

# **Nah-Infrarot Cr(III)- und V(III)-Luminophore: Multiphonon Relaxation und Upconversion- Lumineszenz**

## **Dissertation**

der Mathematisch-Naturwissenschaftlichen Fakultät  
der Eberhard Karls Universität Tübingen  
zur Erlangung des Grades eines  
Doktors der Naturwissenschaften  
(Dr. rer. nat.)

vorgelegt von  
M. Sc. Jens Kalmbach  
aus Hechingen

Tübingen  
2022





Gedruckt mit Genehmigung der Mathematisch-Naturwissenschaftlichen Fakultät der  
Eberhard Karls Universität Tübingen.

Tag der mündlichen Qualifikation:

08.07.2022

Dekan:

Prof. Dr. Thilo Stehle

1. Berichterstatter:

Prof. Dr. Michael Seitz

2. Berichterstatter:

Prof. Dr. Lars Wesemann

3. Berichterstatter:

Prof. Dr. Oliver Wenger

Die vorliegende Arbeit wurde zwischen Mai 2018 und April 2022 in der Arbeitsgruppe von Prof. Dr. Michael Seitz am Institut für Anorganische Chemie der Eberhard Karls Universität Tübingen angefertigt. Großzügige finanzielle Förderung wurde mir durch die Deutsche Forschungsgemeinschaft (DFG) gewährt.

Teile dieser Arbeit wurden in den unten aufgeführten Artikeln veröffentlicht und im Rahmen von Vorträgen oder Posterpräsentationen auf Konferenzen präsentiert.



# Danksagung

Ein besonderer Dank gilt meinem Doktorvater Prof. Dr. Michael Seitz für die Möglichkeit diese Arbeit in seiner Arbeitsgruppe anfertigen zu dürfen, für zahlreiche wertvolle Diskussionen und die vertrauensvolle Zusammenarbeit zu jeder Zeit.

Prof. Dr. Lars Wesemann danke ich für die Übernahme der Zweitbegutachtung.

Bei Prof. Dr. Katja Heinze (Universität Mainz), Prof. Dr. Markus Gerhards und Prof. Dr. Gereon Niedner-Schatteburg (Universität Kaiserslautern), Prof. Dr. Ute Resch-Genger (Bundesanstalt für Materialforschung und -prüfung) und allen beteiligten Mitarbeitern bedanke ich mich für die spannende und sehr produktive Zusammenarbeit.

Dr. Carolin Beil, Dr. Laura Büldt, Tobias Haas, Dr. Elisabeth Kreidt, Dr. Christian Kruck, Dr. Wolfgang Leis, Angelika Oswald und Dr. Markus Trautnitz danke ich für die herzliche, offene Arbeitsatmosphäre und die schöne Zeit in und außerhalb des Labors. Wegen euch war die Ebene 8 für mich mehr als nur ein Arbeitsplatz.

Den aktuellen und ehemaligen Mitgliedern der Arbeitsgruppe von Prof. Dr. Doris Kunz gilt mein Dank für die Unterstützung im Labor, bei Vorträgen und für gemeinsame Mittagessen.

Bei Dr. Hartmut Schubert möchte ich mich für das Messen und Lösen der Kristallstrukturanalysen und die Radsportfachgespräche bedanken.

Wolfgang Bock und Mohammad Ghani danke ich für das Durchführen der Elementaranalysen, Dr. Peter Haiss für die Aufnahme der Massenspektren. Mein Dank gilt allen Mitarbeitern des chemischen Instituts für die entgegengebrachte Unterstützung.

Meinen Mastermodulpraktikanten Aaron, Karsten und Maximilian und danke ich für die geleistete Arbeit.

Fei Yang, Steffen, Semra und Lars danke ich für gemeinsame Praktika und die tolle Zeit während des Studiums.

Bei Markus und Geli möchte ich mich für ihre Freundschaft und viele schöne gemeinsame Aktivitäten und Abende bedanken.

Bei Wolfi möchte ich mich herzlich für sein immer offenes Ohr, seine Unterstützung bei allen chemischen und nicht chemischen Fragen und die Gespräche zu allen erdenklichen Themen bedanken.

Tobi danke ich für die tiefe Freundschaft, das Teilen der Leidenschaft für den Ausdauersport und guten Kaffee und seine Unterstützung in allen Lebenslagen.

Meiner Familie danke ich von ganzem Herzen für ihre Unterstützung und Liebe bei allen Höhen und Tiefen.

Von tiefstem Herzen danke ich Ellen für ihre Liebe und ihren Rückhalt an jedem Tag.

Für das Korrekturlesen dieser Arbeit danke ich herzlich Angelika und Wolfi.

Zuletzt danke ich der Deutschen Forschungsgemeinschaft (DFG) für die finanzielle Unterstützung im Rahmen des Schwerpunktprojekts 2102: „Licht-kontrollierte Reaktivität von Metallkomplexen“.

*Meinen lieben Eltern*



# Inhaltsverzeichnis

Abkürzungsverzeichnis	iv
Kurzzusammenfassung	vi
Abstract	vii
Publikationsliste	viii
Eigenanteil an den Publikationen	x
<b>1 Einleitung</b>	<b>1</b>
<b>2 Zielsetzung</b>	<b>5</b>
<b>3 Lumineszente V(III)-Komplexe</b>	<b>10</b>
3.1 Einführung .....	10
3.2 Ergebnisse und Diskussion.....	18
3.2.1 Ein V(III)-Komplex mit blauer und NIR-II Spin-Flip-Lumineszenz (Publikation 2).....	18
3.2.2 Ein heteroleptischer V(III)-Komplex mit NIR Spin-Flip- Lumineszenz (Publikation 5).....	26
<b>4 Multiphonon Relaxation bei NIR lumineszierenden Cr(III)- und V(III)- Komplexen</b>	<b>31</b>
4.1 Einführung .....	31
4.1.1. Reduzierung von Multiphonon Relaxation .....	38
4.1.1. Quantifizierung von Multiphonon Relaxation .....	43
4.2 Ergebnisse und Diskussion.....	47
4.2.1 Multiphonon Relaxation bei lumineszierenden Cr(III)-Komplexen .	47
4.2.1.1 Schwingungsrelaxation von spezifischen aromatischen C-H-Obertönen bei NIR-emissiven molekularen Rubinen (unveröffentlichte Ergebnisse) .....	47
4.2.1.2 Quantitative Analyse der Schwingungsrelaxation durch C-H- und C-D-Obertöne von Acetonitril bei einem Cr(III)- Komplex mit extrem langlebiger Emission (Publikation 1) ..	63
4.2.1.3 Multiphonon Relaxation im molekularen Rubin [Cr(bpmp) <sub>2</sub> ] <sup>3+</sup> mit intensiver roter Lumineszenz (Publikation 6).....	70



4.2.2	Multiphonon Relaxation bei V(III)-Komplexen mit NIR-II Spin-Flip-Emission .....	76
4.2.2.1	Einfluss der Schwingungsrelaxation auf die NIR-II Lumineszenz von $[V(\text{ddpd})_2](\text{PF}_6)_3$ (Publikation 2) .....	77
4.2.2.2	Einfluss der Schwingungsrelaxation auf die NIR-II Lumineszenz von $[V\text{Cl}_3(\text{ddpd})]$ (Publikation 3) .....	80
<b>5</b>	<b>Photolumineszenz und Upconversion von molekularen Chrom-Lanthanoid-Salzen</b>	<b>83</b>
5.1	Einführung .....	83
5.1.1	Lanthanoiden-Lumineszenz.....	83
5.1.2	Optische Sensibilisierung und Upconversion-Lumineszenz in molekularen Chrom-Lanthanoid-Verbindungen .....	87
5.2	Ergebnisse und Diskussion.....	96
5.2.1	Nah-IR nach Nah-IR-Upconversion in molekularen Chrom-Ytterbium-Salzen (Publikation 3) .....	96
5.2.2	Energietransfer-Prozesse in molekularen Chrom-Lanthanoid-Salzen (unveröffentlichte Ergebnisse) .....	103
5.2.2.1	Chromsensibilisierte $\text{Nd}^{3+}$ -Emission in einem molekularen Chrom-Neodym-Salz .....	105
5.2.2.2	Optische Eigenschaften von molekularen Chrom-Terbium- und Chrom-Europium-Salzen .....	109
<b>6</b>	<b>Ein neues hexadentates Ligandensystem für Spin-Flip-Luminophore (unveröffentlichte Ergebnisse)</b>	<b>115</b>
<b>7</b>	<b>Zusammenfassung</b>	<b>120</b>
<b>8</b>	<b>Experimentalteil / Experimental section</b>	<b>127</b>
8.1	General.....	127
8.2	Synthesis of selectively deuterated compounds .....	130
8.3	Synthesis of chromium-lanthanoid salts .....	143
8.4	Synthesis of L1 .....	144
<b>9</b>	<b>Literaturverzeichnis</b>	<b>148</b>
<b>10</b>	<b>Anhang / Appendix</b>	<b>157</b>
10.1	NMR spectra.....	157
10.2	ESI mass spectra.....	158
10.3	Luminescence measurements .....	160
10.4	Near-IR Absorption data .....	166
10.5	X-ray Single Crystal Structure Analysis .....	173



# Abkürzungsverzeichnis

CASSCF	complete active space self-consistent field
CPL	zirkular polarisierte Lumineszenz
CT	charge transfer
DFG	Deutsche Forschungsgemeinschaft
TD-DFT	time-dependent density-functional theory
DMF	Dimethylformamid
DMSO	Dimethylsulfoxid
eq.	Äquivalente
ESI	Elektrospray-Ionisation
HATU	2-(1H-7-azabenzotriazol-1-yl)-1,1,3,3-tetramethyluronium hexafluorphosphat
HI	Hintergrundinformationen ( <i>engl.</i> supporting information)
HSQC	heteronuclear single quantum coherence
IC	internal conversion
ILCT	interligand charge transfer
ISC	intersystem crossing
LMCT	ligand to metal charge transfer
<i>m</i> -CPBA	<i>meta</i> -Chlorperbenzoesäure
MC	metallzentriert ( <i>engl.</i> metal centered)
MLCT	metal to ligand charge transfer
MS	Massenspektrometrie
NIR	Nah-Infrarot
NMR	Kernresonanzspektroskopie ( <i>engl.</i> nuclear magnetic resonance)
OLED	organische Leuchtdiode ( <i>engl.</i> organic light-emitting diode)

ORTEP	Oak Ridge Thermal Ellipsoid Plot
Pub.	Publikation
ppm	parts per million
R <sub>f</sub>	Retentionsfaktor
SPP	Schwerpunktprogramm
TMS	Trimethylsilan
UV	Ultraviolett
Vis	sichtbares Licht ( <i>engl.</i> visible)

# Kurzzusammenfassung

Diese Arbeit befasst sich mit der Konzeption, Darstellung und photophysikalischen Charakterisierung von neuen lumineszenten Materialien auf Basis der 3d-Übergangsmetalle Vanadium und Chrom.

Dabei konnte das Konzept von bekannten Chrom(III)-Komplexen mit Spin-Flip-Emission auf Metallkomplexe des günstigen und reichlich verfügbaren Metalls Vanadium erweitert werden. Der neu entwickelte **[V(ddpd)<sub>2</sub>](PF<sub>6</sub>)<sub>3</sub>**-Komplex (**ddpd** = *N,N*-dimethyl-*N,N*-dipyridin-2-ylpyridin-2,6-diamin) ist dabei der erste 3d<sup>n</sup>-Metallkomplex ( $n \neq 10$ ) überhaupt, welcher NIR-Lumineszenz oberhalb von 1000 nm bei Raumtemperatur und in Lösung zeigt.

Weiter wurden ausführliche Studien zu Multiphonon Relaxation (**MR**) bei Chrom(III)- und Vanadium(III)-Spin-Flip-Emittern durchgeführt. MR bezeichnet die strahlungslose Deaktivierung der angeregten, emittierenden Metallzustände durch Energietransfer auf Schwingungsobertöne von hochenergetischen Oszillatoren wie beispielsweise O-H-, N-H- oder C-H-Streckschwingungen der Liganden oder des Lösungsmittels. An selektiv deuterierten Liganden und der entsprechenden lumineszenten Chrom(III)-Komplexe konnten erstmals die Obertonsignaturen einzelner aromatischer C-H-Oszillatoren aus gemessenen Obertondaten ermittelt und so die Beiträge spezifischer aromatischer C-H-Oszillatoren des Liganden zur MR beurteilt werden. Zusätzlich wurde der Einfluss von Multiphonon Relaxation auf die Photophysik von neuen Chrom(III)- und Vanadium(III)-Emittern untersucht.

Darüber hinaus wurden im Rahmen dieser Arbeit neue photoaktive heterometallische Chrom-Lanthanoid-Architekturen entwickelt, aufgebaut aus einfach zugänglichen Cr<sup>3+</sup>- und Ln<sup>3+</sup>-Komplexionen. Durch Überarbeitung früherer Cr<sup>3+</sup>/Yb<sup>3+</sup>-Systeme konnte ein neuer molekularer Festkörper realisiert werden, welcher NIR→NIR-Upconversion Lumineszenz in der Gegenwart von Sauerstoff und Wasser zeigt. Des Weiteren wurden die Lumineszenzeigenschaften weiterer Chrom-Lanthanoid-Salze charakterisiert und die zugrundeliegenden Energietransferprozesse zwischen den Metallzentren untersucht.

## Abstract

The work at hand reports the design, synthesis and photophysical characterization of novel luminescent materials based on the earth-abundant first-row transition metals vanadium and chromium.

By transferring the concept of known chromium complexes with spin flip luminescence it was possible to develop novel luminescent metal complexes of the earth-abundant metal vanadium. The complex **[V(ddpd)<sub>2</sub>](PF<sub>6</sub>)<sub>3</sub>** (ddpd = *N,N'*-dimethyl-*N,N'*-dipyridine-2-ylpyridine-2,6-diamine) is the first 3d<sup>n</sup> metal complex (n ≠ 10) that displays NIR luminescence >1000 nm at room temperature in solution.

Furthermore extensive studies on multiphonon relaxation (MR) of chromium(III) and vanadium(III) spin flip luminophors were performed. In these systems MR is one of the dominant non-radiative deactivation pathways involving energy transfer from the emissive metal-centered states to vibrational overtones of high-energy oscillators e.g. O-H, N-H or C-H stretching vibrations of the ligand or solvent. Based on selectively deuterated ligands and their corresponding luminescent chromium(III) complexes the overtone signatures of individual aromatic C-H oscillators were obtained by using measured overtone data. With these overtone signatures in hand the contributions of specific aromatic C-H oscillators of the ligand to MR could be evaluated. In addition the influence of multiphonon relaxation on the optical properties of novel chromium(III) and vanadium(III) emitters were investigated.

In the course of this work new photoactive heterometallic chromium-lanthanoid architectures consisting of easily accessible Cr<sup>3+</sup> and Ln<sup>3+</sup> complex ions were developed. By revisiting earlier Cr<sup>3+</sup>/Yb<sup>3+</sup> systems a novel molecular solid was realized which exhibits NIR→NIR Upconversion luminescence in the presence of oxygen and water. Furthermore, the luminescence properties of chromium-lanthanoid salts were characterized and the underlying energy transfer process between the metal centers were studied.

# Publikationsliste

- Publikation 1* S. Treiling, C. Wang, C. Förster, F. Reichenauer, J. Kalmbach, P. Boden, J.P. Harris, L. M. Carrella, E. Rentschler, U. Resch-Genger, C. Reber, M. Seitz, M. Gerhards, K. Heinze  
**Luminescence and Light-Driven Energy and Electron Transfer from an Exceptionally Long-Lived Excited State of a Non-Innocent Chromium(III) Complex**  
*Angew. Chem. Int. Ed.* **2019**, 58, 18075-18085.
- Publikation 2* M. Dorn, J. Kalmbach, P. Boden, A. Pöpcke, S. Gomez, C. Förster, F. Kuczelinis, L. M. Carella, L. Büldt, N. Bings, E. Rentschler, S. Lochbrunner, L. Gonzalez, M. Gerhards, M. Seitz, K. Heinze  
**A vanadium(III) complex with blue and NIR-II spin-flip luminescence in solution**  
*J. Am. Chem. Soc.* **2020**, 142, 7947-7955.
- Publikation 3* J. Kalmbach, C. Wang, Y. You, C. Förster, H. Schubert, K. Heinze, U. Resch-Genger, M. Seitz  
**Near-IR to Near-IR Upconversion Luminescence in Molecular Chromium Ytterbium Salts**  
*Angew. Chem. Int. Ed.* **2020**, 59, 18804-18808.
- Publikation 4* P. Dierks, A. Kruse, O. S. Bokareva, M. J. Al-Marri, J. Kalmbach, M. Baltrun, A. Neuba, R. Schoch, S. Hohloch, K. Heinze, M. Seitz, O. Kühn, S. Lochbrunner, M. Bauer  
**Distinct photodynamics of  $\kappa$ -N and  $\kappa$ -C pseudoisomeric iron(II) complexes**  
*Chem. Commun.* **2021** 57, 6640-6643.

*Publikation 5*

M. Dorn, J. Kalmbach, P. Boden, A. Kruse, C. Dab, C. Reber, G. Niedner-Schatteburg, S. Lochbrunner, M. Gerhards, M. Seitz, K. Heinze

**Ultrafast and long-time excited state kinetics of an NIR-emissive vanadium(III) complex I: Synthesis, spectroscopy and static quantum chemistry**

*Chem. Sci.* **2021**, *12*, 10780-10790.

*Publikation 6*

F. Reichenauer, C. Wang, C. Förster, P. Boden, N. Ugur, R. Baez-Cruz, J. Kalmbach, L. M. Carella, E. Rentschler, C. Ramanan, G. Niedner-Schatteburg, M. Gerhards, M. Seitz, U. Resch-Genger, K. Heinze

**Strongly Red-Emissive Molecular Ruby [Cr(bpmp)<sub>2</sub>]<sup>3+</sup> surpasses [Ru(bpy)<sub>3</sub>]<sup>2+</sup>**

*J. Am. Chem. Soc.* **2021**, *143*, 11843-11855.



## Eigenanteil an den Publikationen

### **Publikation 1: Luminescence and Light-Driven Energy and Electron Transfer from an Exceptionally Long-Lived Excited State of a Non-Innocent Chromium(III) Complex**

S. Treiling, C. Wang, C. Förster, F. Reichenauer, J. Kalmbach, P. Boden, J.P. Harris, L. M. Carrella, E. Rentschler, U. Resch-Genger, C. Reber, M. Seitz, M. Gerhards, K. Heinze, *Angew. Chem. Int. Ed.* **2019**, *58*, 18075-18085.

Die Messung der Nah-IR-Absorptionsbanden von CH<sub>3</sub>CN und CD<sub>3</sub>CN wurde von mir durchgeführt. Die Analyse der Obertöne, die Berechnung der spektralen Überlappungsintegrale (SOIs) und MR-Raten erfolgten durch mich.

### **Publikation 2: A vanadium(III) complex with blue and NIR-II spin-flip luminescence in solution**

M. Dorn, J. Kalmbach, P. Boden, A. Pöpcke, S. Gomez, C. Förster, F. Kuczelinis, L. M. Carella, L. Büldt, N. Bings, E. Rentschler, S. Lochbrunner, L. Gonzalez, M. Gerhards, M. Seitz, K. Heinze, *J. Am. Chem. Soc.* **2020**, *142*, 7947-7955.

Die Planung und Synthese des perdeuterierten **ddpd**-Liganden wurde von mir durchgeführt. Alle Lumineszenzmessungen (Steady State, Lebensdauern, Quantenausbeuten) der isotopologen Komplexe in Lösung bei 298 und 77 K erfolgten durch mich. Die Obertonanalyse wurde von mir durchgeführt.

### **Publikation 3: Near-IR to Near-IR Upconversion Luminescence in Molecular Chromium Ytterbium Salts**

J. Kalmbach, C. Wang, Y. You, C. Förster, H. Schubert, K. Heinze, U. Resch-Genger, M. Seitz, *Angew. Chem. Int. Ed.* **2020**, *59*, 18804-18808.

Die Planung, Synthese und Charakterisierung der ionischen Festkörper erfolgten durch mich. H. Schubert führte die Röntgenstrukturanalyse an von mir erhaltenen Einkristallen durch. Die Steady-State-Emissionsspektren und die Lebensdauerermessungen bei  $\lambda_{em} = 980$  nm wurden von mir vorgenommen. C. Wang bestimmte die Lebensdauern der Chromemissionen ebenso wie die Quantenausbeuten und führte alle Messungen mit Laseranregung (UC-Messungen) durch.

**Publikation 4: Distinct photodynamics of  $\kappa$ -N and  $\kappa$ -C pseudoisomeric iron(II) complexes**

P. Dierks, A. Kruse, O. S. Bokareva, M. J. Al-Marri, J. Kalmbach, M. Baltrun, A. Neuba, R. Schoch, S. Hohloch, K. Heinze, M. Seitz, O. Kühn, S. Lochbrunner, M. Bauer, *Chem. Commun.* **2021** 57, 6640-6643.

Die Nah-IR-Lumineszenzmessungen zum spektroskopischen Nachweis von Singulett-Sauerstoff wurden von mir durchgeführt.

**Publikation 5: Ultrafast and long-time excited state kinetics of an NIR-emissive vanadium(III) complex I: Synthesis, spectroscopy and static quantum chemistry**

M. Dorn, J. Kalmbach, P. Boden, A. Kruse, C. Dab, C. Reber, G. Niedner-Schatteburg, S. Lochbrunner, M. Gerhards, M. Seitz, K. Heinze, *Chem. Sci.* **2021**, 12, 10780-10790.

Der perdeuterierte **ddpd**-Ligand wurde von mir synthetisiert. Alle Lumineszenz- und Lebensdauer-messungen der Komplexe in Festkörper wurden von mir durchgeführt. Die Analyse der Schwingungsobertöne, die Berechnung der spektralen Überlappungsintegrale (SOIs) und MR-Raten erfolgten durch mich.

**Publikation 6: Strongly Red-Emissive Molecular Ruby  $[\text{Cr}(\text{bpmp})_2]^{3+}$  surpasses  $[\text{Ru}(\text{bpy})_3]^{2+}$**

F. Reichenauer, C. Wang, C. Förster, P. Boden, N. Ugur, R. Baez-Cruz, J. Kalmbach, L. M. Carella, E. Rentschler, C. Ramanan, G. Niedner-Schatteburg, M. Gerhards, M. Seitz, U. Resch-Genger, K. Heinze, *J. Am. Chem. Soc.* **2021**, 143, 11843-11855.

Die Messung der Nah-IR-Absorptionsbanden des **bpmp**-Liganden wurde von mir durchgeführt. Die Analyse der Obertöne, die Berechnung der spektralen Überlappungsintegrale (SOIs) und MR-Raten erfolgten durch mich.



# 1 Einleitung

Derzeit stammen näherungsweise 80 % der vom Menschen verbrauchten Energie aus fossilen Brennstoffen.<sup>[1]</sup> Bei der Verbrennung von fossilen Brennstoffen, namentlich Öl, Gas und Kohle, entstehen große Mengen des Treibhausgases Kohlenstoffdioxid und Luftschadstoffe wie Stickoxide ( $\text{NO}_x$ ) oder Schwefeldioxid ( $\text{SO}_2$ ).<sup>[2]</sup> Sonnenlicht stellt eine kostenfreie und in weiten Teilen der Erde gut verfügbare, alternative Energiequelle dar. So kann Solarenergie in Photovoltaik-Systemen<sup>[3,4]</sup> in Elektrizität oder in photochemischen/photokatalytischen Reaktionen in chemische Energie umgewandelt werden.<sup>[5-7]</sup> Neben der Suche nach nachhaltigen Energiequellen spielt die Reduktion des Energieverbrauchs durch Nutzung von energieeffizienten Technologien wie beispielsweise OLEDS (Organic Light Emitting Diodes)<sup>[8-10]</sup> als Lichtquellen oder das Antreiben von chemischen Reaktionen mit Licht anstatt großer Mengen Wärmeenergie, eine zentrale Rolle.<sup>[5-7]</sup>

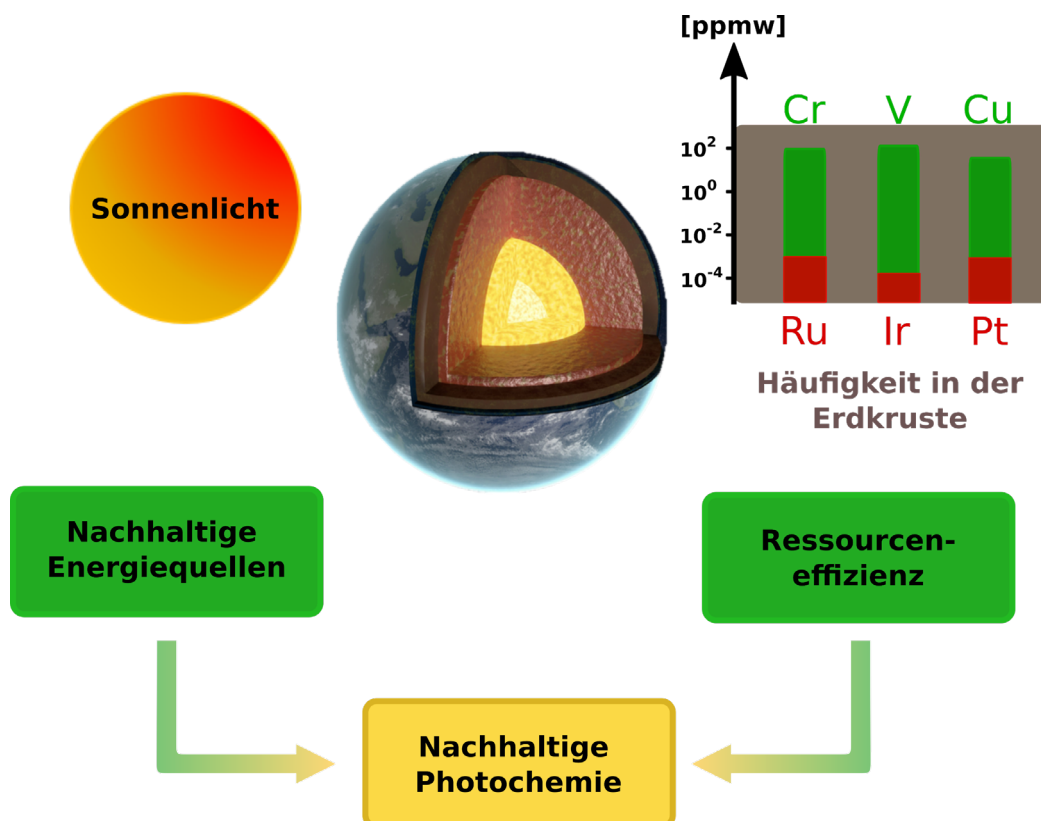


**Abb. 1:** Voraussetzungen für eine nachhaltige Photochemie ist die Kombination aus nachhaltigen Energiequellen und auf der Erde reichlich vorhandenen Metallen (z.B. Cr, V, Cu).<sup>[11]</sup> Abbildung inhaltlich orientiert an Heinze.<sup>[2]</sup>

Bisher kommen in diesen Anwendungen aufgrund ihrer sehr vorteilhaften photophysikalischen Eigenschaften fast ausschließlich Metallkomplexe der schweren Übergangsmetalle (z.B. Ru, Ir, Pt und Au) oder der Lanthanoide zum Einsatz.

Für beide Metallklassen sind die limitierte Verfügbarkeit und der damit verbundene hohe Preis ein zentrales Problem, was ihre Verwendung in großem Maßstab wenig wünschenswert macht. Die Umstellung auf nachhaltige Energiequellen kann daher durch Nutzung der auf der Erde selten vorkommenden Metalle<sup>[12]</sup> (Tab.1) nur unzureichend vollzogen werden vor allem, wenn man berücksichtigt, dass die Gewinnung dieser Metalle sowohl energetisch als auch geopolitisch häufig problematisch ist.<sup>[2]</sup> Es besteht daher ein großer Bedarf die bisher verwendeten Metalle durch günstigere und auf der Erde reichlich vorkommende 3d- und (geeigneten) 4d-Übergangsmetalle zu ersetzen.<sup>[13]</sup> Neue Technologien und Anwendungen welche nachhaltige Energiequellen (Sonnenlicht) und ressourceneffiziente 3d-Metalle wie z.B. Chrom, Eisen oder Kupfer kombinieren, können entscheidend auf dem Weg zu einer nachhaltigen Photochemie sein.

**Tab. 1: Häufigkeit der Elemente in der Erdkruste<sup>a[12,14]</sup>**

Element	Häufigkeit	Element	Häufigkeit	Element	Häufigkeit
V	0.01	Cu	0.005	Re	10 <sup>-7</sup>
Cr	0.01	Zn	0.007	Os	5 × 10 <sup>-7</sup>
Mn	0.091	Zr	0.016	Ir	10 <sup>-7</sup>
Fe	4.7	Mo	1.4 × 10 <sup>-4</sup>	Pt	10 <sup>-6</sup>
Co	2.4 × 10 <sup>-3</sup>	Ru	10 <sup>-6</sup>	Au	4 × 10 <sup>-7</sup>
Ni	7.2 × 10 <sup>-3</sup>	W	1.5 × 10 <sup>-4</sup>	Ce	0.006

<sup>a</sup>in Massenprozent

Die Entwicklung von lumineszierenden 3d-Übergangsmetallkomplexen ist sehr herausfordernd, da wichtige Voraussetzungen erfüllt sein müssen. Im Allgemeinen führt die überwiegende Zahl aller molekularer Verbindungen Anregungsenergie (z.B. Licht) sehr schnell strahlungslos wieder ab. Nur sehr wenige Moleküle haben angeregte elektronische Zustände mit ausreichend langen Lebenszeiten (typischerweise ein paar hundert Pikosekunden) um Lumineszenz oder

photochemische Reaktionen zu ermöglichen.<sup>[14]</sup> In den meisten 3d-Übergangsmetallkomplexen führen effektive strahlungslose Deaktivierungsprozesse allerdings zu sehr kurzen Lebenszeiten der relevanten angeregten Zustände. Eine weitere wichtige Bedingung hinsichtlich zukünftiger Anwendungen ist sowohl Thermo- als auch Photostabilität, welche durch die in 3d-Metallkomplexen häufig labil gebundenen Liganden nicht immer gegeben ist.<sup>[2,15]</sup>

Ein besonders interessantes Forschungsfeld im Gebiet der lumineszenten Materialien sind Luminophore welche im nah-Infrarot (NIR) Spektralbereich emittieren. Das NIR-Spektrum umfasst den Wellenlängenbereich von 780 – 3000 nm und ist zusätzlich in die Bereiche NIR-I (780 - 1000 nm) und NIR-II (1000 – 3000 nm) unterteilt.

NIR-Lumineszenz ermöglicht vielfältige und spannende Anwendungen wie beispielsweise in der optischen Telekommunikation,<sup>[16,17]</sup> Solarzellentechnik,<sup>[3,18]</sup> OLED-Technologie,<sup>[19,20]</sup> in Photon-Upconversion-Materialien<sup>[21–24]</sup> sowie in der bildgebenden medizinischen Diagnostik (Bioimaging).<sup>[20,25]</sup> Insbesondere für die *in vivo* Diagnostik bietet NIR-II-Lumineszenz einige Vorteile. Im Vergleich zu Licht im sichtbaren Wellenlängenbereich sind sowohl die Autofluoreszenz als auch Streueffekte weniger stark ausgeprägt, wodurch sich das Signal-Rausch-Verhältnis wesentlich verbessert. Zudem kann NIR-II-Strahlung tiefer in das Gewebe eindringen und verursacht dabei zusätzlich weniger Schaden.<sup>[25–27]</sup>

Analog zu den metallbasierten Luminophoren mit kurzwelligerer Emission basieren nahezu alle bisher etablierten im NIR lumineszenten Metallkomplexe auf Metallzentren der schweren Übergangsmetallionen (z.B. Ru<sup>2+</sup>, Ir<sup>3+</sup> und Pt<sup>2+</sup>)<sup>[9,20,28,29]</sup> oder den dreifach positiv geladenen Lanthanoidionen (z.B. Yb<sup>3+</sup>, Nd<sup>3+</sup>).<sup>[27,30,31]</sup> Im Hinblick auf eine nachhaltigere Photochemie und dem hohen ökonomischen Wert besteht folglich auch ein großes Interesse an im NIR lumineszierenden 3d- und 4d-Übergangsmetallkomplexen.

Effiziente und langlebige NIR-Lumineszenz ist generell allerdings nur sehr schwer zu erreichen. Ein grundlegendes Problem von energiearmer Emission gründet sich auf dem Energielückengesetz (ELG)<sup>[32]</sup>. Daraus folgt, je kleiner die Energiedifferenz zwischen dem emittierenden Zustand und dem nächst tieferliegenden Niveau desto effektiver sind strahlungslose Deaktivierungsprozesse und je geringer die Lumineszenzquantenausbeute. Einer der wesentlichen strahlungslosen Deaktivierungswege vieler Metallkomplexe mit (metallzentrierter) NIR-Emission ist *Multiphonon Relaxation*. Dieser Prozess bezeichnet die strahlungslose Deaktivierung

der emittierenden, angeregten Metallzustände durch Energietransfer auf Schwingungsobertöne von hochenergetischen Oszillatoren wie beispielsweise O-H-, N-H- oder C-H-Streckschwingungen der Liganden oder des Lösungsmittels.<sup>[33,34]</sup> Die Folge sind stark reduzierte Lumineszenzlebenszeiten und geringe Quantenausbeuten. Nachdem die Entwicklung von Luminophoren der 3d- und 4d-Übergangsmetalle generell bereits sehr herausfordernd ist, stellt die zusätzliche Anforderung der NIR-Emission aufgrund der noch größeren Zahl von effektiven strahlungslosen Deaktivierungsprozessen eine noch schwierigere Aufgabe dar.

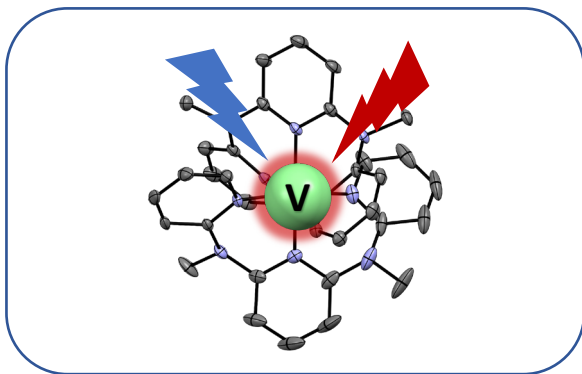
Ein entscheidender Durchbruch gelang mit der Entdeckung von d<sup>3</sup>-Chrom(III)-Metallkomplexen welche intensive, langlebige NIR-Emission zeigen. Angelehnt an den bekannten Rubin-Laser (Cr<sup>3+</sup>:Al<sub>2</sub>O<sub>3</sub>, λ<sub>max</sub> = 694 nm) werden diese neuen Emitter „molekulare Rubine“ genannt. Das allgemeine Strukturmotiv dieser Komplexe ist ein Cr(III)-Metallzentrum, das nahezu perfekt oktaedrisch von zwei tridentaten, häufig pyridinbasierten Starkfeldliganden koordiniert ist.<sup>[35–37]</sup> Im Unterschied zu den meisten bekannten 3d-Luminophoren bei welchen die Emission auf Charge-Transfer-Prozessen zwischen Metall- und Ligand-Orbitalen beruht, resultiert die NIR-Emission der molekularen Rubine aus elektronischen Übergängen zwischen metallzentrierten Spin-Flip-Zuständen (Kapitel 3.1.1).<sup>[2,38]</sup> Aufgrund ihrer scharfen Emission im NIR (λ<sub>max</sub> = 724 nm - 780 nm), den langen Lumineszenzlebenszeiten (τ = 670 – 4500 μs) und hohen Quantenausbeuten (Φ = 5.2 % - 30 %, CH<sub>3</sub>CN) konnten bereits erste Anwendungen dieser Komplexe in Sensortechnik,<sup>[39–41]</sup> Photokatalyse,<sup>[42]</sup> der Photodynamischen Therapie<sup>[43]</sup> oder zirkular polarisierter Emission (CPL)<sup>[44,45]</sup> realisiert werden.

Nach dem Erfolg der chrombasierten Spin-Flip-Emitter rückten vor kurzer Zeit Vanadium-Komplexe als potentielle neue NIR-Luminophore in den Fokus. Das Interesse ist zum einen motiviert durch die hohe natürliche Häufigkeit von Vanadium als 3d-Metall und zum anderen, weil oktaedrische V(III)-Komplexe mit d<sup>2</sup>-Elektronenkonfiguration ebenfalls energetisch tiefliegende Spin-Flip-Zustände aufweisen. Alle bisher bekannten V(III)-Verbindungen zeigen allerdings nur sehr schwache Phosphoreszenz im Festkörper und bei sehr niedrigen Temperaturen, falls überhaupt Lumineszenz beobachtet werden kann.<sup>[46–48]</sup> Nichtsdestotrotz haben V(III)-Komplexe enormes Potential durch Übertragen des erfolgreichen Konzepts der Cr(III)-Luminophore eine neue Klasse an NIR-Emittern mit noch langwelligerer Emission (NIR-II) zu werden.

## 2 Zielsetzung

Lumineszente Metallkomplexe der leichten Übergangsmetalle sind ein derzeit stark wachsendes Forschungsfeld. Dies liegt hauptsächlich an ihrem großen Potential als umweltfreundliche und kostengünstige Alternativen zu Luminophoren der teureren und selteneren Metalle (z.B. Ru, Ir, Pt) in Schlüsseltechnologien wie organischen Leuchtdioden, im Bioimaging oder in Photon-Upconversion-Materialien. Allerdings ist die Zahl der bekannten molekularen 3d-Luminophore, insbesondere mit energiearmer NIR-Emission, bisher sehr gering. Ziel dieser Arbeit ist das Design, die Darstellung und photophysikalische Charakterisierung von neuen lumineszenten Materialien auf Basis der günstigeren und besser verfügbaren Metalle Vanadium und Chrom. Dabei ist diese Arbeit Teil eines Konsortiums bestehend aus den Arbeitskreisen von Michael Seitz (Universität Tübingen), Katja Heinze (Universität Mainz) und Markus Gerhards/Gereon Niedner-Schatteburg (Universität Kaiserslautern) innerhalb des DFG Schwerpunktprojekts „SPP 2102: Licht-kontrollierte Reaktivität von Metallkomplexen“.

Die Zielsetzung dieser Arbeit kann in drei übergeordnete Kategorien eingeteilt werden:



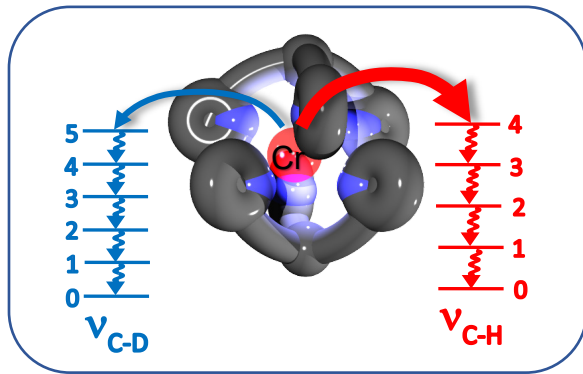
**Lumineszente V(III)-Komplexe**

Oktaedrische Vanadium(III)-Komplexe mit  $d^2$ -Elektronenkonfiguration sind vielversprechende Systeme für die Entwicklung neuer Spin-Flip-Luminophore. Trotzdem sind phosphoreszierende molekulare V(III)-Verbindungen nach wie vor unbekannt. Eines der Hauptziele dieser Arbeit ist die Erweiterung der molekularen 3d-Luminophore um Metallkomplexe des frühen Übergangsmetalls Vanadium. Um dieses Ziel zu erreichen, soll das erfolgreiche Konzept der  $d^3$ -Cr(III)-Spin-Flip-Emitter auf



$d^2$ -V(III)-Komplexe übertragen werden. Für einen erfolgreichen Transfer sind folgende Schritte vorgesehen:

- Voraussetzung für effiziente und langlebige Phosphoreszenz ist eine **große Ligandenfeldaufspaltung**, um die Ligandenfeldzustände zu höherer Energie zu verschieben und so thermischen Rücktransfer in die Ligandenfeldzustände zu verhindern (Kapitel 3.1). Um eine ausreichend große Ligandenfeldaufspaltung zu gewährleisten, sollen möglichst ideal oktaedrische V(III)-Komplexe mit dem tridentaten Starkfeldliganden **ddpd** (ddpd = *N,N'*-dimethyl-*N,N'*-dipyridin-2-ylpyridin-2,6-diamin) dargestellt werden.
- Um den Einfluss einer erhöhten Spin-Bahn-Kopplung durch Halogenid-Liganden in der Nähe des photoaktiven Metallzentrums auf die Photophysik zu untersuchen, soll neben dem homoleptischen **[V(ddpd)<sub>2</sub>]<sup>3+</sup>**-Komplexes auch der heteroleptische **[VCl<sub>3</sub>(ddpd)<sub>2</sub>]**-Komplex synthetisiert werden.
- Mit Absorptions- und (zeitaufgelöster) Lumineszenzspektroskopie sollen die optischen Eigenschaften der neu synthetisierten Komplexe untersucht werden. Dabei sollen auch wichtige photophysikalische Parameter wie die Lebenszeiten der emittierenden Zustände und die Quantenausbeuten unter verschiedenen Bedingungen (Temperatur, Aggregatzustand, Lösungsmittel, Deuterierung) bestimmt werden.
- Zur Unterstützung der spektroskopischen Ergebnisse und Zuordnung der relevanten elektronischen Zustände sollen in Kooperation mit anderen Arbeitskreisen Quantenchemische-Rechnungen (DFT, CASSCF) durchgeführt werden.



## Multiphonon Relaxation

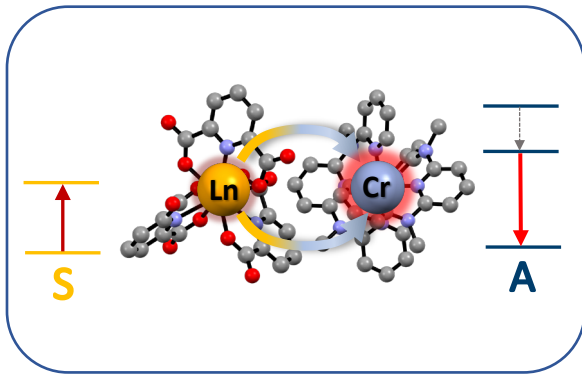
Einer der wichtigsten strahlungslosen Deaktivierungswege von Spin-Flip-Emittern, insbesondere mit energiearmer Emission, ist die Deaktivierung der emittierenden Metallzustände durch Energietransfer auf Schwingungsobertöne von hochenergetischen Oszillatoren wie beispielsweise O-H-, N-H- oder C-H-Streckschwingungen der Liganden oder des Lösungsmittels. Dieser Prozess wird **Multiphonon Relaxation (MR)** genannt. Durch Entfernen hochfrequenter, stark anharmonischer Oszillatoren in räumlicher Nähe des Metalls, z.B. durch Perdeuterierung des Liganden und Verwendung von deuterierten Lösungsmittel können sowohl die Quantenausbeuten als auch die Lebenszeiten der angeregten Zustände wesentlich gesteigert werden. Häufig ist allerdings eine vollständige Deuterierung des Liganden synthetisch nicht praktikabel und eventuell auch nicht besonders effektiv. Um herauszufinden, welche Oszillatoren ausgetauscht werden müssen, muss zunächst bekannt sein, welche C-H-Oszillatoren die Lumineszenz am stärksten löschen. In dieser Arbeit sollen anhand des  $[\text{Cr}(\text{ddpd})_2]^{3+}$ -Komplexes, dem Prototypen der Cr(III)-basierten NIR-Spin-Flip-Luminophore, wichtige Parameter wie z.B. die Energie und die Anharmonizität der deaktivierenden C-H-Oszillatoren an spezifischen aromatischen Positionen bestimmt werden. Dieser Ansatz ermöglicht die Realisierung hoch lumineszenter Spin-Flip-Emitter, welche nur an den entscheidenden Positionen deuteriert sind, um MR effektiv zu unterdrücken. Die wichtigen Zwischenziele dabei sind:

- Entwicklung von Strategien zur Synthese von selektiv deuterierten **ddpd**-Liganden und der entsprechenden isotopologen und isotopomeren  $[\text{Cr}(\text{ddpd})_2]^{3+}$ -Komplexe

- Charakterisierung der photophysikalischen Eigenschaften der isotopologen bzw. der isotopomeren **[Cr(ddpd)<sub>2</sub>]<sup>3+</sup>**-Komplexe
- Experimentelle Bestimmung der Absorptionsbanden der relevanten C-H-Obertöne und Entwicklung einer Methode zur Extraktion der Obertonsignatur von C-H-Oszillatoren an spezifischen aromatischen Positionen
- Quantifizierung des Beitrags einzelner aromatischer C-H-Oszillatoren zur Löschung der Cr(III)-Lumineszenz durch Berechnen der **spektralen Überlappintegrale (SOIs)** auf Basis empirischer Näherungen

Zusätzlich soll der Einfluss von Multiphonon Relaxation auf die Photophysik neuer Chrom(III)- und Vanadium(III)-Luminophore untersucht werden. Dafür sind folgende Schritte vorgesehen:

- Entwicklung von Strategien zur Darstellung (per)-deuterierter Liganden
- Photophysikalische Charakterisierung der isotopologen Metallkomplexe
- Experimentelle Bestimmung der Absorptionsbanden der C-H- und C-D-Obertöne der isotopologen Liganden und des häufig verwendeten Lösungsmittels Acetonitril
- Quantifizierung der Effizienz der Lumineszenz-Löschung durch C-H- und C-D-Obertöne mittels Berechnung der **spektralen Überlappintegrale (SOIs)** auf Basis empirischer Näherungen



## Photolumineszenz und Upconversion in molekularen Chrom-Lanthanoid-Salzen

Die Kombination von Chrom(III)- und Lanthanoid(III)-Ionen in heterometallischen Architekturen ermöglicht das Auftreten von spannenden optischen Phänomenen wie beispielsweise **Photon Upconversion (UC)**. Photon-Upconversion-Prozesse, welche immer mehr Bedeutung in bioanalytischen Anwendungen oder Photovoltaikzellen gewinnen, sind oft auf anorganische Festkörpermateriale oder Nanopartikel beschränkt. Ein weiteres Hauptziel dieser Arbeit ist die Entwicklung von neuen photonischen Materialien aufgebaut aus molekularen  $\text{Cr}^{3+}$ - und  $\text{Ln}^{3+}$ -Komplexionen zur Untersuchung von Energietransferprozessen zwischen den photoaktiven Metallzentren. Hierfür sollen folgende Zwischenziele erreicht werden:

- Konzeption und Darstellung von neuen molekularen  $\text{Ln}^{3+}$ - $\text{Cr}^{3+}$ -Architekturen nach Auswertung der Herausforderungen von bisher bekannten Literaturbeispielen
- Strukturelle Charakterisierung der synthetisierten Materialien
- Ausführliche Untersuchung der Lumineszenzeigenschaften und der zugrundeliegenden Energietransferprozesse nach Laseranregung

## 3 Lumineszente V(III)-Komplexe

### 3.1 Einführung

Lumineszierende Metallkomplexe der ersten Übergangsmetallreihe sind erst seit wenigen Jahren bekannt. Dies liegt im Wesentlichen daran, dass als Folge der inhärent kleineren Ligandenfeldaufspaltung von 3d-Metallen, energetisch tiefliegende metallzentrierte (MC) Zustände zu einer extrem schnellen strahlungslosen Relaxation in den Grundzustand führen und damit das Auftreten von Emission effektiv verhindern.<sup>[14,15,49]</sup> Allerdings konnten in letzter Zeit einige Fortschritte auf dem Gebiet der 3d-Metallluminophore gemacht werden. Die Lumineszenz der überwiegenden Zahl der bekannten 3d-Übergangsmetallluminophore beruht auf relativ langlebigen Charge-Transfer (CT) Zuständen, bei welchen die störenden metallzentrierten Zustände entweder abwesend ( $3d^{10}$ ) oder hoch in der Energie sind. Diese Charge-Transfer-Zustände beruhen in der Regel entweder auf elektronischen Übergängen zwischen besetzten d-Orbitalen und unbesetzten Ligandorbitalen (Metal-to-Ligand Charge-Transfer, MLCT-Zustände) oder auf Übergängen zwischen besetzten Ligandorbitalen und unbesetzten Metallorbitalen (Ligand-to-Metal Charge-Transfer, LMCT-Zustände). Am weitesten verbreitet sind 3d-Luminophore mit MLCT-Emission, welche für  $d^6\text{-Cr(0)}$ ,<sup>[50]</sup>  $d^6\text{-Mn(I)}$ -<sup>[51]</sup> oder  $d^{10}\text{-Ni(0)}$ - /  $d^8\text{-Ni(II)}$ -Komplexe<sup>[52,53]</sup> beobachtet werden konnte. Zu den bekannten LMCT-Emittern gehören low spin  $d^5\text{-Fe(III)}$ -Komplexe<sup>[54,55]</sup> von Wärnmark oder auch  $d^6\text{-Cobalt(III)}$ -Komplexe.<sup>[56]</sup> Die höchsten Quantenausbeuten von bis zu  $\Phi = 99\%$  können mit  $d^{10}\text{-Cu(I)}$ -Komplexen mit zyklischen Carben- und Amidoliganden erreicht werden.<sup>[57]</sup>

Alle genannten CT-Emitter auf Basis der gut verfügbaren Übergangsmetalle zeigen Emission im sichtbaren Spektralbereich, wohingegen NIR-Lumineszenz von CT-Zuständen nach wie vor unbekannt ist. Dies hängt damit zusammen, dass die interkonfigurativen CT-Übergänge mit einem Ladungstransfer und damit mit einer Änderung der Orbitalbesetzung einhergehen. Infolgedessen sind die Gleichgewichtsgeometrien der beim Übergang beteiligten Niveaus sehr unterschiedlich was eine starke Verzerrung des angeregten Zustands gegenüber dem Grundzustand bewirkt. Man spricht auch vom *strong coupling* Limit.<sup>[2]</sup> Da die Wahrscheinlichkeit für strahlungslose Deaktivierungsprozesse aus stark verzerrten Anregungszuständen für energiearme Emission z.B. im NIR sehr hoch ist

(Energilückengesetz),<sup>[32]</sup> sind CT-Zustände für das Beobachten von NIR-Emission eher ungeeignet.

Neben den beschriebenen CT-Emittern gibt es noch eine weitere interessante Klasse an lumineszenten Übergangsmetallkomplexen, den sogenannten Spin-Flip-Luminophoren.

### 3.1.1 Übergangsmetallkomplexe mit Spin-Flip-Emission

Nicht nur CT-Zustände (MLCT und LMCT), sondern auch metallzentrierte Zustände von 3d-Übergangsmetallkomplexen können emissiv sein. Die vielversprechendsten Systeme um intensive d-d-Emission zu beobachten sind Metallionen mit  $d^3$ -Elektronenkonfiguration (z.B. Cr(III), Mo(III), Mn(IV) oder V(II)) in einem starken oktaedrischen Ligandenfeld. Die erfolgreichsten und zudem sehr gut untersuchten Spin-Flip-Luminophore sind dabei oktaedrische Cr(III)-Komplexe.

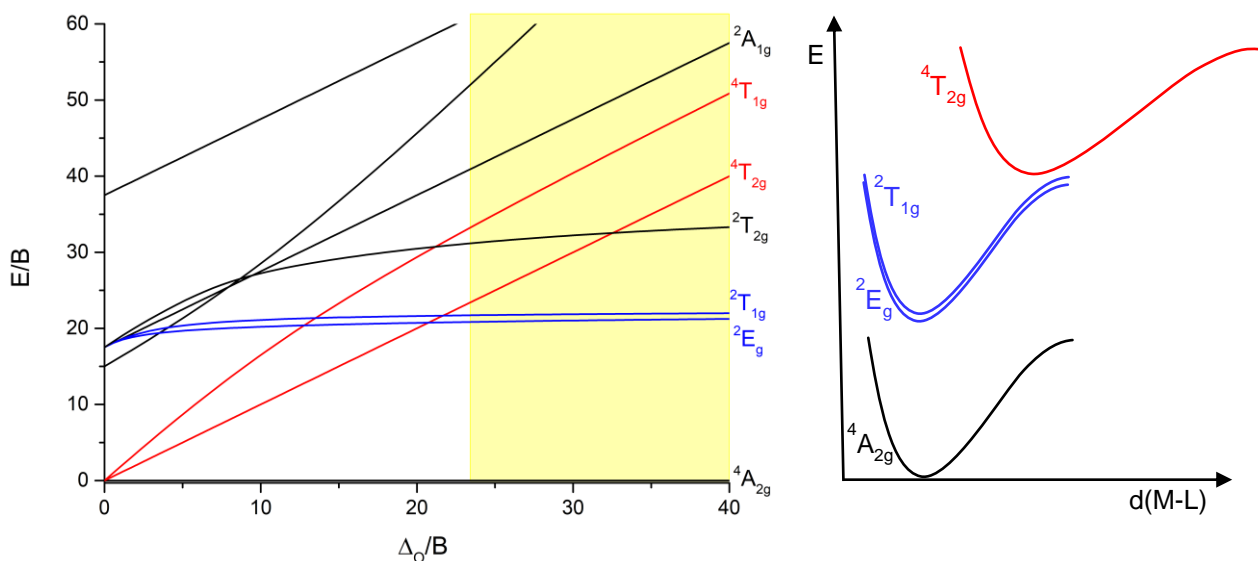


**Abb. 2:** Links: Tanabe-Sugano-Diagramm der  $d^3$ -Elektronenkonfiguration im oktaedrischen Feld ( $C = 4.5 B$ ). Rechts: Potentialkurven der relevanten elektronischen Zustände, der Grundzustand (schwarz), die Spin-Flip-Zustände (blau) und der Ligandenfeldzustand (rot).

Die relevanten elektronischen Zustände sind im Tanabe-Sugano-Diagramm (Abb. 2, links) für oktaedrische Metallkomplexe mit  $d^3$ -Elektronenkonfiguration dargestellt.<sup>[58,59]</sup> Zunächst erfolgt die spin-erlaubte Anregung aus dem elektronischen Grundzustand ( $^4A_{2g}$ ) in einen Ligandenfeldzustand ( $^4T_{2g}$ , Abb. 3). Durch Intersystem Crossing ( $k_{ISC}$ ) können die emittierenden Dublett-Zustände ( $^2E$  und  $^2T_{1g}$ ) populiert werden, welche

schließlich durch einen spin-verbotenen, intrakonfigurativen Übergang in den Grundzustand emittieren können ( $k_p$ , Abb. 3). Sowohl die angeregten Dublett-Zustände als auch der Grundzustand entspringen der  $(t_{2g})^3$ -Elektronenkonfiguration und unterscheiden sich lediglich in der Orientierung des Spins (Spin-Flip). Beim Übergang bleibt daher die Elektronenverteilung am Metall und folglich die Metall-Ligand-Bindungen nahezu unbeeinflusst, die geometrische Reorganisation ist daher sehr gering. Diese Situation wird als *weak coupling* Limit bezeichnet. Die Struktur der Spin-Flip-Zustände ist deshalb nahezu „unverzerrt“ gegenüber der Grundzustandsgeometrie (sogenannte „nested states“) wodurch scharfe und intensive Phosphoreszenz-Emissionen möglich werden.<sup>[38,60]</sup>

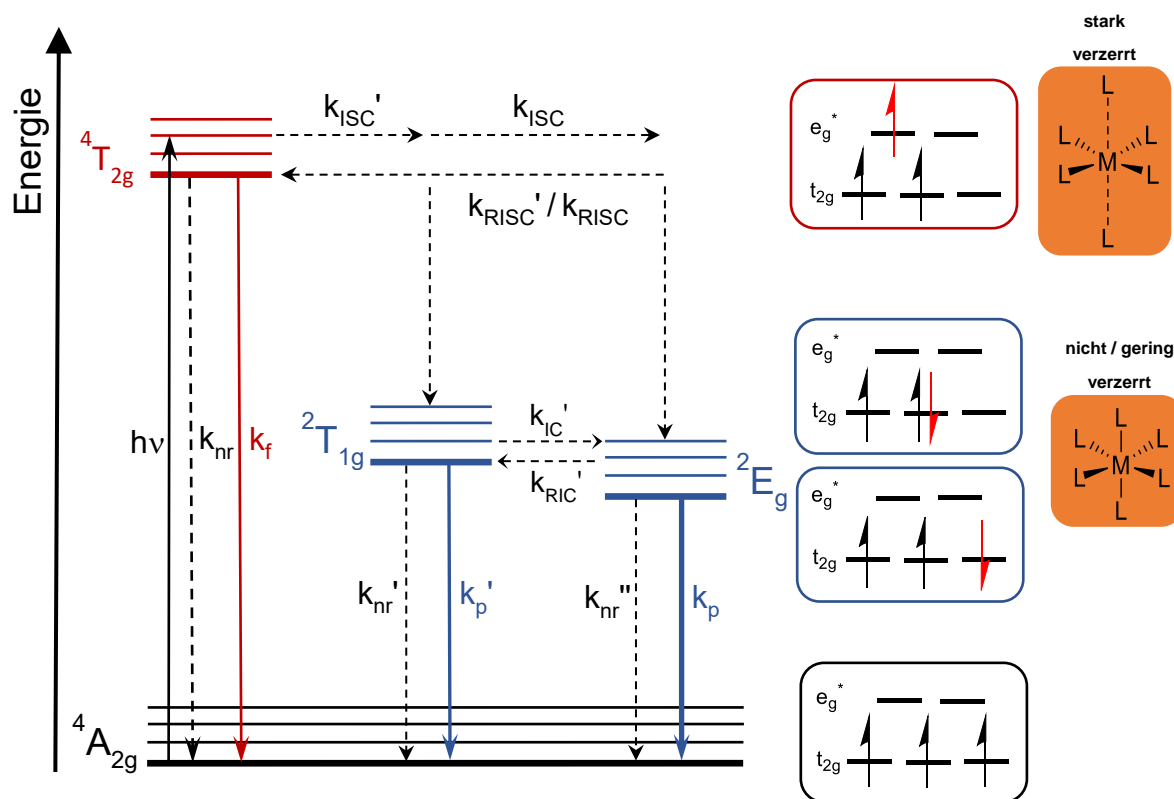


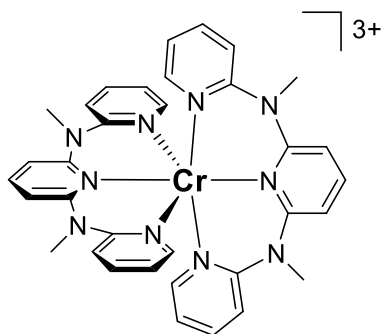
**Abb. 3:** Energiediagramm mit den relevanten photophysikalischen Prozessen, Elektronenkonfigurationen und wichtigsten elektronischen Zuständen für oktaedrische  $d^3$ -Cr(III)-Luminophore ( $k_p$  = Phosphoreszenz,  $k_f$  = Fluoreszenz,  $k_{ISC}$  = Intersystem Crossing,  $k_{RIC}$  = Reverse Intersystem Crossing,  $k_{nr}$  = strahlungslose Deaktivierung,  $k_{IC}$  = internal conversion,  $k_{RIC}$  = reverse internal conversion). Inhaltlich orientiert an Heinze.<sup>[2]</sup>

Im Unterschied zu den Spin-Flip-Zuständen kommt es bei der Besetzung des Ligandenfeldzustands  $^4T_{2g}$  zu einer Änderung der Elektronenkonfiguration von  $(t_{2g})^3$  im Grundzustand zu  $(t_{2g})^2(eg)^1$  im Ligandenfeldzustand und somit auch zu einer

Umverteilung der Elektronendichte um das Chromzentrum (Abb. 3, Elektronenkonfigurationen). Durch die Besetzung der  $e^*_g$ -Orbitale am Chrom, die Metall-Ligand antibindend sind, verändert sich die Struktur des angeregten Zustandes stärker als bei der Besetzung der Spin-Flip-Zustände. Die Population des Ligandenfeldzustands führt also zur Schwächung der Metall-Ligand- $\sigma$ -Bindung und damit auch zur Vergrößerung des Metall-Ligand-Abstandes. Die Struktur dieser angeregten Zustände verändert sich, im Vergleich zur Struktur des Grundzustandes, recht stark ist also „verzerrt“ und stellt das *strong coupling* Limit dar. In analoger Weise ist auch die Besetzung von CT-Zuständen oft mit einer deutlichen Geometrieänderung verbunden. In diesen Fällen ist es sehr wahrscheinlich, dass sich die Potentialhyperflächen von Grund- und angeregtem Zustand schneiden und damit einen sehr effektiven strahlungslosen Deaktivierungsweg via „surface crossing“ darstellen (s. auch Kapitel 4.1).<sup>[34]</sup>

Wie man dem Tanabe-Sugano-Diagramm (Abb. 2, links) entnehmen kann, liegen bei geringer Ligandenfeldstärke (weißer Hintergrund) die Quartett-Zustände (rot) meist unterhalb der Dublett-Zustände (blau) oder ziemlich dicht beieinander. Bei geringen bis mittleren Ligandenfeldstärken ist das Intersystem Crossing in die Spin-Flip-Zustände entweder nicht effektiv möglich oder es kommt zur thermischen Rückbesetzung der Ligandenfeldzustände (Reverse Intersystem Crossing,  $k_{RISC}$ ). Ausgehend von den besetzten Ligandenfeldzuständen tritt nur eine eher breitbandige Fluoreszenz ( $k_f$ ) oder strahlungslose Deaktivierung dieser Zustände wie beispielsweise Fluoreszenzlöschung durch Photo-Redoxreaktionen oder Metall-Ligand-Schwingungen ( $k_{nr}$ ) auf. Zu kleine Ligandenfeldstärken sind daher verbunden mit eher geringen Quantenausbeuten, was an vielen Cr(III)-Komplexen zu beobachten ist. Bei großen Ligandenfeldstärken ( $\Delta_o \gg 20 B$ , Abb. 2 gelb hinterlegt) ist die Energielücke  $\Delta E(^4T_{2g}-^2E)$  immer positiv und groß genug um die thermisch induzierte Rückpopulation zu unterbinden und es kann Phosphoreszenz ( $k_p$ ) aus den Spin-Flip-Zuständen beobachten werden.<sup>[38]</sup>





$\lambda = 775 \text{ nm}$

$\tau = 898 \text{ } \mu\text{s} \text{ (H}_2\text{O, Ar)}$

$\Phi = 11 \text{ \% (H}_2\text{O, Ar)}$

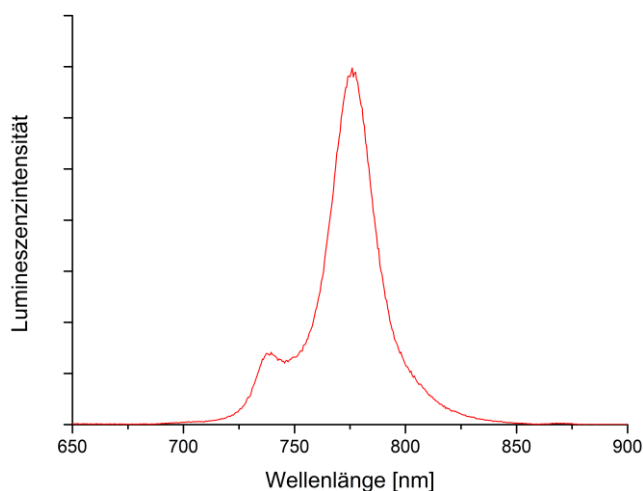


**Abb. 4:** Strukturformel, photophysikalische Daten und Emissionsspektrum von **[Cr(ddpd)<sub>2</sub>]<sup>3+</sup>** ( $\lambda_{\text{exc}} = 435 \text{ nm}$ , H<sub>2</sub>O, entgast).<sup>[35]</sup>

Oktaedrische Cr(III)-Komplexe mit tridentaten, pyridinbasierten Liganden zeigen intensive Spin-Flip-Emission im NIR-Spektralfenster.<sup>[37,61]</sup> Der Prototyp dieser sogenannten „molekularen Rubine“ ist der **[Cr(ddpd)<sub>2</sub>]<sup>3+</sup>**-Komplex (ddpd = *N,N*-dimethyl-*N,N*-dipyridin-2-ylpyridin-2,6-diamin)<sup>[35]</sup> welcher von der Arbeitsgruppe Heinze entwickelt wurde. Der Chelatligand **ddpd** sorgt durch seine großen Bisswinkel und recht starken  $\sigma$ -Donor-Charakter für eine große Ligandenfeldaufspaltung, wodurch die RISC effektiv verhindert wird. Durch die nahezu perfekt oktaedrische Umgebung des Chrom-Ions in Kombination mit dem starken Ligandenfeld emittiert **[Cr(ddpd)<sub>2</sub>]<sup>3+</sup>** im NIR ( $\lambda_{\text{max}} = 775 \text{ nm}$ ) aus dem sehr langlebigen <sup>2</sup>E-Zustand ( $\tau = 898 \text{ } \mu\text{s}$ ) und erreicht Rekordquantenausbeuten von ( $\Phi = 11 \text{ \%}$ ) in entgastem Wasser. Diese ausgezeichneten photophysikalischen Eigenschaften übertreffen bei Weitem die vieler anderer Cr(III)-Luminophore wie beispielsweise **[Cr(en)<sub>3</sub>]<sup>3+</sup>**, **[Cr(bpy)<sub>3</sub>]<sup>3+</sup>** oder **[Cr(tpy)<sub>2</sub>]<sup>3+</sup>** mit Quantenausbeuten von nur  $\Phi = 0.006$ ,  $0.089$  and  $<0.0009 \text{ \%}$  unter vergleichbaren Bedingungen (**en** = ethan-1,2-diamin, **bpy** = 2,2'-bipyridin, **tpy** = 2,6-bis(2-pyridyl)pyridin).<sup>[38]</sup> In den letztgenannten Komplexen ist entweder die Ligandenfeldaufspaltung zu gering oder die Abweichung von der idealen oktaedrischen Umgebung zu groß, wodurch sich ebenfalls die Energien der beteiligten Zustände ändern und effektive strahlungslose Deaktivierung via *surface crossing* auftritt. Im Fall des **[Cr(ddpd)<sub>2</sub>]<sup>3+</sup>**-Komplexes dagegen ist in Abwesenheit von Sauerstoff der einzig verbleibende relevante strahlungslose Deaktivierungsweg der Energietransfer auf Obertöne hochenergetischer Oszillatoren (Abb.3,  $k_{\text{nr}}$ ) wie

beispielsweise O-H-, N-H- oder C-H-Streckschwingungen der Liganden oder des Lösungsmittels (Kapitel 4).

Beim Ziel, das erfolgreiche Konzept der Cr(III)-Spin-Flip-Emitter auf weitere 3d-Metallionen zu übertragen, ist ein vielversprechender Ansatz Metallionen mit  $d^2$ -Elektronenkonfiguration einzusetzen. Beim Blick auf das Tanabe-Sugano-Diagramm für oktaedrische Komplexe mit Metallionen der  $d^2$ -Elektronenkonfiguration (z.B. V(III)) erkennt man einige Parallelen zum entsprechenden Diagramm für  $d^3$ -Systeme.

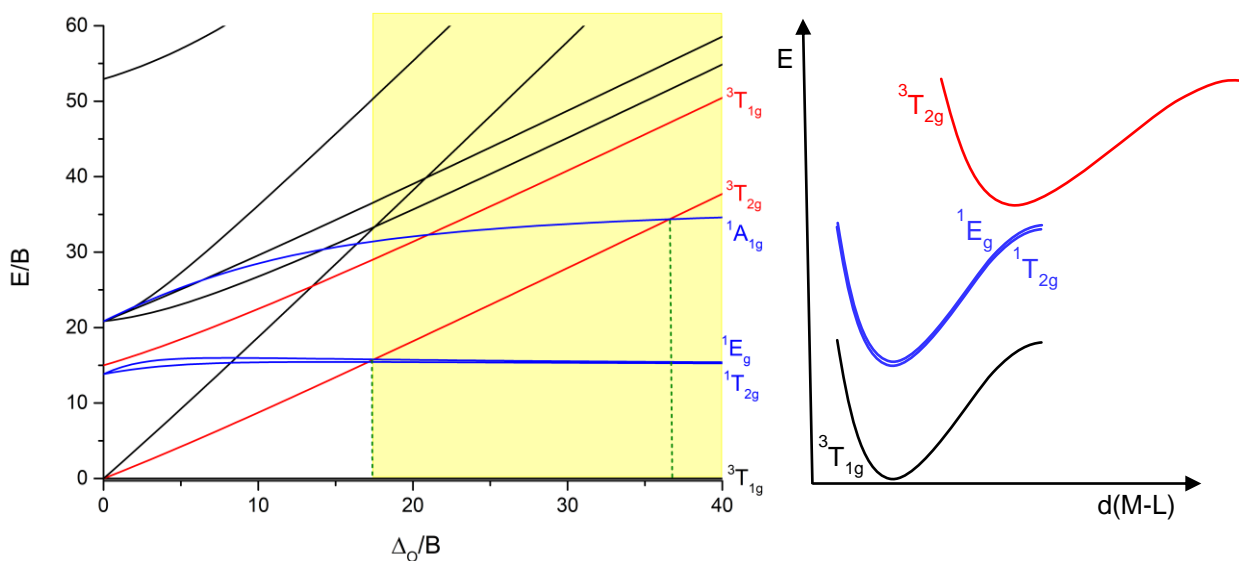


**Abb. 5:** Links: Tanabe-Sugano-Diagramm der  $d^2$ -Elektronenkonfiguration im oktaedrischen Ligandenfeld ( $C = 4.42 B$ ). Rechts: Die Potentialkurven der relevanten elektronischen Zustände: der Grundzustand (schwarz), die Spin-Flip-Zustände (blau) und der Ligandenfeldzustand (rot).

Die wichtigste Analogie sind die energiearmen Spin-Flip-Zustände ( ${}^1E_g$  und  ${}^1T_{2g}$ ), welche oberhalb des  ${}^3T_{1g}$ -Grundzustands liegen. Ein wesentlicher Unterschied von oktaedrischen  $d^2$ -Systemen dagegen ist, dass der Grundzustand  ${}^3T_{1g}$  ein dreifach-entarteter Triplett-Zustand ist, wohingegen der Grundzustand  ${}^4A_{2g}$  in oktaedrischen Komplexen mit  $d^3$ -Elektronenkonfiguration ein nicht-entarteter A-Zustand ist. In nicht hochsymmetrischen  $d^2$ -Komplexen ist die Entartung aufgehoben und der Triplett-Grundzustand spaltet in drei Unterniveaus auf.

Auch für oktaedrische  $d^2$ -Systeme liegen bei schwachen Ligandenfeldern (Abb. 5, weißer Hintergrund) die Ligandenfeldzustände ( ${}^3T_{2g}$  und  ${}^3T_{1g}$ ) energetisch unterhalb oder sehr nahe an den Spin-Flip-Zuständen. Es wird folglich ein großes Ligandenfeld

(Abb. 5, gelb hinterlegt) benötigt um die Energiedifferenz  $\Delta E(^3T_{2g}-^1E_g)$  zwischen den Ligandenfeld- und den Spin-Flip-Zuständen zu vergrößern. Der große energetische Abstand ist entscheidend um die Rückpopulation der Ligandenfeldzustände ( $k_{RISC}$ ) zu verhindern und damit die Voraussetzung für langlebige Phosphoreszenz zu schaffen.

Vanadium(III)-Verbindungen sind aufgrund der großen natürlichen Häufigkeit von Vanadium und der  $d^2$ -Elektronenkonfiguration ideale Kandidaten für die Entwicklung neuer Spin-Flip-Luminophore. Die elektronische Struktur und die photophysikalischen Eigenschaften von Komplexen mit annähernd oktaedrisch umgebenen V(III)-Zentren wurde bereits ausführlich für  $V^{3+}$ -Ionen in oxidischen Matrices oder in Komplexen mit Sauerstoffdonorliganden ( $[V(H_2O)_6]^{3+}$ ,  $V(acac)_3$ ,  $[V(ox)_3]^{3-}$ ,  $[V(urea)_6]^{3+}$ ) untersucht (**acac** = acetylacetonat, **ox** = oxalat).<sup>[46–48,62,63]</sup> Die Energie der Singulett-Zustände in diesen Verbindungen beträgt ca.  $10000\text{ cm}^{-1}$  und dementsprechend einer Wellenlänge von etwa  $\lambda_{em} = 1000\text{ nm}$ . Die Spin-Flip-Emission liegt daher im NIR und somit im optimalen Spektralfenster für potentielle Anwendungen insbesondere für das NIR-Bioimaging.<sup>[26]</sup>

Allerdings zeigen die aktuell bekannten V(III)-Verbindungen nach Anregung und Intersystem Crossing nur extrem schwache Phosphoreszenz bei tiefen Temperaturen und im Festkörper. Sehr häufig kann überhaupt keine Lumineszenz detektiert werden.<sup>[46–48,62,63]</sup> In eine Aluminiumoxid Matrix dotiertes  $V^{3+}$  ( $V^{3+}:Al_2O_3$ ) beispielsweise phosphoresziert dank einer großen Ligandenfeldaufspaltung ausgehend von  $^1T_{2g}$  bei  $1026\text{ nm}$ . Die Emissionsintensität ist dabei aber 3-4 Größenordnungen geringer als im analogen Rubin ( $Cr^{3+}:Al_2O_3$ ) und tritt nur bei extrem tiefen Temperaturen ( $T = 8\text{ K}$ ) auf.<sup>[46,47]</sup>

Statt der gewünschten Spin-Flip-Emission wird bei mäßigen Ligandenfeldstärken ( $\Delta_o$  ca.  $17\text{ B}$ , kurze gestrichelt grüne Linie in Abb. 5) lediglich Fluoreszenz ausgehend vom Ligandenfeldzustand ( $^3T_{2g}$ ) beobachtet.<sup>[64,65]</sup> Dementsprechend wird ein wesentlich größeres Ligandenfeld ( $\Delta_o \gg 17\text{ B}$ ) benötigt, um den  $^3T_{2g}$ -Zustand zu noch höherer Energie zu verschieben und die Rückpopulation ( $^1E_g/^1T_{2g} \rightarrow ^3T_{2g}$ ) effektiver zu verhindern.

Um nach der spin-erlaubten Anregung in die Triplett-Zustände eine effektive Population der emittierenden Singulett-Zustände zu ermöglichen, ist eine möglichst hohe Intersystem-Crossing-Rate entscheidend. Neben einer möglichst starken Spin-Bahn-Kopplung ist dabei eine hohe Dichte an Singulett-Zuständen mit eher geringem

energetischen Abstand zum  ${}^3T_{2g}$ -Zustand vorteilhaft. Grundsätzlich ist dabei direktes ISC in die Spin-Flip-Zustände möglich, mit dem Nachteil von möglichem RISC zurück in den  ${}^3T_{2g}$ -Zustand. Wie im  $d^2$ -Tanabe-Sugano-Diagramm dargestellt, kreuzt bei hohen Ligandenfeldstärken ( $\Delta_o \approx 36.6 B$ , lange gestrichelt grüne Linie in Abb. 5) der zusätzliche Singulett-Zustand ( ${}^1A_{1g}$ ) den Ligandenfeldzustand  ${}^3T_{2g}$ . Folglich ist ein starkes Ligandenfeld im Bereich von  $\Delta_o \approx 37 B$  auch sehr günstig um ISC zu fördern und RISC weitestgehend auszuschließen.

Ebenfalls die bekannten V(II)-Komplexe mit N-Donor-Liganden und  $d^3$ -Elektronenkonfiguration wie beispielsweise  $[V(\text{bpy})_2]^{2+}$  und  $[V(\text{phen})_3]^{2+}$  sind nicht lumineszent.<sup>[66]</sup> Stattdessen relaxieren deren angeregte Spin-Flip-Zustände (analog zu Cr(III) sind das Dublett-Zustände) durch schnelle Besetzung eines energetisch naheliegenden  ${}^2MLCT$ -Zustandes, der dann innerhalb weniger Pikosekunden strahlungslos deaktiviert wird.

## 3.2 Ergebnisse und Diskussion

Dieses Projekt wurde in Zusammenarbeit mit den Arbeitskreisen von Katja Heinze an der Universität Mainz, der Gruppe von Markus Gerhards aus Kaiserslautern und weiteren Kooperationspartnern durchgeführt. Meine Beiträge an der jeweiligen Publikation sind am Anfang der Arbeit dokumentiert.

### 3.2.1 Ein V(III)-Komplex mit blauer und NIR-II Spin-Flip-Lumineszenz (Publikation 2)

Oktaedrische V(III)-Komplexe mit  $d^2$ -Elektronenkonfiguration, welche Spin-Flip-Emission bei Raumtemperatur und in Lösung zeigen, sind trotz ihrer vielversprechenden elektronischen Struktur derzeit nicht bekannt. Das zentrale Problem der bekannten V(III)-Verbindungen ist die zu geringe Ligandenfeldaufspaltung. Ein großes Ligandenfeld ist aber entscheidend um die Rückpopulation in die Ligandenfeldzustände ausgehend von den Spin-Flip-Zuständen zu verhindern, welche höchstens breitbandige Fluoreszenz oder die direkte strahlungslose Deaktivierung zur Folge hätte. Wie in Kap. 3.1.1 beschrieben, wäre auch Intersystem Crossing zur Population der Spin-Flip-Zustände bei starken Ligandenfeldern potentiell effektiver.

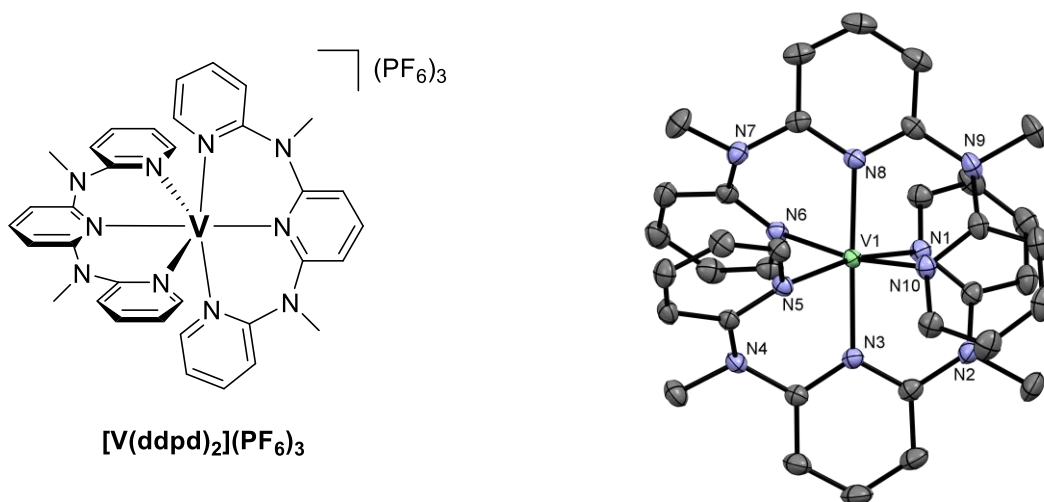


**Abb. 6:** Strukturformel und ORTEP-Darstellung der Molekülstruktur von *mer*- $[V(ddpd)_2](PF_6)_3$ , Ellipsoidenwahrscheinlichkeit 50 %. Wasserstoffatome, Gegenionen und Lösemittelmoleküle sind aus Übersichtlichkeitsgründen nicht dargestellt. Die Details zur Strukturlösung sind den HI zu entnehmen.<sup>[67]</sup>

Um eine möglichst hohe Ligandenfeldstärke zu gewährleisten wurde der Starkfeldligand **ddpd** gewählt. Bei **ddpd** handelt es sich um einen Chelatliganden, der sich durch große Bisswinkel und einen starken  $\sigma$ -Donor-Charakter auszeichnet. Zudem ermöglichte dieser Ligand bereits im **[Cr(ddpd)<sub>2</sub>]<sup>3+</sup>**-Komplex intensive, langlebige Spin-Flip-Lumineszenz im NIR mit Quantenausbeuten von über  $\Phi = 10\%$  in Lösung. Deuterierung des **ddpd**-Liganden und Verwendung von deuteriertem, sauerstofffreien Acetonitril erhöhten die Quantenausbeute auf spektakuläre  $\Phi = 30\%$  und die Lumineszenzlebenszeit auf  $\tau = 2300\ \mu\text{s}$ .<sup>[37]</sup> Daher wurde neben dem **[V(ddpd)<sub>2</sub>](PF<sub>6</sub>)<sub>3</sub>**-Komplex auch sein perdeuteriertes Analogon **[V([D<sub>17</sub>]-ddpd)<sub>2</sub>](PF<sub>6</sub>)<sub>3</sub>** synthetisiert. Die Synthese des perdeuterierten **ddpd**-Liganden und der Einfluss der Deuterierung auf die Photophysik von **[V(ddpd)<sub>2</sub>](PF<sub>6</sub>)<sub>3</sub>** werden in Kapitel 4.2.2 diskutiert. Im Festkörper ist das Vanadium(III)-Zentrum im **[V(ddpd)<sub>2</sub>]<sup>3+</sup>**-Komplexion näherungsweise oktaedrisch von sechs Pyridindonoren koordiniert (Abb. 6). Das *mer*-Isomer wurde gegenüber dem *fac*-Isomer bevorzugt, da die Metall-Ligand-Bindungslängen in *fac*-[M(ddpd)<sub>2</sub>]<sup>n+</sup>-Isomeren aus sterischen Gründen im Allgemeinen länger sind und daher die Ligandenfeldaufspaltung etwas kleiner ist.<sup>[68]</sup>

Die [VN<sub>6</sub>]-Koordinationsgeometrie des d<sup>2</sup>-Vanadiums ist dabei aufgrund des <sup>3</sup>T<sub>2g</sub>-Grundzustandes tetragonal verzerrt (Jahn-Teller-Effekt) und ist verglichen zum d<sup>3</sup>-**[Cr(ddpd)<sub>2</sub>]<sup>3+</sup>**<sup>[35]</sup> weniger ideal oktaedrisch. Trotzdem ist die Abweichung von der idealen Oktaedergeometrie nur gering und daher sollte die gewünschte große Ligandenfeldaufspaltung gewährleistet sein (Details s. Pub. 2: *Results*, HI, Tab. S1+2).

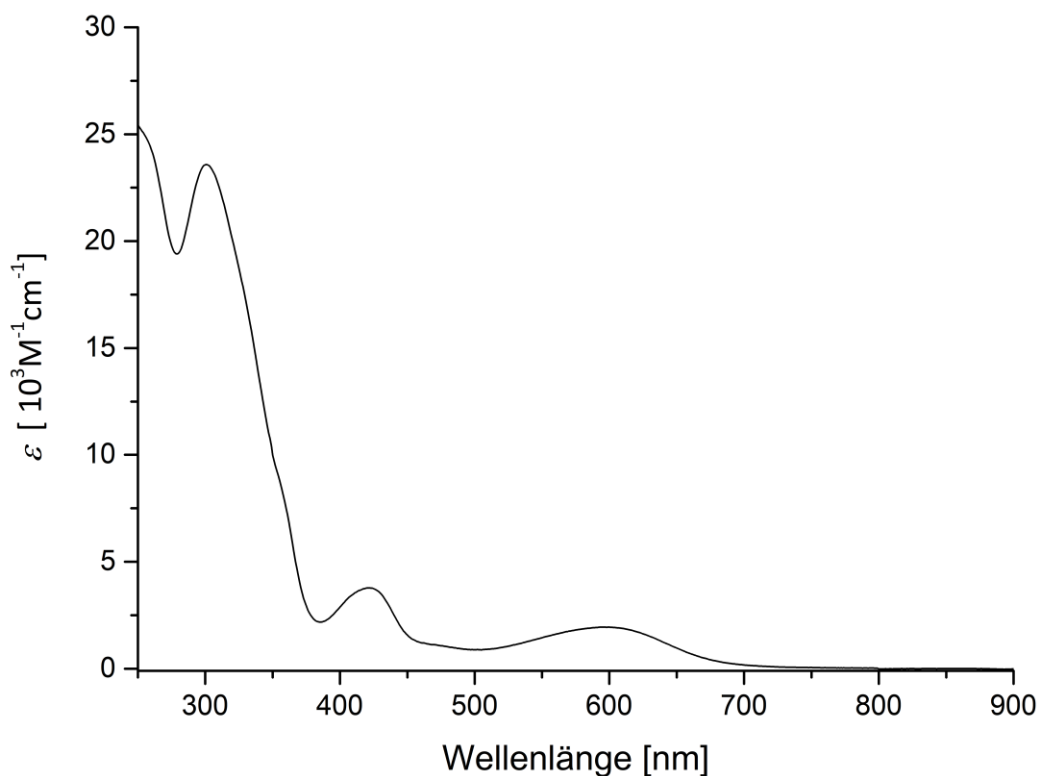


**Abb. 7:** Absorptionsspektrum von  $[\text{V}(\text{ddpd})_2](\text{PF}_6)_3$  in  $\text{CH}_3\text{CN}$ .

Das Absorptionsspektrum von  $[\text{V}(\text{ddpd})_2]^{3+}$  in Acetonitril zeigt eine breite Absorptionsbande bei 597 nm mit einer Schulter bei ca. 475 nm, eine asymmetrische Bande mit Maximum bei 422 nm und intensivere Banden um 300 nm. All diese Banden sind uncharakteristisch intensiv ( $\epsilon \ll 1000 \text{ M}^{-1} \text{ cm}^{-1}$ ) für paritätsverbotene d-d-Übergänge (Laporte-Regel), was auf einen signifikanten CT-Charakter hinweist. Da die CT-Banden die intensitätsschwachen d-d-Zustände überdecken, kann deren energetische Lage und damit die Stärke des Ligandenfelds nicht experimentell bestimmt werden.

Um nun die Energien der relevanten elektronischen Zustände zu erhalten, wurden Quantenchemische-Rechnungen durchgeführt. Durch TD-DFT-UKS- in Kombination mit CASSCF-NEVPT2-Rechnungen von Letizia González konnten die Energien sowohl der CT- als auch der metallzentrierten Zustände abgeschätzt werden (Pub. 2: *Static Quantum Chemical Calculations*). Die relevanten elektronischen Zustände sind im Jablonski-Termschema in Abb. 8 dargestellt. Der angeregte Ligandenfeldzustand  ${}^3\text{T}_{2g}$  (in Oktaedersymmetrie) ist, wie auch der  ${}^3\text{T}_{1g}$  Grundzustand durch Symmetrierniedrigung aufgespalten und von  ${}^3\text{LMCT}$ -Zuständen überlagert.

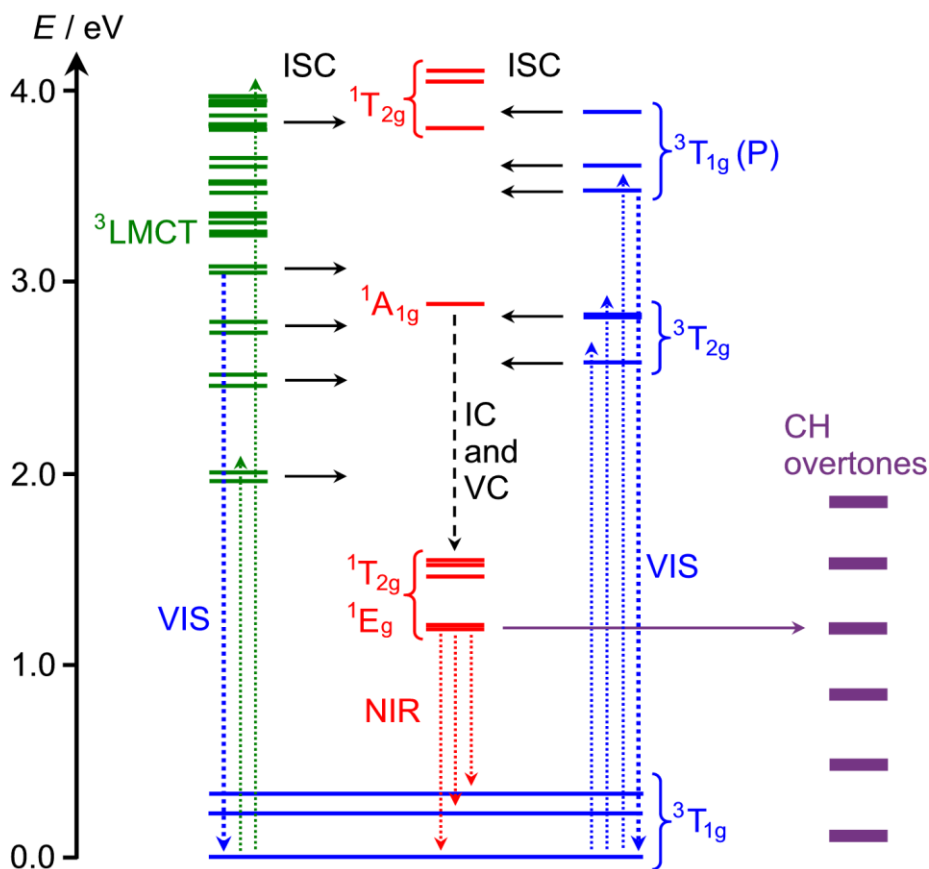


**Abb. 8:** Jablonski Termschema von **[V(ddpd)<sub>2</sub>](PF<sub>6</sub>)** basierend auf TD-DFT-UKS-Rechnungen (<sup>3</sup>LMCT-Zustände in grün) und CASSCF-NEVPT2-Kalkulationen (<sup>3</sup>MC-Zustände in blau; <sup>1</sup>MC-Zustände in rot). Notation der metallzentrierten Zustände nach Oktaedersymmetrie. ISC = intersystem crossing; IC = internal conversion; VC = vibrational cooling; NIR = NIR-Emission; VIS = Emission im sichtbaren Spektralbereich; C-H Obertöne in violett = Multiphonon Relaxation (s.Kapitel 4.2.2). Abbildung übernommen von Heinze.<sup>[67]</sup>

Die Wellenlänge der Anregung aus dem Grundzustand <sup>3</sup>T<sub>1g</sub> in den Ligandenfeldzustand <sup>3</sup>T<sub>2g</sub> wurde mit 441 bzw. 413 nm berechnet. Daraus resultiert für den **[V(ddpd)<sub>2</sub>]<sup>3+</sup>**-Komplex eine Ligandenfeldaufspaltung von ca.  $\Delta_o = 23440 \text{ cm}^{-1}$ . Das ist mehr als  $2500 \text{ cm}^{-1}$  größer als bei V(III)-Komplexen mit Sauerstoffdonorliganden wie beispielsweise **V(acac)<sub>3</sub>**.<sup>[63]</sup> Die Stärke des Ligandenfelds ist daher ausreichend groß um RISC in die <sup>3</sup>LMCT- oder <sup>3</sup>T<sub>2g</sub>-Zustände zu verhindern und Phosphoreszenz aus den Singulett-Zuständen zu beobachten.



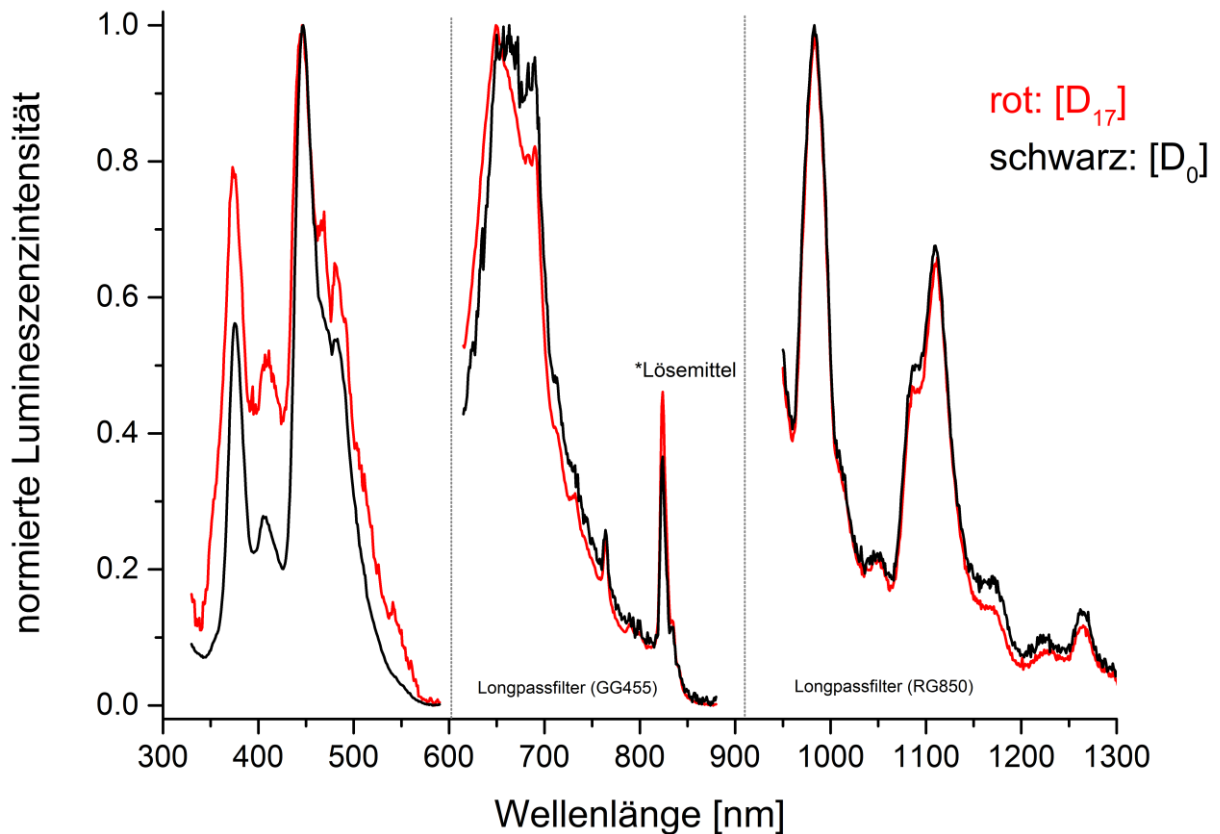


**Abb. 9:** Normierte Steady-State-Emissionsspektren der Komplexe  $[\mathbf{V}(\mathbf{ddpd})_2](\mathbf{PF}_6)_3$  (schwarz) und  $[\mathbf{V}(\mathbf{D}_{17}\text{-ddpd})_2](\mathbf{PF}_6)_3$  (rot) ( $\lambda_{\text{exc}} = 306 \text{ nm}$ , n-BuCN, entgast,  $T = 77 \text{ K}$ ). Die relativen Intensitäten unterschiedlicher Spektralbereiche sind nicht maßstäblich dargestellt. Longpassfilter GG455 bzw. RG850 wurden bei den Messungen der energiearmen Emission verwendet. Bei der mit \* markierten Bande handelt es sich um ein Artefakt aus dem Lösungsmittel.

Der  $[\mathbf{V}(\mathbf{ddpd})_2](\mathbf{PF}_6)_3$ -Komplex zeigt nach Anregung bei  $\lambda_{\text{exc}} = 306 \text{ nm}$  in einer Valeronitril-Glasmatrix bei  $T = 77 \text{ K}$  eine Vielzahl an Emissionsbanden im Wellenlängenbereich zwischen  $\lambda_{\text{em}} = 370 \text{ nm}$  und  $1150 \text{ nm}$  (Abb. 9). Offenbar sind nach kurzweiliger Anregung im UV-Spektralbereich einige Zustände emissiv. Tatsächlich kann auch eine scharfe NIR-II-Emissionsbande bei etwa  $\lambda_{\text{em}} = 1100 \text{ nm}$  beobachtet werden. Die Lebensdauer der Emission bei  $\lambda_{\text{em}} = 1100 \text{ nm}$  zeigt eine biexponentielle Zerfallskinetik und ist einige hundert Nanosekunden lang ( $\tau_1 = 790 \text{ ns}$  (93 %),  $\tau_2 = 8800 \text{ ns}$  (7 %), HI, Tab. S7 u. Abb. S12). Diese Lebenszeit ist phosphoreszenztypisch lang und liegt in einem ähnlichen Bereich wie die Lebenszeit der Spin-Flip-Emission von  $\text{V}^{3+}$ -Ionen dotiert in  $\text{NaMg}(\text{Al}(\text{ox})_3$  bei  $T = 11 \text{ K}$  ( $\tau < 500 \text{ ns}$ ).<sup>[69]</sup> Die Emissionsbanden zeigen eine Feinstruktur was hauptsächlich auf Schwingungsprogression zurückzuführen sein könnte. Erwartungsgemäß hat die Deuterierung keinen Einfluss auf die Lage und Zahl der Emissionsbanden.

Diese experimentellen Befunde sind im Einklang mit den quantenchemischen Rechnungen (Pub. 2: *Steady-State and Time-Resolved Spectroscopy*), welche die NIR-Banden bei  $\lambda_{em} = 982$  und  $\lambda_{em} = 1088/1109$  nm Phosphoreszenz aus den Spin-Flip-Zuständen (am wahrscheinlichsten aus  $^1E_g$ ) in die Niveaus des Grundzustands  $^3T_{1g}$  zuschreiben (NIR, Abb.8). Mit Hilfe der Maxima dieser NIR-I- und NIR-II-Phosphoreszenzbanden kann die Aufspaltung des Grundzustands  $^3T_{1g}$  experimentell auf  $1080\text{ cm}^{-1}$  abgeschätzt werden (1088/1109 nm gemittelt). Dieser Wert ist etwas kleiner als die theoretisch berechnete Grundzustandsaufspaltung ( $1873\text{ cm}^{-1}$ , Abb. 8). Die kurzwelligen Emissionsbanden ( $\lambda_{em} = 374, 447$  und  $660$  nm) wurden, entsprechend den Rechnungen bzw. dem Tanabe-Sugano-Diagramm, spin-erlaubten Emissionen (Fluoreszenz) zugeordnet. Die kurze Lebenszeit der Emission bei  $\lambda_{em} = 396$  nm ( $\tau_1 = 1.7$  ns (51 %),  $\tau_2 = 6.3$  ns (49 %), HI, Tab. S7 u. Abb. S13) von wenigen Nanosekunden bei  $T = 77$  K in Valeronitrilglas bestätigt diese Annahme.

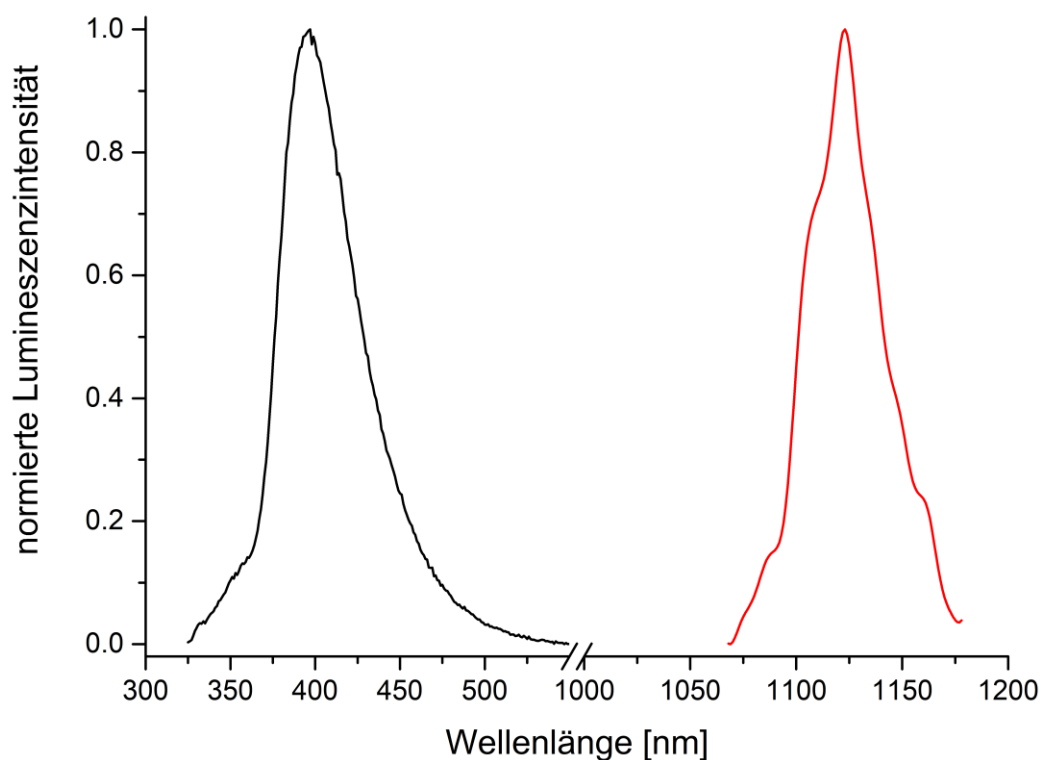


**Abb. 10:** Normierte Steady-State-Emissionsspektren von  $[V(\text{ddpd})_2](\text{PF}_6)_3$  bei Raumtemperatur ( $\lambda_{exc} = 306$  nm,  $\text{CD}_3\text{CN}$ , entgast). Die relativen Intensitäten unterschiedlicher Spektralbereiche sind nicht maßstäblich dargestellt.

In entgastem, deuteriertem Acetonitril emittiert der  $[V(\text{ddpd})_2]^{3+}$ -Komplex nach Anregung bei  $\lambda_{exc} = 306$  nm selbst bei Raumtemperatur gleichzeitig bei  $\lambda_{em} = 396$  nm und  $\lambda_{em} = 1109/1123$  nm (Duale Emission, Abb. 10). Die Quantenausbeute der blauen

Fluoreszenz beträgt  $\Phi = 2.1 \%$  und übertrifft dabei die Quantenausbeute der kürzlich veröffentlichten ebenfalls blau lumineszierenden Cobalt(III)-Komplexe ( $\Phi = 0.7 \%$  /  $0.4 \%$ ).<sup>[56]</sup> Die biexponentiell angepasste Lebenszeit der Fluoreszenz beträgt  $\tau_1 = 3.2 \text{ ns}$  (56 %) und  $\tau_2 = 8.2 \text{ ns}$  (44 %) (HI, Tab. S7 u. Abb. S13). Auf Basis der quantenchemischen Rechnungen kann diese Fluoreszenzbande dem metallzentrierten  ${}^3T_{1g}(P) \rightarrow {}^3T_{1g}$  Übergang zugeordnet werden (Abb. 8). Allerdings liegen auch die berechneten Energien von zwei  ${}^3\text{LMCT}$ -Zuständen in diesem Bereich welche ebenfalls potentiell zur vergleichsweise intensiven Fluoreszenzbande beitragen und die biexponentielle Natur der Lebenszeit erklären könnten (Pub. 2: *Steady-State and Time-Resolved Spectroscopy*). Ferner ist die Fluoreszenz empfindlich gegenüber Luftsauerstoff. Neben der blauen Emission phosphoresziert der **[V(ddpd)<sub>2</sub>](PF<sub>6</sub>)<sub>3</sub>**-Komplex im NIR-II bei Raumtemperatur und in Lösung (Abb. 10). Damit ist der **[V(ddpd)<sub>2</sub>](PF<sub>6</sub>)<sub>3</sub>**-Komplex das erste bekannte Luminophor eines günstigen und leicht verfügbaren Metallions welches NIR-II-Lumineszenz in gefrorener und flüssiger Lösung zeigt. Die relativ scharfe Phosphoreszenz ist eindeutig zu detektieren, auch wenn die Quantenausbeute mit  $\Phi = 2 \times 10^{-4} \%$  nicht besonders hoch ist. Aufgrund der insgesamt sehr niedrigen Quantenausbeute in Kombination mit der herausfordernden Messung ist für den Wert eine relative Abweichung von ca. 50 % zu erwarten. Für die Asymmetrie der NIR-Bande dieses d<sup>2</sup>-V(III)-Komplexes ist hauptsächlich die Aufspaltung des  ${}^3T_{1g}$ -Grundzustands verantwortlich (Abb. 8). Dies ist ein Unterschied zur Bandenform der Spin-Flip-Emission von d<sup>3</sup>-Chrom(III)-Komplexen bei welchen der Grundzustand ( ${}^4A_{2g}$ ) nicht aufgespalten ist und folglich schärfere sowie symmetrischere Phosphoreszenz erfolgt.

Neben strahlungslosen Deaktivierungsprozessen wie Multiphonon Relaxation (Kapitel 4.2.2) spielt das Intersystem Crossing (ISC) eine bedeutende Rolle für die Quantenausbeute der NIR-Emission. Die intensive hochenergetische Fluoreszenz von **[V(ddpd)<sub>2</sub>](PF<sub>6</sub>)<sub>3</sub>** weist auf eine eher geringe ISC-Rate von den  ${}^3\text{LMCT}/{}^3T_{2g}$ -Zuständen in die  ${}^1E_g/{}^1T_{2g}$ -Zustände hin (Abb. 8). Eine niedrige ISC-Rate erhöht die Wahrscheinlichkeit anderer Relaxationsprozesse wie Fluoreszenz oder strahlungslose Deaktivierung der Triplett-Zustände, noch bevor die Spin-Flip-Zustände überhaupt erst populiert werden. Die geringe ISC-Effektivität wurde auch durch Molekulare-Dynamik-Simulationen (Pub. 2: *Molecular Dynamics Calculations*) bestätigt und kann so eine der relevanten Gründe für die geringe NIR-Quantenausbeute liefern.

Zusammenfassend zeigt der  $[\text{V}(\text{ddpd})_2](\text{PF}_6)_3$ -Komplex dank einer großen Ligandenfeldauspaltung intensive blaue Fluoreszenz sowie langlebige NIR-II-Phosphoreszenz und das bei Raumtemperatur und in Lösung. Dieses Konzept erweitert damit die bekannten Luminophore von 3d-Übergangsmetallionen um das günstige und reichlich verfügbare Metall Vanadium. Die duale Emission dieses Vanadium(III)-Komplexes eröffnet zudem potentiell neue Möglichkeiten für zukünftige Anwendungen.

# A Vanadium(III) Complex with Blue and NIR-II Spin-Flip Luminescence in Solution

Matthias Dorn, Jens Kalmbach, Pit Boden, Ayla Pöpcke, Sandra Gómez, Christoph Förster, Felix Kuczelinis, Luca M. Carrella, Laura A. Büldt, Nicolas H. Bings, Eva Rentschler, Stefan Lochbrunner, Leticia González, Markus Gerhards,\* Michael Seitz,\* and Katja Heinze\*

Cite This: *J. Am. Chem. Soc.* 2020, 142, 7947–7955

Read Online

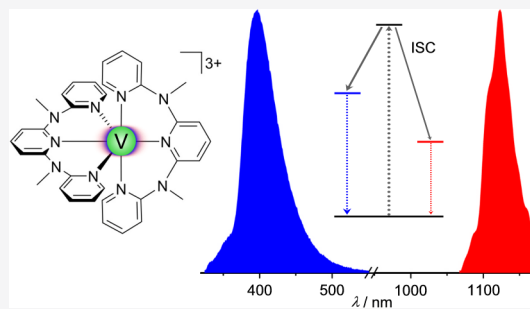
ACCESS |

Metrics & More

Article Recommendations

Supporting Information

**ABSTRACT:** Luminescence from Earth-abundant metal ions in solution at room temperature is a very challenging objective due to the intrinsically weak ligand field splitting of first-row transition metal ions, which leads to efficient nonradiative deactivation via metal-centered states. Only a handful of 3d<sup>n</sup> metal complexes ( $n \neq 10$ ) show sizable luminescence at room temperature. Luminescence in the near-infrared spectral region is even more difficult to achieve as further nonradiative pathways come into play. No Earth-abundant first-row transition metal complexes have displayed emission >1000 nm at room temperature in solution up to now. Here, we report the vanadium(III) complex  $mer\text{-}[V(\text{ddpd})_2][\text{PF}_6]_3$  yielding phosphorescence around 1100 nm in valeronitrile glass at 77 K as well as at room temperature in acetonitrile with  $1.8 \times 10^{-4}\%$  quantum yield (ddpd = *N,N'*-dimethyl-*N,N'*-dipyridine-2-ylpyridine-2,6-diamine). In addition,  $mer\text{-}[V(\text{ddpd})_2][\text{PF}_6]_3$  shows very strong blue fluorescence with 2% quantum yield in acetonitrile at room temperature. Our comprehensive study demonstrates that vanadium(III) complexes with d<sup>2</sup> electron configuration constitute a new class of blue and NIR-II luminophores, which complement the classical established complexes of expensive precious metals and rare-earth elements.



## INTRODUCTION

Luminescent complexes of Earth-abundant metal ions started to emerge only in the past few years.<sup>1–4</sup> Typically, the abundant first-row transition metal ions are prone to subpicosecond nonradiative relaxation via low-energy metal-centered (MC) states, which precluded any useful emission until recently.<sup>4–6</sup> The majority of the very few reported room-temperature luminescent complexes possess rather long-lived charge transfer (CT) states thanks to a high energy or the absence of the detrimental MC states. A d<sup>6</sup>-chromium(0) complex with isocyanide ligands shows <sup>3</sup>MLCT (metal-to-ligand CT) emission at 630 nm ( $\tau = 2.2$  ns,  $\Phi = 0.001\%$ ).<sup>7</sup> d<sup>6</sup>-Cobalt(III) complexes with tridentate strong field ligands display blue emission from <sup>3</sup>LMCT (ligand-to-metal) states (440/412 nm,  $\tau = 5.1/3.2 + 8.7$  ns,  $\Phi = 0.7/0.4\%$ ).<sup>8</sup> Fluorescence from <sup>2</sup>LMCT states is induced in d<sup>5</sup>-iron(III) complexes using carbene ligands (655 nm,  $\tau = 1.96$  ns,  $\Phi = 2.1\%$ ).<sup>9,10</sup> Copper(I) complexes can exhibit quantum yields up to 100%; for example, two-coordinate d<sup>10</sup>-copper(I) complexes of cyclic (alkyl)(amino)carbene and amide ligands emit from ligand-to-ligand charge transfer (LLCT) states between 492–580 nm ( $\tau = 280$ –2500 ns,  $\Phi = 11$ –100%).<sup>11</sup> Clearly, the visible spectral region started to be covered by 3d CT emitters; room-temperature near-infrared (NIR-I, 780–1000 nm; NIR-II, 1000–1700 nm) emission in solution has not yet been reported with CT complexes of Earth-abundant metal ions. On

the other hand, strong NIR luminescence has been achieved by exploiting the spin-flip emission of d<sup>3</sup>-chromium(III) complexes using tridentate strong field ligands, leading to the so-called molecular rubies  $[\text{Cr}(\text{L})_2]^{3+}$  (L = ddpd, tpe; ddpd = *N,N'*-dimethyl-*N,N'*-dipyridine-2-ylpyridine-2,6-diamine; tpe = 1,1,1-tris(pyrid-2-yl)ethane; 782–724 nm,  $\tau = 670$ –4500  $\mu\text{s}$ ,  $\Phi = 5.2$ –30%, CH<sub>3</sub>CN).<sup>12–17</sup> However, emission above 900 nm or even above 1000 nm (NIR-II) at room temperature remains elusive with 3d metal complexes in solution.

In principle, near-infrared (NIR) luminescence enables exciting applications in telecommunications, laser, and LED/OLED or LEC technologies (OLED, organic light-emitting diode; LEC, light-emitting electrochemical cell) as well as in bioanalysis and bioimaging.<sup>18–22</sup> NIR-II luminescence can be particularly beneficial for in vivo imaging with respect to tissue penetration as well as reduced autofluorescence of the background and scattering losses.<sup>18,19</sup> Current materials are based on rare-earth elements, precious metals, and organic dyes often in conjunction with precious metals.<sup>23–28</sup> The rare-

Received: February 22, 2020

Published: April 10, 2020



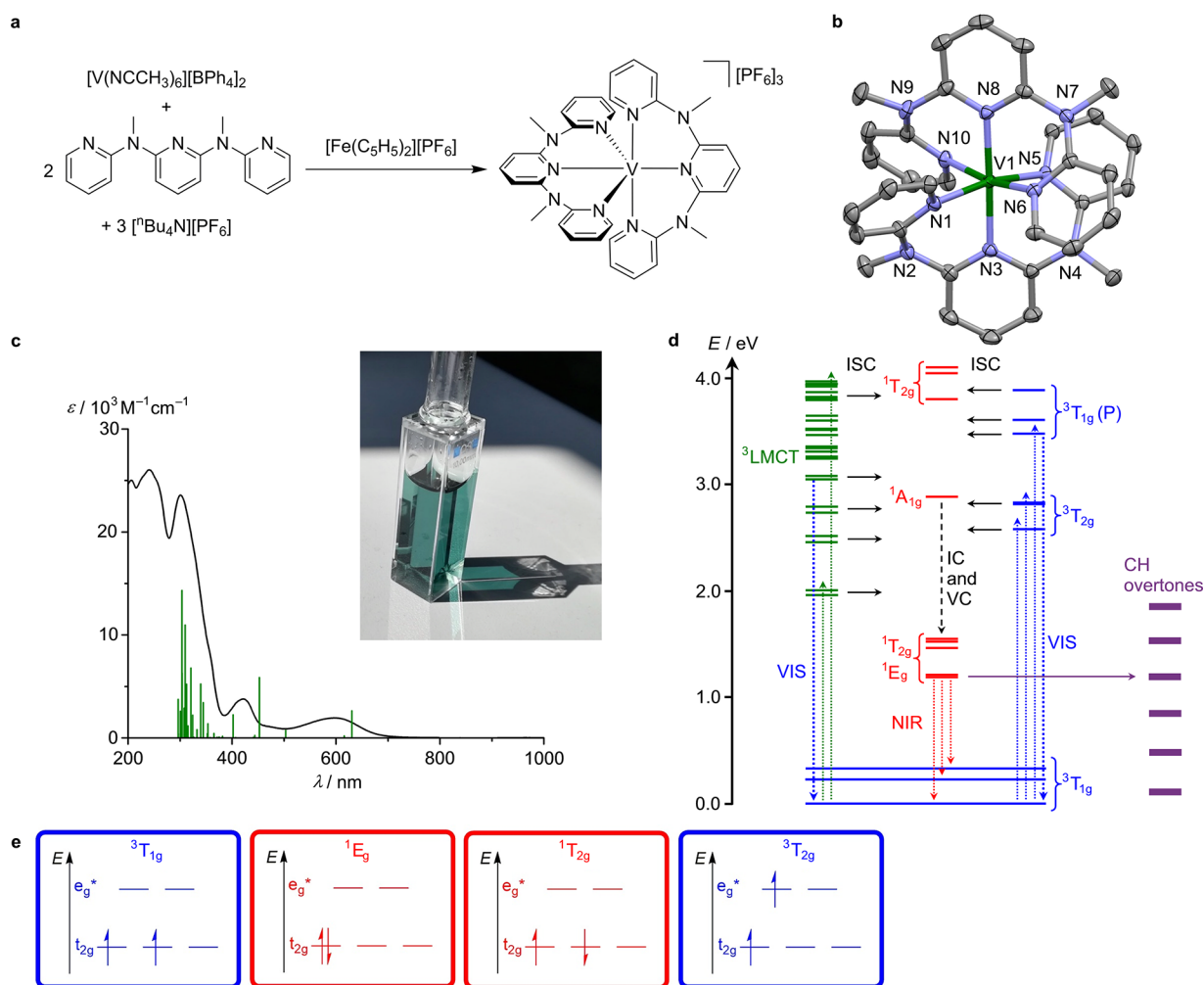


**Figure 1.** Synthesis, molecular structure, absorption spectrum of  $[V(\text{ddpd})_2][\text{PF}_6]_3$ , and Jablonski diagram of  $[V(\text{ddpd})_2]^{3+}$ . (a) Preparation of  $[V(\text{ddpd})_2][\text{PF}_6]_3$ . (b) Molecular structure of the cation of  $[V(\text{ddpd})_2][\text{PF}_6]_3 \times 3\text{CH}_3\text{CN}$ . Thermal ellipsoids are shown at 50% probability. Hydrogen atoms, counterions, and  $\text{CH}_3\text{CN}$  molecules are omitted for clarity. (c) Absorption spectrum and photograph of  $[V(\text{ddpd})_2][\text{PF}_6]_3$  in  $\text{CH}_3\text{CN}$ . The vertical green bars correspond to spin-allowed transitions calculated by TD-DFT-UKS calculations (unshifted). (d) Jablonski diagram constructed from TD-DFT-UKS ( $^3\text{LMCT}$  states in green) and CASSCF-NEVPT2 calculations ( $^3\text{MC}$  states in blue;  $^1\text{MC}$  states in red); notation of MC states according to  $O_h$  symmetry; ISC, intersystem crossing; IC, internal conversion; VC, vibrational cooling; NIR, NIR emission; VIS, emission in the visible spectral region; CH overtones, multiphonon relaxation (experimental overtone energies from ref 13). (e) Representative microstates of the most relevant metal-centered triplet and singlet states.

earth ions typically display comparably sharp emission bands, and yet they are split by electron–electron repulsion, spin–orbit coupling, and the crystal field.<sup>29</sup> Organic emitters often show broad emission bands, which typically merely tail into the NIR spectral region; hence, some emission still occurs in the visible spectral region.

A fundamental problem of low-energy emission derives from the energy-gap law especially for distorted excited states. The rate constant for nonradiative decay that reduces the luminescence quantum yield  $\Phi$  increases with decreasing energy difference between the emitting and the ground states.<sup>30,31</sup> Nested, that is, weakly distorted, states (such as f–f and d–d spin-flip transitions) are hence better suited for NIR emission. Furthermore, high-energy oscillators, for example, OH from water or CH from coordinating ligands, can increase nonradiative decay via energy transfer to suitable OH/CH vibrational overtones.<sup>32,33</sup> Lanthanide compounds, for example, Nd, Sm, Dy, or Yb, very often embedded in nanoparticles that lack detrimental CH oscillators, achieve

NIR-II luminescence due to their favorable excited-state levels originating from f–f transitions and the absence of high-energy oscillators.<sup>18,19,29</sup> The quantum yields for molecular NIR emissive lanthanide complexes are rather small, although deuterated cage and fluorinated porphyrin complexes of  $\text{Yb}^{3+}$  showing emission around 1000 nm recently achieved exceptionally high quantum yields.<sup>34–36</sup> However, rare-earth elements and precious metals are difficult and expensive to mine and purify, so that a huge interest arose in replacing these elements with Earth-abundant metals in luminescence applications.<sup>1–4</sup>

Analogous to the  $d^3$  electron configuration of the abundant metal chromium(III),<sup>2,12–17</sup> an excited-state ordering with low-energy spin-flip states ( $^1E_g/{}^1T_{2g}$ ) emerges from a  $d^2$  electron configuration in an octahedral ligand field ( $^3T_{1g}$  ground state), provided that a strong ligand field is imposed to increase the energy gap between the interconfigurational triplet state ( $^3T_{2g}$ ) and the intraconfigurational singlet states ( $^1E_g/{}^1T_{2g} < {}^3T_{2g}$  at  $\Delta_o > 17.3 B$  in the standard Tanabe–



Sugano diagram; see Figure S1;  $\Delta_o$  and  $B$  are the ligand field parameters). We hypothesized that this situation can be realized by octahedral vanadium(III) complexes in a strong ligand field. The energy of potentially emissive singlet states of vanadium(III) has been determined by absorption spectroscopy on classical vanadium(III) compounds with O-donor ligands, such as  $V^{3+}:Al_2O_3$ ,  $[V(H_2O)_6]^{3+}$ ,  $[V(urea)_6]^{3+}$ , and  $[V(ox)_3]^{3-}$ ,<sup>37–41</sup> and by 2p3d resonant inelastic X-ray scattering on  $V(acac)_3$  as  $\sim 10\,000\text{ cm}^{-1}$  ( $\sim 1000\text{ nm}$ ) (urea =  $OC(NH_2)_2$ , ox =  $[C_2O_4]^{2-}$ , acac =  $[CH_3(CO)CH(CO)CH_3]^-$ ).<sup>42</sup> This energy excellently matches the targeted window for luminescence applications in the NIR-II region. However, the known vanadium(III) compounds display after excitation and intersystem crossing (ISC) only very weak phosphorescence at low temperature, if phosphorescence is observed at all.<sup>37–41</sup> For example, the phosphorescence intensity of  $V^{3+}:Al_2O_3$  is 3–4 orders of magnitude smaller than that of the R lines of ruby ( $Cr^{3+}:Al_2O_3$ ), and the vanadium(III) spin-flip emission has been only detected in the solid state at low temperatures so far.<sup>37,38</sup> Instead, (delayed) fluorescence from vanadium centered  ${}^3T_{2g}$  states occurs in compounds with ligand field strengths close to  $17.3\text{ B}$ .<sup>43,44</sup> Consequently, back-ISC from  ${}^1E_g/{}^1T_{2g}$  to  ${}^3T_{2g}$  states must be suppressed. This can in principle be achieved by further increasing the ligand field strength, thus shifting the  ${}^3T_{2g}$  states to higher energy relative to the singlet states. On the other hand, to promote ISC from the triplets to the singlet manifold besides large spin–orbit coupling, a high density of singlet states in the energy region of the  ${}^3T_{2g}$  states is beneficial.<sup>45</sup> According to ligand field theory, an additional singlet term ( ${}^1A_{1g}$ ) crosses the  ${}^3T_{2g}$  term at very high ligand field strengths ( $\Delta_o > 36.6\text{ B}$  in the standard Tanabe–Sugano diagram; Figure S1). Consequently, an even larger ligand field splitting than  $\Delta_o \gg 17.3\text{ B}$ ,  $\Delta_o \approx 36.6\text{ B}$ , could be advantageous to promote ISC to the singlet states via the high-energy  ${}^1A_{1g}$  state in vanadium(III) complexes. In this study, such a large ligand field splitting will be targeted.

The strong-field ligand ddpd already enabled spectacular room-temperature quantum yields above 10% and microsecond-lifetimes in solution in the prototypical molecular ruby  $[Cr(ddpd)_2]^{3+}$ .<sup>12</sup> Ligand and solvent deuteration even boosted the quantum yield to 30% and the lifetime to  $2300\ \mu\text{s}$ .<sup>13</sup> However, an analogous coordination chemistry of vanadium(III) and oligopyridine ligands is underdeveloped.<sup>46,47</sup> *cis-fac*- $[V(ddpd)_2][PF_6]_3 \times 3CH_3CN$  is the first reported stable homoleptic polypyridine vanadium(III) complex.<sup>46</sup> Yet, the bond lengths in *cis-fac*- $[M(ddpd)_2]^{n+}$  isomers are typically longer than those in *mer*-isomers due to the ligand deformation, which reduces the actual ligand field strength.<sup>46</sup>

Here, we demonstrate that the strong field ligand ddpd promotes ISC in a novel close-to-octahedral vanadium(III) complex *mer*- $[V(ddpd)_2][PF_6]_3$ . Consequently, the complex shows NIR-II phosphorescence at low as well as at room temperature in solution. In addition, a strong blue fluorescence is observed. To deeper elucidate the key challenges for luminescent vanadium(III) complexes, we recorded fs-transient absorption spectra and ns-step-scan FTIR spectra for *mer*- $[V(ddpd)_2][PF_6]_3$ . To judge the influence of multiphonon relaxation via CH overtones, we prepared and studied the deuterated analogue  $[V([D_{17}]\text{-ddpd})_2][PF_6]_3$ . Static quantum chemical and nonadiabatic molecular dynamics simulations provide a comprehensive insight into the electronic

excited-state properties and ultrafast dynamics of *mer*- $[V(ddpd)_2]^{3+}$ .

## RESULTS

**Synthesis, X-ray Structure, and Characterization of  $[V^{III}(ddpd)_2]^{3+}$ .** The dark green complex *mer*- $[V^{III}(ddpd)_2][PF_6]_3$  was efficiently synthesized from  $[V(CH_3CN)_6][BPh_4]_2$  and ddpd<sup>46</sup> followed by oxidation with ferrocenium hexafluorophosphate (Figure 1a). Full characterization is collected in Figures S2–S5. The starting vanadium material  $VCl_3(CH_3CN)_3$  was checked for chromium trace impurities by ICP-MS yielding  $(4.01 \pm 0.31)\ \mu\text{g g}^{-1}\text{ Cr}$ , assuring that emission from conceivable luminescent chromium(III) species will not interfere. The deuterated complex  $[V([D_{17}]\text{-ddpd})_2][PF_6]_3$  was prepared from  $[D_{17}]\text{-ddpd}$  in an analogous manner with a total degree of deuteration of 93.6%D in the ligand and in the complex according to ESI<sup>+</sup> mass spectrometry (Figures S6–S9). Importantly, the  $\alpha$ -protons, closest to the vanadium center, are almost quantitatively substituted by deuterium (99% by <sup>1</sup>H NMR spectroscopy).

The vanadium(III) oxidation state in *mer*- $[V(ddpd)_2][PF_6]_3$  was confirmed by elemental analysis, mass spectrometry, magnetometry, cyclic voltammetry, and single-crystal X-ray diffraction analysis (Figures 1b, S4, S5 and Table S1). The magnetic moment of  $[V(ddpd)_2][PF_6]_3$  between 300 and 50 K amounts to  $\chi T \approx 1.0\text{ cm}^3\text{ K mol}^{-1}$  as expected for an  $S = 1$  ground state. Below 50 K, the magnetic moment decreases due to zero-field splitting. The low-temperature part was modeled with  $g = 1.946$  and a zero-field splitting of  $D_{\text{exp}} = +2.87(11)\text{ cm}^{-1}$  (Figure S4).<sup>47,48</sup> The vanadium(III) complex is reversibly reduced at  $-0.275\text{ V}$  vs ferrocene (Figure S5). In the solid state, the central ion in  $[V(ddpd)_2]^{3+}$  is coordinated by six pyridine donors. The  $[VN_6]$  coordination geometry is nearly octahedral as shown by the octahedral shape parameter being quite close to zero ( $S(\text{OC-6}) = 0.63$ ; Tables S1 and S2). The  $[VN_6]$  symmetry is, however, less perfect than in  $[Cr^{III}(ddpd)_2]^{3+}$  complexes ( $S(\text{OC-6}) = 0.29\text{--}0.43$ ),<sup>46</sup> as a consequence of the Jahn–Teller active partially filled  $t_{2g}$  shell. As compared to the metrics of the *cis-fac*- $[V(ddpd)_2]^{3+}$  isomer, the V–N bond lengths to the four terminal pyridines in *mer*- $[V(ddpd)_2]^{3+}$  decreased by  $0.025\text{--}0.053(9)\ \text{\AA}$ , while V–N distances to the central pyridines increased only slightly by  $0.008/0.022(8)\ \text{\AA}$ .<sup>46</sup> The overall smaller  $[VN_6]$  coordination cage of *mer*- $[V(ddpd)_2]^{3+}$  and its close-to-octahedral symmetry impose the desired large ligand field splitting  $\Delta_o$ .

The electronic absorption spectrum of *mer*- $[V(ddpd)_2][PF_6]_3$  in  $CH_3CN$  reveals a broad absorption band around 597 nm (Gaussian deconvolution: 616, 570 nm), a shoulder at  $\sim 475\text{ nm}$ , an asymmetric band at 422 nm (Gaussian deconvolution: 429, 412 nm), and very intense bands at 301 nm (Figures 1c and S10). All bands are quite intense ( $\epsilon \gg 1000\text{ M}^{-1}\text{ cm}^{-1}$ ) as compared to typical metal-centered transitions, suggesting significant CT character. These intense CT bands conceal the weaker Laporte-forbidden d–d transitions, preventing their observation and hence experimental determination of  $\Delta_o$ . To assign the absorption bands and to obtain the excited-state level ordering including the MC states, quantum chemical calculations were performed (Tables S1–S4).

**Static Quantum Chemical Calculations.** The overall geometry of  $[V(ddpd)_2]^{3+}$  is well reproduced by unrestricted Kohn–Sham Density Functional Theory (DFT-UKS) calculations (CPCM(acetonitrile)-RIJCOSX-UB3LYP-D3BJ-

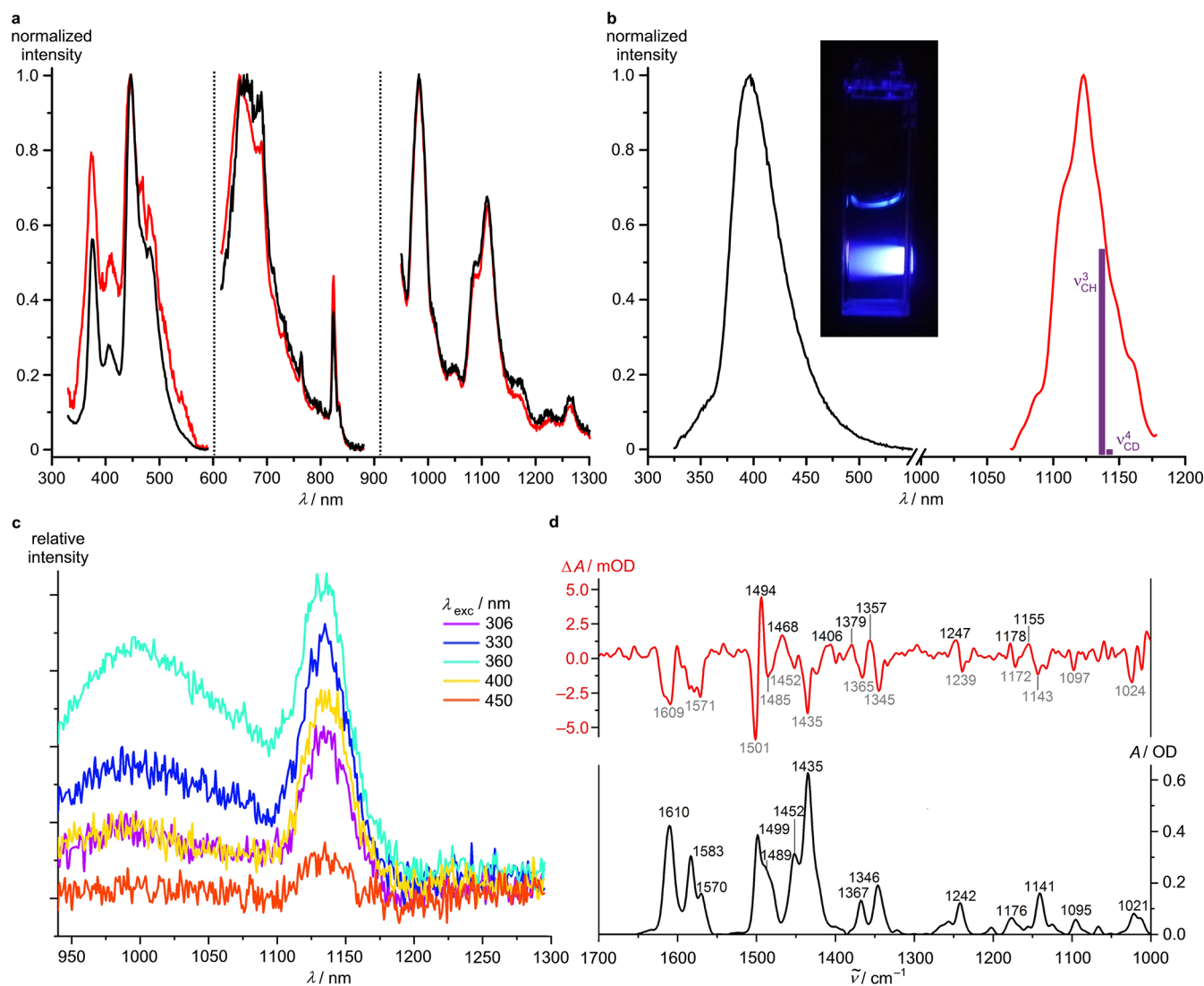


**Figure 2.** (a) Normalized luminescence spectra of  $[\text{V}(\text{ddpd})_2][\text{PF}_6]_3$  (black) and  $[\text{V}([\text{D}_{17}\text{-ddpd}]_2)[\text{PF}_6]_3$  (red) ( $\lambda_{\text{exc}} = 306$  nm,  $n\text{-BuCN}$ , 77 K). Intensities in the different spectral regions are not to scale due to different detectors and gratings used. GG455 and RG850 long pass filters were employed for the low-energy spectra, respectively. (b) Normalized luminescence spectra of  $[\text{V}(\text{ddpd})_2][\text{PF}_6]_3$  ( $\lambda_{\text{exc}} = 306$  nm,  $\text{CD}_3\text{CN}$ , 298 K). Intensities in the different spectral regions are not to scale due to different detectors and gratings used. The integral ratio of the two bands amounts to  $I(\text{VIS}):I(\text{NIR}) = 2.1:1.8 \times 10^{-4}$ . Purple vertical bars indicate relevant CH and CD overtones. Their length approximately illustrates the  $\nu^3_{\text{CH}}:\nu^4_{\text{CD}}$  intensity ratio.<sup>13</sup> The photograph illustrates the blue fluorescence of  $[\text{V}(\text{ddpd})_2][\text{PF}_6]_3$  ( $\lambda_{\text{exc}} = 350$  nm,  $\text{CH}_3\text{CN}$ , 298 K). (c) Luminescence spectra of  $[\text{V}(\text{ddpd})_2][\text{PF}_6]_3$  ( $\lambda_{\text{exc}} = 306\text{--}450$  nm, butyronitrile glass, 20 K). (d) Ground-state FTIR (black) and step-scan FTIR spectra (red) of  $[\text{V}(\text{ddpd})_2][\text{PF}_6]_3$  at 20 K ( $\lambda_{\text{exc}} = 355$  nm, KBr pellet, 0–300 ns).

ZORA/def2-TZVPP) with a maximum deviation in V–N bond lengths of 0.028 Å and N–V–N bond angles of 1.3° (Table S1; octahedral shape parameter  $S(\text{OC-6}) = 0.68$ ). Mulliken spin population analysis yields 2.07 at the vanadium center, similar to that calculated for  $[\text{V}(\text{bpy})_3]^{3+}$  (2.11),<sup>47</sup> accounting for the two unpaired electrons.

To assign the intense CT bands, time-dependent DFT-UKS calculations at the same level of theory were employed (Tables S3 and S4; Figure 1c). The absorption band at 597 nm corresponds to  ${}^3\text{LMCT}$  transitions from the bridging nitrogen atoms to vanadium (calcd 631/616 nm; Figure 1c,d). The shoulder and bands between 500 and 390 nm originate from  ${}^3\text{LMCT}$  transitions as well (calcd 503, 453, 444 nm; Figure 1c,d). The  ${}^3\text{T}_{1g} \rightarrow {}^3\text{T}_{2g}$  ligand field transition (in octahedral symmetry) is split due to the lower symmetry (calcd 441 and 413 nm) and superimposed onto the stronger  ${}^3\text{LMCT}$  bands

in this spectral region (Figure 1c). As compared to vanadium(III) complexes with oxygen donor ligands, for example,  $\text{V}(\text{acac})_3$ ,<sup>37–41,48</sup> the ligand field splitting of  $[\text{V}(\text{ddpd})_2]^{3+}$  ( $\Delta_o \approx 23\,440$   $\text{cm}^{-1}$ ) is larger by more than 2500  $\text{cm}^{-1}$ , confirming our conceptual approach of using ddpd as a strong ligand to prevent back-ISC.<sup>46</sup>

Expectedly, the  ${}^3\text{T}_{1g}$  ground state splits as well, and yet the TD-DFT-UKS calculated energy gaps are unreasonably large (Table S3). To better describe the MC triplet and singlet states (Figure 1e) and the ground-state splitting, complete-active-space self-consistent field (CASSCF) calculations including spin–orbit coupling (SOC for estimation of the zero-field splitting  $D$ ) in conjunction with fully internally contracted N-electron valence perturbation theory to second-order (FIC-NEVPT2) CASSCF(6,12)-FIC-NEVPT2 on optimized  $[\text{V}(\text{ddpd})_2]^{3+}$  were performed (Tables S5, S6 and Figure S11).<sup>39,48</sup> Figure 1d depicts the calculated order of



these MC triplet and singlet states derived from CASSCF-NEVPT2 and the  $^3\text{LMCT}$  states derived from TD-DFT-UKS calculations. The  $^3\text{T}_{1g}$  ground state splits with  $\Delta E = 1873$  and  $2687\text{ cm}^{-1}$ , while the lowest excited triplet state  $^3\text{T}_{2g}$  splits into  $20\,844$ ,  $22\,706$ , and  $22\,803\text{ cm}^{-1}$ . The zero-field splitting was calculated as  $D_{\text{calcd}} = +6.8\text{ cm}^{-1}$ , larger than the experimental value  $D_{\text{exp}} = +2.87(11)\text{ cm}^{-1}$ , yet similar to the experimental and calculated data of  $\text{V}(\text{acac})_3$  ( $D_{\text{exp}} = +6.9\text{ cm}^{-1}$ ;  $D_{\text{calcd}} = +9.6\text{ cm}^{-1}$ ).<sup>48</sup>

A series of five singlet states originating from the  $^1\text{T}_{2g}$  and  $^1\text{E}_g$  terms is located between the triplet ground and excited states. This excited-state ordering confirms the large ligand field splitting with  $\Delta_o > 17.3 B$ . The two lowest singlet states centered at  $9612$  and  $9736\text{ cm}^{-1}$  (Figure S11) are only weakly split by  $\Delta E = 124\text{ cm}^{-1}$ . A sixth (isolated) singlet state ( $^1\text{A}_{1g}$ ) is predicted at  $23\,283\text{ cm}^{-1}$ , slightly above the highest level of the  $^3\text{T}_{2g}$  states by  $480\text{ cm}^{-1}$ . This calculation suggests that  $\Delta_o$  is slightly smaller than  $36.6 B$  (in a standard Tanabe–Sugano diagram with  $C/B = 4.42$ , Figure S1). The combined TD-DFT-UKS and CASSCF-NEVPT2 calculations indicate that several states ( $^3\text{LMCT}$ ,  $^3\text{T}_{2g}$ , and  $^1\text{A}_{1g}$ ) lie in the  $3.1$ – $2.6\text{ eV}$  ( $400$ – $480\text{ nm}$ ) region.

### Steady-State and Time-Resolved Spectroscopy.

Steady-state emission spectra with excitation at  $306\text{ nm}$  ( $4.05\text{ eV}$ ) at  $77\text{ K}$  in a valeronitrile glass matrix show rich spectral features between  $370$  and  $1150\text{ nm}$  (Figure 2a). Obviously, several states are emissive upon high-energy excitation. The NIR-II emission is also observed in butyronitrile glass at  $10\text{ K}$  with excitation wavelengths between  $306$  and  $450\text{ nm}$ . The highest intensity occurs at an excitation wavelength of  $360\text{ nm}$ , where the luminescence is twice as strong as that at  $306\text{ nm}$  excitation, while the luminescence almost vanishes when exciting with  $450\text{ nm}$  (Figure 2c). Tuning the excitation wavelength populates different electronically excited triplet states, which might exhibit different ISC efficiencies as sketched in Figure 1d and consequently lead to different phosphorescence intensities. In the solid state (KBr pellet; Figure S14a,b), the NIR-II emission is not observed, probably resulting from self-quenching. The emission in solution is sensitive to the presence of oxygen. A biexponential lifetime of several hundred nanoseconds is associated with the sharp NIR emission bands at  $1100\text{ nm}$  ( $790\text{ ns}$  ( $93\%$ ),  $8800\text{ ns}$  ( $7\%$ ), Table S7 and Figure S12). The long lifetime is in a similar range as compared to the excited singlet state lifetime reported for  $\text{V}^{3+}$  doped in  $\text{NaMgAl}(\text{ox})_3$  at  $11\text{ K}$  ( $\tau < 500\text{ ns}$ ).<sup>41</sup> All emission bands show vibrational progression, while the ground-state splitting might also account for the observed pattern.

On the basis of the quantum chemical calculations (Figure 1d), the emission energies, and the lifetimes (Figures S12, S13 and Table S7), we assign the high-energy emission bands ( $374$ ,  $447$ , and  $660\text{ nm}$ ) and the NIR-I/NIR-II emission bands ( $982$  and  $1088/1109\text{ nm}$ ) to fluorescence and phosphorescence, respectively. The NIR-I and NIR-II phosphorescence originates from the two almost degenerate lowest excited singlet states (with  $^1\text{E}_g$  and  $^1\text{T}_{2g}$  parentage) decaying radiatively to the split ground-state levels (Figure 1d). From these NIR-I/NIR-II phosphorescence bands, the experimental ground-state splitting is estimated as  $1080\text{ cm}^{-1}$  (averaged  $1088/1109\text{ nm}$ ), which is somewhat smaller than that obtained by the CASSCF-NEVPT2 calculations ( $1873\text{ cm}^{-1}$ ; Figure 1d). As a reference, a splitting of  $880\text{ cm}^{-1}$  was calculated for  $\text{V}(\text{acac})_3$  by SOC-CASSCF(12,10)-NEVPT2,<sup>48</sup> while a value of  $1400\text{ cm}^{-1}$  was

experimentally determined for  $[\text{V}(\text{urea})_6][\text{ClO}_4]_3$ .<sup>40</sup> Excitation of  $^3\text{LMCT}$  states at lower energy ( $600\text{ nm}$ ) does not lead to the NIR-II luminescence, demonstrating that these  $^3\text{LMCT}$  states do not efficiently evolve to the emissive singlet states (Figure 1d).

In diluted deaerated  $\text{CD}_3\text{CN}$  solution, dual emission at  $396$  and  $1109/1123\text{ nm}$  occurs even at  $298\text{ K}$  upon excitation at  $306\text{ nm}$  (Figure 2b). The high-energy blue emission is even observable by the naked eye at room temperature in solution and in a KBr pellet (Figures 2b and S14c). The quantum yield of the high energy fluorescence is very high with  $\Phi = 2.1\%$  and surpasses the quantum yield of the blue emission of the recently reported blue emissive cobalt(III) complexes ( $\Phi = 0.7/0.4\%$ ).<sup>8</sup> The emission decay at  $396\text{ nm}$  is biexponential with  $\tau_{396}$  of  $3.2$  ( $56\%$ ) and  $8.2$  ( $44\%$ ) ns and  $1.7$  ( $51\%$ ) and  $6.3$  ( $49\%$ ) ns at  $298$  and  $77\text{ K}$ , respectively. We assign this fluorescence to  $^3\text{T}_{1g}(\text{P}) \rightarrow ^3\text{T}_{1g}$  or to  $^3\text{LMCT}$  transitions (Figure 1d). Indeed, two  $^3\text{LMCT}$  states are calculated around  $3\text{ eV}$  by TD-DFT calculations and  $^3\text{T}_{2g}(\text{P})$  states around  $3.46\text{ eV}$  by CASSCF-NEVPT2 calculations, which could account for the biexponential decay as sketched in Figure 1d with blue vertical arrows (Tables S3 and S6).

Beyond the intense blue emission of  $[\text{V}(\text{ddpd})_2][\text{PF}_6]_3$ , the observed room-temperature NIR-II phosphorescence of  $[\text{V}(\text{ddpd})_2][\text{PF}_6]_3$  in solution is unique. The NIR quantum yield of  $\Phi = 1.8 \times 10^{-4}\%$  is not very high, but the rather sharp emission band (fwhm ca.  $325\text{ cm}^{-1}$ ) is clearly observable. To the best of our knowledge, no other complexes with Earth-abundant metal ions display NIR-II luminescence in frozen and in fluid solution (Figure 2a–c). The ground-state splitting of the  $^3\text{T}_{1g}$  levels (Figure 1d) rather than vibrational progression likely accounts for the asymmetric band shape. This differs from NIR emission bands of chromium(III) complexes, which possess an orbitally nondegenerate ground state ( $^4\text{A}_g$ ) and consequently deliver sharp phosphorescence bands.<sup>12–17</sup>

To obtain information on the long-lived excited singlet states, the complex (in a KBr pellet) was excited with  $355\text{ nm}$  at  $20\text{ K}$  and probed by step-scan FT-IR spectroscopy. The measured FTIR ground-state spectrum is in excellent agreement with the DFT-UKS calculated spectrum of  $[\text{V}(\text{ddpd})_2]^{3+}$  (Figure S15). The recorded step-scan difference spectrum collected between  $0$  and  $300\text{ ns}$  after the pulse shows the ground-state bleach (negative bands) and excited-state absorption (positive bands) (Figure 2d). The latter vibrational bands correspond to the lowest energy long-lived singlet state. A monoexponential lifetime of about  $290\text{ ns}$  was determined by performing a global exponential fit for the most prominent positive and negative peaks in the step-scan difference spectrum (Figure S16). The observation of step-scan FTIR spectra further confirms the presence of long-lived excited states.

The lifetime of this emissive excited state depends on the efficiency of nonradiative decay processes. Especially, NIR luminescence is prone to multiphonon relaxation via CH overtones, which could be diminished by deuteration.<sup>13,32,33</sup> Indeed, the second aromatic CH overtone ( $\nu^3_{\text{CH}} = 8972\text{ cm}^{-1}$ ) as estimated from CH overtone IR spectroscopy of  $6,6'$ -dimethyl-2,2'-bipyridine<sup>13</sup> has a significant spectral overlap with the NIR-II emission bands of  $[\text{V}(\text{ddpd})_2][\text{PF}_6]_3$  (Figure 2b). For the deuterated derivative, the third CD overtone at  $\nu^4_{\text{CD}} = 8755\text{ cm}^{-1}$  is the most relevant one (Figure 2b).<sup>13</sup> Because of the lower energy and lower extinction coefficient of

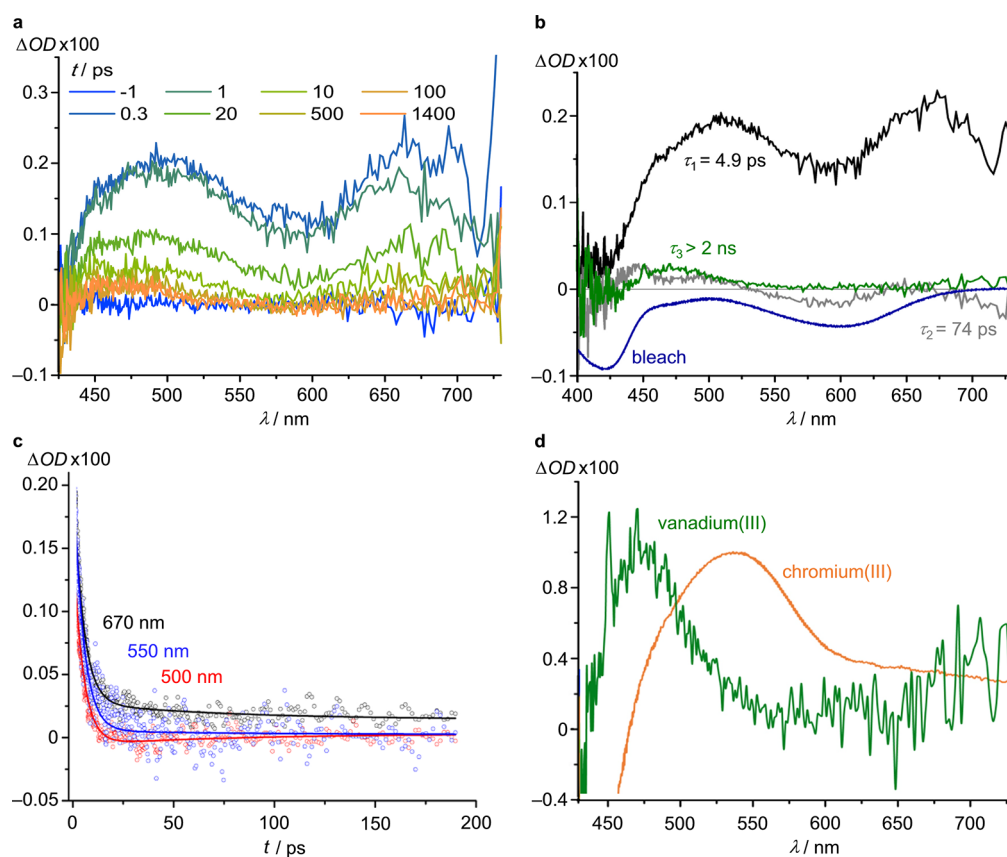


**Figure 3.** Femtosecond-transient absorption spectroscopy of  $[\text{V}(\text{ddpd})_2][\text{PF}_6]_3$ . (a) Transient absorption spectra of  $[\text{V}(\text{ddpd})_2][\text{PF}_6]_3$  in  $\text{CH}_3\text{CN}$  excited with 400 nm laser pulses. (b) Bleach (blue) and decay associated amplitude spectra labeled with the corresponding time constants:  $\tau_1 = 4.9$  ps ( $\sim 70\%$ , black),  $\tau_2 = 74$  ps ( $\sim 20\%$ , gray), and long-living component with a time constant  $\tau_3 > 2$  ns ( $\sim 10\%$ , green). (c) Transient signals as a function of the pump–probe delay time observed at 670 nm (black), 550 nm (blue), and 500 nm (red). The fits to the experimental data correspond to triexponential decays with  $\tau_{1,2} = 4.9, 74$  ps and a time constant  $\tau_3 > 2$  ns. (d) Scaled amplitude spectra of the long-lived components of  $[\text{V}(\text{ddpd})_2][\text{PF}_6]_3$  (green) and  $[\text{Cr}(\text{ddpd})_2][\text{BF}_4]_3$  (orange) (chromium(III) data from ref 49).

the third CD overtone  $\nu_{\text{CD}}^4$ , the spectral overlap with the vanadium NIR-II emission band should be smaller. Consequently, the nonradiative rate constant for the deuterated complex should be smaller than that for the protio derivative. As long as this multiphonon pathway dominates the decay of the singlet states, the NIR quantum yield and lifetime of  $[\text{V}([\text{D}_{17}]\text{-ddpd})_2]^{3+}$  should be larger than those of  $[\text{V}(\text{ddpd})_2]^{3+}$ . However, within experimental uncertainty, we cannot observe significant differences between the NIR emission intensities and lifetimes of  $[\text{V}([\text{D}_{17}]\text{-ddpd})_2]^{3+}$  and  $[\text{V}(\text{ddpd})_2]^{3+}$  at 298 and 77 K (Figures S12, S13, S17, S18 and Table S7). This suggests that other nonradiative pathways dominate the decay of the lowest energy singlet states in  $[\text{V}(\text{ddpd})_2]^{3+}$ . Presumably, the split ground-state levels favor ISC to the ground state (Figure 1d).

The dual emission of  $[\text{V}(\text{ddpd})_2][\text{PF}_6]_3$  in the blue and NIR-II spectral region demonstrates the huge energy difference of ca. 2 eV between these two luminescent states. The observed intense fluorescence of  $[\text{V}(\text{ddpd})_2]^{3+}$  suggests that the ISC rates from the triplets to the singlets are not particularly large. This slow ISC then opens other pathways (fluorescence, nonradiative decay from the triplets) before the singlet states are populated to higher extents.

The initial dynamics was then probed by fs-transient absorption (TA) spectroscopy. TA spectra of  $[\text{V}(\text{ddpd})_2][\text{PF}_6]_3$  in  $\text{CH}_3\text{CN}$  recorded after excitation with femtosecond laser pulses at 620 nm ( $\sim 2$  eV) show excited-state absorptions

(ESA) at around 500 and 670 nm (Figure S19). With a time constant of 6.3 ps, the ground state is essentially recovered. Hence, the  $^3\text{LMCT}$  states do not significantly evolve to the emissive singlets as was already demonstrated by the steady-state luminescence data. This is consistent with the assumption that efficient ISC requires a high density of final states in the energy region of interest.<sup>45</sup> Around 2 eV, such singlet states are unavailable for  $[\text{V}^{\text{III}}(\text{ddpd})_2]^{3+}$  (Figure 1d). However, a singlet state is present at higher energy ( $^1\text{A}_{1g}$ , 2.89 eV from the CASSCF-NEVPT2 calculation; Figure 1d).

TA spectra recorded after excitation at 400 nm (3.1 eV;  $^3\text{LMCT}$  and  $^3\text{T}_{2g}$  states) exhibit a dominant ultrafast decay to the ground state with a time constant of 4.9 ps and a second weaker time constant of 74 ps (Figures 3 and S20). On the nanosecond time scale, a small component persists showing an excited-state absorption around 460 nm (Figure 3c and d). We assign this component to the long-lived singlet state(s), similar to the analogous amplitude spectrum of  $[\text{Cr}(\text{ddpd})_2]^{3+}$ , representing its emissive doublet states, at longer times scales (Figure 3d).<sup>49</sup> These results agree with the observation that a small fraction of the triplet population evolves to the singlet states via ISC. Obviously, the low-energy  $^3\text{LMCT}$  states are less competent to feed the spin-flip singlet states than the  $^3\text{T}_{2g}$  and higher energy  $^3\text{LMCT}$  states. Conceptually, the energy tuning of  $^3\text{LMCT}$  and  $^3\text{T}_{2g}$  states as well as identification of suitable antenna systems should enable an even more efficient

population of the emissive singlet states of vanadium(III) complexes.

**Molecular Dynamics Calculations.** To gain deeper insight into the complex spin-flip dynamics of  $[\text{V}(\text{ddpd})_2]^{3+}$  after excitation, dynamics simulations starting from the  $^3\text{LMCT}$  manifold in acetonitrile were performed. Specifically, nonadiabatic surface hopping including arbitrary couplings (SHARC) dynamics simulations with a linear vibronic coupling (LVC) model were employed.<sup>50</sup> Initially, 100 fs was propagated from the four lowest  $^3\text{LMCT}$  states located at 3.5–3.7 eV (354–333 nm) (Table S3 and Figures S21, S22), where we found one  $^3\text{LMCT}$  state with a significant amount of trapped population. Subsequently and starting from this state ( $2^3\text{LMCT}$ ) located at 3.59 eV (345 nm), we propagated during 50 000 fs and observed IC to the  $^3\text{MC}$  states ( $^3\text{T}_{2g}$  and  $^3\text{T}_{1g}$  ground states) and ISC to a singlet state  $2^1\text{MC}$  (Figures 1d and 4).

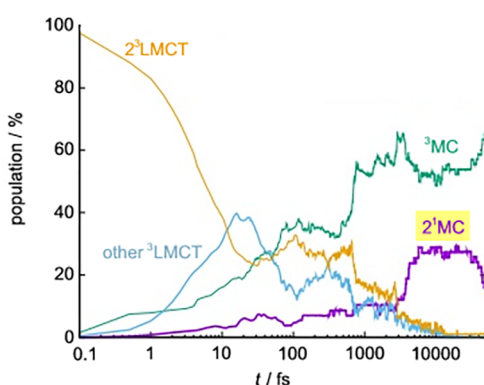


**Figure 4.** Time-evolution of the population of the excited states during 50 000 fs (in logarithmic scale) after starting the dynamics on the  $2^3\text{LMCT}$  state (the longest lived triplet state after 100 fs, Figure S22). The label “other  $^3\text{LMCT}$ ” stands for the population in any other state except for the  $2^3\text{LMCT}$ . The label “ $^3\text{MC}$ ” corresponds to the sum of populations in every triplet MC state, indicating the total amount of internal conversion. Population in any other singlet state except for  $2^1\text{MC}$  is negligible and not plotted.

The singlet  $^1\text{LMCT}$  manifold acts as a mere spectator during the dynamics. The most populated metal-centered singlet state  $2^1\text{MC}$  was then optimized within the LVC method. The optimized geometry (Table S8) lies 1.10 eV (1127 nm) above the  $^3\text{T}_{1g}$  ground state, in very good agreement with the experimental emission energy, thus validating the dynamical approach. The dynamics calculations confirm that the  $2^3\text{LMCT}$  state at high energy (3.59 eV) undergoes ISC to a singlet state of MC character, while no lower energy  $^1\text{LMCT}$  states around 2 eV are involved in the excited-state evolution toward the emissive  $^1\text{MC}$  state, as was already suggested by the steady-state and time-resolved experimental data.

## CONCLUSION

Our study extends the very series of luminescent metal complexes with Earth-abundant 3d metal ions (Cr, Fe, Co, Cu) to the early 3d transition metal vanadium. The vanadium(III) complex  $\text{mer-}[\text{V}(\text{ddpd})_2]^{3+}$  with a tuned large ligand field splitting exhibits a deep-blue emission at room temperature in solution and a long-lived phosphorescence above 1000 nm. This expands the spectral region previously accessible with 3d metal complexes (vis and NIR-I) to the

NIR-II region for the first time. Conceptual design principles for NIR-II luminescent vanadium(III) complexes evolved, highlighting the distinct roles of ligand-to-metal charge transfer states, intersystem crossing, and multiphonon relaxation. This first success in designing blue and NIR-II emissive complexes of the Earth-abundant metal vanadium raises the prospect of employing luminescent vanadium complexes in the future. Especially, dual emissive complexes could find applications as optical probes with a built-in internal reference for chemical or physical perturbations. Work in this direction is currently in progress.

## ASSOCIATED CONTENT

### Supporting Information

The Supporting Information is available free of charge at <https://pubs.acs.org/doi/10.1021/jacs.0c02122>.

Data of quantum chemical calculations, synthetic procedures, and analytical and spectroscopic data of  $[\text{V}(\text{ddpd})_2][\text{PF}_6]_3$  (PDF)

X-ray crystallographic data for  $\text{mer-}[\text{V}(\text{ddpd})_2][\text{PF}_6]_3 \times 3\text{CH}_3\text{CN}$  (CIF)

## AUTHOR INFORMATION

### Corresponding Authors

**Markus Gerhards** – Department of Chemistry and Research Center Optimas, TU Kaiserslautern, Kaiserslautern 67663, Germany; [orcid.org/0000-0002-8748-2940](https://orcid.org/0000-0002-8748-2940); Email: [gerhards@chemie.uni-kl.de](mailto:gerhards@chemie.uni-kl.de)

**Michael Seitz** – Institute of Inorganic Chemistry, University of Tübingen, Tübingen 72076, Germany; [orcid.org/0000-0002-9313-2779](https://orcid.org/0000-0002-9313-2779); Email: [michael.seitz@uni-tuebingen.de](mailto:michael.seitz@uni-tuebingen.de)

**Katja Heinze** – Department of Chemistry, Johannes Gutenberg University of Mainz, Mainz 55128, Germany; [orcid.org/0000-0003-1483-4156](https://orcid.org/0000-0003-1483-4156); Email: [katja.heinze@uni-mainz.de](mailto:katja.heinze@uni-mainz.de)

### Authors

**Matthias Dorn** – Department of Chemistry, Johannes Gutenberg University of Mainz, Mainz 55128, Germany

**Jens Kalmbach** – Institute of Inorganic Chemistry, University of Tübingen, Tübingen 72076, Germany

**Pit Boden** – Department of Chemistry and Research Center Optimas, TU Kaiserslautern, Kaiserslautern 67663, Germany

**Ayla Pöpcke** – Institute for Physics and Department of Life, Light and Matter, University of Rostock, Rostock 18051, Germany

**Sandra Gómez** – Institute of Theoretical Chemistry, Faculty of Chemistry, University of Vienna, Vienna 1090, Austria

**Christoph Förster** – Department of Chemistry, Johannes Gutenberg University of Mainz, Mainz 55128, Germany

**Felix Kuczelinis** – Department of Chemistry, Johannes Gutenberg University of Mainz, Mainz 55128, Germany

**Luca M. Carrella** – Department of Chemistry, Johannes Gutenberg University of Mainz, Mainz 55128, Germany

**Laura A. Büldt** – Institute of Inorganic Chemistry, University of Tübingen, Tübingen 72076, Germany

**Nicolas H. Bings** – Department of Chemistry, Johannes Gutenberg University of Mainz, Mainz 55128, Germany

**Eva Rentschler** – Department of Chemistry, Johannes Gutenberg University of Mainz, Mainz 55128, Germany; [orcid.org/0000-0003-1431-3641](https://orcid.org/0000-0003-1431-3641)



Stefan Lochbrunner – Institute for Physics and Department of Life, Light and Matter, University of Rostock, Rostock 18051, Germany

Leticia González – Institute of Theoretical Chemistry, Faculty of Chemistry, University of Vienna, Vienna 1090, Austria;

orcid.org/0000-0001-5112-794X

Complete contact information is available at:  
<https://pubs.acs.org/10.1021/jacs.0c02122>

## Notes

The authors declare no competing financial interest.

## ACKNOWLEDGMENTS

Financial support from the Deutsche Forschungsgemeinschaft [DFG, Priority Program SPP 2102 “Light-controlled reactivity of metal complexes” (GE 961/10-1, HE 2778/15-1, LO 714/11-1, SE 1448/8-1, GO 1059/8-1)] is gratefully acknowledged. Parts of this research were conducted using the supercomputer Mogon and advisory services offered by Johannes Gutenberg University Mainz (<https://hpc.uni-mainz.de>), which is a member of the AHRP and the Gauss Alliance e.V. as well as at the Vienna Scientific Cluster (VSC3).

## REFERENCES

- (1) (a) Wenger, O. S. Photoactive Complexes with Earth-Abundant Metals. *J. Am. Chem. Soc.* **2018**, *140*, 13522–13533. (b) Förster, C.; Heinze, K. Photophysics and photochemistry with Earth-abundant metals - fundamentals and concepts. *Chem. Soc. Rev.* **2020**, *49*, 1057–1070.
- (2) Otto, S.; Dorn, M.; Förster, C.; Bauer, M.; Seitz, M.; Heinze, K. Understanding and Exploiting Long-lived Near-infrared Emission of a Molecular Ruby. *Coord. Chem. Rev.* **2018**, *359*, 102–111.
- (3) Bizzarria, C.; Spuling, E.; Knoll, D. M.; Volz, D.; Bräse, S. Sustainable metal complexes for organic light-emitting diodes (OLEDs). *Coord. Chem. Rev.* **2018**, *373*, 49–82.
- (4) McCusker, J. K. Electronic structure in the transition metal block and its implications for light harvesting. *Science* **2019**, *363*, 484–488.
- (5) Wagenknecht, P. S.; Ford, P. C. Metal centered ligand field excited states: Their roles in the design and performance of transition metal based photochemical molecular devices. *Coord. Chem. Rev.* **2011**, *255*, 591–616.
- (6) Zhang, W.; Alonso-Mori, R.; Bergmann, U.; Bressler, C.; Chollet, M.; Galler, A.; Gawelda, W.; Hadt, R. G.; Hartssock, R. W.; Kroll, T.; Kjær, K. S.; Kubiček, K.; Lemke, H. T.; Liang, H. W.; Meyer, D. A.; Nielsen, M. M.; Purser, C.; Robinson, J. S.; Solomon, E. I.; Sun, Z.; Sokaras, D.; van Driel, T. B.; Vankó, G.; Weng, T. C.; Zhu, D.; Gaffney, K. J. Tracking excited-state charge and spin dynamics in iron coordination complexes. *Nature* **2014**, *15*, 345–348.
- (7) Büldt, L. A.; Guo, X.; Vogel, R.; Prescimone, A.; Wenger, O. S. A Tris(diisocyanide)chromium(0) Complex Is a Luminescent Analog of Fe(2,2'-Bipyridine)<sub>3</sub><sup>2+</sup>. *J. Am. Chem. Soc.* **2017**, *139*, 985–992.
- (8) Pal, A. K.; Li, C.; Hanan, G. S.; Zysman-Colman, E. Blue Emissive Cobalt(III) Complexes and Their Use in the Photocatalytic Trifluoromethylation of Polycyclic Aromatic Hydrocarbons. *Angew. Chem., Int. Ed.* **2018**, *57*, 8027–8031.
- (9) Chábera, P.; Liu, Y.; Prakash, O.; Thyrahaug, E.; El Nahhas, A.; Honarfar, A.; Essén, S.; Fredin, L. A.; Harlang, T. C. B.; Kjær, K. S.; Handrup, K.; Ericson, F.; Tatsuno, H.; Morgan, K.; Schnadt, J.; Häggström, L.; Ericsson, T.; Sobkowiak, A.; Lidin, S.; Huang, P.; Styring, S.; Uhlig, J.; Bendix, J.; Lomoth, R.; Sundström, V.; Persson, P.; Wärnmark, K. A low-spin Fe(III) complex with 100-ps ligand-to-metal charge transfer photoluminescence. *Nature* **2017**, *543*, 695–699.
- (10) Kjær, K. S.; Kaul, N.; Prakash, O.; Chábera, P.; Rosemann, N. W.; Honarfar, A.; Gordivska, O.; Fredin, L. A.; Bergquist, K.-E.; Häggström, L.; Ericsson, T.; Lindh, L.; Yartsev, A.; Styring, S.; Huang, P.; Uhlig, J.; Bendix, J.; Strand, D.; Sundström, V.; Persson, P.; Lomoth, R.; Wärnmark, K. Luminescence and reactivity of a charge-transfer excited iron complex with nanosecond lifetime. *Science* **2019**, *363*, 249–253.
- (11) Hamze, R.; Peltier, J. L.; Sylvinson, D.; Jung, M.; Cardenas, J.; Haiges, R.; Soleilhavoup, M.; Jazzar, R.; Djurovich, P. I.; Bertrand, G.; Thompson, M. E. Eliminating nonradiative decay in Cu(I) emitters: > 99% quantum efficiency and microsecond lifetime. *Science* **2019**, *36*, 601–606.
- (12) Otto, S.; Grabolle, M.; Förster, C.; Kreitner, C.; Resch-Genger, U.; Heinze, K. [Cr(ddpd)<sub>2</sub>]<sup>3+</sup>: A molecular, water-soluble, highly NIR-emissive ruby analogue. *Angew. Chem., Int. Ed.* **2015**, *54*, 11572–11576.
- (13) Wang, C.; Otto, S.; Dorn, M.; Kreidt, E.; Lebon, J.; Sršan, L.; Di Martino-Fumo, P.; Gerhards, M.; Resch-Genger, U.; Seitz, M.; Heinze, K. Deuterated Molecular Ruby with Record Luminescence Quantum Yield. *Angew. Chem., Int. Ed.* **2018**, *57*, 1112–1116.
- (14) Otto, S.; Förster, C.; Wang, C.; Resch-Genger, U.; Heinze, K. A strongly luminescent chromium(III) complex acid. *Chem. - Eur. J.* **2018**, *24*, 12555–12563.
- (15) Otto, S.; Harris, J.; Heinze, K.; Reber, C. Molecular ruby under pressure. *Angew. Chem., Int. Ed.* **2018**, *57*, 11069–11073.
- (16) Treiling, S.; Wang, C.; Förster, C.; Reichenauer, F.; Kalmbach, J.; Boden, P.; Harris, J. P.; Carrella, L. M.; Rentschler, E.; Resch-Genger, U.; Reber, C.; Seitz, M.; Gerhards, M.; Heinze, K. Luminescence and Light-driven Energy and Electron Transfer from an Exceptionally Long-lived Excited State of a Non-innocent Chromium(III) Complex. *Angew. Chem., Int. Ed.* **2019**, *58*, 18075–18085.
- (17) (a) Jiménez, J. R.; Doistau, B.; Cruz, C. M.; Besnard, C.; Cuerva, J. M.; Campaña, A. G.; Piguet, C. Chiral Molecular Ruby [Cr(dqp)<sub>2</sub>]<sup>3+</sup> with Long-Lived Circularly Polarized Luminescence. *J. Am. Chem. Soc.* **2019**, *141*, 13244–13252. (b) Dee, C.; Zinna, F.; Kitzmann, W. R.; Pescitelli, G.; Heinze, K.; Di Bari, L.; Seitz, M. Strong Circularly Polarized Luminescence of an Octahedral Chromium(III) Complex. *Chem. Commun.* **2019**, *55*, 13078–13081.
- (18) (a) Bünzli, J.-C. G.; Eliseeva, S. V. Lanthanide NIR luminescence for telecommunications, bioanalyses and solar energy conversion. *J. Rare Earths* **2010**, *28*, 824–842. (b) Bünzli, J.-C. G. Lanthanide light for biology and medical diagnosis. *J. Lumin.* **2016**, *170*, 866–878.
- (19) Ibrahim-Ouali, M.; Dumur, F. Recent Advances on Metal-Based Near-Infrared and Infrared Emitting OLEDs. *Molecules* **2019**, *24*, 1412.
- (20) Ye, H. Q.; Li, Z.; Peng, Y.; Wang, C. C.; Li, T. Y.; Zheng, Y. X.; Sapelkin, A.; Adamopoulos, G.; Hernández, I.; Wyatt, P. B.; Gillin, W. P. Organo-erbium systems for optical amplification at telecommunications wavelengths. *Nat. Mater.* **2014**, *13*, 382–386.
- (21) Carlos, L. D.; Ferreira, R. A. S.; Bermudez, V. D. Z.; Ribeiro, S. J. L. Lanthanide-Containing Light-Emitting Organic-Inorganic Hybrids: A Bet on the Future. *Adv. Mater.* **2009**, *21*, 509–534.
- (22) Foucault-Collet, A.; Gogick, K. A.; White, K. A.; Villette, S.; Pallier, A.; Collet, G.; Kieda, C.; Li, T.; Geib, S. J.; Rosi, N. L.; Petoud, S. Lanthanide near infrared imaging in living cells with Yb<sup>3+</sup> nano metal organic frameworks. *Proc. Natl. Acad. Sci. U. S. A.* **2013**, *110*, 17199–17204.
- (23) Yang, Q.; Hu, Z.; Zhu, S.; Ma, R.; Ma, H.; Ma, Z.; Wan, H.; Zhu, T.; Jiang, Z.; Liu, W.; Jiao, L.; Sun, H.; Liang, Y.; Dai, H. Donor Engineering for NIR-II Molecular Fluorophores with Enhanced Fluorescent Performance. *J. Am. Chem. Soc.* **2018**, *140*, 1715–1724.
- (24) Cai, Y.; Wei, Z.; Song, C.; Tang, C.; Han, W.; Dong, X. Optical nano-agents in the second near-infrared window for biomedical applications. *Chem. Soc. Rev.* **2019**, *48*, 22–37.
- (25) Zhang, M.; Zheng, W.; Liu, Y.; Huang, P.; Gong, Z.; Wei, J.; Gao, Y.; Zhou, S.; Li, X.; Chen, X. A New Class of Blue-LED-Excitable NIR-II Luminescent Nanoprobes Based on Lanthanide-Doped CaS Nanoparticles. *Angew. Chem., Int. Ed.* **2019**, *58*, 9556–9560.

- (26) Zhu, S.; Yung, B. C.; Chandra, S.; Niu, G.; Antaris, A. L.; Chen, X. Near Infrared-II (NIR-II) Bioimaging via Off-Peak NIR-I Fluorescence Emission. *Theranostics* **2018**, *8*, 4141–4151.
- (27) Wang, P.; Fan, Y.; Lu, L.; Liu, L.; Fan, L.; Zhao, M.; Xie, Y.; Xu, C.; Zhang, F. NIR II nanoprobe in-vivo assembly to improve image-guided surgery for metastatic ovarian cancer. *Nat. Commun.* **2018**, *9*, 2898.
- (28) Schulze, M.; Steffen, A.; Würthner, F. Near IR Phosphorescent Ruthenium(II) and Iridium(III) Perylene Bisimide Metal Complexes. *Angew. Chem., Int. Ed.* **2015**, *54*, 1570–1573.
- (29) Bünzli, J.-C. G.; Eliseeva, S. V. Basics of Lanthanide Photophysics. In *Lanthanide Luminescence: Photophysical, Analytical and Biological Aspects*; Hänninen, P., Härmä, H., Eds.; Springer-Verlag: Berlin Heidelberg, 2010.
- (30) Englman, R.; Jortner, J. The energy gap law for radiationless transitions in large molecules. *Mol. Phys.* **1970**, *18*, 145–164.
- (31) Casper, J. V.; Kober, E. M.; Sullivan, B. P.; Meyer, T. J. Application of the Energy Gap Law to the Decay of Charge-Transfer Excited States. *J. Am. Chem. Soc.* **1982**, *104*, 630–632.
- (32) Sveshnikova, E. B.; Ermolaev, V. L. Inductive-Resonant Theory of Nonradiative Transitions in Lanthanide and Transition Metal Ions. *Opt. Spectrosc.* **2011**, *111*, 34–50.
- (33) Kreidt, E.; Kruck, C.; Seitz, M. Non-radiative Deactivation of Lanthanoid Luminescence by Multiphonon Relaxation in Molecular Complexes. *Handbook on the Physics and Chemistry of Rare Earths*; Elsevier: Amsterdam, 2018; Vol. 53, pp 35–79.
- (34) Doffek, C.; Seitz, M. The Radiative Lifetime in Near-IR-Luminescent Ytterbium Cryptates: The Key to Extremely High Quantum Yields. *Angew. Chem., Int. Ed.* **2015**, *54*, 9719–9721.
- (35) Hu, J.-Y.; Ning, Y.; Meng, Y.-S.; Zhang, J.; Wu, Z.-Y.; Gao, S.; Zhang, J.-L. Highly near-IR emissive ytterbium(III) complexes with unprecedented quantum yields. *Chem. Sci.* **2017**, *8*, 2702–2709.
- (36) Zhang, J.-X.; Chan, W.-L.; Xie, C.; Zhou, Y.; Chau, H.-F.; Maity, P.; Harrison, G. T.; Amassian, A.; Mohammed, O. F.; Tanner, P. A.; Wong, W.-K.; Wong, K.-L. Impressive near-infrared brightness and singlet oxygen generation from strategic lanthanide-porphyrin double-decker complexes in aqueous solution. *Light: Sci. Appl.* **2019**, *8*, 46.
- (37) Kittilstved, K. R.; Hauser, A. Electronic structure and photophysics of pseudo-octahedral vanadium(III) oxo complexes. *Coord. Chem. Rev.* **2010**, *254*, 2663–2676.
- (38) Reber, C.; Güdel, H. U. Near Infrared Luminescence Spectroscopy of  $\text{Al}_2\text{O}_3:\text{V}^{3+}$  and  $\text{YPO}_4:\text{V}^{3+}$ . *Chem. Phys. Lett.* **1989**, *154*, 425–431.
- (39) Landry-Hum, J.; Bussièrè, G.; Daniel, C.; Reber, C. Triplet Electronic States in  $d^2$  and  $d^8$  Complexes Probed by Absorption Spectroscopy: A CASSCF/CASPT2 Analysis of  $[\text{V}(\text{H}_2\text{O})_6]^{3+}$  and  $[\text{Ni}(\text{H}_2\text{O})_6]^{2+}$ . *Inorg. Chem.* **2001**, *40*, 2595–2601.
- (40) Beaulac, R.; Tregenna-Piggott, P. L. W.; Barra, A.-L.; Høgni, Weihe; Luneau, D.; Reber, C. The Electronic Ground State of  $[\text{V}(\text{urea})_6]^{3+}$  Probed by NIR Luminescence, Electronic Raman, and High-Field EPR Spectroscopies. *Inorg. Chem.* **2006**, *45*, 3399–3407.
- (41) Kittilstved, K. R.; Hauser, A. Electronic structure of  $\text{V}^{3+}$  in  $\text{NaMgAl}(\text{ox})_3 \cdot 9\text{H}_2\text{O}$  probed by Fourier Transform spectroscopy. *J. Lumin.* **2009**, *129*, 1493–1496.
- (42) Van Kuiken, B. E.; Hahn, A. W.; Maganas, D.; DeBeer, S. Measuring Spin-Allowed and Spin-Forbidden d-d Excitations in Vanadium Complexes with 2p3d Resonant Inelastic X-ray Scattering. *Inorg. Chem.* **2016**, *55*, 11497–11501.
- (43) Reber, C.; Güdel, H. U.; Meyer, G.; Schleid, T.; Daul, C. A. Optical Spectroscopic and Structural Properties of  $\text{V}^{3+}$ -Doped Fluoride, Chloride, and Bromide Elpasolite Lattices. *Inorg. Chem.* **1989**, *28*, 3249–3258.
- (44) Wenger, O. S.; Güdel, H. U. Luminescence spectroscopy of  $\text{V}^{3+}$ -doped  $\text{Cs}_2\text{NaYCl}_6$  under high pressure. *Chem. Phys. Lett.* **2002**, *354*, 75–81.
- (45) Penfold, T. J.; Gindensperger, E.; Daniel, C.; Marian, C. M. Spin-Vibronic Mechanism for Intersystem Crossing. *Chem. Rev.* **2018**, *118*, 6975–7025.
- (46) Förster, C.; Dorn, M.; Reuter, T.; Otto, S.; Davarci, G.; Reich, T.; Carrella, L.; Rentschler, E.; Heinze, K. Ddpd as Expanded Terpyridine: Dramatic Effects of Symmetry and Electronic Properties in First Row Transition Metal Complexes. *Inorganics* **2018**, *6*, 86.
- (47) Bowman, A. C.; Sproules, S.; Wieghardt, K. Electronic Structures of the  $[\text{V}^{\text{I}}(\text{bpy})_3]^{z+}$  ( $z = 3+, 2+, 0, 1-$ ) Electron Transfer Series. *Inorg. Chem.* **2012**, *51*, 3707–3717.
- (48) Van Stappen, C.; Maganas, D.; DeBeer, S.; Bill, E.; Neese, F. Investigations of the Magnetic and Spectroscopic Properties of V(III) and V(IV) Complexes. *Inorg. Chem.* **2018**, *57*, 6421–6438.
- (49) Otto, S.; Nauth, A. M.; Ermilov, E.; Scholz, N.; Friedrich, A.; Resch-Genger, U.; Lochbrunner, S.; Opatz, T.; Heinze, K. Photo Chromium: Sensitizer for Visible Light-Induced Oxidative C-H Bond Functionalization - Electron or Energy Transfer? *ChemPhotoChem.* **2017**, *1*, 344–349.
- (50) Plasser, F.; Gómez, S.; Menger, M. F. S. J.; Mai, S.; González, L. Highly efficient surface hopping dynamics using a linear vibronic coupling model. *Phys. Chem. Chem. Phys.* **2019**, *21*, 57–69.

## **A vanadium(III) complex with blue and NIR-II spin-flip luminescence in solution**

Matthias Dorn<sup>1</sup>, Jens Kalmbach<sup>2</sup>, Pit Boden<sup>3</sup>, Ayla Pöpcke<sup>4</sup>, Sandra Gómez<sup>5</sup>, Christoph Förster<sup>1</sup>, Felix Kuczelinis<sup>1</sup>, Luca M. Carrella<sup>1</sup>, Laura A. Büldt<sup>2</sup>, Nicolas H. Bings<sup>1</sup>, Eva Rentschler<sup>1</sup>, Stefan Lochbrunner<sup>4</sup>, Leticia González<sup>5</sup>, Markus Gerhards\*<sup>3</sup>, Michael Seitz\*<sup>2</sup> and Katja Heinze\*<sup>1</sup>

<sup>1</sup>Department of Chemistry, Johannes Gutenberg University of Mainz, Duesbergweg 10-14, 55128 Mainz, Germany.

<sup>2</sup>Institute of Inorganic Chemistry, University of Tübingen, Auf der Morgenstelle 18, 72076 Tübingen, Germany.

<sup>3</sup>Department of Chemistry and Research Center Optimas, TU Kaiserslautern, Erwin-Schrödinger-Straße, 67663 Kaiserslautern, Germany.

<sup>4</sup>Institute for Physics and Department of Life, Light and Matter, University of Rostock, 18051 Rostock, Germany.

<sup>5</sup>Institute of Theoretical Chemistry, Faculty of Chemistry, University of Vienna, Währinger Straße 17, 1090 Vienna, Austria.

### **Supporting Information**

**General Procedures.** Diethyl ether and petroleum ether (40/60) were distilled over sodium, acetonitrile over calcium hydride and butyronitrile over  $\text{Na}_2\text{CO}_3$ .  $\text{VCl}_3$  (anhydrous, 95 %; ABCR), 10% Pd/C (dry, unreduced; Acros Organics),  $\text{CD}_3\text{I}$  (>99.5 %D, stabilized with copper, Sigma-Aldrich) and 2,6-diaminopyridine (Sigma-Aldrich) were used as received. For NMR spectroscopy and synthesis, deuterated solvents with a deuteration level of at least 99.8 % were used. Column chromatography was performed using silica gel 60 (Merck, 0.04-0.063 mm). Analytical thin layer chromatography (TLC) was done on silica gel 60 F254 plates (Merck, coated on aluminum sheets). The ligand  $\text{ddpd}^1$  and  $[\text{V}(\text{NCCH}_3)_6][\text{BPh}_4]_2$ <sup>2</sup> were prepared according to reported procedures. NMR spectroscopic and mass spectrometric data match the literature values. A glovebox (UniLab/MBraun, Ar 4.8,  $\text{O}_2 < 100$  ppm,  $\text{H}_2\text{O} < 1$  ppm) was used for storage and weighing of sensitive compounds.

**NMR spectra** were recorded on a Bruker Avance DRX 400 or AVII+400 NMR spectrometer at 400.31 MHz ( $^1\text{H}$ ). All resonances are reported in ppm versus the solvent signal as internal standard.<sup>3</sup>

**IR spectra** were recorded with a Bruker Alpha FTIR spectrometer with an ATR unit containing a diamond crystal.

**ESI<sup>+</sup> mass spectra** were recorded on a Micromass Q-TOF-Ultima spectrometer by the central analytical facility of the Department of Chemistry (University of Mainz) or on a Bruker Daltonics Esquire 3000 plus mass spectrometer by the central analytical facility of the Department of Chemistry (University of Tübingen).

**DC magnetic studies** were performed with a Quantum Design MPMS-XL-7 SQUID magnetometer on powdered microcrystalline samples. Experimental susceptibility data were corrected for the underlying diamagnetism using Pascal's constants. The temperature dependent magnetic contribution of the holder and of the embedding eicosane matrix was experimentally determined and subtracted from the measured susceptibility data. Variable temperature susceptibility data were collected in a temperature range of 2 – 300 K under an applied field of 0.1 Tesla.

**Electrochemical experiments** were carried out on a BioLogic SP-200 voltammetric analyzer using platinum wires as counter and working electrodes and a 0.01 M Ag/Ag[ $\text{NO}_3$ ] electrode as reference electrode. Cyclic voltammetry and square wave measurements were carried out at scan rates of 50–200  $\text{mV s}^{-1}$  using 0.1 M [ $^n\text{Bu}_4\text{N}$ ][ $\text{PF}_6$ ] in  $\text{CH}_3\text{CN}$  as supporting electrolyte. Potentials are referenced against the ferrocene/ferrocenium couple. UV/Vis/NIR spectra were recorded on a Varian Cary 5000 spectrometer using 1.0 cm cells.

**Luminescence experiments.** For luminescence experiments,  $\text{CD}_3\text{CN}$  (99.8 %D, NMR grade) or spectrophotometric grade toluene as well as  $\text{H}_2\text{O}$  were used. Prior to use, all solvents were deoxygenated by three freeze-pump-thaw cycles and eventually sealed under dry, dioxygen-free argon atmosphere. Luminescence measurements at room temperature and at 77 K were performed on the following instruments:

a) The first instrument was a Horiba Fluorolog-3 spectrofluorimeter equipped with a 450 W Xenon lamp for steady-state measurements. Emitted light was detected either by a Hamamatsu R2658P PMT detector ( $200 \text{ nm} < \lambda_{\text{em}} < 1010 \text{ nm}$ ) or by a Hamamatsu H10330-75 PMT detector ( $950 \text{ nm} < \lambda_{\text{em}} < 1700 \text{ nm}$ ). Spectral selection in the excitation path was accomplished by a DFX monochromator (double gratings: 1200 grooves/mm, 330 nm blaze) and in the emission paths in the visible/NIR spectral region ( $\lambda_{\text{em}} < 1010 \text{ nm}$ ) by a spectrograph iHR550 (single gratings: either 1200 grooves/mm, 500 nm blaze or 950 grooves/mm, 900 nm blaze) and in the NIR spectral region ( $\lambda_{\text{em}} > 950 \text{ nm}$ ) by a spectrograph iHR320 (single grating: 600 grooves/mm, 1000 nm blaze). Luminescence lifetimes of the visible emission around 390 nm was determined at 298 K in standard fluorescence cuvettes (1 cm path length, quartz suprasil) with a pulsed LED (DeltaDiode-310,  $\lambda_{\text{exc}} = 306 \text{ nm} \pm 10 \text{ nm}$ , pulse width ca. 1.0 ns,  $P_{\text{avg}} = 5 \mu\text{W}$ ). Lifetime data analysis (deconvolution, statistical parameters, etc.) was performed using the software package DAS from Horiba. Lifetimes were

determined by deconvolution of the decay profiles with the instrument response function, which was determined using a dilute aqueous dispersion of colloidal silica (Ludox® AM-30).

b) The second instrument was a PTI Quantamaster QM4 spectrofluorimeter equipped with a 75 W continuous xenon short arc lamp as excitation source. Emission was monitored using a PTI P1.7R detector module (Hamamatsu PMT R5509-72 with a Hamamatsu C9525 power supply operated at 1500 V and a Hamamatsu liquid N<sub>2</sub> cooling unit C9940 set to -80°C). For the measurements between 600 nm and 900 nm, a long-pass filter GG-455 (Schott, 3.0 mm thickness, transmission 98 – 95 % in the spectral region mentioned) was used in the emission channel in order to avoid higher order excitation light. The same approach was taken for NIR measurements above 1000 nm with a long-pass filter RG-850 (Schott, 3.0 mm thickness, transmission > 98 % above 970 nm). Spectral selection was achieved by single grating monochromators (excitation: 1200 grooves/mm, 300 nm blaze; vis emission: 1200 grooves/mm, 500 nm blaze; near-IR emission: 600 grooves/mm, 1200 nm blaze). Near-IR luminescence lifetimes of the phosphorescent transition  $^1E_g/{}^1T_{2g} \rightarrow {}^3T_{1g}$  were determined at 77 K (liquid N<sub>2</sub> cuvette, sample dissolved in deoxygenated <sup>n</sup>BuCN in standard NMR tubes under argon) with a xenon flash lamp as excitation source (Hamamatsu L4633: pulse width ca. 1.5 μs FWHM). Lifetime data analysis (deconvolution, statistical parameters, etc.) was performed using the software package FeliX32 from PTI. Lifetimes were determined by deconvolution of the decay profiles with the instrument response function, which was determined using an empty NMR tube as scatterer.

Partial quantum yields in the visible and the NIR spectral regions were determined using the following equation:

$$\Phi_x = \Phi_r * (\text{Grad}_x / \text{Grad}_r) * (\eta_x^2 / \eta_r^2)$$

where  $\eta$  is the refractive index and Grad is the linearly fitted slope from the plot of the integrated luminescence intensity (corrected for instrument response) versus the absorbance at the excitation wavelength. The subscripts 'x' and 'r' refer to the sample and reference, respectively. The vanadium samples were prepared in deoxygenated CD<sub>3</sub>CN ( $\eta_x = 1.341$ ) at 298 K under argon (vide supra). For the emission around 390 nm, quinine sulfate in 0.1 M aqueous H<sub>2</sub>SO<sub>4</sub> ( $\eta_r = 1.33$ ) was used after excitation at  $\lambda_{\text{exc}} = 308$  nm as a reference material with a fluorescence quantum yield of  $\Phi_r = 54.6$  %.<sup>4</sup> For the NIR emission band ( ${}^1E_g/{}^1T_{2g} \rightarrow {}^3T_{1g}$ ), Yb(tta)<sub>3</sub>(phen) in toluene ( $\eta_r = 1.496$ ) was used after excitation at  $\lambda_{\text{exc}} = 308$  nm with a quantum yield of  $\Phi_r = 1.1$  %.<sup>5</sup> For the measurement of the ytterbium standard emission, the signal had to be attenuated by a neutral density filter (Newport, neutral density filter FSQ-ND10, transmission around 1000 nm ca. 11.0±0.2 %) in the emission. The attenuation factor was taken into account mathematically during the integration of the emission bands for the quantum yield calculations.

c) Steady state luminescence measurements in frozen butyronitrile solution down to 20 K were recorded on a Horiba Jobin Yvon Fluorolog 3-22 τ spectrometer equipped with a 450 W xenon lamp and a DSS – IGA020L NIR detector (900 nm <  $\lambda_{\text{em}}$  < 1500 nm). Spectral selection was realized with double and single grating monochromators in the excitation and emission paths, respectively (excitation: 1200 grooves/mm; near-IR emission 600 grooves/mm). A long-pass filter RG-850 (Edmund Optics, transmission > 98 % above 970 nm) was used in the emission channel to avoid higher order excitation light. The butyronitrile solution was cooled down to 20 K with a closed cycle helium cryostat (ARS Model DE-202A). The cryo cooler was equipped with a cuvette holder and CaF<sub>2</sub> windows. Measurements were performed in fluorescence cuvettes (1 cm path length, quartz suprasil).

d) Steady state luminescence measurements by using KBr pellets were performed on a Horiba Jobin Yvon FluoroMax-2 using the described cryostat. A 150 W xenon lamp was used for sample excitation and detection was realized with a R928 photomultiplier detector. Spectral selection was achieved with single grating monochromators in the excitation and emission paths, respectively (excitation: 1200 grooves/mm, 330 nm blaze; emission: 1200 grooves/mm, 500 nm blaze). Long-pass filters with cut-off wavelengths of 420 nm or



600 nm were used depending on the measurement. KBr pellets of  $[V(\text{ddpd})_2][\text{PF}_6]_3$  (ca. 0.5 mg) were prepared by mixing with dry KBr (ca. 200 mg), grinding to a homogeneous mixture and pressing into a pellet.

**Time-resolved FTIR experiments** were performed with an FTIR spectrometer Bruker Vertex 80v, operated in the step-scan mode. KBr pellets of  $[V(\text{ddpd})_2][\text{PF}_6]_3$  (ca. 0.5 mg) were prepared by mixing with dry KBr (ca. 200 mg, stored at 80 °C) and grinding to a homogeneous mixture. This mixture was filled in an evacuable pellet die with a diameter of 13 mm and sintered at a pressure of 0.75 GPa. The strongest peak in the ground state spectrum showed an absorption of about 0.6 OD with the mentioned concentration. Measurements with cryogenically cooled KBr pellets (20 K and 290 K at the sample) were performed with a closed cycle helium cryostat (ARS Model DE-202A). The cryo cooler was equipped with a homebuilt pellet holder and  $\text{CaF}_2$  windows. A liquid-nitrogen-cooled mercury cadmium telluride (MCT) detector (Kolmar Tech., Model KV100-1-B-7/190) with a rise time of 25 ns, connected to a fast preamplifier and a 14-bit transient recorder board (Spectrum Germany, M3I4142, 400  $\text{MS s}^{-1}$ ), was used for signal detection and processing. The laser setup includes a Q-switched Nd:YAG laser (Innolas SpitLight Evo I) generating pulses with a band-width of 6 – 9 ns at a repetition rate of 100 Hz. The third harmonic (355 nm) of the Nd:YAG laser was used for sample excitation. The UV pump beam was attenuated to about 2.0 mJ per shot at a diameter of 9 mm. The beam was directed onto the sample and adjusted to have a maximal overlap with the IR beam of the spectrometer. The sample chamber was equipped with anti-reflection-coated germanium filters to prevent the entrance of laser radiation into the detector and interferometer compartments. The time delay between the start of the experiment and the UV laser pulse was controlled with a Stanford Research Systems DG535 delay generator. A total of 10400 coadditions were recorded at each interferogram point. The spectral region was limited by undersampling to 988 – 1975  $\text{cm}^{-1}$  with a spectral resolution of 4  $\text{cm}^{-1}$  resulting in 555 interferogram points. An IR broad band filter (850 – 1750  $\text{cm}^{-1}$ ) and the  $\text{CaF}_2$  windows (no IR transmission < 1000  $\text{cm}^{-1}$ ) of the cryostat prevented problems when performing a Fourier transformation (*i.e.* no IR intensity outside the measured region should be observed). FTIR ground state spectra were recorded systematically to check for sample degradation. A more detailed description of the step-scan setup is given here.<sup>6</sup>

**Transient absorption spectra** were recorded applying a pump-probe setup with a time resolution of 100 fs. A noncollinear optical parametric amplifier (NOPA) tuned to a center wavelength of 620 nm was used for excitation and a white light continuum, generated with a  $\text{CaF}_2$  crystal, for probing. Both the white light generation and the NOPA were pumped by a regenerative Ti:sapphire laser system operating at 775 nm with a repetition rate of 1 kHz. The polarizations of the pump and probe pulses were set to magic angle with respect to each other to avoid effects due to orientational relaxation. Pump and probe beam were focused onto the sample resulting in overlapping spots with diameters of approximately 270  $\mu\text{m}$  and 110  $\mu\text{m}$ , respectively. The sample was dissolved in acetonitrile and filled into a 1 mm fused silica cuvette. The optical density was set at 600 nm to 0.3 – 0.5 to obtain transient spectra with a good signal to noise ratio. This corresponds to concentrations of 1.8 – 2.5 $\times 10^{-3}$  M for the complex. The solutions were perfused with argon for approximately two minutes. For the measurements with an excitation wavelength of 400 nm a second pump-probe setup was used based on a Ti:Sapphire laser system (Spectra-Physics, Spitfire Pro) with a center wavelength of 800 nm and a repetition rate of 1 kHz. By frequency doubling applying a BBO crystal pump pulses at 400 nm with a pulse duration of 200 fs were obtained. The white light continuum for the probe was again generated with a  $\text{CaF}_2$  crystal. Both beams with polarizations arranged in magic angle were focused onto the sample leading to spots with diameters of 170  $\mu\text{m}$  for the pump and 80  $\mu\text{m}$  for the probe. The sample was dissolved in  $\text{CH}_3\text{CN}$  and filled into a 1 mm fused silica cuvette. The optical density was set to 0.7 at 400 nm which corresponds to an optical density of 0.4 at 600 nm and to a concentration of 2.5 $\times 10^{-3}$  M. The same sample was used as in the aforementioned measurement with an excitation at 620 nm.

**Elemental analyses** were conducted by the microanalytical laboratory of the department of chemistry of the University of Mainz.

**Trace determination of chromium in the presence of vanadium.** Mass spectrometrical analysis of the starting materials for traces of Cr were performed by the Laboratory for Inorganic Trace Analysis and Plasma Spectrometry, University of Mainz. The chromium concentrations in  $\text{VCl}_3(\text{THF})_3$ , and  $\text{VCl}_3(\text{CH}_3\text{CN})_3$  were determined by microwave assisted acid digestion and subsequent SN-ICP-MS (solution nebulization-inductively coupled plasma-mass spectrometry) measurement. Initially, the approximate chromium concentrations were determined via digestion and subsequent ICP-MS measurement of  $\sim 10$  mg of the respective compound using a three point external calibration with concentrations between  $0.5 \text{ ng ml}^{-1}$  and  $50 \text{ ng ml}^{-1}$ . Based on these results, the procedure to achieve valid quantitative results was as follows: An amount of (40–130) mg per sample was weighted and digested in 6 mL nitric acid (70 % p.a. grade, Fisher Chemical, Fisher Scientific GmbH, Germany) and 2 ml hydrogen peroxide solution (30 % p.a. grade, ROTIPURAN®, Carl Roth, Germany) using an Ethos 2000plus microwave assisted digestion system (Milestone Inc, Shelton, CT, USA). The first step of the heating program was a temperature ramp to  $140^\circ\text{C}$  within 7.5 min followed by a second ramp to  $200^\circ\text{C}$  within 5 min. This temperature was held for 10 min and afterwards increased to  $220^\circ\text{C}$  within 5 min before holding this temperature for 20 mins. Prior to digestion,  $100 \mu\text{l}$  of a  $10 \mu\text{g ml}^{-1}$  Y-solution were added to compensate for analyte loss during the digestion and subsequent sample preparation steps. The obtained solutions were diluted to 25 ml with ultrapure water (Millipore, Milli-Q System, USA) from which five aliquots of 1 ml were diluted to 10 ml each. For quantification via standard addition, Cr and Y were added at concentrations between 0 and  $5 \text{ ng ml}^{-1}$ , and 0 and  $8 \text{ ng ml}^{-1}$ , respectively. Sc was added at a concentration of  $4 \text{ ng ml}^{-1}$  as internal standard. For ICP-MS measurements, a sample introduction system consisting of a concentric MicroMist™ nebulizer (Agilent Technologies, Santa Clara, CA, USA) and a double pass spray chamber (Agilent Technologies, Santa Clara, CA, USA) were coupled to a quadrupole ICP-MS instrument 7800 (Agilent Technologies, Santa Clara, CA, USA). The signal intensities of  $^{45}\text{Sc}^+$ ,  $^{52}\text{Cr}^+$ ,  $^{53}\text{Cr}^+$  and  $^{89}\text{Y}^+$  were measured for data evaluation. The optimum instrumental parameters of the developed ICP-MS method are as follows: plasma power: 1550 W, plasma gas flow rate:  $15 \text{ l min}^{-1}$ , auxiliary gas flow rate:  $0.9 \text{ l min}^{-1}$ , nebulizer gas flow rate:  $0.99\text{--}1.05 \text{ l min}^{-1}$ , sampler and skimmer cone: Ni, He gas flow rate (cell gas):  $2 \text{ ml min}^{-1}$ , data acquisition: 0.3 s integration time, 30 sweeps per replicate, 6 replicates.

$\text{VCl}_3(\text{NCMe})_3$ :  $(4.01 \pm 0.31) \mu\text{g/g}$  ( $U$ ;  $k=2$ );  $\text{VCl}_3(\text{THF})_3$ :  $(3.45 \pm 0.10) \mu\text{g/g}$  ( $U$ ;  $k=2$ ).

**Crystal structure determination.** Intensity data were collected with a STOE IPDS-2T diffractometer and an Oxford cooling system and corrected for absorption and other effects using Mo  $K_\alpha$  radiation ( $\lambda = 0.71073 \text{ \AA}$ ). The diffraction frames were integrated using the STOE X-Area software package<sup>7</sup>, and most were corrected for absorption with MULABS<sup>8</sup> of the PLATON package.<sup>9</sup> The structure was solved by direct methods and refined by the full-matrix method based on  $F^2$  using the SHELXTL software package.<sup>10,11</sup> All non-hydrogen atoms were refined anisotropically, while the positions of all hydrogen atoms were generated with appropriate geometric constraints and allowed to ride on their respective parent carbon atoms with fixed isotropic thermal parameters. CCDC 1958562 ( $[\text{V}(\text{ddpd})_2][\text{PF}_6]_3 \times 3\text{CH}_3\text{CN}$ ) contains the supplementary crystallographic data for this paper. These data are provided free of charge by The Cambridge Crystallographic Data Centre.

**Crystallographic Data of *mer*- $[\text{V}(\text{ddpd})_2][\text{PF}_6]_3 \times 3\text{CH}_3\text{CN}$ .**  $\text{C}_{40}\text{H}_{43}\text{F}_{18}\text{N}_{13}\text{P}_3\text{V}$  (1191.72); triclinic;  $P\bar{1}$ ;  $a = 11.483(2) \text{ \AA}$ ,  $b = 11.901(2) \text{ \AA}$ ,  $c = 18.093(4) \text{ \AA}$ ,  $\alpha = 90.88(3)^\circ$ ,  $\beta = 96.38(3)^\circ$ ,  $\gamma = 91.60(3)^\circ$ ;  $V = 2456.0(9) \text{ \AA}^3$ ;  $Z = 2$ ; density, calcd. =  $1.612 \text{ g cm}^{-3}$ ,  $T = 193(2) \text{ K}$ ,  $\mu = 0.415 \text{ mm}^{-1}$ ;  $F(000) = 1208$ ; crystal size  $0.620 \times 0.520 \times 0.460 \text{ mm}$ ;  $\theta = 2.437$  to  $28.426 \text{ deg.}$ ;  $-15 \leq h \leq 15$ ,  $-15 \leq k \leq 14$ ,  $-24 \leq l \leq 24$ ; rfln collected = 25922; rfln unique = 12253 [ $R(\text{int}) = 0.0416$ ]; completeness to  $\theta = 25.242 \text{ deg.} = 99.8 \%$ ; semi empirical absorption correction from equivalents; max. and min. transmission 1.11737 and 0.90264; data 12253; restraints 84, parameters 747; goodness-of-fit on  $F^2 = 1.028$ ; final indices [ $I > 2\sigma(I)$ ]  $R_1 = 0.0409$ ,  $wR_2 = 0.1060$ ;  $R$  indices (all data)  $R_1 = 0.0548$ ,  $wR_2 = 0.11126$ ; largest diff. peak and hole  $0.391$  and  $-0.489 \text{ e \AA}^{-3}$ .

## Computational Details.

The characterization of the absorption spectrum was done employing two types of quantum chemical calculations: i) density functional theory in its unrestricted form, as for open shell species unrestricted orbitals are expected to deliver best geometries and energy values in comparison to restricted orbitals, and ii) multiconfigurational theory with an active space tailored to predict accurately the MC states. The first method is labelled below as “Unrestricted Kohn-Sham orbitals DFT (UKS), the second as “SOC-CASSCF(6,12)-FIC-NEVPT2”. These two methods are complementary to each other, as the first gives the best energetics for the LMCT states, while the second provides accurately the position of the MC states. The simulation of the excited state molecular dynamics states related to the spin-flip was done using surface hopping, below labeled as “non-adiabatic spin-flip dynamics calculations”. As explained in more detailed here, the electronic structure theory calculations underlying the molecular dynamics were done with the same computational protocol as the DFT calculations, but using restricted orbitals, in order to obtain pure spin states.

**Static unrestricted Kohn-Sham orbitals DFT (UKS):** All calculations were performed using the quantum computing suite ORCA 4.0.1.<sup>12</sup> Geometry optimization (Tables S1 – S2) was performed using unrestricted Kohn-Sham orbitals DFT (UKS) and the B3LYP functional<sup>13</sup> in combination with Ahlrichs’ split-valence triple- $\zeta$  basis set def2-TZVPP for all atoms.<sup>14,15</sup> Tight convergence criteria were chosen for DFT-UKS calculations (keywords tightscf and tightopt). All DFT-UKS calculations make use of the resolution of identity (Split-RI-J) approach for the Coulomb term in combination with the chain-of-spheres approximation for the exchange term (COSX).<sup>16,17</sup> The zero order relativistic approximation was used to describe relativistic effects in all calculations (keyword ZORA).<sup>18,19</sup> Grimme’s empirical dispersion correction D3(BJ) was employed (keyword D3BJ).<sup>20,21</sup> To account for solvent effects, a conductor-like screening model (keyword CPCM) modeling acetonitrile was used in all calculations.<sup>22</sup> Explicit counterions and/or solvent molecules were neglected. TD-DFT-UKS calculations were performed at the same level of theory using unrestricted Kohn-Sham orbitals (UKS). Fifty vertical spin-allowed transitions were calculated (Tables S3 – S4).

**SOC-CASSCF(6,12)-FIC-NEVPT2:** Calculations of ground- and excited-state properties with respect to metal-centered (MC) states were performed using the complete-active-space self-consistent field method (including spin-orbit coupling (SOC-CASSCF)<sup>23,24</sup> for calculation of the zero-field splitting  $D$ ) in conjunction with the fully internally contracted N-electron valence perturbation theory to second order (FIC-NEVPT2)<sup>25,26</sup> in order to recover missing dynamic electron correlation. SOC was treated through the mean-field (SOMF) approximation<sup>27,28</sup>, and the effective Hamiltonian approach<sup>29-31</sup> was used to compute the spin-Hamiltonian parameters. In order to accurately model the ligandfield, active spaces were chosen to encompass the dominate bonding/antibonding orbitals formed between vanadium and the ligand. An active space of (6,12) along with 10 triplet roots and 12 singlet roots was selected (Tables S5 – S6). In addition to the minimal active space of (2,5), two occupied V-N  $\sigma$  bonding orbitals and a second d shell<sup>32</sup> were included in these calculations (Table S5).

**Non-adiabatic spin-flip dynamic calculations** were accomplished using the SHARC (Surface Hopping including ARbitrary Couplings)<sup>33-36</sup> molecular dynamics program suite with the pySHARC driver. The electronic Hamiltonian was approximated using a linear vibronic coupling (LVC) method<sup>37</sup> based on TDDFT vertical excitations calculated using the methodological details described above with one essential difference. The open-shell (UKS) ground state electronic wave function used as a reference for the previous TDDFT calculations delivers electronic states that cannot be labelled according to their spin multiplicity (i.e., they are not eigenfunctions of the spin operator). As we need explicit couplings between pure singlet and pure triplet states, a RKS approach, where the two unpaired electrons are forced to be paired in one restricted orbital, is used to do single point calculations on the UKS optimized geometry and obtain pure triplet states as a linear response of a pure singlet state. The obtained RKS energies are also listed in Table S3. Since there is only one reference closed-shell orbital instead of two – as one would have in an open-shell triplet state – some electronic states are missing in the RKS approach with respect to the UKS calculation. In the RKS

approach, the assignment of the state characters has been done dividing the molecule into three fragments (metal center and two ddpd ligands) and calculating charge transfer (CT) numbers, as implemented in the TheoDore software package.<sup>38</sup> The quantitative wave function analysis is presented in Fig. S21 and the largest contribution is used to state the main state character in Table S3.

A total of 48 coupled diabatic electronic states (12x3 triplets and 12 singlets, listed in Table S8) were included in the SHARC-LVC calculations. For the 100 fs simulations (Fig. S22), 4 sets of 54, 69, 60, 59 trajectories were excited 100 % to the lowest  $1^3\text{LMCT}$ ,  $2^3\text{LMCT}$ ,  $3^3\text{LMCT}$  and  $4^3\text{LMCT}$  states, respectively. In the 50 ps simulation (Figure 4), 294 trajectories were included, starting from the  $2^3\text{LMCT}$  state, which was identified as the longest-lived state during the previous 100 fs. The nuclear motion was propagated with a 0.5 fs step, and the electronic wave function was integrated with a 0.02 fs step, using the local diabatization scheme.<sup>39</sup> During a hop, the full momentum vector was rescaled to conserve total energy. The energy-based decoherence correction<sup>40</sup> with the standard parameter of 0.1 a.u. was used. 1000 initial geometries were sampled from a harmonic Wigner distribution of the UKS ground state; from the 231 available normal modes, one imaginary mode ( $-30\text{ cm}^{-1}$ ) and the highest 33 (from  $3047$  to  $3279\text{ cm}^{-1}$ ) were excluded due to anharmonicities. These modes correspond to the large amplitude torsions of the methyl groups, which cannot be described by a linear model potential. For each of the remaining 196 normal modes, 4415 intrastate and 18827 interstate vibronic couplings were calculated using a numerical differentiation scheme and the computation of wave function overlaps between the states at the reference geometry and the displaced geometries. We note that the optimized geometry of the singlet reference state and that of the triplet ground state are very similar (RMSD = 0.584), justifying the use of the UKS frequencies as seed for the initial conditions.

Using the LVC framework, the optimization of the longest-lived singlet state ( $2^1\text{MC}$ ) leads to the structure given in Table S9. This state lays 1.1 eV above the triplet ground state and it is assigned as the NIR emissive state.

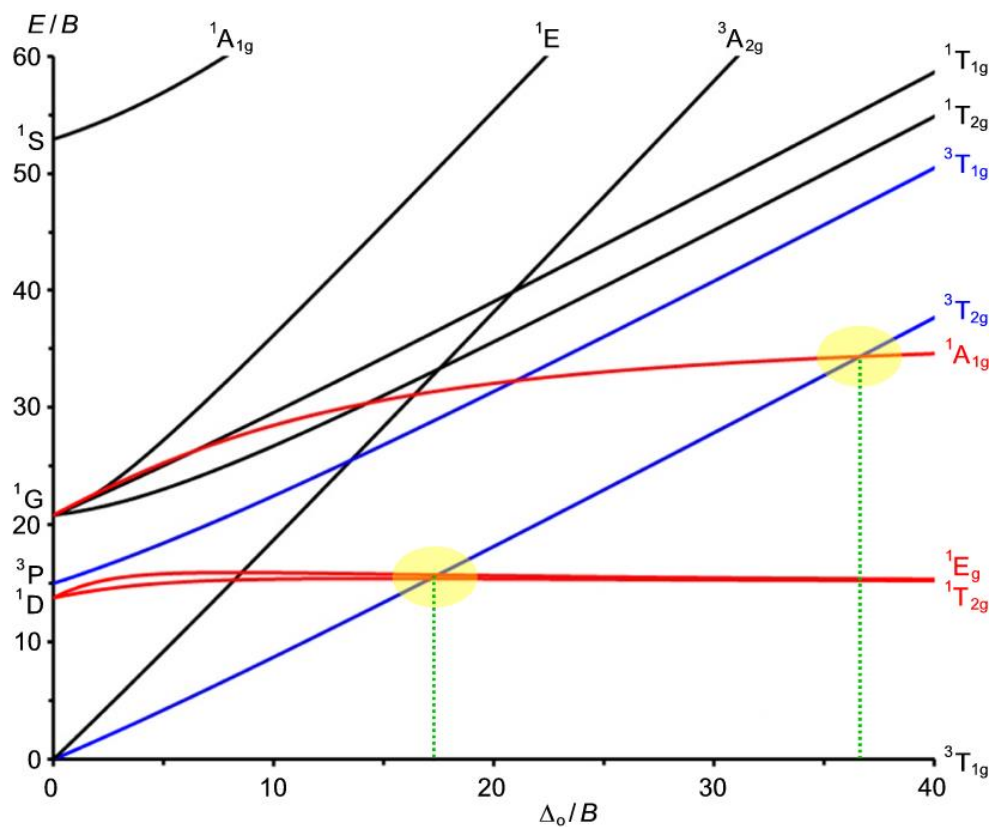


**Figure S1.** Tanabe Sugano diagram for octahedral transition metal complexes with  $d^2$  electron configuration ( $C/B = 4.42$ ). Relevant excited triplet states in blue, relevant singlet states in red, important crossing points highlighted in yellow.<sup>42</sup>

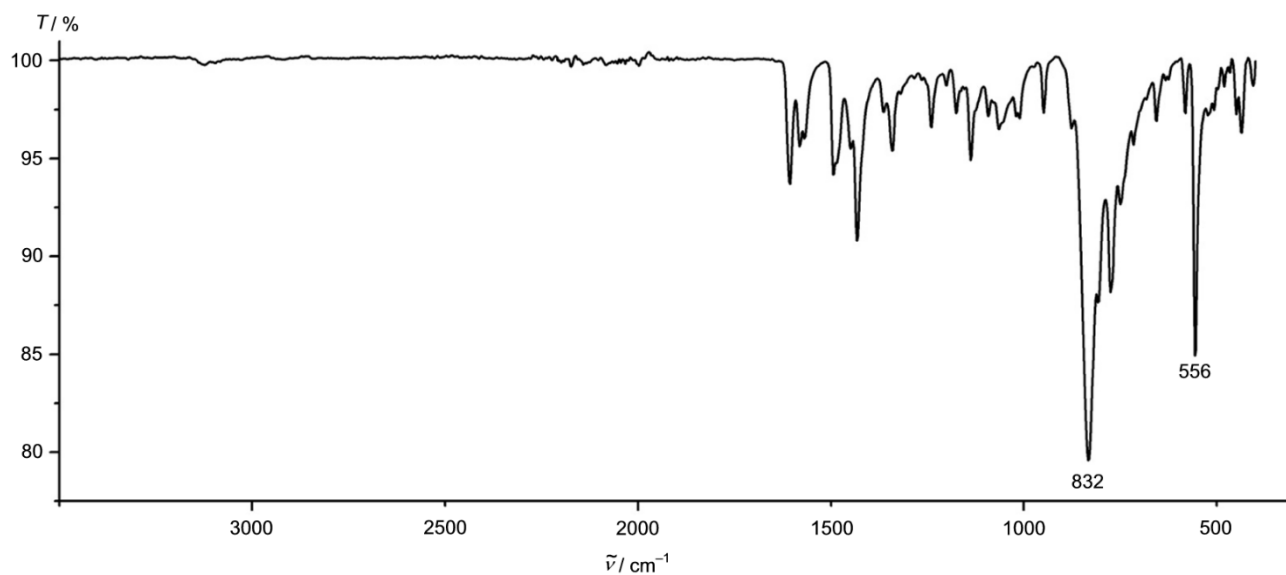


**Figure S2.** ATR IR spectrum of  $\text{mer-}[V^{III}(\text{ddd})_2](\text{PF}_6)_3$ .

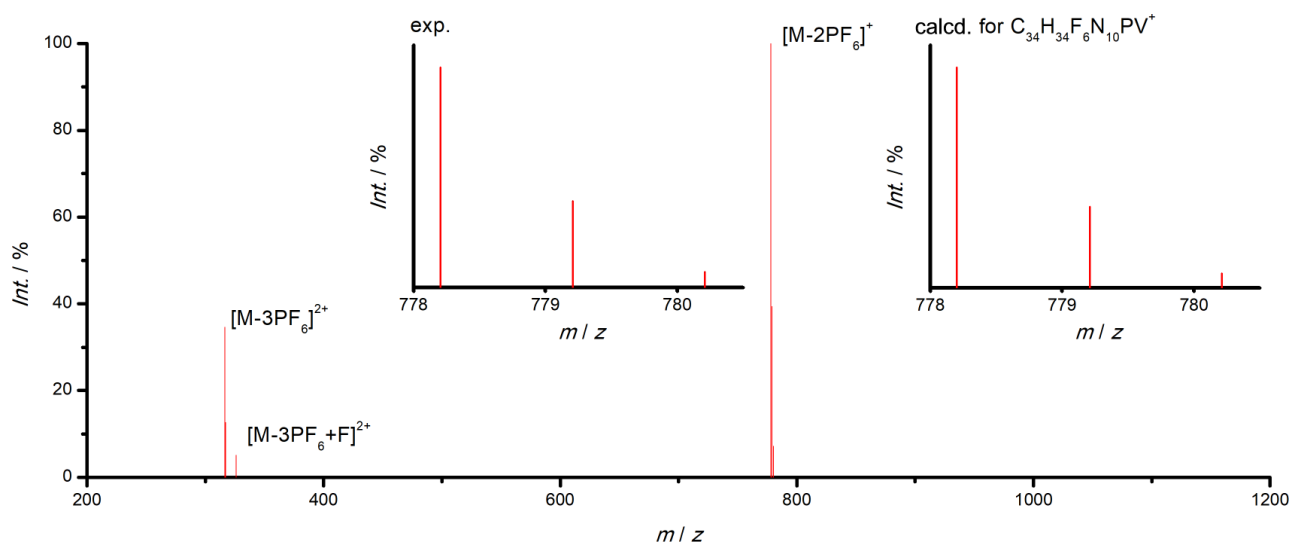


**Figure S3.** ESI<sup>+</sup> mass spectrum of *mer*-[V<sup>III</sup>(dddpd)<sub>2</sub>][PF<sub>6</sub>]<sub>3</sub> in CH<sub>3</sub>CN. The insets show the experimental and calculated isotopic pattern of the largest peak.

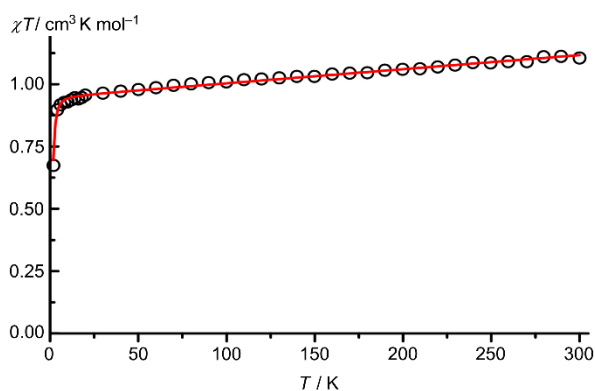


**Figure S4.** Temperature-dependence of  $\chi_M T$  of *mer*-[V(dddpd)<sub>2</sub>][PF<sub>6</sub>]<sub>3</sub> (black circles) with fit (red line,  $g = 1.946(2)$ ,  $D = +2.87(11) \text{ cm}^{-1}$ ; TIP =  $566 \times 10^{-6} \text{ cm}^3 \text{ K mol}^{-1}$ ). Simulation with a negative  $D$  value gave a slightly poorer fit to the experimental data. As obtained by HF-EPR spectroscopy, reported vanadium(III) complexes exhibit positive  $D$  values.<sup>43</sup> Only two oxalates of vanadium(III) are reported to possess negative  $D$  values based on inelastic neutron scattering and single crystal high-resolution FT absorption spectroscopy.<sup>44</sup>

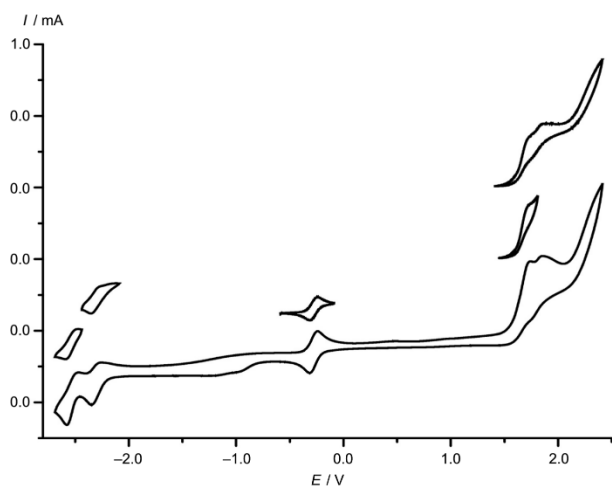
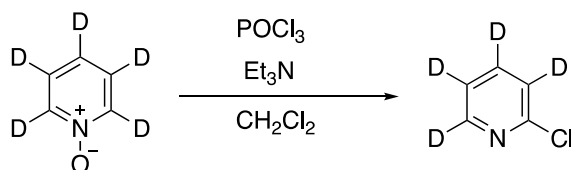


**Figure S5.** Cyclic voltammogram of *mer*-[V<sup>III</sup>(dddpd)<sub>2</sub>][PF<sub>6</sub>]<sub>3</sub> in [<sup>n</sup>Bu<sub>4</sub>N][PF<sub>6</sub>] in CH<sub>3</sub>CN;  $E$  vs. ferrocene.

## Synthesis and characterization of [D<sub>17</sub>]-ddpd

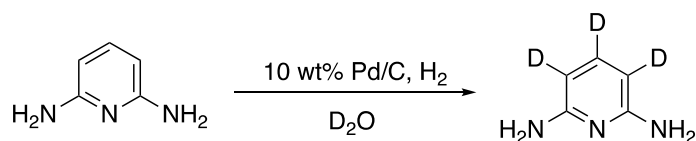
### [D<sub>4</sub>]-2-Chloropyridine<sup>45</sup>



To a stirred solution of [D<sub>5</sub>]-pyridine-N-oxide<sup>46</sup> (8.1 g, 81 mmol, 1.0 eq.) and triethylamine (13.4 ml, 9.8 g, 97 mmol, 1.2 eq.) in dichloromethane (80 ml) was slowly added a solution of POCl<sub>3</sub> (8.8 ml, 14.9 g, 97 mmol, 1.2 eq.) in dichloromethane (50 ml) at 10 °C. After stirring for 30 minutes at room temperature, the reaction mixture was refluxed for 1 h. The solution was cooled to room temperature and ice was slowly added until all excess phosphoroychloride was hydrolysed. After addition of water (30 ml), the solution pH was adjusted to 10 with aq. NaOH (2 M). The organic layer was separated and the aqueous layer was extracted with CH<sub>2</sub>Cl<sub>2</sub> (5 × 30 ml). The combined organic layers were washed with a saturated NaCl solution, dried (MgSO<sub>4</sub>) and concentrated at reduced pressure. The resulting red oil was subjected to column chromatography (SiO<sub>2</sub>, CH<sub>2</sub>Cl<sub>2</sub>, preloading onto SiO<sub>2</sub>, detection: UV). The product was obtained as a colorless oil (3.8 g, 40 %, >99.5 %D).

<sup>13</sup>C{<sup>1</sup>H} NMR (101 MHz, CDCl<sub>3</sub>): δ = 151.4 (s), 149.3 (t, *J* = 28.0 Hz), 138.3 (t, *J* = 25.0 Hz), 124.0 (t, *J* = 26.2 Hz), 121.7 (t, *J* = 25.6 Hz) ppm. MS (ESI<sup>+</sup>): *m/z* (%) = 118.04 (100, [M+H]<sup>+</sup>).

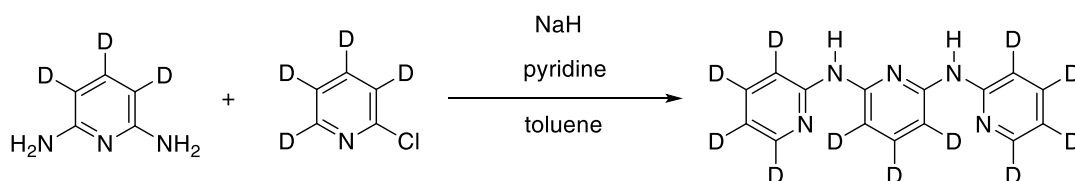
### [D<sub>3</sub>]-2,6-Diaminopyridine



In analogy to a published procedure,<sup>47</sup> a mixture of 2,6-diaminopyridine (500 mg, 4.6 mmol, 1.0 eq.) and 10 % Pd/C (10 wt-%, 50 mg) in D<sub>2</sub>O (20 ml, NMR grade, 99.9 %D) in a steel autoclave was set under an atmosphere of H<sub>2</sub> (1 bar) and stirred at 180°C (bath temperature) for 24 h. After cooling to room temperature, methanol (20 ml) was added and the dark green reaction mixture was filtered through celite. The filter cake was washed with additional methanol (3 × 10 ml) and the combined filtrate was concentrated under reduced pressure. The product was obtained as dark green solid (510 mg, 99 %, H<sup>3/5</sup>: 87 %D, H<sup>4</sup>: 97 %D, overall: 90.5 %D).

<sup>1</sup>H NMR (400 MHz, CD<sub>3</sub>OD): δ = 7.18 (0.03 H, non-deuterated residual signal), 5.84 (0.25 H, non-deuterated residual signal), 4.84 (s, 4 H) ppm. MS (ESI<sup>+</sup>): *m/z* (%) = 113.1 (100, [M+H]<sup>+</sup>).

### [D<sub>11</sub>]-*N,N'*-Bis(2-pyridyl)-2,6-diaminopyridine

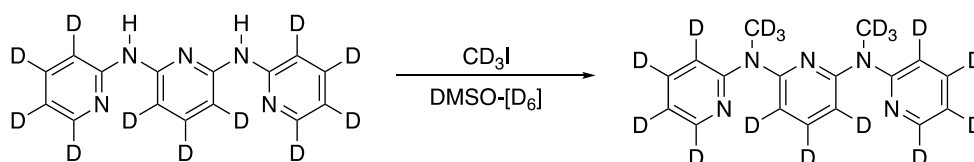


In analogy to a published procedure,<sup>48</sup> under an argon atmosphere a mixture of [D<sub>3</sub>]-2,6-diaminopyridine (0.5 g, 4.4 mmol, 1 eq.) and NaH (60 wt% dispersion in mineral oil, 1.2 g, 29 mmol, 6.8 eq.) was stirred for 5 min

at room temperature. [D<sub>4</sub>]-2-Chloropyridine (1.2 ml, 1.5 g, 13 mmol, 3 eq.) and pyridine (2.5 ml) were added, followed by stirring for 5 min at room temperature. The reaction mixture was immersed in a preheated oil bath at 150 °C resulting in immediate, strong gas evolution. A few minutes later, just before the red brown suspension became a solid mass, dry toluene (15 ml) was added. The mixture was stirred at 150°C (bath temperature) for 4 h. After cooling to room temperature, the solvent was removed under reduced pressure. Cautiously, ice-cold water (30 ml) was added dropwise. After stirring for 10 minutes, the brown precipitate was collected on a sintered-glass frit (porosity 3), washed extensively with water (3 × 20 ml) and *n*-hexane (3 × 10 ml). The light brown solid was dissolved in THF (60 ml) and filtered through a short plug of silica. The plug was washed with additional THF (3 × 10 ml) and the combined THF filtrates were concentrated under reduced pressure resulting in a brown solid. The crude product was transferred into a 25 ml round bottom flask and MeOH (3 ml), CH<sub>2</sub>Cl<sub>2</sub> (3 ml) and Et<sub>2</sub>O (3 ml) were added. After stirring for 3 h at room temperature, the mixture was cooled in an ice bath. The beige solid was collected on a filter, washed with Et<sub>2</sub>O (3 × 5 ml) and dried under vacuum. The product was obtained as beige solid (0.36 g, 29 %, 90.3 %D).

<sup>1</sup>H NMR (400 MHz, [D<sub>6</sub>]-DMSO):  $\delta$  = 9.36 (s, 2 H), 7.12 (0.9 H, non-deuterated residual signal) ppm.

#### [D<sub>17</sub>]-ddpd<sup>49</sup>



Under an argon atmosphere, powdered KOH (99 mg, 1.8 mmol, 4.0 eq.) was added to a yellow solution of [D<sub>11</sub>]-*N,N'*-bis(2-pyridyl)-2,6-diaminopyridine (120 mg, 0.4 mmol, 1.0 eq.) in [D<sub>6</sub>]-DMSO (10 ml, NMR grade, 99.8 %D). The mixture was stirred at room temperature for 30 min. CD<sub>3</sub>I (60  $\mu$ l, 140 mg, 0.97 mmol, 2.2 eq.) was added to the red reaction solution and stirring was continued overnight (16 h). Water (40 ml) was added and the yellow aqueous suspension was extracted with a 1:1 (v/v) mixture of Et<sub>2</sub>O/THF (3 × 30 ml). The combined organic phases were washed with aqueous sat. Na<sub>2</sub>CO<sub>3</sub> (25 ml), dried (MgSO<sub>4</sub>) and concentrated under reduced pressure. The resulting yellow oil was subjected to column chromatography (SiO<sub>2</sub>, *n*-hexane/EtOAc, 12:1) to obtain the product as a pale-yellow oil (75 mg, 55 %, >93.6 %D).

<sup>1</sup>H NMR (400 MHz, CDCl<sub>3</sub>):  $\delta$  = 6.76 (non-deuterated residual signal) ppm (Fig. S6). MS (ESI<sup>+</sup>): *m/z* (%) = 308.3 (100, [M+H]<sup>+</sup>) (Fig. S7 – S8).



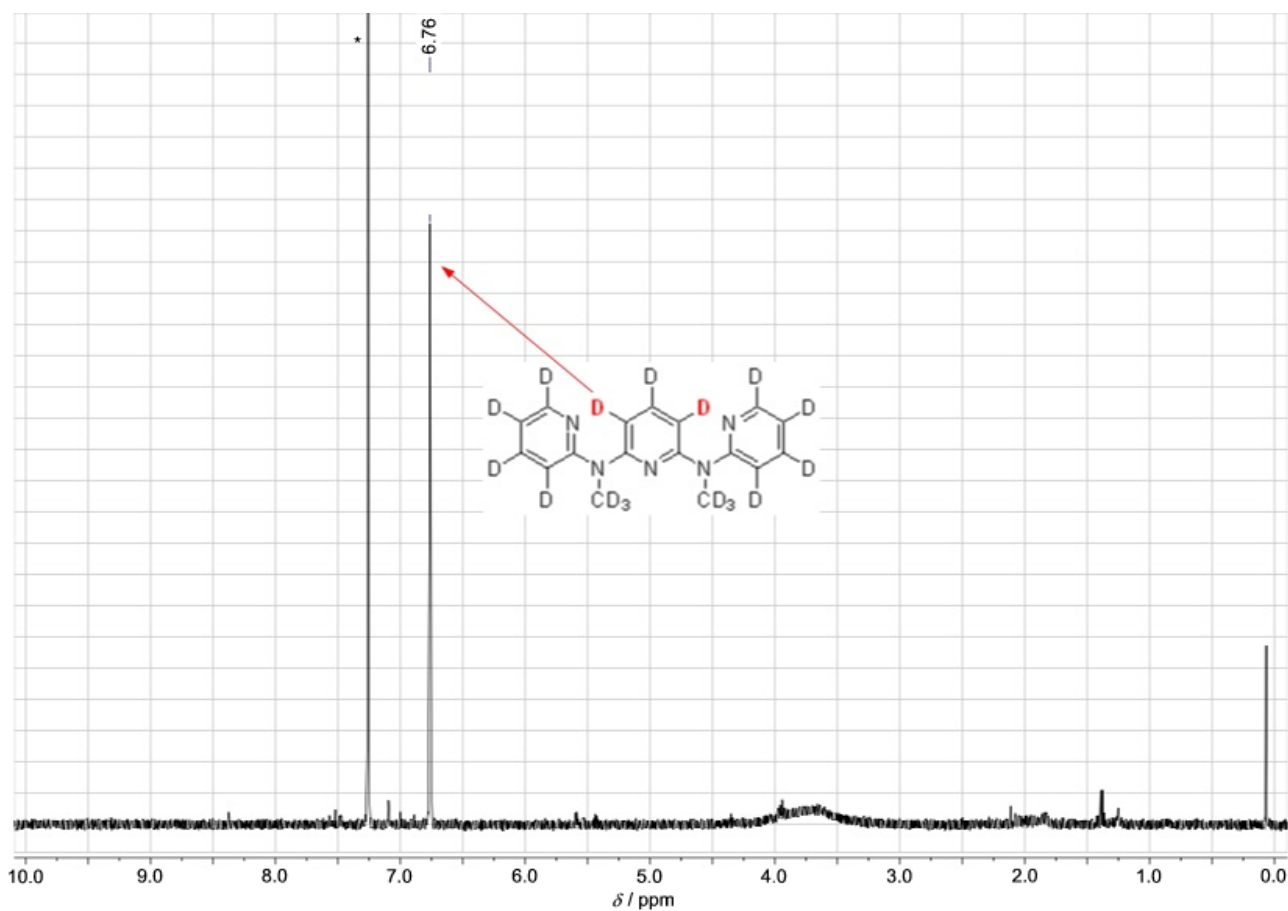


**Figure S6.**  $^1\text{H}$  NMR spectrum (400 MHz) of  $[\text{D}_{17}]$ -ddpd in  $\text{CDCl}_3$  showing the only major residual proton resonance due to incomplete deuteration at the position indicated in bold red. The asterisk marks residual solvent resonance.

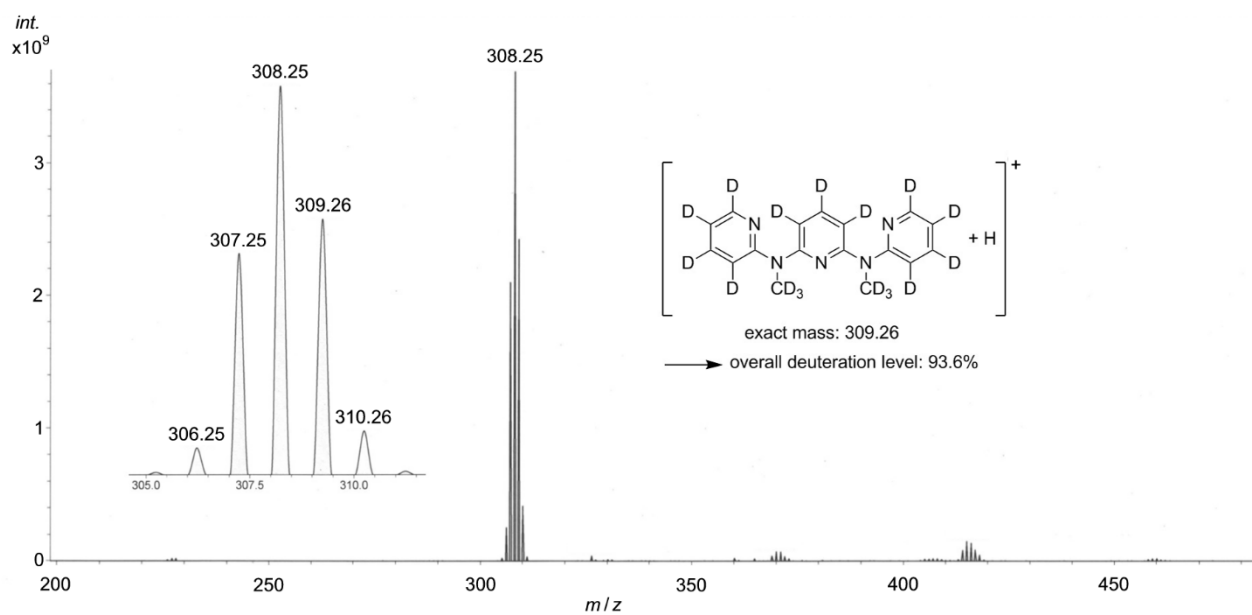


**Figure S7.**  $\text{ESI}^+$  mass spectrum of  $[\text{D}_{17}]$ -ddpd.

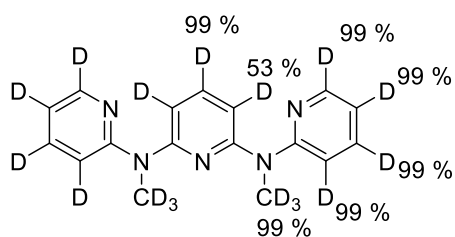


**Figure S8.** Detailed deuteration pattern of  $[D_{17}]$ -ddpd from combined  $^1H$  NMR and mass spectrometry data.

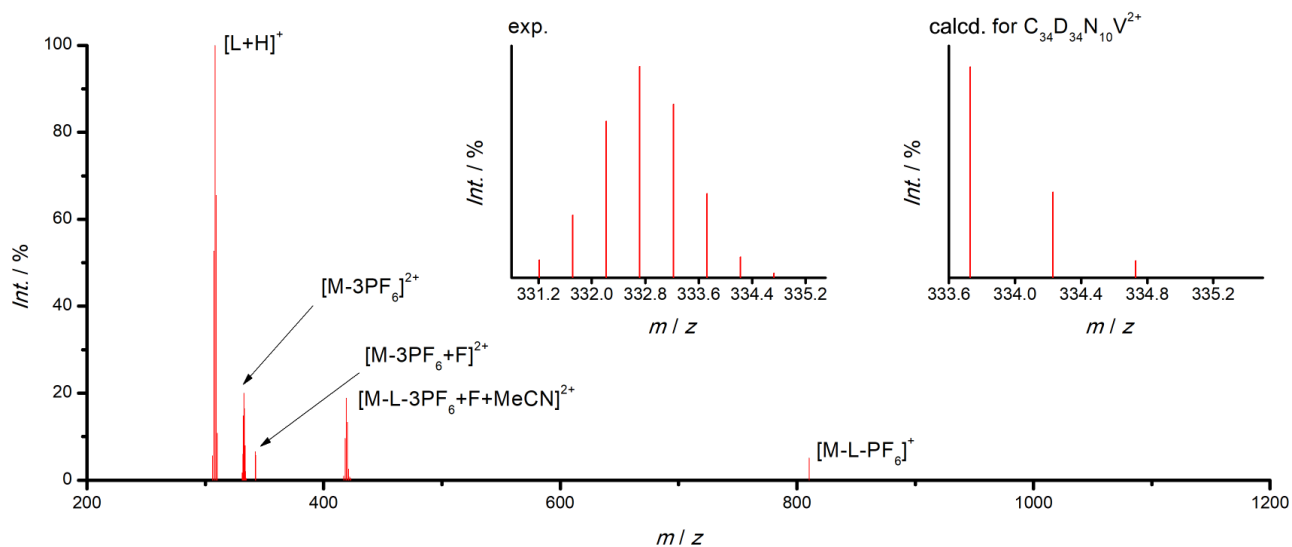


**Figure S9.** ESI<sup>+</sup> mass spectrum of  $mer$ - $[V^{III}]([D_{17}]$ -ddpd)<sub>2</sub>[PF<sub>6</sub>]<sub>3</sub> in CH<sub>3</sub>CN. The insets show the experimental and calculated isotopic pattern of the  $[M-3PF_6]^{2+}$  peak.

**Synthesis of [V(ddpd)<sub>2</sub>][PF<sub>6</sub>]<sub>3</sub>:** [V(NCMe)<sub>6</sub>][BPh<sub>4</sub>]<sub>2</sub> (42.0 mg, 0.05 mmol, 1.0 eq) was dissolved in acetonitrile (4 ml) and [<sup>n</sup>Bu<sub>4</sub>N][PF<sub>6</sub>] (52.2 mg, 0.14 mmol, 2.8 eq.), dissolved in acetonitrile (2 ml), was added under stirring. The ligand ddpd (27.7 mg, 0.09 mmol, 1.8 eq.), dissolved in acetonitrile (2 ml), was added. The turquoise solution was stirred for 18 h and turned dark red within the first several hours. Upon addition of ferrocenium hexafluorophosphate (15.0 mg, 0.05 mmol, 1.0 eq.), dissolved in acetonitrile (4 ml), the red solution turned green. The solvent was removed under reduced pressure and the dark green residue was washed with 2 ml aliquots of petroleum ether (40/60) until the washing solution remained colorless. After dissolving the green product in acetonitrile (4 ml), black crystals were obtained from slow diffusion of diethyl ether into the solution. Yield: 18.2 mg (0.02 mmol, 44 %). C<sub>34</sub>H<sub>34</sub>F<sub>18</sub>N<sub>10</sub>P<sub>3</sub>V: calcd. C 38.22; H 3.21; N 13.11 %; found: C 38.22; H 3.43; N 13.56 %. IR (ATR):  $\tilde{\nu}$  = 1607 (m), 1581 (w), 1568 (w), 1494 (m), 1449 (w), 1432 (m), 1364 (w), 1341 (w), 1319 (w), 1240 (w), 1201 (w), 1175 (w), 1138 (w), 1093 (w), 1065 (w), 1052 (w, sh), 1020 (w), 1011 (w), 949 (w), 876 (w), 832 (s), 807 (s), 775 (s), 750 (m), 716 (w), 656 (w), 633 (w), 582 (w), 556 (s), 523 (w), 507 (w), 480 (w), 467 (w), 449 (w), 436 (w) cm<sup>-1</sup>. MS (ESI<sup>+</sup>, CH<sub>3</sub>CN): *m/z* (%) = 316.6 (35) [M-3PF<sub>6</sub>]<sup>3+</sup>, 326.1 (5) [M-3PF<sub>6</sub>+F]<sup>+</sup>, 778.2 (100) [M-2PF<sub>6</sub>]<sup>+</sup>. UV/VIS/NIR (CH<sub>3</sub>CN):  $\lambda$  ( $\epsilon$  / M<sup>-1</sup>cm<sup>-1</sup>) = 207 (25015), 241 (26040), 301 (23585), 422 (3775) 597 (1945) nm. CV ([<sup>n</sup>Bu<sub>4</sub>N][PF<sub>6</sub>]/CH<sub>3</sub>CN, vs. ferrocene): *E*<sub>1/2</sub> = -2.53 (qrev.), -2.31 (qrev.), -0.275 (rev.) V; *E*<sub>p</sub> = 1.74 (irrev.), 1.86 (irrev.) V.

**Synthesis of [V([D<sub>17</sub>]-ddpd)<sub>2</sub>][PF<sub>6</sub>]<sub>3</sub>:** The deuterated complex was prepared analogously, starting from [D<sub>17</sub>]-ddpd (27.7 mg, 0.09 mmol, 2.0 eq.). Yield: 8.6 mg (0.008 mmol, 13 %). The degree of deuteration was fully retained according to ESI<sup>+</sup> mass spectrometry.

**Table S1.** Bond distances / Å and angles / ° of *mer*-[V<sup>III</sup>(ddpd)<sub>2</sub>][PF<sub>6</sub>]<sub>3</sub>·3CH<sub>3</sub>CN (XRD) and *mer*-[V<sup>III</sup>(ddpd)<sub>2</sub>]<sup>3+</sup> (DFT-UKS).

	ddpd(A)		ddpd(B)		shape parameter <i>S</i> (OC-6) <sup>47</sup>
	V-N1 / V-N2 / V-N3	N1-V-N2 / N1-V-N3 / N2-V-N3	V-N4 / V-N5 / V-N6	N4-V-N5 / N4-V-N6 / N5-V-N6	
XRD	2.079(2)/ 2.062(1)/ 2.068(2)	84.14(6)/ 168.23(6)/ 84.13(6)	2.074(2)/ 2.058(1)/ 2.081(2)	85.12(6)/ 169.73(6)/ 84.69(6)	0.63
DFT-UKS	2.095 2.078 2.097	84.24 168.56 84.32	2.092 2.077 2.096	84.16 168.40 84.25	0.68

**Table S2.** Cartesian Coordinates of the DFT-UKS calculated ground state geometry of *mer*-[V<sup>III</sup>(ddpd)<sub>2</sub>]<sup>3+</sup>.

23	-0.436272000	4.887622000	1.498586000
7	0.057762000	4.359394000	3.465344000
7	0.566002000	2.182490000	2.743718000
7	1.171885000	3.674479000	0.990576000
7	1.735378000	5.193304000	-0.753156000
7	-0.608309000	5.160298000	-0.568481000
7	-1.881315000	3.370031000	1.418202000
7	-2.967475000	4.322157000	3.270756000
7	-2.043433000	6.107196000	1.995698000
7	-1.078209000	7.861890000	0.710978000
7	0.685217000	6.647703000	1.684615000
6	-0.136059000	5.257662000	4.457962000
1	-0.259546000	6.284304000	4.150607000
6	-0.211793000	4.895243000	5.778999000
1	-0.382655000	5.644256000	6.536428000
6	-0.081057000	3.543448000	6.097041000
1	-0.146249000	3.212495000	7.123799000
6	0.163009000	2.623064000	5.098671000
1	0.313028000	1.585384000	5.342659000
6	0.261183000	3.065063000	3.774103000
6	0.413147000	0.745847000	3.014200000
1	-0.540605000	0.588956000	3.509025000
1	1.213525000	0.349688000	3.639044000
1	0.400412000	0.219756000	2.065843000
6	1.420814000	2.536984000	1.690707000
6	2.497005000	1.718823000	1.381436000
1	2.690014000	0.831463000	1.959805000
6	3.346353000	2.091812000	0.355262000
1	4.198093000	1.474345000	0.108427000
6	3.106104000	3.253067000	-0.356363000
1	3.743171000	3.535313000	-1.177084000
6	2.000162000	4.024811000	-0.028203000
6	2.891430000	5.883199000	-1.344184000
1	2.632379000	6.928522000	-1.483488000
1	3.191768000	5.454711000	-2.300306000
1	3.718554000	5.823470000	-0.645115000
6	0.483182000	5.466337000	-1.293928000
6	0.357628000	6.053399000	-2.558570000
1	1.231585000	6.307009000	-3.133546000
6	-0.902124000	6.260699000	-3.081259000
1	-1.006918000	6.701378000	-4.062468000
6	-2.027893000	5.874740000	-2.353587000
1	-3.027361000	6.005690000	-2.738081000
6	-1.836368000	5.328887000	-1.109826000
1	-2.670761000	5.035170000	-0.492501000
6	-1.729583000	2.362329000	0.528906000
1	-1.035394000	2.541877000	-0.277137000
6	-2.384217000	1.162843000	0.651400000
1	-2.220705000	0.380897000	-0.073714000
6	-3.239090000	0.990094000	1.739795000
1	-3.767402000	0.057720000	1.879655000
6	-3.435458000	2.025466000	2.630370000
1	-4.127804000	1.914655000	3.447243000
6	-2.758753000	3.234073000	2.429724000
6	-3.604148000	4.064075000	4.570470000
1	-3.131234000	3.195145000	5.018379000
1	-4.676344000	3.887573000	4.485973000
1	-3.427930000	4.921238000	5.211336000
6	-3.045409000	5.633621000	2.781636000
6	-4.137792000	6.421152000	3.112467000
1	-4.931914000	6.021879000	3.720181000
6	-4.214122000	7.705453000	2.603668000
1	-5.063960000	8.329648000	2.839898000

6	-3.204065000	8.191998000	1.793981000
1	-3.239019000	9.200534000	1.418905000
6	-2.117001000	7.375772000	1.514158000
6	-1.433285000	8.883518000	-0.284577000
1	-0.691772000	8.861308000	-1.077409000
1	-1.478835000	9.886173000	0.140329000
1	-2.398162000	8.626338000	-0.708437000
6	0.257173000	7.779071000	1.094684000
6	1.137328000	8.843198000	0.867841000
1	0.793923000	9.744769000	0.390211000
6	1.954271000	6.577639000	2.147616000
6	2.440965000	8.742728000	1.308045000
6	2.860348000	7.594130000	1.978984000
1	2.229881000	5.657694000	2.639060000
1	3.867457000	7.488226000	2.351171000
1	3.123251000	9.565649000	1.149268000

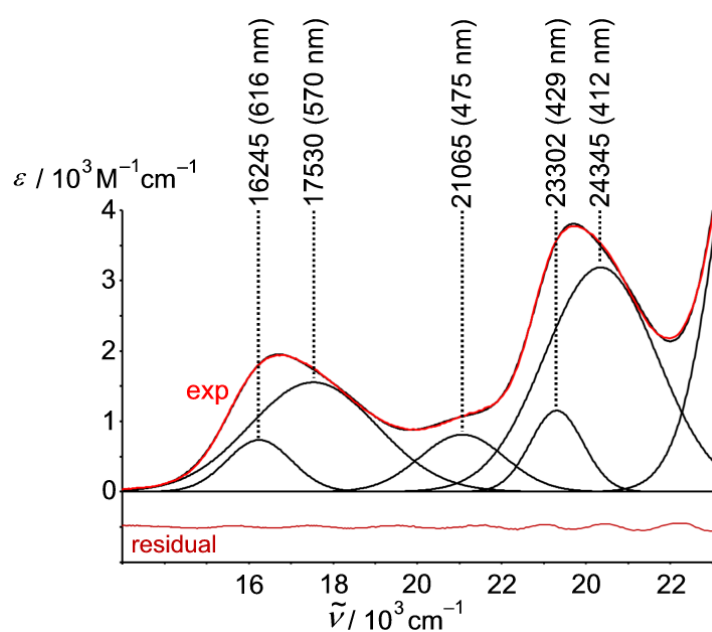
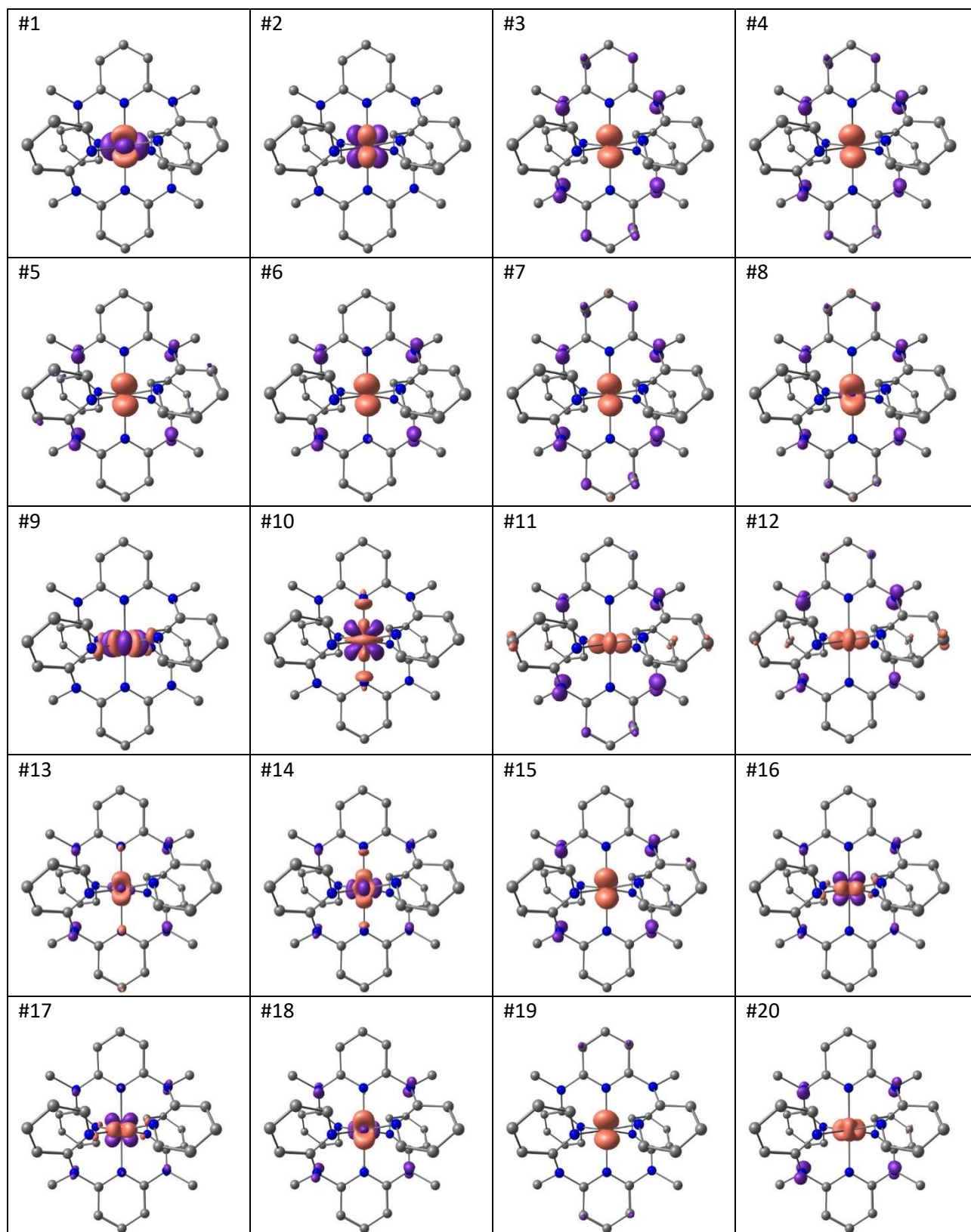


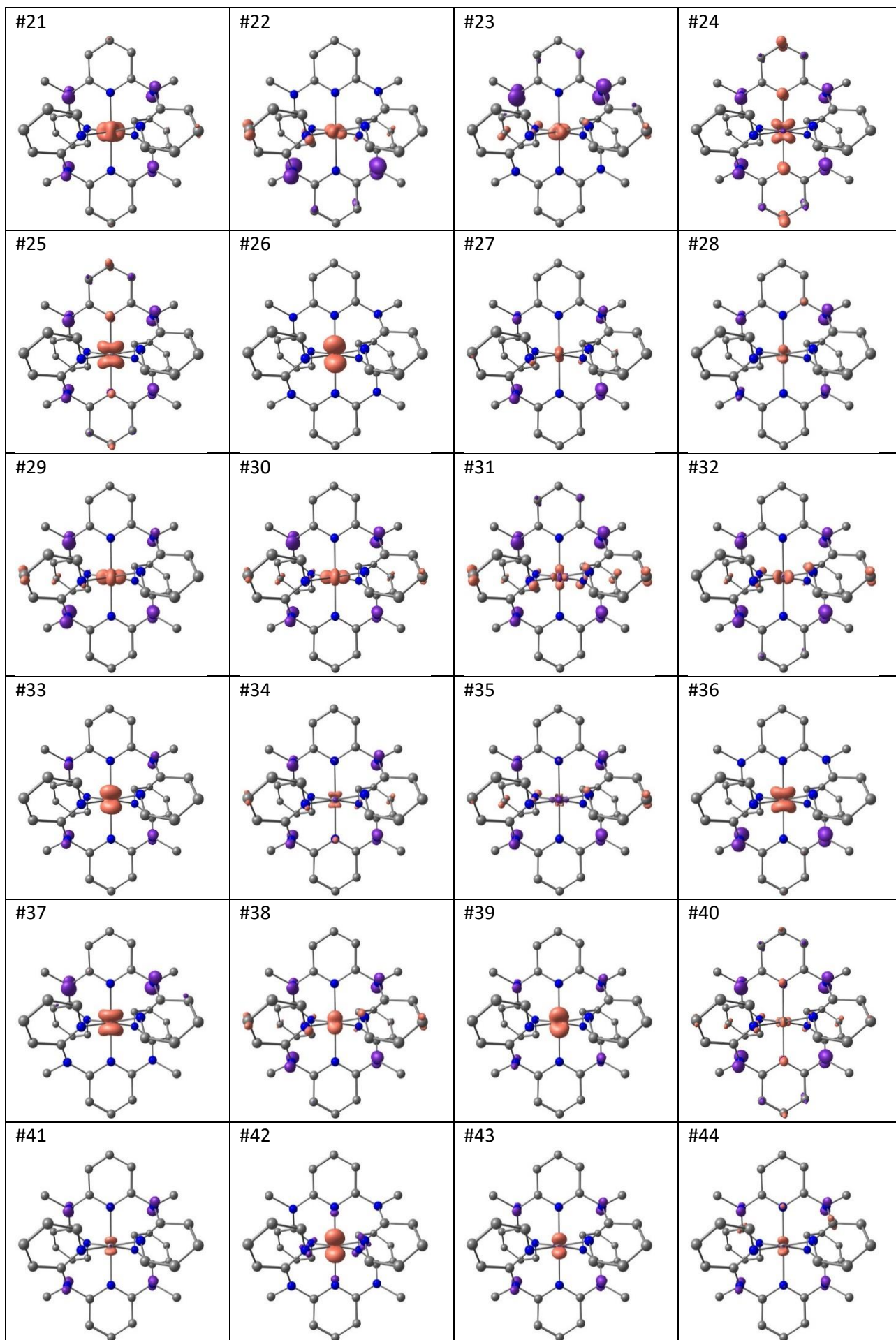
**Figure S10.** UV/Vis spectrum of *mer*-[V<sup>III</sup>(ddd)<sub>2</sub>][PF<sub>6</sub>]<sub>3</sub> in CH<sub>3</sub>CN (red) including Gaussian deconvolution (black).

**Table S3.** TD-DFT calculated spin-allowed transitions (UKS) and triplet states (RKS). The assignment of the UKS states was accomplished by visual inspection of difference electron densities (Table S4). The assignment of the RKS states corresponds to the largest contribution to the charge transfer number (Fig. S21).

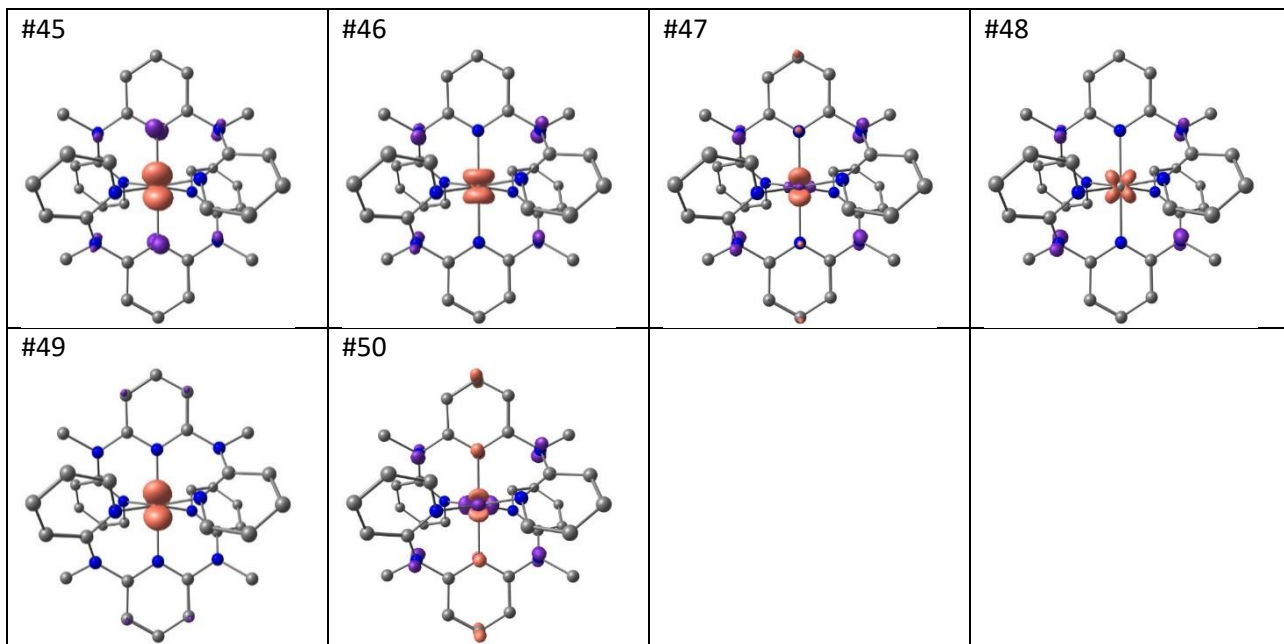
TD-DFT-UKS						TD-DFT-RKS			
state	$\tilde{\nu} / \text{cm}^{-1}$	$\lambda / \text{nm}$	$E / \text{eV}$	$f_{\text{osc}}$	assignment	$\tilde{\nu} / \text{cm}^{-1}$	$\lambda / \text{nm}$	$E / \text{eV}$	assignment
1	3589	2786	0.445	7.71E-04	<sup>3</sup> MC	2084	4800	0.258	<sup>3</sup> MC
2	5077	1970	0.629	7.41E-06	<sup>3</sup> MC				
3	15858	631	1.966	1.31E-02	<sup>3</sup> LMCT(NMe→V)				
4	16237	616	2.013	9.71E-04	<sup>3</sup> LMCT(NMe→V)				
5	19875	503	2.464	3.64E-03	<sup>3</sup> LMCT(NMe→V)				
6	20343	492	2.522	3.32E-06	<sup>3</sup> LMCT(NMe→V)				
7	22097	453	2.740	2.93E-02	<sup>3</sup> LMCT(NMe→V)				
8	22543	444	2.795	1.20E-03	<sup>3</sup> LMCT(NMe→V)				
9	22675	441	2.811	2.66E-04	<sup>3</sup> MC	22529	444	2.793	<sup>3</sup> MC
10	24203	413	3.001	2.42E-06	<sup>3</sup> MC	24786	404	3.073	<sup>3</sup> MC
11	24582	407	3.048	1.62E-04	<sup>3</sup> LMCT(NMe→V)	26901	372	3.335	<sup>3</sup> LMCT
12	24875	402	3.084	1.12E-02	<sup>3</sup> LMCT(NMe→V)	27316	366	3.387	<sup>3</sup> LMCT
13	26190	382	3.247	7.63E-04	<sup>3</sup> LMCT(NMe→V)/ <sup>3</sup> MC	27616	362	3.424	<sup>3</sup> LMCT
14	26214	382	3.250	3.31E-04	<sup>3</sup> MC/LMCT(NMe→V)				
15	26329	380	3.264	1.01E-04	<sup>3</sup> LMCT(NMe→V)				
16	26661	375	3.306	4.13E-04	<sup>3</sup> MC/ <sup>3</sup> LMCT(NMe→V)	28058	356	3.479	<sup>3</sup> LMCT
17	26932	371	3.339	3.68E-04	<sup>3</sup> MC/ <sup>3</sup> LMCT(NMe→V)	30461	328	3.777	<sup>3</sup> LMCT
18	27056	370	3.355	8.04E-07	<sup>3</sup> MC/ <sup>3</sup> LMCT(NMe→V)	30586	327	3.792	<sup>3</sup> LMCT
19	27374	365	3.394	2.14E-03	<sup>3</sup> MC	31428	318	3.897	<sup>3</sup> LMCT
20	27914	358	3.461	2.08E-04	<sup>3</sup> LMCT(NMe→V)	31650	316	3.924	<sup>3</sup> LMCT
21	28340	353	3.514	3.22E-04	<sup>3</sup> LMCT(NMe→V)				
22	28285	354	3.507	6.86E-03	<sup>3</sup> LMCT(NMe→V)/ <sup>3</sup> ILCT				
23	28368	353	3.517	2.12E-03	<sup>3</sup> LMCT(NMe→V)/ <sup>3</sup> ILCT				
24	29010	345	3.597	1.71E-02	<sup>3</sup> LMCT(NMe→V)/ <sup>3</sup> ILCT				
25	29431	340	3.649	2.62E-02	<sup>3</sup> LMCT(NMe→V)/ <sup>3</sup> ILCT				
26	30068	333	3.728	4.04E-03	<sup>3</sup> MC				
27	30568	327	3.790	1.51E-04	<sup>3</sup> LMCT(NMe→V)				
28	30709	326	3.807	9.10E-05	<sup>3</sup> LMCT(NMe→V)/ <sup>3</sup> ILCT				
29	30659	326	3.801	3.28E-04	<sup>3</sup> LMCT(NMe→V)/ <sup>3</sup> ILCT				
30	30835	324	3.823	1.10E-02	<sup>3</sup> LMCT(NMe→V)/ <sup>3</sup> ILCT				
31	30814	325	3.820	2.33E-04	<sup>3</sup> LMCT(NMe→V)/ <sup>3</sup> ILCT				
32	31164	321	3.864	3.39E-02	<sup>3</sup> LMCT(NMe→V)/ <sup>3</sup> ILCT				
33	31585	317	3.916	1.27E-04	<sup>3</sup> LMCT(NMe→V)				
34	31725	315	3.933	1.19E-04	<sup>3</sup> LMCT(NMe→V)/ <sup>3</sup> ILCT				
35	31708	315	3.931	5.79E-03	<sup>3</sup> LMCT(NMe→V)/ <sup>3</sup> ILCT				
36	31789	315	3.941	4.03E-03	<sup>3</sup> LMCT(NMe→V)				
37	31794	315	3.942	2.68E-03	<sup>3</sup> LMCT(NMe→V)				
38	31985	313	3.966	2.60E-02	<sup>3</sup> LMCT(NMe→V)/ <sup>3</sup> ILCT				
39	32267	310	4.001	7.96E-04	<sup>3</sup> LMCT(NMe→V)				
40	32293	310	4.004	5.48E-02	<sup>3</sup> LMCT(NMe→V)/ <sup>3</sup> ILCT				
41	32487	308	4.028	1.44E-02	<sup>3</sup> LMCT(NMe→V)				
42	32451	308	4.023	1.53E-03	<sup>3</sup> LMCT(NMe→V)				
43	32912	304	4.081	3.15E-02	<sup>3</sup> LMCT(NMe→V)				
44	32947	304	4.085	7.00E-03	<sup>3</sup> LMCT(NMe→V)/ <sup>3</sup> ILCT				
45	32928	304	4.083	7.16E-02	<sup>3</sup> LMCT(NMe→V)				
46	33231	301	4.120	3.10E-04	<sup>3</sup> LMCT(NMe→V)				
47	33292	300	4.128	1.29E-02	<sup>3</sup> LMCT(NMe→V)/ <sup>3</sup> ILCT				
48	33381	300	4.139	3.82E-05	<sup>3</sup> LMCT(NMe→V)				
49	33701	297	4.178	2.04E-03	<sup>3</sup> MC				
50	33750	296	4.185	1.87E-02	<sup>3</sup> LMCT(NMe→V)/ <sup>3</sup> ILCT				

**Table S4.** Difference electron densities of the 50 lowest-lying TD-DFT-UKS calculated states. (isosurface value at 0.007 a.u.; purple = electron depletion; orange = electron gain; hydrogen atoms omitted).

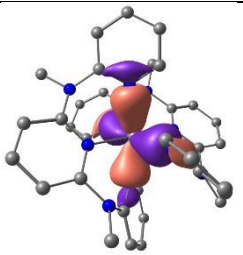
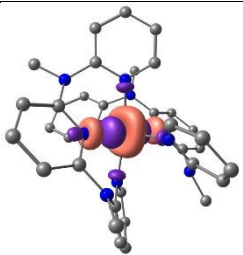
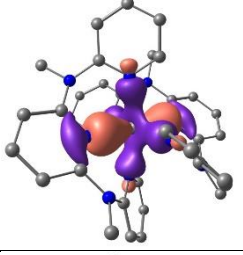
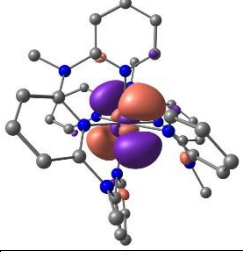
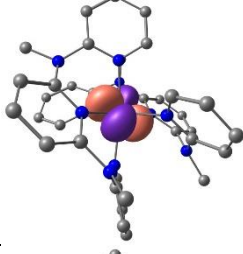
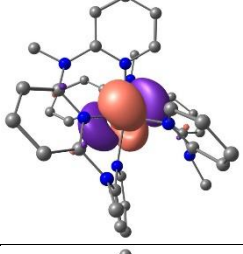
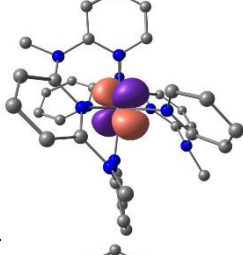
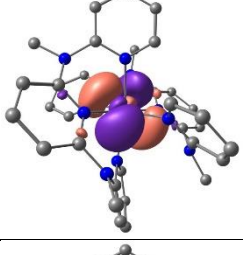
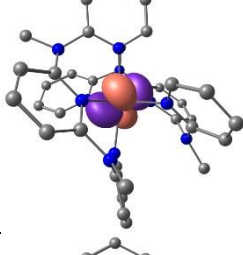
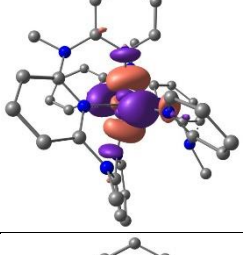
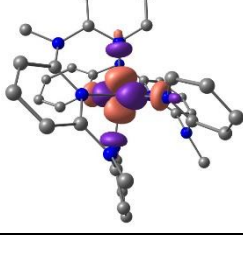
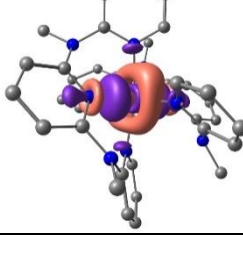








**Table S5.** Orbital energies/Hartree of the canonical orbitals used in the active space of the CASSCF(6,12)-FIC-NEVPT2 calculation, depicted at a contour value of 0.05 a.u. (hydrogen atoms omitted for clarity).

#	$E / H$	orbital	#	$E / H$	orbital
161	-0.59153		167	+0.12076	
162	-0.59466		168	+0.8329	
163	-0.00153		169	+0.85194	
164	+0.00038		170	+0.89659	
165	+0.00753		171	+1.31242	
166	+0.11194		172	+1.49528	

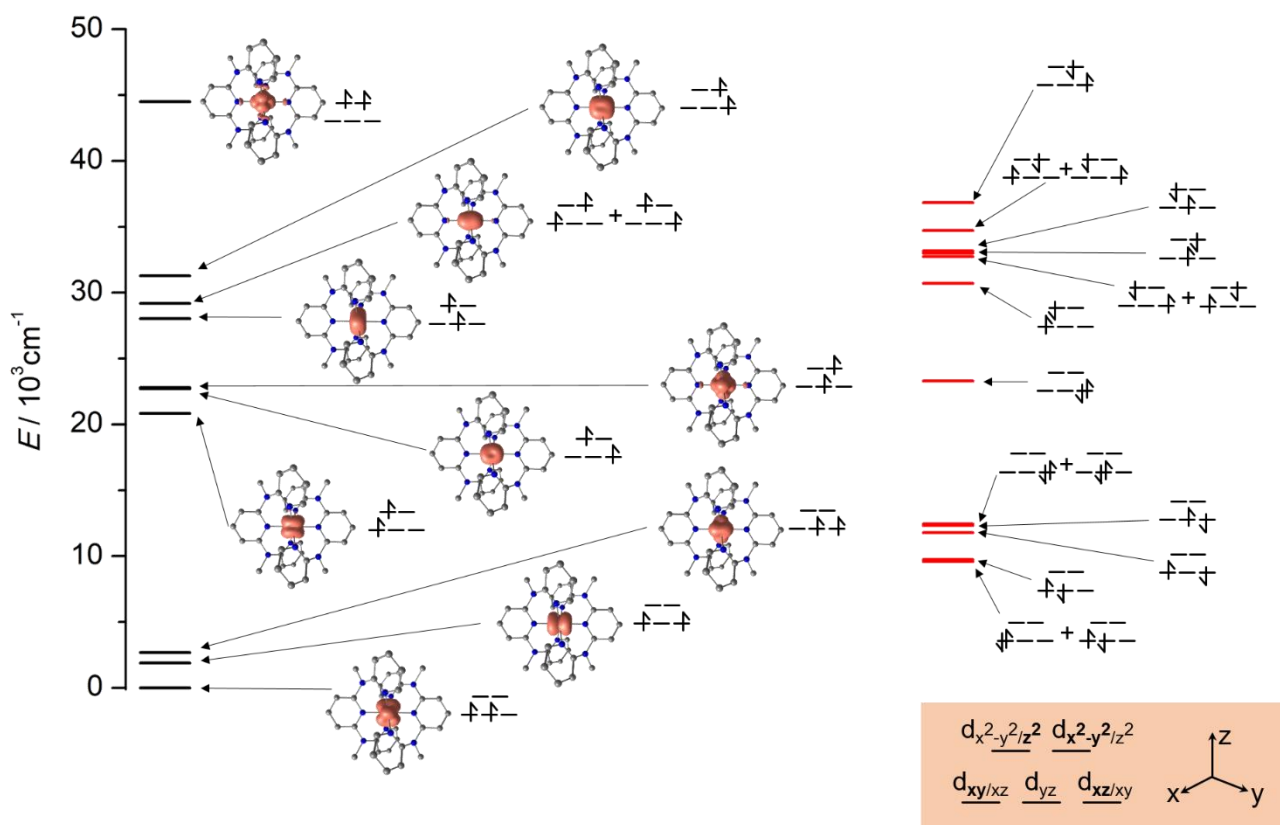


**Figure S11.** Energy diagram of the electronic states of  $mer-[V^{III}(ddpd)_2]^{3+}$  constructed from CASSCF(6,12)-FIC-NEVPT2 energies with spin densities in orange (0.05 a.u. isosurface value, hydrogen atoms omitted for clarity, triplet states in black, singlet states in red; a coordinate system referring to the displayed structures and d orbital labels is shown in the orange box).

**Table S6.** CASSCF(6,12)-FIC-NEVPT2 state compositions (the configurations are the occupation numbers for the individual active orbitals in rising energy (in eV and  $\text{cm}^{-1}$ ). The first two numbers of the configuration represent the ligand-metal  $\sigma$ -bonding orbitals, the next five the metal 3d orbitals and the last five the 4d orbitals (Table S6). Singlet states shown in red, triplet states shown in black.

state	root	mult	configuration	weight	$\Delta E/\text{eV}$	$\tilde{\nu} / \text{cm}^{-1}$	$\lambda/\text{nm}$
0	0	3	221100000000	0.94971	0		
1	1	3	221010000000	0.94790	0.232	1873	5344
2	2	3	220110000000	0.95301	0.333	2687	3723
3	0	1	222000000000	0.65408	1.192	9612	1040
4	1	1	221100000000	0.96124	1.207	9736	1027
5	2	1	221010000000	0.97424	1.459	11769	850
6	3	1	220110000000	0.95454	1.529	12333	811
7	4	1	220020000000	0.48695	1.541	12431	805
8	3	3	221001000000	0.83676	2.584	20844	480
9	4	3	220011000000	0.70074	2.815	22706	440
10	5	3	220100100000	0.42279	2.827	22803	439
11	5	1	220020000000	0.98358	2.887	23283	429
12	6	3	220101000000	0.94490	3.475	28026	357
13	7	3	221000100000	0.67288	3.618	29183	343
14	6	1	221001000000	0.91877	3.809	30720	326
15	8	3	220010100000	0.81832	3.878	31278	320
16	7	1	220011000000	0.57938	4.059	32735	305
17	8	1	220100100000	0.96151	4.095	33028	303
18	9	1	220101000000	0.97839	4.112	33163	302
19	10	1	221000100000	0.58977	4.303	34708	288
20	11	1	220010100000	0.93700	4.567	36835	271
21	9	3	220001100000	0.99098	5.518	44503	225

**Table S7.** Partial quantum yields  $\Phi$  and luminescence lifetimes  $\tau$  for  $[\text{V}(\text{ddpd})_2][\text{PF}_6]_3$  and  $[\text{V}([\text{D}_{17}]\text{-ddpd})_2][\text{PF}_6]_3$  in deoxygenated solutions.

compound	$\Phi_{\text{F}} / \%$ <sup>a</sup>	$\tau_{\text{F}} / \text{ns}$ (fraction) <sup>b</sup>	$\Phi_{\text{P}} / \%$ <sup>c</sup>	$\tau_{\text{P}} / \text{ns}$	$\tau_{\text{F}} / \text{ns}$
				(fraction) <sup>d</sup>	(fraction)
				in <sup>n</sup> BuCN, 77 K	in <sup>n</sup> PrCN, 77 K
		in $\text{CD}_3\text{CN}$ , 298 K			
$[\text{V}(\text{ddpd})_2][\text{PF}_6]_3$	2.1	3.2 (56 %) 8.2 (44 %)	$1.8 \times 10^{-4}$	790 (93 %) 8800 (7 %)	1.7 (51 %) 6.3 (49 %)
$[\text{V}([\text{D}_{17}]\text{-ddpd})_2][\text{PF}_6]_3$	1.2	3.3 (88 %) 7.2 (12 %)	$1.6 \times 10^{-4}$	800 (91 %) 8300 (9 %)	–

<sup>a</sup>  $\lambda_{\text{exc}} = 308 \text{ nm}$ ,  $\lambda_{\text{em}} \approx 340 - 580 \text{ nm}$ , measured relative to the quantum yield standard quinine in 0.1 M aqueous  $\text{H}_2\text{SO}_4$ , estimated uncertainties  $\pm 40 \%$ ; <sup>b</sup>  $\lambda_{\text{exc}} = 306 \text{ nm}$ ,  $\lambda_{\text{em}} 390$ , biexponential fitting, estimated uncertainties  $\pm 10 \%$ ; <sup>c</sup>  $\lambda_{\text{exc}} = 308 \text{ nm}$ ,  $\lambda_{\text{em}} \approx 1050 - 1200 \text{ nm}$ , measured relative to the quantum yield standard  $[\text{Yb}(\text{tta})_3(\text{phen})]$  in toluene, estimated uncertainties  $\pm 50 \%$ ; <sup>d</sup>  $\lambda_{\text{exc}} = 300 \text{ nm}$ ,  $\lambda_{\text{em}} 1110 \text{ nm}$ , biexponential fitting, estimated uncertainties  $\pm 20 \%$ .

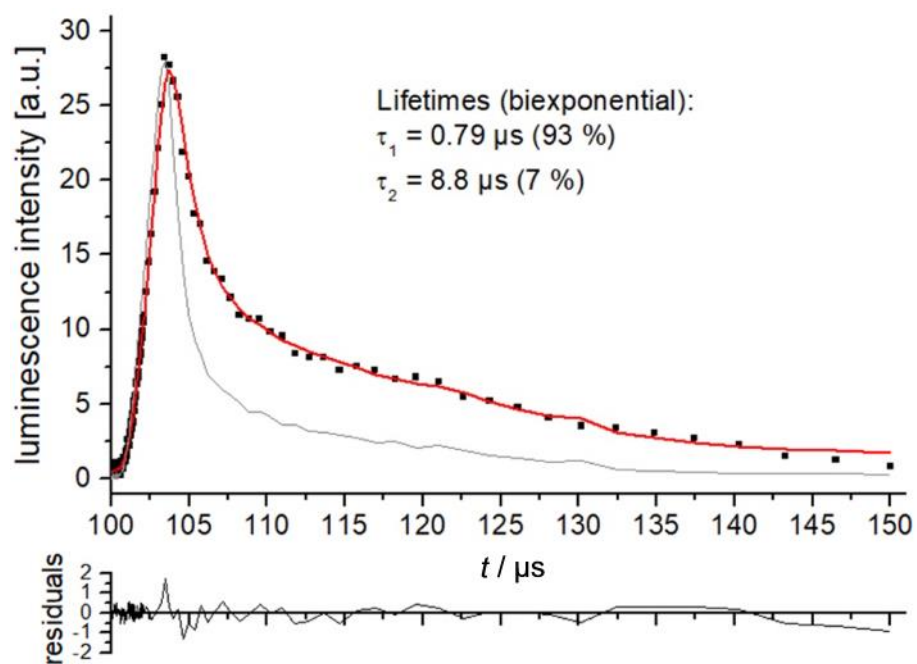


**Figure S12.** Luminescence decay (black scatter) for *mer*-[V(ddpd)<sub>2</sub>][PF<sub>6</sub>]<sub>3</sub> in deoxygenated <sup>n</sup>BuCN at 77 K ( $\lambda_{\text{exc}} = 300 \text{ nm}$ ,  $\lambda_{\text{em}} = 1110 \text{ nm}$ , emission path: long pass filter RG850) with biexponential fit function (red) and instrument response function (gray).

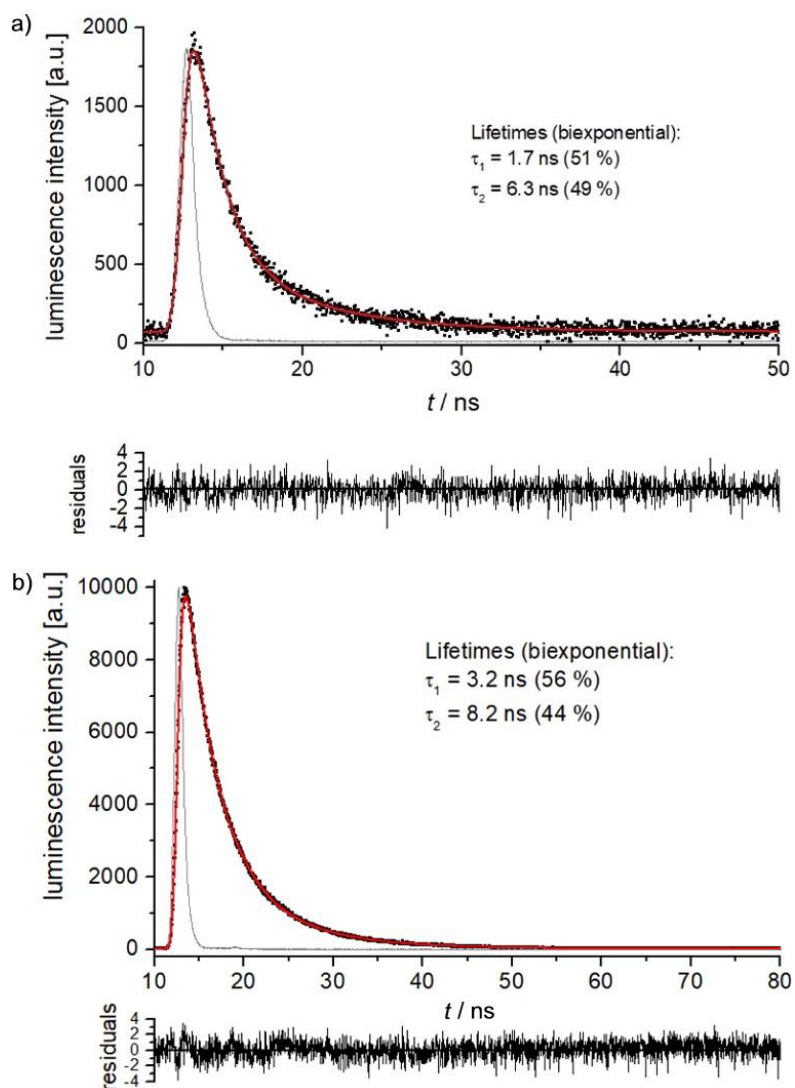


**Figure S13.** a) Luminescence decay (black scatter) for *mer*-[V(ddpd)<sub>2</sub>][PF<sub>6</sub>]<sub>3</sub> in deoxygenated <sup>n</sup>PrCN at 77 K ( $\lambda_{\text{exc}} = 306$  nm,  $\lambda_{\text{em}} = 416$  nm) with biexponential fit function (red) and instrument response function (gray) and b) luminescence decay (black scatter) for *mer*-[V(ddpd)<sub>2</sub>][PF<sub>6</sub>]<sub>3</sub> in deoxygenated CD<sub>3</sub>CN at 298 K ( $\lambda_{\text{exc}} = 306$  nm,  $\lambda_{\text{em}} = 390$  nm) with biexponential fit function (red) and instrument response function (gray).

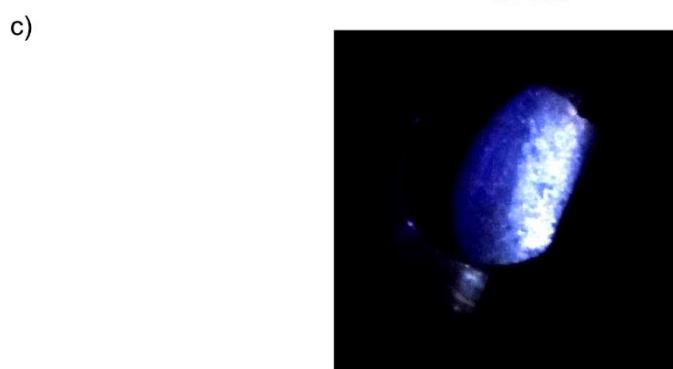
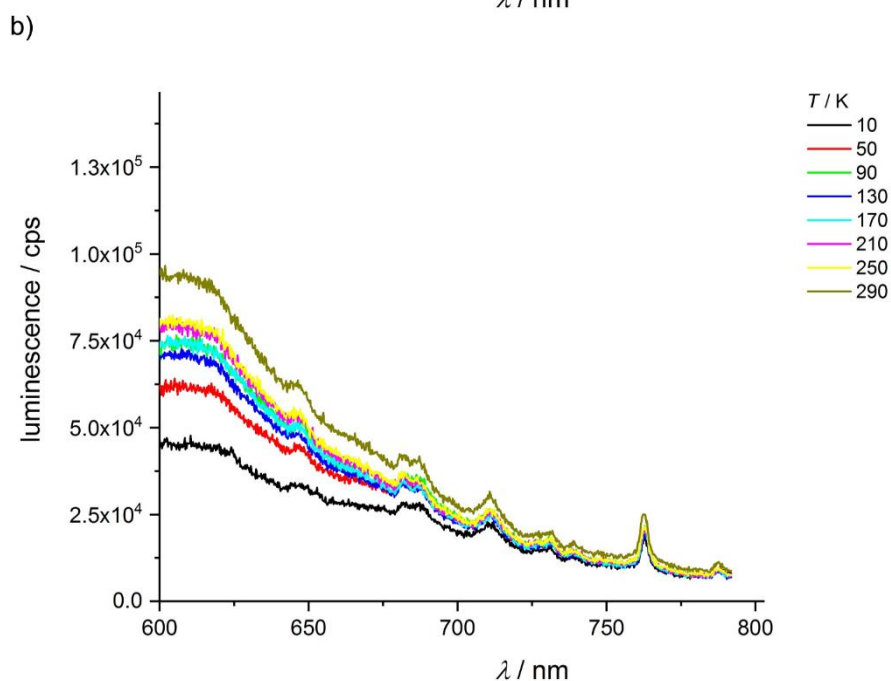
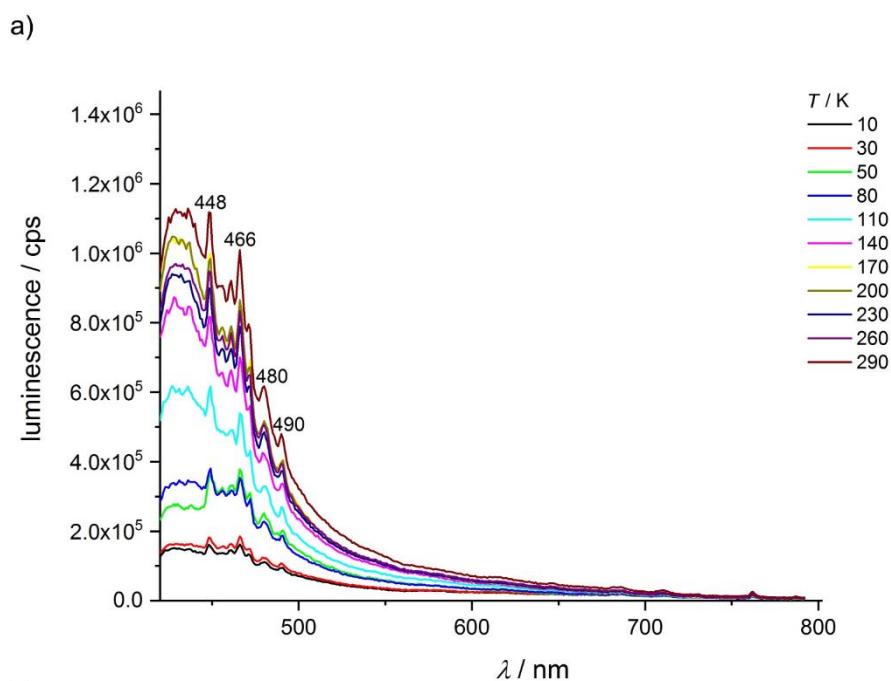


**Figure S14.** Emission spectra of *mer*-[V(ddpd)<sub>2</sub>][PF<sub>6</sub>]<sub>3</sub> in a KBr pellet at different temperatures using **a.** 420 and **b.** 600 nm longpass filters;  $\lambda_{\text{exc}} = 400$  nm. The quite surprising decrease of the intensity of blue fluorescence upon cooling the sample may be explained by a more favorable ISC to the singlet manifold at low temperature, compared to other radiative and non-radiative processes. **c.** Photograph of *mer*-[V(ddpd)<sub>2</sub>][PF<sub>6</sub>]<sub>3</sub> in a KBr pellet under excitation with  $\lambda_{\text{exc}} = 350$  nm (290 K).

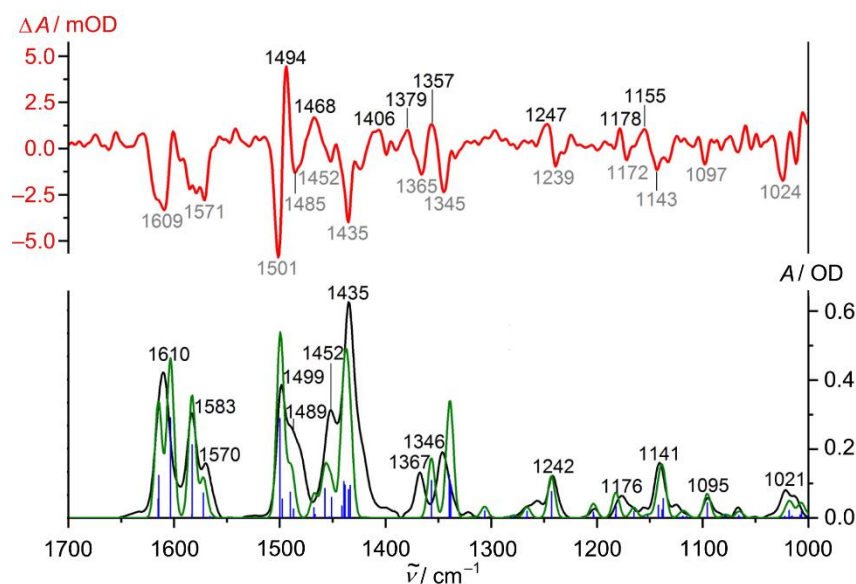


**Figure S15.** Step-scan FTIR spectrum of  $[\text{V}(\text{ddpd})_2][\text{PF}_6]_3$  (KBr pellet, 20 K) 0 to 300 ns after laser excitation at  $\lambda_{\text{exc}} = 355$  nm (red) and ground state FTIR spectrum (black) (KBr pellet, 20 K), DFT-UKS calculated IR absorption transitions (blue) (scaled by 0.98), and DFT-UKS calculated IR spectrum (green) of  $[\text{V}(\text{ddpd})_2]^{3+}$  (scaled by 0.98, FWHM =  $8 \text{ cm}^{-1}$ , gaussian profile).

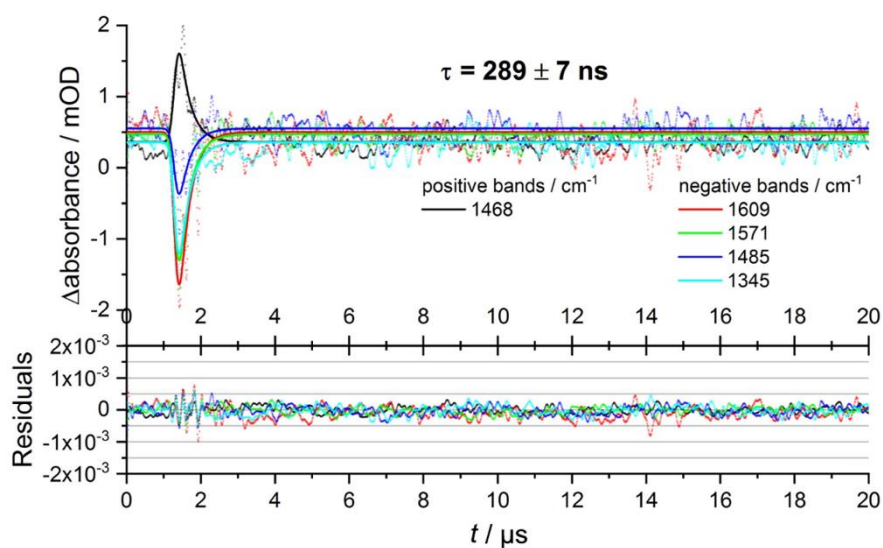


**Figure S16.** Global monoexponential fit and residuals performed for the most prominent positive and negative peaks in the step-scan spectrum of  $[\text{V}(\text{ddpd})_2][\text{PF}_6]_3$  (KBr pellet, 20 K).



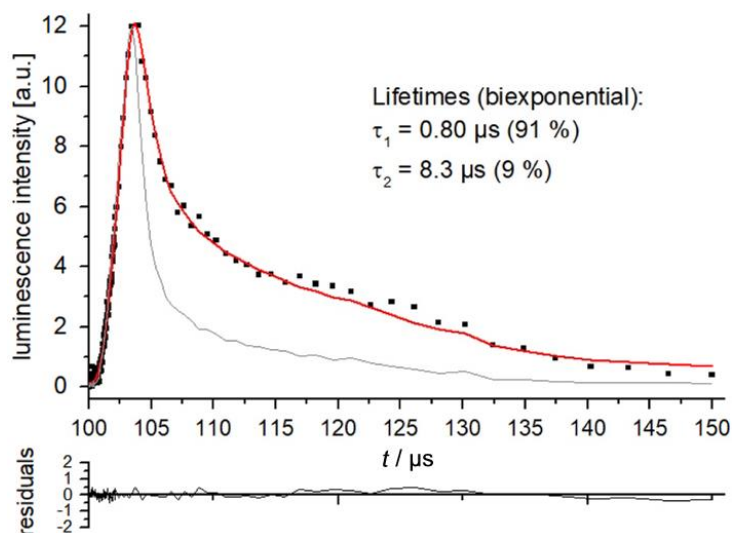


**Figure S17.** Luminescence decay (black scatter) for *mer*-[V([D<sub>17</sub>]-ddpd)<sub>2</sub>][PF<sub>6</sub>]<sub>3</sub> in deoxygenated <sup>t</sup>BuCN at 77 K ( $\lambda_{\text{exc}} = 300 \text{ nm}$ ,  $\lambda_{\text{em}} = 1110 \text{ nm}$ , emission path: long pass filter RG850) with biexponential fit function (red) and instrument response function (gray).

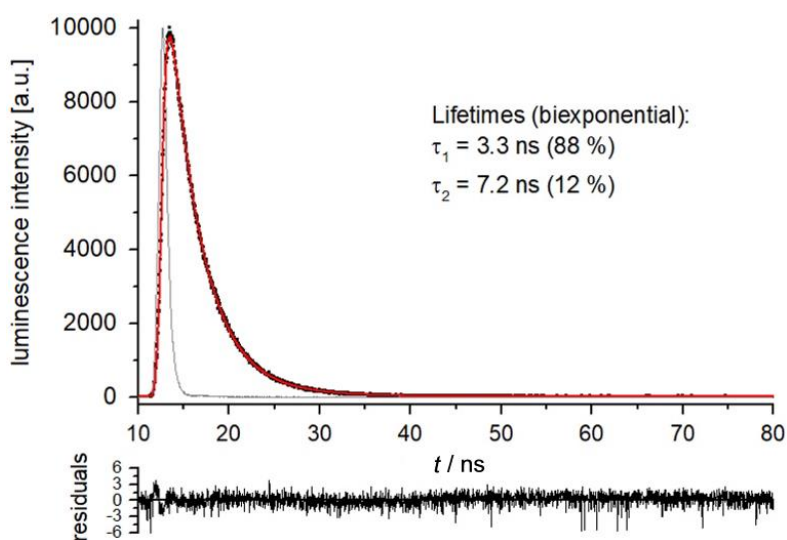


**Figure S18.** Luminescence decay (black scatter) for *mer*-[V([D<sub>17</sub>]-ddpd)<sub>2</sub>][PF<sub>6</sub>]<sub>3</sub> in deoxygenated CD<sub>3</sub>CN at 298 K ( $\lambda_{\text{exc}} = 306 \text{ nm}$ ,  $\lambda_{\text{em}} = 390 \text{ nm}$ ) with biexponential fit function (red) and instrument response function (gray).

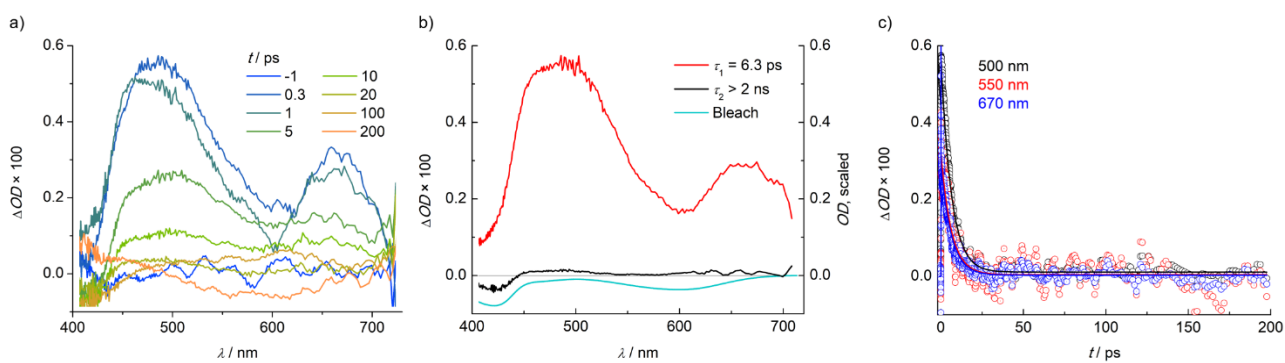


**Figure S19.** **a.** Transient absorption spectra of  $[V^{III}(\text{ddpd})_2][\text{PF}_6]_3$  in  $\text{CH}_3\text{CN}$  excited with 620 nm laser pulses. **b.** Decay associated amplitude spectra labelled by the corresponding time constants and compared to the bleach. **c.** Transient signals as a function of the pump–probe delay time observed at 500 nm (black), 550 nm (red) and 670 nm (blue).

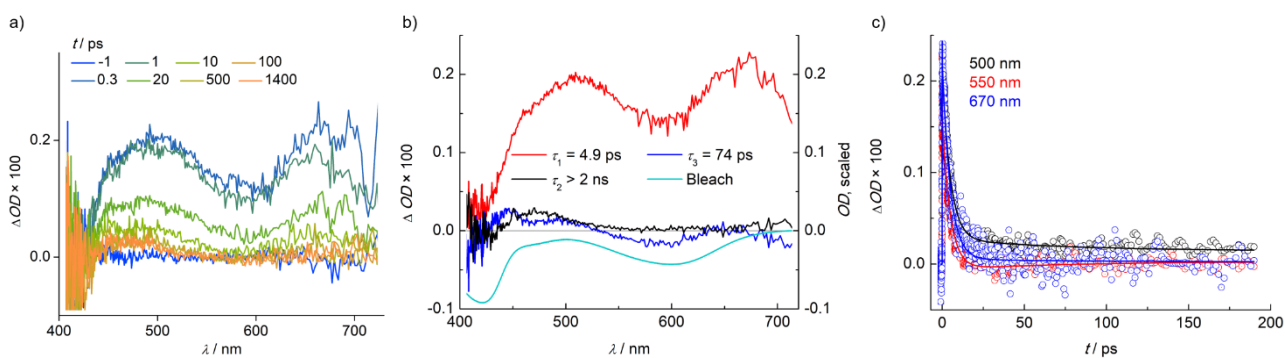


**Figure S20.** **a.** Transient absorption spectra of  $[V^{III}(\text{ddpd})_2][\text{PF}_6]_3$  in  $\text{CH}_3\text{CN}$  excited with 400 nm laser pulses. **b.** Decay associated amplitude spectra labelled by the corresponding time constants and compared to the bleach. **c.** Transient signals as a function of the pump–probe delay time observed at 500 nm (black), 550 nm (red) and 670 nm (blue).

**Table S8.** TD-DFT-RKS relative energies (eV) with respect to the triplet ground state  ${}^3T_{1g}$  and corresponding assignment based on the largest contribution of the charge transfer numbers (Fig. S21) of the electronic states used to parameterize the potential energy surfaces employed in the SHARC-LVC simulations. Irreducible representations labels correspond to an idealized octahedral geometry (Fig. S1).

State	Triplets	$\Delta E$ /eV	Singlets	$\Delta E$ /eV
1	$1^3MC$ ( ${}^3T_{1g}$ )	0	$1^1MC$ ( ${}^1E_g$ )	1.16
2	$2^3MC$ ( ${}^3T_{1g}$ )	0.26	$2^1MC$ ( ${}^1T_{2g}$ )	1.36
3	$3^3MC$ ( ${}^3T_{2g}$ )	2.79	$3^1MC$	1.47
4	$4^3MC$ ( ${}^3T_{2g}$ )	3.07	$1^1LMCT$	3.44
5	$1^3LMCT$	3.33	$2^1LMCT$	3.50
6	$2^3LMCT$	3.39	$3^1LMCT$	3.59
7	$3^3LMCT$	3.42	$4^1LMCT$	3.64
8	$4^3LMCT$	3.48	$4^1MC$	3.72
9	$5^3LMCT$	3.78	$5^1MC$	3.79
10	$6^3LMCT$	3.79	$5^1LMCT$	3.94
11	$7^3LMCT$	3.90	$6^1LMCT$	3.96
12	$8^3LMCT$	3.92	$7^1LMCT$	4.08

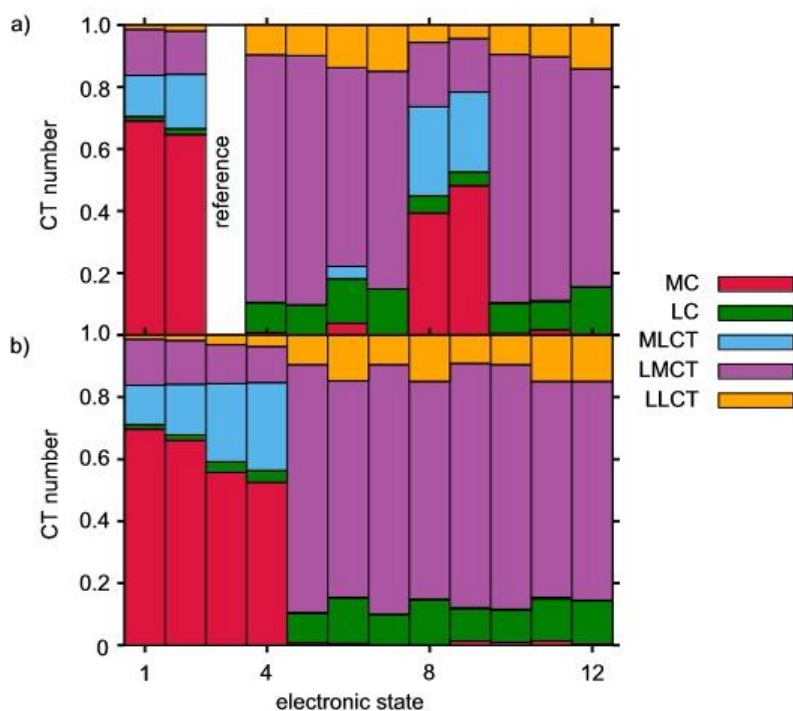


**Figure S21.** TD-DFT-RKS charge transfer (CT) numbers defined from 0 to 1 of the lowest-lying 12 singlets (a) and 12 triplets (b) states, calculated with respect to the closed-shell reference  $3^1MC$  ( ${}^1A_{1g}$ ). The reference state is 100 % closed-shell and serves as a reference for the CT numbers calculated.

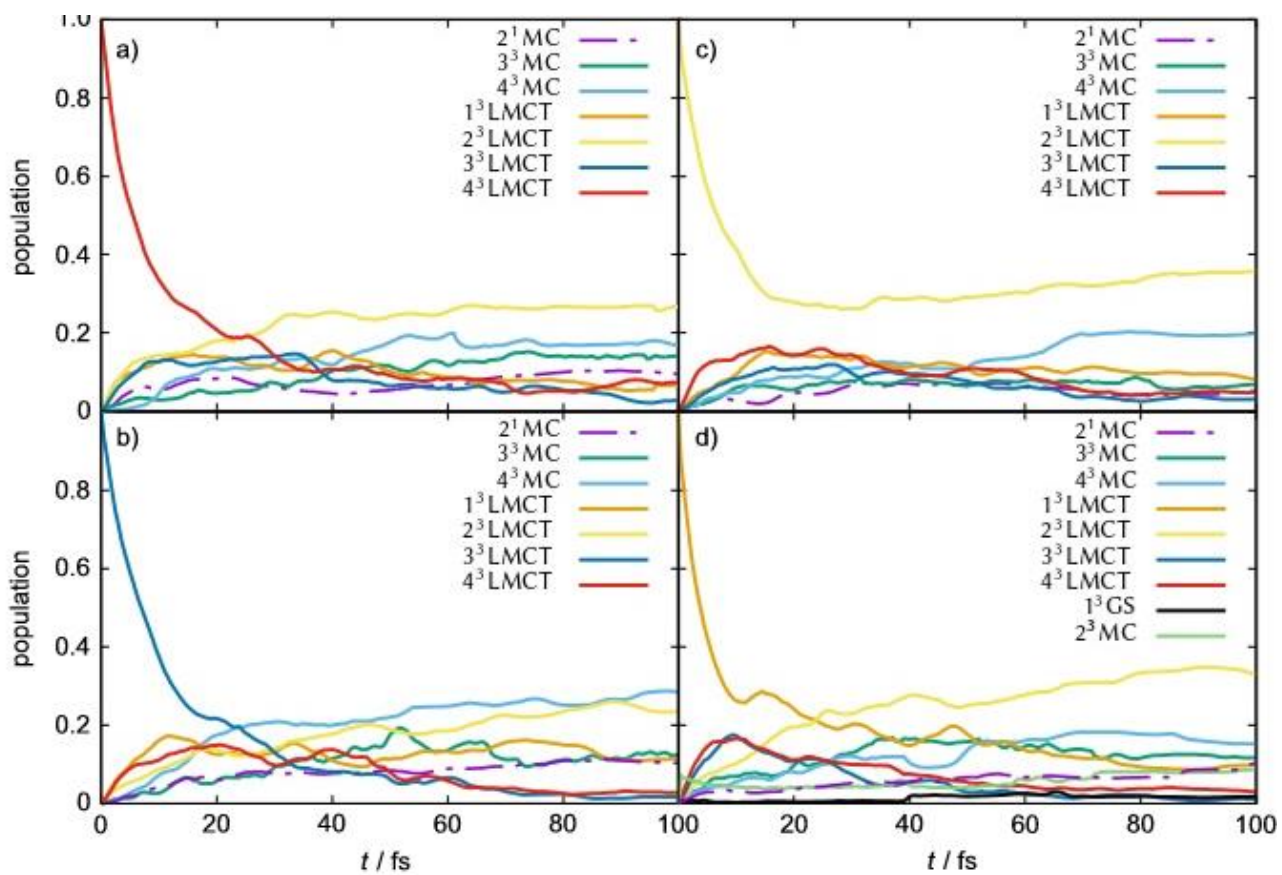


**Figure S22.** Time-evolution of the population on the excited states during the first 100 fs, after starting the dynamics on a)  $4^3\text{LMCT}$ , b)  $3^3\text{LMCT}$ , c)  $2^3\text{LMCT}$ , d)  $1^3\text{LMCT}$  triplet states. Population in any other singlet state other than  $2^1\text{MC}$  is negligible and not plotted.

**Table S9.** Cartesian coordinates of the minimum energy geometry of the 2<sup>1</sup>MC singlet state, optimized within the LVC method.

V	-0.66530157968787	4.73327191559267	1.15414806626787
N	-0.33031990692470	4.49554366729562	3.24011128941319
N	0.41830831745261	2.21830701812423	2.87578640975785
N	0.97362870509963	3.50540643057365	0.94630448773096
N	1.61181540473234	5.06453779574661	-0.70547438832152
N	-0.72354413669044	4.76766598674381	-0.90727949908829
N	-1.96074838838531	3.16994764007497	1.08780284944625
N	-3.22330616437540	4.11306267448654	2.85863757136509
N	-2.21011674159465	5.95501601848848	1.67409350682190
N	-1.11064559695091	7.76960212804624	0.59882839517929
N	0.58976681646651	6.42517020550181	1.45105292787956
C	-0.51902350304275	5.56679860144001	4.08464141971885
H	-0.99699684623169	6.48213429825880	3.63165367747580
C	-0.16320443140994	5.50958067229945	5.48352260559947
H	-0.35556178466572	6.39299189250326	6.10453377228770
C	0.51176234304264	4.31800507016179	6.06408638013690
H	0.89902833180966	4.22851529398475	7.15602764374424
C	0.75868681650198	3.25593348824104	5.19995115897545
H	1.34566669070994	2.36340268708133	5.61351377319930
C	0.27580951908176	3.34952219944841	3.77455144119524
C	0.42018420640678	0.85020353375555	3.57052585170090
H	-0.39584601781559	0.77755344403761	4.32684050305551
H	1.37894137222654	0.67430009465801	4.11198294918403
H	0.26254884577769	0.07566127797111	2.76831582681121
C	1.15439748411093	2.36476309861683	1.67101644509280
C	2.10641939261553	1.42356718411031	1.25941935733429
H	2.25574519220159	0.51061526752509	1.81405784265292
C	2.97403726640090	1.76629990326041	0.23081403718095
H	3.76278574276453	1.08027705090921	-0.05494221860542
C	2.86302853677891	2.99025708861967	-0.42628638110484
H	3.49707496006560	3.31985076379143	-1.23583990510299
C	1.81763156898550	3.82320791161327	-0.07354996768462
C	2.83029928965059	5.97887585408924	-0.90011021511064
H	2.41554656988593	6.99646409452291	-0.96780825332937
H	3.55087333703551	5.67230931017101	-1.75596654545864
H	3.42879715613805	5.96338504169185	0.08606352508797
C	0.44216636160675	5.38973471048780	-1.36280251430980
C	0.46573486730863	6.34793466226565	-2.45814903615440
H	1.41703906901873	6.78735923738471	-2.81081756219200
C	-0.73262762177129	6.65128543688819	-3.09104037879572
H	-0.74238450534174	7.40302113893741	-3.93830763666378
C	-1.92899150285652	5.92906992859351	-2.67105828474415
H	-2.87962140492781	6.11776359400517	-3.16034885436779
C	-1.89273795903647	5.00037101855265	-1.58049928373020
H	-2.81901711234949	4.50676085023559	-1.17595517763402
C	-1.67220076396436	2.11464319120735	0.26628263347842
H	-0.98933712529239	2.32687239570611	-0.54156214987688
C	-2.15687315540798	0.84205131370184	0.48371391037265
H	-1.86512504601290	0.01176335787152	-0.15931420609855
C	-3.01035880731720	0.65100071089963	1.57491682377841
H	-3.40025978996045	-0.34014703517561	1.79390915664606
C	-3.38350807185125	1.73340937704325	2.36839128304000
H	-4.08062037759673	1.60134843901535	3.18276761788482
C	-2.86067965063365	3.01531348345467	2.07944393277739
C	-3.70493630437212	3.82438704648768	4.23523611756562
H	-3.04190831110575	3.05752658744568	4.66273815789241
H	-4.75507503727469	3.49933672866476	4.27620673752258
H	-3.58814105987102	4.72646958234386	4.82478436598885
C	-3.17180039490112	5.50367725461328	2.53685243927383
C	-4.11306109280554	6.48231054318854	3.21399326932164
H	-4.91248388501292	6.10384131769645	3.83079600124229
C	-3.97406588955119	8.00933775827573	3.19294090222228
H	-4.65613641102556	8.81979055084680	3.86077222364849
C	-2.98017046603333	8.45680858404359	2.3222283020250
H	-2.83517191274696	9.63489712391607	2.30759569178623
C	-2.12851454730312	7.37398690254809	1.52735339577138
C	-1.45842223194776	8.99550642510190	-0.17258183971986
H	-0.81466042114834	8.96943559455970	-1.08741231606597
H	-1.27972973059534	9.94759527925353	0.44055814387018
H	-2.56663951869531	8.97082259954718	-0.49474886031302
C	0.22495910042885	7.63515938090614	0.99965310256870
C	1.12055930549567	8.71230282173515	0.98126581737906
H	0.81802530346211	9.67679693582683	0.60260621904721
C	1.83052754324382	6.25881473429048	1.95615033551378
C	2.38955024184869	8.53412485803401	1.50832530143104
C	2.75514231091441	7.28051998723144	2.00643290806222
H	2.07673153270343	5.26299380217903	2.30093049901599
H	3.73629512792687	7.09459911151002	2.42034138169754
H	3.08593957658572	9.36744507524232	1.54281956117543

## References.

1. Breivogel, A.; Förster, C.; Heinze, K. A Heteroleptic Bis(tridentate)ruthenium(II) Polypyridine Complex with Improved Photophysical Properties and Integrated Functionalizability. *Inorg. Chem.* **2010**, *49*, 7052–7056.
2. Anderson, S. J.; Wells, F. J.; Wilkinson, G.; Hussain, B.; Hursthouse, M. B. 1,2-Bis(dimethyl)phosphinoethane complexes of molybdenum and vanadium. X-ray crystal structure of trans-[MoCl( $\eta^2$ -NCMe)(dmpe)<sub>2</sub>]BPh<sub>4</sub>, trans-[(SPh)<sub>2</sub>(dmpe)<sub>2</sub>], trans-[V(NCMe)<sub>2</sub>(dmpe)<sub>2</sub>]BPh<sub>4</sub>, trans-[V(CNBU<sup>t</sup>)<sub>2</sub>(dmpe)<sub>2</sub>](PF<sub>6</sub>)<sub>2</sub>. *Polyhedron* **1988**, *7*, 2615–2626.
3. Fulmer, G. R.; Miller, A. J. M.; Sherden, N. H.; Gottlieb, H. E.; Nudelman, A.; Stoltz, B. M.; Bercaw, J. E.; Goldberg, K. I. NMR Chemical Shifts of Trace Impurities: Common Laboratory Solvents, Organics, and Gases in Deuterated Solvents Relevant to the Organometallic Chemist. *Organometallics* **2010**, *29*, 2176–2179.
4. Melhuish, W. H. Quantum efficiencies of fluorescence of organic substrates: effect of solvent and concentration of the fluorescent solute. *J. Phys. Chem.* **1961**, *65*, 229–235.
5. Meshkova, S. B.; Topilova, Z. M.; Bolshoy, Z. M.; Belyukova, S. V.; Tsvirko, M. P.; Venchikov, V. Y. Quantum Efficiency of the Luminescence of Ytterbium(III)  $\beta$ -Diketonates. *Acta Phys. Pol. A* **1999**, *95*, 983–990.
6. a) Zimmer, M.; Rupp, F.; Singer, P.; Walz, F.; Breher, F.; Klopper, W.; Diller, R.; Gerhards, M. Time-resolved IR spectroscopy of a trinuclear palladium complex in solution. *Phys. Chem. Chem. Phys.* **2015**, *17*, 14138–14144; b) Bäßler, F.; Zimmer, M.; Dietrich, F.; Gruppe, M.; Wallesch, M.; Volz, D.; Bräse, S.; Gerhards, M.; Diller, R. Photophysical dynamics of a binuclear Cu(I)-emitter on the fs to  $\mu$ s timescale, in solid phase and in solution. *Phys. Chem. Chem. Phys.* **2017**, *19*, 29438–29448; c) Zimmer, M.; Dietrich, F.; Volz, D.; Bräse, S.; Gerhards, M. Solid-State Step-Scan FTIR Spectroscopy of Binuclear Copper(I) Complexes. *ChemPhysChem* **2017**, *18*, 3023–3029.
7. STOE & Cie, X-Red, STOE & Cie, Darmstadt, Germany 2002.
8. Blessing, R. H. An empirical correction for absorption anisotropy. *Acta Crystallogr. Sect. A* **1995**, *51*, 33–38.
9. Spek, A. L. Structure validation in chemical crystallography. *Acta Crystallogr. Sect. D* **2009**, *65*, 148–55.
10. Sheldrick, G. M. SHELXL-2014/7, University of Göttingen, Göttingen, Germany, 2014.
11. Sheldrick, G. M. SHELXT – Integrated space-group and crystal-structure determination. *Acta Crystallogr. Sect. A* **2015**, *71*, 3–8.
12. Neese, F. The ORCA program system. *WIREs Comput. Mol. Sci.* **2012**, *2*, 73–78.
13. Becke, A. D. Density-functional thermochemistry. III. The role of exact exchange. *J. Chem. Phys.* **1993**, *98*, 5648–5652.
14. Weigend, F.; Ahlrichs, R. Balanced basis sets of split valence, triple zeta valence and quadruple zeta valence quality for H to Rn: Design and assessment of accuracy. *Phys. Chem. Chem. Phys.* **2005**, *7*, 3297–3305.
15. Weigend, F. Accurate Coulomb-fitting basis sets for H to Rn. *Phys. Chem. Chem. Phys.* **2006**, *8*, 1057–1065.
16. Neese, F.; Wennmohs, F.; Hansen, A.; Becker, U. Efficient, approximate and parallel Hartree–Fock and hybrid DFT calculations. A ‘chain-of-spheres’ algorithm for the Hartree–Fock exchange. *Chem. Phys.* **2009**, *356*, 98–109.
17. Izsák, R.; Neese, F. An overlap fitted chain of spheres exchange method. *J. Chem. Phys.* **2011**, *135*, 144105.
18. Pantazis, D. A.; Chen, X.-Y.; Landis, C. R.; Neese, F. All-Electron Scalar Relativistic Basis Sets for Third-Row Transition Metal Atoms. *J. Chem. Theory Comput.* **2008**, *4*, 908–919.
19. van Lenthe, E.; Baerends, E. J.; Snijders, J. G. Relativistic regular two-component Hamiltonians. *J. Chem. Phys.* **1993**, *99*, 4597–4610.
20. Grimme, S.; Antony, J.; Ehrlich, S.; Krieg, H. A consistent and accurate ab initio parametrization of density functional dispersion correction (DFT-D) for the 94 elements H-Pu. *J. Chem. Phys.* **2010**, *132*, 154104.

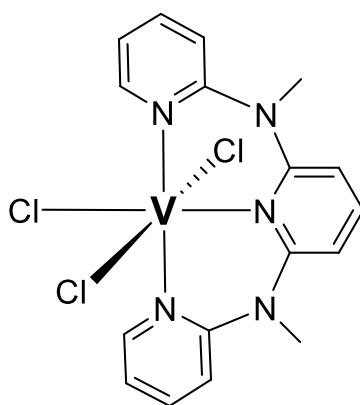
21. Grimme, S.; Ehrlich, S.; Goerigk, L. Effect of the damping function in dispersion corrected density functional theory. *J. Comput. Chem.* **2011**, *32*, 1456–1465.
22. Barone, V.; Cossi, M. Quantum Calculation of Molecular Energies and Energy Gradients in Solution by a Conductor Solvent Model. *J. Phys. Chem. A* **1998**, *102*, 1995–2001.
23. Roos, B. O.; Taylor, P. R.; Siegbahn, P. E. M. A Complete Active Space SCF Method (CASSCF) Using a Density-Matrix Formulated Super-CI Approach. *Chem. Phys.* **1980**, *48*, 157–173.
24. Siegbahn, P. E. M.; Almlof, J.; Heiberg, A.; Roos, B. O. The Complete Active Space Scf (CASSCF) Method in a Newton-Raphson Formulation with Application to the HNO Molecule. *J. Chem. Phys.* **1981**, *74*, 2384–2396.
25. Angeli, C.; Cimiraglia, R.; Evangelisti, S.; Leininger, T.; Malrieu, J.-P. Introduction of n-electron valence states for multireference perturbation theory. *J. Chem. Phys.* **2001**, *114*, 10252–10264.
26. Angeli, C.; Cimiraglia, R. Multireference perturbation configuration interaction V. Third-order energy contributions in the Møller–Plesset and Epstein–Nesbet partitions. *Theor. Chem. Acc.* **2002**, *107*, 313–317.
27. Neese, F. Efficient and accurate approximations to the molecular spin-orbit coupling operator and their use in molecular g-tensor calculations. *J. Chem. Phys.* **2005**, *122*, 34107.
28. Hess, B. A.; Marian, C. M. In *Computational Molecular Spectroscopy*; Jensen, P. B., Ed.; Wiley: New York, 2000; p. 169ff.
29. Cahier, B.; Maurice, R.; Bolvin, H.; Mallah, T.; Guihéry, N. Tools for Predicting the Nature and Magnitude of Magnetic Anisotropy in Transition Metal Complexes: Application to Co(II) Complexes. *Magnetochemistry* **2016**, *2*, 31–45.
30. Roos, B. O.; Malmqvist, P.-Å. Relativistic quantum chemistry: the multiconfigurational approach. *Phys. Chem. Chem. Phys.* **2004**, *6*, 2919–2927.
31. Durand, P.; Malrieu, J.-P. In *Advances in Chemical Physics: Ab Initio Methods in Quantum Chemistry*; Lawley, K. P., Ed.; John Wiley & Sons Ltd.: Hoboken, NJ, 1987; Vol. 67, Part 1, pp 321–412.
32. Pierloot, K. Transition metals compounds: Outstanding challenges for multiconfigurational methods. *Int. J. Quantum Chem.* **2011**, *111*, 3291–3301.
33. Richter, M.; Marquetand, P.; González-Vazquez, J.; Sola, I.; González, L. SHARC: ab Initio Molecular Dynamics with Surface Hopping in the Adiabatic Representation Including Arbitrary Couplings. *J. Chem. Theory Comput.* **2011**, *7*, 1253–1258.
34. Mai, S.; Marquetand, P.; González, L. *WIREs Comput. Mol. Sci.* **2018**, e1370.
35. Mai, S.; Marquetand, P.; González, L. *Int. J. Quantum Chem.* **2015**, *115*, 1215–1231.
36. Mai, S.; Richter, M.; Heindl, M.; Menger, M. F. S. J.; Atkins, A.; Ruckebauer, M.; Plasser, F.; Oppel, M.; Marquetand, P.; González, L. *Sharc2.0: Surface Hopping Including Arbitrary Couplings – Program Package for Non-Adiabatic Dynamics* (2018), available from <http://sharc-md.org>.
37. Plasser, F.; Gómez, S.; Menger, M. F. S. J.; Mai, S.; González, L. Highly efficient surface hopping dynamics using a linear vibronic coupling model. *Phys. Chem. Chem. Phys.* **2019**, *21*, 57–69.
38. a) Mai, S.; Plasser, F.; Dorn, J.; Fumana, M.; Daniel, C.; González, L. Quantitative wave function analysis for excited states of transition metal complexes. *Coord. Chem. Rev.* **2018**, *361*, 74–97; b) <http://theodore-qc.sourceforge.net>.
39. Granucci, G.; Persico, M. Direct semiclassical simulation of photochemical processes with semiempirical wave functions. *J. Chem. Phys.* **2001**, *114*, 10608.
40. Granucci, G.; Persico, M. Critical appraisal of the fewest switches algorithm for surface hopping. *J. Chem. Phys.* **2007**, *126*, 134114.
41. Alemany, P.; Casanova, D.; Alvarez, S.; Dryzun, C.; Avnir, D. Continuous Symmetry Measures: A New Tool in Quantum Chemistry. In *Reviews in Computational Chemistry*. Parrill, A. L., Lipkowitz, K. B., Eds., John Wiley & Sons: Hoboken, NJ, USA, Volume 30, **2017**, pp. 289–352.
42. Tanabe, Y.; Sugano, S. On the Absorption Spectra of Complex Ions. II. *J. Phys. Soc. Jpn.* **1954**, *9*, 766–779.

43. Krzystek, J.; Ozarowski, A.; Telser, J.; Crans, D. C. High-frequency and -field electron paramagnetic resonance of vanadium(IV, III, and II) complexes. *Coord. Chem. Rev.* **2015**, *301–302*, 123–133.
44. Kittilstved, K. R.; Sorgho, L. A.; Amstutz, N.; Tregenna-Piggott, P. L. W.; Hauser, A. Ground-State Electronic Structure of Vanadium(III) Trisoxalate in Hydrated Compounds. *Inorg. Chem.* **2009**, *48*, 7750–7764.
45. Jung, J.; Jung, Y.; Park, O. Preparation of 2-chloropyridine. *Synth. Commun.* **2001**, *31*, 2507–2511.
46. Jha, A. K.; Jain, N. The microwave-assisted ortho-alkylation of azine N-oxides with N-tosylhydrazones catalyzed by copper(I) iodide. *Chem. Commun.* **2016**, *52*, 1831–1834.
47. Esaki, H.; Ito, N.; Sakai, S.; Maegawa, T.; Monguchia, Y.; Sajikia, H. General method of obtaining deuterium-labeled heterocyclic compounds using neutral D<sub>2</sub>O with heterogeneous Pd/C. *Tetrahedron* **2006**, *62*, 10954–10961.
48. Dirvanauskas, A.; Galavotti, R.; Lunghi, A.; Nicolini, A.; Roncaglia, F.; Totti, F.; Cornia, A. Solution structure of a pentachromium(II) single molecule magnet from DFT calculations, isotopic labelling and multinuclear NMR spectroscopy. *Dalton Trans.* **2018**, *47*, 585–595.
49. Wang, C.; Otto, S.; Dorn, M.; Kreidt, E.; Lebon, J.; Sršan, L.; Di Martino-Fumo, P.; Gerhards, M.; Resch-Genger, U.; Seitz, M.; Heinze, K. Deuterated Molecular Ruby with Record Luminescence Quantum Yield. *Angew. Chem. Int. Ed.* **2018**, *57*, 1112–1116.



### 3.2.2 Ein heteroleptischer V(III)-Komplex mit NIR Spin-Flip-Lumineszenz (Publikation 5)

Die Entwicklung von lumineszenten 3d-Übergangsmetallkomplexen ist sehr herausfordernd. Das liegt neben der im Vergleich zu den 4d- bzw. 5d-Übergangsmetallen geringeren Ligandenfeldaufspaltung, auch an den deutlich kleineren Spin-Bahn-Kopplungskonstanten (SOC) der 3d-Elemente. Diese schwache Spin-Bahn-Kopplung ist meist verantwortlich dafür, dass die verbotenen Intersystem Crossing Prozesse eher langsam sind und die energetisch tiefliegenden, emittierenden Zustände ineffizient besetzt werden. Auch für V(III)-Komplexe ist das ISC eher langsam. Das ist auch gut daran zu erkennen, dass die Intensität der spin-verbotenen Spin-Flip-Emission um mehr als drei Größenordnungen kleiner im Vergleich zur Intensität der spin-erlaubten Emission der Ligandenfeldzustände ist.<sup>[70]</sup>



**[VCl<sub>3</sub>(dddpd)]**

**Abb. 11:** Strukturformel des heteroleptischen *mer*-[VCl<sub>3</sub>(dddpd)]-Komplexes.

Auch der lumineszente [V(dddpd)<sub>2</sub>](PF<sub>6</sub>)<sub>3</sub>-Komplex weist eine geringe ISC-Effizienz auf, was neben dem Auftreten von intensiver Fluoreszenz aus den Triplett-Zuständen ebenfalls durch Molekulare-Dynamik-Simulationen bestätigt wurde.<sup>[67]</sup> Um die geringe Spin-Bahn-Kopplungskonstante der V(III)-Komplexe ( $\zeta \approx 210 \text{ cm}^{-1[71]} / 206 \text{ cm}^{-1[72]} / 220 \text{ cm}^{-1[73]}$ ) zu erhöhen, war der Grundgedanke, einen der dreizähligen, pyridinbasierten Donorliganden durch drei Chlorido-Liganden zu ersetzen um die größere SOC ( $\zeta \approx 547 \text{ cm}^{-1[73]}$ ) im Vergleich zu Stickstoff ( $\zeta \approx 76 \text{ cm}^{-1[73]}$ ) auszunutzen. Zusätzlich könnte durch die Symmetrierniedrigung mit den nun stark unterschiedlichen Liganden, das Paritätsverbot der d-d-Übergänge (Laporte-Regel)

umgangen und damit die strahlende Zerfallsrate der metallzentrierten Spin-Flip-Zustände erhöht werden.

Zunächst wurde der heteroleptische **mer-[VCl<sub>3</sub>(ddpd)]**-Komplex nach der bereits bekannten Vorschrift synthetisiert.<sup>[68]</sup> Das Absorptionsspektrum von **[VCl<sub>3</sub>(ddpd)]** in Acetonitril zeigt prominente Banden bei 320 und 463 nm, sowie eine sehr schwache Bande bei 702 nm (14245 cm<sup>-1</sup>). Zur Zuordnung dieser Banden und zur Bestimmung der Energien der metallzentrierten Zustände wurden wie bereits für den **[V(ddpd)<sub>2</sub>]<sup>3+</sup>**-Komplex TD-DFT-Rechnung und zusätzlich CASSCF-NEVPT2-Kalkulationen durchgeführt (Abb. 12, HI, Abb. S1+2 u. Tab. S1-4). Eine detaillierte Beschreibung der quantenchemischen Untersuchungen können auch der dazugehörigen Publikation entnommen werden.<sup>[74]</sup>

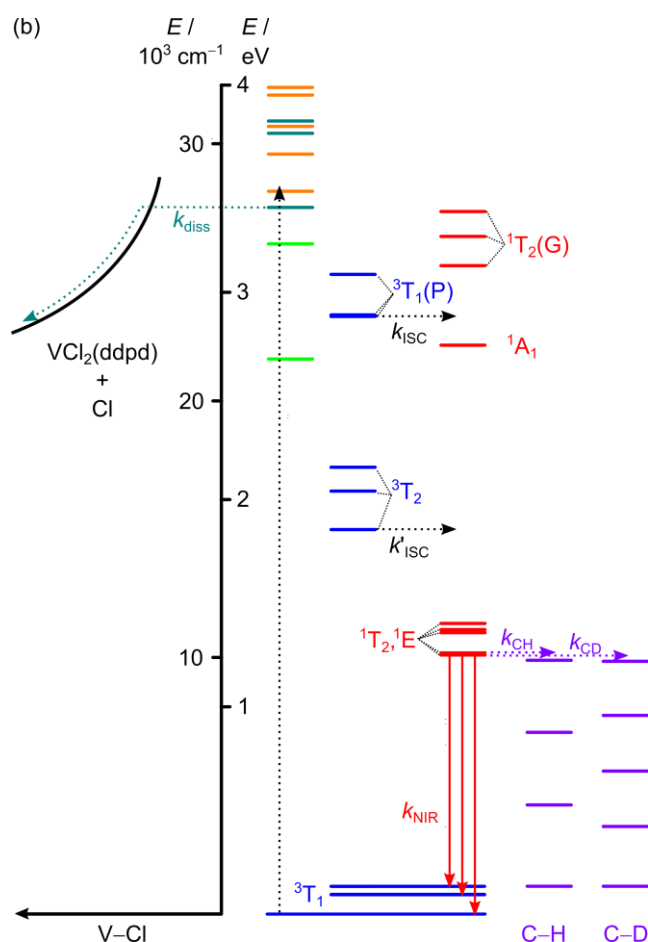


**Abb. 12:** Energiediagramm von **[VCl<sub>3</sub>(ddpd)]** basierend auf TDDFT-UKS-Rechnungen (ddpd→V <sup>3</sup>LMCT (hellgrün), Cl→V <sup>3</sup>LMCT (petrolgrün), ILCT (orange)) und CASSCF-NEVPT2-Kalkulationen (<sup>3</sup>MC (blau); <sup>1</sup>MC (rot)). Notation der metallzentrierten Zustände nach Oktaedersymmetrie. ISC = intersystem crossing; diss = V-Cl Homolytische Bindungsspaltung; NIR = NIR-Emission; C-H- und C-D-Obertöne in violett = Multiphonon Relaxation (s.Kapitel 4.2.2). Abbildung übernommen von Heinze.<sup>[75]</sup>

Aus diesen Rechnungen resultiert das in Abb. 12 dargestellte Energiediagramm, bei welchem die unterschiedlichen Farben den dominanten Charakter der elektronischen Zustände repräsentieren. So können die hochenergetischen Banden des Absorptionsspektrums CT-Zuständen zugeordnet werden, während die intensitätsschwache Bande bei 702 nm ( $14245\text{ cm}^{-1}$ ) auf den metallzentrierten  $^3T_2$ -Zustand zurückgeht (Pub. 5: *Results and discussion*, Fig. 1 a)). Daher ist auch im **[VCl<sub>3</sub>(ddpd)]**-Komplex das Ligandenfeld ausreichend groß um die emittierenden Spin-Flip-Zustände  $^1E / ^1T_2$  energetisch unter den Ligandenfeldzustand  $^3T_2$  zu schieben.

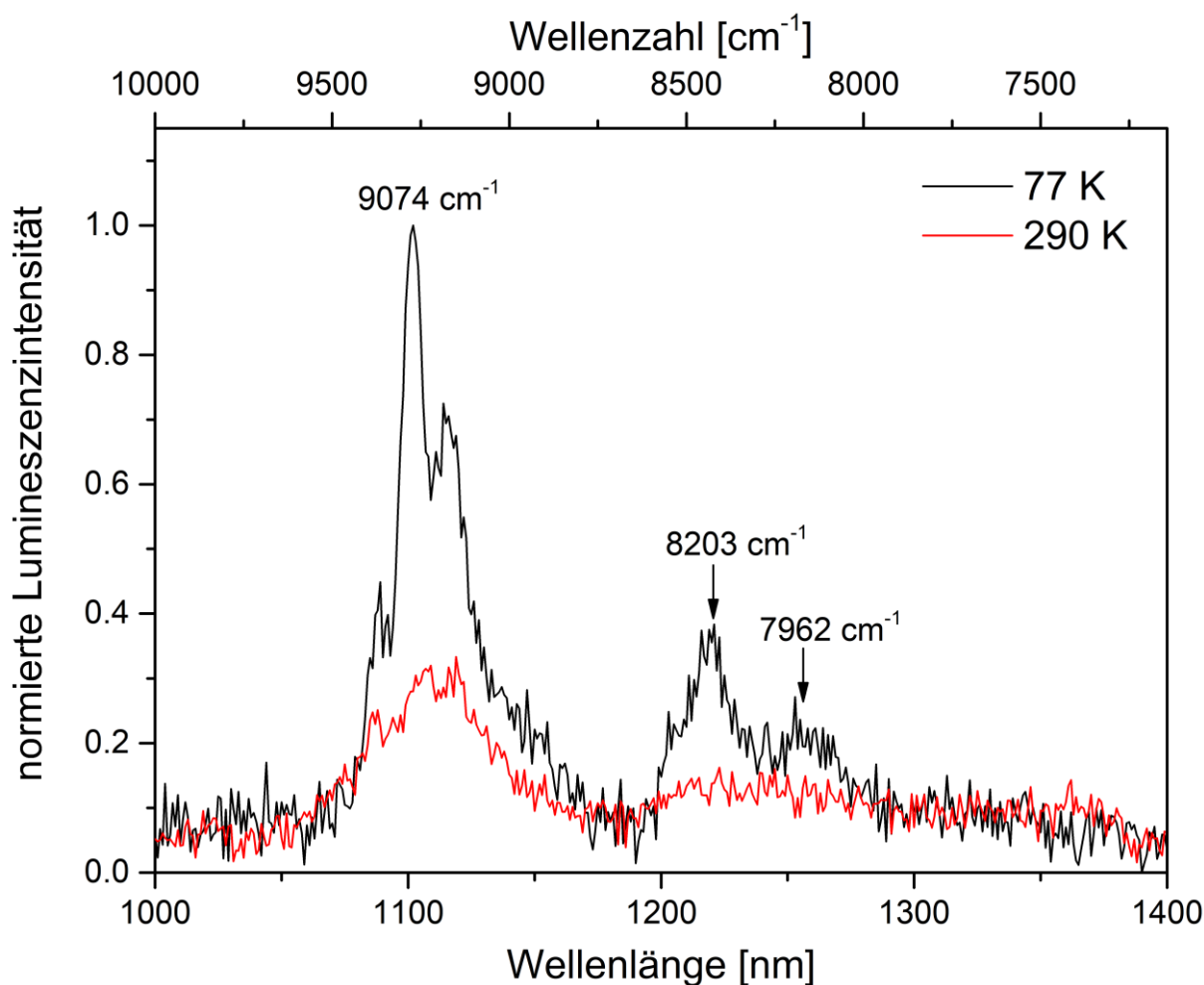


**Abb. 13:** Normierte Steady-State-Emissionsspektren von **[VCl<sub>3</sub>(ddpd)]** bei 290 K (rot) und  $T = 77\text{ K}$  (schwarz) ( $\lambda_{\text{exc}} = 350\text{ nm}$ , Festkörper). Die relativen Intensitäten bei  $T = 290$  bzw.  $77\text{ K}$  sind nicht maßstäblich skaliert.

Nach Anregung von festem **[VCl<sub>3</sub>(ddpd)]** mit  $\lambda_{\text{exc}} = 350\text{ nm}$  bei Raumtemperatur können zwei schwache NIR-Emissionsbanden detektiert werden (Abb. 13). Erwartungsgemäß steigt die Intensität der Emissionsbanden bei  $T = 77\text{ K}$  deutlich an und es tritt zudem eine Feinstruktur auf. Die erkennbaren Maxima der Banden liegen

bei  $\lambda_{em} = 1102, 1219$  und  $1256$  nm ( $9074, 8203, 7962$   $cm^{-1}$ ). Die NIR-Emissionsbanden können den Übergängen vom energetisch tiefliesten Spin-Flip-Zustand in den aufgespaltenen Grundzustand zugeordnet werden (Abb. 12). Dabei stimmt die experimentell bestimmte Grundzustandsaufspaltung von ca.  $800$  und  $1040$   $cm^{-1}$  sehr gut mit der berechneten Aufspaltung ( $755$  und  $1076$   $cm^{-1}$ ) überein. Die sehr große Grundzustandsaufspaltung geht auf die geringere Symmetrie des heteroleptischen **[VCl<sub>3</sub>(ddpd)]**-Komplexes zurück. Da an der NIR-Emission somit mehrere Banden beteiligt sind, erstreckt sich die Emission dieses Komplexes über einen großen Wellenlängenbereich von ca.  $2400$   $cm^{-1}$ . Das ist ein Unterschied zu der scharfen Spin-Flip-Emission von  $d^3$ -Cr(III)-Systemen bei welchen keine Grundzustandsaufspaltung vorhanden ist. Zusätzlich verkleinert die große Grundzustandsaufspaltung die ohnehin schon geringe Energielücke zwischen den Spin-Flip-Zuständen und dem höchsten Niveau des Grundzustandes, was nach dem Energielückengesetz strahlungslose Zerfallsprozesse wahrscheinlicher macht.

Die feineren Details der NIR-Emissionsbanden könnten mit der Besetzung von energetisch sehr nahen weiteren Spin-Flip-Zuständen und mit Schwingungsprogression von Schwingungen mit einer Energie von ca.  $120$   $cm^{-1}$  erklärt werden. Dabei liegen laut DFT-Berechnungen Cl-V-Cl-Deformationsschwingungen im passenden Energiebereich ( $125, 136, 159$   $cm^{-1}$ , HI, Tab. S4).

Die Lebensdauer der NIR-Emission im Festkörper bei  $T = 298$  K und unter Inertatmosphäre ist monoexponentiell mit  $\tau = 0.5$   $\mu s$  (HI, Abb. S7). Diese Lebenszeit bestätigt die Zuordnung zur Phosphoreszenz, auch wenn diese wegen der recht effektiven Löschung durch die große Grundzustandsaufspaltung und Multiphonon Relaxation (Kap. 4.2.2) eher kurz für typische Phosphoreszenz-Lebenszeiten ist. Die gemessene Lebensdauer von einer halben Mikrosekunde liegt dabei auch an der unteren Grenze des Instrumentenlimits. Allerdings validiert die von der Arbeitsgruppe Gerhards unabhängig gemessene Lebenszeit der NIR-Emission von  $\tau = 611$  ns (HI, Abb. S24) den gemessenen Wert.

Die Untersuchung der Photophysik des **[VCl<sub>3</sub>(ddpd)]**-Komplexes konnte zuverlässig nur im Festkörper durchgeführt werden. Das liegt zum einen an der schlechten Löslichkeit in gängigen Lösungsmitteln, zum anderen an der zu geringen Photostabilität in Lösung. Nach UV-Anregung findet Photochemie ausgehend von angeregten LMCT-Zuständen statt, wobei der Ladungstransfer von den Chlorid-Liganden zum V(III) verläuft (HI, Abb. S28-31). Da ein solcher Ladungstransfer sehr

wahrscheinlich die V-Cl-Bindungen schwächt, erscheint damit auch homolytische Bindungsspaltung sehr plausibel (Abb. 12). Damit verbunden wäre erwartungsgemäß eine deutlich niedrigere Lumineszenzquantenausbeute und die Zersetzung des Komplexes.

Zuletzt konnte mit ultraschneller transientser Absorptionsspektroskopie die Geschwindigkeitskonstante des Intersystem Crossings von den Triplett- in die Singulett-Zustände ermittelt werden. Die ISC-Ratenkonstante ist recht hoch ( $k_{ISC} > 6.67 \times 10^{11} \text{ s}^{-1}$ ) und könnte mit der größeren SOC der Chlorido-Liganden zusammenhängen.

Insgesamt zeigt der **[VCl<sub>3</sub>(ddpd)]**-Komplex Spin-Flip-Lumineszenz im Festkörper bei Raumtemperatur im NIR-II bei  $\lambda_{em} = 1102, 1219$  und  $1256$  nm. An diesem Modellkomplex für die Entwicklung von d<sup>2</sup>-NIR-Emittern konnten wichtige Kernparameter wie die ISC-Effizienz, Grundzustandsaufspaltung und Photostabilität untersucht werden, wodurch wertvolle Erkenntnisse für die Entwicklung von Luminophoren auf Basis des günstigen und leicht verfügbaren Metalls Vanadium gewonnen werden konnten.

Cite this: *Chem. Sci.*, 2021, 12, 10780

All publication charges for this article have been paid for by the Royal Society of Chemistry

# Ultrafast and long-time excited state kinetics of an NIR-emissive vanadium(III) complex I: synthesis, spectroscopy and static quantum chemistry†‡

Matthias Dorn,<sup>a</sup> Jens Kalmbach,<sup>b</sup> Pit Boden,<sup>c</sup> Ayla Kruse,<sup>d</sup> Chahinez Dab,<sup>e</sup> Christian Reber,<sup>e</sup> Gereon Niedner-Schatteburg,<sup>c</sup> Stefan Lochbrunner,<sup>d</sup> Markus Gerhards,<sup>c</sup> Michael Seitz<sup>\*b</sup> and Katja Heinze<sup>\*a</sup>

In spite of intense, recent research efforts, luminescent transition metal complexes with Earth-abundant metals are still very rare owing to the small ligand field splitting of 3d transition metal complexes and the resulting non-emissive low-energy metal-centered states. Low-energy excited states decay efficiently non-radiatively, so that near-infrared emissive transition metal complexes with 3d transition metals are even more challenging. We report that the heteroleptic pseudo-octahedral d<sup>2</sup>-vanadium(III) complex VCl<sub>3</sub>(ddpd) (ddpd = *N,N'*-dimethyl-*N,N'*-dipyridine-2-yl-pyridine-2,6-diamine) shows near-infrared singlet → triplet spin-flip phosphorescence maxima at 1102, 1219 and 1256 nm with a lifetime of 0.5 μs at room temperature. Band splitting, ligand deuteration, excitation energy and temperature effects on the excited state dynamics will be discussed on slow and fast timescales using Raman, static and time-resolved photoluminescence, step-scan FTIR and fs-UV pump-vis probe spectroscopy as well as photolysis experiments in combination with static quantum chemical calculations. These results inform future design strategies for molecular materials of Earth-abundant metal ions exhibiting spin-flip luminescence and photoinduced metal–ligand bond homolysis.

Received 16th April 2021  
Accepted 7th July 2021

DOI: 10.1039/d1sc02137k

rsc.li/chemical-science

## Introduction

The control of photophysical properties of transition metal complexes by chemical means, especially for applications in lighting, imaging, sensing, photonics, dye sensitised solar cells, phototherapy or photocatalysis, is a very active research field.<sup>1–8</sup> However, most applications rely on noble metal complexes with d<sup>6</sup> or d<sup>8</sup> electron configurations such as ruthenium(II), iridium(III) or platinum(II).<sup>9</sup> The success of these precious metals in photophysics and photochemistry can be ascribed, among other beneficial features, to their intrinsically large

ligand field splitting<sup>10</sup> and their large spin–orbit coupling (SOC) constants  $\zeta \gg 1000 \text{ cm}^{-1}$ .<sup>11</sup> Finally, these properties enable the efficient population of the photoactive and luminescent long-lived triplet metal-to-ligand charge transfer (<sup>3</sup>MLCT) states as lowest excited states after intersystem crossing (ISC).<sup>12</sup>

Aiming at a sustainable future photochemistry less dependent on rare and precious metals, Earth-abundant metals are currently heavily explored and novel concepts have been put forward<sup>13–18</sup> including some second row metals,<sup>19–22</sup> but in particular the first row transition metals.<sup>13–18</sup> The 3d transition metals possess a weaker ligand field splitting<sup>10</sup> and smaller SOC<sup>11</sup> posing severe challenges to the design of the excited state landscape,<sup>14</sup> yet several recent breakthroughs have been reported, *e.g.* on copper(I),<sup>23,24</sup> nickel(0,II),<sup>25,26</sup> cobalt(III),<sup>27</sup> iron(II,III),<sup>28–31</sup> chromium(0/III)<sup>32–35</sup> and vanadium(III).<sup>36</sup> Beyond the conventionally exploited MLCT excited states,<sup>12</sup> LMCT states of the low-spin d<sup>5</sup> electron configuration of iron(III)<sup>18</sup> and spin-flip states of the d<sup>3</sup> electron configuration of chromium(III)<sup>15</sup> are emerging as novel paradigmatic excited states useful for photoapplications.

The currently most successful spin-flip emitters are based on the so-called molecular ruby motif, *e.g.* in [Cr(ddpd)<sub>2</sub>]<sup>3+</sup>, with tridentate pyridine-type ligands forming six-membered chelate rings (ddpd = *N,N'*-dimethyl-*N,N'*-dipyridine-2-yl-pyridine-2,6-diamine).<sup>33,34,37</sup> Applications already emerged in the areas of sensing,<sup>38–40</sup> photocatalysis,<sup>37</sup> photodynamic therapy,<sup>41</sup> photon

<sup>a</sup>Department of Chemistry, Johannes Gutenberg University of Mainz, Duesbergweg 10-14, 55128 Mainz, Germany. E-mail: katja.heinze@uni-mainz.de

<sup>b</sup>Institute of Inorganic Chemistry, University of Tübingen, Auf der Morgenstelle 18, 72076 Tübingen, Germany

<sup>c</sup>Department of Chemistry and Research Center Optimas, Technical University Kaiserslautern, Erwin-Schrödinger-Straße, 67663 Kaiserslautern, Germany

<sup>d</sup>Institute for Physics and Department of Life Light and Matter, University of Rostock, 18051 Rostock, Germany

<sup>e</sup>Département de chimie, Université de Montréal, Montréal, Québec, H3C 3J7, Canada

† During manuscript finalisation, Prof. Markus Gerhards unexpectedly passed away on Dec. 28th 2020.

‡ Electronic supplementary information (ESI) available: Details the quantum chemical calculations, luminescence spectra, Raman spectra, luminescence decay, vibrational overtone analysis, step-scan FTIR spectra, IR spectral decay, photostability, cyclic voltammogram. See DOI: 10.1039/d1sc02137k



upconversion<sup>42</sup> and the generation of circularly polarised emission.<sup>43–45</sup>

Very recently, vanadium started to spark interest as potential novel near-infrared (NIR) luminophore<sup>46</sup> motivated by its high natural abundance and complementary properties to the chromium(III) spin-flip luminophores and sensitizers.<sup>36,47</sup> Rappé and Damrauer demonstrated, that the d<sup>3</sup>-vanadium(II) electron configuration in the well-known [V(bpy)<sub>3</sub>]<sup>2+</sup> and [V(phen)<sub>3</sub>]<sup>2+</sup> complexes<sup>48</sup> (Chart 1, bpy = 2,2'-bipyridine, phen = 1,10-phenanthroline) leads to the population of non-luminescent excited doublet states with mixed <sup>2</sup>MC/<sup>2</sup>MLCT character within 2.5–3 ps after excitation.<sup>47</sup> The lifetimes of the mixed excited states of [V(bpy)<sub>3</sub>]<sup>2+</sup> and [V(phen)<sub>3</sub>]<sup>2+</sup> are 0.43 ns and 1.6 ns, respectively.<sup>47,49</sup> Yet, emission from these vanadium(II) complexes has not been observed at wavelengths shorter than 1600 nm even at low temperature.<sup>47</sup>

Analogous to the intra- and interconfigurational electronic transitions derived from the d<sup>3</sup> electron configuration (<sup>4</sup>T<sub>2</sub> and <sup>2</sup>E/<sup>2</sup>T<sub>1</sub>), the d<sup>2</sup> electron configuration with a <sup>3</sup>T<sub>1</sub> ground state in octahedral symmetry provides low-energy spin-flip singlet states (<sup>1</sup>E/<sup>1</sup>T<sub>2</sub>) and triplet states (<sup>3</sup>T<sub>2</sub>) with respective intra- and interconfigurational transitions.<sup>50</sup> This electron configuration is realised, for example, in octahedral vanadium(III) complexes and solid state materials with vanadium(III) in octahedral sites.<sup>51–53</sup> The electronic structure of basic d<sup>2</sup>-vanadium(III) complexes, e.g. [V(H<sub>2</sub>O)<sub>6</sub>]<sup>3+</sup> and [V(urea)<sub>6</sub>]<sup>3+</sup>, including the ground state splitting of the orbitally degenerate <sup>3</sup>T<sub>1</sub> ground state and the zero-field splitting, has been obtained from Raman, luminescence, and high-frequency high-field electron paramagnetic resonance spectroscopies.<sup>51–53</sup> A particularly interesting application of d<sup>2</sup>-luminescent materials is upconversion based on sequential ground state and excited state absorption,<sup>54</sup> as has been shown for example with d<sup>2</sup>-titanium(II) solid state materials such as MgCl<sub>2</sub>:Ti.<sup>54</sup>

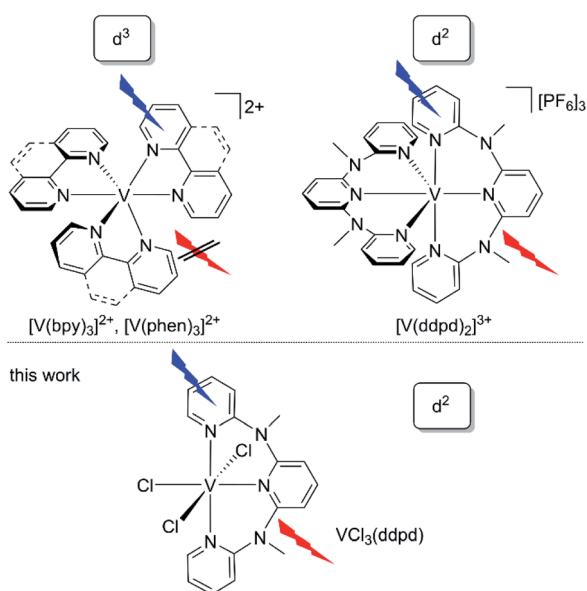


Chart 1 Structures of vanadium(II) and luminescent vanadium(III) polypyridine complexes.

Upconversion with molecular complexes has been demonstrated utilizing d<sup>3</sup>-chromium(III) complexes.<sup>42,55</sup> The five-coordinate d<sup>2</sup>-vanadium(III) complex V((C<sub>6</sub>F<sub>5</sub>)<sub>3</sub>tren)(CN<sup>t</sup>Bu) emits at 1240 nm in the solid state and frozen solution and was suggested as optically addressable molecular quantum bit candidate ((C<sub>6</sub>F<sub>5</sub>)<sub>3</sub>tren = 2,2',2''-tris[(pentafluorophenyl)amino]triethylamine).<sup>56</sup> Consequently, the advancement of emissive molecular materials exploiting the d<sup>2</sup> electronic configuration would be very valuable for diverse photonic applications such as NIR emission, upconversion and quantum technology.

The d<sup>2</sup>-vanadium(III) polypyridine complex [V(ddpd)<sub>2</sub>]<sup>3+</sup> emits in the NIR (1100 nm), observed for the first time even at room temperature in solution (Chart 1).<sup>36</sup> Its phosphorescent singlet state with a lifetime of 0.79 μs/8.8 μs (93%/7%; 77 K in butyronitrile glass) is populated within picoseconds after excitation. Yet, the efficiency of the population transfer to the singlet states by ISC is rather small as confirmed by non-adiabatic molecular dynamics calculations.<sup>36</sup> Unexpectedly, and in contrast to the analogous chromium(III) spin-flip emitters, the decay of the phosphorescent spin-flip states of [V(ddpd)<sub>2</sub>]<sup>3+</sup> is insensitive to ligand deuteration, in spite of the significant spectral overlap of the NIR emission with the second aromatic C–H overtone ν<sub>CH</sub><sup>3</sup> of the ligand. This suggests that other non-radiative decay pathways are more relevant than the multiphonon relaxation involving high-energy C–H oscillators<sup>57</sup> in this particular case.<sup>36</sup>

A profound understanding of the decisive excited states and the excited state dynamics of these polypyridine vanadium(III) chromophores on ultrafast (population of emissive states) and slow timescales (depopulation of emissive states) is lacking. To better understand the novel class of d<sup>2</sup>-spin-flip luminophores based on vanadium(III) with respect to the population and decay of the emissive spin-flip states, we selected the chlorido vanadium(III) complex VCl<sub>3</sub>(ddpd) (Chart 1)<sup>58</sup> for a detailed study of the photodynamics at ultrashort (sub-picosecond) to microsecond timescales (Chart 1).

Spin-orbit effects are weak in vanadium(III) complexes based on the lower intensity of the singlet transitions compared to the triplet bands by more than three orders of magnitude.<sup>59</sup> Our choice of molecular system is guided by two considerations: (i) the slow ISC rate defined by the small SOC constant of vanadium(III) (ζ ≈ 210/206/220 cm<sup>-1</sup>)<sup>11,60,61</sup> can increase due to the influence of the coordinated chlorido ligands with their higher SOC constant (ζ ≈ 547 cm<sup>-1</sup>)<sup>61</sup> as compared to nitrogen (ζ ≈ 76 cm<sup>-1</sup>).<sup>61</sup> (ii) The symmetry reduction by using different ligand types can relax Laporte's rule<sup>62</sup> and increase the radiative rate from metal-centred spin-flip states.<sup>35</sup>

We report here that the heteroleptic VCl<sub>3</sub>(ddpd)<sup>58</sup> complex is NIR-emissive at room temperature (Chart 1). We undertook a detailed photophysical study using Raman spectroscopy, variable temperature and variable pressure steady-state photoluminescence spectroscopy, fs-transient absorption spectroscopy, time-resolved photoluminescence and variable temperature step-scan FTIR spectroscopy to cover the ground state splitting, as well as the ultrafast and slow time regimes of the excited state kinetics. To elucidate whether non-radiative relaxation of the luminescent singlet states *via* aromatic





C–H overtones (C–H<sub>ar</sub>) plays a significant role for the non-radiative relaxation in this particular case, the deuterated complex VCl<sub>3</sub>(ddpd-[D<sub>17</sub>]) was prepared and studied for comparison. The electronic structures of ground and excited states at the ground state geometry were described utilizing relativistic two-component time-dependent density functional theory (TDDFT) and CASSCF-NEVPT2 calculations (NEVPT2 = N-electron valence state perturbation theory to second-order). A detailed kinetic model of the excited state dynamics will be derived by trajectory surface hopping simulations within a linear vibronic coupling model in the accompanying paper.<sup>63</sup>

## Results and discussion

The vanadium(III) complex VCl<sub>3</sub>(ddpd-[D<sub>0</sub>]) has been prepared as reported from VCl<sub>3</sub>(solvent)<sub>3</sub> (solvent = CH<sub>3</sub>CN or THF)<sup>64</sup> and the ligand ddpd-[D<sub>0</sub>]<sup>65</sup> as poorly soluble orange coloured complex.<sup>58</sup> Its structure and magnetic properties in the solid state have been reported.<sup>58</sup> Yet, luminescence, ultrafast and slow excited-state dynamics as well as temperature and pressure effects on the decisive ground and excited states and the excited state kinetics remained unexplored.

The electronic absorption spectrum of VCl<sub>3</sub>(ddpd-[D<sub>0</sub>]) in acetonitrile reveals prominent absorption bands around 320 and 463 nm (31 250 and 21 598 cm<sup>-1</sup>) as well as a very weak band at 702 nm (14 245 cm<sup>-1</sup>;  $\epsilon < 100 \text{ M}^{-1} \text{ cm}^{-1}$ ; Fig. 1a). TDDFT calculations on the geometry optimised triplet ground state (CPCM(acetonitrile)-RIJCOSX-UB3LYP-D3BJ-ZORA/def2-TZVPP; for details see Experimental section) were performed to assign the optical transitions (Fig. 1a, S1, S2 and Tables S1–S4, ESI†). To better match the experiment the calculated transition energies were shifted hypsochromically by 3400 cm<sup>-1</sup> (Fig. 1a). Partitioning of the density-matrix into ddpd, Cl and V fragments for charge transfer number analysis using the TheoDore package<sup>66,67</sup> indicates the major character of the transitions as ddpd → V <sup>3</sup>LMCT (light green), Cl → V <sup>3</sup>LMCT (petrol green), ILCT (orange) and V → ddpd <sup>3</sup>MLCT (purple) (Fig. 1a). CASSCF calculations reported in the accompanying paper<sup>63</sup> suggest some double excitation character of the ILCT transitions which might well lower the energy of these states. The very weak low-energy band at 702 nm ( $\epsilon < 100 \text{ M}^{-1} \text{ cm}^{-1}$ ) corresponds to metal-centred (MC) transitions from t<sub>2g</sub> to e<sub>g</sub> orbitals (<sup>3</sup>T<sub>2</sub>).

To better describe the split <sup>3</sup>T<sub>1</sub> ground state and the intra- and interconfigurational metal-centred transitions of the vanadium(III) ion, we resorted to CASSCF(6,12)-FIC-NEVPT2 calculations on the CPCM(acetonitrile)-RIJCOSX-UB3LYP-D3BJ-ZORA/def2-TZVPP optimised triplet ground state geometry (for details see Experimental section). The active space included five 3d and five 4d orbitals as well as two occupied V–N/Cl  $\sigma$ -bonding orbitals occupied with six electrons (Table S5 and Fig. S3, ESI†).<sup>68</sup> Without including the dynamic correlation with NEVPT2, the <sup>1</sup>E/<sup>1</sup>T<sub>2</sub> and <sup>3</sup>T<sub>2</sub> states are quite close in energy (Table S6, ESI†). Inclusion of the dynamic correlation with NEVPT2 lowers the energy of the <sup>1</sup>E/<sup>1</sup>T<sub>2</sub> states by ca. 2550 cm<sup>-1</sup> and raises the energy of the <sup>3</sup>T<sub>2</sub> states by ca. 1200 cm<sup>-1</sup>. On this level of theory, the energy gap between the lowest singlet and triplet excited states amounts to ca. 3750 cm<sup>-1</sup> (Fig. 1b). These

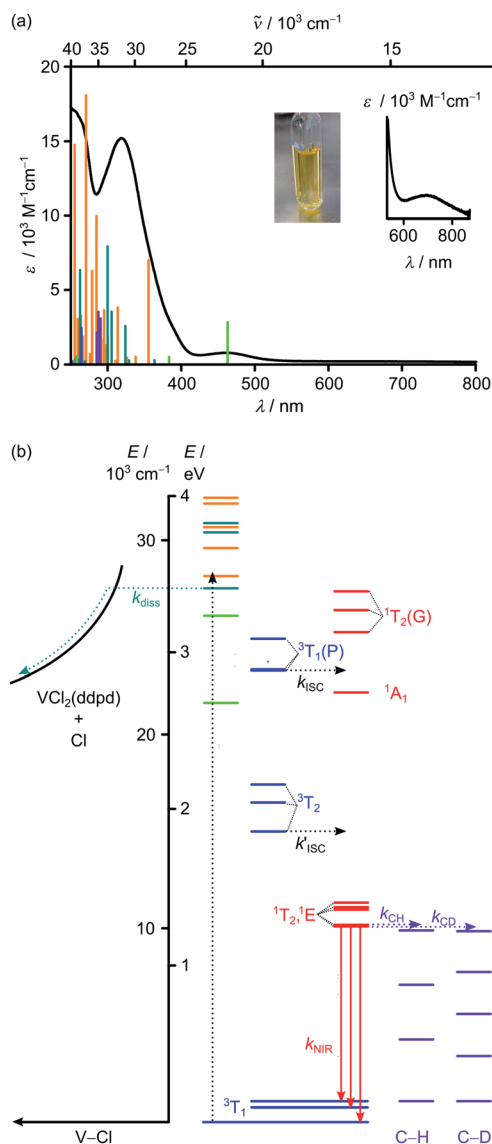


Fig. 1 (a) Absorption spectrum including a zoom into the red spectral region (black) and photograph of VCl<sub>3</sub>(ddpd-[D<sub>0</sub>]) in CH<sub>3</sub>CN. The vertical bars correspond to spin-allowed CT transitions calculated by TDDFT-UKS (hypsochromically shifted by 3400 cm<sup>-1</sup>). The colour code of the vertical bars indicates the major character of the transition as ddpd → V <sup>3</sup>LMCT (light green), Cl → V <sup>3</sup>LMCT (petrol green), ILCT (orange) and V → ddpd <sup>3</sup>MLCT (purple). (b) Jablonski diagram constructed from TDDFT-UKS (ddpd → V <sup>3</sup>LMCT (light green), Cl → V <sup>3</sup>LMCT (petrol green) and ILCT (orange)) and CASSCF-NEVPT2 calculations (<sup>3</sup>MC states in blue; <sup>1</sup>MC states in red). Notation of MC states is according to octahedral symmetry. ISC = intersystem crossing; diss = V–Cl homolysis; NIR = NIR emission; C–H and C–D overtones in purple = multiphonon relaxation (experimental overtone energies from ref. 34).

calculations place the lowest excited triplet states of <sup>3</sup>T<sub>2</sub> parentage at 14 968/16 464/17 393 cm<sup>-1</sup> above the split <sup>3</sup>T<sub>1</sub> ground state (0/755/1076 cm<sup>-1</sup>) (Fig. 1b). The lowest energy spin-allowed transition is calculated at 14 968 cm<sup>-1</sup> in reasonable agreement with the experimental band maximum (14 245 cm<sup>-1</sup>, Fig. 1a inset). The calculated splitting of all





$^3T$  states is substantial reflecting the low symmetry of the complex. The five lowest excited singlet states of  $^1E/{}^1T_2$  parentage are calculated at 10 086/10 161/10 949/11 068/11 309  $\text{cm}^{-1}$ . These spread over 1200  $\text{cm}^{-1}$  (Fig. 1b). As the energy of the lowest singlet state is significantly lower than the lowest excited triplet state by *ca.* 4900  $\text{cm}^{-1}$ , NIR phosphorescence from the singlet state to the split ground state is conceivable (Fig. 1b). Extended calculations using an even larger active space will be presented in the accompanying paper.<sup>63</sup>

Excitation of solid  $\text{VCl}_3(\text{ddpd}[\text{D}_0])$  with 350 nm (ILCT) at 298 K results in the appearance of two NIR emission bands (Fig. 2a). At 77 K, the emission bands increase in intensity and develop a characteristic fine structure (Fig. 2a). Discernible peaks occur at 1102, 1219 and 1256 nm (9074, 8203, 7962  $\text{cm}^{-1}$ ). Considering the calculated ground state splitting, we assign these clearly visible band maxima to radiative transitions from the lowest excited singlet state(s) to the split ground state (Fig. 1b). The resulting experimental ground state splitting of *ca.* 800 and 1100  $\text{cm}^{-1}$  excellently agrees with the CASSCF-NEVPT2 calculated splitting (755 and 1076  $\text{cm}^{-1}$ ). The experimental ground state splitting refers to the geometry minimum of the singlet state, while the CASSCF-NEVPT2 calculated splitting refers to the ground state geometry. As spin-flip states are rather nested, the geometry differences should be marginal. Raman spectra of  $[\text{V}(\text{H}_2\text{O})_6]^{3+}$  and  $[\text{V}(\text{urea})_6]^{3+}$  show broad electronic Raman transitions around 1900–2900  $\text{cm}^{-1}$  and 1400  $\text{cm}^{-1}$ , respectively,<sup>51,52</sup> due to the trigonal ground-state splitting. For  $\text{VCl}_3(\text{ddpd}[\text{D}_0])$ , we observe two broad electronic Raman transitions around 500 and 900  $\text{cm}^{-1}$  in its Raman spectrum in accordance with its lower symmetry (Fig. 2b). These energies fit well to the splitting assigned by luminescence spectroscopy (Fig. 2a) and obtained from the CASSCF-NEVPT2 calculations.

The finer details of the NIR luminescence band structure can be tentatively assigned to population of the close-lying singlet states with the difference between the two lowest singlet states calculated as 75  $\text{cm}^{-1}$  and to enabling vibrations around 120  $\text{cm}^{-1}$ . Indeed, Cl–V–Cl deformation vibrations (125, 136, 159  $\text{cm}^{-1}$ ; unscaled) appear in this energy region according to the DFT calculations (ESI, Fig. S4†).

Upon pressurizing solid  $\text{VCl}_3(\text{ddpd}[\text{D}_0])$  to 7 kbar, two very weak NIR emission bands at approximately 9100 and 9280  $\text{cm}^{-1}$  (lowest energy detectable with the employed detector) shift to higher energy by  $\approx 10 \text{ cm}^{-1} \text{ kbar}^{-1}$ . (Fig. S5, ESI†). This hypsochromic shift of the emission bands differs from the bathochromic behaviour encountered by the  $d^3$  complex  $[\text{Cr}(\text{ddpd})_2]^{3+}$  at increasing pressure.<sup>39</sup> This unusual pressure-sensitivity is probably a combined effect of energy changes of the emissive singlet states and of the ground state splitting under increasing pressure. The broad, electronic Raman bands assigned to transitions within the split  $^3T_{1g}$  ground state experience variations in intensity and broaden strongly with increasing pressure (Fig. S6, ESI†). At pressures higher than 30 kbar the broadening, most likely due to effects of non-hydrostatic pressure, dominates and the bands can no longer be observed. These observations illustrate that luminescence

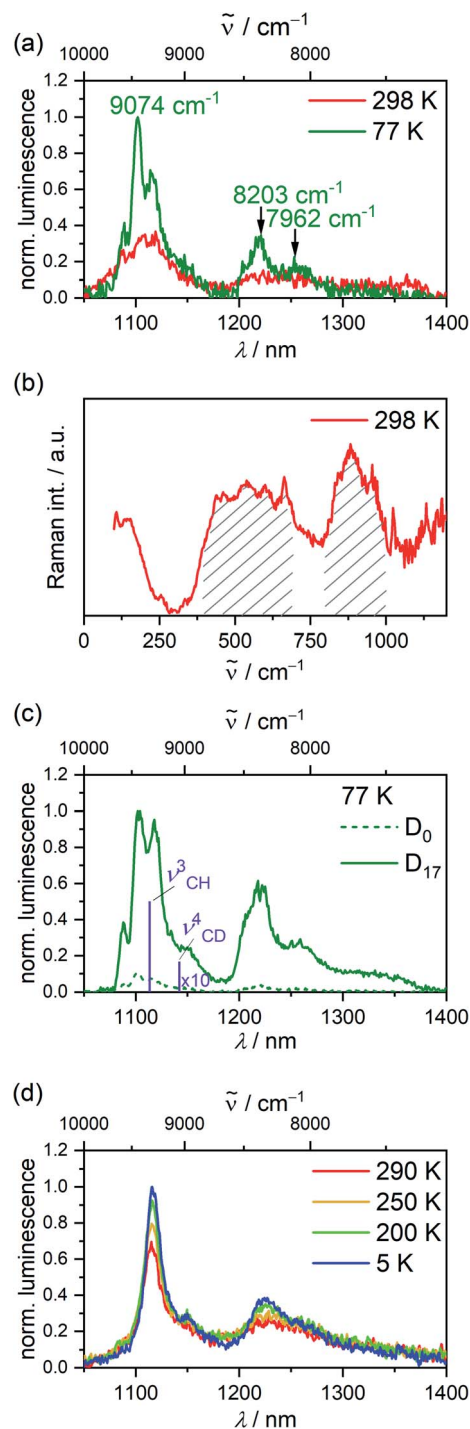


Fig. 2 (a) Luminescence spectra of  $\text{VCl}_3(\text{ddpd}[\text{D}_0])$  at 298 K (red) and 77 K (green) ( $\lambda_{\text{exc}} = 350 \text{ nm}$ ), (b) solid state Raman spectrum of neat  $\text{VCl}_3(\text{ddpd}[\text{D}_0])$  at 298 K ( $\lambda_{\text{exc}} = 785 \text{ nm}$ ). Electronic Raman transitions between the  $^3T_1$  ground state components are highlighted. (c) Luminescence spectra of neat  $\text{VCl}_3(\text{ddpd}[\text{D}_0])$  (green dotted line) and  $\text{VCl}_3(\text{ddpd}[\text{D}_{17}])$  (green solid line) at 77 K ( $\lambda_{\text{exc}} = 350 \text{ nm}$ ). Purple bars indicate the positions of the  $\nu_{\text{CH}}^3$  and  $\nu_{\text{CD}}^4$  overtones. (d) Luminescence spectra of  $\text{VCl}_3(\text{ddpd}[\text{D}_{17}])$  as KBr pellet at 5–290 K ( $\lambda_{\text{exc}} = 350 \text{ nm}$ ).

shifts different from those for spin-flip transitions with nondegenerate ground states are expected for vanadium(III) complexes.



The NIR luminescence of  $\text{VCl}_3(\text{ddpd-}[\text{D}_{17}])$  at 298 K in the solid state under inert conditions ( $\lambda_{\text{exc}} = 350 \text{ nm}$ ) decays monoexponentially with  $\tau_{298}^{\text{H}} = 0.5 \mu\text{s}$  (ESI, Fig. S7†). This long lifetime confirms the assignment as phosphorescence. With the fully deuterated ligand  $\text{ddpd-}[\text{D}_{17}]^{36}$  installed in  $\text{VCl}_3(\text{ddpd-}[\text{D}_{17}])$ , the NIR luminescence intensity strongly increases compared to that of the non-deuterated complex (Fig. 2c). Concomitantly, the luminescence lifetime at 298 K increases to  $\tau_{298}^{\text{D}} = 3.3 \mu\text{s}$  ( $\lambda_{\text{obs}} = 1106 \text{ nm}$ ) and  $3.4 \mu\text{s}$  ( $\lambda_{\text{obs}} = 1222 \text{ nm}$ ) (Fig. S8 and S9, ESI†). The deuteration effect confirms that multiphonon relaxation (Fig. 1b) is substantial in  $\text{VCl}_3(\text{ddpd-}[\text{D}_0])$ . The estimated spectral overlap integral (SOI) of the second C–H<sub>ar</sub> overtone  $\nu_{\text{CH}}^3$  (ref. 34) of the ligand at  $8972 \text{ cm}^{-1}$  is significant, while the relevant third CD<sub>ar</sub> overtone  $\nu_{\text{CD}}^4$  (ref. 34) at  $8755 \text{ cm}^{-1}$  has a much lower SOI due to its lower extinction coefficient (ESI, Fig. S10–S12†). Based on the vibrational overtone analysis and SOI calculation, the rate constant for this overtone-mediated non-radiative decay mechanism should diminish by a factor of 36 (ESI, Fig. S10–S16†). This qualitatively matches the observed intensity enhancement upon deuteration. The observation of an isotope effect confirms that multiphonon relaxation is a major non-radiative decay path of the singlet states in this complex dominating other non-radiative decays. This finding contrasts the observations for the homoleptic complex  $[\text{V}(\text{ddpd})_2][\text{PF}_6]_3$  and its deuterated isotopologue where other decay pathways appear to dominate the non-radiative decay of the NIR-emissive states.<sup>36</sup>

Cooling solid  $\text{VCl}_3(\text{ddpd-}[\text{D}_n])$  both as neat powder and as KBr pellet increases the luminescence intensity (Fig. 2a, d; and S17–S19, ESI†). For example, cooling  $\text{VCl}_3(\text{ddpd-}[\text{D}_{17}])$  from 290 to 200 K yields a 1.5-fold increased integrated NIR intensity, while further cooling to 5 K only has a minor effect (Fig. 2d; and S17–S19, ESI†). This suggests the presence of a thermally activated non-radiative pathway accessible at temperatures above 200 K.

To probe the structure, the vibrational signature and possible distortions of the long-lived excited singlet states at high and low temperature, step-scan FTIR spectra of  $\text{VCl}_3(\text{ddpd-}[\text{D}_0])$  and  $\text{VCl}_3(\text{ddpd-}[\text{D}_{17}])$  were recorded in KBr pellets (Fig. 3; and S20–S23, ESI†). The ground state FTIR spectra of  $\text{VCl}_3(\text{ddpd-}[\text{D}_0])$  and  $\text{VCl}_3(\text{ddpd-}[\text{D}_{17}])$  in KBr pellets at 290 K are well reproduced by DFT calculated frequencies scaled by 0.98 (Fig. 3a and S21, ESI†). The characteristic  $\nu_{\text{CC}}$ ,  $\nu_{\text{CN}}$  and  $\delta_{\text{CH}}$  modes of the terminal and central pyridine rings around  $1599$ ,  $1495$  and  $1442 \text{ cm}^{-1}$  shift to lower energy by approximately  $35\text{--}75 \text{ cm}^{-1}$  upon deuteration of the ligand in  $\text{VCl}_3(\text{ddpd-}[\text{D}_{17}])$ .

Step-scan FTIR spectra recorded for  $\text{VCl}_3(\text{ddpd-}[\text{D}_0])$  and  $\text{VCl}_3(\text{ddpd-}[\text{D}_{17}])$  in a KBr pellet with  $\lambda_{\text{exc}} = 355 \text{ nm}$  collected over 0–500 ns at 290 and 20 K are depicted in Fig. 3a, S20, S21 and S23 (ESI†). The long-lived excited singlet states give rise to positive and negative bands corresponding to the population of the excited singlet states and ground state bleach, respectively. The excited state spectra of  $\text{VCl}_3(\text{ddpd-}[\text{D}_0])$  and  $\text{VCl}_3(\text{ddpd-}[\text{D}_{17}])$  at 290 and 20 K are derived from the respective step-scan and the ground state spectra (Fig. 3b; and S22, ESI†). Temperature has only a minor influence on the excited state spectra of  $\text{VCl}_3(\text{ddpd-}[\text{D}_0])$

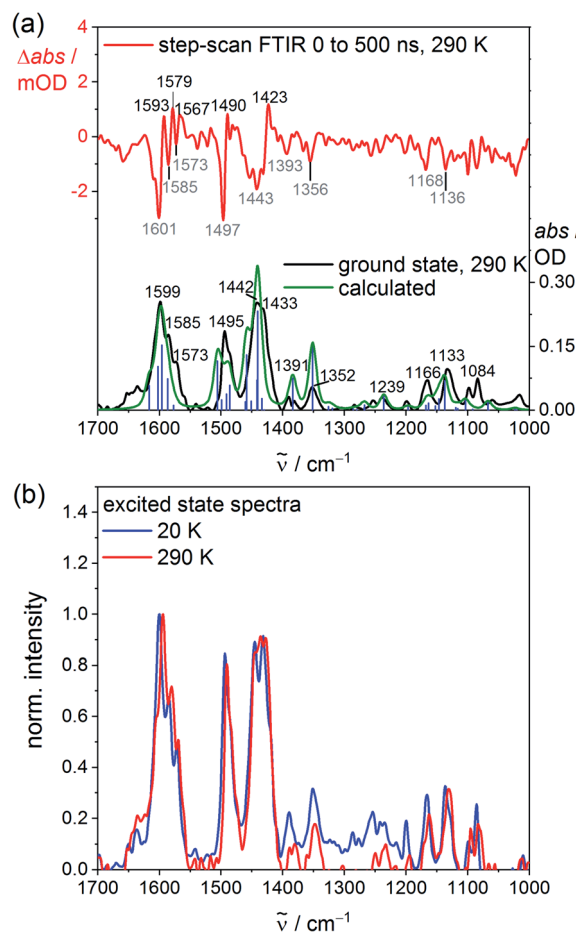


Fig. 3 (a) Experimental (black), DFT-calculated ground state (green) and step-scan FTIR spectra (top,  $\lambda_{\text{exc}} = 355 \text{ nm}$ ; 0–500 ns) of  $\text{VCl}_3(\text{ddpd-}[\text{D}_0])$  in a KBr pellet at 290 K (red) and (b) excited state FTIR spectra of  $\text{VCl}_3(\text{ddpd-}[\text{D}_0])$  in a KBr pellet obtained from step-scan FTIR spectra ( $\lambda_{\text{exc}} = 355 \text{ nm}$ ; 0–500 ns) (small contributions of 3% of the respective ground state spectrum added to the step-scan spectrum) at 20 K (blue) and 290 K (red).

(Fig. 3b), but modifies the relative excited state IR intensities of the deuterated derivative  $\text{VCl}_3(\text{ddpd-}[\text{D}_{17}])$  (Fig. S22, ESI†).

The evolution of prominent IR bands after excitation of  $\text{VCl}_3(\text{ddpd-}[\text{D}_0])$  over time was fitted in a global analysis giving a monoexponential decay with  $\tau_{290\text{K}}^{\text{H}} = 0.6 \mu\text{s}$  at 290 K (Fig. S24, ESI†) excellently fitting to the decay observed by photoluminescence spectroscopy at 298 K. Cooling to 20 K approximately doubles the excited state lifetime to  $\tau_{20\text{K}}^{\text{H}} = 1.3 \mu\text{s}$  (Fig. S25, ESI†). This confirms that thermally activated non-radiative pathways are operative at room temperature in addition to the multiphonon relaxation *via* C–H oscillators,<sup>57</sup> which takes place at all temperatures. Surprisingly, the step-scan data of the deuterated complex  $\text{VCl}_3(\text{ddpd-}[\text{D}_{17}])$  deliver excited state lifetimes of  $\tau_{290\text{K}}^{\text{D}} = 0.6 \mu\text{s}$  and  $\tau_{20\text{K}}^{\text{D}} = 1.2 \mu\text{s}$  at 290 and 20 K, respectively (Fig. S26 and S27, ESI†), similar to  $\text{VCl}_3(\text{ddpd-}[\text{D}_0])$ . This differs from the higher room temperature lifetime of  $\text{VCl}_3(\text{ddpd-}[\text{D}_{17}])$   $\tau_{298}^{\text{D}} = 3.3/3.4 \mu\text{s}$  obtained by time-correlated single photon counting (Fig. S8 and S9, ESI†; see above). Possibly, the step-scan FTIR experiment mainly detects one of



the emissive singlet states but fails to probe the second emissive singlet state. According to the CASSCF-NEVPT2 calculations, the two lowest singlet states derive from terms with essentially  $^1E$  and  $^1T_2$  character, respectively, with a very small energy difference of only  $75\text{ cm}^{-1}$  (Table S6, ESI $^\dagger$ ). As the orbital population of the  $^1T_2$ -derived term matches that of the lowest term of the split  $^3T_2$  ground state (Fig. S3, ESI $^\dagger$ ), this excited state possesses the same equilibrium nuclear configuration as the ground state (nested state). Consequently, step-scan FTIR spectroscopy would not be able to detect this excited state. Clearly, a model of the excited state decay of the two lowest energy singlet excited states to the split ground state requires at least five electronic states. For a kinetic model of the non-radiative decay *via* high- and low-frequency modes<sup>57</sup> these comparably close-lying electronic states (Fig. 1b) would have to be combined with the different anharmonic vibrational C–H/C–D modes as well as the pyridine ring vibrational ladders. The latter modes are also affected by deuteration according to the ground state FTIR spectra of  $\text{VCl}_3(\text{ddpd}-[\text{D}_0])$  and  $\text{VCl}_3(\text{ddpd}-[\text{D}_{17}])$  (Fig. 3a and S21, ESI $^\dagger$ ).

As  $\text{VCl}_3(\text{ddpd})$  is only poorly soluble in typical solvents, a detailed reliable study of its weak NIR luminescence in solution is unfortunately impeded, especially when exciting at the very weak  $^3MC$  band. Furthermore, we noted a follow-up reaction upon irradiating  $\text{VCl}_3(\text{ddpd}-[\text{D}_0])$  at  $350 \pm 5\text{ nm}$  (ILCT) in acetonitrile solution. The absorption spectrum changes and an emission band at *ca.* 400 nm grows in over time (Fig. S28 and S29, ESI $^\dagger$ ). The photostability is much higher under irradiation at  $400 \pm 5\text{ nm}$  including consideration for absorption and light intensity of the light source. (Fig. S30–S32, ESI $^\dagger$ ). This suggests that the low energy  $^3T_2$ ,  $^1T_2/{}^1E$  and  $\text{ddpd} \rightarrow \text{V } ^3LMCT$  states are not responsible for the photoreactivity (Fig. 1b). At the higher excitation energy and with the assumption that LMCT states are likely involved (Fig. 1), we speculate that V–Cl homolysis could occur in solution. The well-known fact, that M–Cl bonds of reducible metal ions are prone to photoinduced homolysis has regained considerable interest in organic photoredox catalysis in particular for copper<sup>69–71</sup> and nickel.<sup>72–75</sup>  $\text{VCl}_3$  itself is photo-reduced to vanadium(II) in alcoholic solutions *via* excitation into LMCT states (chloride-to-vanadium or alkoxide-to-vanadium charge transfer).<sup>76</sup> A  $^3LMCT$  state with chloride-to-vanadium character was found by TDDFT at 324 nm (state 14 shifted hypsochromically by  $3400\text{ cm}^{-1}$ , Tables S3, S4, and Fig. S2, ESI $^\dagger$ ). This  $^3LMCT$  state could qualify as excited state with V–Cl dissociative character. To probe the conceivable  $\text{V}^{\text{III/II}}$  reduction process, a cyclic voltammogram of  $\text{VCl}_3(\text{ddpd}-[\text{D}_0])$  was recorded in  $\text{CH}_3\text{CN}$ . The cathodic scan reveals an irreversible reduction wave at  $E_p = -1.11\text{ V}$  versus ferrocene/ferrocenium with an oxidative follow-up wave at  $E_p = -0.25\text{ V}$  and a reductive wave at  $-0.83\text{ V}$  (Fig. S33, ESI $^\dagger$ ). This behaviour can be associated with chloride loss upon electron capture, similar to the reported preparation of  $\text{VCl}_2(\text{py})_4$  from  $\text{VCl}_3$ , pyridine and zinc dust as reductant.<sup>77</sup> Consequently, we consider V–Cl bond homolysis as a viable reaction path under UV light photolysis in fluid solution. In contrast to this photoreactivity of the chlorido complex, the homoleptic complex  $[\text{V}(\text{ddpd})_2][\text{PF}_6]_3$  appears comparably photostable in solution,

which can be ascribed to the absence of suitable dissociative LMCT states.<sup>36</sup>

Finally we explored the reaction path from the Franck-Condon excited triplet state to the long-lived singlet states by ultrafast transient absorption spectroscopy in  $\text{CH}_3\text{CN}$ . To diminish the dissociative processes assigned to high-energy  $^3LMCT$  states with  $\text{Cl} \rightarrow \text{V}$  character, 400 nm pulses were employed populating essentially  $^3LMCT$  states with  $\text{NMe}(\text{ddpd}) \rightarrow \text{V}$  character (Tables S3, S4 and Fig. S2, ESI $^\dagger$ ). After excitation, a broad excited state absorption (ESA) from 470–700 nm appears in addition to an ESA around 410 nm (Fig. 4a). The ground state bleach fits to the dip in the transient absorption spectrum around 463 nm (Fig. 1a and 4b).

The broad ESA evolves with  $\tau_1 = 1.5\text{ ps}$  to a long-lived state with a maximum at 543 nm (Fig. 4b). This state persists much longer than the time window of 1.4 ns of the pump-probe experiment, which is given by the length of the motorized delay stage in the setup. Since electronic relaxation between electronically excited states of the same spin multiplicity is typically rather fast, one of the lowest excited states of the different spin multiplicities should be responsible for the long-

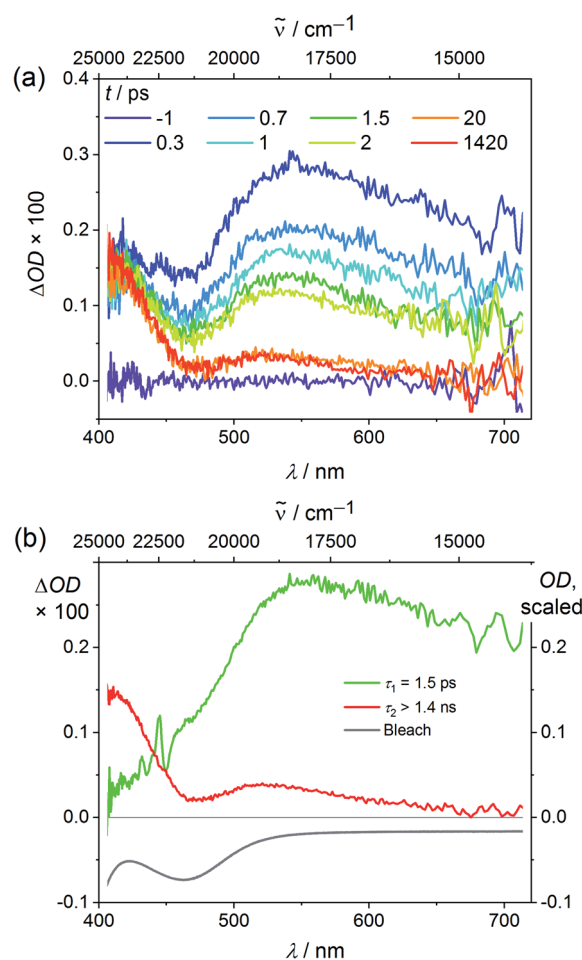


Fig. 4 (a) Transient absorption spectra of  $\text{VCl}_3(\text{ddpd}-[\text{D}_0])$  in  $\text{CH}_3\text{CN}$  excited with fs laser pulses at 400 nm (298 K) and (b) decay associated amplitude spectra (red, green) with indicated lifetimes and the ground state bleach (grey).





lived state, *i.e.* the  $^3T_2$  state or the  $^1E/{}^1T_2$  states (Fig. 1). Significant population in a long living electronically excited triplet state should result in fluorescence, since the radiative transition to the ground state would be spin allowed and Laporte's rule is relaxed in the complex. However, no luminescence is observed at wavelengths below 1050 nm as would be expected for triplet states (Fig. 1). This excludes that a significant excited state population is trapped in any triplet state. A partitioning of excited state population in triplet and singlet states, as it was observed in  $[V(\text{ddpd})_2]^{3+}$  (ref. 36) does not occur with  $VCl_3(\text{ddpd})$ . The persistent TA component is therefore assigned to the long-lived  $^1E/{}^1T_2$  states. Clearly, ISC to the singlet manifold and vibrational cooling proceed to completion within a few ps. The rate constant for ISC  $k_{\text{ISC}}$  is at least  $1/\tau_1 = 6.7 \times 10^{11} \text{ s}^{-1}$ . Trajectory surface hopping simulations within a linear vibronic coupling model will derive a detailed kinetic model of the initial dynamics and the efficiency of the ISC processes ( $\tau_{\text{ISC, simulation}} = 1.7 \pm 0.3 \text{ ps}$ ) in the accompanying paper.<sup>63</sup>

## Experimental

**Synthesis.**  $VCl_3(\text{ddpd}-D_0)$  was prepared according to ref. 58. The deuterated complex  $VCl_3(\text{ddpd}-[D_{17}])$  was prepared analogously using the deuterated ligand  $\text{ddpd}-[D_{17}]$  prepared according to ref. 36.

**Electrochemical experiments** were carried out on a BioLogic SP-200 voltammetric analyser using platinum wires as counter and working electrodes and a 0.01 M  $\text{Ag}/\text{Ag}[\text{NO}_3]$  electrode as reference electrode. Cyclic voltammetry and square wave measurements were carried out at scan rates of 50–200  $\text{mV s}^{-1}$  using 0.1 M  $[^t\text{Bu}_4\text{N}][\text{PF}_6]$  in  $\text{CH}_3\text{CN}$  as supporting electrolyte. Potentials are referenced against the ferrocene/ferrocenium couple.

**Photolysis experiments** were carried out in  $\text{CH}_3\text{CN}$  using an Asahi Spectra Max-303 Xenon Light Source (300 W, Fig. S32, ESI<sup>†</sup>), together with  $350 \pm 5 \text{ nm}$  and  $400 \pm 5 \text{ nm}$  filters, respectively.

**UV/Vis photoluminescence spectra during photolysis experiments** were collected on a Varian Cary Eclipse spectrometer.

**UV/Vis/NIR spectra** were recorded on a Varian Cary 5000 spectrometer using 1.0 cm cells.

**Raman and luminescence spectra under pressure** at wavelengths up to 1050 nm were measured with a Renishaw InVia microscope (488 and 785 nm laser wavelengths) and a HPDO diamond anvil cell.

**Temperature-dependent steady-state NIR luminescence experiments** down to 5 K were conducted on a Horiba Jobin Yvon Fluorolog 3-22  $\tau$  spectrometer equipped with a 450 W xenon lamp and a DSS – IGA020L NIR detector (850 nm  $< \lambda_{\text{em}} < 1550 \text{ nm}$ ). Spectral selection was realized with double and single grating monochromators in the excitation and emission paths, respectively (excitation: 1200 grooves per mm; near-IR emission 600 grooves per mm). A combination of two long-pass filters (FELH0500 Thorlabs, transmission  $\geq 92\%$  above 500 nm and FELH0850 Thorlabs, transmission  $\geq 98\%$  above 1000 nm) was used in the emission channel to avoid higher order excitation light. For the preparation of KBr pellets,

the compounds (*ca.* 1.0 mg for  $VCl_3(\text{ddpd}-[D_0])$  and 0.5 mg for  $VCl_3(\text{ddpd}-[D_{17}])$ ) were mixed with dry KBr (*ca.* 200 mg, stored in a compartment dryer at 80 °C, purchased from Merck) and ground to a homogenous mixture. This mixture was filled into an evacuable pellet die with a diameter of 13 mm and sintered at a pressure of 0.75 GPa. Measurements on neat powders were conducted by homogenous spreading of the neat sample between two  $\text{CaF}_2$  windows (13 mm diameter, 1 mm thick). Experiments at temperatures between 5 K and 290 K were performed using a closed-cycle helium cryostat (ColdEdge, 101J cryocooler). The cryocooler was equipped with a pellet holder (copper) and  $\text{CaF}_2$  windows.

**Steady-state NIR luminescence experiments** on neat samples down to 77 K were conducted on a Horiba Fluorolog-3 spectrofluorimeter equipped with a 450 W xenon lamp for steady-state measurements. Emitted light was detected either by a Hamamatsu R2658P PMT detector (200 nm  $< \lambda_{\text{em}} < 1010 \text{ nm}$ ) or by a Hamamatsu H10330-75 PMT detector (950 nm  $< \lambda_{\text{em}} < 1700 \text{ nm}$ ). Spectral selection in the excitation path was accomplished by a DFX monochromator (double gratings: 1200 grooves per mm, 330 nm blaze) and in the emission paths in the visible/NIR spectral region ( $\lambda_{\text{em}} < 1010 \text{ nm}$ ) by a spectrograph iHR550 (single gratings: either 1200 grooves per mm, 500 nm blaze or 950 grooves per mm, 900 nm blaze) and in the NIR spectral region ( $\lambda_{\text{em}} > 950 \text{ nm}$ ) by a spectrograph iHR320 (single grating: 600 grooves per mm, 1000 nm blaze).

**Near-IR luminescence lifetimes** of the phosphorescent transitions were determined at 298 K (solid samples in standard NMR tubes under argon) with a PTI Quantamaster QM4 spectrofluorimeter equipped with a 75 W continuous xenon short arc lamp as excitation source (Hamamatsu L4633: pulse width *ca.* 1.5  $\mu\text{s}$  FWHM). Emission was monitored using a PTI P1.7R detector module (Hamamatsu PMT R5509-72 with a Hamamatsu C9525 power supply operated at 1500 V and a Hamamatsu liquid  $\text{N}_2$  cooling unit C9940 set to  $-80 \text{ }^\circ\text{C}$ ). For the measurements above 1000 nm, a long-pass filter RG-850 (Schott, 3.0 mm thickness, transmission  $>98\%$  above 970 nm) was used in the emission channel in order to avoid higher order excitation light. Spectral selection was achieved by single grating monochromators (excitation: 1200 grooves per mm, 300 nm blaze; Vis emission: 1200 grooves per mm, 500 nm blaze; near-IR emission: 600 grooves per mm, 1200 nm blaze) and an additional UG11 bandpass filter (Schott, 3.0 mm thickness) in the excitation channel. Lifetime data analysis (deconvolution, statistical parameters, *etc.*) was performed using the software package FeliX32 from PTI. Lifetimes were determined by deconvolution of the decay profiles with the instrument response function, which was determined using an empty NMR tube as scatterer. Estimated uncertainties for the lifetimes of the near-IR emission determined with this setup are 20%.

**Time-resolved FTIR experiments** were performed with the FTIR spectrometer Bruker Vertex 80v, operated in the step-scan mode. A liquid-nitrogen-cooled mercury cadmium telluride (MCT) detector (Kolmar Tech., Model KV100-1-B-7/190) with a rise time of 25 ns, connected to a fast preamplifier and a 14 bit transient recorder board (Spectrum Germany, M314142, 400 MS



$s^{-1}$ ), was used for signal detection and processing. The laser setup used for the measurements includes a Q-switched Nd:YAG laser (Innolas SpitLight Evo I) generating pulses with a pulse duration of about 6 ns at a repetition rate of 100 Hz. The third harmonic (355 nm) of the Nd:YAG laser was used directly for sample excitation. The UV pump beam was attenuated to about 1.8 mJ per shot at a diameter of 9 mm. The beam was directed onto the sample and adjusted to have a maximal overlap with the IR beam of the spectrometer. The sample chamber was equipped with anti-reflection-coated germanium filters to prevent the entrance of laser radiation into the detector and interferometer compartments. The KBr pellets were prepared as described in the section on luminescence spectroscopy, however, with a smaller amount of sample of *ca.* 0.2 mg and *ca.* 200 mg KBr. The strongest peak in the ground state spectrum showed an absorption of about 0.4 OD with the mentioned concentration. *T*-dependent measurements were performed using a closed-cycle helium cryostat (ARS Model DE-202A) reaching a temperature of about 20 K at the sample. The cryocooler was equipped with a pellet holder and CaF<sub>2</sub> windows. The temporal resolution of the 14 bit transient recorder board was chosen to 5 ns for VCl<sub>3</sub>(ddpd-[D<sub>0</sub>]) and 10 ns for VCl<sub>3</sub>(ddpd-[D<sub>17</sub>]). The time where the laser pulse reached the sample was set as zero point in all spectra. The time delay between the start of the experiment and the laser pulse was controlled with a Stanford Research Systems DG535 delay generator. The spectral region was limited by undersampling to 1975 to 0  $cm^{-1}$  for VCl<sub>3</sub>(ddpd-[D<sub>0</sub>]) and 988–1975  $cm^{-1}$  for VCl<sub>3</sub>(ddpd-[D<sub>17</sub>]) with a spectral resolution of 4  $cm^{-1}$  resulting in 1110 and 555 interferogram points, respectively. An IR broadband filter (850–1750  $cm^{-1}$ ) and CaF<sub>2</sub> windows (no IR transmission <1000  $cm^{-1}$ ) prevented problems when performing a Fourier transformation (*i.e.* no IR intensity outside the measured region should be observed). FTIR ground state spectra were recorded systematically to check if there is no sample degradation. Estimated uncertainties for the excited state lifetimes are on the order of 10%.

**Transient absorption spectra** of VCl<sub>3</sub>(ddpd-[D<sub>0</sub>]) were recorded applying a pump-probe setup with an excitation wavelength of 400 nm. The setup is pumped by a Ti:sapphire laser system (Spectra-Physics, Spitfire Pro) which provides ultrashort laser pulses centred at 800 nm with a repetition rate of 1 kHz. By frequency doubling its output with a BBO-crystal pump pulses with a centre wavelength of 400 nm and a pulse duration of 200 fs were obtained. For probing, a white light continuum generated with a CaF<sub>2</sub> crystal was used. Both beams, with polarizations arranged in magic angle, were focused onto the sample leading to pump and probe spots with diameters of 170  $\mu m$  and 80  $\mu m$ , respectively. Transient absorption spectra were recorded by dispersing the probe beam after the sample with a prism and detecting its spectral intensity distribution with a CCD array. The metal complex was dissolved in acetonitrile under argon atmosphere and the obtained sample was filled into a 1 mm fused silica cuvette. The concentration was  $1.5 \times 10^{-3}$  M resulting in an optical density of 0.18 at 400 nm. Significantly higher concentrations

were not accessible because of the moderate solubility of the compound in acetonitrile.

**Quantum chemical calculations.** The characterization of the absorption spectrum was done employing two types of quantum chemical calculations: (i) density functional theory in its unrestricted form and (ii) multiconfigurational theory with an active space tailored to predict the MC states. The first method is labelled as “Unrestricted Kohn–Sham” orbitals DFT (UKS), the second as “SOC-CASSCF(6,12)-FIC-NEVPT2”. These two methods are complementary to each other, as the first gives energies of the CT states, while the second one provides the energies of the MC states and the ground state splitting.<sup>78</sup>

**Unrestricted Kohn–Sham orbitals DFT (UKS):** All calculations were performed using the quantum computing suite ORCA 4.0.1.12.<sup>79</sup> Geometry optimization (Tables S1 and S2†) was performed using unrestricted Kohn–Sham orbitals DFT (UKS) and the B3LYP functional<sup>80–82</sup> in combination with Ahlrichs’ split-valence triple- $\zeta$  basis set def2-TZVPP for all atoms.<sup>83,84</sup> Tight convergence criteria were chosen for DFT-UKS calculations (keywords tightscf and tightopt). All DFT-UKS calculations make use of the resolution of identity RIJ (Split-RI-J) approach for the Coulomb term in combination with the chain-of-spheres approximation for the exchange term (COSX).<sup>85,86</sup> The zero order relativistic approximation was used to describe relativistic effects in all calculations (keyword ZORA).<sup>87</sup> Grimme’s empirical dispersion correction D3(BJ) was employed (keyword D3BJ).<sup>88,89</sup> To account for solvent effects, a conductor-like screening model (keyword CPCM) modelling acetonitrile was used in all calculations.<sup>90,91</sup> TDDFT-UKS calculations were performed at the same level of theory using unrestricted Kohn–Sham orbitals (UKS). Fifty vertical spin-allowed transitions were calculated (Tables S3 and S4†).

Harmonic frequency calculations for the IR assignments were performed using Turbomole 7.4 (ref. 92 and 93) on the optimized geometry (RIJCOSX-UB3LYP-D3BJ/def2-TZVP). The vibrational frequencies were scaled by a factor of 0.98, which is typical for the chosen method and basis set, to minimize the differences between the experimental and calculated frequencies. A Gaussian convolution with a full-width at half-maximum of 15  $cm^{-1}$  was applied to the calculated vibrational transitions.

**SOC-CASSCF(6,12)-FIC-NEVPT2:** calculations of ground- and excited-state properties with respect to metal-centered (MC) states were performed using the complete-active-space self-consistent field method in conjunction with the fully internally contracted N-electron valence perturbation theory to second order based on a fully internally contracted (FIC) wave function (FIC-NEVPT2)<sup>94,95</sup> in order to recover missing dynamic electron correlation. In order to accurately model the ligand field, active spaces were chosen to encompass the dominating bonding/antibonding orbitals formed between vanadium and the ligand. An active space of (6,12) along with 10 triplet roots and 9 singlet roots was selected (Tables S5 and S6†). In addition to the minimal active space of (2,5) comprising the 3d orbitals, two occupied V–N  $\sigma$  bonding orbitals and a second d shell<sup>96</sup> were included in these calculations.



## Conclusions

The pseudo-octahedral vanadium(III) complex  $\text{VCl}_3(\text{ddpd})$  with the strong-field ligand ddpd shows spin-flip phosphorescence at room temperature at 1102, 1219 and 1256 nm after excitation into charge-transfer bands. Several factors are relevant for this emission from a 3d transition metal complex to occur:

(i) The ligand field splitting in  $\text{VCl}_3(\text{ddpd})$  is large enough to place the emissive singlet states  $^1\text{E}/^1\text{T}_2$  below the distorted metal-centred triplet excited states  $^3\text{T}_2$ .

(ii) Lower temperature disables thermally activated non-radiative pathways increasing the photoluminescence, yet even at room temperature a weak emission is still observed.

(iii) Deuteration of the ddpd ligand reduces non-radiative energy transfer to C-H overtones increasing the photoluminescence.

(iv) The radiative rate might be higher in non-centrosymmetric pseudo-octahedral vanadium complexes, although this effect of Laporte's parity rule was not experimentally confirmed in this particular case.

(v) The ISC rate constant from the triplet to the singlet manifold is high ( $k_{\text{ISC}} > 6.7 \times 10^{11} \text{ s}^{-1}$ ) as confirmed by the molecular dynamics simulations in the accompanying paper.<sup>63</sup> This high rate could be an effect of the heavier chloride atoms (heavy atom effect), efficient vibronic coupling and/or enhanced SOC due to large differences in orbital type between the two states ( $^3\text{LMCT} \rightarrow ^1\text{MC}$ ),<sup>97</sup> although other ultrafast pathways might still compete with ISC.

Challenges with the emission from excited states of  $\text{d}^2\text{-VCl}_3(\text{ddpd})$  arise from the large ground state splitting which spreads the emission bands over *ca.* 2400  $\text{cm}^{-1}$ . This range is larger by almost two orders of magnitude than the corresponding spin-flip emission of  $\text{d}^3$ -metal complexes with orbitally non-degenerate ground states, a very significant difference for transitions involving essentially nested states. The considerable ground state splitting further reduces the already small energy gap between the emissive state and the ground state enabling a higher non-radiative decay according to the energy gap law. A second aspect of  $\text{VCl}_3(\text{ddpd})$  as phosphorescent emitter concerns the excited state reactivity of LMCT states with chloride  $\rightarrow$  vanadium charge-transfer character in solution. As these states can lead to V-Cl homolysis in solution reducing the photoluminescence and finally decomposing the complex, solution photostability is a particularly important aspect for future applications of vanadium(III) complexes in solution.

This study emphasises that design strategies toward efficient  $\text{d}^2$ -NIR emitters require a particular attention to the ISC efficiency from the triplets to the singlet states and potential dissociative unimolecular reactions at ultrafast timescales as well as on the radiative and non-radiative relaxation of the singlets at longer times. Details of the ultrafast excited state dynamics of  $\text{VCl}_3(\text{ddpd})$  up to 10 ps are discussed in the accompanying paper.<sup>63</sup>

## Data availability

Experimental and computational data are available as ESI.

## Author contributions

MD prepared the complex, performed all ground state characterization and photolysis experiments and the quantum chemical calculations, JK and MS measured and analysed the luminescence and lifetime data of the neat complex, measured and analysed the NIR absorption data and performed the SOI calculations, CD and CR measured and analysed the Raman spectra and the spectra under pressure, PB, GNS and MG measured and analysed the step-scan FT-IR spectra and the temperature dependent luminescence spectra of the complex in KBr pellets, AK and SL measured and analysed the transient absorption spectra, MS and KH devised the concept. KH supervised the project and wrote the manuscript.

## Conflicts of interest

There are no conflicts to declare.

## Acknowledgements

Financial support from the Deutsche Forschungsgemeinschaft [DFG, Priority Program SPP 2102 "Light-controlled reactivity of metal complexes" GE 961/10-1, HE 2778/15-1, LO 714/11-1, SE 1448/8-1] is gratefully acknowledged. Parts of this research were conducted using the supercomputer Mogon and advisory services offered by Johannes Gutenberg University Mainz (<http://www.hpc.uni-mainz.de>), which is a member of the AHRP and the Gauss Alliance e.V. and the supercomputer Elwetritsch and advisory services offered by the TU Kaiserslautern (<https://elwe.rhrk.uni-kl.de>) which is a member of the AHRP. CR and CD thank the Natural Sciences and Engineering Research Council (Canada) for research grants and the Fonds du recherche du Québec – Nature et technologies for a postdoctoral fellowship (CD).

## Notes and references

- R. D. Costa, E. Ort, H. J. Bolink, F. Monti, G. Accorsi and N. Armaroli, *Angew. Chem., Int. Ed.*, 2012, **51**, 8178.
- K. K.-W. Lo, *Acc. Chem. Res.*, 2015, **48**, 2985.
- M. Schäferling, *Angew. Chem., Int. Ed.*, 2012, **51**, 3532.
- F. Heinemann, J. Karges and G. Gasser, *Acc. Chem. Res.*, 2017, **50**, 2727.
- A. Hagfeldt, G. Boschloo, L. C. Sun, L. Kloo and H. Pettersson, *Chem. Rev.*, 2010, **110**, 6595.
- C. K. Prier, D. A. Rankic and D. W. C. MacMillan, *Chem. Rev.*, 2013, **113**, 5322.
- J. M. R. Narayanam and C. R. J. Stephenson, *Chem. Soc. Rev.*, 2011, **40**, 102.
- T. P. Yoon, M. A. Ischay and J. Du, *Nat. Chem.*, 2010, **2**, 527.
- V. Balzani, G. Bergamini, S. Campagna and F. Puntoriero, *Photochemistry and Photophysics of Coordination Compounds: Overview and General Concepts*. in *Photochemistry and Photophysics of Coordination Compounds I, Topics in Current Chemistry*, ed. V. Balzani and S. Campagna, Springer, Berlin, 2007, pp. 1–36.



- 10 J. K. McCusker, *Science*, 2019, **363**, 484.
- 11 S. Koseki, N. Matsunaga, T. Asada, M. W. Schmidt and M. S. Gordon, *J. Phys. Chem. A*, 2019, **123**, 2325.
- 12 V. W. Yam, A. K. Chan and E. Y. Hong, *Nat. Rev. Chem.*, 2020, **4**, 528.
- 13 O. S. Wenger, *J. Am. Chem. Soc.*, 2018, **140**, 13522.
- 14 C. Förster and K. Heinze, *Chem. Soc. Rev.*, 2020, **49**, 1057.
- 15 S. Otto, M. Dorn, C. Förster, M. Bauer, M. Seitz and K. Heinze, *Coord. Chem. Rev.*, 2018, **359**, 102.
- 16 O. S. Wenger, *Chem.–Eur. J.*, 2019, **25**, 6043.
- 17 C. Bizzarri, E. Spuling, D. M. Knoll, D. Volz and S. Bräse, *Coord. Chem. Rev.*, 2018, **373**, 49.
- 18 P. Chábera, L. Lindh, N. W. Rosemann, O. Prakash, J. Uhlig, A. Yartsev, K. Wärnmark, V. Sundström and P. Persson, *Coord. Chem. Rev.*, 2020, **426**, 213517.
- 19 P. Herr, F. Glaser, L. A. Büldt, C. B. Larsen and O. S. Wenger, *J. Am. Chem. Soc.*, 2019, **141**, 14394.
- 20 L. A. Büldt, X. Guo, A. Prescimone and O. S. Wenger, *Angew. Chem., Int. Ed.*, 2016, **55**, 11247.
- 21 Y. Zhang, T. S. Lee, J. M. Favale, D. C. Leary, J. L. Petersen, G. D. Scholes, F. N. Castellano and C. Milsmann, *Nat. Chem.*, 2020, **12**, 345.
- 22 Y. Zhang, T. S. Lee, J. L. Petersen and C. Milsmann, *J. Am. Chem. Soc.*, 2018, **140**, 5934.
- 23 R. Hamze, J. L. Peltier, D. Sylvinson, M. Jung, J. Cardenas, R. Haiges, M. Soleilhavoup, R. Jazzar, P. I. Djurovich, G. Bertrand and M. E. Thompson, *Science*, 2019, **36**, 601.
- 24 M. Gernert, L. Balles-Wolf, F. Kerner, U. Mueller, A. Schmiedel, M. Holzzapfel, C. M. Marian, J. Pflaum, C. Lambert and A. Steffen, *J. Am. Chem. Soc.*, 2020, **142**, 8897.
- 25 L. A. Büldt, C. B. Larsen and O. S. Wenger, *Chem.–Eur. J.*, 2017, **23**, 8577.
- 26 Y.-S. Wong, M.-C. Tang, M. Ng and V. W.-W. Yam, *J. Am. Chem. Soc.*, 2020, **142**, 7638.
- 27 A. K. Pal, C. Li, G. S. Hanan and E. Zysman-Colman, *Angew. Chem., Int. Ed.*, 2018, **57**, 8027.
- 28 P. Chábera, Y. Liu, O. Prakash, E. Thyrhaug, A. El Nahhas, A. Honarfar, S. Essén, L. A. Fredin, T. C. B. Harlang, K. S. Kjær, K. Handrup, F. Ericson, H. Tatsuno, K. Morgan, J. Schnadt, L. Häggström, T. Ericsson, A. Sobkowiak, S. Lidin, P. Huang, S. Styring, J. Uhlig, J. Bendix, R. Lomoth, V. Sundström, P. Persson and K. Wärnmark, *Nature*, 2017, **543**, 695.
- 29 K. S. Kjær, N. Kaul, O. Prakash, P. Chábera, N. W. Rosemann, A. Honarfar, O. Gordivska, L. A. Fredin, K.-E. Bergquist, L. Häggström, T. Ericsson, L. Lindh, A. Yartsev, S. Styring, P. Huang, J. Uhlig, J. Bendix, D. Strand, V. Sundström, P. Persson, R. Lomoth and K. Wärnmark, *Science*, 2019, **363**, 249.
- 30 T. Jiang, Y. Bai, P. Zhang, Q. Han, D. B. Mitzi and M. J. Therien, *Proc. Natl. Acad. Sci. U. S. A.*, 2020, **117**, 20430.
- 31 J. Steube, A. Pöpcke, O. S. Bokareva, T. Reuter, S. Demeshko, R. Schoch, S. Hohloch, F. Meyer, K. Heinze, O. Kühn, S. Lochbrunner, M. Bauer, submitted (preprint at DOI: 10.21203/rs.3.rs-64316/v1).
- 32 L. A. Büldt, X. Guo, R. Vogel, A. Prescimone and O. S. Wenger, *J. Am. Chem. Soc.*, 2017, **139**, 985.
- 33 S. Otto, M. Grabolle, C. Förster, C. Kreitner, U. Resch-Genger and K. Heinze, *Angew. Chem., Int. Ed.*, 2015, **54**, 11572.
- 34 C. Wang, S. Otto, M. Dorn, E. Kreidt, J. Lebon, L. Sršan, P. Di Martino-Fumo, M. Gerhards, U. Resch-Genger, M. Seitz and K. Heinze, *Angew. Chem., Int. Ed.*, 2018, **57**, 1112.
- 35 S. Treiling, C. Wang, C. Förster, F. Reichenauer, J. Kalmbach, P. Boden, J. P. Harris, L. Carrella, E. Rentschler, U. Resch-Genger, C. Reber, M. Seitz, M. Gerhards and K. Heinze, *Angew. Chem., Int. Ed.*, 2019, **58**, 18075.
- 36 M. Dorn, J. Kalmbach, P. Boden, A. Pöpcke, S. Gómez, C. Förster, F. Kuczelinis, L. M. Carrella, L. Büldt, N. Bings, E. Rentschler, S. Lochbrunner, L. González, M. Gerhards, M. Seitz and K. Heinze, *J. Am. Chem. Soc.*, 2020, **142**, 7947.
- 37 S. Otto, A. M. Nauth, E. Ermilov, N. Scholz, A. Friedrich, U. Resch-Genger, S. Lochbrunner, T. Opatz and K. Heinze, *ChemPhotoChem*, 2017, **1**, 344.
- 38 S. Otto, N. Scholz, T. Behnke, U. Resch-Genger and K. Heinze, *Chem.–Eur. J.*, 2017, **23**, 12131.
- 39 S. Otto, J. Harris, K. Heinze and C. Reber, *Angew. Chem. Int. Ed.*, 2018, **57**, 11069.
- 40 C. Wang, S. Otto, M. Dorn, K. Heinze and U. Resch-Genger, *Anal. Chem.*, 2019, **91**, 2337.
- 41 U. Basu, S. Otto, K. Heinze and G. Gasser, *Eur. J. Inorg. Chem.*, 2019, 37.
- 42 J. Kalmbach, C. Wang, Y. You, C. Förster, H. Schubert, K. Heinze, U. Resch-Genger and M. Seitz, *Angew. Chem. Int. Ed.*, 2020, **59**, 1884.
- 43 J.-R. Jiménez, B. Doistau, C. M. Cruz, C. Besnard, J. M. Cuerva, A. G. Campaña and C. Piguet, *J. Am. Chem. Soc.*, 2019, **141**, 13244.
- 44 C. Dee, F. Zinna, W. R. Kitzmann, G. Pescitelli, K. Heinze, L. Di Bari and M. Seitz, *Chem. Commun.*, 2019, **55**, 13078.
- 45 J.-R. Jiménez, M. Poncet, S. Míguez-Lago, S. Grass, J. Lacour, C. Besnard, J. M. Cuerva, A. G. Campaña and C. Piguet, *Angew. Chem., Int. Ed.*, 2021, **60**, 10095.
- 46 H. Xiang, J. Cheng, X. Ma and X. Zhou, *Chem. Soc. Rev.*, 2013, **42**, 6128.
- 47 R. D. Dill, R. I. Portillo, S. G. Shepard, M. P. Shores, A. K. Rappé and N. H. Damrauer, *Inorg. Chem.*, 2020, **59**, 14706.
- 48 A. C. Bowman, S. Sproules and K. Wieghardt, *Inorg. Chem.*, 2012, **51**, 3707.
- 49 A. W. Maverick, S. S. Shah, C. Kirmaier and D. Holten, *Inorg. Chem.*, 1987, **26**, 774.
- 50 Y. Tanabe and S. Sugano, *J. Phys. Soc. Jpn.*, 1954, **9**, 766.
- 51 P. L. W. Tregenna-Piggott, D. Spichiger, G. Carver and B. Frey, *Inorg. Chem.*, 2004, **43**, 8049.
- 52 R. Beaulac, P. L. W. Tregenna-Piggott, A.-L. Barra, H. Weihe, D. Luneau and C. Reber, *Inorg. Chem.*, 2006, **45**, 3399.
- 53 K. R. Kittilstved and A. Hauser, *Coord. Chem. Rev.*, 2010, **254**, 2663.
- 54 D. R. Gamelin and H. U. Güdel, *Acc. Chem. Res.*, 2000, **33**, 235.
- 55 L. Aboshyan-Sorgho, C. Besnard, P. Pattison, K. R. Kittilstved, A. Aebischer, J.-C. G. Bünzli, A. Hauser and C. Piguet, *Angew. Chem., Int. Ed.*, 2011, **50**, 4108.





- 56 M. S. Fataftah, S. L. Bayliss, D. W. Laorenza, X. Wang, B. T. Phelan, C. B. Wilson, P. J. Mintun, B. D. Kovos, M. R. Wasielewski, S. Han, M. S. Sherwin, D. D. Awschalom and D. E. Freedman, *J. Am. Chem. Soc.*, 2020, **142**, 20400–20408.
- 57 E. Kreidt, C. Kruck and M. Seitz, *Handbook on the Physics and Chemistry of Rare Earths*, Elsevier, Amsterdam, 2018, vol. 53, pp. 35–79.
- 58 C. Förster, M. Dorn, T. Reuter, S. Otto, G. Davarci, T. Reich, L. Carrella, E. Rentschler and K. Heinze, *Inorganics*, 2018, **6**, 86.
- 59 G. Bussière, R. Beaulac, B. Cardinal-David and C. Reber, *Coord. Chem. Rev.*, 2001, **219**, 509.
- 60 J. Bendix, M. Brorson and C. E. Schaffer, *Inorg. Chem.*, 1993, **32**, 2838.
- 61 M. Blume and R. E. Watson, *Proc. R. Soc. London, Ser. A*, 1963, **271**, 565.
- 62 O. Laporte and W. F. Meggers, *J. Opt. Soc. Am.*, 1925, **11**, 459.
- 63 J. P. Zobel, T. Knoll and L. González, *Chem. Sci.*, 2021, DOI: 10.1039/D1SC02149D.
- 64 L. E. Manzer, J. Deaton, P. Sharp and R. R. Schrock, *Inorg. Synth.*, 1982, **21**, 135.
- 65 A. Breivogel, C. Förster and K. Heinze, *Inorg. Chem.*, 2010, **49**, 7052.
- 66 F. Plasser, *J. Chem. Phys.*, 2020, **152**, 084108.
- 67 S. Mai, F. Plasser, J. Dorn, M. Fumanal, C. Daniel and L. González, *Coord. Chem. Rev.*, 2018, **361**, 74.
- 68 C. Van Stappen, D. Maganas, S. DeBeer, E. Bill and F. Neese, *Inorg. Chem.*, 2018, **57**, 6421.
- 69 J. K. Kochi, *J. Am. Chem. Soc.*, 1962, **84**, 2121.
- 70 A. Hossain, S. Engl, E. Lutsker and O. Reiser, *ACS Catal.*, 2019, **9**, 1103.
- 71 R. Fayad, S. Engl, E. O. Danilov, C. E. Hauke, O. Reiser and F. N. Castellano, *J. Phys. Chem. Lett.*, 2020, **11**, 5345.
- 72 S. J. Hwang, D. C. Powers, A. G. Maher, B. L. Anderson, R. G. Hadt, S.-L. Zheng, Y.-S. Chen and D. G. Nocera, *J. Am. Chem. Soc.*, 2015, **137**, 6472.
- 73 S. J. Hwang, B. L. Anderson, D. C. Powers, A. G. Maher, R. G. Hadt and D. G. Nocera, *Organometallics*, 2015, **34**, 4766.
- 74 O. S. Wenger, *Chem.–Eur. J.*, 2021, **27**, 2270.
- 75 S. K. Kariofillis and A. G. Doyle, *Acc. Chem. Res.*, 2021, **54**, 988.
- 76 Y. Doi and M. Tsutsui, *J. Am. Chem. Soc.*, 1978, **100**, 3243.
- 77 J. J. H. Edema, W. Stauthamer, F. Van Bolhuis, S. Gambarotta, W. J. J. Smeets and A. L. Spek, *Inorg. Chem.*, 1990, **29**, 1302.
- 78 D. Reinen, M. Atanasov, P. Köhler and D. Babel, *Coord. Chem. Rev.*, 2010, **254**, 2703.
- 79 F. Neese, *Wiley Interdiscip. Rev.: Comput. Mol. Sci.*, 2018, **8**, e1327.
- 80 A. D. Becke, *J. Chem. Phys.*, 1993, **98**, 5648.
- 81 C. Lee, W. Yang and R. G. Parr, *Phys. Rev. B: Condens. Matter Mater. Phys.*, 1988, **37**, 785.
- 82 B. Miehlich, A. Savin, H. Stoll and H. Preuss, *Chem. Phys. Lett.*, 1989, **157**, 200.
- 83 F. Weigend and R. Ahlrichs, *Phys. Chem. Chem. Phys.*, 2005, **7**, 3297.
- 84 F. Weigend, *Phys. Chem. Chem. Phys.*, 2006, **8**, 1057.
- 85 F. Neese, F. Wennmohs, A. Hansen and U. Becker, *Chem. Phys.*, 2009, **356**, 98.
- 86 R. Izsák and F. Neese, *J. Chem. Phys.*, 2011, **135**, 144105-1–144105-11.
- 87 D. A. Pantazis, X.-Y. Chen, C. R. Landis and F. Neese, *J. Chem. Theory Comput.*, 2008, **4**, 908.
- 88 S. Grimme, S. Ehrlich and L. Goerigk, *J. Comput. Chem.*, 2011, **32**, 1456.
- 89 S. Grimme, J. Antony, S. Ehrlich and H. Krieg, *J. Chem. Phys.*, 2010, **132**, 154104.
- 90 S. Miertus, E. Scrocco and J. Tomasi, *Chem. Phys.*, 1981, **55**, 117.
- 91 V. Barone and M. Cossi, *J. Phys. Chem. A*, 1998, **102**, 1995.
- 92 F. Furche, R. Ahlrichs, C. Hättig, W. Klopper, M. Sierka and F. Weigend, *Wiley Interdiscip. Rev.: Comput. Mol. Sci.*, 2014, **4**, 91.
- 93 TURBOMOLE V7.4 2019, a development of University of Karlsruhe and Forschungszentrum Karlsruhe GmbH, 1989–2007, TURBOMOLE GmbH, since 2007; available from <http://www.turbomole.com>.
- 94 C. Angeli, R. Cimiraglia, S. Evangelisti, T. Leininger and J.-P. Malrieu, *J. Chem. Phys.*, 2001, **114**, 10252.
- 95 C. Angeli and R. Cimiraglia, *Theor. Chem. Acc.*, 2002, **107**, 313.
- 96 K. Pierloot, *Int. J. Quantum Chem.*, 2011, **111**, 3291.
- 97 T. Penfold, E. Gindensperger, C. Daniel and C. M. Marian, *Chem. Rev.*, 2018, **118**, 6975.







**Figure S2.** TD-DFT-UKS charge transfer (CT) numbers of  $VCl_3(\text{ddpd})$  defined from 0 to 1 of the lowest-lying 50 triplet states.

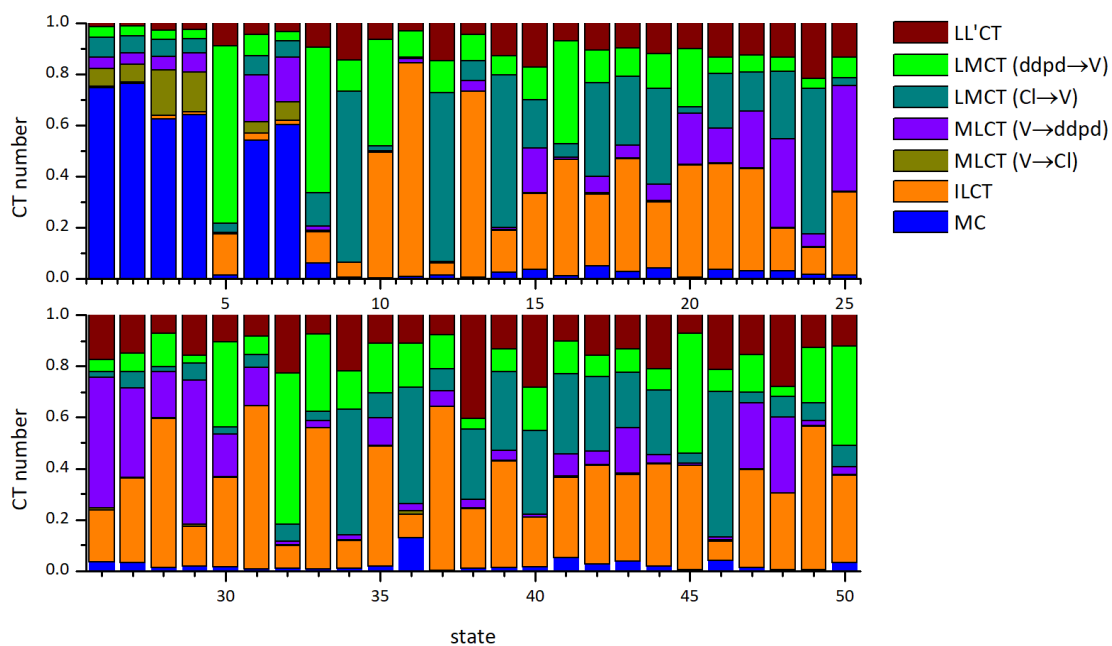


**Table S1** Bond distances / Å and angles / ° of *mer*- $VCl_3(\text{dddpd})^{S1}$  (XRD and DFT-UKS).

	V-N1/ V-N2/ V-N3	N1-V-N2/ N1-V-N3 N2-V-N3	V-Cl1 V-Cl2 V-Cl3	Cl1-V-Cl2 Cl1-V-Cl3 Cl2-V-Cl3	Shape parameter $S(\text{OC-6})$
XRD	2.123(3) 2.119(3) 2.109(3)	84.68(12) 170.41(12) 85.85(12)	2.354(12) 2.325(13) 2.335(12)	90.42(4) 178.75(5) 90.72(4)	0.48
DFT-UKS	2.123 2.114 2.123	84.25 168.53 84.28	2.387 2.375 2.386	90.19 179.66 90.08	0.64

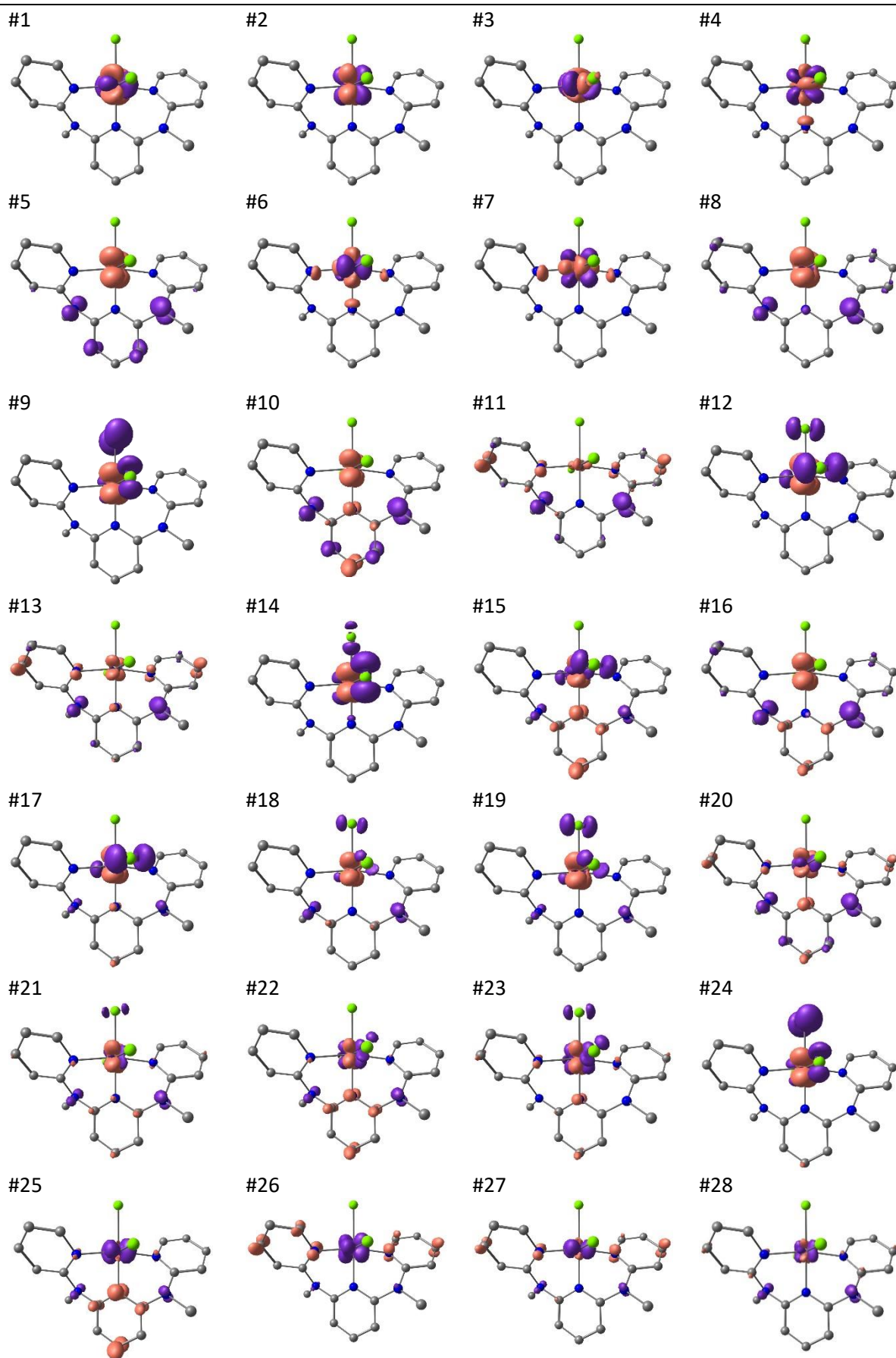
**Table S2.** Cartesian Coordinates of the DFT-UKS calculated ground state geometry of *mer*-VCl<sub>3</sub>(ddpd).

atomic number	x	y	z
23	0.002946000	-0.007579000	0.104116000
7	0.004059000	-0.004113000	-2.010521000
7	-0.150783000	-2.114360000	-0.112225000
7	0.165427000	2.099835000	-0.104000000
6	-0.723824000	-0.918934000	-2.699791000
6	-0.737837000	-0.939401000	-4.091568000
6	0.000253000	-0.000559000	-4.786831000
6	0.740112000	0.936459000	-4.090917000
6	0.729983000	0.912705000	-2.699013000
1	-1.292363000	-1.701307000	-4.613717000
1	1.294128000	1.698627000	-4.613101000
6	0.410027000	-2.897831000	0.830558000
6	0.053717000	-4.212499000	1.014748000
6	-0.929873000	-4.745971000	0.182300000
6	-1.466786000	-3.972585000	-0.825731000
6	-1.029273000	-2.646721000	-0.976471000
1	-1.258101000	-5.768867000	0.305373000
1	1.139025000	-2.414357000	1.459686000
1	0.518604000	-4.795997000	1.794537000
1	-2.188579000	-4.392248000	-1.506323000
6	1.040352000	2.634690000	-0.970096000
6	1.477613000	3.960305000	-0.817174000
6	0.945395000	4.730647000	0.195745000
6	-0.033838000	4.194365000	1.031140000
6	-0.390784000	2.880151000	0.844004000
1	1.274108000	5.753222000	0.320160000
1	2.196282000	4.382386000	-1.499379000
1	-0.494924000	4.775114000	1.815197000
1	-1.116559000	2.394818000	1.475435000
7	-1.495888000	-1.869126000	-2.024261000
6	-2.778623000	-2.243367000	-2.633240000
1	-2.695669000	-3.084717000	-3.323231000
1	-3.470609000	-2.499142000	-1.835582000
1	-3.169494000	-1.382583000	-3.165664000
7	1.503910000	1.860572000	-2.022411000
6	2.781091000	2.242294000	-2.638419000
1	2.689775000	3.085259000	-3.325620000
1	3.477050000	2.499441000	-1.844655000
1	3.172865000	1.384873000	-3.175646000
1	-0.000860000	0.000776000	-5.868145000
17	-0.007942000	-0.016751000	2.479265000
17	-2.374490000	0.195152000	0.090701000
17	2.382361000	-0.201957000	0.106198000

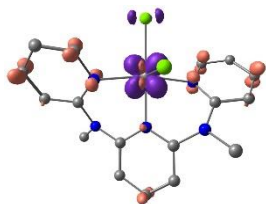
**Table S3.** TD-DFT calculated spin-allowed transitions (UKS, unshifted). The assignment of the UKS states corresponds to the largest contribution to the charge transfer number (Fig. S2).

state	$\tilde{\nu} / \text{cm}^{-1}$	$\lambda / \text{nm}$	$E / \text{eV}$	$f_{\text{osc}}$	assignment
1	2431	4114	0.301	7.24E-05	<sup>3</sup> MC
2	3593	2783	0.445	4.10E-08	<sup>3</sup> MC
3	17221	581	2.135	1.11E-05	<sup>3</sup> MC
4	17358	576	2.152	6.54E-05	<sup>3</sup> MC
5	18198	550	2.256	1.14E-02	<sup>3</sup> LMCT(ddpd→V)
6	21692	461	2.689	1.35E-05	<sup>3</sup> MC
7	22346	448	2.771	1.15E-04	<sup>3</sup> MC
8	22681	441	2.812	2.01E-03	<sup>3</sup> LMCT(ddpd→V)
9	24096	415	2.988	1.18E-03	<sup>3</sup> LMCT(Cl→V)
10	24734	404	3.067	2.80E-02	<sup>3</sup> LMCT(ddpd→V)
11	26178	382	3.246	2.11E-03	<sup>3</sup> ILCT(ddpd)
12	26983	371	3.346	1.16E-03	<sup>3</sup> LMCT(Cl→V)
13	27255	367	3.379	1.89E-03	<sup>3</sup> ILCT(ddpd)
14	27465	364	3.405	1.03E-02	<sup>3</sup> LMCT(Cl→V)
15	28474	351	3.530	1.54E-02	<sup>3</sup> LMCT(Cl→V), <sup>3</sup> ILCT (ddpd)
16	28777	348	3.568	9.71E-04	<sup>3</sup> LMCT(ddpd→V), <sup>3</sup> ILCT (ddpd)
17	29334	341	3.637	1.42E-02	<sup>3</sup> LMCT(ddpd,Cl→V)
18	29878	335	3.704	7.47E-03	<sup>3</sup> LMCT(ddpd,Cl→V), <sup>3</sup> ILCT(ddpd)
19	29940	334	3.712	3.17E-02	<sup>3</sup> LMCT(ddpd,Cl→V)
20	30211	331	3.746	5.13E-03	<sup>3</sup> LMCT(ddpd→V), <sup>3</sup> ILCT(ddpd)
21	30469	328	3.778	1.46E-02	<sup>3</sup> ILCT(ddpd)
22	30562	327	3.789	6.74E-03	<sup>3</sup> ILCT(ddpd)
23	30931	323	3.835	4.33E-04	<sup>3</sup> LMCT(Cl→V)
24	30979	323	3.841	6.18E-05	<sup>3</sup> LMCT(Cl→V)
25	31037	322	3.848	1.24E-02	<sup>3</sup> MLCT(V→ddpd)
26	31397	319	3.893	1.42E-02	<sup>3</sup> MLCT(V→ddpd)
27	31666	316	3.926	8.54E-03	<sup>3</sup> MLCT(V→ddpd)
28	31726	315	3.934	3.99E-02	<sup>3</sup> ILCT(ddpd)
29	32248	310	3.998	1.74E-04	<sup>3</sup> MLCT(V→ddpd)
30	32468	308	4.025	2.51E-02	<sup>3</sup> LMCT(ddpd→V)
31	32489	308	4.028	2.70E-03	<sup>3</sup> ILCT(ddpd)
32	32765	305	4.062	3.27E-05	<sup>3</sup> LMCT(ddpd→V)
33	32819	305	4.069	2.86E-03	<sup>3</sup> LMCT(ddpd→V), <sup>3</sup> ILCT(ddpd)
34	33478	299	4.151	6.89E-06	<sup>3</sup> LMCT(Cl→V)
35	33557	298	4.161	7.23E-02	<sup>3</sup> ILCT(ddpd)
36	33795	296	4.190	8.51E-04	<sup>3</sup> LMCT(Cl→V)
37	34118	293	4.230	7.47E-03	<sup>3</sup> ILCT(ddpd)
38	34423	291	4.268	9.86E-03	<sup>3</sup> LLCT(Cl→ddpd)
39	34530	290	4.281	1.32E-02	<sup>3</sup> LMCT(ddpd,Cl→V), <sup>3</sup> ILCT(ddpd)
40	34674	288	4.299	2.53E-02	<sup>3</sup> LMCT(ddpd,Cl→V)
41	34953	286	4.334	1.29E-03	<sup>3</sup> LMCT(ddpd,Cl→V)
42	35026	286	4.343	4.10E-03	<sup>3</sup> LMCT(ddpd,Cl→V), <sup>3</sup> ILCT(ddpd)
43	35063	285	4.347	7.91E-04	<sup>3</sup> LMCT(ddpd,Cl→V), <sup>3</sup> ILCT(ddpd)
44	35162	284	4.360	1.23E-02	<sup>3</sup> LMCT(ddpd,Cl→V), <sup>3</sup> ILCT(ddpd)
45	35386	283	4.387	2.20E-03	<sup>3</sup> LMCT(ddpd→V)
46	35549	281	4.408	1.64E-03	<sup>3</sup> LMCT(Cl→V)
47	35791	279	4.438	5.90E-02	<sup>3</sup> ILCT(ddpd)
48	36062	277	4.471	9.19E-04	<sup>3</sup> MLCT(V→ddpd)
49	36377	275	4.510	1.06E-05	<sup>3</sup> ILCT(ddpd)
50	36670	273	4.547	4.40E-03	<sup>3</sup> LMCT(ddpd→V)

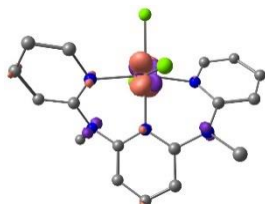
**Table S4.** Difference electron densities of the 50 lowest-lying TD-DFT-UKS calculated states (isosurface value at 0.007 a.u.; purple = electron depletion; orange = electron gain; hydrogen atoms omitted).



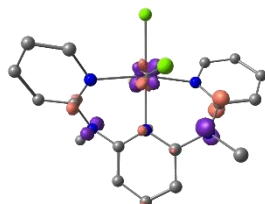
#29



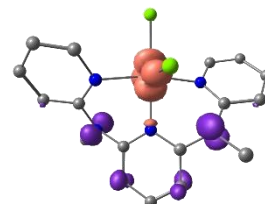
#30



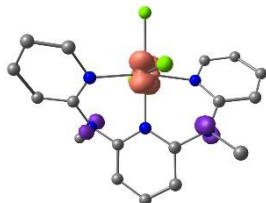
#31



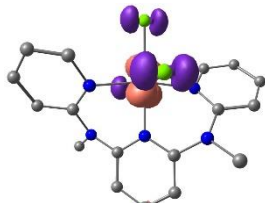
#32



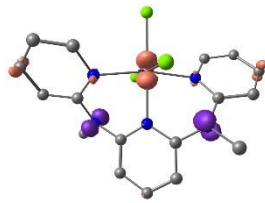
#33



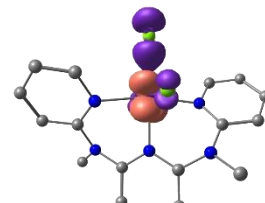
#34



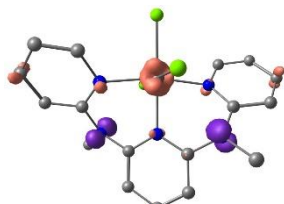
#35



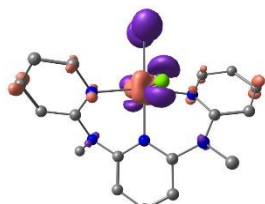
#36



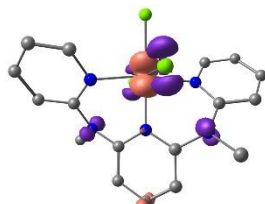
#37



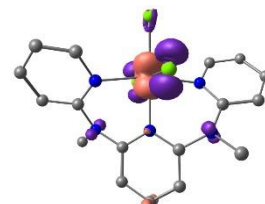
#38



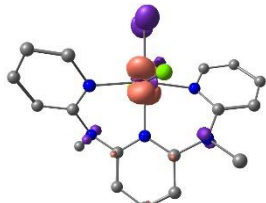
#39



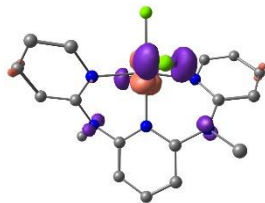
#40



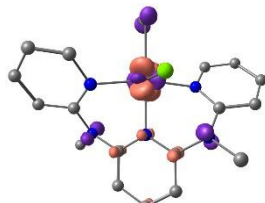
#41



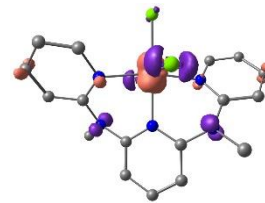
#42



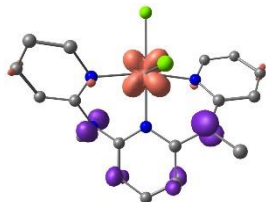
#43



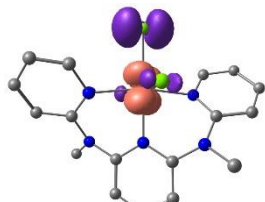
#44



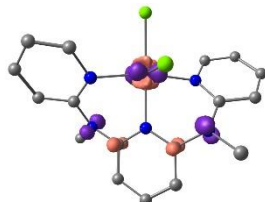
#45



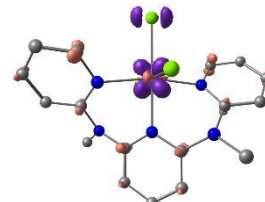
#46



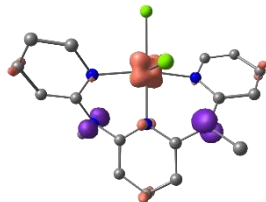
#47



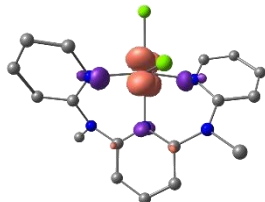
#48



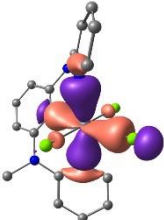
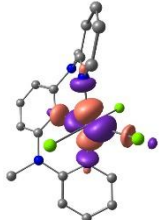
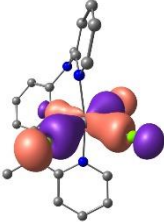
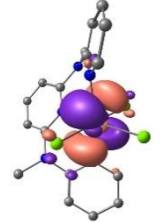
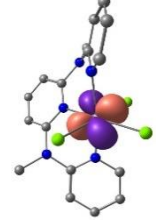
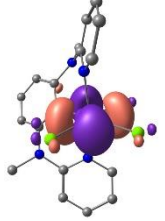
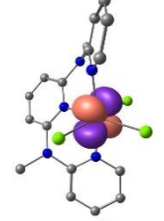
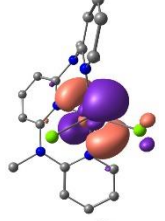
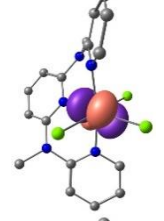
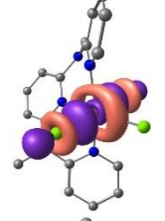
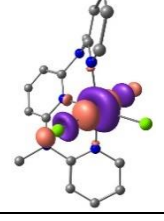
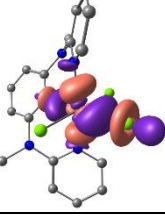
#49



#50



**Table S5.** Orbital energies/Hartree of the canonical orbitals used in the active space of the CASSCF(6,12)-FICNEVPT2 calculation, depicted at a contour value of 0.05 a.u. (hydrogen atoms omitted for clarity).

MO #	$E/H$	orbital	MO #	$E/H$	orbital
111	-0.53269		117	+0.15634	
112	-0.48346		118	+0.87582	
113	+0.02254		119	+0.90233	
114	+0.02553		120	+0.91763	
115	+0.02877		121	+1.13585	
116	+0.10787		122	+1.27999	

**Figure S3.** Energy diagram of the electronic states of  $\text{VCl}_3(\text{ddpd})$  constructed from CASSCF(6,12)-FIC-NEVPT2 energies with spin densities in orange (0.007 a.u. isosurface value, hydrogen atoms omitted for clarity, triplet states in blue, singlet states in red; a coordinate system referring to the displayed structures and d orbital labels is shown in the grey box).

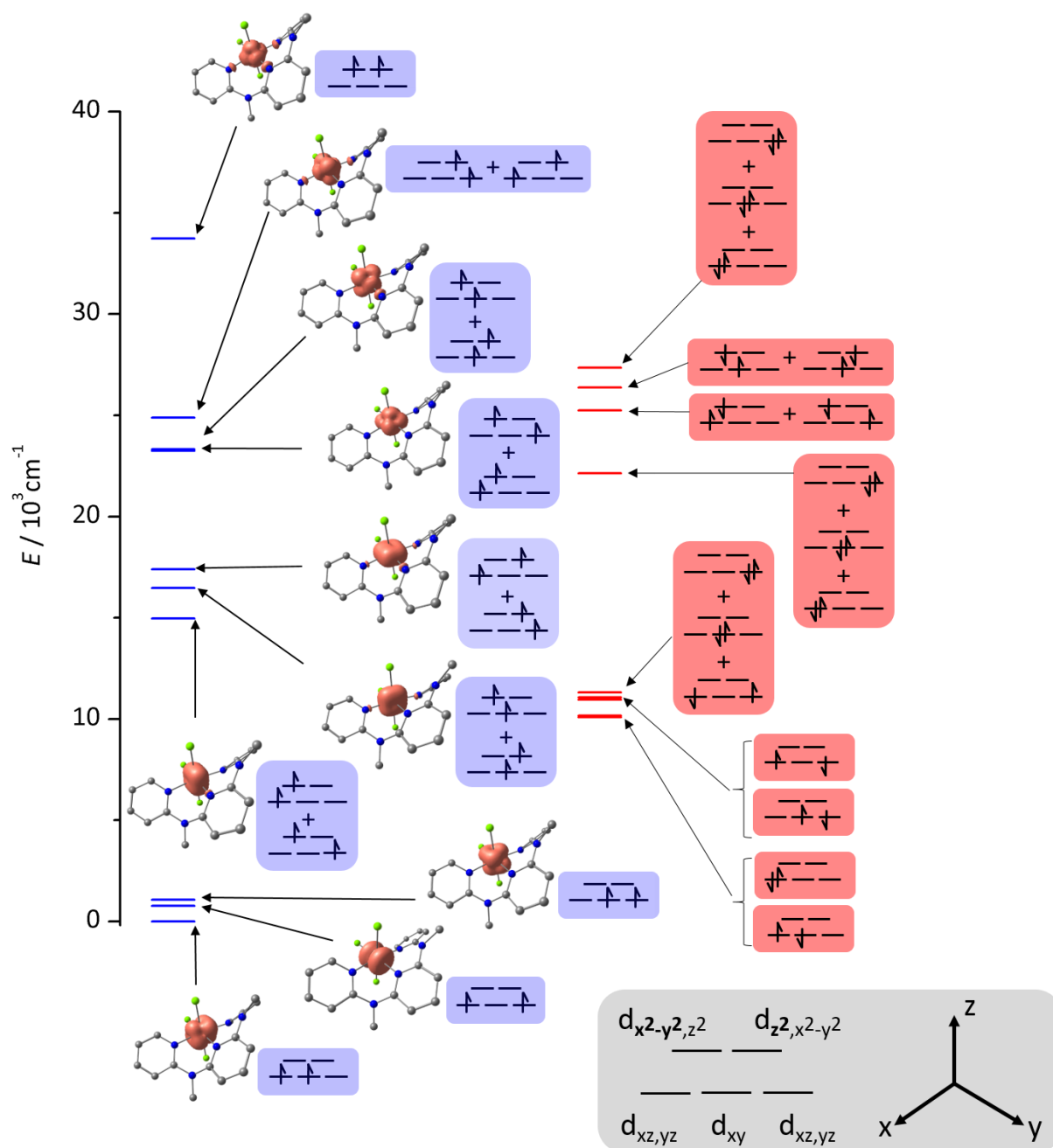




**Table S6.** Energies of triplet and singlet states/cm<sup>-1</sup> from the CASSCF(6,12) calculations without and with NEVPT2 (assignments according to the dominant contribution).

state	<i>E</i> / cm <sup>-1</sup> without NEVPT2	<i>E</i> / cm <sup>-1</sup> with NEVPT2	$\Delta E$ / cm <sup>-1</sup>
GS ( <sup>3</sup> T <sub>1</sub> )	574.7	755.4	180.7
GS ( <sup>3</sup> T <sub>1</sub> )	874.1	1076.3	202.2
<sup>1</sup> E	12658.8	10085.9	-2572.9
<sup>1</sup> T <sub>2</sub>	12804.9	10160.5	-2644.4
<sup>1</sup> E/ <sup>1</sup> T <sub>2</sub>	13456.4	10949.1	-2507.3
<sup>1</sup> E/ <sup>1</sup> T <sub>2</sub>	13580.0	11068.3	-2511.7
<sup>1</sup> E/ <sup>1</sup> T <sub>2</sub>	13837.7	11309.1	-2528.6
<sup>3</sup> T <sub>2</sub>	13857.6	14967.5	1109.9
<sup>3</sup> T <sub>2</sub>	15252.7	16463.5	1210.8
<sup>3</sup> T <sub>2</sub>	16114.6	17393.1	1278.5
<sup>1</sup> A <sub>1</sub>	26337.3	22141.7	-4195.6
<sup>3</sup> T <sub>1</sub> (P)	25522.4	23253.9	-2268.5
<sup>3</sup> T <sub>1</sub> (P)	25841.4	23318.7	-2522.7
<sup>3</sup> T <sub>1</sub> (P)	27384.5	24890.9	-2493.6
<sup>1</sup> T <sub>2</sub> (G)	27538.6	25238.5	-2300.1
<sup>1</sup> T <sub>2</sub> (G)	28592.3	26376.7	-2215.6
<sup>1</sup> T <sub>2</sub> (G)	29508.1	27339.6	-2168.5

**Figure S4.** Displacement vectors of Cl–V–Cl deformation vibrations calculated by DFT at 125, 136, 159 cm<sup>-1</sup> (unscaled).

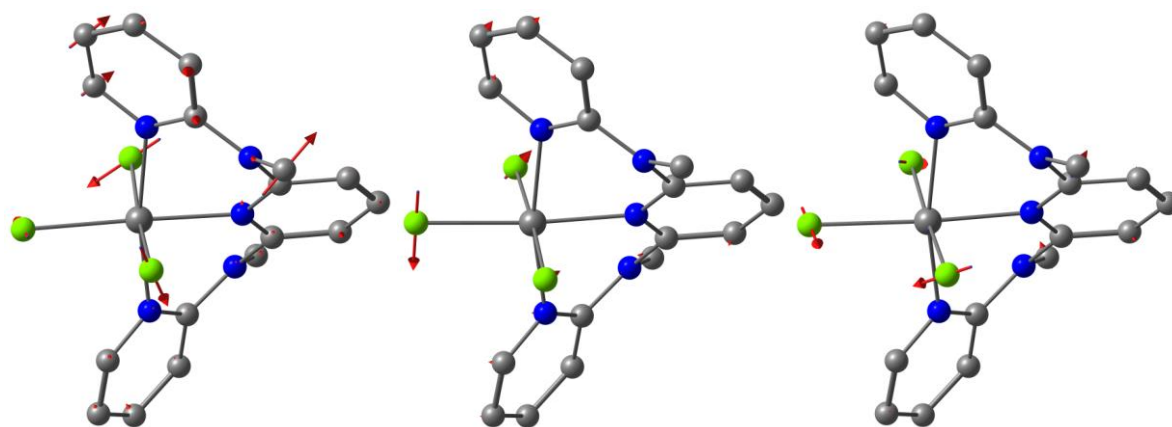
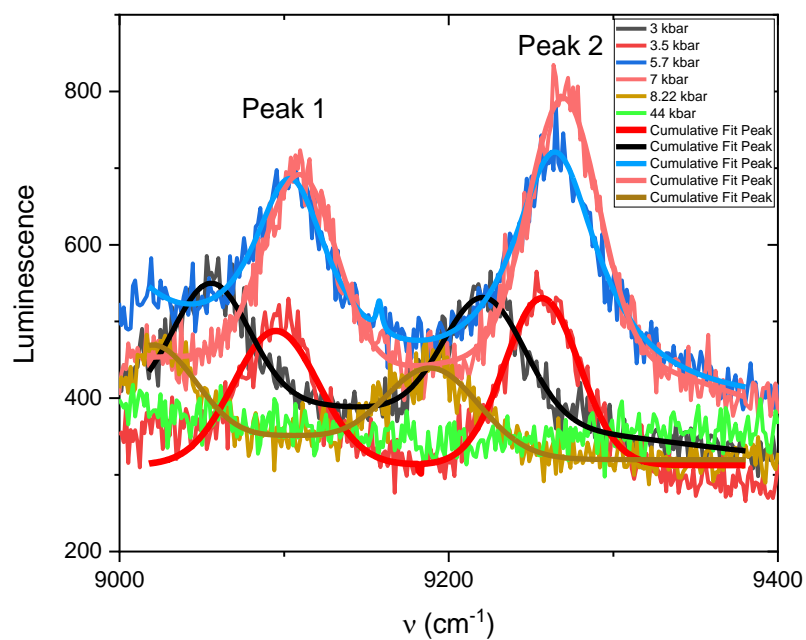


**Figure S5.** (a) NIR emission bands (peak 1 and 2) of solid  $\text{VCl}_3(\text{D}_0\text{-ddpd})$  under hydrostatic pressure and (b) corresponding peak shift (peak 1 and 2) versus pressure plots.

(a)



(b)

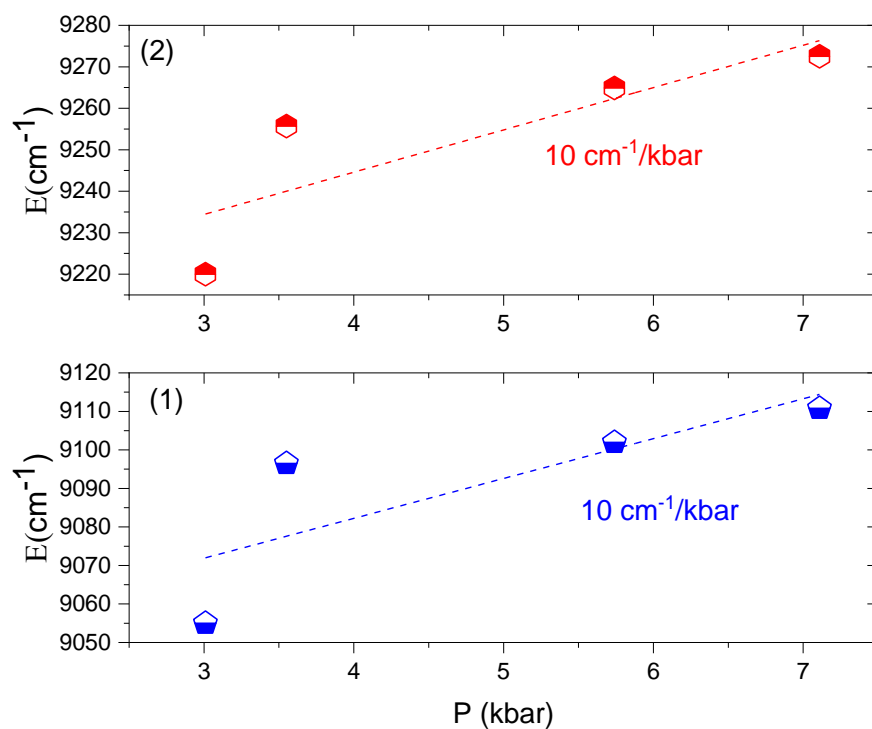
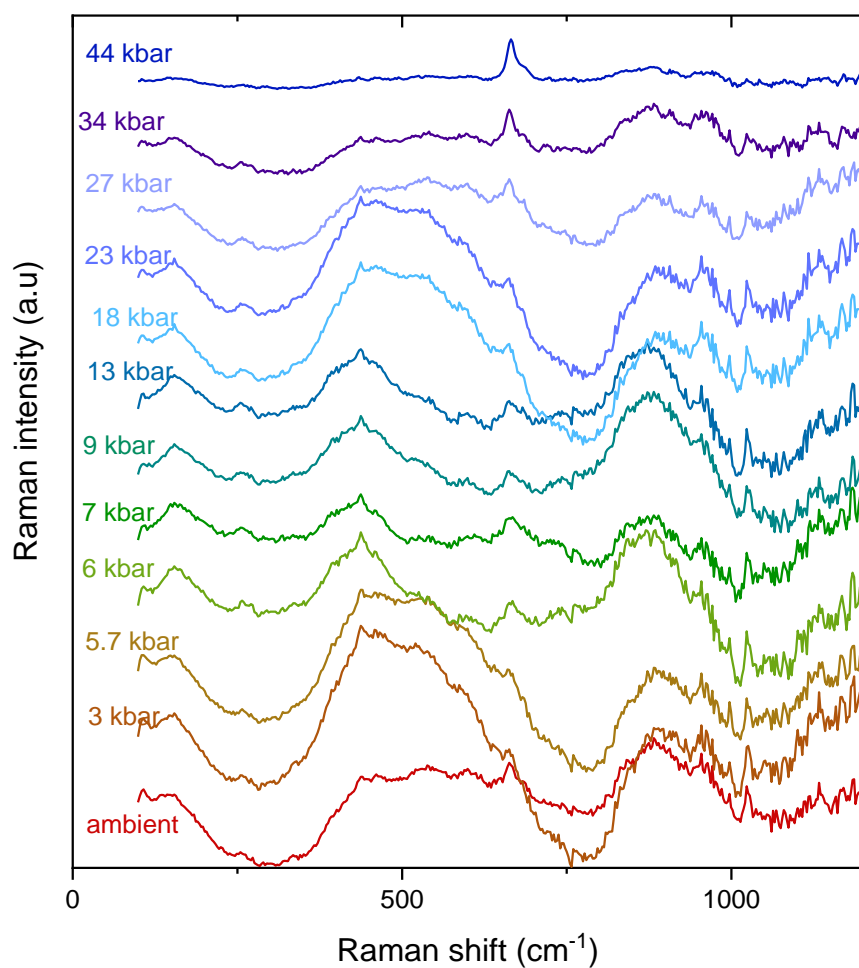


**Figure S6.** Raman spectra of solid  $\text{VCl}_3(\text{D}_0\text{-ddpd})$  under hydrostatic pressure ( $\lambda_{\text{exc}} = 785.0 \text{ nm}$ ).



At 44 kbar, the highest pressure achieved for this study, only the vibrational peaks at approximately  $665 \text{ cm}^{-1}$  are observed, documenting that the electronic Raman signals, dominant at lower pressure, are broadened out to the extreme so that they are no longer clearly identifiable.

**Figure S7.** Luminescence decay (black scatter) for  $\text{VCl}_3(\text{ddpd}-[\text{D}_0])$  in the solid state under a dry and deoxygenated argon atmosphere ( $\lambda_{\text{exc}} = 350 \text{ nm}$ ,  $\lambda_{\text{em}} = 1106 \text{ nm}$ , excitation path: band pass filter UG11, emission path: long pass filter RG850) with monoexponential fit function (red) and instrument response function (grey).

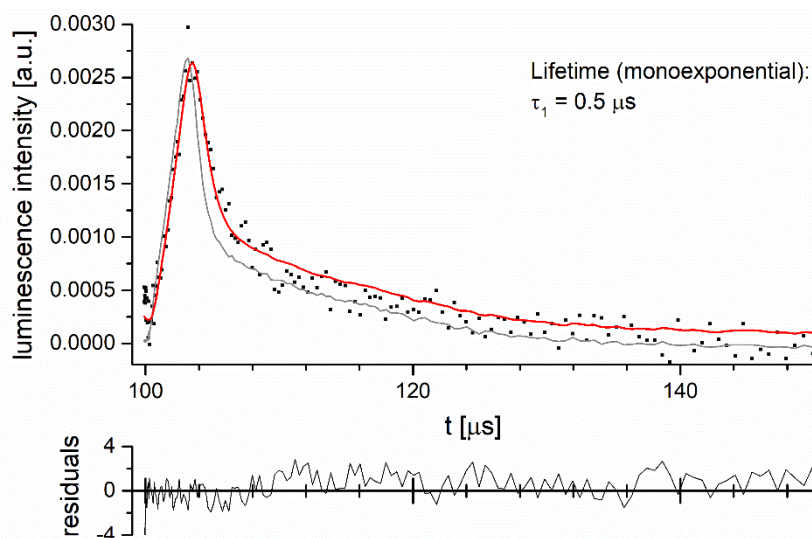


**Figure S8.** Luminescence decay (black scatter) for  $\text{VCl}_3(\text{ddpd}-[\text{D}_{17}])$  in the solid state under a dry and deoxygenated argon atmosphere ( $\lambda_{\text{exc}} = 350 \text{ nm}$ ,  $\lambda_{\text{em}} = 1106 \text{ nm}$ , excitation path: band pass filter UG11, emission path: long pass filter RG850) with monoexponential fit function (red) and instrument response function (grey).

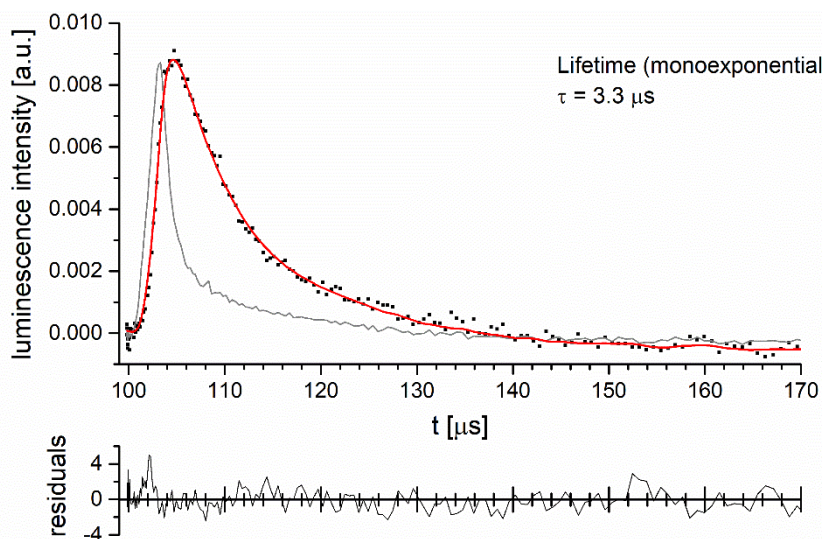
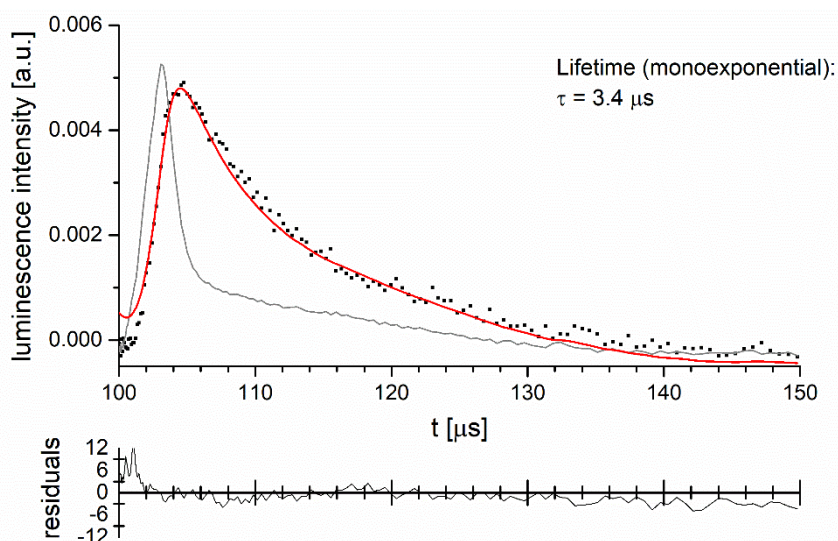


**Figure S9.** Luminescence decay (black scatter) for  $\text{VCl}_3(\text{ddpd}-[\text{D}_{17}])$  in the solid state under a dry and deoxygenated argon atmosphere ( $\lambda_{\text{exc}} = 350 \text{ nm}$ ,  $\lambda_{\text{em}} = 1222 \text{ nm}$ , excitation path: band pass filter UG11, emission path: long pass filter RG850) with monoexponential fit function (red) and instrument response function (grey).



### NIR Absorption Spectroscopy / Vibrational Overtone Analysis

Since the isotopologic vanadium(III) complexes were not available in sufficient quantities, the analysis of the position and intensity of the C–H and C–D vibrational overtones for the vanadium complexes was carried out on simpler pyridine-containing model compounds. The vibrational signatures of the protiated and deuterated methyl protons in ddpd were not investigated due to insufficient quantities and because deuteration did not show an effect on the non-radiative deactivation of the metal centered emission of  $[\text{Cr}(\text{ddpd})_2]^{3+}$ .<sup>S3</sup> Previously, the vibrational overtone data of the isotopologues of 6,6'-dimethyl-2,2'-bipyridine ( $\text{Me}_2\text{-bpy}$  and  $[\text{D}_{12}]\text{-Me}_2\text{-bpy}$ , Figure S11)<sup>S2</sup> proved to be a successful model system for the analysis of the vibrational overtone structure of ddpd.<sup>S3</sup> For the present analysis, we used the previously obtained aromatic C–(H/D) overtone bands (Gaussians)<sup>S2</sup> of  $\text{Me}_2\text{-bpy}$  and  $[\text{D}_{12}]\text{-Me}_2\text{-bpy}$  for the calculations of the spectral overlap integral (SOI) between these oscillators and the vanadium emission.

**Figure S10.** Comparison of ddpd with the model compounds  $\text{Me}_2\text{-bpy}$  and  $[\text{D}_{12}]\text{-Me}_2\text{-bpy}$  used for the analysis of the vibrational C–H and C–D overtones.

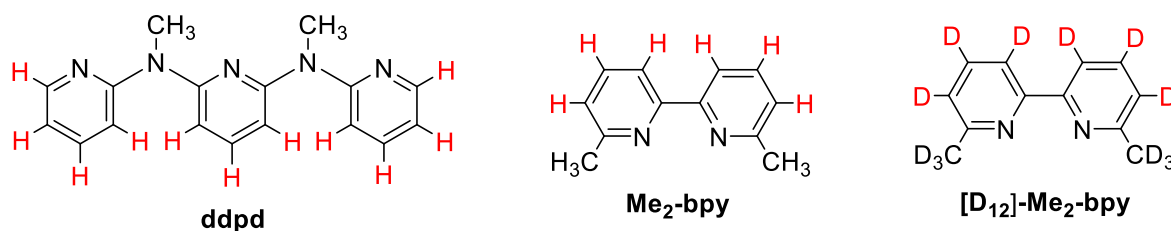




**Figure S11.** Reconstructed vibrational overtone absorption bands ( $\nu = 2, 3,$  and  $4$ ) for the aromatic C–H oscillators of Me<sub>2</sub>-bpy (black) with single Gaussian fits (dashed red).<sup>S3</sup>

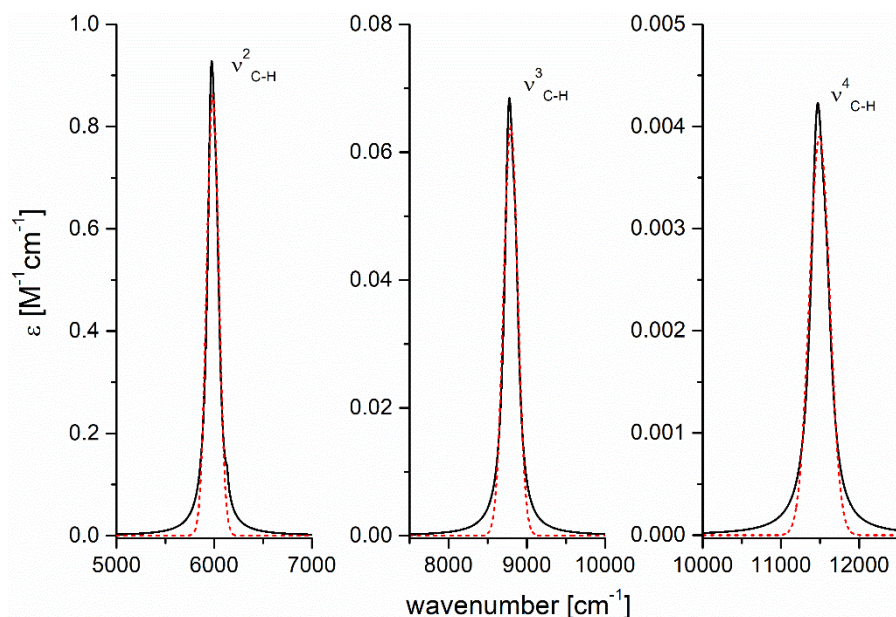
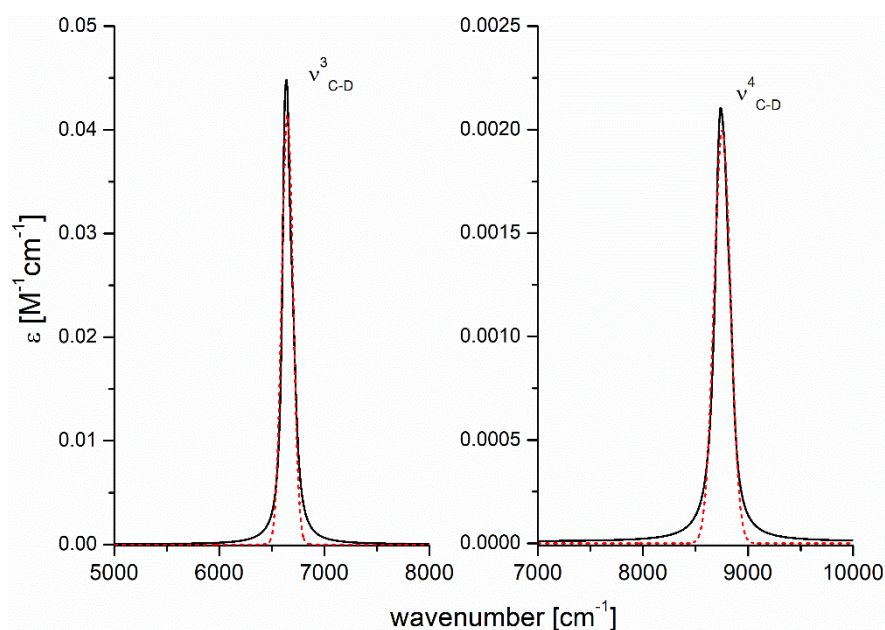


**Figure S12.** Reconstructed vibrational overtone absorption bands ( $\nu = 3$  and  $4$ ) for the aromatic CD oscillators of Me<sub>2</sub>-bpy (black) with single Gaussian fits (dashed red).<sup>S3</sup>



The integrand functions for the SOIs between the vanadium emission and the relevant C–(H/D) overtones were constructed according to the mathematical definition of the SOIs:

$$\text{SOI} = \int I_{\text{norm}}(\tilde{\nu}) \cdot \varepsilon_{\text{vib}}(\tilde{\nu}) \cdot \tilde{\nu}^{-4} d\tilde{\nu}$$

with  $I_{\text{norm}}$  being the vanadium emission spectrum (normalized to unit area) and  $\varepsilon$  the molar vibrational extinction coefficient (extracted and extrapolated absorption spectra of the relevant overtones), both expressed in the wavenumber scale  $\tilde{\nu}$ . The integrand functions were generated with a set of data points with a step size of  $1 \text{ cm}^{-1}$ . Numerical integration gave the corresponding values for SOI.

**Figure S13.** Integrand function of the spectral overlap integral (SOI) for the vanadium emission band in  $\text{VCl}_3(\text{ddpd})$  and the second aromatic C–H ( $\nu = 3$ ) oscillators in  $\text{Me}_2\text{-bpy}$ .

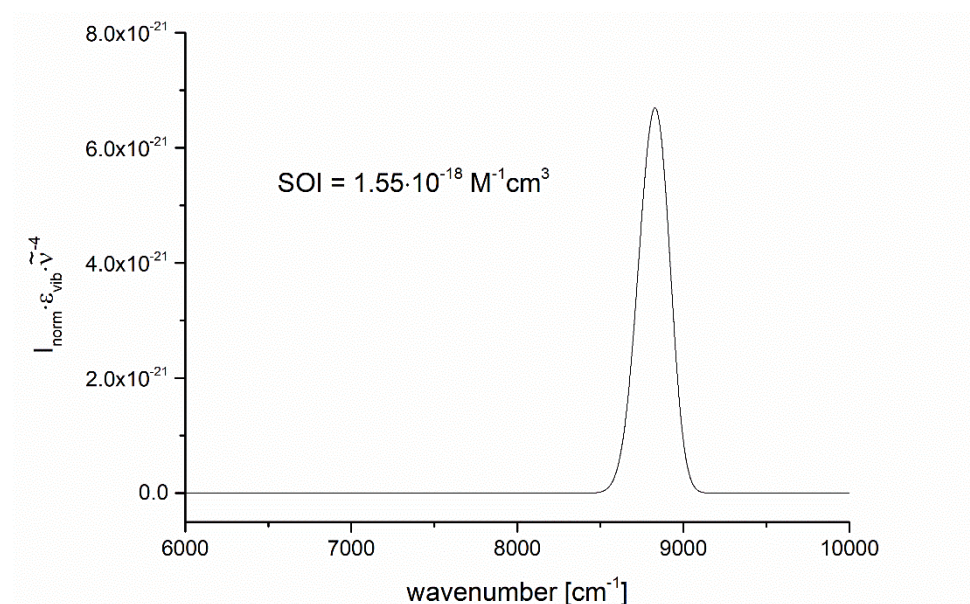
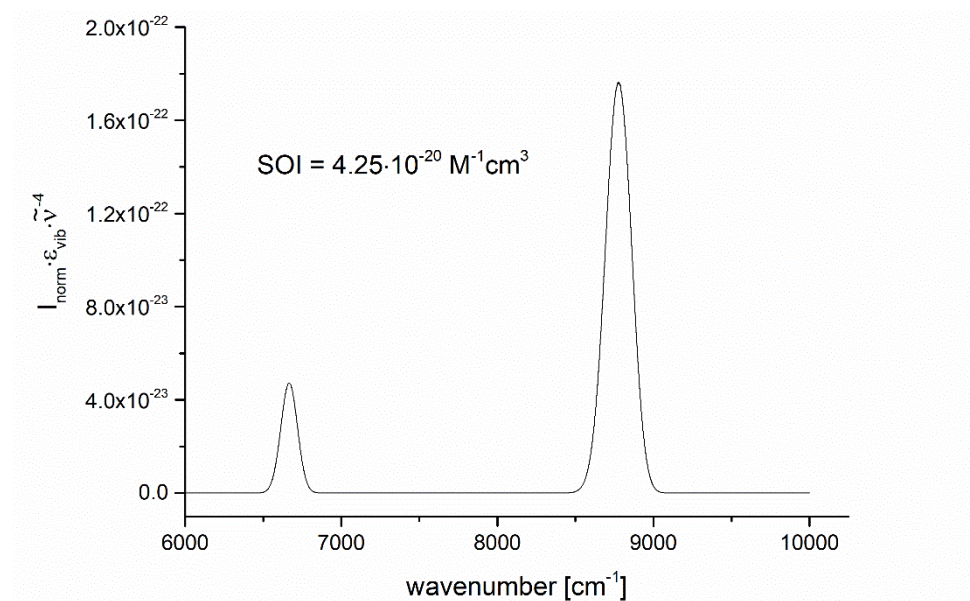


**Figure S14.** Integrand function of the spectral overlap integral (SOI) for the vanadium emission band in  $\text{VCl}_3(\text{ddd})$  and the second ( $\nu = 3$ ) and third ( $\nu = 4$ ) aromatic C–D oscillators in  $[\text{D}_{12}]\text{-Me}_2\text{-bpy}$ .



Based on the obtained SOIs, the ratio of the non-radiative deactivation rates of vanadium excited states from  $\text{VCl}_3(\text{ddpd}-[D_0])$  and  $\text{VCl}_3(\text{ddpd}-[D_{17}])$  is estimated as:

$$\frac{k_{\text{nr}}(\text{C-H})}{k_{\text{nr}}(\text{C-D})} = \frac{\text{SOI}(\text{C-H})}{\text{SOI}(\text{C-D})} = \frac{1.55 \cdot 10^{-18} \text{ M}^{-1}\text{cm}^3}{4.25 \cdot 10^{-20} \text{ M}^{-1}\text{cm}^3} = 3.63 \cdot 10^1$$

**Figure S15.** Normalized spectra for the vanadium  $^1\text{E}$  emission of  $\text{VCl}_3(\text{ddpd})$  (red) and the relevant vibrational aromatic C–H overtone absorption band (dashed black).

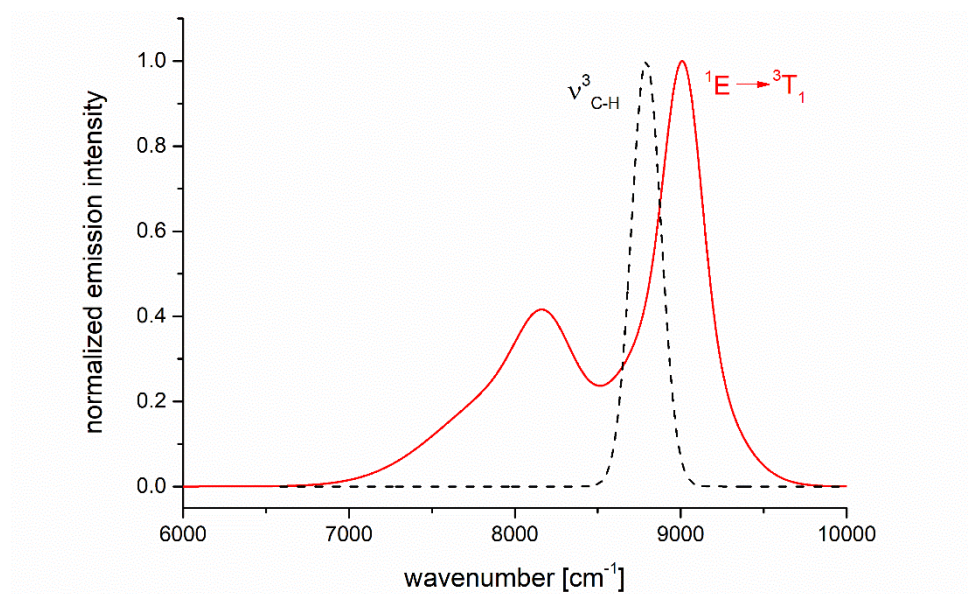


**Figure S16.** Spectra for the vanadium  $^1\text{E}$  emission of  $\text{VCl}_3(\text{ddpd})$  (red) and the relevant vibrational aromatic C–D overtone absorption bands (dashed black). The overtone intensities are shown with their actual intensity ratios.

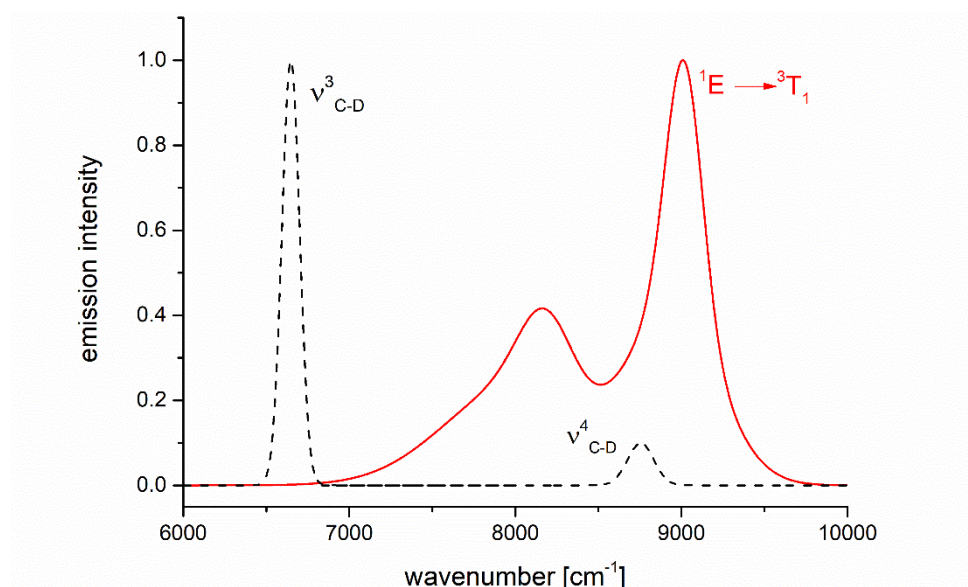




**Figure S17.** Luminescence spectra of  $\text{VCl}_3(\text{ddpd-}[\text{D}_0])$  as neat powder at 5–290 K ( $\lambda_{\text{exc}} = 350 \text{ nm}$ ).

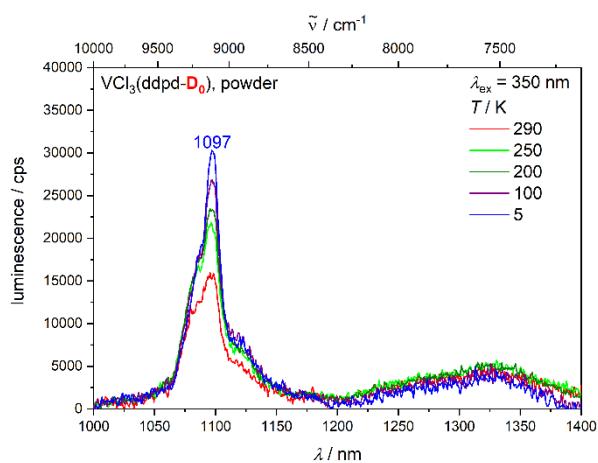


**Figure S18.** Luminescence spectra of  $\text{VCl}_3(\text{ddpd-}[\text{D}_0])$  as KBr pellet at 5–290 K ( $\lambda_{\text{exc}} = 350 \text{ nm}$ ).

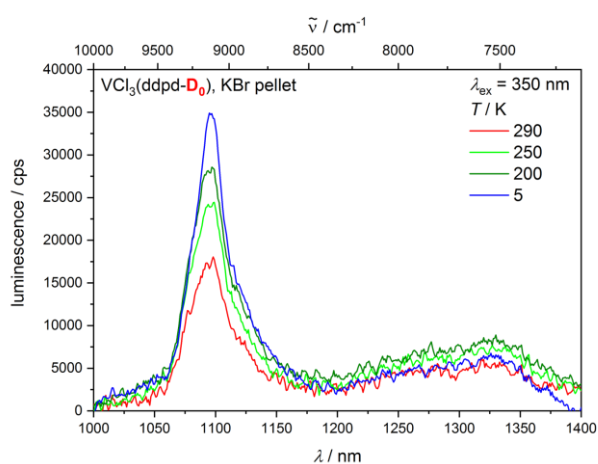


**Figure S19.** Plot of the integrated luminescence versus temperature for  $\text{VCl}_3(\text{ddpd-}[\text{D}_0])$  and  $\text{VCl}_3(\text{ddpd-}[\text{D}_{17}])$ .

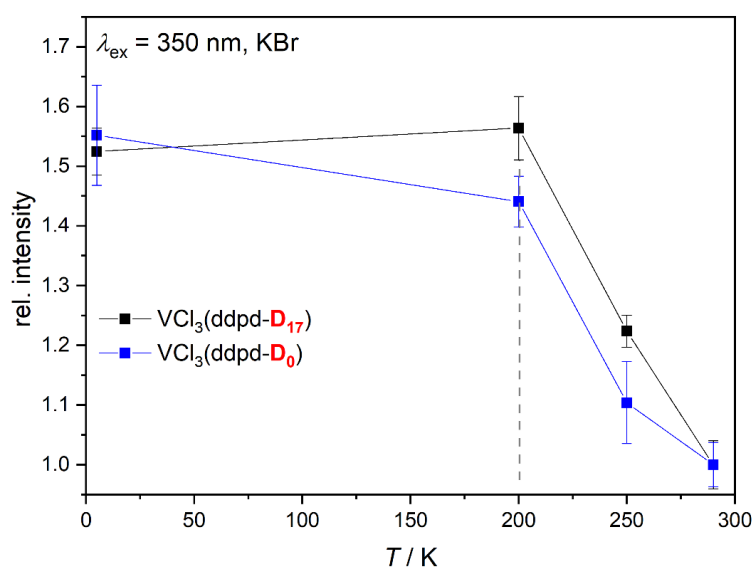


**Figure S20.** Ground state (black) and step-scan FTIR spectrum (red,  $\lambda_{\text{exc}} = 355 \text{ nm}$ ; 0–500 ns) of  $\text{VCl}_3(\text{ddpd}-[\text{D}_0])$  in a KBr pellet at 20 K.

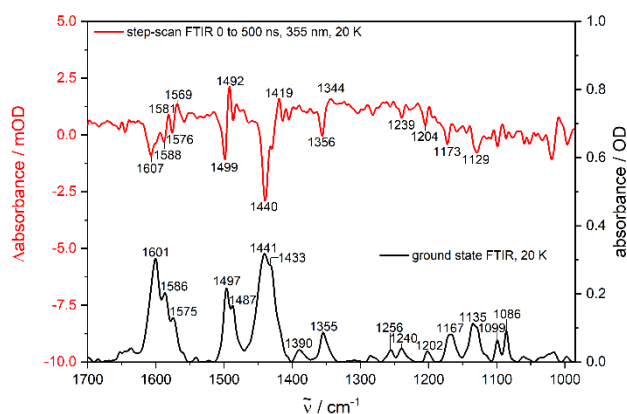


**Figure S21.** Experimental (black), DFT-calculated ground state (green) and step-scan FTIR spectrum (red,  $\lambda_{\text{exc}} = 355 \text{ nm}$ ; 0–500 ns) of  $\text{VCl}_3(\text{ddpd}-[\text{D}_{17}])$  in a KBr pellet at 290 K (red).

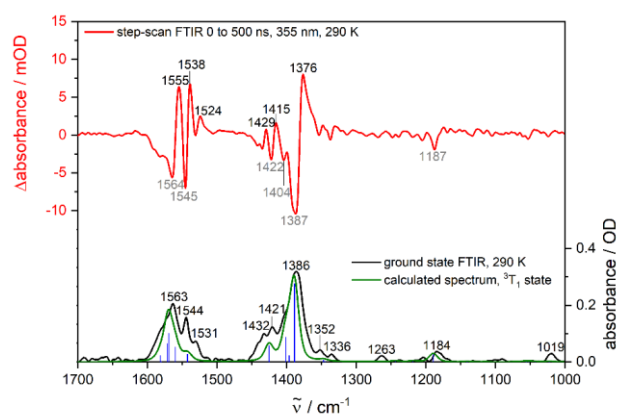


**Figure S22.** Excited state FTIR spectra of  $\text{VCl}_3(\text{ddpd}-[\text{D}_{17}])$  in a KBr pellet obtained from step-scan FTIR spectra ( $\lambda_{\text{exc}} = 355 \text{ nm}$ ; 0–500 ns) (and small contributions of the respective ground state spectrum of 3 %) at 20 K (blue) and 290 K (red).

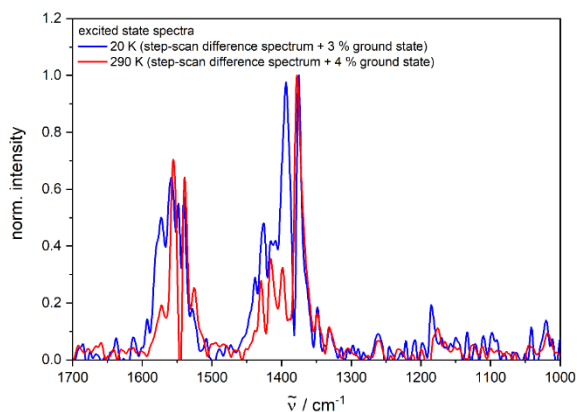


**Figure S23.** Ground state (black) and step-scan FTIR spectrum (red,  $\lambda_{\text{exc}} = 355 \text{ nm}$ ; 0–500 ns) of  $\text{VCl}_3(\text{ddpd-}[D_{17}])$  in a KBr pellet at 20 K.

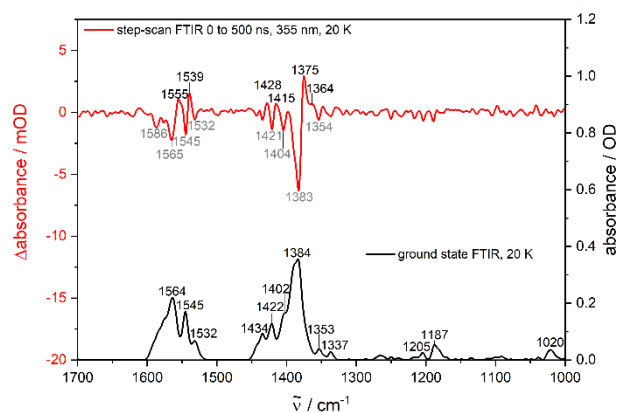


**Figure S24.** Global monoexponential fit and residuals performed for the most prominent positive and negative peaks in the step-scan spectrum of  $\text{VCl}_3(\text{ddpd-}[D_0])$  in a KBr pellet at 290 K.

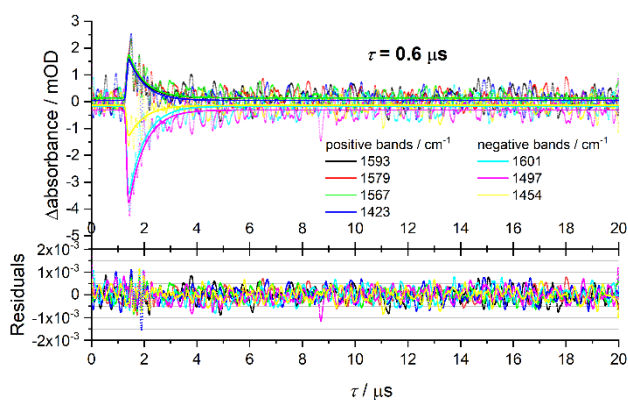


**Figure S25.** Global monoexponential fit and residuals performed for the most prominent positive and negative peaks in the step-scan spectrum of  $\text{VCl}_3(\text{ddpd-}[D_0])$  in a KBr pellet at 20 K.

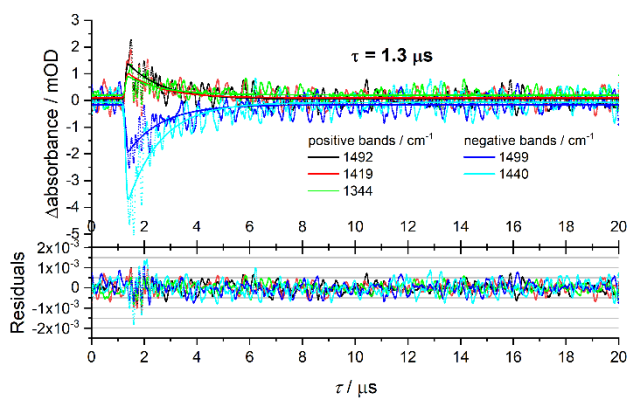


**Figure S26.** Global monoexponential fit and residuals performed for the most prominent positive and negative peaks in the step-scan spectrum of  $\text{VCl}_3(\text{ddpd}-[D_{17}])$  in a KBr pellet at 290 K.

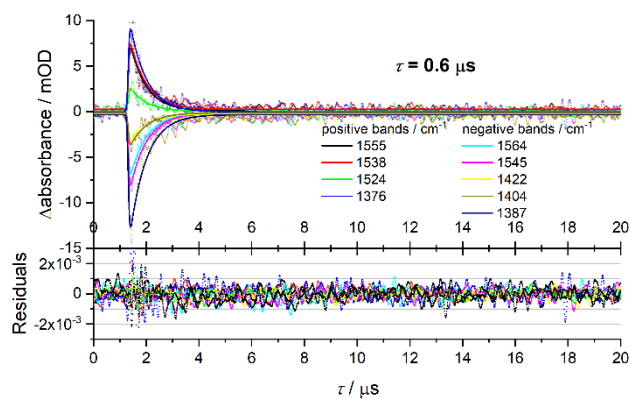


**Figure S27.** Global monoexponential fit and residuals performed for the most prominent positive and negative peaks in the step-scan spectrum of  $\text{VCl}_3(\text{ddpd}-[D_{17}])$  in a KBr pellet at 20 K.

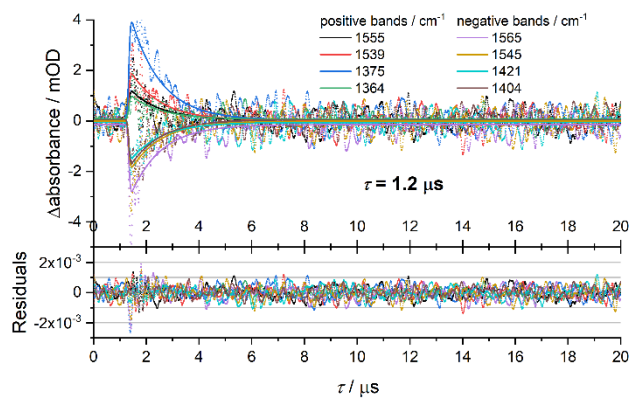


**Figure S28.** Changes of the UV/Vis absorption spectra of  $\text{VCl}_3(\text{ddpd}-[\text{D}_0])$  in  $\text{CH}_3\text{CN}$  under irradiation with a Xe lamp at  $350 \pm 5$  nm.

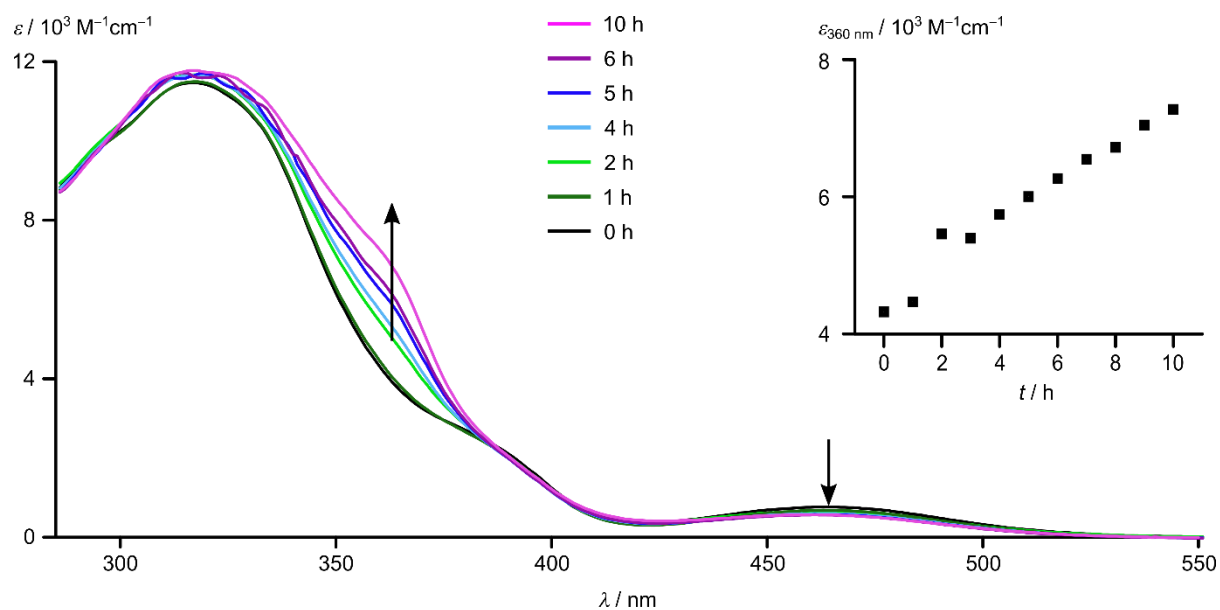


**Figure S29.** Changes of the emission spectra of  $\text{VCl}_3(\text{ddpd}-[\text{D}_0])$  in  $\text{CH}_3\text{CN}$  under irradiation with a Xe lamp at  $350 \pm 5$  nm.

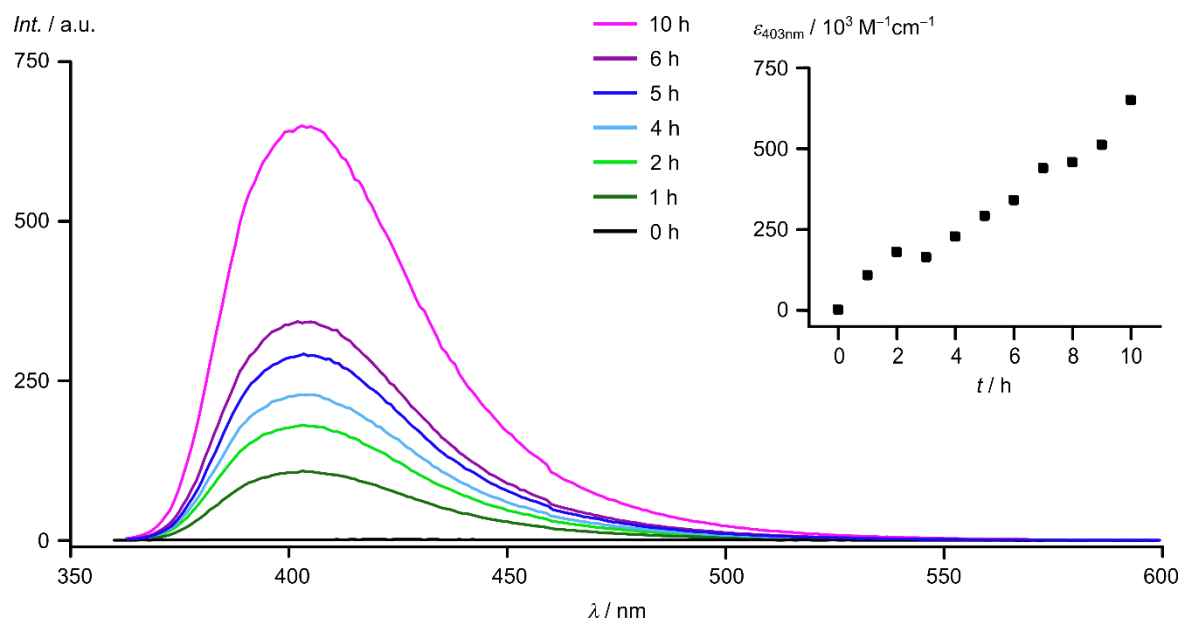


**Figure S30.** Changes of the UV/Vis absorption spectra of  $\text{VCl}_3(\text{ddpd}-[\text{D}_0])$  in  $\text{CH}_3\text{CN}$  under irradiation with a Xe lamp at  $400\pm 5$  nm.

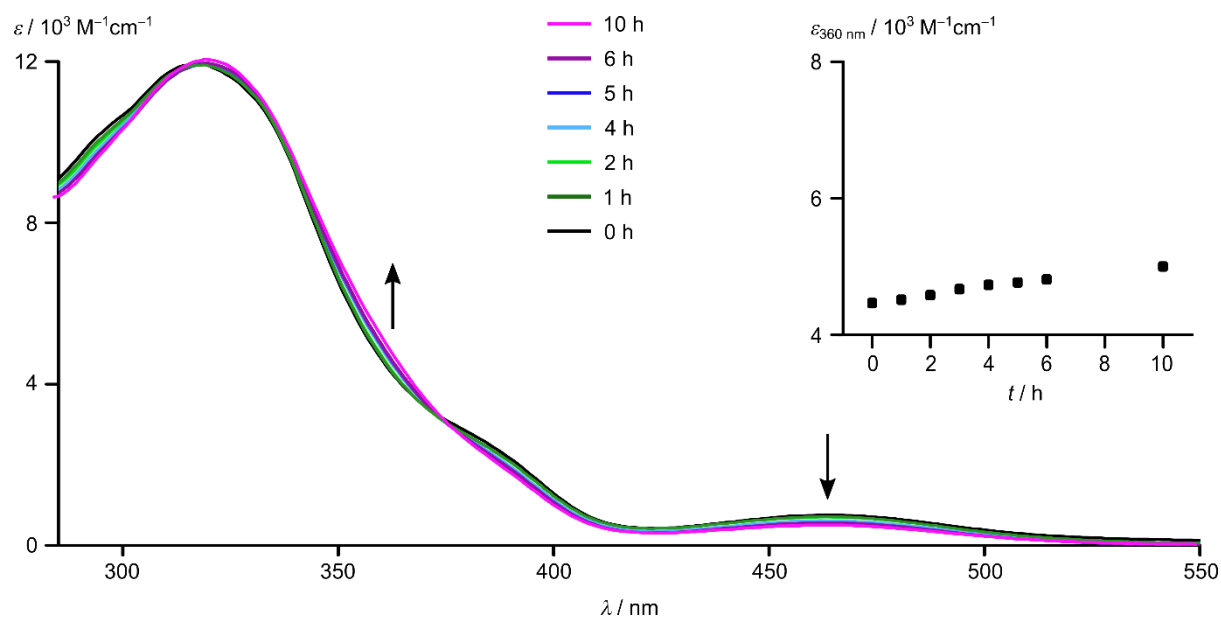


**Figure S31.** Changes of the emission spectra of  $\text{VCl}_3(\text{ddpd}-[\text{D}_0])$  in  $\text{CH}_3\text{CN}$  under irradiation with a Xe lamp at  $400\pm 5$  nm.

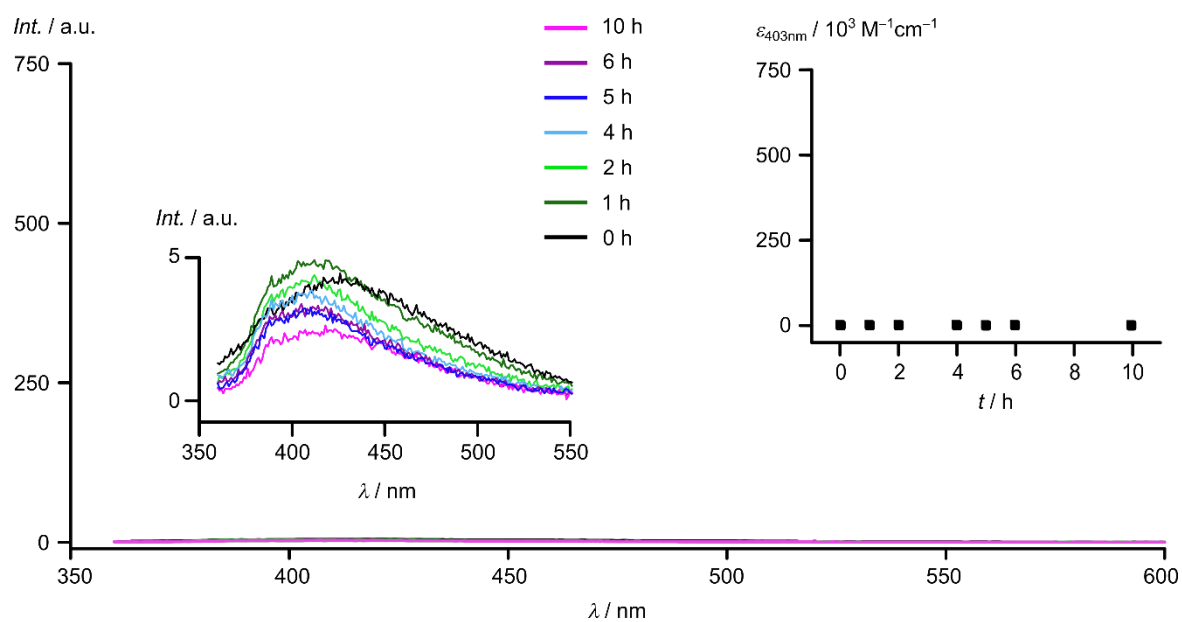


**Figure S32.** Spectral irradiance of the employed light source Asahi Spectra Max-303 Xenon Light Source (300 W).

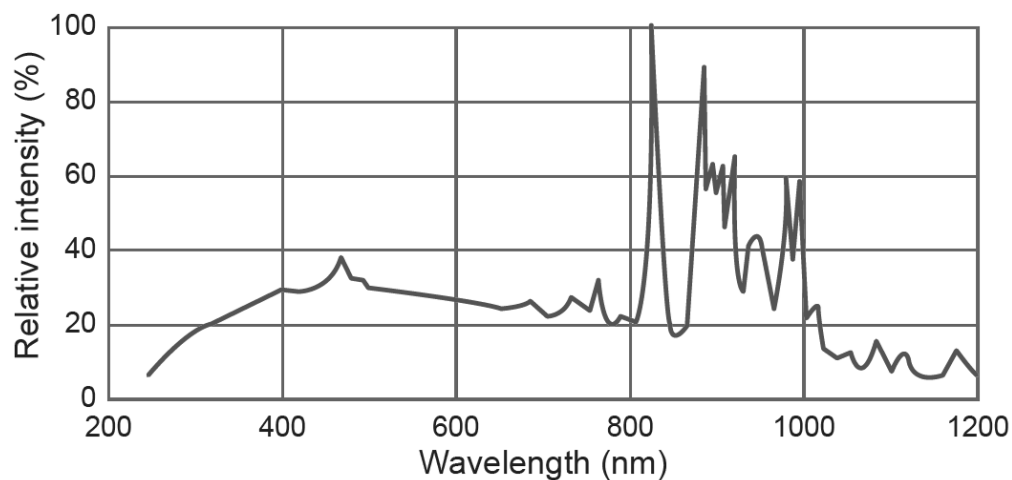
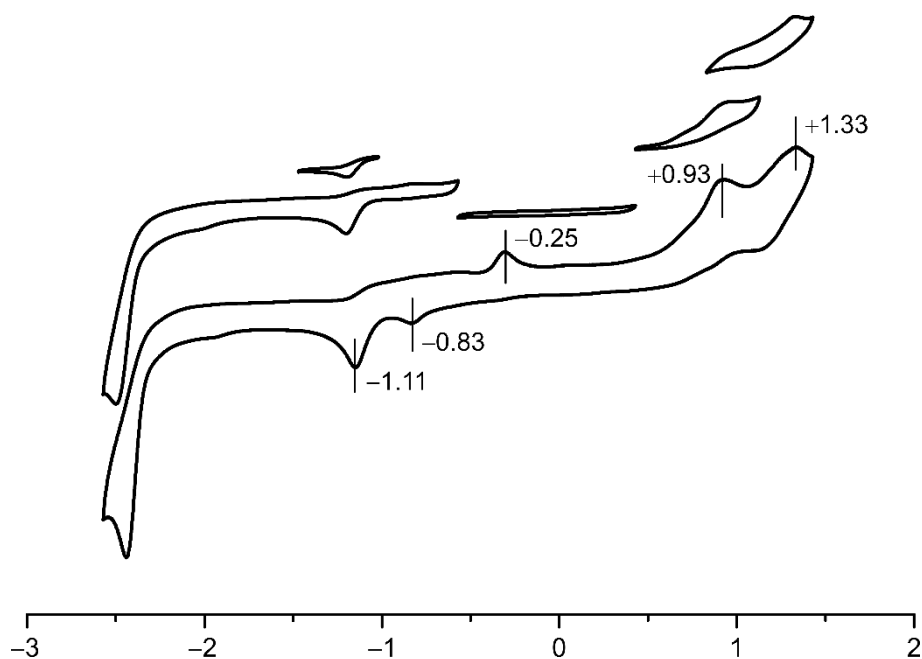


**Figure S33** Cyclic voltammograms of  $VCl_3(\text{ddpd})$  at 298 K in  $[\text{nBu}_4\text{N}][\text{PF}_6]/\text{CH}_3\text{CN}$ . Potentials given vs. ferrocene/ferrocenium.



## References

- S1 C. Förster, M. Dorn, T. Reuter, S. Otto, G. Davarci, T. Reich, L. Carrella, E. Rentschler and K. Heinze, *Inorganics* 2018, **6**, 86.
- S2 C. Doffek, N. Alzakhem, C. Bischof, J. Wahsner, T. Güden-Silber, J. Lügger, C. Platas-Iglesias and M. Seitz, *J. Am. Chem. Soc.* **2012**, *134*, 16413–16423.
- S3 C. Wang, S. Otto, M. Dorn, E. Kreidt, J. Lebon, L. Sršan, P. Di Martino-Fumo, M. Gerhards, U. Resch-Genger, M. Seitz and K. Heinze, *Angew. Chem.* **2018**, *130*, 1125–1130.

## 4 Multiphonon Relaxation bei NIR lumineszierenden Cr(III)- und V(III)-Komplexen

### 4.1 Einführung

In  $d^3$ -Cr(III)-Komplexen mit nahezu ideal oktaedrisch umgebenen Metallzentren und einer großen Ligandenfeldaufspaltung kann die thermische Rückbesetzung der Ligandenfeldzustände ausgehend von den emittierenden Spin-Flip-Zuständen effektiv verhindert werden. Kann zusätzlich Emissions-Löschung durch  $O_2$  ausgeschlossen werden, ist der wichtigste verbleibende strahlungslose Deaktivierungsweg der angeregten Zustände in Spin-Flip-Luminophoren der Energietransfer auf Obertöne hochenergetischer Oszillatoren wie beispielsweise O-H-, N-H- oder C-H-Streckschwingungen der Liganden oder des umgebenden Mediums. Dieser Prozess wurde bereits früher in festen Lanthanoidmaterialien beobachtet und wird als **Multiphonon Relaxation (MR)** bezeichnet. Multiphonon Relaxation ist besonders effektiv für molekulare Luminophore mit energiearmer Emission in Lösung und häufig verantwortlich für die typischerweise geringen Lumineszenzquantenausbeuten und kurzen Lebenszeiten der angeregten Zustände derartiger Verbindungen.

Grundsätzlich können zwei Grenzfälle von MR unterschieden werden, abhängig davon ob sich die Strukturen der am Übergang beteiligten elektronischen Zustände geometrisch stark voneinander unterscheiden oder diese sehr ähnliche Strukturen haben, also das *strong coupling* oder *weak coupling* Limit vorliegt. Wie bereits in Kapitel 3.1.1 erläutert, kommt es in oktaedrischen Cr(III)-Komplexen bei der Besetzung des Ligandenfeldzustands  ${}^4T_{2g}$  zu einer Population von Metall-Ligand antibindenden Orbitalen und dadurch zu einer Verschiebung der Kernkoordinaten (Abb.14: Potentialkurve des  ${}^4T_{2g}$ -Zustands ist nach rechts verschoben). Infolgedessen unterscheiden sich die Geometrien des  ${}^4A_{2g}$ -Grundzustands und des angeregten  ${}^4T_{2g}$ -Niveaus stark voneinander und es liegt das *strong coupling* Limit vor. In diesem Fall ist es sehr wahrscheinlich, dass sich die Potentialhyperflächen des Grundzustands  ${}^4A_{2g}$  und des Ligandenfeldzustands  ${}^4T_{2g}$  sehr nahekommen oder sogar schneiden und so effektive strahlungslose Deaktivierung via *surface crossing* möglich wird. Für diesen Energietransfer sind prinzipiell alle Schwingungen, auch die von Oszillatoren mit niedrigen Schwingungsfrequenzen, geeignet.<sup>[34]</sup>



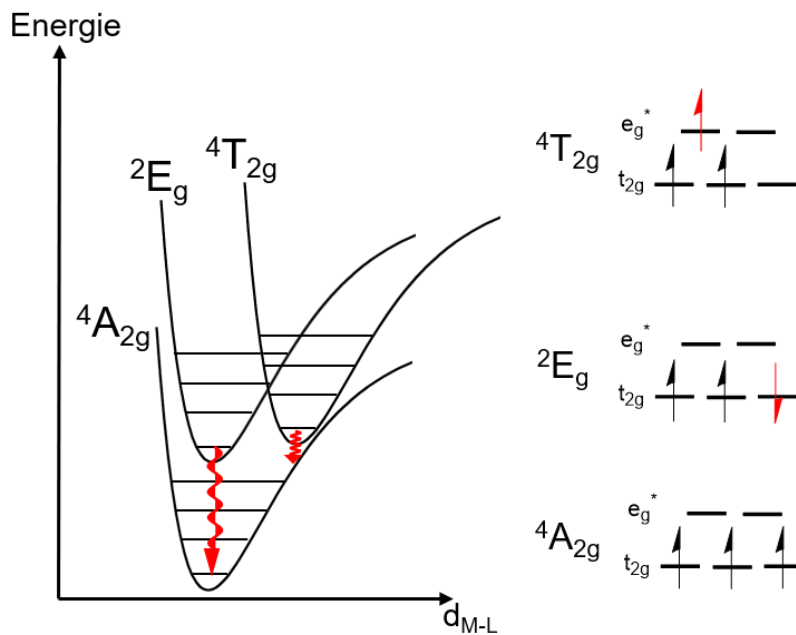


**Abb. 14:** Elektronische Konfigurationen der wichtigsten elektronischen Zustände für oktaedrisch umgebene Cr(III)-Ionen und den schematischen Potentialkurven der dazugehörigen Zustände. Die Strukturen der Zustände  ${}^2E_g$  und  ${}^4A_{2g}$  sind sehr ähnlich (*weak coupling* Limit), dagegen unterscheiden sich die Strukturen der Zustände  ${}^4T_{2g}$  und  ${}^4A_{2g}$  deutlich voneinander (*strong coupling* Limit). Abbildung verändert übernommen von Seitz.<sup>[34]</sup>

Dagegen bleiben die Kernkoordinaten beim Übergang vom Spin-Flip-Zustand  ${}^2E_g$  in den Grundzustand  ${}^4A_{2g}$  nahezu unbeeinflusst (Kapitel 3.1.1) und die Potentialhyperflächen dieser Zustände unterscheiden sich zwar in ihrer Energie aber nicht in Bezug auf die Position ihrer Kernkoordinaten (Abb.14: Potentialkurve des  ${}^2E_g$ -Zustands ist nur vertikal verschoben). Es liegt das *weak coupling* Limit vor. Bei der strahlungslosen Deaktivierung der Spin-Flip-Zustände müssen im Vergleich zu den Ligandenfeldzuständen größere Energien abgeführt werden, weshalb MR hauptsächlich durch Obertöne von hochenergetischen, stark anharmonischen Oszillatoren wie O-H, N-H- oder C-H-Streckschwingungen erfolgen kann. Eine ganz ähnliche Situation findet sich bei lumineszenten Lanthanoidkomplexen, deren Lumineszenz ebenso auf paritäts- und teilweise auch auf spin-verbotenen f-f-Übergängen der  $Ln^{3+}$ -Ionen beruht (Kapitel 5.1.1) für die ebenfalls das *weak coupling* Limit gilt.

Im Allgemeinen hängt die Effektivität von MR von vier wichtigen Faktoren ab:

*Ordnung des Obertons:* In der Regel beträgt die Energielücke zwischen dem emittierenden Zustand und dem nächst tieferen Niveau (für oktaedrische  $\text{Cr}^{3+}$ -Ionen: emittierender Zustand  ${}^2E_g$ , Grundzustand  ${}^4A_{2g}$ , Abb. 15) mehrere Vielfache der Grundswingungsenergie ( $\nu = 1$ ) des Oszillators. So besitzt beispielsweise der dritte C-H-Oberton ( $\nu_{\text{C-H}}^4$ , also der Übergang von  $\nu = 0$  nach  $\nu = 4$ ) die passende Energie (Abb. 15). Je höher der benötigte Oberton ist um den Energieabstand zu überbrücken, desto unwahrscheinlicher wird MR. Aus diesem Grund sind Metallkomplexe mit energiearmer Emission im NIR (z.B.  $\text{Cr}^{3+}$ -,  $\text{Yb}^{3+}$ -,  $\text{Nd}^{3+}$ -Komplexe) am anfälligsten für MR. Durch den geringen Energieabstand zwischen den am Übergang beteiligten Niveaus reicht bereits ein recht niedriger Oberton des Oszillators aus, um den erforderlichen Energietransfer zu ermöglichen, wodurch MR sehr effektiv sein kann. Daher leiden viele NIR-Luminophore an kurzen Lebenszeiten der angeregten Zustände und geringen Quantenausbeuten im niedrigen Prozentbereich, während beispielsweise für Lanthanoid-Komplexe mit energiereicherer, grüner ( $\text{Tb}^{3+}$ )<sup>[76]</sup> oder roter Emission ( $\text{Eu}^{3+}$ )<sup>[77]</sup> Quantenausbeuten von bis zu 60 % in Lösung erreicht werden.

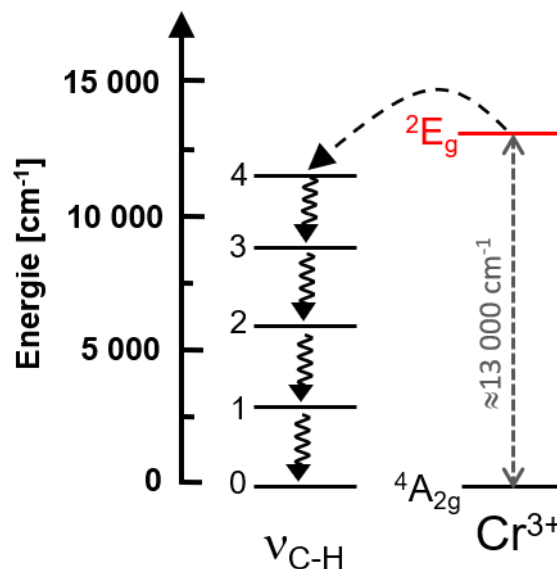


**Abb. 15:** Schematische Darstellung des Energietransfers vom angeregten Spin-Flip-Zustand  ${}^2E_g$  eines oktaedrisch umgebenen  $\text{Cr(III)}$ -Luminophors auf den dritten Oberton eines C-H-Oszillators.

*Resonante Energieniveaus:* Je geringer der Energieabstand zwischen dem emittierenden Niveau des Metallions und dem akzeptierenden Schwingungsoberton, desto effektiver ist MR.<sup>[78,79]</sup>

*Abstand:* MR ist im Allgemeinen umso effektiver, je kleiner der räumliche Abstand zwischen dem photoaktiven Metallzentrum und dem Oszillator ist. In vielen Fällen wird angenommen, dass der Energietransfer auf Schwingungsobertöne *via* eines „försterartigen“ Dipol-Dipol-Mechanismus erfolgt. MR reduziert sich daher proportional zu  $r^{-6}$ .<sup>[80]</sup>

*Anharmonizität:* Die überwiegende Zahl an Untersuchungen zu MR in lumineszenten Materialien beschreiben Schwingungen als ideale, harmonische Oszillatoren. Diese Näherung erlaubt eine relativ einfache und sinnvolle Beschreibung der Schwingungsrelaxation für einige Metallkomplexe mit CT-Emission<sup>[81]</sup> oder für ausgedehnte, mit Lanthanoid- oder Übergangsmetallionen dotierte Festkörper. Die bekannten Charakteristika des harmonischen Oszillators sind die äquidistanten Energieabstände zwischen den Energieniveaus  $E_n$  abhängig von der Vibrationsquantenzahl  $n_{\text{Harm}}$  und die Auswahlregel  $\Delta n \pm 1$ , welche Vibrations-Übergänge ausschließlich zwischen benachbarten Niveaus erlaubt. Das harmonische Modell offenbart aber konzeptionelle Schwächen bei der Behandlung von MR für Spin-Flip-Emitter oder molekulare Lanthanoid-Komplexe, bei welchen für die strahlungslose Deaktivierung der emittierenden Zustände wesentlich größere Energien auf hochenergetische Schwingungsobertöne übertragen werden müssen. Die Besetzung des für den Energietransfer benötigten hohen Schwingungsobertons direkt aus dem Grundzustand ( $n = 0$ ) wäre wegen der Auswahlregel des harmonischen Modells mit  $\Delta n \pm 1$  streng verboten und MR für diese Systeme sehr ineffektiv. Dies steht in Diskrepanz zu den experimentellen Befunden die zeigen, dass MR auch sehr effektiv ist, wenn die Energielücke zwischen elektronisch angeregtem Zustand und Nullpunkts-Schwingungs-Niveau ein Vielfaches der Energie des Grundschwingungsübergangs ( $n = 0$  nach  $n = 1$ ) ist. Daher sind bei der strahlungslosen Deaktivierung der angeregten Zustände im *weak coupling* Limit durch MR fast immer Oszillatoren mit einem hohen Anteil an Anharmonizität beteiligt. Bei der Behandlung von MR für Spin-Flip-Emitter und molekulare Lanthanoidluminophore muss somit die Anharmonizität der Schwingungen mitberücksichtigt werden.

Gut dafür geeignet ist das „local-mode Morse Oszillator Modell“,<sup>[82]</sup> welches bereits für die quantitative Beschreibung der Schwingungsrelaxation molekularer Verbindungen in Lösung erfolgreich eingesetzt werden konnte.<sup>[83,84]</sup>

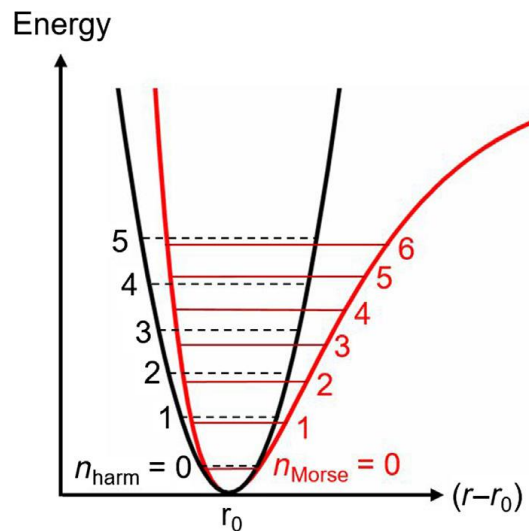


**Abb. 16:** Vergleich der Schwingungszustände und Energien des harmonischen Oszillators (schwarz, Schwingungsquantenzahl  $n_{\text{harm}}$ ) und eines Morse-Oszillators (rot, Schwingungsquantenzahl  $n_{\text{Morse}}$ ). Abbildung übernommen von Seitz.<sup>[34]</sup>

Einer der wichtigsten Bestandteile des Morse-Modells sind die mit höherer Schwingungsquantenzahl  $n_{\text{Morse}}$  immer kleiner werdenden Energieabstände  $\Delta E_n$ . Folglich sind die Abstände zwischen den Obertonbanden auch nicht mehr äquidistant, die Auswahlregel  $n \pm 1$  gilt auch nicht mehr streng, womit die direkte Population eines höheren Schwingungsniveaus aus dem Grundzustand möglich ist. Im Morse-Modell kann die Energie  $\tilde{\nu}_n$  (in Wellenzahlen) für einen Übergang vom Grundzustand in einen angeregten Zustand der Schwingungsquantenzahl  $n$  durch Gl. 1 beschrieben werden:<sup>[83,84]</sup>

$$\tilde{\nu}_n = n \cdot \tilde{\nu}_0 - n(n + 1) \cdot x \quad (1)$$

Nach Gl. 1 hängt  $\tilde{\nu}_n$  zum einen von der Schwingungsquantenzahl  $n$  und der Grundschiebungsfrequenz  $\tilde{\nu}_0$ , zum anderen vom Anharmonizitätsparameter  $x$  ab. Dabei zeigen größere Werte von  $x$  einen höheren Grad an Anharmonizität der Schwingung an. Für einen ideal harmonischen Oszillator muss folglich  $x = 0$  gelten. In Tab. 2 sind die relevanten Morse-Parameter von zweiatomigen Streckschwingungen

aufgeführt, die in typischen Ligandmotiven von lumineszenten Metallkomplexen und verbreiteten Lösungsmitteln auftreten. Es wird deutlich, dass hochenergetische X-H-Streckschwingungen wie  $\nu_{\text{O-H}}$  ( $x = 90 \text{ cm}^{-1}$ ) oder  $\nu_{\text{C-H}}$  ( $x = 58 \text{ cm}^{-1}$ ) die höchsten Anharmonizitäten aufweisen. Demgegenüber stehen die niederfrequenten C-Halogen-Schwingungen welche mit  $\nu_{\text{C-F}}$  ( $x = 5.0 \text{ cm}^{-1}$ ) oder  $\nu_{\text{C-Cl}}$  ( $x = 4.5 \text{ cm}^{-1}$ ) wesentlich harmonischer sind. Vergleicht man die isotopologen C-H- bzw. C-D-Oszillatoren stellt man fest, dass C-D-Oszillatoren sowohl geringere Schwingungsfrequenzen als auch reduzierte Anharmonizitäten besitzen. Dabei kann die Abnahme der Schwingungsfrequenzen durch die größere reduzierte Masse (Gl. 2) erklärt werden:

$$\frac{\tilde{\nu}_{\text{C-H}}}{\tilde{\nu}_{\text{C-D}}} = \sqrt{\frac{\mu_{\text{C-D}}}{\mu_{\text{C-H}}}} = \sqrt{\frac{(m_{\text{C}} \cdot m_{\text{D}})/(m_{\text{C}} + m_{\text{D}})}{(m_{\text{C}} \cdot m_{\text{H}})/(m_{\text{C}} + m_{\text{H}})}} = 1.36 \quad (2)$$

Die Reduzierung der Anharmonizität von  $\nu_{\text{C-H}}$  ( $x = 58 \text{ cm}^{-1}$ ) im Vergleich zu  $\nu_{\text{C-D}}$  ( $x = 28 \text{ cm}^{-1}$ ) ist beachtlich. Als groben Anhaltspunkt kann man im Vergleich  $\nu_{\text{X-H}} / \nu_{\text{X-D}}$  etwa von einer Halbierung des Anharmonizitätsparameters ausgehen.

**Tab. 2:** Typische Parameter für den anharmonischen Morse-Oszillator mit der Grundschwingungsenergie  $\tilde{\nu}_0$  und dem Anharmonizitätsparameter  $x$  für verschiedene Streckschwingungen. Tabellenwerte entnommen von Seitz.<sup>[34]</sup>

Oszillator	$\tilde{\nu}_0$ [ $\text{cm}^{-1}$ ]	$x$ [ $\text{cm}^{-1}$ ]	Verbindung
O-H	3515	90	CH <sub>3</sub> OH (rein)
O-D	2600	50	CH <sub>3</sub> OD (rein)
C-H (arom.)	3161	58	Pyridin (H3, H4, H5)
C-D (arom.)	2325	28	Pyridin (D3, D4, D5)
C=O	1860	12	PP-PBD (perfluorierter Esther)
C-F	1255	5.0	Methyl-Perfluoropropionat
C-Cl	775	4.5	CCl <sub>4</sub> (rein)

Ein entscheidender Punkt ist, dass die Anharmonizität nicht nur die Energie der Obertöne bestimmt, sondern zusätzlich auch die Oszillatorstärke des Übergangs auf höhere Obertöne beeinflusst. Im Allgemeinen weisen die Obertöne stark anharmonischer Oszillatoren im Vergleich zu den Obertönen harmonischer Oszillatoren der gleichen Energie erheblich höhere Oszillatorstärken auf, was naturgemäß MR fördert.<sup>[34]</sup>

#### 4.1.1. Reduzierung von Multiphonon Relaxation

Für die Entwicklung von Luminophoren mit langlebiger und intensiver NIR-Emission muss die strahlungslose Deaktivierung der angeregten Metallzustände unterbunden werden. Im Prinzip kann dies einfach durch Vermeiden von hochenergetischen X-H-Oszillatoren ( $X = O, N, C$ ) in der Nähe des photoaktiven Metallzentrums erreicht werden. In der Praxis ist es aber wegen der allgegenwärtigen C-H-Bindungen in gängigen organischen Liganden und Lösungsmitteln, insbesondere für Metallkomplexe in Lösung, eine große Herausforderung.

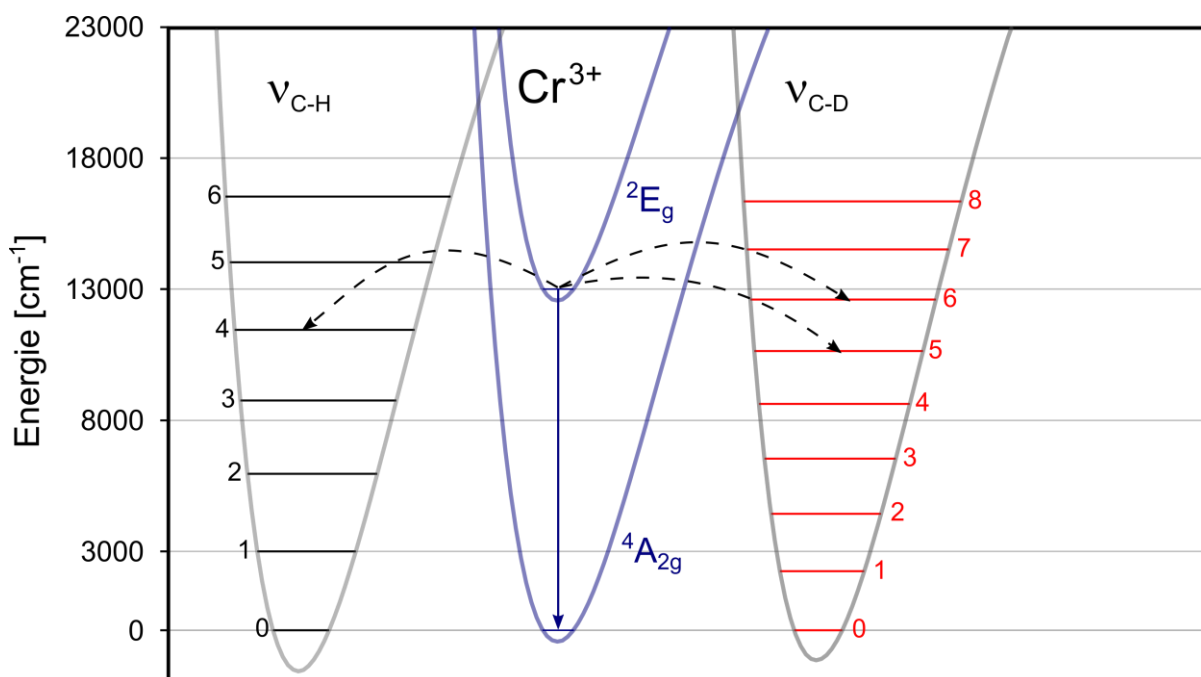
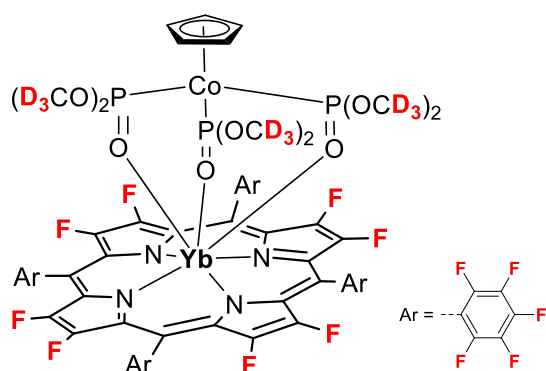


**Abb. 17:** Darstellung des Energietransfers vom angeregten Spin-Flip-Zustand  $^2E_g$  eines oktaedrischen Cr(III)-Luminophors auf Obertöne von aromatischen C-H- und C-D-Oszillatoren.

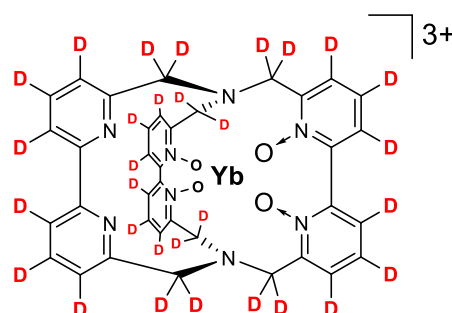
Generell gibt es zwei etablierte Strategien, Halogenierung<sup>[85]</sup> und Deuterierung,<sup>[86,87]</sup> um MR durch Obertöne von C-H-Oszillatoren zu reduzieren. Wie bereits ausgeführt, besitzen C-F/Cl- bzw. C-D-Oszillatoren aufgrund der größeren reduzierten Masse geringere Oszillatorfrequenzen und Anharmonizitäten (Tab. 2). Daher ist ein höherer Oberton des Oszillators erforderlich, um die Energielücke zwischen dem angeregten Zustand und dem nächst tieferliegenden Zustand zu überbrücken (Abb. 17). Da die Besetzungswahrscheinlichkeit für höhere Obertöne abnimmt, kann so die strahlungslose Deaktivierung durch C-H-Oszillatoren reduziert werden.

Grundsätzlich stellt Perhalogenierung im Vergleich zur Perdeuterierung, wegen der noch geringeren Oszillatorfrequenzen und Anharmonizitäten der C-F/Cl-Streckschwingungen, die effektivere Methode dar. So ermöglichte die Perfluorierung der Liganden die Entwicklung der aktuell besten NIR Lanthanoid-Luminophore mit Rekordquantenausbeuten von bis zu  $\Phi = 63\%$ .<sup>[88]</sup> Allerdings ist Halogenierung, besonders Perfluorierung, nur für eine begrenzte Zahl an Ligandensystemen geeignet. Zum einen nimmt mit höherem Fluorierungsgrad oftmals die Stabilität der Liganden ab, zum anderen wird die  $\sigma$ -Donor-Stärke durch den -I Effekt der Fluoratome stark herabgesetzt. Diese Tatsache ist gerade für Spin-Flip-Luminophore ein ernstzunehmendes Problem, da eine hohe  $\sigma$ -Donorstärke des Liganden sowohl für die Komplexstabilität als auch für die benötigte große Ligandfeldaufspaltung unerlässlich ist.



**Gao und Zhang 2017**

LM = CD<sub>2</sub>Cl<sub>2</sub>  
 $\lambda_{em} = 974$  nm  
 $\Phi = 63\%$



**Seitz 2015**

LM = CD<sub>3</sub>OD  
 $\lambda_{em} = 975$  nm  
 $\Phi = 12\%$

**Abb. 18:** Ausgewählte Beispiele von effizienten NIR Metallluminophoren mit reduzierter MR durch Fluorierung oder Deuterierung des Liganden.<sup>[88,89]</sup>

Dagegen beeinflusst Deuterierung die elektronischen und sterischen Ligandeneigenschaften nur minimal und kann daher prinzipiell für alle Liganden eingesetzt werden. Auch die Deuterierung des Liganden sowie die Verwendung von deuterierten Lösungsmitteln stellt eine effektive Möglichkeit dar, um die photophysikalischen Eigenschaften von Metallkomplexen mit energiearmer Emission signifikant zu verbessern. Dies konnte beispielsweise für perdeuterierte Lanthanoidkryptate der Lanthanoidionen Yb<sup>3+</sup> und Nd<sup>3+</sup> gezeigt werden.<sup>[89,90]</sup> Auch für



oktaedrische  $d^3$ -Cr(III)-Komplexe mit NIR Spin-Flip-Emission kann Deuterierung sehr vorteilhaft sein. Einen signifikanten Isotopeneffekt erwartet man für nahezu ideal oktaedrische Cr(III)-Komplexe mit einer großen Ligandenfeldaufspaltung bei welchen strahlungslose Deaktivierungsprozesse stark von MR dominiert sind. Diese Voraussetzungen sind nicht für alle bekannten lumineszierenden Chromkomplexe gegeben. Die Komplexe  $[\text{Cr}(\text{bpy})_3]^{3+}$  und  $[\text{Cr}(\text{CN})_6]^{3-}$  zeigen beispielsweise nur einen sehr geringen (inversen) Isotopeneffekt durch Wechsel des Lösungsmittels von  $\text{H}_2\text{O}$  auf  $\text{D}_2\text{O}$  ( $[\text{Cr}(\text{bpy})_3]^{3+}$ :  $\text{D}_2\text{O}/\text{H}_2\text{O}$  (Ar),  $\tau = 61/66 \mu\text{s}$ , 0.9).<sup>[91,92]</sup> Durch die geringe Ligandenfeldaufspaltung von  $[\text{Cr}(\text{bpy})_3]^{3+}$  kommt es ausgehend von den emittierenden Dublett-Zuständen zur thermischen Rückpopulation der Ligandenfeldzustände. Demzufolge erfolgt die strahlungslose Deaktivierung der Spin-Flip-Zustände vorwiegend durch Reverse Intersystem Crossing und sich daran anschließende Deaktivierungswege wie beispielsweise *surface crossing*. Es ist daher nicht von einem ausgeprägten Deuterierungseffekt auszugehen.

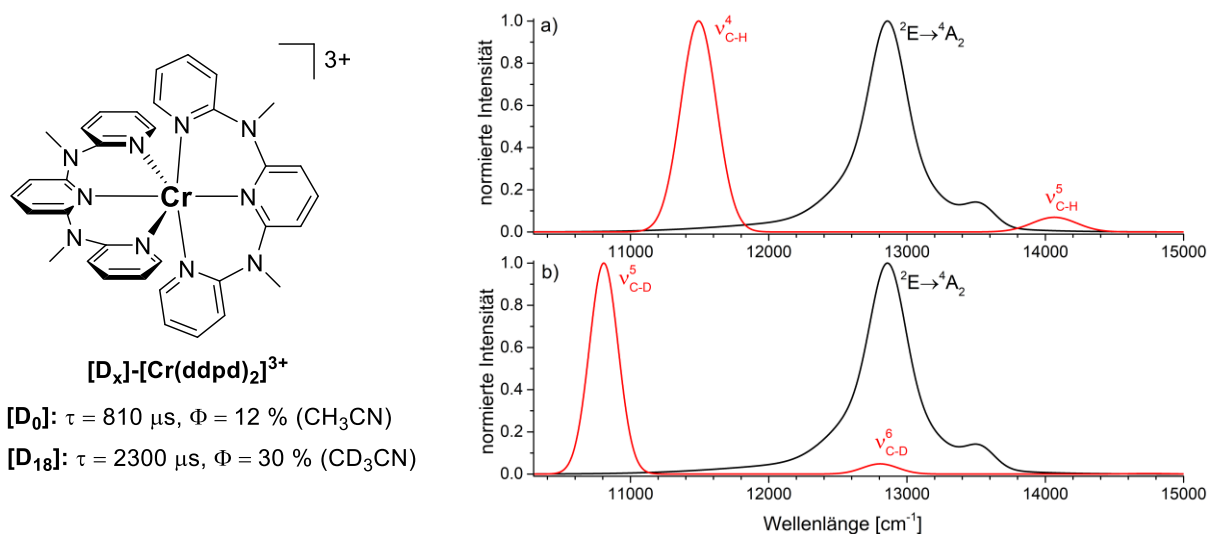


**Abb. 19:** Links: Lebenszeiten und Quantenausbeuten von  $[\text{D}_x]\text{-}[\text{Cr}(\text{ddpd})_2]^{3+}$ . Rechts: Normiertes  ${}^2\text{E}$ -Emissionsspektrum von  $[\text{Cr}(\text{ddpd})_2]^{3+}$  (schwarz) und die aus den gemessenen Spektren extrahierten Absorptionsbanden der relevanten aromatischen C-H-Obertöne (rot) mit nur geringem spektralem Überlapp. b) Normiertes  ${}^2\text{E}$ -Emissionsspektrum von  $[\text{Cr}(\text{ddpd})_2]^{3+}$  (schwarz) und die aus den gemessenen Spektren extrahierten Absorptionsbanden der relevanten aromatischen C-D-Obertöne (rot) mit fast vollständigem spektralem Überlapp des sechsten C-D-Obertons. Abbildung verändert übernommen von Heinze.<sup>[37]</sup>

Anders sieht die Situation für die Spin-Flip Zustände im  $[\text{Cr}(\text{ddpd})_2]^{3+}$ -Komplex aus. Partielle Deuterierung des Liganden ( $\sim 50\%$  D) steigerte die Lumineszenzlebenszeiten

bei Raumtemperatur um die Faktoren 1.4 und 2.0 in H<sub>2</sub>O bzw. CH<sub>3</sub>CN. In sauerstofffreien, deuterierten Acetonitril erreicht der teildeuterierte **[Cr(ddpd)<sub>2</sub>]<sup>3+</sup>**-Komplex neue Rekordwerte für Cr(III)-Luminophore mit einer Quantenausbeute von  $\Phi = 30 \%$  und einer Lebenszeit von  $\tau = 2300 \mu\text{s}$  bei Raumtemperatur.<sup>[37]</sup>

Die Obertonanalyse auf Basis von experimentell zugänglichen aromatischen C-H(D)-Oszillatoren von einfacheren Pyridinliganden wurde im Vorfeld dieser Arbeit in der Arbeitsgruppe bereits durchgeführt und offenbarte einige Besonderheiten.<sup>[37]</sup> Die qualitative Analyse der relativen Positionen der aromatischen C-H-Obertöne und der <sup>2</sup>E-Emissionsbande von **[Cr(ddpd)<sub>2</sub>]<sup>3+</sup>** ergab eine vorteilhaft geringe spektrale Überlappung der Emissionsbande mit den energetisch benachbarten C-H-Obertönen ( $\nu_{\text{C-H}}^4$  und  $\nu_{\text{C-H}}^5$ , Abb. 19). Aufgrund des geringen spektralen Überlapps tragen diese C-H-Oszillatoren nur eingeschränkt zur MR bei, wodurch die bereits ausgezeichneten photophysikalischen Eigenschaften des undeuterierten Komplexes erklärt werden können. Im Gegensatz dazu überlappt der entsprechende C-D-Oberton ( $\nu_{\text{C-D}}^6$ , Abb. 19) nahezu vollständig mit der Emissionsbande, weshalb von einem größeren Beitrag zur strahlungslosen Deaktivierung der angeregten Dublett-Zustände als üblich auszugehen ist. Diese Tatsache begründet die im Vergleich zu Literaturbeispielen eher moderate Steigerung der Lumineszenzlebenszeiten nach Deuterierung.

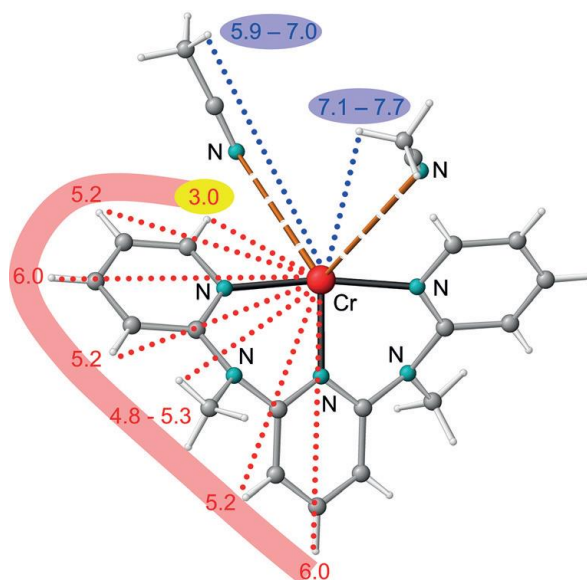


**Abb. 20:** Cr...CH-Abstände zum **ddpd**-Liganden (aus DFT-Berechnungen) und zu kokristallisierendem CH<sub>3</sub>CN (aus der Röntgenstrukturanalyse) bestimmt. Die Abstände der ersten bzw. zweiten Koordinationssphäre sind in rot bzw. blau gezeigt. Der zweite **ddpd**-Ligand wurde aus Übersichtlichkeitsgründen weggelassen. Abstände sind in Å angegeben. Abbildung übernommen von Heinze.<sup>[37]</sup>

Darüber hinaus konnte durch selektive Liganddeuterierung gezeigt werden, dass nicht alle C-H-Oszillatoren gleichwertig zu MR beitragen. So spielen die Methylgruppen für MR praktisch keine Rolle, wohingegen die C-H-Oszillatoren in 6/6“-Position der terminalen Pyridine mit dem geringsten Abstand zum Chromzentrum (3 Å) den größten Einfluss haben (Abb. 20, gelb hinterlegt). Für die Entwicklung zukünftiger d<sup>2</sup>/d<sup>3</sup>-Luminophore mit reduzierter Multiphonon Relaxation sollte daher die Deuterierung der Oszillatoren mit der höchsten Löschungseffizienz ausreichen, um die gewünschte Verbesserung der photophysikalischen Kenngrößen zu erreichen. Um die MR-Raten einzelner Oszillatoren zu ermitteln, ist die Kenntnis wichtiger Parameter wie Abstand, Energie oder Anharmonizität von C-H-Oszillatoren an spezifischen Positionen von großer Bedeutung (s. Kap. 4.1.1). Solche Daten sind allerdings derzeit nur für eher einfache Pyridine und häufig nur in der Gasphase bekannt.<sup>[83,84,93,94]</sup> Auch die C-H- und O-H-Oszillatoren der Lösungsmittelmoleküle in der zweiten Koordinationssphäre tragen zur MR bei. Trotz der im Festkörper relativ großen Abstände zwischen den hochenergetischen Oszillatoren und des photoaktiven Cr<sup>3+</sup>-Ions (ca. 5.9 – 7.7 Å) kann bei Verwendung der isotopologen Lösungsmittel (CD<sub>3</sub>CN und D<sub>2</sub>O) die Lebenszeit der <sup>2</sup>E-Emission um den Faktor 1.7 gesteigert werden. Erwartungsgemäß ist die Löschungseffizienz der O-H-Oszillatoren von H<sub>2</sub>O etwas ausgeprägter als die der C-H-Oszillatoren von Acetonitril. Die Kombination aus der fast vollständigen Deuterierung der metallnächsten C-H-Oszillatoren des **ddpd**-Liganden und der Verwendung von deuteriertem Lösungsmittel war der Schlüssel für die Rekordlebenszeiten und Rekordquantenausbeuten dieses Cr(III)-Luminophors bei Raumtemperatur.<sup>[37,38]</sup>

#### 4.1.1. Quantifizierung von Multiphonon Relaxation

Eine fundierte quantitative Beschreibung der strahlungslosen Deaktivierung durch hochenergetische Oszillatoren ist von zentraler Bedeutung für die Konzeption von hochlumineszenten Metallkomplexen mit NIR-Emission. Allerdings sind Untersuchungen der Ligandschwingungen von Metallkomplexen in Lösung sehr herausfordernd, da in organischen Liganden unterschiedliche Typen von Oszillatorgruppen (z.B. aromatische C-H, aliphatische C-H, CH<sub>2</sub>, CH<sub>3</sub>, N-H) auftreten, welche zusätzlich noch untereinander gekoppelt sind. Üblicherweise sind die Obertonsignaturen unterschiedlicher Oszillatoren auch nicht einfach unterscheidbar, was die Analyse eines einzelnen Oszillators sehr schwierig macht.

Eine erste gute theoretische Beschreibung der strahlungslosen Desaktivierung des emittierenden Metallzustands durch MR gelang durch das Energielückengesetz (EGL).<sup>[32,95]</sup> Dieses Gesetz basiert auf der Korrelation zwischen dem Energieabstand des emittierenden und nächsttieferliegenden Zustands mit der Löschrates des bei der Desaktivierung beteiligten Oszillators. Das EGL liefert eine einfache und gute quantitative Beschreibung für mit Lanthanoid- oder Übergangsmetallionen dotierte ausgedehnte Festkörper und für einige CT-Emitter, versagt aber in vielen Fällen bei Beteiligung von stark anharmonischen Oszillatoren, wie es häufig für Metallkomplexe mit organischen Liganden der Fall ist.<sup>[34]</sup>

Für die quantitative Beschreibung von MR für Spin-Flip-Luminophore oder lumineszenten Lanthanoidkomplexe in Lösung ist das EGL daher ungeeignet. Ein besser geeignetes Modell wurde von Ermolaev und Sveshnikova vorgeschlagen und trägt den Namen *Inductive-resonant mechanism of non-radiative transitions* (IRM).<sup>[96]</sup> Dieses Modell basiert auf der Grundannahme, dass der Energietransfer vom photoaktiven Metallion auf den anharmonischen Oszillator vornehmlich durch elektrische Dipol-Dipol-Wechselwirkungen erfolgt. Das IRM Modell ist daher ganz analog zum besser bekannten Förster-Resonanzenergietransfer (FRET)<sup>[80]</sup> für organische Fluorophore. Im Rahmen des FRET-Modells kommt es zu einem resonanten Energietransfer (RET) von einem Donor, hier der emittierende Zustand des Metallions, auf einen Akzeptor, in diesem Fall der passende Schwingungszustand des Oszillators. Gemäß des IRM kann die Rate der strahlungslosen Deaktivierung (MR-Rate)  $k_{nr}$  infolge des Energietransfers vom angeregten Zustands des Metallions auf einen Oszillator in der Nähe durch Gl. 3 beschrieben werden:<sup>[96]</sup>

$$k_{nr} = \frac{9000 \cdot \ln(10) \cdot \kappa^2}{128 \cdot \pi^5 \cdot N_A} \cdot \frac{k_r}{n^4 \cdot r^6} \cdot \text{SOI} = 5.857 \times 10^{-25} \frac{k_r}{n^4 \cdot r^6} \cdot \text{SOI} \quad (3)$$

dabei sind die Parameter und Konstanten:  $k_r$  ist die Rate des strahlenden Übergangs in Abwesenheit aller strahlungslosen Deaktivierungspfade,  $\kappa^2$  ist ein Faktor, der abhängig von der relativen Orientierung der Übergangsdipolmomente des Donors (Metall) und des Oszillators (Akzeptor) ist. Im Rahmen des dynamischen isotropen Limits gilt  $\kappa^2 = 2/3$ . Der Parameter  $n$  ist der Brechungsindex,  $N_A$  die Avogadrokonstante und  $r$  der Abstand zwischen Metallzentrum und Oszillator mit der für Dipol-Dipol-Wechselwirkungen typischen Abstandsabhängigkeit von  $r^{-6}$ . Das *spectral overlap integral* (SOI) ist ein Ausdruck in der Wellenzahlskala  $\tilde{\nu}$  aus dem FRET-Modell und beschreibt den spektralen Überlapp zwischen Donor und Akzeptor (Gl. 4):

$$\text{SOI} = \int I_{\text{norm}}(\tilde{\nu}) \cdot \varepsilon_{\text{vib}}(\tilde{\nu}) \cdot \tilde{\nu}^{-4} d\tilde{\nu} \quad (4)$$

dabei ist  $\varepsilon_{\text{vib}}(\tilde{\nu})$  der dekadische molare Absorptionskoeffizient bei der Wellenzahl  $\tilde{\nu}$  (in der Einheit  $\text{M}^{-1}\text{cm}^{-1}$ ), in welchem die genaue Energie und indirekt auch die Anharmonizität des jeweiligen Obertons steckt.  $I_{\text{norm}}$  ist die dimensionslose, auf das Integral der Emissionsbande normierte Emissionsintensität (Gl. 5):

$$I_{\text{norm}}(\tilde{\nu}) = \frac{I_{\text{em}}(\tilde{\nu})}{\int I_{\text{em}}(\tilde{\nu}) d\tilde{\nu}} \Rightarrow \int I_{\text{norm}}(\tilde{\nu}) d\tilde{\nu} = 1 \quad (5)$$

Unter ansonsten gleichen Bedingungen können die Parameter  $\kappa$ ,  $k_r$  und  $r$  für die isotopologen C-H(D)-Oszillatoren als unverändert angesehen werden. Dadurch lässt sich das Verhältnis der Raten der strahlungslosen Deaktivierung durch MR bilden und damit Gl. 3 zu Gl. 6 vereinfachen. Gl. 6 hängt dann nur noch von den Überlappintegralen  $\text{SOI}^{\text{H}}$  und  $\text{SOI}^{\text{D}}$  ab:

$$\frac{k_{nr}^{\text{H}}}{k_{nr}^{\text{D}}} = \frac{\int I_{\text{norm}}(\tilde{\nu}) \cdot \varepsilon_{\text{vib}}^{\text{H}}(\tilde{\nu}) \cdot \tilde{\nu}^{-4} d\tilde{\nu}}{\int I_{\text{norm}}(\tilde{\nu}) \cdot \varepsilon_{\text{vib}}^{\text{D}}(\tilde{\nu}) \cdot \tilde{\nu}^{-4} d\tilde{\nu}} = \frac{\text{SOI}^{\text{H}}}{\text{SOI}^{\text{D}}} \quad (6)$$

Das IRM erlaubt im Vergleich zum EGL eine deutlich bessere quantitative Beschreibung von MR auch für molekulare Luminophore in Lösung. Wichtige Vorteile sind die Berücksichtigung der Anharmonizität und die Behandlung individueller Oszillatoren mit ihren Abständen zum Metallzentrum und ihren Schwingungseigenschaften. Auf der anderen Seite werden für den quantitativen Einsatz des IRM spezifische Informationen über wichtige Parameter wie beispielsweise  $k_r$ ,  $r$  oder  $\varepsilon_{\text{vib}}(\tilde{\nu})$  benötigt. Diese Daten sind experimentell oft schwer zugänglich oder unterliegen dynamischen Änderungen in typischen experimentellen Zeitskalen. Insbesondere die quantitativen Daten der Obertonsignaturen  $\varepsilon_{\text{vib}}(\tilde{\nu})$  von hochenergetischen X-H-Oszillatoren sind entscheidend für die Berechnung der SOIs, obgleich diese ausgesprochen schwierig zu ermitteln sind. Ein wesentlicher Grund dafür ist, dass die strukturelle Beziehung zwischen Oszillator und Metallzentrum häufig nicht bekannt ist oder sich dynamisch mit Änderung der Koordinationsgeometrie in Lösung verändert.<sup>[34]</sup> Eine weitere Herausforderung stellen die sehr kleinen Extinktionskoeffizienten gerade für höheren Obertöne dar (Abb. 21). Für die experimentelle Bestimmung von  $\varepsilon_{\text{vib}}(\tilde{\nu})$  sind daher vergleichsweise hohe Konzentrationen der Messlösungen nötig, die nicht immer erreichbar sind. Während nur sehr wenige  $\varepsilon_{\text{vib}}(\tilde{\nu})$  Daten und ihre quantitative Behandlung im Rahmen des IRM für molekulare Koordinationsverbindungen bekannt sind, wurden die Schwingungsobertöne in einfachen organischen Verbindungen wie beispielsweise einfacheren Pyridinliganden sehr gut untersucht.<sup>[83,84,93,94]</sup> In einigen Fällen, bei welchen sich die Oszillatoreigenschaften nicht wesentlich mit der chemischen Umgebung ändern, können diese Obertondaten für die Schwingungsanalyse von Metallkomplexen mit vergleichbaren Ligandenmotiven herangezogen werden. Für diesen Zweck eignen sich besonders gut nicht austauschende, aromatische C-H-Oszillatoren, die in nahezu allen Ligandensystemen von lumineszierenden Lanthanoid- und Spin-Flip-Komplexen vorkommen.<sup>[34]</sup>

Mit dieser Vorgehensweise konnten in vorangegangenen Arbeiten mit Hilfe von experimentell zugänglichen Obertonsignaturen von aromatischen C-H(D)-Oszillatoren, die relevanten SOIs für pyridinbasierte Lanthanoidkryptate mit NIR-Emission quantitativ ermittelt werden.<sup>[87]</sup>

Zudem konnte dieser Ansatz auch auf Cr(III)-Spin-Flip-Komplexe übertragen werden.<sup>[37]</sup> Anhand von isotopologen **[Cr(ddpd)<sub>2</sub>]<sup>3+</sup>**-Komplexen wurde eine qualitative Analyse der relativen Positionen der aromatischen C-H-Obertöne und der <sup>2</sup>E-

Emissionsbande durchgeführt (Kapitel 4.1.1, Abb. 19). Eine quantitative Auswertung der spektralen Überlappintegrale und die Bestimmung der MR-Raten  $k_{nr}$  der aromatischen C-H(D)-Oszillatoren wurde in dieser Analyse aber nicht durchgeführt.

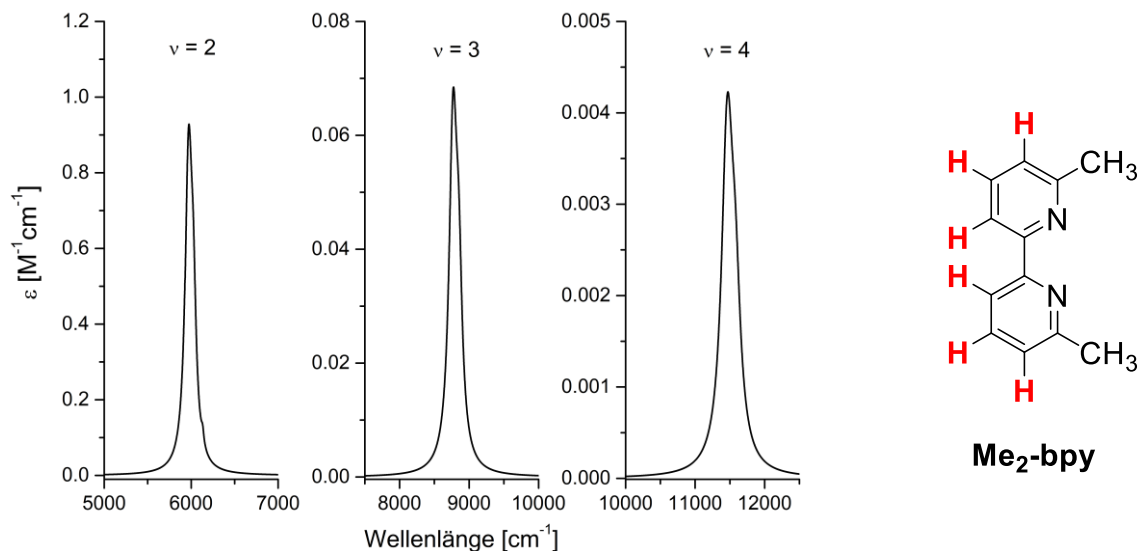


**Abb. 21:** Aus den gemessenen NIR-Absorptionsspektren extrahierte Obertonsignaturen der ersten drei Obertöne ( $\nu = 2 - 4$ ) von **Me<sub>2</sub>-bpy** in  $\text{CDCl}_3$ , wobei drei individuelle aromatische C-H-Oszillatoren überlagern. Daten entnommen von Seitz.<sup>[87]</sup>

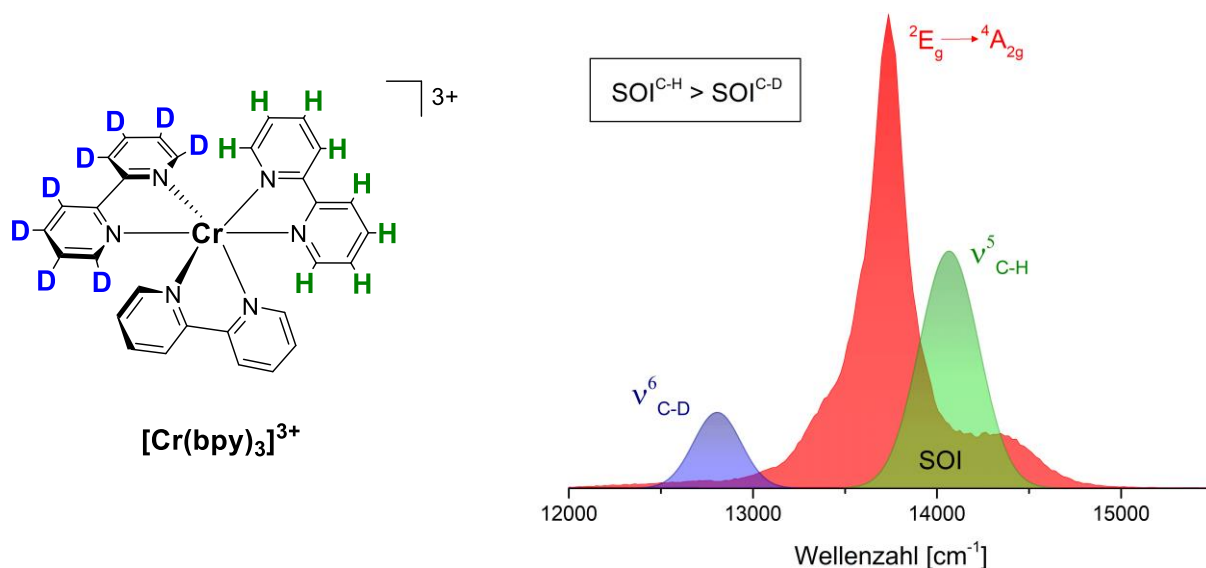


**Abb. 22:** Schematische Darstellung des spektralen Überlapp der  ${}^2E$ -Emission von  $[\text{Cr}(\text{bpy})_3]^{3+}$  mit den relevanten aromatischen C-H- (grün) und C-D-Obertönen (blau). Die relativen Intensitäten sind nicht maßstäblich dargestellt.

## 4.2 Ergebnisse und Diskussion

### 4.2.1 Multiphonon Relaxation bei lumineszierenden Cr(III)-Komplexen

#### 4.2.1.1 Schwingungsrelaxation von spezifischen aromatischen C-H-Obertönen bei NIR-emissiven molekularen Rubinen (unveröffentlichte Ergebnisse)

Die Reduzierung von MR durch Deuterierung von hochfrequenten, anharmonischen C-H-Oszillatoren des Liganden spielt bei Cr(III)-Luminophoren mit NIR Spin-Flip-Emission eine zentrale Rolle um die Quantenausbeuten und Lumineszenzlebenszeiten dieser Emitter zu verbessern. Allerdings tragen nicht alle C-H-Oszillatoren des Liganden gleichwertig zur strahlungslosen Deaktivierung der Spin-Flip-Zustände bei. Dies konnte bereits in ersten Untersuchungen für den **[Cr(ddpd)<sub>2</sub>]<sup>3+</sup>**-Komplex, dem Prototypen dieser Emitterklasse, gezeigt werden (Kapitel 4.1.1). Aus diesem Grund ist eine vollständige Deuterierung des Liganden in vielen Fällen nicht besonders effektiv und zusätzlich manchmal synthetisch auch nicht praktikabel. Um nun herauszufinden, welche Oszillatoren ausgetauscht werden müssen, muss zunächst bekannt sein welche C-H-Oszillatoren die Lumineszenz am stärksten löschen. Mit diesem Wissen könnten neue hoch lumineszente Spin-Flip-Emitter entwickelt werden, die nur an den entscheidenden Positionen deuteriert sind und dadurch MR effektiv zu unterdrücken.

Um die MR-Raten einzelner Oszillatoren bestimmen zu können, werden neben  $k_r$  und dem Abstand  $r$  zwischen Metallzentrum und Oszillator auch die Obertonsignaturen  $\varepsilon_{\text{vib}}(\tilde{\nu})$  einzelner C-H-Oszillatoren an spezifischen Positionen des Liganden benötigt (Kapitel 4.1.1, Gl. 3-5). Die Obertonsignaturen einzelner Oszillatoren sind insbesondere für Metallkomplexe experimentell sehr schwer zugänglich und derzeit weder für Cr(III)- noch für Ln(III)-Luminophore bekannt. Daher war ein wesentliches Ziel dieses Projektes, am Modell des **[Cr(ddpd)<sub>2</sub>]<sup>3+</sup>**-Komplexes eine Methode zu entwickeln, um die Obertonsignaturen  $\varepsilon_{\text{vib}}(\tilde{\nu})$  von spezifischen aromatischen C-H-Oszillatoren des Liganden zu bestimmen. Dazu sollten zunächst selektiv deuterierte **[Cr(ddpd)<sub>2</sub>]<sup>3+</sup>**-Komplexe dargestellt werden, bei welchen an den terminalen Pyridineinheiten des **ddpd**-Liganden nur noch ein C-H-Oszillator vorhanden ist und alle übrigen aromatischen C-H-Oszillatoren vollständig durch C-D-Oszillatoren ausgetauscht wurden. So sind beispielsweise in **[6,6''-H<sub>4</sub>-D<sub>24</sub>]-Cr** (Abb. 23) die aromatischen Protonen der Positionen 3-5 der äußeren Pyridine



weitestgehend deuteriert und es ist nur noch der C-H-Oszillator in 6-Position (**C-H<sup>6</sup>**) existent.

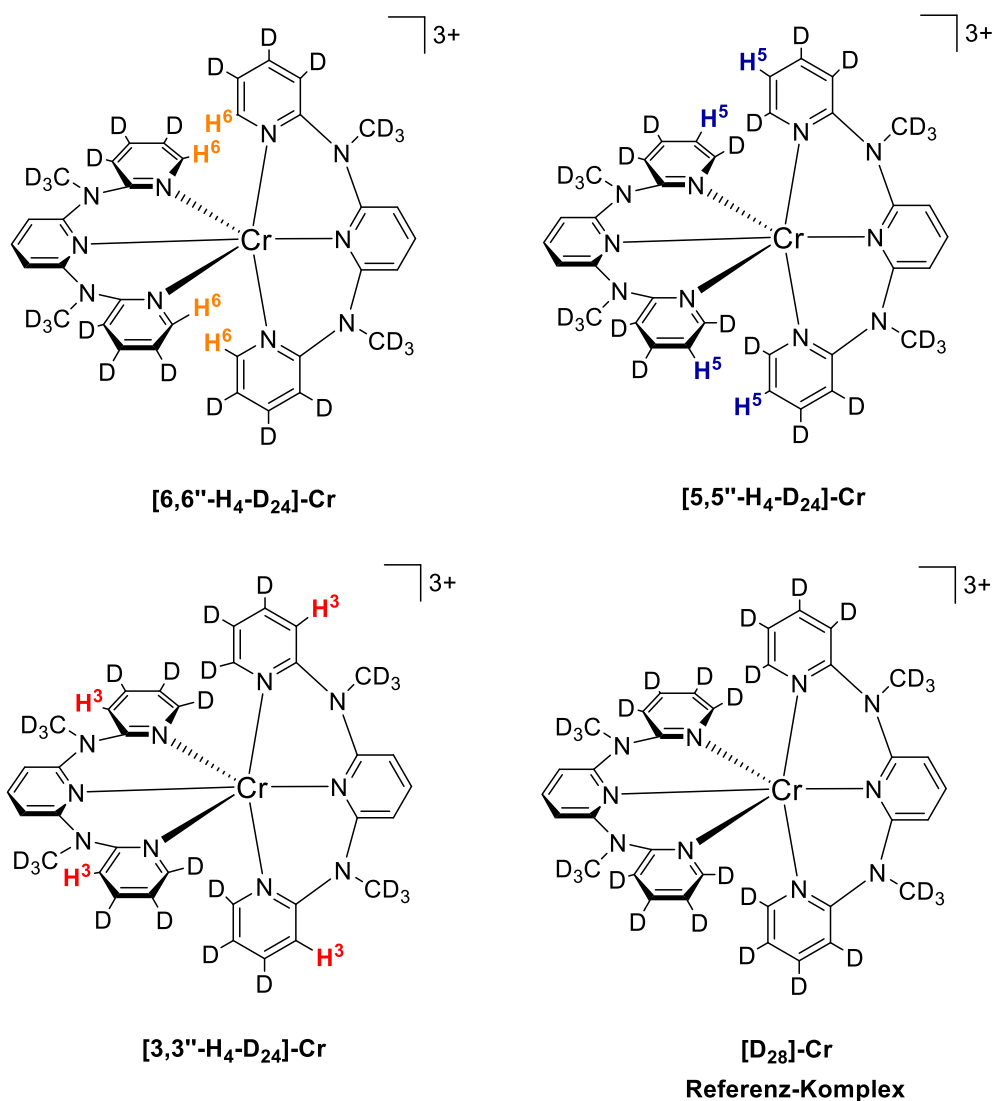


**Abb. 23:** Strukturformeln der selektiv deuterierten, isotopomeren Cr(III)-Komplexe **[6,6''-H<sub>4</sub>-D<sub>24</sub>]-Cr**, **[5,5''-H<sub>4</sub>-D<sub>24</sub>]-Cr** und **[3,3''-H<sub>4</sub>-D<sub>24</sub>]-Cr** mit jeweils nur einem C-H-Oszillator an den terminalen Pyridinen und des isotopologen Referenz-Komplexes **[D<sub>28</sub>]-Cr**, bei welchem die terminalen Pyridine vollständig deuteriert sind.

Bei den zu **[6,6''-H<sub>4</sub>-D<sub>24</sub>]-Cr** isotopomeren Komplexen **[5,5''-H<sub>4</sub>-D<sub>24</sub>]-Cr** und **[3,3''-H<sub>4</sub>-D<sub>24</sub>]-Cr** liegen entsprechend nur die aromatischen C-H-Oszillatoren in 5,5''- (**C-H<sup>5</sup>**) bzw. 3,3''-Position (**C-H<sup>3</sup>**) der äußeren Pyridine undeuteriert vor. Während die Methylgruppen von **ddpd** ebenfalls deuteriert vorliegen, sollte auf den Austausch der aromatischen Protonen der zentralen Pyridineinheit verzichtet werden, da dieser erfahrungsgemäß nur unvollständig möglich ist. Aufgrund des sehr hohen synthetischen Aufwands wurde zudem der Komplex **[4,4''-H<sub>4</sub>-D<sub>24</sub>]-Cr** nicht dargestellt.

Als Referenzsystem sollte das isotopologe **[D<sub>28</sub>]-Cr** hergestellt werden, bei welchem die Protonen der terminalen Pyridine vollständig durch Deuterium ersetzt wurden (Abb. 23).

### Synthese der selektiv deuterierten **ddpd**-Liganden

Das Grundprinzip der Darstellung von selektiv deuterierten **ddpd**-Liganden war, diese sukzessive aus relativ einfach zugänglichen, selektiv deuterierten Bausteinen und unter Verwendung möglichst milder Reaktionsbedingungen aufzubauen, um Verlust von Deuterium oder H/D-Scrambling zu vermeiden.

Generell konnte bei der Synthese der selektiv deuterierten Pyridinbausteine in einigen Fällen auf Arbeitsvorschriften von Pavlik zurückgegriffen werden.<sup>[97]</sup> Die Syntheseroute von **[D<sub>14</sub>]-ddpd** und **[6,6''-H<sub>2</sub>-D<sub>12</sub>]-ddpd** ist in Abb. 24 dargestellt. Die Synthese von **[D<sub>14</sub>]-ddpd** beginnt ausgehend von deuteriertem Pyridin-N-oxid **[D<sub>5</sub>]-1**<sup>[98]</sup>, welches mit POCl<sub>3</sub> und in Gegenwart von Et<sub>3</sub>N selektiv in ortho-Position chloriert werden kann.<sup>[99]</sup> Nach säulenchromatographischer Aufarbeitung konnte **[D<sub>4</sub>]-2** als farblose Flüssigkeit mit einer Ausbeute von 45 % erhalten werden. Das deuterierte 2-Chlorpyridin **[D<sub>4</sub>]-2** wurde im nächsten Schritt in einer nukleophilen aromatischen Substitutionsreaktion mit 2,6-Diaminopyridin (**3**) zum Amin **[D<sub>8</sub>]-4** umgesetzt (Ausbeute: 80 %). Die genaue Auswertung der ESI-Massenspektren ergab einen sehr hohen Deuterierungsgrad von 99 %D, trotz der recht harschen und stark basischen Reaktionsbedingungen (150 °C, 7 Äquivalente NaH). Im nächsten Schritt erfolgt die Methylierung mit kommerziell erhältlichem CD<sub>3</sub>I und KOH in DMSO-d<sub>6</sub>. Nach Reinigung mittels Säulenchromatographie konnte **[D<sub>14</sub>]-ddpd** mit einer Ausbeute von 40 % und einem ebenfalls sehr hohen Gesamtdeuterierungsgrad von 99 %D (Anhang, Fig. A2) als farbloses Öl erhalten werden. Ausgehend von selektiv deuteriertem Pyridin-N-Oxid **[D<sub>3</sub>]-1**<sup>[97]</sup> an Stelle von **[D<sub>5</sub>]-1** konnte **[6,6''-H<sub>2</sub>-D<sub>12</sub>]-ddpd** in analoger Weise mit einem sehr guten Deuterierungsgrad von etwa 99 %D (Anhang, Fig. A3) erhalten werden.

Das Startmaterial bei der Synthese der beiden selektiv deuterierten **ddpd**-Liganden **[3,3''-H<sub>2</sub>-D<sub>12</sub>]-ddpd** und **[5,5''-H<sub>2</sub>-D<sub>12</sub>]-ddpd** ist undeuteriertes 3-Chlorpyridin-N-oxid **5**<sup>[97]</sup> (Abb. 25). In der ersten Reaktionsstufe erfolgte der H/D-Austausch durch Rühren des N-Oxid **5** in einem Stahlautoklaven in D<sub>2</sub>O und in Gegenwart von K<sub>2</sub>CO<sub>3</sub> für 16 h bei 190 °C.<sup>[97]</sup> Um einen möglichst hohen Deuterierungsgrad zu gewährleisten wurde das im ersten Schritt erhaltene Produkt nochmals analog umgesetzt. Für die

weitere Synthese wurden die deuterierten Bausteine 2,3- und 2,5-Dichlorpyridin **[D<sub>3</sub>]-7** und **[D<sub>3</sub>]-10** benötigt.

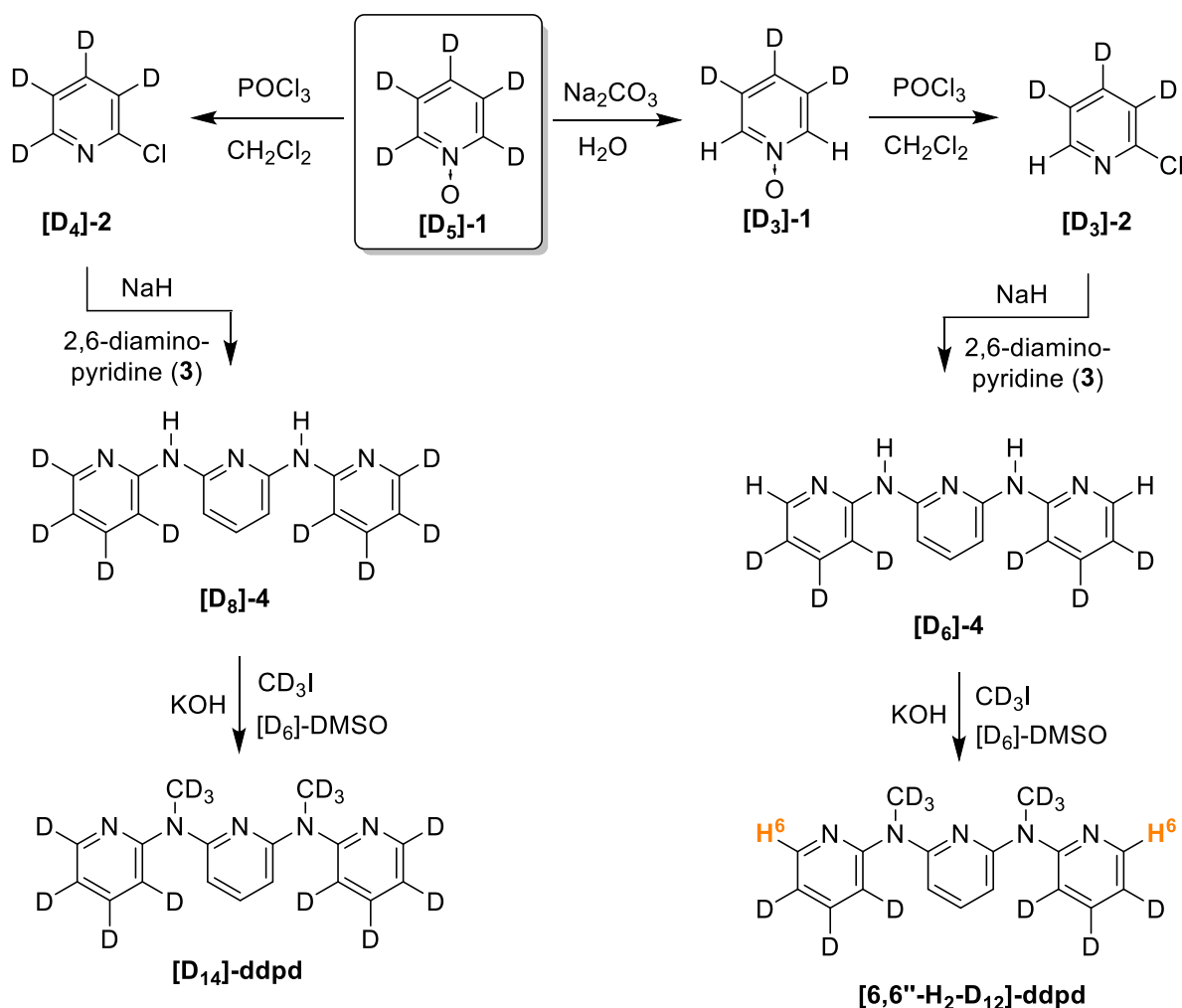


**Abb. 24:** Synthese der selektiv deuterierten **ddpd**-Liganden **[D<sub>14</sub>]-ddpd** und **[6,6''-H<sub>2</sub>-D<sub>12</sub>]-ddpd**.

Beide Verbindungen können durch die Umsetzung von **[D<sub>4</sub>]-6** mit POCl<sub>3</sub> und anschließender säulenchromatographischer Trennung als farblose Feststoffe mit hohen Deuterierungsgraden (99 %D) erhalten werden, wenn auch nur in eher geringen Ausbeuten von 11 - 26 %. Im weiteren Verlauf wurden **[D<sub>3</sub>]-7** und **[D<sub>3</sub>]-10** jeweils zu den Aminen **[D<sub>6</sub>]-8** und **[D<sub>6</sub>]-11** umgesetzt. Die Ausbeuten sind mit 80-90 % sehr gut, allerdings kommt es bei der Reaktion zu **[D<sub>6</sub>]-11** zu einem Verlust von Deuterium an der 4-Position (**C-H<sup>4</sup>**). ESI-Massenspektrometrie und <sup>1</sup>H-NMR-Spektroskopie ergab für **[D<sub>6</sub>]-11** einen Gesamtdeuterierungsgrad von 85 %D, wobei der Oszillator **C-H<sup>4</sup>** noch zu 60 % deuteriert vorliegt. Der Gesamtdeuterierungsgrad von **[D<sub>6</sub>]-8** dagegen liegt bei hohen 97 %D. Nach Methylierung mit CD<sub>3</sub>I folgt im letzten Reaktionsschritt die

palladiumkatalysierte Hydrierung der C-Cl-Bindung von **[D<sub>12</sub>]-9** und **[D<sub>12</sub>]-12** im Autoklaven bei 5 bar Wasserstoff.<sup>[97]</sup> Nach säulenchromatographischer Aufreinigung konnten die Zielliganden **[3,3''-H<sub>2</sub>-D<sub>12</sub>]-ddpd** (67 % Ausbeute, 97 %D, Anhang, Fig. A4) und **[5,5''-H<sub>2</sub>-D<sub>12</sub>]-ddpd** (73 % Ausbeute, 92 %D, Anhang, Fig. A5) als leicht gelbliche Öle erhalten werden.

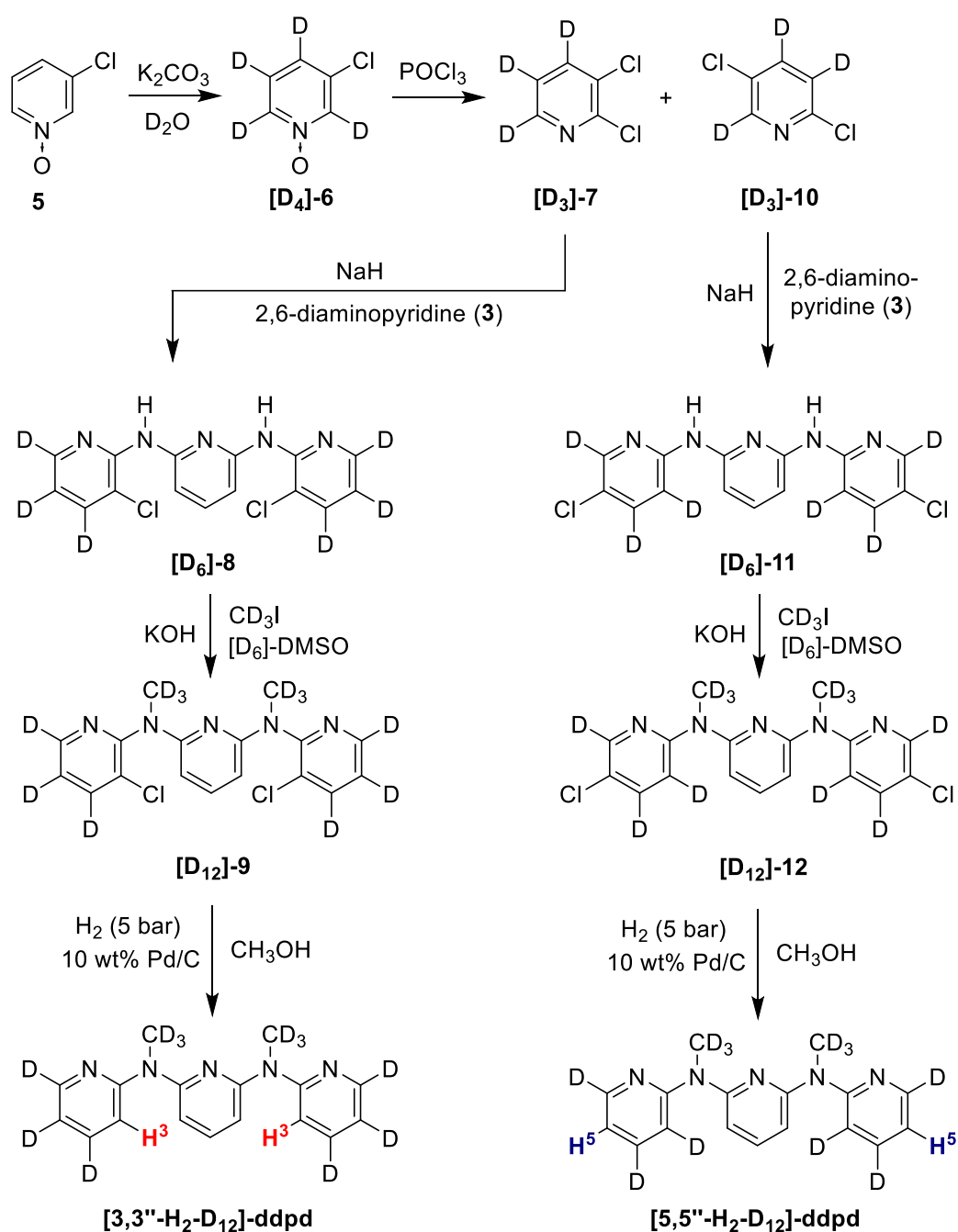


**Abb. 25:** Synthese der selektiv deuterierten **ddpd**-Liganden **[3,3''-H<sub>2</sub>-D<sub>12</sub>]-ddpd** und **[5,5''-H<sub>2</sub>-D<sub>12</sub>]-ddpd**.

## Synthese der selektiv deuterierten Chromkomplexe

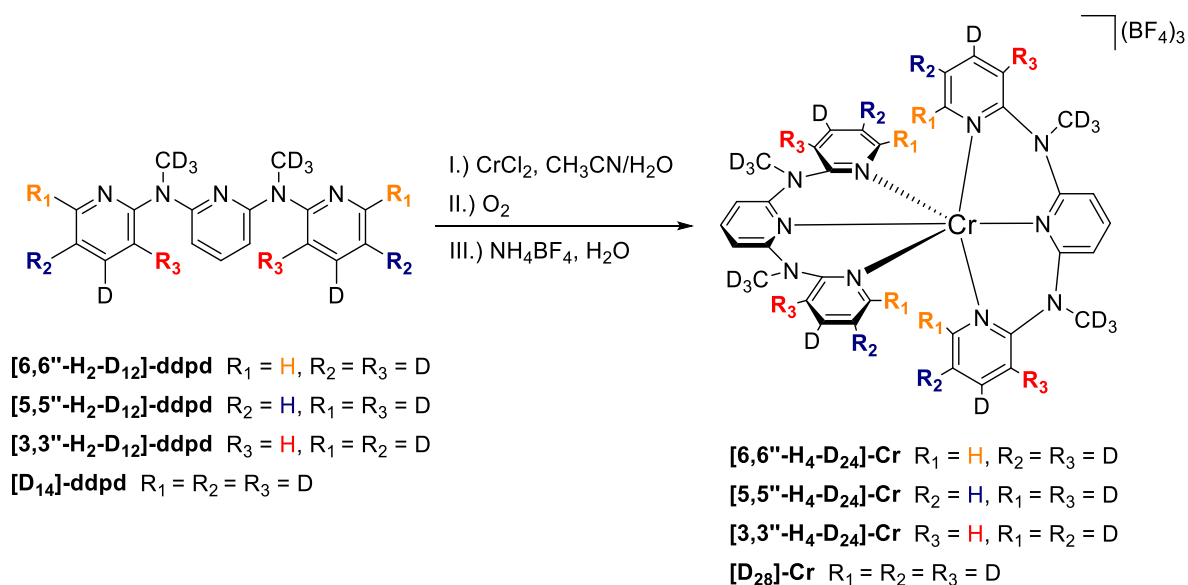


**Abb. 26:** Darstellung der selektiv deuterierten Cr(III)-Komplexe **[6,6''-H<sub>4</sub>-D<sub>24</sub>]-Cr**, **[5,5''-H<sub>4</sub>-D<sub>24</sub>]-Cr**, **[3,3''-H<sub>4</sub>-D<sub>24</sub>]-Cr** und **[D<sub>28</sub>]-Cr**.

Die Synthese der selektiv deuterierten Chromkomplexe gelang analog zur Darstellung des undeuterierten **[Cr(ddpd)<sub>2</sub>]<sup>3+</sup>**-Komplexes durch Umsetzen von 2 Äquivalenten des selektiv deuterierten **ddpd**-Liganden mit  $\text{CrCl}_2$  in Acetonitril/Wasser-Mischungen (Abb. 26).<sup>[35]</sup> Die Auswertung der ESI-Massenspektren ergab, dass sich die Deuterierungsgrade der dargestellten Chromkomplexe und die der eingesetzten Liganden nicht unterscheiden. Es kommt daher bei der Komplexierung zu keinem Verlust an Deuterium, auch wenn bei der Synthese keine deuterierten Lösungsmittel eingesetzt wurden. Um sicherzustellen, dass sich die Geometrien der selektiv deuterierten Chromkomplexe nicht wesentlich von der Struktur des undeuterierten Komplexes unterscheiden, wurden exemplarisch Einkristalle von **[D<sub>28</sub>]-Cr** mittels Röntgendiffraktometrie vermessen. Die Röntgenstrukturanalyse (Details s. Anhang, Tab. A5) zeigte nur sehr geringe Unterschiede zwischen den Komplexgeometrien der isotopologen **[Cr(ddpd)<sub>2</sub>]<sup>3+</sup>**-Komplexe im Festkörper, weshalb die in Abb. 20 aufgeführten  $\text{Cr}\cdots\text{CH}$ -Abstände zum **ddpd**-Liganden auch für die selektiv deuterierten **[Cr(ddpd)<sub>2</sub>]<sup>3+</sup>**-Komplexe korrekt sind.

## Photophysikalische Charakterisierung

Erwartungsgemäß zeigen alle dargestellten Chrom-Komplexe unabhängig vom Deuterierungsgrad das für den  $[\text{Cr}(\text{ddpd})_2]^{3+}$ -Komplex typische Emissionsspektrum mit Emissionsmaximum bei  $\lambda_{\text{em}} = 778 \text{ nm}$  (Anhang, Fig. A6-10). Dagegen sollten sich die Lumineszenzlebenszeiten der unterschiedlich selektiv deuterierten Cr(III)-Komplexe signifikant voneinander unterscheiden, je nachdem wie effektiv die strahlungslose Deaktivierung der Spin-Flip-Zustände durch MR ist. Alle Lebenszeitmessungen wurden unter identischen Bedingungen (in n-Butyronitril Gläsern bei  $T = 77 \text{ K}$  in Gegenwart von Luftsauerstoff) durchgeführt, um zu gewährleisten, dass verschieden lange Lebenszeiten nur auf Unterschiede in der Effektivität von MR zurückzuführen sind. Die Messbedingungen wurden dabei so gewählt, dass möglichst hohe Reproduzierbarkeiten für die Lebenszeiten erhalten werden konnten. Die Messung bei  $T = 77 \text{ K}$  hat zudem den entscheidenden Vorteil, dass die Lumineszenzlöschung durch Sauerstoff nur eine untergeordnete Rolle spielt und eventuell leicht unterschiedliche Sauerstoffkonzentrationen in den Messlösungen die Ergebnisse nicht beeinflussen.

**Tab. 3:** Lumineszenzlebensdauern  $\tau$  der selektiv deuterierten Cr(III)-Komplexe  $[\text{6,6''}\text{-H}_4\text{-D}_{24}\text{]-Cr}$ ,  $[\text{5,5''}\text{-H}_4\text{-D}_{24}\text{]-Cr}$ ,  $[\text{3,3''}\text{-H}_4\text{-D}_{24}\text{]-Cr}$  und  $[\text{D}_{28}\text{]-Cr}$  in n-Butyronitril bei  $T = 77 \text{ K}$  an Luft. Die angegebenen Cr...H-Abstände zum **ddpd**-Liganden wurden ermittelt an einer, mittels DFT optimierten, Struktur von  $[\text{D}_0\text{]-[Cr}(\text{ddpd})_2]^{3+}$ .<sup>[37]</sup>

Verbindung	$\tau$ (780 nm) [ms] <sup>a</sup> ${}^2\text{E}_g \rightarrow {}^4\text{A}_{2g}$	$r_{\text{Cr}\cdots\text{H}}$ [Å]
$[\text{Cr}(\text{ddpd})_2]^{3+}$	1.4	
$[\text{6,6''}\text{-H}_4\text{-D}_{24}\text{]-Cr}$	2.0	<b>3.0</b>
$[\text{5,5''}\text{-H}_4\text{-D}_{24}\text{]-Cr}$	3.2	<b>5.2</b>
$[\text{3,3''}\text{-H}_4\text{-D}_{24}\text{]-Cr}$	3.5	<b>5.2</b>
$[\text{D}_{28}\text{]-Cr}$	4.5	

<sup>a</sup> $\lambda_{\text{ex}} = 435 \text{ nm}$ , Lebensdauern wurden monoexponentiell angepasst.

In Tab. 3 sind die Lebenszeiten der Spin-Flip-Emission bei  $\lambda_{\text{em}} = 780 \text{ nm}$  der isotopologen und isotopomeren  $[\text{Cr}(\text{ddpd})_2]^{3+}$ -Komplexe aufgeführt. Alle gemessenen

Lebenszeiten konnten monoexponentiell angepasst werden. Wie zu erwarten, unterscheiden sich die gemessenen Lebenszeiten der Komplexe in Abhängigkeit vom Deuterierungsmuster beachtlich. Der undeuterierte **[Cr(ddpd)<sub>2</sub>]<sup>3+</sup>**-Komplex weist unter den gewählten Bedingungen mit  $\tau = 1.4$  ms die kürzeste Lebenszeit auf. Die Lebenszeiten der selektiv deuterierten, isotopomeren Komplexe **[6,6''-H<sub>4</sub>-D<sub>24</sub>]-Cr**, **[5,5''-H<sub>4</sub>-D<sub>24</sub>]-Cr** und **[3,3''-H<sub>4</sub>-D<sub>24</sub>]-Cr** zeigen, dass MR umso effektiver ist, je kürzer der räumliche Abstand zwischen dem C-H-Oszillator und photoaktiven Cr<sup>3+</sup>-Zentrum ist. So weist **[6,6''-H<sub>4</sub>-D<sub>24</sub>]-Cr**, bei welchem der Oszillator **C-H<sup>6</sup>** mit dem geringsten Abstand zum Chromzentrum (3 Å) nicht deuteriert ist, auch die zweitkürzeste Lebenszeit ( $\tau = 2.0$  ms) auf. Die Komplexe **[5,5''-H<sub>4</sub>-D<sub>24</sub>]-Cr** und **[3,3''-H<sub>4</sub>-D<sub>24</sub>]-Cr** deren C-H-Oszillatoren an den äußeren Pyridinen **C-H<sup>5</sup>** und **C-H<sup>3</sup>** den gleiche Abstand (5.2 Å) zum Cr(III)-Ion haben, besitzen mit  $\tau = 3.2$  und  $\tau = 3.5$  ms auch sehr ähnliche Lebenszeiten. Da die Effektivität von MR aber auch maßgeblich von anderen Faktoren wie dem spektralen Überlapp mit der Chromemissionsbande (SOI) abhängt (Gl. 3), sind die Unterschiede zwischen den Lebenszeiten geringer, als man auf Grund der Abstandsbeziehung für Dipol-Dipol-Wechselwirkungen ( $k_{nr} \sim r^{-6}$ ) erwarten würde. Der an den äußeren Pyridineinheiten vollständig deuterierte Referenzkomplex **[D<sub>28</sub>]-Cr** weist mit  $\tau = 4.5$  ms erwartungsgemäß die längste Lebenszeit auf.

### Messung der C-H-Obertöne

Mit den selektiv deuterierten **ddpd**-Liganden und **[Cr(ddpd)<sub>2</sub>]<sup>3+</sup>**-Komplexen in Händen sollten im Anschluss an die photophysikalische Charakterisierung nun die Obertonsignaturen der einzelnen aromatischen C-H-Obertöne bestimmt werden. Dazu sollten zunächst NIR-Absorptionsspektren für die Liganden **[6,6''-H<sub>2</sub>-D<sub>12</sub>]-ddpd**, **[5,5''-H<sub>2</sub>-D<sub>12</sub>]-ddpd**, **[3,3''-H<sub>2</sub>-D<sub>12</sub>]-ddpd** und **[D<sub>14</sub>]-ddpd** im erwarteten Wellenlängenbereich der C-H-Obertöne aufgenommen werden. Solche Messungen sind durchaus herausfordernd, weil bei der experimentellen Bestimmung der C-H-Obertonbanden mehrere intrinsischen Probleme auftreten. So sind beispielsweise die Extinktionskoeffizienten insbesondere für höhere Obertöne sehr klein ( $\epsilon < 10^{-3} \text{ M}^{-1} \text{ cm}^{-1}$ ), weshalb auch recht hohe Substanzmengen benötigt werden, um ausreichend konzentrierte Lösungen ( $c \approx 0.3 - 0.4 \text{ M}$ ) herstellen zu können. Zudem ist man bei der Wahl des Lösungsmittels stark eingeschränkt, weil ein Lösungsmittel gebraucht wird, welches nicht selbst im erwarteten

Wellenlängenbereich der C-H-Obertöne absorbiert. Insbesondere Lösungsmittel mit C-H-, O-H- oder O-D-Oszillatoren sind für solche Obertonmessungen ungeeignet. Für die selektiv deuterierten **ddpd**-Liganden konnten quantitative Absorptionsmessungen der aromatischen C-H-Obertöne in CDCl<sub>3</sub> bis zum dritten Oberton ( $\nu_{\text{C-H}}^2 - \nu_{\text{C-H}}^4$ ) durchgeführt werden (Anhang, Fig. A17-25). Exemplarisch ist in Abb. 27 die Messung für **[3,3''-H<sub>2</sub>-D<sub>12</sub>]-ddpd** gezeigt.

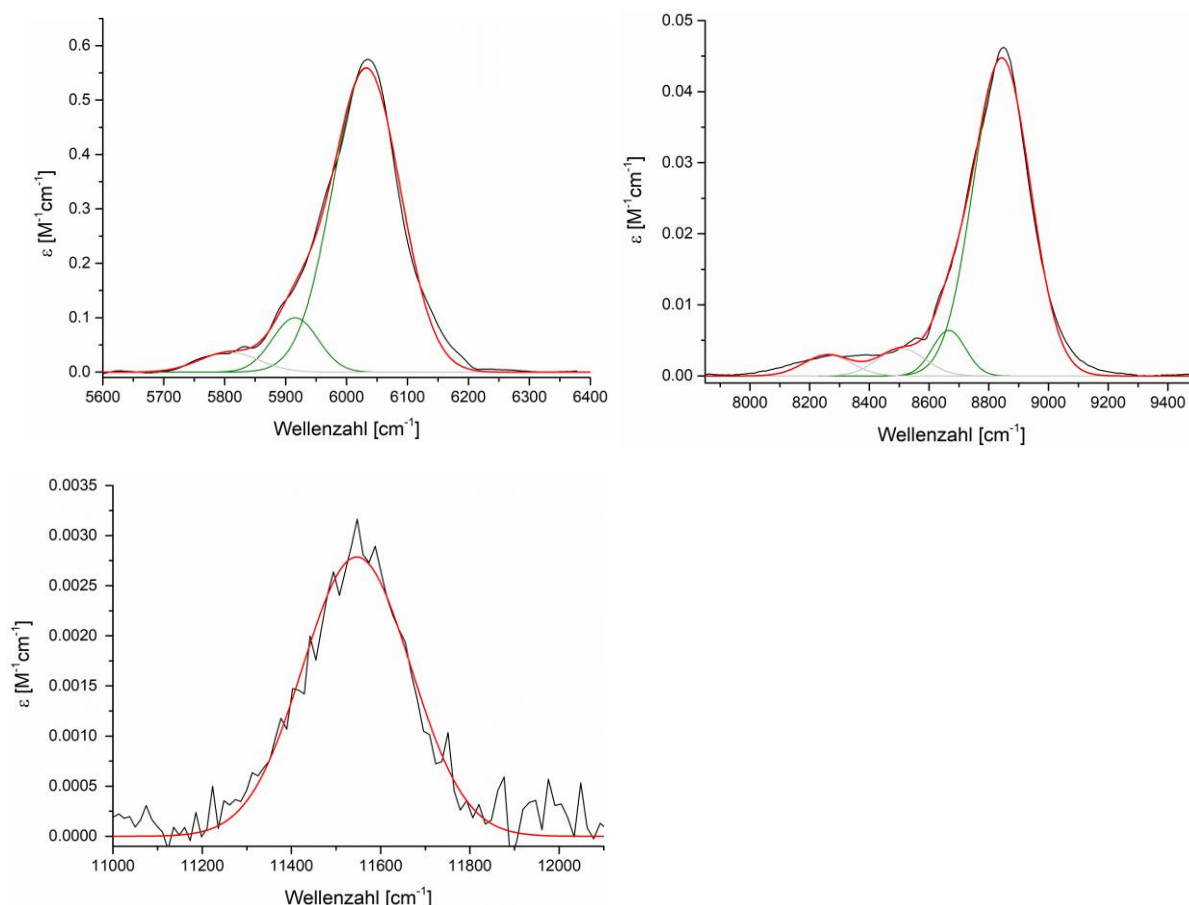


**Abb. 27:** NIR-Absorptionsspektren von **[3,3''-H<sub>2</sub>-D<sub>12</sub>]-ddpd** (schwarz) in CDCl<sub>3</sub> ( $c = 429 \text{ mM}$ , Küvettenlänge  $d = 1.0 \text{ cm}$  für  $\nu_{\text{C-H}}^2$  und  $d = 5.0 \text{ cm}$  für  $\nu_{\text{C-H}}^3$  und  $\nu_{\text{C-H}}^4$  der Obertöne  $\nu_{\text{C-H}}^2$  (oben links),  $\nu_{\text{C-H}}^3$  (oben rechts) und  $\nu_{\text{C-H}}^4$  (unten links) gefittet mit Gaussfunktionen (grün: einzelne Gaussfunktionen, die aromatischen C-H-Oszillatoren zugeordnet werden konnten, grau: einzelne Gaussfunktionen, die nicht aromatischen C-H-Oszillatoren zugeordnet werden konnten, rot: Summe aller Gaussfunktionen).

Die erhaltenen Absorptionsspektren wurden dabei im ersten Schritt basislinienkorrigiert (Abb. 27, schwarz) und anschließend mit einer Serie von Gaussfunktionen gefittet, um die Obertonsignaturen der aromatischen C-H-Oszillatoren zu ermitteln. Die so extrahierten zuordenbaren Absorptionsbanden (Abb. 27, Summe der grün dargestellten Gaussfunktionen) setzen sich jeweils aus den



Beiträgen aller aromatischen C-H-Oszillatoren des jeweiligen **ddpd**-Liganden zusammen. So setzen sich die extrahierten Absorptionsbanden der aromatischen C-H-Obertöne von **[3,3''-H<sub>2</sub>-D<sub>12</sub>]-ddpd** (Abb. 28, grün und Abb. 27, Summe der grün dargestellten Gaussfunktionen) zusammen aus der Absorption der zentralen Pyridineinheit und der Absorption der terminalen Pyridine (**C-H<sup>3</sup>**, Abb. 28, rot markiert). Die entsprechenden extrahierten Absorptionsbanden von **[D<sub>14</sub>]-ddpd** (Abb. 28, schwarz) enthalten dagegen nur die Absorptionen der zentralen Pyridineinheit. Um nun die Obertonsignatur der einzelnen C-H-Oszillatoren **C-H<sup>3</sup>** zu extrahieren, wird das Differenzspektrum (Abb. 28, rot) aus den extrahierten Absorptionsbanden von **[3,3''-H<sub>2</sub>-D<sub>12</sub>]-ddpd** und denen von **[D<sub>14</sub>]-ddpd** gebildet. Dieses Differenzspektrum sollte also nur noch die Beiträge der aromatischen **C-H<sup>3</sup>**-Oszillatoren enthalten und stellt damit die Obertonsignatur  $\varepsilon_{\text{vib}}(\tilde{\nu})$  von **C-H<sup>3</sup>** dar.

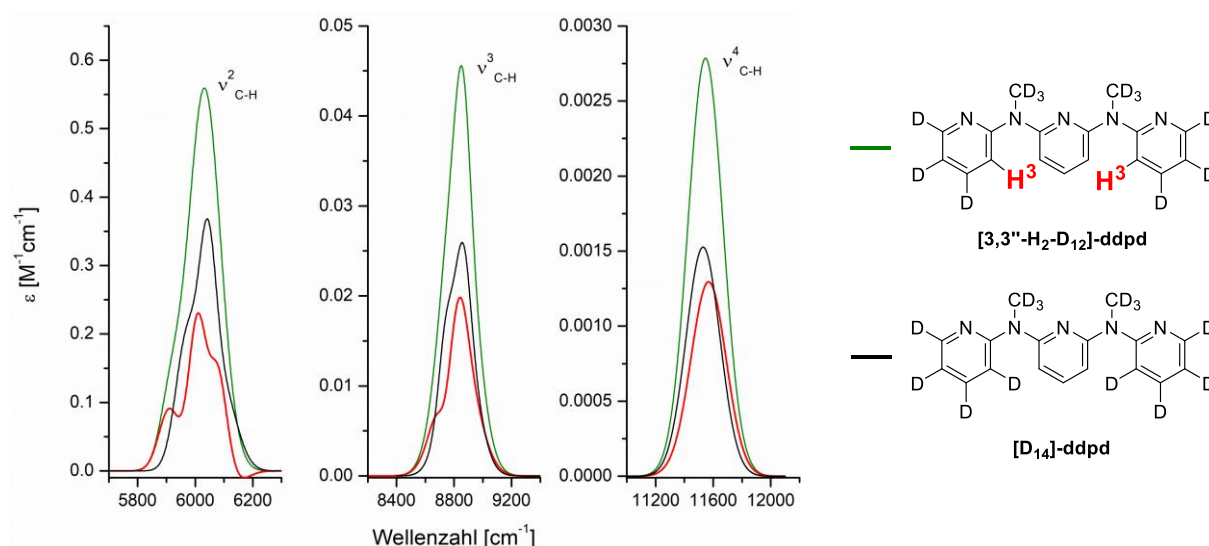


**Abb. 28:** Die aus den gemessenen NIR-Absorptionsspektren extrahierten Obertonsignaturen ( $v_{\text{C-H}}^2 - v_{\text{C-H}}^4$ ) der aromatischen C-H-Oszillatoren von **[3,3''-H<sub>2</sub>-D<sub>12</sub>]-ddpd** (grün), die entsprechend extrahierten Obertonsignaturen von **[D<sub>14</sub>]-ddpd** (schwarz) und das Differenzspektrum aus den letztgenannten Absorptionsspektren, welches die Obertonsignaturen der einzelnen aromatischen C-H-Oszillatoren **C-H<sup>3</sup>** (rot) darstellt.

Diese Methodik konnte ebenfalls auf die NIR-Absorptionsspektren von **[6,6''-H<sub>2</sub>-D<sub>12</sub>]-ddpd** und **[5,5''-H<sub>2</sub>-D<sub>12</sub>]-ddpd** angewendet und so die Obertonsignaturen der aromatischen C-H-Oszillatoren **C-H<sup>6</sup>** und **C-H<sup>5</sup>** erhalten werden. In Abb. 29 sind die Obertonsignaturen der ersten drei Obertöne ( $v_{\text{C-H}}^2 - v_{\text{C-H}}^4$ ) der Oszillatoren **C-H<sup>6</sup>**, **C-H<sup>5</sup>** und **C-H<sup>3</sup>** dargestellt. Man erkennt deutlich, dass sich die Obertonsignaturen der C-H-Oszillatoren an unterschiedlichen aromatischen

Positionen in Form, Amplitude und energetischer Lage voneinander unterscheiden. Während die Energien der Obertonbanden der Oszillatoren **C-H<sup>3</sup>** und **C-H<sup>5</sup>** sehr ähnlich sind, sind die Energien der Obertöne von **C-H<sup>6</sup>** um ca. 100 – 300 cm<sup>-1</sup> (je nach Oberton) zu geringerer Energie verschoben.

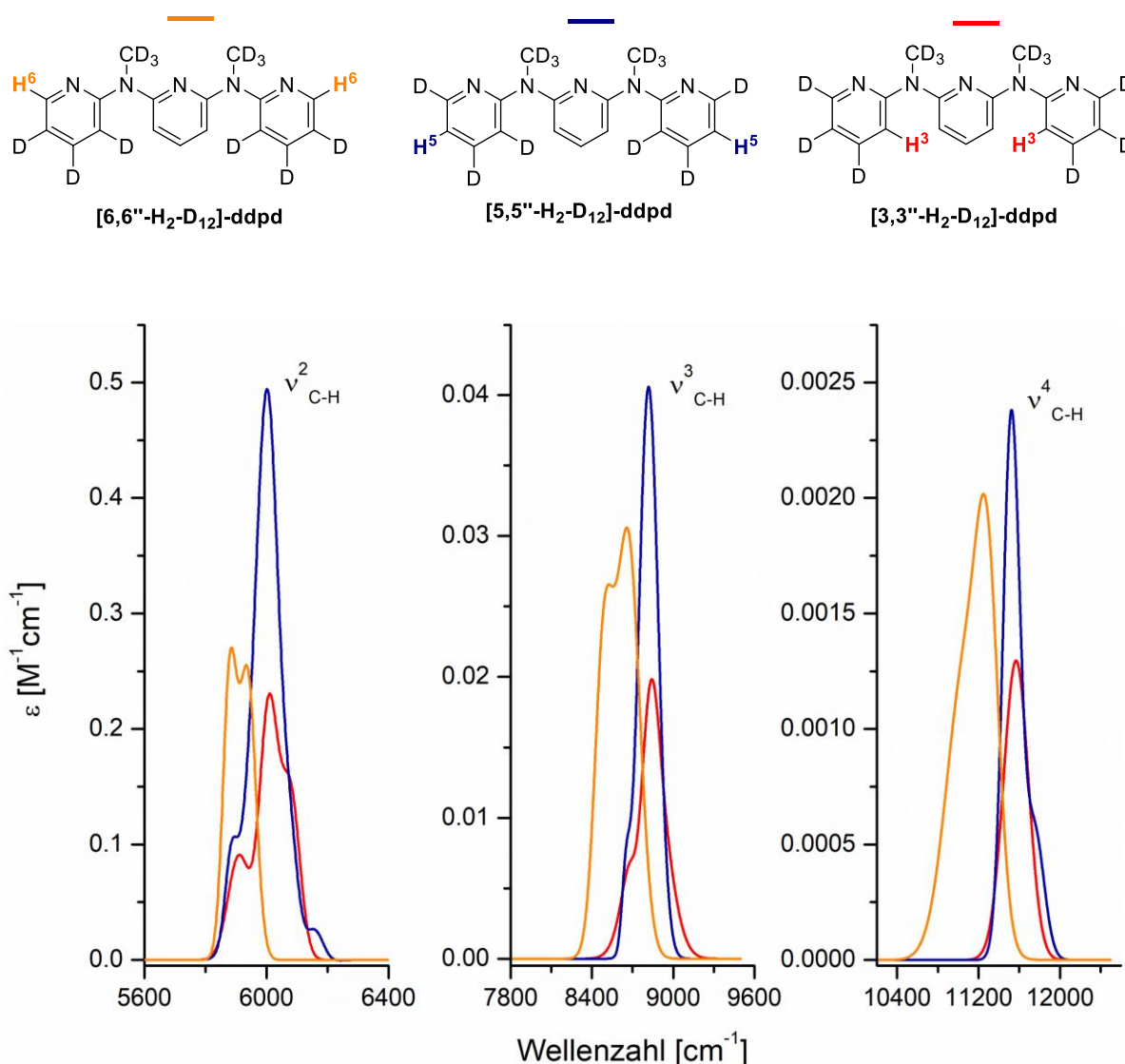


**Abb. 29:** Darstellung der Obertonsignaturen der ersten drei Obertöne ( $v_{\text{C-H}}^2 - v_{\text{C-H}}^4$ ) der aromatischen C-H-Oszillatoren **C-H<sup>6</sup>** (orange), **C-H<sup>5</sup>** (lila) und **C-H<sup>3</sup>** (rot).

Dieser Befund ist im Einklang mit entsprechenden Untersuchungen an einfachen Pyridinen, bei welchen die C-H-Oszillatoren in ortho-Position ebenfalls zu niedrigeren Wellenzahlen verschoben sind.<sup>[93]</sup> Die Amplituden der Obertonbanden von **C-H<sup>5</sup>** sind im Vergleich zu den Amplituden der Absorptionsbanden von **C-H<sup>3</sup>** und **C-H<sup>6</sup>** deutlich größer. Begründet werden kann dies hauptsächlich durch die unvollständige Deuterierung der **C-H<sup>4</sup>**-Oszillatoren von **[5,5''-H<sub>2</sub>-D<sub>12</sub>]-ddpd**. Als Folge davon

enthalten die Obertonsignaturen von **C-H<sup>5</sup>** zusätzlich auch Beiträge von **C-H<sup>4</sup>**, was sich am deutlichsten in größeren Amplituden widerspiegelt. Da sich die Obertonsignaturen der C-H-Oszillatoren an unterschiedlichen aromatischen Positionen voneinander unterscheiden, überlappen diese auch unterschiedlich mit der Emissionsbande von **[Cr(ddpd)<sub>2</sub>]<sup>3+</sup>**. Die daraus resultierenden unterschiedlichen SOIs sollten sich nach Gl. 3 direkt auf die Effektivität von MR auswirken.

Neben den selektiv deuterierten **ddpd**-Liganden wurden ebenfalls quantitative Absorptionsmessungen der aromatischen C-H-Obertöne der entsprechenden **[Cr(ddpd)<sub>2</sub>]<sup>3+</sup>**-Komplexe in deuteriertem CD<sub>3</sub>CN (99.9 %D) durchgeführt. Bei diesen Messungen hat man aber mit einigen experimentellen Herausforderungen zu kämpfen. So reicht beispielsweise die Löslichkeit der Komplexe in einem geeigneten Lösungsmittel nicht aus, um die sehr intensitätsschwachen, höheren Obertöne so zuverlässig messen zu können, dass eine verlässliche Auswertung der Daten möglich war. Daher wurden aus Praktikabilitätsgründen für die nachfolgende Berechnung der SOIs der einzelnen aromatischen C-H-Oszillatoren die Daten der **ddpd**-Liganden herangezogen.

### Berechnung der spektralen Überlappungsintegrale (SOIs)

Für die Berechnung der spektralen Überlappungsintegrale zwischen der Obertonabsorption von **ddpd** und der Spin-Flip-Emission von **[Cr(ddpd)<sub>2</sub>]<sup>3+</sup>** (ca. 11500 - 14000 cm<sup>-1</sup>) werden die Absorptionsbanden  $\varepsilon_{\text{vib}}(\tilde{\nu})$  des dritten ( $\nu_{\text{C-H}}^4$ ) und vierten Obertons ( $\nu_{\text{C-H}}^5$ ) der C-H-Oszillatoren **C-H<sup>6</sup>**, **C-H<sup>5</sup>** und **C-H<sup>3</sup>** benötigt. Allerdings konnten wegen der extrem kleinen Extinktionskoeffizienten nur die Obertonbanden bis zum dritten Oberton ( $\nu_{\text{C-H}}^4$ ) zuverlässig gemessen werden. Um nun trotzdem die SOIs mit der Chromemission bestimmen zu können, wurde die Obertonbande des vierten C-H-Obertons ( $\nu_{\text{C-H}}^5$ ) mit Hilfe der Obertondaten der verlässlich messbaren, niedrigeren C-H-Obertöne ( $\nu_{\text{C-H}}^2 - \nu_{\text{C-H}}^4$ ) ermittelt. Dazu wurde zunächst jede Obertonbande mit nur einer Gaussfunktion der Form  $y(x) = A \cdot e^{\left(-\frac{1}{2} \left(\frac{x-x_c}{\sigma}\right)^2\right)}$  gefittet. Dabei ist A die Amplitude,  $x_c$  die Schwerpunktwellenzahl und  $\sigma$  die Breite. Extrapolation der drei Gaussparameter ermöglichte dann die Berechnung der Absorptionsbanden höherer Obertöne. So können die Obertonpositionen  $x_c$  mit der passenden Morse-Beziehung (Gl. 1) im Rahmen des local-mode Morse-Modells mit Hilfe von Birge-

Sponer-Plots ermittelt werden. Zur Bestimmung der Morse-Parameter  $\tilde{\nu}_0$  (Fundamentalfrequenz) und  $x$  (Anharmonizitätsparameter) wird dabei zunächst im Birge-Sponer-Plot ( $\tilde{\nu}/\nu$ ) gegen  $(\nu+1)$  aufgetragen (Abb. 30, links oben). Die lineare Regression liefert dann  $\tilde{\nu}_0$  als y-Achsenabschnitt und  $-x$  als Steigung der Ausgleichsgeraden. Die Gaussamplitude  $A$  des vierten C-H-Obertons ( $\nu_{\text{C-H}}^5$ ) kann aus der linearen Regression der Auftragung von  $\log(A)$  gegen die Vibrationsquantenzahl  $\nu$  (Abb. 30, links unten) und die Gaussbreite  $\sigma$  von  $\nu_{\text{C-H}}^5$  aus der linearen Regression der Auftragung von  $\sigma$  gegen die Vibrationsquantenzahl  $\nu$  (Abb. 30, unten rechts) errechnet werden. Eine Übersicht der Gaussparameter für die Oszillatoren **C-H<sup>6</sup>**, **C-H<sup>5</sup>** und **C-H<sup>3</sup>** sind dem Anhang (Anhang, Tab. A1-3) zu entnehmen.

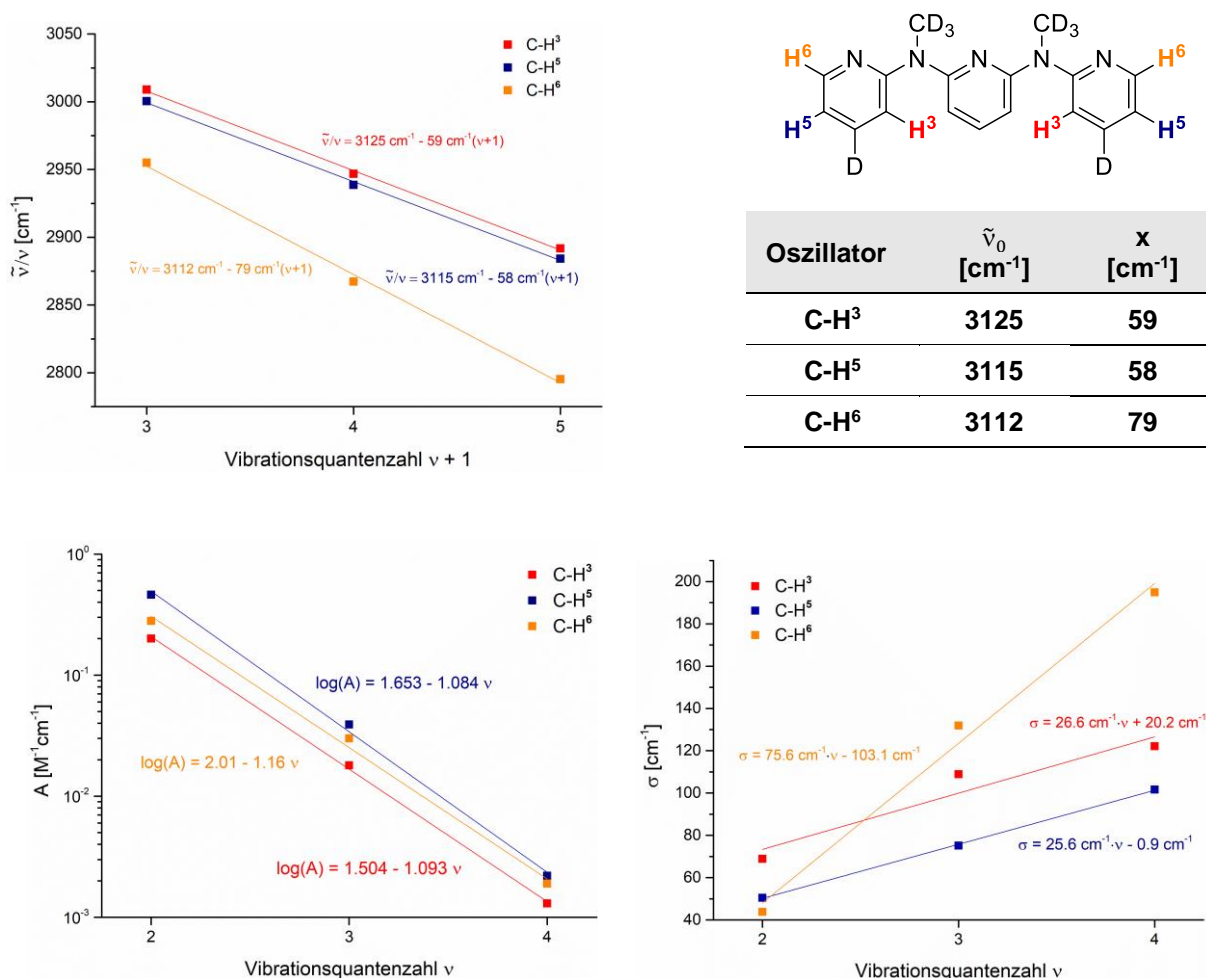


**Abb. 30:** Ermittlung der Gaussparameter für die nicht messbaren Obertöne der Oszillatoren **C-H<sup>6</sup>**, **C-H<sup>5</sup>** und **C-H<sup>3</sup>**: Birge-Sponer-Plot zur Bestimmung des Gaussparamters  $x_c$  (links oben), Graph der Gaussbreiten  $\sigma$  (links unten) und der semi-logarithmische Plot der Gaussamplituden  $A$  (rechts unten) jeweils mit linearen Regressionen. Tabelle mit den Fundamentalfrequenzen  $\tilde{\nu}_0$  und Anharmonizitätsparametern  $x$  der individuellen aromatischen Oszillatoren.

Die Fundamentalfrequenzen  $\tilde{\nu}_0$  von **C-H<sup>6</sup>**, **C-H<sup>5</sup>** und **C-H<sup>3</sup>** (Abb. 30) sind für alle drei aromatischen C-H-Oszillatoren sehr ähnlich und liegen im üblichen Bereich für Pyridine zwischen 3112 - 3125  $\text{cm}^{-1}$ .<sup>[94,100]</sup> Die ermittelten Anharmonizitätsparameter offenbaren dagegen Auffälligkeiten (Abb. 30, Tabelle). Während die Anharmonizitäten von **C-H<sup>5</sup>** und **C-H<sup>3</sup>** mit  $x = 58$  und  $59 \text{ cm}^{-1}$  im erwarteten Bereich für aromatische C-H-Oszillatoren liegen, sind die Oszillatoren **C-H<sup>6</sup>** mit  $x = 79 \text{ cm}^{-1}$  ungewöhnlich stark anharmonisch. Dieser Wert grenzt sich stark von Literaturdaten von einfacher substituierten Pyridinen (z.B. 2-Methylpyridin) ab, bei welchen die C-H-Oszillatoren in ortho-Position üblicherweise Anharmonizitäten von  $x = 60 - 62 \text{ cm}^{-1}$ <sup>[94,100]</sup> aufweisen. Wegen des stark anharmonischen Charakters von **C-H<sup>6</sup>** im Vergleich zu **C-H<sup>5</sup>** und **C-H<sup>3</sup>**, sollte die strahlungslose Deaktivierung der Spin-Flip-Zustände durch **C-H<sup>6</sup>** effektiver sein. Dies ist sehr wahrscheinlich neben dem geringen räumlichen Abstand von **C-H<sup>6</sup>** zum  $\text{Cr}^{3+}$ -Zentrum ein weiterer Grund warum **[6,6''-H<sub>4</sub>-D<sub>24</sub>]-Cr** von den selektiv deuterierten, isotopomeren **[Cr(ddpd)<sub>2</sub>]<sup>3+</sup>**-Komplexen die kürzeste Lebenszeit aufweist.

Mit den Obertonsignaturen  $\varepsilon_{\text{vib}}(\tilde{\nu})$  des dritten und vierten Obertons von **C-H<sup>6</sup>**, **C-H<sup>5</sup>** und **C-H<sup>3</sup>** können jetzt die SOIs mit der Chromemission gemäß Gl. 4 u. 5 berechnet werden. Abb. 31 zeigt das Integral (SOI) mit der Spin-Flip-Emission von **[Cr(ddpd)<sub>2</sub>]<sup>3+</sup>** und des vierten und fünften Obertons des Oszillators **C-H<sup>3</sup>**. Entsprechende Abbildungen der SOIs für die Oszillatoren **C-H<sup>5</sup>** und **C-H<sup>6</sup>** sind im Anhang (Fig. A26+27) dargestellt.

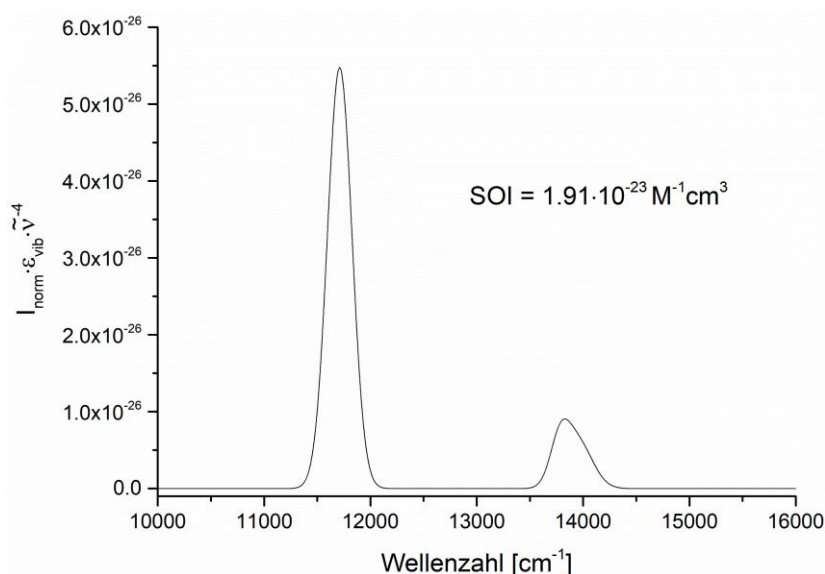


**Abb. 31:** Integralfunktion des spektralen Überlappungsintegrals (SOI) der Spin-Flip-Emission von **[Cr(ddpd)<sub>2</sub>]<sup>3+</sup>** und des vierten und fünften Obertons ( $\nu_{\text{C-H}}^4 + \nu_{\text{C-H}}^5$ ) des Oszillators **C-H<sup>3</sup>**.

In Tab. 4 sind die SOIs für die einzelnen aromatischen C-H-Oszillatoren aufgeführt. Die sich ergebenden SOIs der Oszillatoren **C-H<sup>3</sup>** und **C-H<sup>5</sup>** sind dabei nahezu identisch. Dies ist auch plausibel, da auch die für die Berechnung der SOIs maßgebenden Obertonsignaturen dieser beiden Oszillatoren in Energie und Breite nur wenig voneinander abweichen (Abb. 29). Die Absorptionsbanden der Obertöne von **C-H<sup>6</sup>** dagegen sind, wie bereits oben beschrieben, relativ zu den Obertonbanden von **C-H<sup>3</sup>** und **C-H<sup>5</sup>** zu kleineren Wellenzahlen verschoben und zusätzlich auch noch deutlich breiter (Abb. 29). Beides führt dazu, dass die spektrale Überlappung der Obertöne von **C-H<sup>6</sup>** mit der Chrom-Emission im Vergleich zu den SOIs mit den Obertönen von **C-H<sup>3</sup>** und **C-H<sup>5</sup>** um etwa den Faktor 5 größer ist (Tab. 4). Da das SOI nach Gl. 3 direkt proportional zur strahlungslosen Deaktivierungsrate  $k_{nr}$  ist, löscht **C-H<sup>6</sup>** die Spin-Flip-Emission von **[Cr(ddpd)<sub>2</sub>]<sup>3+</sup>** sehr viel effektiver als die Oszillatoren **C-H<sup>3</sup>** und **C-H<sup>5</sup>**. Anders ausgedrückt würde auf Basis der SOI-Berechnung die Deuterierung von **C-H<sup>6</sup>** die strahlungslose Deaktivierung durch MR im Vergleich zur Deuterierung der Oszillatoren **C-H<sup>3</sup>** oder **C-H<sup>5</sup>** effektiver reduzieren und so eine größere Steigerung der Lumineszenzlebenszeiten und Quantenausbeuten von **[Cr(ddpd)<sub>2</sub>]<sup>3+</sup>** ermöglichen.

**Tab. 4:** Spektrale Überlappungsintegrale (SOIs) der C-H-Oszillatoren **C-H<sup>6</sup>**, **C-H<sup>5</sup>** und **C-H<sup>3</sup>** des **ddpd**-Liganden mit der Spin-Flip-Emission von **[Cr(ddpd)<sub>2</sub>]<sup>3+</sup>** und dem Verhältnis der berechneten SOIs und dem SOI des Oszillators **C-H<sup>3</sup>**.

Oszillator arom.	SOI [M <sup>-1</sup> cm <sup>3</sup> ]	SOI / SOI <sub>C-H<sup>3</sup></sub>
<b>C-H<sup>3</sup></b>	<b>1.91·10<sup>-23</sup></b>	<b>1</b>
<b>C-H<sup>5</sup></b>	<b>1.74·10<sup>-23</sup></b>	<b>0.9</b>
<b>C-H<sup>6</sup></b>	<b>1.00·10<sup>-21</sup></b>	<b>5.2</b>

Im Rahmen dieses Projekts konnte erstmals am Modell des **[Cr(ddpd)<sub>2</sub>]<sup>3+</sup>**-Komplex eine Methode entwickelt werden, um die Obertonsignaturen von einzelnen aromatischen C-H-Oszillatoren eines Pyridin-Liganden für Cr(III)-Spin-Flip-Luminophore zu extrahieren. Dazu wurden zunächst selektiv deuterierte **ddpd**-Liganden und deren entsprechende **[Cr(ddpd)<sub>2</sub>]<sup>3+</sup>**-Komplexe synthetisiert. Durch Messung der NIR-Absorptionsbanden im Bereich der C-H-Obertöne und anschließende Prozessierung der gewonnenen Obertondaten konnten die Obertonsignaturen der C-H-Oszillatoren der terminalen Pyridine von **ddpd** in 6- (**C-H<sup>6</sup>**),

5- (**C-H<sup>5</sup>**) und 3-Position (**C-H<sup>3</sup>**) erhalten werden. Mit diesen Obertonsignaturen in Händen war es möglich die spektralen Überlappungsintegrale (SOIs) mit der Chrom-Emission zu berechnen und so die Effektivität der strahlungslosen Deaktivierung dieser einzelnen C-H-Oszillatoren zu bewerten. Während die Oszillatoren **C-H<sup>3</sup>** und **C-H<sup>5</sup>** auf Basis der SOIs die Chromlumineszenz ähnlich stark löschen, ist die strahlungslose Deaktivierung der Spin-Flip-Zustände durch den **C-H<sup>6</sup>**-Oszillator beträchtlich effektiver. Durch die Gewinnung der Obertonsignaturen und die Berechnung der SOIs konnten wichtige Voraussetzungen zur Berechnung der MR-Raten einzelner aromatischer C-H-Oszillatoren in molekularen Cr(III)-Emittlern geschaffen werden. Diese sind entscheidend auf dem Weg ein Modell zu entwickeln, das Voraussagen darüber erlaubt, wie sich die Deuterierung eines einzelnen aromatischen C-H-Oszillators auf die photophysikalischen Eigenschaften von Cr(III)-Komplexen mit Spin-Flip-Emission auswirkt.



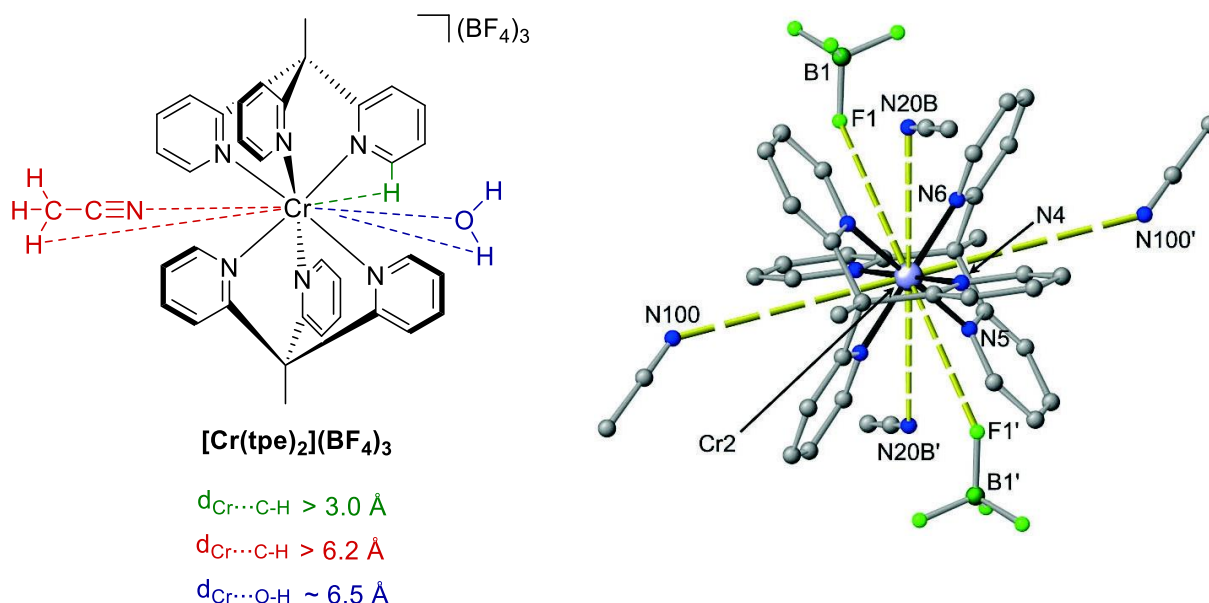


**Abb. 32:** Links: Strukturformel von **[Cr(tpe)<sub>2</sub>](BF<sub>4</sub>)<sub>3</sub>** mit den Cr···H-Abständen im Festkörper von cookristallisierenden Lösemittelmolekülen. Rechts: Molekülstruktur von **[Cr(tpe)<sub>2</sub>](BF<sub>4</sub>)<sub>3</sub>** inklusive der Lösemittelmoleküle und Gegenionen der zweiten Koordinationssphäre. Das zweite unabhängig kristallisierende Kation (mit vier BF<sub>4</sub>-Gegenionen) wurde aus Übersichtlichkeitsgründen weggelassen. Die Details zur Strukturlösung sind den HI zu entnehmen. Abbildung übernommen von Heinze.<sup>[36]</sup>

Die Röntgenstrukturanalyse an Einkristallen von **[Cr(tpe)<sub>2</sub>](BF<sub>4</sub>)<sub>3</sub>** bestätigt die erfolgreiche Darstellung des D<sub>3</sub>-symmetrischen, homoleptischen Komplexes. Das **[Cr(tpe)<sub>2</sub>]<sup>3+</sup>**-Kation weist dabei die kristallographisch auferlegte Inversionssymmetrie auf. Neben den BF<sub>4</sub>-Gegenionen besetzen auch Acetonitril Moleküle die sechs Taschen die durch die Pyridinringe des tripodalen **tpe**-Liganden aufgespannt werden (Abb. 32, rechts). In dieser zweiten Koordinationssphäre beträgt der Cr···C-H-Abstand zwischen dem Chromzentrum und den für die Schwingungsrelaxation relevanten C-H-Oszillatoren von Acetonitril etwa 6.2 Å. Im literaturbekannten low-spin Cobalt(III)-Komplex **[Co(tpe)<sub>2</sub>](ClO<sub>4</sub>)<sub>3</sub>·xH<sub>2</sub>O** sind dagegen alle Taschen ausnahmslos mit Perchlorat-Gegenionen gefüllt.<sup>[102]</sup> Der kürzeste Co···O-Abstand zu O-H-Oszillatoren von koordiniertem H<sub>2</sub>O beträgt im Festkörper ca. 6.5 Å und ist daher nur unwesentlich größer als der Cr···C-H-Abstand von koordinierendem Acetonitril in **[Cr(tpe)<sub>2</sub>]<sup>3+</sup>**. In Lösung ist zusätzlich von einer dynamischen Besetzung der Taschen insbesondere von sterisch wenig anspruchsvollen Acetonitril Molekülen auszugehen. Die Cr···C-H-Abstände von koordinierendem Acetonitril in **[Cr(tpe)<sub>2</sub>]<sup>3+</sup>** sind dabei sehr ähnlich zu denen im **[Cr(ddpd)<sub>2</sub>]<sup>3+</sup>**-Komplex, bei welchem die C-H-Oszillatoren von Acetonitril signifikant zur strahlungslosen Deaktivierung der angeregten Dublett-Zustände



beitragen und durch Verwendung von deuteriertem Acetonitril die Lebenszeit der  $^2E$ -Emission um den Faktor 1.7 gesteigert werden konnte.<sup>[37]</sup>

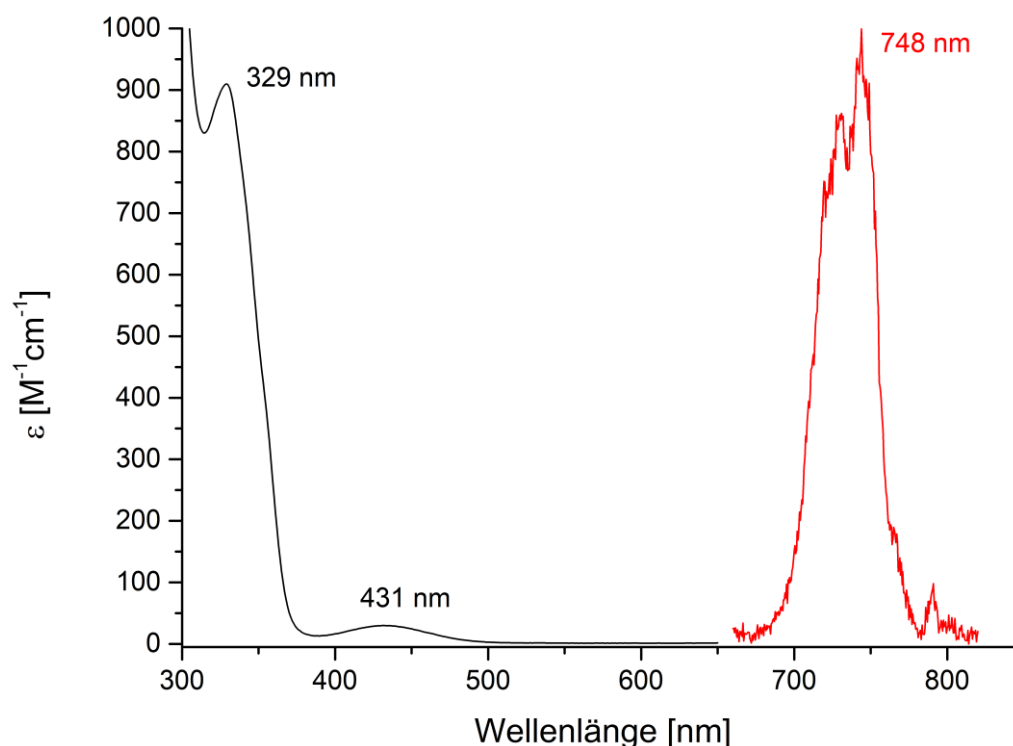


**Abb. 33:** Absorptions- (schwarz) und normiertes Emissionsspektrum (rot) von  $[\text{Cr}(\text{tpe})_2](\text{BF}_4)_3$  in  $\text{D}_2\text{O}/\text{DClO}_4$  bei Raumtemperatur ( $\lambda_{\text{exc}} = 428 \text{ nm}$ ;  $9.0 \mu\text{l DCIO}_4 \text{ mL}^{-1}$  (68 % in  $\text{D}_2\text{O}$ ) unter einer Argonatmosphäre.

Das Absorptionsspektrum von  $[\text{Cr}(\text{tpe})_2]^{3+}$  zeigt zwei prominente Banden bei 329 und 431 nm (Abb. 33, links). Die schwache Bande bei 431 nm ( $\epsilon = 30 \text{ M}^{-1}\text{cm}^{-1}$ ) kann dabei dem streng paritätsverbotenen  $^4A_{2g} \rightarrow ^4T_{2g}$  Übergang (Zustandsbezeichnungen in  $O_h$  Symmetrie) zugeordnet werden. Geometrieoptimierung mittels DFT des  $[\text{Cr}(\text{tpe})_2]^{3+}$ -Ions schlagen aber die weniger symmetrische  $D_{3d}$ -Symmetrie unter Erhalt des Inversionszentrums vor (Pub. 1: *Optical Properties* u. HI, Tab. S1). In der Punktgruppe  $D_{3d}$  spaltet der Ligandenfeldzustand  $^4T_{2g}$  ( $O_h$ ) in die Zustände  $^4E_g$  ( $D_{3d}$ ) und  $^4A_{1g}$  ( $D_{3d}$ ) auf. Wegen der Laporte-Regel sind die berechneten Oszillatorstärken der Übergänge vom Grundzustand in die Ligandenfeldzustände im zentrosymmetrischen  $[\text{Cr}(\text{tpe})_2]^{3+}$ -Komplex etwa zwei Größenordnungen kleiner (HI, Abb. S7) als die Intensität der Absorption der entsprechenden Bande bei 435 nm im nicht zentrosymmetrischen  $[\text{Cr}(\text{ddpd})_2]^{3+}$ -Komplex.<sup>[35]</sup> Dagegen liegt die Ligandenfeldaufspaltung in  $[\text{Cr}(\text{tpe})_2]^{3+}$  mit  $\Delta_o = 23200 \text{ cm}^{-1}$  in einem sehr ähnlichen Bereich. Die Anregung in die Ligandenfeldzustände  $^4A_{1g}$  ( $D_{3d}$ ) und  $^4E_g$  ( $D_{3d}$ ) bei  $\lambda_{\text{ex}} = 428 \text{ nm}$  und darauffolgendes

Intersystem Crossing in die Dublett-Zustände resultiert in einer asymmetrischen Emissionsbande mit Maximum bei  $\lambda_{em} = 748$  nm (Abb. 33). Die recht breite und asymmetrische Bandenform der Spin-Flip-Emission kann auf die Beteiligung mehrerer sich energetisch naheliegender Dublett-Zustände zurückgeführt werden. In der Punktgruppe  $D_{3d}$  von  $[\text{Cr}(\text{tpe})_2]^{3+}$  spaltet der emissive  ${}^2T_{1g}$ -Zustand ( $O_h$ ) in die Zustände  ${}^2A_{2g}$  ( $D_{3d}$ ) und  ${}^2E_g$  ( $D_{3d}$ ) auf, während der Spin-Flip-Zustand  ${}^2E_g$  ( $O_h = D_{3d}$ ) nicht weiter aufspaltet. Dies ist ein wichtiger Unterschied zum  $[\text{Cr}(\text{ddpd})_2]^{3+}$ -Komplex in dem, aufgrund der hohen lokalen Symmetrie um das Chrom-Zentrum (annähernd perfekt oktaedrisch durch Stickstoff-Atome umgeben), die emittierenden Dublett-Zustände  ${}^2E_g/{}^2T_{1g}$  nicht aufspalten und daher zwei recht scharfe Emissionsbanden bei  $\lambda_{em} = 775$  und  $738$  nm beobachtet werden können.

Im  $[\text{Cr}(\text{tpe})_2]^{3+}$ -Komplex spielen bei der strahlungslosen Deaktivierung der Dublett-Zustände durch MR sowohl die aromatischen C-H-Oszillatoren des **tpe**-Liganden als auch die von koordinierenden Lösungsmittelmolekülen eine wichtige Rolle. Der vierte Schwingungsoberton der aromatischen C-H-Oszillatoren von **tpe** zeigt mit einer Energie von ungefähr  $14000\text{ cm}^{-1}$ <sup>[35]</sup> die größte spektrale Überlappung mit der Emissionsbande von  $[\text{Cr}(\text{tpe})_2]^{3+}$  bei Raumtemperatur (HI, Abb. S15). Wegen des erwartungsgemäß großen SOIs ist von einer effektiven strahlungslosen Deaktivierung durch die sechs metallnächsten C-H-Oszillatoren mit dem kürzesten Cr...H Abstand von ca.  $3\text{ \AA}$  auszugehen (Abb. 32, grün markiert). Neben den C-H-Oszillatoren von **tpe** tragen auch die C-H- bzw. O-H-Oszillatoren von Acetonitril bzw. Wasser in der zweiten Koordinationssphäre zur Löschung der Spin-Flip-Emission bei (Abb. 32, rot und blau markiert). Um den zu erwartenden Beitrag von Acetonitril zur MR in  $[\text{Cr}(\text{tpe})_2]^{3+}$  und die potentielle Verbesserung der Lumineszenzlebenszeiten durch Verwendung von deuteriertem Acetonitril abzuschätzen, wurden die MR-Raten  $k_{nr}$  für die C-H(D)-Oszillatoren in  $\text{CH}_3\text{CN}/\text{CD}_3\text{CN}$  bestimmt. Dafür wurden zunächst die Obertonsignaturen von flüssigem Acetonitril im Wellenlängenbereich zwischen  $11500$  und  $16000\text{ cm}^{-1}$  (vierter Oberton ( $\nu_{\text{C-H}}^5$ ) einer C-H-Streckschwingung und Kombinationsschwingungen im Energiebereich des dritten C-H-Obertons ( $\nu_{\text{C-H}}^4$ , HI, Abb. S26+27) gemessen, passend zum Wellenlängenbereich der Dublett-Emission von  $[\text{Cr}(\text{tpe})_2]^{3+}$  (Abb. 34, oben). Die erhaltenen Daten waren dabei konsistent mit vorausgegangen Messungen von flüssigem Acetonitril, die zeigen, dass die Intensitäten der Absorptionsbanden stark von den Obertönen von C-H-Streckschwingungen dominiert sind.<sup>[103]</sup> Der Beitrag durch  $\text{C}\equiv\text{N}$  Schwingungen konnte

deshalb vernachlässigt werden. Die experimentelle Bestimmung der C-D-Obertöne im gleichen Wellenlängenbereich war dagegen wegen der äußerst kleinen Extinktionskoeffizienten nicht zuverlässig möglich. Um nun trotzdem die SOIs mit der Chromemission bestimmen zu können, wurden die Absorptionsbanden der C-D-Obertöne im relevanten Bereich ( $\nu_{\text{C-D}}^6$  und  $\nu_{\text{C-D}}^7$ ) mit Hilfe der Obertondaten von verlässlich messbaren, niedrigeren C-D-Obertönen ( $\nu_{\text{C-D}}^3$  -  $\nu_{\text{C-D}}^5$ ) ermittelt (Abb. 34, unten, Details HI, Abb. S28-31 u. Tab. S4).

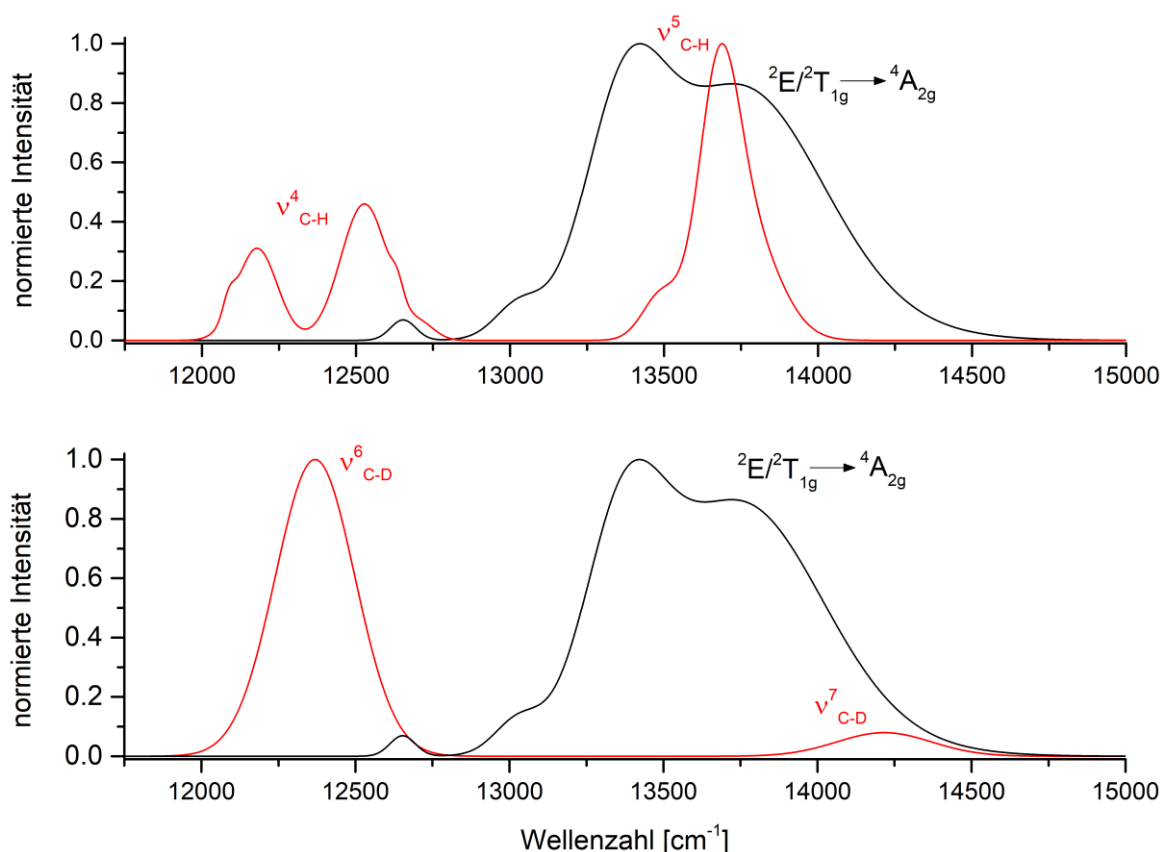


**Abb. 34:** Oben: Normiertes Emissionsspektrum von  $[\text{Cr}(\text{tpe})_2]^{3+}$  (schwarz) und die aus den gemessenen Spektren extrahierten Absorptionsbanden der Kombinationsschwingungen im Energiebereich des dritten Obertons ( $\nu_{\text{C-H}}^4$ ) und des vierten Obertons der C-H-Streckschwingungen ( $\nu_{\text{C-H}}^5$ ) (rot). Unten: Normiertes Emissionsspektrum von  $[\text{Cr}(\text{tpe})_2]^{3+}$  (schwarz) und die anhand gemessener niedrigerer Obertöne extrapolierten Absorptionsbanden des fünften und sechsten C-D-Obertons (rot). Die Obertonintensitäten sind dabei relativ zu ihren tatsächlichen Intensitäten aufgetragen.

Der vierten C-H-Oberton ( $\nu_{\text{C-H}}^5$ ) von Acetonitril überlappt nahezu vollständig mit der Spin-Flip-Emission von  $[\text{Cr}(\text{tpe})_2]^{3+}$ . Wegen des resultierenden großen SOIs ( $\text{SOI}^{\text{H}} = 1.24 \cdot 10^{-21} \text{ M}^{-1}\text{cm}^3$ , HI, Abb. S32), nimmt  $k_{\text{nr}}^{\text{H}}$  große Werte an und MR ist potentiell effektiv. Dagegen fällt die spektrale Überlappung des sechsten C-D-

Obertons ( $\nu_{C-D}^7$ ) mit der Chromemission wegen des viel kleineren Extinktionskoeffizienten weniger stark ins Gewicht ( $SOI^D = 6.28 \cdot 10^{-24} \text{ M}^{-1}\text{cm}^3$ , HI, Abb. S33), weshalb  $k_{nr}^D$  um drei Größenordnungen kleiner im Vergleich zu  $k_{nr}^H$  ist. Anders ausgedrückt, sollte die Verwendung von  $CD_3CN$  statt  $CH_3CN$  zu einer deutlichen Reduzierung von MR durch Acetonitril führen und sich verlängernd auf die Lebensdauern der Spin-Flip-Emission von  $[Cr(tpe)_2]^{3+}$  auswirken.

Die Lumineszenzquantenausbeute von  $[Cr(tpe)_2]^{3+}$  beträgt bei Raumtemperatur in sauerstofffreien  $H_2O$  sehr gute  $\Phi = 3.2 \%$ . Dieser Wert kann durch Zugabe von  $0.1 \text{ M NaClO}_4$  oder  $0.1 \text{ M HClO}_4$  auf die Werte  $\Phi = 4.2 \%$  bzw.  $\Phi = 5.4 \%$  gesteigert werden (HI, Tab. S2). Dabei dürften die Perchlorat-Ionen das Chrom-Zentrum vor Lösemittelmolekülen (s. Abb. 32 zweite Koordinationssphäre von  $[M(tpe)_2]^{3+}$  im Festkörper) abschirmen und reduzieren so die strahlungslose Deaktivierung der Spin-Flip-Zustände.

Die in  $H_2O/HClO_4$  gemessene Lebenszeit von  $\tau = 2800 \mu\text{s}$  ist sehr lang und deutlich länger im Vergleich zur Lebenszeit des nicht zentrosymmetrischen  $[Cr(ddpd)_2]^{3+}$ -Komplexes. In sauerstofffreien  $D_2O/DClO_4$ -Lösungen ist die strahlungslose Deaktivierung wegen der geringeren Oszillatorstärke der O-D-Oszillatoren im Vergleich zu den O-H-Schwingungen von  $H_2O$  weniger effektiv und die Quantenausbeute und Lebenszeit steigert sich um den Faktor 1.5 – 1.6. Der Wechsel der Bedingungen von  $H_2O/HClO_4$  zu  $CH_3CN/HClO_4$  wirkt sich kaum auf die photophysikalischen Eigenschaften von  $[Cr(tpe)_2]^{3+}$  aus. Auch die Lebenszeiten von  $[Cr(tpe)_2]^{3+}$  unterscheiden sich in  $CH_3CN/HClO_4$  und  $CD_3CN/DClO_4$  nur unwesentlich. Dies ist dann plausibel, wenn die Zugabe der Perchlorsäure zur Abschirmung des Chromzentrums vor Lösungsmittelmolekülen führt und die direkte Umgebung des  $Cr^{3+}$ -Ions (Perchlorat-Ionen /  $H_2O$ ) unter allen Bedingungen sehr ähnlich ist. In diesem Fall spielt MR durch Acetonitril Moleküle eine untergeordnete Rolle und es kann auch kein Isotopeneffekt beobachtet werden.

Zusammenfassend zeigt der zentrosymmetrische  $[Cr(tpe)_2]^{3+}$ -Komplex wegen seiner großen Ligandenfeldaufspaltung intensive Spin-Flip-Emission mit einer Quantenausbeute von  $\Phi = 8.2 \%$  bei Raumtemperatur in  $D_2O/DClO_4$ -Lösungen. Die Spin-Flip-Emission bei  $\lambda_{em} = 748 \text{ nm}$  ist Laporte-verboden was zu einer sehr langen Lumineszenzlebenszeit von  $\tau = 4500 \mu\text{s}$  führt. Durch die Zugabe von Perchlorsäure kann die potentiell sehr effektive MR durch solvatisierende Acetonitril Moleküle

verhindert werden. Die äußerst lange Lebenszeit des angeregten Zustands macht den **[Cr(tpe)<sub>2</sub>]<sup>3+</sup>**-Komplex interessant für verschiedene Anwendungen.

**VIP** Photochemistry Very Important Paper

 International Edition: DOI: 10.1002/anie.201909325  
 German Edition: DOI: 10.1002/ange.201909325

# Luminescence and Light-Driven Energy and Electron Transfer from an Exceptionally Long-Lived Excited State of a Non-Innocent Chromium(III) Complex

Steffen Treiling, Cui Wang, Christoph Förster, Florian Reichenauer, Jens Kalmbach, Pit Boden, Joe P. Harris, Luca M. Carrella, Eva Rentschler, Ute Resch-Genger, Christian Reber, Michael Seitz, Markus Gerhards, and Katja Heinze\*

**Abstract:** Photoactive metal complexes employing Earth-abundant metal ions are a key to sustainable photophysical and photochemical applications. We exploit the effects of an inversion center and ligand non-innocence to tune the luminescence and photochemistry of the excited state of the  $[CrN_6]$  chromophore  $[Cr(tpe)_2]^{3+}$  with close to octahedral symmetry ( $tpe = 1,1,1$ -tris(pyrid-2-yl)ethane).  $[Cr(tpe)_2]^{3+}$  exhibits the longest luminescence lifetime ( $\tau = 4500 \mu s$ ) reported up to date for a molecular polypyridyl chromium(III) complex together with a very high luminescence quantum yield of  $\Phi = 8.2\%$  at room temperature in fluid solution. Furthermore, the  $tpe$  ligands in  $[Cr(tpe)_2]^{3+}$  are redox non-innocent, leading to reversible reductive chemistry. The excited state redox potential and lifetime of  $[Cr(tpe)_2]^{3+}$  surpass those of the classical photosensitizer  $[Ru(bpy)_3]^{2+}$  ( $bpy = 2,2'$ -bipyridine) enabling energy transfer (to oxygen) and photoredox processes (with azulene and tri(*n*-butyl)amine).

## Introduction

A strongly growing interest in chromium(III) complexes, especially with polypyridyl ligands, arises from two perspectives, namely from the ambiguity of the ground state electronic structures of their reduced congeners (redox non-innocence)<sup>[1,2]</sup> and their—for first row transition metal complexes—outstanding luminescent properties with long-lived spin-flip emission from doublet states.<sup>[3–5]</sup> The type of polypyridine ligand determines both, redox and photophysical properties of chromium(III) complexes. The classical electron

transfer series  $[Cr(^l\text{bpy})_3]^{n+}$  and  $[Cr(\text{tpy})_2]^{n+}$  ( $n = 3, 2, 1, 0$ ) exclusively comprise ligand-centered redox couples and the chromium center retains its oxidation state +III throughout ( $^l\text{bpy} = 4,4'$ -di-*tert*-butyl-2,2'-bipyridine,  $\text{tpy} = 2,2':6',2''$ -terpyridine; Scheme 1).<sup>[1]</sup> Analogous results have been obtained for  $[Cr(\text{MePDP})_2]^{n+}$  ( $\text{H}_2\text{MePDI} = 2,6$ -bis(5-methyl-3-phenyl-1*H*-pyrrol-2-yl)pyridine) complexes.<sup>[2]</sup> On the other hand, the  $[Cr(\text{ddpd})_2]^{3+/2+}$  redox couple featuring the electron-rich polypyridine ligand ddpd involves a purely metal centered process giving chromium(II) (ddpd = *N,N'*-dimethyl-*N,N'*-dipyridin-2-ylpyridine-2,6-diamine; Scheme 1).<sup>[3,6]</sup>

Bis(terpyridine)chromium(III)  $[Cr(\text{tpy})_2]^{3+}$  and other classical pyridine complexes are weakly emissive (Table 1).<sup>[7–13]</sup> Although electron donating substituents at the  $\text{tpy}$  ligands enhance absorption in the visible spectral region by intraligand charge transfer absorptions, luminescence quantum yields and lifetimes remain poor (Table 1).<sup>[14,15]</sup> Prior to our work on the strongly emissive complex  $[Cr(\text{ddpd})_2]^{3+}$  (Scheme 1, Table 1)<sup>[5]</sup> featuring six-membered chelate rings and hence N-Cr-N angles close to 90°, the highest luminescence lifetimes were reported for the hexamine quasi-cage and cage complexes  $[Cr(\text{TAP}[9]\text{aneN}_3)]^{3+}$  and  $[Cr(\text{fac-Me}_5\text{-D}_{3h}\text{-tricosaneN}_6)]^{3+}$  (Table 1).<sup>[16–18]</sup> Note, that these two ligands form six-membered chelate rings with the chromium ion as well. Chromium(III) cage complexes with five-membered chelate rings show shorter luminescence lifetimes and lower quantum yields.<sup>[19]</sup> Deuteration of the ddpd ligand boosts the key luminescence data of  $[Cr(\text{ddpd})_2]^{3+}$  to  $\Phi = 30.0\%$  and  $\tau = 2300 \mu s$  in deaerated  $\text{CD}_3\text{CN}$

[\*] S. Treiling, Dr. C. Förster, F. Reichenauer, Dr. L. M. Carrella, Prof. E. Rentschler, Prof. K. Heinze  
 Institute of Inorganic Chemistry and Analytical Chemistry,  
 Johannes Gutenberg University of Mainz  
 Duesbergweg 10–14, 55128 Mainz (Germany)  
 E-mail: katja.heinze@uni-mainz.de


C. Wang, Dr. U. Resch-Genger  
 Division Biophotonics,  
 Federal Institute for Materials Research and Testing (BAM)  
 Richard-Willstätter-Straße 11, 12489 Berlin (Germany)


C. Wang  
 Institute of Chemistry and Biochemistry, Freie Universität Berlin  
 Takustraße 3, 14195 Berlin (Germany)

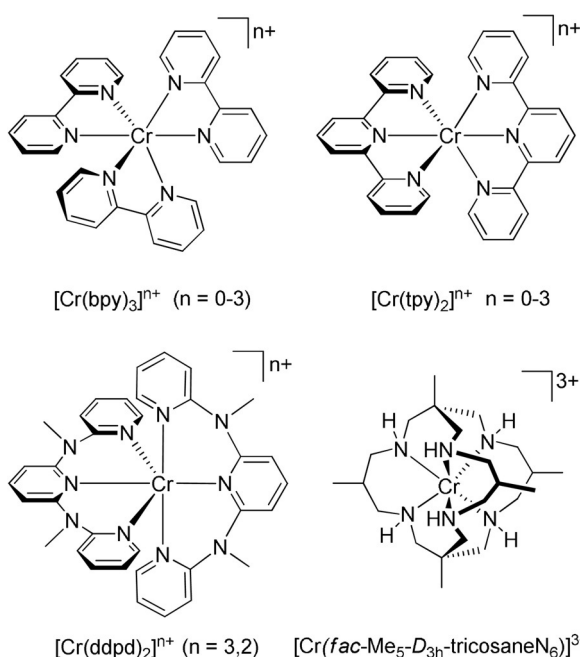
J. Kalmbach, Prof. M. Seitz  
 Institute of Inorganic Chemistry, University of Tübingen  
 Auf der Morgenstelle 18, 72076 Tübingen (Germany)

P. Boden, Prof. M. Gerhards  
 Department of Chemistry and Research Center Optimas,  
 TU Kaiserslautern  
 Erwin-Schrödinger-Straße, 67663 Kaiserslautern (Germany)

Dr. J. P. Harris, Prof. C. Reber  
 Département de chimie, Université de Montréal  
 Montréal, Québec, H3C 3J7 (Canada)

 Supporting information and the ORCID identification number(s) for the author(s) of this article can be found under:  
<https://doi.org/10.1002/anie.201909325>

 © 2019 The Authors. Published by Wiley-VCH Verlag GmbH & Co. KGaA. This is an open access article under the terms of the Creative Commons Attribution License, which permits use, distribution and reproduction in any medium, provided the original work is properly cited.



**Scheme 1.** Selected luminescent chromium(III) complexes ( $n=3$ ) and their reduced counterparts ( $n=2, 1, 0$ ).

**Table 1:** Luminescence data of pertinent chromium(III) complexes. All data refer to deoxygenated solutions.

complex (solvent)	$\tau / \mu\text{s}$	$\Phi / \%$	Ref.
$[\text{Cr}(\text{phen})_3]^{3+}$ ( $\text{CH}_3\text{CN}$ )	224	0.15	[7, 15]
$[\text{Cr}(\text{tpy})_2]^{3+}$ ( $\text{CH}_3\text{CN}$ )	0.14	< 0.00089	[7, 14]
$[\text{Cr}(\text{ddpd})_2]^{3+}$ ( $\text{H}_2\text{O}$ )	898	11.0	[3]
$[\text{Cr}(\text{ddpd})_2]^{3+}$ ( $\text{D}_2\text{O}$ )	1164	14.0	[3]
$[\text{Cr}(\text{D}_n\text{-ddpd})_2]^{3+}$ ( $\text{CD}_3\text{CN}$ )	2300	30.0	[20]
$[\text{Cr}(\text{TAP}[9]\text{aneN}_3)]^{3+}$ ( $\text{H}_2\text{O}$ )	265	–	[16, 17]
$[\text{Cr}(\text{TAP}[9]\text{aneN}_3)]^{3+}$ ( $\text{D}_2\text{O}$ )	850	–	[16, 17]
$[\text{Cr}(\text{fac-Me}_5\text{-D}_{3h}\text{-tricosaneN}_6)]^{3+}$ ( $\text{H}_2\text{O}$ )	235	–	[18]
$[\text{Cr}(\text{fac-Me}_5\text{-D}_{3h}\text{-tricosaneN}_6)]^{3+}$ ( $\text{D}_2\text{O}$ )	1500	–	[18]
$[\text{Cr}(5\text{-C}\equiv\text{CH-bpy})(\text{phen})_2]^{3+}$ ( $\text{CH}_3\text{CN}$ )	259	–	[15]
$[\text{Cr}(\text{ddpd})(\text{tpy})]^{3+}$ ( $\text{CH}_3\text{CN}$ )	1000	0.06	[26]

(Table 1).<sup>[20]</sup> These favorable photophysical data of  $[\text{Cr}(\text{ddpd})_2]^{3+}$  enable its application in temperature, pressure and dioxygen sensing, as well as in photocatalysis and photodynamic therapy.<sup>[21–25]</sup> Replacing one ddpd ligand by tpy slightly increases the excited state lifetime, yet dramatically reduces the quantum yield (Table 1), underlining the positive effect of six-membered chelate rings.<sup>[26]</sup> Photoredox catalytic cycloadditions have been reported using  $[\text{Cr}(\text{phen})_3]^{3+}$  derivatives.<sup>[27–30]</sup> Energy transfer to chromium(III) complexes has been investigated using luminescent  $[\text{Cr}(\text{CN})_6]^{3-}$ ,  $[\text{Cr}(\text{ox})_3]^{3-}$  or *trans*- $[\text{Cr}(\text{CN})_2(\text{cyclam})]^{+}$  acceptors in supramolecular architectures and in solid state materials (cyclam = 1,4,8,11-tetraazacyclotetradecane).<sup>[31–33]</sup> Vice versa, the luminescence of  $[\text{Cr}(\text{alkynyl})_2(\text{cyclam})]^{+}$  complexes is quenched by Dexter energy transfer to ferrocene. Furthermore,  $\text{Cr}^{\text{III}}$  complexes have been exploited as sensitizers in molecular lanthanide-based energy transfer upconversion.<sup>[34]</sup>

All described and conceivable future applications in luminescence, energy and electron transfer would profit from increased quantum yields and lifetimes. Decisive factors elucidated so far comprise i) a strong ligand field to shift the detrimental ligand field states ( ${}^4\text{T}_{2g}$  in octahedral symmetry) to higher energy<sup>[4,35]</sup> and ii) the elimination of high energy XH oscillators from the vicinity of the metal center, for example, by selective deuteration, to reduce non-radiative multiphonon relaxation.<sup>[20,36,37]</sup> A further aspect is to reduce excited state distortion, especially large trigonal twists.<sup>[16,17]</sup>

Similar to the mainly meridionally coordinating tridentate ligand ddpd,<sup>[3,6,38–43]</sup> the tripodal ligand 1,1,1-tris(pyrid-2-yl)ethane (tpe)<sup>[44]</sup> forms 6-membered chelate rings with nearly  $90^\circ$  bite angles with transition metal complexes.<sup>[45,46]</sup> Tetradentate tpe analogues<sup>[47]</sup> were successfully employed in several  $\text{MCl}_2(\text{L})$  complexes.<sup>[48]</sup> However, chromium(III) complexes with tpe, modified tpe or comparable tpm and tpa ligands have, to the best of our knowledge, not yet been reported (tpm = 2,2',2'-tripyridylmethane, tpa = 2,2',2'-tripyridylamine).

We surmised that the tpe ligands should exert a strong ligand field in  $[\text{Cr}(\text{tpe})_2]^{3+}$ . This should place the lowest energy doublet states below the lowest energy quartet excited states in a homoleptic chromium(III) complex leading to phosphorescence. In contrast to  $D_2$ -symmetric *mer*- $[\text{Cr}(\text{ddpd})_2]^{3+}$  and  $D_3$ -symmetric  $[\text{Cr}(\text{N}\cap\text{N})_3]^{3+}$  metal complexes,  $[\text{M}(\text{tpe})_2]^{3+}$  complexes feature an inversion center. According to Laporte's rule for dd transitions in centrosymmetric complexes, the inversion center should affect the absorption and emission properties.<sup>[49]</sup> Furthermore, tpe could be susceptible to ligand-based redox chemistry (ligand non-innocence) similar to 'bpy, tpy or  ${}^{\text{Me}}\text{PDP}^{2-}$ ,<sup>[1,2]</sup> contrasting ddpd as a redox-innocent spectator ligand.<sup>[6]</sup>

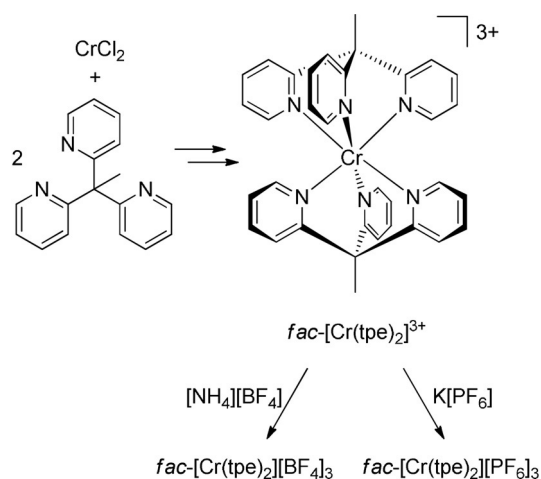
In this study, we exploit the complex  $[\text{Cr}(\text{tpe})_2]^{3+}$  with an Earth-abundant metal ion as a potential substitute for the classical, precious metal containing chromophore  $[\text{Ru}(\text{bpy})_3]^{2+}$  in luminescence, as well as in photoinduced energy and electron transfer reactions. Single crystal X-ray diffraction,<sup>[50–54]</sup> NIR luminescence quantum yields<sup>[55]</sup> and lifetimes, variable temperature luminescence and step-scan FT-IR spectroscopy,<sup>[56–58]</sup> electrochemistry and spectroelectrochemistry, Stern–Volmer analyses as well as quantum chemical calculations<sup>[59–69]</sup> confirm the proposed design guidelines.

## Results and Discussion

### Synthesis and Characterization

The tripodal pyridine ligand tpe<sup>[44]</sup> has been prepared from 2-ethylpyridine and 2-fluoropyridine according to a reported procedure.<sup>[45]</sup> Treatment of  $\text{CrCl}_2$  with two equivalents of tpe results in complexation and oxidation to  $\text{Cr}^{\text{III}}$ . Counterion exchange gives the faint yellow and green complexes *fac*- $[\text{Cr}(\text{tpe})_2][\text{BF}_4]_3$  and *fac*- $[\text{Cr}(\text{tpe})_2][\text{PF}_6]_3$ , respectively (Scheme 2). The salts were characterized by mass spectrometry, IR spectroscopy, magnetic susceptibility measurements and elemental analyses. The data support the composition,





**Scheme 2.** Preparation of the homoleptic chromium(III) complex salts  $fac-[Cr(tpe)_2][BF_4]_3$  and  $fac-[Cr(tpe)_2][PF_6]_3$ .

the high symmetry and the quartet electronic ground state (see Supporting Information, Figures S1–S5).<sup>[70]</sup>

### Structures in the Solid State and Ground State Quantum Chemical Calculations

Single crystals of  $[Cr(tpe)_2][BF_4]_3 \times 3 CH_3CN$  and  $[Cr(tpe)_2][PF_6]_3 \times 3 CH_3CN$  were obtained by diffusion of diethyl ether into acetonitrile solutions of the respective salts (Figure 1). The  $[BF_4]^-$  salt crystallizes in the centrosymmetric triclinic space group  $P\bar{1}$  with two independent trications in the asymmetric unit. Both trications possess crystallographically imposed inversion symmetry. The  $[PF_6]^-$  salt crystallizes in the non-centrosymmetric space group  $R3$ . The trication possesses crystallographically imposed threefold symmetry without inversion symmetry. The metrical data of the two independent tpe ligands are very similar (Table S1). In all

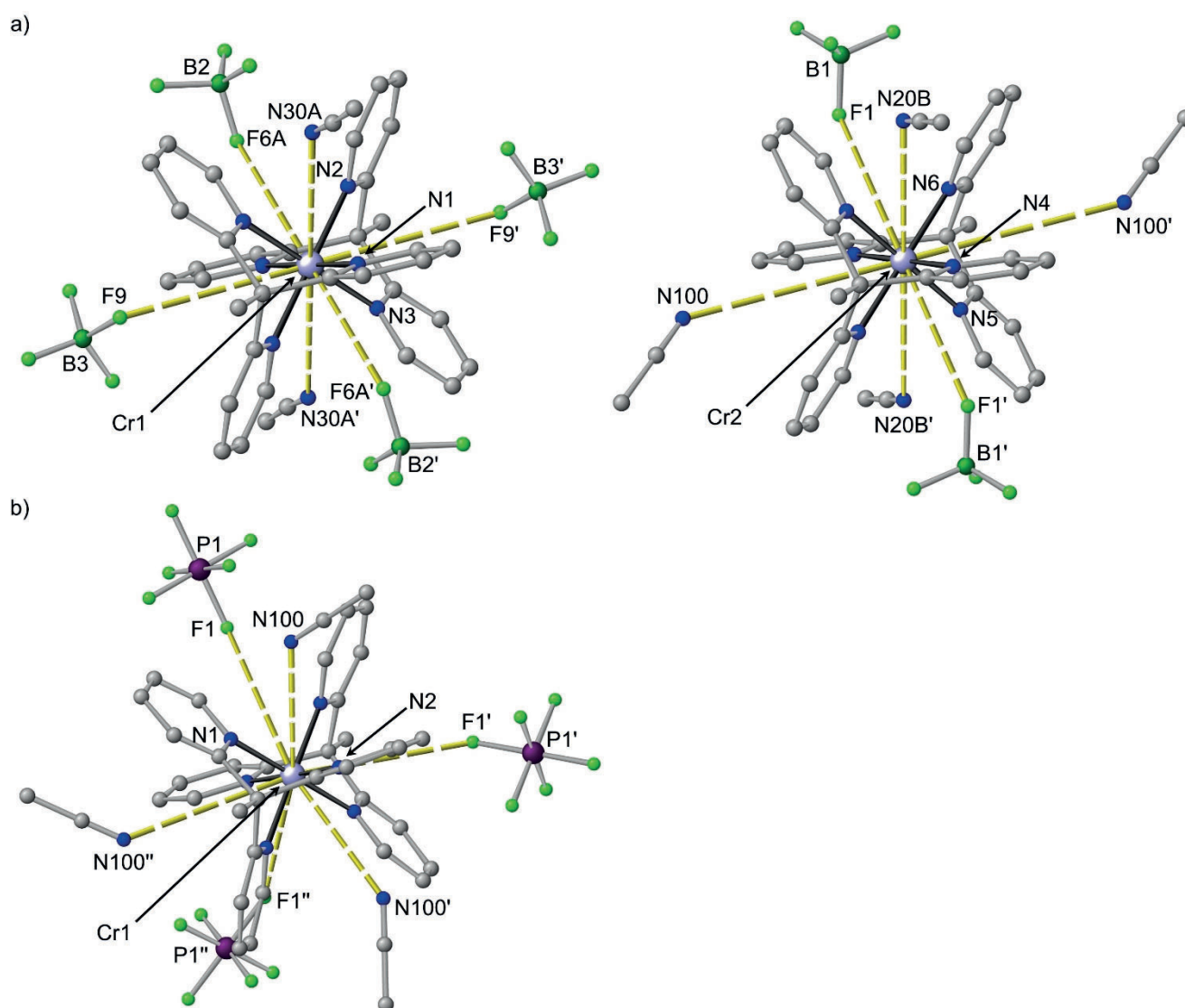


**Figure 1.** Molecular structures of the cations of a)  $[Cr(tpe)_2][BF_4]_3 \times 3 CH_3CN$  with two independent cations and b)  $[Cr(tpe)_2][PF_6]_3 \times 3 CH_3CN$  including the second coordination sphere of solvents and counterions. View approximately along the molecular threefold axes. Plots of the cations with thermal ellipsoids are depicted in Figure S6.<sup>[89]</sup>



three crystallographically characterized trications, the point symmetry of the  $[\text{CrN}_6]$  coordination sphere is close to  $O_h$ . The reported  $d^6$  low spin complexes  $[\text{Fe}(\text{tpe})_2][\text{ClO}_4]_2$  and  $[\text{Co}(\text{tpe})_2][\text{ClO}_4]_3$  exhibit a highly symmetric  $[\text{MN}_6]$  coordination sphere as well.<sup>[45]</sup>

Counterions and acetonitrile molecules occupy the six pockets spanned by the pyridyl rings of the tripodal ligands. This second coordination sphere consists of  $2\text{CH}_3\text{CN}/4[\text{BF}_4]^-$ ,  $4\text{CH}_3\text{CN}/2[\text{BF}_4]^-$  or  $3\text{CH}_3\text{CN}/3[\text{PF}_6]^-$  molecules with  $\text{Cr}\cdots\text{N}/\text{Cr}\cdots\text{F}$  distances ranging from 4.42 to 5.20 Å (Table S1). The low-spin cobalt(III) salt  $[\text{Co}(\text{tpe})_2][\text{ClO}_4]_3 \times 4\text{CH}_3\text{CN}$  displays a fully analogous  $2\text{CH}_3\text{CN}/4[\text{ClO}_4]^-$  environment with a  $\text{Co}\cdots\text{N}(\text{solvent})$  distance of 4.76 Å and  $\text{Co}\cdots\text{O}(\text{counterion})$  distances of 4.20 and 4.50 Å, respectively.<sup>[45]</sup> In the monohydrate  $[\text{Co}(\text{tpe})_2][\text{ClO}_4]_3 \times \text{H}_2\text{O}$ , all pockets are filled exclusively with perchlorate counterions with  $\text{Co}\cdots\text{O}(\text{water})$  distance amounts to 6.49 Å. This is significantly larger than the  $\text{Cr}\cdots\text{N}$  distances to  $\text{CH}_3\text{CN}$ . Dynamic solvation and ion pair formation of  $[\text{M}(\text{tpe})_2]^{3+}$  cations with variable occupation of the pockets by solvent molecules, especially the sterically less demanding  $\text{CH}_3\text{CN}$  molecule, and small counterions is expected in solution.<sup>[71–73]</sup> Furthermore, the terminal methyl groups of the tpe ligands form short  $\text{H}\cdots\text{F}-\text{BF}_3$  and  $\text{H}\cdots\text{F}-\text{PF}_5$  contacts to the counterions with  $\text{H}\cdots\text{F}$  distances around 2.5–2.9 Å.

The DFT optimized geometry of  $[\text{Cr}(\text{tpe})_2]^{3+}$  at the CPCM( $\text{CH}_3\text{CN}$ )-RIJCOSX-B3LYP-D3BJ-ZORA/def2-TZVPP level of theory agrees very well with the experimental data (Table S1). The calculated Mulliken  $\alpha$  spin density at chromium amounts to  $\approx 3.22$  electrons (Figure S7a). Spin polarization ( $\sigma$  pathway) imposes some  $\beta$  spin density to all six nitrogen donor atoms (Figure S7a;  $-0.08$ ) and increases the  $\alpha$  spin density at chromium above three. This is in accordance with a  $(t_{2g})^3$  electron configuration of the chromium(III) ion and the magnetic data (Figure S5). Furthermore, the spin density is consistent with that obtained for  $[\text{Cr}(\text{tpy})_2]^{3+}$ ,  $[\text{Cr}(\text{bpy})_3]^{3+}$  and  $[\text{Cr}(\text{MePDP})_2]^{1-}$  with 3.21, 3.27 and 3.21  $\alpha$  electrons at the chromium centers, respectively,<sup>[1,2]</sup> at the B3LYP/def2-TZVP level of theory.

### Optical Properties

The faint yellow solution of  $[\text{Cr}(\text{tpe})_2]^{3+}$  features absorption bands at 329 and 431 nm, irrespective of the counterion ( $[\text{BF}_4]^-$ ,  $[\text{PF}_6]^-$ ) and the solvent ( $\text{H}_2\text{O}$ ,  $\text{CH}_3\text{CN}$ ) (Figure 2). The weak band at 431 nm ( $\epsilon = 30\text{ M}^{-1}\text{ cm}^{-1}$ ) corresponds to the strongly parity-forbidden  ${}^4\text{A}_{2g} \rightarrow {}^4\text{T}_{2g}$  ligand field transitions (symmetry labels according to idealized  $O_h$  symmetry). Time-dependent DFT calculations on the geometry optimized  $[\text{Cr}(\text{tpe})_2]^{3+}$  ion (Table S1, quartet state) support this assignment. The spin-allowed ligand field transitions were calculated at 378, 379 and 394 nm and hence suggest a splitting of the  ${}^4\text{T}_{2g}$  level ( $O_h$  symmetry) in  ${}^4\text{E}_g$  and  ${}^4\text{A}_{1g}$  levels by ca.  $1000\text{ cm}^{-1}$  due to the actual lower  $D_{3d}$  symmetry. Yet, the inversion center is preserved. In the following discussions, the symmetry labels of the  $D_{3d}$  point group are employed for  $[\text{Cr}(\text{tpe})_2]^{3+}$ . Due to Laporte's rule, the calculated oscillator

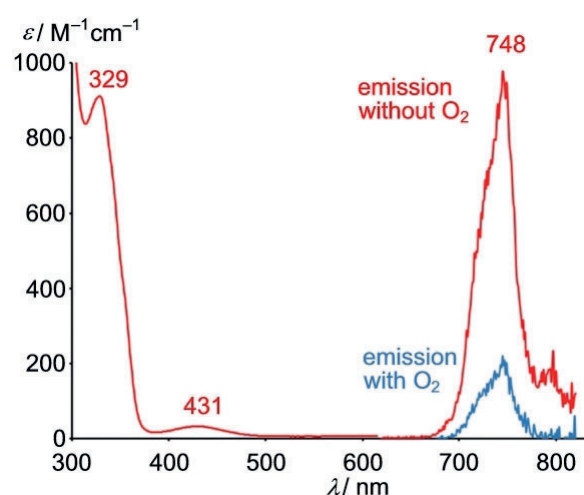


**Figure 2.** Absorption and emission spectra of  $[\text{Cr}(\text{tpe})_2][\text{BF}_4]_3$  in  $\text{D}_2\text{O}/\text{DClO}_4$  at room temperature ( $\lambda_{\text{exc}} = 428\text{ nm}$ ;  $9.0\ \mu\text{l}\ \text{DClO}_4(68\%)\ \text{mL}^{-1}\ \text{D}_2\text{O}$ ) under inert (red) and air-saturated conditions (blue).

strengths are very small ( $1.4\text{--}1.5 \times 10^{-8}$  each; Figure S7). The analogous absorption band of the comparable centrosymmetric bis(hydrotris(1-pyrazolyl)borate)chromium(III) complex  $[\text{Cr}(\text{HBpz}_3)_2]^{3+}$  is of similar intensity ( $456\text{ nm}$ ;  $\epsilon = 35\text{ M}^{-1}\text{ cm}^{-1}$ ),<sup>[74]</sup> while that of  $[\text{Cr}(\text{ddpd})_2]^{3+}$  at  $435\text{ nm}$  is more intense by two orders of magnitude due to the lack of the inversion center in  $[\text{Cr}(\text{ddpd})_2]^{3+}$ .<sup>[3]</sup> The “octahedral” ligand field splitting  $\Delta_o = 23200\text{ cm}^{-1}$  of  $[\text{Cr}(\text{tpe})_2]^{3+}$  (corresponding to the center of the quartet absorption band) is in the same range as that of bpy and ddpd chromium(III) complexes, yet larger than that of  $[\text{Cr}(\text{tpy})_2]^{3+}$  due to the unfavorable metal-ligand orbital overlap of the latter.

Excitation of the ligand field states ( ${}^4\text{A}_{1g}(D_{3d})$  and  ${}^4\text{E}_g(D_{3d})$ ) is followed by intersystem crossing (ISC) to the doublet manifold, leading to an asymmetric emission band centered at  $748\text{ nm}$  (Figure 2). This doublet emission band is relatively broad (FWHM  $785\text{ cm}^{-1}$ ) and appears at higher energy than the corresponding band of  $[\text{Cr}(\text{ddpd})_2]^{3+}$  with sharp bands at  $775$  and  $738\text{ nm}$ , a separation typical for the lowest-energy doublet states of octahedral chromium(III) complexes.<sup>[3,75]</sup>

The  $D_{3d}$  symmetry in  $[\text{Cr}(\text{tpe})_2]^{3+}$  splits the  ${}^2\text{T}_{1g}(O_h)$  excited state into  ${}^2\text{A}_{2g}(D_{3d})$  and  ${}^2\text{E}_g(D_{3d})$  states, while the  ${}^2\text{E}_g(O_h)$  level remains degenerate ( ${}^2\text{E}_g(D_{3d})$ ) (Figure 3). It is conceivable that the lowest doublet state of  $[\text{Cr}(\text{tpe})_2]^{3+}$  is one of the split  ${}^2\text{T}_{1g}(O_h)$  states to which electron configurations with two electrons paired in a  $d(\pi)$  orbital, a half-filled  $d(\pi)$  orbital and an unoccupied  $d(\pi)$  orbital also contribute. This is not the case for  ${}^2\text{E}_g$  in the octahedral limit, a key qualitative difference in electronic structure. Configurations are strongly mixed due to the energetic proximity of the states arising from the  ${}^2\text{G}$  free ion term and to interaction with  ${}^2\text{E}_g$  and  ${}^2\text{T}_{1g}$  states arising from higher energy doublet terms of the chromium(III) ion. Consequently, individual configurations cannot be assigned to a single excited state. As the ordering of the  ${}^2\text{A}_{2g}(D_{3d})$  and  ${}^2\text{E}_g(D_{3d})$  states in  $[\text{Cr}(\text{tpe})_2]^{3+}$  cannot be determined from the luminescence spectra, we denote the lowest energy doublet state as  ${}^2\text{X}_g(D_{3d})$  and the higher one as  ${}^2\text{Y}_g(D_{3d})$ . Both geometries should be slightly distorted due to

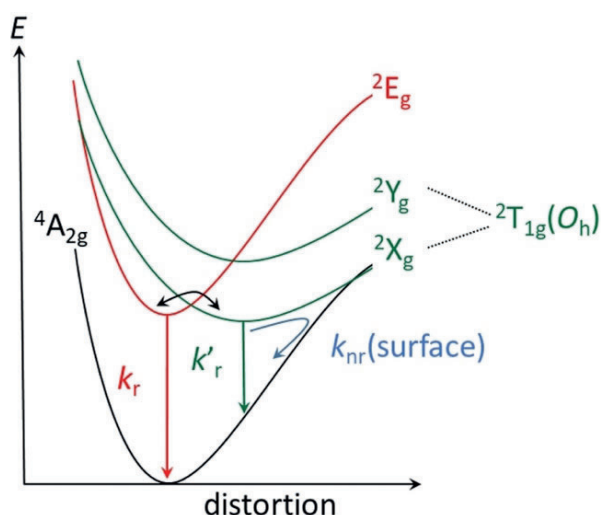


**Figure 3.** Schematic suggested potential energy curve diagram of  $[\text{Cr}(\text{tpe})_2]^{3+}$ ; term symbols refer to  $D_{3d}$  symmetry, yet with an unknown ordering of  ${}^2A_{2g}(D_{3d})$  and  ${}^2E_g(D_{3d})$  which are denoted arbitrarily as  ${}^2X_g(D_{3d})/{}^2Y_g(D_{3d})$ .

the shift in electron density within the  $d(\pi)$  orbitals with respect to the ground state. In the  ${}^2E_g$  state (derived from  ${}^2E_g(O_h)$ ) all three  $d(\pi)$  orbitals are singly occupied and the geometry is very similar to that of the ground state (Figure 3). We will present arguments for this assignment of the doublet levels in the following discussion.

### Excited State Properties

The photoluminescence quantum yield of  $\Phi = 3.2\%$  at room temperature in deaerated  $\text{H}_2\text{O}$  is among the highest reported for chromium(III) complexes, but lower than that of  $[\text{Cr}(\text{ddpd})_2]^{3+}$ .<sup>[3]</sup> The quantum yield of  $[\text{Cr}(\text{tpe})_2]^{3+}$  increases in  $0.1\text{M NaClO}_4$  ( $\Phi = 4.2\%$  in  $\text{H}_2\text{O}/\text{NaClO}_4$ ) or  $0.1\text{M HClO}_4$  ( $\Phi = 5.4\%$  in  $\text{H}_2\text{O}/\text{HClO}_4$ ). Presumably, the perchlorate and the acid protect the complex, for example, from solvent molecules (cf. the microenvironment of  $[\text{M}(\text{tpe})_2]^{n+}$  complexes in the solid state).<sup>[45]</sup> Consequently, all following luminescence measurements in solution were performed in the presence of perchloric acid ( $9.5\ \mu\text{L HClO}_4$  (70% in  $\text{H}_2\text{O}$ )  $\text{mL}^{-1}$  solvent;  $9.0\ \mu\text{L DClO}_4$  (68% in  $\text{D}_2\text{O}$ )  $\text{mL}^{-1}$  solvent).

The lifetime  $\tau = 2800\ \mu\text{s}$  in deaerated  $\text{H}_2\text{O}/\text{HClO}_4$  is extremely long and even surpasses that of  $[\text{Cr}(\text{ddpd})_2]^{3+}$ .<sup>[3]</sup> In deaerated  $\text{D}_2\text{O}/\text{DClO}_4$ , the quantum yield increases to  $\Phi = 8.2\%$  and the luminescence lifetime to a record value of  $\tau = 4500\ \mu\text{s}$ . The photophysical key numbers are similar in deaerated acetonitrile/perchloric acid, which might be an effect of the presence of water in the employed perchloric acid (Table S2). Radiative decay ( $k_r$ ) is governed by the spin and parity selection rules while the non-radiative excited state decay ( $k_{nr}$ ) of  $\text{Cr}^{\text{III}}$  complexes can occur through back-intersystem crossing (bISC) to the quartet states ( $k_{nr}(\text{bISC})$ ), through surface crossing of distorted excited doublet states with the ground state ( $k_{nr}(\text{surface})$ ), through multiphonon

relaxation ( $k_{nr}(\text{XH})$ ),<sup>[20,36,37]</sup> through electronic energy transfer to energy acceptors ( $k_{nr}(\text{EnT})$ ) and through electron transfer from electron donors ( $k_{nr}(\text{ET})$ ).<sup>[4]</sup> These decay pathways will be considered in the following to explain the high lifetimes of  $[\text{Cr}(\text{tpe})_2]^{3+}$  and to suggest possible applications.

Due to the inversion center in  $[\text{Cr}(\text{tpe})_2]^{3+}$ , the luminescence is strictly Laporte-forbidden. In addition, it is spin-forbidden as for all chromium(III) complexes with sufficiently strong ligand fields. In fact, the radiative rate constant  $k_r$  of  $[\text{Cr}(\text{tpe})_2]^{3+}$  is very small ( $\tau_r = \tau / \Phi = 42.9\text{--}61.9\ \text{ms}$ ;  $k_r = 23\text{--}18\ \text{s}^{-1}$ ; Table S2). This is in good agreement with the reported small radiative rate constant  $k_r = 25\ \text{s}^{-1}$  ( $\tau_r = 40\ \text{ms}$ ) of the centrosymmetric  $[\text{Cr}(\text{CN})_6]^{3-}$  ion.<sup>[76]</sup> Vibronic coupling (vibrations of ungerade symmetry) is required to enable this electronic transition in  $[\text{Cr}(\text{tpe})_2]^{3+}$ . A broad emission band at room temperature has also been observed for the centrosymmetric  $d^3$  manganese(IV) complex  $[\text{Mn}(\text{PhB}(\text{Meim})_3)_2]^{2+}$  with approximate  $D_{3d}$  symmetry ( $[\text{PhB}(\text{MeIm})_3]^- = \text{phenyltris}(3\text{-methylimidazol-2-yl})\text{borate anion}$ ). Its band width ( $800\text{--}2000\ \text{cm}^{-1}$ ;  $85\text{--}300\ \text{K}$ ; solid state) has been ascribed to the required vibronic origins involving ungerade parity vibrational modes in centrosymmetric transition metal complexes.<sup>[77,78]</sup> On the other hand, complexes lacking an inversion center such as  $[\text{Cr}(\text{bpy})_3]^{3+}$  and  $[\text{Cr}(\text{ddpd})_2]^{3+}$  feature more symmetric emission bands.<sup>[6]</sup> The electronic origin transition of  $[\text{Cr}(\text{tpe})_2]^{3+}$  is observed at approximately  $13500\ \text{cm}^{-1}$  in the solid-state emission spectrum at  $10\ \text{K}$  (Figure 4). It is both spin and parity forbidden, and therefore vibronic origins dominate the observed intensity, both, to higher and lower energy of the origin as temperature increases. The combination of the easily visible origin and the vibrational frequencies of up to  $1000\ \text{cm}^{-1}$  leads to vibronic origins that cause the relatively broad luminescence band.

Splittings of the asymmetric emission band of  $[\text{Cr}(\text{tpe})_2]^{3+}$  at room temperature in the solid state and in solution are discernible (Figures S14–S15; splittings in solution amount to approximately  $372$  and  $346\ \text{cm}^{-1}$ ). DFT calculations find

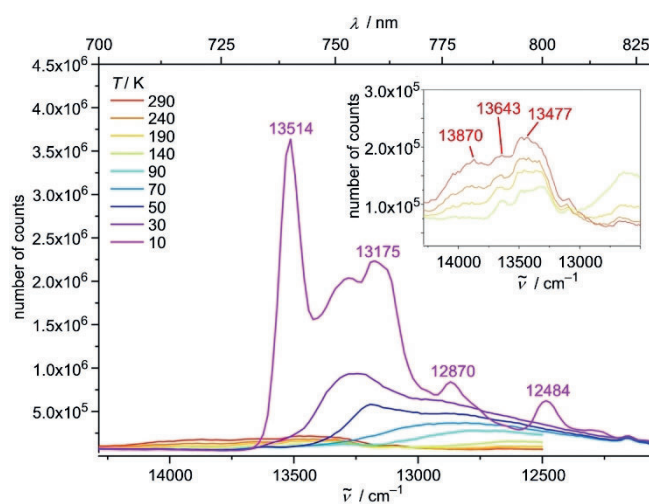


**Figure 4.** Emission spectra of  $[\text{Cr}(\text{tpe})_2][\text{BF}_4]_3$  as KBr disk in the temperature range  $10\text{--}290\ \text{K}$  with  $\lambda_{\text{exc}} = 420\ \text{nm}$ . The inset shows a zoom into the spectra in the temperature range  $140\text{--}290\ \text{K}$ .

Cr–N stretching vibrations with ungerade symmetry in the range of 300–400  $\text{cm}^{-1}$ . These vibrations could be the enabling modes leading to the asymmetric emission band with fine structure. However, as several Cr–N vibrations are present in this energy range and as electronic states derived from slightly higher doublet states should have a similar energy (Figure 3), the observed splittings cannot be straightforwardly assigned to vibrational progressions and the experimental energy gaps should not be overinterpreted. Clearly, the inversion center broadens the emission band and reduces  $k_r$  at higher temperature. Possible contributions to  $k_{nr}$ , namely  $k_{nr}(\text{bISC})$ ,  $k_{nr}(\text{surface})$  and  $k_{nr}(\text{XH})$ , will be discussed next.

As the ligand field splitting and consequently the approximate energy difference between the ligand field quartet states  ${}^4A_{1g}(D_{3d})/{}^4E_g(D_{3d})$  and the luminescent doublet states are large ( $\approx 1.2$  eV), thermally activated bISC to re-populate the quartet states is highly unlikely. Hence, we exclude the bISC pathway from the discussion for the non-radiative decay.

A further potential thermally activated non-radiative decay path could be surface crossing of a distorted doublet state  ${}^2X_g(D_{3d})/{}^2Y_g(D_{3d})$  with the ground state ( $k_{nr}(\text{surface})$ ; Figure 3).<sup>[4,79]</sup> The  ${}^2X_g(D_{3d})/{}^2Y_g(D_{3d})$  potential energy surface should be displaced horizontally relative to the ground state minimum, enabling efficient non-radiative relaxation pathways. Such a doublet potential well displacement has been suggested before and denoted “pseudo-Stokes shift” giving rise to a low energy phosphorescence.<sup>[79]</sup> Upon cooling crystals of  $[\text{Cr}(\text{tpe})_2][\text{BF}_4]_3$  to 80 K the broad emission band centered at 745 nm ( $13425 \text{ cm}^{-1}$ ) disappears while a new broad, structured band at lower energy (centered at ca. 770 nm/ $13000 \text{ cm}^{-1}$ ) grows in (Figure S16). The intensity decrease in the 700 nm to 740 nm range is clearly visible in Figure S16 and is the typical signature of thermally populated electronic or vibrational levels with higher radiative relaxation rates than the lowest-energy electronic transition. In the title compound, the effect is dramatic due to its exact inversion symmetry and leads to exceptional variations of the spectroscopic patterns. Crystals of  $[\text{Cr}(\text{tpe})_2][\text{PF}_6]_3$  display a fully analogous overall behavior upon cooling to 80 K, yet with slightly different vibrational fine structure (Figure S17). Even KBr disks of  $[\text{Cr}(\text{tpe})_2][\text{BF}_4]_3$  show an increasing low-energy emission band at lower temperature at the expense of a high energy band (Figure 4). At 10 K, the low energy band shows resolved fine structure and the intensity dramatically increases (Figure 4). The increase in emission intensity is compatible with the proposed diminished  $k_{nr}(\text{surface})$  at lower temperature of the “pseudo-Stokes shifted”  ${}^2X_g(D_{3d})$  state (Figure 3).<sup>[79]</sup>

To gain more insight into the geometries of the long-lived excited states, we subjected KBr disks of  $[\text{Cr}(\text{tpe})_2][\text{BF}_4]_3$  to time-resolved step-scan FTIR spectroscopy<sup>[56–58,80]</sup> in the energy range of 1750 to  $1200 \text{ cm}^{-1}$  at 290 and 20 K (Figure 5a). The negative bands in the difference spectra indicate depopulation of the ground state while positive bands belong to the electronically excited state(s). DFT calculations excellently reproduce the ground state IR spectrum (Figure S18). In the excited state, nearly all IR bands shift to lower energy and a shoulder appears at approximately  $1433 \text{ cm}^{-1}$  at 290 K (Figure 5b). The shoulder might appear

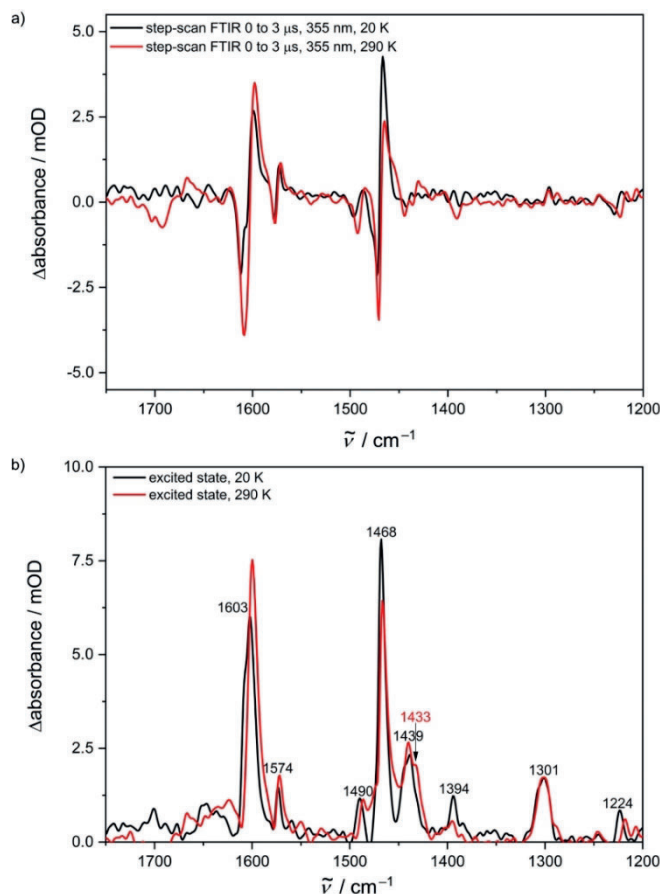


**Figure 5.** a) Step-scan FTIR spectra of  $[\text{Cr}(\text{tpe})_2][\text{BF}_4]_3$  at 290 K (red) and 20 K (black) in a KBr disk 0 to 3  $\mu\text{s}$  after laser excitation at 355 nm and b) IR spectra of the excited state after subtraction of the spectrum of the electronic ground state at 290 K (red) and 20 K (black).

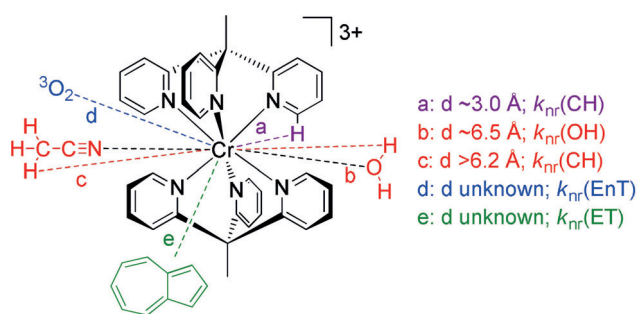
due to the population of two long-lived excited states or to the removal of the inversion center in the doublet states. At 20 K, the IR bands in the step-scan IR spectra sharpen and the shoulder disappears. This might point to a preferred population of a long-lived excited state at 20 K ( ${}^2X_2(D_{3d})$ ) which would match the suggested excited state ordering (Figure 3). From time-resolved IR data at low and high temperature, biexponential decays are extracted (20 K: 66  $\mu\text{s}$  (82 %); 2.2  $\mu\text{s}$  (18 %); 290 K: 10  $\mu\text{s}$  (65 %); 0.71  $\mu\text{s}$  (35 %), Figure S19).

However, the data of the TCSPC experiments at 290 K in KBr disks are fitted with tri- and tetraexponential decay curves (Figures S20–S22). The latter one results in a slightly better description with respect to the residuals. All fits yield two long-lived components, which are associated with two emissive doublet states at 290 K. The triexponential function shows one time constant in the nanosecond regime, whereby the tetraexponential fit yields a further short-lived component with a very small contribution equal or less to 3%. A true photophysical relevance of this fourth component might be questionable. The nanosecond processes may be associated to fluorescence. Static emission and TCSPC investigations on neat films confirm the results from KBr disks and indicate that no matrix effects of KBr are observed (Figure S23).



A biexponential decay is observed in both, the step-scan and the TCSPC experiments at 20 K (Figure S24–S25). The biexponential decay from TCSPC measurements shows a very small, negligible contribution (2–5%) for the shorter-lived component indicating a low population of the energetically higher excited doublet state. The step-scan data also show a smaller, yet significant contribution (18%) of the shorter-lived component at 20 K (compared to 290 K). This comparably high population cannot result from a pure thermalized occupation of the low energy  ${}^2E_g/{}^2X_g$  states but could result from differently efficient population transfer from the initially excited quartet states to the doublets, for example, to  ${}^2X_g/{}^2Y_g$  in an approximately 82:18 ratio. The decay of the second component to the ground state contains a prominent non-radiative pathway based on the different IR and TCSPC results. Some of the non-radiative pathways might be assigned to surface crossing and multiphonon relaxation ( $k_{nr}(XH)$ ).

Indeed, multiphonon relaxation typically plays a decisive role in non-radiative excited state decay of NIR emitters.<sup>[4,20,36,37]</sup> The fourth vibrational overtone of aromatic CH oscillators of pyridyl ligands ( $14065\text{ cm}^{-1}$ )<sup>[22]</sup> falls within the emission band envelope of the room temperature emission band of  $[\text{Cr}(\text{tpe})_2]^{3+}$  (Figure S15). This results in an appreciable spectral overlap integral, hence promoting non-radiative deactivation by nearby CH oscillators (Scheme 3; pyridyl CH group with a  $\text{Cr}\cdots\text{H}$  distance of  $d \approx 3.0\text{ \AA}$ ).  $[\text{Cr}(\text{tpe})_2]^{3+}$  features six nearby CH oscillators (Scheme 3), while  $[\text{Cr}(\text{ddpd})_2]^{3+}$  only provides four of them (Scheme 1). This further increases  $k_{nr}(XH)$  of  $[\text{Cr}(\text{tpe})_2]^{3+}$  with respect to that of  $[\text{Cr}(\text{ddpd})_2]^{3+}$ . However, at 10 K, the emission of the distorted  ${}^2X_2(D_{3d})$  state of  $[\text{Cr}(\text{tpe})_2]^{3+}$  shifts to lower energy (Figure 4), significantly reducing the spectral overlap integral and consequently enhancing the quantum yield.



**Scheme 3.** Possible non-radiative decay pathways of  $[\text{Cr}(\text{tpe})_2]^{3+}$ : multiphonon relaxation by ligand CH modes (a: in purple), by water OH modes (b: in red), by acetonitrile CH modes (c: in red); Dexter energy transfer to  ${}^3\text{O}_2$  (d: in blue) and electron transfer from azulene Az (e: in green). Distances ( $d$ ) to  $\text{CH}_3\text{CN}$  and  $\text{H}_2\text{O}$  estimated from XRD analyses (see above).

Similar to CH oscillators of the ligand, OH oscillators of the solvent quench the phosphorescence (Table S2; Scheme 3;  $\text{Cr}\cdots\text{O}$  distance  $d \approx 6.5\text{ \AA}$ ). This solvent-promoted non-radiative decay is less likely in heavy water due to the required higher overtone of the OD vibration. This increases quantum yield and lifetime by 1.5–1.6. Changing the medium from  $\text{H}_2\text{O}/\text{HClO}_4$  to  $\text{CH}_3\text{CN}/\text{HClO}_4$  (and  $\text{D}_2\text{O}/\text{DClO}_4$  to

$\text{CD}_3\text{CN}/\text{DClO}_4$ ) barely affects the photophysical data (Table S2). This might be an effect of the water/perchlorate present with the perchloric acid providing a similar micro-environment around the complex under all conditions (cf. Figure 1). This assumption is substantiated by estimating the expected effect of  $\text{CH}_3\text{CN}$  deuteration according to the theory of multiphonon relaxation.<sup>[36,37]</sup> Determination of CH/CD overtone and combination mode energies and extinction coefficients of  $\text{CH}_3\text{CN}/\text{CD}_3\text{CN}$  allowed calculating the expected spectral overlap integrals with the luminescence band. In fact,  $k_{nr}(\text{CD})$  should be smaller than  $k_{nr}(\text{CH})$  by more than three orders of magnitude (for details see Figures S26–S33), provided this pathway would play a significant role. This is clearly not the case and hence,  $k_{nr}(\text{CH})$  through acetonitrile CH modes is not particularly relevant under these acidic/wet conditions.

We suggest that a close to octahedral symmetry of the  $[\text{CrN}_6]$  polyhedron with N–Cr–N angles of  $\approx 90^\circ/\approx 180^\circ$  is beneficial for high  $\Phi$  as the resulting strong ligand field shifts the quartet states to higher energy (small  $k_{nr}(\text{BISC})$ ). Yet, an inversion center of the entire complex (e.g.  $O_h$ ,  $D_{4h}$ ,  $D_{3d}$  point groups), including the  $\pi$  planes of the pyridine rings, reduces  $k_r$  and hence, the quantum yield. Shielding of the complex from solvent XH modes decreases  $k_{nr}(\text{XH})$ . Both, small  $k_r$  and  $k_{nr}$  lead to the exceptionally high lifetime  $\tau$  of  $[\text{Cr}(\text{tpe})_2]^{3+}$ . The long lifetime should favor bimolecular reactions with substrates, namely energy transfer ( $k(\text{EnT})$ ) and electron transfer ( $k(\text{ET})$ ) (Scheme 3).

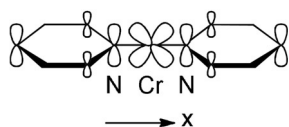
In acidic, air-saturated water, oxygen quenches the spin-flip emission of  $[\text{Cr}(\text{tpe})_2]^{3+}$  with  $\tau(\text{Ar}) : \tau(\text{O}_2)$  ratios of 2.5 ( $\text{H}_2\text{O}$ ) and 2.0 ( $\text{D}_2\text{O}$ ) (Scheme 3, path d;  $k_{nr}(\text{EnT})$ ; Table S2). Similar values are found in acetonitrile/acid mixtures. Obviously, the typical Dexter energy transfer pathway<sup>[81]</sup> of the doublet state(s) to  ${}^3\text{O}_2$  forming  ${}^1\text{O}_2$  is viable for  $[\text{Cr}(\text{tpe})_2]^{3+}$  (Scheme 3, blue quenching pathway).<sup>[26]</sup> The very high lifetime favors this pathway and enables applications of  $[\text{Cr}(\text{tpe})_2]^{3+}$  in photo-induced energy transfer reactions.

### Ground State and Excited State Redox Properties

$[\text{Cr}(\text{tpe})_2]^{3+}$  exhibits two reversible one-electron reduction waves at  $E_{1/2} = -0.88$  and  $-1.54\text{ V}$  and a quasireversible reduction peak at  $E_p = -2.49\text{ V}$  (Figures S34–S35).  $[\text{Cr}(\text{ddpd})_2]^{3+}$  is reduced to the corresponding labile  $d^4$  chromium(II) complex at  $E_{1/2} = -1.11\text{ V}$  and irreversibly at the ddpd ligand at  $-1.94\text{ V}$  vs.  $\text{FcH}/\text{FcH}^+$ .<sup>[3,6]</sup> On the other hand,  $[\text{Cr}(\text{tpy})_2]^{3+}$  ( $E_{1/2} = -0.53, -0.95, -1.45, -2.37\text{ V}$ )<sup>[2]</sup> and  $[\text{Cr}(\text{bpy})_3]^{3+}$  ( $E_{1/2} = -0.63, -1.15, -1.72, -2.34, -2.67, -2.90\text{ V}$ )<sup>[1a]</sup> exhibit several reversible one-electron reduction steps, which have all been assigned to ligand centered reductions yielding the corresponding radical anions and dianions coordinated to  $\text{Cr}^{3+}$ .  $[\text{Cr}(\text{bpy})_3]^{n+}$  and  $[\text{Cr}(\text{tpy})_2]^{n+}$  ( $n = 2, 1$ ) exhibit characteristic intense absorption bands in the red to near-infrared spectral region. On the basis of their intensity ( $\epsilon$  in the order of several  $1000\text{ M}^{-1}\text{ cm}^{-1}$ ) and time-dependent DFT calculations, these bands have been assigned to  $\pi\text{-}\pi^*$  transitions of the  ${}^1\text{bpy}^-/\text{tpy}^-$  radical anions.<sup>[1]</sup>

In order to determine the site of reduction,  $[\text{Cr}(\text{tpe})_2]^{3+}$  was subjected to reductive electrolysis inside a transparent UV/Vis/NIR cell under the in situ conditions of spectroelectrochemistry.<sup>[82]</sup> Exemplary spectra are displayed in Figure S36. Most notably, intense bands in the red to near-infrared spectral region grow in. The intensities of these bands with  $\epsilon > 1000 \text{ M}^{-1} \text{ cm}^{-1}$  are clearly incompatible with a chromium(II) or chromium(I) complex description as these complexes should only display weak Laporte-forbidden transitions. The observed intense bands resemble those of  $[\text{Cr}(\text{bpy})_3]^{n+}$  and  $[\text{Cr}(\text{tpy})_2]^{n+}$  ( $n=2, 1$ ) with coordinated ligand radical anions.<sup>[1]</sup> Consequently, we assign these bands to  $\pi$ - $\pi^*$  transitions of coordinated  $\text{tpe}^-$  radical ligands. TD-DFT calculations on geometry optimized  $[\text{Cr}(\text{tpe})_2]^{2+}$  ( $S=1$ ) and  $[\text{Cr}(\text{tpe})_2]^+$  ( $S=1/2$ ) cations find charge transfer absorption bands in these spectral regions as well (Figure S37). The good agreement substantiates the  $S=1$  and  $S=1/2$  ground state of  $[\text{Cr}(\text{tpe})_2]^{2+}$  and  $[\text{Cr}(\text{tpe})_2]^+$ , respectively. This fully agrees with previously reported complexes of chromium(III) and pyridine radical ligands.<sup>[1,2]</sup>

DFT calculations of the respective di- and monocations are consistent with a description as chromium(III) ions coordinated by radical ligands, although the Mulliken  $\alpha$  spin density at Cr corresponds to less than three unpaired electrons (Figure S7). This suggests strong interactions between the  $3d(\pi)$  orbitals and the  $\pi$  system of the ligands. The  $\beta$  spin density distribution cannot be assigned to individual tpe ligands, but is rather delocalized over two *trans*-coordinated pyridines of different tpe ligands featuring a coplanar orientation (Figure S7 b and S7 c; Scheme 4). This contrasts with



**Scheme 4.** Relevant spin-carrying ligand  $\pi^*$  and metal d orbitals along the x axis in  $[\text{Cr}(\text{tpe})_2]^{n+}$  ( $n=1, 2$ ); analogous combinations are formed along the y and z directions.

the behavior of the radical ligands in  $[\text{Cr}(\text{bpy})_3]^{n+}$ ,  $[\text{Cr}(\text{tpy})_2]^{n+}$  and  $[\text{Cr}(\text{MePDP})_2]^{2-}$  coordinated in an orthogonal arrangement of the ligand planes. The *trans*-coordinated pyridine pairs in  $[\text{Cr}(\text{tpe})_2]^{n+}$  are perfectly co-planar and aligned with the chromium  $d(\pi)$  orbitals (Scheme 4; Figure 6a). This generates three molecular orbitals, each comprised of two pyridine  $\pi^*$  orbitals and a symmetry-corresponding  $d(\pi)$  orbital of the metal (Scheme 4; py-Cr-py). In  $[\text{Cr}(\text{tpe})_2]^{2+}$  (triplet state), three electrons occupy the metal  $d(\pi)$  orbitals with  $\alpha$  spins and the fourth electron occupies a molecular orbital composed of two  $\pi^*$  orbitals of *trans*-coordinated pyridines with a  $\beta$  spin (antiferromagnetic coupling to one  $\alpha$  spin in the corresponding  $d(\pi)$  orbital; Figure S7 b).

In the monocation  $[\text{Cr}(\text{tpe})_2]^+$  (doublet state), three electrons occupy the metal  $d(\pi)$  orbitals with  $\alpha$  spins. The two  $\beta$  electrons are symmetrically delocalized over all six pyridines with a net antiferromagnetic coupling to two  $\alpha$  spins

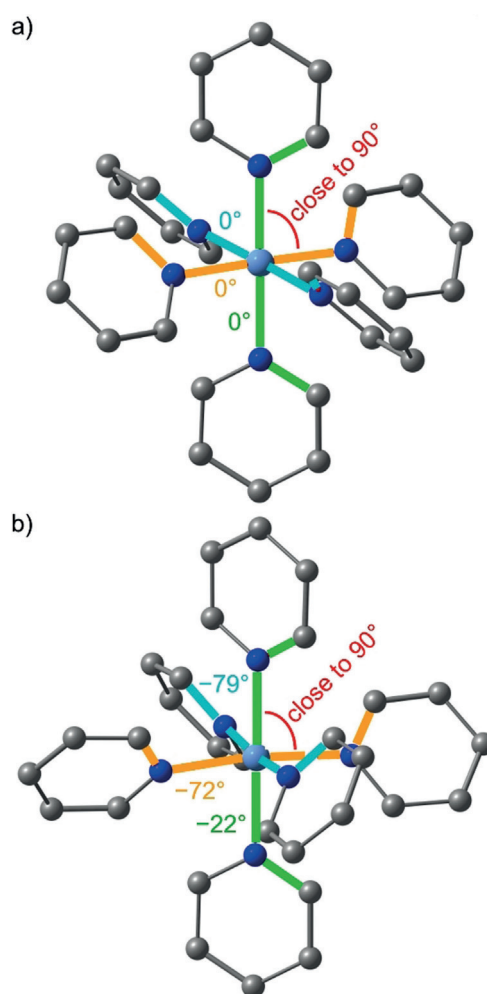


**Figure 6.** Close to octahedral symmetry of the  $[\text{CrN}_6]$  cores and the different orientations of the pyridine ligands in a)  $[\text{Cr}(\text{tpe})_2]^{3+}$  and b)  $[\text{Cr}(\text{ddpd})_2]^{3+}$  complexes. The bridging atoms and hydrogen atoms of the ligands are omitted and the N-Cr-N (in red) and C-N-N-C angles (in blue, green and orange) given in deg.

in the chromium  $d(\pi)$  orbitals (Figure S7 c). A delocalized model has also been calculated for  $[\text{Cr}(\text{bpy})_3]^+$  featuring three identical  $\beta$  spin-carrying bpy ligands (point group  $D_3$ ) although with a larger spin density at the metal center.<sup>[1a]</sup> That delocalized descriptions are favored could be an intrinsic bias of the B3LYP functional<sup>[1]</sup> or due to the lack of charge-localizing and symmetry-breaking counterions in the computational model. The suitable description of the electronic structures of  $[\text{Cr}(\text{bpy})_3]^{n+}$ ,  $[\text{Cr}(\text{tpy})_2]^{n+}$  and  $[\text{Cr}(\text{tpe})_2]^{n+}$  ( $n=2, 1$ ) as chromium(III) ions coordinated by radical ligands is, however, demonstrated in all cases and consistent with UV/Vis/NIR spectroscopic data. Reduction of pyridines coordinated to  $\text{Cr}^{\text{III}}$  becomes more difficult in the series tpy, <sup>4</sup>bpy,<sup>[1]</sup> and tpe and hence, the latter case approaches other limiting electronic situation  $[\text{Cr}^{\text{II}}\text{L}_3]^{2+}$  with an essentially metal centered reduction as realized in  $[\text{Cr}^{\text{II}}(\text{ddpd})_2]^{2+}$ .<sup>[3,6]</sup> This sequence can be attributed to the type and energy of the  $\pi^*$  system hosting the additional electron, namely Cr(**py-py-py**), Cr(**py-py**), and [**py-Cr-py**] (Scheme 4) for  $[\text{Cr}(\text{tpy})_2]^{2+}$ ,  $[\text{Cr}(\text{bpy})_3]^{2+}$ , and  $[\text{Cr}(\text{tpe})_2]^{2+}$ , respectively.

With the doublet state energy of  $[\text{Cr}(\text{tpe})_2]^{3+}$  of ca. 1.75 eV at room temperature (from the 0-0 energy of the emission band fit, Figure S15) and the redox potential of the  $[\text{Cr}(\text{tpe})_2]^{3+/2+}$  couple, the excited state reduction potential amounts to +0.87 V vs.  $\text{FcH}/\text{FcH}^+$  (+1.25 V vs. SCE<sup>[83]</sup>). This exceeds the potential of commonly employed photoredox catalysts  $[\text{Ru}(\text{bpy})_3]^{2+}$  (+0.77 V vs. SCE<sup>[84]</sup>) and *fac*- $\text{Ir}(\text{ppy})_3$  (+0.31 V vs. SCE;<sup>[27]</sup>  $\text{ppy} = \text{anion of 2-phenylpyridine}$ ), yet is smaller than that of the strongest chromium(III) derived photooxidants ( $[\text{Cr}(\text{dmcbpy})_3]^{3+}$ : +1.84 V vs. SCE;  $\text{dmcbpy} = 4,4'$ -di(methylcarboxyl)-2,2'-bipyridine;<sup>[27]</sup>  $[\text{Cr}(\text{ttpy})_2]^{3+}$ : +1.44 V vs. SCE;  $\text{ttpy} = 4'-(p\text{-tolyl})-2,2':6,2''\text{-terpyridine}$ ).<sup>[85]</sup> In terms of excited state lifetime,  $[\text{Cr}(\text{tpe})_2]^{3+}$  surpasses all these sensitizers by orders of magnitude ( $\tau([\text{Ru}(\text{bpy})_3]^{2+}) = 1.1 \mu\text{s}$ ;  $\tau(\text{fac-}\text{Ir}(\text{ppy})_3) = 1.9 \mu\text{s}$ ;  $\tau([\text{Cr}(\text{dmcbpy})_3]^{3+}) = 7.7 \mu\text{s}$ ;  $\tau([\text{Cr}(\text{ttpy})_2]^{3+}) = 0.27 \mu\text{s}$ ).<sup>[27,85]</sup>

To probe the photoredox chemistry of  $[\text{Cr}(\text{tpe})_2]^{3+}$ , azulene (Az) was employed as substrate. The triplet energy of Az (1.74 eV)<sup>[86]</sup> is close to the doublet state energy of  $[\text{Cr}(\text{tpe})_2]^{3+}$ , hence energy transfer to Az is less favorable. On the other hand, Az can be oxidized to its radical cation  $\text{Az}^+$  at 0.50 V vs.  $\text{FcH}/\text{FcH}^+$  (0.88 V vs. SCE)<sup>[87]</sup> which is significantly lower than the excited state redox potential of  $[\text{Cr}(\text{tpe})_2]^{3+}$ , proving enough driving force for the electron transfer. Az quenches the luminescence of  $[\text{Cr}(\text{tpe})_2]^{3+}$  with a Stern–Volmer constant  $K_{\text{SV}} = 41.7 \times 10^3 \text{ M}^{-1}$  (Figure S38). The efficient luminescence quenching by Az supports photoinduced electron transfer from Az to  $^2[\text{Cr}(\text{tpe})_2]^{3+}$  (Scheme 3,  $k_{\text{nr}}$  (ET)), that is, to the redox orbital formed by tpe ligands and the chromium ion (Scheme 4). Additionally, tri(*n*-butyl)amine ( $E^{\text{p}} = 0.38 \text{ V vs. FcH}/\text{FcH}^+$ )<sup>[24]</sup> quenches the luminescence of  $[\text{Cr}(\text{tpe})_2]^{3+}$  forming  $[\text{Cr}(\text{tpe})_2]^{2+}$  according to UV/Vis/NIR spectroscopy (Figure S39). Further substrates suitable for activation by  $[\text{Cr}(\text{tpe})_2]^{3+}$  will be reported in future studies.

## Conclusion

The centrosymmetric complex  $[\text{Cr}(\text{tpe})_2]^{3+}$  is highly luminescent at room temperature in  $\text{D}_2\text{O}/\text{DClO}_4$  ( $\Phi = 8.2\%$ ) due to a large ligand field splitting ( $23200 \text{ cm}^{-1}$ ). The emission ( $13370 \text{ cm}^{-1}$ ) is strongly Laporte-forbidden, leading to an unprecedentedly high luminescence lifetime (4500  $\mu\text{s}$ ). The most relevant non-radiative pathways of the luminescent states are surface crossing with the ground state and multiphonon relaxation through nearby CH oscillators of the tpe ligand as well as through solvent modes (OH in water). Energy transfer from the excited state to triplet oxygen is feasible as well.

The coplanar orientation of *trans*-coordinated pyridine donors in  $[\text{Cr}(\text{tpe})_2]^{3+}$  enables ligand-based reduction processes. The additional electrons occupy  $\pi^*$  orbitals delocalized over two tpe ligands (and some Cr) in  $[\text{Cr}(\text{tpe})_2]^{2+/+}$  ions. These coordinated  $\pi$  radicals show strong NIR absorption bands. Consequently, a conjugated oligopyridine ligand, as found in the electron transfer series  $[\text{Cr}(\text{bpy})_3]^{n+}$  and  $[\text{Cr}(\text{tpy})_2]^{n+}$ , is not required for ligand-based redox-chemistry.

The very long excited state lifetime and ligand-centered reduction of  $[\text{Cr}(\text{tpe})_2]^{3+}$  enable both, energy and electron transfer processes with suitable substrates such as oxygen, azulene and tri(*n*-butyl)amine. This excited state reactivity paves the way for employing this specific  $[\text{CrN}_6]$  chromophore architecture in energy transfer schemes such as singlet oxygen formation,<sup>[26]</sup> triplet sensitizing<sup>[88]</sup> or lanthanide-based energy transfer upconversion<sup>[34b]</sup> as well as in photoredox catalysis.<sup>[27–30]</sup> Work in these directions is currently in progress in our laboratories.

## Acknowledgements

This work was supported by the Deutsche Forschungsgemeinschaft (RE 1203/23-1, Priority Program SPP 2102, “Light-controlled reactivity of metal complexes” HE 2778/15-1, SE 1448/8-1, GE 961/10-1), the Natural Sciences and Engineering Research Council of Canada, and the DAAD for a visiting research fellowship to C.R. Parts of this research were conducted using the supercomputer MOGON and advisory services offered by Johannes Gutenberg University of Mainz (www.hpc.uni-mainz.de), which is a member of the AHRP and the Gauss Alliance e.V. We are grateful to Dr. Dieter Schollmeyer for the X-ray data collection.

## Conflict of interest

The authors declare no conflict of interest.

**Keywords:** Earth-abundant metals · Laporte's rule · Luminescence · Photoredox chemistry · Sustainable Chemistry

**How to cite:** *Angew. Chem. Int. Ed.* **2019**, *58*, 18075–18085  
*Angew. Chem.* **2019**, *131*, 18243–18253

- [1] a) C. C. Scarborough, S. Sproules, T. Weyhermüller, S. DeBeer, K. Wieghardt, *Inorg. Chem.* **2011**, *50*, 12446–12462; b) C. C. Scarborough, K. M. Lancaster, S. DeBeer, T. Weyhermüller, S. Sproules, K. Wieghardt, *Inorg. Chem.* **2012**, *51*, 3718–3732.
- [2] A. Gowda, J. L. Petersen, C. Milsmann, *Inorg. Chem.* **2018**, *57*, 1919–1934.
- [3] S. Otto, M. Grabolle, C. Förster, C. Kreitner, U. Resch-Genger, K. Heinze, *Angew. Chem. Int. Ed.* **2015**, *54*, 11572–11576; *Angew. Chem.* **2015**, *127*, 11735–11739.
- [4] S. Otto, M. Dorn, C. Förster, M. Bauer, M. Seitz, K. Heinze, *Coord. Chem. Rev.* **2018**, *359*, 102–111.
- [5] O. S. Wenger, *J. Am. Chem. Soc.* **2018**, *140*, 13522–13533.
- [6] C. Förster, M. Dorn, T. Reuter, S. Otto, G. Davarci, T. Reich, L. Carrella, E. Rentschler, K. Heinze, *Inorganics* **2018**, *6*, 86.
- [7] H. Xiang, J. Cheng, X. Ma, X. Zhou, *Chem. Soc. Rev.* **2013**, *42*, 6128–6185.
- [8] A. D. Kirk, *Coord. Chem. Rev.* **1981**, *39*, 225–263.
- [9] M. A. Jamieson, N. Serpone, M. Z. Hoffman, *Coord. Chem. Rev.* **1981**, *39*, 121–179.
- [10] L. S. Forster, *Chem. Rev.* **1990**, *90*, 331–353.
- [11] A. D. Kirk, *Chem. Rev.* **1999**, *99*, 1607–1640.
- [12] N. Serpone, M. A. Jamieson, M. S. Henry, M. Z. Hoffman, F. Bolletta, M. Maestri, *J. Am. Chem. Soc.* **1979**, *101*, 2907–2916.



- [13] D. Zare, B. Doistau, H. Nozary, C. Besnard, L. Guenee, Y. Suffren, A.-L. Pele, A. Hauser, C. Piguët, *Dalton Trans.* **2017**, 46, 8992–9009.
- [14] J. C. Barbour, A. J. I. Kim, E. deVries, S. E. Shaner, B. M. Lovaasen, *Inorg. Chem.* **2017**, 56, 8212–8222.
- [15] B. Doistau, G. Collet, E. A. Bolomey, V. Sadat-Noorbakhsh, C. Besnard, C. Piguët, *Inorg. Chem.* **2018**, 57, 14362–14373.
- [16] M. W. Perkovic, M. J. Heeg, J. F. Endicott, *Inorg. Chem.* **1991**, 30, 3140–3147.
- [17] M. W. Perkovic, J. F. Endicott, *J. Phys. Chem.* **1990**, 94, 1217–1219.
- [18] K. N. Brown, R. J. Geue, A. M. Sargeson, G. Moran, S. F. Ralph, H. Riesen, *Chem. Commun.* **1998**, 2291–2292.
- [19] A. M. McDaniel, H.-W. Tseng, E. A. Hill, N. H. Damrauer, A. K. Rappé, M. P. Shores, *Inorg. Chem.* **2013**, 52, 1368–1378.
- [20] C. Wang, S. Otto, M. Dorn, E. Kreidt, J. Lebon, L. Sršan, P. Di Martino-Fumo, M. Gerhards, U. Resch-Genger, M. Seitz, K. Heinze, *Angew. Chem. Int. Ed.* **2018**, 57, 1112–1116; *Angew. Chem.* **2018**, 130, 1125–1130.
- [21] S. Otto, N. Scholz, T. Behnke, U. Resch-Genger, K. Heinze, *Chem. Eur. J.* **2017**, 23, 12131–12135.
- [22] S. Otto, J. Harris, K. Heinze, C. Reber, *Angew. Chem. Int. Ed.* **2018**, 57, 11069–11073; *Angew. Chem.* **2018**, 130, 11236–11240.
- [23] C. Wang, S. Otto, M. Dorn, K. Heinze, U. Resch-Genger, *Anal. Chem.* **2019**, 91, 2337–2344.
- [24] S. Otto, A. M. Nauth, E. Ermilov, N. Scholz, A. Friedrich, U. Resch-Genger, S. Lochbrunner, T. Opatz, K. Heinze, *Chem-PhotoChem* **2017**, 1, 344–349.
- [25] U. Basu, S. Otto, K. Heinze, G. Gasser, *Eur. J. Inorg. Chem.* **2019**, 37–41.
- [26] J.-R. Jiménez, B. Doistau, C. Besnard, C. Piguët, *Chem. Commun.* **2018**, 54, 13228–13231.
- [27] S. M. Stevenson, M. P. Shores, E. M. Ferreira, *Angew. Chem. Int. Ed.* **2015**, 54, 6506–6510; *Angew. Chem.* **2015**, 127, 6606–6610.
- [28] R. F. Higgins, S. M. Fatur, S. G. Shepard, S. M. Stevenson, D. J. Boston, E. M. Ferreira, N. H. Damrauer, A. K. Rappé, M. P. Shores, *J. Am. Chem. Soc.* **2016**, 138, 5451–5464.
- [29] S. M. Stevenson, R. F. Higgins, M. P. Shores, E. M. Ferreira, *Chem. Sci.* **2017**, 8, 654–660.
- [30] F. J. Sarabia, Q. Li, E. M. Ferreira, *Angew. Chem. Int. Ed.* **2018**, 57, 11015–11019; *Angew. Chem.* **2018**, 130, 11181–11185.
- [31] E. Previtera, A. Tissot, *Eur. J. Inorg. Chem.* **2016**, 1972–1979.
- [32] a) A. Cadranel, J. E. Tate, P.-S. Oviedo, S. Yamazaki, J. H. Hodak, L. M. Baraldo, V. D. Kleiman, *Phys. Chem. Chem. Phys.* **2017**, 19, 2882–2893; b) A. Cadranel, P. S. Oviedo, P. Alborés, L. M. Baraldo, D. M. Guldi, J. H. Hodak, *Inorg. Chem.* **2018**, 57, 3042–3053.
- [33] P. T. Burks, A. D. Ostrowski, A. A. Mikhailovsky, E. M. Chan, P. S. Wagenknecht, P. C. Ford, *J. Am. Chem. Soc.* **2012**, 134, 13266–13275.
- [34] a) W. P. Forrest, Z. Cao, H. M. Rhodes Hambrick, B. M. Prentice, P. E. Fanwick, P. S. Wagenknecht, T. T. Ren, *Eur. J. Inorg. Chem.* **2012**, 5616–5620; b) L. Aboshyan-Sorgho, C. Besnard, P. Pattison, K. R. Kittilstved, A. Aebischer, J.-C. G. Bünzli, A. Hauser, C. Piguët, *Angew. Chem. Int. Ed.* **2011**, 50, 4108–4112; *Angew. Chem.* **2011**, 123, 4194–4198.
- [35] P. S. Wagenknecht, P. C. Ford, *Coord. Chem. Rev.* **2011**, 255, 591–616.
- [36] V. L. Ermolaev, E. B. Sveshnikova, *Russ. Chem. Rev.* **1994**, 63, 905–922.
- [37] E. Kreidt, C. Kruck, M. Seitz, *Handbook on the Physics and Chemistry of Rare Earths, Vol. 53* (Eds. J. C.-G. Bünzli, V. K. Pecharsky) **2018**, Elsevier, Amsterdam, pp. 35–79.
- [38] A. Breivogel, C. Förster, K. Heinze, *Inorg. Chem.* **2010**, 49, 7052–7056.
- [39] K. Mack, A. Wünsche von Leupoldt, C. Förster, M. Ezhevskaya, D. Hinderberger, K. W. Klinkhammer, K. Heinze, *Inorg. Chem.* **2012**, 51, 7851–7858.
- [40] C. Förster, K. Mack, L. M. Carrella, V. Ksenofontov, E. Rentschler, K. Heinze, *Polyhedron* **2013**, 52, 576–581.
- [41] A. K. C. Mengel, C. Förster, A. Breivogel, K. Mack, J. R. Ochsmann, F. Laquai, V. Ksenofontov, K. Heinze, *Chem. Eur. J.* **2015**, 21, 704–714.
- [42] S. Otto, J. Moll, C. Förster, D. Geißler, C. Wang, U. Resch-Genger, K. Heinze, *Eur. J. Inorg. Chem.* **2017**, 5033–5040.
- [43] M. Dorn, K. Mack, L. M. Carrella, E. Rentschler, C. Förster, K. Heinze, *Z. Anorg. Allg. Chem.* **2018**, 644, 706–712.
- [44] A. Maleckis, J. W. Kampf, M. S. Sanford, *J. Am. Chem. Soc.* **2013**, 135, 6618–6625.
- [45] A. Santoro, C. Sambiagio, P. C. McGowan, M. A. Halcrow, *Dalton Trans.* **2015**, 44, 1060–1069.
- [46] T. Ishida, T. Kanetomo, M. Yamasaki, *Acta Crystallogr. Sect. C* **2016**, 72, 797–801.
- [47] E. A. Ünal, D. Wiedemann, J. Seiffert, J. P. Boyd, A. Grohmann, *Tetrahedron Lett.* **2012**, 53, 54–55.
- [48] D. Wiedemann, A. Grohmann, *Z. Anorg. Allg. Chem.* **2014**, 640, 1632–1640.
- [49] O. Laporte, W. F. Meggers, *J. Opt. Soc. Am.* **1925**, 11, 459–463.
- [50] STOE & Cie, X-Red, STOE & Cie, Darmstadt, Germany **2002**.
- [51] R. H. Blessing, *Acta Crystallogr. Sect. A* **1995**, 51, 33–38.
- [52] A. L. Spek, *Acta Crystallogr. Sect. D* **2009**, 65, 148–155.
- [53] G. M. Sheldrick, SHELXL-2014/7, University of Göttingen, Göttingen, Germany, **2014**.
- [54] G. M. Sheldrick, *Acta Crystallogr. Sect. A* **2015**, 71, 3–8.
- [55] a) C. Würth, J. Pauli, C. Lochmann, M. Spieles, U. Resch-Genger, *Anal. Chem.* **2012**, 84, 1345–1352; b) C. Würth, M.-G. González, R. Niessner, U. Panne, C. Haisch, U. Resch-Genger, *Talanta* **2012**, 90, 30–37; c) C. Würth, D. Geissler, T. Behnke, M. Kaiser, U. Resch-Genger, *Anal. Bioanal. Chem.* **2015**, 407, 59–78.
- [56] J. R. Schoonover, G. F. Strouse, K. M. Omberg, R. B. Dyer, *Comments Inorg. Chem.* **1996**, 18, 165–188.
- [57] M. Zimmer, F. Rupp, P. Singer, F. Walz, F. Breher, W. Klopfer, R. Diller, M. Gerhards, *Phys. Chem. Chem. Phys.* **2015**, 17, 14138–14144.
- [58] F. Bäßler, M. Zimmer, F. Dietrich, M. Gruppe, M. Wallesch, D. Volz, S. Bräse, M. Gerhards, R. Diller, *Phys. Chem. Chem. Phys.* **2017**, 19, 29438–29448.
- [59] F. Neese, *WIREs Comput. Mol. Sci.* **2012**, 2, 73–78.
- [60] F. Neese, F. Wennmohs, A. Hansen, U. Becker, *Chem. Phys.* **2009**, 356, 98–109.
- [61] R. Izsák, F. Neese, *J. Chem. Phys.* **2011**, 135, 144105.
- [62] A. D. Becke, *J. Chem. Phys.* **1993**, 98, 5648–5652.
- [63] F. Weigend, R. Ahlrichs, *Phys. Chem. Chem. Phys.* **2005**, 7, 3297–3305.
- [64] F. Weigend, *Phys. Chem. Chem. Phys.* **2006**, 8, 1057–1065.
- [65] D. A. Pantazis, X.-Y. Chen, C. R. Landis, F. Neese, *J. Chem. Theory Comput.* **2008**, 4, 908–919.
- [66] E. van Lenthe, E. J. Baerends, J. G. Snijders, *J. Chem. Phys.* **1993**, 99, 4597–4610.
- [67] S. Grimme, J. Antony, S. Ehrlich, H. Krieg, *J. Chem. Phys.* **2010**, 132, 154104.
- [68] S. Grimme, S. Ehrlich, L. Goerigk, *J. Comput. Chem.* **2011**, 32, 1456–1465.
- [69] V. Barone, M. Cossi, *J. Phys. Chem. A* **1998**, 102, 1995–2001.
- [70] a) U. Casellato, R. Graziani, R. P. Bonomo, A. J. Di Bilio, *J. Chem. Soc. Dalton Trans.* **1991**, 23–31; b) R. P. Bonomo, A. J. Di Bilio, F. Riggi, *Chem. Phys.* **1991**, 151, 323–333.
- [71] S. Otto, C. Förster, C. Wang, U. Resch-Genger, K. Heinze, *Chem. Eur. J.* **2018**, 24, 12555–12563.
- [72] A. Breivogel, M. Meister, C. Förster, F. Laquai, K. Heinze, *Chem. Eur. J.* **2013**, 19, 13745–13760.

- [73] a) R. Frantz, A. Pinto, S. Constant, G. Bernadinelli, J. Lacour, *Angew. Chem. Int. Ed.* **2005**, *44*, 5060–5064; *Angew. Chem.* **2005**, *117*, 5188–5192; b) G. Li, M. D. Brady, G. J. Meyer, *J. Am. Chem. Soc.* **2018**, *140*, 5447–5456.
- [74] M. J. Abrams, R. Faggani, C. J. L. Lock, *Inorg. Chim. Acta* **1985**, *106*, 69–74.
- [75] M. G. Brik, A. M. Srivastava, *ECS J. Solid State Sci. Technol.* **2018**, *7*, R3079–R3085.
- [76] R. Dannöhl-Fickler, H. Kelm, F. Wasgestian, *J. Lumin.* **1975**, *10*, 103–112.
- [77] A. P. Forshaw, R. P. Botchev, J. M. Smith, *Inorg. Chem.* **2007**, *46*, 3792–3794.
- [78] V. Baslon, J. P. Harris, C. Reber, H. E. Colmer, T. A. Jackson, A. P. Forshaw, J. R. Smith, R. A. Kinney, J. Telsner, *Can. J. Chem.* **2017**, *95*, 547–552.
- [79] P. E. Hoggard, H.-H. Schmidtke, *Ber. Bunsen-Ges.* **1972**, *76*, 1013–1021.
- [80] M. Zimmer, F. Dietrich, D. Volz, S. Bräse, M. Gerhards, *ChemPhysChem* **2017**, *18*, 3023–3029.
- [81] F. Strieth-Kalthoff, M. J. James, M. Teders, L. Pitzer, F. Glorius, *Chem. Soc. Rev.* **2018**, *47*, 7190–7202.
- [82] a) M. Krejčík, M. Daněk, F. Hartl, *J. Electroanal. Chem. Interfacial Electrochem.* **1991**, *317*, 179–187; b) *Spectroelectrochemistry* (Eds. W. Kaim, A. Klein), RSC Publishing, London, **2008**.
- [83] V. V. Pavlishchuk, A. W. Addison, *Inorg. Chim. Acta* **2000**, *298*, 97–102.
- [84] C. Creutz, N. Sutin, *Inorg. Chem.* **1976**, *15*, 496–499.
- [85] R. Farran, L. Le-Quang, J.-M. Mouesca, V. Maurel, D. Jouvenot, F. Loiseau, A. Deronzier, J. Chauvin, *Dalton Trans.* **2019**, *48*, 6800–6811.
- [86] A. A. Gorman, I. Hamblett, R. J. Harrison, *J. Am. Chem. Soc.* **1984**, *106*, 6952–6955.
- [87] T. Kurihara, T. Suzuki, H. Wakabayashi, S. Ishikawa, K. Shindo, Y. Shimada, H. Chiba, T. Miyashi, M. Yasunami, T. Nozoe, *Bull. Chem. Soc. Jpn.* **1996**, *69*, 2003–2006.
- [88] T. R. Blum, Z. D. Miller, D. M. Bates, I. A. Guzei, T. P. Yoon, *Science* **2016**, *354*, 1391–1395.
- [89] CCDC 1876389 and 1876390 contain the supplementary crystallographic data for this paper. These data can be obtained free of charge from The Cambridge Crystallographic Data Centre.

Manuscript received: July 24, 2019

Revised manuscript received: October 1, 2019

Accepted manuscript online: October 10, 2019

Version of record online: October 31, 2019



Supporting Information

**Luminescence and Light-Driven Energy and Electron Transfer from an Exceptionally Long-Lived Excited State of a Non-Innocent Chromium(III) Complex**

*Steffen Treiling, Cui Wang, Christoph Förster, Florian Reichenauer, Jens Kalmbach, Pit Boden, Joe P. Harris, Luca M. Carrella, Eva Rentschler, Ute Resch-Genger, Christian Reber, Michael Seitz, Markus Gerhards, and Katja Heinze\**

anie\_201909325\_sm\_miscellaneous\_information.pdf

## **Author Contributions**

The manuscript was written through contributions of all authors. ST synthesized the tpe ligand and the tpe complexes, performed ground state IR, MS, CV and SEC studies as well as most DFT calculations. CF performed further DFT calculations, and solved and refined the X-ray structures, CW and URG performed the quantum yield and lifetime measurements in solution, LC and ER performed and analyzed the magnetic measurements, JK and MS performed the IR overtone spectroscopy and SOI calculations, PB and MG performed and interpreted the temperature dependent transient IR spectra and luminescence experiments in KBr disks and neat films, JPH and CR performed and interpreted low-temperature luminescence experiments in the crystals, FR prepared more material and performed the Stern–Volmer analysis. KH designed the concept, interpreted the data and wrote the manuscript. All authors have given approval to the final version of the manuscript.

## Supporting Information

**General Procedures.** Diethyl ether was distilled over sodium, THF over potassium and acetonitrile over calcium hydride. The ligand tpe was prepared similar to a reported procedure.<sup>51</sup> NMR spectroscopic and mass spectrometric data match the literature values. A glovebox (UniLab/MBraun, Ar 4.8, O<sub>2</sub> < 100 ppm, H<sub>2</sub>O < 1 ppm) was used for storage and weighing of sensitive compounds. Reagents were received from usual suppliers (ABCR, Acros Organics, Alfa Aesar, Fischer Scientific, Fluka and Sigma Aldrich). NMR spectra of tpe were recorded on a Bruker Avance DRX 400 spectrometer at 400.31 MHz (<sup>1</sup>H). All resonances are reported in ppm versus the solvent signal as internal standard [CDCl<sub>3</sub> (<sup>1</sup>H:  $\delta$  = 7.26)].<sup>52</sup> IR spectra were recorded with a Bruker Alpha FTIR spectrometer with ATR unit containing a diamond crystal. ESI<sup>+</sup> mass spectra were recorded on a Micromass Q-TOF-Ultima spectrometer. DC magnetic studies were performed with a Quantum Design MPMS-XL-7 SQUID magnetometer on powdered microcrystalline samples. Experimental susceptibility data were corrected for the underlying diamagnetism using Pascal's constants. The temperature dependent magnetic contribution of the holder and of the embedding eicosane matrix was experimentally determined and subtracted from the measured susceptibility data. Variable temperature susceptibility data were collected in a temperature range of 6 – 300 K under an applied field of 0.1 Tesla. Electrochemical experiments were carried out on a BioLogic SP-50 voltammetric analyzer using platinum wires as counter and working electrodes and a 0.01 M Ag/Ag[NO<sub>3</sub>] electrode as reference electrode. Cyclic voltammetry and square wave measurements were carried out at scan rates of 50–200 mV s<sup>-1</sup> using 0.1 M [N<sup>n</sup>Bu<sub>4</sub>][BF<sub>4</sub>] in CH<sub>3</sub>CN as supporting electrolyte. Potentials are referenced against the ferrocene/ferrocenium couple. Spectroelectrochemical experiments were performed using a Specac omni-cell liquid transmission cell with CaF<sub>2</sub> windows equipped with a Pt gauze working electrode, a Pt gauze counter electrode and a Ag wire as pseudo reference electrode, melt-sealed in a polyethylene spacer (approximate path length 0.5 mm) in 10<sup>-5</sup> M solutions in CH<sub>3</sub>CN, containing 0.1 M [N<sup>n</sup>Bu<sub>4</sub>][BF<sub>4</sub>]. UV/Vis/NIR spectra were recorded on a Varian Cary 5000 spectrometer using 1.0 cm cells. Luminescence emission spectra and decays in solution were reported with a calibrated spectrofluorometer FSP 920 from Edinburgh Instruments. For the measurement of the emission spectra, a continuous xenon lamp was applied as excitation light source, while the time-resolved luminescence measurements were completed with a  $\mu$ s xenon flashlamp and detection in a multi-channel scaling mode. All measurements were performed at magic angle condition (polarization 0° in the excitation and 54.7° in the emission channel). The luminescence decays in solution were analyzed by fitting the obtained decay curves mono-exponentially with the program FAST (Fluorescence Analysis Software Technology, Edinburgh Instruments Ltd.). The luminescence quantum yields in solution were determined using an Ulbricht integrating sphere (Quantaaurus-QY C11347-11, Hamamatsu).<sup>53-55</sup> Relative uncertainty is estimated to be  $\pm 5$  %. NIR absorption spectra of CH<sub>3</sub>CN and CD<sub>3</sub>CN for overtone determination were measured in absorption mode using a JASCO V-770 spectrophotometer (equipped with a long cuvette holder LSE-701). The spectra were recorded in rectangular semimicro cuvettes (Starna, type 28/B/SX/50, path length 5.0 cm). CH<sub>3</sub>CN was spectrophotometric grade and CD<sub>3</sub>CN was NMR grade (99.8% D). The spectra were corrected for baseline drift with OriginPro 9.0. The component peaks of the spectra were deconvoluted by fitting of the spectra with a series of Gaussian functions (Levenberg-Marquardt on  $\chi^2$ ). All time-resolved FTIR experiments were performed with an FTIR spectrometer Bruker Vertex 80v, operated in the step-scan mode. KBr pellets of [Cr(tpe)<sub>2</sub>][BF<sub>4</sub>]<sub>3</sub> (ca. 0.75 mg) were prepared by mixing with dry KBr (ca. 200 mg, stored at 80 °C) and grinding to a homogeneous mixture. The strongest peak in the ground state spectrum showed an absorption of about 0.6 OD with the mentioned concentration. Measurements with cryogenically cooled KBr pellets (20 K and 290 K at the sample) were performed with a closed cycle helium cryostat (ARS Model DE-202A). The cryo cooler was equipped with a

homebuilt pellet holder and CaF<sub>2</sub> windows. A liquid-nitrogen-cooled mercury cadmium telluride (MCT) detector (Kolmar Tech., Model KV100-1-B-7/190) with a rise time of 25 ns, connected to a fast preamplifier and a 14-bit transient recorder board (Spectrum Germany, M3I4142, 400 MS s<sup>-1</sup>), was used for signal detection and processing. The laser setup includes a Q-switched Nd:YAG laser (Innolas SpitLight Evo I) generating pulses with a band-width of 6 – 9 ns at a repetition rate of 100 Hz. The third harmonic (355 nm) of the Nd:YAG laser was used for sample excitation. The UV pump beam was attenuated to about 2.0 mJ per shot at a diameter of 9 mm. The beam was directed onto the sample and adjusted to have a maximal overlap with the IR beam of the spectrometer. The sample chamber was equipped with anti-reflection-coated germanium filters to prevent the entrance of laser radiation into the detector and interferometer compartments. The time delay between the start of the experiment and the UV laser pulse was controlled with a Stanford Research Systems DG535 delay generator. A total of more than 2000 coadditions were recorded at each interferogram point. The spectral region was limited by undersampling to 988 – 1975 cm<sup>-1</sup> with a spectral resolution of 4 cm<sup>-1</sup> resulting in 555 interferogram points. An IR broad band filter (850 – 1750 cm<sup>-1</sup>) and the CaF<sub>2</sub> windows (no IR transmission < 1000 cm<sup>-1</sup>) of the cryostat prevented problems when performing a Fourier transformation (*i.e.* no IR intensity outside the measured region should be observed). FTIR ground state spectra were recorded systematically to check for sample degradation. A more detailed description of the step-scan setup is given here.<sup>56-58</sup> Temperature dependent emission spectra of KBr disks were recorded with a FluoroMax-2 (Horiba Scientific) device using the described cryostat. Time-correlated single photon counting measurements were performed with a DeltaFlex (Horiba Scientific) instrument at a repetition rate of 10 kHz with a time resolution of 13 or 27 ns, depending on the experiment. Temperature dependent emission spectra of crystals of [Cr(tpe)<sub>2</sub>][BF<sub>4</sub>]<sub>3</sub> and [Cr(tpe)<sub>2</sub>][PF<sub>6</sub>]<sub>3</sub> were recorded with a Renishaw Invia Raman microscope equipped with a Peltier-cooled CCD camera. The excitation source was a 488 nm Argon ion laser. Variable-temperature spectra were obtained by coupling a Linkam cryostat to the microscope with liquid nitrogen used as the coolant. Elemental analyses were conducted by the microanalytical laboratory of the chemical institutes of the University of Mainz.

**Caution!** Although we have not experienced any problems in handling the perchlorate solutions, all materials should be handled with extreme care.

**Crystal structure determinations.** Diffusion of diethyl ether into concentrated solutions of [Cr(tpe)<sub>2</sub>][BF<sub>4</sub>]<sub>3</sub> or [Cr(tpe)<sub>2</sub>][PF<sub>6</sub>]<sub>3</sub> in CH<sub>3</sub>CN yielded diffraction quality crystals. Intensity data were collected with a STOE IPDS-2T diffractometer and an Oxford cooling system and corrected for absorption and other effects using Mo K<sub>α</sub> radiation ( $\lambda = 0.71073 \text{ \AA}$ ). The diffraction frames were integrated using the SAINT package, and most were corrected for absorption with MULABS.<sup>59,510,511</sup> The structures were solved by direct methods and refined by the full-matrix method based on  $F^2$  using the SHELXTL software package.<sup>512,513</sup> All non-hydrogen atoms were refined anisotropically, while the positions of all hydrogen atoms were generated with appropriate geometric constraints and allowed to ride on their respective parent carbon atoms with fixed isotropic thermal parameters. CCDC 1876389 ([Cr(tpe)<sub>2</sub>][BF<sub>4</sub>]<sub>3</sub>×3CH<sub>3</sub>CN) and 1876390 ([Cr(tpe)<sub>2</sub>][PF<sub>6</sub>]<sub>3</sub>×3CH<sub>3</sub>CN) contain the supplementary crystallographic data for this paper. These data are provided free of charge by The Cambridge Crystallographic Data Centre.

**Crystallographic Data of [Cr(tpe)<sub>2</sub>][BF<sub>4</sub>]<sub>3</sub>×3CH<sub>3</sub>CN:** C<sub>40</sub>H<sub>39</sub>B<sub>3</sub>CrF<sub>12</sub>N<sub>9</sub> (958.23); triclinic;  $P\bar{1}$ ;  $a = 11.3010(8) \text{ \AA}$ ,  $b = 13.5207(8) \text{ \AA}$ ,  $c = 15.5147(9) \text{ \AA}$ ,  $\alpha = 74.575(4)^\circ$ ,  $\beta = 76.869(5)^\circ$ ,  $\gamma = 73.432(5)^\circ$ ;  $V = 2150.6(2) \text{ \AA}^3$ ;  $Z = 2$ ; density, calcd. = 1.480 g cm<sup>-3</sup>,  $T = 120(2) \text{ K}$ ,  $\mu = 0.361 \text{ mm}^{-1}$ ;  $F(000) = 978$ ; crystal size 0.600 × 0.310 × 0.187 mm;  $\theta = 1.915$  to  $28.318 \text{ deg.}$ ;  $-15 \leq h \leq 15$ ,  $-17 \leq k \leq 18$ ,  $-20 \leq l \leq 20$ ; rfln collected = 39128; rfln unique = 10667 [ $R(\text{int}) = 0.0604$ ]; completeness to  $\theta = 25.242 \text{ deg.} = 99.9\%$ ; semi empirical

absorption correction from equivalents; max. and min. transmission 1.11561 and 0.88170; data 10667; restraints 300, parameters 861; goodness-of-fit on  $F^2 = 1.038$ ; final indices [ $I > 2\sigma(I)$ ]  $R_1 = 0.0556$ ,  $wR_2 = 0.1342$ ;  $R$  indices (all data)  $R_1 = 0.0871$ ,  $wR_2 = 0.1546$ ; largest diff. peak and hole 0.454 and  $-0.557 \text{ e } \text{\AA}^{-3}$ .

**Crystallographic Data of  $[\text{Cr}(\text{tpe})_2][\text{PF}_6]_3 \times 3\text{CH}_3\text{CN}$ :**  $\text{C}_{40}\text{H}_{39}\text{CrF}_{18}\text{N}_9\text{P}_3$  (1132.71); trigonal;  $R\bar{3}$ ;  $a = b = 16.953(2) \text{ \AA}$ ,  $c = 13.901(3) \text{ \AA}$ ;  $V = 3459.9(11) \text{ \AA}^3$ ;  $Z = 3$ ; density, calcd. =  $1.631 \text{ g cm}^{-3}$ ,  $T = 193(2) \text{ K}$ ,  $\mu = 0.468 \text{ mm}^{-1}$ ;  $F(000) = 1719$ ; crystal size  $0.310 \times 0.240 \times 0.190 \text{ mm}$ ;  $\theta = 2.403$  to  $28.293 \text{ deg.}$ ;  $-20 \leq h \leq 19$ ,  $-19 \leq k \leq 22$ ,  $-18 \leq l \leq 18$ ; rfln collected = 6617; rfln unique = 3811 [ $R(\text{int}) = 0.0213$ ]; completeness to  $\theta = 25.242 \text{ deg.} = 99.9 \%$ ; semi empirical absorption correction from equivalents; max. and min. transmission 1.04896 and 0.95585; data 3811; restraints 1, parameters 217; goodness-of-fit on  $F^2 = 1.071$ ; final indices [ $I > 2\sigma(I)$ ]  $R_1 = 0.0334$ ,  $wR_2 = 0.0838$ ;  $R$  indices (all data)  $R_1 = 0.0378$ ,  $wR_2 = 0.0865$ ; largest diff. peak and hole  $0.375$  and  $-0.195 \text{ e } \text{\AA}^{-3}$ .

**Density functional theoretical calculations** on the chromium complex cations  $[\text{Cr}(\text{tpe})_2]^{n+}$  were carried out using the ORCA program package (version 4.0.1).<sup>S14</sup> Tight convergence criteria were chosen for all calculations (keywords tightscf and tightopt). All calculations make use of the resolution of identity (Split-RJ) approach for the Coulomb term in combination with the chain-of-spheres approximation for the exchange term (COSX).<sup>S15,S16</sup> Geometry optimization was performed using the B3LYP functional<sup>S17</sup> in combination with Ahlrichs' split-valence triple- $\zeta$  basis set def2-TZVPP for all atoms.<sup>S18,S19</sup> The optimized geometries were confirmed to be local minima on the respective potential energy surface by subsequent numerical frequency analysis ( $N_{\text{imag}} = 0$ ). TD-DFT calculations were performed at the same level of theory. Fifty vertical spin-allowed transitions were calculated. The zero order relativistic approximation was used to describe relativistic effects in all calculations (keyword ZORA).<sup>S20,S21</sup> Grimme's empirical dispersion correction D3(BJ) was employed (keyword D3BJ).<sup>S22,S23</sup> To account for solvent effects, a conductor-like screening model (keyword CPCM) modeling acetonitrile was used in all calculations.<sup>S24</sup> Explicit counterions and/or solvent molecules were neglected.

**Synthesis of 1,1,1-tris(pyrid-2-yl)ethane tpe:**<sup>S1</sup> 2-Ethylpyridine (2.1 ml, 18.7 mmol) in dry THF (60 ml) were cooled to  $-78^\circ\text{C}$ .  $n$ -Butyl lithium (2.5 M in hexane; 7.5 ml; 18.75 mmol) was added dropwise. After stirring for 50 min and warming to  $-40^\circ\text{C}$ , 2-fluoropyridine (3.6 g, 37.4 mmol) was added to the red solution with the temperature kept below  $-30^\circ\text{C}$ . The resulting colorless reaction mixture was warmed to room temperature and then heated under reflux for 12 h. After cooling to room temperature, the solvents were removed under reduced pressure. The resulting solid was dissolved in THF (60 ml) and filtered. The solvent was removed under reduced pressure and the brown raw product was purified by column chromatography (alumina, hexanes/ethyl acetate 2:1,  $R_f = 0.30$ ) giving tpe as off-white solid (2.0 g, 7.6 mmol, 41 %).  $\text{C}_{17}\text{H}_{15}\text{N}_3$  (261.33).  $^1\text{H NMR}$  ( $\text{CDCl}_3$ ):  $\delta = 8.50$  (d,  $^3J_{\text{HH}} = 3.5 \text{ Hz}$ , 3H,  $\text{H}^4$ ), 7.65 (dt,  $^3J_{\text{HH}} = 7.7 \text{ Hz}$ ,  $^3J_{\text{HH}} = 1.6 \text{ Hz}$ , 3H,  $\text{H}^2$ ), 7.21 (dd,  $^3J_{\text{HH}} = 6.7 \text{ Hz}$ ,  $^3J_{\text{HH}} = 4.9 \text{ Hz}$ , 3H,  $\text{H}^3$ ), 7.11 (d,  $^3J_{\text{HH}} = 8.1 \text{ Hz}$ , 3H,  $\text{H}^1$ ), 2.25 (s, 3H,  $\text{H}^5$ ). MS (ESI<sup>+</sup>,  $\text{CH}_3\text{CN}$ ):  $m/z$  (%) = 262.13 (100,  $[\text{tpe}+\text{H}]^+$ ), 545.24 (9,  $[\text{2tpe}+\text{Na}]^+$ ).

**Synthesis of  $[\text{Cr}(\text{tpe})_2][\text{BF}_4]_3$ :** Under oxygen-free conditions, tpe (500 mg, 1.91 mmol) was dissolved in a  $\text{CH}_3\text{CN}/\text{H}_2\text{O}$  mixture (50 ml, 1:1 v/v) and  $\text{CrCl}_2$  (118 mg, 0.96 mmol) was added as a solid. The resulting dark green solution was stirred for 2 h at room temperature, heated to reflux for 3 h and stirred for 5 d at room temperature.  $[\text{NH}_4][\text{BF}_4]$  (312 mg, 2.98 mmol) dissolved in deaerated water (3 ml) was added to the reaction mixture. After stirring for 2 h under inert conditions, the mixture was left to stand for 16 h under air giving a pale-red solution. The solvents were removed under reduced pressure and the resulting red solid suspended in  $\text{CH}_3\text{CN}$  (5 ml). A colorless solid was removed by filtration. Diffusion of diethyl ether into the concentrated  $\text{CH}_3\text{CN}$  solution yielded golden crystals (495 mg, 0.59 mmol, 62 %). MS (ESI<sup>+</sup>,  $\text{CH}_3\text{CN}$ ):  $m/z$  (%) = 191.39 (18)  $[\text{Cr}(\text{tpe})_2]^{3+}$ , 262.13 (12)  $[\text{tpe}+\text{H}]^+$ , 287.09 (60)  $[\text{Cr}(\text{tpe})_2]^{2+}$ , 296.59 (13)  $[\text{Cr}(\text{tpe})_2+\text{F}]^{2+}$ , 330.59 (100)  $[\text{Cr}(\text{tpe})_2+\text{BF}_4]^{2+}$ , 364.05 (10), 576.15 (12), 593.19 (25)

$[\text{Cr}(\text{tpe})_2+\text{F}]^+$ , 639.20 (14), 661.19 (35)  $[\text{Cr}(\text{tpe})_2+(\text{BF}_4)]^+$ , 706.19 (12), 748.20 (44)  $[\text{Cr}(\text{tpe})_2+(\text{BF}_4)_2]^+$ . IR (ATR):  $\tilde{\nu} = 3102$  (w br, CH), 1601 (s), 1581 (w), 1492 (w), 1470 (s), 1441 (s), 1387 (w), 1307 (w), 1284 (w), 1294 (w), 1216 (w), 1175 (w), 1030 (vs br, BF), 847 (m), 773 (m), 758 (s), 750 (s), 721 (w), 660 (m), 639 (s), 564 (m), 519 (s), 449 (s), 400 (s)  $\text{cm}^{-1}$ . UV/Vis ( $\text{CH}_3\text{CN}$ ):  $\lambda(\varepsilon) = 431$  (30), 329 (910), 274 (13700), 238 (30300  $\text{M}^{-1} \text{cm}^{-1}$ ) nm. Emission ( $\text{CH}_3\text{CN}$ ;  $\lambda_{\text{exc}} = 436$  nm):  $\lambda = 790, 749, 743, 727, 719$  nm (structured band). Magnetism:  $\chi T = 1.875 \text{ cm}^3 \text{ K mol}^{-1}$  (6 – 300 K; solvate-free sample). CV ( $\text{CH}_3\text{CN}$ ,  $[\text{N}^n\text{Bu}_4][\text{BF}_4]$ , vs.  $\text{FcH}/\text{FcH}^+$ ) =  $-0.88$  (rev.),  $-1.54$  (rev.),  $-2.49$  (qrev.) V. Elemental analysis calcd. (%) for  $\text{C}_{34}\text{H}_{30}\text{B}_3\text{CrF}_{12}\text{N}_6$  (835.06): C 48.90 H 3.62, N 10.06; found C 48.89, H 3.63 N 10.21.

**Synthesis of  $[\text{Cr}(\text{tpe})_2][\text{PF}_6]_3$ :** Under oxygen-free conditions, tpe (99.4 mg, 0.38 mmol) was dissolved in  $\text{H}_2\text{O}$  (17 ml) and  $\text{CrCl}_2$  (23.4 mg, 0.19 mmol) was added as a solid. The resulting dark green solution was stirred for 3 d at room temperature.  $\text{K}[\text{PF}_6]$  (105 mg, 0.57 mmol) was dissolved in deaerated water (3 ml) and added to the reaction mixture. The solvent was removed under reduced pressure and the resulting solid dissolved in  $\text{CH}_3\text{CN}$  (3 ml). Diffusion of diethyl ether into the concentrated  $\text{CH}_3\text{CN}$  solution yielded dark green crystals (23 mg, 0.022 mmol, 12 %). MS (ESI<sup>+</sup>,  $\text{CH}_3\text{CN}$ ):  $m/z$  (%) = 144.98 (11), 287.09 (100)  $[\text{Cr}(\text{tpe})_2]^{2+}$ , 359.57 (27)  $[\text{Cr}(\text{tpe})_2+\text{PF}_6]^{2+}$ , 393.29 (10), 413.26 (11), 419.31 (10), 441.29 (27), 568.73 (6), 719.15 (69)  $[\text{Cr}(\text{tpe})_2+\text{PF}_6]^+$ , 864.17 (6)  $[\text{Cr}(\text{tpe})_2+(\text{PF}_6)_2]^+$ . IR (ATR):  $\tilde{\nu} = 3102$  (w br, CH), 2253 (w, CN), 1604 (m), 1470 (m), 1439 (m), 1389 (w), 1311 (w), 1218 (w), 1173 (w), 1113 (w), 1060 (m), 1037 (m), 824 (vs, PF), 775 (s), 762 (m), 660 (m), 639 (s), 555 (s,  $\text{PF}_2$ ), 511 (m), 449 (m), 400 (m)  $\text{cm}^{-1}$ . Elemental analysis calcd. (%) for  $\text{C}_{34}\text{H}_{30}\text{CrF}_{18}\text{N}_6\text{P}_3$  (1009.54)  $\times 0.5\text{H}_2\text{O}$ : C 40.09 H 3.07, N 8.25; found C 39.70, H 3.03 N 8.11.

Both salts crystallize with three acetonitrile solvate molecules according to single crystal XRD analyses (see below). However, the actual amount of solvent in a given sample depends on the grinding and drying procedure after crystallization.

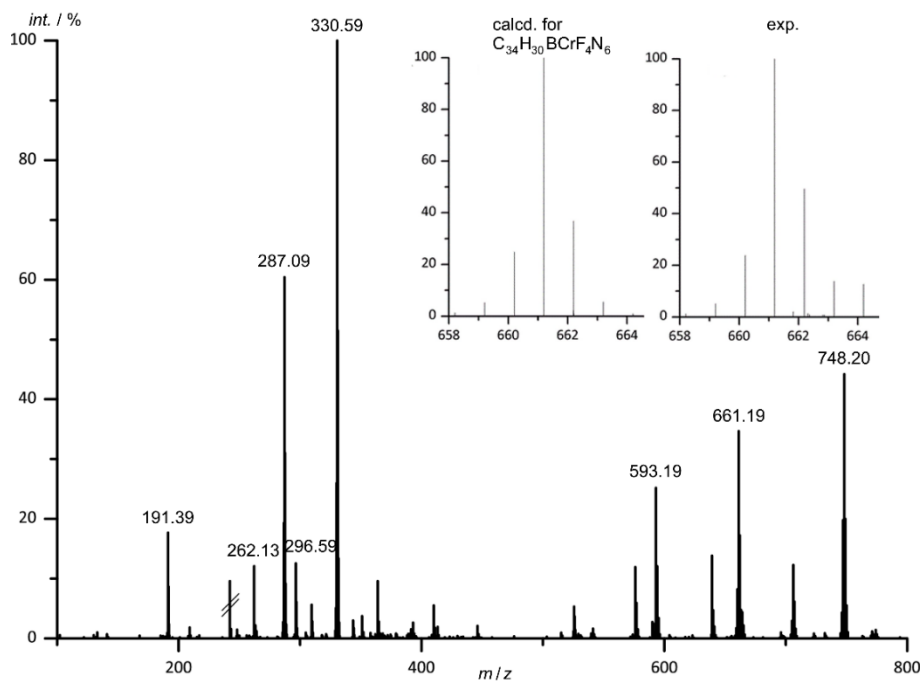


**Figure S1.** a) ESI<sup>+</sup> mass spectrum of [Cr(tpe)<sub>2</sub>][BF<sub>4</sub>]<sub>3</sub> in CH<sub>3</sub>CN. The inset shows the calculated and experimental isotope distribution of the ion cluster {[Cr(tpe)<sub>2</sub>][BF<sub>4</sub>]}<sup>+</sup>.

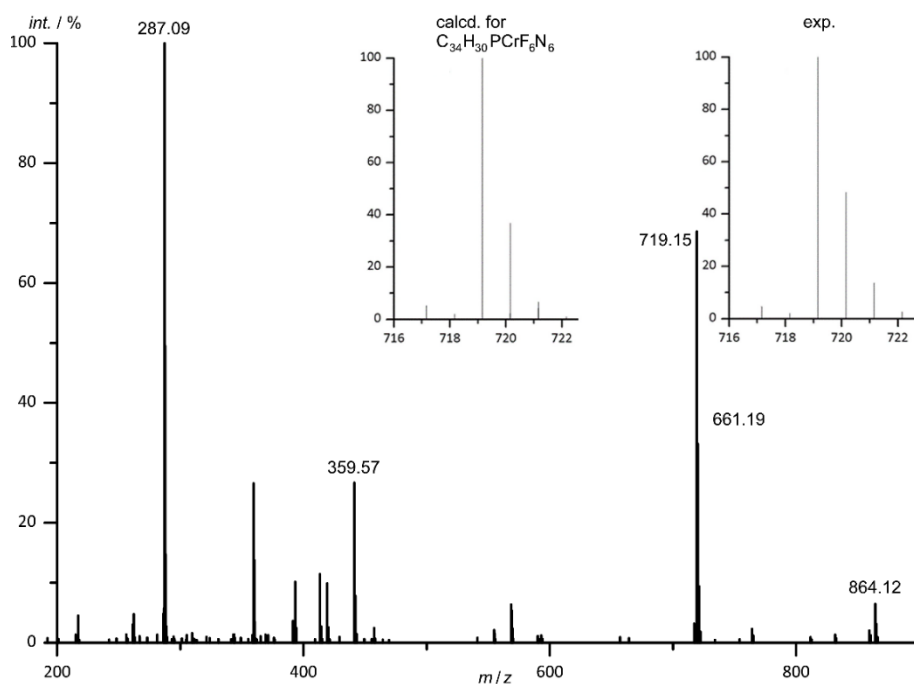


**Figure S2.** a) ESI<sup>+</sup> mass spectrum of [Cr(tpe)<sub>2</sub>][PF<sub>6</sub>]<sub>3</sub> in CH<sub>3</sub>CN. The inset shows the calculated and experimental isotope distribution of the ion cluster {[Cr(tpe)<sub>2</sub>][PF<sub>6</sub>]}<sup>+</sup>.

The cations of the salts are observed in the ESI<sup>+</sup> mass spectra as the trication [Cr(tpe)<sub>2</sub>]<sup>3+</sup> and the dication [Cr(tpe)<sub>2</sub>]<sup>2+</sup> and as ion clusters with the respective counter ions such as {[Cr(tpe)<sub>2</sub>][X]}<sup>2+</sup> and {[Cr(tpe)<sub>2</sub>][X]<sub>2</sub>}<sup>+</sup> with X<sup>-</sup> = [BF<sub>4</sub>]<sup>-</sup>, [PF<sub>6</sub>]<sup>-</sup> or F<sup>-</sup>.

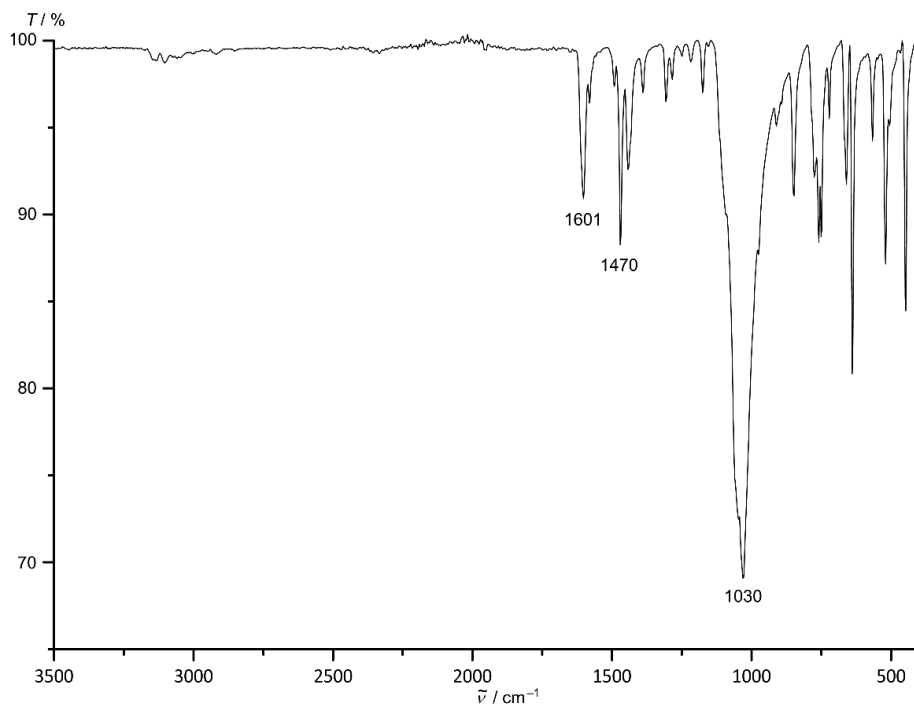


**Figure S3.** ATR-IR spectrum of  $[\text{Cr}(\text{tpe})_2][\text{BF}_4]_3$  (solvent-free sample).

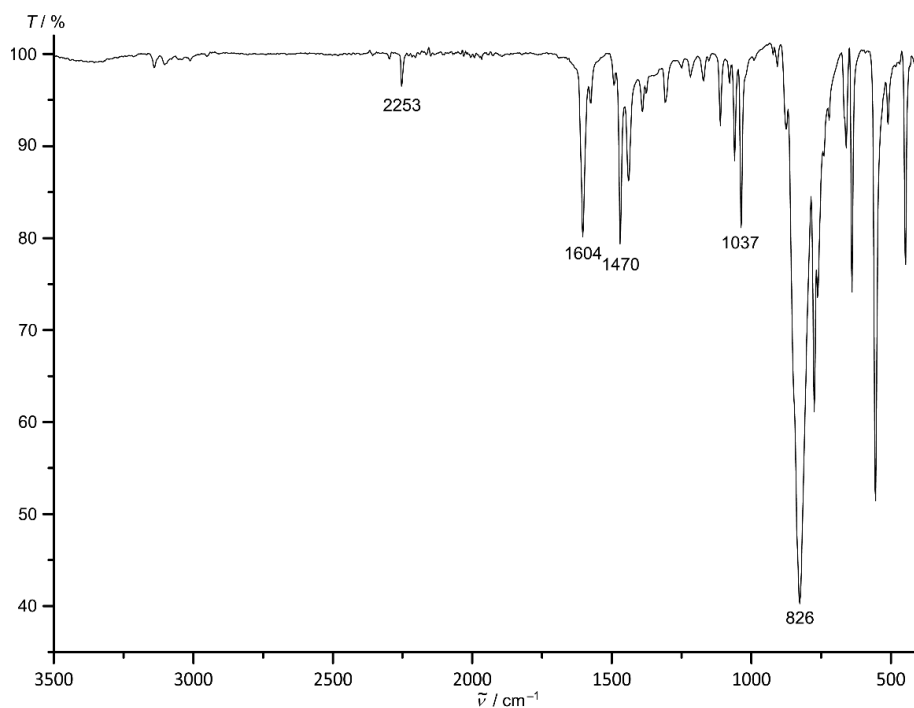


**Figure S4.** ATR-IR spectrum of  $[\text{Cr}(\text{tpe})_2][\text{PF}_6]_3 \cdot x\text{CH}_3\text{CN}$ .

The counter ions show characteristic absorption bands for BF and PF stretching vibrations in the respective ATR-IR spectra. Crystals of *fac*- $[\text{Cr}(\text{tpe})_2][\text{PF}_6]_3 \cdot 3\text{CH}_3\text{CN}$  display a sharp absorption band at  $2253 \text{ cm}^{-1}$  which is assigned to the CN stretching vibration of co-crystallized  $\text{CH}_3\text{CN}$ . The fingerprint region of both complex salts displays comparably few bands for CC and skeletal vibrations. This points to the high symmetry of the complex cations.



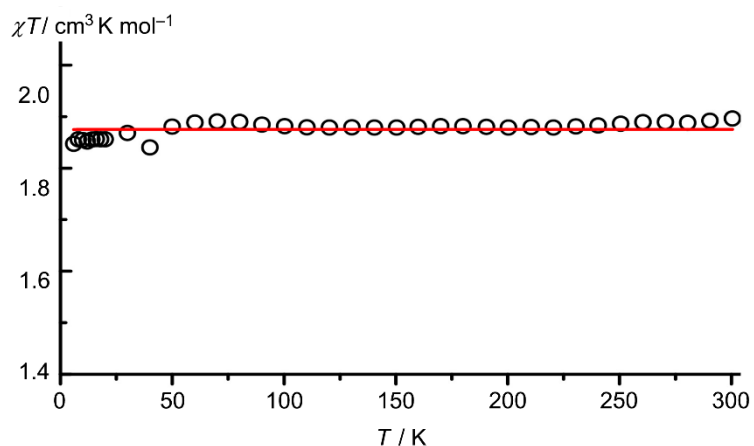


**Figure S5.** a)  $\chi T$  vs.  $T$  plot of  $[\text{Cr}(\text{tpe})_2][\text{BF}_4]_3$  (solvent-free sample); fit with  $g = 2.000$  shown in red.

The temperature dependence of the magnetic susceptibility of a solvent-free sample of  $[\text{Cr}(\text{tpe})_2][\text{BF}_4]_3$  has been studied in the range 6 – 300 K in an external field of 0.1 T. In this temperature range,  $\chi T$  is essentially temperature independent and with  $1.875 \text{ cm}^3 \text{ K mol}^{-1}$  very close to the spin-only value of a  $S = 3/2$  system ( $^4\text{A}_{2g}$  ground state;  $g = 2.000$ ;  $\mu = 3.87 \mu_{\text{B}}$ ). The fitted  $g$  value matches those of  $[\text{Cr}(\text{ddpd})_2][\text{BF}_4]_3$  and of  $[\text{Cr}(\text{tpy})_2][\text{ClO}_4]_3$ .<sup>S25-S27</sup>

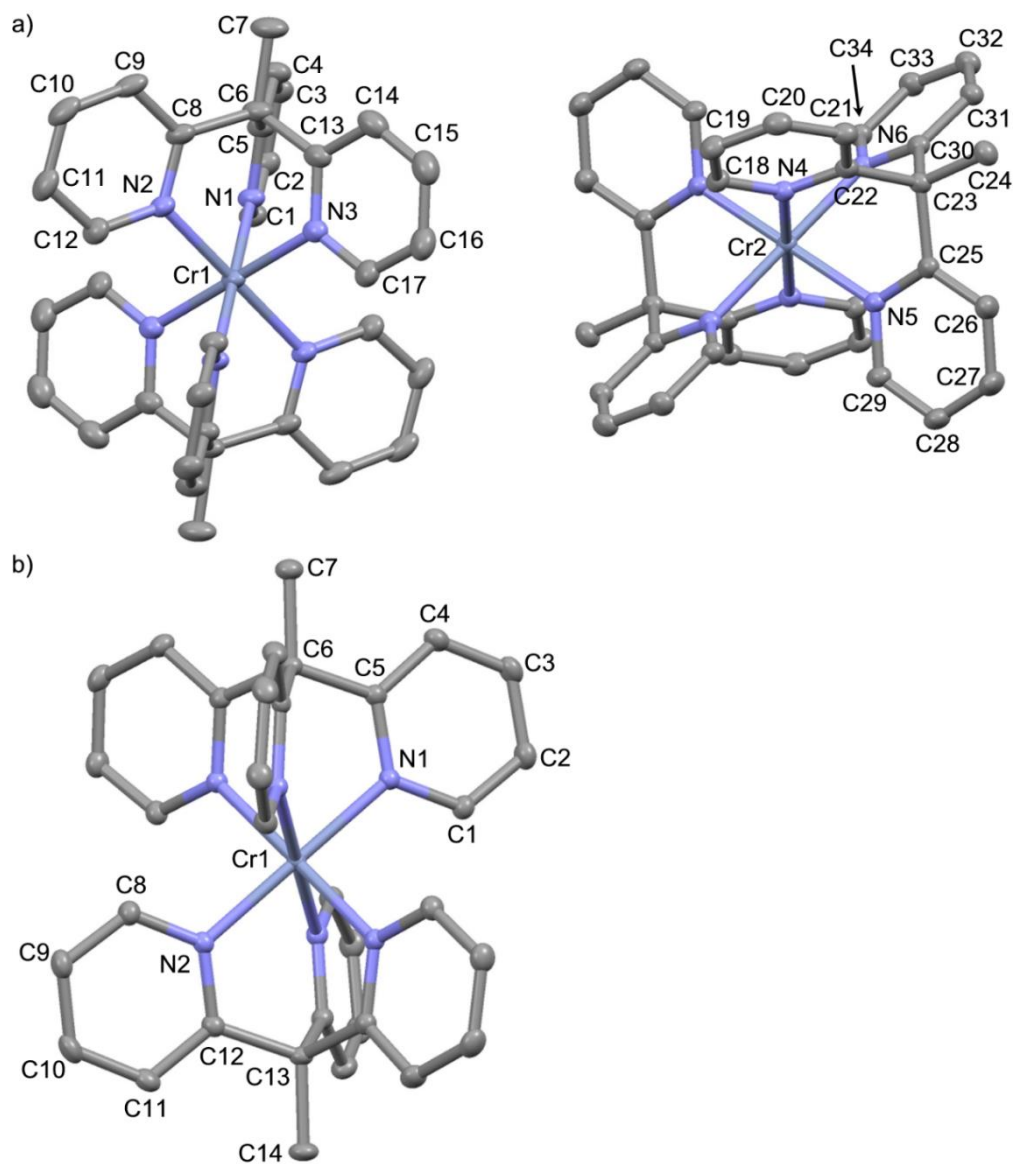


**Figure S6.** Plots of the cations of a)  $[\text{Cr}(\text{tpe})_2][\text{BF}_4]_3 \cdot 3\text{CH}_3\text{CN}$  with two independent cations and b)  $[\text{Cr}(\text{tpe})_2][\text{PF}_6]_3 \cdot 3\text{CH}_3\text{CN}$  with thermal ellipsoids set 30 % probability.

**Table S1.** Selected distances (Å) and angles (°) for [Cr(tpe)<sub>2</sub>][BF<sub>4</sub>]<sub>3</sub>×3CH<sub>3</sub>CN,<sup>a</sup> [Cr(tpe)<sub>2</sub>][PF<sub>6</sub>]<sub>3</sub>×3CH<sub>3</sub>CN,<sup>b</sup> and [Cr(tpe)<sub>2</sub>]<sup>3+</sup> (DFT).

	[Cr(tpe) <sub>2</sub> ][BF <sub>4</sub> ] <sub>3</sub> ×3CH <sub>3</sub> CN	[Cr(tpe) <sub>2</sub> ][PF <sub>6</sub> ] <sub>3</sub> ×3CH <sub>3</sub> CN	[Cr(tpe) <sub>2</sub> ] <sup>3+</sup>
Cr1-N1	2.041(2)	2.046(3) / 2.044(3)	2.055 / 2.055
Cr1-N2	2.041(2)	2.046(3) / 2.044(3)	2.055 / 2.055
Cr1-N3	2.031(2)	2.046(3) / 2.044(3)	2.053 / 2.053
tpe (intraligand)			
N1-Cr1-N2	86.34(8)	86.48(11) / 86.08(11)	86.74 / 86.78
N1-Cr1-N3	86.66(9)	86.48(11) / 86.08(11)	86.73 / 86.73
N2-Cr1-N3	86.57(9)	86.48(11) / 86.08(11)	86.79 / 86.75
tpe (interligand)			
N1-Cr1-N1'	180.0	93.22(10)	179.96
N1-Cr1-N2'	93.66(8)	179.22(12)	93.26
N1-Cr1-N3'	93.34(9)	94.22(10)	93.29
N2-Cr1-N2'	180.0	94.22(10)	179.99
N2-Cr1-N3'	93.43(9)	93.22(10)	93.27
N3-Cr1-N3'	180.0	179.22(12)	179.95
Cr2-N4	2.052(2)	—	—
Cr2-N5	2.048(2)	—	—
Cr2-N6	2.049(2)	—	—
N4-Cr2-N5	86.00(8)	—	—
N4-Cr2-N6	86.85(8)	—	—
N5-Cr2-N6	86.29(8)	—	—
N4-Cr2-N4'	180.0	—	—
N4-Cr2-N5'	93.99(8)	—	—
N4-Cr2-N6'	93.15(8)	—	—
N5-Cr2-N5'	180.0	—	—
N5-Cr2-N6'	93.71(8)	—	—
N6-Cr2-N6'	180.0	—	—
Cr1···N(solvent)	4.47 (2×)	4.53 (3×)	—
Cr1···F(counterion)	4.46 (2×), 4.55 (2×)	4.64 (3×)	—
Cr2···N(solvent)	4.45 (2×), 5.20 (2×)	—	—
Cr2···F(counterion)	4.42 (2×)	—	—

<sup>a</sup> Two independent centrosymmetric trications Cr1/Cr2 in the unit cell.

<sup>b</sup> A single trication in the unit cell with two crystallographically independent C<sub>3</sub> symmetric tpe ligands.

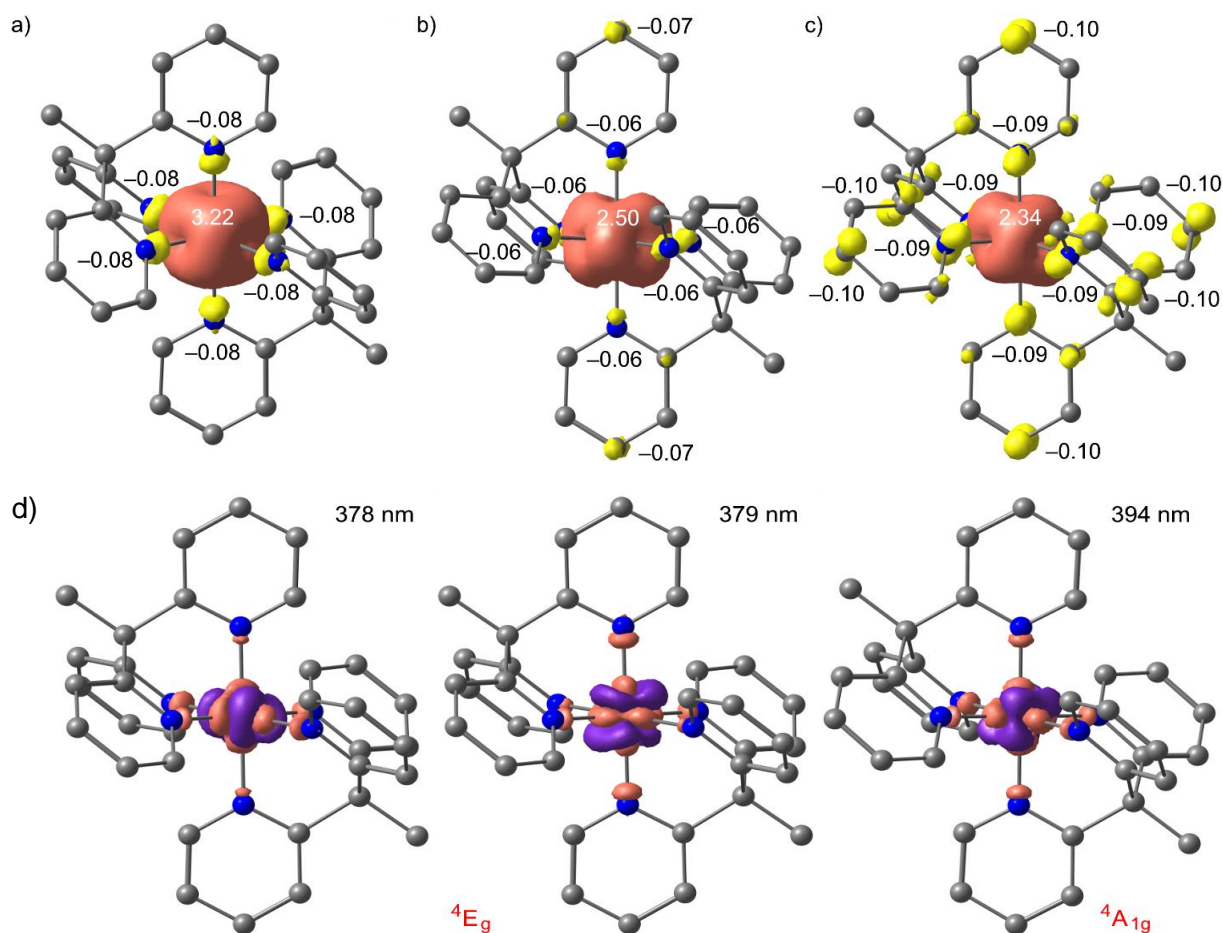


**Figure S7.** DFT optimized geometries of a) [Cr(tpe)<sub>2</sub>]<sup>3+</sup> (quartet state), b) [Cr(tpe)<sub>2</sub>]<sup>2+</sup> (triplet state) and c) [Cr(tpe)<sub>2</sub>]<sup>+</sup> (doublet state), and corresponding Mulliken spin densities plotted at 0.006 a.u. with the  $\alpha$  spin in orange and the  $\beta$  spin in yellow. d) Three lowest TD-DFT calculated spin-allowed transitions; these correspond to the spin-allowed  ${}^4A_{2g} \rightarrow {}^4E_g$  and  ${}^4A_{2g} \rightarrow {}^4A_{1g}$  ligand field transitions (in  $D_{3d}$  symmetry). Hydrogen atoms omitted. Difference electron densities plotted with an isosurface value of 0.01 a.u.; purple = depletion; orange = gain.

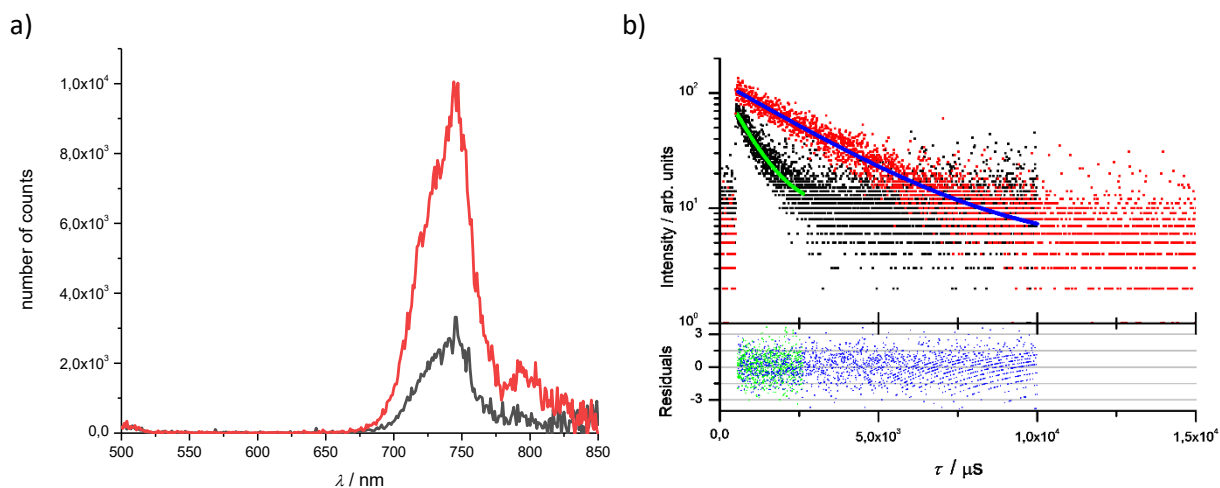


**Figure S8.** a) Emission spectra of  $[\text{Cr}(\text{tpe})_2][\text{BF}_4]_3$  in  $\text{H}_2\text{O}/\text{HClO}_4$  at room temperature ( $\lambda_{\text{exc}} = 428 \text{ nm}$ ) under inert (red) and air-saturated conditions (black) and b) corresponding emission decay curves.

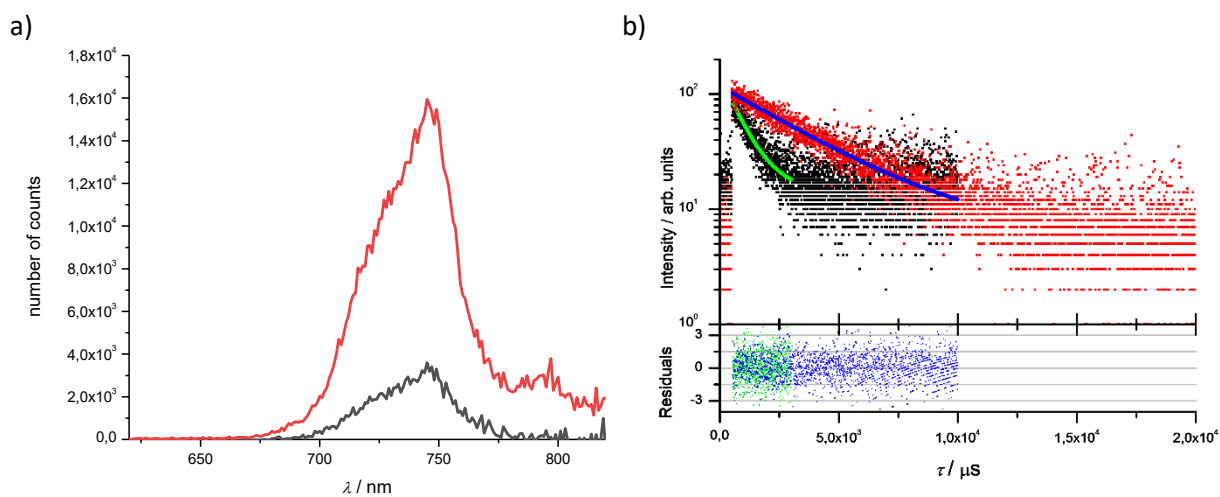


**Figure S9.** a) Emission spectra of  $[\text{Cr}(\text{tpe})_2][\text{BF}_4]_3$  in  $\text{D}_2\text{O}/\text{DClO}_4$  at room temperature ( $\lambda_{\text{exc}} = 428 \text{ nm}$ ) under inert (red) and air-saturated conditions (black) and b) corresponding emission decay curves.

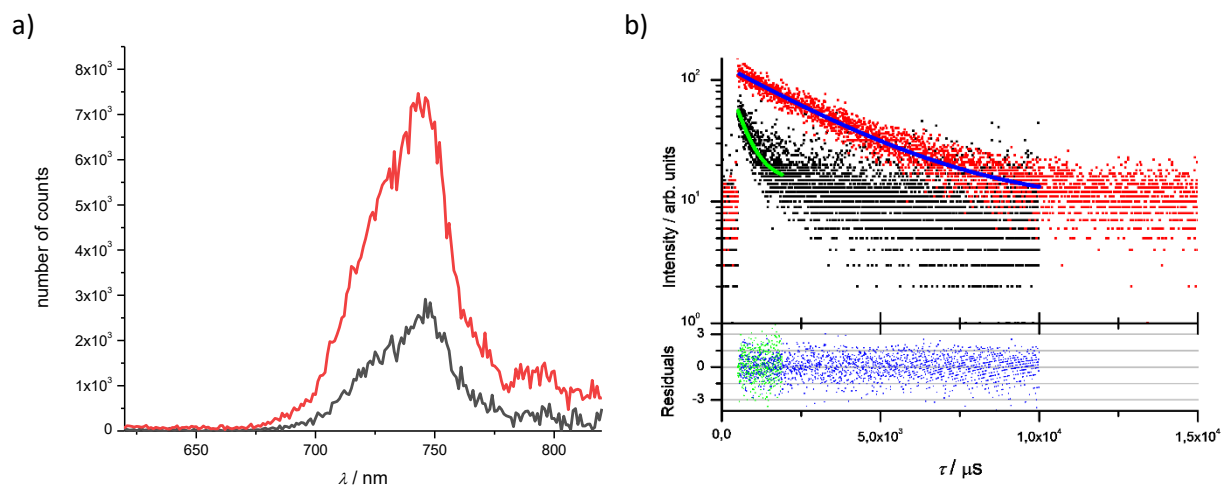


**Figure S10.** a) Emission spectra of  $[\text{Cr}(\text{tpe})_2][\text{BF}_4]_3$  in  $\text{CH}_3\text{CN}/\text{HClO}_4$  at room temperature ( $\lambda_{\text{exc}} = 428$  nm) under inert (red) and air-saturated conditions (black) and b) corresponding emission decay curves.

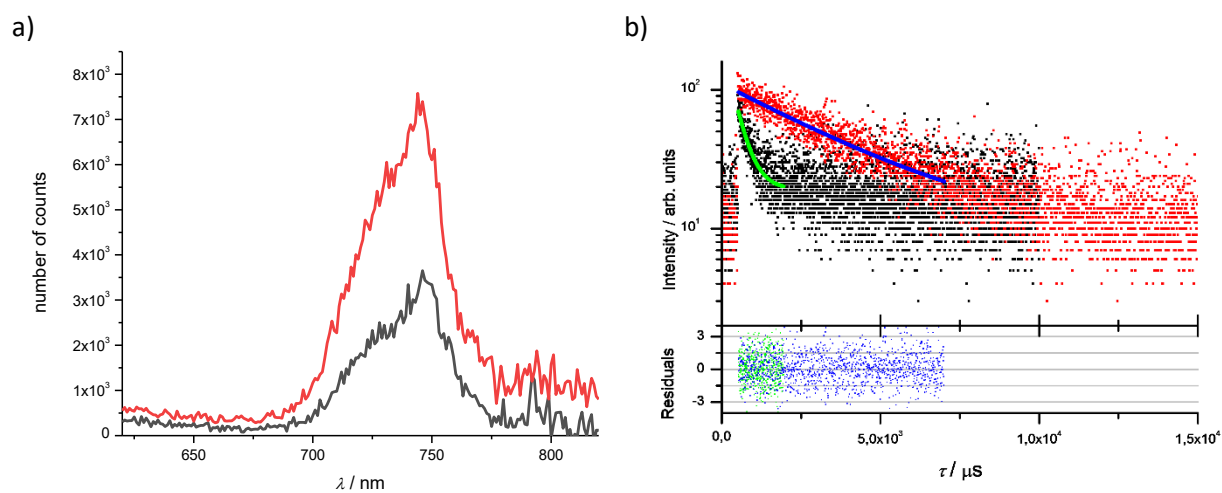


**Figure S11.** a) Emission spectra of  $[\text{Cr}(\text{tpe})_2][\text{BF}_4]_3$  in  $\text{CD}_3\text{CN}/\text{DClO}_4$  at room temperature ( $\lambda_{\text{exc}} = 428$  nm) under inert (red) and air-saturated conditions (black) and b) corresponding emission decay curves.

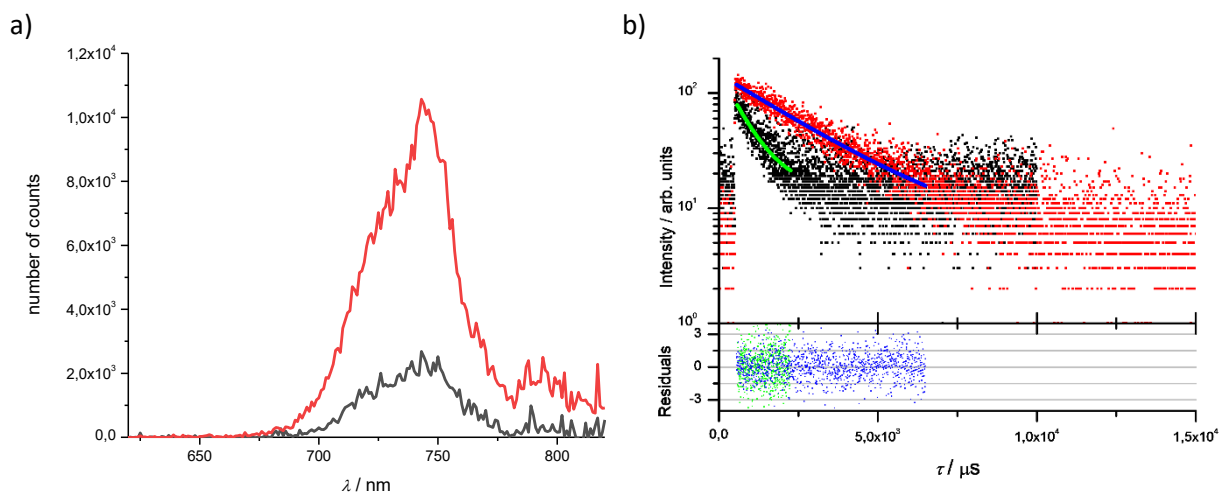


**Figure S12.** a) Emission spectra of  $[\text{Cr}(\text{tpe})_2][\text{BF}_4]_3$  in  $\text{H}_2\text{O}/\text{NaClO}_4$  at room temperature ( $\lambda_{\text{exc}} = 428$  nm) under inert (red) and air-saturated conditions (black) and b) corresponding emission decay curves.

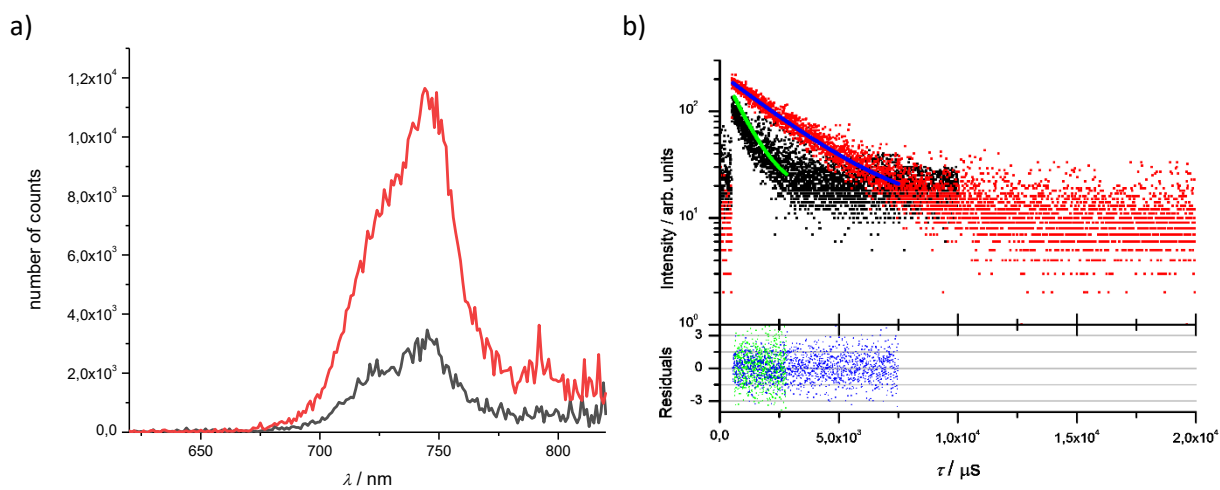
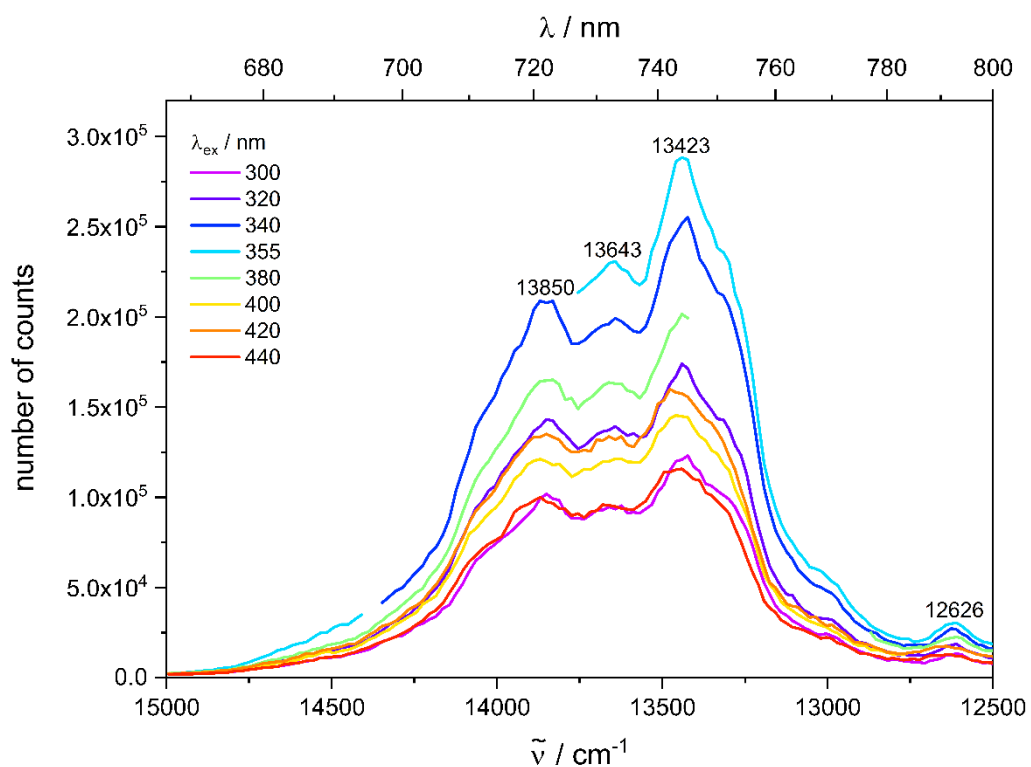


**Figure S13.** a) Emission spectra of  $[\text{Cr}(\text{tpe})_2][\text{BF}_4]_3$  in  $\text{D}_2\text{O}/\text{NaClO}_4$  at room temperature ( $\lambda_{\text{exc}} = 428$  nm) under inert (red) and air-saturated conditions (black) and b) corresponding emission decay curves.

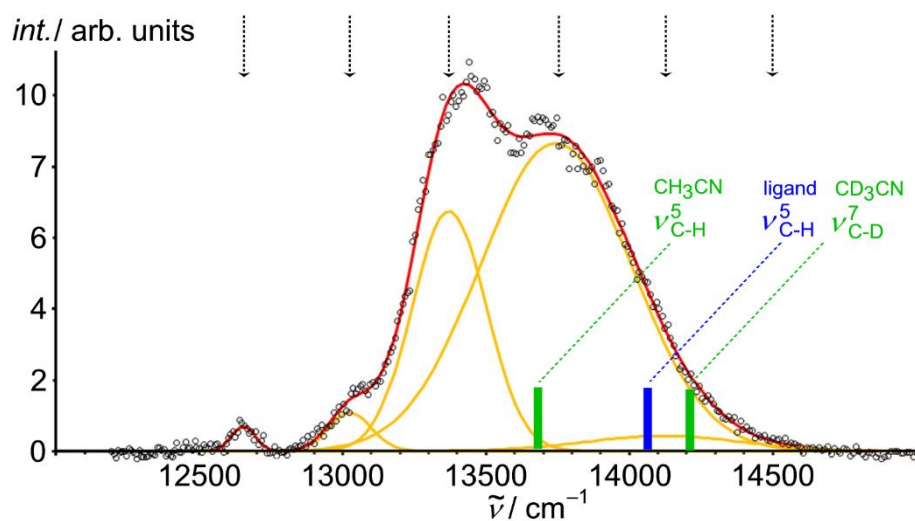
**Table S2.** Quantum yields  $\Phi$ , luminescence lifetimes  $\tau$  and radiative lifetimes  $\tau_r$  of  $[\text{Cr}(\text{tpe})_2][\text{BF}_4]_3$  and  $[\text{Cr}(\text{ddpd})_2][\text{BF}_4]_3$  <sup>S29</sup> under inert and under air-saturated conditions ( $\tau_r = \tau / \Phi$ ).  $[\text{Cr}(\text{tpe})_2][\text{BF}_4]_3$  was measured in the presence of  $\text{HClO}_4$ ,  $\text{DClO}_4$  or  $\text{NaClO}_4$  (0.1 M), respectively, while no acid was employed for  $[\text{Cr}(\text{ddpd})_2][\text{BF}_4]_3$ . Please note, that the solubility of  $\text{O}_2$  in  $\text{H}_2\text{O}$  changes with pH so that the quenching data of  $[\text{Cr}(\text{tpe})_2][\text{BF}_4]_3$  and  $[\text{Cr}(\text{ddpd})_2][\text{BF}_4]_3$  should not be compared directly (Figures S8 – S13).

	$[\text{Cr}(\text{tpe})_2][\text{BF}_4]_3$ (inert)	$[\text{Cr}(\text{tpe})_2][\text{BF}_4]_3$ ( $\text{O}_2$ -sat.)	$[\text{Cr}(\text{ddpd})_2][\text{BF}_4]_3$ (inert)	$[\text{Cr}(\text{ddpd})_2][\text{BF}_4]_3$ ( $\text{O}_2$ -sat.)
$\Phi(\text{H}_2\text{O}/\text{HClO}_4) / \%$	5.4	2.2	11.0	2.1
$\tau(\text{H}_2\text{O}/\text{HClO}_4) / \mu\text{s}$	2800	780	898	177
$\tau_r(\text{H}_2\text{O}/\text{HClO}_4) / \text{ms}$	51.9	35.5	8.2	8.4
$\Phi(\text{D}_2\text{O}/\text{DClO}_4) / \%$	8.2	4.1	14.2	2.0
$\tau(\text{D}_2\text{O}/\text{DClO}_4) / \mu\text{s}$	4500	890	1164	150
$\tau_r(\text{D}_2\text{O}/\text{DClO}_4) / \text{ms}$	54.9	21.7	8.2	7.5
$\Phi(\text{CH}_3\text{CN}/\text{HClO}_4) / \%$	6.1	3.4	12.1	0.60
$\tau(\text{CH}_3\text{CN}/\text{HClO}_4) / \mu\text{s}$	2900	320	899	44
$\tau_r(\text{CH}_3\text{CN}/\text{HClO}_4) / \text{ms}$	47.5	9.4	7.4	7.3
$\Phi(\text{CD}_3\text{CN}/\text{DClO}_4) / \%$	7.7	4.5	11.7	0.60
$\tau(\text{CD}_3\text{CN}/\text{DClO}_4) / \mu\text{s}$	3300	360	810	24
$\tau_r(\text{CD}_3\text{CN}/\text{DClO}_4) / \text{ms}$	42.9	8.0	6.9	4.0
$\Phi(\text{H}_2\text{O}/\text{NaClO}_4) / \%$	4.2	2.1		
$\tau(\text{H}_2\text{O}/\text{NaClO}_4) / \mu\text{s}$	2500	760		
$\tau_r(\text{H}_2\text{O}/\text{NaClO}_4) / \text{ms}$	59.5	36.2		
$\Phi(\text{D}_2\text{O}/\text{NaClO}_4) / \%$	6.3	4.1		
$\tau(\text{D}_2\text{O}/\text{NaClO}_4) / \mu\text{s}$	3900	880		
$\tau_r(\text{D}_2\text{O}/\text{NaClO}_4) / \text{ms}$	61.9	21.5		

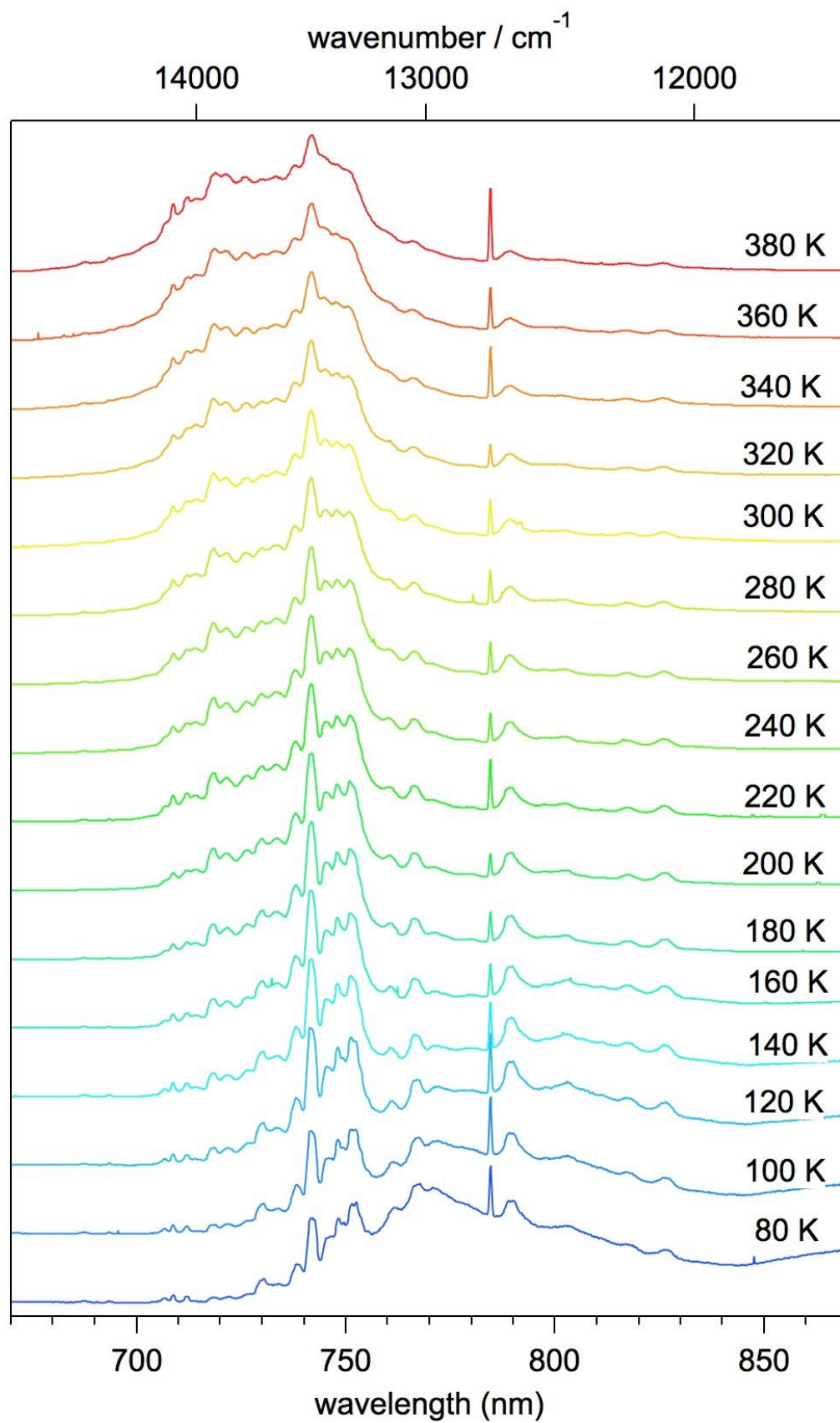




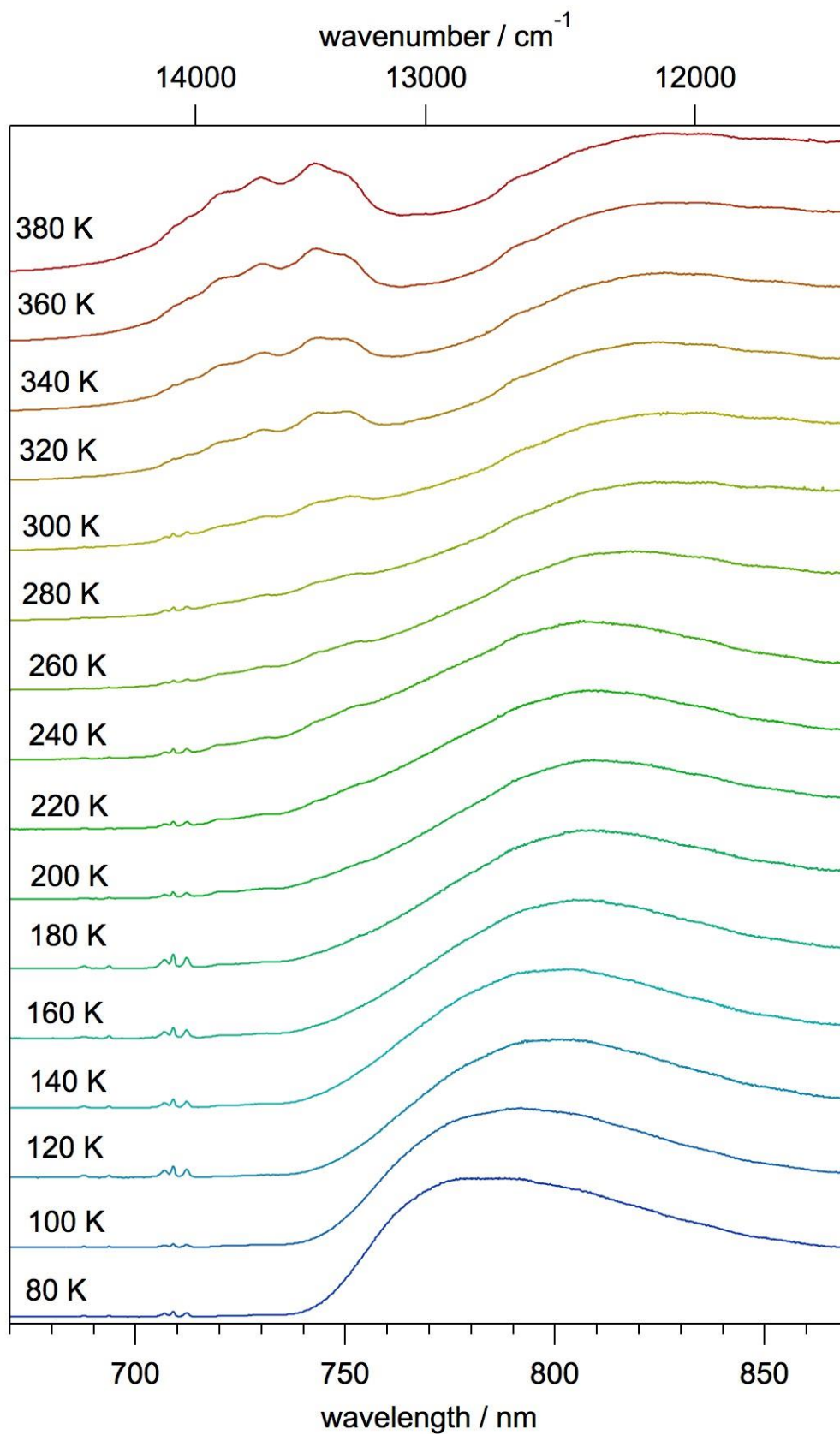
**Figure S14.** Emission spectra of  $[\text{Cr}(\text{tpe})_2][\text{BF}_4]_3$  as KBr disk at 290 K with different excitation wavelengths.



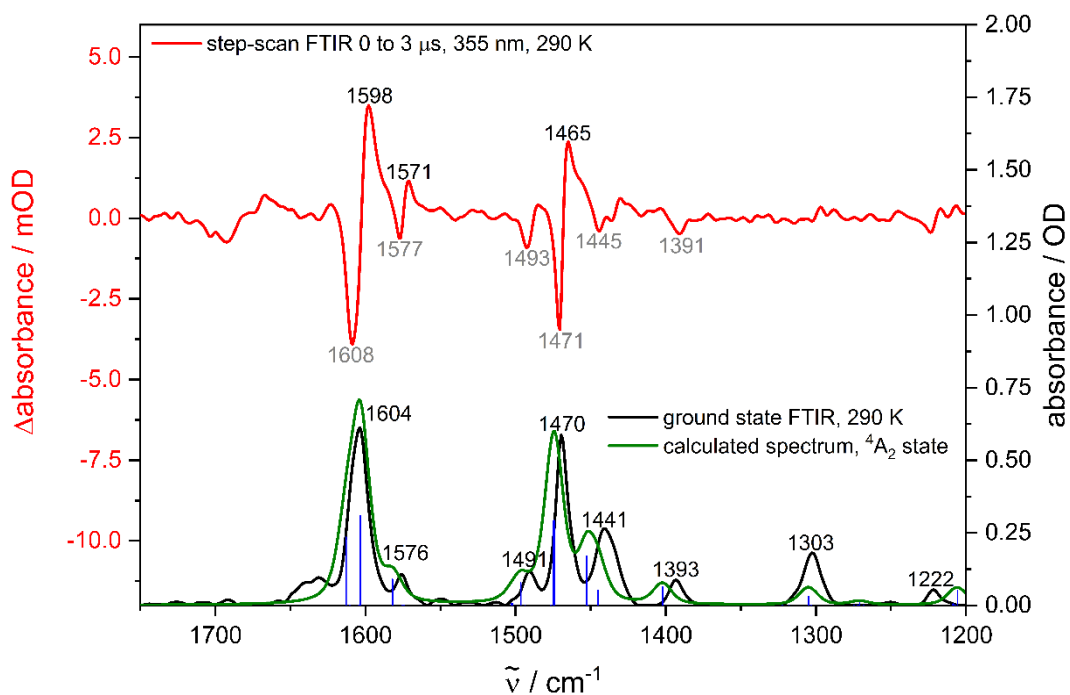
**Figure S15.** Room temperature emission band of  $[\text{Cr}(\text{tpe})_2][\text{BF}_4]_3$  in  $\text{CH}_3\text{CN}$  ( $\lambda_{\text{exc}} = 436 \text{ nm}$ ) and a fit of the band envelope by five Gaussians ( $12653, 13026, 13372, 13744, 14120 \text{ cm}^{-1}$ ;  $R^2 = 0.99684$ ). The energies of vibrational C-H(ligand), C-H( $\text{CH}_3\text{CN}$ ) and C-D( $\text{CD}_3\text{CN}$ ) overtones relevant for multiphonon relaxation are indicated by blue and green bars.



**Figure S16.** Emission spectra of crystals of  $[\text{Cr}(\text{tpe})_2][\text{BF}_4]_3$  at different temperatures ( $\lambda_{\text{exc}} = 488 \text{ nm}$ ).



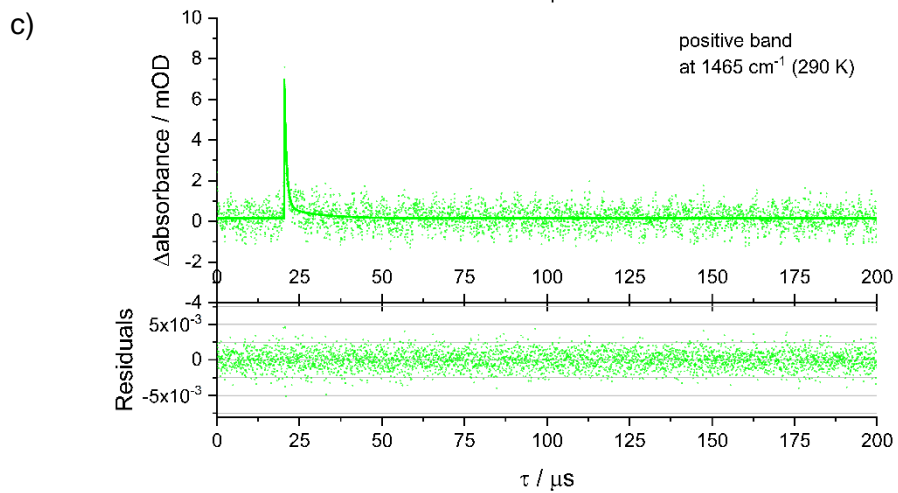
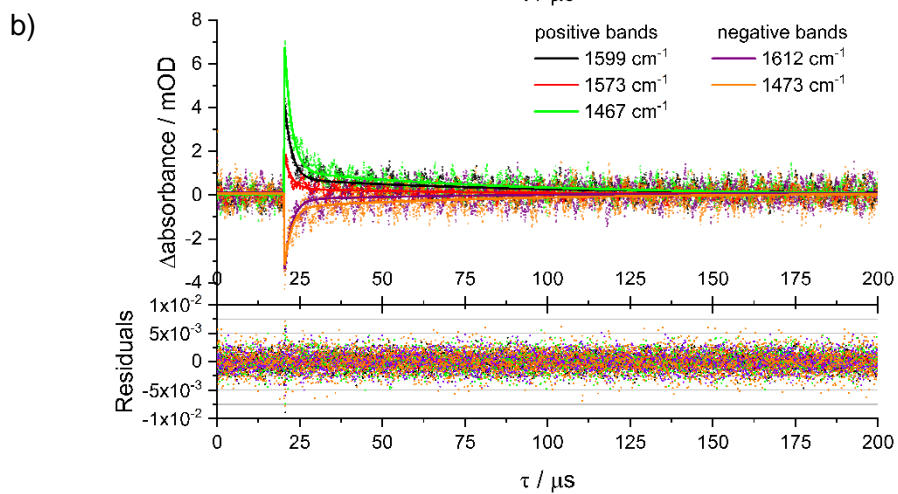
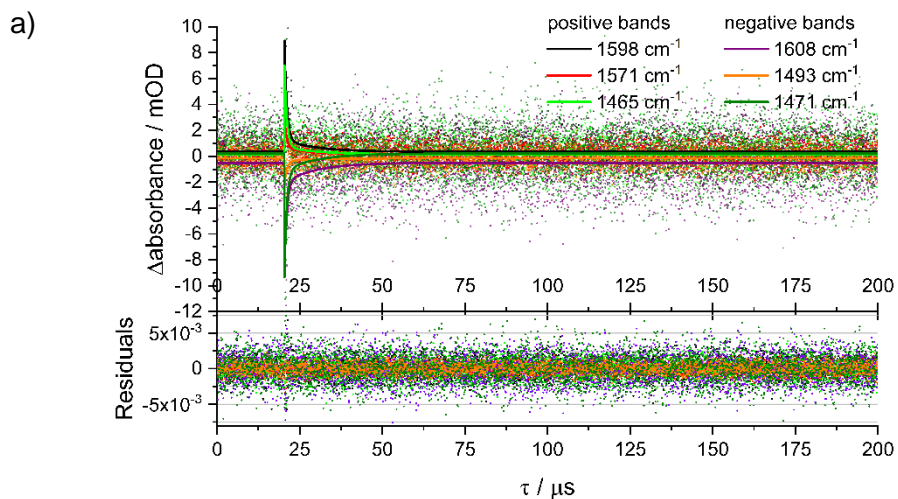
**Figure S17.** Emission spectra of crystals of  $[\text{Cr}(\text{tpe})_2][\text{PF}_6]_3$  at different temperatures ( $\lambda_{\text{exc}} = 488 \text{ nm}$ ).

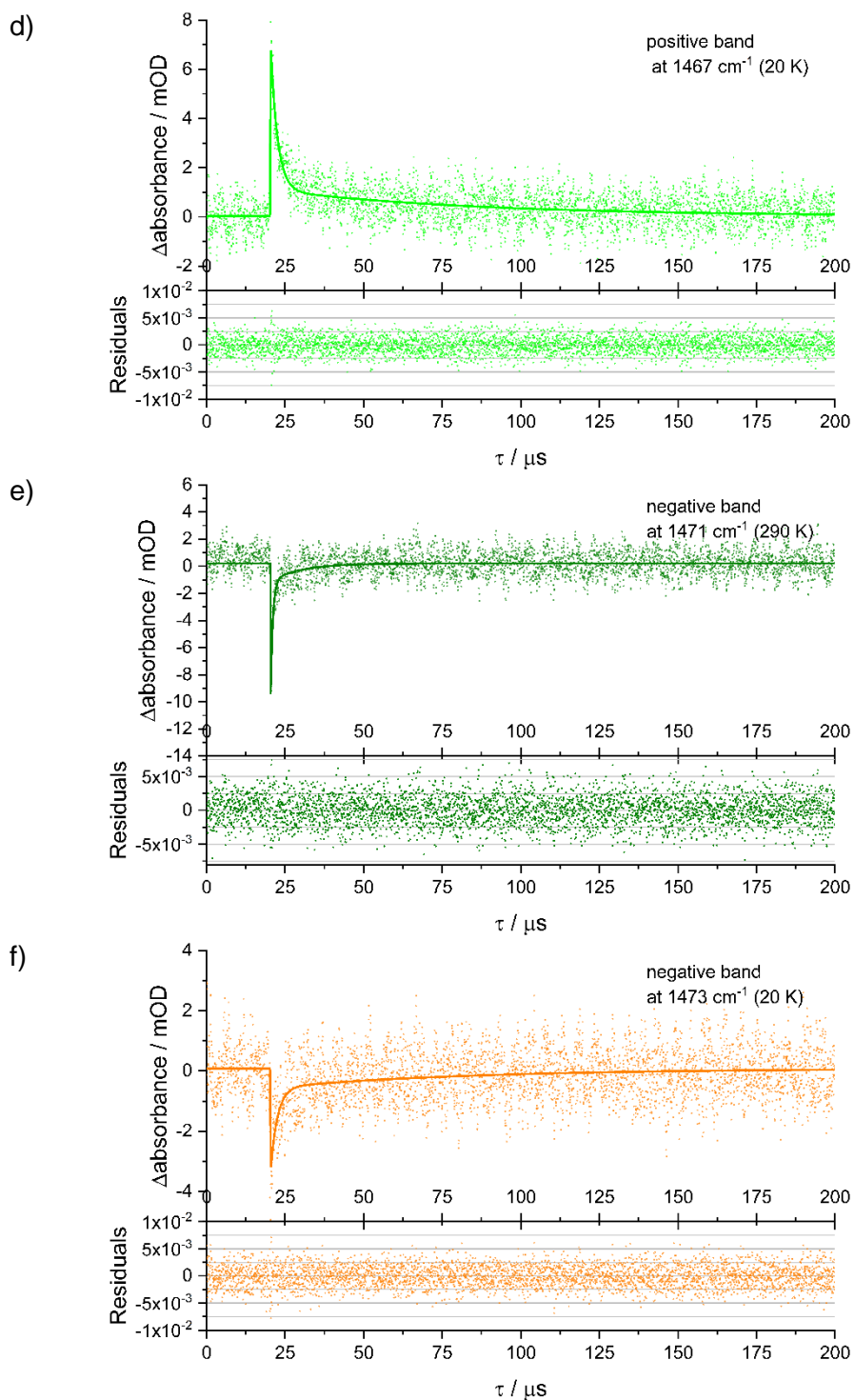


**Figure S18.** Step-scan FT-IR spectrum (red) and ground state IR spectrum (black) of  $[\text{Cr}(\text{tpe})_2][\text{BF}_4]_3$  as KBr disk at 290 K and DFT calculated IR absorption bands (blue, scaled by 0.98) and DFT calculated IR spectrum (green, pseudo-Voigt functions with  $\text{FWHM} = 15 \text{ cm}^{-1}$ ).

**Table S3.** Excited state lifetimes of  $[\text{Cr}(\text{tpe})_2][\text{BF}_4]_3$  as obtained from KBr disk or from a neat film. For the measurements at 290 K both the results of the tri- and tetraexponential fits are given.

method	medium	$T / \text{K}$	$\tau_1 / \text{ns}$ (fraction / %)	$\tau_2 / \text{ns}$ (fraction / %)	$\tau_3 / \mu\text{s}$ (fraction / %)	$\tau_4 / \mu\text{s}$ (fraction / %)
step-scan	KBr	290	-	-	$0.71 \pm 0.07$ (35)	$10 \pm 2$ (65)
step-scan	KBr	20	-	-	$2.2 \pm 0.2$ (18)	$66 \pm 7$ (82)
TCSPC $\lambda_{\text{exc}} = 389 \text{ nm}$ $\lambda_{\text{em}} = 745 \text{ nm}$	KBr	290	-	$88 \pm 2$ (8)	$0.71 \pm 0.01$ (21)	$10.9 \pm 0.1$ (71)
TCSPC $\lambda_{\text{exc}} = 389 \text{ nm}$ $\lambda_{\text{em}} = 745 \text{ nm}$	KBr	290	$38 \pm 3$ (2)	$276 \pm 8$ (10)	$1.49 \pm 0.05$ (17)	$14.4 \pm 0.3$ (71)
TCSPC $\lambda_{\text{exc}} = 389 \text{ nm}$ $\lambda_{\text{em}} = 733 \text{ nm}$	KBr	290	-	$96 \pm 1$ (8)	$0.72 \pm 0.01$ (22)	$9.5 \pm 0.1$ (70)
TCSPC $\lambda_{\text{exc}} = 389 \text{ nm}$ $\lambda_{\text{em}} = 733 \text{ nm}$	KBr	290	$47 \pm 2$ (3)	$305 \pm 8$ (12)	$1.57 \pm 0.05$ (19)	$13.7 \pm 0.3$ (67)
TCSPC $\lambda_{\text{exc}} = 389 \text{ nm}$ $\lambda_{\text{em}} = 722 \text{ nm}$	KBr	290	-	$105 \pm 2$ (8)	$0.83 \pm 0.02$ (21)	$12.2 \pm 0.3$ (72)
TCSPC $\lambda_{\text{exc}} = 389 \text{ nm}$ $\lambda_{\text{em}} = 722 \text{ nm}$	KBr	290	$58 \pm 4$ (3)	$310 \pm 20$ (9)	$1.5 \pm 0.1$ (17)	$15.3 \pm 0.5$ (70)
TCSPC $\lambda_{\text{exc}} = 389 \text{ nm}$ $\lambda_{\text{em}} = 759 \text{ nm}$	KBr	20	-	-	$0.5 \pm 0.1$ (2)	$55 \pm 13$ (98)
TCSPC $\lambda_{\text{exc}} = 389 \text{ nm}$ $\lambda_{\text{em}} = 740 \text{ nm}$	KBr	20	-	-	$0.60 \pm 0.07$ (5)	$50 \pm 10$ (95)
TCSPC $\lambda_{\text{exc}} = 389 \text{ nm}$ $\lambda_{\text{em}} = 740 \text{ nm}$	Neat film	290	-	$190 \pm 5$ (8)	$1.30 \pm 0.05$ (21)	$12.0 \pm 0.4$ (71)
TCSPC $\lambda_{\text{exc}} = 389 \text{ nm}$ $\lambda_{\text{em}} = 740 \text{ nm}$	Neat film	290	$47 \pm 7$ (1)	$290 \pm 20$ (9)	$1.5 \pm 0.1$ (19)	$13.5 \pm 0.5$ (72)
TCSPC $\lambda_{\text{exc}} = 389 \text{ nm}$ $\lambda_{\text{em}} = 717 \text{ nm}$	Neat film	290	-	$172 \pm 6$ (5)	$0.94 \pm 0.03$ (21)	$10.6 \pm 0.2$ (74)
TCSPC $\lambda_{\text{exc}} = 389 \text{ nm}$ $\lambda_{\text{em}} = 717 \text{ nm}$	Neat film	290	$120 \pm 20$ (2)	$400 \pm 50$ (10)	$1.7 \pm 0.1$ (19)	$12.5 \pm 0.2$ (69)

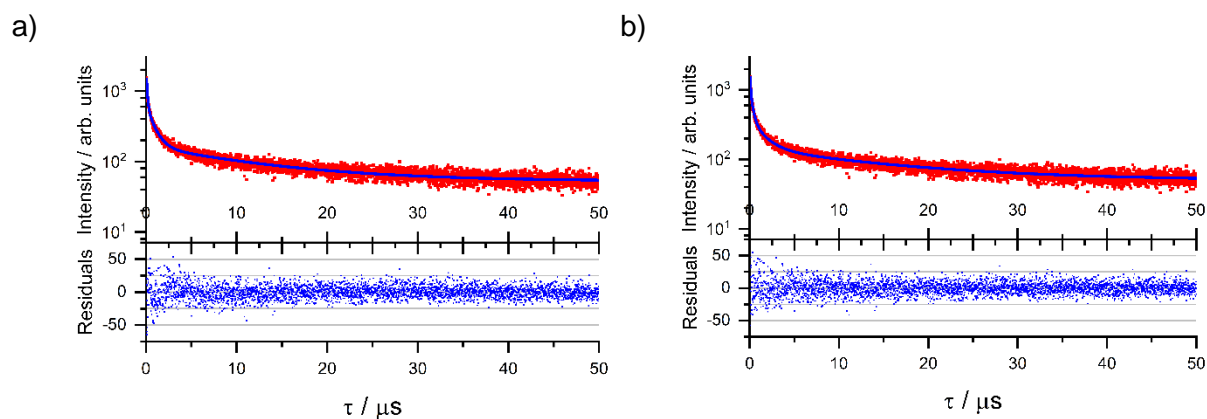




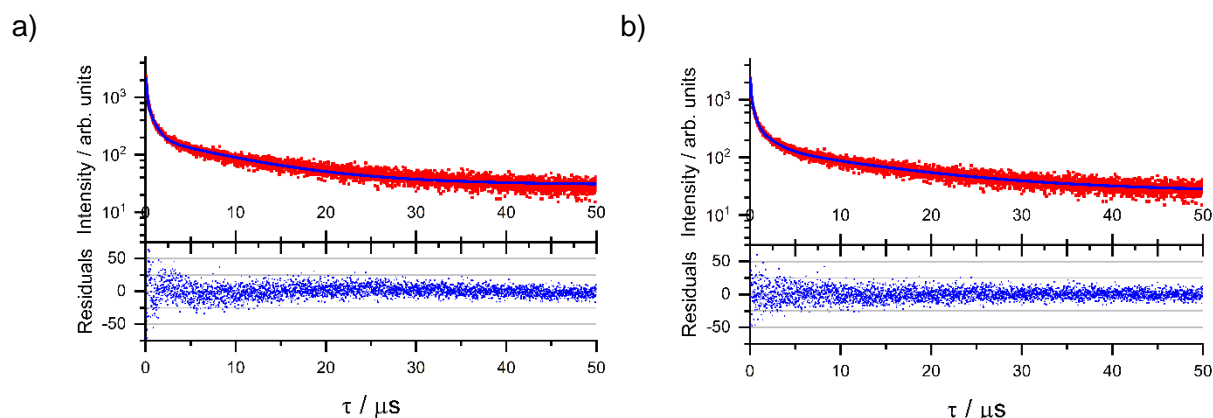
**Figure S19.** Decay curves and global fits obtained from step-scan FT-IR data at a) 290 K and b) 20 K including residuals. c) – f) Fits of the transition around  $1465\text{ cm}^{-1}$  at 290 K and 20 K (positive band that belongs to the excited state) and transition around  $1470\text{ cm}^{-1}$  at 290 K and 20 K (negative band that belongs to the electronic ground state) including residuals.



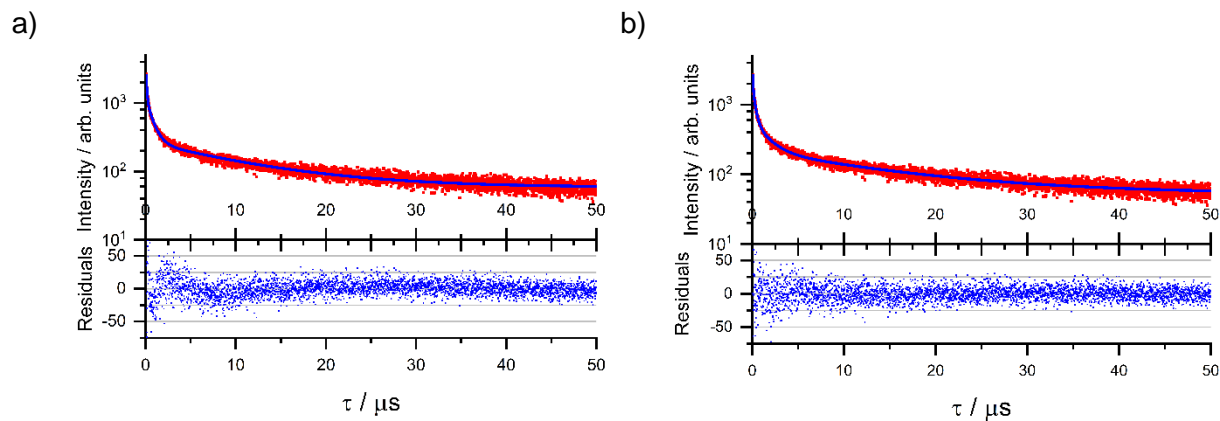
**Figure S20.** Decay curves as well as a) tri- and b) tetraexponential fits obtained from TCSPC data at 290 K ( $\lambda_{\text{obs}} = 722$  nm, KBr). The offset results from the dark current.



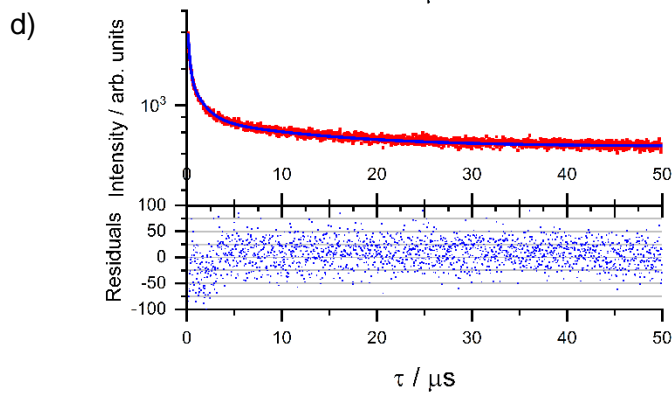
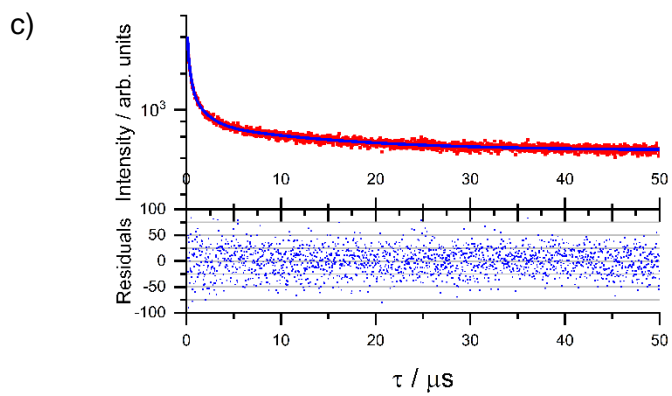
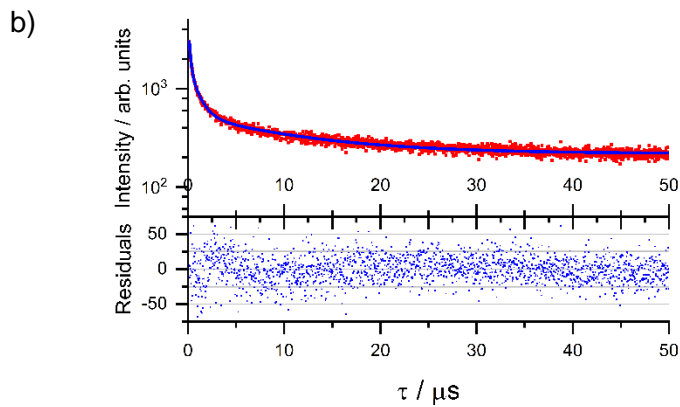
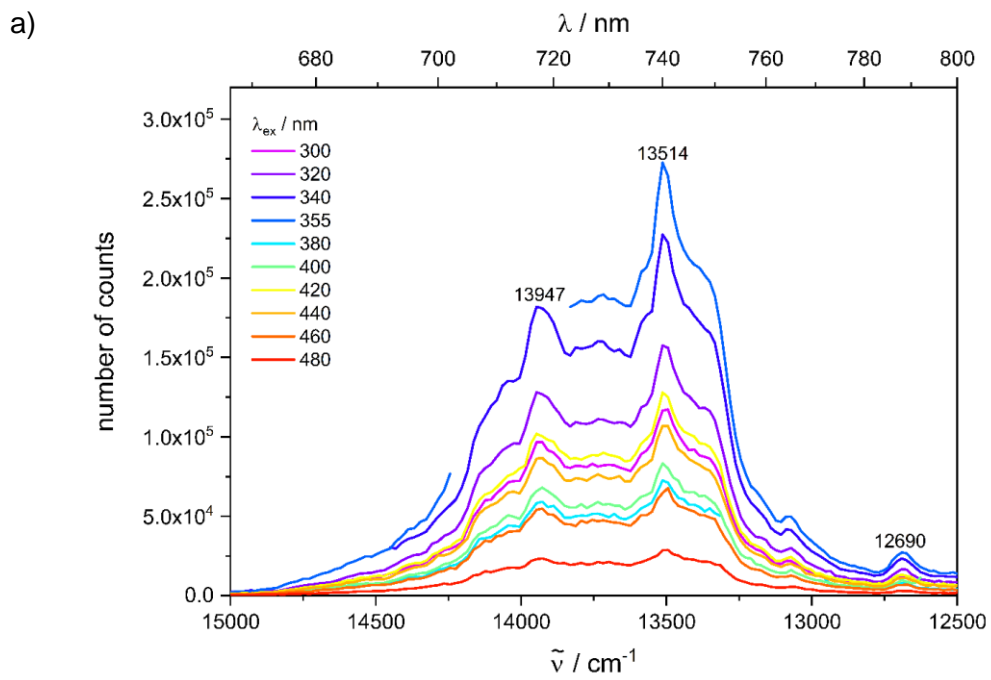
**Figure S21.** Decay curves as well as a) tri- and b) tetraexponential fits obtained from TCSPC data at 290 K ( $\lambda_{\text{obs}} = 733$  nm, KBr). The offset results from the dark current.



**Figure S22.** Decay curves as well as a) tri- and b) tetraexponential fits obtained from TCSPC data at 290 K ( $\lambda_{\text{obs}} = 745$  nm, KBr). The offset results from the dark current.







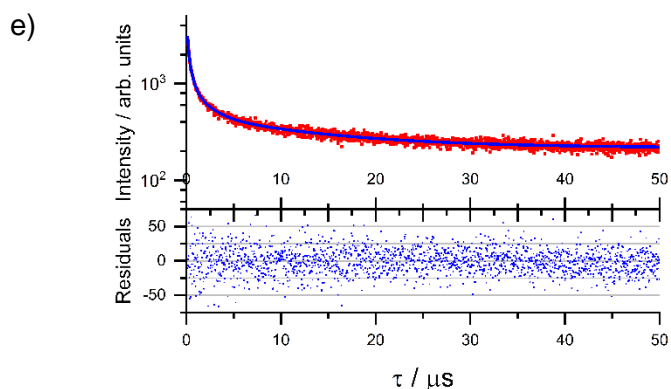


**Figure S23.** a) Emission spectra of  $[\text{Cr}(\text{tpe})_2][\text{BF}_4]_3$  as neat film at 290 K with different excitation wavelengths, decay curves as well as b) tri- and c) tetraexponential fits obtained from TCSPC data at 290 K ( $\lambda_{\text{obs}} = 717$  nm), decay curves as well as d) tri- and e) tetraexponential fits obtained from TCSPC data at 290 K ( $\lambda_{\text{obs}} = 740$  nm).

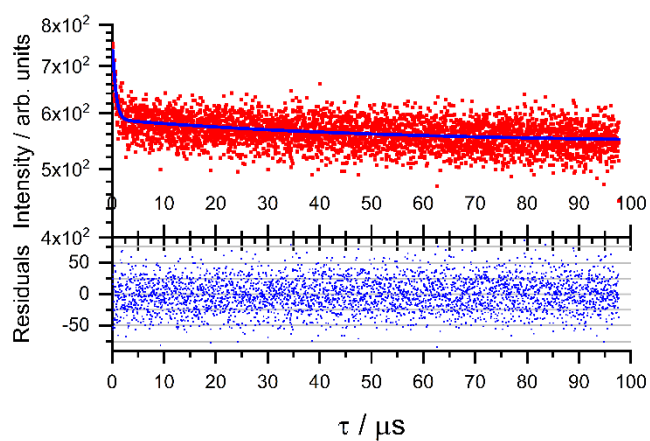


**Figure S24.** Decay curves and biexponential fits obtained from TCSPC data at 20 K ( $\lambda_{\text{obs}} = 740$  nm, KBr).

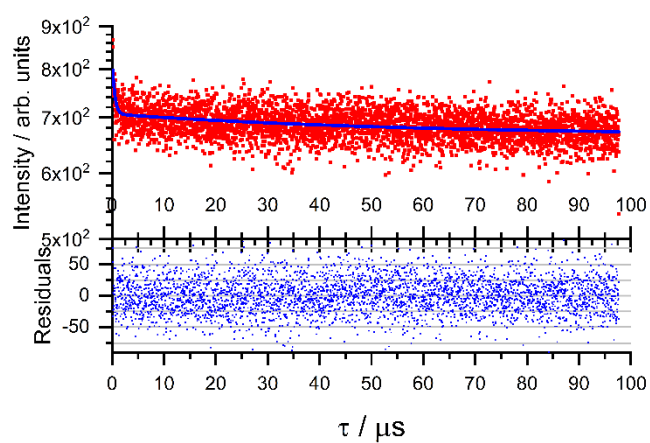


**Figure S25.** Decay curves and biexponential fits obtained from TCSPC data at 20 K ( $\lambda_{\text{obs}} = 759$  nm, KBr).

### Spectral overlap integral (SOI) calculations for $[\text{Cr}(\text{tpe})_2]^{3+} / \text{CH}_3\text{CN}$ and $\text{CD}_3\text{CN}$ :

The C-H overtone bands of  $\text{CH}_3\text{CN}$  in solution (Figures S26 and S27) were measured in the relevant spectral region ( $11500$  to  $16000 \text{ cm}^{-1} \equiv$  fourth C-H stretch overtone and third combination region) corresponding to the spectral region of the doublet emission of  $[\text{Cr}(\text{tpe})_2]^{3+}$ . The obtained data are consistent with previous measurements in liquid  $\text{CH}_3\text{CN}$  and show that the band intensities are largely dominated by C-H stretching overtones without significant participation of  $\text{C}\equiv\text{N}$  vibrations.<sup>S28</sup> The measured bands were fitted by a series of Gaussian functions in order to extract a coherent expression of the band shape for the SOI calculation (vide infra).

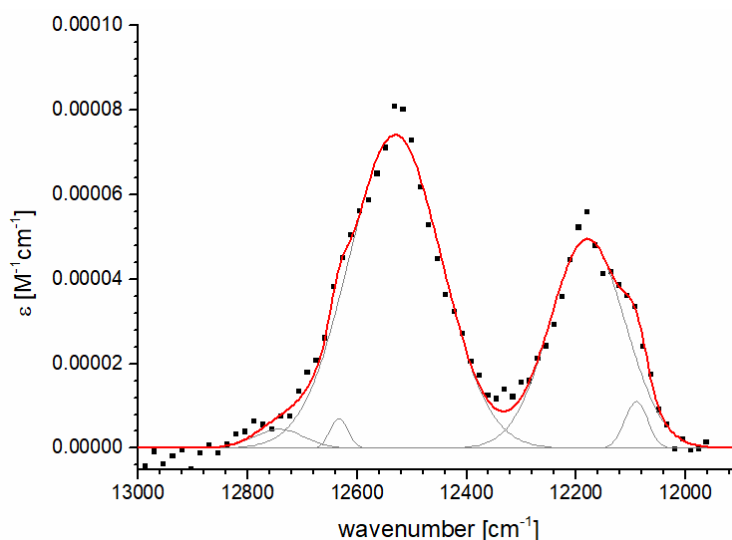


**Figure S26.** Near-IR absorption spectrum of neat  $\text{CH}_3\text{CN}$  (black,  $c = 19.15 \text{ M}$ ,  $d = 5 \text{ cm}$ ) in the third C-H combination region. Gaussian fit functions for the analytical extraction of the band shape (grey: individual Gaussians; red: sum of the Gaussians).

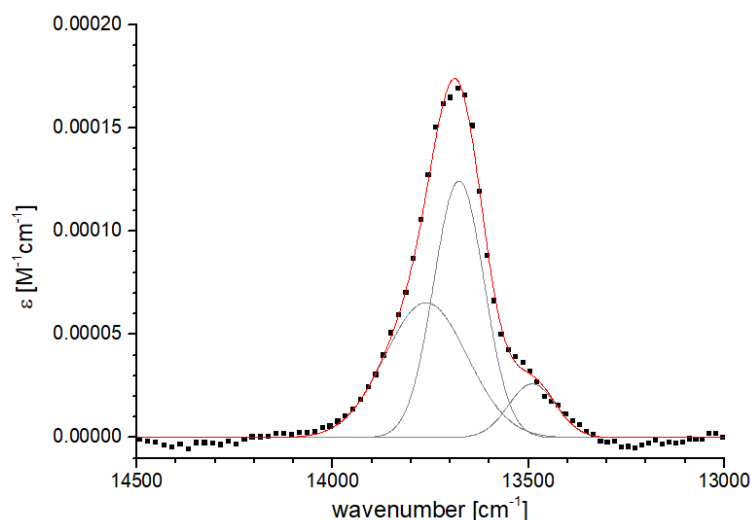


**Figure S27.** Near-IR absorption spectrum of neat  $\text{CH}_3\text{CN}$  (black,  $c = 19.15 \text{ M}$ ,  $d = 5 \text{ cm}$ ) in the fourth C-H overtone region (vibrational quantum number  $\nu = 5$ ). Gaussian fit functions for the analytical extraction of the band shape (grey: individual Gaussians; red: sum of the Gaussians).

The C-D absorption bands in the same region as for the C-H overtones (11500 to 16000  $\text{cm}^{-1}$ ) could not be reliably measured due to the extremely small molar extinction values associated with these overtones. In order to be able to calculate the corresponding SOI with the chromium emission, the spectral characteristics of the required higher overtones C-D (in particular the overtones  $\nu = 6$  and 7) were extrapolated from the systematic changes seen in the lower overtones ( $\nu = 3 - 5$ ) that could be measured. For this purpose, each measured overtone band was fitted with a single Gaussian function of the form  $y(x) = A \cdot \exp(-0.5 \cdot ((x-x_c)/\sigma)^2)$  defined by amplitude  $A$ , center wavenumber  $x_c$ , and Gaussian width  $\sigma$ . As can be seen from Figures S28–S30, this is a rather crude approximation for the lower overtone bands (especially seen in Figure S28) but improves with increasing vibrational quantum number as the vibrations gain more local-mode character and coupling between oscillators is diminishing.

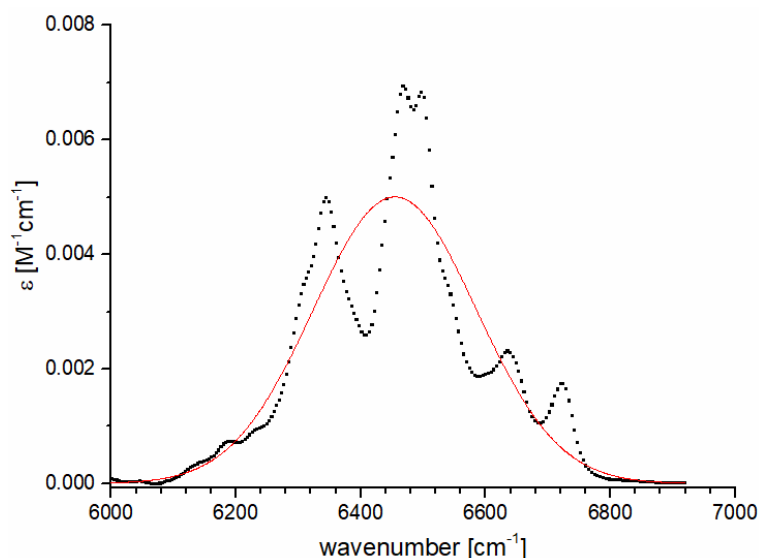


**Figure S28.** Near-IR absorption spectrum of neat  $\text{CD}_3\text{CN}$  (black,  $c = 19.15 \text{ M}$ ,  $d = 5 \text{ cm}$ ) in the third C-D combination region. Single Gaussian fit function (red) for the extrapolation procedure to higher overtones (see text).

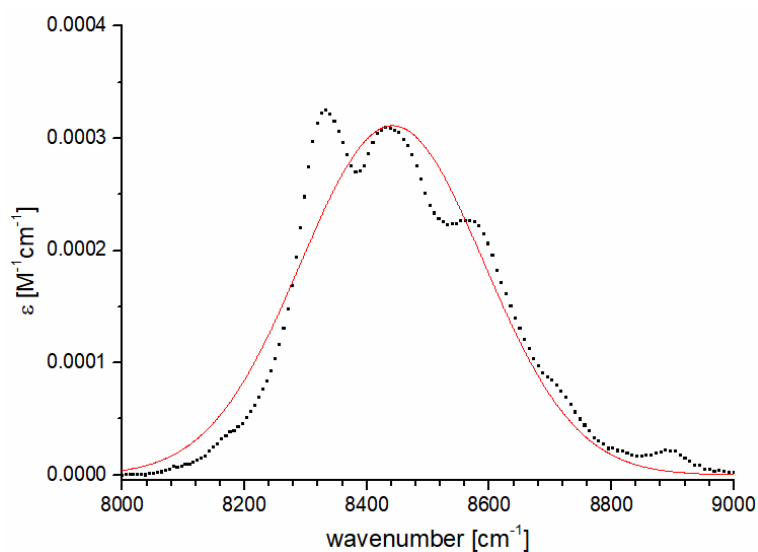


**Figure S29.** Near-IR absorption spectrum of neat  $\text{CD}_3\text{CN}$  (black,  $c = 19.15 \text{ M}$ ,  $d = 5 \text{ cm}$ ) in the fourth C-D combination region. Single Gaussian fit function (red) for the extrapolation procedure to higher overtones (see text).

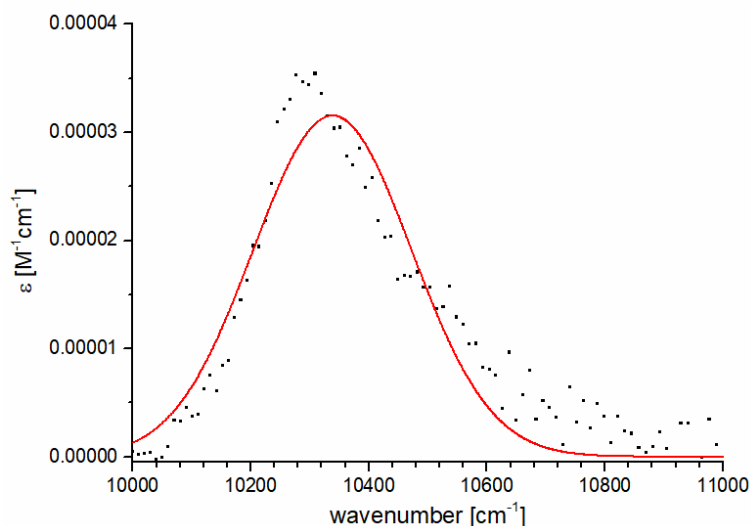


**Figure S30.** Near-IR absorption spectrum of neat CD<sub>3</sub>CN (black,  $c = 19.15$  M,  $d = 5$  cm) in the fifth C-D combination region. Single Gaussian fit function (red) for the extrapolation procedure to higher overtones (see text).

Due to the high degree of coupling in the overtones, the only Gaussian parameter that turned out to be reliable for the extrapolation was the amplitude  $A$ . As already successfully shown in previous work,<sup>S29</sup> the semilogarithmic plot of  $\log(A)$  vs. vibrational quantum number  $\nu$  could be fitted well by a linear relationship (Figure S31).

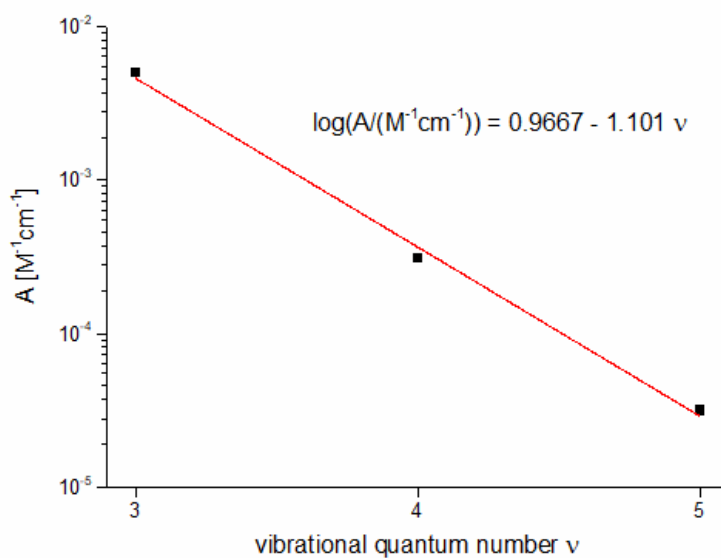


**Figure S31.** Semi-logarithmic plot of the amplitudes  $A$  of the Gaussians describing the C-D oscillators vs. the vibrational quantum number  $\nu$  in CD<sub>3</sub>CN and linear fit (solid red).

The other two Gaussian parameters ( $x_c$  and  $\sigma$ ) necessary for the construction of the higher C-D overtone bands were estimated using the published data. The  $x_c$  values were calculated using the known Morse parameters for liquid CD<sub>3</sub>CN (fundamental  $\tilde{\nu}_0 = 2175$  cm<sup>-1</sup> and anharmonicity  $x = 30.5$  cm<sup>-1</sup>),<sup>S30</sup> whereas the Gaussian widths for the required overtones  $\sigma$  were estimated to be equal to the corresponding C-D overtone band widths for aromatic C-D oscillators.<sup>S29,S31</sup> The properties of the

measured and extrapolated Gaussians are summarized in Table S4 and were used for the SOI calculations (vide infra).

**Table S4.** Parameters of the Gaussians ( $x_c$ : wavenumber of the maximum;  $\sigma$ : Gaussian width;  $A$ : amplitude) describing the C-D-oscillators in CD<sub>3</sub>CN.

$\nu$	maximum $x_c / \text{cm}^{-1}$	$\sigma / \text{cm}^{-1}$	$A / \text{M}^{-1}\text{cm}^{-1}$
3 <sup>[a]</sup>	-	-	$5.01 \cdot 10^{-3}$
4 <sup>[a]</sup>	-	-	$3.11 \cdot 10^{-4}$
5	-	-	$3.15 \cdot 10^{-5}$
6	12369 <sup>[b]</sup>	129.05 <sup>[c]</sup>	$2.29 \cdot 10^{-6}$ <sup>[d]</sup>
7	14217 <sup>[b]</sup>	154.35 <sup>[c]</sup>	$1.82 \cdot 10^{-7}$ <sup>[d]</sup>

<sup>[a]</sup> Based on Gaussian fits of measured data.

<sup>[b]</sup> Calculated using  $x_c = \nu \cdot 2175 \text{ cm}^{-1} - \nu(\nu+1) \cdot 30.5 \text{ cm}^{-1}$  from ref. S30.

<sup>[c]</sup> Calculated using  $\sigma = \nu \cdot 25 \text{ cm}^{-1} - 22.8 \text{ cm}^{-1}$  from ref. S29.

<sup>[d]</sup> Extrapolated using the equation  $\log(A/(\text{M}^{-1}\text{cm}^{-1})) = 0.9667 - \nu \cdot 1.101$ , obtained by linear fitting of  $\log(A)$  vs. vibrational quantum number  $\nu$  (obtained by Gaussian fitting for the overtones  $\nu = 3$  to  $5$ , see Figures S28–S30).

The integrand functions for the SOIs between the chromium complex emission and C-(H/D) overtones in the isotopologic bulk acetonitriles were constructed according to the mathematical definition of the SOIs:

$$\text{SOI} = \int I_{\text{norm}}(\tilde{\nu}) \cdot \varepsilon(\tilde{\nu}) \cdot \tilde{\nu}^{-4} d\tilde{\nu}$$

with  $I_{\text{norm}}$  being the chromium emission spectrum normalized to unit area and  $\varepsilon$  the decimal molar vibrational absorption coefficient (see extracted and extrapolated absorption spectra above), both expressed in the wavenumber scale  $\tilde{\nu}$ . The integrand functions were generated with a set of data points with a step size of  $1 \text{ cm}^{-1}$  (Figures S32 and S33). Numerical integration of the integrand functions (OriginPro 9.0) gave the corresponding values for the SOIs.

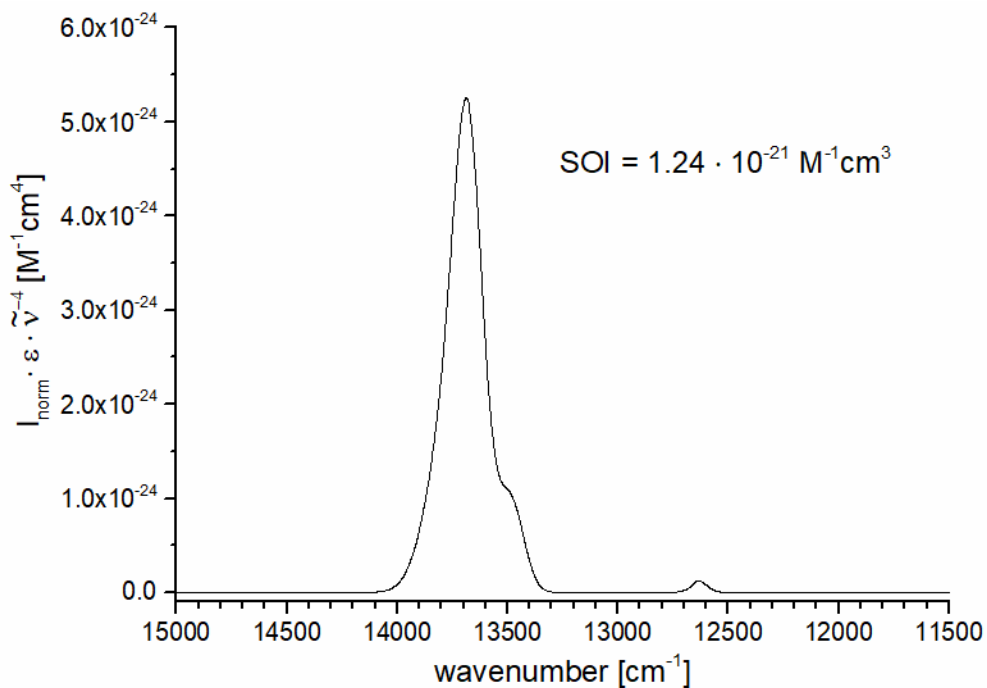


**Figure S32.** Integrand function of the spectral overlap integral (SOI) for chromium emission band in  $[\text{Cr}(\text{tpe})_2]^{3+}$  and the measured fourth overtone C-H ( $\nu = 5$ ) and the measured third combination region of bulk  $\text{CH}_3\text{CN}$ .

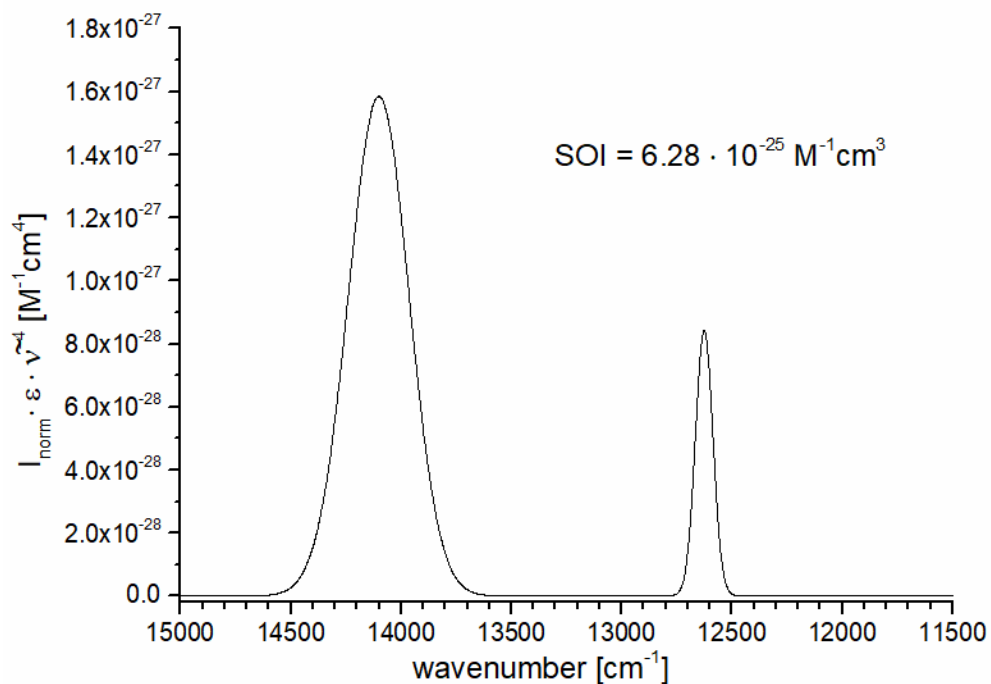


**Figure S33.** Integrand function of the spectral overlap integral (SOI) for chromium emission band in  $[\text{Cr}(\text{tpe})_2]^{3+}$  and the extrapolated fifth and sixth overtone C-D ( $\nu = 6$  and  $\nu = 7$ ) of bulk  $\text{CD}_3\text{CN}$ .

Based on the obtained SOIs, the ratio of the non-radiative deactivation rates of chromium excited states in  $[\text{Cr}(\text{tpe})_2]^{3+}$  in the acetonitrile isotopologues is estimated as:<sup>S31</sup>

$$\frac{k_{\text{nr}}(\text{CH}_3\text{CN})}{k_{\text{nr}}(\text{CD}_3\text{CN})} = \frac{\text{SOI}(\text{CH}_3\text{CN})}{\text{SOI}(\text{CD}_3\text{CN})} = \frac{1.24 \cdot 10^{-21} \text{ M}^{-1}\text{cm}^3}{6.28 \cdot 10^{-25} \text{ M}^{-1}\text{cm}^3} = 1.97 \cdot 10^3$$

This ratio would suggest a massive reduction in multiphonon relaxation rates and a concomitant increase in luminescence intensity and lifetimes by exchanging  $\text{CH}_3\text{CN}$  versus  $\text{CD}_3\text{CN}$ . Yet, this is not observed. For a discussion, see main text.

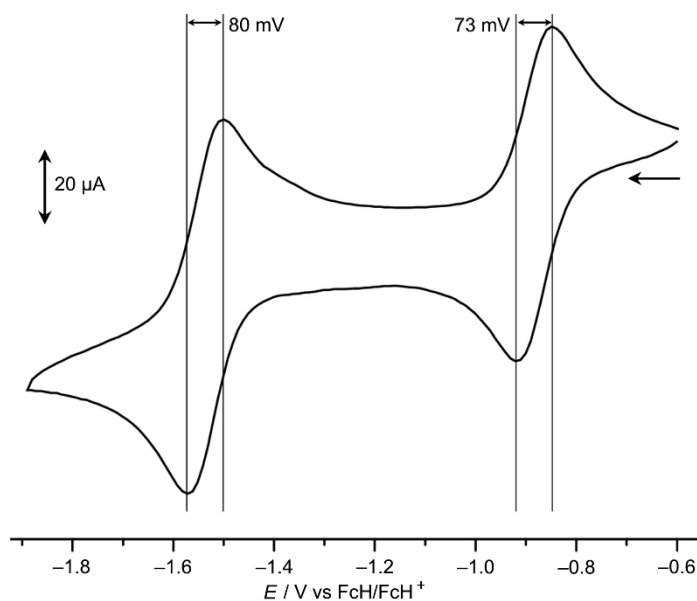


**Figure S34.** Cyclic voltammogram of  $[\text{Cr}(\text{tpe})_2][\text{BF}_4]_3$  ( $\text{CH}_3\text{CN}$ ,  $[\text{N}^n\text{Bu}_4][\text{BF}_4]$ ,  $T = 293 \text{ K}$ ).

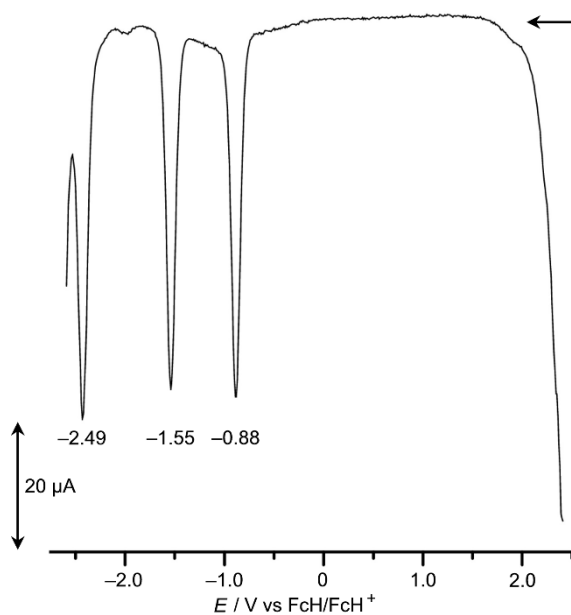


**Figure S35.** Square wave voltammogram of  $[\text{Cr}(\text{tpe})_2][\text{BF}_4]_3$  ( $\text{CH}_3\text{CN}$ ,  $[\text{N}^n\text{Bu}_4][\text{BF}_4]$ ,  $T = 293 \text{ K}$ ).



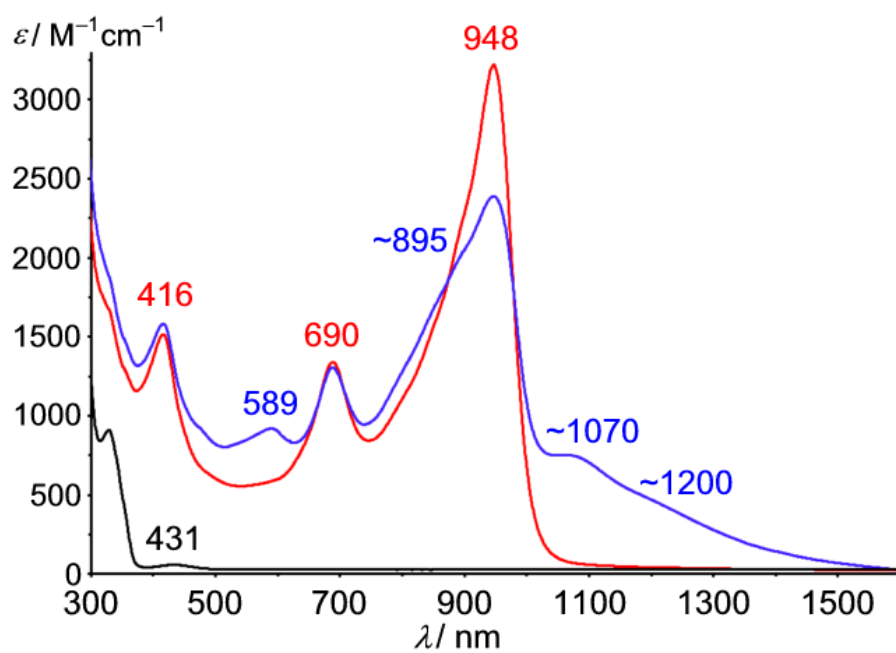


**Figure S36.** UV/Vis/NIR absorption spectra ( $\text{CH}_3\text{CN}$ ,  $[\text{N}^{\text{t}}\text{Bu}_4][\text{BF}_4]$ ,  $T = 293 \text{ K}$ ) of  $[\text{Cr}(\text{tpe})_2][\text{BF}_4]_3$  (black), after the first reduction (red) and approximately after the second reduction (blue) in an OTTLE cell.

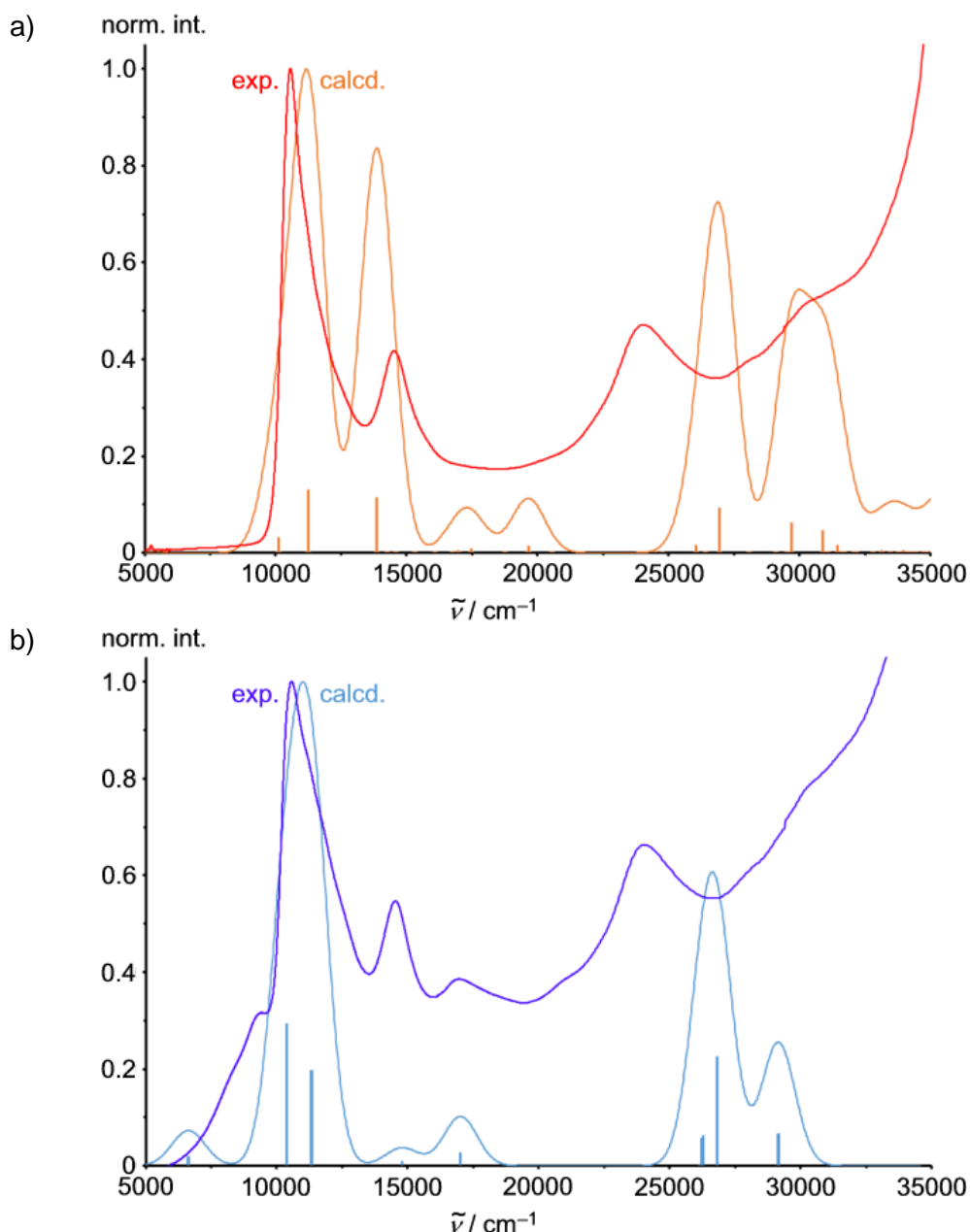


**Figure S37.** a) UV/Vis/NIR spectrum of  $[\text{Cr}(\text{tpe})_2][\text{BF}_4]_3$  after the first reduction in an OTTLE cell ( $\text{CH}_3\text{CN}$ ,  $[\text{N}^n\text{Bu}_4][\text{BF}_4]$ ,  $T = 293 \text{ K}$ ) and TD-DFT calculated 50 vertical transitions of geometry optimized  $[\text{Cr}(\text{tpe})_2]^{2+}$  ( $S = 1$ ). Stick spectrum was approximated by Gaussian bands with FWHM of  $1500 \text{ cm}^{-1}$ . b) UV/Vis/NIR spectrum of  $[\text{Cr}(\text{tpe})_2][\text{BF}_4]_3$  approximately after the second reduction in an OTTLE cell ( $\text{CH}_3\text{CN}$ ,  $[\text{N}^n\text{Bu}_4][\text{BF}_4]$ ,  $T = 293 \text{ K}$ ) and TD-DFT calculated 50 vertical transitions of geometry optimized  $[\text{Cr}(\text{tpe})_2]^+$  ( $S = 1/2$ ). The stick spectrum was approximated by Gaussian bands with FWHM of  $1500 \text{ cm}^{-1}$ .

**Figure S38.** a) Emission spectra of  $[\text{Cr}(\text{tpe})_2][\text{BF}_4]_3$  in  $\text{CH}_3\text{CN}$  during titration with azulene and b) corresponding Stern-Volmer analysis;  $K_{\text{SV}} = 41.7 \times 10^3 \text{ M}^{-1}$ ;  $R^2 = 0.9887$ .

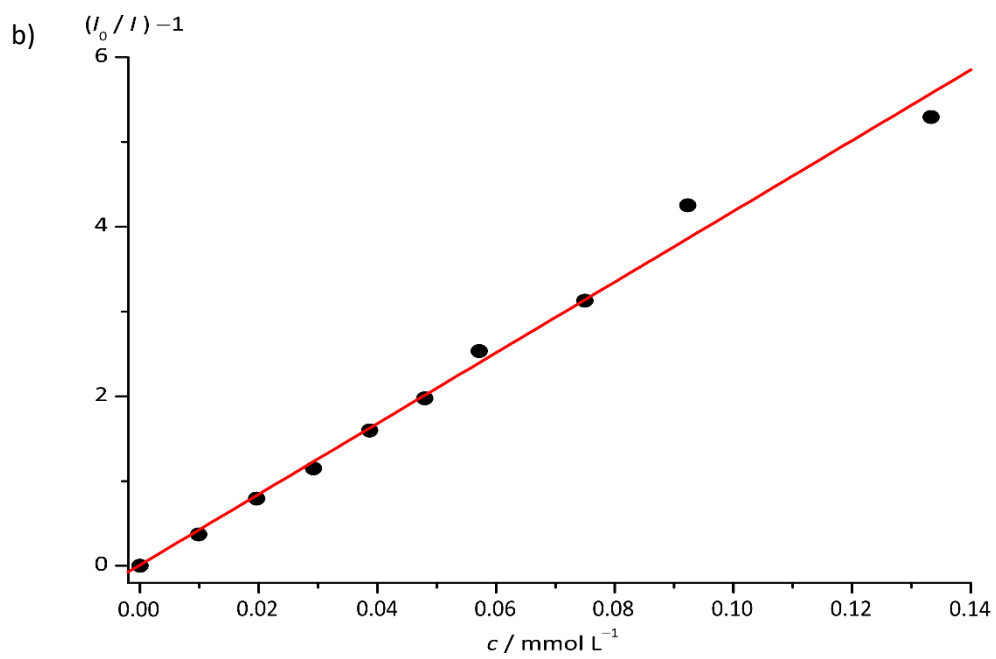
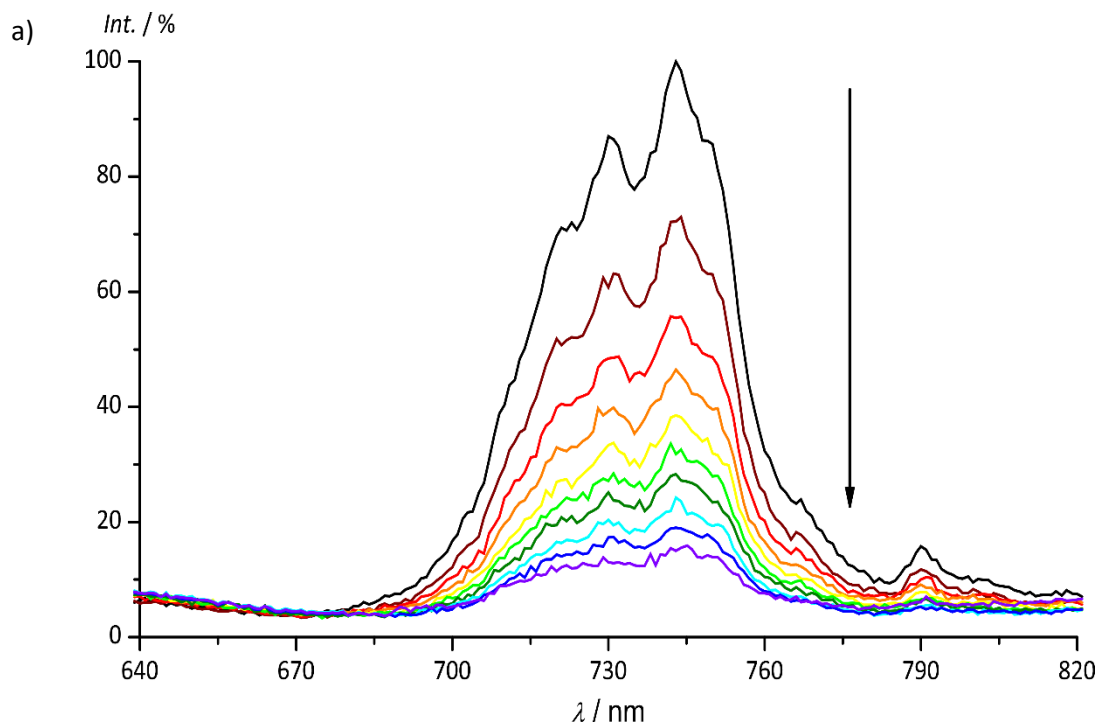
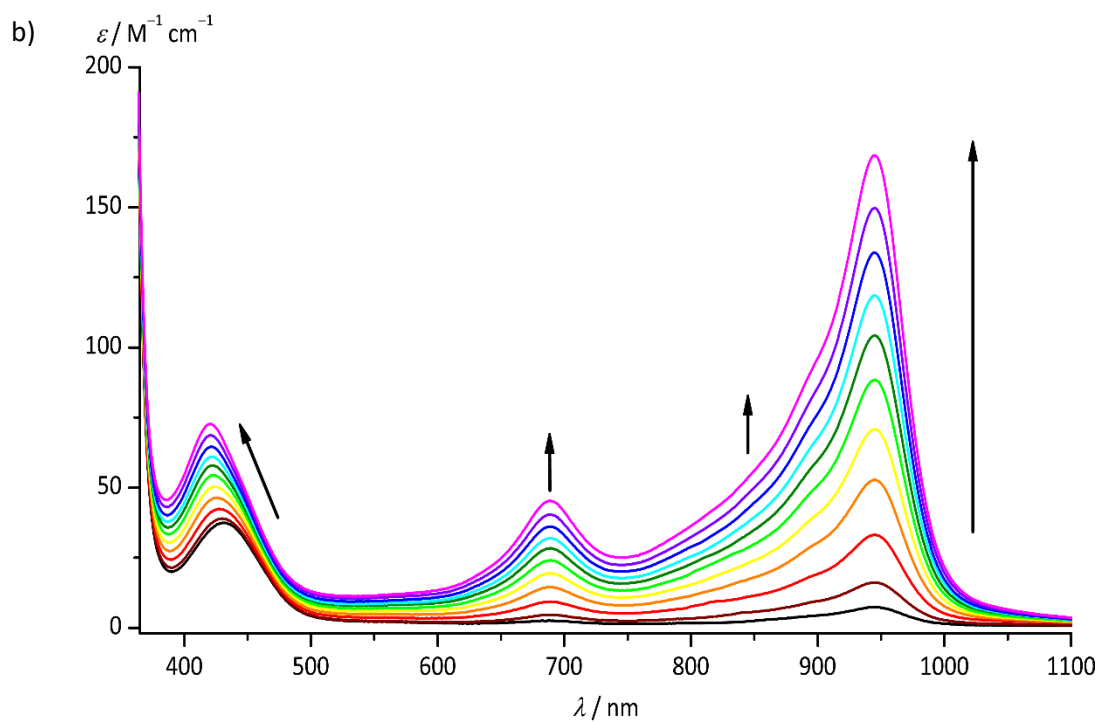
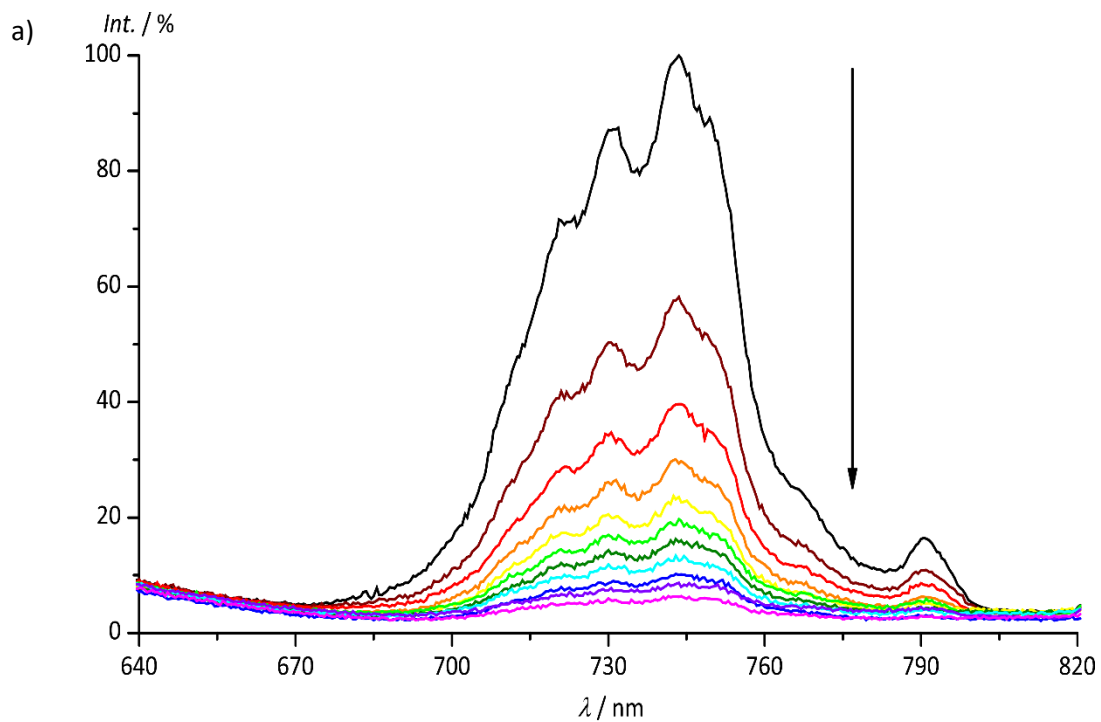


**Figure S39.** a) Emission spectra of  $[\text{Cr}(\text{tpe})_2][\text{BF}_4]_3$  in  $\text{CH}_3\text{CN}$  during titration with tri(*n*-butyl)amine and b) corresponding UV/Vis/NIR spectra showing the formation of  $[\text{Cr}(\text{tpe})_2]^{2+}$ .



Cartesian coordinates of geometry optimized  $[\text{Cr}(\text{tpe})_2]^{3+}$  (quartet)

24	1.762771000	1.606228000	7.381007000
7	2.830770000	-0.144294000	7.240533000
7	3.574703000	2.576281000	7.360545000
7	1.999852000	1.450063000	9.414141000
6	2.282182000	1.228497000	12.141658000
1	2.407825000	1.137064000	13.211060000
6	4.347961000	0.830627000	8.934733000
6	4.925456000	4.374585000	6.567885000
1	5.009734000	5.258080000	5.953904000
6	5.818187000	2.759259000	8.095045000
1	6.641381000	2.392373000	8.681911000
6	5.985648000	3.902130000	7.325487000
1	6.937537000	4.413672000	7.322873000
6	3.734575000	3.682390000	6.612350000
1	2.880694000	4.010291000	6.041053000
6	3.195355000	1.095685000	9.924119000
6	1.059404000	1.593406000	11.600656000
1	0.198357000	1.797327000	12.218341000
6	0.958789000	1.693926000	10.229930000
1	0.029109000	1.973827000	9.760494000
6	3.355162000	0.979524000	11.297150000
1	4.303831000	0.698371000	11.718436000
6	5.617490000	0.450082000	9.700725000
1	5.454435000	-0.447613000	10.290063000
1	5.912650000	1.250249000	10.373200000
1	6.438000000	0.262482000	9.014423000
6	3.940119000	-0.313864000	7.985653000
6	4.672431000	-1.487289000	7.880572000
1	5.561553000	-1.634504000	8.467456000
6	4.258268000	-2.484912000	7.009139000
1	4.829710000	-3.398427000	6.927396000
6	3.113048000	-2.295775000	6.251873000
1	2.753137000	-3.043865000	5.562343000
6	2.426108000	-1.109847000	6.396155000
1	1.530843000	-0.913869000	5.827767000
6	4.595929000	2.103517000	8.101120000
7	0.696087000	3.357379000	7.521995000
7	-0.049255000	0.636280000	7.401840000
7	1.523873000	1.761864000	5.347984000
6	1.237859000	1.979350000	2.620485000
1	1.110769000	2.069156000	1.551117000
6	-0.823540000	2.382905000	5.829598000
6	-1.400067000	-1.161356000	8.195807000
1	-1.483852000	-2.045396000	8.809077000
6	-2.294516000	0.456196000	6.672047000
1	-3.118584000	0.824433000	6.087263000
6	-2.461529000	-0.687034000	7.441181000
1	-3.413989000	-1.197502000	7.445598000
6	-0.208554000	-0.470337000	8.149390000
1	0.646375000	-0.799644000	8.718321000
6	0.327725000	2.115777000	4.839094000
6	2.461322000	1.615108000	3.160374000
1	3.321517000	1.410118000	2.541856000
6	2.563695000	1.516592000	4.531110000
1	3.493936000	1.237063000	4.999662000

6	0.166097000	2.229852000	3.466096000
1	-0.783092000	2.510543000	3.045661000
6	-2.093597000	2.764279000	5.064868000
1	-1.930302000	3.661405000	4.474741000
1	-2.390443000	1.963945000	4.393344000
1	-2.913124000	2.953188000	5.752049000
6	-0.414013000	3.527356000	6.778089000
6	-1.145703000	4.701108000	6.883898000
1	-2.035236000	4.848806000	6.297773000
6	-0.730106000	5.698635000	7.754757000
1	-1.301065000	6.612402000	7.837066000
6	0.415789000	5.508997000	8.510876000
1	0.776788000	6.257006000	9.199928000
6	1.102166000	4.322831000	8.365854000
1	1.998506000	4.127165000	8.932734000
6	-1.071558000	1.110548000	6.663726000

Cartesian coordinates of geometry optimized  $[\text{Cr}(\text{tpe})_2]^{2+}$  (triplet)

24	1.762401000	1.606268000	7.381618000
7	2.822961000	-0.118886000	7.246885000
7	3.580216000	2.587258000	7.359208000
7	2.000140000	1.453165000	9.414812000
6	2.278355000	1.185517000	12.150257000
1	2.402419000	1.079833000	13.218706000
6	4.350078000	0.844738000	8.937164000
6	4.944986000	4.370987000	6.547859000
1	5.032580000	5.251609000	5.929500000
6	5.833203000	2.758446000	8.078059000
1	6.657104000	2.389794000	8.663185000
6	6.008026000	3.894138000	7.299974000
1	6.964002000	4.398479000	7.289250000
6	3.747213000	3.689660000	6.609901000
1	2.886739000	4.021380000	6.050191000
6	3.195477000	1.097469000	9.928105000
6	1.056784000	1.558276000	11.608680000
1	0.194010000	1.753150000	12.227783000
6	0.962480000	1.687256000	10.239109000
1	0.037291000	1.982751000	9.769728000
6	3.352260000	0.955997000	11.301502000
1	4.301872000	0.672893000	11.720185000
6	5.621502000	0.468616000	9.703175000
1	5.463034000	-0.428380000	10.294866000
1	5.916572000	1.270402000	10.374611000
1	6.442682000	0.279876000	9.017491000
6	3.938609000	-0.301741000	7.992349000
6	4.666410000	-1.480389000	7.896904000
1	5.553710000	-1.623685000	8.488537000
6	4.257092000	-2.487228000	7.033121000
1	4.825534000	-3.403062000	6.957912000
6	3.111868000	-2.290116000	6.272769000
1	2.749403000	-3.039698000	5.584922000
6	2.429088000	-1.101179000	6.405807000
1	1.537284000	-0.908070000	5.830717000
6	4.602107000	2.113577000	8.096955000
7	0.702123000	3.331533000	7.516586000
7	-0.055403000	0.625265000	7.404141000
7	1.524240000	1.759277000	5.348418000
6	1.245436000	2.026866000	2.613021000
1	1.121155000	2.132566000	1.544599000
6	-0.825482000	2.368029000	5.826602000
6	-1.420024000	-1.158680000	8.215271000
1	-1.507512000	-2.039445000	8.833442000
6	-2.308497000	0.454192000	6.685583000
1	-3.132469000	0.823004000	6.100656000
6	-2.483190000	-0.681674000	7.463435000
1	-3.439157000	-1.186032000	7.474197000
6	-0.222283000	-0.477299000	8.153229000
1	0.638258000	-0.809091000	8.712779000
6	0.328869000	2.115194000	4.835394000
6	2.467028000	1.653791000	3.154322000
1	3.329615000	1.458660000	2.535043000
6	2.561571000	1.524840000	4.523877000
1	3.486823000	1.229178000	4.993021000

6	0.171788000	2.256661000	3.462022000
1	-0.777878000	2.539972000	3.043603000
6	-2.097035000	2.744322000	5.060881000
1	-1.938613000	3.641410000	4.469317000
1	-2.392211000	1.942666000	4.389336000
1	-2.918098000	2.932924000	5.746738000
6	-0.413788000	3.514383000	6.771513000
6	-1.141706000	4.692926000	6.867403000
1	-2.029200000	4.836211000	6.276062000
6	-0.732228000	5.699701000	7.731182000
1	-1.300767000	6.615446000	7.806728000
6	0.413327000	5.502650000	8.491048000
1	0.776004000	6.252203000	9.178817000
6	1.096196000	4.313821000	8.357564000
1	1.988402000	4.121056000	8.932183000
6	-1.077403000	1.099070000	6.666644000



Cartesian coordinates of geometry optimized  $[\text{Cr}(\text{tpe})_2]^+$  (doublet)

24	1.762423000	1.606357000	7.381618000
7	2.807608000	-0.121602000	7.231621000
7	3.542356000	2.571934000	7.354993000
7	1.983413000	1.453542000	9.386812000
6	2.274256000	1.236047000	12.145636000
1	2.400994000	1.148099000	13.215267000
6	4.334773000	0.834002000	8.926777000
6	4.911342000	4.376345000	6.561578000
1	4.992564000	5.260842000	5.946344000
6	5.805289000	2.762513000	8.082882000
1	6.628232000	2.391243000	8.669101000
6	5.983295000	3.908177000	7.315142000
1	6.935914000	4.418429000	7.309628000
6	3.720293000	3.687325000	6.608163000
1	2.864114000	4.015384000	6.040177000
6	3.183570000	1.099987000	9.915421000
6	1.049692000	1.597838000	11.592868000
1	0.186384000	1.802645000	12.209372000
6	0.946469000	1.695105000	10.223487000
1	0.016537000	1.972263000	9.752677000
6	3.342122000	0.988165000	11.290169000
1	4.293917000	0.708879000	11.708073000
6	5.605044000	0.452851000	9.691889000
1	5.443900000	-0.444084000	10.283724000
1	5.904098000	1.252525000	10.363968000
1	6.426274000	0.262817000	9.006216000
6	3.925852000	-0.309250000	7.978949000
6	4.654062000	-1.486695000	7.873917000
1	5.541272000	-1.633168000	8.465577000
6	4.247986000	-2.491496000	7.002876000
1	4.817127000	-3.406657000	6.922733000
6	3.099812000	-2.288981000	6.243699000
1	2.737538000	-3.035330000	5.551491000
6	2.414736000	-1.103338000	6.385728000
1	1.520683000	-0.904326000	5.816293000
6	4.582276000	2.105685000	8.093766000
7	0.717281000	3.334326000	7.531654000
7	-0.017446000	0.640580000	7.408405000
7	1.541141000	1.759176000	5.376496000
6	1.249706000	1.976393000	2.617682000
1	1.122738000	2.064237000	1.548071000
6	-0.810240000	2.378531000	5.836908000
6	-1.386133000	-1.163954000	8.201994000
1	-1.467192000	-2.048514000	8.817165000
6	-2.280556000	0.449979000	6.681079000
1	-3.103661000	0.821274000	6.095103000
6	-2.458312000	-0.695742000	7.448780000
1	-3.410918000	-1.206018000	7.454525000
6	-0.195087000	-0.474912000	8.155199000
1	0.661307000	-0.802982000	8.722877000
6	0.340819000	2.112563000	4.848082000
6	2.474429000	1.614790000	3.170240000
1	3.337642000	1.410024000	2.553588000
6	2.577919000	1.517653000	4.539597000
1	3.508006000	1.240710000	5.010228000

6	0.181997000	2.224246000	3.473357000
1	-0.769910000	2.503401000	3.055616000
6	-2.080640000	2.759638000	5.071987000
1	-1.919631000	3.656603000	4.480158000
1	-2.379746000	1.959961000	4.399935000
1	-2.901787000	2.949597000	5.757778000
6	-0.401248000	3.521791000	6.784708000
6	-1.129700000	4.699057000	6.890096000
1	-2.017158000	4.845366000	6.298769000
6	-0.723559000	5.703873000	7.761092000
1	-1.292914000	6.618874000	7.841548000
6	0.424984000	5.501594000	8.519776000
1	0.787388000	6.248025000	9.211831000
6	1.110313000	4.316139000	8.377402000
1	2.004885000	4.117514000	8.946171000
6	-1.057554000	1.106832000	6.669929000

## References

- [S1] A. Santoro, C. Sambiagio, P. C. McGowan, M. A. Halcrow, *Dalton Trans.* **2015**, *44*, 1060–1069.
- [S2] G. R. Fulmer, A. J. M. Miller, N. H. Sherden, H. E. Gottlieb, A. Nudelman, B. M. Stoltz, J. E. Bercaw, K. I. Goldberg, *Organometallics* **2010**, *29*, 2176–2179.
- [S3] C. Würth, J. Pauli, C. Lochmann, M. Spieles, U. Resch-Genger, *Anal. Chem.* **2012**, *84*, 1345–1352.
- [S4] C. Würth, M.-G. González, R. Niessner, U. Panne, C. Haisch, U. Resch-Genger, *Talanta* **2012**, *90*, 30–37.
- [S5] C. Würth, D. Geissler, T. Behnke, M. Kaiser, U. Resch-Genger, *Anal. Bioanal. Chem.* **2015**, *407*, 59–78.
- [S6] M. Zimmer, F. Rupp, P. Singer, F. Walz, F. Breher, W. Klopper, R. Diller, M. Gerhards, *Phys. Chem. Chem. Phys.* **2015**, *17*, 14138–14144.
- [S7] F. Bäppler, M. Zimmer, F. Dietrich, M. Gruppe, M. Wallesch, D. Volz, S. Bräse, M. Gerhards, R. Diller, *Phys. Chem. Chem. Phys.* **2017**, *19*, 29438–29448.
- [S8] M. Zimmer, F. Dietrich, D. Volz, S. Bräse, M. Gerhards, *ChemPhysChem* **2017**, *18*, 3023–3029.
- [S9] STOE & Cie, X-Red, STOE & Cie, Darmstadt, Germany **2002**.
- [S10] R. H. Blessing, *Acta Crystallogr. Sect. A* **1995**, *51*, 33–38.
- [S11] A. L. Spek, *Acta Crystallogr. Sect. D* **2009**, *65*, 148–55.
- [S12] G. M. Sheldrick, SHELXL-2014/7, University of Göttingen, Göttingen, Germany, **2014**.
- [S13] G. M. Sheldrick, *Acta Crystallogr. Sect. A* **2015**, *71*, 3–8.
- [S14] F. Neese, *WIREs Comput. Mol. Sci.* **2012**, *2*, 73–78.
- [S15] F. Neese, F. Wennmohs, A. Hansen, U. Becker, *Chem. Phys.* **2009**, *356*, 98–109.
- [S16] R. Izsák, F. Neese, *J. Chem. Phys.* **2011**, *135*, 144105.
- [S17] A. D. Becke, *J. Chem. Phys.* **1993**, *98*, 5648–5652.
- [S18] F. Weigend, R. Ahlrichs, *Phys. Chem. Chem. Phys.* **2005**, *7*, 3297–3305.
- [S19] F. Weigend, *Phys. Chem. Chem. Phys.* **2006**, *8*, 1057–1065.
- [S20] D. A. Pantazis, X.-Y. Chen, C. R. Landis, F. Neese, *J. Chem. Theory Comput.* **2008**, *4*, 908–919.
- [S21] E. van Lenthe, E. J. Baerends, J. G. Snijders, *J. Chem. Phys.* **1993**, *99*, 4597–4610.
- [S22] S. Grimme, J. Antony, S. Ehrlich, H. Krieg, *J. Chem. Phys.* **2010**, *132*, 154104.
- [S23] S. Grimme, S. Ehrlich, L. Goerigk, *J. Comput. Chem.* **2011**, *32*, 1456–1465.
- [S24] V. Barone, M. Cossi, *J. Phys. Chem. A* **1998**, *102*, 1995–2001.
- [S25] S. Otto, M. Grabolle, C. Förster, C. Kreitner, U. Resch-Genger, K. Heinze, *Angew. Chem.* **2015**, *127*, 11735–11739; *Angew. Chem. Int. Ed.* **2015**, *54*, 11572–11576;

- [S26] S. Lenz, H. Bamberger, P. P. Hallmen, Y. Thiebes, S. Otto, K. Heinze, J. van Slageren, *Phys. Chem. Chem. Phys.* **2019**, *21*, 6976–6983.
- [S27] a) U. Casellato, R. Graziani, R. P. Bonomo, A. J. Di Bilio, *J. Chem. Soc. Dalton Trans.* **1991**, 23–31; b) R. P. Bonomo, A. J. DiBilio, *F. Chem. Phys.* **1991**, *151*, 323–333.
- [S28] M. K. Ahmed, B. R. Henry, *J. Chem. Phys.* **1987**, *87*, 3724.
- [S29] C. Wang, S. Otto, M. Dorn, E. Kreidt, J. Lebon, L. Srsan, P. Di Martino-Fumo, M. Gerhards, U. Resch-Genger, M. Seitz, K. Heinze, *Angew. Chem.* **2018**, *130*, 1125–1130; *Angew. Chem. Int. Ed.* **2018**, *57*, 1112–1116.
- [S30] M. K. Ahmed, B. R. Henry, *Can. J. Chem.* **1988**, *66*, 628–632.
- [S31] C. Doffek, N. Alzakhem, C. Bischof, J. Wahsner, T. Güden-Silber, J. Lügger, C. Platas-Iglesias, M. Seitz, *J. Am. Chem. Soc.* **2012**, *134*, 16413–16423.

#### 4.2.1.3 Multiphonon Relaxation im molekularen Rubin $[\text{Cr}(\text{bpmp})_2]^{3+}$ mit intensiver roter Lumineszenz (Publikation 6)

Lumineszente Cr(III)-Komplexe mit intensiver Spin-Flip-Emission emittieren bisher ausschließlich oberhalb des sichtbaren Wellenlängenbereichs an der Grenze zum oder im Nah-IR ( $\gg 700 \text{ nm}$ ). Für manche Anwendungen, wie beispielsweise auch im Bioimaging, ist aber langlebige rote Emission ( $\leq 700 \text{ nm}$ ) vorteilhaft. Diese konnte bereits mit Eu(III)- und Ru(II)-Komplexen erreicht werden.<sup>[104]</sup> Allerdings sind diese Metalle im Vergleich zu Chrom um die Faktoren von ca. 100 und 10000 seltener und dadurch auch wesentlich teurer.<sup>[12]</sup>

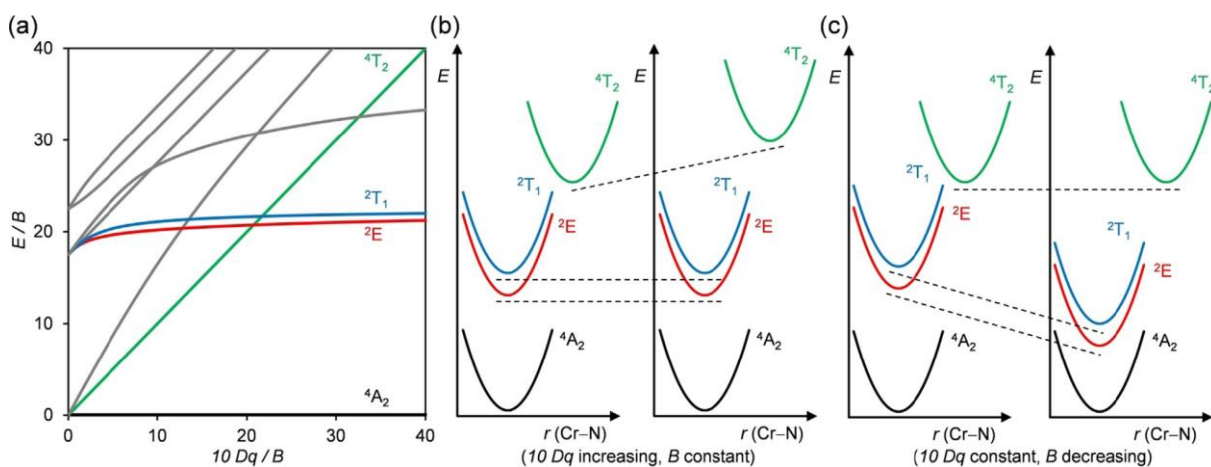


**Abb. 35:** a) Tanabe-Sugano-Diagramm der  $d^3$ -Elektronenkonfiguration im oktaedrischen Feld b) Einfluss der Steigerung des Ligandenfeldparameters ( $10 Dq$ ) auf die Energien der Zustände  $^4T_2$ ,  $^2E$  und  $^2T_1$ . c) Einfluss des Racah-Parameters  $B$  (in diesem Fall mit abnehmenden Werten von  $B$ ) auf die Energien der entsprechenden Zustände. Abbildung übernommen von Wenger.<sup>[105]</sup>

Das Erreichen von intensiver roter Emission ausgehend von angeregten Spin-Flip-Zuständen in molekularen Chrom(III)-Komplexen ist herausfordernd. Man benötigt ein Ligandensystem, dass zum einen die emissiven Spin-Flip-Zustände ( $^2E$  und  $^2T_{1g}$ ) zu höherer Energie verschiebt, aber gleichzeitig eine ausreichend große Energielücke zu den Ligandenfeldzuständen ( $^4T_{2g}$ ) sicherstellt, um strahlungslose Deaktivierung der Dublett-Zustände durch Reverse Intersystem Crossing zu verhindern. Während die Lage der Ligandenfeldzustände durch die Größe der Ligandenfeldaufspaltung gesteuert werden kann, sind die Dublett-Zustände davon nahezu unbeeinflusst (Abb. 35 b). Die energetische Lage der Dublett-Zustände kann aber durch Variieren des Racah-Parameters  $B$  beeinflusst werden, wobei größere Wert von  $B$  die Spin-Flip-

Zustände zu höherer Energie verschieben. Entsprechend würde der in Abb. 35 c) gezeigte umgekehrte Fall, also eine Reduzierung des Racah-Parameters  $B$ , auch zu einer Reduzierung der Energie der Dublett-Zustände führen.

Ausgangspunkt für die Suche nach einem geeigneten Ligandensystem war der tridentate **ddpd**-Ligand, welcher im  $[\text{Cr}(\text{ddpd})_2]^{3+}$ -Komplex intensive und langlebige Spin-Flip-Emission im NIR ermöglicht (Kapitel 3.1.1). Ersetzen der N-Methyl-Einheiten im **ddpd**-Liganden durch  $\text{CH}_2$ -Brücken, führte zum Zielliganden 2,6-bis(2-pyridylmethyl)-pyridin (**bpmp**), der im homoleptischen  $[\text{Cr}(\text{bpmp})_2](\text{CF}_3\text{SO}_3)_3$ -Komplex (Abb. 36) für eine hohe Energie der Dublett- und Ligandenfeldzustände sorgen sollte. Die Wahl von  $[\text{Cr}(\text{bpmp})_2]^{3+}$  war motiviert durch den hohen berechneten Racah-Parameter  $B$  ( $B = 1003 \text{ cm}^{-1}$ ), welcher größer als der von  $[\text{Cr}(\text{ddpd})_2]^{3+}$  ( $B = 760 \text{ cm}^{-1}$ ) ist, bei gleichzeitiger Gewährleistung einer ausreichend großen ( $\Delta_o = 20882 \text{ cm}^{-1}$ ) Ligandenfeldauspaltung (Pub. 6: *Quantum Chemical Screening* und HI, Tab. S1-3).

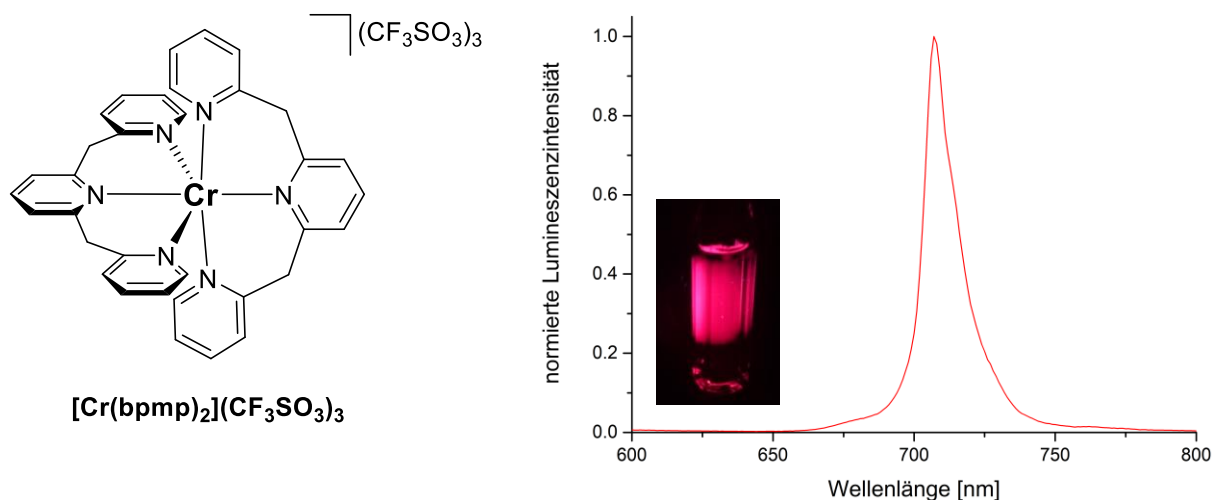


**Abb. 36:** Links: Strukturformel von  $[\text{Cr}(\text{bpmp})_2](\text{CF}_3\text{SO}_3)_3$  Rechts: Normiertes Emissionsspektrum gemessen bei Raumtemperatur ( $\lambda_{\text{exc}} = 462 \text{ nm}$ ;  $0.1 \text{ M DCIO}_4$  in  $\text{D}_2\text{O}$ ) unter einer Argonatmosphäre. Teile der Abbildung übernommen von Heinze.<sup>[106]</sup>

Anregung von  $[\text{Cr}(\text{bpmp})_2]^{3+}$  bei  $\lambda_{\text{exc}} = 462 \text{ nm}$  in den Ligandenfeldzustand ruft eine scharfe Emission mit Maximum bei  $\lambda_{\text{em}} = 709 \text{ nm}$  hervor. Damit reicht die im Vergleich zu  $[\text{Cr}(\text{ddpd})_2]^{3+}$  ( $\lambda_{\text{em}} = 775 \text{ nm}$ ) hypsochrom verschobene Emission in das sichtbare Spektrum hinein und ist als tief rote Lumineszenz beobachtbar (Abb. 36).

Die Lumineszenzquantenausbeute von **[Cr(bpmp)<sub>2</sub>]<sup>3+</sup>** beträgt in entgaster wässriger Lösung  $\Phi = 12.3\%$ . Sowohl in trockenem CH<sub>3</sub>CN als auch in phosphatgepufferten Salzlösungen (0.1 M PBS, pH = 6.5) sinkt die Quantenausbeute auf unter  $\Phi = 2\%$  (Pub. 6: *Excited State Properties and Dynamics*, Tab. 1). Dies liegt sehr wahrscheinlich an der Deprotonierung der recht aciden CH<sub>2</sub>-Brücken des koordinierten **bpmp**-Liganden bereits im Grundzustand unter diesen Bedingungen. Durch Zugabe von HClO<sub>4</sub> wird die Deprotonierung der CH<sub>2</sub>-Gruppen in wässriger Lösung verhindert und die Quantenausbeute steigt auf  $\Phi = 15.8\%$ . Aufgrund der Acidität der Methylenbrücken kommt es zu einem Austausch der CH-aciden Protonen der CH<sub>2</sub>-Brücken mit den Wassermolekülen des Lösungsmittels.

Durch Wechsel der Bedingungen von H<sub>2</sub>O/HClO<sub>4</sub> zu D<sub>2</sub>O/DClO<sub>4</sub> erhöht sich die Quantenausbeute bzw. Lumineszenzlebenszeit von **[Cr(bpmp)<sub>2</sub>]<sup>3+</sup>** von  $\Phi = 15.8\%$  auf  $\Phi = 19.6\%$  bzw. von  $\tau = 1550\ \mu\text{s}$  auf  $\tau = 1800\ \mu\text{s}$  (Pub. 6: *Excited State Properties and Dynamics*, Tab. 1). Diese Anstiege beruhen im Wesentlichen auf zwei unterschiedlichen Beiträgen: Zum einen kommt es in D<sub>2</sub>O/DClO<sub>4</sub>-Lösungen zu einem C-H/C-D-Austausch in den Methylenbrücken (HI, Abb. S26+27). Die aliphatischen C-D-Oszillatoren mit Cr...H-Abständen von 3.1 – 4.3 Å tragen wegen der im Vergleich zu den C-H-Oszillatoren geringeren Oszillatorstärken weniger stark zur strahlungslosen Deaktivierung der angeregten Dublett-Zustände bei. Zum anderen führt das Ersetzen der O-H- durch O-D-Oszillatoren durch Verwendung von D<sub>2</sub>O statt H<sub>2</sub>O zu reduzierter MR durch Lösungsmittelmoleküle der zweiten Koordinationssphäre. Die CH<sub>2</sub>-Gruppen von **bpmp** sind wegen des C-H/C-D-Austauschs in deuterierten Lösungsmitteln für die Obertonanalyse und damit auch für die Berechnung der SOIs mit der Emissionsbande von **[Cr(bpmp)<sub>2</sub>]<sup>3+</sup>** nicht geeignet. Die aromatischen C-H-Oszillatoren des **bpmp**-Liganden dagegen unterliegen nicht dieser Austauschdynamik und sind für die quantitative Analyse der MR geeignet. Wie in Kapitel 4.1.1 beschrieben, kommt es beim **[Cr(ddpd)<sub>2</sub>]<sup>3+</sup>**-Komplex mit der energieärmeren Emission bei  $\lambda_{\text{em}} = 775\ \text{nm}$  zu einem spektralen Überlapp mit dem dritten aromatischen C-H-Oberton ( $\nu_{\text{C-H}}^4 = 11493\ \text{cm}^{-1}$ ). Die Deuterierung von **ddpd** mit einem hohen Deuterierungsgrad der metallnächsten C-H-Oszillatoren in 6/6''-Position der terminalen Pyridine, ermöglichte das Erreichen von Rekordwerten unter den Spin-Flip-Emittern für die Lumineszenzlebensdauer ( $\tau = 2300\ \mu\text{s}$ ) und Quantenausbeute ( $\Phi = 30\%$ ) in CD<sub>3</sub>CN. In der für den **[Cr(ddpd)<sub>2</sub>]<sup>3+</sup>**-Komplex durchgeführten Obertonanalyse<sup>[37]</sup> erwiesen sich die Daten der aromatischen

Schwingungsobertöne von isotopologen 6,6'-Dimethyl-2,2'-bipyridin (**Me<sub>2</sub>bpy** und **[D<sub>12</sub>]-Me<sub>2</sub>bpy**)<sup>[37]</sup> als gut geeignetes Modellsystem für die aromatischen Obertonsignaturen des **ddpd**-Liganden. Grundsätzlich werden für die Analyse der Schwingungsrelaxation in lumineszenten Komplexen häufig die Obertonsignaturen der Liganden herangezogen, weil die isotopologen Komplexe nicht in ausreichend großer Menge vorliegen um die benötigten äußerst intensitätsschwachen Banden höherer Obertöne verlässlich messen zu können. Um nun zu prüfen ob sich die Obertondaten von istopologem **Me<sub>2</sub>bpy** auch zur Beschreibung der Obertöne im **[Cr(bpmp)<sub>2</sub>]<sup>3+</sup>**-Komplex eignen, wurden zunächst die aus den gemessenen Spektren extrahierten Obertonsignaturen des **bpmp**-Liganden mit denen von **Me<sub>2</sub>bpy** verglichen (Abb. 37, HI, Abb. S38+39). Wegen der sehr guten Übereinstimmung in Form und energetischer Lage wurde für die Berechnung der SOIs und MR-Raten  $k_{nr}$  ebenfalls die Obertondaten von (**Me<sub>2</sub>bpy**) und (**[D<sub>12</sub>]-Me<sub>2</sub>bpy**) herangezogen.<sup>[37]</sup>

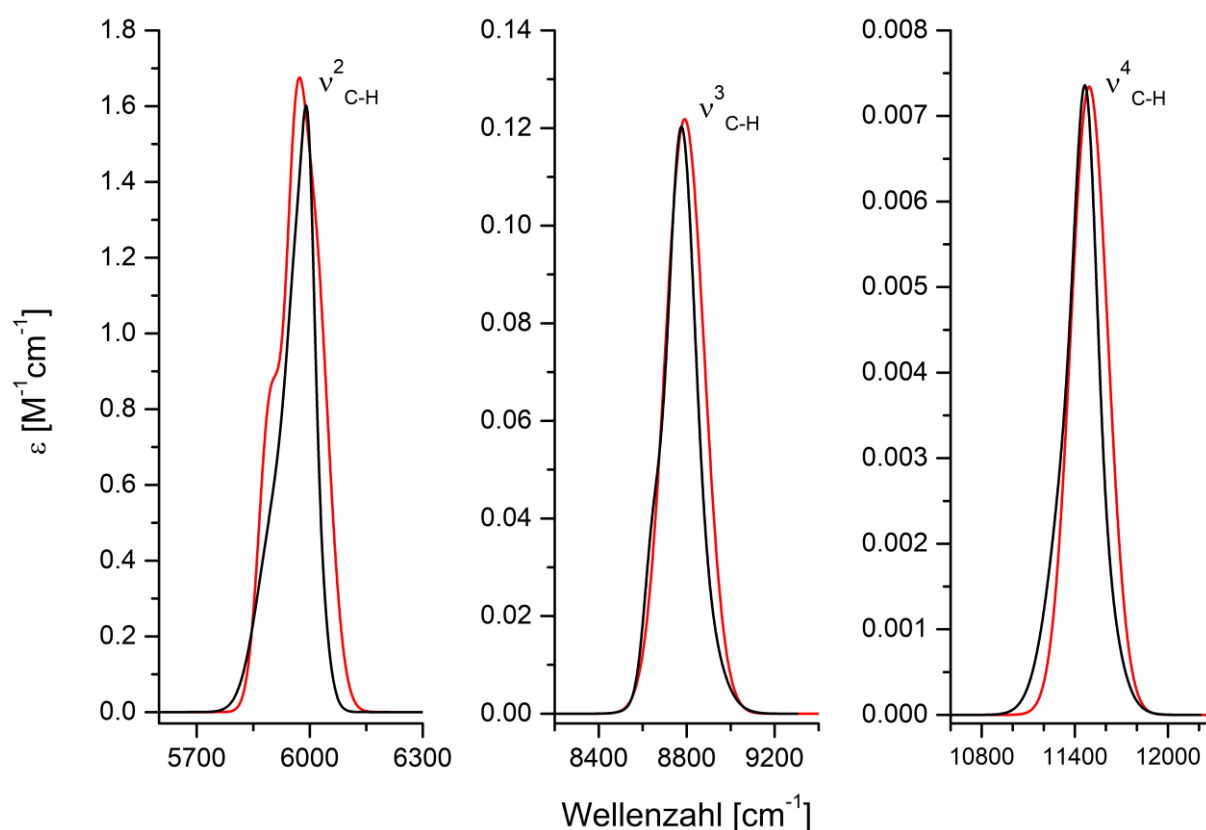


**Abb. 37:** Aus den gemessenen Spektren extrahierte NIR-Absorptionsbanden der aromatischen C-H-Schwingungsobertöne von **Me<sub>2</sub>bpy**<sup>[37]</sup> (schwarz) und **bpmp** (rot) in CDCl<sub>3</sub> in der Region von  $\nu_{C-H}^2$  (links),  $\nu_{C-H}^3$  (Mitte) und  $\nu_{C-H}^4$  (rechts). Wegen der kleineren Zahl an aromatischen C-H-Oszillatoren in **Me<sub>2</sub>bpy** (6) im Vergleich zu **bpmp** (11) wurden die Gaussfunktionen von **Me<sub>2</sub>bpy** um den Faktor 11/6 skaliert.



Durch die zu höherer Energie verschobenen Emission von  $[\text{Cr}(\text{bpmp})_2]^{3+}$  gegenüber der von  $[\text{Cr}(\text{ddpd})_2]^{3+}$  zeigt nun der vierte C-H-Oberton ( $\nu_{\text{C-H}}^5 = 14065 \text{ cm}^{-1}$ ) den größten spektralen Überlapp mit der Dublett-Emission (Abb. 38, oben). Dieser hohe Oberton besitzt einen sehr kleinen Extinktionskoeffizienten, liegt aber energetisch direkt unter der Emissionsbande von  $[\text{Cr}(\text{bpmp})_2]^{3+}$  und trägt deshalb substantiell zur strahlungslosen Deaktivierung der angeregten Spin-Flip-Zustände bei (HI, Abb. S40). Hingegen überlappen die relevanten C-D-Obertöne (Abb. 28, unten,  $\nu_{\text{C-H}}^6 = 12806 \text{ cm}^{-1}$  und  $\nu_{\text{C-H}}^7 = 14755 \text{ cm}^{-1}$ ) nur wenig mit der Chromemission und haben zusätzlich auch noch geringere Extinktionskoeffizienten (s. HI, Abb. S41). Damit ist  $k_{\text{nr}}^{\text{H}}$  signifikant größer als  $k_{\text{nr}}^{\text{D}}$  und bezüglich MR ist von verbesserten photophysikalischen Eigenschaften des deuterierten  $[\text{Cr}(\text{bpmp})_2]^{3+}$ -Komplexes auszugehen.

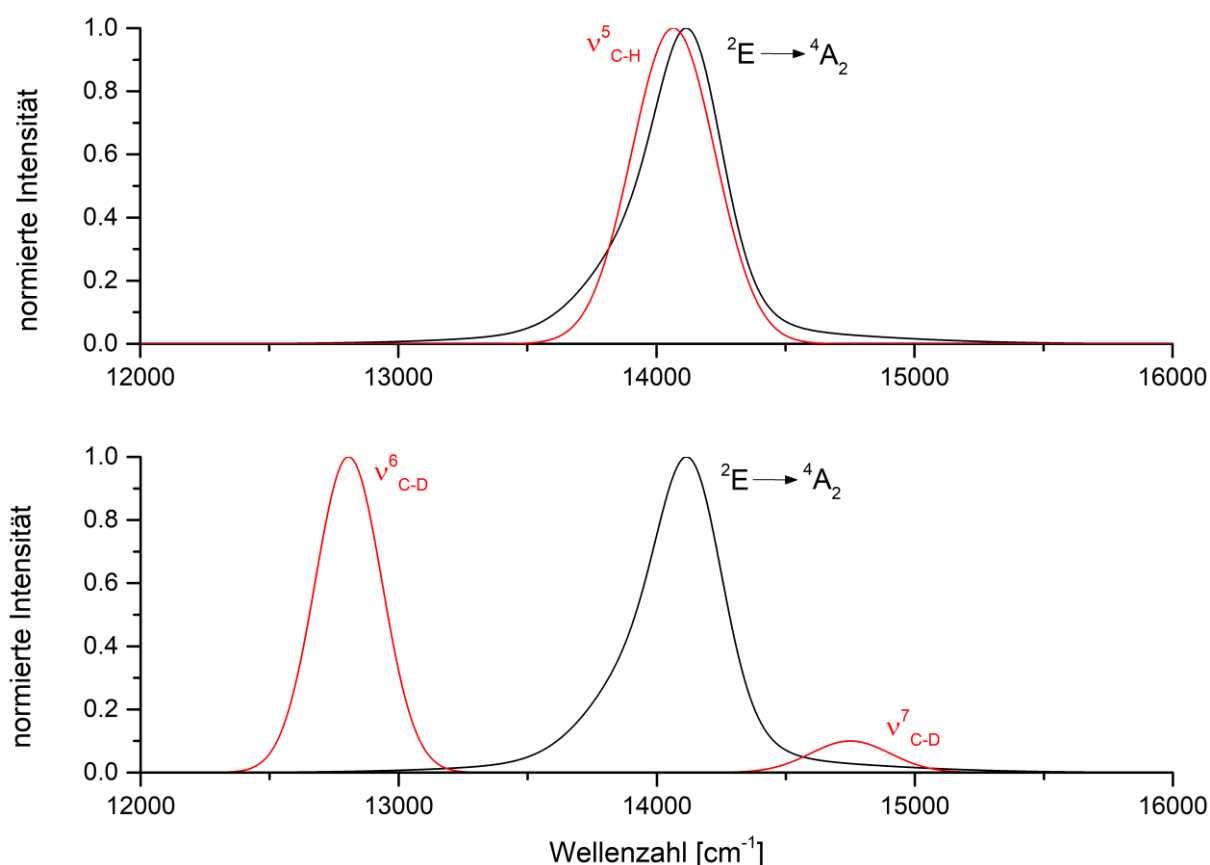


**Abb. 38:** Oben: Normiertes Emissionsspektrum von  $[\text{Cr}(\text{bpmp})_2]^{3+}$  (schwarz) und die aus den gemessenen Spektren extrahierten Absorptionsbanden des vierten C-H-Obertons ( $\nu_{\text{C-H}}^5$ , rot). Unten: Normiertes Emissionsspektrum von  $[\text{Cr}(\text{bpmp})_2]^{3+}$  (schwarz) und die aus den gemessenen Spektren extrahierten Absorptionsbanden des fünften und sechsten C-D-Obertons ( $\nu_{\text{C-H}}^6$  und  $\nu_{\text{C-H}}^7$ , rot). Die Obertonintensitäten sind dabei relativ zu ihren tatsächlichen Intensitäten aufgetragen.

Um experimentell zu überprüfen ob die Quantenausbeuten und Lumineszenzlebenszeiten durch Reduzierung von MR weiter gesteigert werden können, wurde der  $[\text{Cr}(\text{D}_2\text{-bpmp})_2]^{3+}$ -Komplex synthetisiert (Details HI, Abb. S28-37), bei welchem die metallnächsten C-H-Oszillatoren in 6/6"-Position der terminalen Pyridine fast quantitativ deuteriert sind. Durch selektive Deuterierung dieser potentiell am stärksten zur strahlungslosen Deaktivierung beitragenden C-H-Oszillatoren, kann in sauerstofffreien  $\text{DClO}_4/\text{D}_2\text{O}$ -Lösungen die Quantenausbeute von  $\Phi = 19.6\%$  auf  $\Phi = 24.6\%$  und die Lebenszeit von  $\tau = 1800\ \mu\text{s}$  auf  $\tau = 2500\ \mu\text{s}$  gesteigert werden (Tab. 5). In Gegenwart von Luftsauerstoff wird die strahlungslose Deaktivierung der angeregten Zustände dagegen in beiden isotopologen Komplexen von der Löschung durch  $\text{O}_2$ -Moleküle dominiert und MR spielt eine untergeordnete Rolle (Tab. 5).

**Tab. 5:** Lumineszenzlebensdauern  $\tau$  und Quantenausbeuten  $\Phi$  von  $[\text{Cr}(\text{bpmp})_2]^{3+}$  und  $[\text{Cr}([\text{D}_2]\text{-bpmp})_2]^{3+}$  jeweils entgast und unter Argonatmosphäre (Ar) oder nicht entgast unter Luft ( $\text{O}_2$ ) bei Raumtemperatur.

Komplex	$\tau\ [\mu\text{s}]^{\text{a}}$	$\tau\ [\mu\text{s}]^{\text{a}}$	$\Phi\ [\%]^{\text{b}}$	$\Phi\ [\%]^{\text{b}}$
	Ar	$\text{O}_2$	Ar	$\text{O}_2$
$[\text{Cr}(\text{bpmp})_2]^{3+}$	1800	840	19.6	9.8
$[\text{Cr}([\text{D}_2]\text{-bpmp})_2]^{3+}$	2500	990	24.6	9.5

<sup>a</sup> $\lambda_{\text{exc}} = 462\ \text{nm}$ , 0.1 M  $\text{DClO}_4$  in  $\text{D}_2\text{O}$ , unter diesen Bedingungen ist von einem H/D Austausch der Methylenbrücken auszugehen; <sup>b</sup> $\lambda_{\text{exc}} = 462\ \text{nm}$ , 0.1 M  $\text{DClO}_4$  in  $\text{D}_2\text{O}$ .

Das durch theoretische Rechnungen gestützte Ligandendesign ermöglichte die Entwicklung des neuen Spin-Flip-Luminophors  $[\text{Cr}(\text{bpmp})_2]^{3+}$  mit Emission im roten Spektralbereich. Der Komplex zeigt eine intensive Spin-Flip-Emission aus den Dublett-Zuständen mit Quantenausbeuten von bis zu  $\Phi = 20\%$  und Lumineszenzlebenszeiten von bis zu  $\tau = 1800\ \mu\text{s}$  in  $\text{DClO}_4 / \text{D}_2\text{O}$ -Lösungen. Durch selektive Deuterierung der metallnächsten C-H-Obertöne kann die Quantenausbeute auf  $\Phi = 25\%$  und die Lebenszeit auf  $\tau = 2500\ \mu\text{s}$  gesteigert werden.

# Strongly Red-Emissive Molecular Ruby $[\text{Cr}(\text{bpmp})_2]^{3+}$ Surpasses $[\text{Ru}(\text{bpy})_3]^{2+}$

Florian Reichenauer, Cui Wang, Christoph Förster, Pit Boden, Naz Ugur, Ricardo Báez-Cruz, Jens Kalmbach, Luca M. Carrella, Eva Rentschler, Charusheela Ramanan, Gereon Niedner-Schatteburg, Markus Gerhards, Michael Seitz,\* Ute Resch-Genger,\* and Katja Heinze\*



Cite This: *J. Am. Chem. Soc.* 2021, 143, 11843–11855



Read Online

ACCESS |



Metrics & More

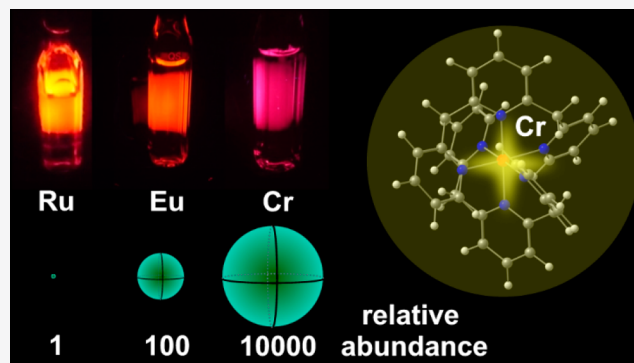


Article Recommendations



Supporting Information

**ABSTRACT:** Gaining chemical control over the thermodynamics and kinetics of photoexcited states is paramount to an efficient and sustainable utilization of photoactive transition metal complexes in a plethora of technologies. In contrast to energies of charge transfer states described by spatially separated orbitals, the energies of spin-flip states cannot straightforwardly be predicted as Pauli repulsion and the nephelauxetic effect play key roles. Guided by multi-reference quantum chemical calculations, we report a novel highly luminescent spin-flip emitter with a quantum chemically predicted blue-shifted luminescence. The spin-flip emission band of the chromium complex  $[\text{Cr}(\text{bpmp})_2]^{3+}$  (bpmp = 2,6-bis(2-pyridylmethyl)pyridine) shifted to higher energy from ca. 780 nm observed for known highly emissive chromium(III) complexes to 709 nm. The photoluminescence quantum yields climb to 20%, and very long excited state lifetimes in the millisecond range are achieved at room temperature in acidic  $\text{D}_2\text{O}$  solution. Partial ligand deuteration increases the quantum yield to 25%. The high excited state energy of  $[\text{Cr}(\text{bpmp})_2]^{3+}$  and its facile reduction to  $[\text{Cr}(\text{bpmp})_2]^{2+}$  result in a high excited state redox potential. The ligand's methylene bridge acts as a Brønsted acid quenching the luminescence at high pH. Combined with a pH-insensitive chromium(III) emitter, ratiometric optical pH sensing is achieved with single wavelength excitation. The photophysical and ground state properties (quantum yield, lifetime, redox potential, and acid/base) of this spin-flip complex incorporating an earth-abundant metal surpass those of the classical precious metal  $[\text{Ru}(\alpha\text{-diimine})_3]^{2+}$  charge transfer complexes, which are commonly employed in optical sensing and photo(redox) catalysis, underlining the bright future of these molecular ruby analogues.



## INTRODUCTION

In optical sensing, imaging, and photo(redox) chemistry, complexes with  $d^6$  (e.g.,  $\text{Ru}^{\text{II}}$ ,  $\text{Ir}^{\text{III}}$ ,  $\text{Os}^{\text{II}}$ , or  $\text{Re}^{\text{I}}$  and recently  $\text{Mo}^0$ ),  $d^8$  ( $\text{Pt}^{\text{II}}$ ,  $\text{Au}^{\text{III}}$ ),  $d^9$  ( $\text{Cu}^{\text{I}}$ )<sup>15–22</sup> electron configuration and electron deficient ligands are typically employed. Complexes of these metal ions with suitable electron accepting ligands such as 2,2'-bipyridine (bpy) or 2,2':6',2''-terpyridine (tpy) can possess favorable long-lived, luminescent, and/or redox active triplet metal-to-ligand charge transfer ( $^3\text{MLCT}$ ) states. Such complexes are hence ubiquitous in photosensitized reactions, OLEDs, bioimaging probes, optical sensors, photodrugs, and dye-sensitized solar cells.<sup>1–10</sup> In the past few years, the substitution of precious metals by earth-abundant base metals has become a vivid and important research area aiming at sustainable photochemistry and photophysical applications.<sup>23–40</sup> Luminescent ligand-to-metal (LMCT) states of earth-abundant  $\text{Fe}^{\text{III}}$  and  $\text{Co}^{\text{III}}$  complexes have emerged very recently as alternative useful excited states of 3d transition metal complexes.<sup>38–40</sup> The highest quantum yields achieved so far with charge transfer (CT) emitters of LMCT or LMCT

character based on earth-abundant 3d metals (except from the special case of copper(I)) are 0.001% ( $\text{Cr}^0$ ),<sup>33</sup> 0.7% ( $\text{Co}^{\text{III}}$ ),<sup>40</sup> and 2.1% ( $\text{Fe}^{\text{III}}$ ).<sup>38</sup>

Fundamentally different from charge transfer states, which involve spatially separated metal and ligand frontier orbitals,<sup>41</sup> are metal-centered spin-flip states.<sup>26,42–48</sup> Such localized spin-flip states can be phosphorescent, in particular in the near-infrared spectral region.<sup>26,44,49</sup> These excited states could be useful for optical applications (sensing, imaging, and lasing) as well as excited state electron and energy transfer reactions. However, most transition metal complexes with a  $d^2$  or  $d^3$  electron configuration suitable for a spin-flip luminescence<sup>50</sup> are only weakly emissive ( $\Phi \ll 0.15\%$ ).<sup>44,49</sup> With the development

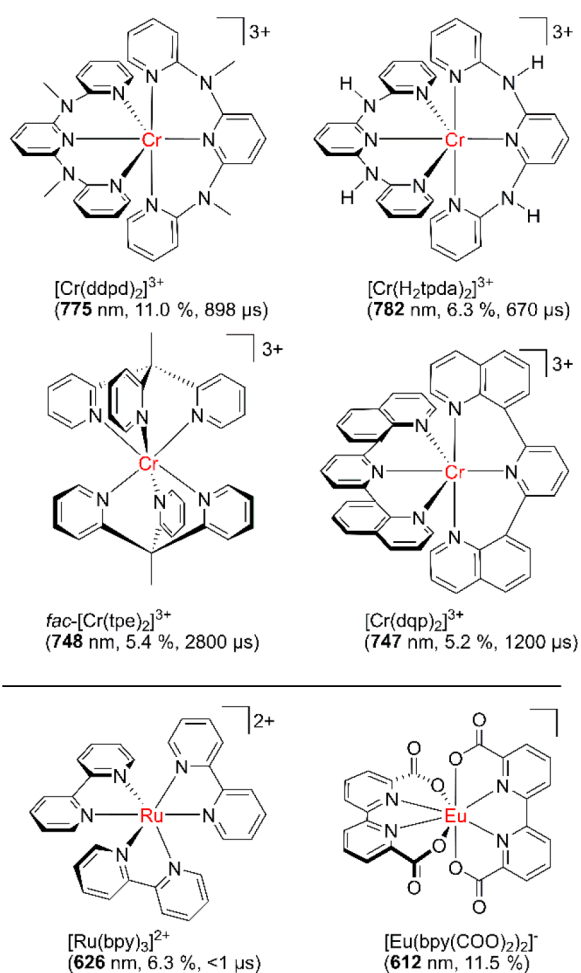
Received: June 9, 2021

Published: July 23, 2021



of the so-called molecular ruby  $[\text{Cr}(\text{ddpd})_2]^{3+}$  ( $\text{ddpd} = N,N'$ -dimethyl- $N,N'$ -dipyridine-2-ylpyridine-2,6-diamine<sup>51,52</sup>), we achieved record photoluminescence quantum yields of  $\Phi = 11\%$  ( $\Phi = 30\%$  with a partially deuterated  $\text{ddpd}$  ligand) of the NIR luminescence ( $\lambda_{\text{em}} = 775 \text{ nm}$ ).<sup>53,54</sup> Several applications in the fields of sensing, photocatalysis, upconversion, and circularly polarized luminescence already emerged in the past few years.<sup>55–64</sup> Variations of the ligand and the complex symmetry increased the lifetime of the luminescent excited spin-flip state up to the current record value of  $4500 \mu\text{s}$ .<sup>65</sup> However, all these highly emissive chromium(III) complexes based on the molecular ruby motif emit in the near-infrared spectral region ( $\gg 700 \text{ nm}$ ;  $\ll 1.77 \text{ eV}$ ) up to now (Scheme 1).<sup>53–65</sup>

**Scheme 1. NIR-Emissive Chromium(III) Complexes and Classical Red-Emissive Complexes Based on Ruthenium(II) and Europium(III)**



Red, long-lived emission (i.e.,  $\approx 700 \text{ nm}$ ) has been achieved by using europium(III)<sup>66,67</sup> and ruthenium(II) complexes (Scheme 1). Consequently, complexes of these metals are heavily exploited for example in biosensing.<sup>68–70,48</sup> However, these metals are dramatically less abundant than chromium by factors of ca. 100 and 10000. This scarcity is also reflected by the prices of ca. 30, 7300, and 16250  $\text{€ mol}^{-1}$  for  $\text{CrCl}_3$ ,  $\text{EuCl}_3$ , and  $\text{RuCl}_3$ , respectively (based on the hydrated chlorides; commercial supplier, May 2021). Bright red emission from spin-flip excited states has only been realized in solid  $\text{Cr}^{\text{III}}$  materials such as ruby  $\text{Al}_2\text{O}_3:\text{Cr}^{3+}$  itself (695 nm)<sup>71–74</sup> and in

$\text{Mn}^{\text{IV}}$ -doped solids, e.g.,  $\text{K}_2\text{SiF}_6:\text{Mn}^{4+}$  (630 nm),<sup>75</sup> but remained elusive for molecular chromium(III) complexes. Either the spin-flip states of previously reported molecular  $\text{Cr}^{\text{III}}$  complexes are at a too low energy as in the molecular rubies (Scheme 1),<sup>53,57,64,65</sup> or the quantum yields are extremely poor (0.024%–0.000005%).<sup>49</sup>

Unlike the straightforward and well-founded correlations elucidated for charge transfer complexes with MLCT, LMCT, or LL'CT excited states and organic emitters with donor–acceptor character, shifting of the excited doublet state levels of such spin-flip emitters and hence the emission color by chemical measures, such as donor atom variation or substitution patterns of the ligands, is extremely difficult to predict. A clear-cut correlation with ligand types for chromium(III) spin-flip emitters<sup>49</sup> remains elusive beyond the classical ligand field parameters of the covalently reduced d–d interelectronic repulsion ( $B$  and  $C$  ligand field parameters), that is, the nephelauxetic series of simple classical ligands such as halides.<sup>76–78</sup> The accurate description<sup>79–82</sup> of the relevant excited quartet and doublet states<sup>83–86,58</sup> is challenging due to the required consideration of interelectronic repulsion.<sup>81</sup> The localized spin-flip character instead of the charge transfer nature of the classical CT luminophores with separately addressable spatially distinct wave functions has furthermore precluded reliable predictions for spin-flip levels so far. However, recent method developments in quantum chemistry and coding suitable for open-shell complexes of realistic size in general and chromium(III) in particular conceptually tackled this challenge.<sup>79–87</sup>

In this study, we address the challenge to increase the energy of the spin-flip state in molecular chromium(III) complexes, while concomitantly maintaining a high quantum yield by providing a large enough energy gap between the detrimental metal centered quartet states and the emissive spin-flip level(s) using high-level quantum chemical calculations and the translation to synthesis, spectroscopy, and first applications of the resulting complex.

## RESULTS AND DISCUSSION

**Quantum Chemical Screening.** To identify a ligand modification, which shifts the energy of the emissive spin-flip state(s) ( ${}^2\text{E}$  and  ${}^2\text{T}_1$ ) of chromium(III) complexes to higher energy while maintaining a large enough quartet state energy ( ${}^4\text{T}_2$ ), we screened six-coordinate chromium(III) complexes with several monodentate and chelate ligands ( $\text{NH}_3$ ,  $\text{CN}^-$ ,  $\text{acac}^-$ ) and in particular pyridine-based ligands (py, bpy, tpy, ddpd) by high-level quantum chemical methods. As density functional theory (DFT) methods failed to give the correct ordering of doublet ( ${}^2\text{E}$ ,  ${}^2\text{T}_1$ ) and quartet excited states ( ${}^4\text{T}_2$ ),<sup>81</sup> an ab initio multireference method was selected.<sup>83–86</sup> Complete active space self-consistent field (CASSCF) calculations combined with  $N$ -electron valence state perturbation theory (NEVPT2) to account for dynamic electron correlation based on a fully internally contracted (FIC) wave function have been successfully used for open-shell metal complexes.<sup>83–86,58,44</sup> This method was employed in the following for the complexes selected.

First, DFT calculations on the CPCM(acetonitrile)-UB3LYP-D3BJ-ZORA/def2-TZVPP level deliver the optimized geometries of the chromium(III) complexes in their respective  ${}^4\text{A}_2$  ground states. Subsequently, CASSCF-FIC-NEVPT2 calculations with an active space comprising the five 3d orbitals and the three d electrons CAS(3,5) estimate the required excited state energies (Table S1, Supporting Information). These calcu-



lations were followed by an ab initio ligand field theory (AILFT) analysis to yield the Racah parameters  $B$  and  $C$  and the ligand field splitting  $\Delta_0$  (Table S2).<sup>83,84</sup>

This initial screening of DFT-optimized chromium(III) complexes coordinated by monodentate and chelate ligands  $\text{Cr}(\text{acac})_3$ ,  $[\text{Cr}(\text{NH}_3)_6]^{3+}$ ,  $[\text{Cr}(\text{py})_6]^{3+}$ ,  $[\text{Cr}(\text{tpy})_2]^{3+}$ ,  $[\text{Cr}(\text{bpy})_3]^{3+}$ ,  $[\text{Cr}(\text{ddpd})_2]^{3+}$ , and  $[\text{Cr}(\text{CN})_6]^{3-}$  yielded ligand field splittings  $\Delta_0$  ( ${}^4\text{T}_2$  energies) increasing in the order of  $\text{acac}^- < \text{py} < \text{tpy} < \text{ddpd} < \text{NH}_3 < \text{bpy} < \text{CN}^-$  (Table S1). The experimental spectrochemical series  $\text{acac}^- < \text{tpy} < \text{ddpd} < \text{bpy} < \text{CN}^-$ , that is, the experimentally observed ligand field transitions  ${}^4\text{A}_2 \rightarrow {}^4\text{T}_2$ , confirms this approach. As the ligand field splitting  $\Delta_0$  of all these complexes is large enough to enable luminescence from doublet states, the decisive parameter is the Racah parameter  $B$ , which determines the energy of the doublet states. The calculated  $B$  values increase in the order  $\text{CN}^-$  (888  $\text{cm}^{-1}$ )  $< \text{tpy} < \text{ddpd} < \text{py} < \text{acac}^- \approx \text{bpy} < \text{NH}_3$  (988  $\text{cm}^{-1}$ ) (Table S2). Clearly, this nephelauxetic series is difficult to explain or even to predict based on simple guidelines. As the tridentate ddpd ligand performed well in previous luminescence studies of its chromium(III) complex due to its large enough  $\Delta_0$  and relative rigidity,<sup>26,53,54</sup> we attempted simple modifications of ddpd maintaining the tridentate ligation and the six-membered chelate rings.

Replacing the NMe groups of the ddpd ligand by  $\text{CH}_2$  bridges provided a hit structure based on the two conditions of high energy doublet and high energy excited quartet levels. The chromium(III) complex  $[\text{Cr}(\text{bpmp})_2]^{3+}$  with the ligand 2,6-bis(2-pyridylmethyl)pyridine (bpmp) shows the highest calculated  $B = 1003 \text{ cm}^{-1}$  in the series, while maintaining a large enough  $\Delta_0 = 20882 \text{ cm}^{-1}$  (Tables S1 and S2).

For  $[\text{Cr}(\text{bpmp})_2]^{3+}$  and its parent complex  $[\text{Cr}(\text{ddpd})_2]^{3+}$  the active space was then expanded to CAS(7,12) with the two filled Cr–N  $\sigma$ -bonding orbitals and a second d shell.<sup>86,87</sup> This methodology had proven to be sufficiently accurate to predict the relative energies of excited quartet and doublet states and even the energy gap between the two lowest doublet states for  $[\text{Cr}(\text{ddpd})_2]^{3+}$ .<sup>58</sup>

The refined calculation of the doublet and quartet excited states of  $[\text{Cr}(\text{bpmp})_2]^{3+}$  using CASSCF(7,12)-FIC-NEVPT2 confirmed the relative doublet and quartet energies (Figure 1; Tables S1 and S3). Interestingly, one doublet microstate of  ${}^2\text{T}_1$  parentage drops below the lowest energy doublet microstate of  ${}^2\text{E}$  parentage in the CASSCF(7,12)-FIC-NEVPT2 calculation, similar to the doublet state ordering of the parent complex  $[\text{Cr}(\text{ddpd})_2]^{3+}$  (Figure 1 and Table S3).<sup>58</sup> The energy gap between the lowest doublet state and the lowest excited quartet level (from the  ${}^4\text{T}_2$  set) in  $[\text{Cr}(\text{bpmp})_2]^{3+}$  amounts to 6010  $\text{cm}^{-1}$  ( $>70 \text{ kJ mol}^{-1}$ ) on this level of theory. After excitation, intersystem crossing (ISC), and vibrational cooling (VC), this large gap prohibits back-intersystem crossing (back-ISC) at room temperature. Consequently, the detrimental nonradiative relaxation via the  ${}^4\text{T}_2$  state is eliminated. Importantly, the calculated energy of the lowest emissive doublet level of  $[\text{Cr}(\text{bpmp})_2]^{3+}$  exceeds that calculated for  $[\text{Cr}(\text{ddpd})_2]^{3+}$  by 766  $\text{cm}^{-1}$  at the same level of theory as desired (Figure 1 and Table S3).

**Synthesis, Structure, and Ground State Reactivity of  $[\text{Cr}(\text{bpmp})_2]^{3+}$ .** Encouraged by the quantum chemical predictions and the facile synthesis of the proposed suitable ligand bpmp,<sup>88</sup> the corresponding chromium(III) complex  $[\text{Cr}(\text{bpmp})_2]^{3+}$  was prepared. However, unlike the straightforward synthesis of  $[\text{Cr}(\text{ddpd})_2]^{3+}$ ,<sup>53</sup> simple mixing of bpmp and

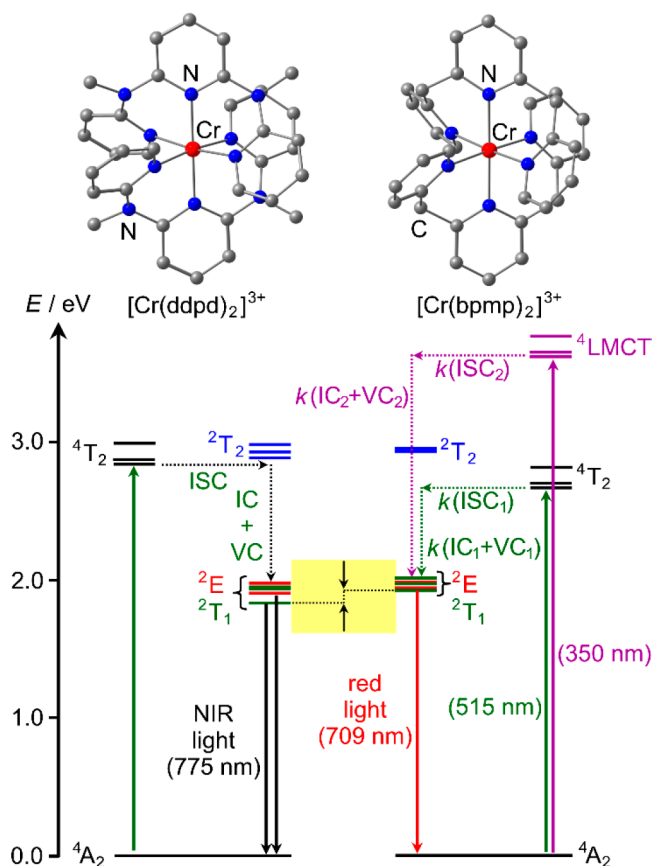


**Figure 1.** DFT-optimized geometries and Jablonski diagrams derived from CASSCF(7,12)-FIC-NEVPT2 calculations of  $[\text{Cr}(\text{ddpd})_2]^{3+}$  (left)<sup>58</sup> and  $[\text{Cr}(\text{bpmp})_2]^{3+}$  (right). The energy difference between the two lowest doublet levels of the complexes is indicated by arrows and highlighted in yellow. ISC = intersystem crossing, IC = internal conversion, and VC = vibrational cooling. Decay cascades starting from  ${}^4\text{LMCT}$  and  ${}^4\text{T}_2$  states are indicated with dotted purple and green arrows, respectively. The experimentally employed excitation and observed emission wavelengths are given in parentheses.

$\text{CrCl}_2$  resulted in redox reactions instead of the desired complexation. Consequently, a stepwise route starting from chromium(III) chloride<sup>89,90</sup> instead of chromium(II) chloride was applied (Figure 2a).

Refluxing the inexpensive starting material  $\text{CrCl}_3 \cdot 6\text{H}_2\text{O}$  with 1 equiv of the ligand bpmp in isopropanol gives the green chlorido complex  $\text{Cr}(\text{bpmp})\text{Cl}_3$  in nearly quantitative yield (Figure 2a). The heteroleptic complex  $\text{Cr}(\text{bpmp})\text{Cl}_3$  was characterized by IR spectroscopy, mass spectrometry, and elemental analysis (Figures S1 and S2). Quantitative substitution of the three coordinated chlorido ligands of  $\text{Cr}(\text{bpmp})\text{Cl}_3$  by more labile triflates with triflic acid yields the red-brown complex  $\text{Cr}(\text{bpmp})(\text{OTf})_3$  under release of gaseous HCl (Figure 2a). An analogous procedure starts from  $\text{CrBr}_3 \cdot 6\text{H}_2\text{O}$  but gives no further advantage (Figures S3 and S4). The constitution of  $\text{Cr}(\text{bpmp})(\text{OTf})_3$  is confirmed by IR spectroscopy, mass spectrometry, and single crystal X-ray diffraction (Figure 2b, Figures S5 and S6).

XRD analysis of a single crystal of  $\text{Cr}(\text{bpmp})(\text{OTf})_3 \cdot 1/4\text{CH}_3\text{CN}$  confirms the meridional configuration of the cation (Figure 2b). Interestingly, the triflate ligands form intra- and intermolecular  $\text{CH} \cdots \text{O}$  hydrogen bonds to the methylene bridges of the bpmp ligand, indicating a significant

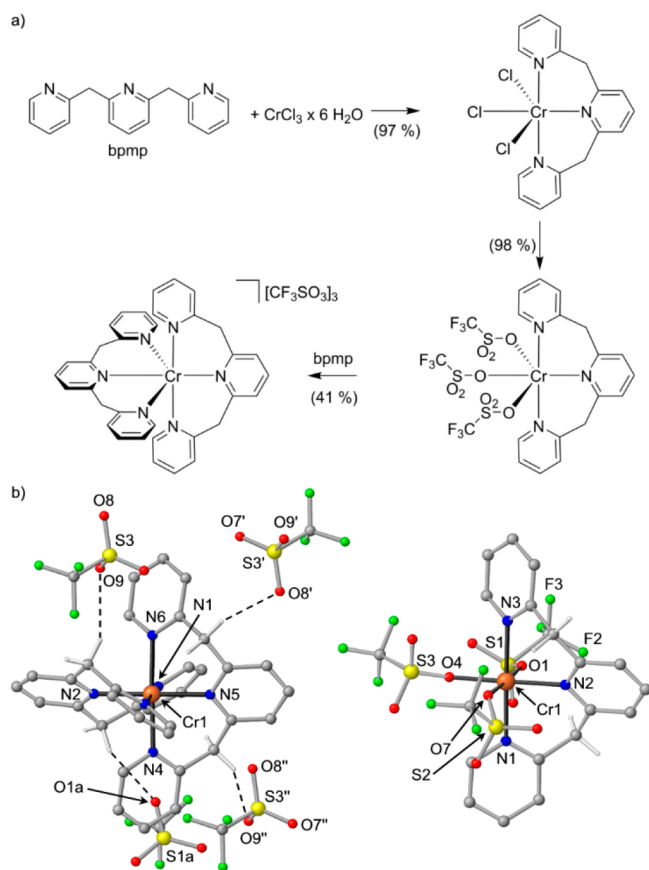


**Figure 2.** (a) Synthesis of  $[\text{Cr}(\text{bpmp})_2][\text{OTf}]_3$  via  $\text{Cr}(\text{bpmp})\text{Cl}_2$  and  $\text{Cr}(\text{bpmp})(\text{OTf})_3$  and (b) molecular structures of the complexes in the solid state. Hydrogen bonding of triflate ions to the  $\text{CH}_2$  groups is illustrated in  $[\text{Cr}(\text{bpmp})_2][\text{OTf}]_3$  by dashed lines. Hydrogen atoms (except for the  $\text{CH}_2$  groups) are omitted.

CH acidity of the coordinated ligand ( $d(\text{C}\cdots\text{O}_{\text{intra}}) = 3.00\text{--}3.36$  Å;  $d(\text{C}\cdots\text{O}_{\text{inter}}) = 3.52\text{--}3.56$  Å). Ligand exchange by a further equivalent of bpmp furnishes the cationic paramagnetic orange complex as triflate salt  $[\text{Cr}(\text{bpmp})_2][\text{OTf}]_3$  (Figure 2a) substantiated by IR spectroscopy, mass spectrometry, elemental analysis, and SQUID magnetometry (Figures S7–S9). Its constitution and meridional configuration was confirmed by single crystal X-ray diffraction of  $[\text{Cr}(\text{bpmp})_2][\text{OTf}]_3 \cdot \text{CH}_3\text{CH}_2\text{OH}$  (Figure 2b and Table S6).

The experimental structure of the cation fits to the geometry calculated by DFT (Figures 1 and 2b, Table S6). Notably, the  $[\text{CrN}_6]$  core is highly octahedral with balanced Cr–N distances and N–Cr–N angles close to  $90^\circ$ . This ensures a large Cr/N orbital overlap and consequently a large ligand field splitting and high energy excited quartet levels.

In the solid state, the methylene bridges of the bpmp ligands form  $\text{CH}\cdots\text{O}$  hydrogen bonds with the triflate counterions ( $d(\text{C}\cdots\text{O}) = 3.12\text{--}3.49$  Å; Figure 2b) similar to  $\text{Cr}(\text{bpmp})(\text{OTf})_3$ . Exchange of the triflates could be achieved with  $[\text{Bu}_4\text{N}][\text{BF}_4]$ ,  $[\text{Bu}_4\text{N}][\text{PF}_6]$ , or  $[\text{Bu}_4\text{N}][\text{ClO}_4]$  as shown by IR spectroscopy, mass spectrometry, elemental analysis, and single crystal XRD analysis of the tetrafluoroborate salt (Figures S10–S14). Hydrogen bonds of the ligand's  $\text{CH}_2$  bridges to  $\text{BF}_4^-$  counterions are present with  $\text{C}\cdots\text{F}$  distances between 2.90 and 3.70 Å in the solid state (Figure S14).

At pH above 7–8,  $[\text{Cr}(\text{bpmp})_2]^{3+}$  converts to a dark yellow to brown complex in solution (Video S1). Even a solid sample

reacts with gaseous ammonia to the brown complex and back to starting material with gaseous HCl (Video S2). UV/vis spectroscopy in  $\text{H}_2\text{O}$  reveals intense broad bands at ca. 350, 455, 540, 615, and 730 nm tailing up to 950 nm (Figure S15). This reactivity is associated with the acidity of the bridging  $\text{CH}_2$  units in the cationic complex, which is already reflected in the hydrogen bonding of the triflates to the  $\text{CH}_2$  groups in the solid state (Figure 2b). Comparing the experimental UV/vis spectrum with the time-dependent (TD)-DFT calculated transitions for the corresponding base  $[\text{Cr}(\text{bpmp})(\text{bpmp-H})]^{2+}$  supports this acid/base chemistry (Figure S15 and Table S7). Photometric titration yields a  $\text{pK}_a$  value of 8.6 (Figure S16).  $[\text{Cr}(\text{bpmp})_2]^{3+}$  is similarly acidic as the NH analogue  $[\text{Cr}(\text{H}_2\text{tpda})_2]^{3+}$  with NH bridging units ( $\text{pK}_a$  8.8; Scheme 1).<sup>57</sup> The methylene bridge can be reversibly de- and reprotonated by NaOH and  $\text{HCl}_{\text{aq}}$  or HOTf, respectively, several times as demonstrated optically and photometrically (Figure S17). However, above ca. pH 10 further processes set in which are partially irreversible, as suggested by the optical spectra (Figure S17). ESI mass spectra of  $[\text{Cr}(\text{bpmp})_2][\text{OTf}]_3$  display peaks at mass-to-charge ratios of 191.4 (7%), 286.6 (13%), and 572.2 (100%), corresponding to  $\{[\text{Cr}(\text{bpmp})_2]^{3+}\}$ ,  $\{[\text{Cr}(\text{bpmp})_2\text{-H}]^{2+}\}$ , and  $\{[\text{Cr}(\text{bpmp})_2\text{-2H}]^{+}\}$ , respectively (Figure S7). The  $\text{BF}_4^-$  and  $\text{PF}_6^-$  salts exhibits similar mass spectroscopic patterns (Figures S10 and S12). This further underscores the high acidity of  $[\text{Cr}(\text{bpmp})_2]^{3+}$ . To ensure full protonation of the bridge and prohibit any decomposition, pertinent optical measurements were performed in the presence of aqueous perchloric acid.

A reversible  $[\text{Cr}(\text{bpmp})_2]^{3+/2+}$  reduction wave appears at  $-0.81$  V vs ferrocene in the cyclic voltammogram followed by the waves for the  $[\text{Cr}(\text{bpmp})_2]^{2+/+}$ ,  $[\text{Cr}(\text{bpmp})_2]^{+/0}$ , and  $[\text{Cr}(\text{bpmp})_2]^{0/1-}$  couples at  $-1.80$ ,  $-2.13$ , and  $-2.31$  V, respectively (Figures S18 and S19). The  $[\text{Cr}(\text{bpmp})_2]^{3+/2+}$  wave is shifted anodically by 0.3 V compared to that of the  $[\text{Cr}(\text{ddpd})_2]^{3+/2+}$  couple.<sup>53</sup> The more electron-deficient nature of the bpmp ligand as compared to ddpd accounts for this redox potential shift. Indeed, DFT calculations of  $[\text{Cr}(\text{bpmp})_2]^{2+}$  suggest an electronic structure of a low-spin chromium(II) ion admixed with a chromium(III) ion antiferromagnetically coupled to a ligand-centered radical (Figure S20). With this assignment, the electronic structure of  $[\text{Cr}(\text{bpmp})_2]^{2+}$  is between a genuine chromium(II) ion as found for  $[\text{Cr}(\text{ddpd})_2]^{2+}$ <sup>53,93</sup> and a ligand-centered radical found for  $[\text{Cr}(\text{bpy})_3]^{2+}/[\text{Cr}(\text{tpy})_2]^{2+}$ <sup>91,92</sup> and  $[\text{Cr}(\text{tpe})_2]^{2+}$ <sup>65</sup> complexes (Figure 1, tpe = 1,1,1-tris(pyrid-2-yl)ethane).

**Excited State Properties and Dynamics.** The absorption spectrum of  $[\text{Cr}(\text{bpmp})_2]^{3+}$  in solution ( $\text{H}_2\text{O}$  or  $\text{CH}_3\text{CN}$ ) can be divided into three spectral regions (Figure 3a). According to TD-DFT calculations (Figure S21), bands at 239 and 270 nm are assigned to  $\pi\text{--}\pi^*$  transitions of the ligand, the band at 340 nm to  $^4\text{LMCT}$  transitions, and the weak band at 465 nm ( $\epsilon = 60$   $\text{M}^{-1}\text{cm}^{-1}$ , Figure 3a) to Laporte-forbidden  $^4\text{A}_2 \rightarrow ^4\text{T}_2$  transitions.

The latter absorption band reflects the ligand field splitting ( $\Delta_{0,\text{exp}} \approx 21500$   $\text{cm}^{-1}$ ). This splitting is somewhat smaller than that of  $[\text{Cr}(\text{ddpd})_2]^{3+}$  with  $\Delta_{0,\text{exp}} \approx 22990$   $\text{cm}^{-1}$ .<sup>53</sup> The CASSCF-NEVPT2 calculations confirm this smaller ligand field splitting (Figure 1). The splitting is still sufficiently large to prevent nonradiative decay via back-ISC. Yet, this lower energy for excitation might be beneficial for future applications. Excitation with 462 nm light gives rise to a very sharp emission band (FWHM 280  $\text{cm}^{-1}$ ) peaking at 709 nm (Figure 3a). This is at the lower energy side of the visible spectral region giving a

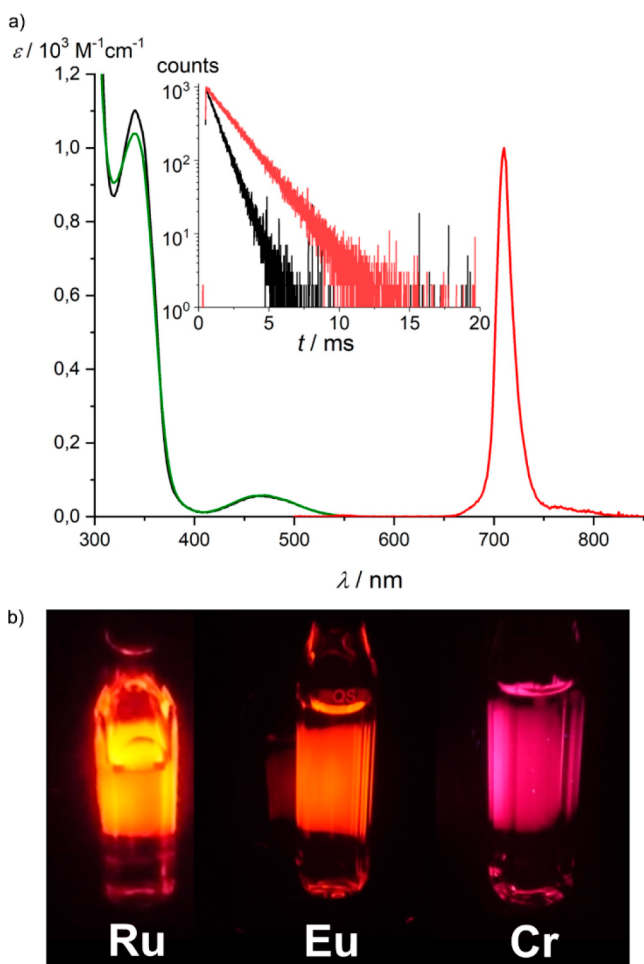


**Figure 3.** (a) UV/vis absorption spectrum (black), excitation spectrum ( $\lambda_{\text{obs}} = 709$  nm, green), and emission spectrum ( $\lambda_{\text{exc}} = 462$  nm, red) of  $[\text{Cr}(\text{bpmp})_2][\text{OTf}]_3$  in deaerated  $\text{H}_2\text{O}$  (0.1 M  $\text{HClO}_4$ ) at room temperature; the inset shows the emission decay curves of  $[\text{Cr}(\text{bpmp})_2][\text{OTf}]_3$  in  $\text{D}_2\text{O}$  (0.1 M  $\text{DClO}_4$ ) deaerated (red) and saturated with  $\text{O}_2$  (black). (b) Photographs of the red/orange emitters  $[\text{Ru}(\text{bpy})_3]^{2+}$ ,  $[\text{Eu}(\text{H}_2\text{O})(\text{OTf})_2(\text{tpy})_2]^+$ , and the deep red emitter  $[\text{Cr}(\text{bpmp})_2]^{3+}$  in  $\text{H}_2\text{O}$  under irradiation with  $\lambda_{\text{exc}} = 340$  nm.

deep red emission with CIE coordinates of  $x = 0.7326$  and  $y = 0.2674$  at the utmost corner of the CIE 1931 diagram (Figure 3b and Figure S22).<sup>94</sup>

The excitation spectrum ( $\lambda_{\text{obs}} = 709$  nm) closely follows the absorption spectrum in the region of 300–600 nm. This confirms that the emission arises from the  $[\text{Cr}(\text{bpmp})_2]^{3+}$  chromophore. Furthermore, higher energy  $^4\text{LMCT}$  states around 350 nm efficiently evolve to the luminescent state as well bypassing further loss channels (Figure 3a).

Gratifyingly, this emission band is higher in energy than that of  $[\text{Cr}(\text{ddpd})_2]^{3+}$  by  $1200\text{ cm}^{-1}$ , in agreement with the predicted trend of the CASSCF-NEVPT2 calculations (Figure 1). The experimentally determined excited state energies (lowest excited quartet and doublet states) reflect the quantum chemically predicted trends and confirm the validity of our screening strategy. The most important aspect is the red emission of  $[\text{Cr}(\text{bpmp})_2]^{3+}$  which is readily detected with conventional detectors. Although only a fraction of the sharp emission band tails into the visible red region (Figure 3a), the red emission under illumination in solution can even be observed by the naked eye (Figure 3b).

Upon cooling, the emission band sharpens further with a FWHM =  $230\text{ cm}^{-1}$  at 130 K in frozen butyronitrile solution. Fine structure appears at the lower energy side of the emission band at lower temperature. The pattern can be fitted by five Voigt functions centered at 14140, 14017, 13788, 13483, and  $13099\text{ cm}^{-1}$  (Figure S23). At lower temperature, the intensity of the three lower energy bands increases relative to the prominent 709 nm band at room temperature. This behavior is similar to that of  $[\text{Cr}(\text{ddpd})_2]^{3+}$  describing a Boltzmann distribution between two equilibrating emissive states.<sup>53,55</sup> The higher energy state is more emissive, that is, less prone to thermally activated nonradiative decay. This is confirmed by the luminescence spectra of a KBr pellet of  $[\text{Cr}(\text{bpmp})_2][\text{BF}_4]_3$  cooled to 10 K. Below ca. 130 K the low-energy emission ( $719.5\text{ nm}$ ;  $13900\text{ cm}^{-1}$ ) dramatically increases in intensity, suggesting less efficient nonradiative decay pathways for this state at low temperature (Figure 4). Concomitantly, the high-energy

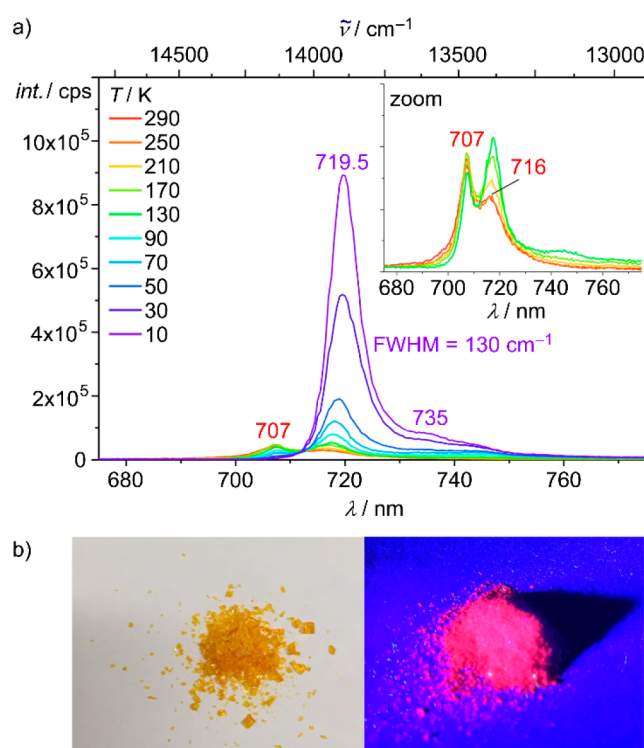


**Figure 4.** (a) Temperature-dependent luminescence spectra of  $[\text{Cr}(\text{bpmp})_2][\text{BF}_4]_3$  in a KBr matrix recorded between 10 K (purple) and 290 K (red) with  $\lambda_{\text{exc}} = 355$  nm. The inset shows the spectra between 130 and 290 K. (b) Photographs of crystalline  $[\text{Cr}(\text{bpmp})_2][\text{OTf}]_3$  under ambient light and under irradiation with  $\lambda_{\text{exc}} = 340$  nm.

emission ( $709\text{ nm}$ ;  $14105\text{ cm}^{-1}$ ) vanishes. The energy difference is in the range predicted by the CASSCF(7,12)-NEVPT2 calculations for the two lowest doublet states ( $\Delta E_{\text{exp}} = 245\text{ cm}^{-1}$ ;  $\Delta E_{\text{CASSCF}} = 154\text{ cm}^{-1}$ ). The thermally activated nonradiative decay could be enabled by a surface crossing with the ground state, similar to the effects observed for  $[\text{Cr}(\text{tpe})_2]^{3+}$ .<sup>65</sup> For this path to be operative, the lowest emissive state should be distorted relative to the ground state. This fits to a slightly distorted microstate of  $^2\text{T}_1$  parentage which has been predicted by CASSCF(7,12)-NEVPT2 as the lowest doublet state. The presence of a vibrational fine structure of the low energy band confirms the distortion of this excited doublet state. Tentatively,



the vibrational progression of ca. 290  $\text{cm}^{-1}$  could correspond to a Cr–N vibration (in the  $xy$ -plane) of the ground state according to the DFT calculations (308  $\text{cm}^{-1}$ , scaled by 0.98; 302  $\text{cm}^{-1}$ ; Figure S24). For  $[\text{Cr}(\text{NH}_3)_6]^{3+}$ , vibrations of odd symmetry  $\delta(\text{T}_{1u}, \text{N–Cr–N})$  and  $\nu(\text{T}_{1u}, \text{Cr–N})$  have been found at 267 and 458  $\text{cm}^{-1}$ , respectively.<sup>95</sup>

The much higher integrated emission intensity upon cooling a sample of  $[\text{Cr}(\text{bpmp})_2][\text{BF}_4]_3$  in a KBr pellet from 290 to 10 K parallels an increase of the average photoluminescence lifetime from 38.0 to 1900  $\mu\text{s}$ , respectively (Figure S25 and Table S8). The observed temperature dependence supports the model of reduced thermally available nonradiative decay pathways below ca. 130 K.

The photoluminescence quantum yield of  $[\text{Cr}(\text{bpmp})_2][\text{OTf}]_3$  reaches 12.3% at room temperature in deaerated  $\text{H}_2\text{O}$  solution (Table 1). This is similar to the quantum yield of the

**Table 1. Quantum Yields  $\Phi$  and Luminescence Lifetimes  $\tau$  of  $[\text{Cr}(\text{bpmp})_2][\text{OTf}]_3$  and  $[\text{Cr}([\text{D}_2]\text{-bpmp})_2][\text{OTf}]_3$  in Various Environments at Room Temperature ( $\lambda_{\text{exc}} = 462 \text{ nm}$ )**

solvent	acid <sup>a</sup>	O <sub>2</sub> <sup>c</sup>	$\Phi$ (%)	$\tau$ ( $\mu\text{s}$ )
$[\text{Cr}(\text{bpmp})_2]^{3+}$				
$\text{H}_2\text{O}$	–	–	12.3	1360
$\text{H}_2\text{O}$	$\text{HClO}_4$	–	15.8	1550
$\text{H}_2\text{O}$	$\text{HClO}_4$	+	9.8	880
$\text{D}_2\text{O}$	$\text{DClO}_4$ <sup>b</sup>	–	19.6	1800
$\text{D}_2\text{O}$	$\text{DClO}_4$ <sup>b</sup>	+	9.8	840
$\text{CH}_3\text{CN}$	–	–	0.8	840
$\text{CH}_3\text{CN}$	$\text{HClO}_4$	–	11.4	1290
$\text{CH}_3\text{CN}$	$\text{HClO}_4$	+	4.6	390
$\text{CD}_3\text{CN}$	$\text{DClO}_4$ <sup>b</sup>	–	15.5	1340
$\text{CD}_3\text{CN}$	$\text{DClO}_4$ <sup>b</sup>	+	4.3	380
PBS (pH 6.6)	–	–	1.4	600
PBS (pH 6.4)	–	+	1.4	470
$[\text{Cr}([\text{D}_2]\text{-bpmp})_2]^{3+}$				
$\text{D}_2\text{O}$	$\text{DClO}_4$	–	24.6	2500
$\text{D}_2\text{O}$	$\text{DClO}_4$	+	9.5	990

<sup>a</sup>Final  $\text{HClO}_4$  ( $\text{DClO}_4$ ) concentration  $c = 0.1 \text{ M}$ . <sup>b</sup>Under these conditions,  $\text{H} \rightarrow \text{D}$  exchange at the methylene bridge is expected. “+” refers to atmospheric conditions and “–” to inert conditions.

NIR emissive molecular ruby  $[\text{Cr}(\text{ddpd})_2]^{3+}$  and larger by several orders of magnitude compared to other reported chromium(III) emitters with emission in the red spectral region.<sup>49</sup> In pure and dry  $\text{CH}_3\text{CN}$  as well as in phosphate-buffered saline (PBS) buffer (0.1 M) the quantum yield drops below 2%, likely due to the deprotonation of the coordinated bpmp ligand in the ground state. Preventing  $\text{CH}_2$  bridge deprotonation by adding  $\text{HClO}_4$  increases the quantum yield to 15.8%. In the deuterated environments  $\text{CD}_3\text{CN}$  ( $\text{DClO}_4$ ) and  $\text{D}_2\text{O}$  ( $\text{DClO}_4$ ) the quantum yields increase to record numbers of 15.5% and 19.6%, respectively (Table 1). Other salts of  $[\text{Cr}(\text{bpmp})_2]^{3+}$  ( $\text{ClO}_4^-$ ,  $\text{PF}_6^-$ ,  $\text{BF}_4^-$ ) show a similar behavior under acidic conditions (Table S9). The  $\text{PF}_6^-$  salt even reaches a quantum yield of 20% in  $\text{D}_2\text{O}/\text{DClO}_4$  solution (Table S9). The acid/base chemistry and consequently the luminescence depend on the counterion in neutral to basic environments (Table S9).

In line with the above-mentioned acid/base chemistry, the CH acidic protons of the  $\text{CH}_2$  bridges readily exchange with deuterium in  $\text{D}_2\text{O}$  (Figures S26 and S27). Replacement of CH by CD oscillators reduces the nonradiative excited state decay via multiphonon relaxation<sup>54,57,96</sup> involving the aliphatic CH/

CD oscillators with  $\text{Cr}\cdots\text{H}$  distances of 3.1–4.3 Å. Indeed, the quantum yield of  $[\text{Cr}(\text{bpmp})_2][\text{OTf}]_3$  increases from 15.8 to 19.6% by replacing  $\text{H}_2\text{O}/\text{HClO}_4$  by  $\text{D}_2\text{O}/\text{DClO}_4$  (Table 1). This gain results from the combined effect of the CH/CD replacement in the ligand methylene bridges and the OH/OD replacement in the aqueous solution. As the bridges rapidly exchange H/D in  $\text{H}_2\text{O}$  or  $\text{D}_2\text{O}$ , these first- and second-sphere isotope effects cannot be disentangled.

$[\text{Cr}(\text{ddpd})_2]^{3+}$  with a lower emission energy has some spectral overlap with the third aromatic CH vibrational overtone  $\nu_{\text{CH}}^4$  at  $\approx 11493 \text{ cm}^{-1}$  with a comparably high extinction coefficient.<sup>54</sup> Deuteration of  $[\text{Cr}(\text{ddpd})_2]^{3+}$  to  $[\text{Cr}([\text{D}_x]\text{-ddpd})_2]^{3+}$  (>95% D at the pyridine  $\alpha$ -positions which are closest to the metal center) increased the quantum yield to 30% in  $\text{CD}_3\text{CN}$ .<sup>54</sup> The spectral overlap integral of the sharp  $[\text{Cr}(\text{bpmp})_2]^{3+}$  emission band at 14124  $\text{cm}^{-1}$  with overtones of aromatic CH oscillators is rather small as the accepting energy level derives from the fourth vibrational overtone  $\nu_{\text{CH}}^5$  at  $\approx 14065 \text{ cm}^{-1}$ .<sup>54</sup> This high overtone possesses a very small extinction coefficient.<sup>54</sup> To ascertain whether a further boost of the quantum yield could be achieved by deuteration of aromatic ligand protons, the ligand  $[\text{D}_2]\text{-bpmp}$  with the pyridine's  $\alpha$ -positions deuterated and its chromium complex  $[\text{Cr}([\text{D}_2]\text{-bpmp})_2]^{3+}$  were synthesized as detailed in the Supporting Information (Figures S28–S37). This deuteration at the  $\alpha$ -position increases the luminescence quantum yield from  $\Phi = 19.6\%$  to  $\Phi = 24.6\%$  in  $\text{D}_2\text{O}/\text{DClO}_4$  (Table 1). Concomitantly, the lifetime increases from 1800 to 2500  $\mu\text{s}$  (Table 1). This substantial increase in luminescence efficiency can be traced back to the comparison of spectral overlap of the relevant isotopologic C–(H/D) overtones with the doublet emission of chromium (Figures S38–S43). The fourth CH overtone ( $\nu_{\text{CH}}^5$ ) shows good spectral overlap (Figure S42), leading to a substantial nonradiative relaxation, while CD oscillators have a much smaller spectral overlap (Figure S43), in addition to the generally decreased oscillator strength compared to CH oscillators.

The photophysical properties of  $[\text{Cr}(\text{bpmp})_2]^{3+}$  and  $[\text{Cr}([\text{D}_2]\text{-bpmp})_2]^{3+}$  outperform the record NIR photoluminescence data of the molecular ruby  $[\text{Cr}(\text{ddpd})_2]^{3+}$ <sup>54</sup> and the standard red-orange emitter  $[\text{Ru}(\text{bpy})_3]^{2+}$  ( $\Phi(\text{CH}_3\text{CN}) = 9.5\%$ ;  $\tau(\text{CH}_3\text{CN}) = 1.1 \mu\text{s}$ ;  $\Phi(\text{H}_2\text{O}) = 6.3\%$ ;  $\tau(\text{H}_2\text{O}) = 0.65 \mu\text{s}$ ; Scheme 1).<sup>97–99</sup>

In the solid state, the details of the photoluminescence quantum yield and lifetime depend on the counterion. The quantum yield increases in the series  $\text{BF}_4^-$ ,  $\text{ClO}_4^-$ ,  $\text{PF}_6^-$ , and  $\text{OTf}^-$  ( $\Phi = 0.5, 1.7, 2.0,$  and  $7.1\%$ ) under aerated conditions. The luminescence decay was fitted mono-, bi-, or triexponentially and follows the same increasing trend with 36  $\mu\text{s}$ , 89/230  $\mu\text{s}$  (52:48), 530/250/110  $\mu\text{s}$  (13:66:21), and 1100/520/190  $\mu\text{s}$  (54:41:5), respectively. Clearly, the different packing and possible counterion association modify the solid state luminescence. Counterion effects on solid state and solution luminescence and photoreactivity have been reported previously for MLCT emitters,<sup>100,101</sup> yet a clear structure–activity relationship of counterion and luminescence in general, and spin-flip luminescence in particular,<sup>102</sup> is still elusive and more data are required.

The very long lifetime of the emissive state(s) allowed recording step-scan FT-IR spectra<sup>44,65,103–105</sup> after excitation of  $[\text{Cr}(\text{bpmp})_2][\text{BF}_4]_3$  in a KBr pellet with 355 nm excitation at 290 and 20 K (Figure 5a and Figures S44–S49). This high energy pulse likely populates allowed <sup>4</sup>LMCT states with



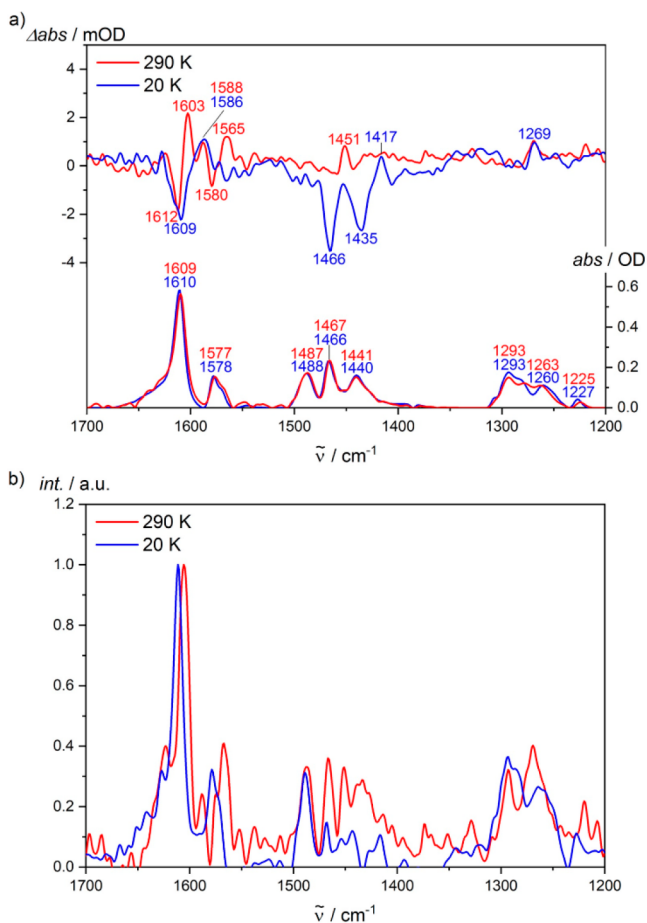


**Figure 5.** (a) Ground state (bottom) and step-scan FT-IR spectra (top,  $\lambda_{\text{exc}} = 355 \text{ nm}$ ;  $0\text{--}1 \mu\text{s}$ ) of  $[\text{Cr}(\text{bpmp})_2][\text{BF}_4]_3$  in a KBr pellet at 20 K (blue) and 290 K (red) and (b) excited state FT-IR spectra of  $[\text{Cr}(\text{bpmp})_2][\text{BF}_4]_3$  in a KBr pellet obtained from step-scan FT-IR spectra ( $\lambda_{\text{exc}} = 355 \text{ nm}$ ;  $0\text{--}1 \mu\text{s}$ ) (small contributions of 2% and 0.8% added to the respective ground state spectrum) at 20 K (blue) and 290 K (red). At 20 K, essentially the lowest doublet state is populated.

pyridine  $\rightarrow t_{2g}$  CT character according to TD-DFT calculations (Figure 1 and Figure S21). The absorption and emission spectra are hardly affected by the matrix (solution, KBr pellet, thin film; Figures S50 and S51). The ground state FT-IR spectra are essentially superimposable at 290 and 20 K (Figure S44). On the other hand, the normalized excited state spectra show significant differences around  $1600 \text{ cm}^{-1}$ ,  $1550 \text{ cm}^{-1}$ , and between  $1400$  and  $1450 \text{ cm}^{-1}$  at 290 and 20 K (Figure 5b). This is an indication for a temperature-dependent population of the contributing long-lived excited doublet states. With an estimated energy difference of the two lowest doublet microstates of  ${}^2T_1$  and  ${}^2E$  parentage of  $245 \text{ cm}^{-1}$  from the luminescence spectra ( $155 \text{ cm}^{-1}$  from the CASSCF-NEVPT2 calculations), the derived Boltzmann population ratio amounts to 77:23 (CASSCF: 68:32) and 100:0 (CASSCF: 100:0) at 290 and 20 K, respectively. Consequently, only the lowest energy excited state is populated at 20 K. At 290 K, the rise and decay of the most prominent IR bands at  $1612$ ,  $1603$ ,  $1588$ , and  $1451 \text{ cm}^{-1}$  were considered in a global fit to yield biexponential decays of 37 and  $2.5 \mu\text{s}$  with contributions of 77% and 23%, respectively (Figure S48). This ratio matches the population ratio estimated from the luminescence energies. At 20 K, the higher doublet state is hardly populated. Indeed, the global fit of the IR bands

yields a major time constant of  $372 \mu\text{s}$  (96%) and a minor one of  $13 \mu\text{s}$  (4%) (Figure S49). As thermal equilibration is not feasible at 20 K, the minor component might arise from the branching dynamics along the decay cascade after  ${}^4\text{LMCT}$  excitation to the final excited  ${}^2E/{}^2T_1$  states (Figure 1, purple arrows).

To experimentally probe the initial dynamics after excitation, subpicosecond transient absorption (TA) spectra of  $[\text{Cr}(\text{bpmp})_2][\text{OTf}]_3$  in  $\text{CH}_3\text{CN}$  ( $\text{HClO}_4$ ) were recorded with excitation at  $515 \text{ nm}$  ( ${}^4T_2$ ),  $460 \text{ nm}$  ( ${}^4T_2$ ), and  $350 \text{ nm}$  ( ${}^4\text{LMCT}$ ) (Figure 6 and Figures S52–S54). The TA spectra of

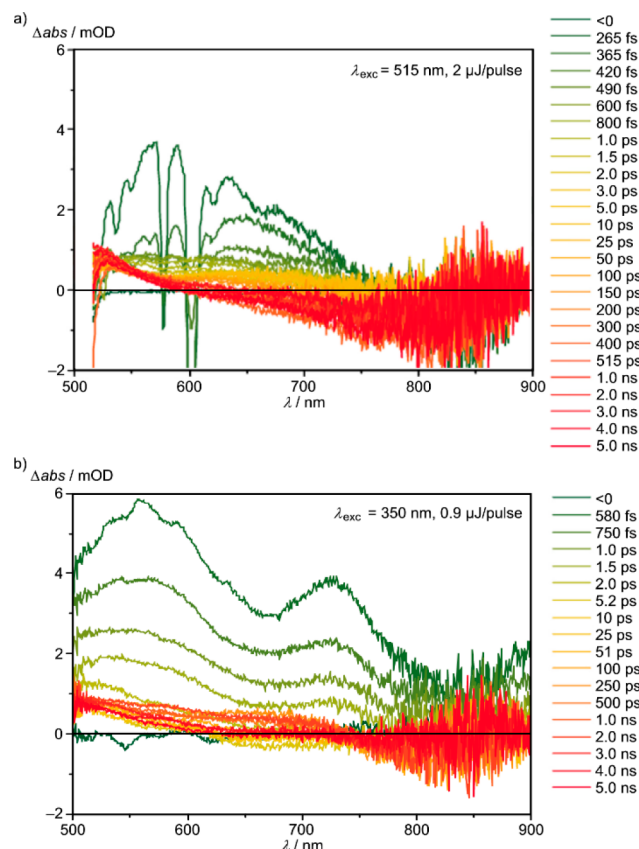


**Figure 6.** Transient absorption spectra of  $[\text{Cr}(\text{bpmp})_2][\text{OTf}]_3$  in  $\text{CH}_3\text{CN}$  ( $\text{HClO}_4$ ) excited with femtosecond laser pulses (a) at  $515 \text{ nm}$  ( ${}^4T_2$  states) and (b) at  $350 \text{ nm}$  ( ${}^4\text{LMCT}$  states).

the  $515$  and  $460 \text{ nm}$  excitation are very similar apart from the lower pump laser power at  $460 \text{ nm}$ , confirming that the same initial states are populated (Figure 6a and Figure S54). The TA spectra after  ${}^4T_2$  excitation with  $515 \text{ nm}$  (Figure 6a) were fitted with three time constants  $\tau^{515}_{1,2,3}$  of  $<200 \text{ fs}$ ,  $300 \text{ ps}$ , and a nondecaying component within the  $8 \text{ ns}$  time window, respectively. The fast decaying component  $\tau^{515}_1$  is attributed to a coherent artifact necessary for the fit. The slow decaying component  $\tau^{515}_3$  is straightforwardly assigned to the long-lived  ${}^2E/{}^2T_1$  states. As the evolution-associated difference spectra (EADS) relating to  $\tau_2$  and  $\tau_3$  are similar lacking significant spectral shifts (Figure S52), they correspond to states of similar nature. A kinetic model assigns  $\tau^{515}_2 = 300 \text{ ps}$  to internal conversion (IC) and vibrational cooling (VC) within doublet states  $k(\text{IC}_1 + \text{VC}_1)$  (Figure 1) while intersystem crossing (ISC) is faster than the instrument's time resolution ( $\tau^{515}_1(\text{ISC}_1) < 200 \text{ fs}$ ). The combined  $\text{ISC}_1$ ,  $\text{IC}_1$ , and  $\text{VC}_1$  processes are slower than observed for  $[\text{Cr}(\text{ddpd})_2]^{3+}$  with  $3.5 \text{ ps}$ ,  ${}^{56}\text{Cr}(\text{acac})_3$  with  $1.1 \text{ ps}$

( $\tau(\text{ISC}) < 100 \text{ fs}$ ),<sup>107</sup>  $\text{Cr}(t\text{Buacac})_3$  with 1.6 ps,<sup>108</sup> and  $[\text{Cr}(\text{CN})_6]^{3-}$  in a  $\text{Cr}^{\text{III}}-\text{V}^{\text{III}}$  Prussian blue analogue with  $\tau(\text{ISC}) = 250 \text{ fs}$  and  $\tau(\text{VC}) = 1.1 \text{ ps}$ <sup>109</sup> after  ${}^4\text{T}_2$  excitation, while ISC occurs in the ultrafast time regime within hundreds of femtoseconds. The density of doublet states in the  ${}^4\text{T}_2$  energy region and spin-orbit coupling (SOC) determine the ISC rates. For  $\text{Cr}(\text{acac})_3$  with nearly isoenergetic  ${}^4\text{T}_2$  and  ${}^2\text{E}/{}^2\text{T}_1$  states, SOC matrix elements between the  ${}^4\text{T}_2$  and the  ${}^2\text{E}/{}^2\text{T}_1$  states at geometries close to potential energy crossing points were calculated as 21–371  $\text{cm}^{-1}$  (at the SOC-CASSCF(3,5) level of theory).<sup>106</sup> SOC-CASSCF(7,12)-NEVPT2 calculations for  $[\text{Cr}(\text{bpmp})_2]^{3+}$  (in the ground state geometry) deliver SOCs between the lowest quartet state  ${}^4\text{T}_2(1)$  and the lowest doublet states derived from  ${}^2\text{E}$  and  ${}^2\text{T}_1$  states ranging from 6 to 97  $\text{cm}^{-1}$  accounting for an ISC pathway from  ${}^4\text{T}_2(1)$  to the doublet states, in particular the  ${}^2\text{E}(1)$  state (Table S4). These values closely match those obtained for  $[\text{Cr}(\text{ddpd})_2]^{3+}$  (Table S4). The different SOCs for states of  ${}^2\text{E}$  and  ${}^2\text{T}_1$  parentage might account for the population of both  ${}^2\text{E}(1)$  and states  ${}^2\text{T}_1(1)$  at very low temperature without equilibration of these states.

The TA spectra after  ${}^4\text{LMCT}$  excitation at 350 nm excitation (~Figure 6b) were fitted with three time constants  $\tau^{350}_{1,2,3}$  of 540 fs, 75 ps, and a nondecaying component within the 8 ns time window. Again,  $\tau^{350}_3$  is assigned to the lifetime of the  ${}^2\text{E}/{}^2\text{T}_1$  states. The first EADS comprises a broad excited state absorption (ESA), with peaks at 560 and 740 nm (Figure S53). This decays in 540 fs to yield the second EADS, which shows an ESA at 525 nm. This evolves in 75 ps to the final EADS with a broad ESA, spanning 500–750 nm. The ESAs of the second and third EADS are rather similar and distinct from the first EADS. A plausible kinetic model assigns the fast component  $\tau^{350}_1$  to ISC (and possibly electron redistribution) from  ${}^4\text{LMCT}$  states to the metal-centered or charge-transfer doublet manifold [Figure 1;  $\tau(\text{ISC}_2) = 540 \text{ fs}$ ] and the picosecond component  $\tau^{350}_2$  to IC and VC within the doublets (Figure 1;  $\tau(\text{IC}_2+\text{VC}_2) = 75 \text{ ps}$ ).  ${}^4\text{LMCT}$  excitation of  $\text{Cr}(\text{acac})_3$  yielded a process of ~50 fs which had been tentatively assigned to the  ${}^4\text{LMCT}$  to  ${}^2\text{E}$  population transfer.<sup>107</sup> With these assignments, the conversion from the LMCT to the ligand field manifold is ~10 times slower in  $[\text{Cr}(\text{bpmp})_2]^{3+}$  than in  $\text{Cr}(\text{acac})_3$  which might be ascribed to a different density of (electronic and associated vibrational) doublet states in the respective CT energy regions and the very different ligand types.

Irrespective of the excitation energy and the decay pathway, the relaxed long-lived doublet state(s) of  $[\text{Cr}(\text{bpmp})_2]^{3+}$  are characterized by an ESA around 500–750 nm (Figure 6 and Figure S54), similar to the excited doublet states of  $[\text{Cr}(\text{ddpd})_2]^{3+}$  (530 nm)<sup>56</sup> and  $\text{Cr}(\text{acac})_3$  (510 nm).<sup>108</sup>

**Singlet Oxygen Generation, Photoredox Chemistry, and Optical pH Sensing.** The excited state reactivity of the long-lived doublet states of  $[\text{Cr}(\text{bpmp})_2][\text{OTf}]_3$  was probed by excited state quenching with oxygen in  $\text{H}_2\text{O}/\text{HClO}_4$  and  $\text{CH}_3\text{CN}/\text{HClO}_4$  (Table 1). In air-saturated solutions, the luminescence quantum yields were diminished by factors of 1.6 and 2.0, respectively. This is considerably less than observed for  $[\text{Cr}(\text{ddpd})_2][\text{BF}_4]_3$  with factors of 5.2 and 17, respectively.<sup>53</sup> The product of this reaction is singlet oxygen  ${}^1\text{O}_2$  as confirmed by the observation of its characteristic emission at 1275 nm (Figure S55). Steady-state and time-resolved Stern–Volmer analyses yield Stern–Volmer constants  $K_{\text{SV}} = 0.44 \times 10^4$  and  $0.46 \times 10^4 \text{ M}^{-1}$ , respectively (Figures S56 and S57), demonstrating the dynamic character of the Dexter-type energy transfer quenching without significant static contributions.<sup>110</sup>

With  $\tau = 1550 \mu\text{s}$ , the bimolecular quenching rate constant  $k_q$  amounts to  $0.29 \times 10^7 \text{ M}^{-1} \text{ s}^{-1}$ . The longer lifetime of  $[\text{Cr}(\text{bpmp})_2]^{3+}$  and the lower  $K_{\text{SV}}$  as compared to those of  $[\text{Cr}(\text{ddpd})_2]^{3+}$ <sup>53</sup> yield a lower bimolecular quenching rate constant  $k_q$ . The Stern–Volmer constants of the tetrafluoroborate salt are even lower than those of the triflate with  $K_{\text{SV}} = 0.35 \times 10^4$  and  $0.36 \times 10^4 \text{ M}^{-1}$  (intensity and lifetime based; Figures S58 and S59). The quenching rate constant was calculated to  $k_q = 0.25 \times 10^7 \text{ M}^{-1} \text{ s}^{-1}$  ( $\tau = 1400 \mu\text{s}$ ). The singlet oxygen quantum yields of  $[\text{Cr}(\text{bpmp})_2][\text{X}]_3$  were determined by using the comparative method as 55, 44, and 39% in DMF/ $\text{HClO}_4$  for  $\text{X}^- = \text{OTf}^-$ ,  $\text{PF}_6^-$ , and  $\text{BF}_4^-$ , respectively. These values are smaller than those of  $[\text{Cr}(\text{ddpd})_2][\text{BF}_4]_3$  in DMF (61%)<sup>56</sup> and in DMF/ $\text{HClO}_4$  (86%) (Figure S55 and Table S5).

Although the driving force for energy transfer to oxygen is larger for  $[\text{Cr}(\text{bpmp})_2]^{3+}$  by 1200  $\text{cm}^{-1}$  than for  $[\text{Cr}(\text{ddpd})_2]^{3+}$ , and although the chromium center is somewhat less shielded by the  $\text{CH}_2$  bridges than by the larger  $\text{NCH}_3$  bridges of the ligands,  $[\text{Cr}(\text{bpmp})_2]^{3+}$  is less sensitive to oxygen than  $[\text{Cr}(\text{ddpd})_2]^{3+}$ . A hypothesis for explaining this surprising result might be the dynamic association with the  $\text{X}^-$  counterions at the C–H acidic methylene bridges of the ligands, fully analogous to the coordination of triflates and tetrafluoroborates in the solid state structure (Figure 2b and Figure S14). Possibly, this dynamic coordination of the anions to the bridges in solution shields the chromium center in  $[\text{Cr}(\text{bpmp})_2]^{3+}$  from successful quenching encounters with  $\text{O}_2$  more efficiently than the larger  $\text{NCH}_3$  bridges which cannot hydrogen-bond to counterions. Consequently, the pockets spanned by the tridentate ligands are on average more often filled by counterions in the bpmp complex. These results might pave the way to successfully design oxygen-insensitive and anion-sensitive spin-flip emitters in the future.

Apart from excited state energy transfer, photoinduced single electron transfer could occur from suitable substrates to the excited chromium(III) complex. The favorable redox and excited state properties suggest the use of  $[\text{Cr}(\text{bpmp})_2][\text{OTf}]_3$  as photoredox sensitizer. The excited state is strongly oxidizing (0.94 V vs ferrocene), slightly more oxidizing than  $*[\text{Cr}(\text{tpe})_2]^{3+}/[\text{Cr}(\text{tpe})_2]^{2+}$  (0.87 V vs ferrocene)<sup>65</sup> and significantly more oxidizing than  $*[\text{Ru}(\text{bpy})_3]^{2+}/[\text{Ru}(\text{bpy})_3]^+$  (0.41 V vs ferrocene) or classical ground state ruthenium(III) oxidants  $[\text{Ru}(\text{bpy})_3]^{3+}$  (0.84 V vs ferrocene) and  $[\text{Ru}(\text{phen})_3]^{3+}$  (0.87 V vs ferrocene).<sup>111</sup>

In fact, azulene ( $E_{1/2} = 0.50 \text{ V}$  vs ferrocene)<sup>112</sup> quenches the emission of  $[\text{Cr}(\text{bpmp})_2]^{3+}$  ( $K_{\text{SV}} = 3.73 \times 10^4 \text{ M}^{-1}$ ;  $k_q = 4.4 \times 10^7 \text{ M}^{-1} \text{ s}^{-1}$  in  $\text{CH}_3\text{CN}$ ;  $\tau = 840 \mu\text{s}$ ; Figure S60) slightly more efficiently than that of  $[\text{Cr}(\text{tpe})_2]^{3+}$  ( $K_{\text{SV}} = 4.17 \times 10^4 \text{ M}^{-1}$ ;  $k_q = 1.4 \times 10^7 \text{ M}^{-1} \text{ s}^{-1}$ ). The larger driving force and hence a smaller activation barrier for the electron transfer between  $*[\text{Cr}(\text{bpmp})_2]^{3+}$  and azulene might account for this small difference. The small quenching rate constants of both complexes might be associated with a weak electronic coupling in the collision complex as a result of the metal-localized excited state and the formation of contact ion pairs with the counterions shielding the sensitizer. Unfortunately, photoinduced oxidation of amines as useful redox partners is not feasible due to the deprotonation of the  $\text{CH}_2$  bridge of the coordinated ligand by amines already in the ground state (Figure 7). Yet, this intriguing feature can be turned into an advantage for sensing applications.

The reversible ground state acid/base chemistry forms dearomatized/rearomatized pyridine ligands.<sup>113</sup> Deprotonation at the methylene bridge leads to a coordinated nitrogen donor

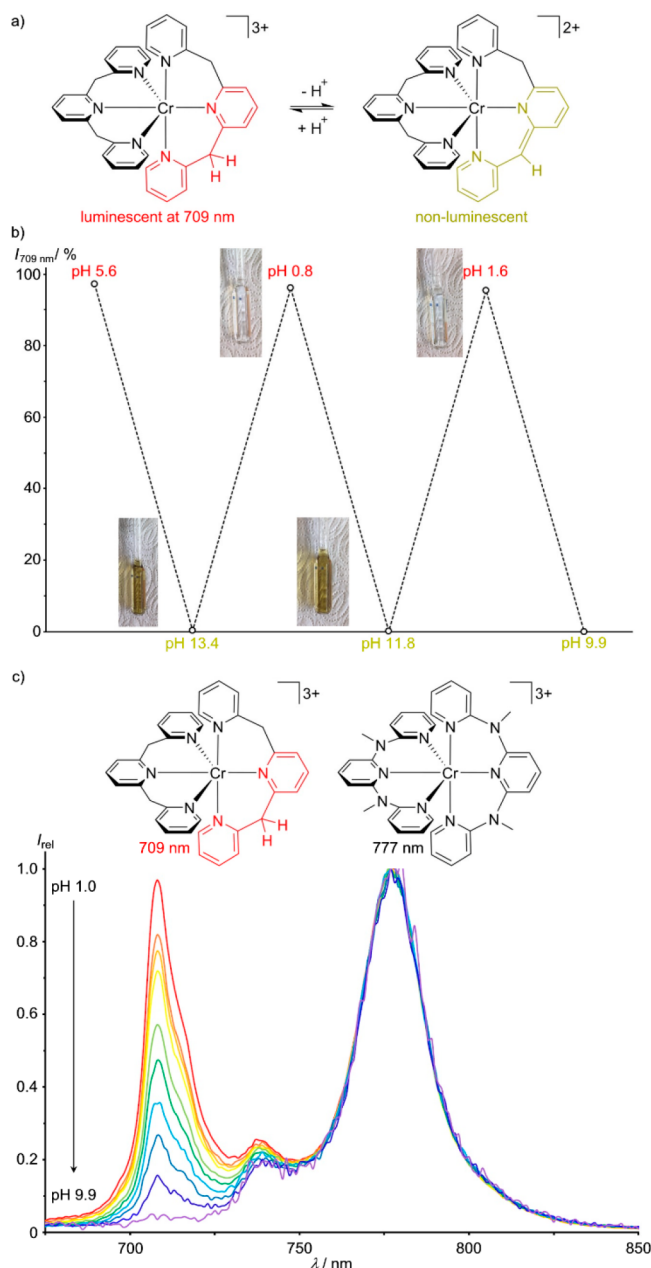


**Figure 7.** (a) Deprotonation/reprotonation equilibrium of an aqueous solution of  $[\text{Cr}(\text{bpmp})_2]^{3+}$  with concomitant dearomatization/rearomatization of a pyridine donor. (b) Intensity of the emission band at 709 nm during deprotonation/reprotonation cycles with NaOH and HOTf ( $\lambda_{\text{exc}} = 466 \text{ nm}$ ). (c) Normalized pH-dependent emission spectra of a mixture of  $[\text{Cr}(\text{bpmp})_2]^{3+}$  and  $[\text{Cr}(\text{ddpd})_2]^{3+}$  (molar fraction 25:2;  $\lambda_{\text{exc}} = 452 \text{ nm}$ ) in  $\text{H}_2\text{O}$  under ambient conditions. Note that dissolved  $\text{O}_2$  reduces the quantum yield of both complexes especially at higher pH, and the nonemissive deprotonated complexes absorb strongly at the excitation wavelength. Both effects result in a poorer S/N ratio at high pH.

atom with enamide character dramatically changing the donor properties (Figure 7a). As a result, the luminescence of  $[\text{Cr}(\text{bpmp})_2]^{3+}$  at 709 nm is completely quenched at higher pH and reinstated at lower pH (Figure 7b). As the emission of  $[\text{Cr}(\text{ddpd})_2]^{3+}$  at 777 nm is pH-insensitive, the combination of these two emitters gives a ratiometric optical pH sensor operating in the red to near-infrared spectral region with single-wavelength excitation in the blue (Figure 7c). The sharp

emission bands of both complexes in the red/near-IR spectral region and the excitation with blue light would even allow combination with further luminophores utilizing the visible part of the spectral region.<sup>60</sup> Consequently, this luminophore combination will be further developed towards multicolor multianalyte optical probes in the future.<sup>60</sup>

## CONCLUSIONS

On the basis of high-level computer-aided design, we developed the first molecular highly luminescent chromium(III) complex emitting in the red spectral region. After excitation of the  $[\text{Cr}(\text{bpmp})_2]^{3+}$  luminophore, ultrafast and efficient population transfer by intersystem crossing and vibrational cooling to the long-lived doublet states of  $^*[\text{Cr}(\text{bpmp})_2]^{3+}$  occurs. These doublet states emit in the deep red spectral region with photoluminescence quantum yields up to 20% and excited state lifetimes up to 1800  $\mu\text{s}$ . Deuteration of the  $\alpha$ -positions of the terminal pyridines increases the quantum yield to 25% and the lifetime to 2500  $\mu\text{s}$ . The key photophysical properties of the purely red-emissive molecular ruby  $[\text{Cr}(\text{bpmp})_2]^{3+}$  (emission color, photoluminescence quantum yield, excited state lifetime, and excited state redox potential) outperform those of the classical ruthenium(II) sensitizers and the often-used europium(III)-based red-emissive complexes. Furthermore, the reversible ground state (de)protonation of  $[\text{Cr}(\text{bpmp})_2]^{3+}$  coupled with an off/on luminescence enables ratiometric optical pH sensing. Future work will further exploit this novel red emitter with an earth-abundant chromium center in bioimaging, multicolor sensing (e.g., pH,  $\text{O}_2$ , and anions), photocatalysis, molecular upconversion,<sup>61,114</sup> and circularly polarized luminescence.<sup>63,64,115–117</sup>

## ASSOCIATED CONTENT

### Supporting Information

The Supporting Information is available free of charge at <https://pubs.acs.org/doi/10.1021/jacs.1c05971>.

Details of quantum chemical calculations, synthetic procedures, analytical and spectroscopic data of  $\text{Cr}(\text{bpmp})\text{Cl}_3$ ,  $\text{Cr}(\text{bpmp})\text{Br}_3$ ,  $\text{Cr}(\text{bpmp})(\text{OTf})_3$ ,  $[\text{Cr}(\text{bpmp})_2][\text{OTf}]_3$ ,  $[\text{Cr}(\text{bpmp})_2][\text{BF}_4]_3$ ,  $[\text{Cr}(\text{bpmp})_2][\text{PF}_6]_3$ ,  $[\text{D}_2\text{-bpmp}]$ ,  $\text{Cr}([\text{D}_2\text{-bpmp}])\text{Cl}_3$ ,  $\text{Cr}([\text{D}_2\text{-bpmp}](\text{OTf})_3$ , and  $[\text{Cr}([\text{D}_2\text{-bpmp})_2][\text{OTf}]_3$  (PDF)

Video S1 (MP4)

Video S2 (MP4)

### Accession Codes

CCDC 1989536–1989537 and 2083757 contain the supplementary crystallographic data for this paper. These data can be obtained free of charge via [www.ccdc.cam.ac.uk/data\\_request/cif](http://www.ccdc.cam.ac.uk/data_request/cif), or by emailing [data\\_request@ccdc.cam.ac.uk](mailto:data_request@ccdc.cam.ac.uk), or by contacting The Cambridge Crystallographic Data Centre, 12 Union Road, Cambridge CB2 1EZ, UK; fax: +44 1223 336033.

## AUTHOR INFORMATION

### Corresponding Authors

Katja Heinze – Department of Chemistry, Johannes Gutenberg University of Mainz, 55128 Mainz, Germany; [orcid.org/0000-0003-1483-4156](https://orcid.org/0000-0003-1483-4156); Email: [katja.heinze@uni-mainz.de](mailto:katja.heinze@uni-mainz.de)

Ute Resch-Genger – Division Biophotonics, Federal Institute for Materials Research and Testing (BAM), 12489 Berlin, Germany; [orcid.org/0000-0002-0944-1115](https://orcid.org/0000-0002-0944-1115); Email: [ute.resch@bam.de](mailto:ute.resch@bam.de)



Michael Seitz – Institute of Inorganic Chemistry, University of Tübingen, 72076 Tübingen, Germany; [orcid.org/0000-0002-9313-2779](https://orcid.org/0000-0002-9313-2779); Email: [michael.seitz@uni-tuebingen.de](mailto:michael.seitz@uni-tuebingen.de)

## Authors

Florian Reichenauer – Department of Chemistry, Johannes Gutenberg University of Mainz, 55128 Mainz, Germany

Cui Wang – Division Biophotonics, Federal Institute for Materials Research and Testing (BAM), 12489 Berlin, Germany; Institut für Chemie und Biochemie, Freie Universität Berlin, 14195 Berlin, Germany

Christoph Förster – Department of Chemistry, Johannes Gutenberg University of Mainz, 55128 Mainz, Germany

Pit Boden – Department of Chemistry and Research Center Optimas, University Kaiserslautern, 67663 Kaiserslautern, Germany

Naz Ugur – Max Planck Institute for Polymer Research, 55128 Mainz, Germany

Ricardo Báez-Cruz – Max Planck Institute for Polymer Research, 55128 Mainz, Germany

Jens Kalmbach – Institute of Inorganic Chemistry, University of Tübingen, 72076 Tübingen, Germany

Luca M. Carrella – Department of Chemistry, Johannes Gutenberg University of Mainz, 55128 Mainz, Germany

Eva Rentschler – Department of Chemistry, Johannes Gutenberg University of Mainz, 55128 Mainz, Germany; [orcid.org/0000-0003-1431-3641](https://orcid.org/0000-0003-1431-3641)

Charusheela Ramanan – Max Planck Institute for Polymer Research, 55128 Mainz, Germany

Gereon Niedner-Schatteburg – Department of Chemistry and Research Center Optimas, University Kaiserslautern, 67663 Kaiserslautern, Germany; [orcid.org/0000-0001-7240-6673](https://orcid.org/0000-0001-7240-6673)

Markus Gerhards – Department of Chemistry and Research Center Optimas, University Kaiserslautern, 67663 Kaiserslautern, Germany; [orcid.org/0000-0002-8748-2940](https://orcid.org/0000-0002-8748-2940)

Complete contact information is available at: <https://pubs.acs.org/10.1021/jacs.1c05971>

## Notes

The authors declare no competing financial interest. During manuscript finalization, Prof. Markus Gerhards unexpectedly passed away on Dec 28th 2020.

## ACKNOWLEDGMENTS

Financial support from the Deutsche Forschungsgemeinschaft [DFG, Priority Program SPP 2102 “Light-controlled reactivity of metal complexes” (GE 961/10-1, HE 2778/15-1, SE 1448/8-1) and RE 1203/23-1] is gratefully acknowledged. Parts of this research were conducted by using the supercomputer Mogon and advisory services offered by Johannes Gutenberg University Mainz ([www.hpc.uni-mainz.de](http://www.hpc.uni-mainz.de)), which is a member of the AHRP and the Gauss Alliance e.V., and the supercomputer Elwetritsch and advisory services offered by the TU Kaiserslautern (<https://elwe.rhrk.uni-kl.de>), which is a member of the AHRP. We thank Marius Bauer and Leander Geske for assistance with photography and IR spectroscopy, respectively.

## REFERENCES

(1) Baldo, M. A.; Thompson, M. E.; Forrest, S. R. High-Efficiency Fluorescent Organic Light-Emitting Devices using a Phosphorescent Sensitizer. *Nature* **2000**, *403*, 750–753.

(2) Li, A.; Turro, C.; Kodanko, J. J. Ru(II) Polypyridyl Complexes Derived from Tetradentate Ancillary Ligands for Effective Photocaging. *Acc. Chem. Res.* **2018**, *51*, 1415–1421.

(3) Mari, C.; Pierroz, V.; Ferrari, S.; Gasser, G. Combination of Ru(II) Complexes and Light: New Frontiers in Cancer Therapy. *Chem. Sci.* **2015**, *6*, 2660–2686.

(4) Hagfeldt, A.; Grätzel, M. Molecular Photovoltaics. *Acc. Chem. Res.* **2000**, *33*, 269–277.

(5) Yoon, T. P.; Ischay, M. A.; Du, J. N. Visible Light Photocatalysis as a Greener Approach to Photochemical Synthesis. *Nat. Chem.* **2010**, *2*, 527–532.

(6) Marzo, L.; Pagire, S. K.; Reiser, O.; König, B. Visible-light photocatalysis: does it make a difference in organic synthesis? *Angew. Chem., Int. Ed.* **2018**, *57*, 10034–10072.

(7) Romero, N. A.; Nicewicz, D. A. Organic photoredox catalysis. *Chem. Rev.* **2016**, *116*, 10075–10166.

(8) Skubi, K. L.; Blum, T. R.; Yoon, T. P. Dual Catalysis Strategies in Photochemical Synthesis. *Chem. Rev.* **2016**, *116*, 10035–10074.

(9) Shaw, M. H.; Twilton, J.; MacMillan, D. W. Photoredox catalysis in organic chemistry. *J. Org. Chem.* **2016**, *81*, 6898–926.

(10) Narayanam, J. M.; Stephenson, C. R. Visible light photoredox catalysis. Applications in organic synthesis. *Chem. Soc. Rev.* **2011**, *40*, 102–113.

(11) Herr, P.; Glaser, F.; Büldt, L. A.; Larsen, C. B.; Wenger, O. S. Long-Lived, Strongly Emissive, and Highly Reducing Excited States in Mo(0) Complexes with Chelating Isocyanides. *J. Am. Chem. Soc.* **2019**, *141*, 14394–14402.

(12) Büldt, L. A.; Wenger, O. S. Chromium(0), Molybdenum(0), and Tungsten(0) Isocyanide Complexes as Luminophores and Photosensitizers with Long-Lived Excited States. *Angew. Chem., Int. Ed.* **2017**, *56*, 5676–5682.

(13) Büldt, L. A.; Guo, X.; Prescimone, A.; Wenger, O. S. A Molybdenum(0) Isocyanide Analogue of Ru(2,2-Bipyridine)<sub>3</sub><sup>2+</sup>: A Strong Reductant for Photoredox Catalysis. *Angew. Chem., Int. Ed.* **2016**, *55*, 11247–11250.

(14) Yam, V. W.; Wong, K. M.-C. Luminescent metal complexes of d<sup>6</sup>, d<sup>8</sup> and d<sup>10</sup> transition metal centres. *Chem. Commun.* **2011**, *47*, 11579–11592.

(15) Hamze, R.; Peltier, J. L.; Sylvinson, D.; Jung, M.; Cardenas, J.; Haiges, R.; Soleilhavoup, M.; Jazzar, R.; Djurovich, P. I.; Bertrand, G.; Thompson, M. E. Eliminating Nonradiative Decay in Cu(I) Emitters: > 99% Quantum Efficiency and Microsecond Lifetime. *Science* **2019**, *363*, 601–606.

(16) Gernert, M.; Müller, U.; Haehnel, M.; Pflaum, J.; Steffen, A. A Cyclic Alkyl(amino)carbene as Two-Atom  $\pi$ -Chromophore Leading to the First Phosphorescent Linear Cu<sup>I</sup> Complexes. *Chem. - Eur. J.* **2017**, *23*, 2206–2216.

(17) Di, D. W.; Romanov, A. S.; Yang, L.; Richter, J. M.; Rivett, J. P. H.; Jones, S.; Thomas, T. H.; Abdi Jalebi, M.; Friend, R. H.; Linnolahti, M.; Bochmann, M.; Credgington, D. High-Performance Light-Emitting Diodes based on Carbene-Metal-Amides. *Science* **2017**, *356*, 159–163.

(18) Hossain, A.; Bhattacharyya, A.; Reiser, O. Copper's Rapid Ascent in Visible-Light Photoredox Catalysis. *Science* **2019**, *364*, eaav9713.

(19) Hernandez-Perez, A. C.; Collins, S. K. Heteroleptic Cu-Based Sensitizers in Photoredox Catalysis. *Acc. Chem. Res.* **2016**, *49*, 1557–1565.

(20) Housecroft, C. E.; Constable, E. C. The emergence of copper(i)-based dye sensitized solar cells. *Chem. Soc. Rev.* **2015**, *44*, 8386–8398.

(21) Yersin, H.; Rausch, A. F.; Czerwieńiec, R.; Hofbeck, T.; Fischer, T. The triplet state of organo-transition metal compounds. Triplet harvesting and singlet harvesting for efficient OLEDs. *Coord. Chem. Rev.* **2011**, *255*, 2622–2652.

(22) Zhang, Y.; Schulz, M.; Wächter, M.; Karnahl, M.; Dietzek, B. Heteroleptic diimine–diphosphine Cu(I) complexes as an alternative towards noble-metal based photosensitizers: Design strategies, photophysical properties and perspective applications. *Coord. Chem. Rev.* **2018**, *356*, 127–146.

- (23) Förster, C.; Heinze, K. Photophysics and photochemistry with Earth-abundant metals - fundamentals and concepts. *Chem. Soc. Rev.* **2020**, *49*, 1057–1070.
- (24) Hockin, B. M.; Li, C.; Robertson, N.; Zysman-Colman, E. Photoredox catalysts based on earth-abundant metal complexes. *Catal. Sci. Technol.* **2019**, *9*, 889–915.
- (25) Wenger, O. S. Photoactive Complexes with Earth-Abundant Metals. *J. Am. Chem. Soc.* **2018**, *140*, 13522–13533.
- (26) Otto, S.; Dorn, M.; Förster, C.; Bauer, M.; Seitz, M.; Heinze, K. Understanding and Exploiting Long-lived Near-infrared Emission of a Molecular Ruby. *Coord. Chem. Rev.* **2018**, *359*, 102–111.
- (27) Bizzarri, C.; Spuling, E.; Knoll, D. M.; Volz, D.; Bräse, S. Sustainable metal complexes for organic light-emitting diodes (OLEDs). *Coord. Chem. Rev.* **2018**, *373*, 49–82.
- (28) Larsen, C. B.; Wenger, O. S. Photoredox Catalysis with Metal Complexes Made from Earth-Abundant Elements. *Chem. - Eur. J.* **2018**, *24*, 2039–2058.
- (29) Bozic-Weber, B.; Constable, E. C.; Housecroft, C. E. Light harvesting with Earth abundant d-block metals: development of sensitizers in dye-sensitized solar cells (DSCs). *Coord. Chem. Rev.* **2013**, *257*, 3089–3106.
- (30) Barbieri, A.; Accorsi, G.; Armaroli, N. Luminescent complexes beyond the platinum group: the d<sup>10</sup> avenue. *Chem. Commun.* **2008**, 2185–2193.
- (31) Harlang, T. C. B.; Liu, Y. Z.; Gordivska, O.; Fredin, L. A.; Ponceca, C. S.; Huang, P.; Chabera, P.; Kjaer, K. S.; Mateos, H.; Uhlig, J.; Lomoth, R.; Wallenberg, R.; Styring, S.; Persson, P.; Sundström, V.; Wärnmark, K. Iron Sensitizer Converts Light to Electrons with 92% Yield. *Nat. Chem.* **2015**, *7*, 883–889.
- (32) Chábera, P.; Kjaer, K. S.; Prakash, O.; Honarfar, A.; Liu, Y. Z.; Fredin, L. A.; Harlang, T. C. B.; Lidin, S.; Uhlig, J.; Sundström, V.; Lomoth, R.; Persson, P.; Wärnmark, K. Fe<sup>II</sup> Hexa N-Heterocyclic Carbene Complex with a 528 ps Metal-to-Ligand Charge-Transfer Excited-State Lifetime. *J. Phys. Chem. Lett.* **2018**, *9*, 459–463.
- (33) Büldt, L. A.; Guo, X.; Vogel, R.; Prescimone, A.; Wenger, O. S. A Tris(diisocyanide)chromium(0) Complex Is a Luminescent Analog of Fe(2,2'-Bipyridine)<sub>3</sub><sup>2+</sup>. *J. Am. Chem. Soc.* **2017**, *139*, 985–992.
- (34) Stevenson, S. M.; Shores, M. P.; Ferreira, E. M. Photoredox Chromium Catalysts for Promoting Radical Cation Cycloadditions. *Angew. Chem., Int. Ed.* **2015**, *54*, 6506–6510.
- (35) Higgins, R. F.; Fatur, S. M.; Shepard, S. G.; Stevenson, S. M.; Boston, D. J.; Ferreira, E. M.; Damrauer, N. H.; Rappé, A. K.; Shores, M. P. Uncovering the Roles of Oxygen in Cr(III) Photoredox Catalysis. *J. Am. Chem. Soc.* **2016**, *138*, 5451–5464.
- (36) Stevenson, S. M.; Higgins, R. F.; Shores, M. P.; Ferreira, E. M. Chromium photocatalysis: accessing structural complements to Diels–Alder adducts with electron-deficient dienophiles. *Chem. Sci.* **2017**, *8*, 654–660.
- (37) Zhang, Y.; Lee, T. S.; Favale, J. M.; Leary, D. C.; Petersen, J. L.; Scholes, G. D.; Castellano, F. N.; Milsmann, C. Delayed fluorescence from a zirconium (iv) photosensitizer with ligand-to-metal charge-transfer excited states. *Nat. Chem.* **2020**, *12*, 345–352.
- (38) Kjaer, K. S.; Kaul, N.; Prakash, O.; Chábera, P.; Rosemann, N. W.; Honarfar, A.; Gordivska, O.; Fredin, L. A.; Bergquist, K. E.; Hægström, L.; Ericsson, T.; Lindh, L.; Yartsev, A.; Styring, S.; Huang, P.; Uhlig, J.; Bendix, J.; Strand, D.; Sundström, V.; Persson, P.; Lomoth, R.; Wärnmark, K. Luminescence and Reactivity of a Charge-Transfer Excited Iron Complex with Nanosecond Lifetime. *Science* **2019**, *363*, 249–253.
- (39) Chábera, P.; Lindh, L.; Rosemann, N. W.; Prakash, O.; Uhlig, J.; Yartsev, A.; Wärnmark, K.; Sundström, V.; Persson, P. *Coord. Chem. Rev.* **2021**, *426*, 213517.
- (40) Pal, A. K.; Li, C. F.; Hanan, G. S.; Zysman-Colman, E. Blue-Emissive Cobalt(III) Complexes and Their Use in the Photocatalytic Trifluoromethylation of Polycyclic Aromatic Hydrocarbons. *Angew. Chem., Int. Ed.* **2018**, *57*, 8027–8031.
- (41) Yam, V. W.; Chan, A. K.; Hong, E. Y. Charge-transfer processes in metal complexes enable luminescence and memory functions. *Nat. Rev. Chem.* **2020**, *4*, 528–541.
- (42) Jamieson, M. A.; Serpone, N.; Hoffman, M. Z. Advances in the photochemistry and photophysics of chromium(III) polypyridyl complexes in fluid media. *Coord. Chem. Rev.* **1981**, *39*, 121–179.
- (43) Kirk, A. D. Photochemistry and Photophysics of Chromium(III) Complexes. *Chem. Rev.* **1999**, *99*, 1607–1640.
- (44) Dorn, M.; Kalmbach, J.; Boden, P.; Pöpcke, A.; Gómez, S.; Förster, C.; Kuczelinis, F.; Carrella, L. M.; Büldt, L.; Bings, N.; Rentschler, E.; Lochbrunner, S.; González, L.; Gerhards, M.; Seitz, M.; Heinze, K. A vanadium(III) complex with blue and NIR-II spin-flip luminescence in solution. *J. Am. Chem. Soc.* **2020**, *142*, 7947–7955.
- (45) Forster, L. S. Thermal relaxation in excited electronic states of d<sup>3</sup> and d<sup>6</sup> metal complexes. *Coord. Chem. Rev.* **2002**, *227*, 59–92.
- (46) Forster, L. S. Intersystem crossing in transition metal complexes. *Coord. Chem. Rev.* **2006**, *250*, 2023–2033.
- (47) Kane-Maguire, N. A. P. Photochemistry and Photophysics of Coordination Compounds: Chromium. *Top. Curr. Chem.* **2007**, *280*, 37–67.
- (48) Balzani, V.; Ceroni, P.; Juris, A. *Photochemistry and Photophysics*; Wiley-VCH: Weinheim, 2014; pp 216–219.
- (49) Xiang, H.; Cheng, J.; Ma, X.; Zhou, X.; Chruma, J. J. Near-infrared phosphorescence: materials and applications. *Chem. Soc. Rev.* **2013**, *42*, 6128–6185.
- (50) Jørgenson, C. K. Recent Progress in Ligand Field Theory. *Struct. Bonding (Berlin)* **1966**, *1*, 3–31.
- (51) Breivogel, A.; Förster, C.; Heinze, K. A Heteroleptic Bis(tridentate)ruthenium(II) Polypyridine Complex with Improved Photophysical Properties and Integrated Functionalizability. *Inorg. Chem.* **2010**, *49*, 7052–7056.
- (52) Förster, C.; Dorn, M.; Reuter, T.; Otto, S.; Davarci, G.; Reich, T.; Carrella, L.; Rentschler, E.; Heinze, K. Ddpd as Expanded Terpyridine: Dramatic Effects of Symmetry and Electronic Properties in First Row Transition Metal Complexes. *Inorganics* **2018**, *6*, 86.
- (53) Otto, S.; Grabolle, M.; Förster, C.; Kreitner, C.; Resch-Genger, U.; Heinze, K. [Cr(ddpd)<sub>2</sub>]<sup>3+</sup>: A molecular, water-soluble, highly NIR-emissive ruby analogue. *Angew. Chem., Int. Ed.* **2015**, *54*, 11572–11576.
- (54) Wang, C.; Otto, S.; Dorn, M.; Kreidt, E.; Lebon, J.; Sršan, L.; Di Martino-Fumo, P.; Gerhards, M.; Resch-Genger, U.; Seitz, M.; Heinze, K. Deuterated Molecular Ruby with Record Luminescence Quantum Yield. *Angew. Chem., Int. Ed.* **2018**, *57*, 1112–1116.
- (55) Otto, S.; Scholz, N.; Behnke, T.; Resch-Genger, U.; Heinze, K. Thermo-Chromium: A Contactless Optical Molecular Thermometer. *Chem. - Eur. J.* **2017**, *23*, 12131–12135.
- (56) Otto, S.; Nauth, A. M.; Ermilov, E.; Scholz, N.; Friedrich, A.; Resch-Genger, U.; Lochbrunner, S.; Opatz, T.; Heinze, T. Photo-Chromium: Sensitizer for Visible Light-Induced Oxidative C-H Bond Functionalization – Electron or Energy Transfer? *ChemPhotoChem.* **2017**, *1*, 344–349.
- (57) Otto, S.; Förster, C.; Wang, C.; Resch-Genger, U.; Heinze, K. A strongly luminescent chromium(III) complex acid. *Chem. - Eur. J.* **2018**, *24*, 12555–12563.
- (58) Otto, S.; Harris, J.; Heinze, K.; Reber, C. Molecular ruby under pressure. *Angew. Chem., Int. Ed.* **2018**, *57*, 11069–11073.
- (59) Basu, U.; Otto, S.; Heinze, K.; Gasser, G. Biological Evaluation of the NIR-Emissive Ruby Analogue [Cr(ddpd)<sub>2</sub>][BF<sub>4</sub>]<sub>3</sub> as a Photodynamic Therapy Photosensitizer. *Eur. J. Inorg. Chem.* **2019**, *2019*, 37–41.
- (60) Wang, C.; Otto, S.; Dorn, M.; Heinze, K.; Resch-Genger, U. Luminescent TOP Nanosensors for Simultaneously Measuring Temperature, Oxygen, and pH at a Single Excitation Wavelength. *Anal. Chem.* **2019**, *91*, 2337–2344.
- (61) Kalmbach, J.; Wang, C.; You, Y.; Förster, C.; Schubert, H.; Heinze, K.; Resch-Genger, U.; Seitz, M. Near-IR to Near-IR Upconversion Luminescence in Molecular Chromium Ytterbium Salts. *Angew. Chem., Int. Ed.* **2020**, *59*, 18804–18808.
- (62) Jiménez, J.-R.; Doistau, B.; Besnard, C.; Piguet, C. Versatile heteroleptic bis-terdentate Cr(III) chromophores displaying room temperature millisecond excited state lifetimes. *Chem. Commun.* **2018**, *54*, 13228–13231.



- (63) Jiménez, J. R.; Doistau, B.; Cruz, C. M.; Besnard, C.; Cuerva, J. M.; Campaña, A. G.; Pigué, C. Chiral Molecular Ruby  $[\text{Cr}(\text{dqp})_2]^{3+}$  with Long-Lived Circularly Polarized Luminescence. *J. Am. Chem. Soc.* **2019**, *141*, 13244–13252.
- (64) Dee, C.; Zinna, F.; Kitzmann, W. R.; Pescitelli, G.; Heinze, K.; Di Bari, L.; Seitz, M. Strong Circularly Polarized Luminescence of an Octahedral Chromium(III) Complex. *Chem. Commun.* **2019**, *55*, 13078–13081.
- (65) Treiling, S.; Wang, C.; Förster, C.; Reichenauer, F.; Kalmbach, J.; Boden, P.; Harris, J. P.; Carrella, L. M.; Rentschler, E.; Resch-Genger, U.; Reber, C.; Seitz, M.; Gerhards, M.; Heinze, K. Luminescence and Light-driven Energy and Electron Transfer from an Exceptionally Long-lived Excited State of a Non-innocent Chromium(III) Complex. *Angew. Chem., Int. Ed.* **2019**, *58*, 18075–18085.
- (66) Bünzli, J.-C. G.; Charbonniere, L. J.; Ziessel, R. F. Structural and photophysical properties of  $\text{Ln}^{\text{III}}$  complexes with 2,2'-bipyridine-6,6'-dicarboxylic acid: surprising formation of a H-bonded network of bimetallic entities. *J. Chem. Soc., Dalton Trans.* **2000**, 1917–1923.
- (67) Wahsner, J.; Seitz, M. Nonradiative Deactivation of Lanthanoid Excited States by Inner-Sphere Carboxylates. *Inorg. Chem.* **2015**, *54*, 10841–10848.
- (68) Bünzli, J.-C. G. Lanthanide Luminescence for Biomedical Analyses and Imaging. *Chem. Rev.* **2010**, *110*, 2729–2755.
- (69) Heffern, M. C.; Matosziuk, L. M.; Meade, T. J. Lanthanide Probes for Bioresponsive Imaging. *Chem. Rev.* **2014**, *114*, 4496–4539.
- (70) Amoroso, A. J.; Pope, S. J. A. Using lanthanide ions in molecular bioimaging. *Chem. Soc. Rev.* **2015**, *44*, 4723–4742.
- (71) Degli Esposti, C.; Bizzocchi, L. Absorption and Emission Spectroscopy of a Lasing Material: Ruby. *J. Chem. Educ.* **2007**, *84*, 1316–1318.
- (72) Dominiak-Dzik, G.; Ryba-Romanowski, W.; Grinberg, M.; Beregi, E.; Kovacs, L. Excited-state relaxation dynamics of  $\text{Cr}^{3+}$  in  $\text{YAl}_3(\text{BO}_3)_4$ . *J. Phys.: Condens. Matter* **2002**, *14*, 5229–5237.
- (73) Malysa, B.; Meijerink, A.; Jüstel, T. Temperature dependent luminescence  $\text{Cr}^{3+}$ -doped  $\text{GdAl}_3(\text{BO}_3)_4$  and  $\text{YAl}_3(\text{BO}_3)_4$ . *J. Lumin.* **2016**, *171*, 246–253.
- (74) Harris, J. P.; Sonnevile, C.; Villain, O.; Calas, G.; Reber, C. Analytical fitting of temperature-dependent spin-flip transitions in absorption spectra of  $\text{Cr}^{3+}$ -doped silicate glasses. *Chem. Phys. Lett.: X* **2019**, *2*, 100003.
- (75) Sijbom, H.; Verstraete, R.; Joos, J. J.; Poelman, D.; Smet, P. F.  $\text{K}_2\text{SiF}_6:\text{Mn}^{4+}$  as a red phosphor for displays and warm-white LEDs: a review of properties and perspectives. *Opt. Mater. Express* **2017**, *7*, 3332–3365.
- (76) Ballhausen, C. J. *Introduction to Ligand Field Theory*; McGraw-Hill: New York, 1962; p 222.
- (77) Ballhausen, C. J. *Molecular Electronic Structures of Transition Metal Complexes*; McGraw-Hill: New York, 1979; p 1.
- (78) Avram, N. M.; Brik, M. G., Eds.; *Optical Properties of 3d-Ions in Crystals: Spectroscopy and Crystal Field Analysis*; Springer: 2013; p 62.
- (79) Daniel, C. Photochemistry and photophysics of transition metal complexes: quantum chemistry. *Coord. Chem. Rev.* **2015**, *282*–283, 19–32.
- (80) Sousa, C.; Alías, M.; Domingo, A.; de Graaf, C. Deactivation of Excited States in Transition-Metal Complexes: Insight from Computational Chemistry. *Chem. - Eur. J.* **2019**, *25*, 1152–1164.
- (81) Reinen, D.; Atanasov, M.; Köhler, P.; Babel, D. Jahn–Teller coupling and the influence of strain in  $T_g$  and  $E_g$  ground and excited states – A ligand field and DFT study on halide  $\text{M}^{\text{III}}\text{X}_6$  model complexes  $[\text{M} = \text{Ti}^{\text{III}} - \text{Cu}^{\text{III}}; \text{X} = \text{F}^-, \text{Cl}^-]$ . *Coord. Chem. Rev.* **2010**, *254*, 2703–2754.
- (82) Escudero, D. Photodeactivation Channels of Transition Metal Complexes: A Computational Chemistry Perspective. In *Transition Metals in Coordination Environments*; Broclawik, E., Borowski, T., Radoń, M., Eds; Challenges and Advances in Computational Chemistry and Physics; Springer: Cham, 2019; Vol. 29.
- (83) Atanasov, M.; Ganyushin, D.; Sivalingam, K.; Neese, F. A Modern First-Principles View on Ligand Field Theory Through the Eyes of Correlated Multireference Wavefunctions. *Struct. Bonding (Berlin, Ger.)* **2011**, *143*, 149–220.
- (84) Singh, S. K.; Eng, J.; Atanasov, M.; Neese, F. Covalency and chemical bonding in transition metal complexes: An ab initio based ligand field perspective. *Coord. Chem. Rev.* **2017**, *344*, 2–25.
- (85) Lang, L.; Atanasov, M.; Neese, F. Improvement of Ab Initio Ligand Field Theory by Means of Multistate Perturbation Theory. *J. Phys. Chem. A* **2020**, *124*, 1025–1037.
- (86) Pierloot, K.; Vancoillie, S. Relative energy of the high- $(^5T_{2g})$  and low- $(^1A_{1g})$  spin states of  $\text{Fe}(\text{H}_2\text{O})_6^{2+}$ ,  $\text{Fe}(\text{NH}_3)_6^{2+}$ , and  $[\text{Fe}(\text{bpy})_3]^{2+}$ : CASPT2 versus density functional theory. *J. Chem. Phys.* **2006**, *125*, 124303.
- (87) Pierloot, K. Transition metals compounds: Outstanding challenges for multiconfigurational methods. *Int. J. Quantum Chem.* **2011**, *111*, 3291–3301.
- (88) Dyker, G.; Muth, O. Synthesis of Methylene- and Methine-Bridged Oligopyridines. *Eur. J. Org. Chem.* **2004**, *2004*, 4319–4322.
- (89) Constable, E. C.; Housecroft, C. E.; Neuburger, M.; Schönle, J.; Zampese, J. A. The surprising lability of bis(2,2':6',2''-terpyridine)-chromium(III) complexes. *Dalton Trans.* **2014**, *43*, 7227–7235.
- (90) Zare, D.; Doistau, B.; Nozary, H.; Besnard, C.; Guénee, L.; Suffren, Y.; Pelé, A.-L.; Hauser, A.; Pigué, C.  $\text{Cr}^{\text{III}}$  as an alternative to  $\text{Ru}^{\text{II}}$  in metallo-supramolecular chemistry. *Dalton Trans.* **2017**, *46*, 8992–9009.
- (91) Scarborough, C. C.; Sproules, S.; Weyhermüller, T.; DeBeer, S.; Wieghardt, K. Electronic and Molecular Structures of the Members of the Electron Transfer Series  $[\text{Cr}(\text{tppy})_3]^n$  ( $n = 3+, 2+, 1+, 0$ ): An X-ray Absorption Spectroscopic and Density Functional Theoretical Study. *Inorg. Chem.* **2011**, *50*, 12446–12462.
- (92) Scarborough, C. C.; Lancaster, K. M.; DeBeer, S.; Weyhermüller, T.; Sproules, S.; Wieghardt, K. Experimental Fingerprints for Redox-Active Terpyridine in  $[\text{Cr}(\text{tpy})_2](\text{PF}_6)_n$  ( $n = 3-0$ ), and the Remarkable Electronic Structure of  $[\text{Cr}(\text{tpy})_2]^{1+}$ . *Inorg. Chem.* **2012**, *51*, 3718–3732.
- (93) Becker, P. M.; Forster, C.; Carrella, L. M.; Boden, P.; Hunger, D.; Slagereen, J.; Gerhards, M.; Rentschler, E.; Heinze, K. Spin Crossover and Long-lived Excited States in a Reduced Molecular Ruby. *Chem. - Eur. J.* **2020**, *26*, 7199–7204.
- (94) CIE (1932). *Commission internationale de l'Eclairage proceedings*; Cambridge University Press: Cambridge, 1931.
- (95) Eysel, H. H. Absorptions- und Lumineszenzspektrum von Hexamminchrom(III)-salzen. *Z. Phys. Chem.* **1970**, *72*, 82–90.
- (96) Kreidt, E.; Kruck, C.; Seitz, M. *Handbook on the Physics and Chemistry of Rare Earths*; Bünzli, J. C.-G., Pecharsky, V. K., Eds.; Elsevier: Amsterdam, 2018; Vol. 53, pp 35–79.
- (97) Suzuki, K.; Kobayashi, A.; Kaneko, S.; Takehira, K.; Yoshihara, T.; Ishida, H.; Shiina, Y.; Oishi, S.; Tobita, S. Reevaluation of absolute luminescence quantum yields of standard solutions using a spectrometer with an integrating sphere and a back-thinned CCD detector. *Phys. Chem. Chem. Phys.* **2009**, *11*, 9850–9860.
- (98) Young, R. C.; Meyer, T. J.; Whitten, D. G. Electron transfer quenching of excited states of metal complexes. *J. Am. Chem. Soc.* **1976**, *98*, 286–287.
- (99) Juris, A.; Balzani, V.; Barigelletti, F.; Campagna, S.; Belser, P.; von Zelewsky, A. Ru(II) polypyridine complexes: photophysics, photochemistry, electrochemistry, and chemiluminescence. *Coord. Chem. Rev.* **1988**, *84*, 85–277.
- (100) Farney, E. P.; Chapman, S. J.; Swords, W. B.; Torelli, M. D.; Hamers, R. J.; Yoon, T. P. Discovery and Elucidation of Counteranion Dependence in Photoredox Catalysis. *J. Am. Chem. Soc.* **2019**, *141*, 6385–6391.
- (101) Ma, D.; Duan, L.; Wei, Y.; He, L.; Wang, L.; Qiu, Y. Increased phosphorescent quantum yields of cationic iridium(III) complexes by wisely controlling the counter anions. *Chem. Commun.* **2014**, *50*, 530–532.
- (102) Henry, M. S. Prolongation of the Lifetime of the  $^2E$  State of Tris(2,2'-bipyridine)chromium(III) Ion by Anions in Aqueous Solution. *J. Am. Chem. Soc.* **1977**, *99*, 6138–6139.

(103) Schoonover, J. R.; Strouse, G. F.; Omberg, K. M.; Dyer, R. B. Application of transient vibrational spectroscopies to the excited states of metal polypyridyl complexes. *Comments Inorg. Chem.* **1996**, *18*, 165–188.

(104) B pppler, F.; Zimmer, M.; Dietrich, F.; Grupe, M.; Wallesch, M.; Volz, D.; Br se, S.; Gerhards, M.; Diller, R. Photophysical dynamics of a binuclear Cu(I)-emitter on the fs to  $\mu$ s timescale, in solid phase and in solution. *Phys. Chem. Chem. Phys.* **2017**, *19*, 29438–29448.

(105) Boden, P.; Di Martino-Fumo, P.; Otto, S.; Seidel, W.; Heinze, K.; Gerhards, M. Transient FTIR spectroscopy after pump/pump vs. pump/dump excitation and temperature dependent luminescence investigations on a highly luminescent chromium(III) complex. *Phys. Chem. Chem. Phys.* **2021**, *23*, 13808–13818.

(106) Ando, H.; Iuchi, S.; Sato, H. Theoretical study on ultrafast intersystem crossing of chromium(III) acetylacetonate. *Chem. Phys. Lett.* **2012**, *535*, 177–181.

(107) Juban, E. A.; McCusker, J. K. Ultrafast Dynamics of  ${}^2E$  State Formation in  $\text{Cr}(\text{acac})_3$ . *J. Am. Chem. Soc.* **2005**, *127*, 6857–6865.

(108) Schraubens, J. N.; Dillman, K. L.; Beck, W. F.; McCusker, J. K. Vibrational coherence in the excited state dynamics of  $\text{Cr}(\text{acac})_3$ : probing the reaction coordinate for ultrafast intersystem crossing. *Chem. Sci.* **2010**, *1*, 405–410.

(109) Johansson, J. O.; Kim, J.-W.; Allwright, E.; Rogers, D. M.; Robertson, N.; Bigot, J.-Y. Directly probing spin dynamics in a molecular magnet with femtosecond time-resolution. *Chem. Sci.* **2016**, *7*, 7061–7067.

(110) Arias-Rotondo, D. A.; McCusker, J. K. The photophysics of photoredox catalysis: a roadmap for catalyst design. *Chem. Soc. Rev.* **2016**, *45*, 5803–5820.

(111) Connelly, N. G.; Geiger, W. E. Chemical Redox Agents for Organometallic Chemistry. *Chem. Rev.* **1996**, *96*, 877–910.

(112) Kurihara, T.; Suzuki, T.; Wakabayashi, H.; Ishikawa, S.; Shindo, K.; Shimada, Y.; Chiba, H.; Miyashi, T.; Yasunami, M.; Nozoe, T. Electronic Structures and Oxidation Potentials of Some Azulene Derivatives. *Bull. Chem. Soc. Jpn.* **1996**, *69*, 2003–2006.

(113) Khusnutdinova, J. R.; Milstein, D. Metal–Ligand Cooperation. *Angew. Chem., Int. Ed.* **2015**, *54*, 12236–12273.

(114) Aboshyan-Sorgho, L.; Besnard, C.; Pattison, P.; Kittilstved, K. R.; Aebischer, A.; B nzli, J.-C. G.; Hauser, A.; Piguet, C. Near-Infrared/Visible Light Upconversion in a Molecular Trinuclear d–f–d Complex. *Angew. Chem., Int. Ed.* **2011**, *50*, 4108–4112.

(115) Jimenez, J.; Cerdan, L.; Moreno, F.; Maroto, B. L.; Garc a-Moreno, I.; Lunkley, J. L.; Muller, G.; de la Moya, S. Chiral Organic Dyes Endowed with Circularly Polarized Laser Emission. *J. Phys. Chem. C* **2017**, *121*, 5287–5292.

(116) Zhang, D.-W.; Li, M.; Chen, C.-F. Recent advances in circularly polarized electroluminescence based on organic light-emitting diodes. *Chem. Soc. Rev.* **2020**, *49*, 1331–1343.

(117) Jim nez, J.-R.; Poncet, M.; M guez-Lago, S.; Grass, S.; Lacour, J.; Besnard, C.; Cuerva, J. M.; Campa a, A. G.; Piguet, C. Bright Long-Lived Circularly Polarized Luminescence in Chiral Chromium(III) Complexes. *Angew. Chem., Int. Ed.* **2021**, *60*, 10095–10102.

# Strongly Red-Emissive Molecular Ruby $[\text{Cr}(\text{bpmp})_2]^{3+}$ surpasses $[\text{Ru}(\text{bpy})_3]^{2+}$

Florian Reichenauer<sup>a</sup>, Cui Wang<sup>b,c</sup>, Christoph Förster<sup>a</sup>, Pit Boden<sup>d</sup>, Naz Ugur<sup>e</sup>, Ricardo Báez-Cruz<sup>e</sup>, Jens Kalmbach<sup>f</sup>, Luca M. Carrella<sup>a</sup>, Eva Rentschler<sup>a</sup>, Charusheela Ramanan<sup>e</sup>, Gereon Niedner-Schatteburg<sup>d</sup>, Markus Gerhards<sup>d†</sup>, Michael Seitz<sup>f,\*</sup>, Ute Resch-Genger<sup>b,\*</sup> and Katja Heinze<sup>a,\*</sup>

<sup>a</sup> Department of Chemistry, Johannes Gutenberg University of Mainz, Duesbergweg 10-14, 55128 Mainz, Germany

<sup>b</sup> Federal Institute for Materials Research and Testing (BAM), Division Biophotonics, Richard-Willstätter-Str. 11, 12489 Berlin, Germany

<sup>c</sup> Institut für Chemie und Biochemie, Freie Universität Berlin, Arnimallee 22, 14195 Berlin, Germany

<sup>d</sup> Department of Chemistry and Research Center Optimas, University Kaiserslautern, Erwin-Schrödinger-Straße, 67663 Kaiserslautern, Germany

<sup>e</sup> Max Planck Institute for Polymer Research, Ackermannweg 10, 55128 Mainz, Germany

<sup>f</sup> Institute of Inorganic Chemistry, University of Tübingen, Auf der Morgenstelle 18, 72076 Tübingen, Germany.

† During manuscript finalization, Prof. Markus Gerhards unexpectedly passed away on Dec. 28<sup>th</sup> 2020.

**Supporting Information**



## Contents

<b>Quantum Chemical Screening and Refinement</b>	<b>S3</b>
Table S1. CASSCF(3,5)-NEVPT results	S4
Table S2. LFT parameters from CASSCF(3,5)-NEVPT results	S4
Table S3. CASSCF(7,12)-NEVPT results of $[\text{Cr}(\text{ddpd})_2]^{3+}$ and $[\text{Cr}(\text{bpmp})_2]^{3+}$	S4
Table S4. Root-mean-squared spin-orbit coupling (SOC) matrix elements	S4
<b>Methods and Synthetic Procedures</b>	<b>S5</b>
General Procedures	S5
Syntheses	S9
Synthesis of $\text{Cr}(\text{bpmp})\text{Cl}_3$	S9
Synthesis of $\text{Cr}(\text{bpmp})\text{Br}_3$	S9
Synthesis of $\text{Cr}(\text{bpmp})(\text{OTf})_3$	S9
Synthesis of $[\text{Cr}(\text{bpmp})_2][\text{OTf}]_3$	S9
Synthesis of $[\text{Cr}(\text{bpmp})_2][\text{PF}_6]_3$	S9
Synthesis of $[\text{Cr}(\text{bpmp})_2][\text{BF}_4]_3$	S10
Synthesis of $[\text{Cr}(\text{bpmp})_2][\text{ClO}_4]_3$	S10
Synthesis of $[\text{Cr}([\text{D}_4]\text{-bpmp})_2][\text{PF}_6]_3$	S10
Synthesis of 6-deutero-2-methylpyridine	S10
Synthesis of $[\text{D}_2]\text{-bpmp}$	S11
Synthesis of $\text{Cr}([\text{D}_2]\text{-bpmp})\text{Cl}_3$	S11
Synthesis of $\text{Cr}([\text{D}_2]\text{-bpmp})(\text{O}_3\text{SCF}_3)_3$	S11
Synthesis of $[\text{Cr}([\text{D}_2/\text{D}_6]\text{-bpmp})_2](\text{O}_3\text{SCF}_3)_3$	S12
<b>Spectra, analytical data and Tables</b>	<b>S13</b>
Figure S1. ESI <sup>+</sup> mass spectrum of $\text{Cr}(\text{bpmp})\text{Cl}_3$	S13
Figure S2. ATR-IR spectrum of $\text{Cr}(\text{bpmp})\text{Cl}_3$	S13
Figure S3. ESI <sup>+</sup> mass spectrum of $\text{Cr}(\text{bpmp})\text{Br}_3$	S14
Figure S4. ATR-IR spectrum of $\text{Cr}(\text{bpmp})\text{Br}_3$	S14
Figure S5. APCI mass spectrum of $\text{Cr}(\text{bpmp})(\text{OTf})_3$	S15
Figure S6. ATR-IR spectrum of $\text{Cr}(\text{bpmp})(\text{OTf})_3$	S15
Figure S7. ESI <sup>+</sup> mass spectrum of $[\text{Cr}(\text{bpmp})_2][\text{OTf}]_3$	S16
Figure S8. ATR-IR spectrum of $[\text{Cr}(\text{bpmp})_2][\text{OTf}]_3$	S16
Figure S9. Temperature-dependence of $\chi_{\text{MT}}$ of $[\text{Cr}(\text{bpmp})_2][\text{BF}_4]_3$	S17
Table S6. Bond lengths [Å] and angles [deg] of $[\text{Cr}(\text{bpmp})_2]^{3+}$ .	S17
Figure S10. ESI <sup>+</sup> mass spectrum of $[\text{Cr}(\text{bpmp})_2][\text{BF}_4]_3$	S18
Figure S11. ATR-IR spectrum of $[\text{Cr}(\text{bpmp})_2][\text{BF}_4]_3$	S18
Figure S12. ESI <sup>+</sup> mass spectrum of $[\text{Cr}(\text{bpmp})_2][\text{PF}_6]_3$	S19
Figure S13. ATR-IR spectrum of $[\text{Cr}(\text{bpmp})_2][\text{PF}_6]_3$	S19
Figure S14. Molecular structure of $[\text{Cr}(\text{bpmp})_2][\text{BF}_4]_3$ in the solid state	S20
Figure S15. Absorption spectrum of $[\text{Cr}(\text{bpmp})_2][\text{OTf}]_3$ in H <sub>2</sub> O at pH 9.9 and TD-DFT calculated oscillator strengths of $[\text{Cr}(\text{bpmp})(\text{bpmp-H})]^{2+}$ .	S20
Table S7. TD-DFT calculated transitions of $[\text{Cr}(\text{bpmp-H})(\text{bpmp})]^{2+}$	S21
Figure S16. Photometric titration of $[\text{Cr}(\text{bpmp})_2][\text{OTf}]_3$ in H <sub>2</sub> O	S28
Figure S17. Absorption spectra of $[\text{Cr}(\text{bpmp})_2][\text{OTf}]_3$ in H <sub>2</sub> O cycling between pH $\approx$ 1.5 and $>$ 12	S29
Figure S18. Cyclic voltammogram of $[\text{Cr}(\text{bpmp})_2][\text{PF}_6]_3$ in CH <sub>3</sub> CN/[ <sup>n</sup> Bu <sub>4</sub> N][PF <sub>6</sub> ]	S30
Figure S19. Square wave voltammogram of $[\text{Cr}(\text{bpmp})_2][\text{PF}_6]_3$ in CH <sub>3</sub> CN/[ <sup>n</sup> Bu <sub>4</sub> N][PF <sub>6</sub> ]	S30
Figure S20. DFT optimized geometries of a) $[\text{Cr}(\text{bpmp})_2]^{3+}$ and b) $[\text{Cr}(\text{bpmp})_2]^{2+}$	S31
Figure S21. TD-DFT calculated absorption spectrum of $[\text{Cr}(\text{bpmp})_2]^{3+}$ and difference electron densities	S31
Figure S22. CIE 1931 diagram and CIE coordinates of $[\text{Cr}(\text{bpmp})_2]^{3+}$	S32
Figure S23. Normalized emission spectra of $[\text{Cr}(\text{bpmp})_2][\text{OTf}]_3$ at 300 – 80 K	S33
Figure S24. Illustration of the 308 cm <sup>-1</sup> vibrational mode of $[\text{Cr}(\text{bpmp})_2]^{3+}$	S34
Figure S25. Plot of the average luminescence lifetime $\tau_{\text{av}}$ of $[\text{Cr}(\text{bpmp})_2][\text{BF}_4]_3$ and the integrated luminescence versus temperature	S34
Table S8. Temperature-dependent luminescence lifetimes of $[\text{Cr}(\text{bpmp})_2][\text{BF}_4]_3$ (KBr pellet)	S35
Table S9. Quantum yields and luminescence lifetimes of $[\text{Cr}(\text{bpmp})_2][\text{ClO}_4]_3$ , $[\text{Cr}(\text{bpmp})_2][\text{PF}_6]_3$ , $[\text{Cr}(\text{bpmp})_2][\text{BF}_4]_3$ in various environments at room temperature	S36

Figure S26. ESI <sup>+</sup> mass spectrum of [Cr([D <sub>4</sub> ]-bpmp) <sub>2</sub> ][PF <sub>6</sub> ] <sub>3</sub>	S37
Figure S27. ATR-IR spectra of [Cr([D <sub>4</sub> ]-bpmp) <sub>2</sub> ][PF <sub>6</sub> ] <sub>3</sub> with deuterated methylene bridges and [Cr(bpmp) <sub>2</sub> ][PF <sub>6</sub> ] <sub>3</sub>	S37
Figure S28. <sup>1</sup> H NMR spectrum of 6-deutero-2-methylpyridine	S38
Figure S29. Zoom into the aromatic region of the <sup>1</sup> H NMR spectrum of 6-deutero-2-methylpyridine	S38
Figure S30. <sup>1</sup> H NMR spectra of bpmp and [D <sub>2</sub> ]-bpmp	S39
Figure S31. ESI <sup>+</sup> mass spectrum of [D <sub>2</sub> ]-bpmp	S39
Figure S32. ESI <sup>+</sup> and APCI mass spectra of Cr([D <sub>2</sub> ]-bpmp)Cl <sub>3</sub>	S40
Figure S33. ATR-IR spectrum of Cr([D <sub>2</sub> ]-bpmp)Cl <sub>3</sub>	S41
Figure S34. ESI <sup>+</sup> and APCI mass spectra of Cr([D <sub>2</sub> ]-bpmp)(OTf) <sub>3</sub>	S42
Figure S35. ATR-IR spectrum of Cr([D <sub>2</sub> ]-bpmp)(OTf) <sub>3</sub>	S43
Figure S36. ESI <sup>+</sup> and APCI mass spectra of [Cr([D <sub>2</sub> ]-bpmp) <sub>2</sub> ][OTf] <sub>3</sub>	S44
Figure S37. ATR-IR spectrum of [Cr([D <sub>2</sub> ]-bpmp) <sub>2</sub> ][OTf] <sub>3</sub>	S45
NIR Absorption Spectroscopy / Vibrational Overtone Analysis	S46
Figure S38. Pyridine-based ligands in chromium complexes and model compounds	S46
Figure S39. NIR absorption bands of the aromatic C–H vibrational overtones of Me <sub>2</sub> bpy and bpmp	S47
Figure S40. Integrand function of the spectral overlap integral (SOI); C–H (ν = 5)	S47
Figure S41. Integrand function of the spectral overlap integral (SOI); C–H (ν = 6, 7)	S48
Figure S42. Normalized spectra for the emission of [Cr(bpmp) <sub>2</sub> ] <sup>3+</sup> and the relevant vibrational aromatic C–H overtone absorption band	S48
Figure S43. Spectra for the emission of [Cr(bpmp) <sub>2</sub> ] <sup>3+</sup> and the relevant vibrational aromatic C–D overtone absorption bands	S49
Figure S44. FTIR spectra of [Cr(bpmp) <sub>2</sub> ][BF <sub>4</sub> ] <sub>3</sub> as KBr pellets at 290 K and 20 K	S50
Figure S45. Ground state FTIR spectrum of [Cr(bpmp) <sub>2</sub> ][BF <sub>4</sub> ] <sub>3</sub> (KBr pellet, 20 K) and calculated IR frequencies and calculated IR spectrum	S50
Figure S46. FTIR ground state spectrum and step-scan spectra difference spectrum of [Cr(bpmp) <sub>2</sub> ][BF <sub>4</sub> ] <sub>3</sub> (T = 290 K)	S51
Figure S47. FTIR ground state spectrum and step-scan spectra difference spectrum of [Cr(bpmp) <sub>2</sub> ][BF <sub>4</sub> ] <sub>3</sub> (T = 20 K)	S51
Figure S48. Global biexponential fit and residuals of [Cr(bpmp) <sub>2</sub> ][BF <sub>4</sub> ] <sub>3</sub> at 290 K	S52
Figure S49. Global biexponential fit and residuals of [Cr(bpmp) <sub>2</sub> ][BF <sub>4</sub> ] <sub>3</sub> at 20 K	S52
Figure S50. UV/Vis absorption spectrum of [Cr(bpmp) <sub>2</sub> ][BF <sub>4</sub> ] <sub>3</sub> (thin film) at 290 K	S53
Figure S51. Luminescence spectrum of [Cr(bpmp) <sub>2</sub> ][BF <sub>4</sub> ] <sub>3</sub> (thin film and KBr pellet) at 290 K	S53
Figure S52. EADS of [Cr(bpmp) <sub>2</sub> ][OTf] <sub>3</sub> excited with λ <sub>exc</sub> = 551 nm at 290 K	S54
Figure S53. EADS of [Cr(bpmp) <sub>2</sub> ][OTf] <sub>3</sub> excited with λ <sub>exc</sub> = 350 nm at 290 K	S54
Figure S54. Transient absorption spectra of [Cr(bpmp) <sub>2</sub> ][OTf] <sub>3</sub> with λ <sub>exc</sub> = 460 nm	S55
Figure S55. <sup>1</sup> O <sub>2</sub> emission sensitized by [Cr(ddpd) <sub>2</sub> ][BF <sub>4</sub> ] <sub>3</sub> , [Cr(ddpd) <sub>2</sub> ][PF <sub>6</sub> ] <sub>3</sub> and [Cr(ddpd) <sub>2</sub> ][OTf] <sub>3</sub>	S55
Figure S56. Emission spectra of [Cr(bpmp) <sub>2</sub> ][OTf] <sub>3</sub> with O <sub>2</sub> and Stern-Volmer plot	S56
Figure S57. Luminescence decays of [Cr(bpmp) <sub>2</sub> ][OTf] <sub>3</sub> with O <sub>2</sub> and Stern-Volmer plot	S56
Figure S58. Emission spectra of [Cr(bpmp) <sub>2</sub> ][BF <sub>4</sub> ] <sub>3</sub> with O <sub>2</sub> and Stern-Volmer plot	S57
Figure S59. Luminescence decays of [Cr(bpmp) <sub>2</sub> ][BF <sub>4</sub> ] <sub>3</sub> with O <sub>2</sub> and Stern-Volmer plot	S57
Figure S60. Emission spectra of [Cr(bpmp) <sub>2</sub> ][OTf] <sub>3</sub> with azulene and Stern-Volmer plot	S58
<b>Cartesian Coordinates</b>	<b>S59</b>
Table S10. Cartesian Coordinates of Cr(acac) <sub>3</sub>	S59
Table S11. Cartesian Coordinates of [Cr(NH <sub>3</sub> ) <sub>6</sub> ] <sup>3+</sup>	S59
Table S12. Cartesian Coordinates of [Cr(py) <sub>6</sub> ] <sup>3+</sup>	S60
Table S13. Cartesian Coordinates of [Cr(tpy) <sub>2</sub> ] <sup>3+</sup>	S61
Table S14. Cartesian Coordinates of [Cr(bpy) <sub>3</sub> ] <sup>3+</sup>	S62
Table S15. Cartesian Coordinates of [Cr(ddpd) <sub>2</sub> ] <sup>3+</sup>	S63
Table S16. Cartesian Coordinates of [Cr(bpmp) <sub>6</sub> ] <sup>3+</sup>	S64
Table S17. Cartesian Coordinates of [Cr(CN) <sub>6</sub> ] <sup>3-</sup>	S65
<b>References</b>	<b>S66</b>

## Quantum Chemical Screening and Refinement

**Static unrestricted Kohn-Sham orbitals DFT (UKS):** All calculations were performed using the quantum computing suite ORCA 4.0.1.<sup>1</sup> Geometry optimization was performed using unrestricted Kohn-Sham orbitals DFT (UKS) and the B3LYP functional<sup>2</sup> in combination with Ahlrichs' split-valence triple- $\zeta$  basis set def2-TZVPP for all atoms.<sup>3,4</sup> Tight convergence criteria were chosen for DFT-UKS calculations (keywords *tightscf* and *tightopt*). All DFT-UKS calculations make use of the resolution of identity (Split-RI-J) approach for the Coulomb term in combination with the chain-of-spheres approximation for the exchange term (*COSX*).<sup>5,6</sup> The zero order relativistic approximation was used to describe relativistic effects in all calculations (keyword *ZORA*).<sup>7,8</sup> Grimme's empirical dispersion correction D3(BJ) was employed (keyword *D3BJ*).<sup>9,10</sup> To account for solvent effects, a conductor-like screening model (keyword *CPCM* acetonitrile) modeling acetonitrile was used in all calculations.<sup>11</sup> Explicit counter ions and/or solvent molecules were neglected.

**SOC-CASSCF(x,y)-FIC-NEVPT2:** Calculations of ground and excited state properties with respect to metal-centered (MC) states were performed using the complete-active-space self-consistent field method including spin-orbit coupling (SOC-CASSCF)<sup>12,13</sup> in conjunction with the fully internally contracted N-electron valence perturbation theory to second order (FIC-NEVPT2)<sup>14,15</sup> in order to recover missing dynamic electron correlation. All electronic states are classified by irreducible representations of the *O* point group, in spite of the lower actual symmetries of the considered complexes. In the screening procedure, a small active space of the three d electrons and five d orbitals was selected CAS(3,5) (Table S1). In order to accurately model the ligand field of the hit structure and the reference structure, the active space was expanded to encompass the dominant bonding/antibonding orbitals formed between chromium and the ligand. In addition to the minimal active space of (3,5), two occupied Cr–N  $\sigma$  bonding orbitals and a second d shell<sup>16</sup> were included in these calculations giving an active space of (7,12) (Table S3). 7 quartet and 9 doublet roots were calculated with this active space. 10 quartet and 40 doublet roots were calculated to invoke an ab initio ligand field theory (AILFT)<sup>17,18</sup> analysis from CASSCF(3,5)-NEVPT results (keyword *actorbs dorbs*) (Table S2). SOC was treated through the mean-field (SOMF) approximation<sup>19,20</sup>, and the effective Hamiltonian approach<sup>21-23</sup> was used to compute the spin-Hamiltonian parameters (Table S4). From these SOC matrix elements, we obtain an approximate guess of conceivable ISC processes at the Franck-Condon geometry, i.e. before vibrational cooling in the excited quartet state.

**Table S1. CASSCF(3,5)-NEVPT results; energies in  $\text{cm}^{-1}$  (bold values indicate the lowest state of each multiplicity).**

	<sup>2</sup> E(1)	<sup>2</sup> E(2)	<sup>2</sup> T <sub>1</sub> (1)	<sup>2</sup> T <sub>1</sub> (2)	<sup>2</sup> T <sub>1</sub> (3)	<sup>2</sup> T <sub>2</sub> (1)	<sup>2</sup> T <sub>2</sub> (2)	<sup>2</sup> T <sub>2</sub> (3)	<sup>4</sup> T <sub>2</sub> (1)	<sup>4</sup> T <sub>2</sub> (2)	<sup>4</sup> T <sub>2</sub> (3)
Cr(acac) <sub>3</sub>	<b>16577</b>	16630	17290	17564	17598	24793	24874	25479	<b>19006</b>	19427	19526
[Cr(NH <sub>3</sub> ) <sub>6</sub> ] <sup>3+</sup>	<b>16784</b>	16786	17554	17605	17698	25608	25841	25953	<b>22731</b>	22789	22823
[Cr(py) <sub>6</sub> ] <sup>3+</sup>	<b>16589</b>	16589	17428	17432	17445	25159	25192	25202	<b>20213</b>	20245	2026
[Cr(tpy) <sub>2</sub> ] <sup>3+</sup>	<b>16021</b>	16087	16819	16820	16911	24694	24738	24739	<b>20386</b>	23113	23119
[Cr(bpy) <sub>3</sub> ] <sup>3+</sup>	<b>16278</b>	16288	16817	17210	17233	24810	24864	25762	<b>23300</b>	23440	23539
[Cr(ddpd) <sub>2</sub> ] <sup>3+</sup>	<b>15605</b>	16269	16804	16919	17089	25069	25423	25781	<b>22448</b>	22767	23907
[Cr(bpmp) <sub>2</sub> ] <sup>3+</sup>	<b>16299</b>	16515	17096	17354	17391	25246	25440	25488	<b>20882</b>	21203	22186
[Cr(CN) <sub>6</sub> ] <sup>3-</sup>	<b>15623</b>	15624	16332	16333	16333	24651	24653	24653	<b>28470</b>	28483	28484

**Table S2. LFT parameters from CASSCF(3,5)-NEVPT results; B, C in  $\text{cm}^{-1}$ .**

	B	C	C/B
Cr(acac) <sub>3</sub>	982	3116	3.17
[Cr(NH <sub>3</sub> ) <sub>6</sub> ] <sup>3+</sup>	988	3053	3.09
[Cr(py) <sub>6</sub> ] <sup>3+</sup>	976	3011	3.08
[Cr(tpy) <sub>2</sub> ] <sup>3+</sup>	947	2962	3.13
[Cr(bpy) <sub>3</sub> ] <sup>3+</sup>	982	2942	2.99
[Cr(ddpd) <sub>2</sub> ] <sup>3+</sup>	964	2972	3.08
[Cr(bpmp) <sub>2</sub> ] <sup>3+</sup>	1003	2937	2.93
[Cr(CN) <sub>6</sub> ] <sup>3-</sup>	888	2939	3.31

**Table S3. CASSCF(7,12)-NEVPT results of [Cr(ddpd)<sub>2</sub>]<sup>3+</sup> and [Cr(bpmp)<sub>2</sub>]<sup>3+</sup>; energies in  $\text{cm}^{-1}$  (bold values indicate the lowest state of each multiplicity).**

	<sup>2</sup> E(1)	<sup>2</sup> E(2)	<sup>2</sup> T <sub>1</sub> (1)	<sup>2</sup> T <sub>1</sub> (2)	<sup>2</sup> T <sub>1</sub> (3)	<sup>2</sup> T <sub>2</sub> (1)	<sup>2</sup> T <sub>2</sub> (2)	<sup>2</sup> T <sub>3</sub> (3)	<sup>4</sup> T <sub>2</sub> (1)	<sup>4</sup> T <sub>2</sub> (2)	<sup>4</sup> T <sub>2</sub> (3)
[Cr(ddpd) <sub>2</sub> ] <sup>3+</sup>	<b>15355</b>	<b>15916</b>	<b>14769</b>	15647	15719	23328	23600	24033	<b>22899</b>	23230	24174
[Cr(bpmp) <sub>2</sub> ] <sup>3+</sup>	<b>15689</b>	<b>16225</b>	<b>15535</b>	16000	16245	23649	23670	23848	<b>21546</b>	21822	22733

**Table S4. Root-mean-squared spin-orbit coupling (SOC)<sup>a</sup> matrix elements /  $\text{cm}^{-1}$  between the lowest excited quartet <sup>4</sup>T<sub>2</sub>(1) and the 8 lowest doublet states of [Cr(ddpd)<sub>2</sub>]<sup>3+</sup> and [Cr(bpmp)<sub>2</sub>]<sup>3+</sup> at their ground state geometry (the Franck-Condon point) from SOC-CASSCF(7,12)-NEVPT results.**

	<sup>2</sup> E(1)	<sup>2</sup> E(2)	<sup>2</sup> T <sub>1</sub> (1)	<sup>2</sup> T <sub>1</sub> (2)	<sup>2</sup> T <sub>1</sub> (3)	<sup>2</sup> T <sub>2</sub> (1)	<sup>2</sup> T <sub>2</sub> (2)	<sup>2</sup> T <sub>3</sub> (3)
[Cr(ddpd) <sub>2</sub> ] <sup>3+</sup>	97	10	1	45	36	32	42	3
[Cr(bpmp) <sub>2</sub> ] <sup>3+</sup>	98	12	6	46	40	32	38	4

<sup>a</sup> The listed SOC values are root-mean-square values for SOC matrix elements over all possible M<sub>s</sub> states.

## Methods and Synthetic Procedures

### General procedures

Acetonitrile was distilled over calcium hydride and butyronitrile over  $\text{Na}_2\text{CO}_3/\text{KMnO}_4$ . Ethanol, isopropanol, tetrahydrofuran, diethyl ether,  $\text{CrCl}_3 \cdot 6\text{H}_2\text{O}$  and  $\text{CrBr}_3 \cdot 6\text{H}_2\text{O}$  (Alfa Aesar),  $\text{D}_2\text{O}$  (99.9 % D, Deutero or Sigma Aldrich),  $\text{CD}_3\text{CN}$  (99 % D, abcr), triflic acid (Alfa Aesar), deuterated triflic acid (98 % D, Sigma Aldrich), tetrafluoroboric acid diethyl ether complex (Sigma Aldrich), tetra-*n*-butylammonium hexafluorophosphate (TCl), tetra-*n*-butylammonium tetrafluoroborate (Acros), tetra-*n*-butylammonium perchlorate (Aldrich),  $\text{HClO}_4$  (70 %, Merck),  $\text{DClO}_4$  (99 % D, Bernd Kraft), 2-bromo-6-methylpyridine (abcr) and 2,6-difluoropyridine (abcr) were used as received. The ligand  $\text{bpmp}^{24}$  and  $[\text{Cr}(\text{ddpd})_2][\text{BF}_4]_3^{25}$  were prepared according to reported procedures. NMR spectroscopic and mass spectrometric data match the literature values. Column chromatography was performed using aluminum oxide (neutral, Brockmann I). Analytical thin layer chromatography (TLC) was done on aluminum oxide F254 (Macherey-Nagel, coated on polyester sheets). A glovebox (UniLab/MBraun, Ar 4.8,  $\text{O}_2 < 1$  ppm,  $\text{H}_2\text{O} < 0.1$  ppm) was used for storage and weighing of sensitive compounds.

**NMR spectra** were recorded on a Bruker Avance DRX 400 or AVII+400 NMR spectrometer at 400.31 MHz ( $^1\text{H}$ ). All resonances are reported in ppm versus the solvent signal as internal standard.<sup>26</sup>

**IR spectra** were recorded with a Bruker Alpha FTIR spectrometer with an ATR unit containing a diamond crystal.

**ESI<sup>+</sup> mass spectra** were recorded on a Micromass Q-TOF-Ultima spectrometer by the central analytical facility of the Department of Chemistry (University of Mainz).

**APCI mass spectra** were recorded on an Advion expresson-L CMS spectrometer by the central analytical facility of the Department of Chemistry (University of Mainz).

**DC magnetic studies** were performed with a Quantum Design MPMS-XL-7 SQUID magnetometer on powdered microcrystalline samples. Experimental susceptibility data were corrected for the underlying diamagnetism using Pascal's constants. The temperature dependent magnetic contribution of the holder and of the embedding eicosane matrix was experimentally determined and subtracted from the measured susceptibility data. Variable temperature susceptibility data were collected in a temperature range of 2 – 300 K under an applied field of 0.1 Tesla.

**Electrochemical experiments** were carried out on a BioLogic SP-200 voltammetric analyzer using platinum wires as counter and working electrodes and a 0.01 M  $\text{Ag}/\text{Ag}[\text{NO}_3]$  electrode as reference electrode. Cyclic voltammetry and square wave measurements were carried out at scan rates of 50–200  $\text{mV s}^{-1}$  using 0.1 M  $[\text{Bu}_4\text{N}][\text{PF}_6]$  in  $\text{CH}_3\text{CN}$  as supporting electrolyte. Potentials are referenced against the ferrocene/ferrocenium couple.

**UV/Vis/NIR spectra** were recorded on a Varian Cary 5000 spectrometer using 1.0 cm cells.

**Luminescence experiments.** Luminescence emission spectra and luminescence decay kinetics in solution were obtained with a calibrated spectrofluorometer FSP 920 from Edinburgh Instruments. For the measurement of the emission spectra, a CW xenon lamp was applied as excitation light source, while the time-resolved luminescence measurements were performed with a  $\mu\text{s}$  xenon flashlamp and single photon counting detection in a multi-channel scaling mode. Emission spectra of singlet oxygen were obtained with the FSP 920 spectrometer as well, yet with a cooled NIR-detector (R5509P PMT). All measurements were performed at magic angle conditions using polarizers in the excitation and emission channel set to  $0^\circ$  and  $54.7^\circ$ , respectively. The luminescence decays in solution were analyzed by fitting the obtained decay curves with the program FAST (Fluorescence Analysis Software Technology, Edinburgh Instruments Ltd.). The luminescence quantum yields in solution were determined absolutely using an Ulbricht integrating sphere

setup (Quantaaurus-QY C11347-11, Hamamatsu). Relative uncertainties are estimated to be  $\pm 5\%$ . pH- and  $T$ -dependent emission spectra in solution and Stern-Volmer analyses with azulene were recorded on a Varian Cary Eclipse fluorescence spectrometer.

**Stern-Volmer studies with oxygen** were carried out by measuring the luminescence response (emission intensity and lifetime) of complex solutions to oxygen at different oxygen concentrations. The general procedure was achieved by following the measuring order: oxygen concentration determination of the sample – luminescence emission spectra and lifetimes measurements – control the oxygen concentration in the sample. The oxygen concentration was taken from the average value of the oxygen concentrations before and after the luminescent measurements cycle to minimize the effect of oxygen diffusion during the measurements. Determination of the oxygen partial pressure  $p(\text{O}_2)$  in solution was completed with a commercial fiber-optic oxygen meter Firesting  $\text{O}_2$  from PyroScience and a solvent-resistant oxygen probe tip (OXSOVLPT) from the manufacturer.

**Luminescence emission spectra and decays in KBr pellets** at variable temperature (20 – 290 K at the sample) were recorded in the solid state with a FluoroMax-2 (Horiba Jobin-Yvon) spectrometer using a closed cycle helium cryostat (ARS Model DE-202A). The cryo cooler was equipped with a copper pellet holder and  $\text{CaF}_2$  windows. KBr pellets of  $[\text{Cr}(\text{bpmp})_2][\text{BF}_4]_3$  (ca. 0.7 mg) were prepared by mixing with dry KBr (ca. 200 mg, stored in a compartment dryer at 80 °C, purchased from Merck) and grinding to a homogeneous mixture. Neat films were prepared by spraying a solution of the compound in  $\text{CH}_3\text{CN}$  on a  $\text{CaF}_2$  substrate (13 mm diameter, 1 mm thick), followed by evaporation of the solvent. The luminescence lifetimes were determined with the time-correlated single photon counting technique (TCSPC). Data were recorded with a DeltaFlex (Horiba Scientific) spectrometer. The sample was excited with short light pulses of a SpectraLED (390 nm) and the emission monochromator was set to 707 – 720 nm. The emitted light was detected with a picosecond photon counting (PPT) detection module. In all the static and time-resolved luminescence experiments, a long pass filter (600 nm) was mounted between the sample and the emission monochromator to prevent scattered excitation light from reaching the detector.

**Time-resolved FTIR experiments** were performed with an FTIR spectrometer Bruker Vertex 80v, operated in the step-scan mode. Temperature dependent measurements were performed at 290 K and 20 K by the use of KBr pellets and the cryostat described above. The strongest peak in the ground state spectrum at  $1610\text{ cm}^{-1}$  showed an absorption of about 0.6 OD with the mentioned concentration. A liquid-nitrogen-cooled mercury cadmium telluride (MCT) detector (Kolmar Tech., Model KV100-1-B-7/190) with a rise time of 25 ns, connected to a fast preamplifier and a 14-bit transient recorder board (Spectrum Germany, M3I4142,  $400\text{ MS s}^{-1}$ ), was used for signal detection and processing. The laser setup includes a Q-switched Nd:YAG laser (Innolas SpitLight Evo I) generating pulses with a band-width of 6 ns at a repetition rate of 100 Hz. The third harmonic (355 nm) of the Nd:YAG laser was used for sample excitation. The UV pump beam was attenuated to about 2.0 mJ per shot at a diameter of 9 mm. The beam was directed onto the sample and adjusted to have a maximal overlap with the IR beam of the spectrometer. The sample chamber was equipped with anti-reflection-coated germanium filters to prevent the entrance of laser radiation into the detector and interferometer compartments. The time delay between the start of the experiment and the UV laser pulse was controlled with a Stanford Research Systems DG535 delay generator and the time where the laser pulse reached the sample was set as zero point in all spectra. The temporal resolution was set to 50 ns at 290 K and 100 ns at 20 K. A total of 4000 and 4400 coadditions were recorded at each interferogram point at 290 K and 20 K, respectively. The spectral region was limited by undersampling to  $988 - 1975\text{ cm}^{-1}$  with a spectral resolution of  $4\text{ cm}^{-1}$  resulting in 555 interferogram points. An IR broad band filter ( $850 - 1750\text{ cm}^{-1}$ ) and the  $\text{CaF}_2$  windows (no IR transmission  $< 1000\text{ cm}^{-1}$ ) of the cryostat prevented problems when performing a Fourier transformation (*i.e.* no IR intensity outside the measured region should be observed). FTIR ground state spectra were recorded systematically to check for sample degradation. A more detailed description of the step-scan setup is given here.<sup>27-29</sup>

**Transient absorption spectra** were measured using a Helios-Fire pump-probe setup (Ultrafast systems) paired with a regeneratively amplified 1030 nm laser (Pharos, Light Conversion, 1030 nm, 200 fs, 200  $\mu$ ). The effective laser repetition rate of 1 kHz was set via an internal pulse picker. A small portion of the 1030 nm fundamental is directed to the optical delay line and is subsequently used to generate broadband probe light by focusing onto a sapphire crystal. The pump pulse is generated with an optical parametric amplifier (Orpheus-F, Light Conversion). The pump fluence at the sample was 0.9–2  $\mu$ J/pulse, as noted in the respective experiments. The experiments were run with 5 seconds of averaging at each time delay. Samples were measured in 2 mm path length cuvettes, with an OD of  $\sim$ 1 at 500 nm. Global analysis of the TA data was done using the R-package TAMP software<sup>30</sup> with the graphical interface Glotaran 1.5.1.<sup>31</sup>

**Singlet oxygen quantum yields** were determined optically using the reference [Cr(ddpd)<sub>2</sub>][BF<sub>4</sub>]<sub>3</sub> with a known <sup>1</sup>O<sub>2</sub> quantum yield (0.61 in DMF).<sup>32</sup> Samples and reference were excited at the same wavelength (462 nm) and measured under the same conditions, i.e. using the same fluorimeter settings.  $\Phi[{}^1\text{O}_2]$  was calculated using the following equation:

$$\Phi_S[{}^1\text{O}_2] = \Phi_{Ref}[{}^1\text{O}_2] * \frac{I_S}{I_{Ref}} * \frac{A_{Ref}}{A_S}$$

Here  $\Phi_{Ref}[{}^1\text{O}_2]$ ,  $I_{Ref}$  and  $A_{Ref}$  are assigned to the singlet oxygen quantum yield, the integrated emission intensity ( $\lambda = 1240 - 1360$  nm) and the absorbance of the reference compound in DMF solution, respectively;  $I_S$  and  $A_S$  denote the integrated emission intensity and absorbance of the sample, respectively. As the [Cr(bpmp)<sub>2</sub>]<sup>3+</sup> complexes tend to deprotonate in pure DMF, an acidic environment was provided by adding 2  $\mu$ L HClO<sub>4</sub> (70 – 72 %) to 3 mL DMF solution, achieving a final HClO<sub>4</sub> concentration of ca. 0.01 M. The singlet oxygen quantum yield of [Cr(ddpd)<sub>2</sub>][BF<sub>4</sub>]<sub>3</sub> was determined in DMF/HClO<sub>4</sub> (0.01 M), which was then used as a reference for the [Cr(bpmp)<sub>2</sub>]<sup>3+</sup> complexes in DMF/HClO<sub>4</sub> (0.01 M).

**Table S5. <sup>1</sup>O<sub>2</sub> quantum yields.**

	solvent	$\Phi$ / %
[Cr(ddpd) <sub>3</sub> ][BF <sub>4</sub> ] <sub>3</sub>	DMF	61
[Cr(ddpd) <sub>3</sub> ][BF <sub>4</sub> ] <sub>3</sub>	DMF/HClO <sub>4</sub>	86
[Cr(bpmp) <sub>3</sub> ][OTf] <sub>3</sub>	DMF/HClO <sub>4</sub>	55
[Cr(bpmp) <sub>3</sub> ][PF <sub>6</sub> ] <sub>3</sub>	DMF/HClO <sub>4</sub>	44
[Cr(bpmp) <sub>3</sub> ][BF <sub>4</sub> ] <sub>3</sub>	DMF/HClO <sub>4</sub>	39

**Elemental analyses** were conducted by the microanalytical laboratory of the department of chemistry of the University of Mainz.

**Caution!** Although we have not experienced any problems in handling the perchlorate *solutions*, all materials should be handled with extreme care. Especially, we avoided isolation of *dried perchlorate salts*.

**Crystal structure determinations.** Intensity data were collected with a STOE STADIVARI diffractometer with an Oxford cooling using Mo- $K_{\alpha}$  radiation ( $\lambda = 0.71073 \text{ \AA}$ ). The diffraction frames were integrated using the STOE X-Area software package<sup>33</sup> and most were corrected for absorption with MULABS<sup>34</sup> of the PLATON software package<sup>35</sup> or with STOE LANA<sup>36,37</sup>. The structures were solved by direct methods and refined by the full-matrix method based on  $F^2$  using the SHELX software package<sup>38</sup> using the ShelXle graphical interface<sup>39</sup>. All non-hydrogen atoms were refined anisotropically while the positions of all hydrogen atoms were generated with appropriate geometric constraints and allowed to ride on their respective parent atoms with fixed isotropic thermal parameters. CCDC 1989536 (Cr(bpmp)(OTf)<sub>3</sub>), 1989537 ([Cr(bpmp)<sub>2</sub>][OTf]<sub>3</sub>×CH<sub>3</sub>CH<sub>2</sub>OH) and 2083757 ([Cr(bpmp)<sub>2</sub>][BF<sub>4</sub>]<sub>3</sub>×<sup>5</sup>/<sub>3</sub>CH<sub>3</sub>CN) contain the supplementary crystallographic data for this paper. These data are provided free of charge by The Cambridge Crystallographic Data Centre.

**Crystallographic Data of *mer*-Cr(bpmp)(OTf)<sub>3</sub>×0.25CH<sub>3</sub>CN.** C<sub>20</sub>H<sub>15</sub>CrF<sub>9</sub>N<sub>3</sub>O<sub>9</sub>S<sub>3</sub>×0.25CH<sub>3</sub>CN (770.79); triclinic;  $P\bar{1}$ ;  $a = 9.872(2) \text{ \AA}$ ,  $b = 10.578(2) \text{ \AA}$ ,  $c = 15.838(3) \text{ \AA}$ ,  $\alpha = 70.84(3)^\circ$ ,  $\beta = 86.05(3)^\circ$ ,  $\gamma = 66.13(3)^\circ$ ;  $V = 1424.7(7) \text{ \AA}^3$ ;  $Z = 2$ ; density, calcd. =  $1.797 \text{ g cm}^{-3}$ ,  $T = 120(2) \text{ K}$ ,  $\mu = 0.736 \text{ mm}^{-1}$ ;  $F(000) = 773$ ; crystal size  $0.240 \times 0.214 \times 0.200 \text{ mm}$ ;  $\theta = 2.198$  to  $30.701 \text{ deg.}$ ;  $-14 \leq h \leq 13$ ,  $-14 \leq k \leq 13$ ,  $-22 \leq l \leq 21$ ; rfln collected = 28517; rfln unique = 7881 [ $R(\text{int}) = 0.0349$ ]; completeness to  $\theta = 25.242 \text{ deg.} = 99.9 \%$ ; semi empirical absorption correction from equivalents; max. and min. transmission 1.07582 and 0.94806; data 7881; restraints 24, parameters 434; goodness-of-fit on  $F^2 = 1.031$ ; final indices [ $I > 2\sigma(I)$ ]  $R_1 = 0.0313$ ,  $wR_2 = 0.0854$ ;  $R$  indices (all data)  $R_1 = 0.0391$ ,  $wR_2 = 0.0882$ ; largest diff. peak and hole  $0.562$  and  $-0.656 \text{ e \AA}^{-3}$ .

**Crystallographic Data of *mer*-[Cr(bpmp)<sub>2</sub>][OTf]<sub>3</sub>×CH<sub>3</sub>CH<sub>2</sub>OH.** C<sub>37</sub>H<sub>30</sub>CrF<sub>3</sub>N<sub>6</sub>O<sub>3</sub>S×CH<sub>3</sub>CH<sub>2</sub>OH (1067.92); triclinic;  $P\bar{1}$ ;  $a = 10.550(2) \text{ \AA}$ ,  $b = 12.178(2) \text{ \AA}$ ,  $c = 16.714(3) \text{ \AA}$ ,  $\alpha = 81.77(3)^\circ$ ,  $\beta = 78.79(3)^\circ$ ,  $\gamma = 85.55(3)^\circ$ ;  $V = 2082.0(7) \text{ \AA}^3$ ;  $Z = 2$ ; density, calcd. =  $1.465 \text{ g cm}^{-3}$ ,  $T = 120(2) \text{ K}$ ,  $\mu = 0.533 \text{ mm}^{-1}$ ;  $F(000) = 1090$ ; crystal size  $0.370 \times 0.250 \times 0.120 \text{ mm}$ ;  $\theta = 1.969$  to  $30.985 \text{ deg.}$ ;  $-15 \leq h \leq 15$ ,  $-17 \leq k \leq 17$ ,  $-23 \leq l \leq 24$ ; rfln collected = 42354; rfln unique = 11665 [ $R(\text{int}) = 0.0486$ ]; completeness to  $\theta = 25.242 \text{ deg.} = 100.0 \%$ ; semi empirical absorption correction from equivalents; max. and min. transmission 1.16976 and 0.90213; data 11665; restraints 774, parameters 689; goodness-of-fit on  $F^2 = 1.018$ ; final indices [ $I > 2\sigma(I)$ ]  $R_1 = 0.0340$ ,  $wR_2 = 0.0908$ ;  $R$  indices (all data)  $R_1 = 0.0430$ ,  $wR_2 = 0.0937$ ; largest diff. peak and hole  $0.637$  and  $-0.806 \text{ e \AA}^{-3}$ .

**Crystallographic Data of *mer*-[Cr(bpmp)<sub>2</sub>][BF<sub>4</sub>]<sub>3</sub>×<sup>5</sup>/<sub>3</sub>CH<sub>3</sub>CN.** C<sub>34</sub>H<sub>30</sub>B<sub>3</sub>CrF<sub>12</sub>N<sub>6</sub>×<sup>5</sup>/<sub>3</sub>CH<sub>3</sub>CN (903.49); trigonal;  $P\bar{3}c1$ ;  $a = b = 19.2795(3) \text{ \AA}$ ,  $c = 38.1826(8) \text{ \AA}$ ,  $\alpha = \beta = 90^\circ$ ,  $\gamma = 120^\circ$ ;  $V = 12291.0(5) \text{ \AA}^3$ ;  $Z = 12$ ; density, calcd. =  $1.704 \text{ g cm}^{-3}$ ,  $T = 173(2) \text{ K}$ ,  $\mu = 0.373 \text{ mm}^{-1}$ ;  $F(000) = 5516$ ; crystal size  $0.480 \times 0.245 \times 0.056 \text{ mm}$ ;  $\theta = 2.113$  to  $24.992 \text{ deg.}$ ;  $-20 \leq h \leq 21$ ,  $-20 \leq k \leq 21$ ,  $-42 \leq l \leq 37$ ; rfln collected = 54247; rfln unique = 6527 [ $R(\text{int}) = 0.0283$ ]; completeness to  $\theta = 24.992 \text{ deg.} = 90.3 \%$ ; semi empirical absorption correction from equivalents; max. and min. transmission 0.9949 and 0.2028; data 6527; restraints 276, parameters 688; goodness-of-fit on  $F^2 = 1.111$ ; final indices [ $I > 2\sigma(I)$ ]  $R_1 = 0.0463$ ,  $wR_2 = 0.0685$ ;  $R$  indices (all data)  $R_1 = 0.1339$ ,  $wR_2 = 0.1395$ ; largest diff. peak and hole  $1.553$  and  $-0.711 \text{ e \AA}^{-3}$ .



**Synthesis of Cr(bpmp)Cl<sub>3</sub>** (procedure adapted from ref. 40). A pale yellow solution of bpmp (2.07 g, 7.92 mmol) in isopropanol (50 mL) was added to a green solution of chromium(III) chloride hexahydrate (2.11 g, 7.92 mmol) in isopropanol (150 mL). The green mixture was heated to 82 °C for 15 hours yielding a dark green precipitate. After cooling, the suspension was filtered and the solid was washed with warm ethanol (2 x 50 mL) and diethyl ether (2 x 70 mL). The dark green product was dried under reduced pressure. Yield: 3.22 g (7.67 mmol, 97 %). MS (ESI<sup>+</sup>, CH<sub>3</sub>CN): *m/z* (%) = 383.00 (100) [Cr(bpmp)Cl<sub>3</sub>-Cl]<sup>+</sup>. IR (ATR):  $\tilde{\nu}$  = 2890 (w), 1604 (s), 1577 (m), 1566 (w), 1483 (m), 1459 (s), 1432 (s), 1416 (m), 1292 (m), 1238 (vw), 1221 (vw), 1172 (w), 1156 (vw), 1131 (vw), 1107 (w), 1060 (m), 1025 (m), 1004 (vw), 977 (vw), 930 (m), 913 (vw), 887 (vw), 849 (m), 792 (m), 771 (vs), 739 (m), 724 (vw), 667 (vw), 651 (m), 621 (s), 604 (w), 594 (w), 554 (vw), 474 (m), 458 (w), 443 (s), 413 (m) cm<sup>-1</sup>. Elemental analysis calcd. (%) for C<sub>17</sub>H<sub>15</sub>Cl<sub>3</sub>CrN<sub>3</sub> (419.68): C 48.65 H 3.60, N 10.01; found C 48.45, H 3.31 N 9.31.

**Synthesis of Cr(bpmp)Br<sub>3</sub>** (procedure adapted from ref. 40). A pale yellow solution of bpmp (2.52 g, 9.64 mmol) in isopropanol (50 mL) was added to a green solution of chromium(III) bromide hexahydrate (3.85 g, 9.64 mmol) in isopropanol (200 mL). The green mixture was heated to 82 °C for 15 hours yielding a green precipitate. After cooling, the suspension was filtered and the solid was washed with warm ethanol (2 x 50 mL) and diethyl ether (2 x 70 mL). The green product was dried under reduced pressure. Yield: 5.01 g (9.06 mmol, 94 %). MS (ESI<sup>+</sup>, CH<sub>3</sub>CN): *m/z* (%) = 450.01 (100) [Cr(bpmp)Br<sub>3</sub>-2Br+OH+CH<sub>3</sub>CN]<sup>+</sup>, 472.90 (51) [Cr(bpmp)Br<sub>3</sub>-Br]<sup>+</sup>, 513.93 (28) [Cr(bpmp)Br<sub>3</sub>-Br+CH<sub>3</sub>CN]<sup>+</sup>. IR (ATR):  $\tilde{\nu}$  = 2873 (w), 1604 (s), 1576 (m), 1565 (w), 1483 (m), 1458 (s), 1431 (m), 1412 (m), 1292 (m), 1276 (vw), 1237 (vw), 1219 (vw), 1172 (w), 1157 (vw), 1131 (vw), 1107 (w), 1062 (m), 1023 (m), 1001 (vw), 974 (vw), 927 (m), 885 (vw), 849 (m), 789 (m), 769 (vs), 737 (m), 649 (m), 621 (s), 604 (w), 594 (w), 553 (vw), 517 (vw), 472 (m), 454 (w), 441 (s), 421 (vw), 408 (m) cm<sup>-1</sup>. Elemental analysis calcd. (%) for C<sub>17</sub>H<sub>15</sub>Br<sub>3</sub>CrN<sub>3</sub> (553.03): C 36.92 H 2.73, N 7.60; found C 36.38, H 2.81 N 7.13.

**Synthesis of Cr(bpmp)(OTf)<sub>3</sub>** (procedure adapted from ref. 41). Anhydrous triflic acid (6.0 mL, 68.4 mmol) was added under argon atmosphere to Cr(bpmp)Cl<sub>3</sub> (2.15 g, 5.12 mmol) or [Cr(bpmp)Br<sub>3</sub>] (2.83 g, 5.12 mmol), respectively. The reaction mixture turned dark red immediately together with gas evolution. The HCl (HBr) was detected by bubbling the gas into an aqueous solution of silver nitrate. After stirring at room temperature for four hours, the solution was cooled with ice and dry diethylether (400 mL) was added. The precipitate was collected by filtration, washed with dry diethyl ether (2 x 80 mL) and dried under reduced pressure. Yield: 3.82 g (5.02 mmol, 98 %) (from Cr(bpmp)Cl<sub>3</sub>) and 3.67 g (4.8 mmol, 94 %) (from Cr(bpmp)Br<sub>3</sub>). Cooling a concentrated solution of Cr(bpmp)(OTf)<sub>3</sub> in acetonitrile yielded dichroic green/purple single crystals of Cr(bpmp)(OTf)<sub>3</sub>·<sup>1</sup>/<sub>4</sub>CH<sub>3</sub>CN suitable for single crystal XRD. MS (APCI, CH<sub>3</sub>CN): *m/z* (%) = 610.97 (100) [Cr(bpmp)(OTf)<sub>3</sub>-OTf]<sup>+</sup>, 628.98 (14) [Cr(bpmp)(OTf)<sub>3</sub>-OTf+H<sub>2</sub>O]<sup>+</sup>, 652.00 (66) [Cr(bpmp)(OTf)<sub>3</sub>-OTf+CH<sub>3</sub>CN]<sup>+</sup>. IR (ATR):  $\tilde{\nu}$  = 3094 (vw), 2936 (vw), 1613 (m), 1580 (w), 1496 (w), 1465 (m), 1441 (m), 1347 (s), 1260 (m), 1236 (s), 1201 (vs), 1114 (w), 1073 (w), 1031 (s), 986 (s), 931 (w), 850 (w), 769 (m), 738 (vw), 660 (w), 634 (s), 594 (w), 572 (w), 513 (m), 458 (w), 441 (m), 416 (w) cm<sup>-1</sup>.

**Synthesis of [Cr(bpmp)<sub>2</sub>][OTf]<sub>3</sub>**. A pale yellow solution of bpmp (1.38 g, 5.28 mmol) in dry acetonitrile (20 mL) was added to a dark green solution of Cr(bpmp)(OTf)<sub>3</sub> (2.01 g, 2.64 mmol) in dry acetonitrile (80 mL). The solution was heated at 60 °C for 20 hours. The solvent of the resulting dark yellow/brown solution was removed under reduced pressure. The residue was heated in tetrahydrofuran (200 mL) and the insoluble yellow solid was collected by filtration, washed with THF (50 mL) and diethyl ether (50 mL) und dried under reduced pressure. Diffusion of diethyl ether into a concentrated solution of [Cr(bpmp)<sub>2</sub>](OTf)<sub>3</sub> in ethanol/anhydrous triflic acid (100:1) yielded orange diffraction quality crystals of [Cr(bpmp)<sub>2</sub>](OTf)<sub>3</sub>·C<sub>2</sub>H<sub>5</sub>OH. Yield: 1.11 g (1.09 mmol, 41 %). MS (ESI<sup>+</sup>, CH<sub>3</sub>CN): *m/z* (%) = 191.73 (4) [Cr(bpmp)<sub>2</sub>]<sup>3+</sup>, 286.59 (13) [Cr(bpmp)<sub>2</sub>-H]<sup>2+</sup>, 572.18 (100) [Cr(bpmp)<sub>2</sub>-2H]<sup>+</sup>. IR (ATR):  $\tilde{\nu}$  = 3554 (w), 3091 (vw), 1610 (s), 1578 (m), 1491 (m), 1466 (m), 1442 (m), 1259 (vs), 1225 (s), 1157 (s), 1112 (w), 1073 (w), 1029 (vs), 929 (vw), 847 (w), 776 (m), 737 (vw), 657 (m), 637 (s), 592 (w), 574 (m), 518 (m), 445 (m) cm<sup>-1</sup>. Elemental analysis calcd. (%) for C<sub>37</sub>H<sub>30</sub>CrN<sub>6</sub>O<sub>9</sub>F<sub>9</sub>S<sub>3</sub> (1021.85): C 43.49 H 2.96, N 8.22; found C 43.68, H 2.47 N 7.84.

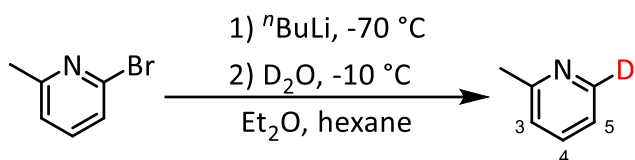
**Synthesis of [Cr(bpmp)<sub>2</sub>][PF<sub>6</sub>]<sub>3</sub>.** A dark yellow solution of [Cr(bpmp)<sub>2</sub>](O<sub>3</sub>SCF<sub>3</sub>)<sub>3</sub> (0.50 g, 0.489 mmol) in ethanol (200 mL) was acidified with two drops of triflic acid resulting in a pale yellow solution. A solution of tetra-*n*-butylammonium hexafluorophosphate (1.14 g, 2.94 mmol) in ethanol (80 mL) was added while stirring. A yellow solid precipitated immediately. After stirring for one hour, the suspension was filtered. The collected solid was washed with ethanol (3 × 20 ml) and diethyl ether (3 × 20 ml) and dried under reduced pressure. Yield: 0.29 g (0.287 mmol, 59 %). MS (ESI<sup>+</sup>, CH<sub>3</sub>CN): *m/z* (%) = 191.40 (1) [Cr(bpmp)<sub>2</sub>]<sup>3+</sup>, 286.59 (10) [Cr(bpmp)<sub>2</sub>-H]<sup>2+</sup>, 572.18 (100) [Cr(bpmp)<sub>2</sub>-2H]<sup>+</sup>, 718.15 (41) [Cr(bpmp)<sub>2</sub>-H+PF<sub>6</sub>]<sup>+</sup>. IR (ATR):  $\tilde{\nu}$  = 3103 (vw), 1608 (s), 1576 (m), 1490 (m), 1463 (m), 1444 (m), 1410 (m), 1296 (m), 1243 (w), 1220 (w), 1173 (m), 1124 (w), 1112 (w), 1074 (m), 1028 (s), 928 (w), 888 (m), 824 (vs, PF), 771 (s), 656 (m), 620 (m), 593 (w), 554 (vs, PF), 471 (m), 440 (s) cm<sup>-1</sup>. Elemental analysis calcd. (%) for C<sub>34</sub>H<sub>30</sub>CrN<sub>6</sub>F<sub>18</sub>P<sub>3</sub> (1009.53): C 40.45 H 3.00, N 8.32; found C 40.12, H 2.93 N 8.16.

**Synthesis of [Cr(bpmp)<sub>2</sub>][BF<sub>4</sub>]<sub>3</sub>.** A dark yellow solution of [Cr(bpmp)<sub>2</sub>](O<sub>3</sub>SCF<sub>3</sub>)<sub>3</sub> (0.50 g, 0.489 mmol) in ethanol (200 mL) was acidified with two drops of tetrafluoroboric acid diethyl ether complex resulting in a pale yellow solution. A solution of tetra-*n*-butylammonium tetrafluoroborate (0.97 g, 2.94 mmol) in ethanol (20 ml) was added while stirring. A yellow solid precipitated immediately. After stirring for one hour, the suspension was filtered. The collected solid was washed with ethanol (3 × 20 ml) and diethyl ether (3 × 20 ml) and dried under reduced pressure. Diffusion of diethyl ether into a concentrated solution of the complex in acetonitrile/tetrafluoroboric acid diethyl ether complex (100:1) yielded orange diffraction quality crystals of [Cr(bpmp)<sub>2</sub>](BF<sub>4</sub>)<sub>3</sub>×3CH<sub>3</sub>CN. Yield: 0.28 g (0.335 mmol, 69 %). MS (ESI<sup>+</sup>, CH<sub>3</sub>CN): *m/z* (%) = 191.40 (1) [Cr(bpmp)<sub>2</sub>]<sup>3+</sup>, 286.59 (8) [Cr(bpmp)<sub>2</sub>-H]<sup>2+</sup>, 572.18 (100) [Cr(bpmp)<sub>2</sub>-2H]<sup>+</sup>, 660.19 (15) [Cr(bpmp)<sub>2</sub>-H+BF<sub>4</sub>]<sup>+</sup>. IR (ATR):  $\tilde{\nu}$  = 1610 (s), 1578 (m), 1491 (m), 1464 (m), 1438 (m), 1422 (m), 1296 (m), 1171 (w), 1054 (vs, B-F), 1026 (vs, B-F), 928 (m), 845 (m), 773 (s, -B-F), 695 (w), 657 (m), 637 (m), 619 (m), 594 (m), 543 (w), 564 (w), 519 (s), 474 (m), 456 (s), 440 (s), 430 (m), 412 (s) cm<sup>-1</sup>. Elemental analysis calcd. (%) for C<sub>34</sub>H<sub>30</sub>CrN<sub>6</sub>F<sub>12</sub>B<sub>3</sub> (835.05)×3H<sub>2</sub>O: C 45.93 H 4.08, N 9.45; found C 46.02, H 3.25 N 9.46.

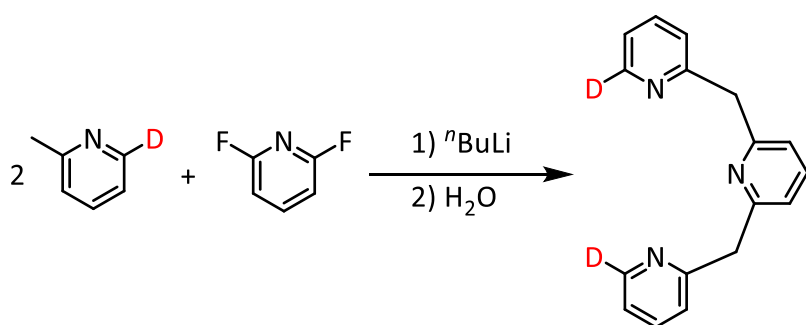
**Synthesis of [Cr(bpmp)<sub>2</sub>][ClO<sub>4</sub>]<sub>3</sub>.** The synthesis of this salt is in principle analogous to the preparation of the PF<sub>6</sub><sup>-</sup> and BF<sub>4</sub><sup>-</sup> salts. However, the *dried* perchlorate salt can be explosive and we do not wish to report its isolation and full characterization as dried material. Instead, we merely report some photophysical data in solution obtained from the *non-dried complex*.

**Synthesis of [Cr([D<sub>4</sub>]-bpmp)<sub>2</sub>][PF<sub>6</sub>]<sub>3</sub>.** [Cr(bpmp)<sub>2</sub>](PF<sub>6</sub>)<sub>3</sub> (200 mg, 0.20 mmol) was suspended in D<sub>2</sub>O (8 mL, NMR grade, 99.9 % D) and stirred under argon for 10 h. The solvent was removed under reduced pressure. This procedure was repeated twice. Diffusion of diethyl ether into a solution of the complex in CH<sub>3</sub>OD yielded crystals of [Cr([D<sub>4</sub>]-bpmp)<sub>2</sub>][PF<sub>6</sub>]<sub>3</sub> (142 mg, 0.14 mmol, 70 %) as orange needles. MS (ESI<sup>+</sup>, CH<sub>3</sub>CN): *m/z* (%) = 193.07 (5), 289.11 (21), 576.20 (100), 723.18 (88) (partial H/D exchange at the methylene groups occurs in the mass spectrometer). IR (ATR):  $\tilde{\nu}$  = 1611 (s), 1577 (m), 1491 (m), 1464 (m), 1438 (m), 1266 (m), 1171 (m), 1113 (w), 1074 (w), 1029 (s), 836 (vs, PF), 765 (s), 740 (m), 656 (m), 639 (s), 621 (w), 556 (vs, PF), 518 (m), 457 (m), 437 (s) cm<sup>-1</sup>.

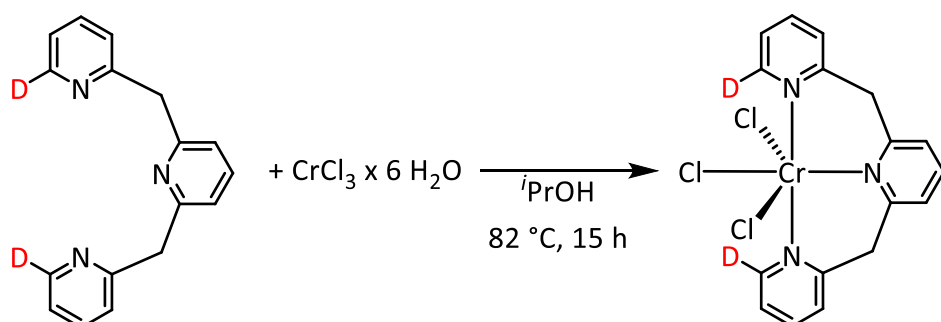
**Synthesis of 6-deutero-2-methylpyridine:** A solution of *n*-butyllithium in hexane (56 mL, 2.5 M) was added dropwise within half an hour to a solution of 2-bromo-6-methylpyridine (15.9 mL, 140 mmol) in dry diethyl ether (600 mL) while cooling to -70 °C (ethanol/dry ice). The orange reaction mixture was stirred for three hours at -70 °C and then warmed to -10 °C. Deuterium oxide (100 mL, 99.9 % D) was added dropwise within half an hour. After phase separation, the aqueous phase was extracted with diethylether (3 × 100 mL). The combined organic phases were dried with sodium sulfate and the solvent was removed under reduced pressure. The colorless to yellow product was isolated by distillation (128°C, ambient pressure). Yield: 11.49 g (122 mmol, 87 %). C<sub>5</sub>H<sub>6</sub>DNBr (162.03). <sup>1</sup>H NMR (400 MHz, CDCl<sub>3</sub>):  $\delta$  = 7.50 (t, <sup>3</sup>J<sub>HH</sub> = 7.7 Hz, 1H, H<sup>4</sup>), 7.09 (d, <sup>3</sup>J<sub>HH</sub> = 7.8 Hz, 1H, H<sup>5</sup>), 7.02 (d, <sup>3</sup>J<sub>HH</sub> = 7.5 Hz, 1H, H<sup>3</sup>), 2.50 (s, 3H, CH<sub>3</sub>).



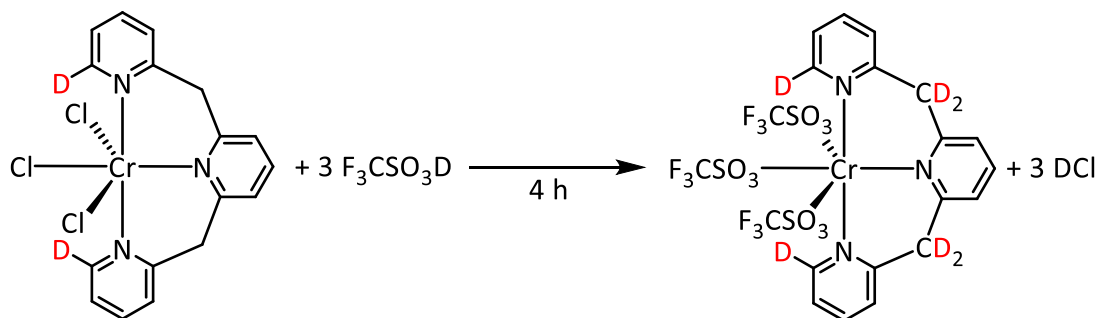
**Synthesis of [D<sub>2</sub>]-bpmp (analogous to the synthesis of the non-deuterated ligand, ref. 24):** A solution of *n*-butyllithium in hexane (48 mL, 2.5 M) was added dropwise within half an hour to a pale yellow solution of 6-deutero-2-methylpyridine (11.33 g, 120 mmol) in dried tetrahydrofuran (80 mL) while cooling to  $-70\text{ }^{\circ}\text{C}$  (ethanol/dry ice). The orange mixture was stirred at  $-70\text{ }^{\circ}\text{C}$  for two hours and then warmed to  $-20\text{ }^{\circ}\text{C}$ . 2,6-Difluoropyridine (1.09 mL, 12.0 mmol) was added and the mixture was heated to reflux at  $60\text{ }^{\circ}\text{C}$  for 24 hours. After cooling to room temperature, water (50 mL) was added dropwise and the phases were separated. The aqueous phase was extracted with dichloromethane ( $3 \times 50\text{ mL}$ ), the combined organic layers were dried with sodium sulfate and the solvents were removed under reduced pressure. The product was purified by column chromatography (Alox, 1:1 cyclohexane/ethyl acetate) yielding a yellow oil ( $R_f = 0.32$ ). Yield: 0.80 g (3.04 mmol, 25 %).  $\text{C}_{17}\text{H}_{13}\text{D}_2\text{N}_3$  (263.33).  $^1\text{H NMR}$  (400 MHz,  $\text{CD}_2\text{Cl}_2$ ):  $\delta = 7.59$  (t,  $^3J_{\text{HH}} = 7.6\text{ Hz}$ , 2H, H<sup>7</sup>), 7.52 (t,  $^3J_{\text{HH}} = 7.7\text{ Hz}$ , 1H, H<sup>1</sup>), 7.23 (d,  $^3J_{\text{HH}} = 7.8\text{ Hz}$ , 2H, H<sup>6</sup>), 7.12 (d,  $^3J_{\text{HH}} = 7.5\text{ Hz}$ , 2H, H<sup>8</sup>), 7.06 (d,  $^3J_{\text{HH}} = 7.7\text{ Hz}$ , 2H, H<sup>2</sup>), 4.27 (s, 4H, H<sup>4</sup>). MS (ESI<sup>+</sup>,  $\text{CH}_3\text{CN}$ ):  $m/z$  (%) = 264.1 (100) [[D<sub>2</sub>]-bpmp+H]<sup>+</sup>, 286.1 (41) [[D<sub>2</sub>]-bpmp+Na]<sup>+</sup>, 326.1 (21) [[D<sub>2</sub>]-bpmp+Cu]<sup>+</sup>, 550.3 (43) [2x[D<sub>2</sub>]-bpmp+Na]<sup>+</sup>.



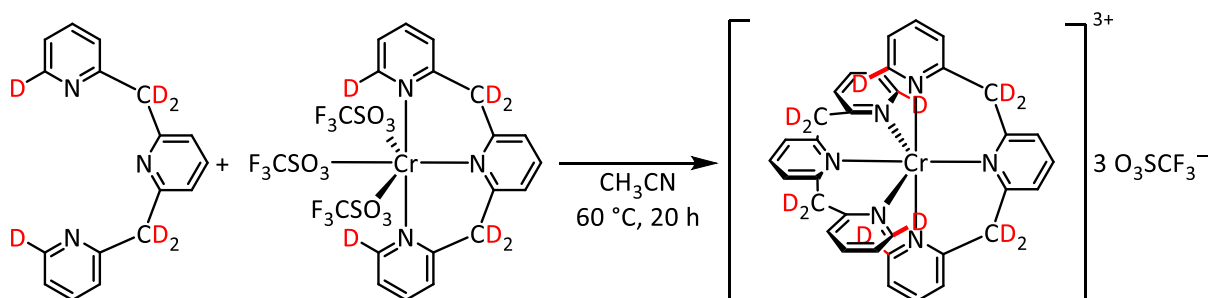
**Synthesis of Cr([D<sub>2</sub>]-bpmp)Cl<sub>3</sub>:** A pale yellow solution of [D<sub>2</sub>]-bpmp (0.30 g, 1.14 mmol) in isopropanol (8 mL) was added to a green solution of chromium(III) chloride hexahydrate (0.30 g, 1.14 mmol) in isopropanol (25 mL). The reaction mixture was heated for 15 hours to  $82\text{ }^{\circ}\text{C}$  yielding a dark green precipitate. After cooling to room temperature, the solution was decanted and the solid was washed with warm ethanol ( $2 \times 10\text{ mL}$ ) and diethyl ether ( $2 \times 10\text{ mL}$ ). The dark green product was dried under reduced pressure. Yield: 0.47 g (1.11 mmol, 98 %). MS (ESI<sup>+</sup>,  $\text{CH}_3\text{CN}$ ):  $m/z$  (%) = 385.0 (33) [Cr([D<sub>2</sub>]-bpmp)Cl<sub>3</sub>-Cl]<sup>+</sup>, 426.0 (100) [Cr([D<sub>2</sub>]-bpmp)Cl<sub>3</sub>-Cl+CH<sub>3</sub>CN]<sup>+</sup>, 445.0 (24) [Cr([D<sub>2</sub>]-bpmp)Cl<sub>3</sub>+Na]<sup>+</sup>, 867.0 (56) [2x Cr([D<sub>2</sub>]-bpmp)Cl<sub>3</sub>+Na]<sup>+</sup>. MS (APCI,  $\text{CH}_3\text{CN}$ ):  $m/z$  (%) = 385.0 (100) [Cr([D<sub>2</sub>]-bpmp)Cl<sub>3</sub>-Cl]<sup>+</sup>. IR (ATR):  $\tilde{\nu} = 3088$  (w), 2975 (vw), 2982 (m), 1597 (s), 1577 (m), 1562 (m), 1461 (s), 1447 (s), 1420 (s), 1286 (vw), 1237 (m), 1167 (m), 1132 (w), 1099 (m), 1061 (w), 1026 (m), 938 (m), 915 (m), 876 (w), 865 (w), 838 (m), 825 (m), 794 (m), 774 (m), 757 (s), 701 (m), 605 (s), 555 (w), 458 (m), 443 (m), 424 (vs), 410 (m)  $\text{cm}^{-1}$ .



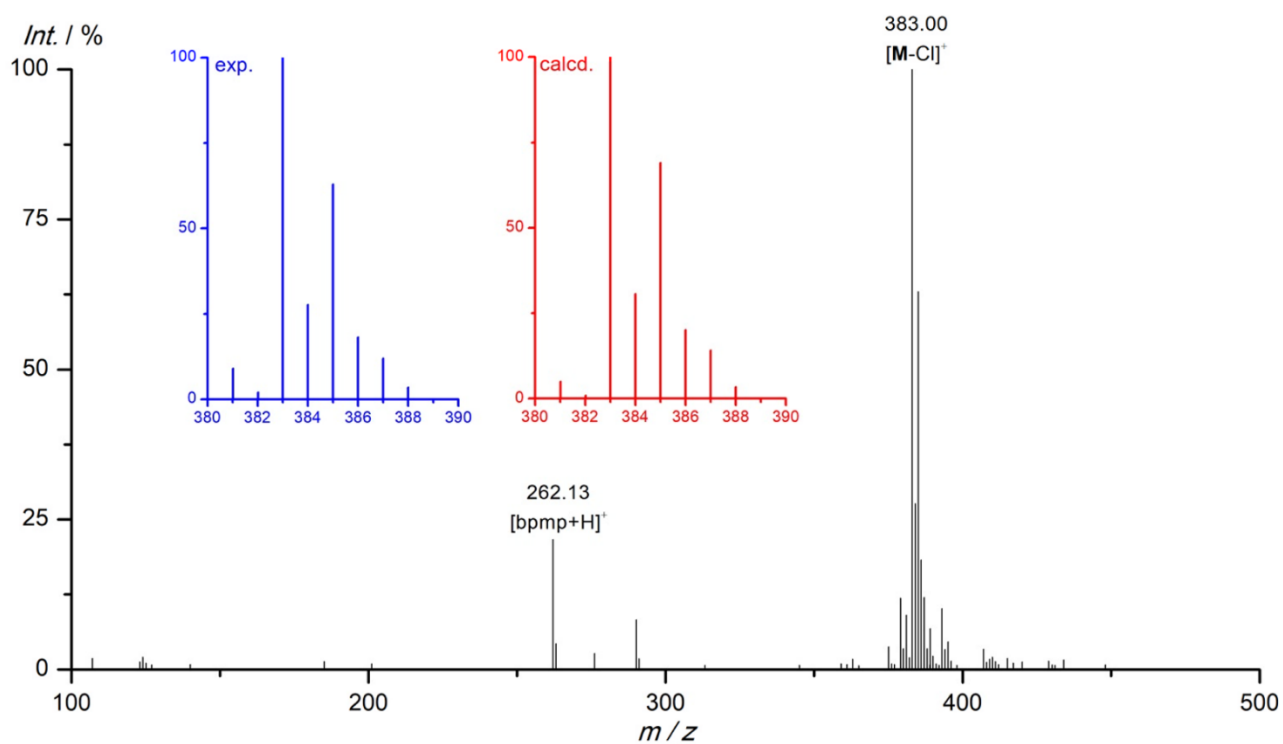
**Synthesis of  $\text{Cr}([\text{D}_2\text{-bpmp}])\text{(O}_3\text{SCF}_3)_3$ :** Anhydrous deuterated triflic acid (0.76 mL, 8.54 mmol, 98 % D) was added under inert conditions to  $\text{Cr}([\text{D}_2\text{-bpmp}])\text{Cl}_3$  (0.24 g, 0.569 mmol). The reaction mixture turned dark red immediately together with evolution of hydrogen chloride gas. After stirring at room temperature for two hours, dry diethylether (10 mL) was added giving a red brown solid. After decanting, the product was washed with dried diethyl ether ( $2 \times 10$  mL) and dried under reduced pressure. Yield: 0.42 g (0.551 mmol, 97 %). MS (ESI<sup>+</sup>, CH<sub>3</sub>CN):  $m/z$  (%) = 613.0 (4)  $[\text{Cr}([\text{D}_2\text{-bpmp}])\text{(OTf)}_3\text{-OTf}]^+$ , 654.0 (2)  $[\text{Cr}([\text{D}_2\text{-bpmp}])\text{(OTf)}_3\text{-OTf+CH}_3\text{CN}]^+$ . MS (APCI, CH<sub>3</sub>CN):  $m/z$  (%) = 613.0 (100)  $[\text{Cr}([\text{D}_2\text{-bpmp}])\text{(OTf)}_3\text{-OTf}]^+$ , 631.0 (10)  $[\text{Cr}([\text{D}_2\text{-bpmp}])\text{(OTf)}_3\text{-OTf+H}_2\text{O}]^+$ , 654.0 (49)  $[\text{Cr}([\text{D}_2\text{-bpmp}])\text{(OTf)}_3\text{-OTf+CH}_3\text{CN}]^+$ . IR (ATR):  $\tilde{\nu}$  = 3107 (w), 2939 (w), 1633 (m), 1609 (m), 1536 (vw), 1464 (vw), 1345 (s), 1286 (m), 1235 (vs), 1199 (vs), 1028 (s), 997 (s), 843 (vw), 764 (w), 634 (vs), 574 (m), 516 (m), 426 (m) cm<sup>-1</sup>.



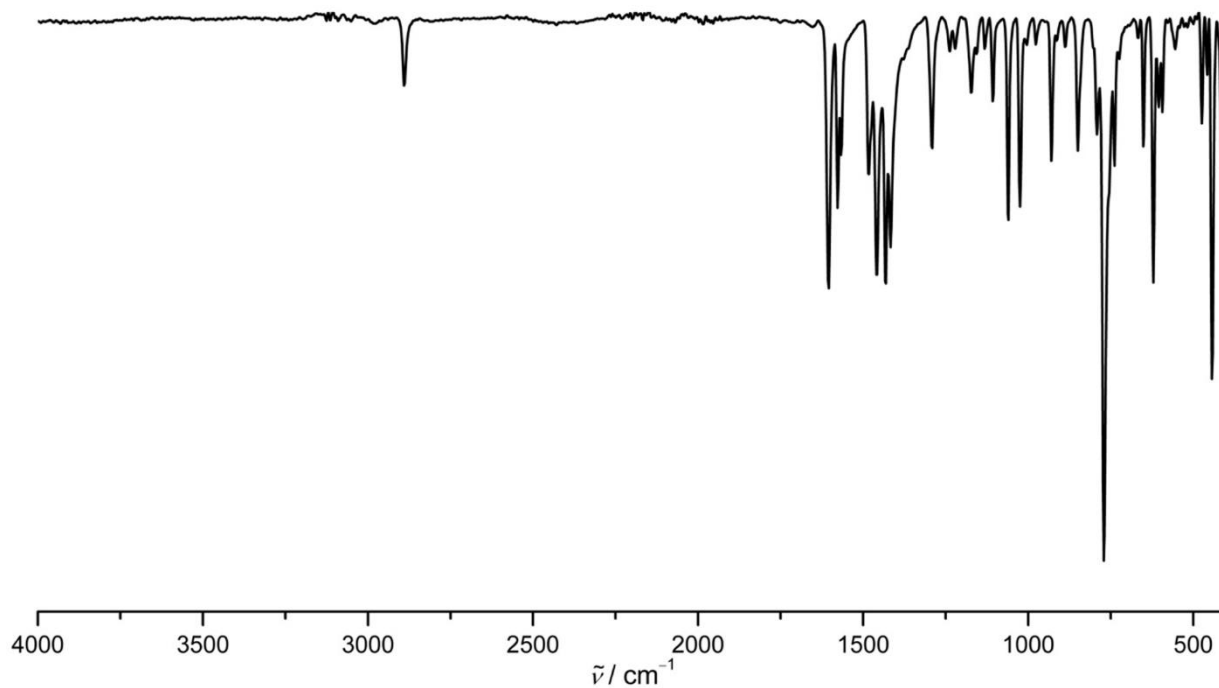
**Synthesis of  $[\text{Cr}([\text{D}_2/\text{D}_6\text{-bpmp}]_2)]\text{(O}_3\text{SCF}_3)_3$ :** A pale yellow solution of  $[\text{D}_2\text{-bpmp}]$  (0.28 g, 1.05 mmol) in dry acetonitrile (4 mL) was added dropwise to a green solution of  $\text{Cr}([\text{D}_2\text{-bpmp}])\text{(O}_3\text{SCF}_3)_3$  (0.40 g, 0.525 mmol) in dry acetonitrile (16 mL). The initially dark green solution was heated for 20 hours to 60 °C, resulting in a dark yellow to brown mixture. The solvent was removed under reduced pressure and the residue was heated in tetrahydrofuran (50 mL). After cooling to room temperature, the solvent was decanted and the yellow solid was washed with tetrahydrofuran (20 mL) and diethyl ether (20 mL) and dried under reduced pressure. Yield: 0.23 g (0.224 mmol, 43 %). MS (ESI<sup>+</sup>, CH<sub>3</sub>CN):  $m/z$  (%) = 193.1 (5)  $[\text{Cr}([\text{D}_2\text{-bpmp}]_2)]^{3+}$ , 289.1 (12)  $[[\text{Cr}([\text{D}_2\text{-bpmp}]_2)\text{-H}]^{2+}$ , 577.2 (100)  $[[\text{Cr}([\text{D}_2\text{-bpmp}]_2)\text{-2H}]^+$ . MS (APCI, CH<sub>3</sub>CN):  $m/z$  (%) = 576.2 (100)  $[[\text{Cr}([\text{D}_2\text{-bpmp}]_2)\text{-2H}]^+$ , 617.2 (3)  $[[\text{Cr}([\text{D}_2\text{-bpmp}]_2)\text{-2H+CH}_3\text{CN}]^+$ . Partial H/D exchange at the methylene groups occurs in the mass spectrometer. IR (ATR):  $\tilde{\nu}$  = 3091 (vw), 2998 (vw), 1604 (s), 1577 (m), 1465 (m), 1432 (m), 1258 (vs), 1224 (s), 1155 (s), 1107 (m), 1029 (vs), 934 (vw), 917 (w), 839 (m), 785 (m), 755 (m), 700 (vw), 636 (vs), 606 (m), 573 (m), 517 (m), 455 (m), 430 (m) cm<sup>-1</sup>.



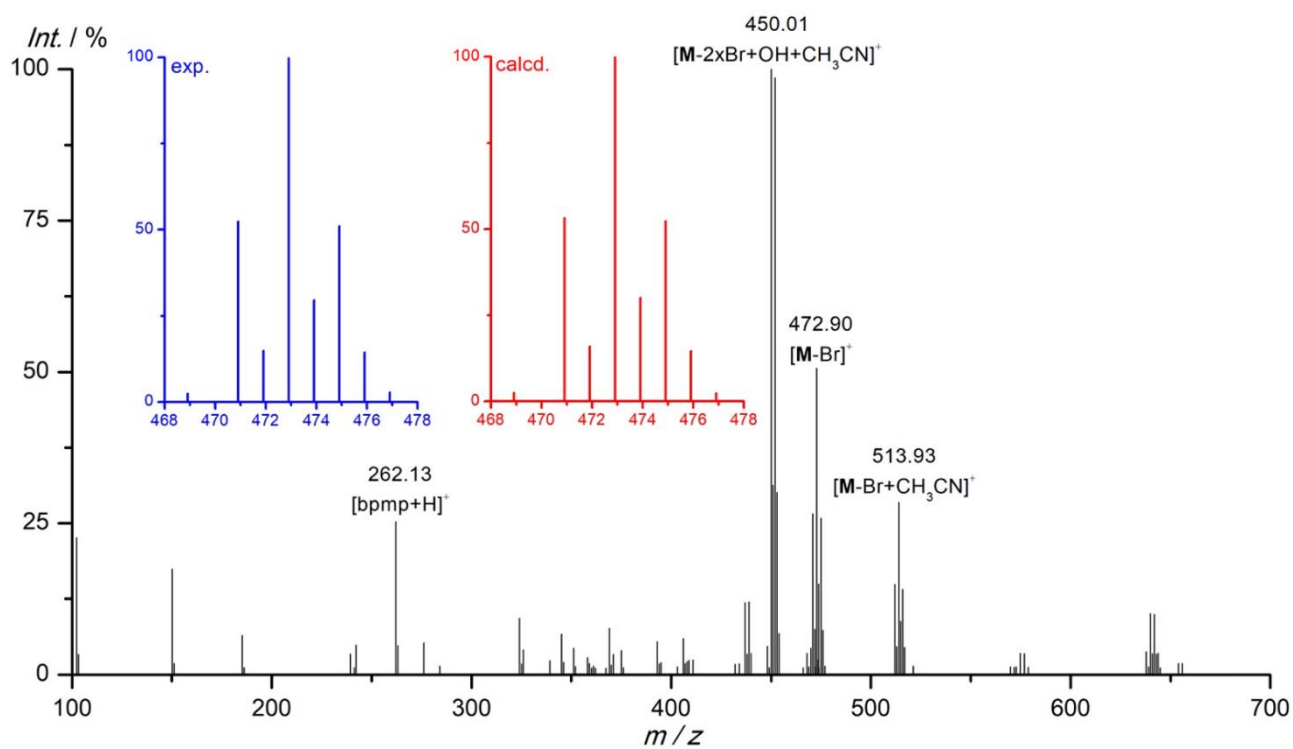
**pH sensing with  $[\text{Cr}(\text{bpmp})_2][\text{O}_3\text{SCF}_3]_3$  and  $[\text{Cr}(\text{ddpd})_2][\text{BF}_4]_3$ .** An aqueous solution of  $[\text{Cr}(\text{bpmp})_2][\text{O}_3\text{SCF}_3]_3$  and  $[\text{Cr}(\text{ddpd})_2][\text{BF}_4]_3$  (25:2 molar ratio) was set to various pH values under ambient conditions. Luminescence spectra were obtained using  $\lambda_{\text{exc}} = 452$  nm and normalized to the emission band at ca. 777 nm.



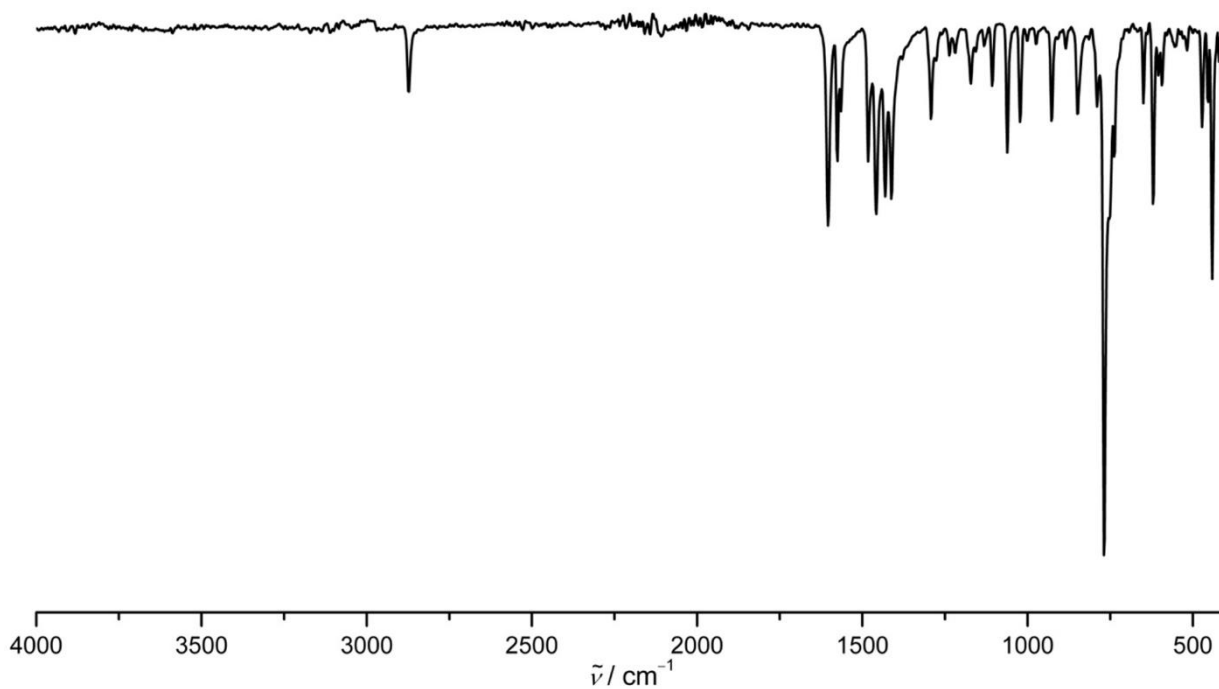
**Figure S1.** ESI<sup>+</sup> mass spectrum of Cr(bmp)Cl<sub>3</sub> in CH<sub>3</sub>CN. The insets depict the experimental (blue) and calculated (red) isotopic pattern of the peak at *m/z* 383 ([Cr(bmp)Cl<sub>3</sub>-Cl]<sup>+</sup>).



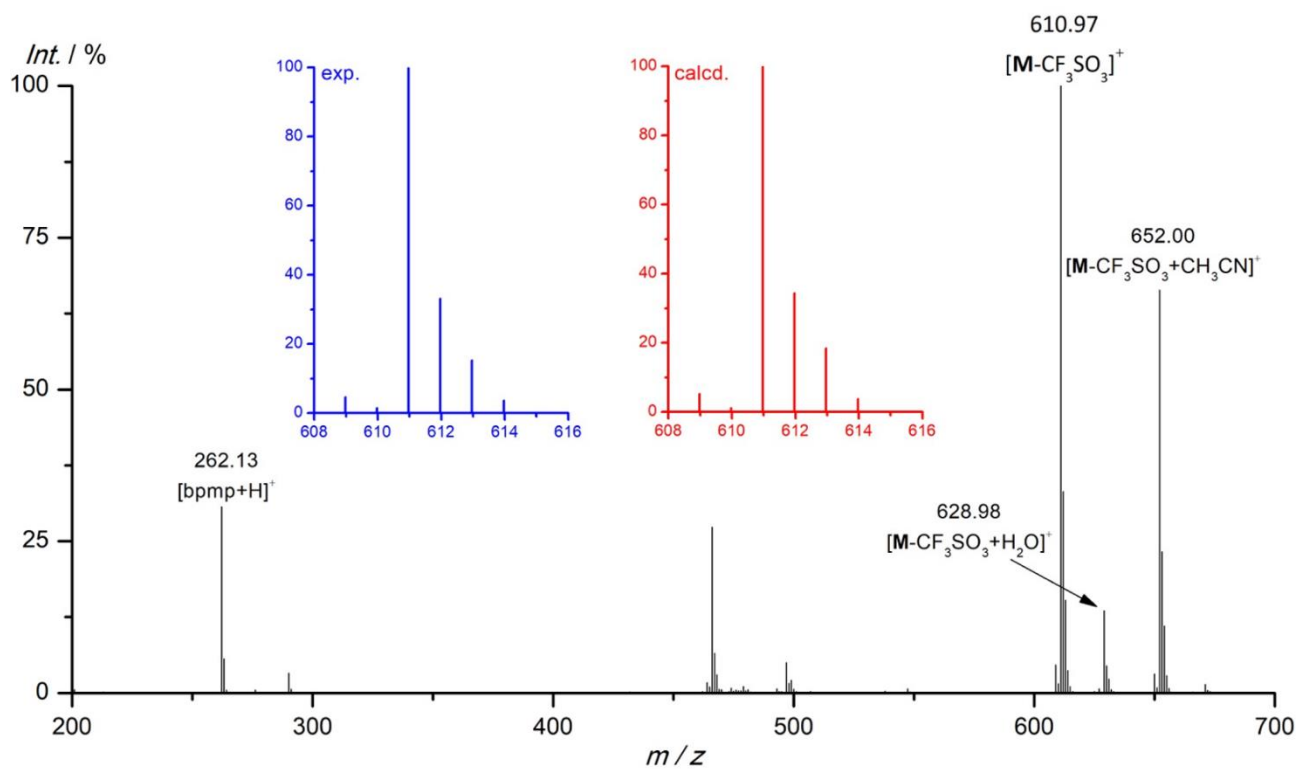
**Figure S2.** ATR-IR spectrum of Cr(bmp)Cl<sub>3</sub>.



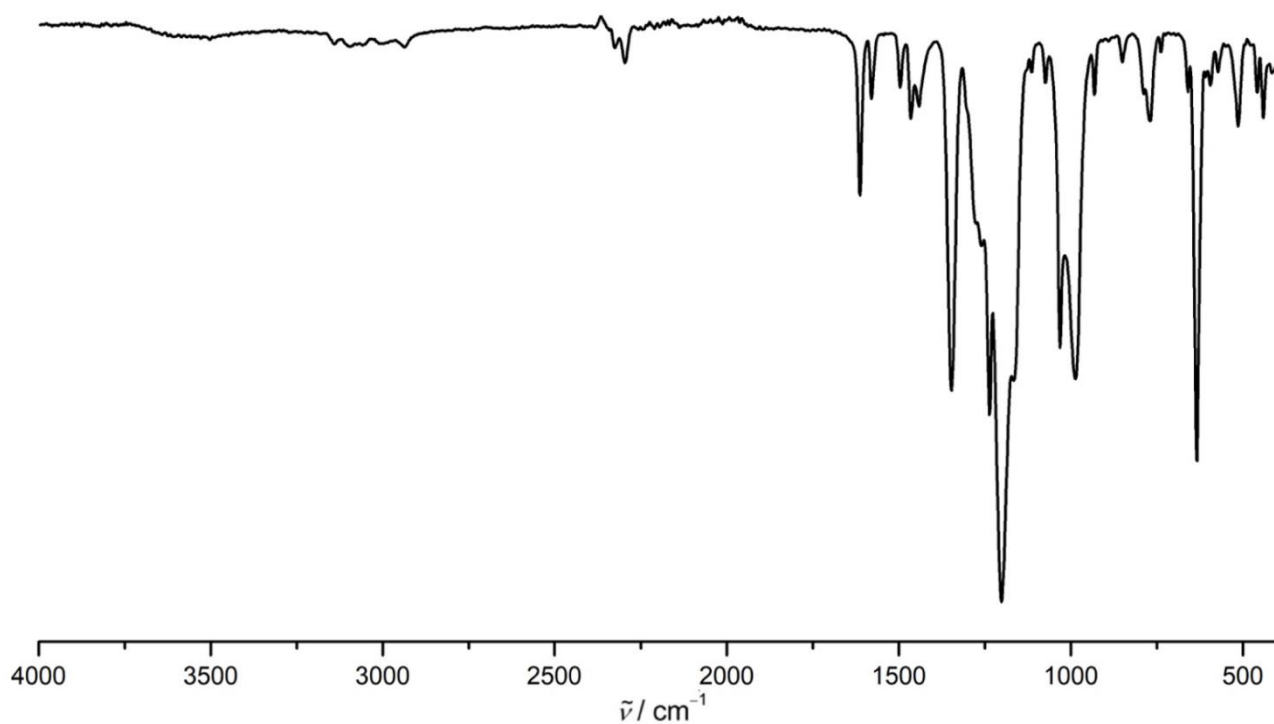
**Figure S3.** ESI<sup>+</sup> mass spectrum of Cr(bpmp)Br<sub>3</sub> in CH<sub>3</sub>CN. The insets depict the experimental (blue) and calculated (red) isotopic pattern of the peak at *m/z* 473 ([Cr(bpmp)Br<sub>3</sub>-Br]<sup>+</sup>).



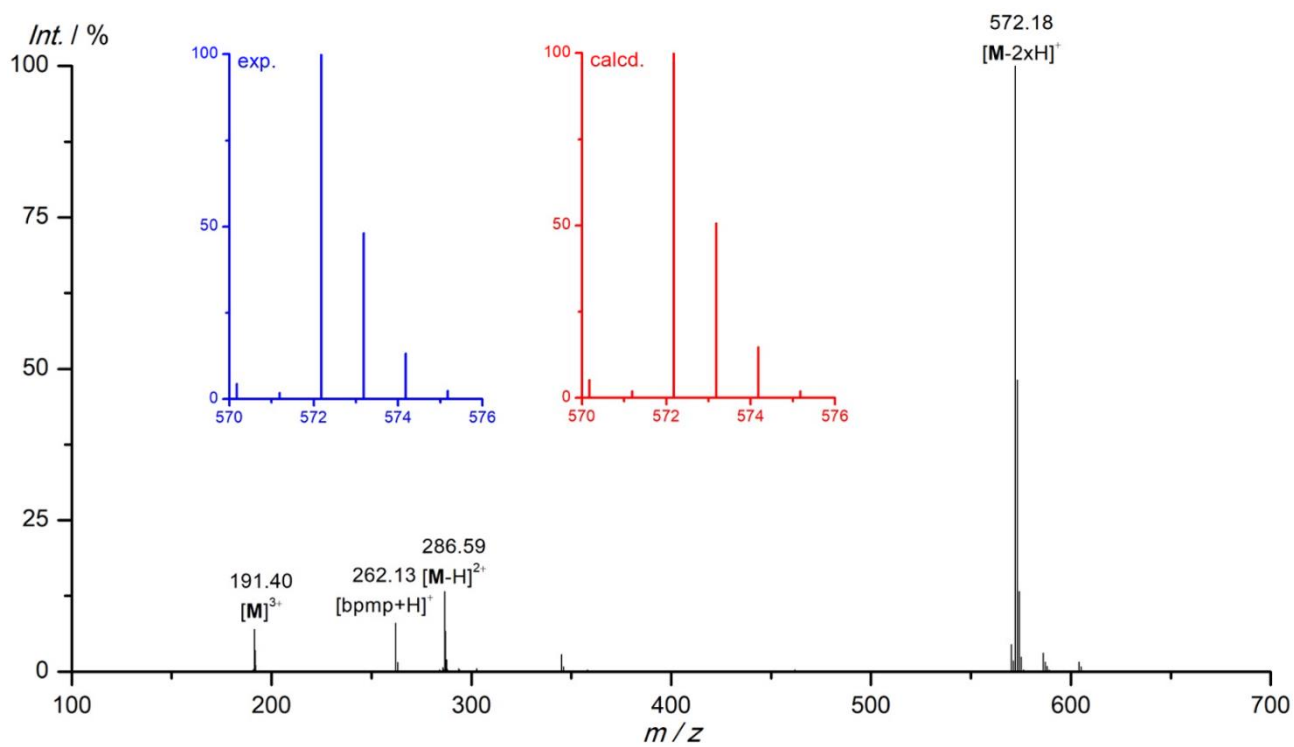
**Figure S4.** ATR-IR spectrum of Cr(bpmp)Br<sub>3</sub>.



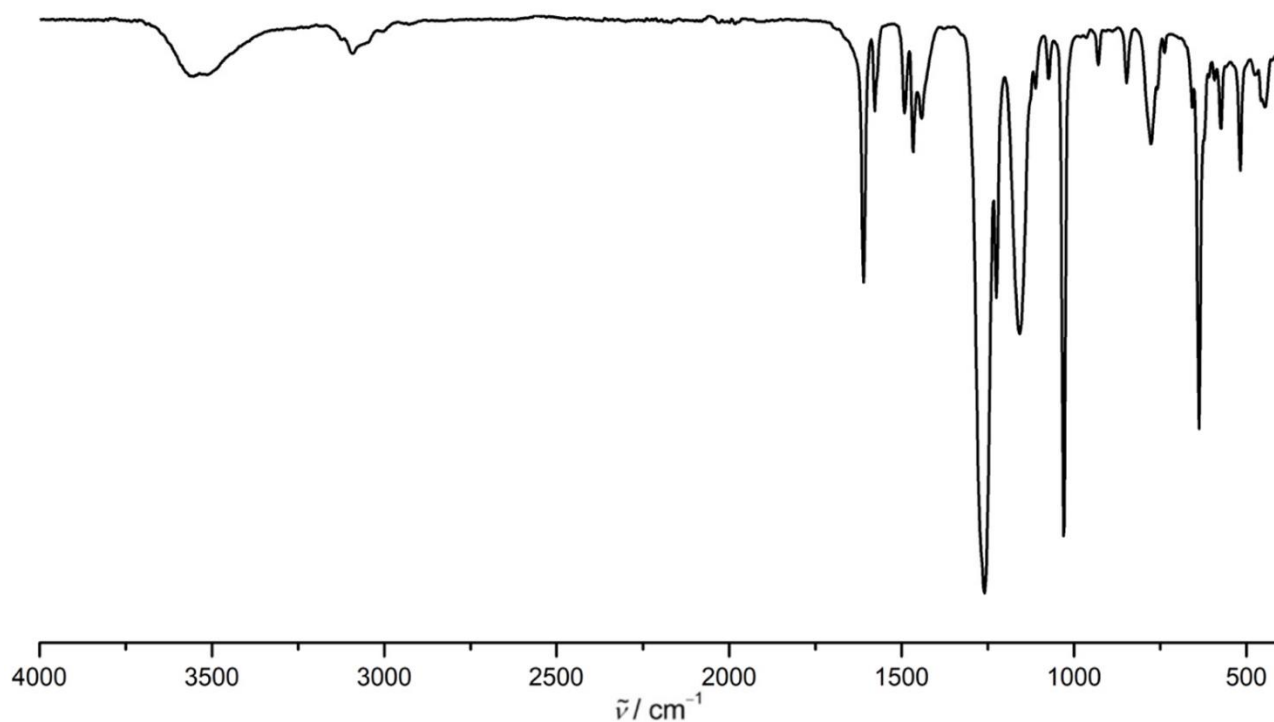
**Figure S5.** APCI mass spectrum of  $\text{Cr}(\text{bpmp})(\text{OTf})_3$ . The insets depict the experimental (blue) and calculated (red) isotopic pattern of the peak at  $m/z$  611 ( $[\text{Cr}(\text{bpmp})(\text{OTf})_3-\text{OTf}]^+$ ).



**Figure S6.** ATR-IR spectrum of  $\text{Cr}(\text{bpmp})(\text{OTf})_3$ .

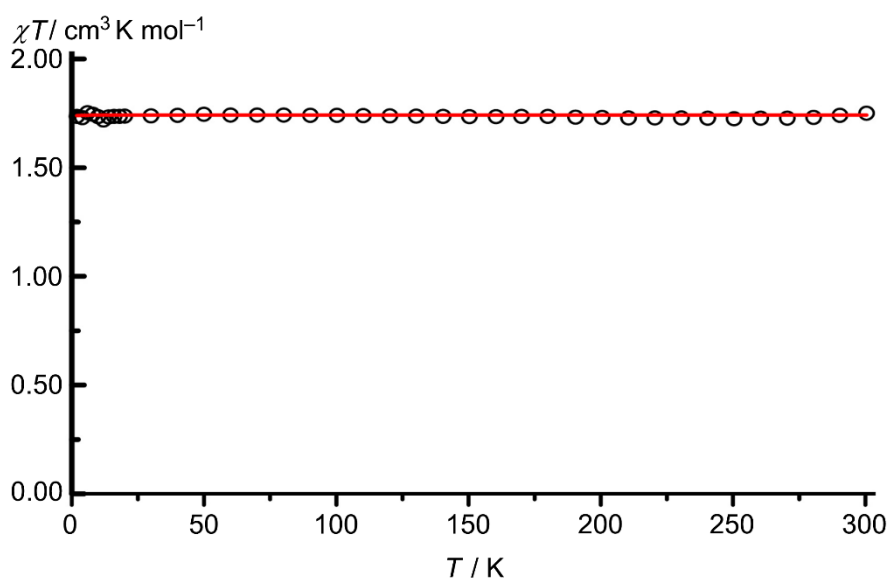


**Figure S7.** ESI<sup>+</sup> mass spectrum of  $[\text{Cr}(\text{bpmp})_2][\text{OTf}]_3$  in  $\text{CH}_3\text{CN}$ . The insets depict the experimental (blue) and calculated (red) isotopic pattern of the peak at  $m/z$  572 ( $[\text{Cr}(\text{bpmp})_2-2\text{H}]^+$ ).



**Figure S8.** ATR-IR spectrum of  $[\text{Cr}(\text{bpmp})_2][\text{OTf}]_3$ .

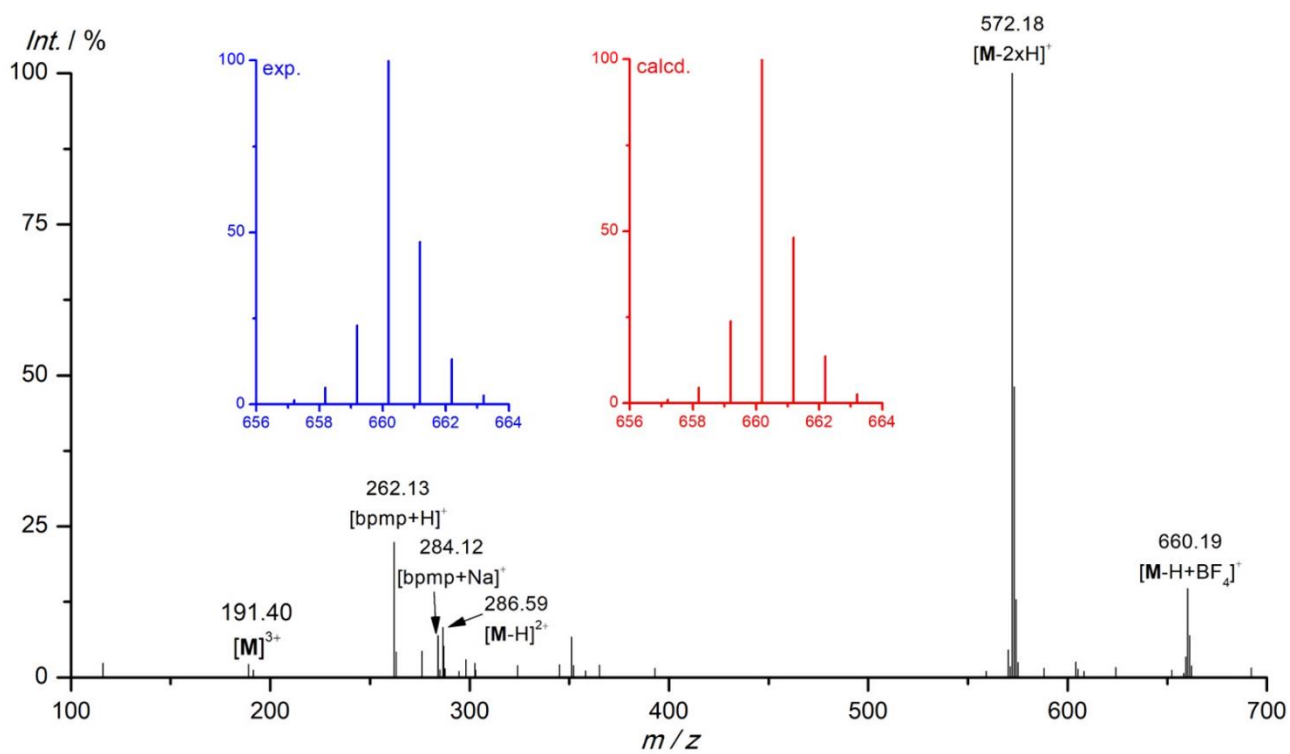




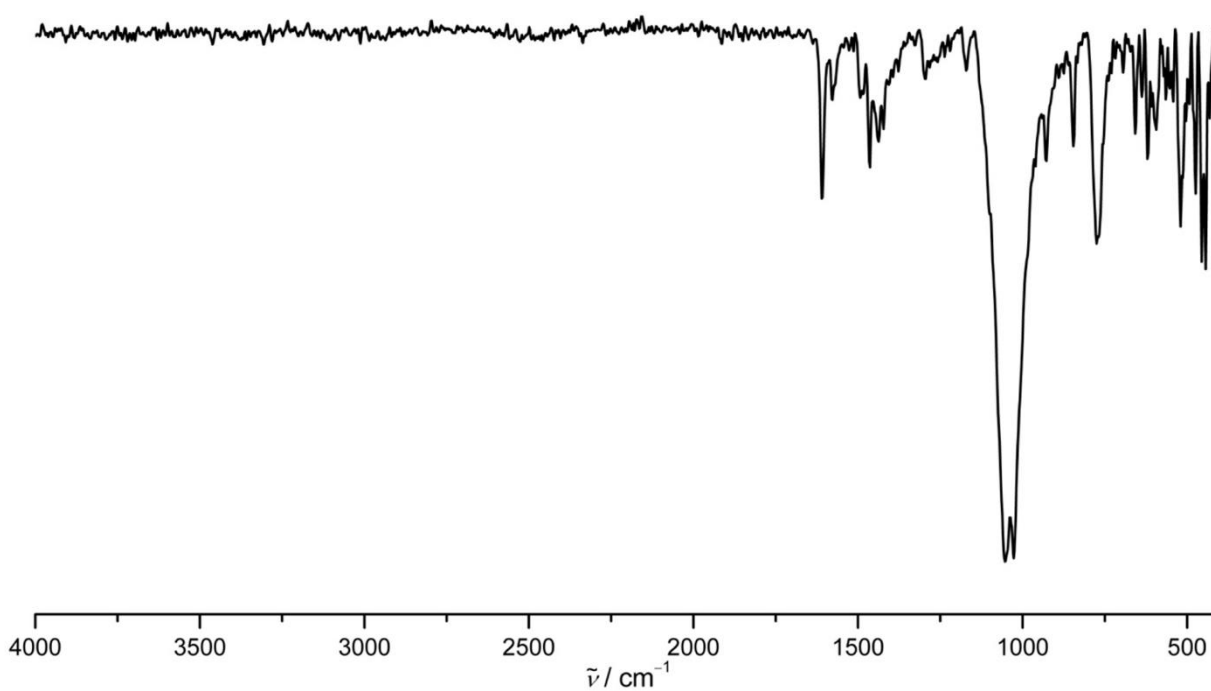
**Figure S9.** Temperature-dependence of  $\chi_{MT}$  of  $[\text{Cr}(\text{bpmp})_2][\text{BF}_4]_3$  (black circles) with fit (red line,  $g = 1.972$ ).

**Table S6.** Bond lengths [ $\text{\AA}$ ] and angles [deg] of  $[\text{Cr}(\text{bpmp})_2]^{3+}$  from XRD measurements of  $[\text{Cr}(\text{bpmp})_2][\text{OTf}]_3$  and  $[\text{Cr}(\text{bpmp})_2][\text{BF}_4]_3$  and DFT calculations of  $[\text{Cr}(\text{bpmp})_2]^{3+}$ .

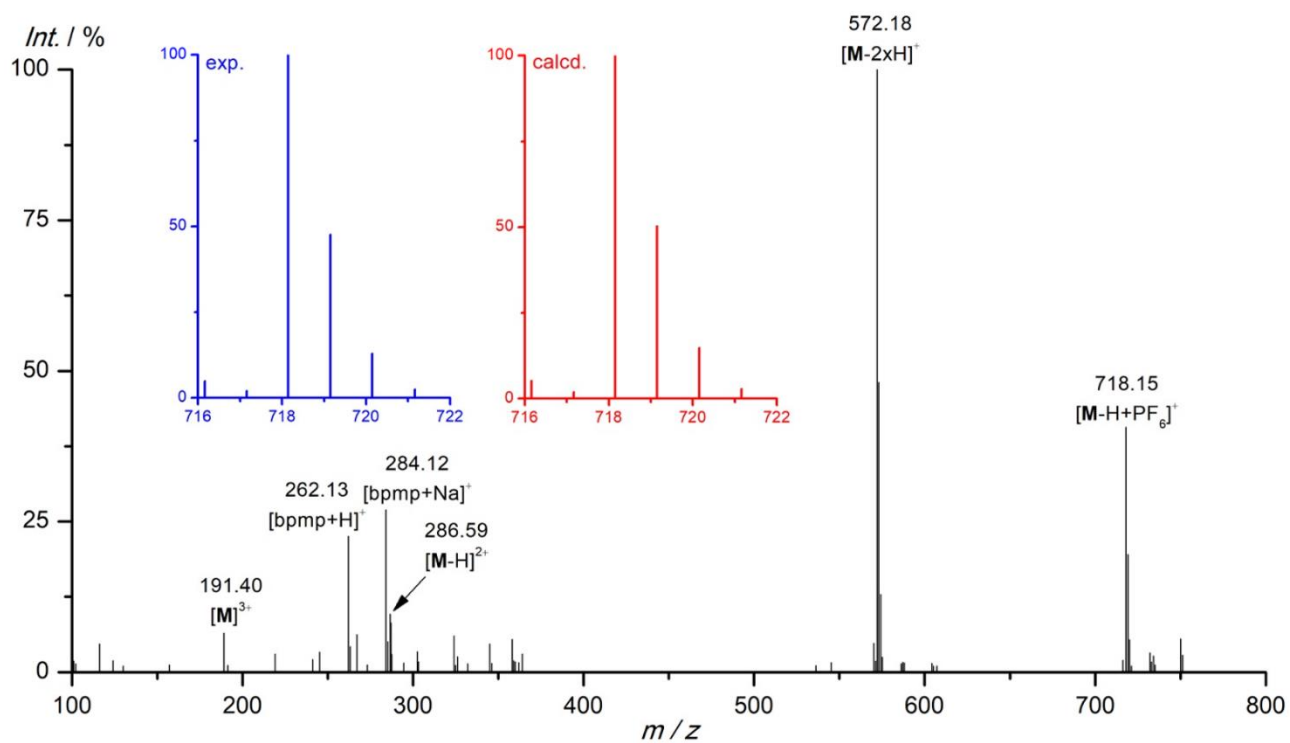
	$[\text{Cr}(\text{bpmp})_2][\text{OTf}]_3$	$[\text{Cr}(\text{bpmp})_2][\text{BF}_4]_3$	DFT
Cr1–N1	2.0755(13)	2.069(2)	2.1233
Cr1–N2	2.0599(13)	2.083(2)	2.1183
Cr1–N3	2.0691(13)	2.061(2)	2.1174
Cr1–N4	2.0703(13)	2.073(2)	2.1089
Cr1–N5	2.0771(13)	2.078(3)	2.0996
Cr1–N6	2.0886(13)	2.084(2)	2.1075
N1–Cr1–N2	89.55(5)	88.72(9)	88.46
N1–Cr1–N3	177.65(4)	176.71(10)	176.85
N1–Cr1–N4	93.04(5)	94.93(9)	96.50
N1–Cr1–N5	89.11(5)	92.85(9)	91.39
N1–Cr1–N6	85.08(5)	84.85(9)	84.14
N2–Cr1–N3	90.11(5)	88.01(10)	88.53
N2–Cr1–N4	91.00(5)	91.97(9)	90.81
N2–Cr1–N5	178.58(4)	178.42(9)	179.41
N2–Cr1–N6	90.68(5)	92.05(10)	91.77
N3–Cr1–N4	84.63(5)	85.54(9)	84.45
N3–Cr1–N5	91.20(5)	90.42(10)	91.64
N3–Cr1–N6	97.25(5)	94.91(9)	95.05
N4–Cr1–N5	88.59(5)	87.72(10)	88.64
N4–Cr1–N6	177.47(4)	175.97(10)	177.35
N5–Cr1–N6	89.69(5)	88.27(10)	88.78
$S(\text{OC-6})^{42}$	0.16	0.20	0.21



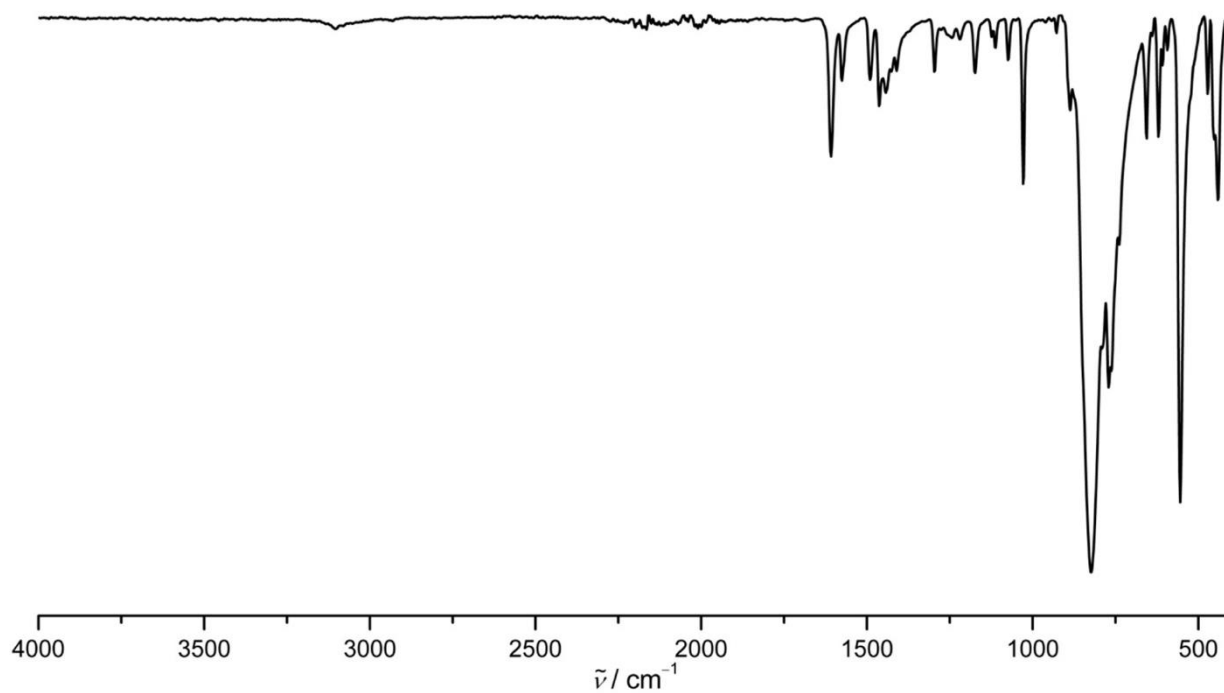
**Figure S10.** ESI<sup>+</sup> mass spectrum of [Cr(bpmp)<sub>2</sub>][BF<sub>4</sub>]<sub>3</sub> in CH<sub>3</sub>CN. The insets depict the experimental (blue) and calculated (red) isotopic pattern of the peak at *m/z* 660 ([Cr(bpmp)<sub>2</sub>-H+BF<sub>4</sub>]<sup>+</sup>).



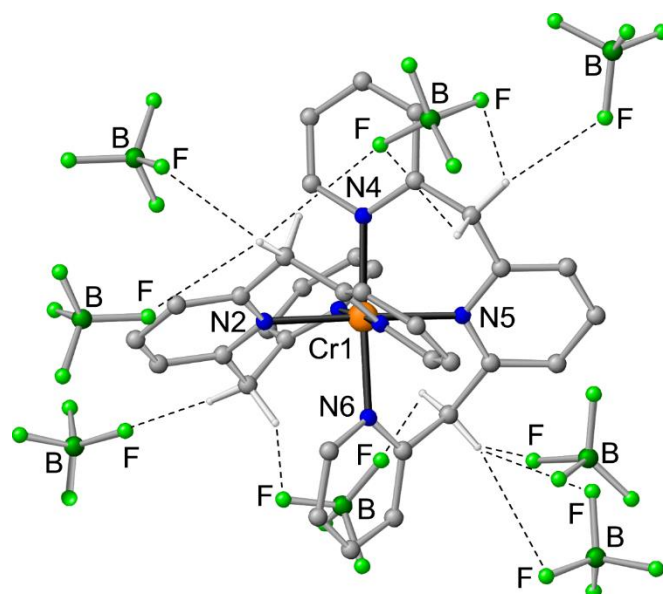
**Figure S11.** ATR-IR spectrum of [Cr(bpmp)<sub>2</sub>][BF<sub>4</sub>]<sub>3</sub>.



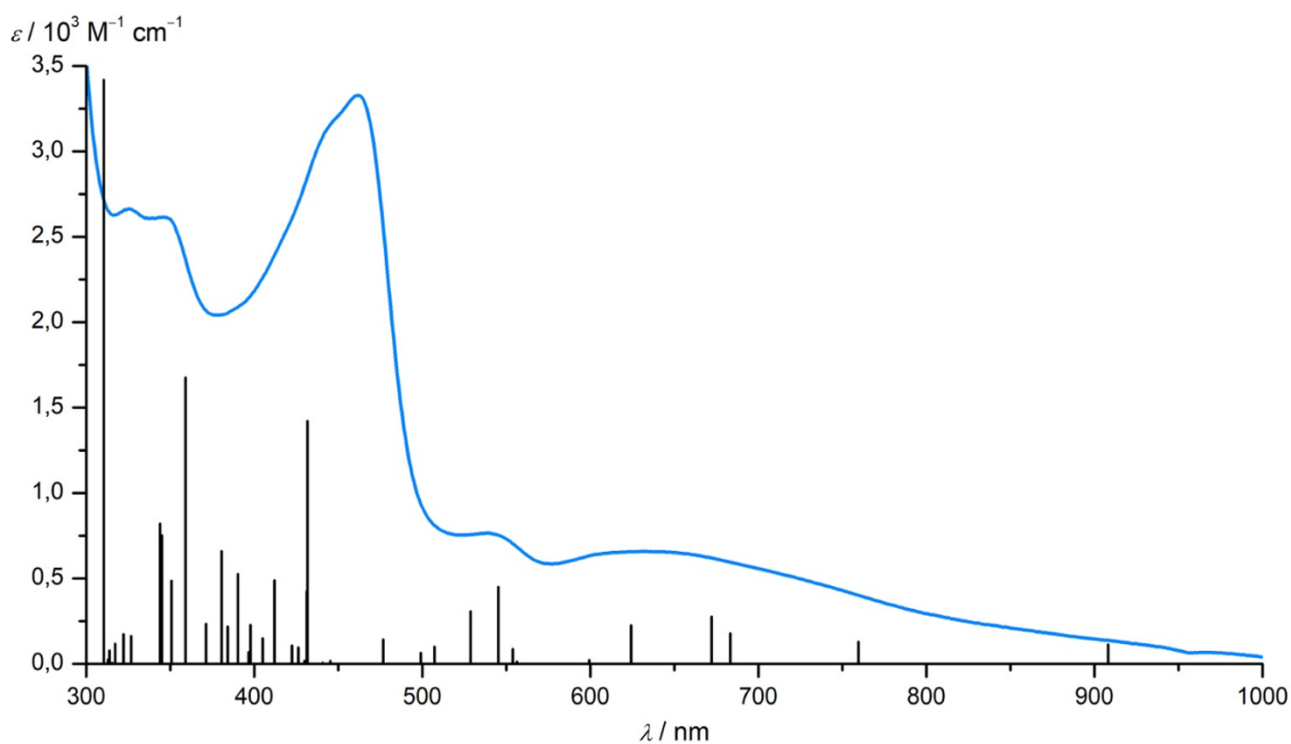
**Figure S12.** ESI<sup>+</sup> mass spectrum of [Cr(bpmp)<sub>2</sub>][PF<sub>6</sub>]<sub>3</sub> in CH<sub>3</sub>CN. The insets depict the experimental (blue) and calculated (red) isotopic pattern of the peak at *m/z* 718 ([Cr(bpmp)<sub>2</sub>-H+PF<sub>6</sub>]<sup>+</sup>).



**Figure S13.** ATR-IR spectrum of [Cr(bpmp)<sub>2</sub>][PF<sub>6</sub>]<sub>3</sub>.

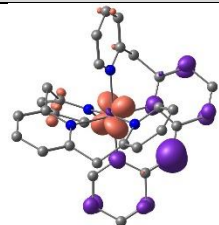
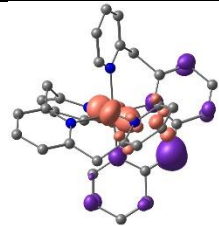
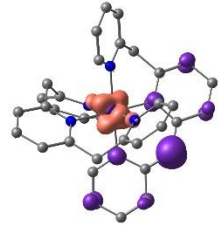
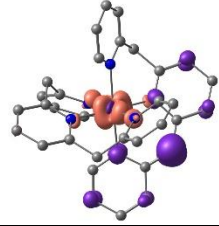
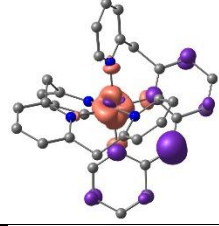
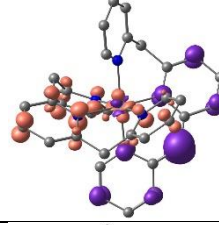
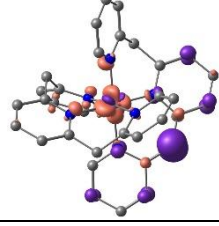


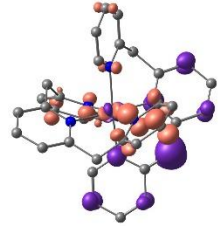
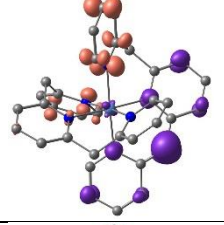
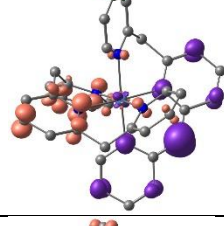
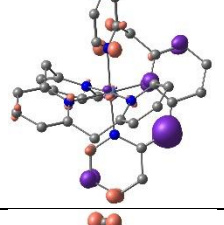
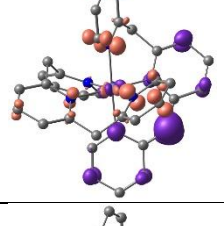
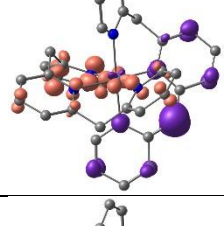
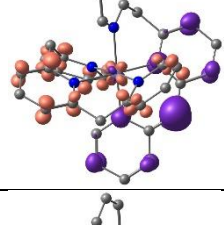
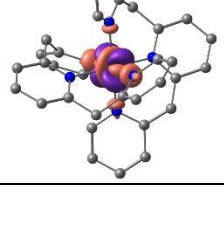
**Figure S14.** Molecular structure of  $[\text{Cr}(\text{bpmp})_2][\text{BF}_4]_3$  in the solid state. Hydrogen bonding of the tetrafluoroborate ions to the  $\text{CH}_2$  groups is illustrated by dashed lines. Hydrogen atoms (except for the  $\text{CH}_2$  groups) are omitted.

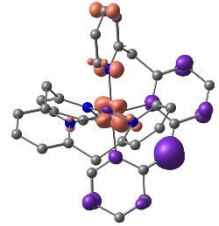
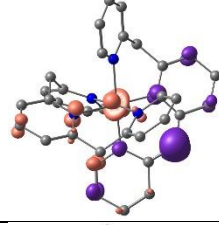
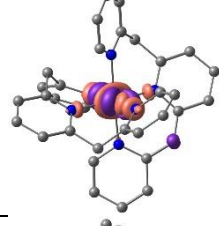
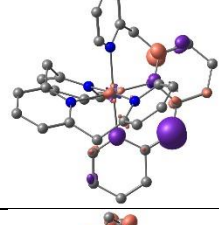
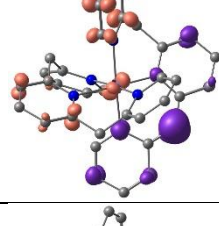
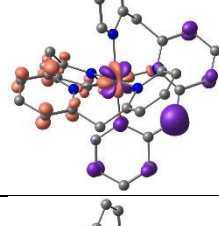
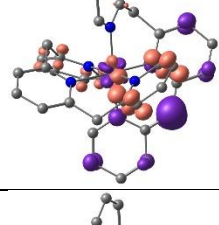
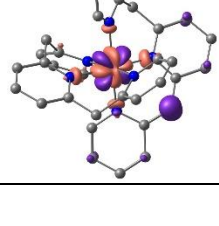


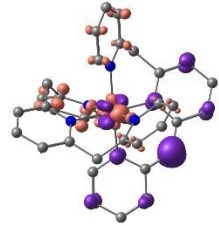
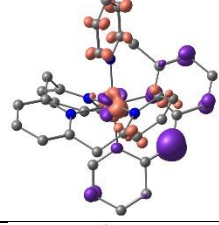
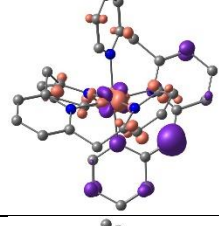
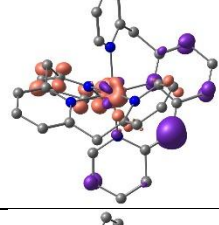
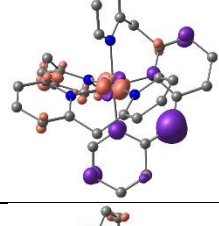
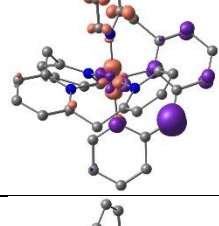
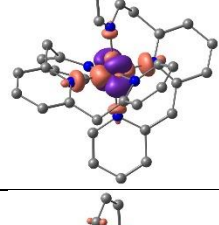
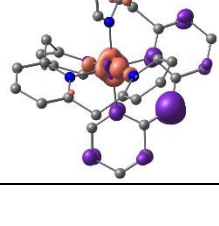
**Figure S15.** Absorption spectrum of  $[\text{Cr}(\text{bpmp})_2][\text{OTf}]_3$  in  $\text{H}_2\text{O}$  at pH 9.9 and TD-DFT calculated oscillator strengths of  $[\text{Cr}(\text{bpmp})(\text{bpmp-H})]^{2+}$ .

**Table S7. TD-DFT calculated transitions of [Cr(bpmp-H)(bpmp)]<sup>2+</sup>.**

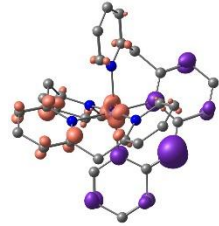
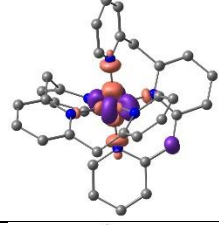
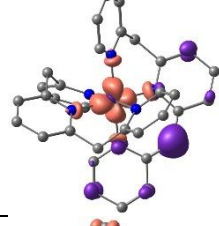
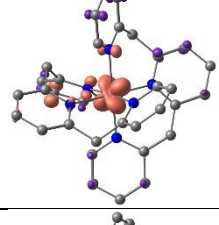
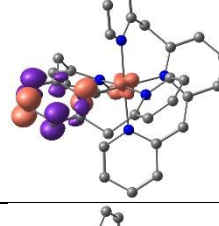
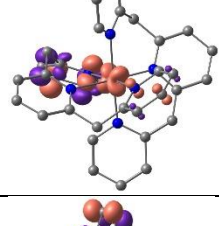
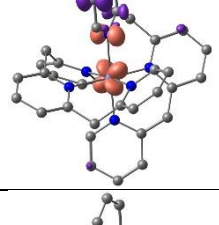
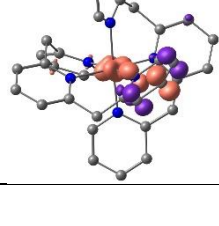
#	$\lambda$ / nm	oscillator strength	character	from	to	difference electron density (purple = electron loss; orange = electron gain)
1	908.3	0.004200695	LMCT + LL'CT	p (CH) + p (py)	$t_{2g} (d_{xz}) + p (py)$	
2	759.5	0.004813556	LMCT + LL'CT	p (CH) + p (py)	$t_{2g} (d_{xz}+d_{yz}) + p (py)$	
3	683.4	0.006631138	LMCT	p (CH) + p (py)	$t_{2g} (d_{xy}) + e_g (d_{z2})$	
4	672.2	0.010283469	LMCT	p (CH) + p (py)	$e_g (d_{z2})$	
5	624.3	0.008371426	LMCT + MC	p (CH) + p (py) + $t_{2g} (d_{xy})$	$e_g (d_{x2-y2})$	
6	599.3	0.000772506	LL'CT + LMCT + MC	p (CH) + p (py) + $t_{2g} (d_{xy})$	p (py) + $e_g (d_{x2-y2})$	
7	556.3	0.000436185	LMCT + LL'CT + MC	p (CH) + p (py) + $t_{2g} (d_{xy})$	$e_g (d_{x2-y2}) + p (py)$	

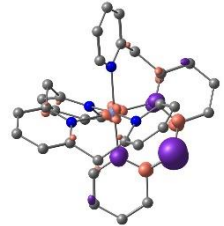
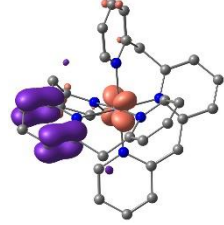
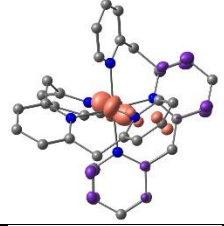
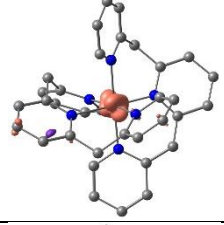
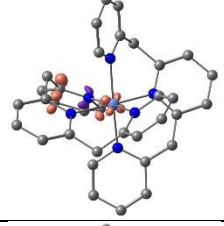
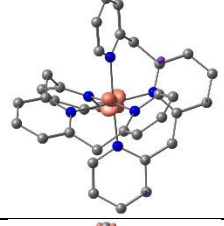
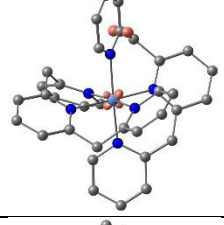
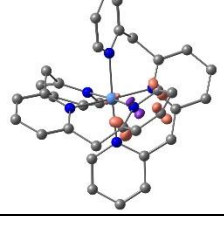
8	554	0.003206402	LL'CT + MC	$p(\text{CH}) + p(\text{py}) + t_{2g}(d_{xz} + d_{yz})$	$p(\text{py}) + e_g(d_{x^2-y^2} + d_{z^2})$	
9	545.4	0.016762453	ILCT + LL'CT	$p(\text{CH}) + p(\text{py})$	$p(\text{py})$	
10	528.9	0.011456804	LL'CT	$p(\text{CH}) + p(\text{py})$	$p(\text{py})$	
11	507.4	0.003737418	ILCT	$p(\text{CH}) + p(\text{py})$	$p(\text{py})$	
12	499.2	0.00234963	ILCT + MC	$p(\text{CH}) + p(\text{py}) + t_{2g}(d_{yz})$	$p(\text{py}) + e_g(d_{x^2-y^2} + d_{z^2})$	
13	476.8	0.005313119	LL'CT + MC	$p(\text{CH}) + p(\text{py}) + t_{2g}(d_{xy})$	$p(\text{py}) + t_{2g}(d_{yz})$	
14	445.2	0.000607987	LL'CT	$p(\text{CH}) + p(\text{py})$	$p(\text{py})$	
15	440.8	0.000222206	MC	$t_{2g}(d_{xz})$	$e_g(d_{z^2})$	

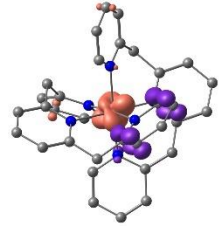
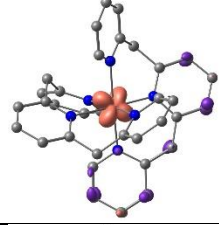
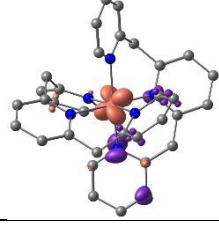
16	431.7	0.05277057	ILCT + MC	p (CH) + p (py) + t <sub>2g</sub> (d <sub>xy</sub> )	p (py) + t <sub>2g</sub> (d <sub>xy</sub> +d <sub>xz</sub> )	
17	431.3	0.015787377	LMCT + LL'CT	p (CH) + p (py)	t <sub>2g</sub> (d <sub>xy</sub> +d <sub>xz</sub> +d <sub>yz</sub> ) + p (py)	
18	430	0.000617098	MC + LMCT	t <sub>2g</sub> (d <sub>yz</sub> ) + p (CH)	e <sub>g</sub> (d <sub>x2-y2</sub> +d <sub>z2</sub> )	
19	426.4	0.003518558	ILCT	p (CH) + p (py)	p (py)	
20	422.4	0.003935425	ILCT + LL'CT + LMCT	p (CH) + p (py)	p (py) + t <sub>2g</sub> (d <sub>xy</sub> +d <sub>yz</sub> )	
21	412.1	0.018123465	LL'CT + MC	p (CH) + p (py) + t <sub>2g</sub> (d <sub>xy</sub> )	p (py) + e <sub>g</sub> (d <sub>x2-y2</sub> )	
22	405.1	0.005534688	LL'CT + MC	p (CH) + p (py) + t <sub>2g</sub> (d <sub>xy</sub> )	p (py) + e <sub>g</sub> (d <sub>x2-y2</sub> +d <sub>z2</sub> )	
23	397.7	0.008474711	MC + LMCT	t <sub>2g</sub> (d <sub>xy</sub> ) + p (CH)	e <sub>g</sub> (d <sub>x2-y2</sub> )	

24	396.7	0.002528534	ILCT + LL'CT + MC	$p(\text{CH}) + p(\text{py}) + t_{2g}(d_{xy})$	$p(\text{py}) + e_g(d_{x^2-y^2} + d_{z^2})$	
25	390.3	0.019580503	ILCT + MC	$p(\text{CH}) + p(\text{py}) + t_{2g}(d_{xy})$	$p(\text{py}) + e_g(d_{x^2-y^2} + d_{z^2})$	
26	384.3	0.008136465	LL'CT + ILCT + MC	$p(\text{CH}) + p(\text{py}) + t_{2g}(d_{xy})$	$p(\text{py}) + e_g(d_{x^2-y^2} + d_{z^2})$	
27	380.5	0.024575727	LL'CT + MC	$p(\text{CH}) + p(\text{py}) + t_{2g}(d_{xy})$	$p(\text{py}) + e_g(d_{x^2-y^2} + d_{z^2})$	
28	371.4	0.008661558	LL'CT + MC	$p(\text{CH}) + p(\text{py}) + t_{2g}(d_{xy})$	$p(\text{py}) + e_g(d_{x^2-y^2} + d_{z^2})$	
29	359.2	0.062219373	ILCT + MC	$p(\text{CH}) + p(\text{py}) + t_{2g}(d_{xy} + d_{xz} + d_{yz})$	$p(\text{py}) + e_g(d_{x^2-y^2} + d_{z^2})$	
30	350.7	0.000959514	MC	$t_{2g}(d_{xz})$	$e_g(d_{x^2-y^2})$	
31	350.7	0.01803702	LMCT + ILCT	$p(\text{CH}) + p(\text{py})$	$e_g(d_{x^2-y^2} + d_{z^2}) + p(\text{py})$	



32	345.1	0.027927026	LL'CT + LMCT	p (CH) + p (py)	p (py) + e <sub>g</sub> (d <sub>x<sup>2</sup>-y<sup>2</sup>+d<sub>z<sup>2</sup></sub>)</sub>	
33	343.9	0.030471736	MC + LMCT	t <sub>2g</sub> (d <sub>yz</sub> ) + p (CH)	e <sub>g</sub> (d <sub>x<sup>2</sup>-y<sup>2</sup>+d<sub>z<sup>2</sup></sub>)</sub>	
34	326.7	0.006043994	LMCT	p (CH) + p (py)	e <sub>g</sub> (d <sub>x<sup>2</sup>-y<sup>2</sup>)</sub>	
35	322.2	0.006409311	LMCT + ILCT	p (py)	t <sub>2g</sub> (d <sub>xz</sub> ) + p (py)	
36	317.3	0.004341205	ILCT + LMCT	p (py)	p (py) + t <sub>2g</sub> (d <sub>xy</sub> +d <sub>xz</sub> +d <sub>yz</sub> )	
37	315.5	0.000239335	ILCT + LMCT	p (py)	p (py) + t <sub>2g</sub> (d <sub>xz</sub> )	
38	313.9	0.002920282	ILCT + LMCT	p (py)	p (py) + t <sub>2g</sub> (d <sub>xz</sub> )	
39	312.9	0.000853879	ILCT + LMCT	p (py)	p (py) + t <sub>2g</sub> (d <sub>yz</sub> )	

40	310.4	0.127030531	ILCT + LMCT	p (py) + p (CH)	p (py) + t <sub>2g</sub> (d <sub>xy</sub> +d <sub>yz</sub> )	
41	299.9	0.003619984	LMCT	p (py)	t <sub>2g</sub> (d <sub>xz</sub> )	
42	293.3	0.015512516	LMCT + LL'CT	p (py)	t <sub>2g</sub> (d <sub>xz</sub> +d <sub>yz</sub> ) + p (py)	
43	293	0.02365423	ILCT + LMCT	p (py)	p (py) + t <sub>2g</sub> (d <sub>xy</sub> +d <sub>xz</sub> +d <sub>yz</sub> )	
44	290.3	0.002589746	ILCT + LMCT	p (py)	p (py) + t <sub>2g</sub> (d <sub>xy</sub> )	
45	290.1	0.021949923	LMCT	p (py)	t <sub>2g</sub> (d <sub>xy</sub> )	
46	289.8	0.001517601	ILCT + LMCT	p (py)	p (py) + t <sub>2g</sub> (d <sub>xy</sub> )	
47	288.4	0.000490673	ILCT	p (py)	p (py)	

48	287.6	0.005138237	LMCT + ILCT	p (py)	$t_{2g} (d_{xy}+d_{xz}+d_{yz}) +$ p (py)	
49	285.1	0.007037636	LMCT	p (CH) + p (py)	$t_{2g} (d_{xy}+d_{yz})$	
50	279.2	0.005036221	LMCT + ILCT	p (py)	$t_{2g} (d_{xy}+d_{xz}) +$ p (py)	

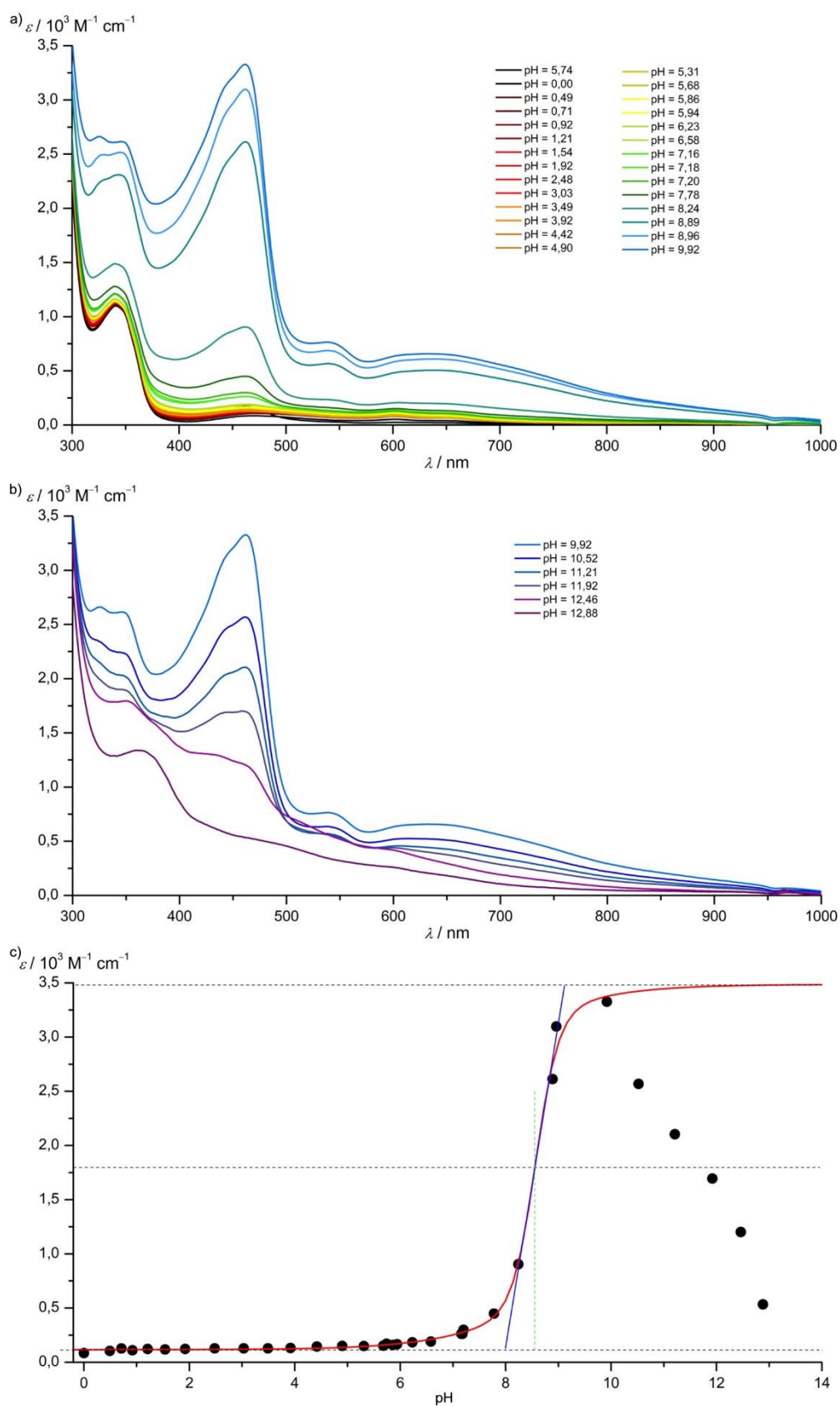


**Figure S16.** Photometric titration of  $[\text{Cr}(\text{bmpm})_2][\text{OTf}]_3$  in  $\text{H}_2\text{O}$  a) pH 0 – 9.9; b) pH 9.9 – 12.9 and c)  $\text{pK}_a$  determination at 445 nm.

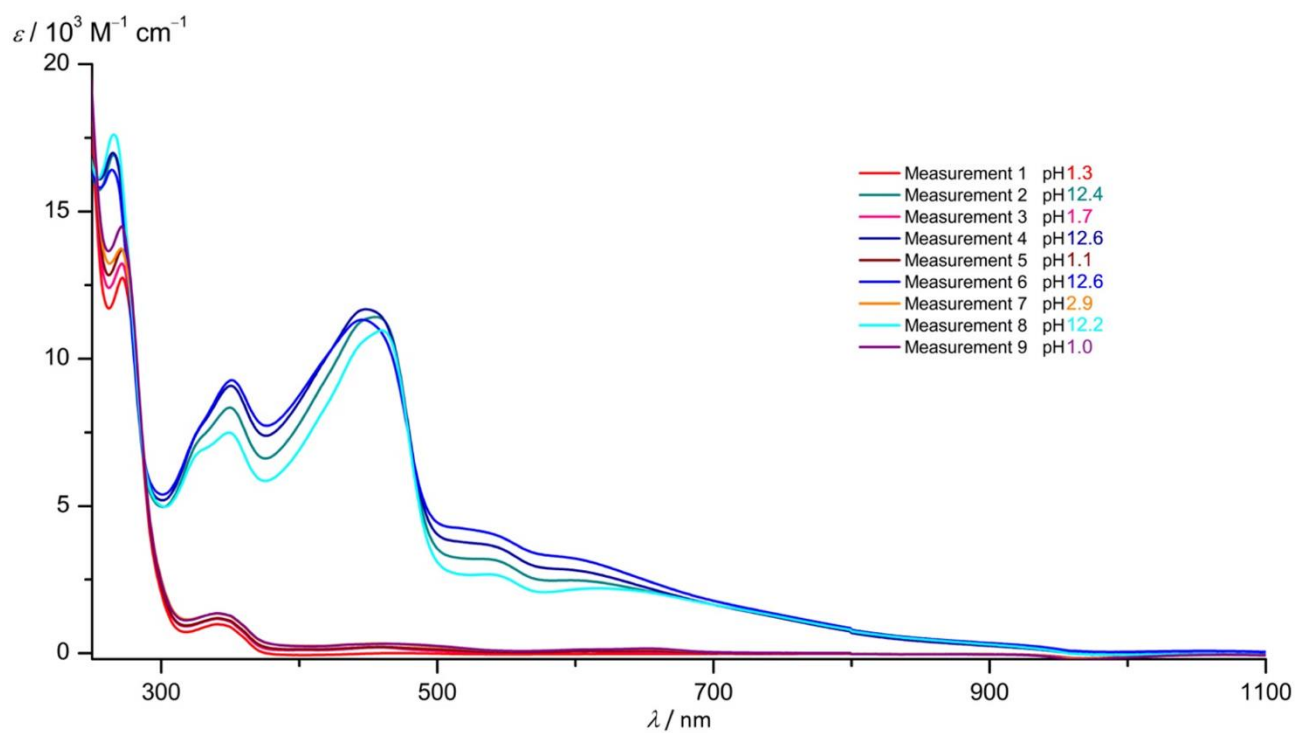


**Figure S17.** Absorption spectra of  $[\text{Cr}(\text{bpmp})_2][\text{OTf}]_3$  in  $\text{H}_2\text{O}$  cycling between  $\text{pH} \approx 1.5$  and  $\text{pH} > 12$ .  $\text{pH} > 12$  causes some degradation.

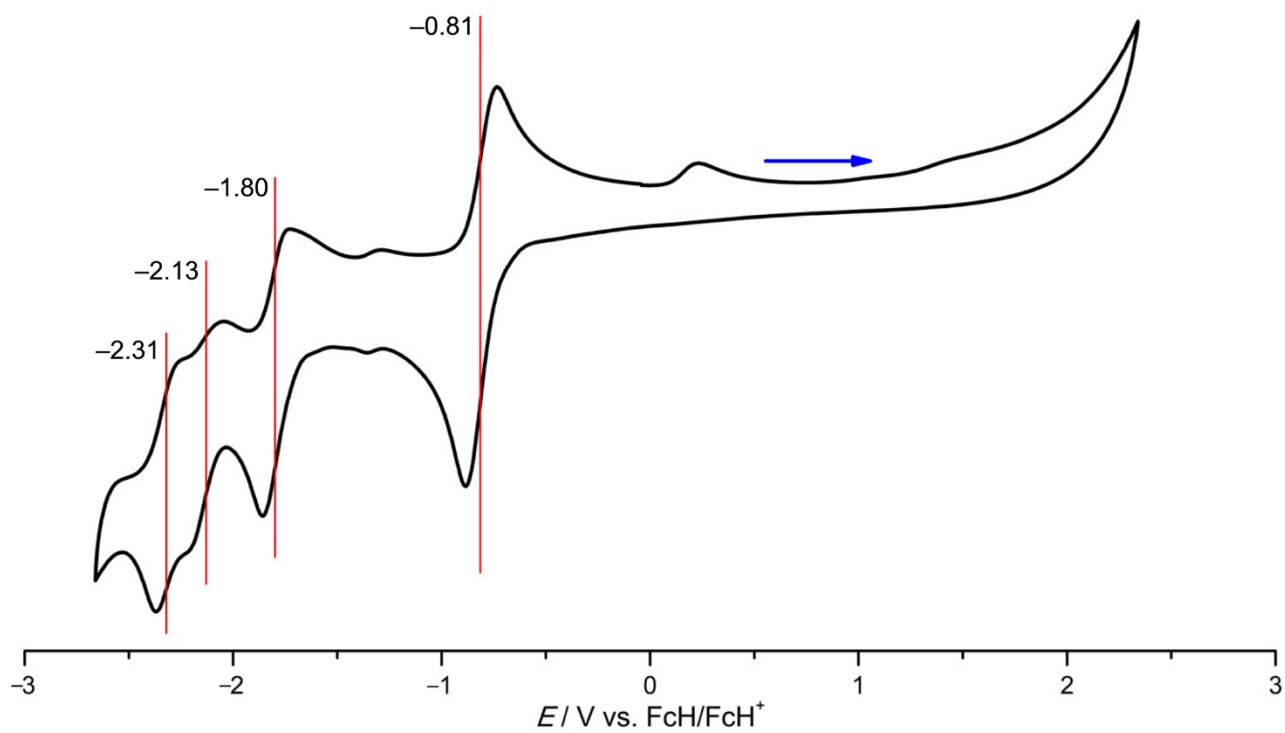


**Figure S18.** Cyclic voltammogram of  $[\text{Cr}(\text{bpmp})_2][\text{PF}_6]_3$  in  $\text{CH}_3\text{CN}/[\text{tBu}_4\text{N}][\text{PF}_6]$ .

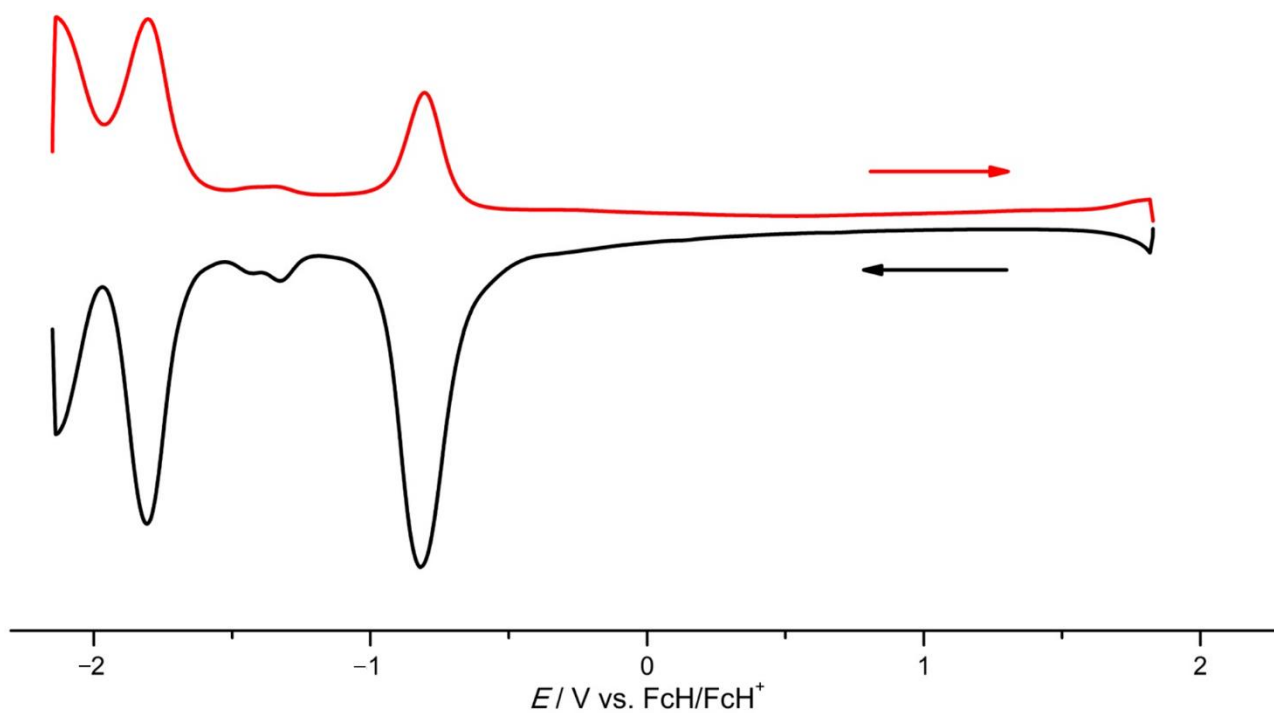


**Figure S19.** Square wave voltammogram of  $[\text{Cr}(\text{bpmp})_2][\text{PF}_6]_3$  in  $\text{CH}_3\text{CN}/[\text{tBu}_4\text{N}][\text{PF}_6]$ .

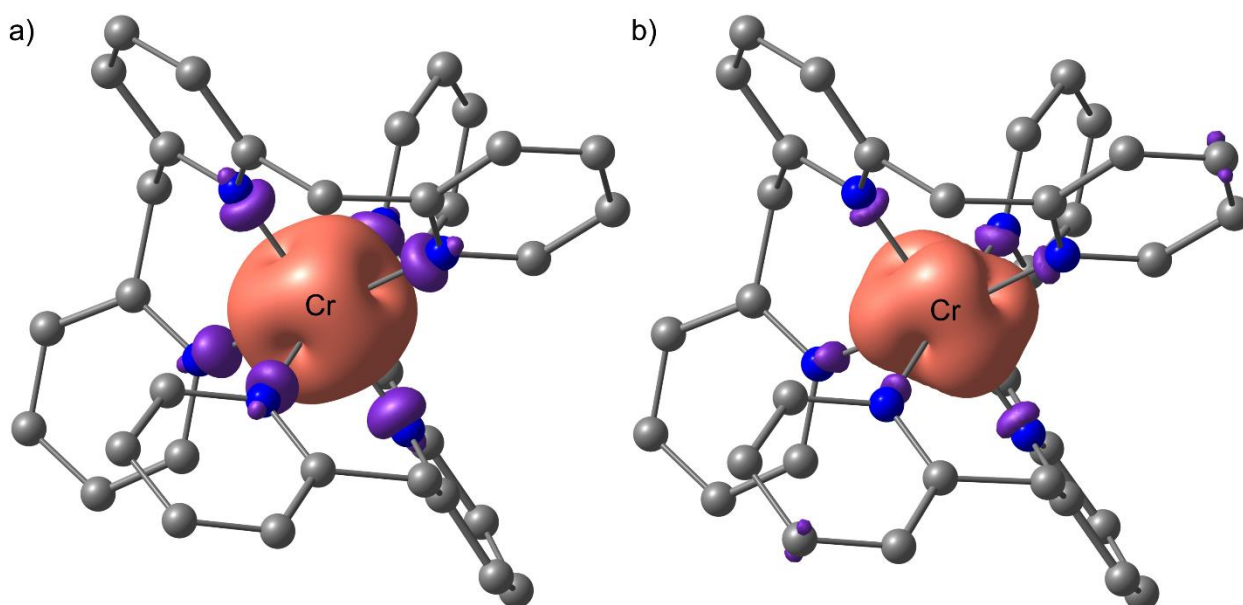


**Figure S20.** DFT optimized geometries of a) [Cr(bpmp)<sub>2</sub>]<sup>3+</sup> (quartet state) and b) [Cr(bpmp)<sub>2</sub>]<sup>2+</sup> (triplet state), and corresponding Mulliken spin densities plotted at 0.006 a.u. with the α spin in orange and the β spin in purple.

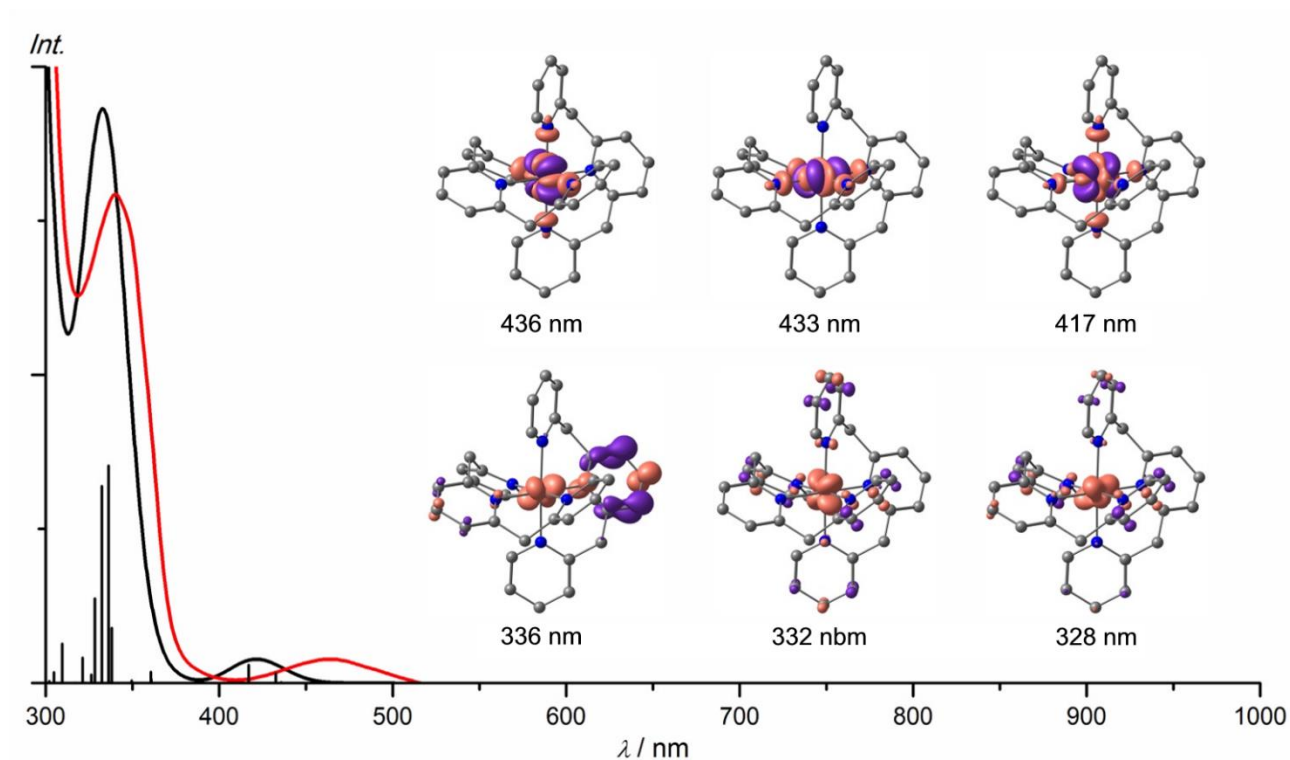


**Figure S21.** Experimental (red) and TD-DFT calculated absorption spectrum (black) of [Cr(bpmp)<sub>2</sub>]<sup>3+</sup> and difference electron densities of the major transitions of <sup>4</sup>LMCT and <sup>4</sup>T<sub>2</sub> character calculated by TD-DFT.

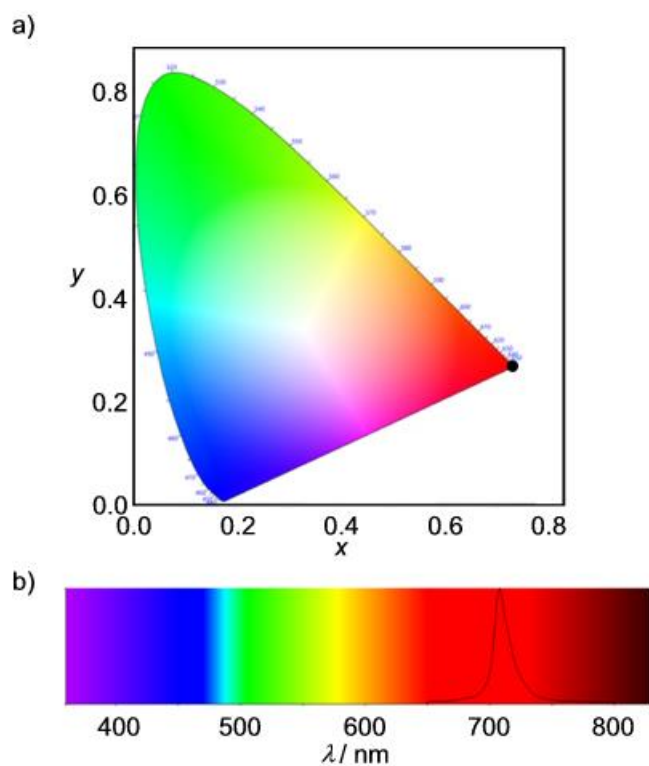


**Figure S22.** a) CIE 1931 diagram and CIE coordinates of  $[\text{Cr}(\text{bmp})_2]^{3+}$  (0.7326, 0.2674) and b) emission spectrum plotted with a background colored with the visible spectral region.



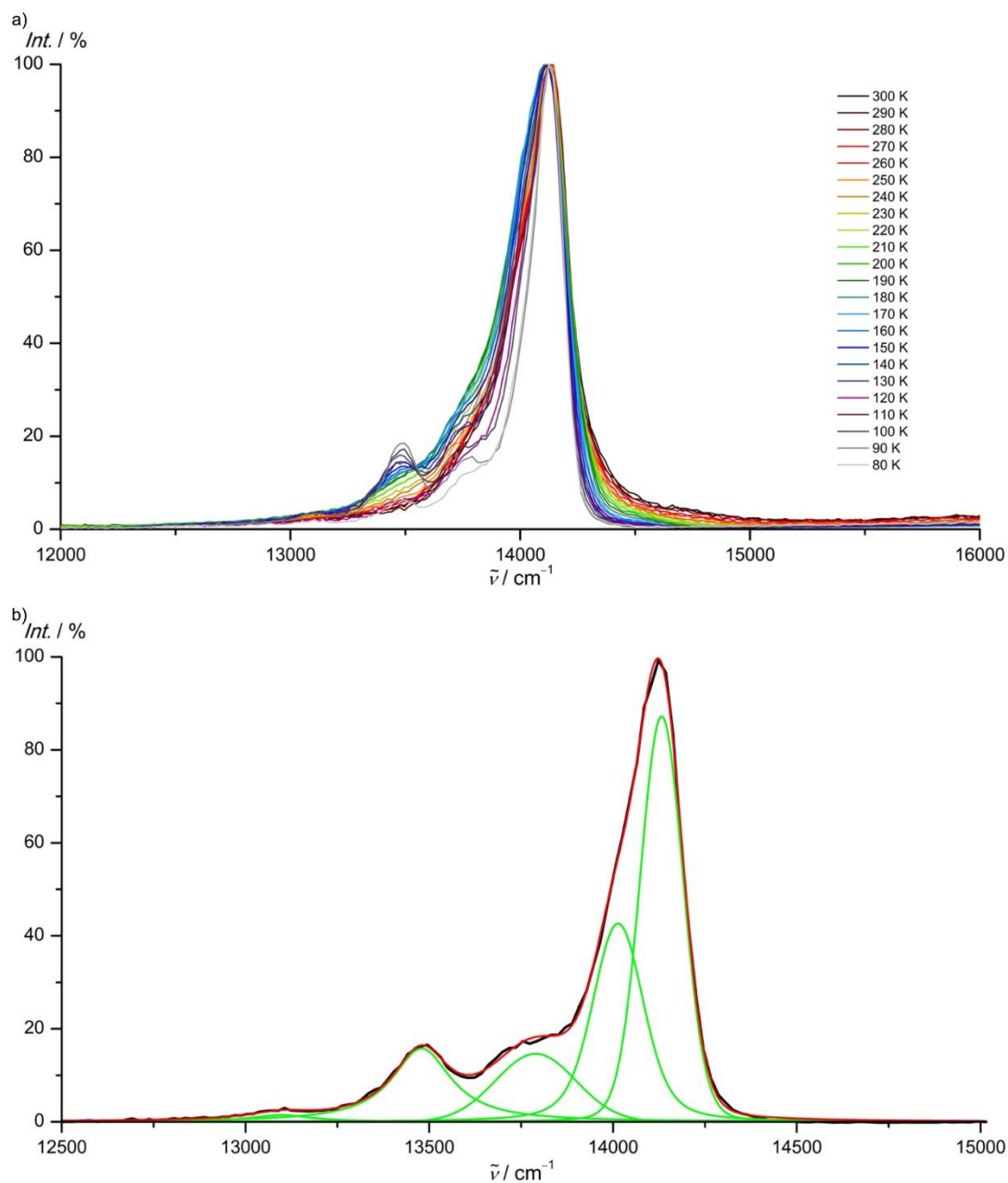


**Figure S23.** a) Normalized emission spectra of  $[\text{Cr}(\text{bpmp})_2][\text{OTf}]_3$  in butyronitrile at 300 – 80 K and b) emission spectrum of  $[\text{Cr}(\text{bpmp})_2][\text{OTf}]_3$  in butyronitrile at 100 K (black) fitted with five Voigt functions (green; peak centers at 14140, 14017, 13788, 13483 and 13099  $\text{cm}^{-1}$ ).

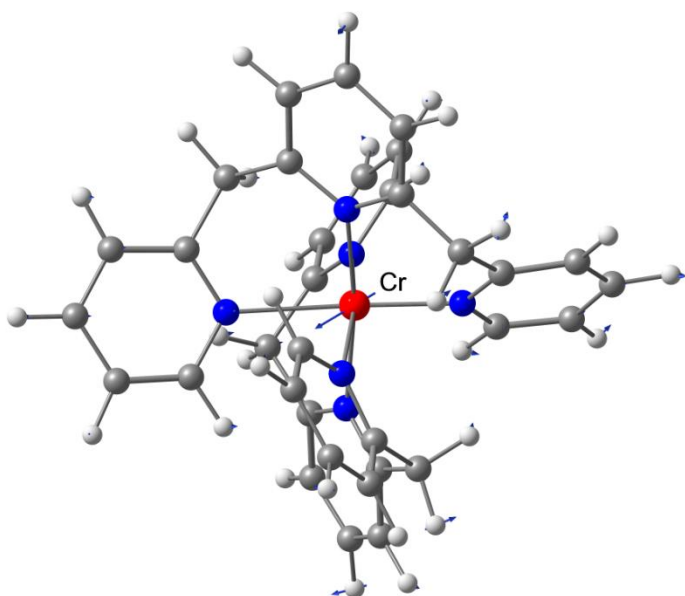


**Figure S24.** Illustration of the  $308\text{ cm}^{-1}$  vibrational mode of  $[\text{Cr}(\text{bpmp})_2]^{3+}$  calculated by DFT. Scaled displacement vectors are shown as blue arrows.

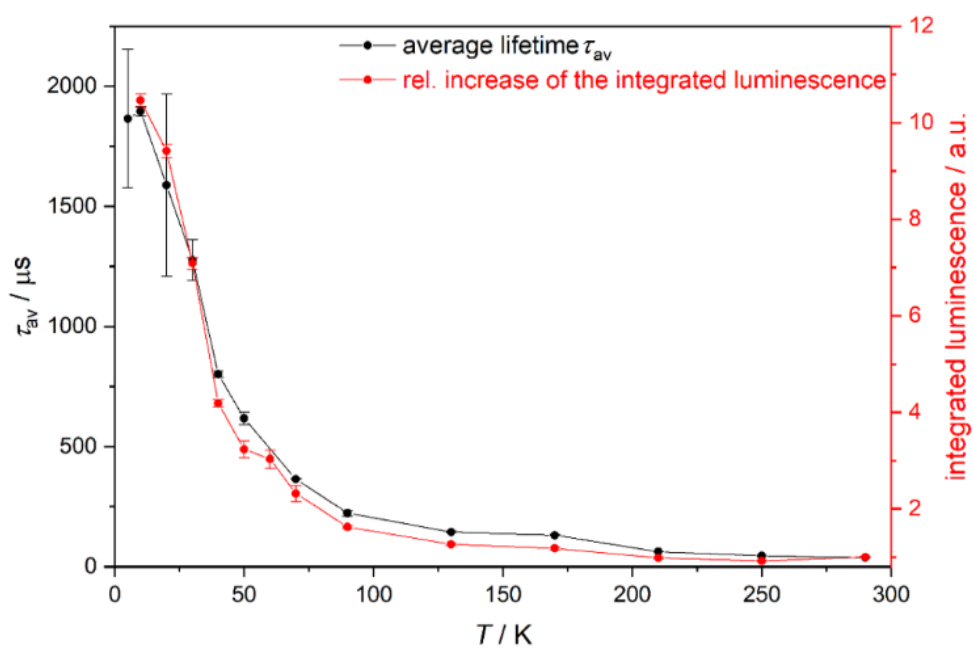


**Figure S25.** Plot of the average luminescence lifetime  $\tau_{av}$  of  $[\text{Cr}(\text{bpmp})_2][\text{BF}_4]_3$  and the integrated luminescence (normalized to 290 K) versus temperature.

**Table S8.** Temperature-dependent luminescence lifetimes of  $[\text{Cr}(\text{bpmp})_2][\text{BF}_4]_3$  measured by TCSPC (KBr pellet,  $\lambda_{\text{exc}} = 390 \text{ nm}$ )

$T / \text{K}$	$\lambda_{\text{em}} / \text{nm}$	$\tau_1 / \mu\text{s}$	$\tau_2 / \mu\text{s}$	$\tau_{\text{av}} / \mu\text{s}^{\text{a}}$
290	707	$5.17 \pm 0.07$ (20%)	$46.0 \pm 0.3$ (80%)	$38.0 \pm 0.3$
	716	$5.37 \pm 0.09$ (19%)	$46.6 \pm 0.3$ (81%)	$38.6 \pm 0.3$
250	707	$6.00 \pm 0.08$ (19%)	$55.4 \pm 0.4$ (81%)	$45.8 \pm 0.4$
	717	$7.6 \pm 0.2$ (14%)	$63.4 \pm 0.7$ (86%)	$55.3 \pm 0.6$
210	707	$11.1 \pm 0.1$ (25%)	$80.0 \pm 0.5$ (75%)	$62.5 \pm 0.4$
	717	$12.5 \pm 0.1$ (24%)	$90.0 \pm 0.7$ (76%)	$71.2 \pm 0.5$
170	707	$21.7 \pm 0.2$ (21%)	$160 \pm 1$ (79%)	$131 \pm 1$
	718	$29.5 \pm 0.2$ (24%)	$200 \pm 2$ (76%)	$159 \pm 1$
130	708	$55.0 \pm 0.5$ (68%)	$339 \pm 13$ (32%)	$145 \pm 4$
	718	$41.9 \pm 0.3$ (56%)	$225 \pm 3$ (44%)	$122 \pm 2$
90	718	$120 \pm 2$ (79%)	$600 \pm 50$ (21%)	$220 \pm 10$
70	718	$160 \pm 2$ (66%)	$770 \pm 40$ (34%)	$365 \pm 1$
50	719	$300 \pm 6$ (60%)	$1100 \pm 60$ (40%)	$620 \pm 30$
40	719	$273 \pm 3$ (49%)	$1300 \pm 20$ (51%)	$800 \pm 10$
30	720	$420 \pm 30$ (33%)	$1700 \pm 100$ (67%)	$1300 \pm 80$
20	720	$640 \pm 200$ (28%)	$2000 \pm 400$ (72%)	$1600 \pm 400$
10	720	$680 \pm 20$ (28%)	$2150 \pm 20$ (72%)	$1900 \pm 20$
5	720	$550 \pm 60$ (15%)	$2050 \pm 50$ (85%)	$1900 \pm 300$

<sup>a</sup> The average lifetime was calculated by considering the relative contributions of the time constants  $\tau_1$  and  $\tau_2$  to get an impression of the sharp increase of the emission lifetimes at low temperatures (especially below 70 K). However, one should be aware of the fact that  $\tau_{\text{av}}$  is indicated here for illustration and does not correspond directly to the decay of an excited state. The biexponential decay of the luminescence over the whole temperature range of 290 – 5 K is assigned to contributions of at least two different emissive doublet microstates. Additionally, different microenvironments in the KBr matrix (e.g.  $[\text{Cr}(\text{bpmp})_2]^{3+}$  with differently close contacts to counter ions or co-crystallized solvent molecules in the microcrystalline state) might contribute to the multiexponential decay.

**Table S9. Quantum yields  $\Phi$  and luminescence lifetimes  $\tau$  of  $[\text{Cr}(\text{bpmp})_2][\text{ClO}_4]_3$ ,  $[\text{Cr}(\text{bpmp})_2][\text{PF}_6]_3$ ,  $[\text{Cr}(\text{bpmp})_2][\text{BF}_4]_3$  in various environments at room temperature ( $\lambda_{\text{exc}} = 462 \text{ nm}$ ).**

X	solvent	acid <sup>a</sup>	oxygen	$\Phi / \%$	$\tau / \mu\text{s}$
$\text{ClO}_4$	$\text{H}_2\text{O}$	–	–	12.9	1500
$\text{ClO}_4$	$\text{H}_2\text{O}$	$\text{HClO}_4$	–	12.0	1500
$\text{ClO}_4$	$\text{H}_2\text{O}$	$\text{HClO}_4$	+	6.2	820
$\text{ClO}_4$	$\text{D}_2\text{O}$	$\text{DClO}_4$	–	15.7	1800
$\text{ClO}_4$	$\text{D}_2\text{O}$	$\text{DClO}_4$	+	8.0	810
$\text{ClO}_4$	$\text{CH}_3\text{CN}$	–	–	9.1	1000
$\text{ClO}_4$	$\text{CH}_3\text{CN}$	$\text{HClO}_4$	–	10.6	1200
$\text{ClO}_4$	$\text{CH}_3\text{CN}$	$\text{HClO}_4$	+	3.7	380
$\text{ClO}_4$	$\text{CD}_3\text{CN}$	$\text{DClO}_4$	–	9.7	1200
$\text{ClO}_4$	$\text{CD}_3\text{CN}$	$\text{DClO}_4$	+	2.8	370
$\text{ClO}_4$	PBS (pH 6.9) <sup>b</sup>	–	–	0.9	310
$\text{ClO}_4$	PBS (pH 6.5) <sup>b</sup>	–	–	1.7	570
$\text{PF}_6$	$\text{H}_2\text{O}$	–	–	0.3	220
$\text{PF}_6$	$\text{H}_2\text{O}$	$\text{HClO}_4$	–	16.0	1500
$\text{PF}_6$	$\text{H}_2\text{O}$	$\text{HClO}_4$	+	9.2	870
$\text{PF}_6$	$\text{D}_2\text{O}$	$\text{DClO}_4$	–	20.0	1800
$\text{PF}_6$	$\text{D}_2\text{O}$	$\text{DClO}_4$	+	9.2	860
$\text{PF}_6$	$\text{CH}_3\text{CN}$	–	–	0.5	550
$\text{PF}_6$	$\text{CH}_3\text{CN}$	$\text{HClO}_4$	–	11.1	1000
$\text{PF}_6$	$\text{CH}_3\text{CN}$	$\text{HClO}_4$	+	4.0	380
$\text{PF}_6$	$\text{CD}_3\text{CN}$	$\text{DClO}_4$	–	15.6	1300
$\text{PF}_6$	$\text{CD}_3\text{CN}$	$\text{DClO}_4$	+	4.8	410
$\text{PF}_6$	PBS (pH 6.9) <sup>b</sup>	–	–	0.5	310
$\text{PF}_6$	PBS (pH 6.5) <sup>b</sup>	–	–	3.2	800
$\text{BF}_4$	$\text{H}_2\text{O}$	–	–	0.4	480
$\text{BF}_4$	$\text{H}_2\text{O}$	$\text{HClO}_4$	–	12.0	1400
$\text{BF}_4$	$\text{H}_2\text{O}$	$\text{HClO}_4$	+	7.6	840
$\text{BF}_4$	$\text{D}_2\text{O}$	$\text{DClO}_4$	–	13.4	1500
$\text{BF}_4$	$\text{D}_2\text{O}$	$\text{DClO}_4$	+	7.4	840
$\text{BF}_4$	$\text{CH}_3\text{CN}$	–	–	0.6	950
$\text{BF}_4$	$\text{CH}_3\text{CN}$	$\text{HClO}_4$	–	10.4	1100
$\text{BF}_4$	$\text{CH}_3\text{CN}$	$\text{HClO}_4$	+	3.8	390
$\text{BF}_4$	$\text{CD}_3\text{CN}$	$\text{DClO}_4$	–	11.2	1200
$\text{BF}_4$	$\text{CD}_3\text{CN}$	$\text{DClO}_4$	+	4.2	400
$\text{BF}_4$	PBS (pH 6.9) <sup>b</sup>	–	–	0.4	480
$\text{BF}_4$	PBS (pH 6.5) <sup>b</sup>	–	–	3.2	860

<sup>a</sup> final  $\text{HClO}_4$  ( $\text{DClO}_4$ ) concentration  $c = 0.1 \text{ M}$ . <sup>b</sup> PBS = phosphate buffered saline (0.1 M).

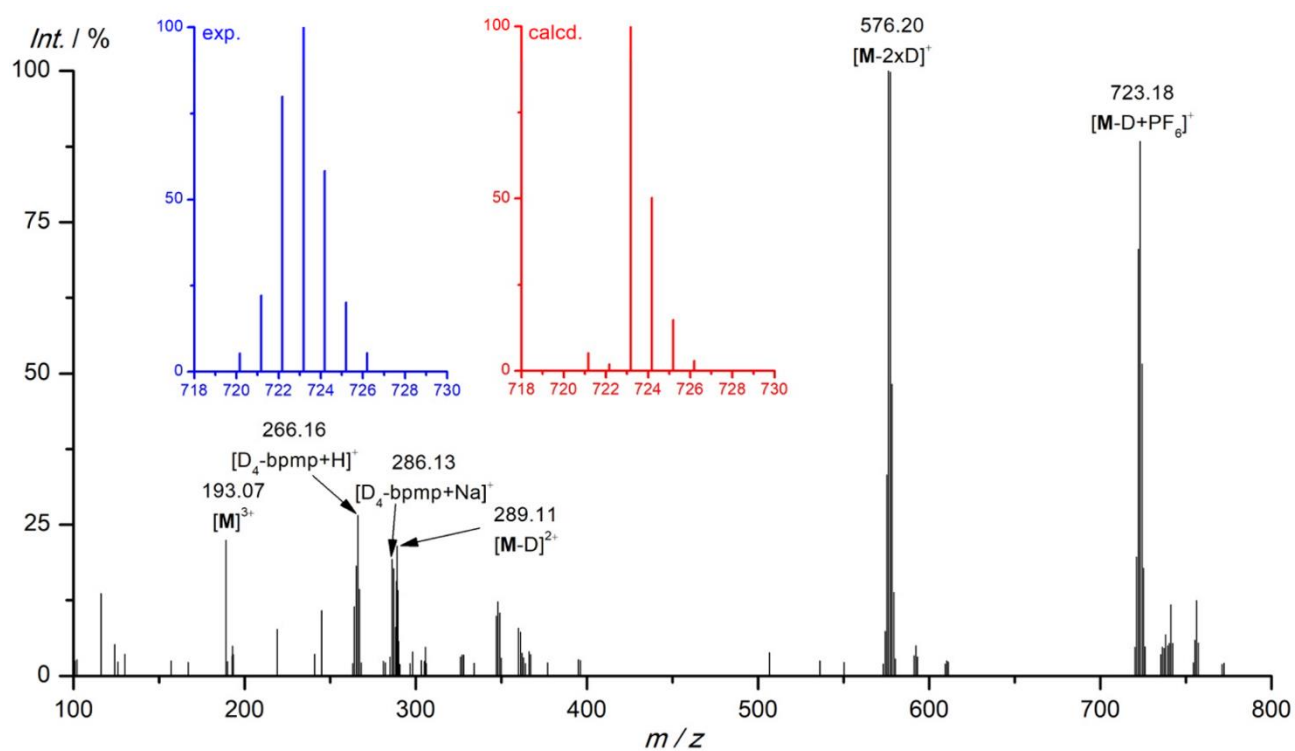


**Figure S26.** ESI<sup>+</sup> mass spectrum of [Cr([D<sub>4</sub>]-bpmp)<sub>2</sub>][PF<sub>6</sub>]<sub>3</sub> in CH<sub>3</sub>CN. The insets depict the experimental (blue) isotopic pattern of the peak at *m/z* 723 and calculated isotopic patterns of the D<sub>6</sub> (red) and D<sub>8</sub> (black) isotopologues for illustration.

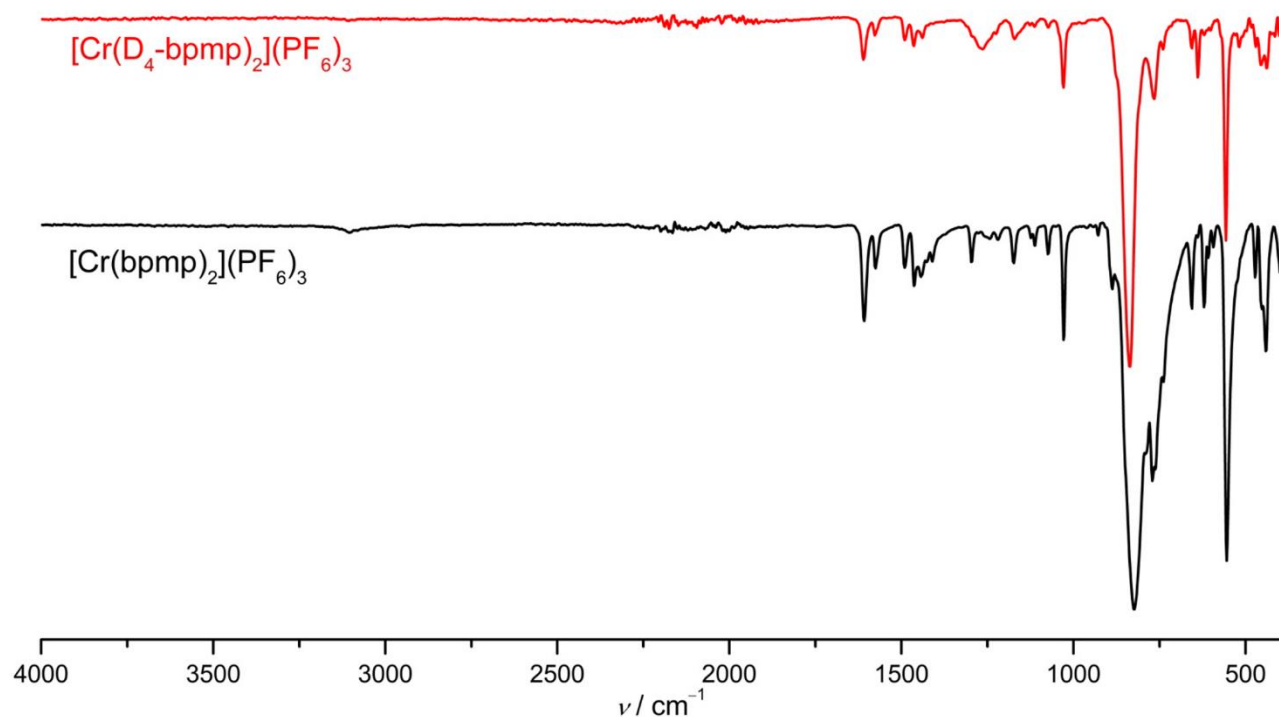


**Figure S27.** ATR-IR spectra of [Cr([D<sub>4</sub>]-bpmp)<sub>2</sub>][PF<sub>6</sub>]<sub>3</sub> with deuterated methylene bridges (red) and [Cr(bpmp)<sub>2</sub>][PF<sub>6</sub>]<sub>3</sub> (black).

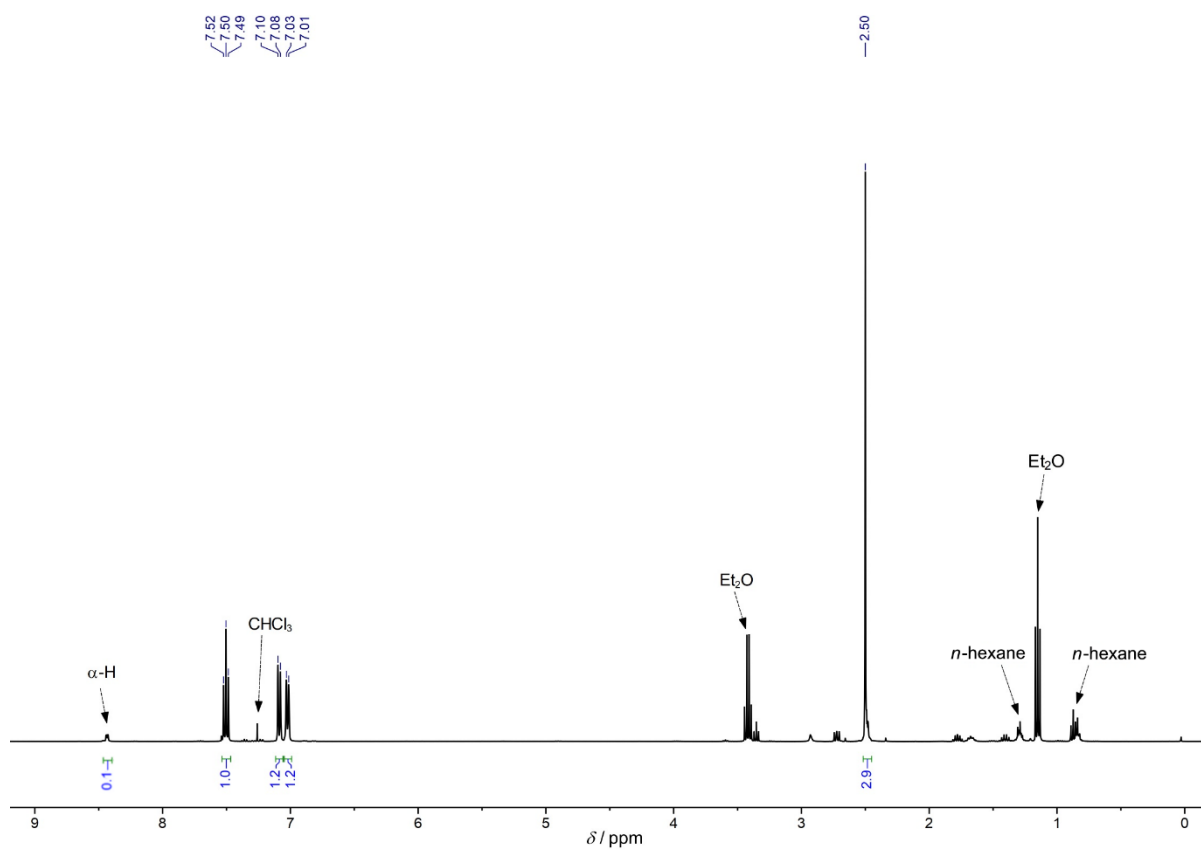


**Figure S28.**  $^1\text{H}$  NMR spectrum of 6-deutero-2-methylpyridine in  $\text{CDCl}_3$ .

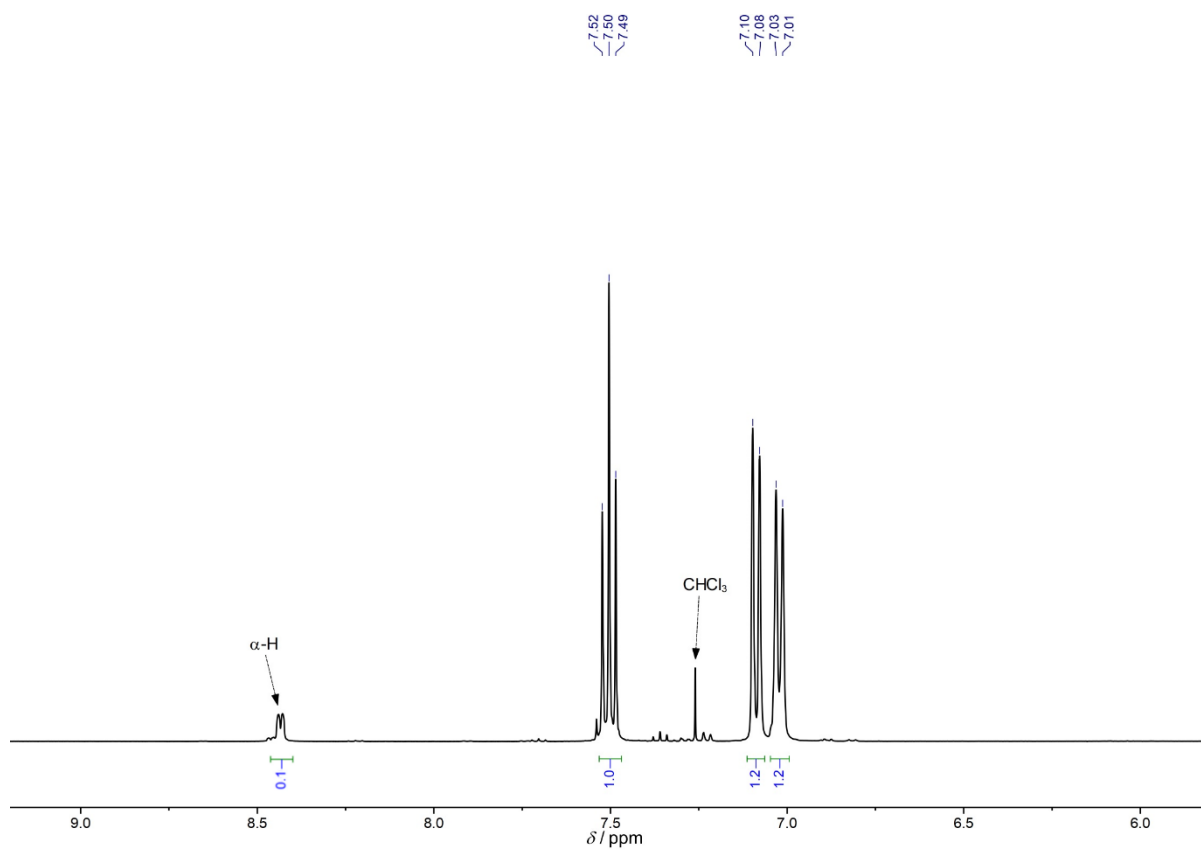


**Figure S29.** Zoom into the aromatic region of the  $^1\text{H}$  NMR spectrum of 6-deutero-2-methylpyridine in  $\text{CDCl}_3$ .

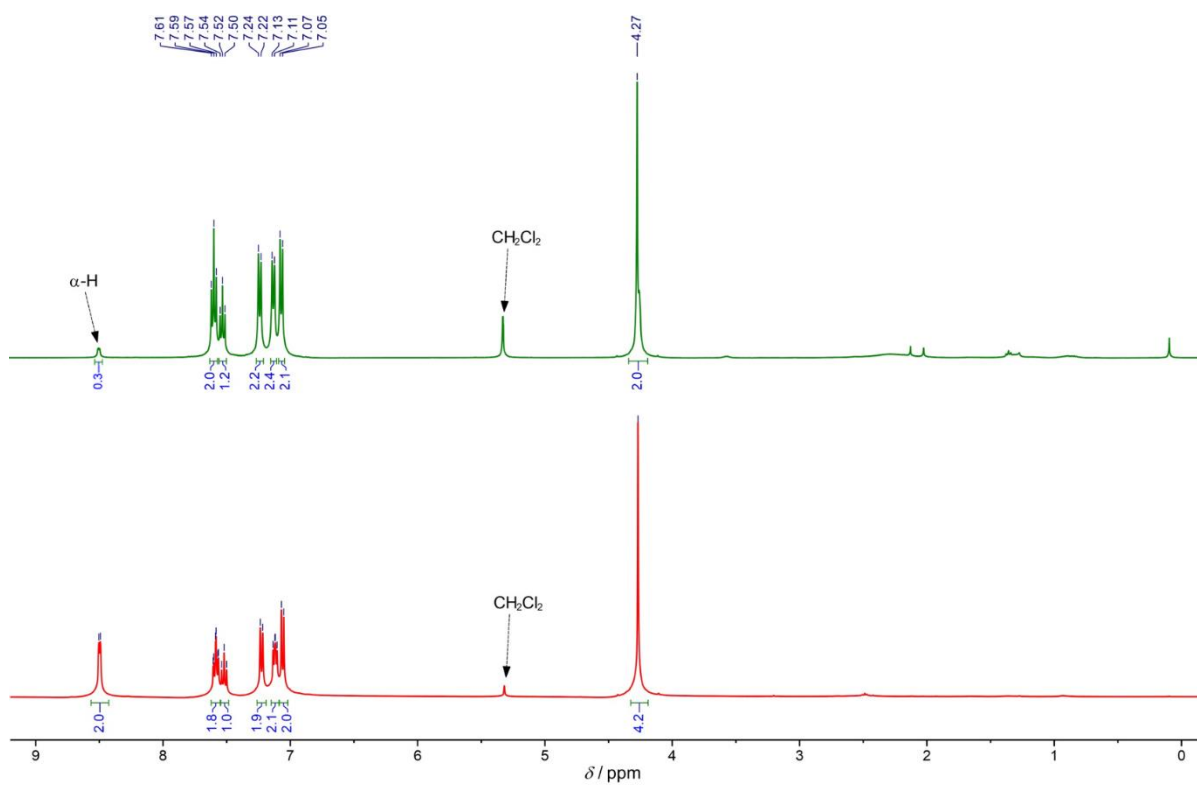


**Figure S30.**  $^1\text{H}$  NMR spectra of  $[\text{D}_{2/4}]$ -bpm (green) and bpm (red) in  $\text{CD}_2\text{Cl}_2$ .

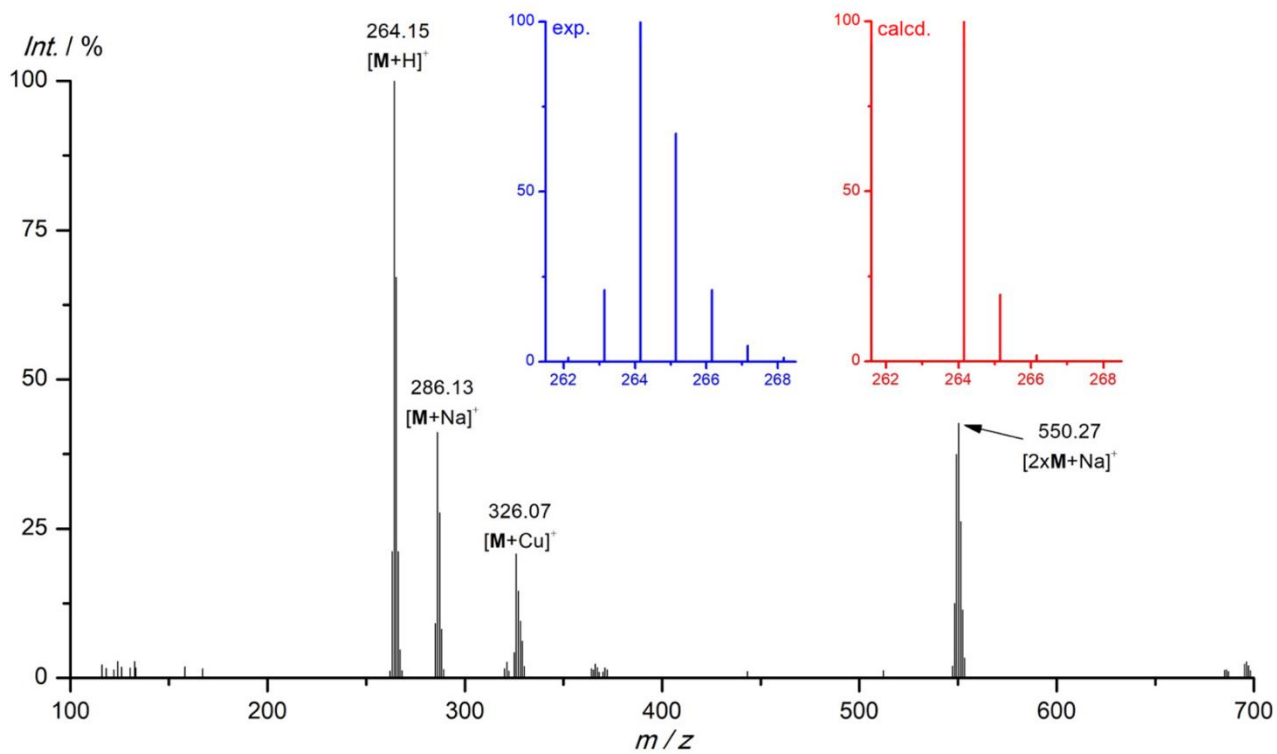
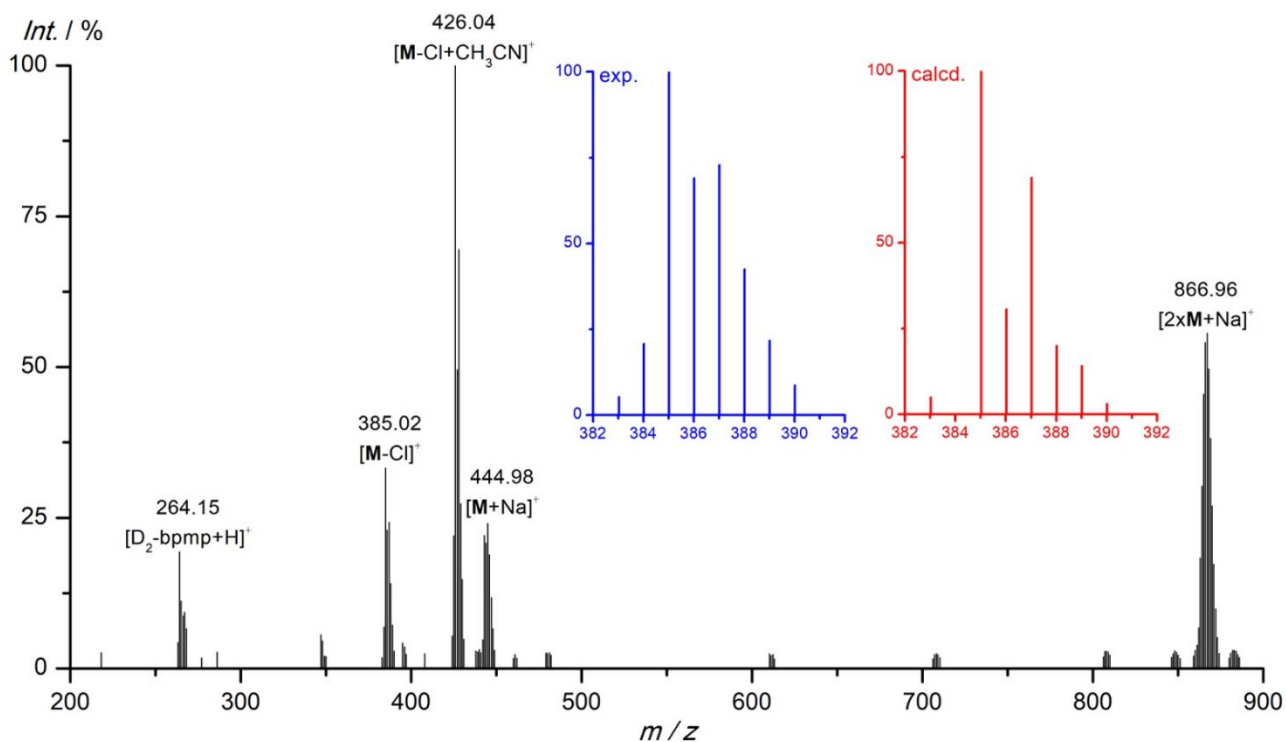


**Figure S31.**  $\text{ESI}^+$  mass spectrum of  $[\text{D}_2]$ -bpm in  $\text{CH}_3\text{CN}$ . The insets depict the experimental (blue) and calculated (red) isotopic pattern of the peak at  $m/z$  264.

a)



b)

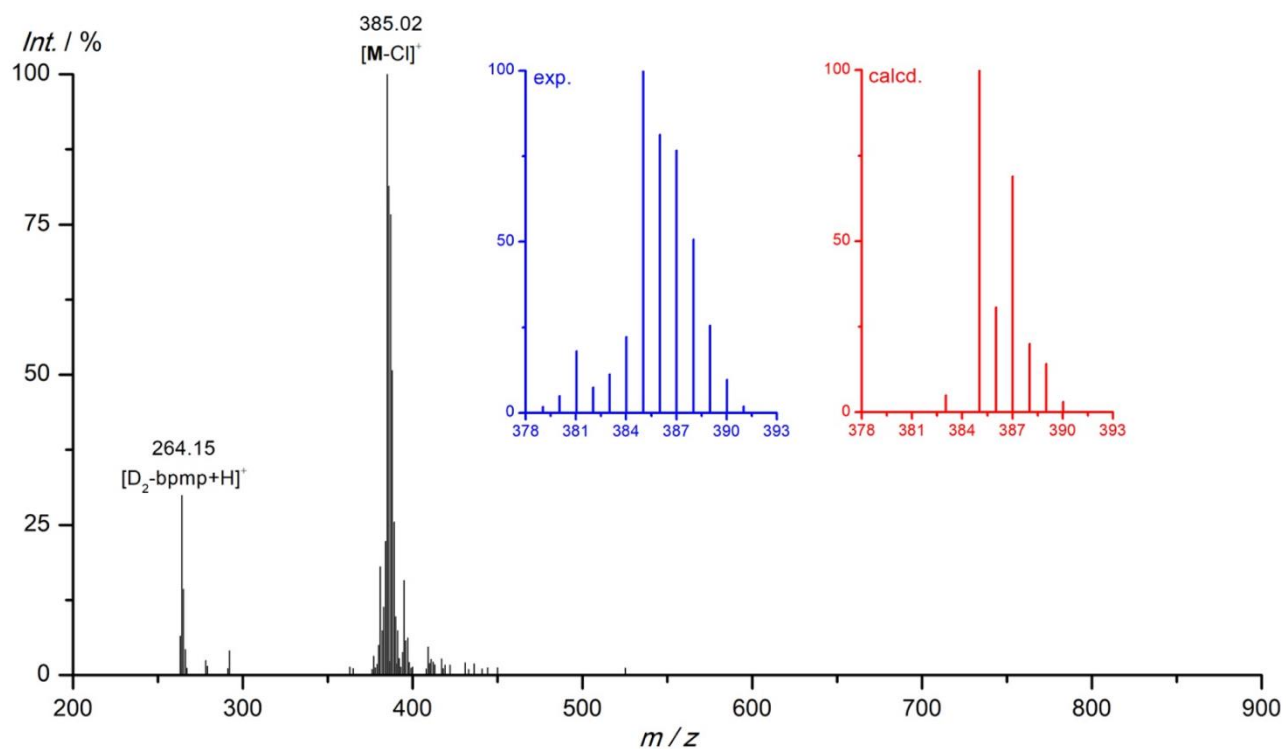


**Figure S32.** a) ESI<sup>+</sup> mass spectrum of Cr([D<sub>2</sub>]-bpm)Cl<sub>3</sub> in CH<sub>3</sub>CN. The insets depict the experimental (blue) and calculated (red) isotopic pattern of the peak at  $m/z$  385. b) APCI mass spectrum of Cr([D<sub>2</sub>]-bpm)Cl<sub>3</sub>. The insets depict the experimental (blue) and calculated (red) isotopic pattern of the peak at  $m/z$  385.



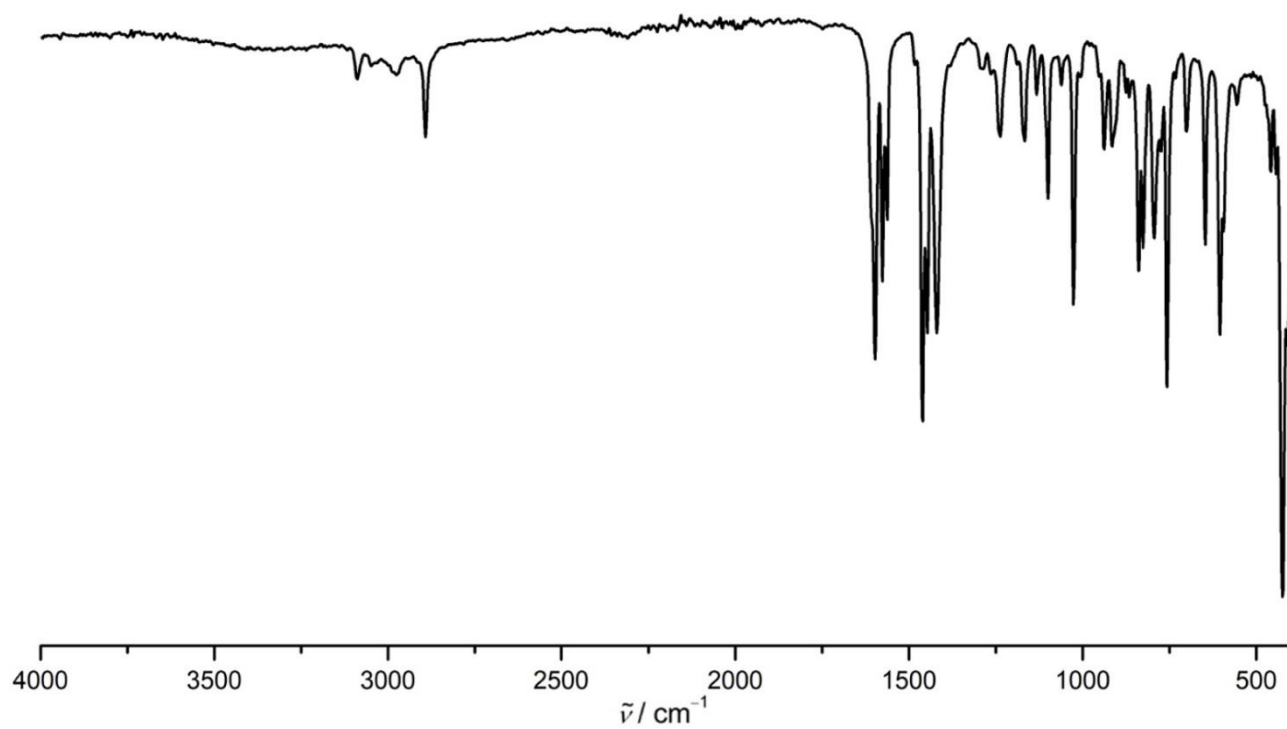
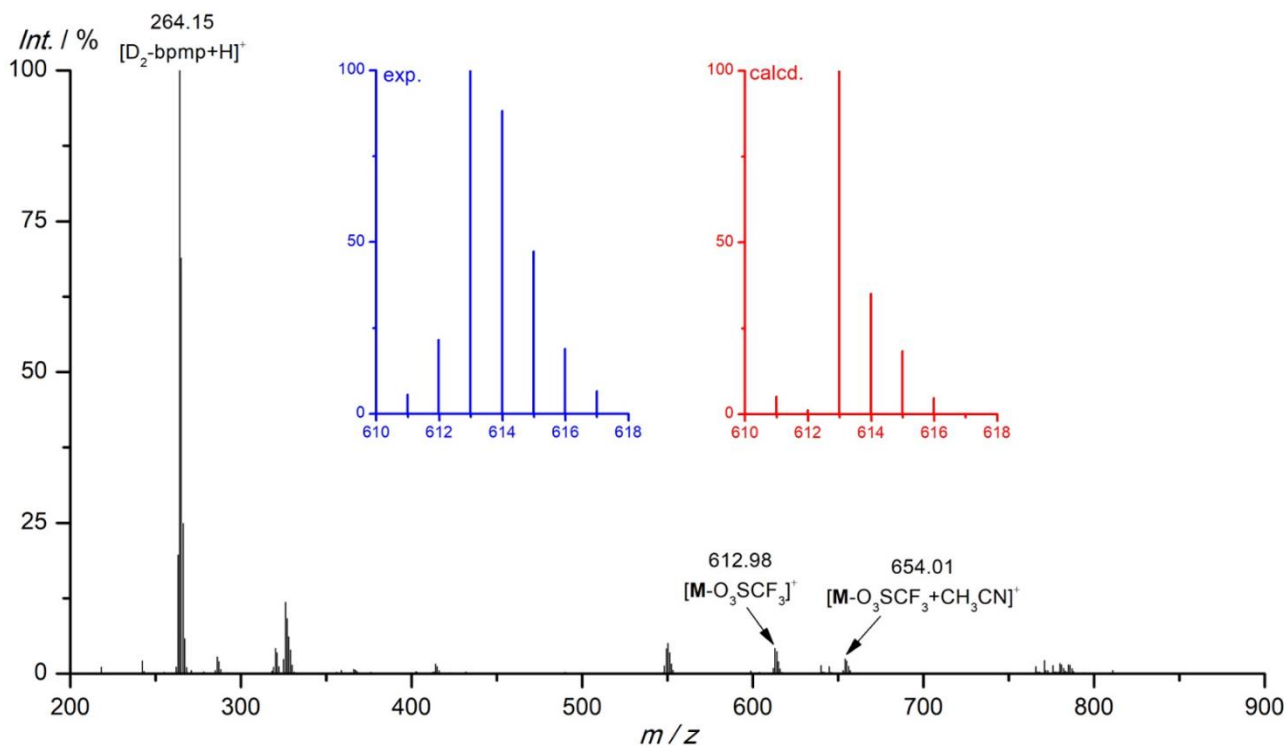


**Figure S33.** ATR-IR spectrum of Cr([D<sub>2</sub>]-bpm)Cl<sub>3</sub>.

a)



b)

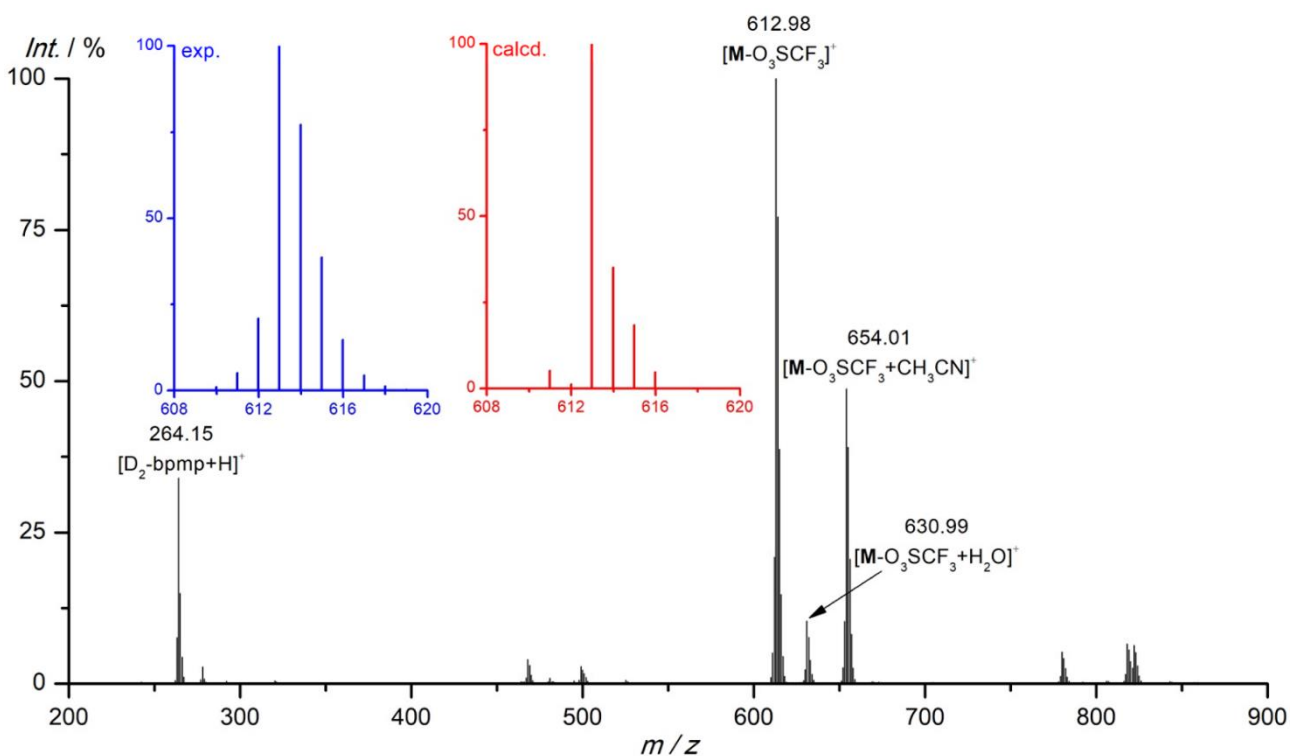


**Figure S34.** a) ESI<sup>+</sup> mass spectrum of Cr([D<sub>2</sub>]-bpmmp)(OTf)<sub>3</sub> in CH<sub>3</sub>CN. The insets depict the experimental (blue) and calculated (red) isotopic pattern of the peak at  $m/z$  613. b) APCI mass spectrum of Cr([D<sub>2</sub>]-bpmmp)(OTf)<sub>3</sub>. The insets depict the experimental (blue) and calculated (red) isotopic pattern of the peak at  $m/z$  613.

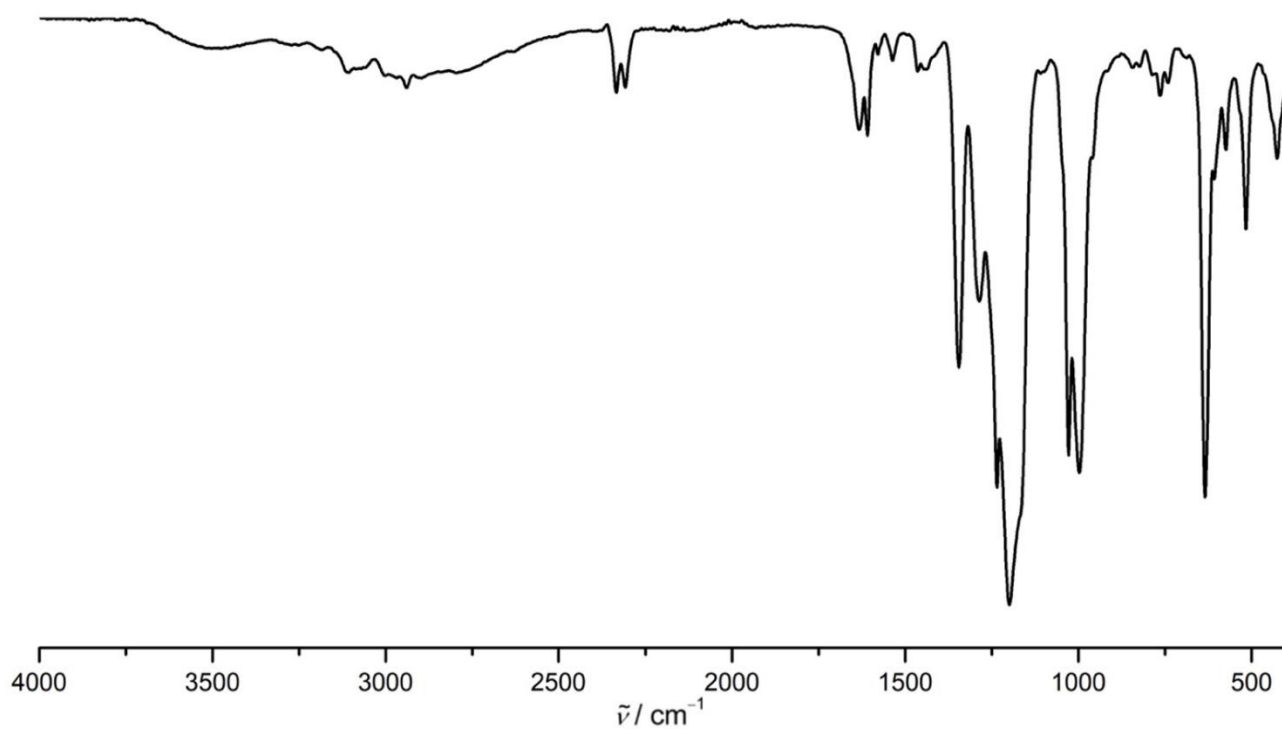


**Figure S35.** ATR-IR spectrum of  $\text{Cr}([\text{D}_2]\text{-bpmp})(\text{OTf})_3$ .

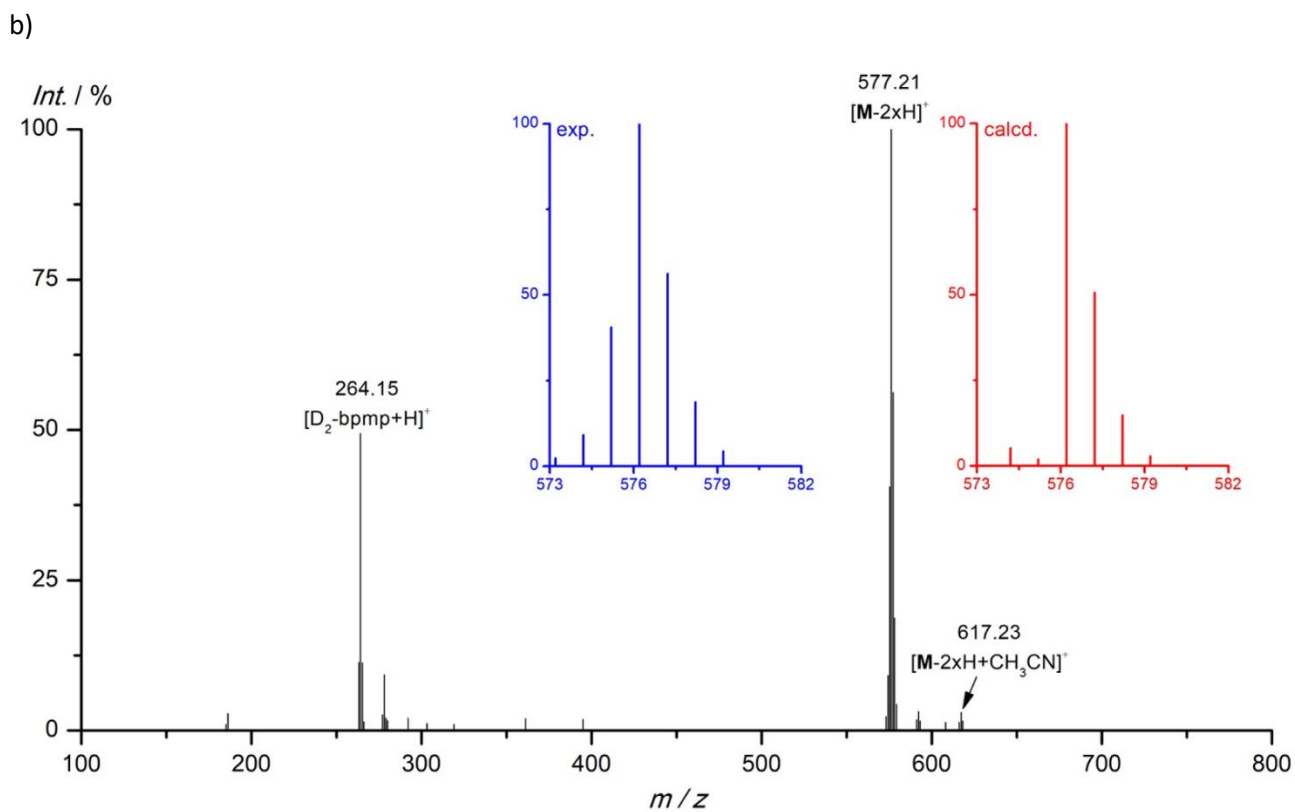
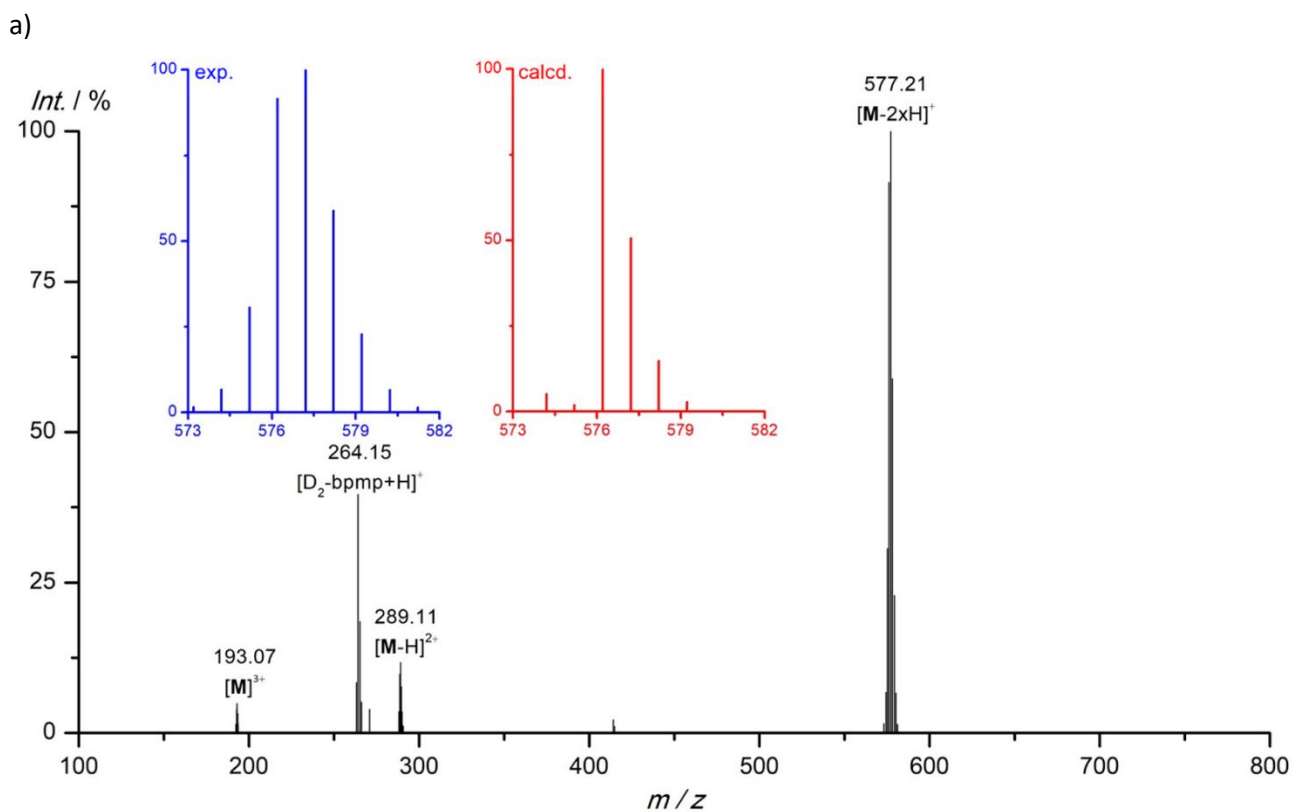


**Figure S36.** a) ESI<sup>+</sup> mass spectrum of  $[\text{Cr}([\text{D}_2\text{-bpmp}]_2)[\text{OTf}]_3]$  in  $\text{CH}_3\text{CN}$ . The insets depict the experimental (blue) and calculated (red) isotopic pattern of the peak at  $m/z$  576. b) APCI mass spectrum of  $[\text{Cr}([\text{D}_2\text{-bpmp}]_2)[\text{OTf}]_3]$ . The insets depict the experimental (blue) and calculated (red) isotopic pattern of the peak at  $m/z$  576.

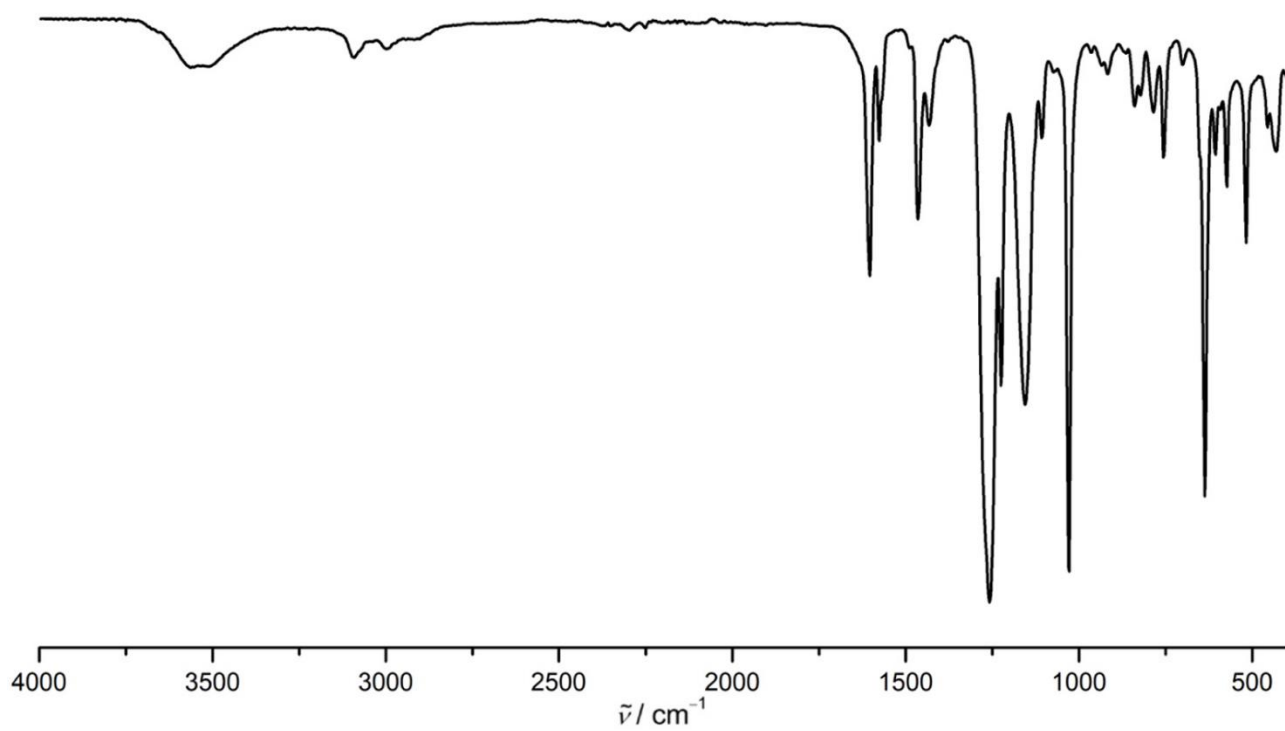


**Figure S37.** ATR-IR spectrum of  $[\text{Cr}([\text{D}_2]\text{-bpm})_2][\text{OTf}]_3$ .

## NIR Absorption Spectroscopy / Vibrational Overtone Analysis

Since the isotopologic chromium(III) complexes were not available in sufficient quantities, the analysis of the position and intensity of the C–H and C–D vibrational overtones for the chromium complexes was carried out on simpler pyridine-containing model compounds. The vibrational signatures of the methylene groups in **bpmp** were not investigated. Previously, the vibrational overtone data from the isotopologues of 6,6'-dimethyl-2,2'-bipyridine (**Me<sub>2</sub>-bpy** and **[D<sub>12</sub>]-Me<sub>2</sub>-bpy**, Figure Sx) proved to be a successful model system for the very similar **ddpd** ligand (Figure S38).<sup>43</sup>

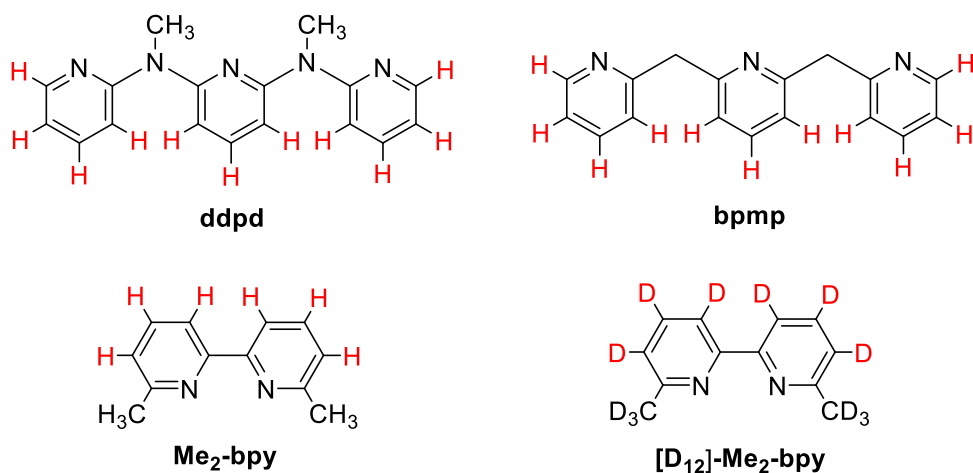


**Figure S38.** Top row: pyridine-based ligands in luminescent chromium complexes. Bottom row: model compounds used for the analysis of vibrational CH and CD overtones.

In order to verify if **Me<sub>2</sub>-bpy** and **[D<sub>12</sub>]-Me<sub>2</sub>-bpy** are also good model compounds for the isotopologues of **bpmp**, we measured the aromatic C–H overtone energies of **bpmp** up to the third overtone ( $\nu = 4$ ) and compared them to the previously obtained overtone data from **Me<sub>2</sub>-bpy** (Figure S39). The C–H overtones of **bpmp** showed a well-behaved Morse progression and could reasonably well be fitted with Gaussian functions of the form  $y(x) = A * \exp(-0.5 * ((x - x_c) / \sigma)^2)$ , defined by amplitude  $A$ , center wavenumber  $x_c$ , and Gaussian width  $\sigma$ . Despite the structural differences of **Me<sub>2</sub>-bpy** and **bpmp** the Gaussian functions of the aromatic C–H vibrational overtones were very similar and confirmed the validity of **Me<sub>2</sub>-bpy** as our model system.

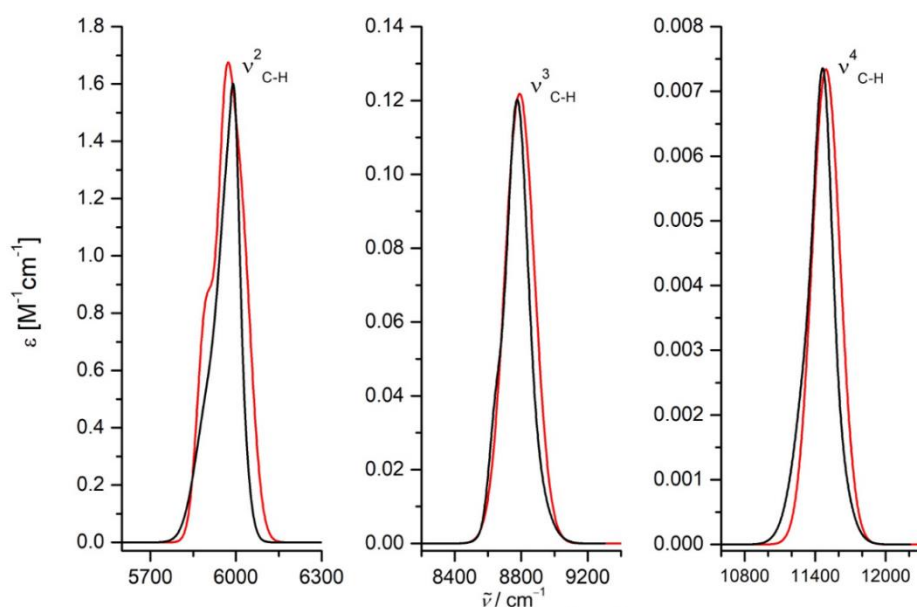


**Figure S39.** NIR absorption bands of the aromatic C–H vibrational overtones of **Me<sub>2</sub>bpy** (black) and **bpmp** (red) in CDCl<sub>3</sub> in the region  $\nu = 2$  (left),  $\nu = 3$  (middle), and  $\nu = 4$  (right). Due to the smaller number of aromatic C–H oscillators in **Me<sub>2</sub>bpy** (**6**) compared to **bpmp** (**11**) the Gaussians of **Me<sub>2</sub>bpy** have been scaled by a factor of 11/6.

Hence, we exploited the earlier calculated Gaussians of the aromatic C–(H/D) overtones<sup>43</sup> of **Me<sub>2</sub>-bpy** and **[D<sub>12</sub>]-Me<sub>2</sub>-bpy** for the SOI calculations. The integrand functions for the SOIs between the chromium complex emission and the relevant C–(H/D) overtones were constructed according to the mathematical definition of the SOIs:

$$\text{SOI} = \int I_{\text{norm}}(\tilde{\nu}) \cdot \varepsilon_{\text{vib}}(\tilde{\nu}) \cdot \tilde{\nu}^{-4} d\tilde{\nu}$$

with  $I_{\text{norm}}$  being the chromium emission spectrum (normalized to unit area) and  $\varepsilon$  the molar vibrational extinction coefficient (extracted and extrapolated absorption spectra of the relevant overtones), both expressed in the wavenumber scale  $\tilde{\nu}$ . The integrand functions were generated with a set of data points with a step size of 1 cm<sup>-1</sup>. Numerical integration (OriginPro 9.0) gave the corresponding values for SOI.

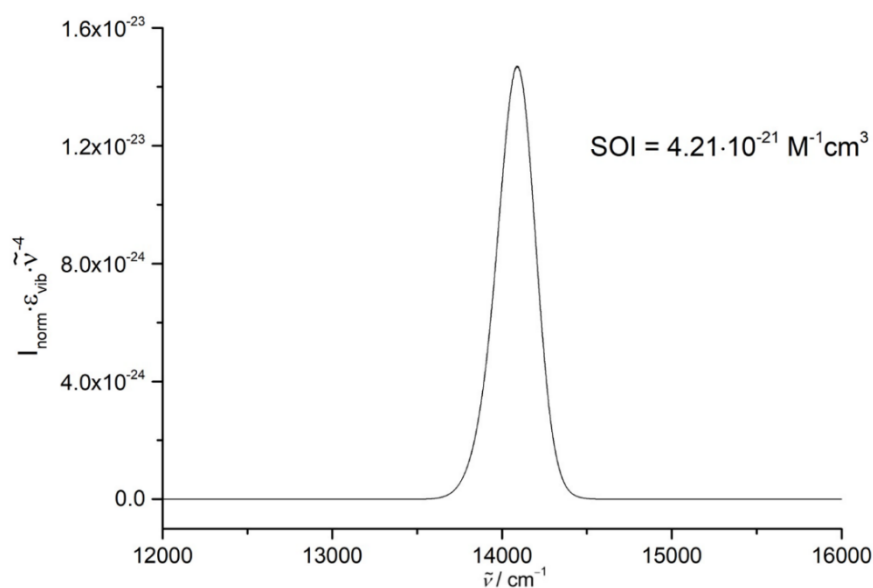


**Figure S40.** Integrand function of the spectral overlap integral (SOI) for the chromium emission band in **[Cr(bpmp)<sub>2</sub>]<sup>3+</sup>** and the fourth aromatic C–H ( $\nu = 5$ ) oscillators in **Me<sub>2</sub>-bpy**.

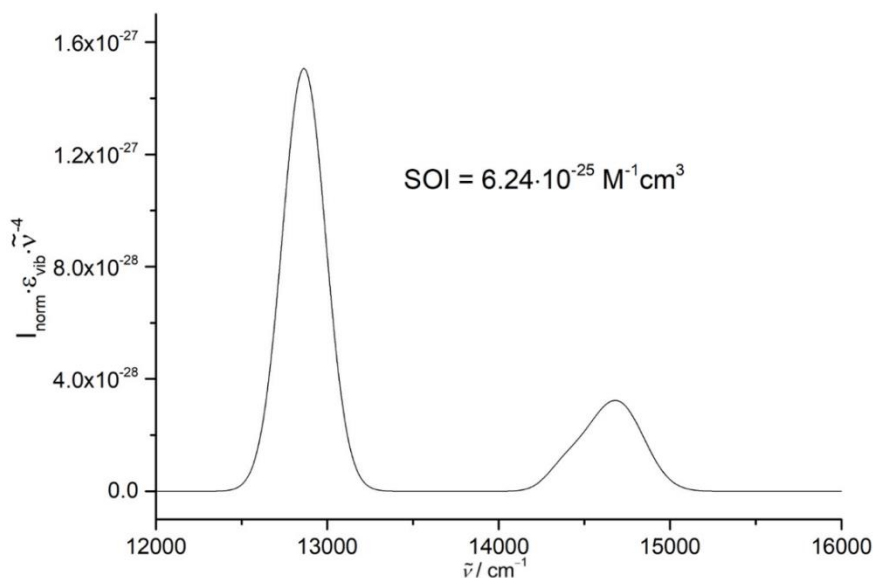


**Figure S41.** Integrand function of the spectral overlap integral (SOI) for the chromium emission band in  $[\text{Cr}(\text{bpmp})_2]^{3+}$  and the fifth ( $\nu = 6$ ) and sixth ( $\nu = 7$ ) aromatic C–D oscillators in  $[\text{D}_{12}]\text{-Me}_2\text{-bpy}$ .

Based on the obtained SOIs, the ratio of the non-radiative deactivation rates of chromium excited states from  $[\text{Cr}(\text{bpmp})_2]^{3+}$  and fully deuterated  $[\text{Cr}(\text{bpmp})_2]^{3+}$  is estimated as:

$$\frac{k_{\text{nr}}(\text{C-H})}{k_{\text{nr}}(\text{C-D})} = \frac{\text{SOI}(\text{C-H})}{\text{SOI}(\text{C-D})} = \frac{4.21 \cdot 10^{-21} \text{ M}^{-1} \text{ cm}^3}{6.24 \cdot 10^{-25} \text{ M}^{-1} \text{ cm}^3} = 6.75 \cdot 10^3$$

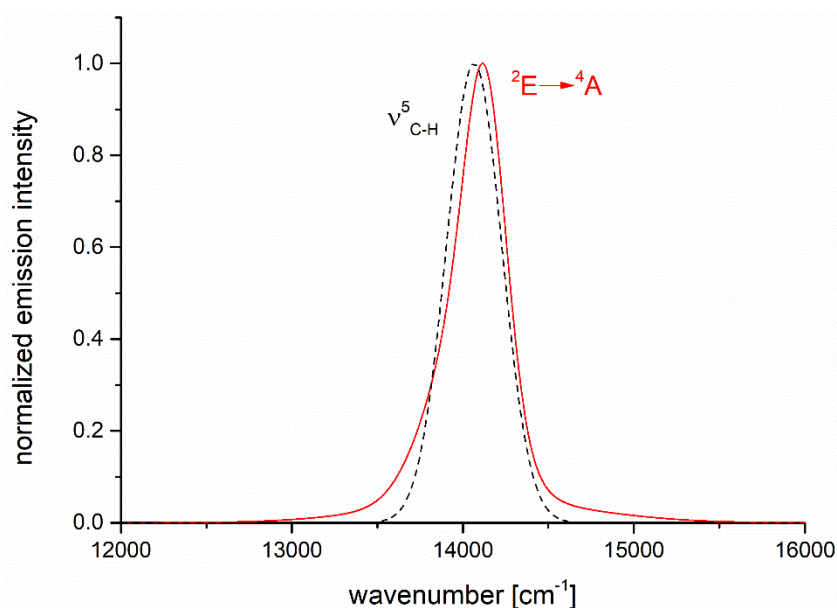


**Figure S42.** Normalized spectra for the chromium  ${}^2\text{E}$  emission of  $[\text{Cr}(\text{bpmp})_2]^{3+}$  (red) and the relevant vibrational aromatic C–H overtone absorption band (dashed black).



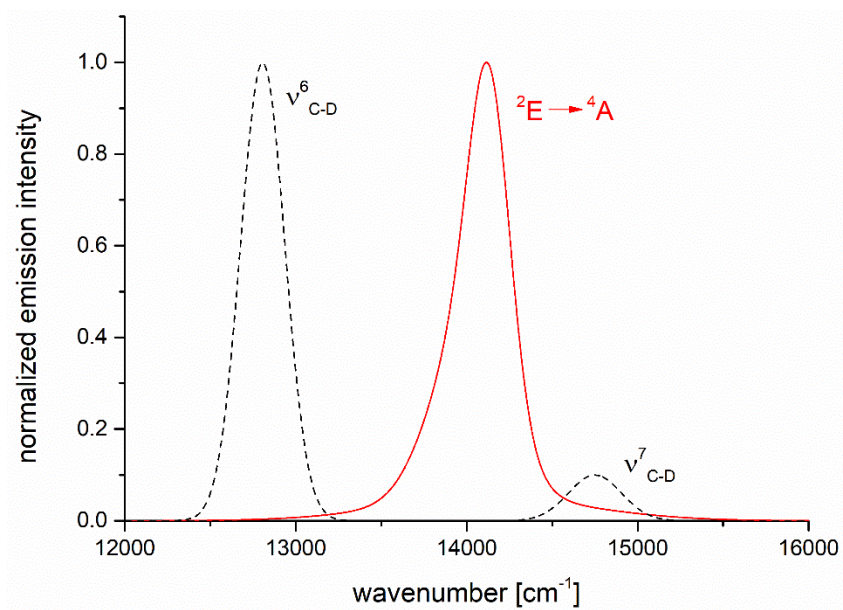


**Figure S43.** Spectra for the chromium  ${}^2E$  emission of  $[\text{Cr}(\text{bpmp})_2]^{3+}$  (red) and the relevant vibrational aromatic C–D overtone absorption bands (dashed black). The overtone intensities are shown with their actual intensity ratios.

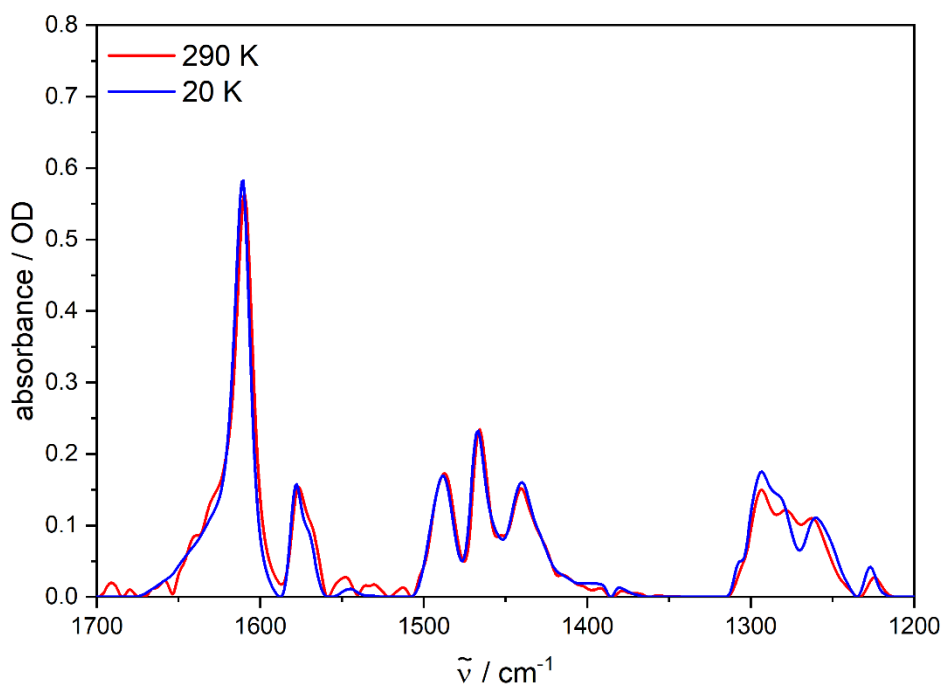


**Figure S44.** FTIR spectra of [Cr(bmpm)<sub>2</sub>][BF<sub>4</sub>]<sub>3</sub> as KBr pellets at 290 K (red) and 20 K (blue).

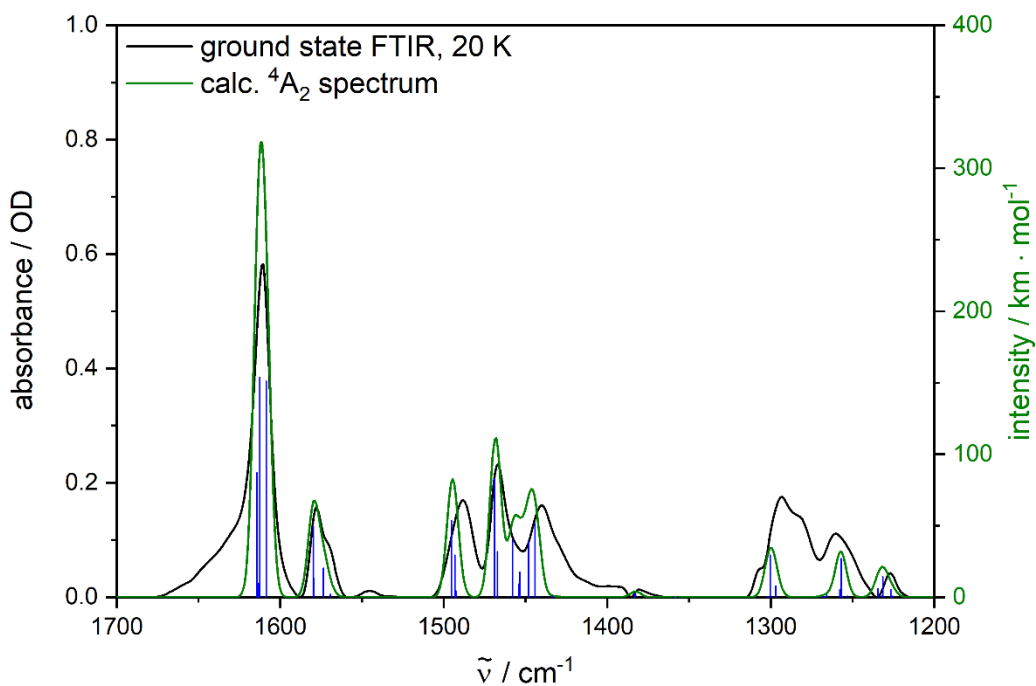


**Figure S45.** Ground state FTIR spectrum of [Cr(bmpm)<sub>2</sub>][BF<sub>4</sub>]<sub>3</sub> (KBr pellet, 20 K) (black) and calculated IR frequencies (blue sticks) and calculated IR spectrum (green) of [Cr(bmpm)<sub>2</sub>]<sup>3+</sup> (scaled by 0.98, FWHM = 8 cm<sup>-1</sup>, pseudo-Voigt profile) (DFT/B3LYP/def2-TZVP/D3-BJ).

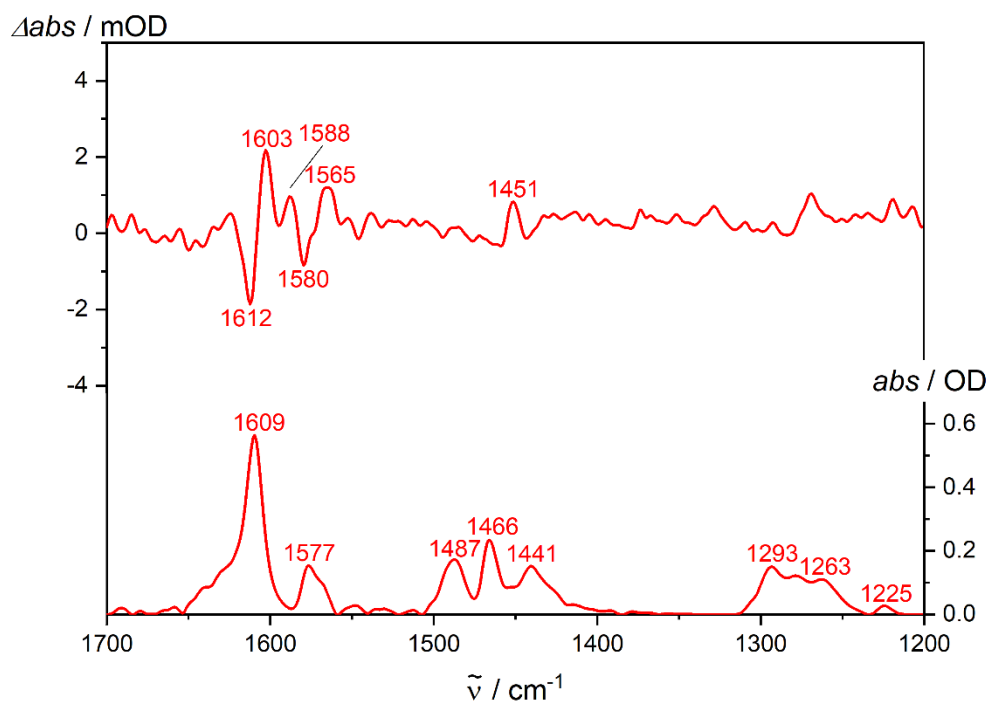


**Figure S46.** FTIR ground state spectrum (bottom) and step-scan spectra difference spectrum (top) of  $[\text{Cr}(\text{bpmp})_2][\text{BF}_4]_3$  (KBr pellet) recorded 0 – 1  $\mu\text{s}$  after laser excitation at 355 nm ( $T = 290$  K).

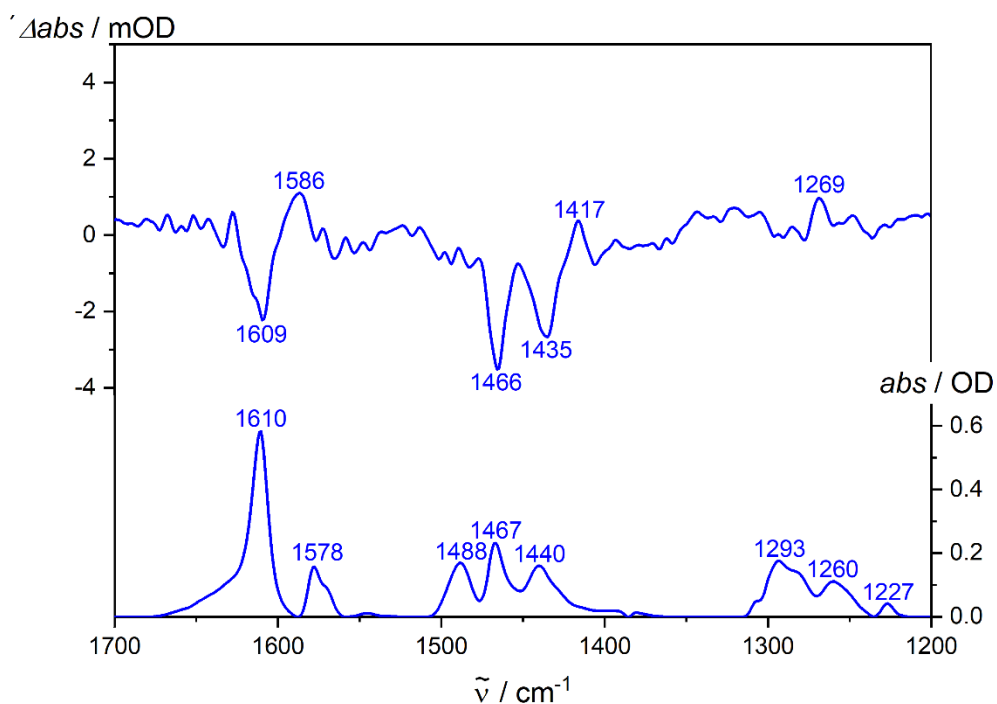


**Figure S47.** FTIR ground state spectrum (bottom) and step-scan spectra difference spectrum (top) of  $[\text{Cr}(\text{bpmp})_2][\text{BF}_4]_3$  (KBr pellet) recorded 0 – 1  $\mu\text{s}$  after laser excitation at 355 nm ( $T = 20$  K).

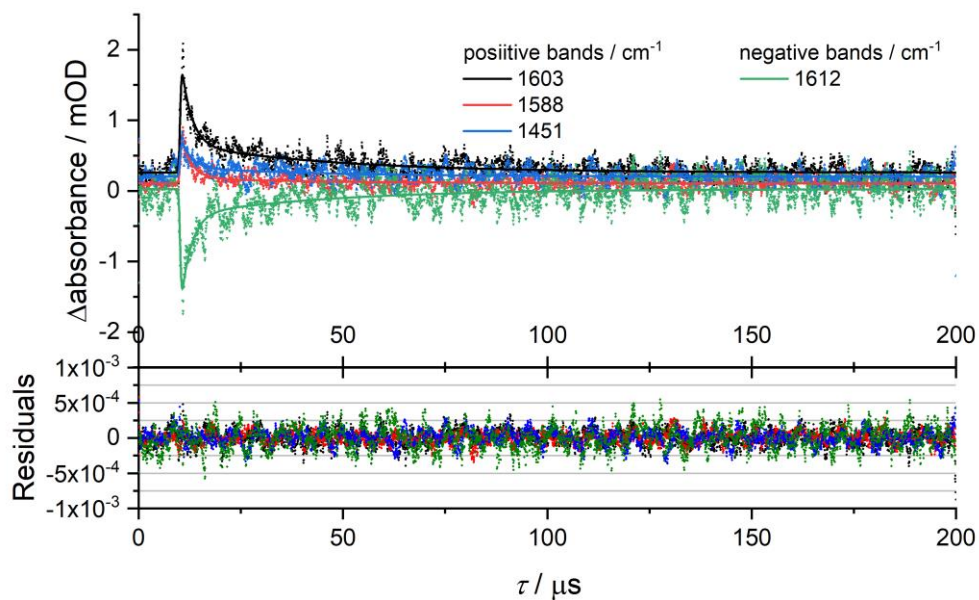


**Figure S48.** Global biexponential fit and residuals of [Cr(bmpm)<sub>2</sub>][BF<sub>4</sub>]<sub>3</sub> (KBr pellet) at 290 K.

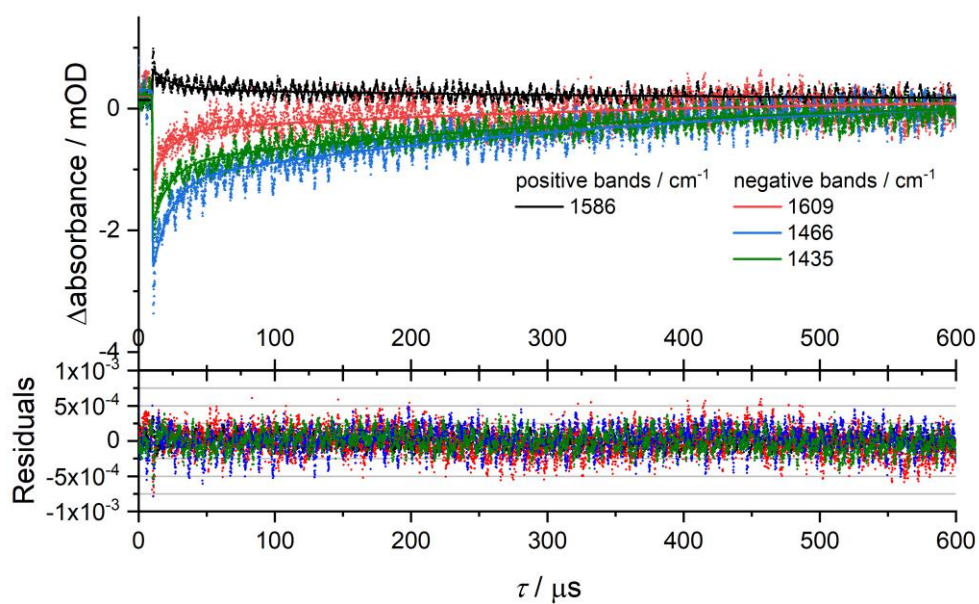


**Figure S49.** Global biexponential fit and residuals of [Cr(bmpm)<sub>2</sub>][BF<sub>4</sub>]<sub>3</sub> (KBr pellet) at 20 K.

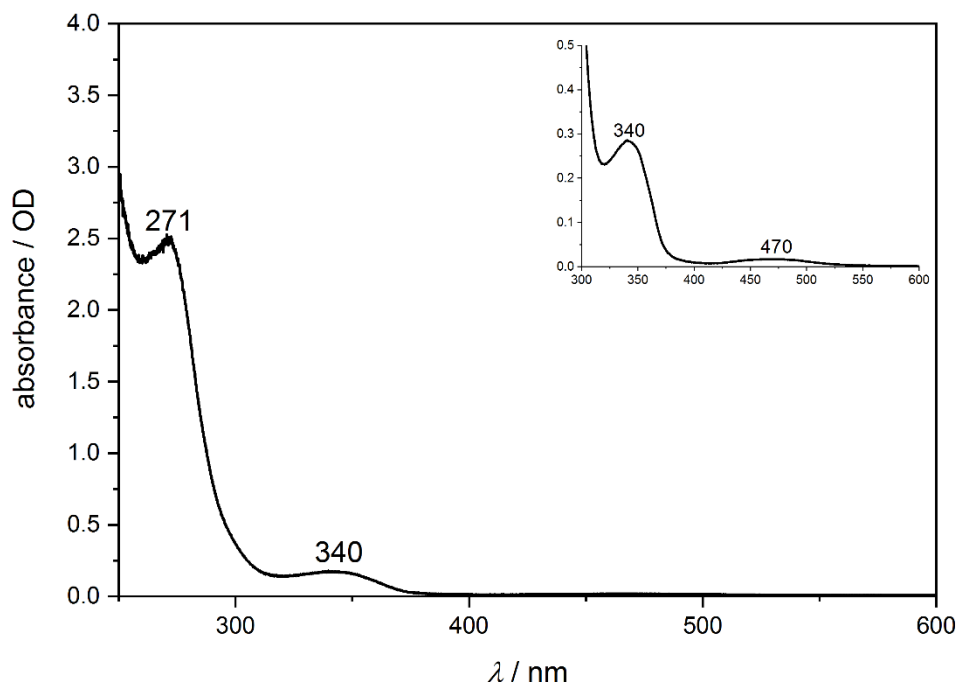


**Figure S50.** UV/Vis absorption spectrum of [Cr(bpmp)<sub>2</sub>][BF<sub>4</sub>]<sub>3</sub> (thin film) at 290 K.

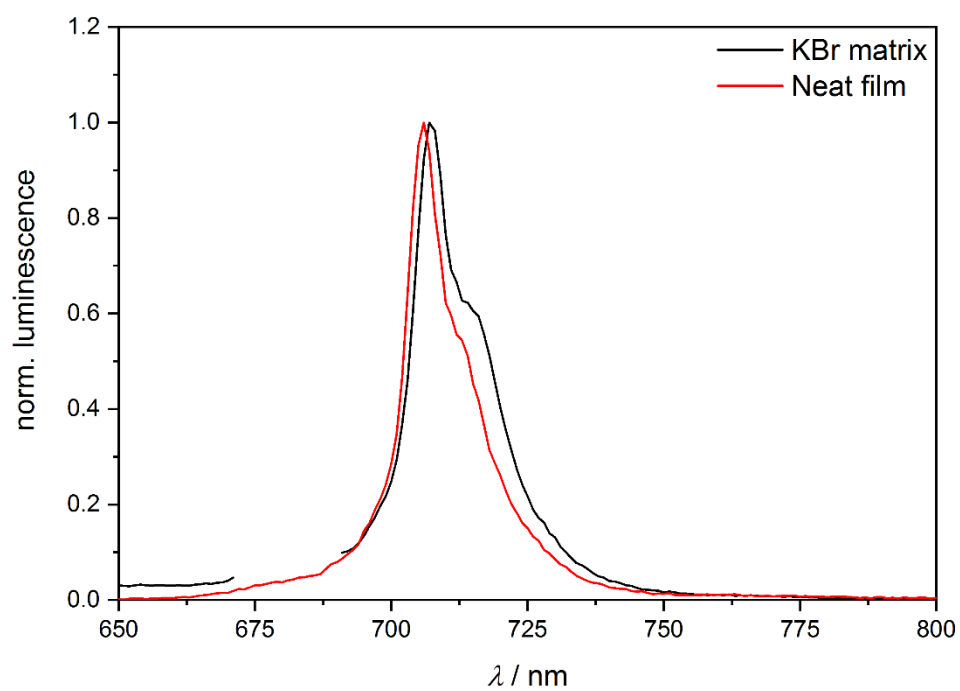


**Figure S51.** Luminescence spectrum of [Cr(bpmp)<sub>2</sub>][BF<sub>4</sub>]<sub>3</sub> (thin film and KBr pellet) at 290 K,  $\lambda_{exc} = 340$  nm.

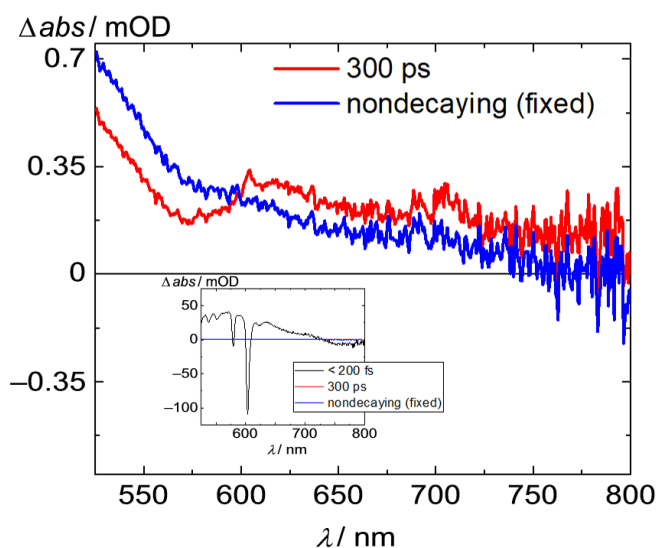


**Figure S52.** EADS of  $[\text{Cr}(\text{bpmp})_2][\text{OTf}]_3$  in  $\text{CH}_3\text{CN}/\text{HClO}_4$  excited with  $\lambda_{\text{exc}} = 515$  nm at 290 K. The inset displays the EADS of the very short component included in the fit, which is probably a coherent artefact.

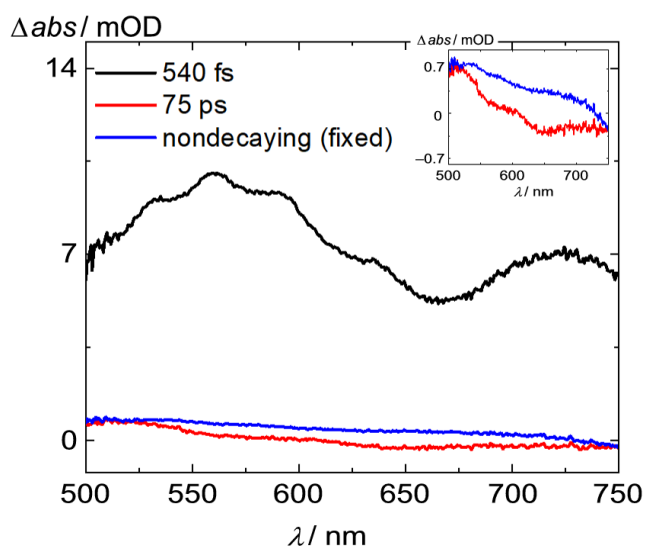


**Figure S53.** EADS of  $[\text{Cr}(\text{bpmp})_2][\text{OTf}]_3$  in  $\text{CH}_3\text{CN}/\text{HClO}_4$  excited with  $\lambda_{\text{exc}} = 350$  nm at 290 K. The inset displays the EADS of the longer components for better comparison.

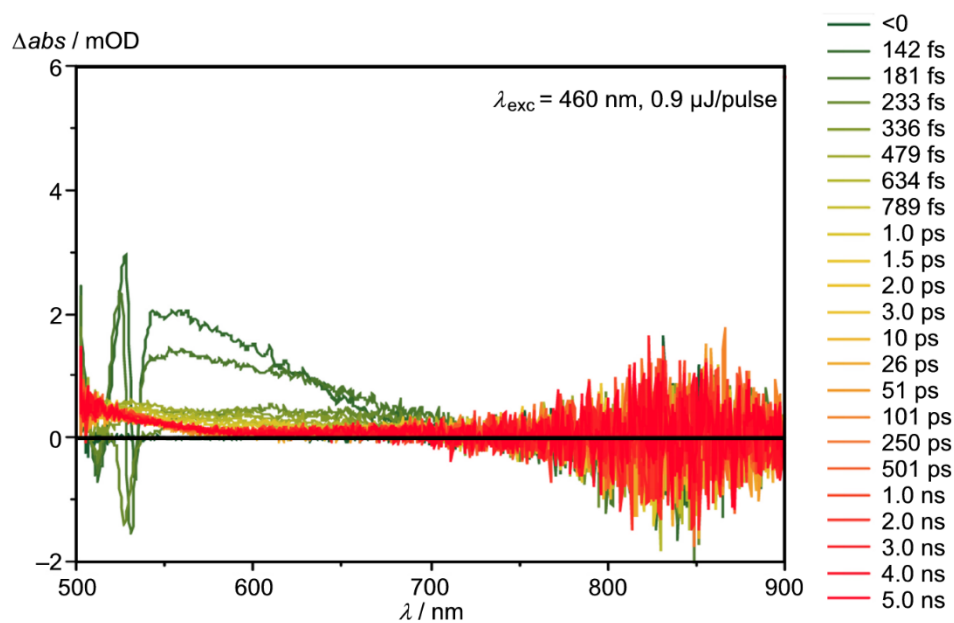


**Figure S54.** Transient absorption spectra of  $[\text{Cr}(\text{bpmp})_2][\text{OTf}]_3$  in  $\text{CH}_3\text{CN}$  ( $\text{HClO}_4$ ) excited with fs laser pulses at 460 nm ( $^4\text{T}_2$  states). The TA spectra are very similar to the ones obtained with 515 nm excitation shown in Fig. 6a ( $^4\text{T}_2$  states), only the pump laser power is lower.

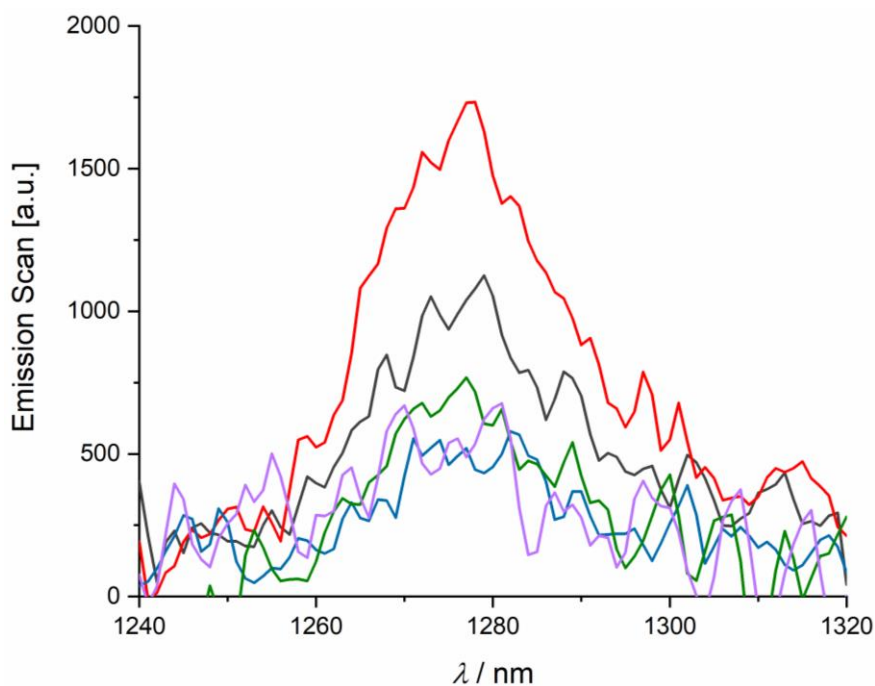


**Figure S55.**  $^1\text{O}_2$  emission sensitized by  $[\text{Cr}(\text{ddpd})_2][\text{BF}_4]_3$  in DMF (black),  $[\text{Cr}(\text{ddpd})_2][\text{BF}_4]_3$  in DMF/ $\text{HClO}_4$  (red),  $[\text{Cr}(\text{bpmp})_2][\text{BF}_4]_3$  in DMF/ $\text{HClO}_4$  (green),  $[\text{Cr}(\text{bpmp})_2][\text{PF}_6]_3$  in DMF/ $\text{HClO}_4$  (blue) and  $[\text{Cr}(\text{bpmp})_2][\text{OTf}]_3$  in DMF/ $\text{HClO}_4$  (purple).

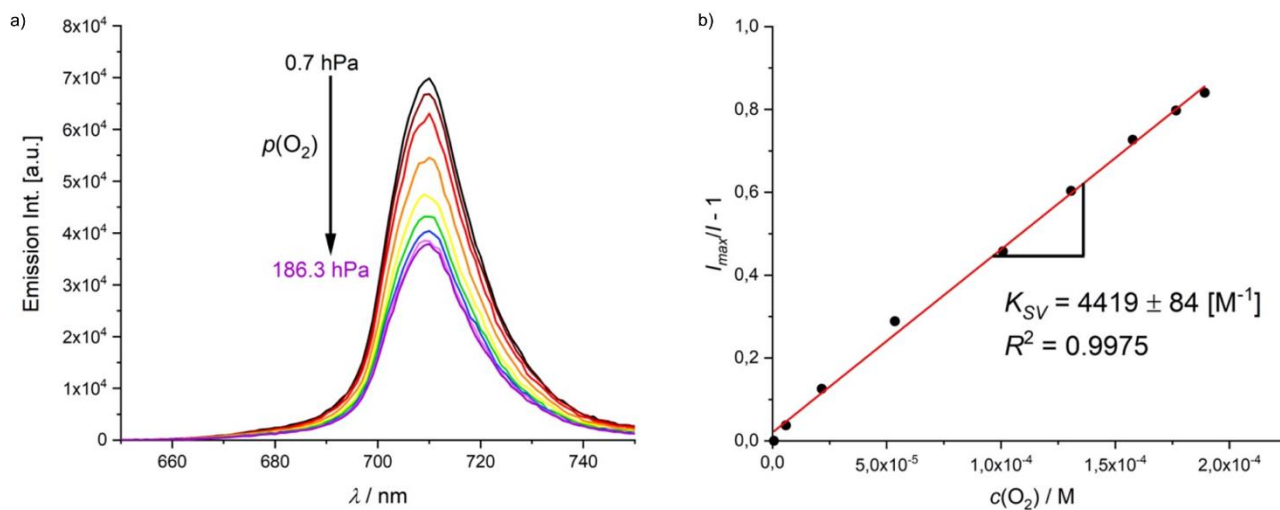


**Figure S56.** A) Emission spectra of  $[\text{Cr}(\text{bpmp})_2][\text{OTf}]_3$  with  $\text{O}_2$  in  $\text{H}_2\text{O}/\text{HClO}_4$  and b) corresponding steady-state Stern-Volmer plot. Steady-state implies that the emission intensities at different oxygen concentration/partial pressure were exploited for the Stern-Volmer plot.

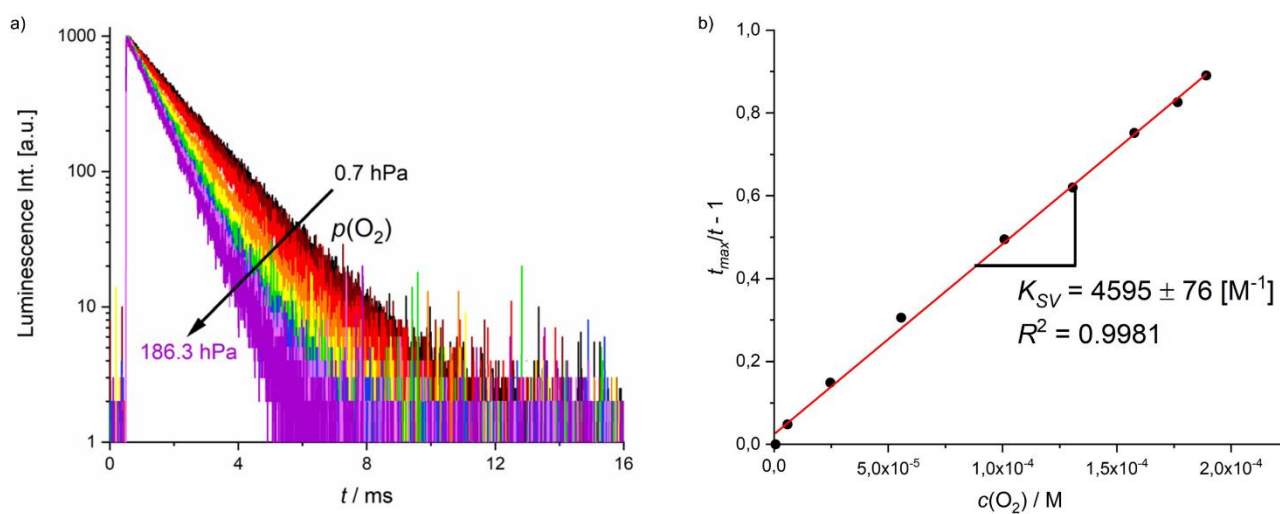


**Figure S57.** A) Luminescence decays of  $[\text{Cr}(\text{bpmp})_2][\text{OTf}]_3$  with  $\text{O}_2$  in  $\text{H}_2\text{O}/\text{HClO}_4$  and b) corresponding time-resolved Stern-Volmer plot. Time-resolved implies that the oxygen concentration/partial pressure-dependent luminescence lifetimes were utilized for the Stern-Volmer plot.



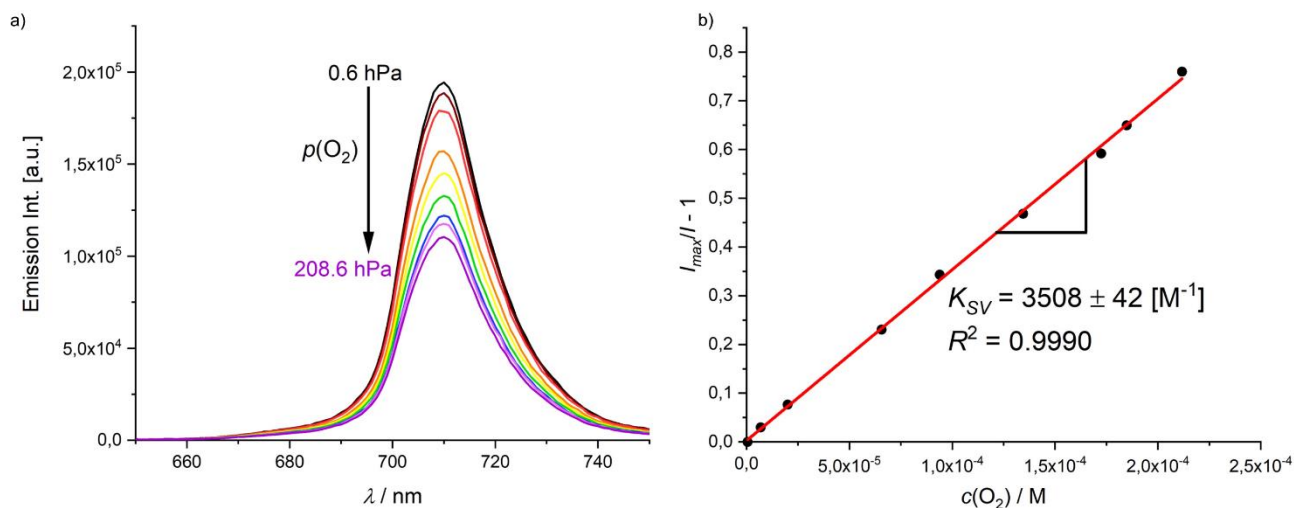


**Figure S58.** A) Emission spectra of  $[\text{Cr}(\text{bmpm})_2][\text{BF}_4]_3$  with  $\text{O}_2$  in  $\text{H}_2\text{O}/\text{HClO}_4$  and b) corresponding steady-state Stern-Volmer plot.

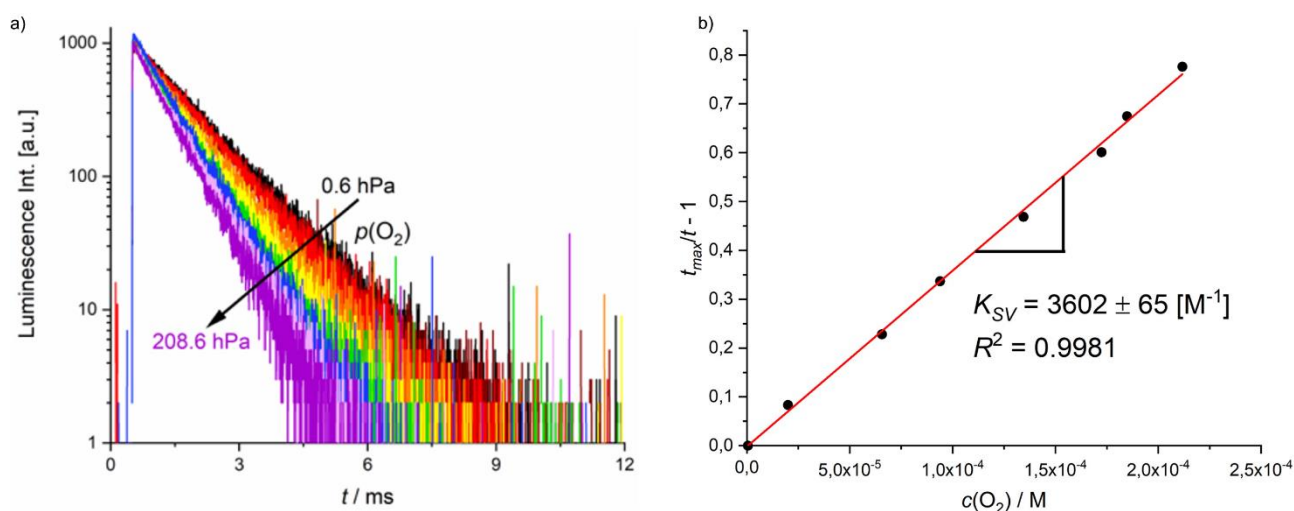


**Figure S59.** A) Luminescence decays of  $[\text{Cr}(\text{bmpm})_2][\text{BF}_4]_3$  with  $\text{O}_2$  in  $\text{H}_2\text{O}/\text{HClO}_4$  and b) corresponding time-resolved Stern-Volmer plot.

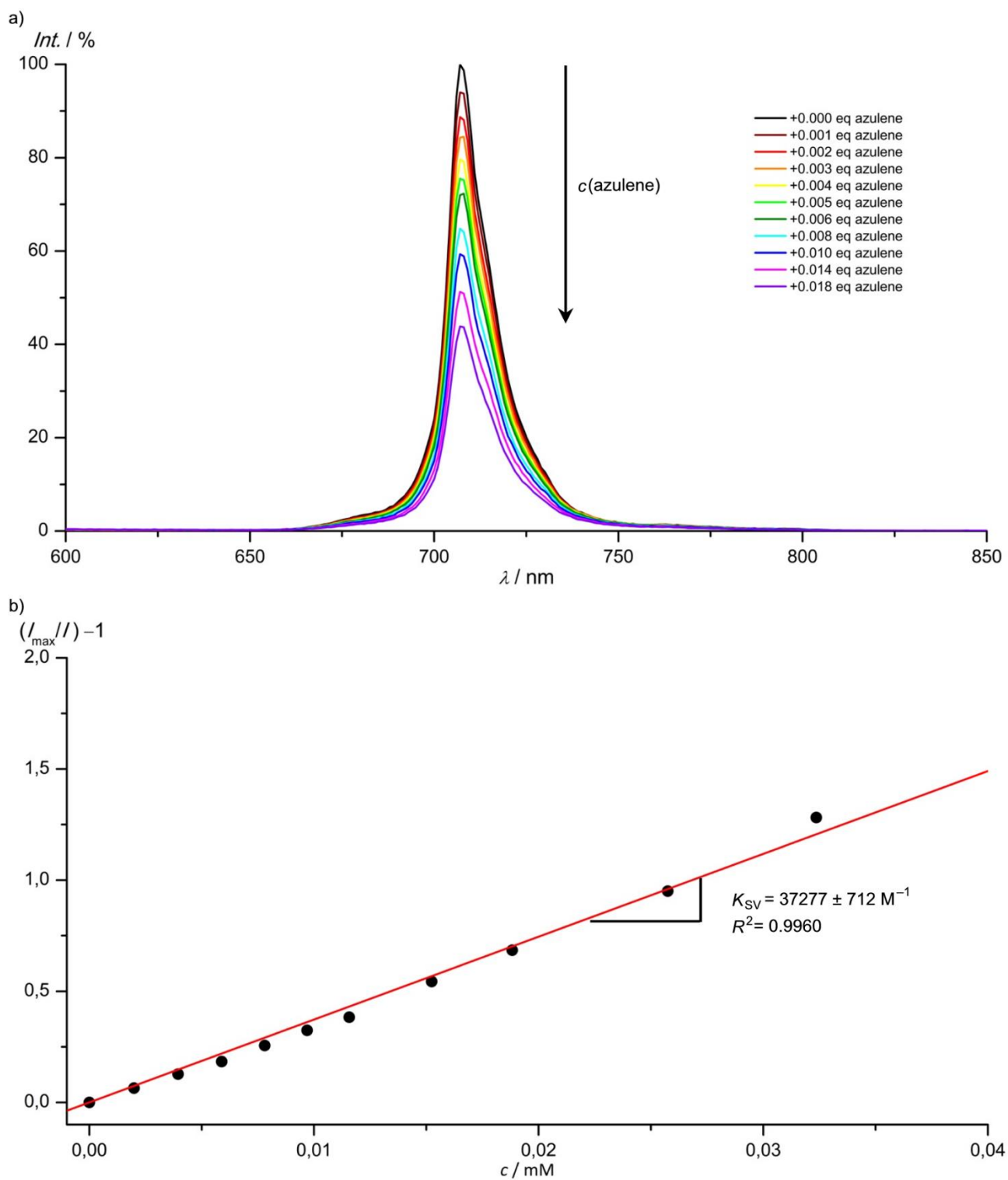


**Figure S60.** a) Emission spectra of  $[\text{Cr}(\text{bpmp})_2][\text{OTf}]_3$  with azulene in  $\text{CH}_3\text{CN}$  (undried) and b) corresponding steady-state Stern-Volmer plot.

**Table S10. Cartesian Coordinates of Cr(acac)<sub>3</sub>.**

Cr	0.00000000	0.00000000	0.00000000
O	-0.02290600	-1.96960100	-0.06688100
O	-1.97178200	0.05676800	-0.00207400
O	0.01112900	0.05236700	-1.96915900
O	-0.00510600	1.96650500	0.08139500
O	1.96631200	-0.05780900	-0.01374200
O	-0.01005300	-0.06689200	1.97593900
C	-1.05104800	-2.72488300	-0.07937200
C	-2.37672800	-2.27814000	-0.08523400
C	-2.77045300	-0.93637600	-0.04718300
C	-0.76513700	-4.19843600	-0.09174800
C	-4.23124300	-0.58854900	-0.05937300
C	-0.06318200	1.08498600	-2.71343000
C	-0.14158400	2.40168500	-2.24698700
C	-0.12587000	2.77464400	-0.89926600
C	-0.06063200	0.81681300	-4.19059300
C	-0.25815000	4.22276700	-0.52771300
C	2.73895700	-0.26332700	0.98241200
C	2.32042400	-0.35534800	2.31025200
C	0.99543700	-0.22754400	2.74209200
C	4.19733700	-0.39431000	0.65494100
C	0.71612400	-0.24809500	4.21678700
H	-3.15408300	-3.02519900	-0.10814300
H	-0.25928800	-4.45602200	-1.02514200
H	-1.66922600	-4.79411200	0.00400800
H	-0.08077400	-4.43965300	0.72242500
H	-4.47050200	-0.09416600	-1.00438000
H	-4.44270600	0.12308300	0.73876000
H	-4.86298200	-1.46566800	0.05628900
H	-0.22556900	3.18699400	-2.98130300
H	-0.80524600	0.05556800	-4.42432200
H	0.91417000	0.41355000	-4.47592000
H	-0.26176600	1.71404100	-4.77056500
H	0.64172000	4.54424400	0.00067700
H	-1.09503600	4.33858400	0.16288200
H	-0.41598000	4.85771700	-1.39568700
H	3.07414500	-0.51625800	3.06486800
H	4.32767100	-1.13918800	-0.13081200
H	4.78651800	-0.67611600	1.52414400
H	4.56296100	0.55774600	0.26364800
H	-0.29677300	-0.59880100	4.40735700
H	0.81019300	0.76964800	4.60528600
H	1.43180500	-0.87108000	4.74829400

**Table S11. Cartesian Coordinates of [Cr(NH<sub>3</sub>)<sub>6</sub>]<sup>3+</sup>.**

Cr	0.00000000	0.00000000	0.00000000
N	2.08466100	-0.00106600	0.08888200
N	-0.12671900	-2.08282900	-0.00089300
N	0.01548500	-0.01898900	2.08714200
N	0.00597100	2.08898900	0.00949000
N	-2.08272600	0.11904800	-0.10656600
N	0.10907000	-0.10922000	-2.08118200
H	2.47902800	-0.90987200	0.31891200
H	2.51544400	0.28056200	-0.78870700
H	2.44607900	0.63749200	0.79224800
H	0.76227200	-2.54080800	-0.18550100
H	-0.45777600	-2.45684500	0.88527100
H	-0.76633100	-2.43645000	-0.70766200
H	0.67254500	-0.70103200	2.45789800
H	-0.88517900	-0.24772200	2.50033500
H	0.29088300	0.87496200	2.48688800

H	0.915772000	2.494086000	0.214334000
H	-0.280992000	2.486218000	-0.882097000
H	-0.633674000	2.476835000	0.698455000
H	-2.533743000	-0.773598000	-0.289232000
H	-2.501852000	0.472458000	0.750337000
H	-2.397187000	0.746622000	-0.842460000
H	0.755324000	-0.829633000	-2.394150000
H	-0.784967000	-0.334458000	-2.510740000
H	0.423193000	0.753526000	-2.518408000

**Table S12. Cartesian Coordinates of [Cr(py)<sub>6</sub>]<sup>3+</sup>.**

Cr	0.000000000	0.000000000	0.000000000
N	-2.128157000	-0.000639000	0.006060000
N	2.127862000	0.000000000	-0.006692000
N	0.000000000	0.000000000	-2.128537000
N	0.000032000	0.000498000	2.127814000
N	0.004339000	-2.127702000	-0.002536000
N	-0.004570000	2.127760000	0.003554000
C	0.016073000	-2.827904000	1.151995000
C	-2.826117000	-1.156555000	-0.005645000
C	-1.151369000	-0.026928000	2.832796000
C	-0.012058000	2.827726000	-1.151180000
C	1.151656000	-0.017657000	-2.833418000
C	2.825580000	1.155856000	-0.031102000
C	-2.831111000	1.152082000	0.026873000
C	-1.156952000	0.014097000	-2.824792000
C	-0.002975000	2.828678000	1.157713000
C	1.156781000	0.028974000	2.823806000
C	2.830987000	-1.152691000	0.009183000
C	-0.002586000	-2.828424000	-1.156805000
C	-4.211623000	1.185456000	0.037962000
C	-4.206385000	-1.196599000	0.004417000
C	-1.182330000	-0.026877000	4.213392000
C	1.199194000	0.029965000	4.204023000
C	-0.008649000	4.209160000	1.193596000
C	-0.018699000	4.208089000	-1.188626000
C	4.205860000	1.195831000	-0.041216000
C	4.211491000	-1.186118000	0.000259000
C	-1.199245000	0.009604000	-4.204979000
C	1.182739000	-0.021906000	-4.214023000
C	0.002200000	-4.208868000	-1.193105000
C	0.020981000	-4.208322000	1.189034000
C	-0.011016000	-0.008749000	-4.920873000
C	-4.920321000	-0.007270000	0.027196000
C	-0.016803000	4.919998000	0.002144000
C	0.011304000	0.001523000	4.920036000
C	0.014068000	-4.919979000	-0.001845000
C	4.919986000	0.006471000	-0.025669000
H	-4.712325000	2.141860000	0.055463000
H	-2.277234000	2.071867000	0.035017000
H	-2.268184000	-2.073729000	-0.023990000
H	-4.702792000	-2.155284000	-0.006396000
H	-6.001018000	-0.009685000	0.035644000
H	0.023382000	-2.272160000	2.070720000
H	0.029673000	-4.706701000	2.146722000
H	0.017446000	-6.000708000	-0.001769000
H	-0.003653000	-4.707745000	-2.150596000
H	-0.013340000	-2.272856000	-2.075603000
H	-2.073311000	0.031530000	-2.265510000
H	2.072731000	-0.030969000	-2.281481000
H	2.138408000	-0.036915000	-4.716196000
H	-0.014996000	-0.012243000	-6.001643000
H	-2.158745000	0.021830000	-4.699837000

H	2.277157000	-2.072333000	0.030261000
H	4.712364000	-2.142495000	0.014216000
H	6.000688000	0.008791000	-0.033090000
H	4.702103000	2.154454000	-0.061328000
H	2.267418000	2.072984000	-0.043458000
H	2.072936000	0.054163000	2.264491000
H	2.158540000	0.053357000	4.698788000
H	0.015402000	0.001395000	6.000817000
H	-2.137753000	-0.050347000	4.715709000
H	-2.072241000	-0.051267000	2.280869000
H	0.001180000	2.273418000	2.076769000
H	-0.007336000	4.708258000	2.150991000
H	-0.021287000	6.000721000	0.001831000
H	-0.023856000	4.706225000	-2.146464000
H	-0.011904000	2.271439000	-2.069540000

**Table S13. Cartesian Coordinates of [Cr(tpy)<sub>2</sub>]<sup>3+</sup>.**

Cr	0.000000000	0.000000000	0.000000000
N	2.028840000	-0.000772000	-0.385480000
N	-2.020130000	0.000000000	-0.429392000
N	0.021555000	0.000000000	-1.991949000
N	-0.023487000	0.000225000	1.991915000
N	-0.004933000	2.024790000	0.407330000
N	-0.005317000	-2.024705000	0.407594000
C	-0.022593000	2.337991000	1.731200000
C	2.995918000	-0.001775000	0.535806000
C	-0.031204000	1.179762000	2.635961000
C	-0.022151000	-2.337718000	1.731524000
C	-1.150982000	0.000259000	-2.648866000
C	-3.006834000	-0.000227000	0.470826000
C	2.356330000	-0.000683000	-1.705998000
C	1.207967000	0.000124000	-2.623272000
C	0.003893000	-3.001819000	-0.503000000
C	-0.030990000	-1.179302000	2.636121000
C	-2.318969000	-0.000202000	-1.756654000
C	0.004493000	3.001780000	-0.503401000
C	3.678707000	-0.001635000	-2.114408000
C	4.337335000	-0.002778000	0.189683000
C	-0.046491000	1.208758000	4.023086000
C	-0.046220000	-1.208220000	4.023189000
C	-0.004103000	-4.339347000	-0.142249000
C	-0.031404000	-3.655538000	2.154347000
C	-4.340457000	-0.001035000	0.095835000
C	-3.632204000	-0.000885000	-2.193511000
C	1.251800000	0.000870000	-4.010076000
C	-1.165053000	0.000959000	-4.036263000
C	-0.004021000	4.339366000	-0.142880000
C	-0.032206000	3.655879000	2.153793000
C	0.050843000	0.001357000	-4.710610000
C	4.681832000	-0.002690000	-1.153438000
C	-0.022422000	-4.669130000	1.204458000
C	-0.053933000	0.000318000	4.710550000
C	-0.023004000	4.669340000	1.203761000
C	-4.655857000	-0.001398000	-1.254447000
H	3.926582000	-0.001632000	-3.164632000
H	2.688054000	-0.001626000	1.571038000
H	5.087287000	-0.003609000	0.965580000
H	5.719046000	-0.003484000	-1.455865000
H	-0.047218000	3.892256000	3.206526000
H	-0.031251000	5.703242000	1.517286000
H	0.003621000	5.097585000	-0.910634000
H	0.018165000	2.705186000	-1.541730000
H	-2.094204000	0.001264000	-4.583341000

H	0.062663000	0.001994000	-5.791022000
H	2.192537000	0.001087000	-4.537181000
H	-3.857173000	-0.001089000	-3.248913000
H	-5.686315000	-0.002038000	-1.579183000
H	-5.107104000	-0.001322000	0.855227000
H	-2.721046000	0.000401000	1.512212000
H	-0.051752000	-2.143210000	4.560194000
H	-0.066391000	0.000349000	5.790958000
H	-0.052454000	2.143782000	4.560064000
H	0.017518000	-2.705258000	-1.541309000
H	0.003387000	-5.097728000	-0.909850000
H	-0.030316000	-5.702989000	1.518130000
H	-0.046089000	-3.891729000	3.207143000

**Table S14. Cartesian Coordinates of [Cr(bpy)<sub>3</sub>]<sup>3+</sup>.**

Cr	0.000000000	0.000000000	0.000000000
N	-0.001798000	-0.044487000	2.056062000
N	-0.223854000	0.178612000	-2.033802000
N	-2.016505000	-0.183910000	0.367197000
N	2.043434000	0.043541000	-0.195510000
N	0.415985000	-2.011844000	-0.027069000
N	-0.217731000	2.032906000	-0.167822000
C	1.733579000	-2.320624000	-0.117371000
C	1.088377000	0.000762000	2.833332000
C	2.783879000	1.154797000	-0.304360000
C	-0.395965000	2.483714000	-1.433034000
C	-2.975838000	-0.197317000	-0.567352000
C	-0.414761000	1.446386000	-2.474100000
C	-1.224711000	-0.203483000	2.619399000
C	-2.353286000	-0.237774000	1.678457000
C	-0.177754000	2.901378000	0.850799000
C	2.640805000	-1.171685000	-0.243039000
C	-0.223407000	-0.837458000	-2.906317000
C	-0.492185000	-2.989809000	0.085497000
C	-1.363568000	-0.321197000	3.994184000
C	1.013334000	-0.112148000	4.208817000
C	4.156725000	1.109689000	-0.460602000
C	4.014798000	-1.281173000	-0.400919000
C	-0.301771000	4.264371000	0.656443000
C	-0.535004000	3.839488000	-1.689850000
C	-0.617777000	1.706388000	-3.821345000
C	-0.431142000	-0.642084000	-4.259242000
C	-3.682892000	-0.311001000	2.067793000
C	-4.317348000	-0.270127000	-0.242109000
C	-0.130235000	-4.324078000	0.115362000
C	2.157117000	-3.640778000	-0.087966000
C	-4.674547000	-0.327719000	1.096973000
C	-0.232531000	-0.278005000	4.796667000
C	-0.482460000	4.739059000	-0.634633000
C	4.780213000	-0.128307000	-0.509592000
C	1.215003000	-4.652497000	0.029935000
C	-0.633918000	0.650440000	-4.721484000
H	-2.338228000	-0.450839000	4.436170000
H	2.037673000	0.133716000	2.339739000
H	1.917547000	-0.071696000	4.796249000
H	-0.327318000	-0.373981000	5.868756000
H	3.206280000	-3.881137000	-0.152976000
H	1.532499000	-5.684949000	0.054412000
H	-0.893657000	-5.081334000	0.205324000
H	-1.527273000	-2.692532000	0.146981000
H	-2.659400000	-0.149186000	-1.596505000
H	-5.056149000	-0.280352000	-1.028483000
H	-5.713761000	-0.383851000	1.387983000

H	-3.945470000	-0.350349000	3.112785000
H	-0.060012000	-1.825342000	-2.506980000
H	-0.432633000	-1.490730000	-4.925695000
H	-0.802605000	0.839193000	-5.772021000
H	-0.770641000	2.716290000	-4.166771000
H	4.485978000	-2.250103000	-0.441053000
H	5.851361000	-0.201115000	-0.632487000
H	4.714214000	2.030073000	-0.541860000
H	2.263726000	2.097650000	-0.260671000
H	-0.034497000	2.492042000	1.838067000
H	-0.257278000	4.929321000	1.505072000
H	-0.582651000	5.798306000	-0.823042000
H	-0.674496000	4.192383000	-2.698831000

**Table S15. Cartesian Coordinates of [Cr(ddpd)<sub>2</sub>]<sup>3+</sup>.**

Cr	0.000000000	0.000000000	0.000000000
N	-0.063391000	-0.002063000	-2.040076000
N	0.056068000	-0.000994000	2.038359000
N	0.064332000	-2.053516000	-0.125516000
N	-0.071070000	2.051921000	-0.126429000
N	-2.047138000	-0.015009000	0.187929000
N	2.054912000	0.018135000	0.066023000
C	-0.735201000	-0.977917000	-2.697787000
C	-0.791085000	-1.002697000	-4.084742000
C	-0.154503000	-0.002615000	-4.797532000
C	0.526743000	0.998473000	-4.128816000
C	0.561329000	0.974650000	-2.741247000
H	-1.298855000	-1.803721000	-4.594691000
H	1.001586000	1.798527000	-4.671143000
C	0.747183000	-2.758791000	0.803969000
C	0.540327000	-4.097421000	1.015670000
C	-0.407385000	-4.748227000	0.225803000
C	-1.065763000	-4.052616000	-0.766696000
C	-0.788549000	-2.691905000	-0.948813000
H	-0.620473000	-5.797416000	0.375083000
H	1.447927000	-2.200083000	1.403603000
H	1.092680000	-4.613868000	1.785038000
H	-1.762206000	-4.559507000	-1.412479000
C	0.735855000	2.686747000	-0.997181000
C	1.039765000	4.043142000	-0.822327000
C	0.454724000	4.736329000	0.216761000
C	-0.451178000	4.090750000	1.058474000
C	-0.685946000	2.756496000	0.849851000
H	0.689534000	5.781495000	0.361338000
H	1.700565000	4.547933000	-1.506013000
H	-0.949287000	4.607438000	1.863740000
H	-1.355041000	2.199876000	1.486294000
C	-0.875782000	-0.687987000	2.743373000
C	-0.865985000	-0.693405000	4.131454000
C	0.122631000	0.009893000	4.796334000
C	1.076681000	0.708922000	4.079242000
C	1.020883000	0.690875000	2.692169000
H	-1.632110000	-1.216777000	4.678044000
H	1.867638000	1.236123000	4.584955000
C	-2.801365000	0.604412000	-0.747257000
C	-4.124725000	0.306810000	-0.944237000
C	-4.702333000	-0.674120000	-0.138079000
C	-3.960557000	-1.265375000	0.863117000
C	-2.620815000	-0.890693000	1.034620000
H	-5.733896000	-0.963598000	-0.280687000
H	-2.291678000	1.327427000	-1.363457000
H	-4.682502000	0.810589000	-1.717938000
H	-4.416257000	-1.986125000	1.520025000

C	2.681739000	0.870214000	0.898936000
C	4.024275000	1.209565000	0.686192000
C	4.715225000	0.612709000	-0.347854000
C	4.080598000	-0.335597000	-1.149640000
C	2.758275000	-0.603861000	-0.906574000
H	5.750347000	0.872480000	-0.519171000
H	4.522993000	1.905019000	1.339234000
H	4.596123000	-0.842135000	-1.950375000
H	2.209945000	-1.307182000	-1.512568000
N	-1.852228000	-1.426352000	2.058636000
C	-2.345035000	-2.646295000	2.718646000
H	-3.160065000	-2.446771000	3.414351000
H	-2.684548000	-3.336134000	1.952013000
H	-1.517735000	-3.102620000	3.251073000
N	1.963881000	1.420574000	1.953716000
C	2.502594000	2.635170000	2.586193000
H	3.335913000	2.426638000	3.257387000
H	2.830835000	3.311243000	1.802696000
H	1.702267000	3.112556000	3.141118000
N	-1.403815000	-1.966791000	-1.961860000
N	1.276591000	1.964143000	-2.052445000
C	-2.613215000	-2.539223000	-2.573577000
H	-2.389962000	-3.339101000	-3.279253000
H	-3.247451000	-2.924060000	-1.780923000
H	-3.143418000	-1.742928000	-3.084565000
C	2.451206000	2.527552000	-2.735704000
H	2.192694000	3.339239000	-3.415511000
H	3.141866000	2.893365000	-1.981626000
H	2.935799000	1.731051000	-3.290315000
H	-0.189922000	-0.003594000	-5.877783000
H	0.149669000	0.013581000	5.876821000

**Table S16. Cartesian Coordinates of [Cr(bmp)<sub>2</sub>]<sup>3+</sup>.**

Cr	0.000000000	0.000000000	0.000000000
N	-0.2392231150	-2.1091667910	-0.0513686530
N	2.1082842930	0.0000000000	0.0499894260
N	0.0000000000	0.0000000000	2.0996350620
N	-2.1069259780	0.0212638970	0.0450142550
N	0.2063853300	2.1064869570	-0.0604850260
C	-2.7913533870	-0.6749825610	-0.8873822620
C	-2.7834471940	0.6672820620	1.0141205650
C	-4.1662740780	-0.7375001930	-0.9034745460
C	-4.1719785930	0.6345219000	1.0536648770
C	-4.8737485900	-0.0666915060	0.0874396440
N	0.0201332680	-0.0081525660	-2.1181372370
C	-0.9527232910	0.6773031080	2.7849439450
C	0.9722827730	-0.6584638400	2.7774931060
C	-0.9503471600	0.7082687700	4.1698782490
C	1.0197583430	-0.6333371500	4.1609687800
C	0.0499852550	0.0552595590	4.8686549340
C	2.7863310940	-0.6619628030	1.0073501620
C	2.7918381000	0.7174001540	-0.8665231350
C	4.1745144010	-0.6295498400	1.0489474310
C	4.1668980980	0.7850116810	-0.8773936150
C	4.8756268060	0.0933443900	0.0979595550
C	-0.5266830220	1.0191819110	-2.8114667000
C	0.5857662100	-1.0377685650	-2.7930259750
C	-0.5051752450	1.0431914230	-4.1956300990
C	0.6083548660	-1.0637791970	-4.1770181680
C	0.0637676360	-0.0099867610	-4.8907552180
C	0.2531851980	-2.8410746360	-1.0696000460
C	-1.0665160750	-2.6954509720	0.8393386210
C	-0.1042445890	-4.1727895350	-1.2299554840



C	-1.4493884940	-4.0144732890	0.7385237060
C	-0.9707074110	-4.7667653800	-0.3269955960
C	-0.3113948450	2.8341824500	-1.0700356540
C	0.9874342950	2.7172098220	0.8551550510
C	1.2829682200	4.0608589770	0.8011335900
C	-0.0427696380	4.1913284600	-1.1811850640
C	0.7636226970	4.8146329920	-0.2440894000
H	1.3857612200	2.1007930270	1.6441661350
H	-0.4668693550	4.7430091350	-2.0065858600
H	-4.6876897650	1.1567406070	1.8456970550
H	-2.2090897110	-1.1875904110	-1.6354346450
H	2.2110828090	1.2423933270	-1.6066756760
H	4.6895758750	-1.1682267760	1.8302272190
H	0.2989510310	-4.7273103670	-2.0639726010
H	-1.4343117740	-2.0786872400	1.6428336160
H	0.0743190890	0.0826250500	5.9486312630
H	-1.7275472780	1.2512583650	4.6856502690
H	1.8156804510	-1.1549496100	4.6699689960
H	-0.9442542810	1.8823638640	-4.7128771720
H	1.0577064660	-1.9064255110	-4.6795756660
H	0.0788456730	-0.0118507470	-5.9713888320
C	-1.1912027560	2.1471192680	-2.0711314390
H	-1.5311318230	2.8766166080	-2.7981808610
H	-2.0837308350	1.7781968650	-1.5672104070
C	1.1981278680	-2.1798420600	-2.0282246760
H	2.0748207900	-1.8326056730	-1.4834787620
H	1.5517757440	-2.9165823950	-2.7414554490
C	2.0114992390	-1.4463028840	2.0256325920
H	2.7100331780	-1.8570091780	2.7459896290
H	1.5405343030	-2.3000632400	1.5370549470
C	-2.0160501290	1.4438707110	2.0438777230
H	-1.5664733800	2.3161886430	1.5668196700
H	-2.7195365140	1.8303277720	2.7731175500
H	-2.1186362280	-4.4313591760	1.4752787580
H	-1.2660559490	-5.7986159990	-0.4518416570
H	-4.6650010010	-1.3023014470	-1.6763548640
H	-5.9540480990	-0.0960103720	0.1098276680
H	4.6650790790	1.3674743680	-1.6374875930
H	5.9559241870	0.1230833800	0.1200063550
H	0.9853253720	5.8687323310	-0.3297031160
H	1.9148958170	4.4976615750	1.5588958720

**Table S17. Cartesian Coordinates of  $[\text{Cr}(\text{CN})_6]^{3-}$ .**

Cr	0.000000000	0.000000000	0.000000000
C	-0.000058000	-2.084352000	-0.000015000
C	-2.084493000	0.000004000	-0.000212000
C	-0.000053000	2.084346000	-0.000005000
C	2.084479000	0.000007000	0.000233000
C	0.000078000	-0.000030000	2.084189000
C	-0.000216000	-0.000033000	-2.084186000
N	3.245160000	0.000011000	0.000206000
N	-0.000119000	-3.245041000	-0.000026000
N	0.000112000	-0.000050000	3.244873000
N	-3.245173000	0.000005000	-0.000165000
N	-0.000114000	3.245036000	-0.000011000
N	-0.000357000	-0.000070000	-3.244871000

## References

1. Neese, F. The ORCA program system. *WIREs Comput. Mol. Sci.* **2012**, *2*, 73–78.
2. a) Becke, A. D. Density-functional thermochemistry. III. The role of exact exchange. *J. Chem. Phys.* **1993**, *98*, 5648–5652. b) Lee, C.; Yang, W.; Parr, R. G. *Phys. Rev. B* **1988**, *37*, 785–789. c) Miehlich, B.; Savin, A.; Stoll, H.; Preuss., H. *Chem. Phys. Lett.* **1989**, *157*, 200–206.
3. Weigend, F.; Ahlrichs, R. Balanced basis sets of split valence, triple zeta valence and quadruple zeta valence quality for H to Rn: Design and assessment of accuracy. *Phys. Chem. Chem. Phys.* **2005**, *7*, 3297–3305.
4. Weigend, F. Accurate Coulomb-fitting basis sets for H to Rn. *Phys. Chem. Chem. Phys.* **2006**, *8*, 1057–1065.
5. Neese, F.; Wennmohs, F.; Hansen, A.; Becker, U. Efficient, approximate and parallel Hartree–Fock and hybrid DFT calculations. A ‘chain-of-spheres’ algorithm for the Hartree–Fock exchange. *Chem. Phys.* **2009**, *356*, 98–109.
6. Izsák, R.; Neese, F. An overlap fitted chain of spheres exchange method. *J. Chem. Phys.* **2011**, *135*, 144105.
7. Pantazis, D. A.; Chen, X.-Y.; Landis, C. R.; Neese, F. All-Electron Scalar Relativistic Basis Sets for Third-Row Transition Metal Atoms. *J. Chem. Theory Comput.* **2008**, *4*, 908–919.
8. a) van Lenthe, E.; Baerends, E. J.; Snijders, J. G. Relativistic regular two-component Hamiltonians. *J. Chem. Phys.* **1993**, *99*, 4597–4610; b) van Wüllen, C. *J. Chem. Phys.* **1998**, *109*, 392–399.
9. Grimme, S.; Antony, J.; Ehrlich, S.; Krieg, H. A consistent and accurate ab initio parametrization of density functional dispersion correction (DFT-D) for the 94 elements H–Pu. *J. Chem. Phys.* **2010**, *132*, 154104.
10. Grimme, S.; Ehrlich, S.; Goerigk, L. Effect of the damping function in dispersion corrected density functional theory. *J. Comput. Chem.* **2011**, *32*, 1456–1465.
11. Barone, V.; Cossi, M. Quantum Calculation of Molecular Energies and Energy Gradients in Solution by a Conductor Solvent Model. *J. Phys. Chem. A* **1998**, *102*, 1995–2001.
12. Roos, B. O.; Taylor, P. R.; Siegbahn, P. E. M. A Complete Active Space SCF Method (CASSCF) Using a Density-Matrix Formulated Super-CI Approach. *Chem. Phys.* **1980**, *48*, 157–173.
13. Siegbahn, P. E. M.; Almlof, J.; Heiberg, A.; Roos, B. O. The Complete Active Space SCF (CASSCF) Method in a Newton-Raphson Formulation with Application to the HNO Molecule. *J. Chem. Phys.* **1981**, *74*, 2384–2396.
14. Angeli, C.; Cimiraglia, R.; Evangelisti, S.; Leininger, T.; Malrieu, J.-P. Introduction of n-electron valence states for multireference perturbation theory. *J. Chem. Phys.* **2001**, *114*, 10252–10264.
15. Angeli, C.; Cimiraglia, R.; Malrieu, J.-P. *J. Chem. Phys.* **2002**, *117*, 9138–9153.
16. Pierloot, K. Transition metals compounds: Outstanding challenges for multiconfigurational methods. *Int. J. Quantum Chem.* **2011**, *111*, 3291–3301.
17. Atanasov, M.; Ganyushin, D.; Sivalingam, K.; Neese, F. A Modern First-Principles View on Ligand Field Theory Through the Eyes of Correlated Multireference Wavefunctions. *Struct. Bond.* **2012**, *143*, 149–220.
18. Singh, S. K.; Eng, J.; Atanasov, M.; Neese, F. Covalency and chemical bonding in transition metal complexes: An ab initio based ligand field perspective. *Coord. Chem. Rev.* **2017**, *344*, 2–25.
19. Neese, F. Efficient and accurate approximations to the molecular spin-orbit coupling operator and their use in molecular g-tensor calculations. *J. Chem. Phys.* **2005**, *122*, 34107.
20. Hess, B. A.; Marian, C. M. In *Computational Molecular Spectroscopy*; Jensen, P. B., Ed.; Wiley: New York, 2000; p. 169ff.
21. Cahier, B.; Maurice, R.; Bolvin, H.; Mallah, T.; Guihéry, N. Tools for Predicting the Nature and Magnitude of Magnetic Anisotropy in Transition Metal Complexes: Application to Co(II) Complexes. *Magnetochemistry* **2016**, *2*, 31–45.
22. Roos, B. O.; Malmqvist, P.-Å. Relativistic quantum chemistry: the multiconfigurational approach. *Phys. Chem. Chem. Phys.* **2004**, *6*, 2919–2927.
23. Durand, P.; Malrieu, J.-P. In *Advances in Chemical Physics: Ab Initio Methods in Quantum Chemistry*; Lawley, K. P., Ed.; John Wiley & Sons Ltd.: Hoboken, NJ, 1987; Vol. 67, Part 1, pp 321–412.

24. Dyker, G.; Muth, O. Synthesis of Methylene- and Methine-Bridged Oligopyridines. *Eur. J. Org. Chem.* **2004**, 4319–4322.
25. Otto, S.; Grabolle, M.; Förster, C.; Kreitner, C.; Resch-Genger, U.; Heinze, K. [Cr(ddpd)<sub>2</sub>]<sup>3+</sup>: A molecular, water-soluble, highly NIR-emissive ruby analogue. *Angew. Chem., Int. Ed.* **2015**, *54*, 11572–11576.
26. Fulmer, G. R.; Miller, A. J. M.; Sherden, N. H.; Gottlieb, H. E.; Nudelman, A.; Stoltz, B. M.; Bercaw, J. E.; Goldberg, K. I. NMR Chemical Shifts of Trace Impurities: Common Laboratory Solvents, Organics, and Gases in Deuterated Solvents Relevant to the Organometallic Chemist. *Organometallics* **2010**, *29*, 2176–2179.
27. Zimmer, M.; Rupp, F.; Singer, P.; Walz, F.; Breher, F.; Kloppe, W.; Diller, R.; Gerhards, M. Time-resolved IR spectroscopy of a trinuclear palladium complex in solution. *Phys. Chem. Chem. Phys.* **2015**, *17*, 14138–14144.
28. Bäßler, F.; Zimmer, M.; Dietrich, F.; Gruppe, M.; Wallesch, M.; Volz, D.; Bräse, S.; Gerhards, M.; Diller, R. Photophysical dynamics of a binuclear Cu(I)-emitter on the fs to  $\mu$ s timescale, in solid phase and in solution. *Phys. Chem. Chem. Phys.* **2017**, *19*, 29438–29448.
29. Zimmer, M.; Dietrich, F.; Volz, D.; Bräse, S.; Gerhards, M. Solid-State Step-Scan FTIR Spectroscopy of Binuclear Copper(I) Complexes. *ChemPhysChem* **2017**, *18*, 3023–3029.
30. Mullen, K. M.; van Stokkum, I. H. M. TIMP: An R Package for Modeling Multi-Way Spectroscopic Measurements. *J. Stat. Softw.* **2007**, *18*, 1–46.
31. Snellenburg, J. J.; Liptonok, S. P.; Seger, R.; Mullen, K. M.; van Stokkum, I. H. M. Glotaran: a Java-based Graphical User Interface for the R-package TIMP. *J. Stat. Softw.* **2012**, *49*, 1–22.
32. Otto, S.; Nauth, A. M.; Ermilov, E.; Scholz, N.; Friedrich, A.; Resch-Genger, U.; Lochbrunner, S.; Opatz, T.; Heinze, T. Photo-Chromium: Sensitizer for Visible Light-Induced Oxidative C-H Bond Functionalization – Electron or Energy Transfer? *ChemPhotoChem* **2017**, *1*, 344–349.
33. STOE & Cie, X-Area, STOE & Cie, Darmstadt, Germany.
34. Blessing, R. H. An empirical correction for absorption anisotropy. *Acta Crystallogr. Sect. A* **1995**, *51*, 33–38.
35. Spek, A. L. Structure validation in chemical crystallography. *Acta Crystallogr. Sect. D* **2009**, *65*, 148–55.
36. STOE & Cie, LANA, STOE & Cie, Darmstadt, Germany.
37. Koziskova, J.; Hahn, F.; Richter, J.; Kozisek, J. Comparison of different absorption corrections on the model structure of tetrakis( $\mu_2$ -acetato)-diaqua-di-copper(II). *Acta Chim. Slov.* **2016**, *9*, 136–140.
38. a) Sheldrick, G. M. SHELXT – Integrated space-group and crystal-structure determination. *Acta Crystallogr. Sect. A* **2015**, *71*, 3–8. b) Sheldrick, G. M. SHELXL-2018/3, University of Göttingen, Göttingen, Germany, 2018.
39. Hübsche, C. B.; Sheldrick, G. M.; Dittrich, B. *J. Appl. Cryst.* **2011**, *44*, 1281–1284.
40. Jiménez, J.-R.; Doistau, B.; Besnard, C.; Piguet, C. Versatile heteroleptic bis-terdentate Cr(III) chromophores displaying room temperature millisecond excited state lifetimes. *Chem. Commun.* **2018**, *54*, 13228–13231.
41. Zare, D.; Doistau, B.; Nozary, H.; Besnard, C.; Guénée, L.; Suffren, Y.; Pelé, A.-L.; Hauser, A.; Piguet, C. Cr<sup>III</sup> as an alternative to Ru<sup>II</sup> in metallo-supramolecular chemistry. *Dalton Trans.* **2017**, *46*, 8992–9009.
42. Alemany, P.; Casanova, D.; Alvarez, S.; Dryzun, C.; Avnir, D. Continuous Symmetry Measures: A New Tool in Quantum Chemistry In *Reviews in Computational Chemistry*, John Wiley & Sons, Hoboken, NJ, USA, 2017, pp 289–352.
43. Wang, C.; Otto, S.; Dorn, M.; Kreidt, E.; Lebon, J.; Srsan, L.; Di Martino-Fumo, P.; Gerhards, M.; Resch-Genger, U.; Seitz, M.; Heinze, K. Deuterated Molecular Ruby with Record Luminescence Quantum Yield. *Angew. Chem. Int. Ed.* **2018**, *57*, 1112–1116.

#### 4.2.2 Multiphonon Relaxation bei V(III)-Komplexen mit NIR-II Spin-Flip-Emission

Lumineszente Vanadium(III)-Komplexe sind wegen ihrer sehr energiearmen NIR-II-Emission grundsätzlich sehr anfällig für die strahlungslose Deaktivierung der Spin-Flip-Zustände durch Obertöne von hochenergetischen, anharmonischen C-H-Oszillatoren.

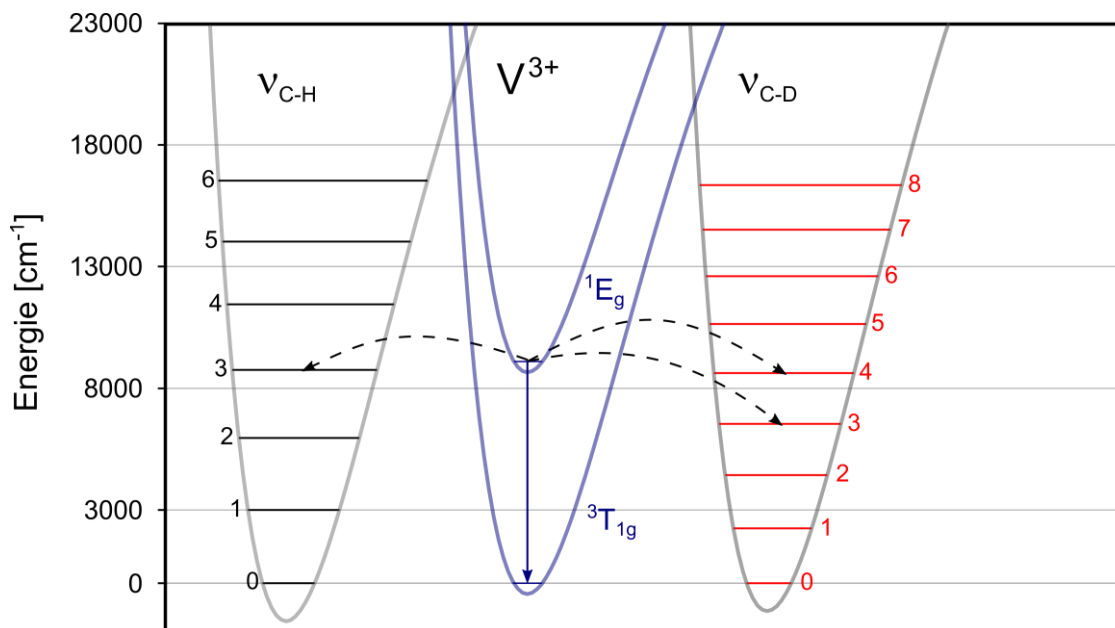


**Abb. 39:** Darstellung des Energietransfers vom angeregten Spin-Flip-Zustand  ${}^1E_g$  eines oktaedrisch umgebenen V(III)-Luminophors auf die Obertöne von aromatischen C-H- und C-D-Oszillatoren.

Da die Spin-Flip-Emission von V(III)-Luminophoren üblicherweise bei etwa  $\lambda_{em} = 1100 \text{ nm}$  (ca.  $9100 \text{ cm}^{-1}$ ) liegt, ist der zweite aromatische C-H-Oberton ( $\nu_{C-H}^3$ ) mit seiner fast identischen Energie von etwa  $9000 \text{ cm}^{-1}$  in pyridinbasierten Liganden prädestiniert für die strahlungslose Deaktivierung der Spin-Flip-Zustände (Abb. 39). In perdeuterierten Komplexen zeigt der dritte Oberton ( $\nu_{C-D}^4$ ) von aromatischen C-D-Oszillatoren potentiell den größten spektralen Überlapp mit der Emissionsbande. Dieser sollte aber wegen der im Vergleich zu C-H-Oszillatoren deutlich geringeren Oszillatorstärke auch in geringerem Maße zur Schwingungsrelaxation beitragen. Es ist daher generell zu erwarten, dass  $k_{nr}^H \gg k_{nr}^D$  ist und damit ein merklicher Isotopeneffekt beobachtet werden kann. Ob sich aber die Lebenszeiten der Spin-Flip-Zustände und die Quantenausbeuten der isotopologen Vanadiumkomplexe wirklich verbessern, hängt aber zunächst davon ab, ob MR in diesen Systemen ein relevanter strahlungsloser Deaktivierungsweg ist oder ob stattdessen andere strahlungslose

Mechanismen dominieren. Für die bereits oben beschriebenen neuen lumineszenten Vanadium-Emitter  $[\text{V}(\text{ddpd})_2](\text{PF}_6)_3$  (Kap. 3.2.1) und  $[\text{VCl}_3(\text{ddpd})]$  (Kapitel 3.2.2) wurde der Einfluss der Deuterierung auf die Lumineszenzeigenschaften genauer untersucht.

#### 4.2.2.1 Einfluss der Schwingungsrelaxation auf die NIR-II Lumineszenz von $[\text{V}(\text{ddpd})_2](\text{PF}_6)_3$ (Publikation 2)

Um die potentiell effektive strahlungslose Deaktivierung der emissiven Singulett-Zustände durch MR im  $[\text{V}(\text{ddpd})_2](\text{PF}_6)_3$ -Komplex zu reduzieren, war das Ziel auch das perdeuterierte Analogon  $[\text{V}([\text{D}_{17}]\text{-ddpd})_2](\text{PF}_6)_3$  darzustellen (Abb. 41). Dafür wurde zunächst eine Strategie zur Synthese des perdeuterierten **ddpd**-Liganden entwickelt (Abb. 40).

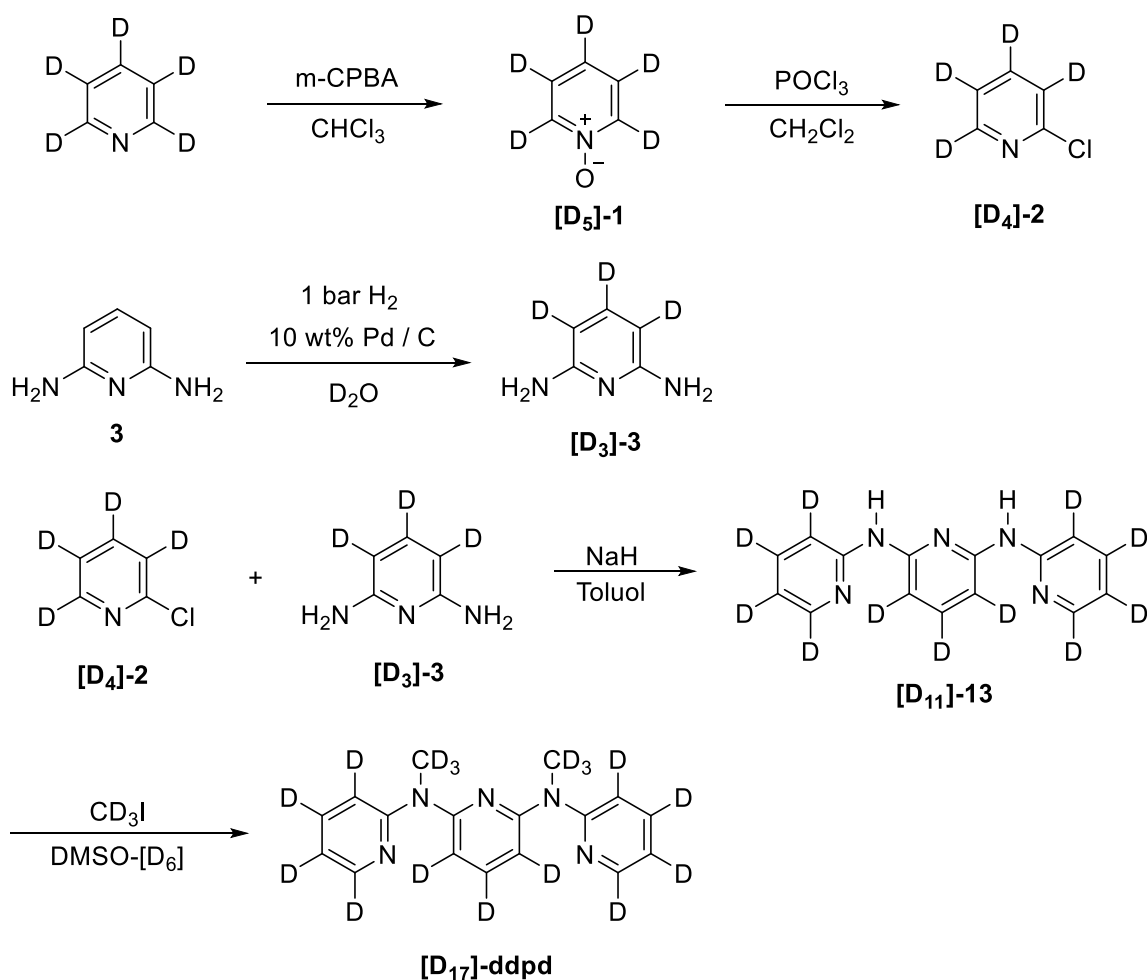


**Abb. 40:** Durchgeführte Syntheseroute zu Darstellung des perdeuterierten Liganden  $[\text{D}_{17}]\text{-ddpd}$ .

Die gezeigte Syntheseroute verfolgt dabei, analog zur Darstellung der selektiv deuterierten **ddpd**-Liganden (Kapitel 4.2.1.1) den modularen Ansatz, bei welchem der perdeuterierte Ligand aus relativ einfach zugänglichen deuterierten Bausteinen und unter Verwendung möglichst milder Reaktionsbedingungen aufgebaut wird, um Verlust an Deuterium oder H/D-Scrambling zu vermeiden. Auf diese Weise konnte **[D<sub>17</sub>]-ddpd** mit einem sehr guten Gesamtdeuterierungsgrad von 93.6 %D erhalten werden (HI, Abb. S6-8). Die alternative Herangehensweise, den H/D-Austausch am zunächst undeuteriert synthetisierten **ddpd**-Liganden durchzuführen, ermöglichte dagegen nur den statistischen Einbau von Deuterium.<sup>[37]</sup> Der **[V([D<sub>17</sub>]-ddpd)<sub>2</sub>](PF<sub>6</sub>)<sub>3</sub>**-Komplex konnte anschließend ausgehend von **[D<sub>17</sub>]-ddpd** analog zur Syntheseroute des undeuterierten Komplex unter Erhalt des sehr guten Gesamtdeuterierungsgrad von 93.6 %D dargestellt werden (HI, Abb. S9). Wichtig dabei ist, dass die metallnächsten C-H-Oszillatoren in 6,6'-Position der terminalen Pyridine, die potentiell am stärksten zu MR beitragen, nahezu quantitativ (99 %D) deuteriert sind.

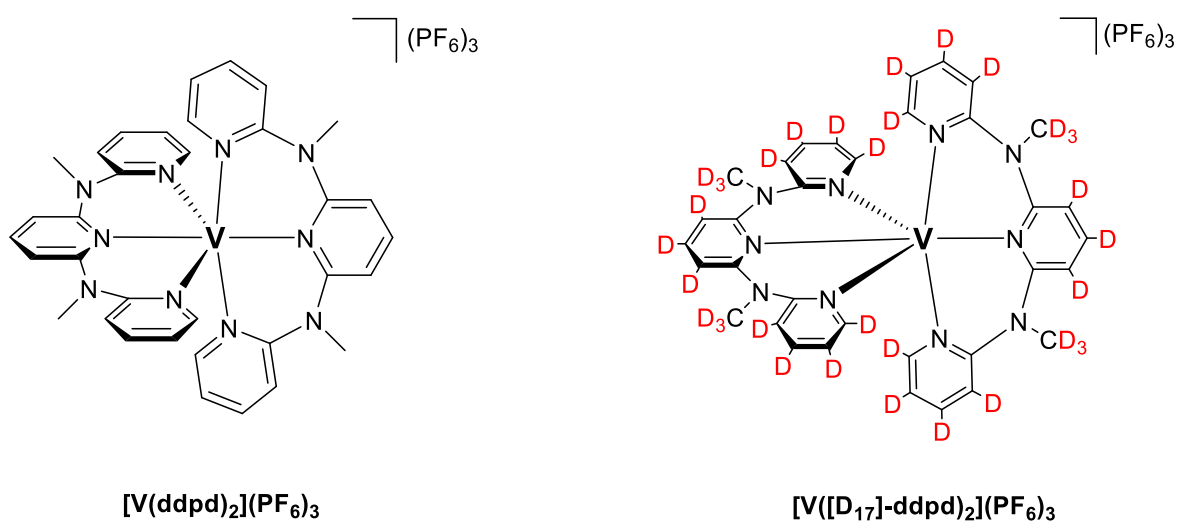


**Abb. 41:** Strukturformeln der untersuchten isotopologen Komplexe **[V(ddpd)<sub>2</sub>](PF<sub>6</sub>)<sub>3</sub>** und **[V([D<sub>17</sub>]-ddpd)<sub>2</sub>](PF<sub>6</sub>)<sub>3</sub>**.

In der für den **[Cr(ddpd)<sub>2</sub>]<sup>3+</sup>**-Komplex durchgeführten Obertonanalyse<sup>[37]</sup> erwiesen sich die Daten der aromatischen Schwingungsobertöne von isotopologen 6,6'-Dimethyl-2,2'-bipyridin (**Me<sub>2</sub>bpy** und **[D<sub>12</sub>]-Me<sub>2</sub>bpy**) als gut geeignetes Modellsystem für die aromatischen Obertonsignaturen des **ddpd**-Liganden. Aus den gemessenen Spektren extrahierten Obertondaten von **Me<sub>2</sub>bpy** konnte die Energie des zweiten aromatischen C-H-Obertons auf  $\nu_{\text{C-H}}^3 = 8970 \text{ cm}^{-1}$  abgeschätzt werden. Es kommt daher zu der

erwarteten großen spektralen Überlappung mit der Spin-Flip-Emissionsbande von  $[\mathbf{V}(\mathbf{ddpd})_2]^{3+}$  bei ca.  $\lambda_{em} = 1100 \text{ nm}$  ( $9090 \text{ cm}^{-1}$ , Abb. 10). Für den entsprechenden  $[\mathbf{V}([\mathbf{D}_{17}]\text{-ddpd})_2]^{3+}$ -Komplex ist der dritte C-D-Oberton mit  $\nu_{\text{C-D}}^4 = 8760 \text{ cm}^{-1}$  am relevantesten, welcher in analoger Weise aus den Obertonsignaturen von  $[\mathbf{D}_{12}]\text{-Me}_2\text{bpy}$  erhalten werden konnte. Wegen des erwartungsgemäß kleineren spektralen Überlapp im Fall des perdeuterierten  $[\mathbf{V}([\mathbf{D}_{17}]\text{-ddpd})_2](\text{PF}_6)_3$ -Komplexes, sollten die demzufolge kleineren MR-Raten  $k_{nr}^D$  zu längeren Lumineszenzlebenszeiten der emittierenden Singulett-Zustände führen. Das Ergebnis der Lumineszenzlebenszeitmessungen ist in Tab. 6 gezeigt.

**Tab. 6:** Lumineszenzlebensdauern  $\tau$  und Quantenausbeuten  $\Phi$  von  $[\mathbf{V}(\mathbf{ddpd})_2](\text{PF}_6)_3$  und  $[\mathbf{V}([\mathbf{D}_{17}]\text{-ddpd})_2](\text{PF}_6)_3$  in entgasten Lösungen unter Argonatmosphäre.

Komplex	$\tau_F$ [ns] <sup>a</sup> in CD <sub>3</sub> CN, 298 K	$\tau_P$ [ns] <sup>b</sup> in <sup>n</sup> BuCN, 77 K	$\Phi_P$ [%] <sup>c</sup>
$[\mathbf{V}(\mathbf{ddpd})_2](\text{PF}_6)_3$	3.2 (56 %) 8.2 (44 %)	790 (93 %) 8800 (7 %)	$1.8 \times 10^{-4}$
$[\mathbf{V}([\mathbf{D}_{17}]\text{-ddpd})_2](\text{PF}_6)_3$	3.3 (88 %) 7.2 (12 %)	800 (91 %) 8300 (9 %)	$1.6 \times 10^{-4}$

<sup>a</sup> $\lambda_{exc} = 306 \text{ nm}$ ,  $\lambda_{em} = 390 \text{ nm}$ , biexponentielles Fitting.

<sup>b</sup> $\lambda_{exc} = 300 \text{ nm}$ ,  $\lambda_{em} = 1110 \text{ nm}$ , biexponentielles Fitting.

<sup>c</sup> $\lambda_{exc} = 308 \text{ nm}$ ,  $\lambda_{em} = 1050\text{--}1200 \text{ nm}$ , gemessen relativ zum Quantenausbeutestandard  $[\text{Yb}(\text{tta})_3(\text{phen})]$  in Toluol (HI, Tab. S7 u. Abb. S12+13, S17+18).

Überraschenderweise kann im Rahmen der Messunsicherheit kein signifikanter Unterschied in der Lebenszeit oder Quantenausbeute der NIR-Emission von  $[\mathbf{V}([\mathbf{D}_{17}]\text{-ddpd})_2](\text{PF}_6)$  und  $[\mathbf{V}(\mathbf{ddpd})_2](\text{PF}_6)_3$  bei  $T = 298$  oder  $77 \text{ K}$  festgestellt werden. Es ist daher davon auszugehen, dass MR zwar ein strahlungsloser Deaktivierungsweg der energieärmsten Singulett-Zustände in diesem Luminophor ist, aber andere strahlungslose Mechanismen dominieren. Dadurch fallen die relativ dazu nur sehr kleinen Unterschiede durch Reduzierung von MR nur sehr wenig ins Gewicht und die beobachteten Lebenszeiten der isotopologen Komplexe sind ähnlich. Welche die dominierenden strahlungslosen Mechanismen genau sind, konnte nicht abschließend geklärt werden. Vermutlich fördert aber die große Grundzustandsaufspaltung direktes ISC in den Grundzustand.

#### 4.2.2.2 Einfluss der Schwingungsrelaxation auf die NIR-II Lumineszenz von $[\text{VCl}_3(\text{ddpd})]$ (Publikation 3)

Nachdem überraschenderweise MR im homoleptischen  $[\text{V}(\text{ddpd})_2](\text{PF}_6)_3$ -Komplex keinen relevanten strahlungslosen Deaktivierungsweg darstellt, sollte nun für den heteroleptischen  $[\text{VCl}_3(\text{ddpd})]$ -Komplex überprüft werden, ob in diesem Luminophor die strahlungslose Deaktivierung der lumineszenten Spin-Flip-Zustände durch MR hochenergetischer, aromatischer C-H-Oszillatoren eine signifikante Rolle spielt. Dazu sollte zunächst der isotopologe  $[\text{VCl}_3([\text{D}_{17}\text{-ddpd})]$  synthetisiert und im nächsten Schritt die Lumineszenzlebenszeiten der NIR-II-Emission bestimmt werden.

Die Synthese von  $[\text{VCl}_3([\text{D}_{17}\text{-ddpd})]$  gelang analog zur Darstellung des undeutierten Komplexes ausgehend vom perdeutierten Liganden  $[\text{D}_{17}\text{-ddpd}]$ , welcher nach der oben beschriebenen Methode erhalten werden konnte (Abb. 40).<sup>[67]</sup>

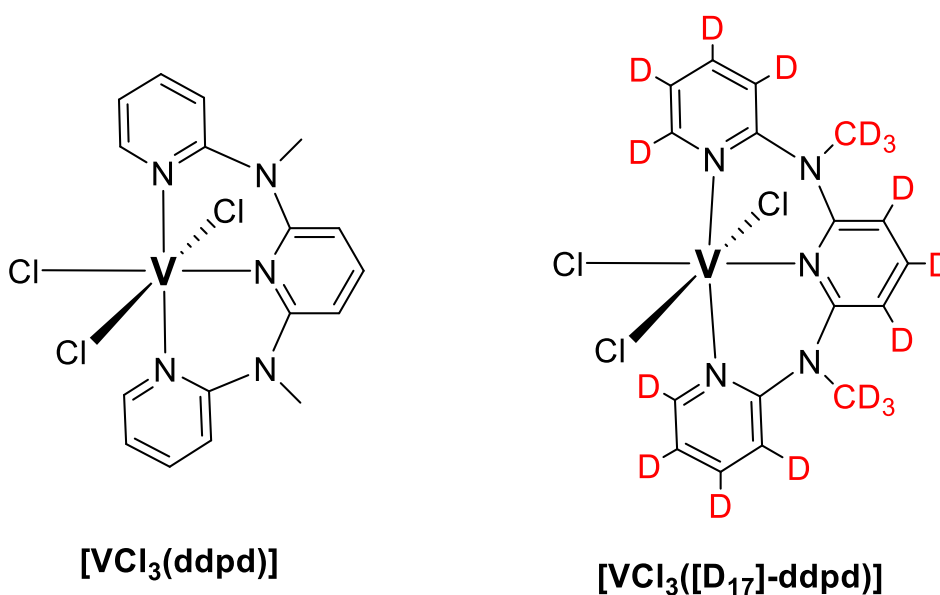


**Abb. 42:** Strukturformeln der untersuchten isotopologen Komplexe  $[\text{VCl}_3(\text{ddpd})]$  und  $[\text{VCl}_3([\text{D}_{17}\text{-ddpd})]$ .

Um die potentielle Steigerung der Lumineszenzlebenszeiten nach Deuterierung zu quantifizieren, wurden die spektralen Überlappintegrale (SOIs) der relevanten C-H(D)-Obertöne mit der <sup>1</sup>E-Emission von  $[\text{VCl}_3(\text{ddpd})]$  bestimmt. Dabei wurden erneut die Obertondaten von **Me<sub>2</sub>bpy** und **[D<sub>12</sub>]-Me<sub>2</sub>bpy** als Modellsysteme für die aromatischen Obertonsignaturen von **[D<sub>0</sub>]/[D<sub>17</sub>]-ddpd** herangezogen (HI, Abb. S10-12).<sup>[37]</sup> Wie in Abb. 43 gezeigt, kommt es zu einer signifikanten spektralen Überlappung ( $\text{SOI}^{\text{H}} = 1.55 \cdot 10^{-18} \text{ M}^{-1}\text{cm}^3$ , HI, Abb. S13) des zweiten aromatischen



C-H-Obertons ( $\nu_{\text{C-H}}^3 = 8970 \text{ cm}^{-1}$ ) mit der  $^1\text{E}$ -Emissionsbande. Auch der dritte C-D-Oberton ( $\nu_{\text{C-D}}^4 = 8760 \text{ cm}^{-1}$ ) überlappt mit der Emission von **[VCl<sub>3</sub>(ddpd)]**. Allerdings ist leicht zu erkennen, dass die spektrale Überlappung ( $\text{SOI}^{\text{D}} = 4.25 \cdot 10^{-20} \text{ M}^{-1} \text{cm}^3$ , HI, Abb. S14) mit dem dritten C-D-Oberton aufgrund des wesentlich geringeren Extinktionskoeffizienten von  $\nu_{\text{C-D}}^4$  im Vergleich zu  $\nu_{\text{C-H}}^3$  beträchtlich kleiner ist.

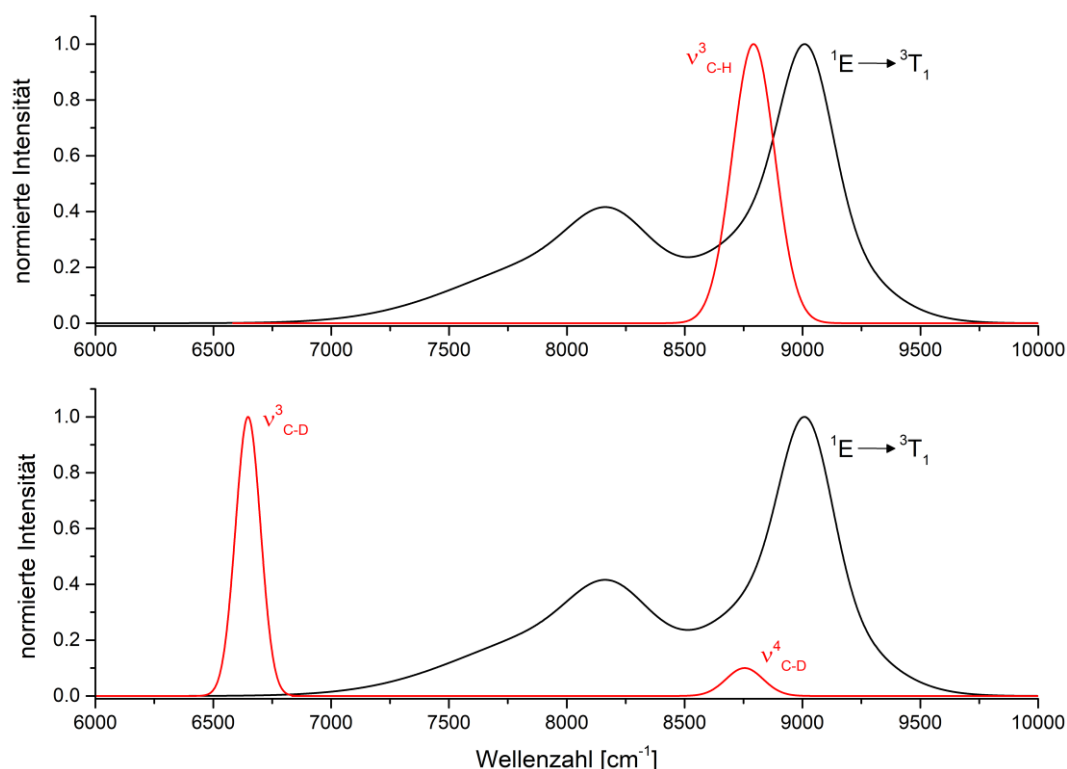


**Abb. 43:** Oben: Normiertes  $^1\text{E}$ -Emissionsspektrum von **[VCl<sub>3</sub>(ddpd)]** (schwarz) und die gemessenen Spektren extrahierten Absorptionsbande des zweiten aromatischen C-H-Obertons ( $\nu_{\text{C-H}}^3$ , rot). Unten: Normiertes  $^1\text{E}$ -Emissionsspektrum von **[VCl<sub>3</sub>(ddpd)]** (schwarz) und die aus gemessenen Spektren extrahierten Absorptionsbanden des zweiten und dritten aromatischen C-D-Obertons ( $\nu_{\text{C-D}}^3$  und  $\nu_{\text{C-D}}^4$ , rot). Die Obertonintensitäten sind dabei maßstäblich zu ihren tatsächlichen Intensitäten skaliert.

Basierend auf dieser Analyse reduziert sich die Rate der strahlungslosen Deaktivierung durch MR in **[VCl<sub>3</sub>(D<sub>17</sub>)-ddpd]** im Vergleich zu **[VCl<sub>3</sub>(ddpd)]** um den Faktor  $\text{SOI}^{\text{H}} / \text{SOI}^{\text{D}} \approx 36$ .

Um diese Prognose mit experimentellen Daten zu untermauern, wurden die Lumineszenzlebenszeiten der isotopologen Komplexe im Festkörper unter Argonatmosphäre ermittelt (Tab. 7). Tatsächlich kann ein Anstieg der Lebenszeit der NIR-Emission von  $\tau^{\text{H}} = 0.5 \mu\text{s}$  (HI, Abb. S7) für den undeuterierten

**[VCl<sub>3</sub>(ddpd)]**-Komplex auf  $\tau^D = 3.3 \mu\text{s}$  für **[VCl<sub>3</sub>([D<sub>17</sub>]-ddpd)]** bei 298 K beobachtet werden (HI, Abb. S8). Dabei unterscheiden sich die Lebensdauern der Emissionsbanden bei  $\lambda_{\text{em}} = 1102 \text{ nm}$  ( $9074 \text{ cm}^{-1}$ ) und  $\lambda_{\text{em}} = 1219 \text{ nm}$  ( $8203 \text{ cm}^{-1}$ ) im Rahmen der Messungengenauigkeit nicht werden (HI, Abb. S9). Dies bestätigt, dass die NIR-II-Emissionen ausgehend vom gleichen emittierenden Singulett-Zustand in zwei verschiedene Unterniveaus des aufgespaltenen Grundzustands erfolgt.

**Tab. 7:** Lumineszenzlebensdauern  $\tau$  von **[VCl<sub>3</sub>(ddpd)]<sub>2</sub>** und **[VCl<sub>3</sub>([D<sub>17</sub>]-ddpd)]** im Festkörper unter trockener und sauerstofffreier Argonatmosphäre.

Komplex	$\tau_{1106} [\mu\text{s}]^a$	$\tau_{1222} [\mu\text{s}]^b$
<b>[VCl<sub>3</sub>(ddpd)]</b>	0.5	-
<b>[VCl<sub>3</sub>([D<sub>17</sub>]-ddpd)]</b>	3.3	3.4

<sup>a</sup> $\lambda_{\text{exc}} = 350 \text{ nm}$ ,  $\lambda_{\text{em}} = 1106 \text{ nm}$ , monoexponentielles Fitting; <sup>b</sup> $\lambda_{\text{exc}} = 350 \text{ nm}$ ,  $\lambda_{\text{em}} = 1222 \text{ nm}$ , monoexponentielles Fitting.

Der beobachtete Anstieg der Lumineszenzlebenszeit des perdeutერიerten Komplexes passt qualitativ zu der Steigerung die auf Basis der berechneten SOIs prognostiziert wurde. Das Auftreten dieses Isotopeneffekts belegt, dass MR ein relevanter strahlungsloser Deaktivierungsweg der emittierenden Singulett-Zustände in diesem Komplex ist. Diese Beobachtung steht im Kontrast zu den Untersuchungen von MR im homoleptischen **[V(ddpd)<sub>2</sub>]<sup>3+</sup>**-Komplex und seines deuterierten Analogons **[V([D<sub>17</sub>]-ddpd)<sub>2</sub>](PF<sub>6</sub>)**, bei welchen andere strahlungslose Deaktivierungswege dominieren und Deuterierung keinen messbaren Einfluss auf NIR Lebenszeit hat.

# 5 Photolumineszenz und Upconversion von molekularen Chrom-Lanthanoid-Salzen

## 5.1 Einführung

Chrom(III)-Ionen in einem starken, oktaedrischen Ligandenfeld zeigen, wie in den vorangegangenen Kapiteln erläutert, sehr vorteilhafte optische Eigenschaften wie scharfe, metallzentrierte Emission aus Spin-Flip-Zuständen und lange Lumineszenzlebenszeiten. Wird zusätzlich Multiphonon Relaxation als einer der dominierenden strahlungslosen Deaktivierungswege reduziert, können Lebensdauern im ms-Bereich und hohe Lumineszenzquantenausbeuten von bis zu 30 % erreicht werden.<sup>[37]</sup>

Diese besonderen optischen Eigenschaften ähneln in einigen Punkten denen von  $\text{Ln}^{3+}$ -Ionen, die in Lanthanoid-Komplexen oder Nanomaterialien bereits vielfältig in optischen Anwendungen zum Einsatz kommen.<sup>[24,107]</sup> Neben einigen Gemeinsamkeiten, gibt es aber auch gewisse Unterschiede beider Verbindungsklassen, welche vorteilhaft in gemischten Chrom-Lanthanoid-Architekturen ausgenutzt werden können und das Auftreten spannender optischer Phänomene ermöglichen.<sup>[24]</sup>

Nachdem die Photophysik der  $\text{Cr}^{3+}$ -Ionen in einer oktaedrischen Umgebung bereits in Kapitel 3.1.1 erläutert wurde, wird im nächsten Abschnitt kurz die der  $\text{Ln}^{3+}$ -Ionen beschrieben.

### 5.1.1 Lanthanoiden-Lumineszenz

La	Ce	Pr	Nd	Pm	Sm	Eu	Gd	Tb	Dy	Ho	Er	Tm	Yb	Lu
Lanthanum	Cerium	Praseodymium	Neodymium	Promethium	Samarium	Europium	Gadolinium	Terbium	Dysprosium	Holmium	Erbium	Thulium	Ytterbium	Lutetium

Die Lanthanoide („dem Lanthan ähnlich“) sind Lanthan und die im Periodensystem folgenden Elemente Cer bis Lutetium. Sie treten in der Regel in der Oxidationstufe +III mit der Elektronenkonfigurationen  $[\text{Xe}]4f^n$  mit  $n = 0$  (für  $\text{La}^{3+}$ ) bis  $n = 14$  (für  $\text{Lu}^{3+}$ ) auf. Die  $\text{Ln}^{3+}$ -Ionen weisen eine besondere elektronische Struktur auf, da die zu besetzenden 4f-Valenzorbitale nicht am weitesten vom Atomkern entfernt sind. Die bereits gefüllten 5s- und 5p-Orbitale sind weiter entfernt und schirmen die von Cer bis

Lutetium sukzessive gefüllten 4f-Orbitale von der Umgebung ab. Dies hat zur Folge, dass die f-Orbitale nur wenig für kovalente Wechselwirkungen zur Verfügung stehen und sich die Lanthanoide chemisch auch sehr ähnlich sind. Da kovalente Bindungsanteile für  $\text{Ln}^{3+}$ -Ionen nur sehr gering sind, dominieren in Koordinationsverbindungen ionische Metall-Ligand-Wechselwirkungen. Im Unterschied zu Übergangsmetallen spielt die Ligandenfeldstabilisierungsenergie eine untergeordnete Rolle, weshalb es keine Vorzugsgeometrie gibt und die Bildung von Lanthanoidkomplexen vor allem von sterischen Effekten abhängt.

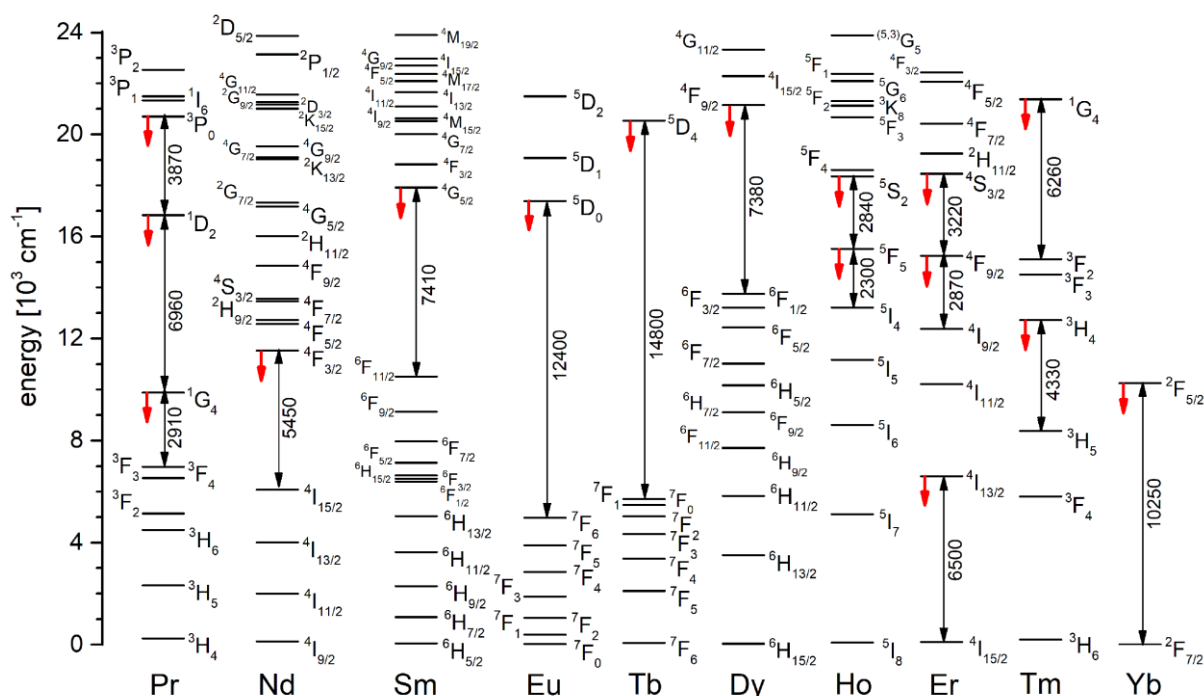


**Abb. 44:** Ausschnitt aus dem Energiediagramm der elektronischen Zustände von ausgewählten  $\text{Ln}^{3+}$ -Ionen mit den jeweils hauptsächlich emittierenden Zuständen (roter Pfeil nach unten) und deren Energieabständen (Werte in  $\text{cm}^{-1}$ , Doppelpfeile). Abbildung übernommen von Seitz.<sup>[34]</sup>

Die elektronische Struktur hat auch entscheidende Konsequenzen für die photophysikalischen Eigenschaften der  $\text{Ln}^{3+}$ -Ionen:

- Durch die Abwesenheit von kovalenten Wechselwirkungen der 4f-Orbitale des Metallions mit den Liganden wird die Struktur der Lanthanoidkomplexe nur sehr wenig von der Konfiguration der f-Orbitale beeinflusst. Bei elektronischen Übergängen zwischen f-Orbitalen bleibt die Bindungssituation folglich nahezu unbeeinflusst und die geometrische Reorganisation ist sehr gering. Es liegt

daher das *weak coupling* Limit vor (Kapitel 3.1.1). Die Emissionbanden der  $\text{Ln}^{3+}$ -Ionen aus den f-Zuständen sind somit scharf und zeigen nur geringe bis keine Stokes-Shifts.

- Die energetische Lage der metallzentrierten Zustände ist fast völlig unabhängig von der Ligandenumgebung. Folglich zeigt jedes  $\text{Ln}^{3+}$ -Ion charakteristische Emissionslinien.
- Aufgrund der sehr schwachen kovalenten Wechselwirkung mit ligandlokalisierten Orbitalen sind elektronische Übergänge in  $\text{Ln}^{3+}$ -Ionen annähernd reine f-f-Übergänge. Diese sind immer paritäts- und teilweise auch spin-verbotten.

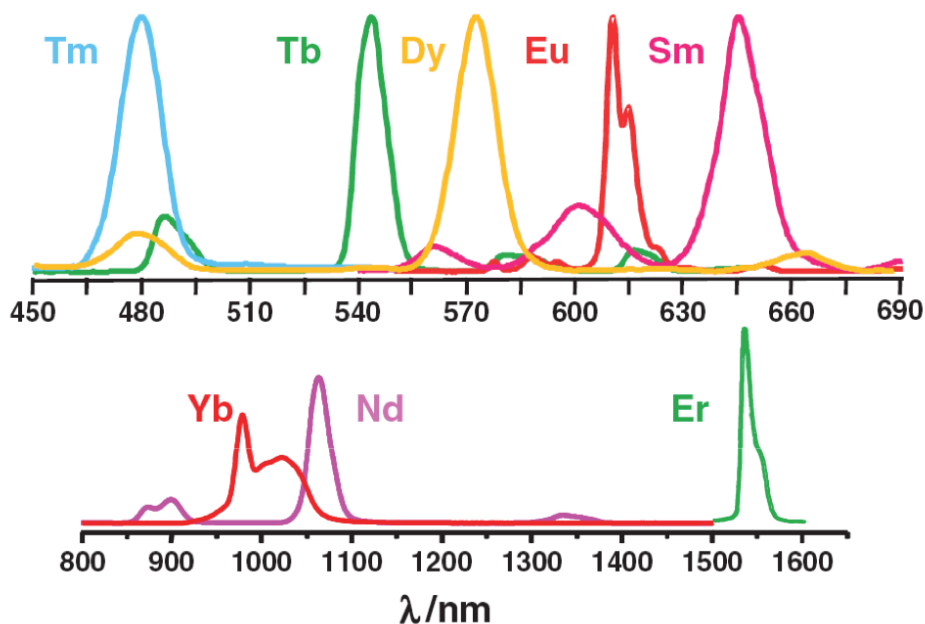


**Abb. 45:** Charakteristische Emissionsbanden unterschiedlicher Lanthanoide vom sichtbaren bis in den NIR-Wellenlängenbereich. Abbildung übernommen von Bünzli.<sup>[104]</sup>

Aus der verbotenen Natur der f-f-Übergänge folgt, dass die Übergangswahrscheinlichkeiten sehr niedrig sind. Daraus resultieren wiederum im Wesentlichen zwei Dinge. Auf der einen Seite haben metallzentrierten Zustände lange Lumineszenzlebensdauern im Bereich von  $\tau \approx \mu\text{s} - \text{ms}$ , auf der anderen Seite auch sehr niedrige Extinktionskoeffizienten ( $\epsilon \approx 0.1 - 10 \text{ M}^{-1}\text{cm}^{-1}$ ).<sup>[108]</sup> Während die langen Lumineszenzlebenszeiten in vielen Fällen wünschenswert sind, ist die sehr schlechte Anregbarkeit häufig problematisch. Grundsätzlich gibt es verschiedene Möglichkeiten  $\text{Ln}^{3+}$ -Ionen trotz der sehr geringen Extinktionskoeffizienten anzuregen. Die erste

Möglichkeit ist die direkte Anregung mit einer sehr starken Energiequelle wie beispielsweise einem Laser. Für die indirekte Anregung kann man sich den sogenannten *Antennen Effekt* zu nutze machen (Abb. 46).

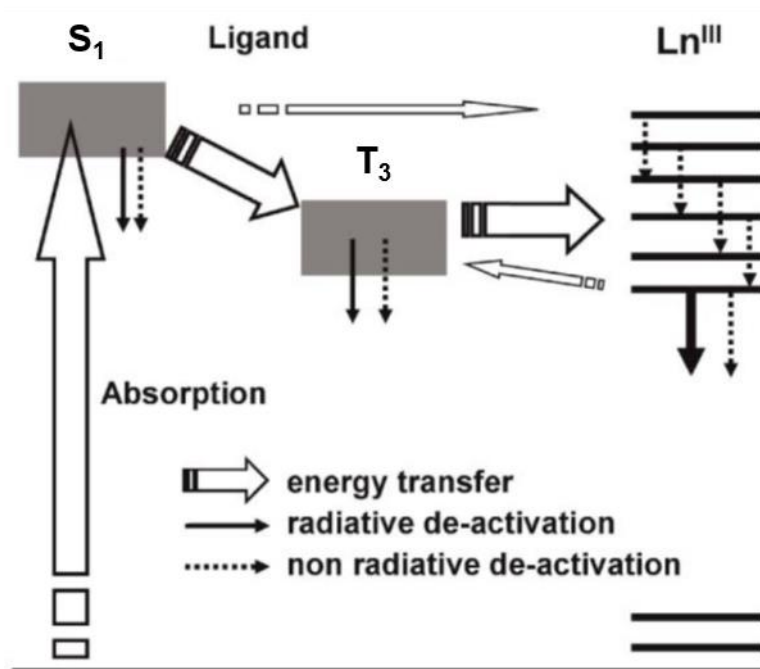


**Abb. 46:** Schematische Darstellung des Antenneneffekts. Bearbeitet übernommen von Bünzli.<sup>[107]</sup>

Als Antennen werden in der Regel organische Liganden mit  $\pi$ -Systemen eingesetzt, welche mit Extinktionskoeffizienten von  $\epsilon \approx 10^4 - 10^5 \text{ M}^{-1}\text{cm}^{-1}$  um einige Größenordnungen besser angeregt werden können als die  $Ln^{3+}$ -Ionen.<sup>[109]</sup>

Zunächst kann mit einer Lichtquelle mit passender Wellenlänge der Ligand in den elektronischen Zustand  $S_1$  angeregt werden. Nach Intersystem Crossing (ISC) kommt es zur Population des ligandzentrierten Triplett-Zustands  $T_3$ . Die Lebenszeit des  $T_3$ -Zustands ist aufgrund des verbotenen Übergangs in den Grundzustand dabei lang genug, sodass Energietransfer auf das  $Ln^{3+}$ -Ion erfolgen kann. Gleichzeitig kann  $T_3$  strahlend oder strahlungslos deaktiviert werden. Ausgehend vom angeregten Zustand des  $Ln^{3+}$ -Ions erfolgt dann strahlende oder strahlungslose Deaktivierung in den  $Ln^{3+}$ -Grundzustand. Beim Antennen Effekt spielt die energetische Lage des Triplett-Zustands des Liganden eine zentrale Rolle. Generell muss die Energie des Triplett-Niveaus größer sein als die der emittierenden Zustände des  $Ln^{3+}$ -Ions. Um thermischen Rücktransfer vom metallzentrierten Niveau auf den Liganden zu vermeiden, muss die Energie des Triplett-Niveaus des Liganden größer sein als die der emittierenden Zustände des  $Ln^{3+}$ -Ions.

unterdrücken, sollte die Energielücke üblicherweise mindestens ca.  $2000\text{ cm}^{-1}$  betragen.<sup>[110]</sup>

In Polymetallischenverbindungen mit gemischten Lanthanoid- und Übergangsmetallzentren kann man sich einen anderen Mechanismus zu Nutze machen um  $\text{Ln}^{3+}$ -Ionen anzuregen. In solchen Systemen, bei welchen Energietransfer zwischen den Metallzentren möglich ist, kann die Anregung des  $\text{Ln}^{3+}$ -Ions auch ausgehend von energetisch höherliegenden metallzentrierten Zuständen des Übergangsmetallions erfolgen. Man spricht bei diesem Prozess auch von  $\text{ÜM} \rightarrow \text{Ln}$ -Downshifting-Energietransfer oder Übergangsmetall sensibilisierter Lumineszenz.<sup>[111,112]</sup>

### 5.1.2 Optische Sensibilisierung und Upconversion-Lumineszenz in molekularen Chrom-Lanthanoid-Verbindungen

Im Allgemeinen gilt, regt man eine lumineszierende Verbindung mit Licht einer bestimmten Wellenlänge an, so ist die ausgesendete Emission immer langwelliger bzw. energieärmer als das Anregungslicht. Dieses Phänomen wurde intensiv von Stokes untersucht und wird deshalb *Stokes-Shift* genannt.<sup>[113]</sup>

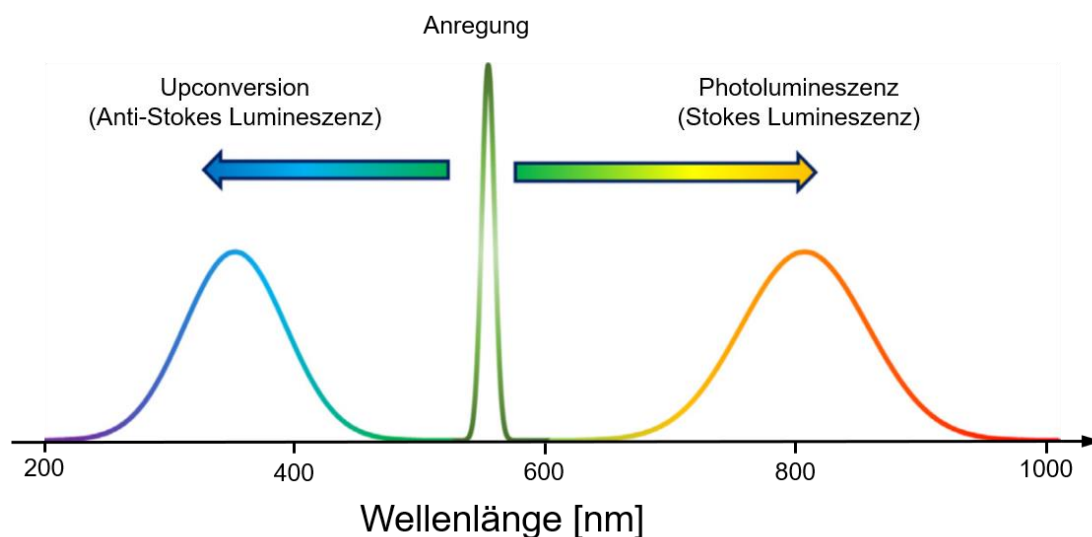


**Abb. 47:** Schematische Darstellung von *Photolumineszenz* (Stokes-Lumineszenz) und *Photon Upconversion* (Anti-Stokes-Lumineszenz). Abbildung bearbeitet übernommen von Charbonnière.<sup>[114]</sup>

In selteneren Fällen ist es einer Verbindung aber möglich, nach der ersten Anregung sehr schnell noch ein weiteres Photon zu absorbieren, um einen höheren angeregten Zustand zu erreichen. Die beim Übergang in den Grundzustand erfolgende Emission

ist nun kurzwelliger bzw. energiereicher als das Anregungslicht. Dieser nicht-lineare Prozess bei dem mehrere energiearme Photonen in Anti-Stokes verschobene Lumineszenz umgewandelt werden, wird *Photon Upconversion (UC)* genannt.<sup>[21]</sup>

Für das Auftreten dieses zunächst „magisch“ erscheinenden Phänomens sind grundsätzlich verschiedene Mechanismen möglich. Eine Auswahl der relevantesten UC-Mechanismen ist in Abb. 48 gezeigt.

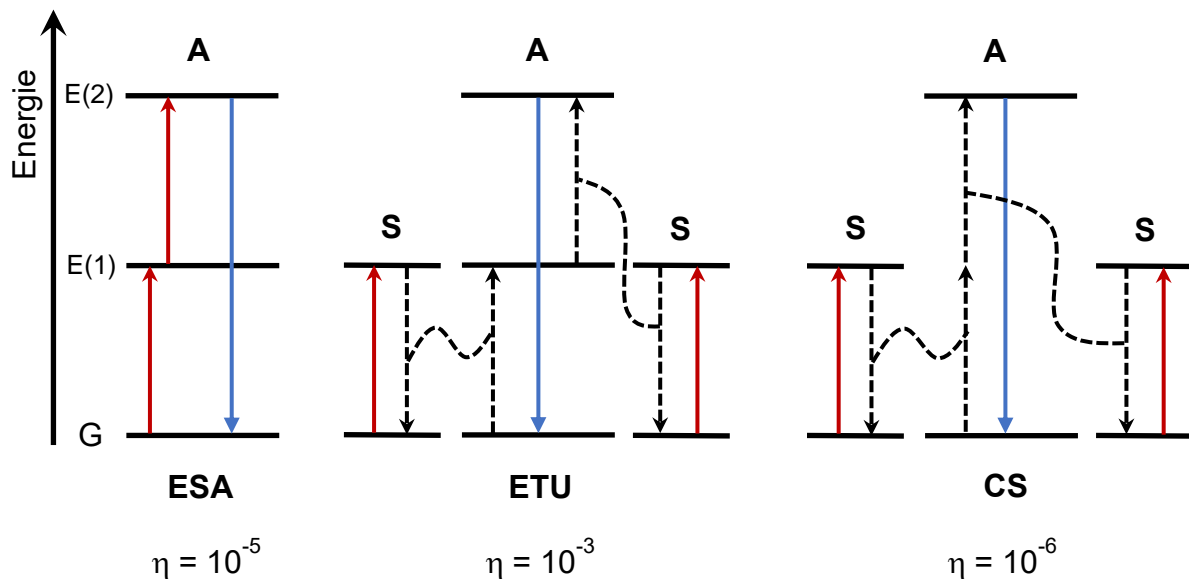


**Abb. 48:** Schematische Darstellung der relevantesten Zwei-Photonen-Upconversion-Mechanismen (G = Grundzustand, E(1), E(2) = angeregte Zustände, A = Aktivator, S = Sensibilisator). Gezeigt sind die Mechanismen *excited state absorption* (ESA), *energy transfer upconversion* (ETU) und *cooperative sensitization* (CS) mit den normierten relativen Effizienzen ( $\eta$ ). Durchgezogene Pfeile nach oben stehen für Anregung, gestrichelte Pfeile für Energietransfer und durchgezogene Pfeile nach unten für Lumineszenz. Inhaltlich orientiert an Piguet.<sup>[24]</sup>

Im Jahr 1966 postulierte Auzel UC-Mechanismen, bei welchen sich ein emittierendes Metallion (**Aktivator**) bereits in einem angeregten Zustand befindet und in der Lage ist ein zusätzliches Photon aufzunehmen. Die dazu benötigte Energie kann entweder durch ein Photon der externen Lichtquelle (*excited state absorption* = ESA) oder von räumlich nahen Metallionen (**Sensibilisatoren**) unter Beteiligung eines Energietransfers (*energy transfer upconversion* = ETU, *cooperative sensitization* = CS) stammen.<sup>[21,24]</sup>

Beim ESA-Mechanismus (Abb. 48, links) führt die Absorption eines Photons zunächst zur Besetzung des ersten angeregten Zustands E(1). Anschließend wird ein weiteres Photon absorbiert, wodurch ein energetisch höherer Anregungszustand E(2) besetzt



wird, von welchem aus die UC-Lumineszenz resultiert. Beim ETU-Mechanismus (Abb. 48, Mitte) wird zunächst ein Sensibilisator (**S**) angeregt, welcher anschließend seine Energie auf den Aktivator (**A**) überträgt. Während sich der Aktivator noch im ersten angeregten Zustand befindet, erfolgt der Energietransfer ausgehend von einem weiteren angeregten Sensibilisator, wodurch der höhere angeregte Zustand des Aktivators erreicht wird. Im letzten Schritt kann die strahlende Relaxation in den Grundzustand des Aktivators als UC-Emission beobachtet werden.

Eine weitere Möglichkeit ist kooperativ sensibilisierte Upconversion, welche durch den *cooperative sensitization* Mechanismus (CS) (Abb. 48, rechts) möglich wird. Hier steht in der elektronischen Struktur des Aktivators kein passender angeregter Zwischenzustand zur Verfügung, was folglich einen schrittweisen Energietransfer ausschließt. Stattdessen übertragen zwei angeregte Sensibilisatorionen gleichzeitig ihre Energie auf den Aktivator um einen angeregten Zustand mit etwa der doppelten Energie des angeregten Sensibilisator-Zustands zu populieren. Dieser kann schließlich strahlend in den Grundzustand relaxieren.

Von den beschriebenen Mechanismen zeichnet sich der ETU-Prozess durch die höchste Effizienz aus (Abb. 48). Der Grund dafür ist, dass sich die Energien des angeregten Zwischenzustands des Aktivators und die angeregten Sensibilisator-Zustände entsprechen, was vorteilhaft für resonanten Energietransfer ist.<sup>[115]</sup>

Für alle beschriebenen UC-Mechanismen müssen zwei wichtige Voraussetzungen erfüllt sein. Zum einen sollte das emissive Aktivator-Ion eine „leiterartige“ elektronische Struktur aufweisen, um in der Lage zu sein einen höheren angeregten Zustand zu „erklimmen“. Ein Ausnahme von dieser Regel stellt der CS-Mechanismus dar, da hier kein angeregter Zwischenzustand benötigt wird. Die zweite Notwendigkeit sind ausreichend lange Lebenszeiten der angeregten Zwischenzustände. Nur wenn diese lange genug leben, können die Prozesse zur Besetzung des höheren angeregten Aktivator-Zustands ablaufen, bevor Relaxation in den Grundzustand erfolgt.<sup>[115]</sup>

Diese beiden Voraussetzungen machen deutlich, warum in den meisten bisher bekannten Upconversion-Materialien entweder Lanthanoid- oder Übergangsmetallkationen mit langen Lumineszenzlebenszeiten eingesetzt werden. Wegen der wesentlich größeren Zahl an strahlungslosen Deaktivierungsmechanismen in Lösung ist es auch wenig verwunderlich, dass die ersten Upconversion-Prozesse in Festkörpermateriale beobachtet wurden. Beispiele sind mit Übergangsmetall- oder Lanthanoidkationen dotierte, feste, anorganische Wirtgitter mit geringen Phononen-

Energien, entweder als Bulkmaterial<sup>[21,115–117]</sup> oder in den letzten Jahren vermehrt als Nanopartikel.<sup>[22,118]</sup> Vor allem Letztere gewinnen immer mehr Bedeutung in der Entwicklung neuer Photovoltaik-Zellen<sup>[18]</sup> oder in vielfältigen bioanalytischen Anwendungen.<sup>[119]</sup> So kann beispielsweise ein UC-Nanopartikel zunächst an ein zu detektierendes Biomolekül gebunden werden. Im nächsten Schritt ist es möglich das UC-Material mit energiearmen NIR-Licht anzuregen, dann aber grünes Licht zu detektieren (Abb. 49). Die große spektrale Trennung zwischen Anregungs- und Detektionslicht bietet dabei spezifische Vorteile.<sup>[120]</sup>

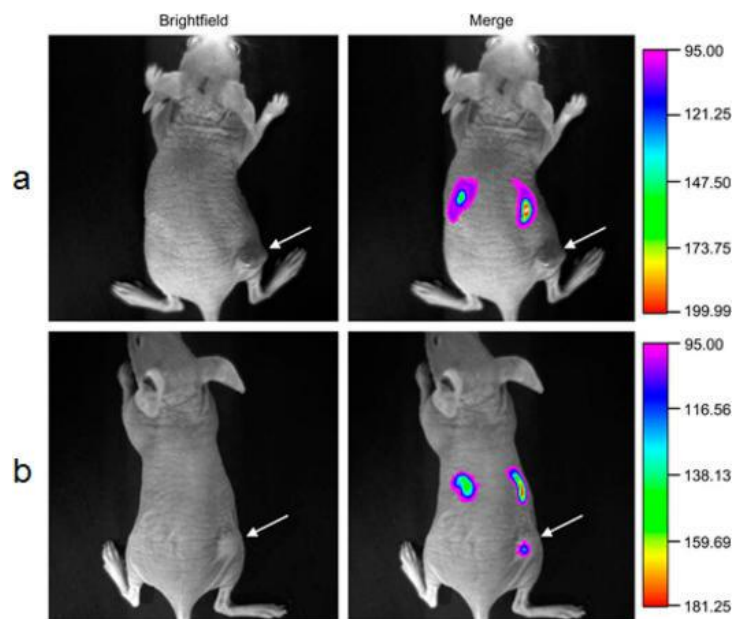


**Abb. 49:** In-vivo Imaging nach intravenöser Injektion eines NaYF<sub>4</sub>:Yb,Er-Nanopartikel-Materials ( $\lambda_{\text{ex}} = 980 \text{ nm}$ ,  $\lambda_{\text{em}} = 600\text{-}700 \text{ nm}$ ). Abbildung übernommen von Huang.<sup>[120]</sup>

Bis vor kurzem hielt man UC in diskreten Metallkomplexen mit organischen Liganden wegen der ausgeprägten strahlungslosen Desaktivierung der angeregten Metallzustände z.B. durch Multiphonon Relaxation für nicht möglich. In den letzten Jahren konnten aber viele Fortschritte bei der Erweiterung von metallbasierter UC auf molekulare Komplexverbindungen erzielt werden, teilweise sogar bei Raumtemperatur und in Lösung.<sup>[24,114,121,122]</sup> Dazu gehören Kombinationen aus Metallkomplexen und organischen Chromophoren,<sup>[123,124]</sup> einkernige Metallkomplexe<sup>[125–128]</sup> und heterooligometallische Sensibilisator-Aktivator-Architekturen.<sup>[129–137]</sup> Insbesondere letztgenannte zeigen das größte Potential für effiziente UC, entweder durch den ETU- oder CS-Mechanismus.

Neben den in molekularen UC-Verbindungen am weitesten verbreiteten Ln<sup>3+</sup>-Ionen (z.B. Yb<sup>3+</sup>, Er<sup>3+</sup>, Tb<sup>3+</sup>) sind auch Cr<sup>3+</sup>-Ionen wegen ihrer guten Anregbarkeit und der langlebigen, intensiven Spin-Flip-Emission geeignete Kandidaten für den Einsatz in Sensibilisator-Aktivator-Architekturen. Die Kombination von Ln<sup>3+</sup>- und Cr<sup>3+</sup>-Ionen in einem molekularen Sensibilisator-Aktivator-Paar ist daher so naheliegend wie vielsprechend. Ob in solchen Systemen das Cr<sup>3+</sup>-Ion als Aktivator oder Sensibilisator auftritt, hängt von der Wahl des dazugehörigen Lanthanoidions ab.<sup>[24]</sup>

Cr<sup>3+</sup>-Ionen als *Sensibilisatoren*:

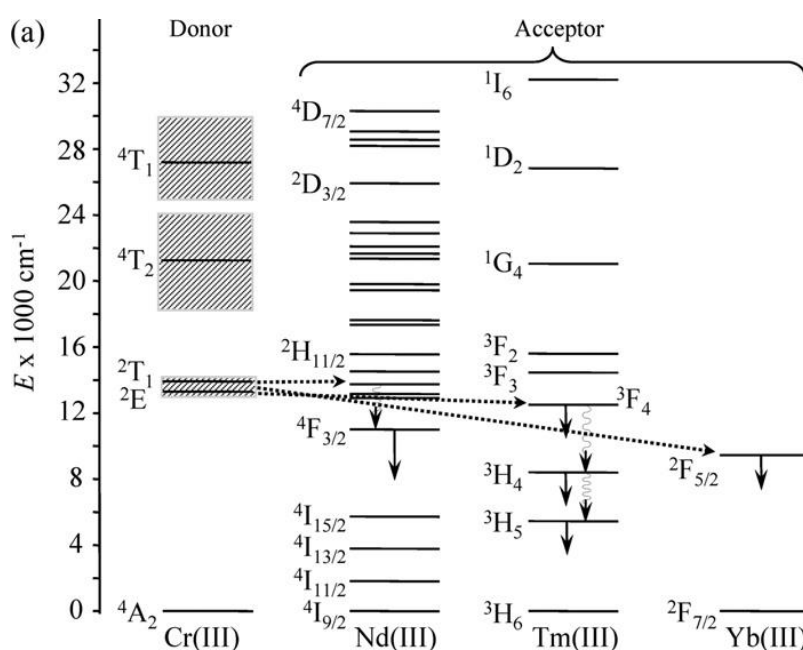


**Abb. 50:** Vereinfachtes Energiediagramm mit den relevanten elektronischen Zuständen von Cr<sup>3+</sup>-Ionen in einem starken oktaedrischen Ligandenfeld, die als Donoren unter Beteiligung von Cr→Ln-Downshifting-Energietransfer die NIR-Lumineszenz von Nd<sup>3+</sup>-, Tm<sup>3+</sup>-, Yb<sup>3+</sup>-Ionen sensibilisieren. Gepunktete Pfeile stehen für Energietransfer, wellenförmige Pfeile für internal conversion und ein durchgezogener Pfeil nach unten für emittierende Zustände. Abbildung übernommen von Piguet.<sup>[24]</sup>

Cr(III)-Komplexe in einem starken oktaedrischen Ligandenfeld sind wegen ihrer langlebigen Spin-Flip-Zustände sehr gut geeignet um als effiziente Sensibilisatoren/Downshifting-Luminophore die NIR-Lumineszenz von Lanthanoidkomplexen durch intermetallischen Cr→Ln-Downshifting-Energietransfer anzuregen.<sup>[111,138]</sup> Dabei besitzen die Lanthanoidkationen Tm<sup>3+</sup>, Nd<sup>3+</sup> und Yb<sup>3+</sup> passende energetisch tief liegende Akzeptor-Niveaus (Abb. 50). Passende Beispiele

sind Hexacyanochromate  $[\text{Cr}(\text{CN})_6]^{3-}$ , die erfolgreich als Antennenmotiv für die Sensibilisierung der NIR-Lumineszenz von  $\text{Yb}^{3+}$ - oder  $\text{Nd}^{3+}$ -Ionen eingesetzt werden können.<sup>[139,140]</sup> Außerdem konnte Piguet in einer trinuklearen Cr-Er-Cr-Koordinationsverbindung NIR nach VIS-Upconversion-Lumineszenz nachweisen. In diesem molekularen System wurden  $\text{Cr}^{3+}$ -Ionen zur Sensibilisierung von  $\text{Er}^{3+}$ -Aktivatoren eingesetzt.<sup>[137]</sup>

#### $\text{Cr}^{3+}$ -Ionen als *Aktivatoren*:

Die langlebigen Spin-Flip-Zustände  ${}^2\text{E}/{}^2\text{T}_1$  von Chrom(III)-Luminophoren können auch als emittierende Akzeptor-Zustände für Ln $\rightarrow$ Cr-Energietransfer ausgehend von energetisch höheren Sensibilisator-Zuständen von beispielsweise  $\text{Eu}^{3+}$ - oder  $\text{Tb}^{3+}$ -Ionen auftreten (Abb. 51). So kann beispielsweise in einem aus Lanthanoid- und  $\text{Cr}[\text{N}_6]$ -Komplexionen aufgebauten Festkörper effizienter  $\text{Tb}^{3+}\rightarrow\text{Cr}^{3+}$ - und  $\text{Eu}^{3+}\rightarrow\text{Cr}^{3+}$ -Energietransfer beobachtet werden.<sup>[141]</sup>

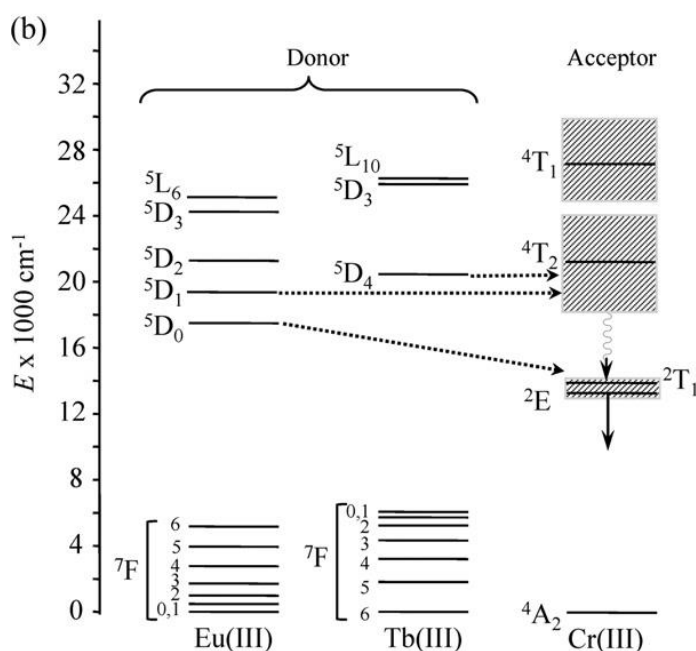


**Abb. 51:** Vereinfachtes Energiediagramm mit den relevanten elektronischen Zuständen von  $\text{Cr}^{3+}$ -Ionen in einem starken oktaedrischen Ligandenfeld, die als Akzeptor-Niveaus für Ln $\rightarrow$ Cr-Energietransfer ausgehend von angeregten Zuständen von  $\text{Eu}^{3+}$ - und  $\text{Tb}^{3+}$ -Ionen auftreten. Gepunktete Pfeile stehen für Energietransfer, wellenförmige Pfeile für internal conversion und ein durchgezogener Pfeil nach unten für emittierende Zustände. Abbildung übernommen von Piguet.<sup>[24]</sup>

Ebenfalls können  $\text{Cr}^{3+}$ -Ionen in Kombination mit  $\text{Yb}^{3+}$ -Ionen als Aktivatoren auftreten. Generell gehören  $\text{Yb}^{3+}$ -Ionen wegen ihres energiearmen, langlebigen  $^2\text{F}_{5/2}$ -Zustand ( $^2\text{F}_{5/2}$  bei  $\approx 10250 \text{ cm}^{-1}$ ,  $\approx 976 \text{ nm}$ ) zu den besten Sensibilisator-Metallzentren und werden beispielsweise in molekularen Systemen zur Sensibilisierung von  $\text{Er}^{3+}$ - oder  $\text{Tb}^{3+}$ -Aktivatoren eingesetzt.<sup>[129–137]</sup>

Güdel postulierte vor gut 20 Jahren einen interessanten UC-Mechanismus (Abb. 52) für das Auftreten von UC-Emission aus dem  $^2\text{E}$ -Zustand eines  $\text{Cr}(\text{III})$ -Ions, die er in einem mit  $\text{Yb}^{3+}$ -Sensibilisatoren und  $\text{Cr}^{3+}$ -Aktivatoren dotierten festen anorganischen Wirtgitter ( $\text{Y}_3\text{Ga}_5\text{O}_{12}$ ) beobachtet hatte.<sup>[142]</sup> Dieses System funktioniert via CSU, bei welchem zwei angeregte  $\text{Yb}^{3+}$ -Ionen kooperativ Energie von deren  $^2\text{F}_{5/2}$ -Zuständen auf den Quartettzustand des  $\text{Cr}^{3+}$ -Ions ( $^4\text{T}_2/^4\text{T}_1$ ) übertragen. Nach Intersystem Crossing kommt es zur Population des emittierenden  $^2\text{E}$ -Zustands. Dieses UC-Material ist besonders deshalb interessant, weil sich sowohl Anregung ( $\lambda_{\text{ex}} = 970 \text{ nm}$ ) als auch die UC-Lumineszenz ( $\lambda_{\text{em}} = 695 \text{ nm}$ ) im NIR-Spektralfenster befinden, welches wie bereits erläutert, zunehmend im Bioimaging eingesetzt wird.<sup>[26]</sup>

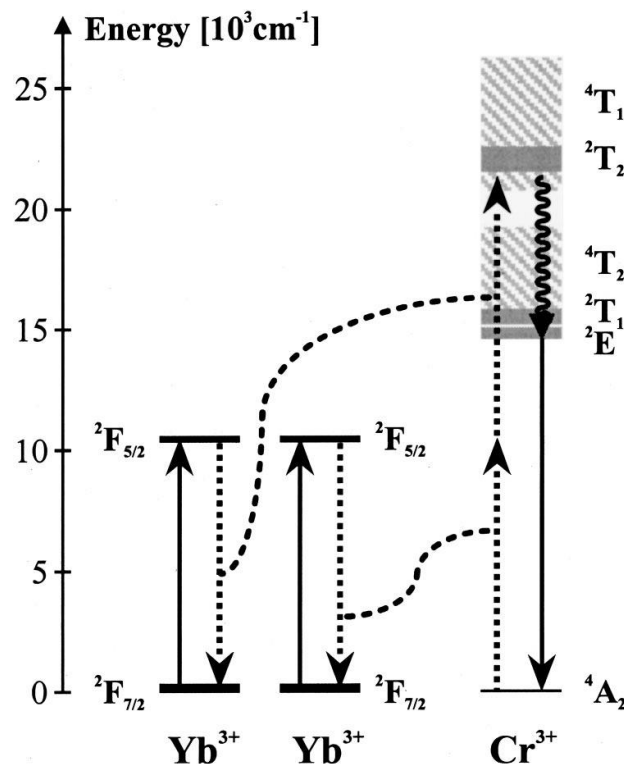


**Abb. 52:** Vereinfachtes Energiediagramm mit den relevanten Zuständen und Prozessen für die UC-Emission in  $\text{Cr}^{3+}$  und  $\text{Yb}^{3+}$  dotiertem  $\text{Y}_3\text{Ga}_5\text{O}_{12}$ . Durchgezogene Pfeile nach oben stehen für Anregung, gestrichelte Pfeile für Energietransfer, geringelte Pfeile für internal conversion und durchgezogener Pfeil nach unten = UC-Lumineszenz. Abbildung übernommen von Güdel.<sup>[142]</sup>

Allerdings zeigen die wenigen bekannten Beispiele, die sich das Yb<sup>3+</sup>/Cr<sup>3+</sup>-Paar zu Nutze machen, UC nur bei sehr niedrigen Temperaturen (meist unter 100 K) und in ausgedehnten, festen, anorganischen Matrizes.<sup>[142–146]</sup> In molekularen Systemen ist NIR nach NIR-Upconversion nach wie vor unbekannt.

### Energietransfer-Mechanismen:

In diesen Sensibilisator-Akzeptor-Paaren kann der Energietransfer (EnT) zwischen den Metallzentren grundsätzlich durch zwei unterschiedliche Mechanismen erfolgen. Das ist zum einen der im Rahmen der MR-Theorie bereits behandelte Förster-EnT<sup>[80]</sup> und zum anderen Dexter-EnT.<sup>[147]</sup>

Beim auf Dipol-Dipol-Wechselwirkungen basierenden Förster-EnT induziert der angeregte Donor eine Oszillation im Akzeptor und gibt so seine Energie strahlungslos und vollständig an den Akzeptor ab. Die Energietransferrate des Förster-EnT ist in Gl. 7 ausgedrückt:

$$k_{\text{ET}}^{\text{F}} = \frac{8.8 \times 10^{-25} \cdot \kappa^2 \cdot \phi}{n^4 \cdot \tau \cdot r^6} \cdot J_{\text{F}} \quad (7)$$

Dabei ist  $\kappa^2$  ein Faktor, der abhängig von der relativen Orientierung der Übergangsdipolmomente des Donors und des Akzeptors ist (für ein isotropes System gilt:  $\kappa^2 = 2/3$ ).  $\phi$  ist die Lumineszenzquantenausbeute und  $\tau$  die Emissionslebensdauer des Donors in Abwesenheit aller strahlungslosen Prozesse. Der Parameter  $n$  ist der Brechungsindex des Lösungsmittels und  $r$  der Abstand zwischen Donor und Akzeptor mit der für Dipol-Dipol-Wechselwirkungen typischen Abstandsabhängigkeit von  $r^{-6}$ . Die Effizienz des Förster-EnT hängt maßgeblich von  $J_{\text{F}}$  ab. Dabei ist  $J_{\text{F}}$  der integrierte spektrale Überlapp (SOI) des (normierten) Emissionsspektrums des Donors und des Absorptionsspektrum des Akzeptors. Das heißt, für einen effektiven Energietransfer müssen Absorptions- und Emissionsspektrum intensiv sein. Darunter verbirgt sich indirekt eine Spinauswahlregel: Da für intensive Absorptions- und Emissionsbanden die beteiligten Übergänge spin-erlaubt sein müssen, darf sich weder im Donor noch im Akzeptor der Spin beim Übergang ändern.<sup>[111]</sup> Dies gilt allerdings streng nur organische Chromophore ohne Beteiligung von Schweratomen.

Beim Dexter-Mechanismus erfolgt der Energietransfer durch einen doppelten Elektronenaustausch-Prozess. Bei diesem überträgt der Donor ein energetisch angeregtes Elektron auf den Akzeptor, welcher wiederum ein nicht angeregtes Elektron zurück auf den Donor transferiert. Dieser Vorgang setzt notwendigerweise eine räumliche Überlappung der Orbitale von Donor und Akzeptor voraus, weshalb Dexter-EnT nur über sehr kurze Distanzen (häufig über kovalente Bindungen) hinweg stattfinden kann. Dies ist ein wichtiger Unterschied zum Förster-EnT, der auch über größere Distanzen und durch den Raum erfolgen kann. Durch den doppelten Elektronenaustausch des Dexter-Mechanismus muss nur der Gesamtspin des Systems erhalten bleiben, wodurch Dexter-EnT in Situationen möglich ist, bei welchem der Förster-Mechanismus wegen verbotenen Übergängen sehr ineffektiv wäre.<sup>[111]</sup>

Die Energietransferrate des Dexter-EnT ergibt sich nach Gl. 8:

$$k_{\text{ET}}^{\text{D}} \propto J_{\text{D}} \cdot \exp\left(\frac{-2r}{L}\right) \quad (8)$$

Auch hier ist  $J_{\text{D}}$  das spektrale Überlappungsintegral und  $L$  ist ein Parameter, der mit den Van-der-Waals-Radien korreliert. Die Dexter-Energietransferrate hängt exponentiell vom Abstand  $r$  zwischen Donor und Akzeptor ab. Dies hat zur Folge, dass Dexter-EnT im Vergleich zu Förster-EnT wesentlich kurzreichweitiger ist und nur über Distanzen von maximal 10 Å erfolgen kann, während Förster-EnT über Entfernungen von bis zu 100 Å noch möglich sind.





Insbesondere  $\text{Cr}^{3+}/\text{Yb}^{3+}$ -Architekturen mit hocheffizientem Dexter-EnT, wie er beispielsweise in hexacyanidochromat- und oxalatverbrückten Koordinationsverbindungen auftritt, schienen für dieses Ziel unbrauchbar.<sup>[139,149,150]</sup> Dexter-EnT ist in diesen molekularen Verbindungen spin-erlaubt (Gesamtdrehimpuls-Quantenzahl  $\Delta J = 1$ )<sup>[139,151]</sup> und sollte daher in zukünftigen UC-Systemen unbedingt vermieden werden. Auf der anderen Seite zeigte  $\text{Cr}^{3+} \rightarrow \text{Yb}^{3+}$ -Dipol-Dipol-EnT (Förster) in oligometallischen, molekularen Systemen ebenfalls unvorteilhaft hohe EnT-Effizienzen von bis zu ca. 50 %. Allerdings ist Förster-EnT in  $\text{Cr}^{3+}/\text{Yb}^{3+}$ -Architekturen durch die entsprechende Auswahlregel ( $\Delta J = 2,4,6$ ) verboten und sollte im Allgemeinen daher ineffektiver sein als Energietransfer via des erlaubten Dexter-Mechanismus.<sup>[139,151]</sup>

Mit diesen Herausforderungen im Blick entwickelten wir ein neues photonisches Material aufgebaut aus einfach zugänglichen  $\text{Cr}^{3+}$ - und  $\text{Yb}^{3+}$ -Komplexionen (Abb. 54).

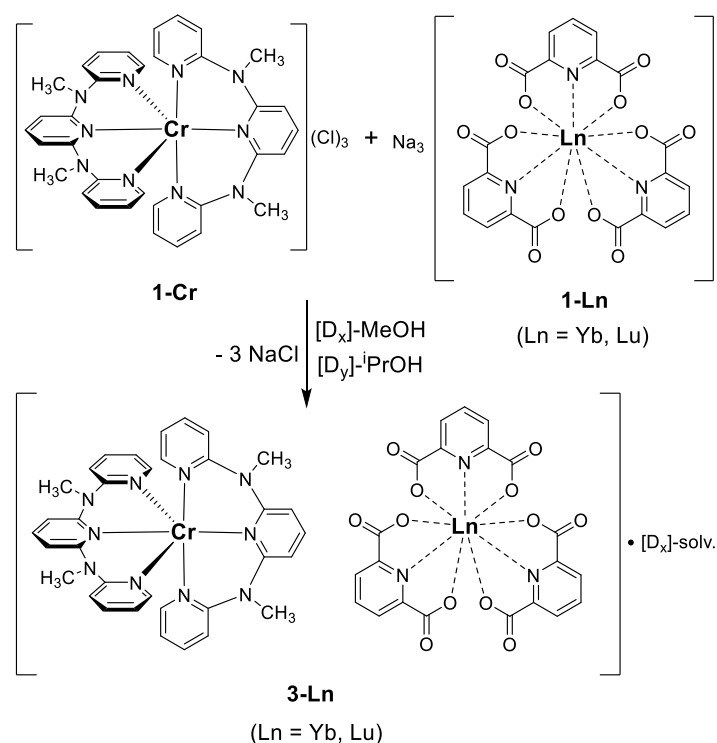


**Abb. 54:** Synthese der Chrom-Lanthanoid-Salze **3-Ln**.

Dabei war der Grundgedanke, Dexter-EnT von  ${}^2\text{E}(\text{Cr}^{3+})$  nach  ${}^2\text{F}_{5/2}(\text{Yb}^{3+})$  zu vermeiden und ein System auszuwählen, bei welchem  $\text{Cr}^{3+} \rightarrow \text{Yb}^{3+}$ -EnT nur durch den weniger effizienten Förster-Mechanismus möglich ist. Hierbei sollte die räumliche Trennung der

Metallzentren in diskrete Koordinationsumgebungen ausgenutzt werden. Für die Realisierung dieses Konzepts, wurde als Aktivator der **mer-[Cr(ddpd)<sub>2</sub>]<sup>3+</sup>**-Komplex (**1-Cr**) wegen seiner bekannt vorteilhaften photophysikalischen Eigenschaften ausgewählt. Bei der Suche nach dem passenden Sensibilisator fiel die Wahl auf den **[Yb(dpa)<sub>3</sub>]<sup>3+</sup>**-Komplex (**dpa** = 2,6-Pyridindicarboxylat). Der dreifach anionische Komplex **1-Yb** besitzt zwar nur mäßig lange Lebensdauern der angeregten <sup>2</sup>F<sub>5/2</sub>-Zustände (Festkörper: **1-Yb** bei T = 295 K: τ = 2.9 μs)<sup>[150,152]</sup>, ist aber synthetisch sehr leicht zugänglich und weist zusätzlich eine hohen Kongruenz mit **1-Cr** in Bezug auf Größe und entgegengesetzter Ladung auf.

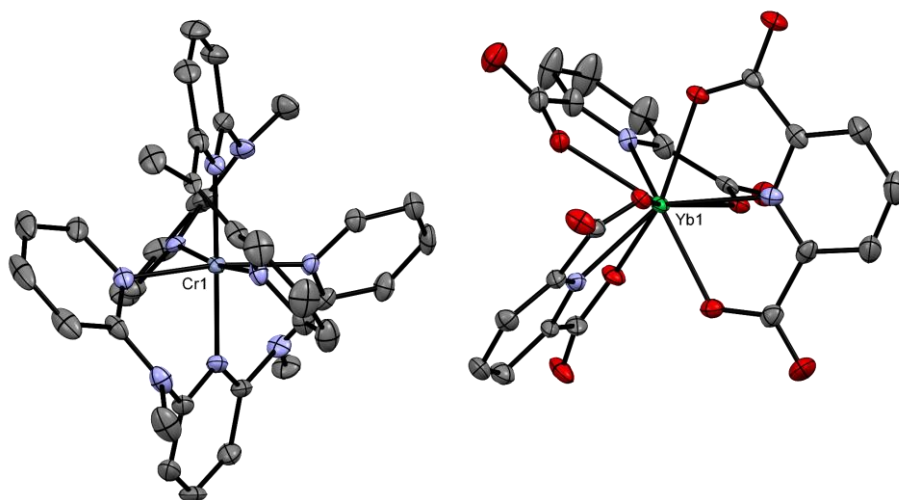


**Abb. 55:** ORTEP-Darstellung der asymmetrischen Einheit von **3-Yb**, Ellipsoidenwahrscheinlichkeit 50 %. Lösemittelmoleküle im Kristallgitter und Wasserstoffatome wurden aus Übersichtlichkeitsgründen weggelassen. Die Details zur Strukturlösung sind den HI zu entnehmen. Abbildung übernommen von Seitz.<sup>[148]</sup>

Die Synthese von **3-Yb** gelang durch Rühren von Na<sub>3</sub>[Yb(dpa)<sub>3</sub>]·6 H<sub>2</sub>O (**1-Yb**)<sup>[153]</sup> mit **[Cr(ddpd)<sub>2</sub>]Cl<sub>3</sub>** (**1-Cr**) in methanolischer Lösung (Abb. 54). Neben dem Cr/Yb-Komplexpaar wurde als strukturelles Analogon von **3-Yb** die Referenzverbindung **3-Lu** dargestellt. Das Lu<sup>3+</sup>-Ion in **3-Lu** ist wegen seiner 4f<sup>14</sup>-Elektronenkonfiguration photoinaktiv und stellt daher ein ideales Kontrollsystem dar. Die Elementaranalyse der beiden Festkörper offenbarte größere Mengen Wasser und Methanol im Material (Details s. HI). Um die potentiell starke strahlungslose Deaktivierung der energetisch tief liegenden <sup>2</sup>E/<sup>2</sup>T<sub>1</sub>- und auch der <sup>2</sup>F<sub>5/2</sub>-Zustände durch

Multiphonon Relaxation von Schwingungsobertönen von C-H- und O-H-Streckschwingungen zu unterdrücken, wurde die Synthese ebenfalls in  $[D_4]\text{-MeOH}/[D_8]\text{-iPrOH}$  durchgeführt.

Die Röntgenstrukturanalyse an Einkristallen von **3-Ln** zeigte, dass alle Salze isostrukturelle, racemische Mischungen der Komplexionen sind (Abb. 55, HI, Tab. S1 u. Abb. S1). Da keine kovalenten Wechselwirkungen zwischen den beiden Metallzentren möglich sind, sollte in festem **3-Yb** unerwünschter Downshifting-EnT nur durch den verbotenen Förster-Mechanismus möglich sein. Im kristallinen Material ist jeder  $\text{Cr}^{3+}$ -Aktivator von fünf  $\text{Yb}^{3+}$ -Sensibilisatoren als nächste Nachbarn umgeben (HI, Abb. S2). Die Cr-Yb-Abstände variieren mit  $8.75 \text{ \AA} < r_{\text{Cr-Yb}} < 9.07 \text{ \AA}$  nur sehr wenig, weshalb unter Annahme von ähnlichen Werten für andere Parameter (z.B. Orientierung der Chromophore, Dipolmomente, etc.) von vergleichbaren Energietransferraten auf den zentralen  $\text{Cr}^{3+}$ -Aktivator für alle fünf Sensibilisatoren auszugehen ist.

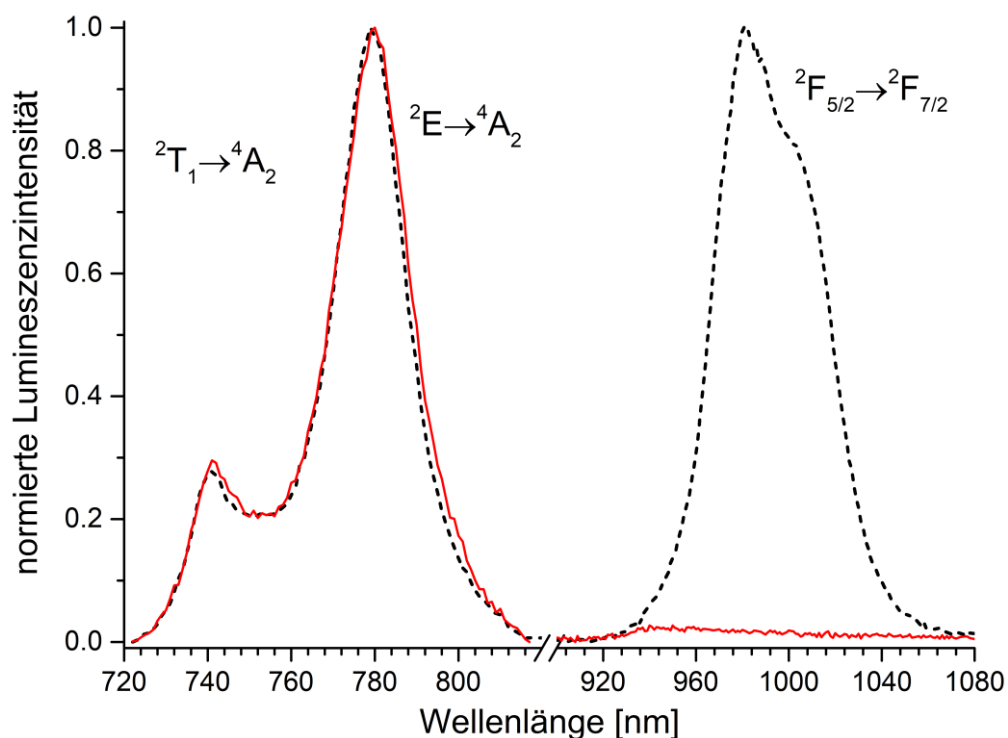


**Abb. 56:** Normierte Steady-State-Emissionsspektren ( $\lambda_{\text{exc}} = 435 \text{ nm}$ ) von **3-Yb** (gestrichelte schwarze Linie) und **3-Lu** (durchgezogene rote Linie) im Festkörper bei  $T = 298 \text{ K}$  an Luft. Die relativen Intensitäten der Emissionsspektren der unterschiedlichen  $\text{Cr}^{3+}$ - und  $\text{Yb}^{3+}$ -Emissionsbanden sind nicht maßstäblich gezeichnet. Abbildung übernommen von Seitz.<sup>[148]</sup>

Selektive Anregung von **3-Ln** bei  $\lambda_{\text{exc}} = 435 \text{ nm}$  in die  ${}^4\text{A}_2 \rightarrow {}^4\text{T}_2$  Bande von **1-Cr** bewirkt die erwartete  ${}^2\text{E}/{}^2\text{T}_1$ -Phosphoreszenz von Chrom mit dem Emissionsmaximum bei etwa  $\lambda_{\text{em}} = 780 \text{ nm}$  (Abb. 56). Die Anregung von **3-Yb** bei  $\lambda_{\text{exc}} = 435 \text{ nm}$  führt nicht nur zum Auftreten der  $\text{Cr}^{3+}$ -Emission, sondern zusätzlich auch der  $\text{Yb}^{3+}$ -Lumineszenz ( ${}^2\text{F}_{5/2} \rightarrow {}^2\text{F}_{7/2}$ ) bei ungefähr  $\lambda_{\text{em}} = 1000 \text{ nm}$ . Da die chromfreie Vorstufe **1-Yb** nach Anregung bei  $\lambda_{\text{exc}} = 435 \text{ nm}$  nicht emittiert (HI, Abb. S3), weist dies deutlich auf unerwünschten  $\text{Cr}^{3+} \rightarrow \text{Yb}^{3+}$ -EnT in **3-Yb** hin. Dieser ungewollte Downshifting-EnT zwischen  $\text{Cr}^{3+}$  und  $\text{Yb}^{3+}$  konnte ebenfalls durch zeitaufgelöste Lumineszenzmessungen unter gleichen Bedingungen belegt werden (Tab. 8).

**Tab. 8:** Lumineszenzlebensdauern  $\tau$  und Quantenausbeuten  $\Phi$  der Komponenten **3-Ln** (Ln = Yb, Lu) im Festkörper bei  $T = 298 \text{ K}$  nach Anregung bei  $\lambda_{\text{exc}} = 435 \text{ nm}$  (Pub. 3: Tab.1).

Verbindung	$\tau$ ( ${}^2\text{E} \rightarrow {}^4\text{A}_2$ ) [ $\mu\text{s}$ ] <sup>a</sup> $\lambda_{\text{em}} = 783 \text{ nm}$	$\tau$ ( ${}^2\text{F}_{5/2} \rightarrow {}^2\text{F}_{7/2}$ ) [ $\mu\text{s}$ ] <sup>a</sup> $\lambda_{\text{em}} = 980 \text{ nm}$	$\Phi$ ( ${}^2\text{E} \rightarrow {}^4\text{A}_2$ ) [%] <sup>b</sup>
<b>3-Yb</b>	160 (15 %) 390 (85 %)	9 (Anstieg, 2 %) 369 (Abnahme, 102 %)	5.9
<b>3-Lu</b>	280 (11%) 660 (89 %)	n.a	6.8

<sup>a</sup>Lebensdauern wurden biexponentiell angepasst, die Prozentangaben in den Klammern geben die relative Amplituden der Komponenten an (HI, Abb. S4-8).

<sup>b</sup>Bestimmt in einer Ulbricht-Kugel Quantaurus-QY C11347-11 (siehe HI für Details).

Die Lebenszeit der  ${}^2\text{E}/{}^2\text{T}_1$ -Emission des  $\text{Cr}^{3+}$ -Zentrums von **3-Yb** zeigt eine monoexponentielle Zerfallskinetik mit einer langen Lebensdauer von  $\tau = 390 \mu\text{s}$ . Das entsprechende Profil der  $\text{Yb}^{3+}$ -Emission zeigt eine biexponentielle Kinetik mit einer annähernd gleich langen Lumineszenzlebensdauer von  $\tau = 369 \mu\text{s}$ . Letztere ist uncharakteristisch lang für molekulare  $\text{Yb}^{3+}$ -Verbindungen, welche üblicherweise Lumineszenzlebensdauern im niedrigen  $\mu\text{s}$ -Bereich aufweisen. Die Lebensdauer von  $\tau = 369 \mu\text{s}$  passt gut zur  ${}^2\text{E}/{}^2\text{T}_1$ -Lebensdauer der  $\text{Cr}^{3+}$ -Emission von  $\tau = 390 \mu\text{s}$ . Zusätzlich weist das Zerfallsprofil der  $\text{Yb}^{3+}$ -Lebenszeit eine Anstiegskomponente (*rise time*) auf, was ein weiterer Beleg für EnT ausgehend vom langlebigen  ${}^2\text{E}$ -Zustand auf das  $\text{Yb}^{3+}$ -Ion ist.

Um nun die Effizienz des unerwünschten Downshifting-Energietransfers zu quantifizieren, wurden die Quantenausbeuten der  ${}^2\text{E}/{}^2\text{T}_1$ -Phosphoreszenz von **3-Yb** und **3-Lu** nach Anregung bei  $\lambda_{\text{exc}} = 435 \text{ nm}$  bestimmt (Tab. 8). Die Quantenausbeutemessungen ergaben  $\Phi$ -Werte von 6.8 bzw. 5.8 % für deuteriertes

**3-Lu** bzw. deuteriertes **3-Yb**. Die Reduzierung der  ${}^2E$ -Quantenausbeute durch Förster-EnT für **3-Yb** im Vergleich zu **3-Lu** ist folglich mit ca. 15 % eher moderat. Dieser Effizienzverlust ist im Vergleich zu ähnlichen Downshifting-Systemen mit Verlusten von ca. 20 % - 50 %<sup>[140,154,155]</sup> erfreulicherweise gering und bestätigt den konzeptionellen Ansatz durch räumliche Trennung der Metallzentren den effizienteren Dexter-EnT von  ${}^2E(\text{Cr}^{3+})$  nach  ${}^2F_{5/2}(\text{Yb}^{3+})$  zu unterbinden.

Überraschenderweise hat weder die Kristallisation von **3-Yb** aus deuterierten Lösemitteln noch die Anwesenheit von Sauerstoff einen signifikanten Einfluss auf die Lumineszenzlebensdauern der  $\text{Cr}^{3+}$ -Emission in **3-Yb** und **3-Lu** (Pub. 3: Tab.1).

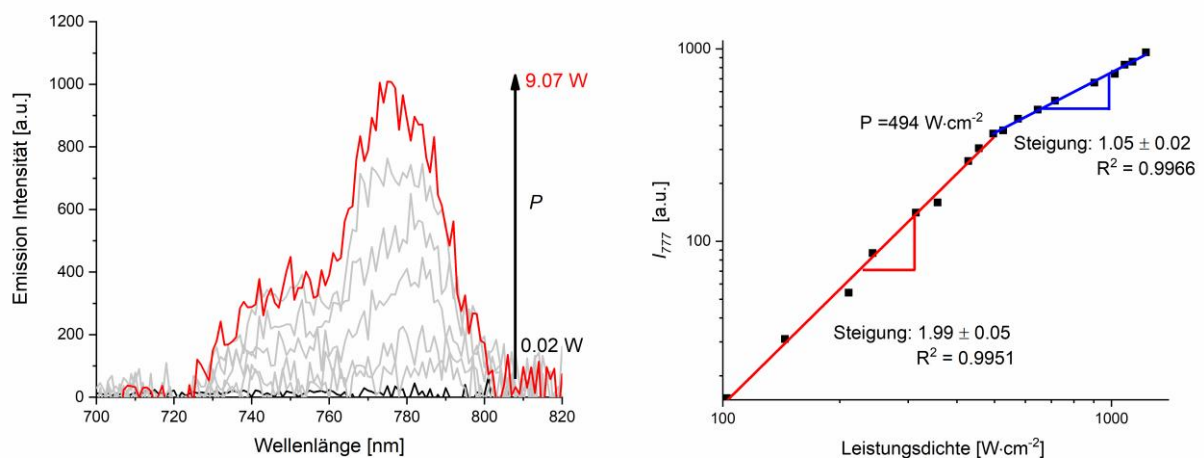


**Abb. 57:** Links: Abhängigkeit der UC-Lumineszenz ( ${}^2E/{}^2T_1 \rightarrow {}^4A$ ) von der Anregungsleistungsdichte  $P$  von **3-Yb** ( $T = 298 \text{ K}$ , Festkörper, Luft) mit  $\text{Yb}^{3+}$ -Anregung bei  $\lambda_{\text{ex}} = 976 \text{ nm}$ . Rechts: Log-log-Plot der Intensität der  ${}^2E$ -Upconversion ( $\lambda_{\text{em}} = 777 \text{ nm}$ ) gegen die Anregungsleistungsdichte von **3-Yb** ( $\lambda_{\text{ex}} = 976 \text{ nm}$ ,  $T = 298 \text{ K}$ , Festkörper). Die Steigungswerte wurden durch lineare Anpassung für niedrige (rot) und hohe (blau) Leistungsdichte-Bereiche bestimmt.

Schließlich wurden UC-Messungen von **3-Yb** und **3-Lu** bei Raumtemperatur und unter Umgebungsatmosphäre durchgeführt. Laseranregung der  $\text{Yb}^{3+}$ -Sensibilisatoren bei  $\lambda_{\text{ex}} = 976 \text{ nm}$  produziert in **3-Yb** intensive  ${}^2E/{}^2T_1$ -UC-Emission des  $\text{Cr}^{3+}$ -Aktivators mit einem Maximum bei etwa  $\lambda_{\text{em}} = 780 \text{ nm}$  (Abb. 57), während wie erwartet für **3-Lu** keine UC-Emission nachgewiesen werden konnte. Dabei reichte für **3-Yb** eine Anregungsleistungsdichte von  $P \approx 67 \text{ W}\cdot\text{cm}^{-2}$  aus, um UC zu beobachten, was einen angemessen niedriger Grenzwert für UC durch den häufig nicht sehr effizienten CSU-Mechanismus darstellt.<sup>[24]</sup> Der in Abb. 57 rechts gezeigte Graph beschreibt die Abhängigkeit der UC-Emissionsintensität von Anregungsleistungsdichte  $P$ . Das Diagramm ist in zwei wesentliche Bereiche unterteilt. Im Bereich unterhalb von

$P \approx 494 \text{ W}\cdot\text{cm}^{-2}$ , also bei niedrigen Anregungsleistungsdichten, ist die Zahl der angeregten  $\text{Yb}^{3+}$ -Kationen gering und die UC hängt, einem Zweiphotonen-Prozess folgend, quadratisch von  $P$  ab (log-log Plot: Steigung oder photonische Ordnung von 1.99). Bei hohen Anregungsleistungsdichten oberhalb von  $P \approx 494 \text{ W}\cdot\text{cm}^{-2}$ , kommt es nach und nach zu einer Sättigung der  $\text{Yb}^{3+}$ -Sensibilisatoren, weshalb die photonische Ordnung Werte kleiner 2 annimmt, bevor sie sich schließlich dem Grenzwert 1 annähert. Dies ist charakteristisch für einen Einphotonen-Prozess (Steigung oder photonische Ordnung von 1.05).<sup>[156]</sup>

Die sorgfältige Überarbeitung des Designs früherer Downshifting- $\text{Cr}^{3+}/\text{Yb}^{3+}$ -Systeme führte zur Entwicklung des neuen ionischen Festkörpers **3-Yb**, welcher NIR→NIR-Upconversion bei Raumtemperatur und in der Gegenwart von Sauerstoff bzw. Wasser zeigt. Dies erweitert die kleine Zahl von UC-Beispielen an molekularen Festkörpern um ein neues Sensibilisator/Aktivator-Metallkomplekxpaar.

## Upconversion

## Near-IR to Near-IR Upconversion Luminescence in Molecular Chromium Ytterbium Salts

Jens Kalmbach<sup>+</sup>, Cui Wang<sup>+</sup>, Yi You, Christoph Förster, Hartmut Schubert, Katja Heinze,<sup>\*</sup> Ute Resch-Genger,<sup>\*</sup> and Michael Seitz<sup>\*</sup>

**Abstract:** Upconversion photoluminescence in hetero-oligonuclear metal complex architectures featuring organic ligands is an interesting but still rarely observed phenomenon, despite its great potential from a basic research and application perspective. In this context, a new photonic material consisting of molecular chromium(III) and ytterbium(III) complex ions was developed that exhibits excitation-power density-dependent cooperative sensitization of the chromium-centered  $^2E/{}^2T_1$  phosphorescence at approximately 775 nm after excitation of the ytterbium band  ${}^2F_{7/2} \rightarrow {}^2F_{5/2}$  at approximately 980 nm in the solid state at ambient temperature. The upconversion process is insensitive to atmospheric oxygen and can be observed in the presence of water molecules in the crystal lattice.

## Introduction

Metal-based upconversion (UC) transforming low-energy photons into an anti-Stokes-shifted luminescence is a very attractive non-linear process for fundamental studies as well as for future applications. Examples are solid inorganic host matrices with low-phonon energies doped with transition metal or lanthanoid cations, either as bulk materials<sup>[1]</sup> or, more recently, as nanocrystalline systems.<sup>[2]</sup> UC was long considered to be impossible in discrete metal-organic com-

How to cite: *Angew. Chem. Int. Ed.* **2020**, *59*, 18804–18808  
 International Edition: doi.org/10.1002/anie.202007200  
 German Edition: doi.org/10.1002/ange.202007200

plexes<sup>[3]</sup> due to the pronounced non-radiative deactivation of the excited metal states by high-frequency oscillators present in organic ligands like -OH, -NH or -CH groups.<sup>[4]</sup> In the past few years, however, many advances have been achieved in implementing metal-based UC in molecular complex species, some even at ambient temperature and in solution.<sup>[5]</sup> This includes metal chelate-organic chromophore combinations,<sup>[6]</sup> mononuclear metal complexes,<sup>[7]</sup> and hetero-oligometallic sensitizer-activator architectures.<sup>[8,9]</sup> The latter have shown to hold the greatest potential for efficient UC, especially for energy transfer upconversion (ETU) but also for cooperatively sensitized upconversion (CSU). For both UC schemes, sensitizer metal centers (S) with appropriate energy levels and sufficiently long luminescence lifetime are necessary to successfully populate an activator (A) excited state with approximately twice the energy of the excited sensitizer state at relatively low excitation power densities. Among the best sensitizing metal centers are Yb<sup>3+</sup> ( ${}^2F_{5/2}$  at  $\approx 10250\text{ cm}^{-1}$ ,  $\approx 976\text{ nm}$ ) and Cr<sup>3+</sup> (octahedral geometry:  ${}^2E/{}^2T_1$  at  $\approx 15000\text{--}12400\text{ cm}^{-1}$ ,  $\approx 665\text{--}805\text{ nm}$  depending on the ligand field). This has been demonstrated for several emissive UC activators in molecular systems, for example the lanthanoids Er<sup>3+</sup> and Tb<sup>3+</sup>.<sup>[8,9]</sup> The earth-abundant metal Cr<sup>3+</sup> has also gained renewed interest as downshifting luminophore/sensitizer,<sup>[10]</sup> on one hand because of the recently developed class of “molecular ruby” emitters which show very high luminescence quantum yields of the  ${}^2E/{}^2T_1$  phosphorescence of up to 30% at room temperature in solution in the absence of oxygen,<sup>[11]</sup> and on the other hand as successful antenna moieties for the downshifting sensitization of near-IR lanthanoid luminescence.<sup>[12,13]</sup>

Two decades ago, Güdel et al. reported an interesting UC Scheme for the generation of  ${}^2E$  UC emission for solid state hosts such as Y<sub>3</sub>Ga<sub>5</sub>O<sub>12</sub> co-doped with Yb<sup>3+</sup> as sensitizer and Cr<sup>3+</sup> as activator.<sup>[14]</sup> These compounds operate via CSU where two excited Yb<sup>3+</sup> cooperatively transfer the energy from their  ${}^2F_{5/2}$  states to an excited quartet state of Cr<sup>3+</sup> ( ${}^4T_2/{}^4T_1$ ) which subsequently populates the emissive  ${}^2E$  state by intersystem crossing (ISC) (Figure 1). This Scheme is particularly interesting because both, excitation and UC emission, are in the near-IR spectral window, increasingly used for bioimaging.<sup>[15]</sup> In molecular systems, near-IR to near-IR upconversion is unknown and the few systems utilizing the couple Yb/Cr reported so far exhibited UC only at very low temperatures (usually below 100 K) in extended solid inorganic matrices. In the past, however, reports on efficient downshifting energy transfer (EnT)  ${}^2E(\text{Cr}^{3+}) \rightarrow {}^2F_{5/2}(\text{Yb}^{3+})$ ,<sup>[12,13]</sup> that led to deactivation of the UC-emissive  ${}^2E$  state, made the successful

[\*] J. Kalmbach,<sup>[†]</sup> Dr. H. Schubert, Prof. Dr. M. Seitz  
 Institute of Inorganic Chemistry  
 University of Tübingen  
 Auf der Morgenstelle 18, 72076 Tübingen (Germany)  
 E-mail: michael.seitz@uni-tuebingen.de

C. Wang,<sup>[†]</sup> Dr. Y. You, Dr. U. Resch-Genger  
 Division Biophotonics  
 Federal Institute for Materials Research and Testing (BAM)  
 Richard-Willstätter-Strasse 11, 12489 Berlin (Germany)  
 E-mail: ute.resch@bam.de

C. Wang<sup>[†]</sup>  
 Institute of Chemistry and Biochemistry, Freie Universität Berlin  
 Arnimallee 22, 14195 Berlin (Germany)

Dr. C. Förster, Prof. Dr. K. Heinze  
 Department of Chemistry, Johannes Gutenberg University of Mainz  
 Duesbergweg 10–14, 55128 Mainz (Germany)  
 E-mail: katja.heinze@uni-mainz.de

[†] These authors contributed equally to this work.

Supporting information and the ORCID identification number(s) for the author(s) of this article can be found under:  
<https://doi.org/10.1002/anie.202007200>.

© 2020 The Authors. Published by Wiley-VCH GmbH. This is an open access article under the terms of the Creative Commons Attribution License, which permits use, distribution and reproduction in any medium, provided the original work is properly cited.



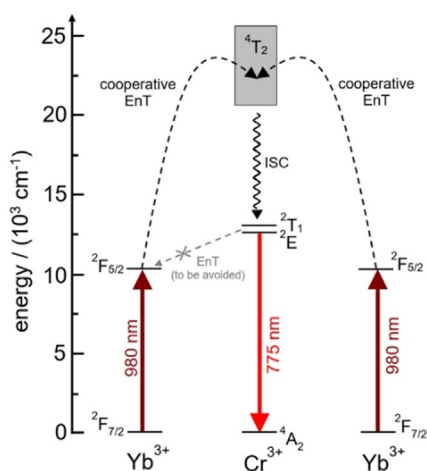


**Figure 1.** Schematic partial energy-level diagram of the energy levels of  $\text{Yb}^{3+}$  and  $\text{Cr}^{3+}$  (energies given for  $\text{mer}[\text{Cr}(\text{ddpd})_2]^{3+}$ ) relevant for cooperatively sensitized UC involving two  $\text{Yb}^{3+}$  centers absorbing 980 nm light and sensitizing the emission of the  $\text{Cr}^{3+}$  activator.

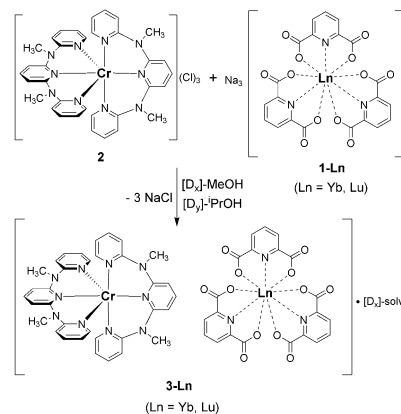
implementation of this attractive UC Scheme unlikely. Especially  $\text{Cr}^{3+}/\text{Yb}^{3+}$ -architectures with highly efficient Dexter EnT (here total angular momentum allowed for  $\Delta J = 1$ )<sup>[16]</sup> in hexacyanidochromate- and oxalato-bridged coordination compounds<sup>[13a-c]</sup> seemed unsuitable for this purpose. On the other hand, dipole-dipole EnT (Förster)  $\text{Cr}^{3+} \rightarrow \text{Yb}^{3+}$  in oligometallic molecular systems also showed unfavorably high EnT efficiencies of up to ca. 50% despite being forbidden by the total angular momentum selection rule ( $\Delta J = 2, 4, 6$ ).<sup>[13a, 16]</sup>

With these challenges of the  $\text{Cr}^{3+}/\text{Yb}^{3+}$  pair in mind, we revisited the design concept for molecular Yb-Cr-UC. This led to a new photonic material composed of easily accessible  $\text{Cr}^{3+}$  and  $\text{Yb}^{3+}$  complex ions which shows  ${}^2\text{E}/{}^2\text{T}_1$  UC at room temperature already at relatively low excitation power densities.

## Results and Discussion

The main idea was to avoid Dexter EnT from  ${}^2\text{E}(\text{Cr}^{3+})$  to  ${}^2\text{F}_{5/2}(\text{Yb}^{3+})$  and opt for a system, where  $\text{Cr}^{3+} \rightarrow \text{Yb}^{3+}$  EnT was only possible by a less efficient Förster mechanism. Therefore, we utilized spatially separated metal centers in discrete coordination environments. For the realization of this design, we chose the complex  $\text{mer}[\text{Cr}(\text{ddpd})_2]^{3+}$  (ddpd = *N,N'*-dimethyl-*N,N'*-dipyridine-2-ylpyridine-2,6-diamine). This  $\text{Cr}^{3+}$  complex shows a very high phosphorescence quantum yield  $\Phi$  of up to 30% in argon-saturated  $\text{CD}_3\text{CN}$  solution at room temperature (298 K) and even remains quite emissive in air-saturated water with  $\Phi = 2.1\%$ .<sup>[11c,d]</sup> Despite earlier reports on the complex  $[\text{Yb}(\text{dpa})_3]^{3-}$  (dpa = 2,6-pyridine-dicarboxylate) and the only moderately long lifetime of its excited  ${}^2\text{F}_{5/2}$  energy level in the solid state (solid **1-Yb** at 295 K:  $\tau = 2.9 \mu\text{s}$ ),<sup>[3, 13c]</sup> we chose this anion as counterpart for the  $\text{Cr}^{3+}$  complex because of its straightforward synthetic accessibility and its good match with  $[\text{Cr}(\text{ddpd})_2]^{3+}$  in terms of comparable size and opposite charge. The latter parameters were ex-

pected to facilitate the crystallization of the desired Cr/Yb ionic solid, where only intermolecular  $\pi$ - $\pi$ -stacking interactions between the different ions occurs. The synthesis of our novel photonic material **3-Yb** was achieved by mixing  $\text{Na}_3[\text{Yb}(\text{dpa})_3] \cdot 6\text{H}_2\text{O}$  (**1-Yb**)<sup>[17]</sup> with  $[\text{Cr}(\text{ddpd})_2]\text{Cl}_3$  (**2**, see SI for details) in an alcoholic solution (Scheme 1). We also prepared



**Scheme 1.** Synthesis of the chromium-lanthanoid salts **3-Ln**.

the reference compound **3-Lu** as a structural analogue of **3-Yb**, thereby utilizing the photoinactive nature of  $\text{Lu}^{3+}$  with its  $4f^{14}$  electronic configuration. **3-Yb** and **3-Lu** were obtained as bright yellow solids in good to excellent yields (57–88%). Both, complex anion and cation,<sup>[18]</sup> are chiral but were used as racemates. Elemental analysis of both compounds revealed large amounts of lattice water and methanol in the material (see SI for details). To suppress potentially severe non-radiative deactivation of both the  ${}^2\text{E}/{}^2\text{T}_1$  and  ${}^2\text{F}_{5/2}$  excited states via multiphonon relaxation by C-H and O-H oscillators,<sup>[4]</sup> the syntheses were also repeated with  $[\text{D}_4]\text{-MeOH}/[\text{D}_8]\text{-iPrOH}$ . The X-ray structural analysis of single crystals of **3-Ln** grown from MeOH/*i*PrOH mixtures confirmed that all salts are isostructural, racemic mixtures of the complex ions (Figure 2, see also Table S1 and Figure S1 in the SI).<sup>[19]</sup>

As intended, in the solid material, downshifting EnT in **3-Yb** should only be possible by the forbidden Förster mechanism. In our crystal, each  $\text{Cr}^{3+}$  activator is surrounded

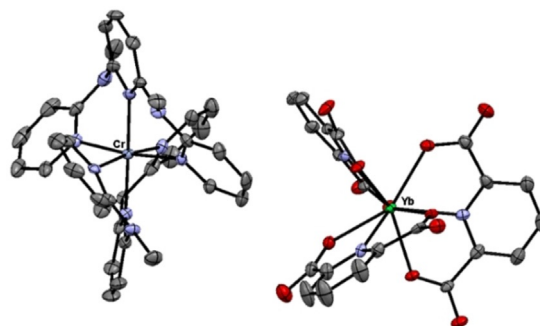


**Figure 2.** Thermal ellipsoid plot of the asymmetric unit in **3-Yb** (Ortep 3 for Windows,<sup>[20]</sup> 50% probability level). Lattice solvent molecules and hydrogen atoms are omitted for clarity.



by five  $\text{Yb}^{3+}$  sensitizers as nearest neighbors with a distance distribution of  $8.75 \text{ \AA} < r_{\text{Cr-Yb}} < 9.07 \text{ \AA}$  (Figure S2 in the SI). Taking into account the distance relationship for  $\text{S} \rightarrow \text{A}$  EnT ( $k_{\text{EnT}} \propto r^{-6}$ ) and assuming similar contributions from all other parameters (e.g. orientation of the chromophores, dipole moments etc.), similar energy transfer rates to the central  $\text{Cr}^{3+}$  activator were expected for the five nearest sensitizers that should hence only vary by a factor of up to  $(8.75/9.07)^{-6} = 1.24$ . Selective excitation of **3-Ln** at  $\lambda_{\text{exc}} = 435 \text{ nm}$  into the  ${}^4\text{A}_2 \rightarrow {}^4\text{T}_2$  band<sup>[11c,d]</sup> of  $[\text{Cr}(\text{ddpd})_2]^{3+}$  produces the expected chromium phosphorescence  ${}^2\text{E}/{}^2\text{T}_1$  with an emission maximum around 780 nm. For **3-Yb**, excitation at 435 nm leads not only to the  $\text{Cr}^{3+}$  emission (Figure 3) but also to the appearance of a  $\text{Yb}^{3+}$  luminescence ( ${}^2\text{F}_{5/2} \rightarrow {}^2\text{F}_{7/2}$ ) at around 1000 nm (Figure 3). Since the chromium-free precursor **1-Yb** is not emissive upon excitation at 435 nm (Figure S3), this clearly indicated undesired  $\text{Cr} \rightarrow \text{Yb}$  EnT in **3-Yb**. Further evidence for a downshifting EnT between  $\text{Cr}^{3+}$  and  $\text{Yb}^{3+}$  was obtained by time-resolved luminescence measurements under the same conditions (Table 1).

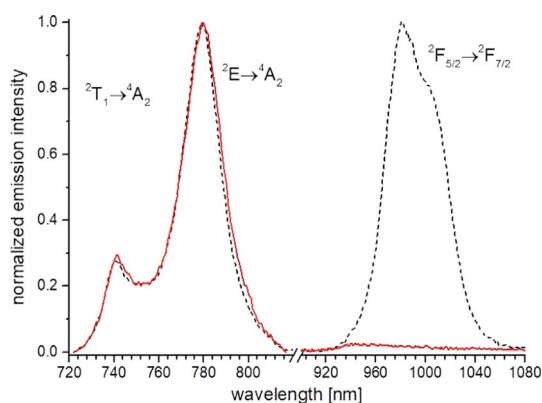


**Figure 3.** Normalized steady-state emission spectra ( $\lambda_{\text{exc}} = 435 \text{ nm}$ ) of **3-Yb** (dashed black line) and **3-Lu** (solid red line) in the solid state at  $T = 298 \text{ K}$  in air. Excitation was at 435 nm. The relative intensities of the emission spectra of the different  $\text{Cr}^{3+}$  and  $\text{Yb}^{3+}$  emission bands were not comparable.

**Table 1:** Luminescence lifetimes  $\tau$  and quantum yields  $\Phi$  of compounds **3-Ln** ( $\text{Ln} = \text{Yb}, \text{Lu}$ ) in the solid state at 298 K for excitation at 435 nm.

Species	$\tau_{2\text{E} \rightarrow 4\text{A}_2}^{\text{air}}$ (783 nm) [ $\mu\text{s}$ ] <sup>[a]</sup>	$\tau_{2\text{E} \rightarrow 4\text{A}_2}^{\text{argon}}$ (783 nm) [ $\mu\text{s}$ ] <sup>[a]</sup>	$\tau_{2\text{F}_{5/2} \rightarrow 2\text{F}_{7/2}}^{\text{air}}$ (980 nm) [ $\mu\text{s}$ ] <sup>[a]</sup>	$\Phi_{2\text{E} \rightarrow 4\text{A}_2}^{\text{air}}$ [%] <sup>[b]</sup>
<b>3-Yb</b>	390 (100%)	380 (100%)	9 (rise, 2%) 369 (decay, 102%)	5.9
<b>3-Yb</b> (deut.)	160 (15%) 390 (85%)	180 (12%) 370 (88%)	12 (rise, 3%) 373 (decay, 103%)	5.8
<b>3-Lu</b> (deut.)	280 (11%) 660 (89%)	320 (12%) 720 (88%)	n.a.	6.8

[a] Lifetimes are fitted mono- or biexponentially, percentages in parentheses give relative amplitudes of the components, estimated uncertainty of  $\tau \pm 5\%$ . [b] Measured using an integrating sphere setup Quantaaurus-QY C11347-11 (see Supporting Information for details), estimated uncertainty  $\pm 5\%$ .

The decay curve of the  $\text{Cr}^{3+}$ -centered  ${}^2\text{E}/{}^2\text{T}_1$  emission of **3-Yb** exhibited monoexponential decay kinetics with a long lifetime  $\tau = 390 \mu\text{s}$ . The decay profile of the  $\text{Yb}^{3+}$  emission revealed biexponential kinetics with a long luminescence lifetime of 369  $\mu\text{s}$ , uncharacteristic for molecular  $\text{Yb}^{3+}$  species<sup>[4]</sup> which normally show luminescence lifetimes in the low  $\mu\text{s}$ -range. The lifetime of 369  $\mu\text{s}$  closely matches the  ${}^2\text{E}/{}^2\text{T}_1$  lifetime of the  $\text{Cr}^{3+}$  emission of 390  $\mu\text{s}$ . In addition, a noticeable rise time component ( $\tau = 9 \mu\text{s}$ ) was present. These observations are all typical for EnT from the long-lived  ${}^2\text{E}$  state to  $\text{Yb}^{3+}$ .<sup>[13d-f]</sup> As detailed before, this EnT could reduce the efficiency of the  ${}^2\text{E}$  upconversion luminescence by non-radiatively depopulating this state. To quantify the potential loss in efficiency, we determined the quantum yield of the  ${}^2\text{E}/{}^2\text{T}_1$  phosphorescence of **3-Yb** and **3-Lu** upon excitation at 435 nm (Table 1). These measurements yielded  $\Phi$  values of 6.8% and 5.8% for deuterated **3-Lu** and **3-Yb**, respectively, and hence revealed only a moderate decrease of 15%  ${}^2\text{E}$  quantum yield for **3-Yb** relative to **3-Lu**. This is favorably low compared to the loss due to Förster EnT reported for analogous downshifting systems in the literature (ca. 20–50%),<sup>[13d-f]</sup> especially when considering that in our case each  $\text{Cr}^{3+}$  has considerably more next  $\text{Yb}^{3+}$  neighbors (here 5, previously 1 at similar distances  $r_{\text{Cr-Yb}}$ ) as EnT acceptors. Surprisingly, neither the crystallization of **3-Yb** from deuterated solvents nor the presence of oxygen significantly affected the luminescence decay kinetics of  $\text{Cr}^{3+}$  in **3-Yb** and **3-Lu** (Table 1). The decay profile of the  $\text{Cr}^{3+}$   ${}^2\text{E}/{}^2\text{T}_1$  emission in deuterated **3-Lu** in air also showed biexponential decay kinetics and revealed considerably longer lifetimes than observed for **3-Yb** (Table 1). Deuterated **3-Lu**:  $\tau_1 = 660 \mu\text{s}$ , 89% and  $\tau_2 = 280 \mu\text{s}$ , 11%.

Finally, UC measurements of **3-Yb** and **3-Lu** were performed at 298 K under ambient atmosphere. Expectedly, **3-Lu** did not yield any UC emission upon excitation at 976 nm. In contrast, excitation of the  $\text{Yb}^{3+}$  sensitizers in **3-Yb** produced intense  ${}^2\text{E}/{}^2\text{T}_1$  UC emission of the activator  $\text{Cr}^{3+}$  with a maximum around  $\lambda_{\text{em}} = 780 \text{ nm}$  (Figure 4). Time-resolved studies confirmed successful UC in **3-Yb** and deuterated **3-Yb**, while no luminescence signal was observed for **3-Lu** (Figure S9). For **3-Yb**, excitation power densities ( $P$ )

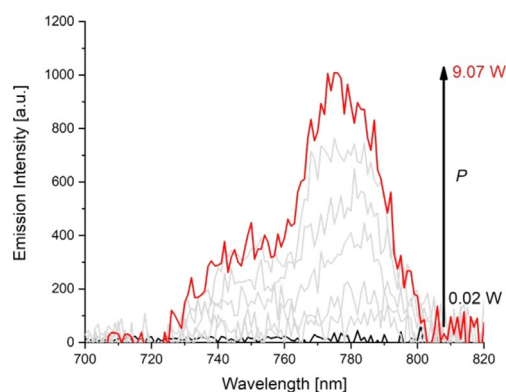


**Figure 4.** Excitation power-density ( $P$ ) dependence of the UC luminescence ( ${}^2\text{E}/{}^2\text{T}_1 \rightarrow {}^4\text{A}$ ) of **3-Yb** (298 K, solid, air) for  $\text{Yb}^{3+}$  excitation at  $\lambda_{\text{ex}} = 976 \text{ nm}$ .

as low as  $P \approx 67 \text{ W cm}^{-2}$  were sufficient for the observation of UC which is a reasonably low threshold for UC by a normally not very efficient CSU mechanism.<sup>[5]</sup> The  $P$  dependence of the UC emission intensity depicted in Figure 5 shows two distinct regions. Below  $P \approx 494 \text{ W cm}^{-2}$ , the number of excited  $\text{Yb}^{3+}$  is low and UC depends quadratically on  $P$  indicating a biphotonic process (log-log plot: slope or photonic order of 1.99). At higher  $P$ , sensitizer saturation slowly occurs as indicated by a photonic order below 2 which eventually approaches 1 as is typical for a one-photon process (slope or photonic order of 1.05).<sup>[21]</sup>

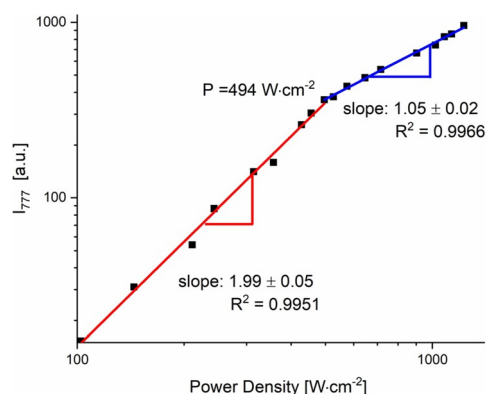


**Figure 5.** Log–log plot of the upconversion  ${}^2\text{E}$  luminescence ( $\lambda_{\text{em}} = 777 \text{ nm}$ ) versus the incident power density in **3-Yb** ( $\lambda_{\text{ex}} = 976 \text{ nm}$ , 298 K, solid)—gradients obtained by linear fitting for the low (red) and high (blue) power density regimes.

## Conclusion

In conclusion, by carefully revisiting earlier downshifting  $\text{Cr}^{3+}/\text{Yb}^{3+}$  systems, we realized a novel near-IR to near-IR upconversion (UC) material by simply combining  $\text{Cr}^{3+}$  and  $\text{Yb}^{3+}$  complexes in an ionic solid. This expands the small number of molecular UC examples by a new pair of sensitizer/activator metal complexes. Importantly, UC can be realized with synthetically easily accessible non-deuterated/non-halogenated building blocks at room temperature in the presence of oxygen and water molecules. This proof-of-concept study will pave the way to a new class of photonic materials and enable new possibilities for the field of molecular UC.

## Acknowledgements

Financial support from the German Research Foundation (DFG, Priority Program SPP 2102 “Light-controlled reactivity of metal complexes”, grant no. SE 1448/8-1 and HE 2778/10-1) is gratefully acknowledged. URG and CW gratefully acknowledge support from DFG (grant no. RE 1203/23-1). The authors thank Taro Lieberth (Johannes Gutenberg University of Mainz) for help with the synthesis of **2**. Open access funding enabled and organized by Projekt DEAL.

## Conflict of interest

The authors declare no conflict of interest.

**Keywords:** chromium · energy transfer · luminescence · upconversion · ytterbium

- [1] a) S. Ye, E.-H. Song, Q.-Y. Zhang, *Adv. Sci.* **2016**, *3*, 1600302; b) J. F. Suyver, A. Aebischer, D. Biner, P. Gerner, J. Grimm, S. Heer, K. W. Krämer, C. Reinhard, H. U. Güdel, *Opt. Mater.* **2005**, *27*, 1111; c) F. Auzel, *Chem. Rev.* **2004**, *104*, 139; d) D. R. Gamelin, H. U. Güdel, *Acc. Chem. Res.* **2000**, *33*, 235.
- [2] a) F. Wang, X. Liu, *Chem. Soc. Rev.* **2009**, *38*, 976; b) B. Zhou, B. Shi, D. Jin, X. Liu, *Nat. Nanotechnol.* **2015**, *10*, 924.
- [3] C. Reinhard, H. U. Güdel, *Inorg. Chem.* **2002**, *41*, 1048.
- [4] E. Kreidt, C. Kruck, M. Seitz, in *Handbook on the Physics and Chemistry of Rare Earths, Vol. 53* (Eds.: J.-C. G. Bünzli, V. K. Pecharsky), Elsevier, Amsterdam, **2018**, pp. 35–79.
- [5] a) B. Golesorkhi, H. Nozary, A. Fürstenberg, C. Piguet, *Mater. Horiz.* **2020**, *7*, 1279; b) A. M. Nonat, L. J. Charbonnière, *Coord. Chem. Rev.* **2020**, *409*, 213192; c) L. J. Charbonnière, *Dalton Trans.* **2018**, *47*, 8566; d) L. Aboshyan-Sorgho, M. Cantuela, S. Petoud, A. Hauser, C. Piguet, *Coord. Chem. Rev.* **2012**, *256*, 1644.
- [6] Selected examples: a) N. Kiseleva, P. Nazari, C. Dee, D. Busko, B. S. Richards, M. Seitz, I. A. Howard, A. Turshatov, *J. Phys. Chem. Lett.* **2020**, *11*, 2477; b) I. Hyppänen, S. Lahtinen, T. Äärilä, J. Mäkelä, J. Kankare, T. Soukka, *ACS Photonics* **2014**, *1*, 394.
- [7] Selected examples: a) B. Golesorkhi, A. Fürstenberg, H. Nozary, C. Piguet, *Chem. Sci.* **2019**, *10*, 6876; b) T. J. Sørensen, O. A. Blackburn, M. Tropiano, S. Faulkner, *Chem. Phys. Lett.* **2012**, *541*, 16; c) O. A. Blackburn, M. Tropiano, T. J. Sørensen, J. Thom, A. Beeby, L. M. Bushby, D. Parker, L. S. Natrajan, S. Faulkner, *Phys. Chem. Chem. Phys.* **2012**, *14*, 13378; d) X. Xiao, J. P. Haushalter, G. W. Faris, *Opt. Lett.* **2005**, *30*, 1674; e) B. Golesorkhi, H. Nozary, L. Guenee, A. Fürstenberg, C. Piguet, *Angew. Chem. Int. Ed.* **2018**, *57*, 15172; *Angew. Chem.* **2018**, *130*, 15392.
- [8] Selected examples: a) A. Nonat, S. Bahamyirou, A. Lecointre, F. Przybilla, Y. Mely, C. Platas-Iglesias, F. Camerel, O. Jeannin, L. J. Charbonnière, *J. Am. Chem. Soc.* **2019**, *141*, 1568; b) T. V. Balashova, A. P. Pushkarev, A. N. Yablonskiy, B. A. Andreev, I. D. Grishin, R. V. Rummyantsev, G. K. Fukin, M. N. Bochkarev, *J. Lumin.* **2017**, *192*, 208; c) H. Ye, V. Bogdanov, S. Liu, S. Vajandar, T. Osipowicz, I. Hernandez, Q. Xiong, *J. Phys. Chem. Lett.* **2017**, *8*, 5695; d) N. Souri, P. Tian, C. Platas-Iglesias, S. Chafaa, K.-L. Wong, A. Nonat, L. J. Charbonnière, *J. Am. Chem. Soc.* **2017**, *139*, 1456; e) A. Nonat, C. F. Chan, T. Liu, C. Platas-Iglesias, K.-L. Wong, L. J. Charbonnière, *Nat. Commun.* **2016**, *7*, 11978; f) I. Hernández, N. Pathumakanthar, P. B. Wyatt, W. P. Gillin, *Adv. Mater.* **2010**, *22*, 5356.
- [9] a) D. Zare, Y. Suffren, H. Nozary, A. Hauser, C. Piguet, *Angew. Chem. Int. Ed.* **2017**, *56*, 14612; *Angew. Chem.* **2017**, *129*, 14804; b) D. Zare, Y. Suffren, L. Guenee, S. V. Eliseeva, H. Nozary, L. Aboshyan-Sorgho, S. Petoud, A. Hauser, C. Piguet, *Dalton Trans.* **2015**, *44*, 2529; c) Y. Suffren, D. Zare, S. V. Eliseeva, L. Guénéee, H. Nozary, T. Lathion, L. Abogoshyan-Sorgho, S. Petoud, A. Hauser, C. Piguet, *J. Phys. Chem. C* **2013**, *117*, 26957; d) L. Aboshyan-Sorgho, C. Besnard, P. Pattison, K. R. Kitilstved, A. Aebischer, J.-C. G. Bünzli, A. Hauser, C. Piguet, *Angew. Chem. Int. Ed.* **2011**, *50*, 4108; *Angew. Chem.* **2011**, *123*, 4194.
- [10] a) C. Förster, K. Heinze, *Chem. Soc. Rev.* **2020**, *49*, 1057; b) O. S. Wenger, *J. Am. Chem. Soc.* **2018**, *140*, 13522; c) S. Otto, M. Dorn, C. Förster, M. Bauer, M. Seitz, K. Heinze, *Coord. Chem. Rev.*

- 2018, 359, 102; d) P. S. Wagenknecht, P. C. Ford, *Coord. Chem. Rev.* **2011**, 255, 591.
- [11] Selected examples: a) S. Treiling, C. Wang, C. Förster, F. Reichenauer, J. Kalmbach, P. Boden, J. P. Harris, L. Carrella, E. Rentschler, U. Resch-Genger, C. Reber, M. Seitz, M. Gerhards, K. Heinze, *Angew. Chem. Int. Ed.* **2019**, 58, 18075; *Angew. Chem.* **2019**, 131, 18243; b) J. R. Jiménez, B. Doistau, C. M. Cruz, C. Besnard, J. M. Cuerva, A. G. Campaña, C. Piguet, *J. Am. Chem. Soc.* **2019**, 141, 13244; c) C. Wang, S. Otto, M. Dorn, E. Kreidt, J. Lebon, L. Sršan, P. Di Martino-Fumo, M. Gerhards, U. Resch-Genger, M. Seitz, K. Heinze, *Angew. Chem. Int. Ed.* **2018**, 57, 1112; *Angew. Chem.* **2018**, 130, 1125; d) S. Otto, M. Grabolle, C. Förster, C. Kreitner, U. Resch-Genger, K. Heinze, *Angew. Chem. Int. Ed.* **2015**, 54, 11572; *Angew. Chem.* **2015**, 127, 11735.
- [12] Reviews: a) S. Chorazy, M. Wyczesany, B. Sieklucka, *Molecules* **2017**, 22, 1902; b) L.-J. Xu, G.-T. Xu, Z.-N. Chen, *Coord. Chem. Rev.* **2014**, 273–274, 47; c) F.-F. Chen, Z.-Q. Chen, Z.-Q. Bian, C.-H. Huang, *Coord. Chem. Rev.* **2010**, 254, 991; d) M. D. Ward, *Coord. Chem. Rev.* **2007**, 251, 1663.
- [13] Selected examples: a) T. Lazarides, G. M. Davies, H. Adams, C. Sabatini, F. Barigelletti, A. Barbieri, S. J. A. Pope, S. Faulkner, M. D. Ward, *Photochem. Photobiol. Sci.* **2007**, 6, 1152; b) T. Sanada, T. Suzuki, T. Yoshida, S. Kaizaki, *Inorg. Chem.* **1998**, 37, 4712; c) P. A. Brayshaw, J.-C. G. Bünzli, P. Froidevaux, J. M. Harrowfield, Y. Kim, A. N. Sobolev, *Inorg. Chem.* **1995**, 34, 2068; d) D. Imbert, M. Cantuel, J.-C. G. Bünzli, G. Bernardinelli, C. Piguet, *J. Am. Chem. Soc.* **2003**, 125, 15698; e) L. Aboshyan-Sorgho, H. Nozari, A. Aebischer, J.-C. G. Bünzli, P.-Y. Morgantini, K. R. Kittilstved, A. Hauser, S. V. Eliseeva, S. Petoud, C. Piguet, *J. Am. Chem. Soc.* **2012**, 134, 12675; f) S. Torelli, D. Imbert, M. Cantuel, G. Bernardinelli, S. Delahaye, A. Hauser, J.-C. G. Bünzli, C. Piguet, *Chem. Eur. J.* **2005**, 11, 3228.
- [14] a) S. Heer, K. Petermann, H. U. Güdel, *J. Lumin.* **2003**, 102–103, 144; b) S. Heer, M. Wermuth, K. Krämer, H. U. Güdel, *Phys. Rev. B* **2002**, 65, 125112; c) S. Heer, M. Wermuth, K. Krämer, D. Ehrentraut, H. U. Güdel, *J. Lumin.* **2001**, 94–95, 337; d) S. Heer, M. Wermuth, K. Krämer, H. U. Güdel, *Chem. Phys. Lett.* **2001**, 334, 293; e) H. K. Dan, N. M. Ty, T. D. Tap, D.-N. Le, L. T. Vinh, D. Zhou, J. Qiu, *Opt. Mater.* **2020**, 100, 109662.
- [15] Y. Ning, M. Zhu, J.-L. Zhang, *Coord. Chem. Rev.* **2019**, 399, 213028.
- [16] G. F. de Sá, O. L. Malta, C. de Mello Donegá, A. M. Simas, R. L. Longo, P. A. Santa-Cruz, E. F. da Silva, Jr., *Coord. Chem. Rev.* **2000**, 196, 165.
- [17] a) G. Kervern, A. D'Aléo, L. Toupet, O. Maury, L. Emsley, G. Pintacuda, *Angew. Chem. Int. Ed.* **2009**, 48, 3082; *Angew. Chem.* **2009**, 121, 3128; b) A. Aebischer, F. Gumy, J.-C. G. Bünzli, *Phys. Chem. Chem. Phys.* **2009**, 11, 1346.
- [18] C. Dee, F. Zinna, W. R. Kitzmann, G. Pescitelli, K. Heinze, L. Di Bari, M. Seitz, *Chem. Commun.* **2019**, 55, 13078.
- [19] Deposition numbers 2003420, 2003421 contain the supplementary crystallographic data for this paper. These data are provided free of charge by the joint Cambridge Crystallographic Data Centre and Fachinformationszentrum Karlsruhe Access Structures service.
- [20] L. J. Farrugia, *J. Appl. Crystallogr.* **1997**, 30, 565.
- [21] a) M. Pollnau, D. R. Gamelin, S. R. Lüthi, H. U. Güdel, M. P. Hehlen, *Phys. Rev. B* **2000**, 61, 3337; b) V. Gray, K. Moth-Poulsen, B. Albinsson, M. Abrahamsson, *Coord. Chem. Rev.* **2018**, 362, 54; c) S. Gharaati, C. Wang, C. Förster, F. Weigert, U. Resch-Genger, K. Heinze, *Chem. Eur. J.* **2020**, 26, 1003; d) M. Kaiser, C. Würth, M. Kraft, I. Hyppänen, T. Soukka, U. Resch-Genger, *Nanoscale* **2017**, 9, 10051; e) C. Würth, M. Kaiser, S. Wilhelm, B. Grauel, T. Hirsch, U. Resch-Genger, *Nanoscale* **2017**, 9, 4283.

Manuscript received: May 18, 2020

Accepted manuscript online: June 17, 2020

Version of record online: August 18, 2020

## Supporting Information

### **Near-IR to Near-IR Upconversion Luminescence in Molecular Chromium Ytterbium Salts**

*Jens Kalmbach<sup>+</sup>, Cui Wang<sup>+</sup>, Yi You, Christoph Förster, Hartmut Schubert, Katja Heinze,<sup>\*</sup> Ute Resch-Genger,<sup>\*</sup> and Michael Seitz<sup>\*</sup>*

anie\_202007200\_sm\_miscellaneous\_information.pdf  
anie\_202007200\_sm\_cif.zip

## Supporting Information

### Table of Contents

1. Materials / Methods	S2
2. X-ray Single Crystal Structure Analysis	S4
3. Luminescence Measurements	S6
3.1 Instruments	S6
3.2 Steady-State and Time-Resolved Luminescence Measurements	S8
3.3 Upconversion Measurements	S11
4. References	S13

## 1. Materials / Methods

### General Information

Acetonitrile (HPLC grade) and methanol (HPLC grade) were purchased by commercial suppliers and used without further purification.  $\text{Na}_3[\text{Ln}(\text{dpa})_3] \cdot x \text{H}_2\text{O}$ <sup>[S1]</sup> (**1-Ln**, Ln = Yb, Lu, dpa = 2,6-dipicolinate) and ligand ddpd<sup>[S2]</sup> were synthesized in-house according to a literature procedure. Elemental analyses were performed by the Analytical Facility of the Institute of Inorganic Chemistry (University of Tübingen) using a Vario MICRO EL analyser. ESI mass spectrometry was performed on a Bruker Daltonics Esquire 6000 mass spectrometer by the central analytical facility of the Department of Chemistry (University of Tübingen).

### Syntheses

#### Synthesis of $[\text{Cr}(\text{ddpd})_2]\text{Cl}_3$ (**2**)

The ligand ddpd<sup>[S2]</sup> (500 mg, 1.72 mmol) was dissolved in methanol and the solution was deoxygenated with argon. Solid  $\text{CrCl}_2$  (105 mg, 0.85 mmol) was added under inert conditions and the resulting solution was stirred for 12 h giving a green solution. After opening the flask to ambient conditions, the solution turned yellow and some dark material precipitated. The dark precipitate was removed by filtration over celite. Gaseous hydrochloric acid was slowly bubbled into the solution for 15 min. The solvent was removed under reduced pressure and the yellow solid was dissolved in a minimum amount of acetonitrile. This solution was layered with diethylether. Over 12 h at  $-25^\circ\text{C}$ , a fine yellow solid precipitated. The product was collected by filtration and washed with diethylether. From the mother liquor, a further crop of material can be obtained by layering again with diethylether and storing at  $-25^\circ\text{C}$ . Larger crystals can be obtained by diffusion of diethylether into a concentrated acetonitrile solution.

MS (ESI, pos. mode):  $m/z$  (%) = 211.37 (100,  $[\text{Cr}(\text{ddpd})_2]^{3+}$ ), 291.12 (20,  $\{\text{ddpd}+\text{H}\}^+$ ), 334.57 (11,  $\{[\text{Cr}(\text{ddpd})_2]+\text{Cl}\}^{2+}$ ).

Optical properties in solution ( $\lambda_{\text{exc}} = 435 \text{ nm}$ ,  $\lambda_{\text{em}} = 775 \text{ nm}$ ):

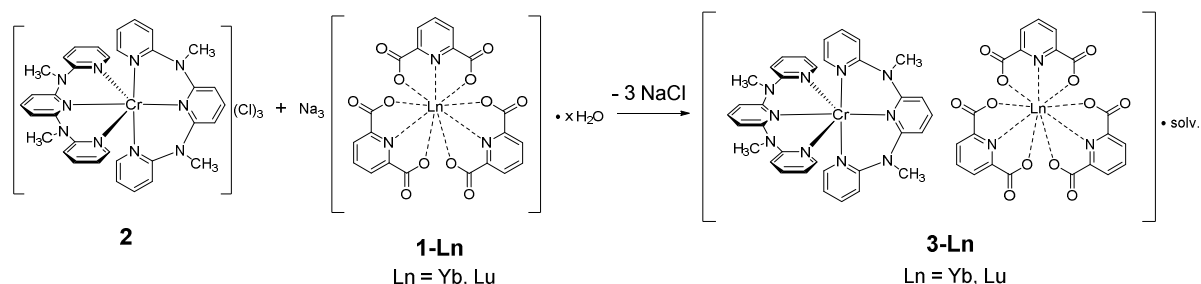
$\Phi(\text{H}_2\text{O}, \text{air}) = 1.93 \%$ ,  $\tau(\text{H}_2\text{O}, \text{air}) = 198 \mu\text{s}$

$\Phi(\text{H}_2\text{O}, \text{Ar}) = 8.30 \%$ ,  $\tau(\text{H}_2\text{O}, \text{Ar}) = 793 \mu\text{s}$

$\Phi(\text{CH}_3\text{CN}, \text{air}) = 0.50 \%$ ,  $\tau(\text{CH}_3\text{CN}, \text{air}) = 21 \mu\text{s}$

$\Phi(\text{CH}_3\text{CN}, \text{Ar}) = 6.85 \%$ ,  $\tau(\text{CH}_3\text{CN}, \text{Ar}) = 535 \mu\text{s}$

### 3-Ln (Ln = Yb, Lu)



General procedure:

In a 10 ml screw cap vial,  $\text{Na}_3[\text{Ln}(\text{dpa})_3] \cdot x \text{H}_2\text{O}^{[\text{S}1]}$  (**1-Ln**, 1.0 equiv., Ln = Yb:  $x = 6$ ; Ln = Lu:  $x = 8$ ) and  $[\text{Cr}(\text{ddpd})_2]\text{Cl}_3$  (**2**, 1.0 equiv.) were suspended in methanol ( $[\text{D}_0]/[\text{D}_4]$ ). The yellow mixture was stirred until all components were dissolved. After stirring for additional 30 minutes at room temperature, the solution was layered with isopropanol ( $[\text{D}_0]/[\text{D}_8]$ , 2 mL). Upon standing for 1 to 3 days, large orange crystals of **3-Ln** were obtained which were also suitable for X-ray crystallographic analysis. The crystals were collected, washed with isopropanol ( $[\text{D}_0]/[\text{D}_8]$ ,  $3 \times 1$  ml), ice-cold methanol ( $[\text{D}_0]/[\text{D}_4]$ ,  $1 \times 2$  ml), and finally dried under reduced pressure. The product was obtained as yellow solid.

#### 3-Yb:

$\text{Na}_3[\text{Yb}(\text{dpa})_3] \cdot 6 \text{H}_2\text{O}$  (33 mg, 39 mmol) and  $[\text{Cr}(\text{ddpd})_2]\text{Cl}_3$  (29 mg, 39 mmol) in MeOH (4 mL), precipitation with  $^i\text{PrOH} \rightarrow$  Yield: 45 mg (34 mmol, 88%).

Anal. Calcd. for:  $\text{C}_{55}\text{H}_{43}\text{CrN}_{13}\text{O}_{12}\text{Yb} \cdot 5 \text{CH}_3\text{OH} \cdot \text{H}_2\text{O}$  (%): C 48.65, H 4.42, N 12.29; Found: C 48.43, H 4.34, N 12.20.

#### 3-Yb (deuterated):

$\text{Na}_3[\text{Yb}(\text{dpa})_3] \cdot 6 \text{H}_2\text{O}$  (28 mg, 32 mmol) and  $[\text{Cr}(\text{ddpd})_2]\text{Cl}_3$  (24 mg, 32 mmol) in  $\text{CD}_3\text{OD}$  (2 mL), precipitation with  $[\text{D}_8]\text{-}^i\text{PrOH} \rightarrow$  Yield: 33 mg (29 mmol, 79 %).

Anal. Calcd. for:  $\text{C}_{55}\text{H}_{43}\text{CrN}_{13}\text{O}_{12}\text{Yb} \cdot 2 \text{CD}_3\text{OD} \cdot 5 \text{H}_2\text{O}$  (%): C 46.72, H 4.75, N 12.43; Found: C 46.21, H 4.55, N 12.21.

#### 3-Lu (deuterated):

$\text{Na}_3[\text{Lu}(\text{dpa})_3] \cdot 8 \text{H}_2\text{O}$  (40 mg, 45 mmol);  $[\text{Cr}(\text{ddpd})_2]\text{Cl}_3$  (34 mg, 45 mmol) in  $\text{CD}_3\text{OD}$  (3 mL), precipitation with  $[\text{D}_8]\text{-}^i\text{PrOH} \rightarrow$  Yield: 35 mg (26 mmol, 57 %).

Anal. Calcd. for:  $\text{C}_{55}\text{H}_{43}\text{CrN}_{13}\text{O}_{12}\text{Lu} \cdot 2 \text{CD}_3\text{OD} \cdot 5 \text{H}_2\text{O}$  (%): C 46.66, H 4.74, N 12.41; Found: C 46.38, H 4.77, N 12.89.

## 2. X-ray Single Crystal Structure Analysis

X-ray data were collected with a Bruker Smart APEX II diffractometer with graphite-monochromated Mo  $K_{\alpha}$  radiation or a Bruker APEX II Duo diffractometer with a Mo  $\mu$ S microfocus tube and a TRIUMPH monochromator. The programs used were Bruker's APEX2 v2011.8-0, including SADABS for absorption correction, SAINT for data reduction and SHELXS for structure solution, as well as the WinGX suite of programs version 1.70.01 or the GUI ShelXle, including SHELXL for structure refinement.<sup>[S3]</sup> Deposition numbers CCDC 2003420-2003421 contain the supplementary crystallographic data for this paper. These data are provided free of charge by the joint Cambridge Crystallographic Data Centre ([www.ccdc.cam.ac.uk/structures](http://www.ccdc.cam.ac.uk/structures)).

**Table S1.** Selected crystallographic data for **3-Yb** and **3-Lu**.

	<b>3-Yb</b>	<b>3-Lu</b>
Empirical formula	C <sub>63</sub> H <sub>71</sub> CrN <sub>12</sub> O <sub>19</sub> Yb	C <sub>62</sub> H <sub>68</sub> CrLuN <sub>12</sub> O <sub>18</sub>
M <sub>r</sub> [g mol <sup>-1</sup> ]	1525.35	1496.25
Crystal appearance	orange prisms	yellow prisms
T [K]	100(2)	100(2)
$\lambda$ [Å]	0.71073 (Mo $K_{\alpha}$ )	0.71073 (Mo $K_{\alpha}$ )
Crystal system	monoclinic	monoclinic
Space group	P2 <sub>1</sub> /n	P2 <sub>1</sub> /n
Z	4	4
a [Å]	16.1841(5)	16.1542(3)
b [Å]	23.2508(6)	23.3848(4)
c [Å]	17.6628(4)	17.6738(3)
$\beta$ [°]	91.979(2)	91.789(1)
V [Å <sup>3</sup> ]	6642.4(3)	6673.2(2)
D <sub>calc</sub> [g cm <sup>-3</sup> ]	1.525	1.489
$\mu$ [mm <sup>-1</sup> ]	1.644	1.712
F(000)	3116	3052.0
Crystal size [mm × mm × mm]	0.17 × 0.15 × 0.14	0.22 × 0.20 × 0.18
$\theta$ range [°]	1.45-27.56	1.45-29.18
Limiting indices	-21 ≤ h ≤ 16 -25 ≤ k ≤ 30 -21 ≤ l ≤ 21	-21 ≤ h ≤ 22 -32 ≤ k ≤ 31 -24 ≤ l ≤ 24
Collected refl.	41041	140668
Independent refl.	15071	17940
Absorption corr.	multi-scan	multi-scan
Transm. (max., min.)	0.746, 0.651	0.746, 0.650
Parameters/restraints	878/1	878/2
R <sub>1</sub> [ $ I > 2\sigma(I) $ ] <sup>a</sup>	0.0549	0.0540
wR <sub>2</sub> [ $ I > 2\sigma(I) $ ] <sup>b</sup>	0.1148	0.1268
R <sub>1</sub> (all data) <sup>a</sup>	0.0871	0.0592
wR <sub>2</sub> (all data) <sup>b</sup>	0.1290	0.1302
GOF on F <sup>2</sup>	1.024	1.251
$\Delta\rho_{\max,\min}$ [e Å <sup>-3</sup> ]	1.621 / -1.630	3.134 / -3.250

<sup>a</sup> R<sub>1</sub> factor definition:  $R_1 = \sum (|F_o| - |F_c|) / \sum |F_o|$

<sup>b</sup> wR<sub>2</sub> factor definition:  $wR_2 = [\sum w(F_o^2 - F_c^2)^2 / \sum w(F_o^2)]^{1/2}$ . Weighting scheme:  $w = 1 / [\sigma^2(F_o^2) + (np)^2]$ ,  $p = [F_o^2 + 2 F_c^2] / 3$



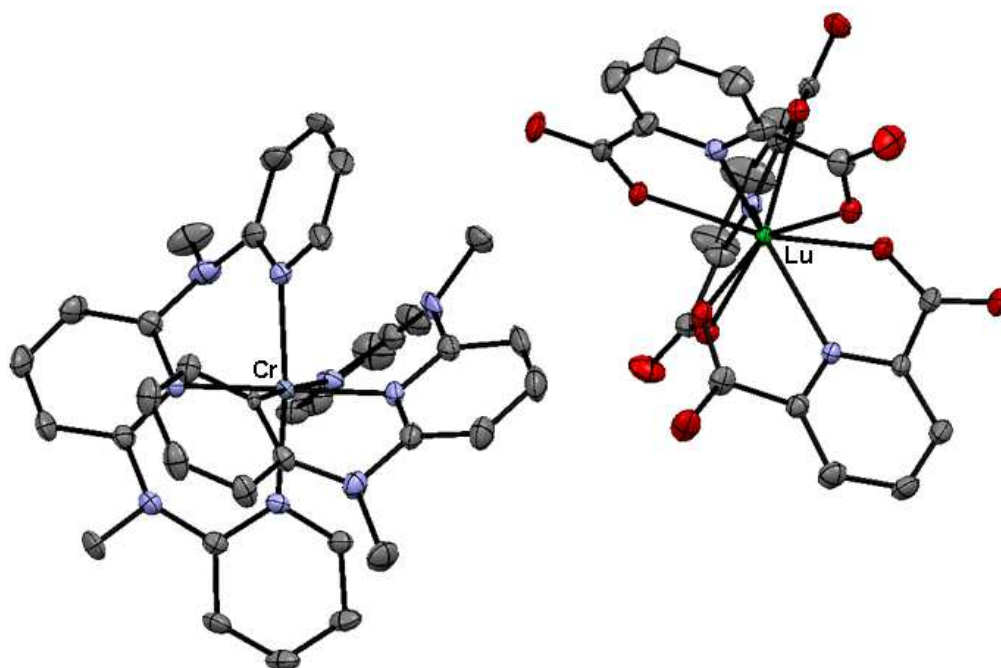


**Figure S1.** Thermal ellipsoid plot for **3-Lu** (Ortep 3 for Windows,<sup>[S4]</sup> 50% probability level). The lattice solvent molecules and hydrogen atoms in the complexes are omitted for clarity.

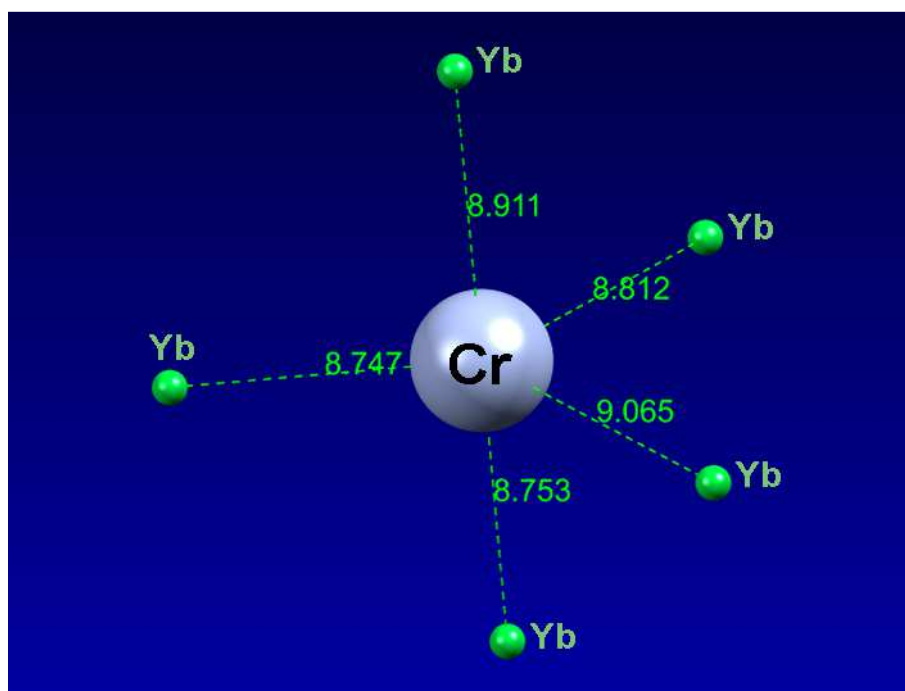


**Figure S2.** Distances Cr-Yb (Å) in the closest shell of Yb<sup>3+</sup> sensitizers around each Cr<sup>3+</sup> center in the solid state structure of **3-Yb**.

### 3. Luminescence Measurements

#### 3.1 Instruments

The measurements were performed on different instruments:

- 1) For photophysical measurements under 435 nm excitation, two different spectrofluorometers were applied:
  - a) A Horiba Fluorolog-3 spectrofluorometer equipped with a 450-W Xenon lamp was used for steady-state measurements. The emitted light was detected at an angle  $90^\circ$  to the excitation light using either a Hamamatsu R2658P PMT detector ( $300 \text{ nm} < \lambda_{\text{em}} < 1010 \text{ nm}$ ) or by a Hamamatsu H10330-75 PMT detector ( $950 \text{ nm} < \lambda_{\text{em}} < 1700 \text{ nm}$ ). Spectral selection in the excitation channel was accomplished by a DFX double monochromator (gratings: 1200 grooves/mm, 330 nm blaze) and in the emission channel by a spectrograph iHR550 (single grating: 1200 grooves/mm, 500 nm blaze) in the visible/NIR spectral region ( $\lambda_{\text{em}} < 1010 \text{ nm}$ ) and a spectrograph iHR320 (single grating: 600 grooves/mm, 1000 nm blaze) in the NIR spectral region ( $\lambda_{\text{em}} > 950 \text{ nm}$ ). Spectral correction of the emission spectra was performed with a correction curve implemented by the instrument manufacturer. The luminescence decay kinetics were determined at 298 K with a pulsed xenon flash lamp (pulse width of ca. 1.5  $\mu\text{s}$  FWHM). The analysis of the luminescence decay kinetics (deconvolution, statistical parameters, etc.) was performed using the software package DAS from Horiba.
  - b) A calibrated spectrofluorometer FSP 920 from Edinburgh Instruments was equipped with different excitation light sources and detectors covering a wavelength region of about 300 to 1700 nm.<sup>[S5]</sup> Luminescence decay curves were also obtained at 298 K with spectrofluorometer FSP 920; yet in this case a  $\mu\text{s}$  xenon flashlamp (100 Hz, pulse width ca. 2.4  $\mu\text{s}$  FWHM) and a Hamamatsu R2658P PMT detector were used. The luminescence decays were analyzed by fitting the obtained decay curves with the software FAST (Fluorescence Analysis Software Technology, Edinburgh Instruments Ltd.).
  - c) The luminescence quantum yields of the solid samples were determined by an absolute method using the commercial integrating sphere setup Quantaury-QY C11347-11 from Hamamatsu<sup>[S6]</sup> using an excitation wavelength of 435 nm (direct excitation of the  $\text{Cr}^{3+}$  complex). For measurements of these solid-state samples,

miniaturized Petri dishes made from quartz from the instrument manufacturer were used.

- 2) For upconversion luminescence measurements, a calibrated photoluminescence spectrofluorometer FLS 980 from Edinburgh Instruments was used. The FLS 980 spectrofluorometer is equipped with an ca. 8-W 976-nm laser diode (Roithner Lasertechnik GmbH, Vienna, Austria), which can be used in a continuous wave (cw) or pulsed mode. The excitation power of the laser at the sample position was previously characterized with a power meter (Newport 841-PE Powermeter). By adjusting the current of the laser, laser power ranges from 0.02 to 9.07 W. As the samples were sealed between two glass slides and measured in a sealed cuvette (4 x 10 mm), reflection of excitation source must be considered. The power losses caused by laser reflections on the glass/quartz surfaces were determined to be ca. 11% by undergoing five separate measurements with different laser power.<sup>[S7]</sup> To gauge the excitation power density, a digital microscope was used to determine the laser spot size using ImageJ. The magnification factor of the microscope was calibrated with a standard calibration target (R1DS1N, USAF 1951 pattern, Thorlabs). This yielded an average spot size of about  $6.6 \cdot 10^{-3} \text{ cm}^2$ . The excitation power density was then calculated with respect to each laser power used in this study, which ranged from ca. 50 to  $1230 \text{ W}\cdot\text{cm}^{-2}$ . UC lifetime measurements were performed with pulsed 976-nm laser excitation (100 Hz, pulse width ca. 200  $\mu\text{s}$ ) with multi-channel scaling mode (MCS). A 645 nm long pass filter was applied to exclude the second order emission from the laser at 490 nm.

### 3.2 Steady-State and Time-Resolved Luminescence Measurements

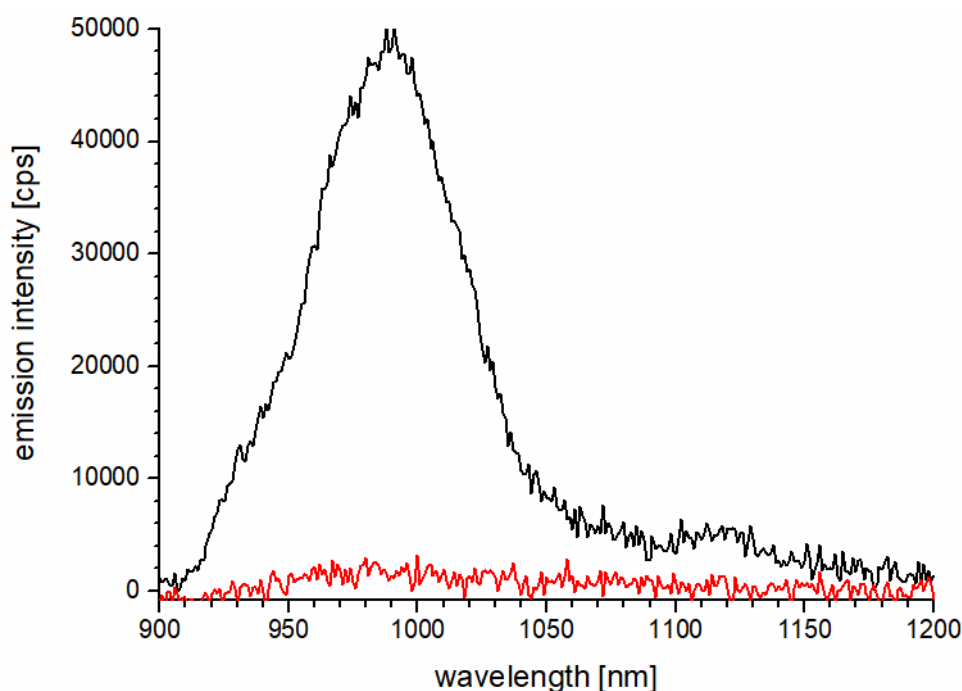


**Figure S3.** Steady-state emission spectra for **1-Yb** (solid state, 298 K, air) after excitation at 290 nm (black) and 435 nm (red).

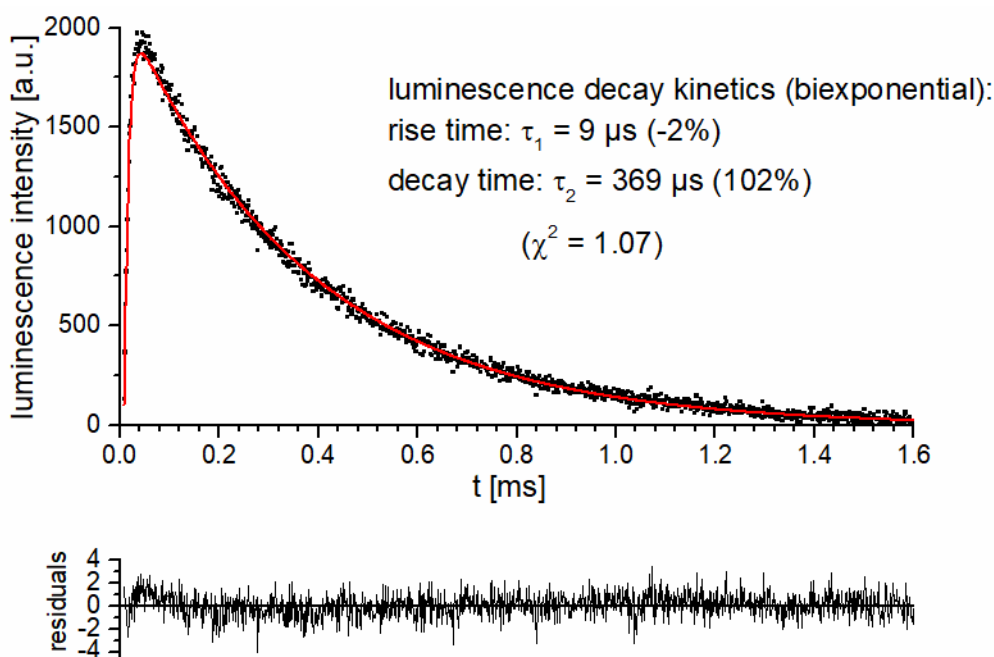


**Figure S4.** Luminescence decay profile (black scatter plot) obtained at 980 nm ( ${}^2F_{5/2} \rightarrow {}^2F_{7/2}$  transition of  $\text{Yb}^{3+}$ ) in **3-Yb** resulting for excitation at the  $\text{Cr}^{3+}$  absorption band at 435 nm ( ${}^4A_2 \rightarrow {}^4T_2$  transition) at  $T = 298$  K in air. The biexponential fit (red solid line) was obtained using a single rise time of  $9 \mu\text{s}$  and a single decay component with a decay time of  $369 \mu\text{s}$ . The residual shown below underlines the suitability of the fit.

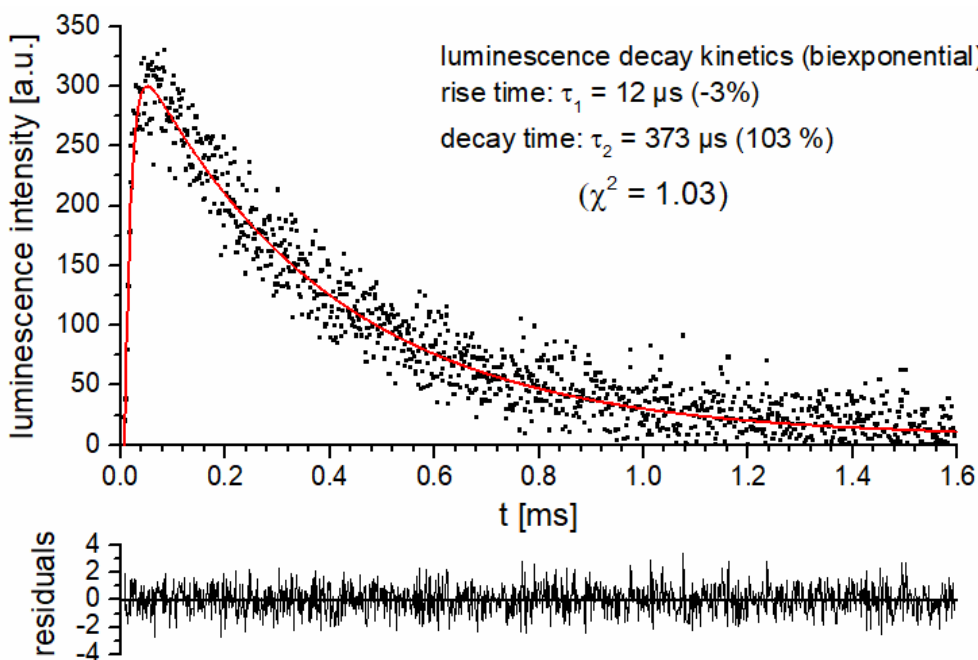


**Figure S5.** Luminescence decay profile (black scatter plot) for the transition  ${}^2F_{5/2} \rightarrow {}^2F_{7/2}$  of  $\text{Yb}^{3+}$  ( $\lambda_{\text{em}} = 980 \text{ nm}$ ) in **3-Yb** (deuterated) after selective excitation into the  $\text{Cr}^{3+}$  absorption band  ${}^4A_2 \rightarrow {}^4T_2$  ( $\lambda_{\text{exc}} = 435 \text{ nm}$ ) at  $T = 298 \text{ K}$  in air – Biexponential fit (red solid line) with one rise time and one decay time component.

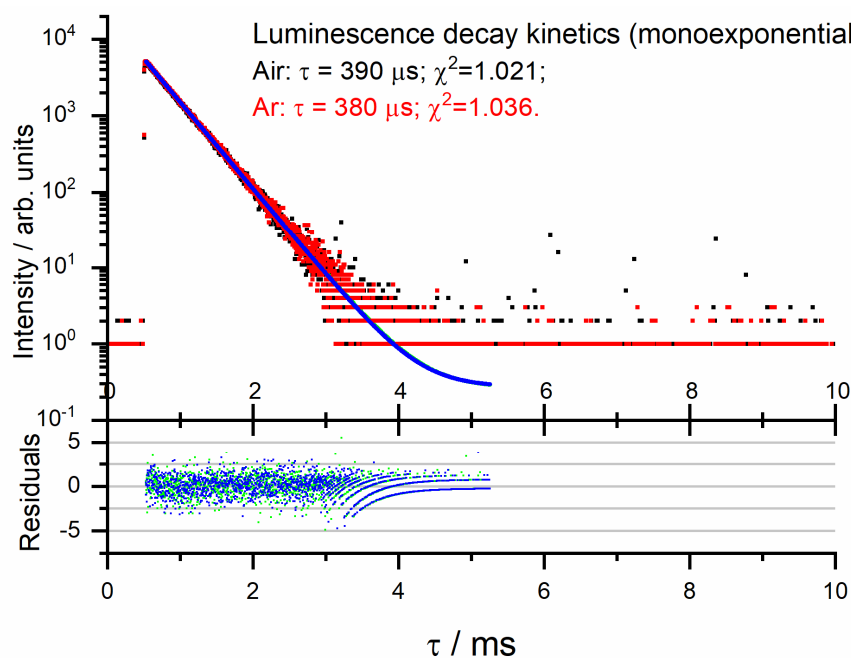


**Figure S6.** Luminescence decay profile under air- (black scatter plot) and Ar-saturation (red scatter plot) for the transition  ${}^2E/{}^2T_1 \rightarrow {}^4A_2$  of  $\text{Cr}^{3+}$  ( $\lambda_{\text{em}} = 783 \text{ nm}$ ) in **3-Yb** after selective excitation into the  $\text{Cr}^{3+}$  absorption band  ${}^4A_2 \rightarrow {}^4T_2$  ( $\lambda_{\text{exc}} = 435 \text{ nm}$ ) at  $T = 298 \text{ K}$  – Monoexponential fits of the decay in air (green solid line) and in Ar (blue solid line).

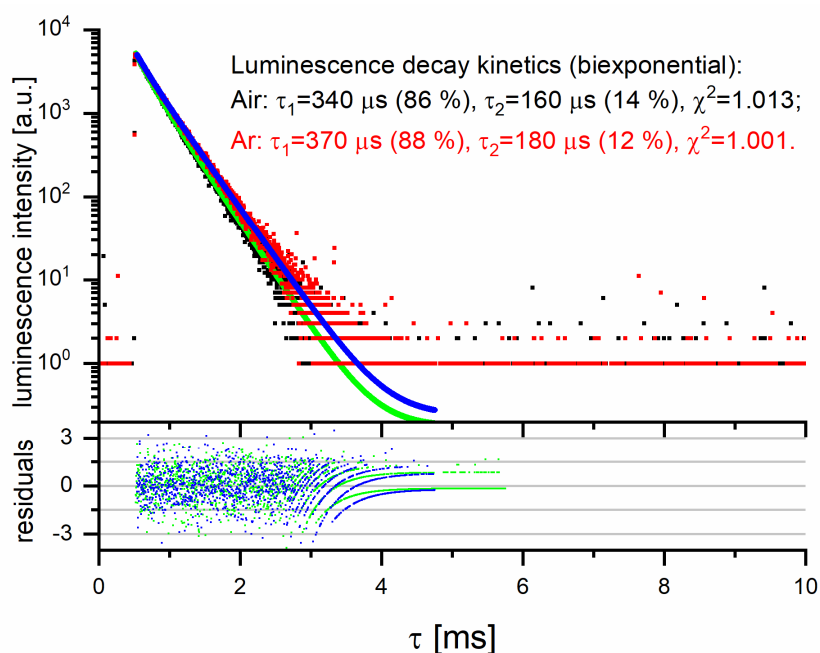


**Figure S7.** Luminescence decay profile under air- (black scatter plot) and Ar-saturation (red scatter plot) for the transition  ${}^2E/{}^2T_1 \rightarrow {}^4A_2$  of  $\text{Cr}^{3+}$  ( $\lambda_{\text{em}} = 783 \text{ nm}$ ) in **3-Yb** (deuterated) after selective excitation into the  $\text{Cr}^{3+}$  absorption band  ${}^4A_2 \rightarrow {}^4T_2$  ( $\lambda_{\text{exc}} = 435 \text{ nm}$ ) at  $T = 298 \text{ K}$  – Biexponential fit of the decay in air (green solid line) and in Ar (blue solid line).

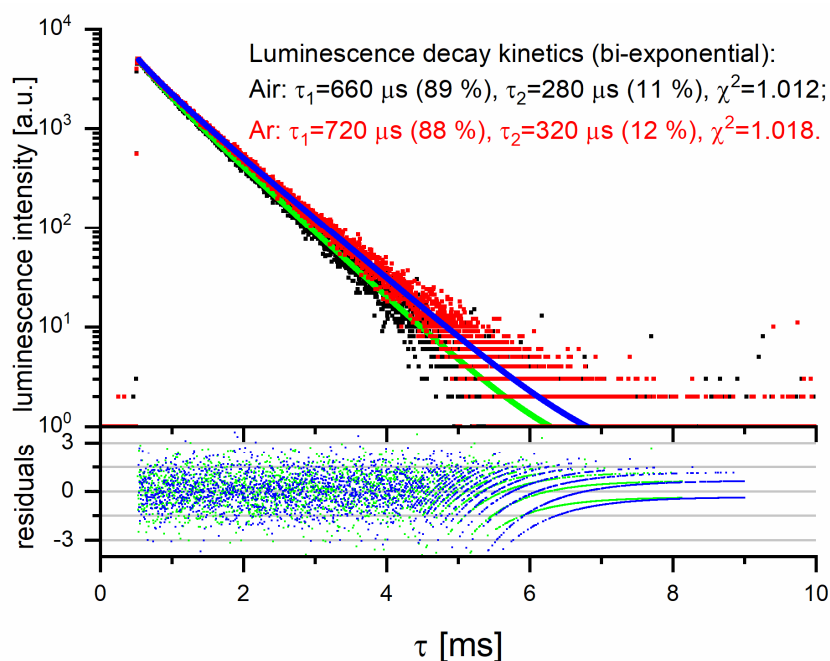


**Figure S8.** Luminescence decay profile under air- (black scatter plot) and Ar-saturation (red scatter plot) for the transition  ${}^2E/{}^2T_1 \rightarrow {}^4A_2$  of  $\text{Cr}^{3+}$  ( $\lambda_{\text{em}} = 783 \text{ nm}$ ) in **3-Lu** after selective excitation into the  $\text{Cr}^{3+}$  absorption band  ${}^4A_2 \rightarrow {}^4T_2$  ( $\lambda_{\text{exc}} = 435 \text{ nm}$ ) at  $T = 298 \text{ K}$  – Biexponential fit of the decay in air (green solid line) and in Ar (blue solid line).

### 3.3 Upconversion Measurements

Within the optical UC emission spectrum, unfortunately, several spectral components cluttered the spectrum for peak interpretation. Thus, a mathematical approach was applied to flag and remove the undesired features from the spectra. Under the current experimental condition, the residual irradiation stemming from the excitation laser at 976 nm was removed from the spectra. The data points corresponding to the range 810 to 820 nm were fitted with a Gaussian function, where the center of this kernel function was constrained at 976 nm, to mimic the residual laser irradiation. Thereafter, this fitted model was applied across the entire measurement range, *i.e.* 700-840 nm, resulting in processed spectra containing only emission signals originating from the samples. Further, the spectra after removing the laser component were decomposed by:

$$f(\nu) = \sum_i A_i \cdot e^{-\left(\frac{\nu - \nu_{0,i}}{\sigma_i}\right)^2} + C \quad \text{eq. S1}$$

where  $f(\nu)$  is the fitted model,  $\nu$  is the independent variable in the unit of  $\text{cm}^{-1}$ ,  $A_i$  is the amplitude of spectral component  $i$ ,  $\nu_{0,i}$  is the peak center of component  $i$ ,  $\sigma_i$  is the corresponding peak width of component  $i$ , and  $C$  is the bias constant. Specifically, the wavelength was converted to wavenumber in order to reflect the Gaussian nature of the fluorescence. In this scenario, three Gaussian kernels were used to interpret all spectra, in which the spectral components of interest fell onto the ones centered at 745 and 777 nm. All calculations were performed with Matlab 2017a.

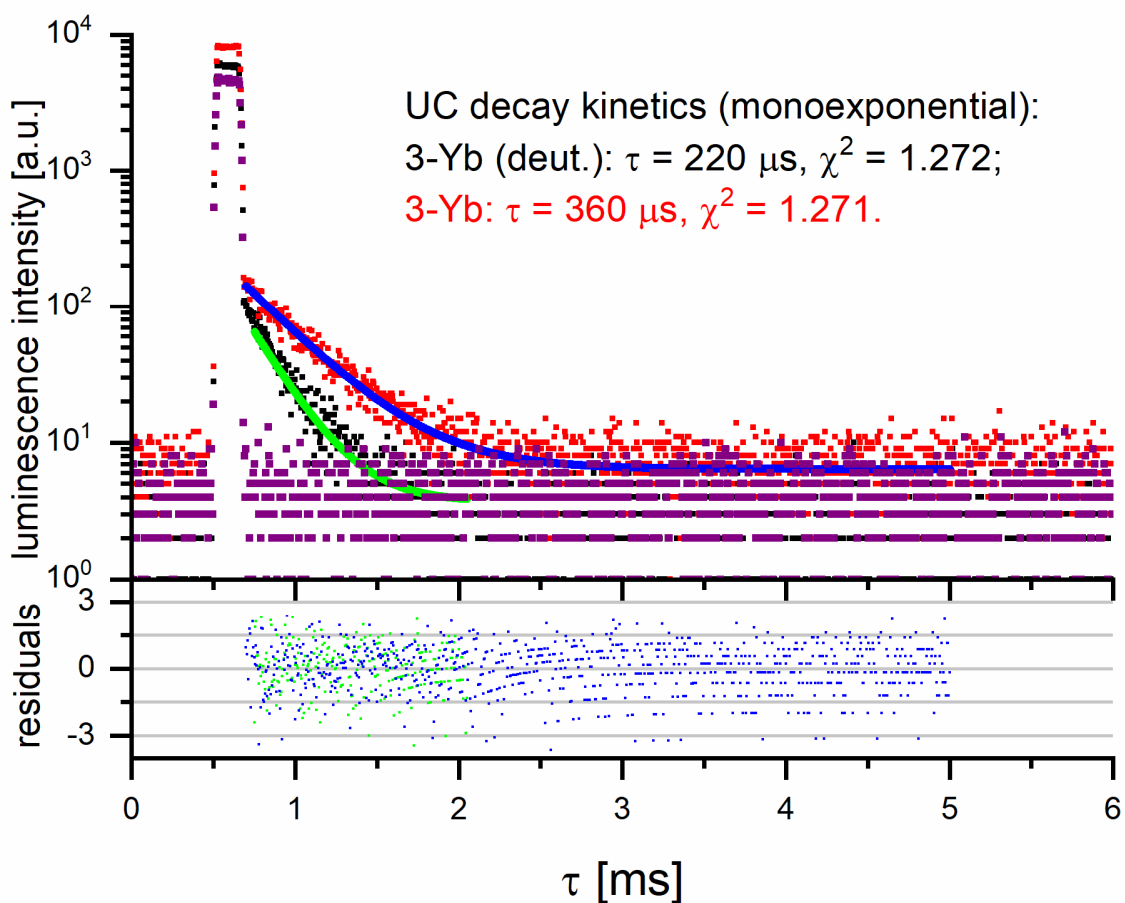


**Figure S9.** UC Luminescence decay profile of deuterated **3-Yb** (black scatter plot), **3-Yb** (red scatter plot) and **3-Lu** (purple scatter plot) for the transition  ${}^2E/{}^2T_1 \rightarrow {}^4A_2$  of  $\text{Cr}^{3+}$  ( $\lambda_{\text{em}} = 778 \text{ nm}$ ) under selective excitation into the  $\text{Yb}^{3+}$  absorption band  ${}^2F_{7/2} \rightarrow {}^2F_{5/2}$  ( $\lambda_{\text{exc}} = 976 \text{ nm}$ ) at  $T = 298 \text{ K}$  – Monoexponential fit of the decay for deuterated **3-Yb** (green solid line) and of **3-Yb** (blue solid line).



#### 4. References

- [S1] G. Kervern, A. D'Aléo, L. Toupet, O. Maury, L. Emsley, G. Pintacuda, *Angew. Chem. Int. Ed.* **2009**, *48*, 3082.
- [S2] A. Breivogel, C. Förster, K. Heinze, *Inorg. Chem.* **2010**, *49*, 7052.
- [S3] a) L. J. Farrugia, *J. Appl. Crystallogr.* **1999**, *32*, 837; b) C. B. Hübschle, G. M. Sheldrick, B. Dittrich, *J. Appl. Crystallogr.* **2011**, *44*, 1281; c) G. M. Sheldrick, *Acta Cryst., Sect. A* **2008**, *64*, 112; d) Bruker AXS Inc. Madison, Wisconsin, USA, **2007**; e) G. M. Sheldrick, *SADABS, University of Göttingen, Germany*, **2008**.
- [S4] L. J. Farrugia, *J. Appl. Crystallogr.* **1997**, *30*, 565.
- [S5] S. Hatami, C. Würth, M. Kaiser, S. Leubner, S. Gabriel, L. Bahrig, V. Lesnyak, J. Pauli, N. Gaponik, A. Eychmüller, U. Resch-Genger, *Nanoscale* **2015**, *7*, 133.
- [S6] a) S. Würth, D. Geißler, T. Behnke, M. Kaiser, U. Resch-Genger, *Anal. Bioanal. Chem.* **2015**, *407*, 59; b) C. Würth, M. G. González, R. Niessner, U. Panne, C. Haisch, U. Resch-Genger, *Talanta* **2012**, *90*, 30; c) C. Würth, J. Pauli, C. Lochmann, M. Speles, U. Resch-Genger, *Anal. Chem.* **2012**, *84*, 1345.
- [S7] S. Gharaati, C. Wang, C. Förster, F. Weigert, U. Resch-Genger, K. Heinze, *Chem. Eur. J.* **2020**, *26*, 1003.

## 5.2.2 Energietransfer-Prozesse in molekularen Chrom-Lanthanoid-Salzen (unveröffentlichte Ergebnisse)

Im Festkörper **3-Ln** können durch Förster-Energietransfer die  $\text{Cr}^{3+}$ - und  $\text{Ln}^{3+}$ -Metallzentren der beiden Komplexionen miteinander „kommunizieren“. Dieser Prozess ermöglicht in festem **3-Yb** das Auftreten von  $^2\text{E}$ -Upconversion-Lumineszenz nach Anregung der Ytterbium-Sensibilisatoren bei  $\lambda_{\text{ex}} = 976 \text{ nm}$  (Kapitel 5.2.1). Neben dem  $\text{Cr}^{3+}/\text{Yb}^{3+}$ -Paar sind auch andere Ln/Cr Kombinationen und deren photophysikalischen Eigenschaften sehr interessant. Abhängig von der Wahl des  $\text{Ln}^{3+}$ -Ions können unterschiedliche Arten von EnT-Prozessen auftreten, bei welchem das Cr(III)-Komplexion mal als Sensibilisator oder auch als Aktivator auftritt (Kapitel 5.1.1, Abb. 50 u. 51).

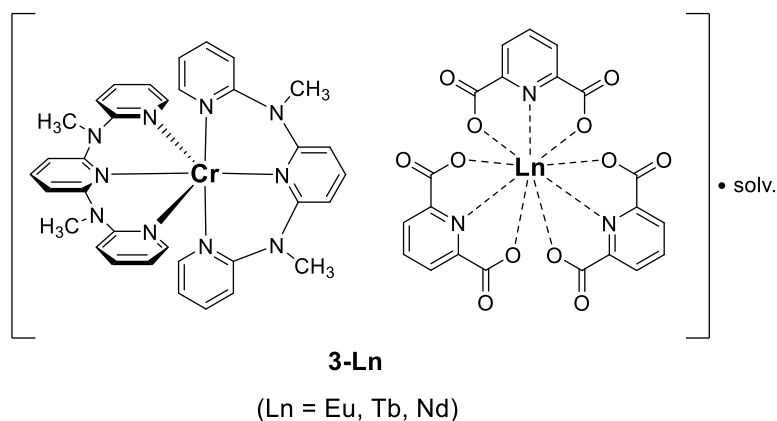


**Abb. 58:** Strukturformeln der dargestellten Chrom-Lanthanoid-Salze **3-Ln**.

Zur Untersuchung der Energietransferprozesse in neuen vielversprechenden Chrom-Lanthanoid-Komplexpaaren wurden die Salze **3-Eu**, **3-Tb** und **3-Nd** ausgewählt (Abb. 58). Die Darstellung der **3-Ln** Salze wurde analog zur Synthese von **3-Yb** und **3-Lu** durchgeführt.<sup>[148]</sup> Die Elementaranalysen der neu synthetisierten Komplexpaare offenbarten ebenfalls große Mengen kokristallisiertes Wassers. Die Kristallisation von **3-Eu**, **3-Tb** und **3-Nd** erfolgte aus  $\text{H}_2\text{O}/\text{PrOH}$ -Mischungen. Auf die Kristallisation aus deuterierten Lösungsmitteln wurde verzichtet, da diese keinen Einfluss auf die Lumineszenzeigenschaften von **3-Yb** und **3-Lu** hatte.

Die Röntgenstrukturanalyse der Einkristalle von **3-Eu**, **3-Tb** und **3-Nd** zeigt große Übereinstimmungen mit den Festkörperstrukturen von **3-Yb** und **3-Lu**, wiesen aber auch auf einen gewissen Einfluss des Lösungsmittels hin. Unabhängig vom

Lösungsmittel kristallisieren alle **3-Ln** Salze als isostrukturelle, racemische Mischungen der beiden Komplexionen. Einkristalle von **3-Ln**, welche aus Wasser erhalten werden konnten, kristallisieren aber nicht in der Raumgruppe  $P2_1/n$ , sondern in der triklinen Raumgruppe  $P\bar{1}$  (Anhang, Tab. A4).

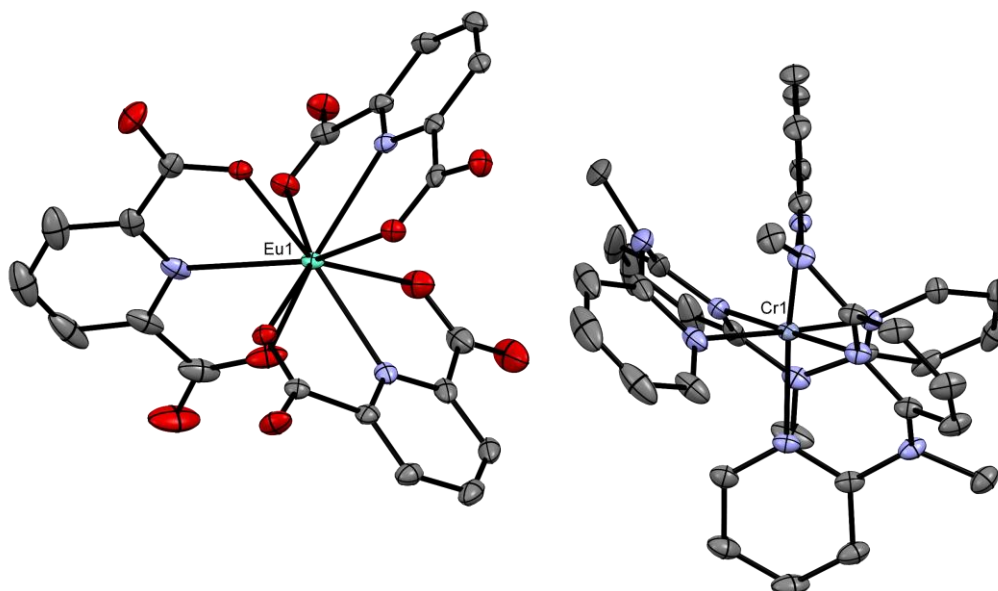


**Abb. 59:** ORTEP-Darstellung der asymmetrischen Einheit von **3-Eu** kristallisiert aus einer  $H_2O/PrOH$ -Mischungen, Ellipsoidenwahrscheinlichkeit 50 %. Lösemittelmoleküle im Kristallgitter und Wasserstoffatome wurden aus Übersichtlichkeitsgründen weggelassen.

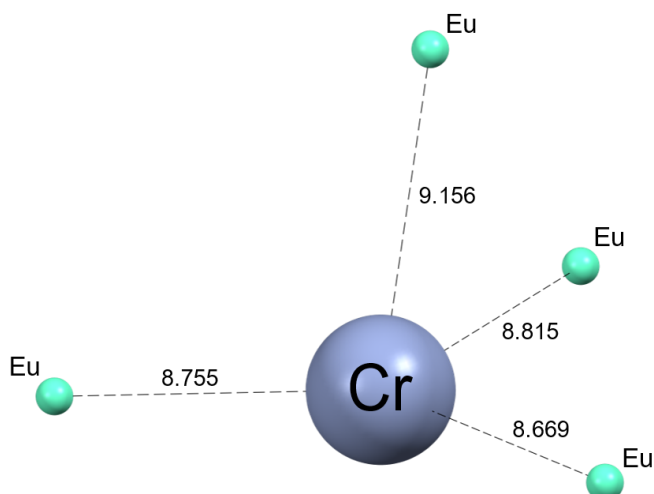


**Abb. 60:** Cr-Eu-Abstände der räumlich nächsten  $Eu^{3+}$ -Sensibilisatoren um je ein  $Cr^{3+}$ -Zentrum im Festkörper von **3-Eu**. Abstände sind in Å angegeben.

Ein weiterer Unterschied ist, dass im kristallinen Festkörper von **3-Eu**, **3-Tb** und **3-Nd** das  $\text{Cr}^{3+}$ -Ion von nur vier (anstatt fünf in **3-Yb** u. **3-Lu**)  $\text{Ln}^{3+}$ -Ionen als nächste Nachbarn umgeben ist. Die Chrom-Lanthanoid-Abstände hingegen sind sehr ähnlich und variieren z.B. in der Festkörperstruktur von **3-Eu** nur zwischen  $8.76 \text{ \AA} < r_{\text{Cr-Eu}} < 9.16 \text{ \AA}$  (Abb. 60). Auf Grund der nur geringen Unterschiede ist auch hier von ähnlichen Energietransferraten für  $\text{Ln} \rightarrow \text{Cr}$ -Energietransfer auszugehen. Diese Energietransferprozesse werden in den folgenden beiden Abschnitten diskutiert.

### 5.2.2.1 Chromsensibilisierte $\text{Nd}^{3+}$ -Emission in einem molekularen Chrom-Neodym-Salz

In der Regel werden, wie in Kapitel 4.1.1 beschrieben, organische Liganden mit  $\pi$ -Systemen als Antennenmotive eingesetzt um das Problem der schlechten Anregbarkeit der  $\text{Ln}^{3+}$ -Ionen zu überwinden. In den vergangenen Jahren wurden auch mehr und mehr Übergangsmetall-Chromophore als Sensibilisatoren für  $\text{Ln}^{3+}$ -basierte Lumineszenz eingesetzt. In diesen d-f-Hybridssystemen kann nach Anregung des Übergangsmetallkomplexes, häufig in einen langlebigen MLCT-Zustand,  $\text{ÜM} \rightarrow \text{Ln}$ -Downshifting-Energietransfer zur Sensibilisierung der NIR-Lumineszenz von beispielsweise  $\text{Nd}^{3+}$ -,  $\text{Er}^{3+}$ - und  $\text{Yb}^{3+}$ -Ionen genutzt werden. Dabei bietet die Verwendung von Übergangsmetallkomplexen als Antennenmotiv beispielsweise den Vorteil, dass die NIR-Lanthanoiden-Lumineszenz oft mit sichtbarem Licht angeregt werden kann, wohingegen die Anregung mit organischen Liganden in der Regel kurzwelliges Licht im UV erfordert.<sup>[111,112]</sup>

Dieses Prinzip konnte auch schon erfolgreich in molekularen Chrom-Lanthanoid-Architekturen angewendet werden. Beispiele hierfür sind hexacyanidochromat- und oxalatverbrückte Koordinationsverbindungen, bei welchem durch effektiven Dexter-Energietransfer ( $\text{EnT}$ )  ${}^2\text{E}(\text{Cr}^{3+}) \rightarrow {}^2\text{F}_{5/2}(\text{Yb}^{3+})$  die NIR-Lumineszenz von  $\text{Yb}^{3+}$ - oder  $\text{Nd}^{3+}$ -Ionen sensibilisiert werden konnte.<sup>[139,149]</sup> Auch konnte Piguet in polymetallischen Chrom-Lanthanoid-Komplexen durch Einsatz von  $\text{Cr}^{3+}$ -Ionen als Sensibilisatoren die Lebenszeit der NIR-emissiven Zustände von  $\text{Nd}^{3+}$ - und  $\text{Yb}^{3+}$ -Ionen in den Millisekunden-Bereich verlängern.<sup>[140,154,155]</sup>

Um das Auftreten von Cr→Nd-Downshifting-EnT in **3-Nd** zu untersuchen, wurden zunächst Emissionsspektren nach Anregung bei  $\lambda_{\text{exc}} = 435 \text{ nm}$  in die  ${}^4A_2 \rightarrow {}^4T$ -Bande des  $\text{Cr}^{3+}$ -Ions bei 298 und 77 K aufgenommen (Abb. 61).

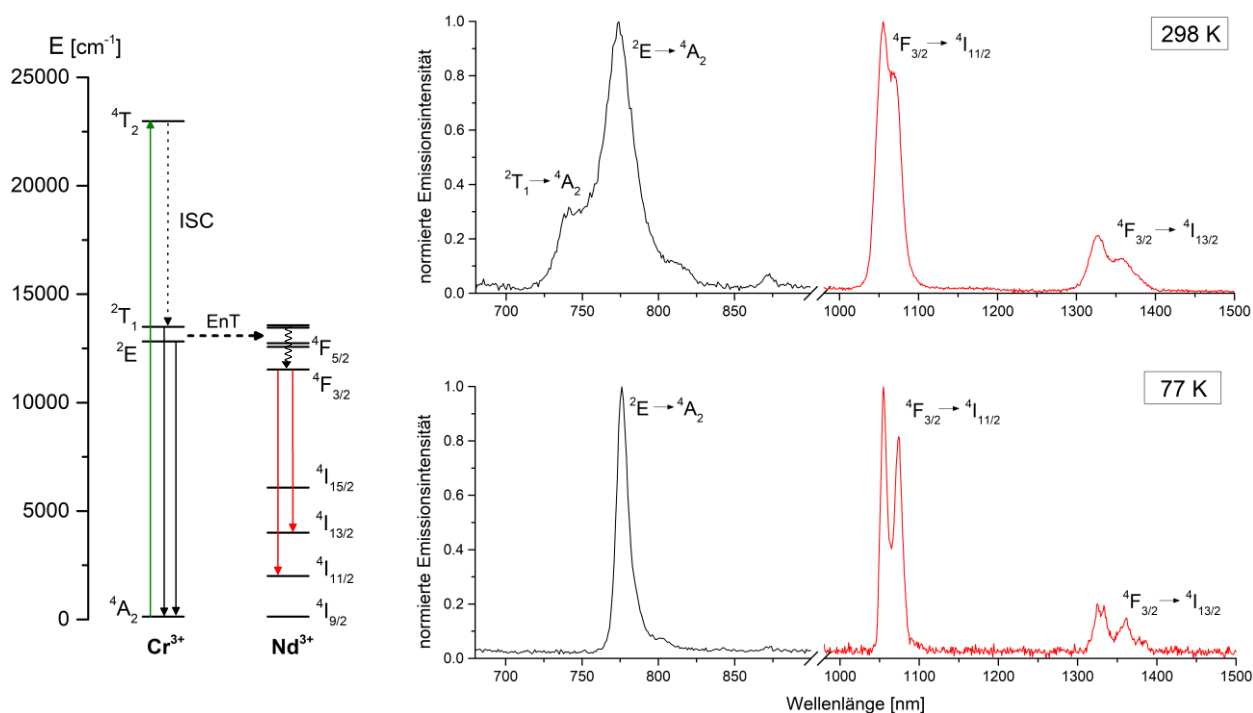


**Abb. 61:** Links: Schematische Darstellung des vereinfachten Energiediagramms von **3-Nd** mit den relevanten Zuständen von  $\text{Nd}^{3+}$  und  $\text{Cr}^{3+}$ . Die Beschriftung der Zustände des  $\text{Nd}^{3+}$ -Ions oberhalb des  ${}^4F_{5/2}$ -Zustands wurden aus Übersichtlichkeitsgründen weggelassen. Grüne Pfeile nach oben stehen für Anregung, Pfeile nach unten für Emission, gepunktete Pfeile für ISC, gestrichelte Pfeile für Energietransfer und ein gewellter Pfeil für Internal Conversion. Rechts: Normierte Steady-State-Emissionsspektren ( $\lambda_{\text{exc}} = 435 \text{ nm}$ ) von **3-Nd** im Festkörper bei  $T = 298 \text{ K}$  (oben) und  $77 \text{ K}$  (unten) an Luft.

Bei Raumtemperatur kann neben einer schwachen Spin-Flip-Emission des  $[\text{Cr}(\text{ddpd})_2]^{3+}$ -Komplexions auch recht intensive  $\text{Nd}^{3+}$ -Emission beobachtet werden (Abb. 61, rechts oben). Dabei können die charakteristischen  $\text{Nd}^{3+}$ -Emissionsbanden bei  $\lambda_{\text{em}} = 1055$  und  $1328 \text{ nm}$  den  ${}^4F_{3/2} \rightarrow {}^4I_{11/2}$  und  ${}^4F_{3/2} \rightarrow {}^4I_{13/2}$  Übergängen zugeordnet werden (Abb. 61, links). Der strahlende Übergang vom emittierenden  ${}^4F_{3/2}$ -Zustand in das energetisch tieflyingende Grundzustandsniveau  ${}^4I_{9/2}$  bei ca.  $\lambda_{\text{em}} = 880 \text{ nm}$  kann dagegen nicht beobachtet werden. Weil die chromfreie Vorstufe **Na<sub>3</sub>[Nd(dpa)<sub>3</sub>] (1-Nd)** nur unterhalb von  $\lambda_{\text{ex}} = 300 \text{ nm}$  angeregt werden kann (Anhang, Fig. A11), ist das Auftreten der  $\text{Nd}^{3+}$ -Emission ein erstes sehr starkes Indiz für  $\text{Cr}^{3+} \rightarrow \text{Nd}^{3+}$ -Energietransfer. Generell emittiert **1-Nd** nach Anregung des **dpa**-Liganden

mit  $\lambda_{\text{exc}} = 275 \text{ nm}$  nur sehr schwach und bei Temperaturen weit unter Raumtemperatur.<sup>[157]</sup> Zusätzlich weist die intensitätsschwache Spin-Flip-Emission des **[Cr(ddpd)<sub>2</sub>]<sup>3+</sup>**-Komplexions von **3-Nd** auf effektive strahlungslose Deaktivierung der Spin-Flip-Zustände hin, was sehr wahrscheinlich auf den Energietransfer auf das Nd<sup>3+</sup>-Ion zurückzuführen ist.

Die Emissionsspektren von **3-Nd** bei T = 77 K zeigen qualitativ ein sehr ähnliches Bild. Erwartungsgemäß nehmen Intensität und Schärfe der Emission bei tieferen Temperaturen zu (Abb. 61, rechts unten). Bei T = 77 K sollte thermisch vorwiegend der energetisch tiefere Spin-Flip-Zustand (<sup>2</sup>E) des Cr<sup>3+</sup>-Ions besetzt sein, weshalb die Schulter der Raumtemperaturemission bei ca.  $\lambda_{\text{em}} = 745 \text{ nm}$  nicht mehr beobachtet werden kann. Zusätzlich kann nun die Feinstruktur der Nd<sup>3+</sup>-Emissionsbanden aufgelöst werden, welche aus der Kristallfeldaufspaltung resultiert. In diesem Zusammenhang wurde in der Literatur für **Na<sub>3</sub>[Ln(dpa)<sub>3</sub>·H<sub>2</sub>O]** und die Cr<sup>3+</sup>/Co<sup>3+</sup>-Ln<sup>3+</sup>-Salze von Sobolev beschrieben, dass die unterschiedliche Orientierung von Wassermolekülen im kristallinen Festkörper zu unterschiedlichen Kristallfeldaufspaltungen führt, was sich auch in den Emissionsspektren widerspiegelt.<sup>[141]</sup>

**Tab. 9:** Lumineszenzlebensdauern  $\tau$  der Komponenten **3-Ln** (Ln = Nd, Lu) im Festkörper bei T = 298 K nach Anregung bei  $\lambda_{\text{exc}} = 435 \text{ nm}$ .

Verbindung	$\tau$ (774 nm) [ $\mu\text{s}$ ] <sup>a</sup> <sup>2</sup> T <sub>1/2</sub> E → <sup>4</sup> A <sub>2</sub>	$\tau$ (1060 nm) [ $\mu\text{s}$ ] <sup>a</sup> <sup>4</sup> F <sub>3/2</sub> → <sup>4</sup> I <sub>11/2</sub>
<b>3-Nd</b>	20 (100 %)	20 (95 %) 58 (5 %)
<b>3-Lu</b>	280 (11%) 660 (89 %)	n.a

<sup>a</sup>Lebensdauern wurden mono- oder biexponentiell angepasst, die Prozentangaben in den Klammern geben die relative Amplituden der Komponenten an (Anhang, Fig. A12+13).

Im nächsten Schritt wurden die Lumineszenzlebensdauern der Emissionsbanden von **3-Nd** bei Raumtemperatur bestimmt. Die zeitliche Abnahme der Nd<sup>3+</sup>-Emission bei  $\lambda_{\text{em}} = 1060 \text{ nm}$  zeigt eine biexponentielle Kinetik mit einer Lebenszeit der dominierenden Komponente von  $\tau = 20 \mu\text{s}$  (Tab. 9). Diese Lebenszeit ist uncharakteristisch lang für vergleichbare Nd-Komplexe bei Raumtemperatur.<sup>[85]</sup> So beträgt beispielsweise die Lebenszeit der Nd<sup>3+</sup>-Emission von **1-Nd** in D<sub>2</sub>O lediglich  $\tau = 1 \mu\text{s}$ .<sup>[157]</sup> Die entsprechende Lebenszeit im Festkörper konnte bisher nicht

bestimmt werden. Die untypisch lange Lebensdauer der  $\text{Nd}^{3+}$ -Emission von **3-Nd** ist ein weiterer Hinweis für die Besetzung des emittierenden  $^4\text{F}_{3/2}$ -Niveaus ausgehend vom langlebigen  $^2\text{E}$ -Zustand des  $\text{Cr}^{3+}$ -Ions. Dazu passt auch die monoexponentielle Lebenszeit der Chromemission von **3-Nd** bei  $\lambda_{\text{em}} = 774 \text{ nm}$ , welche mit  $\tau = 20 \mu\text{s}$  identisch mit der Lebensdauer der  $\text{Nd}^{3+}$ -Emission ist. Diese gemessene Lebensdauer ist im Vergleich zur Lebenszeit  $^2\text{E}$ -Emission der Referenzverbindung **3-Lu** stark verkürzt, was ebenfalls typisch für  $\text{Cr}^{3+} \rightarrow \text{Nd}^{3+}$ -Energietransfer ist.

Zusammengefasst tritt im ionischen Festkörper **3-Nd** nach Anregung bei  $\lambda_{\text{exc}} = 435 \text{ nm}$  in die  $^4\text{A}_2 \rightarrow ^4\text{T}_2$  Bande des Chrom(III)-Komplexions  $\text{Cr}^{3+} \rightarrow \text{Nd}^{3+}$ -Downshifting-EnT bei  $T = 298$  und  $77 \text{ K}$  auf. Die chromsensibilisierte  $\text{Nd}^{3+}$ -Emission ist dabei intensiver und langlebiger als die Lumineszenz in der chromfreien Vorstufe **1-Nd**. Im Unterschied zu den bekannten Literaturbeispielen mit  $\text{Cr}^{3+} \rightarrow \text{Nd}^{3+}$ -Dexter-Energietransfer erfolgt der Energietransfer wegen des recht großen räumlichen Abstands der Metallzentren in **3-Nd** durch den Förster-Mechanismus.

### 5.2.2.2 Optische Eigenschaften von molekularen Chrom-Terbium- und Chrom-Europium-Salzen

Lumineszente Lanthanoid-Komplexe von  $\text{Eu}^{3+}$  und  $\text{Tb}^{3+}$  werden seit einigen Jahren wegen ihrer oft intensiven Emission im sichtbaren Wellenlängenbereich ( $\text{Eu}^{3+}$ :  $\lambda_{\text{em}} \approx 620 \text{ nm}$  und  $\text{Tb}^{3+}$ :  $\lambda_{\text{em}} \approx 550 \text{ nm}$ ) ausgiebig untersucht.<sup>[107]</sup> Kombiniert man diese  $\text{Eu(III)}$ - und  $\text{Tb(III)}$ -Luminophore mit  $\text{Cr(III)}$ -Emittern in polymetallischen Verbindungen, so kann in einigen Fällen  $\text{Ln}^{3+} \rightarrow \text{Cr}^{3+}$ -Energietransfer ausgehend von den Sensibilisator-Zuständen  $^5\text{D}_0$  ( $\text{Eu}^{3+}$ ) und  $^5\text{D}_4$  ( $\text{Tb}^{3+}$ ) auf die  $^2\text{E}/^2\text{T}_1$ -Akzeptorniveaus der  $\text{Cr}^{3+}$ -Ionen beobachtet werden (Kapitel 5.1.1, Abb. 51).<sup>[24]</sup> Die Arbeitsgruppe um Sobolev untersuchte diese Energietransferprozesse in Festkörpermateriale, bei welchen sie die anionischen  $[\text{Ln}(\text{dpa})_3]^{3-}$ -Komplexionen von  $\text{Eu}^{3+}$  und  $\text{Tb}^{3+}$  mit verschiedenen dreifach kationischen, lumineszenten  $\text{Cr(III)}$ - und  $\text{Co(III)}$ -Komplexen in einem molekularen Salz kombinierten.<sup>[141]</sup> In den untersuchten  $\text{ÜM}^{3+}/\text{Ln}^{3+}$ -Paaren wurde nach Laseranregung der  $\text{Ln}^{3+}$ -Ionen die sonst langlebige ( $\tau \approx 2 \text{ ms}$ ) und intensive Emission von  $[\text{Eu/Tb}(\text{dpa})_3]^{3-}$  aufgrund des sehr effektiven  $\text{Ln}^{3+} \rightarrow \text{Cr}^{3+}$ -Energietransfer fast vollständig gelöscht. Es wurde also nur noch schwache Emission und stark verkürzte Lumineszenzlebensdauern beobachtet.

Die ionischen Festkörper **3-Eu** und **3-Tb** sind ebenfalls aus einem  $[\text{Eu/Tb}(\text{dpa})_3]^{3-}$ -Anion und einem kationischen  $\text{Cr(III)}$ -Komplex als Gegenstück aufgebaut. Allerdings weist das  $[\text{Cr}(\text{ddpd})_2]^{3+}$ -Komplekation in **3-Eu** und **3-Tb** wesentlich höhere Quantenausbeuten und Lumineszenzlebensdauern der Spin-Flip-Zustände auf, welche zudem um ca.  $2000 \text{ cm}^{-1}$  energetisch tiefer liegen. Diese Tatsache hat beispielsweise zur Folge, dass der Energieabstand zwischen dem emittierenden  $^5\text{D}_0$ -Zustand von  $\text{Eu}^{3+}$  und den emittierenden Spin-Flip-Zuständen  $^2\text{E}/^2\text{T}_1$  in **3-Eu** größer ist als in den  $\text{Cr}^{3+}/\text{Eu}^{3+}$ -Festkörpern aus der Literatur.

Anregung von festem **3-Eu** über den Antennenliganden **dpa** mit  $\lambda_{\text{exc}} = 275 \text{ nm}$  bei Raumtemperatur führt zum Auftreten von intensiver  $\text{Eu}^{3+}$ -Emission mit den charakteristischen Emissionsbanden bei  $\lambda_{\text{em}} = 593, 616$  und  $690 \text{ nm}$  (Abb. 62). Der 0-0-Übergang ( $^5\text{D}_0 \rightarrow ^7\text{F}_0$ ) sowie der  $^5\text{D}_0 \rightarrow ^7\text{F}_3$  Übergang werden auch beobachtet, sind aber sehr viel intensitätsschwächer. Dagegen kann unter diesen Bedingungen keine Chrom-Emission beobachtet werden. Wechselt man die Anregungswellenlänge auf  $\lambda_{\text{exc}} = 435 \text{ nm}$ , regt also in die  $^4\text{A}_2 \rightarrow ^4\text{T}_2$  Bande des  $\text{Cr}^{3+}$ -Ions an, tritt ausschließlich Spin-Flip-Emission bei ca.  $\lambda_{\text{em}} = 774 \text{ nm}$  von  $[\text{Cr}(\text{ddpd})_2]^{3+}$  auf (Abb. 62, unten).



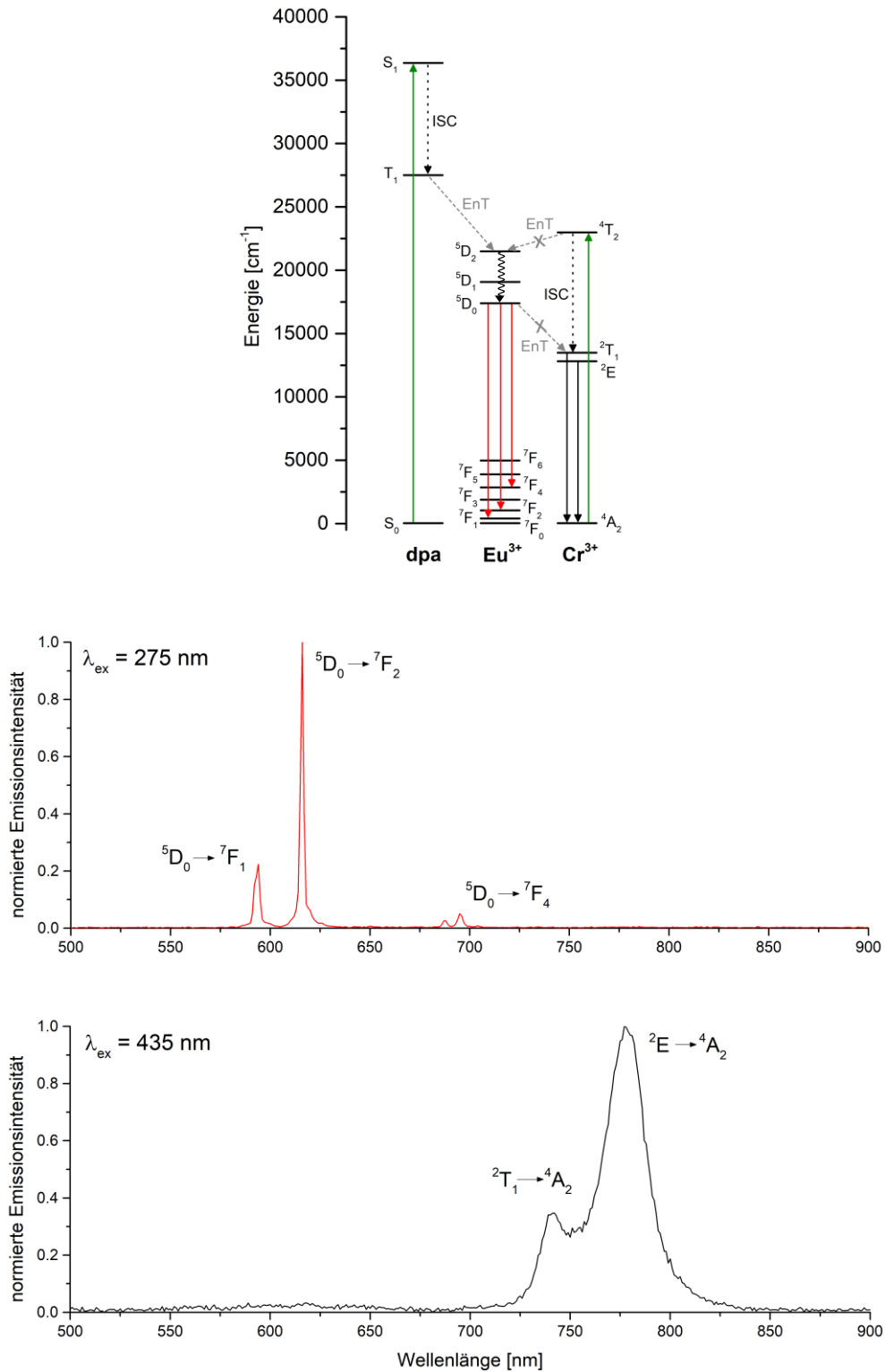


**Abb. 62:** Oben: Schematische Darstellung des vereinfachten Energiediagramms von **3-Eu** mit den Energiezuständen von Eu<sup>3+</sup> und Cr<sup>3+</sup> und des **dpa**-Liganden. Grüne Pfeile nach oben stehen für Anregung, Pfeile nach unten für Emission, gepunktete Pfeile für ISC, gestrichelte Pfeile für Energietransfer und ein gewellter Pfeil für internal conversion. Unten: Normierte Steady-State-Emissionsspektren von **3-Eu** nach Anregung mit λ<sub>exc</sub> = 275 nm (oben) und λ<sub>exc</sub> = 435 nm (unten) im Festkörper bei T = 298 K an Luft.

Die Steady-State Emissionsspektren von **3-Eu** weisen daher darauf hin, dass unter den gewählten Bedingungen kein Energietransfer zwischen den beiden Metallzentren stattfindet (Abb. 62, oben). Um diese Annahme mit weiteren Daten zu untermauern, wurden zeitaufgelöste Lumineszenzmessungen unter gleichen Bedingungen durchgeführt (Tab. 10). Die Lebensdauer der  $\text{Eu}^{3+}$ -Emission zeigt eine monoexponentielle Zerfallskinetik und beträgt  $\tau = 1.7$  ms. Das Profil der Lebensdauer der  ${}^2\text{E}/{}^2\text{T}_1$ -Emission von **3-Eu** zerfällt biexponentiell und ist  $\tau = 295$   $\mu\text{s}$  (15 %) und 718  $\mu\text{s}$  (85 %) lang. Damit sind die gemessenen Lebensdauern im Rahmen der Messunsicherheit identisch mit denen, die für das Natrium-Salz **1-Eu** und die Referenzverbindung **3-Lu** (Tab. 10) bestimmt wurden. Dieser Befund bestätigt, dass sehr wahrscheinlich kein  $\text{Eu}^{3+} \rightarrow \text{Cr}^{3+}$ -Energietransfer stattfindet. Dies ist ein zentraler Unterschied zur Photophysik der strukturell verwandten  $\text{Eu}^{3+}/\text{Cr}^{3+}$ -Salze von Sobolev.<sup>[141]</sup> Da in beiden Europium-Chrom-Architekturen die Metallzentren räumlich voneinander getrennt sind, würde auch in beiden System der Energietransfer zwischen den Metallzentren durch den Förster-Mechanismus dominiert werden. Allerdings sind im kristallinen Festkörper von **3-Eu** die  $\text{Eu} \cdots \text{Cr}$ -Abstände ( $r_{\text{Cr-Eu}} \approx 9.0$  Å) im Vergleich zu den Metall-Metall-Abständen der ionischen Festkörpern aus der Literatur ( $r_{\text{Co-Eu}} \approx 7.4$  Å) größer, was sich negativ auf den stark abstandsabhängigen EnT auswirken könnte. Zudem liegen wie bereits erwähnt, die  ${}^2\text{E}/{}^2\text{T}_1$ -Zustände des **[Cr(ddpd)<sub>2</sub>]<sup>3+</sup>**-Komplexions in **3-Eu** ca. 2000  $\text{cm}^{-1}$  tiefer, woraus ein größerer Abstand  $\Delta E({}^5\text{D}_0 - {}^2\text{E}/{}^2\text{T}_1)$  resultiert und das Auftreten von resonanten Energietransfer ebenfalls erschweren sollte. Eine Übersicht der relevanten Prozesse ist in Abb. 62 oben dargestellt. Vermutlich sind die ablaufenden Mechanismen aber wesentlich komplizierter als in diesem vereinfachten Schema gezeigt. So wäre es beispielsweise durchaus vorstellbar, dass bei energiereicher Anregung im UV auch die Ligandzustände des **ddpd**-Liganden oder energetisch höhere liegende metallzentrierte Zustände des  $\text{Cr}^{3+}$ -Ions an Energietransferprozessen beteiligt sein könnten. Um die ablaufenden Mechanismen näher zu beleuchten, sind weitere spektroskopische Untersuchungen nötig, die im Rahmen dieser Arbeit aber nicht durchgeführt werden konnten.

**Tab. 10:** Lumineszenzlebensdauern  $\tau$  der Komponenten **3-Ln** (Ln = Eu, Tb, Lu) und **1-Ln** (Ln = Eu, Tb) im Festkörper bei T = 298 K unter Umgebungsatmosphäre.

Verbindung	$\tau$ (774 nm) [ $\mu\text{s}$ ] <sup>a</sup> ${}^2T_1/{}^2E \rightarrow {}^4A_2$	$\tau$ (616 nm) [ms] <sup>b</sup> ${}^5D_0 \rightarrow {}^7F_2$	$\tau$ (545 nm) [ $\mu\text{s}$ ] <sup>b</sup> ${}^5D_4 \rightarrow {}^7F_5$
<b>3-Eu</b>	295 (15 %) 718 (85 %)	1.7	-
<b>3-Tb</b>	219 (33 %) 464 (64 %) 50 (3 %)	-	nicht messbar
<b>3-Lu</b>	280 (11 %) <sup>[148]</sup> 660 (89 %)	-	-
<b>1-Eu</b>	-	1.8 <sup>[158]</sup>	-
<b>1-Tb</b>	-	-	1.3 <sup>[158]</sup>

<sup>a</sup> $\lambda_{\text{exc}} = 430$  nm, Lebensdauern wurden bi- oder triexponentiell angepasst, die Prozentangaben in den Klammern geben die relative Amplituden der Komponenten an (Anhang, Fig. 14+16).

<sup>b</sup> $\lambda_{\text{exc}} = 280$  nm, Lebensdauern wurden monoexponentiell angepasst (Anhang, Fig. 15).

Im nächsten Schritt wurden in analoger Weise die Lumineszenzeigenschaften von **3-Tb** untersucht. Regt man festes **3-Tb** über den **dpa**-Liganden mit  $\lambda_{\text{exc}} = 275$  nm bei Raumtemperatur an, kann man neben einer sehr schwachen Tb<sup>3+</sup>-Emission hauptsächlich Emission aus den  ${}^2E/{}^2T_1$ -Zuständen des Chromzentrums beobachten (Abb. 63, oben). Im Gegensatz zur langlebigen und intensiven grünen Emission von **1-Tb**, kommt es in **3-Tb** zu einer effektiven strahlungslosen Deaktivierung des emissiven  ${}^5D_4$ - Zustands, wahrscheinlich durch  ${}^5D_4 \rightarrow {}^2T_1/{}^2E$ -Downshifting-EnT auf das Cr<sup>3+</sup>-Ion (Abb. 64). Da **1-Cr** aber mit  $\lambda_{\text{exc}} = 275$  nm grundsätzlich auch angeregt werden könnte, ist das Auftreten der Chrom-Emission in **3-Tb** noch kein stichfester Beweis für diese Annahme. Die selektive Anregung bei  $\lambda_{\text{exc}} = 435$  nm in den Ligandenfeldzustand  ${}^4T_2$  des Cr<sup>3+</sup>-Komplexions führt ausschließlich zum Auftreten der Spin-Flip-Emission von **[Cr(ddpd)<sub>2</sub>]<sup>3+</sup>** (Abb. 63, unten). Dies weist darauf hin, dass es vermutlich keinen EnT zwischen dem Ligandenfeldzustand  ${}^4T_2$  von Cr<sup>3+</sup> und des  ${}^5D_4$ -Zustand von Tb<sup>3+</sup> gibt (Abb. 64).

Die Lebensdauer der sehr schwachen Tb<sup>3+</sup>-Emission in **3-Tb** konnte experimentell nicht bestimmt werden. Es ist aber davon auszugehen, dass die Lebenszeit des  ${}^5D_4$ -Zustands sehr viel kürzer als die entsprechende Lebensdauer in **1-Tb** ist (Tab. 10). Die Zerfallskinetik der  ${}^2E$ -Emission lässt sich triexponentiell anpassen und weist daher auf die Beteiligung von mindestens drei unterschiedlichen Übergängen und damit auf eine recht komplizierte Photophysik hin. Die Lebensdauern der beiden dominierenden

Komponenten betragen  $\tau = 219 \mu\text{s}$  (33 %) und  $\tau = 464 \mu\text{s}$  (64 %) und weichen damit nur geringfügig von den Lebensdauern der  ${}^2\text{E}/{}^2\text{T}_1$ -Emission von **3-Lu** ab (Tab. 10). Es kann daher geschlossen werden, dass es zu keiner weiteren wesentlichen strahlungslosen Deaktivierung beispielsweise durch Energietransfer auf das  $\text{Tb}^{3+}$ -Komplexion kommt. Nichtsdestotrotz könnte die verkürzte Lebenszeitkomponente von  $\tau = 50 \mu\text{s}$  (3 %) eventuell auf die geringe Beteiligung eines Energietransfers von den Spin-Flip-Zuständen in eines der  ${}^7\text{F}_x$ -Unterniveaus des  $\text{Tb}^{3+}$ -Grundzustands hindeuten, welcher bereits in der Literatur für polymetallische Ln-Cr-Koordinationsverbindungen beschrieben wurde.<sup>[24]</sup>

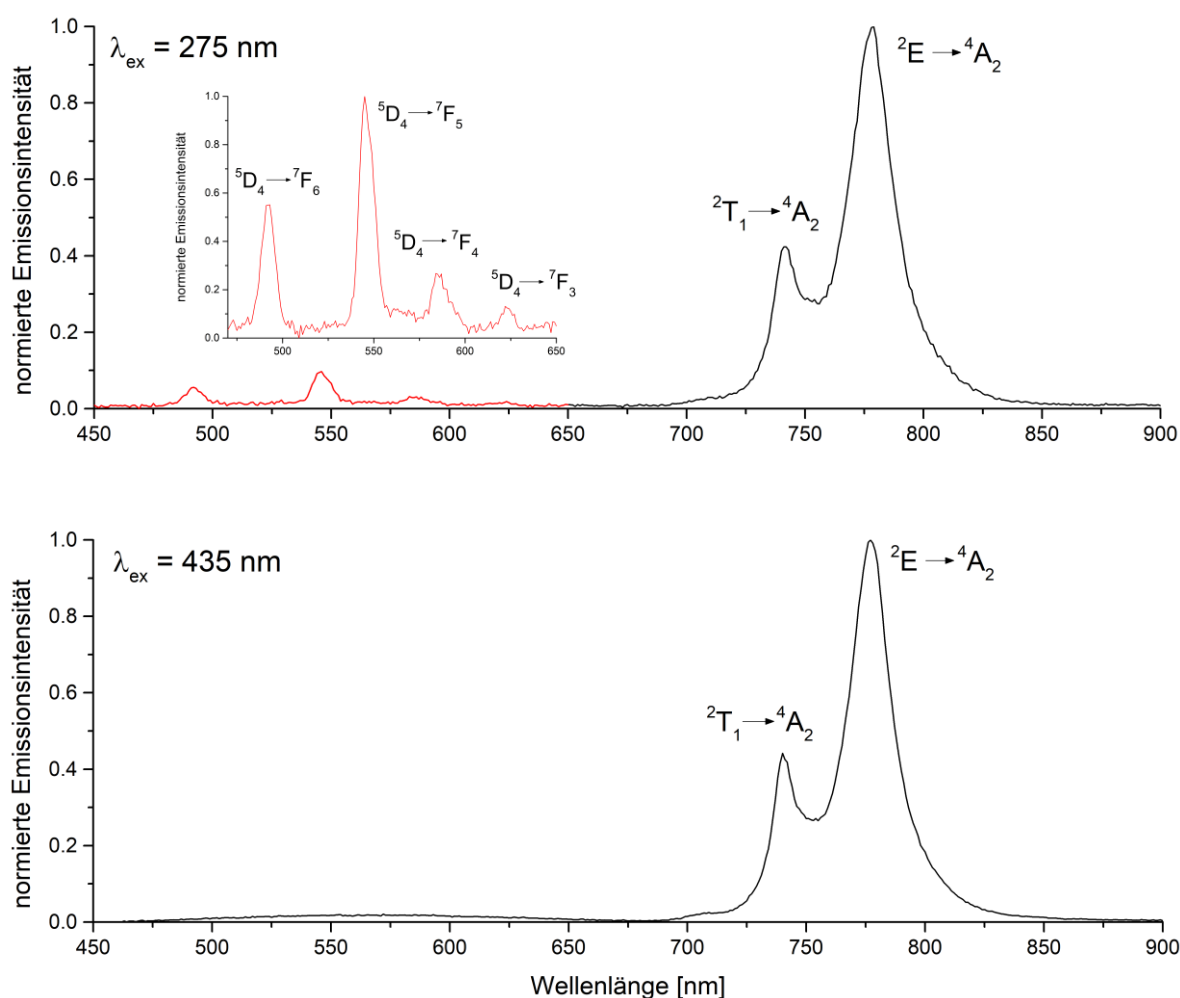


**Abb. 63:** Normierte Steady-State-Emissionsspektren von **3-Tb** nach Anregung mit  $\lambda_{\text{exc}} = 275 \text{ nm}$  (oben) und  $\lambda_{\text{exc}} = 435 \text{ nm}$  (unten) im Festkörper bei  $T = 298 \text{ K}$  an Luft.

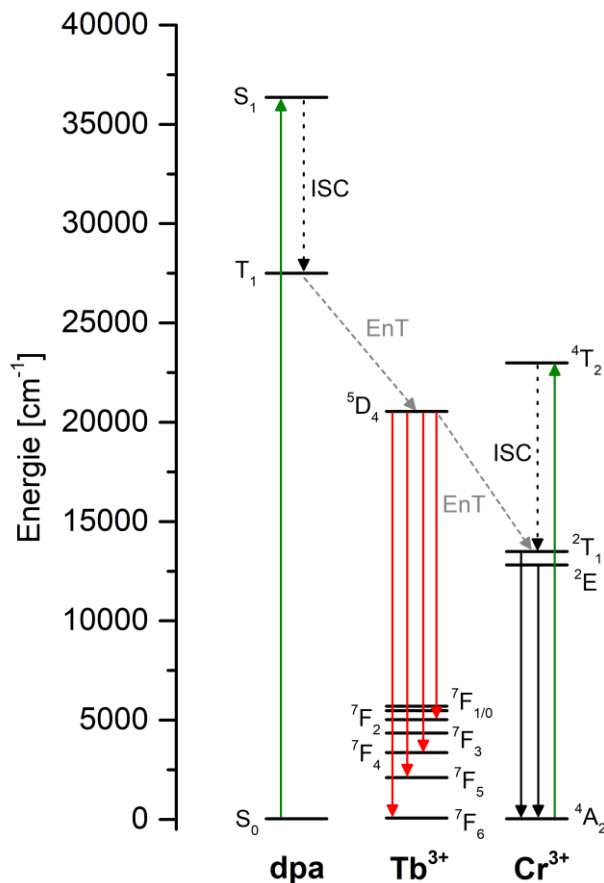


**Abb. 64:** Schematische Darstellung des vereinfachten Energiediagramms von **3-Tb** mit den Energiezuständen von  $Tb^{3+}$  und  $Cr^{3+}$  und des **dpa**-Liganden. Grüne Pfeile nach oben stehen für Anregung, Pfeile nach unten für Emission, gepunktete Pfeile für ISC und gestrichelte Pfeile für Energietransfer.

Zusammengefasst konnte in den ionischen Festkörpern **3-Eu** und **3-Tb** das Auftreten von  $Ln^{3+} \rightarrow Cr^{3+}$ -Energietransfer untersucht werden. In **3-Eu** führt die Anregung des **dpa**-Liganden ausschließlich zu intensiver  $Eu^{3+}$ -Emission, während nach Anregung in den Ligandenfeldzustand  ${}^4T_2$  des Chrom(III)-Komplexions nur Spin-Flip-Emission bei etwa  $\lambda_{em} = 780 \text{ nm}$  beobachtet werden kann. Durch Messung der Lumineszenzlebensdauern konnte bestätigt werden, dass kein messbarer EnT zwischen den Metallzentren stattfindet. So besitzt das photonische Material **3-Eu** die interessante Eigenschaft, je nach gewählter Anregungswellenlänge selektiv im sichtbaren ( $\lambda_{ex} = 275 \text{ nm} \rightarrow \lambda_{em} \approx 616 \text{ nm}$ ) oder im NIR-Spektralbereich ( $\lambda_{ex} = 435 \text{ nm} \rightarrow \lambda_{em} \approx 780 \text{ nm}$ ) zu emittieren. Im Unterschied dazu findet in **3-Tb** nach Anregung des **dpa**-Liganden effektiver  ${}^5D_4(Tb^{3+}) \rightarrow {}^2T_1/{}^2E(Cr^{3+})$ -Downshifting-EnT statt, was zu einer fast vollständigen Löschung der  $Tb^{3+}$ -Emission führt.

## 6 Ein neues hexadentates Ligandensystem für Spin-Flip-Luminophore (unveröffentlichte Ergebnisse)

Bei der Entwicklung von intensiv lumineszierenden Spin-Flip-Luminophoren der 3d-Übergangsmetalle, insbesondere mit Cr(III)- und V(III)-Metallionen, spielt das Ligandensystem eine entscheidende Rolle. Wie in Kapitel 3.1.1. erläutert, sollte der eingesetzte Ligand folgende Voraussetzungen erfüllen:

- $\sigma$ -Donorstärke: Um effiziente Phosphoreszenz aus den Spin-Flip-Zuständen zu gewährleisten ist eine große Ligandenfeldaufspaltung entscheidend, um thermische Rückpopulation in die Ligandenfeldzustände zu verhindern. Für diesen Zweck haben sich in der Vergangenheit vor allem pyridinbasierte Liganden mit einem relativ starken  $\sigma$ -Donor und schwachen  $\pi$ -Akzeptor-Charakter bewährt. Insbesondere starke  $\pi$ -Donoren sind für Einsatz in Spin-Flip-Emittern ungeeignet.
- Große Bisswinkel: Um die Metall-Ligand-Orbitalüberlappung zu optimieren und so die Ligandenfeldaufspaltung zu vergrößern, haben sich mehrzählige Liganden mit großen Bisswinkeln (idealerweise  $90^\circ$ ) bewährt, die eine nahezu perfekt oktaedrische Komplexgeometrie erlauben.
- Rigidität: Ein in Cr(III)-Luminophoren häufig beobachtetes Phänomen ist die strahlungslose Deaktivierung durch Kreuzung der Potentialhyperflächen des Ligandenfeldzustands  ${}^4T_{2g}$  mit dem  ${}^4A_{2g}$ -Grundzustand (*surface crossing*, Kapitel 4.1.1). Dieser Deaktivierungspfad tritt häufig in trigonal verzerrten Komplexen auf, bei welchen durch Symmetrierniedrigung die Entartung der d-Orbitale aufgehoben wird. Dadurch verkleinern sich die Abstände zwischen den elektronischen Zuständen (z.B. bei  $Cr^{3+}$  zwischen  ${}^4T_{2g}$  und  ${}^4A_{2g}$ ), wodurch das Schneiden der Potentialhyperflächen benachbarter Zustände sehr wahrscheinlich wird.<sup>[38]</sup> Um diesen Prozess zu vermeiden, sollte das Ligandensystem rigide sein und zusätzlich eine möglichst ideal oktaedrische Umgebung um das Metallzentrum ermöglichen.

Die Zielsetzung dieses Projekts bestand darin, einen neuen Liganden für Spin-Flip-Luminophore zu entwickeln, welcher die oben genannten Voraussetzungen erfüllt. Ausgangspunkt der Suche war dabei der **ddpd**-Ligand, welcher im **[Cr(ddpd)<sub>2</sub>]<sup>3+</sup>**-Komplex die ausgezeichneten Lumineszenzeigenschaften verantwortlich ist. Der Zielligand sollte die vorteilhaften Eigenschaften von **ddpd** aufweisen, aber zusätzlich noch rigider sein. Das Ergebnis des Ligandendesigns ist der Ligand **L1** (Abb. 65). Der hexadentate Ligand **L1** enthält drei **dpma**-Einheiten (**dpma** = di(pyrid-2-yl)(methyl)amin), welche durch eine Tris(2-aminoethyl)amido-„Kappe“ miteinander verbunden sind. Die hohe Zähigkeit von **L1** sollte dabei die Bildung eines möglichst rigiden und stabilen Cr(III)-Komplexes fördern. Die N-Methyl-Brücke zwischen den Pyridinen sollte, analog zum **ddpd**-Liganden, zum einen die Elektronendichte und damit auch die  $\sigma$ -Donor-Stärke erhöhen und zum anderen für einen ausreichend großen Bisswinkel sorgen, um eine möglichst ideal oktaedrische Umgebung der Cr<sup>3+</sup>-Ionen zu ermöglichen.

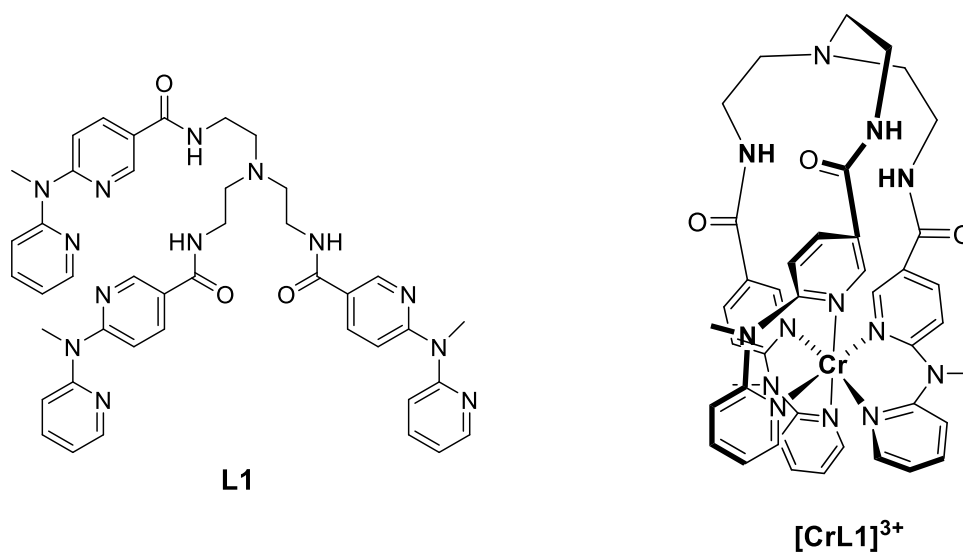


**Abb. 65:** Strukturformeln der Zielverbindungen: Ligand **L1** und der entsprechende Cr(III)-Komplex **[CrL1]<sup>3+</sup>**.

Die Syntheseroute von **L1** (Abb. 66) beinhaltet fünf Stufen und beginnt mit der Oxidation von kommerziell erhältlichen Methylnicotinat **14** mit *m*-CPBA zum Methylnicotinat-N-Oxid **15** (Ausbeute: 82 %). Im nächsten Schritt kann das erhaltene N-Oxid **15** mithilfe von PyBroP in einer milden Aminierungsreaktion mit 2-Aminopyridin

zum Amin **16** umgesetzt werden.<sup>[159]</sup> Nach säulenchromatographischer Aufarbeitung konnte das Amin **16** mit einer akzeptablen Ausbeute von 45 % erhalten werden. Dabei bieten die sehr milden Reaktionsbedingungen den Vorteil, dass die Reaktion auch zur Synthese des deuterierten, isotopologen Liganden potentiell gut geeignet ist. Die Methylierung desamins **16** erfolgt anschließend mit CH<sub>3</sub>I und der nicht nukleophilen Base NaH.

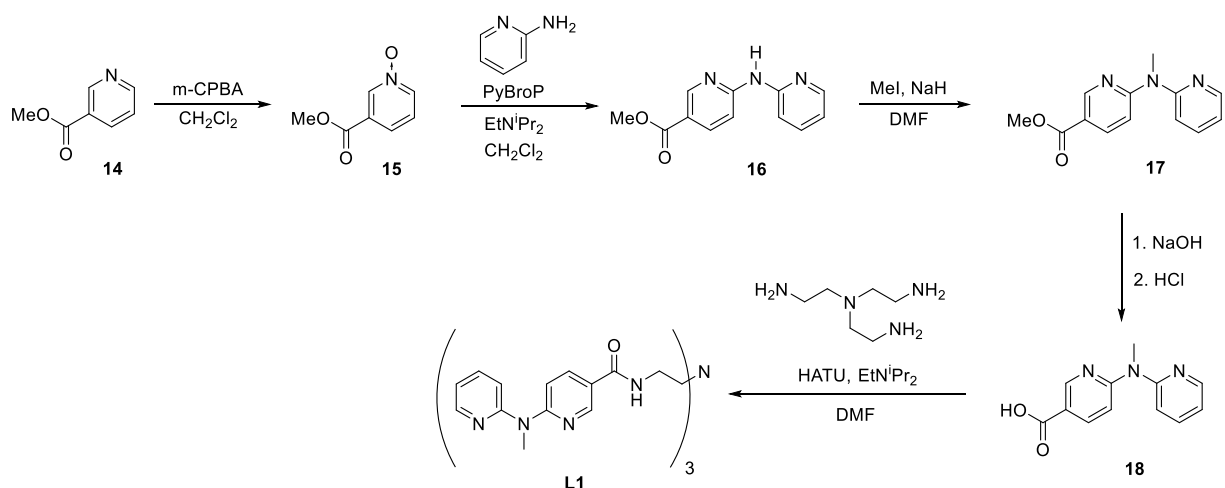


**Abb. 66:** Durchgeführte Syntheseroute zu Darstellung des Liganden **L1**.

Die Verwendung einer nicht nukleophilen Base ist dabei wichtig, um einen nukleophilen Angriff an den Ester zu vermeiden. Nach säulenchromatographischer Reinigung konnte Verbindung **17** mit einer guten Ausbeute von 78 % erhalten werden. Durch Verseifen des Methylrestes **17** mit NaOH und anschließender Protonierung mit wässriger HCl konnte die Carbonsäure **18** mit einer Ausbeute von 75 % dargestellt werden.

Im letzten Schritt konnten in einer HATU<sup>[160]</sup> vermittelten Peptidkupplungsreaktion die drei Amidbindungen zwischen den Aminfunktionen der TREN-„Kappe“ (TREN = Tris(2-aminoethyl)amin) und der Carboxygruppe der **dpma**-Einheiten geknüpft werden. Durch Verwendung von Diisopropylethylamin (DIPEA) als Base und dem Einsatz von 3.5 Äquivalenten der Carbonsäure **18** konnte der Zielligand **L1** in hervorragenden Ausbeuten von 92 % erhalten werden.

In Abb. 67 ist das <sup>1</sup>H-NMR-Spektrum von **L1** in deuteriertem DMSO gezeigt. Erwartungsgemäß erhält man aufgrund der C<sub>3</sub>-Symmetrie für die **dpma**-Ärmchen nur einen Signalsatz. Die Signale der Ethylengruppen bei ca. 3.4 und 2.7 ppm sind im Spektrum recht breit. Dies liegt vermutlich an der leicht eingeschränkten Rotation der



Ethylenprotonen, wodurch diese nicht mehr vollständig magnetisch äquivalent sind. Zusätzlich wurde **L1** mit  $^1\text{H}$ - $^{13}\text{C}$  HSQC-NMR-Spektroskopie (Anhang, Fig. A1) sowie massenspektrometrisch charakterisiert.

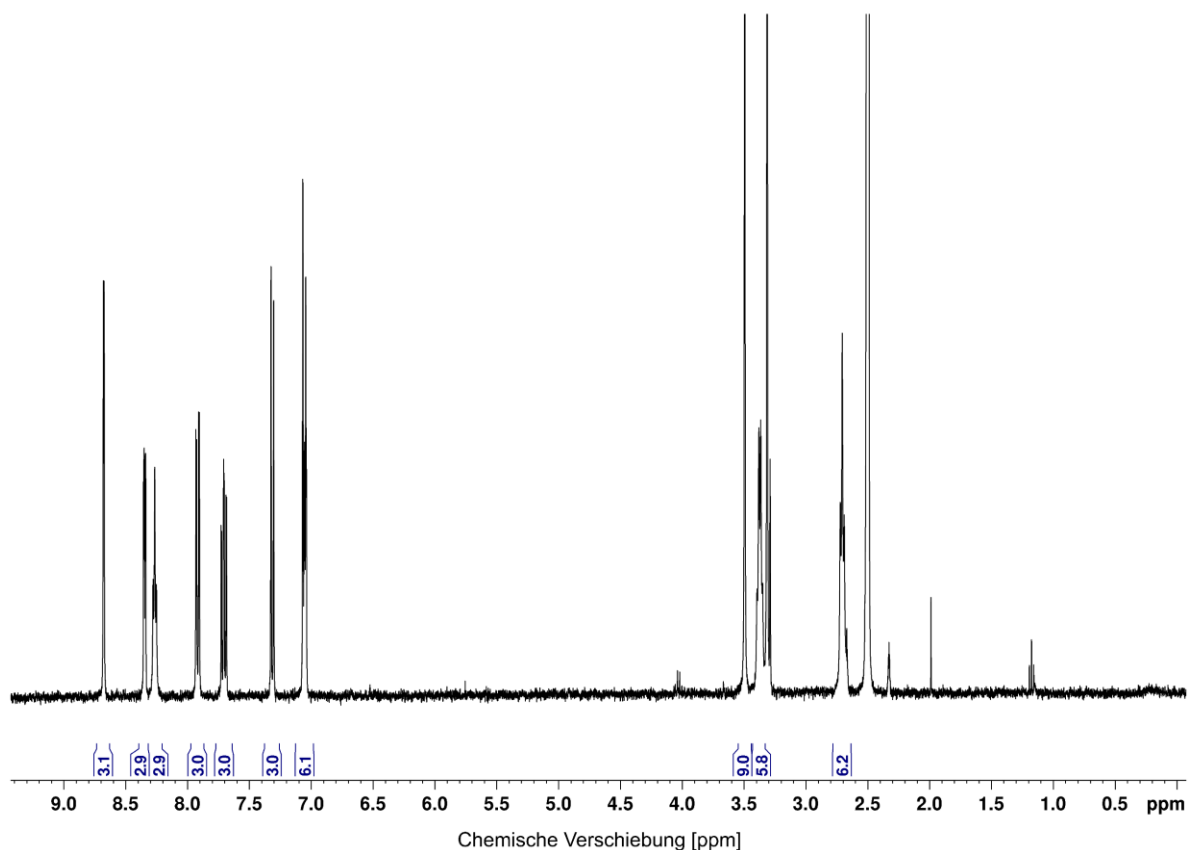


**Abb. 67:**  $^1\text{H}$ -NMR-Spektrum (400 MHz,  $\text{DMSO-d}_6$ ) des Liganden **L1**.

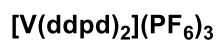
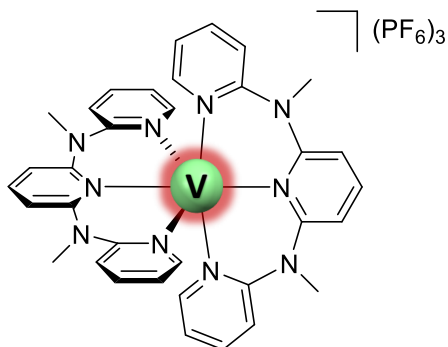
Nach erfolgreicher Darstellung von **L1** sollte im nächsten Schritt die Synthese des  $[\text{CrL1}]^{3+}$ -Komplexes erfolgen (Abb. 65, rechts). Die etablierte Syntheseroute zur Darstellung von homoleptischen pyridinbasierten Cr(III)-Komplexen ist die Umsetzung des Liganden mit labilem  $\text{CrCl}_2$  in Acetonitril und anschließender Oxidation mit Luftsauerstoff zum inerten Cr(III)-Komplex. Nach Austausch der Chlorid-Gegenionen durch schwach koordinierende Anionen wie  $\text{BF}_4^-$  oder  $\text{PF}_6^-$  und anschließender Kristallisation aus  $\text{CH}_3\text{CN}/\text{Et}_2\text{O}$ -Mischungen können die Chromkomplexe oft sauber und in soliden Ausbeuten erhalten werden.<sup>[35,36]</sup> Die Umsetzung von **L1** mit  $\text{CrCl}_2$  führte allerdings nicht zum Zielkomplex  $[\text{CrL1}]^{3+}$ . Stattdessen konnte nach der Aufarbeitung lediglich  $\text{CrCl}_3$  und nicht umgesetzter Ligand isoliert werden. Da **L1** nach der Reaktion unzersetzt vorliegt, kann das Reduktionsvermögen von  $\text{CrCl}_2$  als mögliches Problem vernachlässigt werden. Als etwaiger Grund für die nicht erfolgte Bildung des

Zielkomplexes wurde identifiziert, dass unter den genannten Reaktionsbedingungen Ligand **L1** nicht in der Lage ist die an Chrom gebundenen Chlorid-Liganden zu verdrängen. Um die Chloridabstraktion zu erleichtern, wurde bei der Umsetzung von **L1** mit  $\text{CrCl}_2$  zusätzlich  $\text{AgPF}_6$  zugegeben um die hohe Affinität von  $\text{Ag}^+$  für Chlorid-Ionen und das niedrige Löslichkeitsprodukt von  $\text{AgCl}$  in Acetonitril ( $K_L(\text{AgCl}) = 10^{-12}$ )<sup>[161]</sup> auszunutzen. Als diese Strategie ebenfalls nicht erfolgreich war, wurden in einer alternativen Herangehensweise verschiedene labile, chloridfreie Chromvorstufen ( $[\text{Cr}(\text{CF}_3\text{SO}_3)_2](\text{CH}_3\text{CN})_2$ ,<sup>[162]</sup>  $[\text{Cr}(\text{CH}_3\text{CN})_4](\text{BF}_4)_2$ <sup>[163]</sup>) mit **L1** umgesetzt. Auch hier konnten lediglich in gängigen Lösungsmitteln unlösliche, grün/gräuliche Feststoffe isoliert werden. Dies ist ein Indiz für die Bildung von polymeren Produkten, was aufgrund der Struktur von **L1** durchaus auch plausibel scheint. Die Verwendung von Cr(III)-Vorstufen führte ebenfalls nicht zur Bildung des gewünschten Produkts. Zusammengefasst konnte erfolgreich das neue hexadentate Ligandsystem **L1** synthetisiert und mit NMR- und Massenspektrometrie charakterisiert werden. Die Darstellung des entsprechenden Chrom(III)-Komplex war hingegen nicht möglich, weshalb dieses Projekt nicht weiter verfolgt wurde.

## 7 Zusammenfassung

In dieser Arbeit wurden verschiedene wichtige Ziele auf dem Forschungsgebiet der molekularen Cr(III)- und V(III)-Luminophore erreicht:

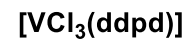
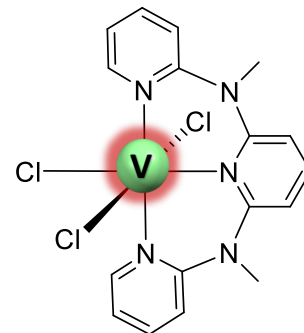
### Lumineszente V(III)-Komplexe



$\lambda_{em} = 396 \text{ nm}$   
 $\tau_1 = 3.2 / 8.2 \text{ ns (56 / 44 \%)}$   
 $\Phi = 2 \%$



$\lambda_{em} = 1109/1123 \text{ nm}$   
 $\tau_2 = 0.8 / 8.8 \text{ }\mu\text{s (93 / 7 \%)}$   
 $\Phi = 2 \times 10^{-4} \%$



$\lambda_{em} = 1106/1222 \text{ nm}$   
**[D<sub>0</sub>]:**  $\tau = 0.5 \text{ }\mu\text{s}$   
**[D<sub>17</sub>]:**  $\tau = 3.3 \text{ }\mu\text{s}$

**Abb. 68:** Übersicht der neu entwickelten d<sup>2</sup>-V(III)-Luminophore und deren photophysikalische Kernparameter. **[V(ddpd)<sub>2</sub>](PF<sub>6</sub>)<sub>3</sub>**: Die Lebenszeit  $\tau_1$  und die Quantenausbeuten  $\Phi$  wurden in entgasten CD<sub>3</sub>CN-Lösungen bei T = 298 K und  $\tau_2$  in entgasten n-Valeronitril bei T = 77 K bestimmt. **[VCl<sub>3</sub>(ddpd)]**: Die Lebenszeiten wurden im Festkörper unter Argon bei T = 298 K gemessen.

- Konzeption und Darstellung lumineszenter  $d^2$ -V(III)-Komplexe **[V(ddpd)<sub>2</sub>](PF<sub>6</sub>)<sub>3</sub>** und **[VCl<sub>3</sub>(ddpd)<sub>2</sub>]** und deren perdeuterierte Analoga
- Umfassende Charakterisierung der optischen Eigenschaften der synthetisierten Vanadiumkomplexe mittels Absorptions- und Lumineszenzspektroskopie im sichtbaren und NIR-Spektralbereich, sowie Bestimmung der Lumineszenzlebenszeiten und Quantenausbeuten
- Korrelation der spektroskopischen Ergebnisse mit den zugrundeliegenden elektronischen Zuständen, gestützt durch Quantenchemische-Rechnungen
- Beurteilung des Einflusses von Multiphonon Relaxation auf die NIR-Lumineszenz von **[V(ddpd)<sub>2</sub>](PF<sub>6</sub>)<sub>3</sub>** und **[VCl<sub>3</sub>(ddpd)<sub>2</sub>]** durch Messung der Phosphoreszenzlebenszeiten isotopologer V(III)-Komplexe und Quantifizierung des potentiellen Einflusses der Liganddeuterierung
- Durch Untersuchen von wichtigen Eigenschaften wie der Intersystem Crossing-Effizienz, Grundzustandsaufspaltung und der Photostabilität konnten wertvolle Erkenntnisse für Entwicklung von neuen Vanadiumluminophoren gewonnen werden

Im Rahmen dieser Arbeit war es möglich die bekannten lumineszenten Metallkomplexe mit 3d-Übergangsmetallionen um das günstige und reichlich verfügbare Metall Vanadium zu erweitern. **[V(ddpd)<sub>2</sub>](PF<sub>6</sub>)<sub>3</sub>** ist dabei der erste 3d<sup>n</sup>-Metallkomplex ( $n \neq 10$ ) überhaupt, welcher NIR-Lumineszenz oberhalb von  $\lambda_{em} = 1000$  nm bei Raumtemperatur und in Lösung zeigt. Diese ersten erfolgreichen Beispiele von  $d^2$ -V(III)-Emitttern eröffnen die Perspektive lumineszente Vanadium-Komplexe in zukünftigen Anwendungen wie beispielsweise in der bildgebenden medizinischen Diagnostik einzusetzen.

## Multiphonon Relaxation

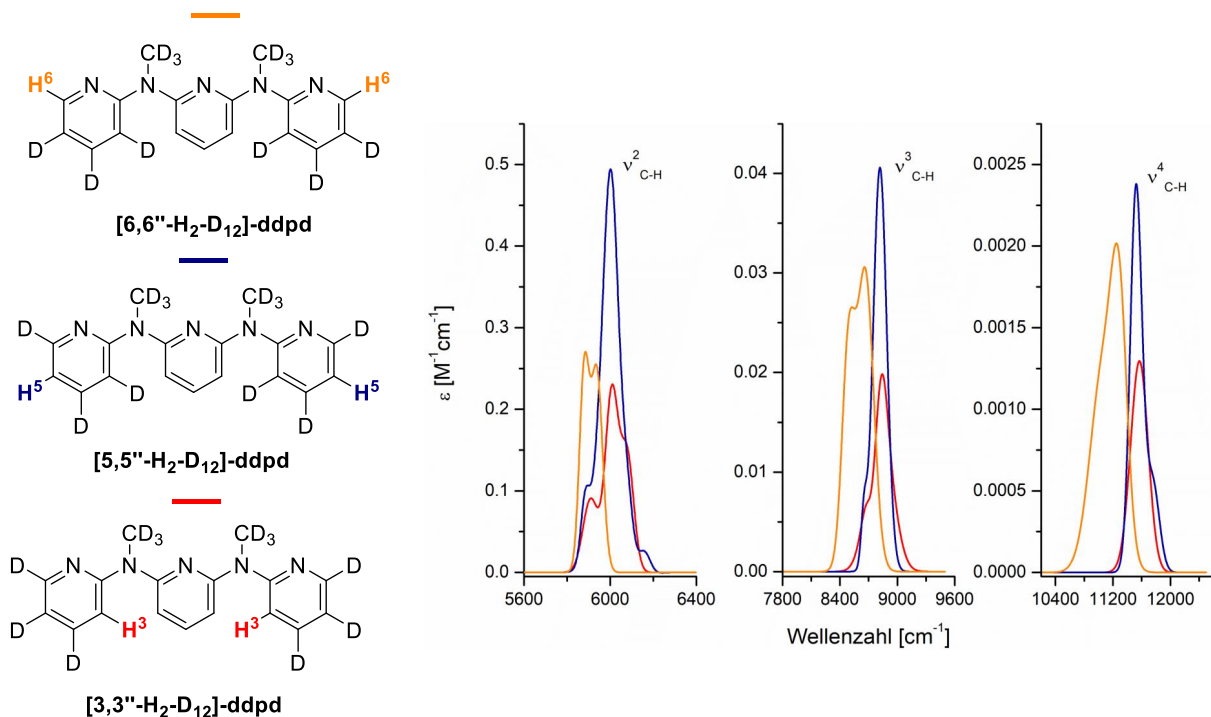


**Abb. 69:** Obertonsignaturen der ersten drei Obertöne ( $v_{\text{C-H}}^2 - v_{\text{C-H}}^4$ ) der aromatischen C-H-Oszillatoren **C-H<sup>6</sup>** (orange), **C-H<sup>5</sup>** (lila) und **C-H<sup>3</sup>** (rot).

- Erfolgreiche Synthese von selektiv deuterierten **ddpd**-Liganden und deren entsprechenden isotopologen und isotopomeren **[Cr(ddpd)<sub>2</sub>]<sup>3+</sup>**-Komplexen
- Messung der Absorptionsbanden der ersten drei C-H-Obertöne der selektiv deuterierten **ddpd**-Liganden und Entwicklung einer Methode zur Extraktion der Obertonsignaturen von einzelnen aromatischen C-H-Oszillatoren
- Bewertung des Beitrags einzelner aromatischer C-H-Oszillatoren zur strahlungslosen Deaktivierung durch Multiphonon Relaxation (MR). Dafür wurden räumliche Abstände zwischen dem Cr<sup>3+</sup>-Zentrum und individuellen C-H-Oszillatoren sowie die spektralen Überlappungsintegrale (SOIs) zwischen der Emissionsbande und individuellen Obertonsignaturen ermittelt. Mittels dieser Daten konnte der Einfluss der spezifischen aromatischen Oszillatoren **C-H<sup>6</sup>**, **C-H<sup>5</sup>** und **C-H<sup>3</sup>** auf die Lumineszenzlebenszeiten der selektiv deuterierten **[Cr(ddpd)<sub>2</sub>]<sup>3+</sup>**-Komplexe quantifiziert werden.

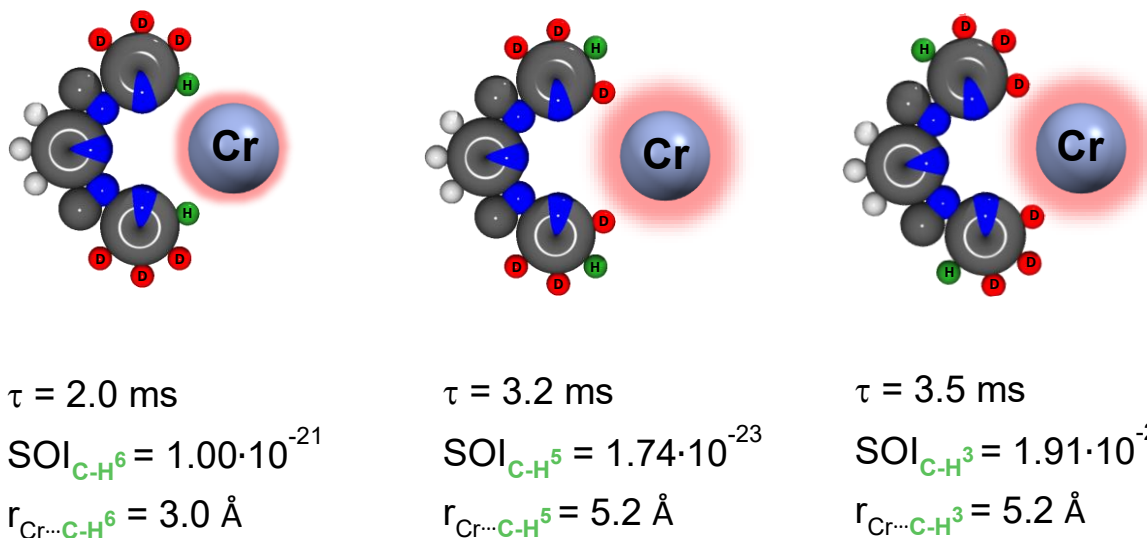


**Abb. 70:** Lumineszenzlebenszeiten  $\tau$  und Cr $\cdots$ CH-Abstände für die selektiv deuterierten **[Cr(ddpd)<sub>2</sub>]<sup>3+</sup>**-Komplexe, sowie die berechneten SOIs der Oszillatoren **C-H<sup>6</sup>**, **C-H<sup>5</sup>** und **C-H<sup>3</sup>** des **ddpd**-Liganden. In dieser schematischen Abbildung wurde auf die Darstellung des zweiten **ddpd**-Liganden verzichtet.

- Quantifizierung des Einflusses der C-H(D)-Obertöne von CH<sub>3</sub>CN und CD<sub>3</sub>CN auf die NIR-Emission des neuen, zentrosymmetrischen **[Cr(tpe)<sub>2</sub>]<sup>3+</sup>**-Komplexes. Durch Zugabe von Perchlorsäure kann die potentiell sehr effektive MR durch solvatisierende Acetonitril-Moleküle verhindert werden, was zu intensiverer Spin-Flip-Emission bei  $\lambda_{\text{em}} = 748 \text{ nm}$  und der sehr langen Lumineszenzlebenszeit von  $\tau = 4500 \text{ }\mu\text{s}$  in D<sub>2</sub>O/DCIO<sub>4</sub>-Lösungen führt.
- Für den neu entwickelten **[Cr(bpmp)<sub>2</sub>]<sup>3+</sup>**-Komplex mit intensiver Spin-Flip-Emission im roten Spektralbereich wurden die C-H(D)-Obertöne des **bpmp**-Liganden quantitativ untersucht, um das Potential für Verbesserungen der photophysikalischen Eigenschaften von **[Cr(bpmp)<sub>2</sub>]<sup>3+</sup>** durch Deuterierung des Liganden auszuloten. Durch selektive Deuterierung der metallnächsten C-H-Obertöne kann dabei die Quantenausbeute von  $\Phi = 20 \%$  auf  $25 \%$  und die Lebenszeit von  $\tau = 1800 \text{ }\mu\text{s}$  auf  $2500 \text{ }\mu\text{s}$  in DCIO<sub>4</sub> / D<sub>2</sub>O-Lösungen gesteigert werden.

Die in dieser Arbeit erzielten Ergebnisse leisten einen wichtigen Beitrag zum allgemeinen Verständnis der strahlungslosen Deaktivierung durch Multiphonon Relaxation bei Spin-Flip-Emittern. Von besonderer Bedeutung dabei ist die im Rahmen dieser Arbeit entwickelte Methode zur Extraktion und Analyse der Obertonsignaturen einzelner aromatischer C-H-Oszillatoren. Dies ist ein Durchbruch auf dem Weg neue und lumineszenterere Spin-Flip-Emitter mit reduzierter MR zu entwickeln, welche interessant für vielfältige optische Anwendungen sind.

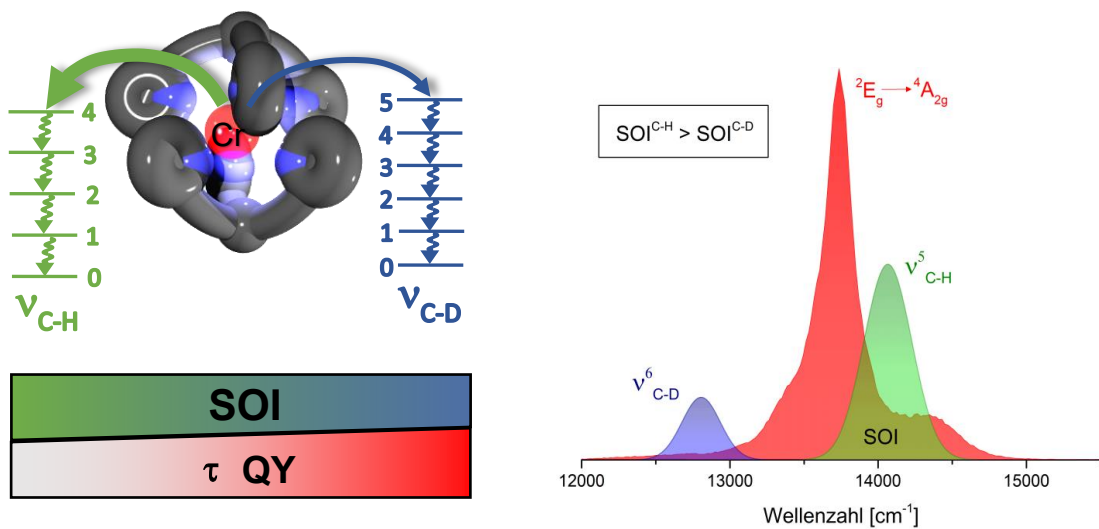
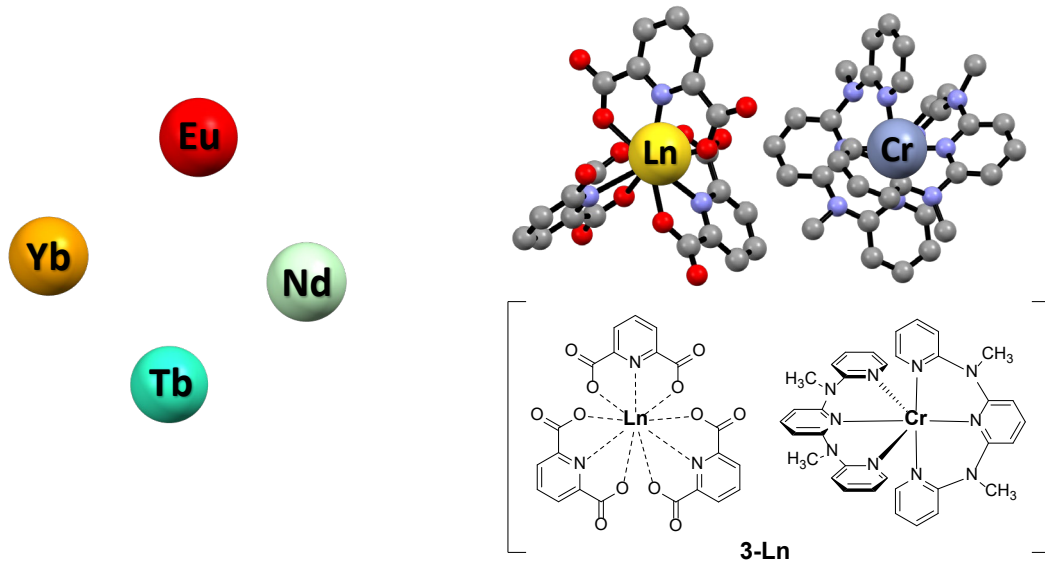


**Abb. 71:** Schematische Darstellung von Multiphonon Relaxation bei Cr(III)-Emittoren mit dem Einfluss von Ligandendeuterierung auf die spektralen Überlappintegrale (SOIs) und den photophysikalischen Eigenschaften dieser Luminophore.

## Photolumineszenz und Upconversion in molekularen Chrom-Lanthanoid-Salzen



### NIR nach NIR-Upconversion

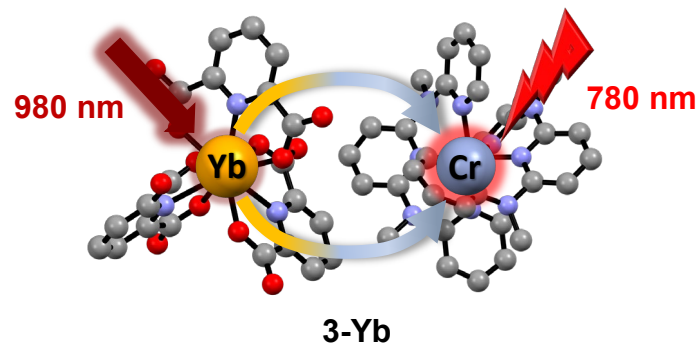


**Abb. 72:** Übersicht der dargestellten Chrom-Lanthanoid-Salze **3-Ln**. Darunter zeigt **3-Yb** NIR→NIR-Upconversion Lumineszenz bei  $\lambda_{em} = 780 \text{ nm}$  nach Laseranregung der  $\text{Yb}^{3+}$ -Sensibilisatoren bei  $\lambda_{ex} = 976 \text{ nm}$ .

- Konzeption, Darstellung und strukturelle Charakterisierung der neuen molekularen Festkörper **3-Ln**
- Im molekularen Festkörper **3-Yb** tritt nach Laseranregung der  $\text{Yb}^{3+}$ -Sensibilisatoren bei  $\lambda_{ex} = 776 \text{ nm}$  intensive  ${}^2E/{}^2T_1$ -UC-Emission des  $\text{Cr}^{3+}$ -Aktivators mit einem Maximum bei etwa  $\lambda_{em} = 780 \text{ nm}$  in Gegenwart von Sauerstoff bzw. Wasser auf



- Die Chrom-Lanthanoid-Salze **3-Ln** (Ln = Nd, Tb, Eu) wurden mit (zeitaufgelöster) Lumineszenzspektroskopie charakterisiert und die zugrundeliegenden EnT-Prozesse zwischen den Metallzentren untersucht

In dieser Arbeit konnte durch die sorgfältige Überarbeitung des Designs früherer Cr<sup>3+</sup>/Yb<sup>3+</sup>-Systeme erstmals ein molekularer Festkörper realisiert werden, welcher NIR→NIR-Upconversion Lumineszenz selbst in der Gegenwart von Sauerstoff bzw. Wasser zeigt. Dies erweitert die kleine Zahl an bekannten UC-Beispielen an molekularen Festkörpern um ein weiteres Sensibilisator/Aktivator-Metallkomplekxpaar. Diese konzeptionelle Studie ermöglicht den Zugang zu einer neuen Klasse von photonischen Materialien und eröffnet vielfältige neue Möglichkeiten auf dem Forschungsgebiet der molekularen Upconversion.

## 8 Experimentalteil / Experimental section

Um den Experimentalteil dieser Arbeit einer breiteren Leserschaft zugänglich zu machen und eine eventuelle Verwendung in späteren Publikationen zu erleichtern, ist das folgende Kapitel in englischer Sprache verfasst.

### 8.1 General

All chemicals were purchased from commercial suppliers and used as received unless stated otherwise. For the preparation of the lanthanoid compounds lanthanoid salts with at least 99.99 % purity (REO, in regards to contaminations with different lanthanoids) were used. The used solvents were of HPLC grade purity. Dichloromethane was dried over  $\text{CaH}_2$ . Diisopropylethylamine ( $\text{EtNiPr}_2$ ) was dried by refluxing over  $\text{CaOH}_2$  for several hours and distilling off. Water-free DMF (Acros Organics) was used as purchased. Deuterated solvents for nmr spectroscopy and syntheses had deuterium contents  $>99.8\%D$ .  $\text{CD}_3\text{l}$  ( $>99.5\%D$ , stabilized with copper) was purchased from Sigma Aldrich. All air-sensitive reactions were performed under a dry, dioxygen-free atmosphere of argon using Schlenk technique. Column-chromatography was performed with silica gel 60 (Merck, 0.063 - 0.200 mm). Analytical thin layer chromatography (TLC) was done on silica gel 60 F 254 plates (Merck, coated on aluminium sheets).

### NMR

NMR spectra were measured on a Bruker AVII+300 ( $^1\text{H}$ : 300 MHz,  $^{13}\text{C}$ : 75 MHz) and Bruker AVII+400 ( $^1\text{H}$ : 400 MHz,  $^{13}\text{C}$ : 101 MHz). The chemical shifts ( $\delta$ ) are reported in ppm relative to TMS and the residual solvent signals were used as internal reference. The following abbreviations are used for signal multiplicities: s (singlet), d (doublet), t (triplet), q (quartet). Signals with markedly broad lines are marked with the prefix "br". Spectra processing, analysis and plotting was performed with the Bruker software TopSpin.

### Mass spectrometry

ESI mass spectrometry was performed on a Bruker Daltonics Esquire 6000 as well as on a Bruker amaZon SL mass spectrometer by the central analytical facility of the Department of Chemistry (University of Tübingen).

## Elemental analysis

Elemental analyses were performed by the Analytical Facility of the Institute of Inorganic Chemistry (University of Tübingen) using a Vario MICRO EL analyser.

## X-ray Single Crystal Structure Analysis

X-ray data were collected with a Bruker Smart APEX II diffractometer with graphite-monochromated Mo  $K_{\alpha}$  radiation or a Bruker APEX II Duo diffractometer with a Mo  $\mu$ S microfocus tube and a TRIUMPH monochromator. The programs used were Bruker's APEX2 v2011.8-0,<sup>[164]</sup> including SADABS for absorption correction,<sup>[165]</sup> SAINT for data reduction<sup>[166]</sup> and SHELXS for structure solution, as well as the WinGX suite of programs version 1.70.01 or the GUI ShelXle, including SHELXL for structure refinement.<sup>[167–169]</sup> All X-ray measurements and refinements were done by Dr. Hartmut Schubert (AG Wesemann, Institute of Inorganic Chemistry, University of Tübingen). The X-ray structures were presented using Mercury 3.8.

## Luminescence Measurements

All luminescence measurements were performed either on solid samples in standard quartz or NMR tubes or on frozen samples dissolved in n-butyronitrile in standard NMR tubes at 298 and 77 K under ambient conditions.

For photophysical measurements two different spectrofluorometers were applied:

a) A Horiba Fluorolog-3 spectrofluorometer equipped with a 450-W Xenon lamp was used for steady-state measurements. The emitted light was detected at an angle  $90^{\circ}$  to the excitation light using either a Hamamatsu R2658P PMT detector ( $300 \text{ nm} < \lambda_{\text{em}} < 1010 \text{ nm}$ ) or by a Hamamatsu H10330-75 PMT detector ( $950 \text{ nm} < \lambda_{\text{em}} < 1700 \text{ nm}$ ). Spectral selection in the excitation channel was accomplished by a DFX double monochromator (gratings: 1200 grooves/mm, 330 nm blaze) and in the emission channel by a spectrograph iHR550 (single grating: 1200 grooves/mm, 500 nm blaze) in the visible/NIR spectral region ( $\lambda_{\text{em}} < 1010 \text{ nm}$ ) and a spectrograph iHR320 (single grating: 600 grooves/mm, 1000 nm blaze) in the NIR spectral region ( $\lambda_{\text{em}} > 950 \text{ nm}$ ). Spectral correction of the emission spectra was performed with a correction curve implemented by the instrument manufacturer. The luminescence decay kinetics were determined at 298 K and 77 K with a pulsed xenon flash lamp (pulse width of ca. 1.5  $\mu$ s FWHM). The analysis of the luminescence decay

kinetics (deconvolution, statistical parameters, etc.) was performed using the software package DAS from Horiba.

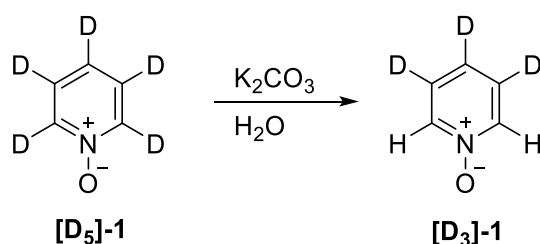
b) The second instrument was a PTI Quantamaster QM4 spectrofluorimeter equipped with a 75 W continuous xenon short arc lamp as excitation source. Emission was monitored using a PTI P1.7R detector module (Hamamatsu PMT R5509-72 with a Hamamatsu C9525 power supply operated at 1500 V and a Hamamatsu liquid N<sub>2</sub> cooling unit C9940 set to -80°C). For the measurements between 600 nm and 900 nm, a long-pass filter GG-455 (Schott, 3.0 mm thickness, transmission 98 – 95 % in the spectral region mentioned) was used in the emission channel in order to avoid higher order excitation light. The same approach was taken for NIR measurements above 1000 nm with a long-pass filter RG-850 (Schott, 3.0 mm thickness, transmission > 98 % above 970 nm). Spectral selection was achieved by single grating monochromators (excitation: 1200 grooves/mm, 300 nm blaze; vis emission: 1200 grooves/mm, 500 nm blaze; near-IR emission: 600 grooves/mm, 1200 nm blaze). Near-IR luminescence lifetimes were determined with a xenon flash lamp as excitation source (Hamamatsu L4633: pulse width ca. 1.5 μs FWHM). Lifetime data analysis (deconvolution, statistical parameters, etc.) was performed using the software package FeliX32 from PTI. Lifetimes were determined by deconvolution of the decay profiles with the instrument response function, which was determined using an empty NMR tube as scatterer.

### Near-IR Absorption Spectra

NIR absorption measurements were performed with a JASCO V-770 spectrophotometer (equipped with a long cuvette holder LSE-701) on solutions of isotopologic **ddpd-[d<sub>x</sub>]** ligands in CDCl<sub>3</sub> (Sigma Aldrich, 99.9%D) and solutions of isotopologic chromium complexes (**[D<sub>x</sub>]- [Cr(ddpd)<sub>2</sub>](BF<sub>4</sub>)<sub>3</sub>** in CD<sub>3</sub>CN (Sigma Aldrich, 99.96 %D). Depending on the intensity of the C-H overtones, rectangular quartz micro cuvettes (Starna, type 28/B/SX, Suprasil 300) with different path lengths were used (ν = 1: 1.0 cm and ν = 2: 5.0 cm). The spectra were corrected for baseline drift by b-spline interpolation with OriginPro 9.0. The component peaks of the spectra were deconvoluted by fitting of the spectra with a series of Gaussian functions (Levenberg-Marquardt on  $\chi^2$ ) without any constraints for the C-H oscillators.

## 8.2 Synthesis of selectively deuterated compounds

### Pyridine N-oxide-[3,4,5-d<sub>3</sub>]<sup>[97]</sup>

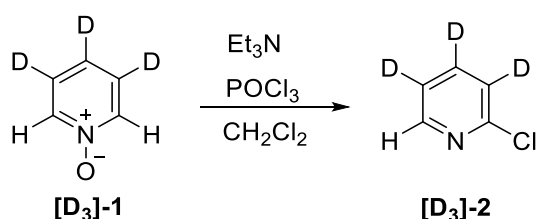


**[D<sub>5</sub>]-pyridine-N-oxide<sup>[98]</sup>** (5.6 g, 56 mmol, 1.0 eq.) was dissolved in 10% aqueous potassium carbonate (700 mL) and heated at reflux temperature for 16 h. After cooling to room temperature the resulting solution was extracted with dichloromethane (7 x 100 mL). The combined organic layers were dried (MgSO<sub>4</sub>) and concentrated under reduced pressure. The resulting colorless solid (4.7 g, 48 mmol, 86 %, >99.5 %D) was dried in vacuo.

<sup>1</sup>H-NMR (400 MHz, CDCl<sub>3</sub>): δ = 8.25 (s) ppm.

MS (ESI, pos. mode): m/z (% assignment) = 99.13 (100, {[M]+H}<sup>+</sup>).

### **[D<sub>3</sub>]-2-Chloropyridine**



The reaction was performed in analogy to the literature procedure by Park.<sup>[99]</sup>

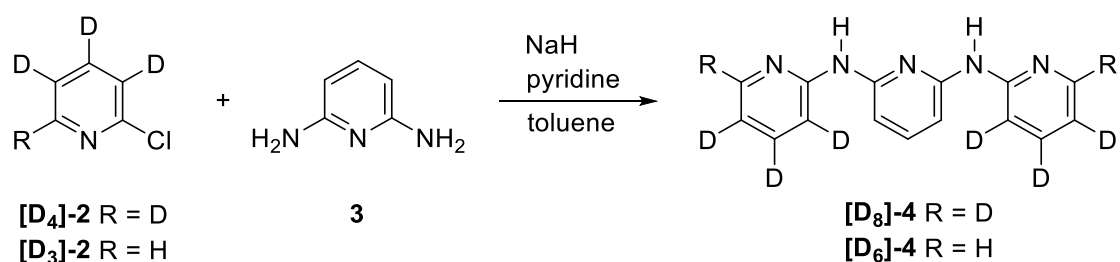
**[D<sub>3</sub>]-pyridine-N-oxide** (4.7 g, 48 mmol, 1.0 eq.) was dissolved in 45 mL dichloromethane and triethylamine (8.0 mL, 5.9 g, 58 mmol, 1.2 eq.) was added. To this mixture a solution of phosphoroyl chloride (5.3 mL, 8.9 g, 58 mmol, 1.2 eq.) in 25 mL dichloromethane was slowly added at 10 °C while stirring. After stirring for 30 minutes at room temperature, the reaction mixture was refluxed for 1 h. The solution was cooled to room temperature and ice was slowly added until all excessive phosphoroyl chloride was hydrolysed. After addition of water (25 mL) the solution was

made alkaline (pH = 10) with 2 M aqueous NaOH. The organic layer was separated and the aqueous layer was extracted with CH<sub>2</sub>Cl<sub>2</sub> (5 x 25 mL). The combined organic layers were washed with saturated NaCl solution, dried (MgSO<sub>4</sub>) and concentrated at reduced pressure. The resulting red oil was subjected to column chromatography (SiO<sub>2</sub>, CH<sub>2</sub>Cl<sub>2</sub>, preloading onto SiO<sub>2</sub>, detection: UV). The product **[D<sub>3</sub>]-2** was obtained as a colorless liquid (2.6 g, 22 mmol, 46 %, >99.5 %D).

<sup>1</sup>H-NMR (400 MHz, CDCl<sub>3</sub>): δ = 8.36 (s) ppm.

MS (ESI, pos. mode): m/z (% , assignment) = 117.06 (100, {[M]+H}<sup>+</sup>).

### **[D<sub>6</sub>]/[D<sub>8</sub>]-N,N'-Bis(2-pyridyl)-2,6-diaminopyridine**



The reaction was performed in analogy to the literature procedure by Cornia.<sup>[170]</sup> Under an argon atmosphere a mixture of 2,6-Diaminopyridine (1 eq.) and NaH (60 wt% oil dispersion, 6.8 eq.) was stirred for 5 min at room temperature. 2-Chloropyridine ([D<sub>3</sub>]/[D<sub>4</sub>]<sup>[98]</sup>, 3.1 eq.) and pyridine were added and after stirring for 5 min, the flask was immersed in a preheated oil bath at 150 °C. Immediately strong gas evolution occurred and a few minutes later, just before the red brown suspension became a solid mass, dry toluene (15 mL) was added. Then the mixture was stirred at 150 °C for 4 h. After cooling to room temperature using a water bath the solvent was removed under reduced pressure. Carefully ice-cold water (30 g) was added. After stirring for 10 minutes the mixture was filtered through a gooch funnel (porosity no. 3) and the filtered brown solid was extensively washed with water (3 x 20 mL) and n-hexan (3 x 10 mL). The light brown solid was dissolved in THF (80 mL) and filtered through a silica plug. The filtered residue was washed with THF (3 x 20 ml) and the combined THF phases were concentrated under reduced pressure resulting in a brown solid. The brown solid was transferred into a 25 ml round bottom flask and MeOH (3 mL), CH<sub>2</sub>Cl<sub>2</sub> (3 mL) and

Et<sub>2</sub>O (3 mL) were added. After stirring for 3 h at room temperature the mixture was cooled with an ice bath and then filtered through a gooch funnel (porosity no. 3). The filtered beige solid was washed with Et<sub>2</sub>O (3 x 5 mL) and dried under vacuum.

#### [D<sub>8</sub>]-4:

[D<sub>4</sub>]-2 (2.5 mL, 3.0 g, 26 mmol), **3** (900 mg, 8.2 mmol), NaH (2.2 g, 56 mmol) and pyridine (4.3 mL) → Yield: 1.8 g (6.6 mmol, 80 %, 99.3 %D).

<sup>1</sup>H-NMR (400 MHz, DMSO-d<sub>6</sub>): δ = 9.37 (s, 2H), 7.50 (t, *J* = 7.9 Hz, 1H), 7.13 (d, *J* = 7.9 Hz, 2H).

MS (ESI, pos. mode): *m/z* (% assignment) = 272.18 (100, {[M]+H}<sup>+</sup>).

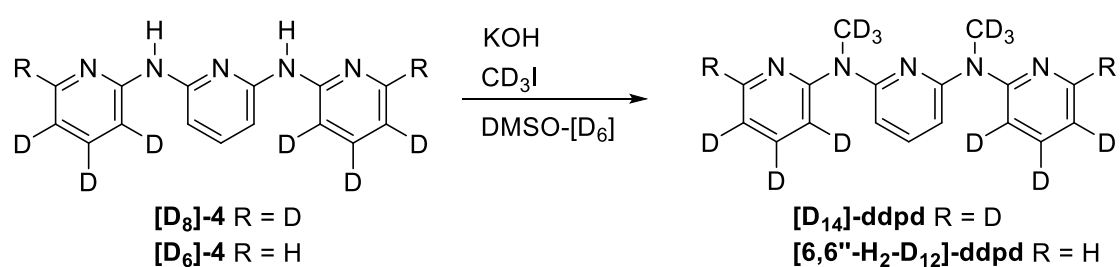
#### [D<sub>6</sub>]-4:

[D<sub>3</sub>]-2 (2.1 mL, 2.5 g, 21 mmol), **3** (775 mg, 7.1 mmol), NaH (1.9 g, 48 mmol) and pyridine (3.6 mL) → Yield: 680 mg (2.6 mmol, 37 %, 97.6 %D).

<sup>1</sup>H-NMR (400 MHz, DMSO-d<sub>6</sub>): δ = 9.37 (s, 2H), 8.21 (s, 2H), 7.50 (t, *J* = 8.0 Hz, 1H), 7.13 (d, *J* = 8.0 Hz, 2H).

MS (ESI, pos. mode): *m/z* (% assignment) = 270.13 (100, {[M]+H}<sup>+</sup>).

#### [D<sub>x</sub>]-ddpd



The reaction was performed in analogy to the literature procedure by Heinze.<sup>[67]</sup>

Under an argon atmosphere powdered KOH (4.0 eq.) was added to a yellow solution of **4** ([D<sub>8</sub>]/[D<sub>6</sub>], 1.0 eq.) in [D<sub>6</sub>]-DMSO (NMR grade). The mixture was stirred at room temperature for 10 min. CD<sub>3</sub>I (2.2 eq.) was added to the red solution and stirring was continued for 2 h. Water was added and the yellow aqueous suspension was extracted with a 1:1 (v/v) mixture of Et<sub>2</sub>O/THF (5 × 30 mL). The combined organic phases were washed with saturated aqueous Na<sub>2</sub>CO<sub>3</sub> (25 mL), dried (MgSO<sub>4</sub>) and concentrated

under reduced pressure. The resulting yellow oil was subjected to column chromatography (SiO<sub>2</sub>, n-hexane/EtOAc, 2:1, detection: UV) to obtain the product as a pale-yellow oil.

**[D<sub>14</sub>]-ddpd:**

**[D<sub>8</sub>]-4** (1.8 g, 6.6 mmol), CD<sub>3</sub>I (0.9 mL, 2.1 g, 14.6 mmol), KOH (1.5 g, 26.5 mmol) and 40 mL [D<sub>6</sub>]-DMSO → Yield: 800 mg (2.6 mmol, 40 %, 99.3 %D).

R<sub>f</sub>: 0.32 (SiO<sub>2</sub>, n-hexane/EtOAc, 2:1, detection: UV).

<sup>1</sup>H-NMR (400 MHz, CD<sub>3</sub>Cl): δ = 7.56 (t, *J* = 8.0 Hz, 1H), 6.84 (d, *J* = 8.0 Hz, 2H).

MS (ESI, pos. mode): *m/z* (% , assignment) = 306.21 (100, {[M]+H}<sup>+</sup>).

**[6,6''-H<sub>2</sub>-D<sub>12</sub>]-ddpd:**

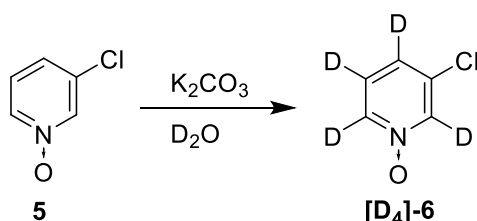
**[D<sub>6</sub>]-4** (550 mg, 2.0 mmol), CD<sub>3</sub>I (284 μL, 652 mg, 4.4 mmol), KOH (457 mg, 8.1 mmol) and 50 mL [D<sub>6</sub>]-DMSO → Yield: 540 mg (1.7 mmol, 88 %, 98.7 %D).

R<sub>f</sub>: 0.32 (SiO<sub>2</sub>, n-hexane/EtOAc, 2:1, detection: UV).

<sup>1</sup>H-NMR (400 MHz, CD<sub>3</sub>Cl): δ = 8.36 (s, 2H), 7.41 (t, *J* = 8.0 Hz, 1H), 6.70 (d, *J* = 8.0 Hz, 2H).

MS (ESI, pos. mode): *m/z* (% , assignment) = 304.21 (100, {[M]+H}<sup>+</sup>).

**[D<sub>4</sub>]-3-Chloropyridine N-oxide<sup>[97]</sup>**



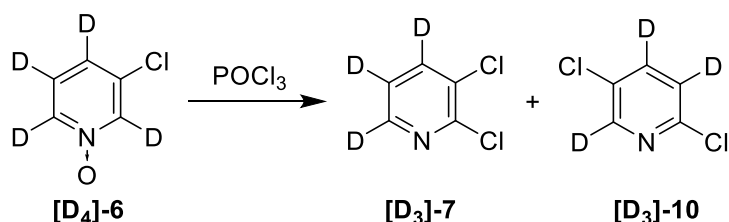
In a steel autoclave 3-Chloropyridine N-oxide<sup>[97]</sup> (3.5 g, 27.0 mmol, 1.0 eq.) was dissolved in D<sub>2</sub>O (25 mL, NMR grade, 99.9 %D) and K<sub>2</sub>CO<sub>3</sub> (2.0 g) was added. The vessel was sealed and the mixture was stirred at 190 °C for 16 h. After cooling to room temperature, the solvent was evaporated. The residue was dissolved in fresh D<sub>2</sub>O (25 mL, NMR grade) and heated at 190 °C for another 5 h. After cooling to room temperature and evaporation of the solvent, the light brown residue was extracted with CH<sub>2</sub>Cl<sub>2</sub> (1 x 100 mL). Water (10 mL) was added and the aqueous phase was extracted with CH<sub>2</sub>Cl<sub>2</sub> (5 x 40 mL). The solvents of the combined organic phases were dried



(MgSO<sub>4</sub>) and concentrated under reduced pressure. The product was obtained as a highly hygroscopic, off-white solid (1.7 g, 12.7 mmol, 47 %, 99 %D).

MS (ESI, pos. mode): m/z (% assignment) = 134.04 (25, {[M]+H}<sup>+</sup>), 155.99 (100, {[M]+Na}<sup>+</sup>), 171.95 (68, {[M]+K}<sup>+</sup>), 289.00 (100, {[2M]+Na}<sup>+</sup>).

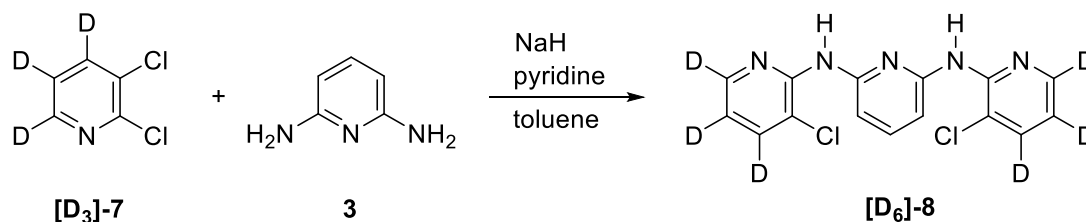
### [D<sub>3</sub>]-2,3-Dichloropyridine, [D<sub>3</sub>]-2,5-Dichloropyridine<sup>[97]</sup>



Under an argon atmosphere [D<sub>4</sub>]-3-Chloropyridine N-oxide (2.2 g, 16.5 mmol, 1.0 eq.) was carefully dissolved in phosphoroylchloride (2.3 mL, 3.8 g, 24.6 mmol, 1.5 eq.) and heated to reflux at 120 °C for 2 h. After cooling to room temperature, the red-brown solution was poured on ice. The liquid was made basic with saturated aqueous K<sub>2</sub>CO<sub>3</sub> and extracted with CH<sub>2</sub>Cl<sub>2</sub> (5 x 30 mL). The combined organic phases were concentrated under reduced pressure. For further purification two different procedures were carried out. In the first procedure the concentrated brown solution was transferred to a sublimation device equipped with a cool finger for liquid nitrogen. After careful sublimation (298 K, 0.1 mbar) a colorless solid was obtained which contains mainly the desired products [D<sub>3</sub>]-7 and [D<sub>3</sub>]-10. After column chromatography (SiO<sub>2</sub>, n-hexane/CH<sub>2</sub>Cl<sub>2</sub>, 1:9, detection: UV) the separated products can be obtained as colorless solids ([D<sub>3</sub>]-7: 620 mg, 4.1 mmol, 25 %, >99%D, [D<sub>3</sub>]-10: 230 mg, 1.5 mmol, 9 %, >99 %D). In the second procedure<sup>[97]</sup> the concentrated brown solution, which also contains other side products, was directly subjected to column chromatography (SiO<sub>2</sub>, n-hexane/CH<sub>2</sub>Cl<sub>2</sub>, 1:9, detection: UV) to give [D<sub>3</sub>]-7 (650 mg, 4.3 mmol, 26 %, >99%D) and [D<sub>3</sub>]-10 (280 mg, 1.9 mmol, 11 %, >99 %D).

[D<sub>3</sub>]-7: R<sub>f</sub>: 0.45 (SiO<sub>2</sub>, n-hexane/ CH<sub>2</sub>Cl<sub>2</sub>, 1:9, detection: UV).

[D<sub>3</sub>]-10: R<sub>f</sub>: 0.55 (SiO<sub>2</sub>, n-hexane/ CH<sub>2</sub>Cl<sub>2</sub>, 1:9, detection: UV).

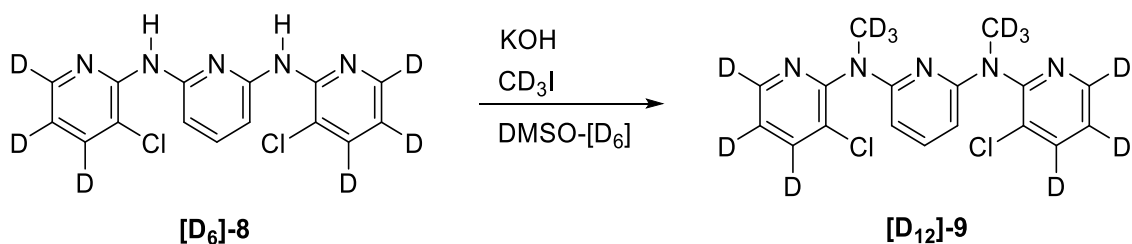
**[D<sub>6</sub>]-8**

The reaction was performed in analogy to the literature procedure by Cornia.<sup>[170]</sup> Under an argon atmosphere a mixture of 2,6-Diaminopyridine (578 mg, 5.3 mmol, 1 eq.) and NaH (60 wt% oil dispersion, 1.4 g, 36 mmol, 6.8 eq.) was stirred for 5 min at room temperature. **[D<sub>3</sub>]-7** (2.4 g, 15.9 mmol, 3 eq.) and dry pyridine (2.7 mL) were added and after stirring for 10 min, the flask was immersed in a preheated oil bath at 120 °C. Immediately strong gas evolution occurred and a few minutes later, just before the red brown suspension became a solid mass, dry toluene (8 mL) was added. Then the mixture was stirred at 150 °C for 4 h. After cooling to room temperature using a water bath the solvent was removed under reduced pressure. Carefully ice-cold water (60 mL) was added. After stirring for 10 minutes the mixture was filtered through a gooch funnel (porosity no. 3) and the filtered brown solid was extensively washed with water (3 x 20 mL) and n-hexan (3 x 10 mL). The light brown solid was dissolved in THF (80 mL) and filtered through a silica plug. The filtered residue was washed with THF (3 x 20 ml) and the combined THF phases were concentrated under reduced pressure resulting in a red-brown solid (1.5 g, 4.4 mmol, 84 %, 94 %D).

R<sub>f</sub>: 0.83 (SiO<sub>2</sub>, CH<sub>2</sub>Cl<sub>2</sub>/MeOH, 25:1, detection: UV).

<sup>1</sup>H-NMR (400 MHz, [D<sub>6</sub>]-DMSO): δ = 8.15 (s, 2H), 7.90 (s, 0.2H non-deuterated residual signal), 7.83 (m, 2H), 7.73 (m, 1H).

MS (ESI, pos. mode): m/z (% , assignment) = 338.02 (100, {[M]+H}<sup>+</sup>).

**[D<sub>12</sub>]-9**

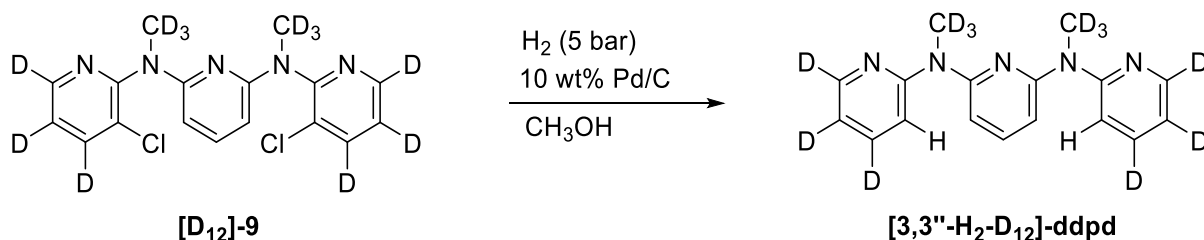
The reaction was performed in analogy to the literature procedure by Heinze.<sup>[67]</sup> Under an argon atmosphere powdered KOH (994 mg, 17.7 mmol, 4.0 eq.) was added to a red-brown solution of [D<sub>6</sub>]-8 (1.5 g, 4.4 mmol, 1.0 eq.) in 150 mL [D<sub>6</sub>]-DMSO (NMR grade). The mixture was stirred at room temperature for 10 min. CD<sub>3</sub>I (704 μL, 1.6 g, 11.1 mmol, 2.5 eq.) was added to the dark red reaction solution and stirring was continued for 3 h. Water (200 mL) was added and the dark yellow aqueous suspension was extracted with a 1:1 (v/v) mixture of Et<sub>2</sub>O/THF (4 × 150 mL). The combined organic phases were washed with aqueous sat. NaCl (30 mL), dried (MgSO<sub>4</sub>) and concentrated under reduced pressure. The resulting yellow oil was subjected to column chromatography (SiO<sub>2</sub>, CH<sub>2</sub>Cl<sub>2</sub>/MeOH, 25:1, detection: UV) to obtain the product as a beige solid (980 mg, 2.6 mmol, 59%, 94 %D).

R<sub>f</sub>: 0.51 (SiO<sub>2</sub>, CH<sub>2</sub>Cl<sub>2</sub>/MeOH, 25:1, detection: UV).

<sup>1</sup>H-NMR (400 MHz, CD<sub>3</sub>Cl): δ = 7.66 (s, 0.3H non-deuterated residual signal), 7.31 (t, *J* = 8.0 Hz, 1H), 5.98 (d, *J* = 8.0 Hz, 2H).

MS (ESI, pos. mode): *m/z* (% , assignment) = 372.08 (100, {[M]+H}<sup>+</sup>).

### [3,3''-H<sub>2</sub>-D<sub>12</sub>]-ddpd



The reaction was performed in analogy to the literature procedure by Pavlik.<sup>[97]</sup>

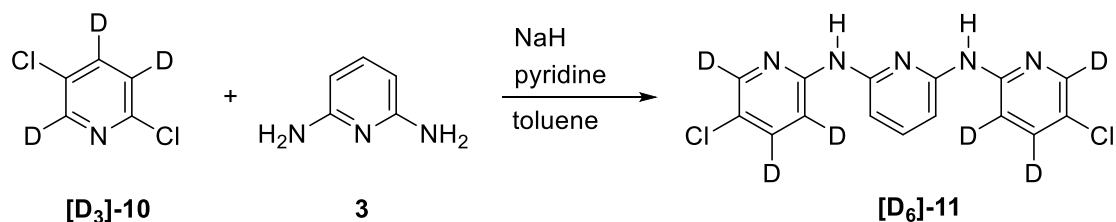
In a steel autoclave **[D<sub>12</sub>]-9** (570 mg, 1.5 mmol, 1.0 eq.) and potassium carbonate (600 mg) were dissolved in MeOH (15 mL) and Pd/C (10 wt%, dry and unreduced, 163 mg, 0.15 mmol, 0.1 eq.) was added. The vessel was flushed three times with hydrogen gas and the mixture was stirred at 5 bar hydrogen pressure and room temperature for 68 h. The vessel was unsealed and the catalyst was removed by filtration over celite. The solvents of the yellow filtrate were evaporated and the resulting yellow oil was subjected to column chromatography (SiO<sub>2</sub>, CH<sub>2</sub>Cl<sub>2</sub>/MeOH, 25:1, detection: UV) to obtain the product as a yellow oil (305 mg, 1.0 mmol, 67 %, 97 %D).

R<sub>f</sub>: 0.35 (SiO<sub>2</sub>, CH<sub>2</sub>Cl<sub>2</sub>/MeOH, 25:1, detection: UV).

<sup>1</sup>H-NMR (400 MHz, CD<sub>3</sub>Cl): δ = 7.52 (m, 0.33H non-deuterated residual signal), 7.43 (t, *J* = 8.0 Hz, 1H), 7.26 (m, 2H), 6.72 (d, *J* = 8.0 Hz, 2H).

MS (ESI, pos. mode): *m/z* (% , assignment) = 304.17 (100, {[M]+H}<sup>+</sup>).

## [D<sub>6</sub>]-11

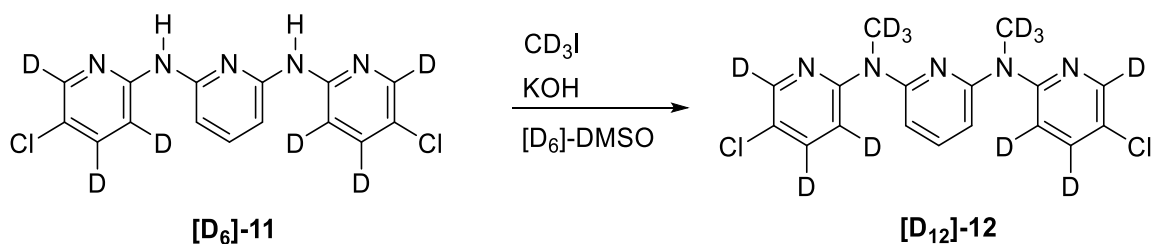


The reaction was performed in analogy to the literature procedure by Cornia.<sup>[170]</sup> Under an argon atmosphere a mixture of 2,6-Diaminopyridine (409 mg, 3.7 mmol, 1 eq.) and NaH (60 wt% oil dispersion, 1.0 g, 26 mmol, 6.8 eq.) was stirred for 5 min at room temperature. [D<sub>3</sub>]-10 (1.7 g, 11.2 mmol, 3 eq.) and dry pyridine (1.9 mL) were added and after stirring for 10 min, the flask was immersed in a preheated oil bath at 120 °C. Immediately strong gas evolution occurred and a few minutes later, just before the dark brown suspension became a solid mass, dry toluene (7 mL) was added. Then the mixture was stirred at 150 °C for 4 h. After cooling to room temperature using a water bath the solvent was removed under reduced pressure. Carefully ice-cold water (50 mL) was added. After stirring for 10 minutes the mixture was filtered through a gooch funnel (porosity no. 3) and the filtered dark brown solid was extensively washed with water (3 x 20 mL) and n-hexan (3 x 10 mL). The light brown solid was dissolved in THF (70 mL) and filtered through a silica plug. The filtered residue was washed with THF (3 x 20 ml) and the combined THF phases were concentrated under reduced pressure resulting in a brown solid (1.1 g, 3.3 mmol, 87 %, 85 %D).

R<sub>f</sub>: 0.32 (SiO<sub>2</sub>, CH<sub>2</sub>Cl<sub>2</sub>/MeOH, 20:1, detection: UV).

<sup>1</sup>H-NMR (400 MHz, [D<sub>6</sub>]-DMSO): δ = 9.64 (s, 2H), 7.74 (s, 0.6H non-deuterated residual signal), 7.54 (m, 1H), 7.08 (d, *J* = 8.0 Hz, 2H).

MS (ESI, pos. mode): *m/z* (% , assignment) = 338.02 (100, {[M]+H}<sup>+</sup>).

**[D<sub>6</sub>]-12**

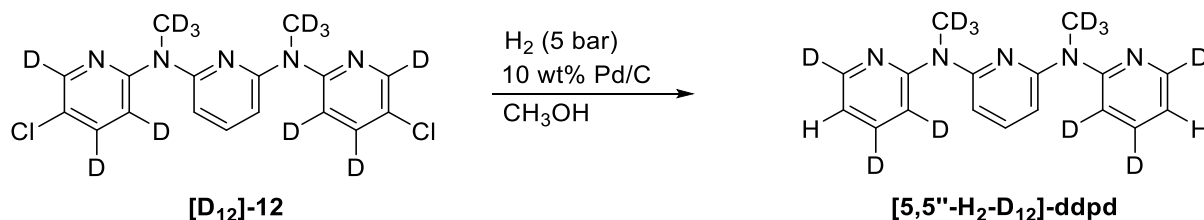
The reaction was performed in analogy to the literature procedure by Heinze.<sup>[67]</sup> Under an argon atmosphere powdered KOH (717 mg, 12.8 mmol, 4.0 eq.) was added to a red-brown solution of **[D<sub>6</sub>]-11** (1.1 g, 3.2 mmol, 1.0 eq.) in 110 mL [D<sub>6</sub>]-DMSO (NMR grade). The mixture was stirred at room temperature for 10 min. CD<sub>3</sub>I (507 μL, 1.2 g, 7.9 mmol, 2.5 eq.) was added to the dark red reaction solution and stirring was continued for 3 h. Water (150 mL) was added and the dark yellow aqueous suspension was extracted with a 1:1 (v/v) mixture of Et<sub>2</sub>O/THF (4 × 100 mL). The combined organic phases were washed with saturated aqueous NaCl (30 mL), dried (MgSO<sub>4</sub>) and concentrated under reduced pressure. The resulting yellow oil was subjected to column chromatography (SiO<sub>2</sub>, n-hexane/EtOAc, 2:1, detection: UV) to obtain the product as a colorless solid (465 mg, 1.2 mmol, 39 %, 93 %D).

R<sub>f</sub>: 0.76 (SiO<sub>2</sub>, n-hexane/EtOAc, 2:1, detection: UV).

<sup>1</sup>H-NMR (400 MHz, CD<sub>3</sub>Cl): δ = 8.30 (s, 0.1H non-deuterated residual signal), 7.59 (m, 0.2H non-deuterated residual signal), 7.51 (m, 2H), 6.75 (d, *J* = 8.0 Hz, 2H).

MS (ESI, pos. mode): *m/z* (% , assignment) = 372.08 (100, {[M]+H}<sup>+</sup>).

## [5,5''-H<sub>2</sub>-D<sub>12</sub>]-ddpd



The reaction was performed in analogy to the literature procedure by Pavlik.<sup>[97]</sup>

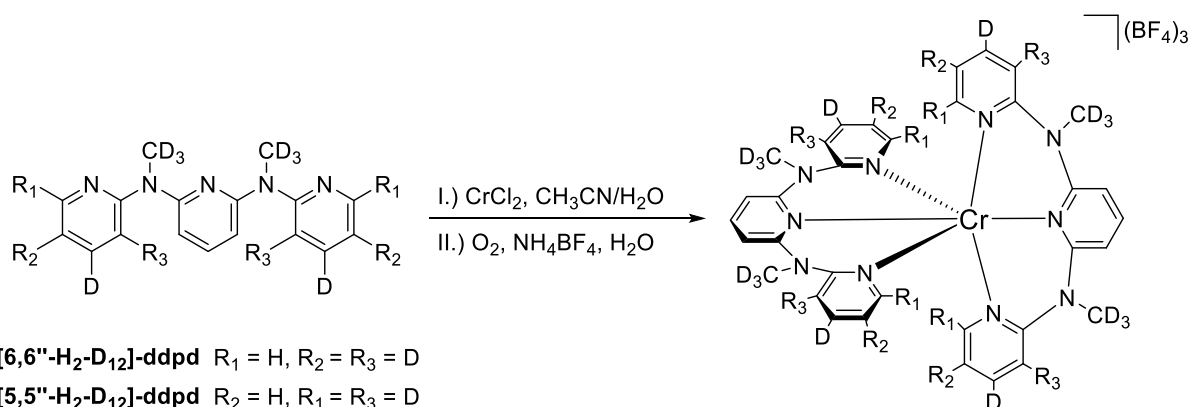
In a steel autoclave **[D<sub>12</sub>]-12** (323 mg, 0.9 mmol, 1.0 eq.) and potassium carbonate (600 mg) were dissolved in MeOH (50 mL) and Pd/C (10 wt%, dry and unreduced, 92 mg, 0.09 mmol, 0.1 eq.) was added. The vessel was flushed three times with hydrogen gas and the mixture was stirred at 5 bar hydrogen pressure and room temperature for 19 h. The vessel was unsealed and the catalyst was removed by filtration over celite. The solvents of the yellow filtrate were evaporated and the resulting yellow oil was subjected to column chromatography (SiO<sub>2</sub>, CH<sub>2</sub>Cl<sub>2</sub>/MeOH, 25:1, detection: UV) to obtain the product as a yellow oil (200 mg, 0.7 mmol, 73 %, 92 %D).

R<sub>f</sub>: 0.35 (SiO<sub>2</sub>, CH<sub>2</sub>Cl<sub>2</sub>/MeOH, 25:1, detection: UV).

<sup>1</sup>H-NMR (400 MHz, CD<sub>3</sub>Cl): δ = 8.33 (m, 0.13H non-deuterated residual signal), 7.47 (m, 0.82H non-deuterated residual signal), 7.40 (m, 1H), 7.26 (m, 0.38H non-deuterated residual signal), 6.81 (m, 2H), 6.68 (d, *J* = 8.0 Hz, 2H).

MS (ESI, pos. mode): *m/z* (% , assignment) = 303.16 (100, {[M-D]+H}<sup>+</sup>).

## [D<sub>x</sub>]-Cr



**[6,6''-H<sub>2</sub>-D<sub>12</sub>]-ddpd** R<sub>1</sub> = H, R<sub>2</sub> = R<sub>3</sub> = D

**[5,5''-H<sub>2</sub>-D<sub>12</sub>]-ddpd** R<sub>2</sub> = H, R<sub>1</sub> = R<sub>3</sub> = D

**[3,3''-H<sub>2</sub>-D<sub>12</sub>]-ddpd** R<sub>3</sub> = H, R<sub>1</sub> = R<sub>2</sub> = D

**[D<sub>14</sub>]-ddpd** R<sub>1</sub> = R<sub>2</sub> = R<sub>3</sub> = D

**[6,6''-H<sub>4</sub>-D<sub>24</sub>]-Cr** R<sub>1</sub> = H, R<sub>2</sub> = R<sub>3</sub> = D

**[5,5''-H<sub>4</sub>-D<sub>24</sub>]-Cr** R<sub>2</sub> = H, R<sub>1</sub> = R<sub>3</sub> = D

**[3,3''-H<sub>4</sub>-D<sub>24</sub>]-Cr** R<sub>3</sub> = H, R<sub>1</sub> = R<sub>2</sub> = D

**[D<sub>28</sub>]-Cr** R<sub>1</sub> = R<sub>2</sub> = R<sub>3</sub> = D

### General Procedure:

The reaction was performed in analogy to the literature procedure by Heinze.<sup>[35]</sup>

The **ddpd** ligand was dissolved in degassed H<sub>2</sub>O / CH<sub>3</sub>CN (v/v, 1:1) and a blue solution of CrCl<sub>2</sub> (1 eq.) in deaerated H<sub>2</sub>O (4 mL) was added. The deep green solution was stirred at room temperature for 12 h. After addition of aqueous NH<sub>4</sub>BF<sub>4</sub> the solution was stirred under presence of oxygen for 1 h and the colour of the reaction mixture turned to orange. A green solid was removed by filtration and the solvents of the filtrate were removed under reduced pressure. The orange residue was suspended in CH<sub>3</sub>CN and an insoluble colourless solid was removed by filtration. To this filtrate Et<sub>2</sub>O was added until the resulting solid is just about to dissolve. Standing overnight yielded in an orange crystalline solid which was collected and dried in vacuo.

### **[6,6''-H<sub>4</sub>-D<sub>24</sub>]-Cr:**

**[6,6''-H<sub>2</sub>-D<sub>12</sub>]-ddpd** (280 mg, 0.9 mmol, 1.9 eq.), CrCl<sub>2</sub> (60 mg, 0.5 mmol, 1 eq.), H<sub>2</sub>O / CH<sub>3</sub>CN (15 mL), NH<sub>4</sub>BF<sub>4</sub> (151 mg, 1.4 mmol, 3 eq. in 4 mL H<sub>2</sub>O) → Yield: 120 mg (0.13 mmol, 27 %, 98 %D).

MS (ESI, pos. mode): m/z (% assignment) = 219.42 (100, [M]<sup>3+</sup>).

### **[5,5''-H<sub>4</sub>-D<sub>24</sub>]-Cr:**

**[5,5''-H<sub>2</sub>-D<sub>12</sub>]-ddpd** (150 mg, 0.5 mmol, 1.4 eq.), CrCl<sub>2</sub> (42 mg, 0.3 mmol, 1 eq.), H<sub>2</sub>O / CH<sub>3</sub>CN (12 mL), NH<sub>4</sub>BF<sub>4</sub> (107 mg, 1.0 mmol, 3 eq. in 3 mL H<sub>2</sub>O) → Yield: 108 mg (0.12 mmol, 39 %, 92 %D).



MS (ESI, pos. mode): m/z (% , assignment) = 219.05 (100, [M]<sup>3+</sup>).

**[3,3''-H<sub>4</sub>-D<sub>24</sub>]-Cr:**

**[3,3''-H<sub>2</sub>-D<sub>12</sub>]-ddpd** (240 mg, 0.7 mmol, 1.4 eq.), CrCl<sub>2</sub> (67 mg, 0.6 mmol, 1 eq.), H<sub>2</sub>O / CH<sub>3</sub>CN (15 mL), NH<sub>4</sub>BF<sub>4</sub> (173 mg, 1.7 mmol, 3 eq. in 4 mL H<sub>2</sub>O) → Yield: 205 mg (0.22 mmol, 40 %, 97 %D).

MS (ESI, pos. mode): m/z (% , assignment) = 219.39 (100, [M]<sup>3+</sup>).

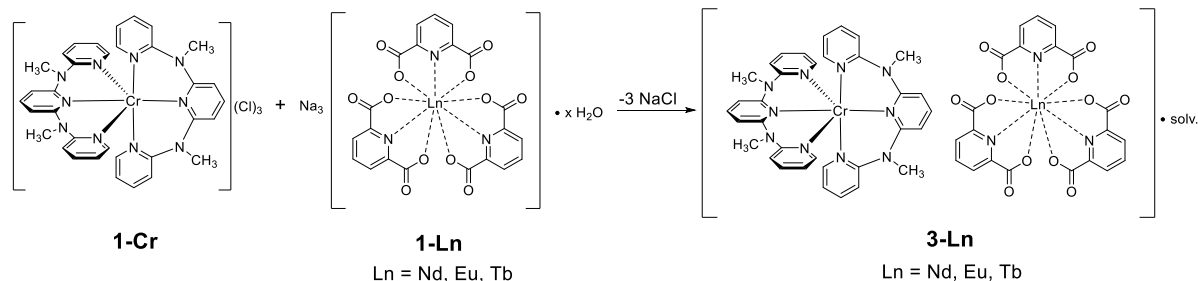
**[D<sub>28</sub>]-Cr**

**[D<sub>14</sub>]-ddpd** (520 mg, 1.7 mmol, 1.9 eq.), CrCl<sub>2</sub> (116 mg, 0.9 mmol, 1 eq.), H<sub>2</sub>O / CH<sub>3</sub>CN (30 mL), NH<sub>4</sub>BF<sub>4</sub> (283 mg, 2.7 mmol, 3 eq. in 6 mL H<sub>2</sub>O) → Yield: 230 mg (0.35 mmol, 40 %, 99 %D).

MS (ESI, pos. mode): m/z (% , assignment) = 220.76 (100, [M]<sup>3+</sup>).

## 8.3 Synthesis of chromium-lanthanoid salts

### 3-Ln (Ln = Nd, Eu, Tb)



General procedure:

In a 10 ml screw cap vial,  $\text{Na}_3[\text{Ln}(\text{dpa})_3] \cdot 6 \text{H}_2\text{O}$ <sup>[153]</sup> (**1-Ln**, 1.0 eq., Ln = Nd, Eu, Tb) and  $[\text{Cr}(\text{ddpd})_2]\text{Cl}_3$ <sup>[148]</sup> (**1-Cr**, 1.0 eq.) were suspended in water. The yellow mixture was stirred until all components were dissolved. After stirring for additional 30 minutes at room temperature, the solution was layered with isopropanol (2 mL). Upon standing for 1 to 4 days, large orange crystals of **3-Ln** were obtained which were also suitable for X-ray crystallographic analysis. The crystals were collected, washed with isopropanol (3 × 1 ml), ice-cold water (1 × 2 ml), and finally dried under reduced pressure. The product was obtained as yellow to orange solid.

#### 3-Nd:

$\text{Na}_3[\text{Nd}(\text{dpa})_3] \cdot 6 \text{H}_2\text{O}$  (30 mg, 37  $\mu\text{mol}$ ) and  $[\text{Cr}(\text{ddpd})_2]\text{Cl}_3$  (27 mg, 37  $\mu\text{mol}$ ) in  $\text{H}_2\text{O}$  (2 mL), Yield: 38 mg (30  $\mu\text{mol}$ , 81 %).

#### 3-Eu:

$\text{Na}_3[\text{Eu}(\text{dpa})_3] \cdot 6 \text{H}_2\text{O}$  (30 mg, 36  $\mu\text{mol}$ ) and  $[\text{Cr}(\text{ddpd})_2]\text{Cl}_3$  (27 mg, 36  $\mu\text{mol}$ ) in  $\text{H}_2\text{O}$  (2 mL), Yield: 40 mg (31  $\mu\text{mol}$ , 86 %).

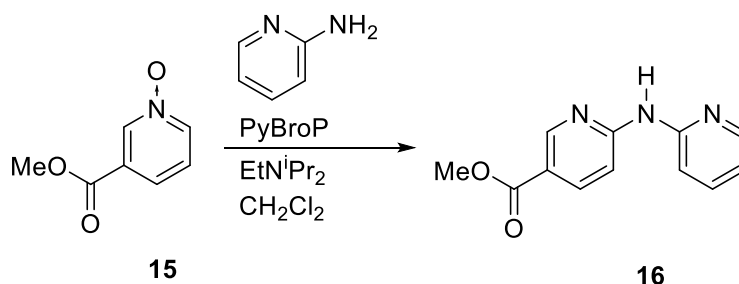
#### 3-Tb:

$\text{Na}_3[\text{Tb}(\text{dpa})_3] \cdot 6 \text{H}_2\text{O}$  (30 mg, 36  $\mu\text{mol}$ ) and  $[\text{Cr}(\text{ddpd})_2]\text{Cl}_3$  (27 mg, 36  $\mu\text{mol}$ ) in  $\text{H}_2\text{O}$  (2 mL), Yield: 37 mg (29  $\mu\text{mol}$ , 81 %).

For crystallographic data for **3-Nd**, **3-Eu** and **3-Tb** see section 10.4 tab. A4.

## 8.4 Synthesis of L1

### Methyl 6-(pyridin-2-ylamino)nicotinate **16**



The reaction was performed in analogy to the literature procedure by Wei.<sup>[159]</sup> Under an argon atmosphere 2-aminopyridine (2.5 g, 26 mmol, 1.0 eq.) was dissolved in dry CH<sub>2</sub>Cl<sub>2</sub> (30 mL) and dry EtN<sup>i</sup>Pr<sub>2</sub> (17.3 mL, 12.8 g, 99 mmol, 3.8 eq.) was added. The solution was stirred at room temperature for 15 min, followed by the addition of methyl nicotinate N-oxide<sup>[171]</sup> (4.0 g, 26 mmol, 1.0 eq) in dry CH<sub>2</sub>Cl<sub>2</sub> (40 mL). PyBroP (15.8 g, 34 mmol, 1.3 eq.) was added and the mixture was stirred at room temperature for 22 h. To the red/orange solution saturated aqueous Na<sub>2</sub>CO<sub>3</sub> (150 mL) was added, the phases were separated and the aqueous phase was extracted with CH<sub>2</sub>Cl<sub>2</sub> (3 × 150 mL). The combined organic phases were washed with saturated aqueous NaCl (100 mL), dried (MgSO<sub>4</sub>), concentrated, and the residue was subjected to column chromatography (SiO<sub>2</sub>, gradient: n-hexane/EtOAc 4:1 → 2:1, detection: UV). After recrystallization from n-hexane/EtOAc 2:1 product **16** was obtained as a colorless solid (2.7 g, 12 mmol 45 %).

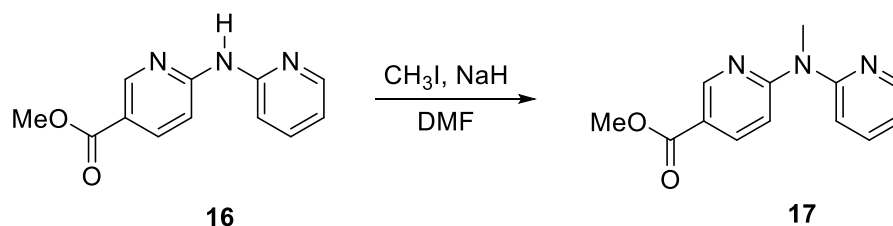
<sup>1</sup>H-NMR (400 MHz, DMSO-d<sub>6</sub>) δ [ppm] = 10.25 (s, 1 H), 8.77 (dd, J = 2.4, 0.7 Hz, 1H), 8.28 (m, 1 H), 8.12 (dd, J = 8.7, 2.4 Hz, 1 H), 7.86 (dd, J = 8.8, 0.7 Hz, 1 H), 7.74-7.70 (m, 2 H), 6.99-6.95 (m, 1 H), 3.83 (s, 3 H).

R<sub>f</sub>: 0.39 (SiO<sub>2</sub>, n-hexane/EtOAc, 2:1, detection: UV).

MS (ESI, pos. mode): m/z (% , assignment) = 229.97 (100, {[M]+H}<sup>+</sup>).

Anal. Calcd. for: C<sub>12</sub>H<sub>11</sub>N<sub>3</sub>O<sub>2</sub>: 62.87 C, 4.84 H, 18.33 N; found: 62.90 C, 4.74 H, 18.58 N.

## Methyl 6-(methyl(pyridin-2-yl)amino)nicotinate **17**



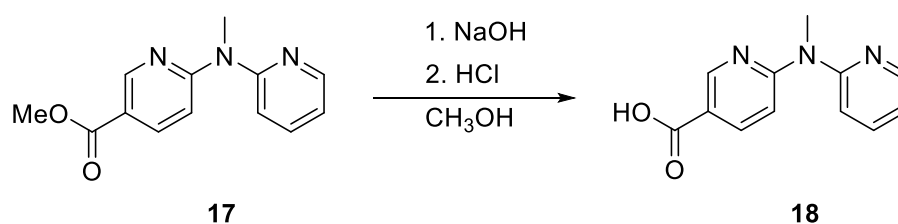
Under an argon atmosphere NaH (60 wt% oil dispersion, 1.0 g, 26 mmol, 3.0 eq.) was added in portions to a slightly yellow solution of **16** (2.0 g, 9 mmol, 1.0 eq.) in dry DMF (60 mL) at 0 °C. The mixture was stirred for 15 min at 0 °C. CH<sub>3</sub>I (1.4 mL, 3.2 g, 22 mmol, 2.5 eq.) was added, the temperature was slowly raised to room temperature and stirring was continued for 20 h. The solvent was evaporated and CH<sub>2</sub>Cl<sub>2</sub> (40 mL) was added. Carefully first ice, then water (40 mL) was added under stirring. The mixture was made basic (pH = 9) with saturated aqueous NaHCO<sub>3</sub> and the aqueous phase was extracted with CH<sub>2</sub>Cl<sub>2</sub> (5 x 60 mL). The combined organic phases were dried (MgSO<sub>4</sub>) and concentrated under reduced pressure. The residue was subjected to column chromatography (SiO<sub>2</sub>, n-hexane/EtOAc, 2:1, detection: UV) to obtain the product **17** as a pale-yellow oil (1.6 g, 6.8 mmol 78 %).

<sup>1</sup>H-NMR (400 MHz, DMSO-d<sub>6</sub>) δ [ppm] = 8.77 (dd, J = 2.4, 0.8 Hz, 1 H), 8.43 (ddd, J = 4.9, 2.1, 1.0 Hz, 1 H), 8.01 (dd, J = 9.1, 2.4 Hz, 1 H), 7.85-7.80 (m, 1 H), 7.44-7.41 (m, 1 H), 7.16 (ddd, J = 7.4, 4.8, 1.0 Hz, 1 H), 7.11 (dd, J = 9.0, 0.8 Hz, 1 H), 3.82 (s, 3 H), 3.55 (s, 3 H).

R<sub>f</sub>: 0.32 (SiO<sub>2</sub>, n-hexane/EtOAc, 2:1, detection: UV).

MS (ESI, pos. mode): m/z (% , assignment) = 244.03 (100, {[M]+H}<sup>+</sup>).

## 6-(methyl(pyridin-2-yl)amino)nicotinic acid **18**

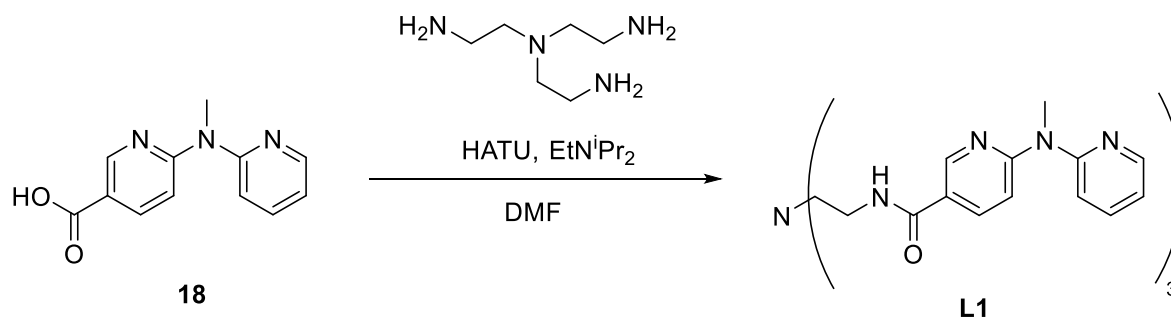


To a solution of **17** (980 mg, 4.0 mmol, 1.0 eq.) in CH<sub>3</sub>OH (60 mL) 1.2 M aqueous NaOH (20 mL, 24 mmol, 6.0 eq.) was slowly added. After complete addition the solution was stirred for 18 h at 50 °C. CH<sub>3</sub>OH was distilled off and aqueous HCl (10 %) was added dropwise till a colorless precipitate was formed. The precipitate was filtered using a Büchner funnel and the filtrate was concentrated resulting in the anew precipitation of the colorless solid. The precipitates were collected and dried under reduced pressure. Product **18** was obtained as a colorless solid (680 mg, 3.0 mmol, 75 %).

<sup>1</sup>H-NMR (400 MHz, DMSO-d<sub>6</sub>) δ [ppm] = 12.78 (s, 1 H), 8.74 (dd, J = 2.4, 0.8 Hz, 1H), 8.42 (ddd, J = 4.9, 2.0, 0.9 Hz, 1 H), 8.01 (dd, J = 9.1, 2.4 Hz, 1 H), 7.84-7.82 (m, 1 H), 7.44-7.40 (m, 1 H), 7.16 (ddd, J = 7.5, 4.1, 0.9 Hz, 1 H), 7.11 (dd, J = 9.0, 0.7 Hz, 1 H), 3.56 (s, 3 H).

MS (ESI, pos. mode): m/z (% , assignment) = 229.98 (100, {[M]+H}<sup>+</sup>).

## L1



Under an argon atmosphere **18** (200 mg, 0.9 mmol, 3.5 eq.) was dissolved in dry and degassed DMF (30 mL). HATU<sup>[160]</sup> (321 mg, 0.8 mmol, 3.4 eq.) and dry EtNIPr<sub>2</sub> (304  $\mu$ L, 1.7 mmol, 7.0 eq.) were sequentially added resulting in a slightly yellow solution. After stirring for 15 minutes at room temperature TREN (37  $\mu$ L, 36 mg, 0.3 mmol, 1.0 eq.) in 2 mL dry and degassed DMF was added dropwise and the solution was stirred for 16 h at room temperature. The volatiles were evaporated and the oily residue was dissolved in CH<sub>2</sub>Cl<sub>2</sub> (50 mL). The mixture was concentrated to about 10 mL and saturated aqueous NaHCO<sub>3</sub> (2 mL) was added slowly until a colorless precipitate began to form. The addition was continued until no additional precipitate was formed and the colorless solid was collected using a Büchner funnel. The organic phase of the filtrate was separated and saturated aqueous NaHCO<sub>3</sub> was added which led to the precipitation of more of the colorless solid. After filtration, the combined precipitates were washed with ice-cold water (10 mL) and CH<sub>2</sub>Cl<sub>2</sub> (10 mL) and dried *in vacuo*. Compound **L1** was obtained as colorless solid (171 mg, 0.3 mmol, 92 %).

<sup>1</sup>H-NMR (400 MHz, DMSO-d<sub>6</sub>)  $\delta$  [ppm] = 8.67 (dd, J = 2.5, 0.7 Hz, 3 H), 8.34 (ddd, J = 4.7, 2.0, 0.7 Hz, 3 H), 8.27 (t, J = 5.4 Hz, 3H), 7.92 (dd, J = 9.0, 2.4 Hz, 3 H), 7.73-7.68 (m, 3 H), 7.33-7.29 (m, 3 H), 7.07-7.03 (m, 6 H), 3.49 (s, 9 H), 3.40-3.33 (m, 6 H), 2.70 (t, J = 6.6 Hz, 6 H).

MS (ESI, pos. mode): m/z (% , assignment) = 390.75 (100, {[M]+2H}<sup>2+</sup>), (40, {[M]+H}<sup>+</sup>).

## 9 Literaturverzeichnis

- [1] N. Armaroli, V. Balzani, *Chem. Asian J.* **2011**, *6*, 768–784.
- [2] C. Förster, K. Heinze, *Chem. Soc. Rev.* **2020**, *49*, 1057–1070.
- [3] X. Huang, S. Han, W. Huang, X. Liu, *Chem. Soc. Rev.* **2013**, *42*, 173–201.
- [4] S. Zhang, X. Yang, Y. Numata, L. Han, *Energy Environ. Sci.* **2013**, *6*, 1443–1464.
- [5] D. M. Arias-Rotondo, J. K. McCusker, *Chem. Soc. Rev.* **2016**, *45*, 5803–5820.
- [6] L. Marzo, S. K. Pagire, O. Reiser, B. König, *Angew. Chem. Int. Ed.* **2018**, *57*, 10034–10072.
- [7] C. B. Larsen, O. S. Wenger, *Chem. Eur. J.* **2017**, *23*, 1–21.
- [8] C. Bizzarri, E. Spuling, D. M. Knoll, D. Volz, S. Bräse, *Coord. Chem. Rev.* **2018**, *373*, 49–82.
- [9] H. Yersin, A. F. Rausch, R. Czerwieńiec, T. Hofbeck, T. Fischer, *Coord. Chem. Rev.* **2011**, *255*, 2622–2652.
- [10] H. Xu, R. Chen, Q. Sun, W. Lai, Q. Su, W. Huang, X. Liu, *Chem. Soc. Rev.* **2014**, *43*, 3259–3302.
- [11] "<https://www.weltderphysik.de/gebiet/erde/news/2021/wie-viel-kohlenstoff-enthaelt-der-erdkern/>" Zuletzt abgerufen am 16.12.2021.
- [12] A. F. Hollemann, N. Wiberg, *Lehrbuch Der Anorganische Chemie*, Walter De Gruyter, Berlin, **2007**.
- [13] R. M. Izatt, S. R. Izatt, R. L. Bruening, N. E. Izatt, B. A. Moyer, *Chem. Soc. Rev.* **2014**, *43*, 2451–2475.
- [14] O. S. Wenger, *J. Am. Chem. Soc.* **2018**, *140*, 13522–13533.
- [15] J. K. McCusker, *Science* **2019**, *363*, 484–488.
- [16] K. Kuriki, Y. Koike, Y. Okamoto, *Chem. Rev.* **2002**, *102*, 2347–2356.
- [17] H. Q. Ye, Z. Li, Y. Peng, C. C. Wang, T. Y. Li, Y. X. Zheng, A. Sapelkin, G. Adamopoulos, I. Hernández, P. B. Wyatt, W. P. Gillin, *Nat. Mater.* **2014**, *13*, 382–386.
- [18] B. M. van der Ende, L. Aarts, A. Meijerink, *Phys. Chem. Chem. Phys.* **2009**, *11*, 11081–11095.
- [19] M. Ibrahim-Ouali, F. Dumur, *Molecules* **2019**, *24*, 1–39.
- [20] H. Xiang, J. Cheng, X. Ma, X. Zhou, J. J. Chruma, *Chem. Soc. Rev.* **2013**, *42*, 6128–6185.

- [21] F. Auzel, *Chem. Rev.* **2004**, *104*, 139–173.
- [22] F. Wang, X. Liu, *Chem. Soc. Rev.* **2009**, *38*, 976–989.
- [23] M. Haase, H. Schäfer, *Angew. Chem. Int. Ed.* **2011**, *50*, 5808–5829.
- [24] L. Aboshyan-Sorgho, M. Cantuel, S. Petoud, A. Hauser, C. Piguet, *Coord. Chem. Rev.* **2012**, *256*, 1644–1663.
- [25] J. C. G. Bünzli, *J. Lumin.* **2016**, *170*, 866–878.
- [26] Y. Ning, M. Zhu, J. L. Zhang, *Coord. Chem. Rev.* **2019**, *399*, 213028.
- [27] S. V. Eliseeva, J. C. G. Bünzli, *New J. Chem.* **2011**, *35*, 1165–1176.
- [28] M. Schulze, A. Steffen, F. Würthner, *Angew. Chem. Int. Ed.* **2015**, *54*, 1570–1573.
- [29] P. T. Chou, Y. Chi, *Chem. - A Eur. J.* **2007**, *13*, 380–395.
- [30] J.-C. G. Bünzli, *Coord. Chem. Rev.* **2015**, *293–294*, 19–47.
- [31] M. Zhang, W. Zheng, Y. Liu, P. Huang, Z. Gong, J. Wei, Y. Gao, S. Zhou, X. Li, X. Chen, *Angew. Chem. Int. Ed.* **2019**, *58*, 9556–9560.
- [32] R. Englman, J. Jortner, *Mol. Phys.* **1970**, *18*, 145–164.
- [33] V. L. Ermolaev, E. B. Sveshnikova, *Russ. Chem. Rev.* **1994**, *63*, 905–922.
- [34] E. Kreidt, C. Kruck, M. Seitz, *Handbook on the Physics and Chemistry of Rare Earths* **2018**, Elsevier, 35–79.
- [35] S. Otto, M. Grabolle, C. Förster, C. Kreitner, U. Resch-Genger, K. Heinze, *Angew. Chem.* **2015**, *127*, 11735–11739.
- [36] S. Treiling, C. Wang, C. Förster, F. Reichenauer, J. Kalmbach, P. Boden, J. P. Harris, L. M. Carrella, E. Rentschler, U. Resch-Genger, C. Reber, M. Seitz, M. Gerhards, K. Heinze, *Angew. Chem. Int. Ed.* **2019**, *58*, 2–13.
- [37] C. Wang, S. Otto, M. Dorn, E. Kreidt, J. Lebon, L. Srsan, P. Di Martino-Fumo, M. Gerhards, U. Resch-Genger, M. Seitz, K. Heinze, *Angew. Chem. Int. Ed.* **2018**, *57*, 1112–1116.
- [38] S. Otto, M. Dorn, C. Förster, M. Bauer, M. Seitz, K. Heinze, *Coord. Chem. Rev.* **2018**, *359*, 102–111.
- [39] S. Otto, J. P. Harris, K. Heinze, C. Reber, *Angew. Chem. Int. Ed.* **2018**, *57*, 11069–11073.
- [40] S. Otto, N. Scholz, T. Behnke, U. Resch-Genger, K. Heinze, *Chem. - A Eur. J.* **2017**, *23*, 12131–12135.
- [41] C. Wang, S. Otto, M. Dorn, K. Heinze, U. Resch-Genger, *Anal. Chem.* **2019**, *91*, 2337–2344.



- [42] S. Otto, A. M. Nauth, E. Ermilov, N. Scholz, A. Friedrich, U. Resch-Genger, S. Lochbrunner, T. Opatz, K. Heinze, *ChemPhotoChem* **2017**, *1*, 344–349.
- [43] U. Basu, S. Otto, K. Heinze, G. Gasser, *Eur. J. Inorg. Chem.* **2019**, *2019*, 37–41.
- [44] J. R. Jiménez, B. Doistau, C. M. Cruz, C. Besnard, J. M. Cuerva, A. G. Campaña, C. Piguet, *J. Am. Chem. Soc.* **2019**, *141*, 13244–13252.
- [45] C. Dee, F. Zinna, W. R. Kitzmann, G. Pescitelli, K. Heinze, L. Di Bari, M. Seitz, *Chem. Commun.* **2019**, *55*, 13078–13081.
- [46] C. Reber, H. U. Güdel, *Chem. Phys. Lett.* **1989**, *154*, 425–431.
- [47] K. R. Kittilstved, A. Hauser, *Coord. Chem. Rev.* **2010**, *254*, 2663–2676.
- [48] R. Beaulac, P. L. W. Tregenna-Piggott, A. L. Barra, H. Weihe, D. Luneau, C. Reber, *Inorg. Chem.* **2006**, *45*, 3399–3407.
- [49] P. S. Wagenknecht, P. C. Ford, *Coord. Chem. Rev.* **2011**, *255*, 591–616.
- [50] L. A. Büldt, X. Guo, R. Vogel, A. Prescimone, O. S. Wenger, *J. Am. Chem. Soc.* **2017**, *139*, 985–992.
- [51] P. Herr, C. Kerzig, C. B. Larsen, D. Häussinger, O. S. Wenger, *Nat. Chem.* **2021**, *13*, 956–962.
- [52] L. A. Büldt, C. B. Larsen, O. S. Wenger, *Chem. Eur. J.* **2017**, *23*, 8577–8580.
- [53] Y. S. Wong, M. C. Tang, M. Ng, V. W. W. Yam, *J. Am. Chem. Soc.* **2020**, *142*, 7638–7646.
- [54] P. Chábera, Y. Liu, O. Prakash, E. Thyraug, A. El Nahhas, A. Honarfar, S. Essén, L. A. Fredin, T. C. B. Harlang, K. S. Kjær, K. Handrup, F. Ericson, H. Tatsuno, K. Morgan, J. Schnadt, L. Häggström, T. Ericsson, A. Sobkowiak, S. Lidin, P. Huang, S. Styring, J. Uhlig, J. Bendix, R. Lomoth, V. Sundström, P. Persson, K. Wärnmark, *Nature* **2017**, *543*, 695–699.
- [55] P. Chábera, L. Lindh, N. W. Rosemann, O. Prakash, J. Uhlig, A. Yartsev, K. Wärnmark, V. Sundström, P. Persson, *Coord. Chem. Rev.* **2021**, *426*.
- [56] A. K. Pal, C. Li, G. S. Hanan, E. Zysman-Colman, *Angew. Chem. Int. Ed.* **2018**, *57*, 8027–8031.
- [57] R. Hamze, J. L. Peltier, D. Sylvinson, M. Jung, J. Cardenas, R. Haiges, M. Soleilhavoup, R. Jazzar, P. I. Djurovich, G. Bertrand, M. E. Thompson, *Science* **2019**, *363*, 601–606.
- [58] Y. Tanabe, S. Sugano, *J. Phys. Soc. Jpn.* **1954**, *9*, 753–766.
- [59] Y. Tanabe, S. Sugano, *J. Phys. Soc. Jpn.* **1954**, *9*, 766–779.

- [60] L. A. Büldt, O. S. Wenger, *Chem. Sci.* **2017**, *8*, 7359–7367.
- [61] J. R. Jiménez, B. Doistau, C. M. Cruz, C. Besnard, J. M. Cuerva, A. G. Campaña, C. Piguet, *J. Am. Chem. Soc.* **2019**, *141*, 13244–13252.
- [62] J. Landry-Hum, G. Bussière, C. Daniel, C. Reber, *Inorg. Chem.* **2001**, *40*, 2595–2601.
- [63] B. E. Van Kuiken, A. W. Hahn, D. Maganas, S. DeBeer, *Inorg. Chem.* **2016**, *55*, 11497–11501.
- [64] C. Reber, H. U. Güdel, G. Meyer, T. Schleid, C. A. Daul, *Inorg. Chem.* **1989**, *28*, 3249–3258.
- [65] O. S. Wenger, H. U. Güdel, *Chem. Phys. Lett.* **2002**, *354*, 75–81.
- [66] R. D. Dill, R. I. Portillo, S. G. Shepard, M. P. Shores, A. K. Rappé, N. H. Damrauer, *Inorg. Chem.* **2020**, *59*, 14706–14715.
- [67] M. Dorn, J. Kalmbach, P. Boden, A. Pöpcke, S. Gómez, C. Förster, F. Kuczelinis, L. M. Carrella, L. A. Büldt, N. H. Bings, E. Rentschler, S. Lochbrunner, L. González, M. Gerhards, M. Seitz, K. Heinze, *J. Am. Chem. Soc.* **2020**, *142*, 7947–7955.
- [68] C. Förster, M. Dorn, T. Reuter, S. Otto, G. Davarci, T. Reich, L. Carrella, E. Rentschler, K. Heinze, *Inorganics* **2018**, *6*, 86.
- [69] K. R. Kittilstved, A. Hauser, *J. Lumin.* **2009**, *129*, 1493–1496.
- [70] G. Bussière, R. Beaulac, B. Cardinal-David, C. Reber, *Coord. Chem. Rev.* **2001**, *219–221*, 509–543.
- [71] S. Koseki, N. Matsunaga, T. Asada, M. W. Schmidt, M. S. Gordon, *J. Phys. Chem. A* **2019**, *123*, 2325–2339.
- [72] J. Bendix, M. Brorson, C. E. Schäffer, *Inorg. Chem.* **1993**, *32*, 2838–2849.
- [73] R. E. Watson, M. Blume, *Proc. R. Soc. Lond. A* **1963**, *271*, 565–578.
- [74] J. P. Zobel, T. Knoll, L. González, *Chem. Sci.* **2021**, *12*, 10791–10801.
- [75] M. Dorn, J. Kalmbach, P. Boden, A. Kruse, C. Dab, C. Reber, G. Niedner-Schatteburg, S. Lochbrunner, M. Gerhards, M. Seitz, K. Heinze, *Chem. Sci.* **2021**, *12*, 10780–10790.
- [76] S. Petoud, S. M. Cohen, J. C. G. Bünzli, K. N. Raymond, *J. Am. Chem. Soc.* **2003**, *125*, 13324–13325.
- [77] A. De Bettencourt-Dias, P. S. Barber, S. Bauer, *J. Am. Chem. Soc.* **2012**, *134*, 6987–6994.
- [78] J. Scholten, G. A. Rosser, J. Wahsner, N. Alzakhem, C. Bischof, F. Stog, A.

- Beeby, M. Seitz, *J. Am. Chem. Soc.* **2012**, *134*, 13915–13917.
- [79] C. Doffek, J. Wahsner, E. Kreidt, M. Seitz, *Inorg. Chem.* **2014**, *53*, 3263–3265.
- [80] T. Förster, *Ann. Phys.* **1948**, *437*, 55–75.
- [81] J. V Caspar, E. M. Kober, B. P. Sullivan, T. J. Meyer, *J. Am. Chem. Soc.* **1982**, *104*, 630–632.
- [82] P. M. Morse, *Phys. Rev.* **1929**, *34*, 57–64.
- [83] B. R. Henry, *Acc. Chem. Res.* **1977**, *10*, 207–213.
- [84] M. S. Child, L. Halonen, *Adv. Chem. Phys.* **1984**, *57*, 1–58.
- [85] S. Yanagida, Y. Hasegawa, K. Murakoshi, Y. Wada, N. Nakashima, T. Yamanaka, *Coord. Chem. Rev.* **1998**, *171*, 461–480.
- [86] W. R. Browne, J. G. Vos, *Coord. Chem. Rev.* **2001**, *219–221*, 761–787.
- [87] C. Doffek, N. Alzakhem, C. Bischof, J. Wahsner, T. Güden-Silber, J. Lügger, C. Platas-Iglesias, M. Seitz, *J. Am. Chem. Soc.* **2012**, *134*, 16413–16423.
- [88] J.-Y. Hu, Y. Ning, Y.-S. Meng, J. Zhang, Z.-Y. Wu, S. Gao, J.-L. Zhang, *Chem. Sci.* **2017**, *8*, 2702–2709.
- [89] C. Doffek, M. Seitz, *Angew. Chem. Int. Ed.* **2015**, *54*, 9719–9721.
- [90] C. Bischof, J. Wahsner, J. Scholten, S. Trosien, M. Seitz, *J. Am. Chem. Soc.* **2010**, *132*, 14334–14335.
- [91] N. A. P. Kane-Maguire, R. C. Kerr, J. R. Walters, *Inorganica Chim. Acta* **1979**, *33*, 163–165.
- [92] R. Dannöhl-Fickler, H. Kelm, F. Wasgestian, *J. Lumin.* **1975**, *10*, 103–112.
- [93] H. G. Kjaergaard, R. J. Proos, D. M. Turnbull, B. R. Henry, *J. Phys. Chem.* **1996**, *100*, 19273–19279.
- [94] R. J. Proos, B. R. Henry, *J. Phys. Chem. A* **1999**, *103*, 8762–8771.
- [95] G. W. Robinson, R. P. Frosch, *J. Chem. Phys.* **1963**, *38*, 1187–1203.
- [96] E. B. Sveshnikova, V. L. Ermolaev, *Opt. Spectrosc.* **2011**, *111*, 34–50.
- [97] J. W. Pavlik, S. Laohhasurayotin, *J. Heterocycl. Chem.* **2007**, *44*, 1485–1492.
- [98] A. K. Jha, N. Jain, *Chem. Commun.* **2016**, *52*, 1831–1834.
- [99] J.-C. Jung, Y.-J. Jung, O.-S. Park, *Synth. Commun.* **2001**, *31*, 2507–2511.
- [100] R. Bini, P. Foggi, R. G. Della Valle, *J. Phys. Chem.* **1991**, *95*, 3027–3031.
- [101] L. Aboshyan-Sorgho, C. Besnard, P. Pattison, K. R. Kittilstved, A. Aebischer, J. C. G. Bünzli, A. Hauser, C. Piguet, *Angew. Chem. Int. Ed.* **2011**, *50*, 4108–4112.
- [102] A. Santoro, C. Sambigiagio, P. C. McGowan, M. A. Halcrow, *Dalt. Trans.* **2015**,

- 44, 1060–1069.
- [103] M. K. Ahmed, B. R. Henry, *J. Chem. Phys.* **1987**, *87*, 3724–3730.
- [104] J. C. G. Bünzli, *Chem. Rev.* **2010**, *110*, 2729–2755.
- [105] N. Sinha, J. Jiménez, B. Pfund, A. Prescimone, C. Piguet, O. S. Wenger, *Angew. Chem.* **2021**, *133*, 2–9.
- [106] F. Reichenauer, C. Wang, C. Förster, P. Boden, N. Ugur, R. Báez-Cruz, J. Kalmbach, L. M. Carrella, E. Rentschler, C. Ramanan, G. Niedner-Schatteburg, M. Gerhards, M. Seitz, U. Resch-Genger, K. Heinze, *J. Am. Chem. Soc.* **2021**, *143*, 11843–11855.
- [107] J. C. G. Bünzli, C. Piguet, *Chem. Soc. Rev.* **2005**, *34*, 1048–1077.
- [108] J.-C. G. Bünzli, S. V. Eliseeva, *Photophysics of Lanthanoid Coordination Compounds in Comprehensive Inorganic Chemistry II*, Elsevier, **2013**.
- [109] J. F. Joung, M. Han, M. Jeong, S. Park, *Sci. Data* **2020**, *7*, 1–6.
- [110] S. Sato, M. Wada, *Bull. Chem. Soc. Jpn.* **1970**, *43*, 1955–1962.
- [111] M. D. Ward, *Coord. Chem. Rev.* **2010**, *254*, 2634–2642.
- [112] M. D. Ward, *Coord. Chem. Rev.* **2007**, *251*, 1663–1677.
- [113] G. Stokes, *Philos. Trans. R. Soc. London* **1852**, *142*, 463–562.
- [114] A. M. Nonat, L. J. Charbonnière, *Coord. Chem. Rev.* **2020**, *409*, 213192.
- [115] S. Ye, E. H. Song, Q. Y. Zhang, *Adv. Sci.* **2016**, *3*, 16600302.
- [116] J. F. Suyver, A. Aebischer, D. Biner, P. Gerner, J. Grimm, S. Heer, K. W. Krämer, C. Reinhard, H. U. Güdel, *Opt. Mater.* **2005**, *27*, 1111–1130.
- [117] D. R. Gamelin, H. U. Güdel, *Acc. Chem. Res.* **2000**, *33*, 235–242.
- [118] B. Zhou, B. Shi, D. Jin, X. Liu, *Nat. Nanotechnol.* **2015**, *10*, 924–936.
- [119] Y. Il Park, K. T. Lee, Y. D. Suh, T. Hyeon, *Chem. Soc. Rev.* **2015**, *44*, 1302–1317.
- [120] L. Q. Xiong, Z. G. Chen, M. X. Yu, F. Y. Li, C. Liu, C. H. Huang, *Biomaterials* **2009**, *30*, 5592–5600.
- [121] B. Golesorkhi, H. Nozary, A. Fürstenberg, C. Piguet, *Mater. Horizons* **2020**, *7*, 1279–1296.
- [122] L. J. Charbonnière, *Dalt. Trans.* **2018**, *47*, 8566–8570.
- [123] N. Kiseleva, P. Nazari, C. Dee, D. Busko, B. S. Richards, M. Seitz, I. A. Howard, A. Turshatov, *J. Phys. Chem. Lett.* **2020**, *11*, 2477–2481.
- [124] I. Hyppänen, S. Lahtinen, T. Ääritalo, J. Mäkelä, J. Kankare, T. Soukka, *ACS Photonics* **2014**, *1*, 394–397.

- [125] B. Golesorkhi, A. Fürstenberg, H. Nozary, C. Piguet, *Chem. Sci.* **2019**, *10*, 6876–6885.
- [126] T. J. Sorensen, O. A. Blackburn, M. Tropiano, S. Faulkner, *Chem. Phys. Lett.* **2012**, *541*, 16–20.
- [127] O. A. Blackburn, M. Tropiano, T. J. Sorensen, J. Thom, A. Beeby, L. M. Bushby, D. Parker, L. S. Natrajan, S. Faulkner, *Phys. Chem. Chem. Phys.* **2012**, *14*, 13378–13384.
- [128] B. Golesorkhi, H. Nozary, L. Guénée, A. Fürstenberg, C. Piguet, *Angew. Chem. Int. Ed.* **2018**, *57*, 15172–15176.
- [129] A. Nonat, S. Bahamyirou, A. Lecointre, F. Przybilla, Y. Mély, C. Platas-Iglesias, F. Camerel, O. Jeannin, L. J. Charbonnière, *J. Am. Chem. Soc.* **2019**, *141*, 1568–1576.
- [130] T. V. Balashova, A. P. Pushkarev, A. N. Yablonskiy, B. A. Andreev, M. N. Bochkarev, *J. Lumin.* **2017**, *192*, 208–211.
- [131] H. Ye, V. Bogdanov, S. Liu, S. Vajandar, T. Osipowicz, I. Hernández, Q. Xiong, *J. Phys. Chem. Lett.* **2017**, *8*, 5695–5699.
- [132] A. Nonat, C. F. Chan, T. Liu, C. Platas-Iglesias, Z. Liu, W. T. Wong, W. K. Wong, K. L. Wong, L. J. Charbonnière, *Nat. Commun.* **2016**, *7*, 11978.
- [133] N. Souri, P. Tian, C. Platas-Iglesias, K. L. Wong, A. Nonat, L. J. Charbonnière, *J. Am. Chem. Soc.* **2017**, *139*, 1456–1459.
- [134] I. Hernández, N. Pathumakanthar, P. B. Wyatt, W. P. Gillin, *Adv. Mater.* **2010**, *22*, 5356–5360.
- [135] D. Zare, Y. Suffren, H. Nozary, A. Hauser, C. Piguet, *Angew. Chem. Int. Ed.* **2017**, *56*, 14612–14617.
- [136] D. Zare, Y. Suffren, L. Guénée, S. V. Eliseeva, H. Nozary, L. Aboshyan-Sorgho, S. Petoud, A. Hauser, C. Piguet, *Dalt. Trans.* **2015**, *44*, 2529–2540.
- [137] L. Aboshyan-Sorgho, C. Besnard, P. Pattison, K. R. Kittilstved, A. Aebischer, J. C. G. Bünzli, A. Hauser, C. Piguet, *Angew. Chem. Int. Ed.* **2011**, *50*, 4108–4112.
- [138] S. Chorazy, M. Wyczesany, B. Sieklucka, *Molecules* **2017**, *22*, 1902.
- [139] T. Lazarides, G. M. Davies, H. Adams, C. Sabatini, F. Barigelletti, A. Barbieri, S. J. A. Pope, S. Faulkner, M. D. Ward, *Photochem. Photobiol. Sci.* **2007**, *6*, 1152–1157.
- [140] D. Imbert, M. Cantuel, J. C. G. Bünzli, G. Bernardinelli, C. Piguet, *J. Am.*

- Chem. Soc.* **2003**, *125*, 15698–15699.
- [141] P. A. Brayshaw, J. C. Bünzli, P. Froidevaux, J. M. Harrowfield, Y. Kim, A. N. Sobolev, *Inorg. Chem.* **1995**, *34*, 2068–2076.
- [142] S. Heer, M. Wermuth, K. Krämer, H. U. Güdel, *Phys. Rev. B - Condens. Matter Mater. Phys.* **2002**, *65*, 1–10.
- [143] S. Heer, K. Petermann, H. U. Güdel, *J. Lumin.* **2003**, *102–103*, 144–150.
- [144] S. Heer, M. Wermuth, K. Krämer, D. Ehrentraut, H. U. Güdel, *J. Lumin.* **2001**, *94–95*, 337–341.
- [145] S. Heer, M. Wermuth, K. Krämer, H. U. Güdel, *Chem. Phys. Lett.* **2001**, *334*, 293–297.
- [146] H. Dan, N. Ty, T. Tap, D. Le, L. Vinh, D. Zhou, J. Qiu, *Opt. Mater.* **2020**, *100*, 109662.
- [147] D. L. Dexter, *J. Chem. Phys.* **1953**, *21*, 836–850.
- [148] J. Kalmbach, C. Wang, Y. You, C. Förster, H. Schubert, K. Heinze, U. Resch-Genger, M. Seitz, *Angew. Chem. Int. Ed.* **2020**, *59*, 18804–18808.
- [149] T. Sanada, T. Suzuki, T. Yoshida, S. Kaizaki, *Inorg. Chem.* **1998**, *37*, 4712–4717.
- [150] P. A. Brayshaw, J. C. Bünzli, P. Froidevaux, J. M. Harrowfield, Y. Kim, A. N. Sobolev, *Inorg. Chem.* **1995**, *34*, 2068–2076.
- [151] G. F. De Sá, O. L. Malta, C. De Mello Donegá, A. M. Simas, R. L. Longo, P. A. Santa-Cruz, E. F. Da Silva, *Coord. Chem. Rev.* **2000**, *196*, 165–195.
- [152] C. Reinhard, H. U. Güdel, *Inorg. Chem.* **2002**, *41*, 1048–1055.
- [153] G. Kervern, A. D'Aléo, L. Toupet, O. Maury, L. Emsley, G. Pintacuda, *Angew. Chem. Int. Ed.* **2009**, *48*, 3082–3086.
- [154] L. Aboshyan-Sorgho, H. Nozary, A. Aebischer, J. C. G. Bünzli, P. Y. Morgantini, K. R. Kittilstved, A. Hauser, S. V. Eliseeva, S. Petoud, C. Piguet, *J. Am. Chem. Soc.* **2012**, *134*, 12675–12684.
- [155] S. Torelli, D. Imbert, M. Cantuel, G. Bernardinelli, S. Delahaye, A. Hauser, J. C. G. Bünzli, C. Piguet, *Chem. Eur. J.* **2005**, *11*, 3228–3242.
- [156] C. H. Stevens, D. C. Greene, *Bull. Geol. Soc. Am.* **1999**, *111*, 919–933.
- [157] E. B. Sveshnikova, P. A. Shakhverdov, T. A. Shakhverdov, V. E. Lanin, R. U. Safina, B. M. Bolotin, V. L. Ermolaev, *Opt. Spectrosc.* **2003**, *95*, 898–907.
- [158] A. Aebischer, F. Gummy, J. C. G. Bünzli, *Phys. Chem. Chem. Phys.* **2009**, *11*, 1346–1353.

- [159] A. T. Londregan, S. Jennings, L. Wei, *Org. Lett.* **2010**, *12*, 5254–5257.
- [160] C. A. G. N. Montalbetti, V. Falque, *Tetrahedron* **2005**, *61*, 10827–10852.
- [161] J. R. Jiménez, B. Doistau, C. Besnard, C. Piguet, *Chem. Commun.* **2018**, *54*, 13228–13231.
- [162] A. Zhou, S. T. Kleespies, K. M. Van Heuvelen, L. Que, *Chem. Commun.* **2015**, *51*, 14326–14329.
- [163] R. T. Henriques, E. Herdtweck, F. E. Kühn, A. D. Lopes, C. C. Romão, *J. Chem. Soc. Dalt. Trans. Dalt. Trans.* **1998**, 1293–1297.
- [164] *Bruker AXS Inc. Madison, Wisconsin, USA 2007.*
- [165] G. M. Sheldrick, *SADABS, Univ. Göttingen, Ger.* **2008.**
- [166] *Bruker SAINT-V6.28A, Madison, Wisconsin, USA 2001.*
- [167] L. J. Farrugia, *J. Appl. Crystallogr.* **1997**, *30*, 565.
- [168] G. M. Sheldrick, *Acta Crystallogr., Sect. C* **2015**, *71*, 3–8.
- [169] L. J. Farrugia, *J. Appl. Crystallogr.* **1999**, *32*, 837.
- [170] A. Dirvanauskas, R. Galavotti, A. Lunghi, A. Nicolini, F. Roncaglia, F. Totti, A. Cornia, *Dalt. Trans.* **2018**, *47*, 585–595.
- [171] J. D. Vasta, R. T. Raines, *Bioorg. Med. Chem.* **2015**, *23*, 3081–3090.

# 10 Anhang / Appendix

## 10.1 NMR spectra

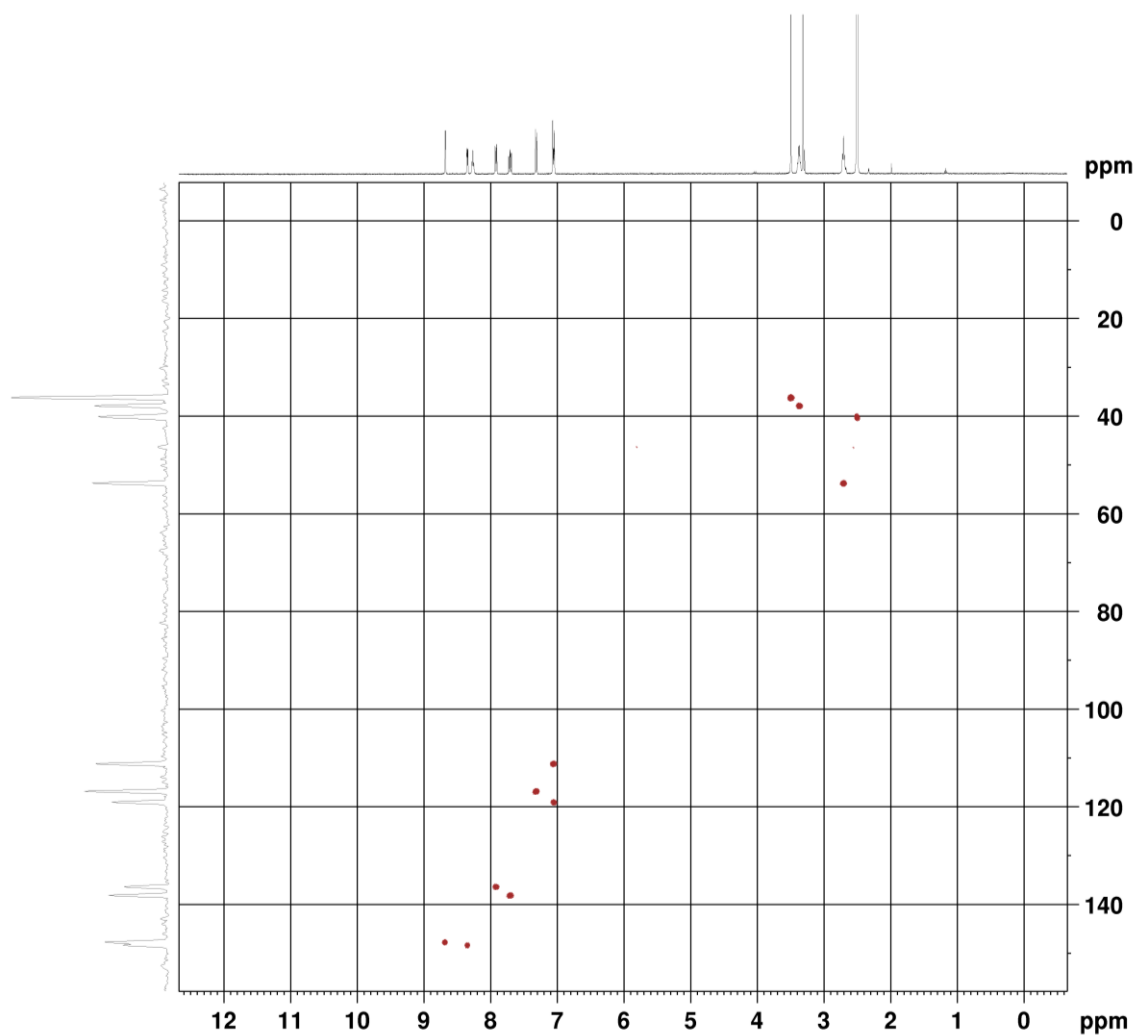


**Fig. A1:**  $^1\text{H}$ - $^{13}\text{C}$  HSQC NMR spectrum ( $^1\text{H}$ : 400 MHz,  $\text{DMSO-d}_6$ ) of L1.



## 10.2 ESI mass spectra

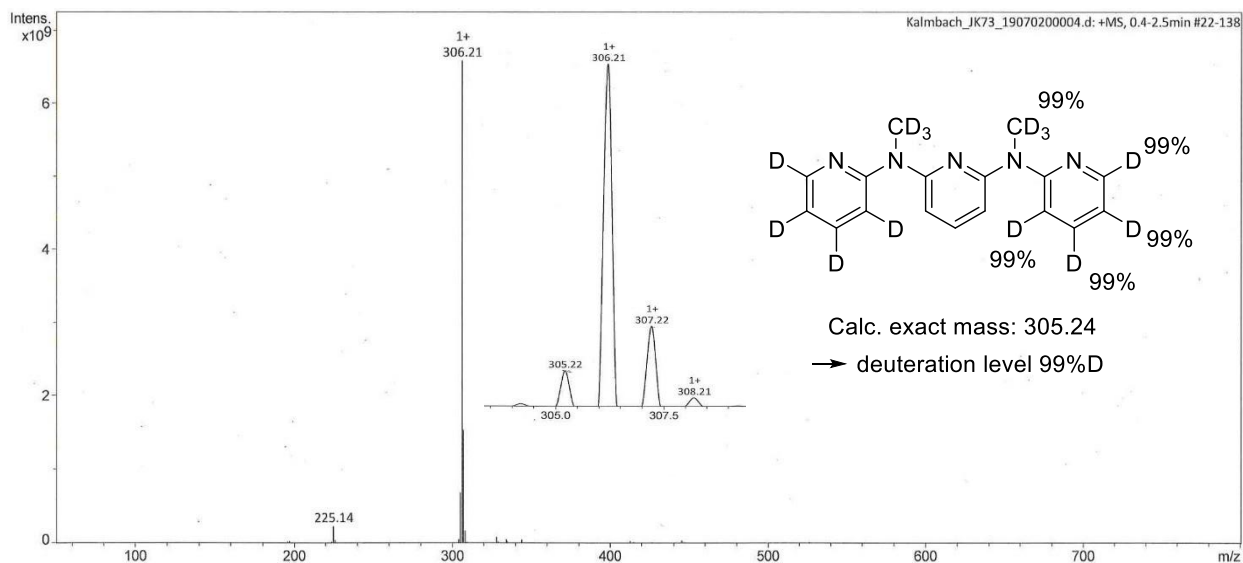


Fig. A2: Mass spectrum (ESI, pos. mode) of  $[D_{14}]$ -ddpd

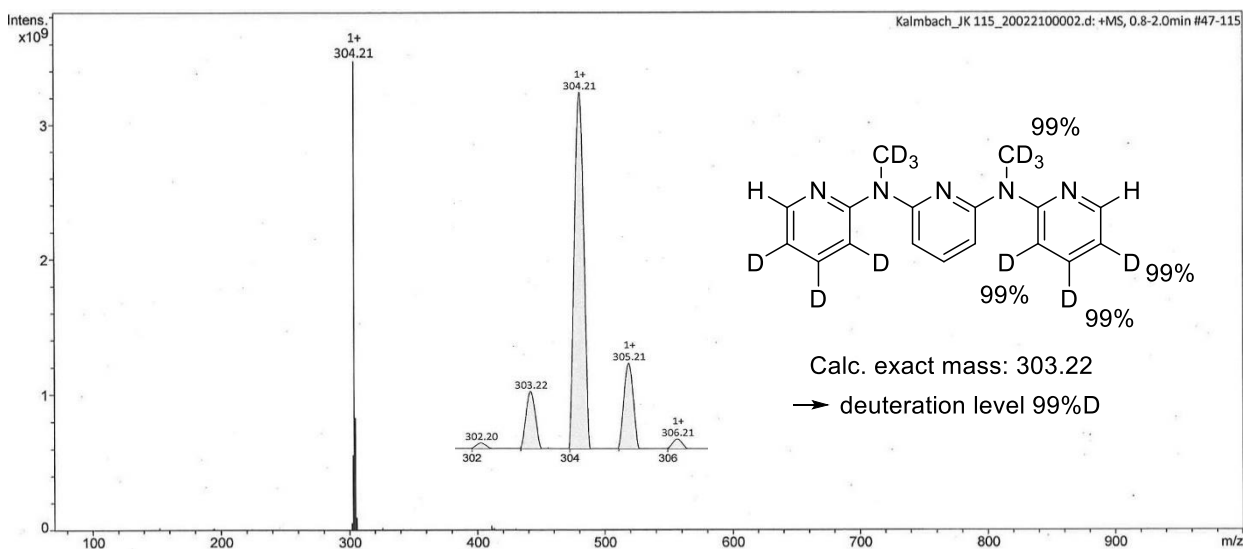
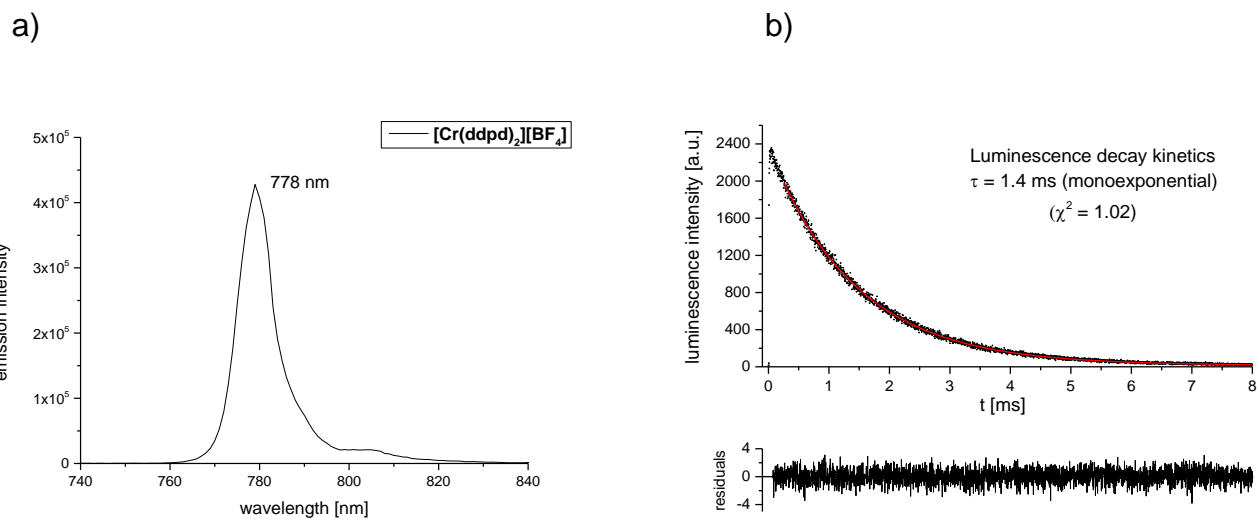


Fig. A3: Mass spectrum (ESI, pos. mode) of  $[6,6''-H_2-D_{12}]$  ddpd.



### 10.3 Luminescence measurements



**Fig. A6:** a) Spectrally corrected emission spectrum and b) luminescence decay profile of  $[\text{Cr}(\text{ddpd})_2][\text{BF}_4]_3$  in n-BuCN at  $T = 77\text{K}$  and under air conditions [ $\lambda_{\text{exc}} = 435$  nm;  $\lambda_{\text{em}} = 778$  nm].

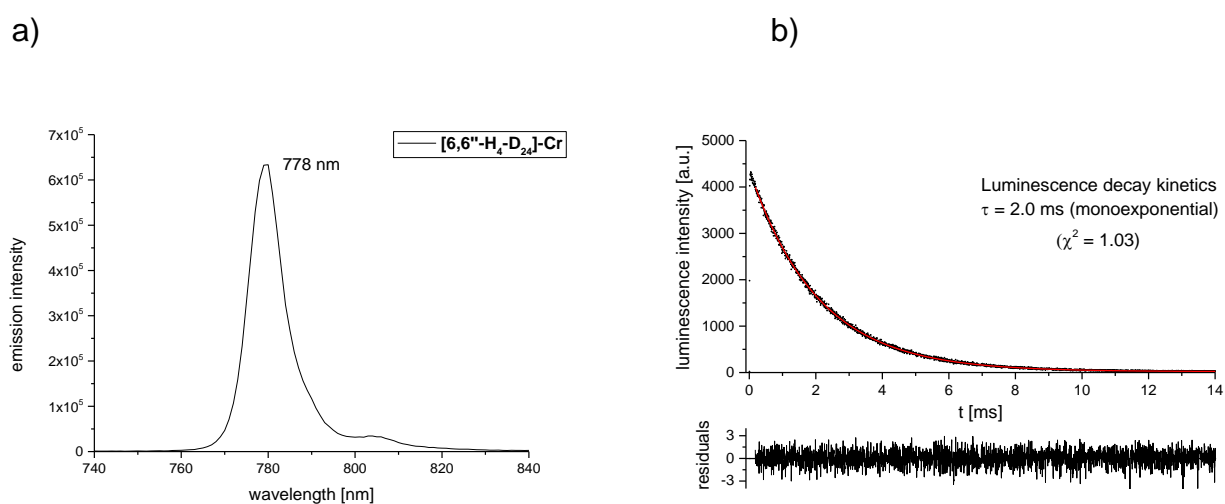


**Fig. A7:** a) Spectrally corrected emission spectrum and b) luminescence decay profile of  $[6,6''\text{-H}_2\text{-D}_{12}]\text{-Cr}$  in n-BuCN at  $T = 77\text{K}$  and under air conditions [ $\lambda_{\text{exc}} = 435$  nm;  $\lambda_{\text{em}} = 778$  nm].

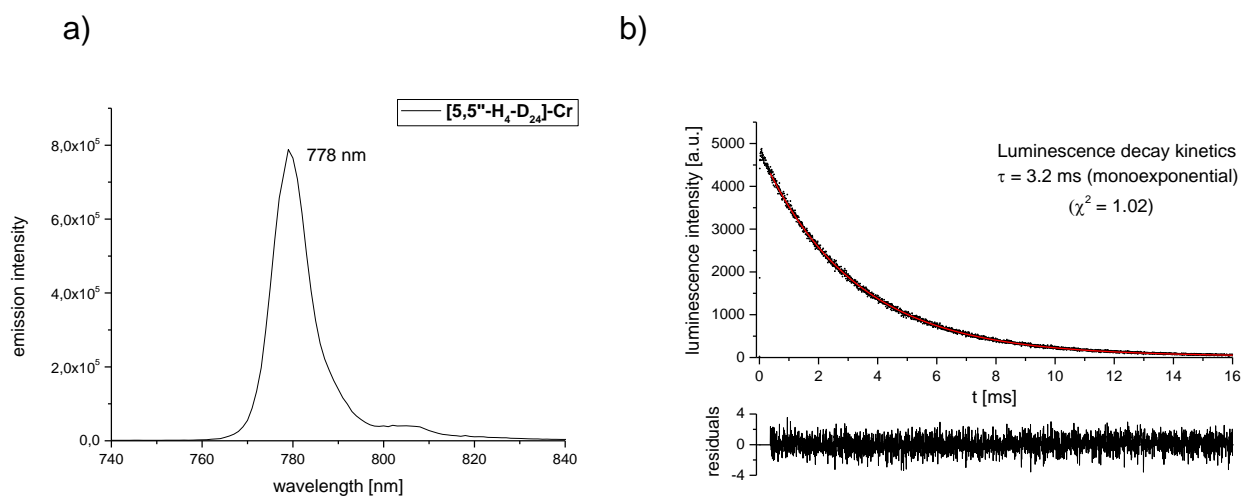


**Fig. A8:** a) Spectrally corrected emission spectrum and b) luminescence decay profile of **[5,5''-H<sub>4</sub>-D<sub>24</sub>]-Cr** in n-BuCN at T = 77K and under air conditions [ $\lambda_{\text{exc}} = 435 \text{ nm}$ ;  $\lambda_{\text{em}} = 778 \text{ nm}$ ].

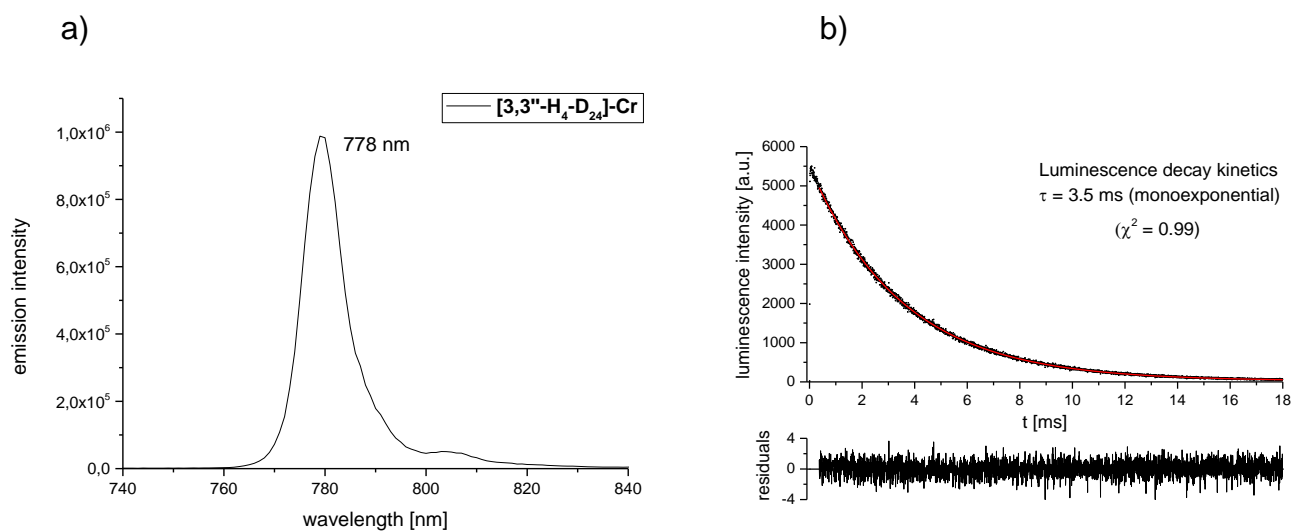


**Fig. A9:** a) Spectrally corrected emission spectrum and b) luminescence decay profile of **[3,3''-H<sub>4</sub>-D<sub>24</sub>]-Cr** in n-BuCN at T = 77K and under air conditions [ $\lambda_{\text{exc}} = 435 \text{ nm}$ ;  $\lambda_{\text{em}} = 778 \text{ nm}$ ].

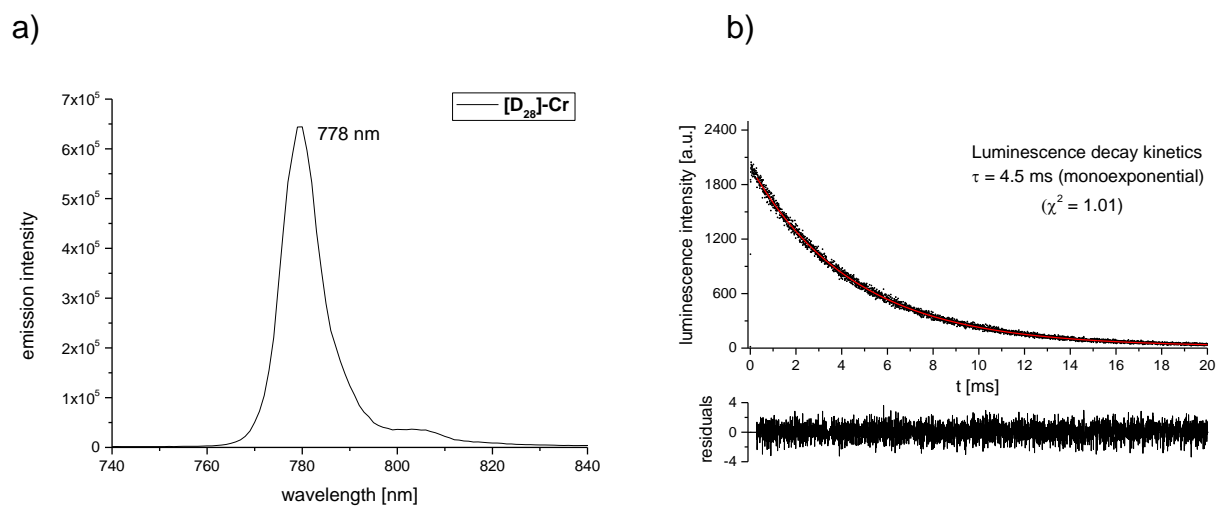


**Fig. A10:** a) Spectrally corrected emission spectrum and b) luminescence decay profile of  $[D_{28}]\text{-Cr}$  in n-BuCN at  $T = 77\text{K}$  and under air conditions [ $\lambda_{\text{exc}} = 435$  nm;  $\lambda_{\text{em}} = 778$  nm].

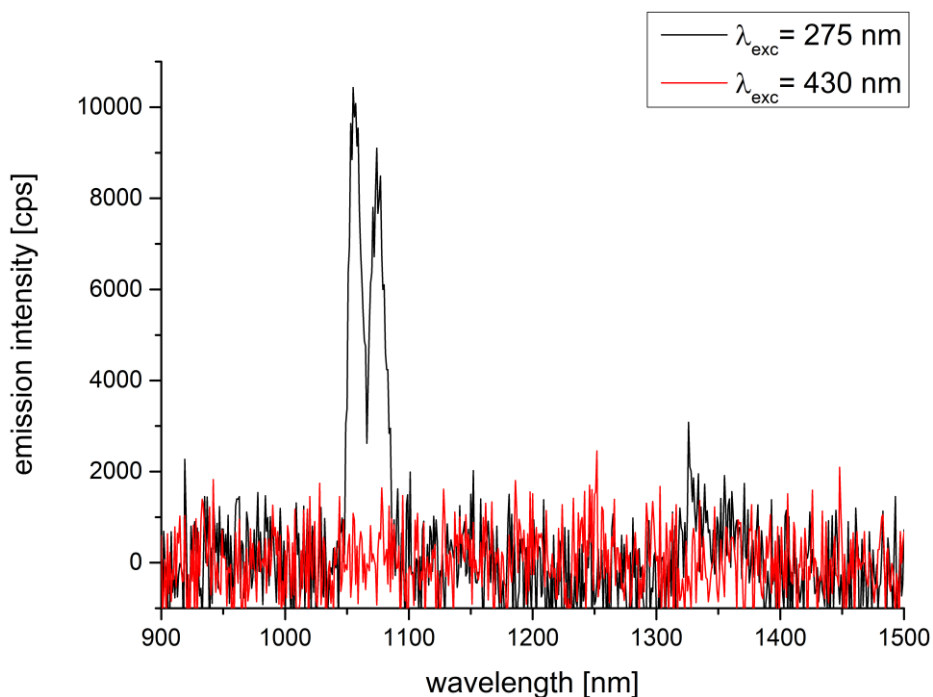


**Fig. A11:** Steady-state emission spectra for **1-Nd** (solid state,  $T = 298$  K, air) after excitation at  $\lambda_{\text{exc}} = 275$  nm (black) and  $\lambda_{\text{exc}} = 430$  nm (red).

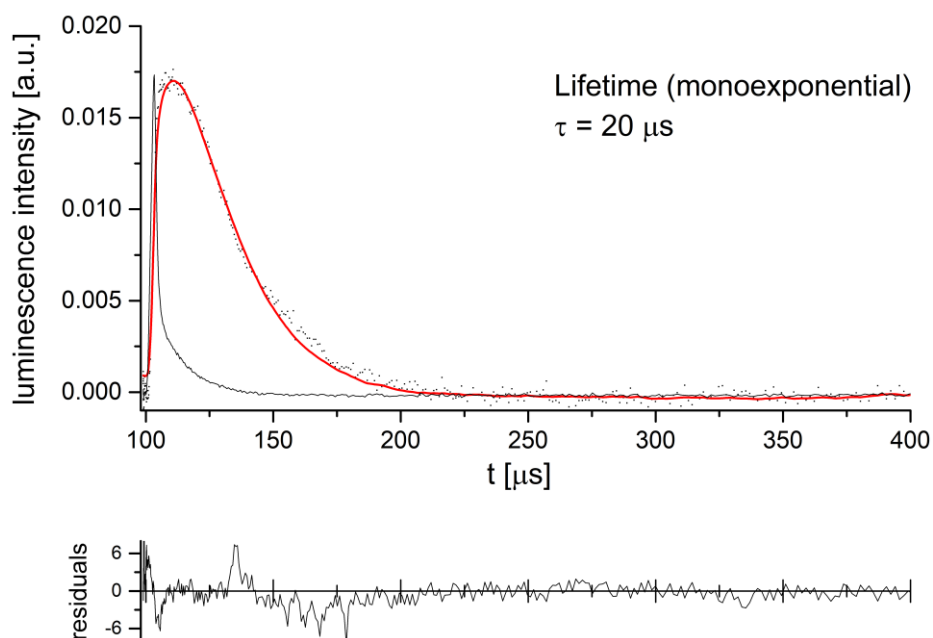


**Fig. A12:** Luminescence decay profile (black scatter plot) for the transition  ${}^2E \rightarrow {}^4A_2$  of  $\text{Cr}^{3+}$  ( $\lambda_{\text{em}} = 774$  nm) in solid **3-Nd** after selective excitation at the  $\text{Cr}^{3+}$  absorption band  ${}^4A_2 \rightarrow {}^4T_2$  ( $\lambda_{\text{exc}} = 430$  nm) at  $T = 298$  K in air. The monoexponential fit (red solid line) was obtained using a single decay component. The residual shown below underlines the suitability of the fit.

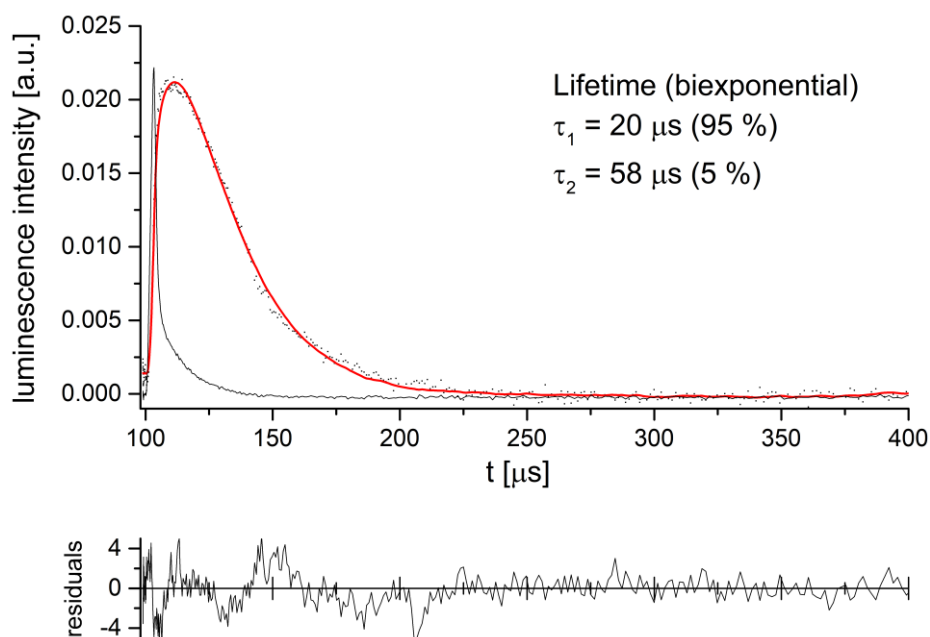


**Fig. A13:** Luminescence decay profile (black scatter plot) for the transition  ${}^4F_{3/2} \rightarrow {}^4I_{11/2}$  of  $\text{Nd}^{3+}$  ( $\lambda_{\text{em}} = 1060 \text{ nm}$ ) in solid **3-Nd** after selective excitation at the  $\text{Cr}^{3+}$  absorption band  ${}^4A_2 \rightarrow {}^4T_2$  ( $\lambda_{\text{exc}} = 430 \text{ nm}$ ) at  $T = 298 \text{ K}$  in air. Biexponential fit (red solid line) two decay time components. The residual shown below underlines the suitability of the fit.

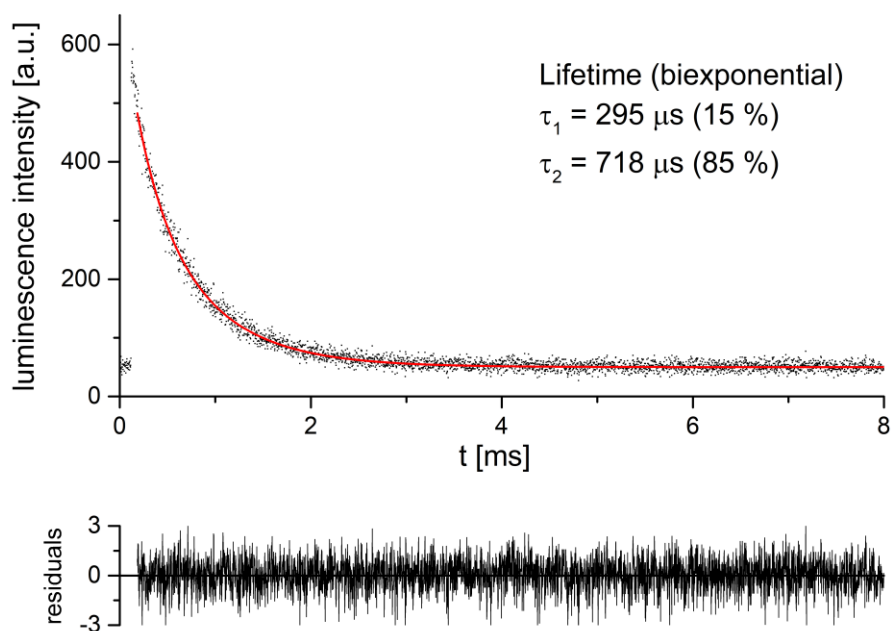


**Fig. A14:** Luminescence decay profile (black scatter plot) for the transition  ${}^2E \rightarrow {}^4A_2$  of  $\text{Cr}^{3+}$  ( $\lambda_{\text{em}} = 774 \text{ nm}$ ) in solid **3-Eu** after selective excitation at the  $\text{Cr}^{3+}$  absorption band  ${}^4A_2 \rightarrow {}^4T_2$  ( $\lambda_{\text{exc}} = 430 \text{ nm}$ ) at  $T = 298 \text{ K}$  in air. The biexponential fit (red solid line) was obtained using two decay components. The residual shown below underlines the suitability of the fit.

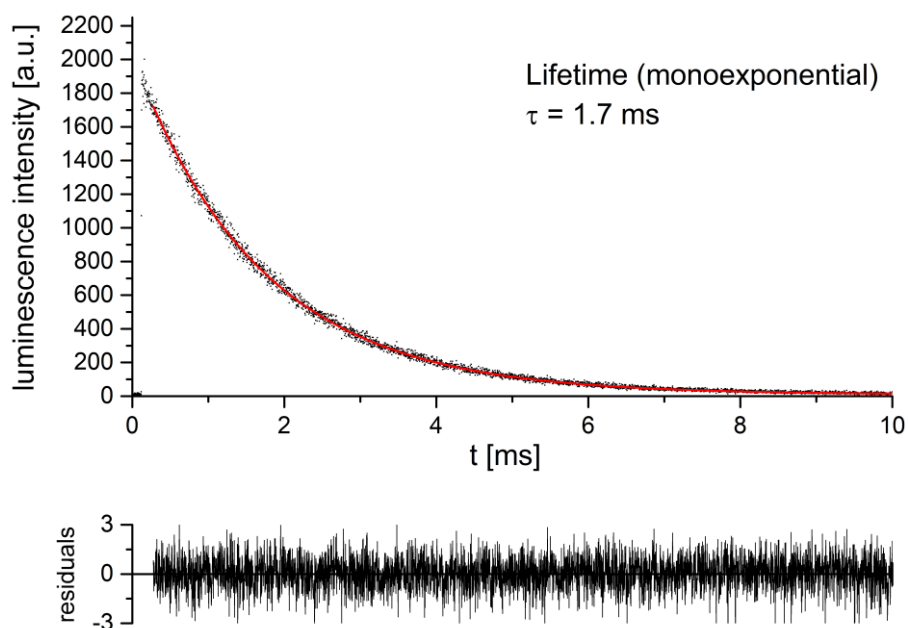


**Fig. A15:** Luminescence decay profile (black scatter plot) for the transition  ${}^5D_0 \rightarrow {}^7F_2$  of  $\text{Eu}^{3+}$  ( $\lambda_{\text{em}} = 545$  nm) in solid **3-Eu** after selective excitation at  $\lambda_{\text{exc}} = 280$  nm at  $T = 298$  K in air. Monoexponential fit (red solid line) one decay time component. The residual shown below underlines the suitability of the fit.

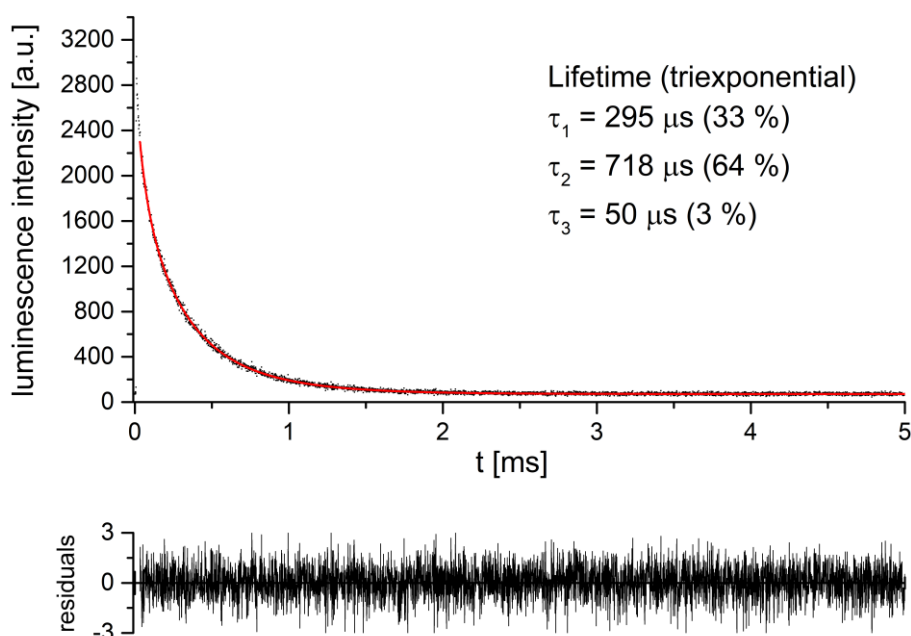


**Fig. A16:** Luminescence decay profile (black scatter plot) for the transition  ${}^2E \rightarrow {}^4A_2$  of  $\text{Cr}^{3+}$  ( $\lambda_{\text{em}} = 774$  nm) in **3-Tb** after selective excitation at the  $\text{Cr}^{3+}$  absorption band  ${}^4A_2 \rightarrow {}^4T_2$  ( $\lambda_{\text{exc}} = 430$  nm) at  $T = 298$  K in air. The triexponential fit (red solid line) was obtained using three decay components. The residual shown below underlines the suitability of the fit.



## 10.4 Near-IR Absorption data

### [D<sub>14</sub>]-ddpd

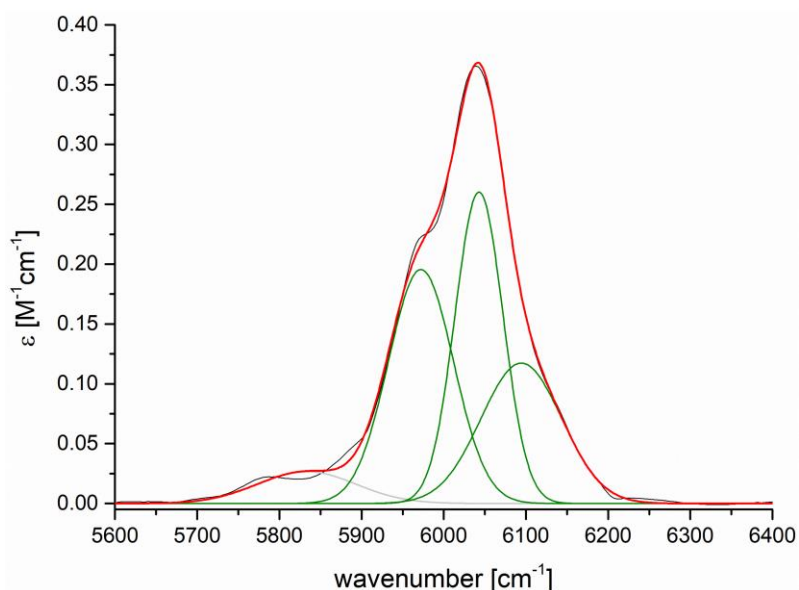


**Fig. A17:** Near-IR absorption spectrum (baseline corrected) of **[D<sub>14</sub>]-ddpd** (solid black) in CDCl<sub>3</sub> (c = 362 mM, d = 1 cm) in the region  $\nu_{\text{C-H}}^2$  with Gaussian fit functions (green: individual Gaussians assigned as aromatic C–H-oscillators; grey: individual Gaussians assigned as non-aromatic C–H-oscillators red: sum of the Gaussians).

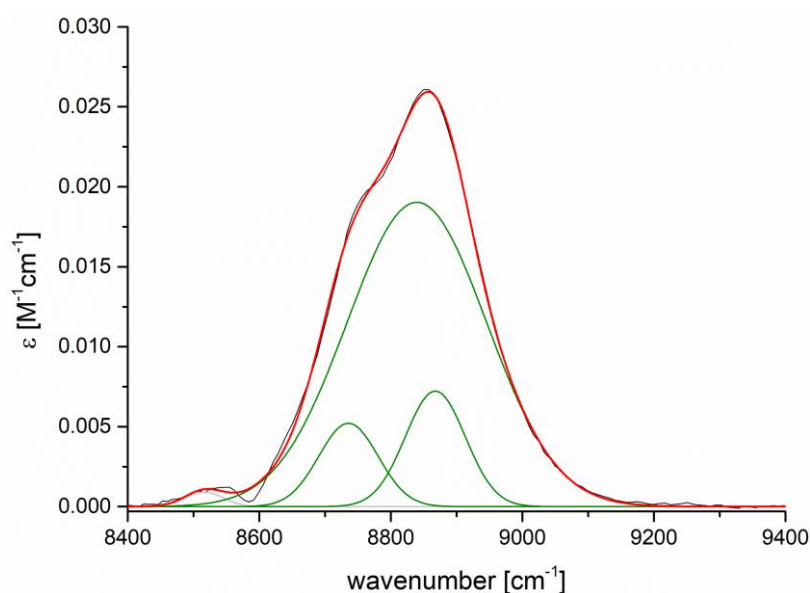


**Fig. A18:** Near-IR absorption spectrum (baseline corrected) of **[D<sub>14</sub>]-ddpd** (solid black) in CDCl<sub>3</sub> (c = 362 mM, d = 5 cm) in the region  $\nu_{\text{C-H}}^3$  with Gaussian fit functions (green: individual Gaussians assigned as aromatic C–H-oscillators; grey: individual Gaussians assigned as non-aromatic C–H-oscillators red: sum of the Gaussians).

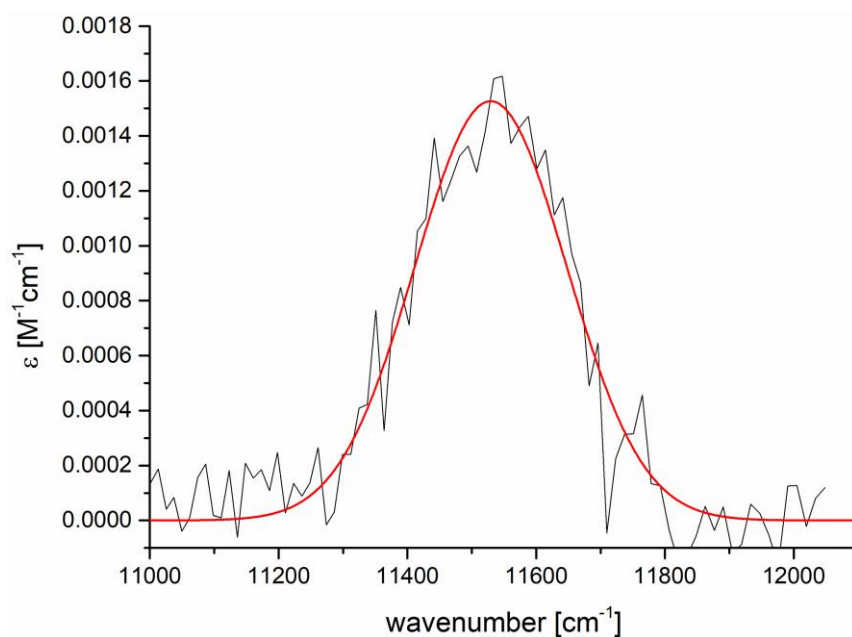


**Fig. A19:** Near-IR absorption spectrum (baseline corrected) of **[D<sub>14</sub>]-ddpd** (solid black) in CDCl<sub>3</sub> (c = 362 mM, d = 5 cm) in the region  $\nu_{\text{C-H}}^4$  with Gaussian fit functions (green: individual Gaussians assigned as aromatic C–H-oscillators; grey: individual Gaussians assigned as non-aromatic C–H-oscillators red: sum of the Gaussians).

**[6,6''-H<sub>2</sub>-D<sub>12</sub>]-ddpd:**

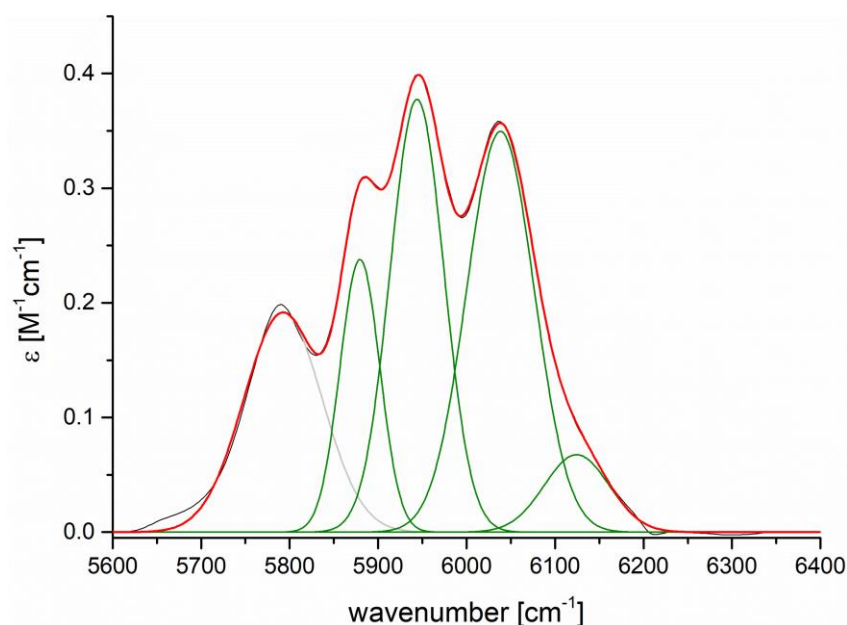


**Fig. A20:** Near-IR absorption spectrum (baseline corrected) of **[6,6''-H<sub>2</sub>-D<sub>12</sub>]-ddpd** (solid black) in CDCl<sub>3</sub> (c = 348 mM, d = 1 cm) in the region  $\nu_{\text{C-H}}^2$  with Gaussian fit functions (green: individual Gaussians assigned as aromatic C–H-oscillators; grey: individual Gaussians assigned as non-aromatic C–H-oscillators red: sum of the Gaussians).

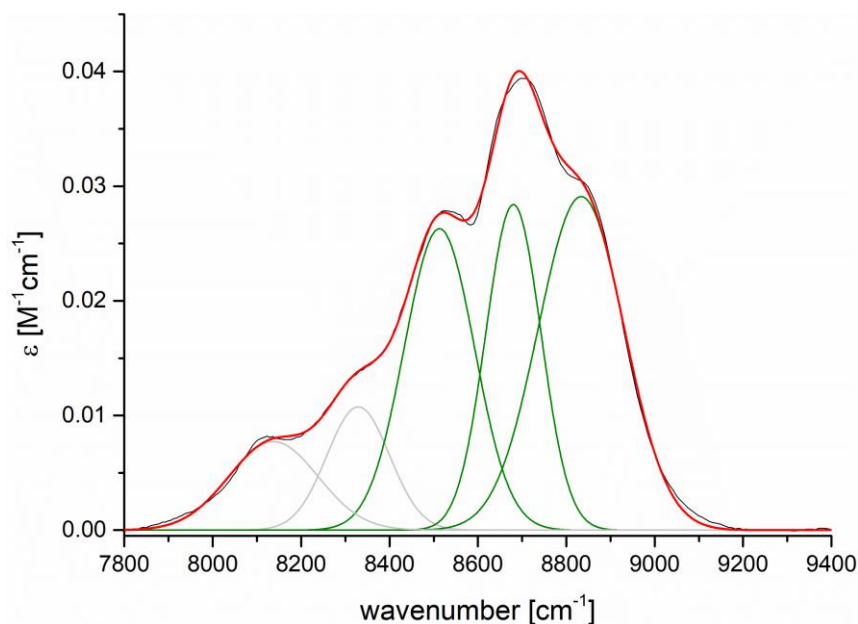


**Fig. A21:** Near-IR absorption spectrum (baseline corrected) of **[6,6''-H<sub>2</sub>-D<sub>12</sub>]-ddpd** (solid black) in CDCl<sub>3</sub> (c = 348 mM, d = 5 cm) in the region  $\nu_{\text{C-H}}^3$  with Gaussian fit functions (green: individual Gaussians assigned as aromatic C–H-oscillators; grey: individual Gaussians assigned as non-aromatic C–H-oscillators red: sum of the Gaussians).

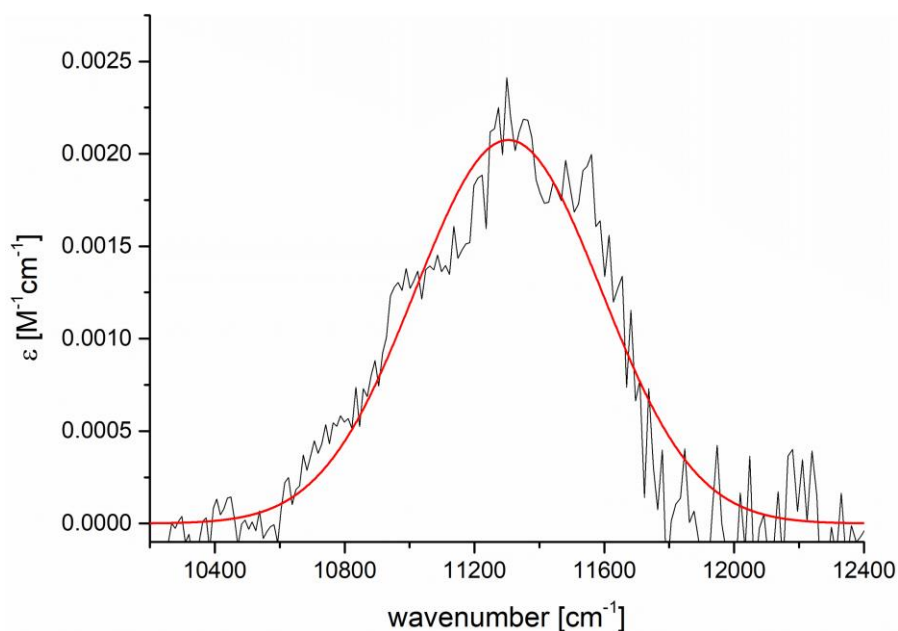


**Fig. A22:** Near-IR absorption spectrum (baseline corrected) of **[6,6''-H<sub>2</sub>-D<sub>12</sub>]-ddpd** (solid black) in CDCl<sub>3</sub> (c = 348 mM, d = 5 cm) in the region  $\nu_{\text{C-H}}^4$  with Gaussian fit functions (green: individual Gaussians assigned as aromatic C–H-oscillators; grey: individual Gaussians assigned as non-aromatic C–H-oscillators red: sum of the Gaussians).

**[5,5''-H<sub>2</sub>-D<sub>12</sub>]-ddpd:**

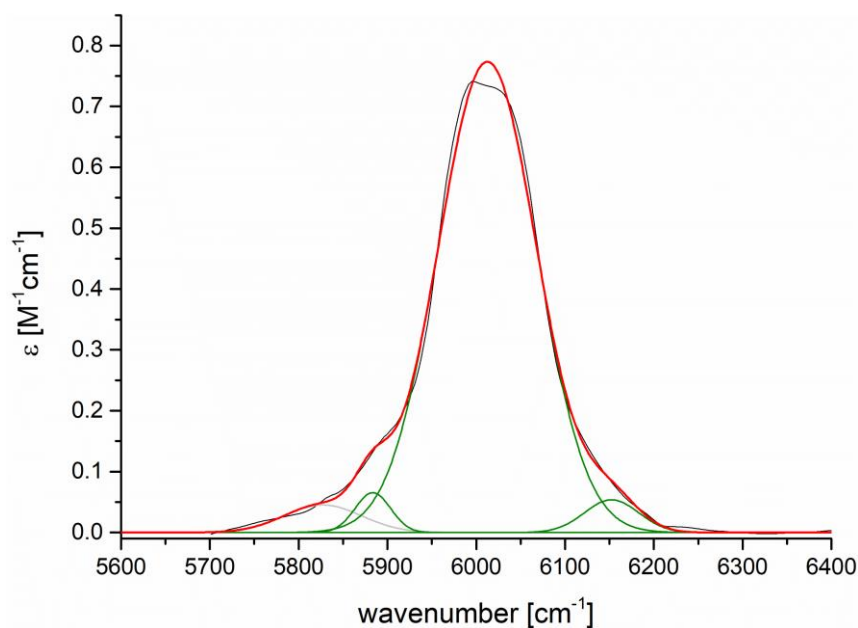


**Fig. A23:** Near-IR absorption spectrum (baseline corrected) of **[5,5''-H<sub>2</sub>-D<sub>12</sub>]-ddpd** (solid black) in CDCl<sub>3</sub> ( $c = 315$  mM,  $d = 1$  cm) in the region  $\nu_{\text{C-H}}^2$  with Gaussian fit functions (green: individual Gaussians assigned as aromatic C–H-oscillators; grey: individual Gaussians assigned as non-aromatic C–H-oscillators red: sum of the Gaussians).

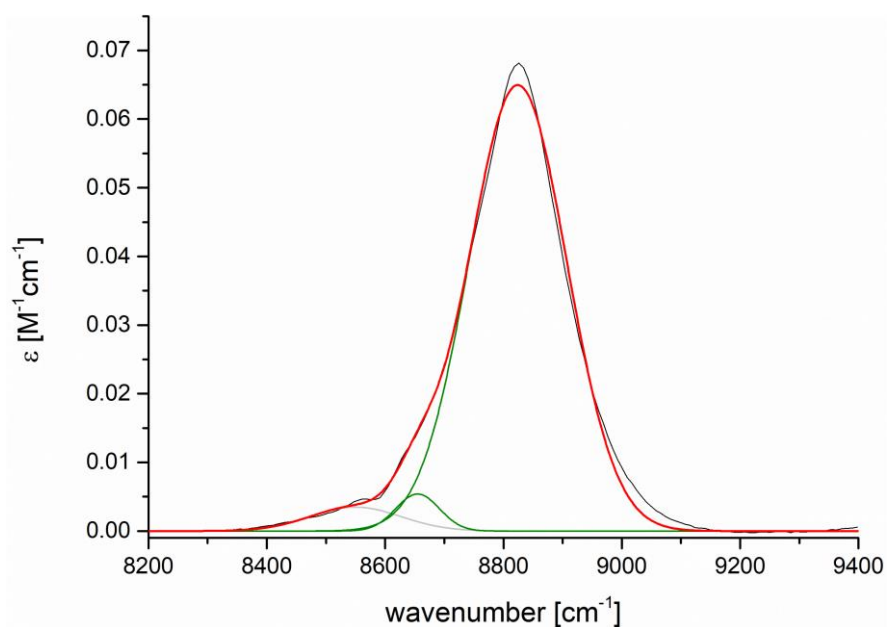


**Fig. A24:** Near-IR absorption spectrum (baseline corrected) of **[5,5''-H<sub>2</sub>-D<sub>12</sub>]-ddpd** (solid black) in CDCl<sub>3</sub> ( $c = 315$  mM,  $d = 5$  cm) in the region  $\nu_{\text{C-H}}^3$  with Gaussian fit functions (green: individual Gaussians assigned as aromatic C–H-oscillators; grey: individual Gaussians assigned as non-aromatic C–H-oscillators red: sum of the Gaussians).

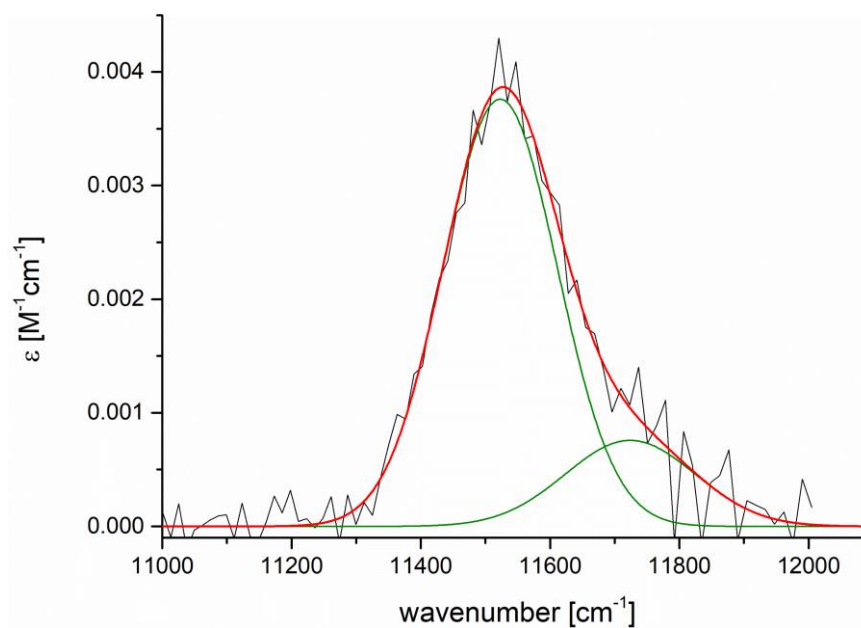


**Fig. A25:** Near-IR absorption spectrum (baseline corrected) of **[5,5''-H<sub>2</sub>-D<sub>12</sub>]-ddpd** (solid black) in CDCl<sub>3</sub> (*c* = 315 mM, *d* = 5 cm) in the region  $\nu_{\text{C-H}}^4$  with Gaussian fit functions (green: individual Gaussians assigned as aromatic C–H-oscillators; grey: individual Gaussians assigned as non-aromatic C–H-oscillators red: sum of the Gaussians).

### Gaussian parameters of C-H<sup>3</sup>, C-H<sup>5</sup> and C-H<sup>6</sup>:

**Tab. A1:** Gaussian parameters ( $x_c$ : center wavenumber;  $\sigma$ : Gaussian width;  $A$ : amplitude) describing the overtones of the aromatic oscillator C-H<sup>3</sup>.

$\nu$	maximum $x_c$ [cm <sup>-1</sup> ]	$\sigma$ [cm <sup>-1</sup> ]	$A$ [M <sup>-1</sup> cm <sup>-1</sup> ]
2 <sup>[a]</sup>	6018.3	68.9	0.2
3 <sup>[a]</sup>	8840.4	108.9	0.018
4 <sup>[a]</sup>	11567.0	122.1	0.0013
5 <sup>[b]</sup>	14159.3	153.2	0.00011

<sup>[a]</sup> Based on Gaussian fits of measured data.

<sup>[b]</sup> Based on extrapolated parameters using the fit relations (Kap. 4.2.1.1, Abb. 30).

**Tab. A2:** Gaussian parameters ( $x_c$ : center wavenumber;  $\sigma$ : Gaussian width;  $A$ : amplitude) describing the overtones of the aromatic oscillator C-H<sup>5</sup>.

$\nu$	maximum $x_c$ [cm <sup>-1</sup> ]	$\sigma$ [cm <sup>-1</sup> ]	$A$ [M <sup>-1</sup> cm <sup>-1</sup> ]
2 <sup>[a]</sup>	6000.9	50.5	0.4
3 <sup>[a]</sup>	8815.8	75.2	0.039
4 <sup>[a]</sup>	11536.7	101.6	0.0022
5 <sup>[b]</sup>	14123.9	126.8	0.00016

<sup>[a]</sup> Based on Gaussian fits of measured data.

<sup>[b]</sup> Based on extrapolated parameters using the fit relations (Kap. 4.2.1.1, Abb. 30).

**Tab. A3:** Gaussian parameters ( $x_c$ : center wavenumber;  $\sigma$ : Gaussian width;  $A$ : amplitude) describing the overtones of the aromatic oscillator C-H<sup>6</sup>.

$\nu$	maximum $x_c$ [cm <sup>-1</sup> ]	$\sigma$ [cm <sup>-1</sup> ]	$A$ [M <sup>-1</sup> cm <sup>-1</sup> ]
2 <sup>[a]</sup>	5910.0	43.8	0.3
3 <sup>[a]</sup>	8601.9	131.9	0.03
4 <sup>[a]</sup>	11181.1	194.9	0.0019
5 <sup>[b]</sup>	13564.1	274.9	0.00017

<sup>[a]</sup> Based on Gaussian fits of measured data.

<sup>[b]</sup> Based on extrapolated parameters using the fit relations (Kap. 4.2.1.1, Abb. 30).

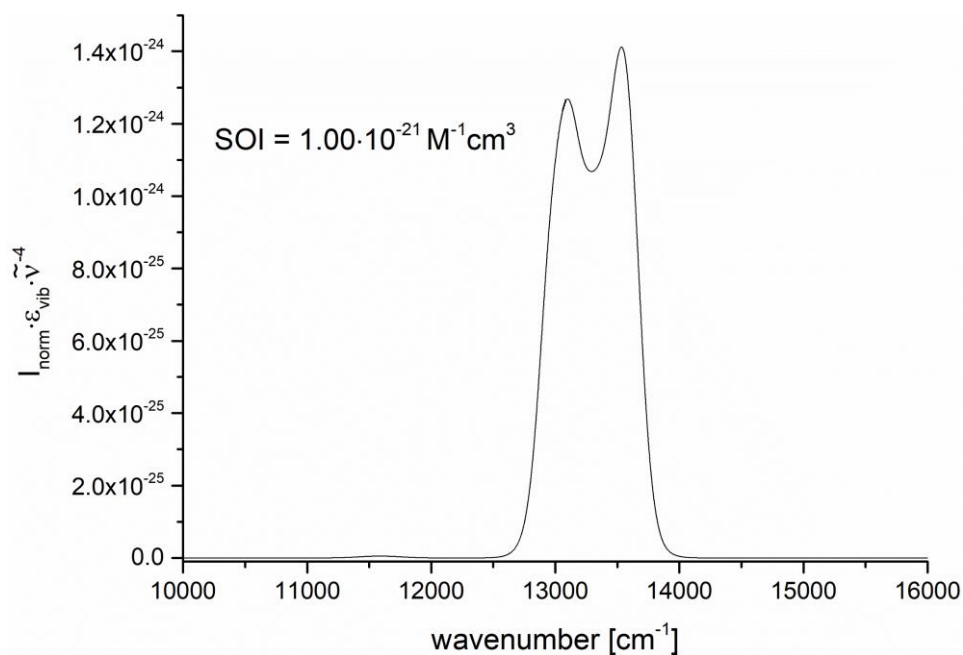


**Fig. A26:** Integrand function of the spectral overlap integral (SOI) for the emission band of  $[\text{Cr}(\text{ddpd})_2]^{3+}$  and the third and fourth overtone ( $\nu_{\text{C-H}}^4$  and  $\nu_{\text{C-H}}^5$ ) of the aromatic C-H oscillator C-H<sup>6</sup>.

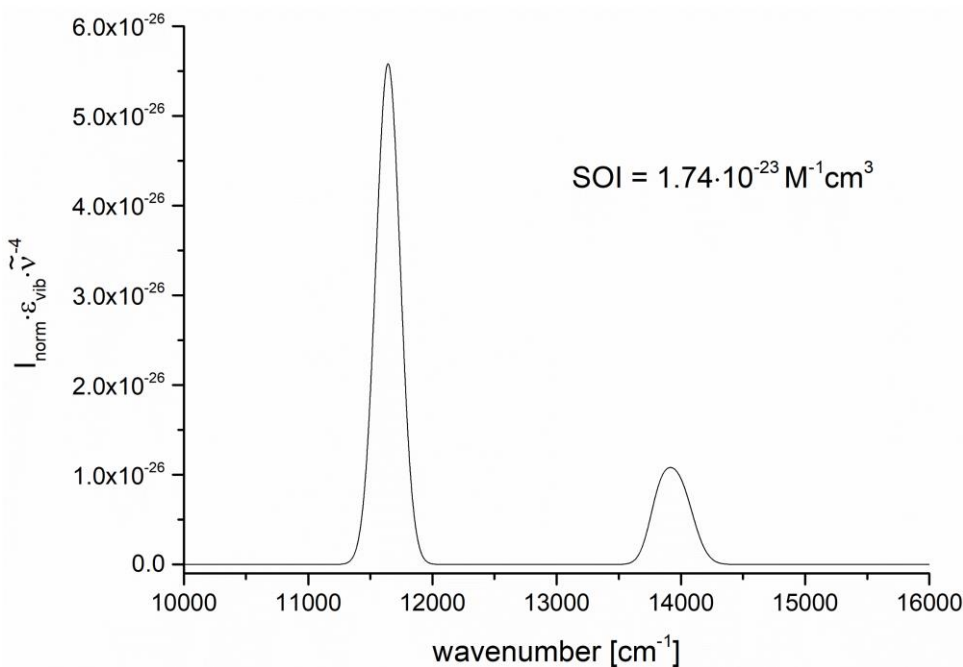


**Fig. A27:** Integrand function of the spectral overlap integral (SOI) for the emission band of  $[\text{Cr}(\text{ddpd})_2]^{3+}$  and the third and fourth overtone ( $\nu_{\text{C-H}}^4$  and  $\nu_{\text{C-H}}^5$ ) of the aromatic C-H oscillator C-H<sup>5</sup>.

## 10.5 X-ray Single Crystal Structure Analysis

**Tab. A4:** Selected crystallographic data for **3-Nd**, **3-Eu** and **3-Tb**.

	<b>3-Nd</b>	<b>3-Eu</b>	<b>3-Tb</b>
Empirical formula	C <sub>55</sub> H <sub>43</sub> CrN <sub>13</sub> NdO <sub>12</sub>	C <sub>55</sub> H <sub>75</sub> CrEuN <sub>13</sub> O <sub>28</sub>	C <sub>55</sub> H <sub>75</sub> CrN <sub>13</sub> O <sub>28</sub> Tb
M <sub>r</sub> [g mol <sup>-1</sup> ]	1274.26	1570.24	1577.21
Crystal appearance	yellow prism	yellow prism	orange prism
T [K]	100(2)	100(2)	100(2)
λ [Å]	0.71073 (Mo K <sub>α</sub> )	0.71073 (Mo K <sub>α</sub> )	0.71073 (Mo K <sub>α</sub> )
Crystal system	triclinic	triclinic	triclinic
Space group	P $\bar{1}$	P $\bar{1}$	P $\bar{1}$
Z	4	2	2
a [Å]	13.3194(3)	13.3002(3)	13.3346(2)
b [Å]	15.2374(3)	15.3640(3)	15.3808(3)
c [Å]	35.3837(7)	17.7457(4)	17.7548(3)
α [°]	99.0170(10)	76.1290(10)	76.0180(10)
β [°]	95.2120(10)	75.8070(10)	75.5820(10)
γ [°]	111.1890(10)	68.9740(10)	68.9400(10)
V [Å <sup>3</sup> ]	6527.61	3234.99	3244.23
D <sub>calc</sub> [g cm <sup>-3</sup> ]	1.297	1.226	1.615
μ [mm <sup>-1</sup> ]	1.016	1.712	1.345
F(000)	2576	1614	1618
Crystal size [mm × mm × mm]	0.31 × 0.26 × 0.25	0.17 × 0.15 × 0.11	0.24 × 0.22 × 0.20
θ range [°]	1.771-27.560	2.46-27.69	2.87-26.37
Limiting indices	-17 ≤ h ≤ 17 -19 ≤ k ≤ 19 -46 ≤ l ≤ 45	-17 ≤ h ≤ 17 -20 ≤ k ≤ 20 -23 ≤ l ≤ 23	-16 ≤ h ≤ 16 -19 ≤ k ≤ 19 -22 ≤ l ≤ 22
Collected refl.	180251	115545	73025
Independent refl.	29879	15281	13218
Absorption corr.	multi-scan	multi-scan	multi-scan
Transm. (max., min.)	0.746, 0.697	0.746, 0.699	0.746, 0.695
Parameters/restraints	1578/716	906/0	977/2
R <sub>1</sub> [I > 2σ(I)] <sup>a</sup>	0.0462	0.0361	0.0778
wR <sub>2</sub> [I > 2σ(I)] <sup>b</sup>	0.1130	0.0893	0.0308
R <sub>1</sub> (all data) <sup>a</sup>	0.0712	0.0429	0.0340
wR <sub>2</sub> (all data) <sup>b</sup>	0.1243	0.0929	0.0811
GOF on F <sup>2</sup>	1.041	1.048	0.788
Δρ <sub>max,min</sub> [e Å <sup>-3</sup> ]	1.345 / -1.203	1.871 / -1.191	1.806 / -0.906

<sup>a</sup>R<sub>1</sub> factor definition:  $R_1 = \sum (||F_o| - |F_c||) / \sum |F_o|$

<sup>b</sup>wR<sub>2</sub> factor definition:  $wR_2 = [\sum w(F_o^2 - F_c^2)^2 / \sum w(F_o^2)]^{1/2}$ . Weighting scheme:  $w = 1 / [\sigma^2(F_o)^2 + (np)^2]$ ,  $p = [F_o^2 + 2 F_c^2] / 3$



**Tab. A5:** Selected crystallographic data for **[D<sub>28</sub>]-Cr** and **[Cr(ddpd)<sub>2</sub>](BF<sub>4</sub>)<sub>3</sub>**.

	<b>[D<sub>28</sub>]-Cr x 3CH<sub>3</sub>CN</b>	<b>[Cr(ddpd)<sub>2</sub>](BF<sub>4</sub>)<sub>3</sub> x 3CH<sub>3</sub>CN<sup>[35]</sup></b>
Empirical formula	C <sub>40</sub> H <sub>43</sub> B <sub>3</sub> CrF <sub>12</sub> N <sub>13</sub>	C <sub>40</sub> H <sub>43</sub> B <sub>3</sub> CrF <sub>12</sub> N <sub>13</sub>
M <sub>r</sub> [g mol <sup>-1</sup> ]	1061.39	1018.30
Crystal appearance	red block	red block
T [K]	100(2)	
λ [Å]	0.71073 (Mo K <sub>α</sub> )	
Crystal system	monoclinic	monoclinic
Space group	<i>Pn</i>	<i>Pn</i>
Z	2	2
a [Å]	11.4744(2)	11.5125(8)
b [Å]	16.4678(3)	16.5554(11)
c [Å]	12.8890(2)	12.9721(9)
α [°]	90	90
β [°]	111.7670(10)	111.890(2)
γ [°]	90	90
V [Å <sup>3</sup> ]	2261.83(7)	2294.2(3)
D <sub>calc</sub> [g cm <sup>-3</sup> ]	1.559	1.474
μ [mm <sup>-1</sup> ]	0.350	0.345
F(000)	1042	1042
Crystal size [mm × mm × mm]	0.28 × 0.27 × 0.25	0.74 × 0.50 × 0.34
θ range [°]	3.203-29.104	2.02 – 27.90
Limiting indices	-15 ≤ h ≤ 15 -22 ≤ k ≤ 22 -17 ≤ l ≤ 17	-14 ≤ h ≤ 15 -21 ≤ k ≤ 21 -17 ≤ l ≤ 17
Collected refl.	77627	27213
Independent refl.	12051	9828
Absorption corr.	multi-scan	
Transm. (max., min.)	0.746, 0.720	0.892, 0.784
Parameters/restraints	629/2	666/22
R <sub>1</sub> [I > 2σ(I)] <sup>a</sup>	0.0274	0.0409
wR <sub>2</sub> [I > 2σ(I)] <sup>b</sup>	0.0717	0.1105
R <sub>1</sub> (all data) <sup>a</sup>	0.0293	0.0439
wR <sub>2</sub> (all data) <sup>b</sup>	0.0727	0.1127
GOF on F <sup>2</sup>	1.045	1.041
Δρ <sub>max,min</sub> [e Å <sup>-3</sup> ]	0.327 / -0.213	0.315 / -0.347

<sup>a</sup> R<sub>1</sub> factor definition:  $R_1 = \sum (|F_o| - |F_c|) / \sum |F_o|$ <sup>b</sup> wR<sub>2</sub> factor definition:  $wR_2 = [\sum w(F_o^2 - F_c^2)^2 / \sum w(F_o^2)]^{1/2}$ . Weighting scheme:  $w = 1 / [\sigma^2(F_o^2) + (np)^2]$ ,  $p = [F_o^2 + 2 F_c^2] / 3$